Advances in Experimental Medicine and Biology 880

Jean-Michel Escoffre
Ayache Bouakaz *Editors*

Therapeutic Ultrasound

Springer

Advances in Experimental Medicine and Biology

Volume 880

Advances in Experimental Medicine and Biology presents multidisciplinary and dynamic findings in the broad fields of experimental medicine and biology. The wide variety in topics it presents offers readers multiple perspectives on a variety of disciplines including neuroscience, microbiology, immunology, biochemistry, biomedical engineering and cancer research.

Advances in Experimental Medicine and Biology has been publishing exceptional works in the field for over 30 years and is indexed in Medline, Scopus, EMBASE, BIOSIS, Biological Abstracts, CSA, Biological Sciences and Living Resources (ASFA-1), and Biological Sciences. The series also provides scientists with up to date information on emerging topics and techniques.

2014 Impact Factor: 1.958

More information about this series at http://www.springer.com/series/5584

Jean-Michel Escoffre • Ayache Bouakaz
Editors

Therapeutic Ultrasound

Volume 880

Springer

Editors
Jean-Michel Escoffre
Inserm U930 “Imagerie et Cerveau”
Université François Rabelais
de Tours - Faculté de Médecine
Tours Cedex 1
France

Ayache Bouakaz
Inserm U930 “Imagerie et Cerveau”
Université François Rabelais
de Tours - Faculté de Médecine
Tours Cedex 1
France

ISSN 0065-2598 ISSN 2214-8019 (electronic)
Advances in Experimental Medicine and Biology
ISBN 978-3-319-22535-7 ISBN 978-3-319-22536-4 (eBook)
DOI 10.1007/978-3-319-22536-4

Library of Congress Control Number: 2015953337

Springer Cham Heidelberg New York Dordrecht London
© Springer International Publishing Switzerland 2016
This work is subject to copyright. All rights are reserved by the Publisher, whether the whole or part of the material is concerned, specifically the rights of translation, reprinting, reuse of illustrations, recitation, broadcasting, reproduction on microfilms or in any other physical way, and transmission or information storage and retrieval, electronic adaptation, computer software, or by similar or dissimilar methodology now known or hereafter developed.
The use of general descriptive names, registered names, trademarks, service marks, etc. in this publication does not imply, even in the absence of a specific statement, that such names are exempt from the relevant protective laws and regulations and therefore free for general use.
The publisher, the authors and the editors are safe to assume that the advice and information in this book are believed to be true and accurate at the date of publication. Neither the publisher nor the authors or the editors give a warranty, express or implied, with respect to the material contained herein or for any errors or omissions that may have been made.

Printed on acid-free paper

Springer International Publishing AG Switzerland is part of Springer Science+Business Media (www.springer.com)

Preface

Besides the well-known and wide use of ultrasound in diagnostics, the therapeutic use of ultrasound has recently emerged. The understanding of the action of ultrasound waves at the cellular level has prompted an increased use of these waves alone or in combination with local activators in several domains. A book on therapeutic ultrasound needs to cover a broad spectrum of techniques and indications, which is quite a challenge. In addition, it should provide an up-to-date review and evidence of treatment efficacy.

All this is presented in three different parts within this book. The first part describes the use of high intensity ultrasound (HIFU) waves to perform tissue ablation: Following a thorough review of the underlying concepts, seven chapters provide detailed reports on different organs of interest. In addition, this part also mentions the synergy between ultrasound and other techniques, such as MRI, for certain indications while others might be achieved with ultrasound techniques exclusively. This underlines the high adaptability of ultrasound to different constraints with respect to the desired objectives. Last but not least, while bone typically represents a barrier for the propagation of ultrasound waves, results obtained in brain applications are absolutely amazing and pave the way for a new method of treating brain diseases.

The second part is based on the existing synergy between ultrasound waves, microbubbles and nanodroplets to exhibit a new therapeutic approach. Here again, after a detailed explanation of underlying mechanisms, even those that are not totally clarified, the following chapters report on the use of this synergy in several domains with a demonstration of efficacy. Conversely to the first part, where clinical trials have clearly demonstrated the high potential of HIFU in several indications, there is less clinical evidence for "sonoporation" to be an invaluable therapeutic improvement, with the exception of sonothrombolysis. However, more and more evidence is now emerging, and no doubt this will be the main challenge for the years to come and might eventually result in a second edition of this book.

The last part of the book deals with further therapeutic applications of ultrasound which do not rely on high intensity focused ultrasound or synergy with microbubbles and nanodroplets. This part illustrates the flexibility of ultrasound which can be used for bone repair or as a new approach for cancer treatment named "sonodynamic therapy".

Altogether, the three parts provide a near-complete overview of the therapeutic potential of ultrasound and offer researchers and clinicians an extensive review on the topic. There is clear evidence of the value of therapeutic

ultrasound in several domains but, this will surely be further substantiated in the coming years based on the clinical evidence of sonoporation and the increased number of clinical results demonstrating a highly positive therapeutic index.

Many thanks to the Editors Jean-Michel Escoffre and Ayache Bouakaz for accepting the challenge of putting together a reference book on this subject, to Jacqueline Butterworth for the English proofreading of the book and to all the authors for their voluntary contribution.

Plan-Les-Ouates, Switzerland François Tranquart, PhD, MD

Contents

Part I

High Intensity Focused Ultrasound Ablation of Pathological Tissue

HIFU Tissue Ablation: Concept and Devices

1

Gail ter Haar

Abstract

High intensity focused ultrasound (HIFU) is rapidly gaining clinical acceptance as a technique capable of providing non-invasive heating and ablation for a wide range of applications. Usually requiring only a single session, treatments are often conducted as day case procedures, with the patient either fully conscious, lightly sedated or under light general anesthesia. HIFU scores over other thermal ablation techniques because of the lack of necessity for the transcutaneous insertion of probes into the target tissue. Sources placed either outside the body (for treatment of tumors or abnormalities of the liver, kidney, breast, uterus, pancreas brain and bone), or in the rectum (for treatment of the prostate), provide rapid heating of a target tissue volume, the highly focused nature of the field leaving tissue in the ultrasound propagation path relatively unaffected. Numerous extra-corporeal, transrectal and interstitial devices have been designed to optimize application-specific treatment delivery for the wide-ranging areas of application that are now being explored with HIFU. Their principle of operation is described here, and an overview of their design principles is given.

Keywords

Ultrasound therapy • Thermal ablation • Cancer • Heating • High Intensity Focused Ultrasound (HIFU) • Ultrasound transducers

G. ter Haar
Joint Department of Physics,
The Institute of Cancer Research,
Sutton, London, UK
e-mail: gail.terhaar@icr.ac.uk

© Springer International Publishing Switzerland 2016

J.-M. Escoffre, A. Bouakaz (eds.), *Therapeutic Ultrasound*, Advances in Experimental Medicine and Biology, Vol. 880, DOI 10.1007/978-3-319-22536-4_1

1.1 Introduction

As the name suggests, High Intensity Focused Ultrasound, HIFU, is the term used to describe the application of focused beams of high power ultrasound for therapeutic benefit. The technique is also sometimes referred to as focused ultrasound surgery, FUS. The common feature of the now many, and varied, HIFU treatments is the need to provide a beam in which the energy is sufficient to produce biological change solely within the focal volume. With few exceptions, the aim is to induce irreversible damage, although in some applications, such as drug delivery, the goal is to produce more transient effects.

1.2 Principles of HIFU

In the frequency range 0.8–5 MHz, the wavelength of ultrasound in tissue is ~2–0.3 mm. This means that small regions of high pressure (intensity) can be created at a distance from the source, in the focal plane. In principle, therefore, if there is sufficient energy in the ultrasound beam travelling through an absorbing medium, it is possible to obtain a biologically significant temperature rise solely in this region, with negligible rises elsewhere.

A common analogy here is that of a magnifying glass used to concentrate the sun's rays, with the purpose of igniting dry kindling. This is only successful when the fuel is placed where the bright spot is at its most intense, that is, in the focal plane of the lens. When the spot is more diffuse, it is not possible to set fire to the kindling, as the fuel is no longer in the focal region. Similarly, when a HIFU focus is placed at depth inside soft tissue, it is possible to raise the temperature at the focus to levels at which thermal necrosis occurs (>56 °C) while leaving the temperatures elsewhere close to their original levels, including those of tissues lying in the beam path overlying the focal volume. Figure 1.1a shows the principle of this technique. The gross appearance of a HIFU lesion (the term used to describe the region of damage induced) can be seen in Fig. 1.1b, while Fig. 1.1c shows a histological section taken at the lesion's edge. The very sharp drop off in temperature is reflected in the sharp demarcation between live and dead cells.

1.3 History of HIFU

Since this use of high intensity focused beams was first proposed in ~1942 (Lynn et al. 1942), it has been explored for a number of different potential medical applications. The aim in the 1940 and 1950s was to destroy regions of the brain selectively, in the quest for a better understanding of neurobehavior (Fry et al. 1954, 1958; Fry 1953; Fry and Fry 1960). These early efforts were hampered not only by the poor quality of the ultrasound images used for targeting, but also by the necessity of removing a portion of the skull to provide an acoustic window for the focused beam into the brain. Despite these limitations, it was possible to destroy pre-determined regions of the brains of experimental animals with good selectivity, and some human treatments of Parkinson's disease were also carried out (Ballantine et al. 1960). The early work achieved 'focusing' by using several plane transducers whose beams all crossed in the same plane. The development of HIFU coincided with the introduction of the drug L-dopa. From a patient's perspective, L-dopa proved to be a more acceptable treatment for Parkinsonism, and from a clinical viewpoint, was easier to administer.

HIFU did not really gain significant clinical acceptance until the 1990s, despite successful ophthalmological treatments before this date. The first proposal to use focused ultrasound in ophthalmology came from Lavine et al. (1952) who demonstrated cataract formation when the lens of the eye was targeted with a focused beam. Other studies demonstrated that HIFU can decrease intra-ocular pressure (Rosenberg and Purnell 1967) and produce lesions in the vitreous, lens, retina and choroid (Coleman et al. 1980, 1985a, b; Lizzi et al. 1978). The first human treatments of glaucoma, undertaken in 1982, gave encouraging results. 79 % of the patient cohort treated had a sustained lowered intra-ocular

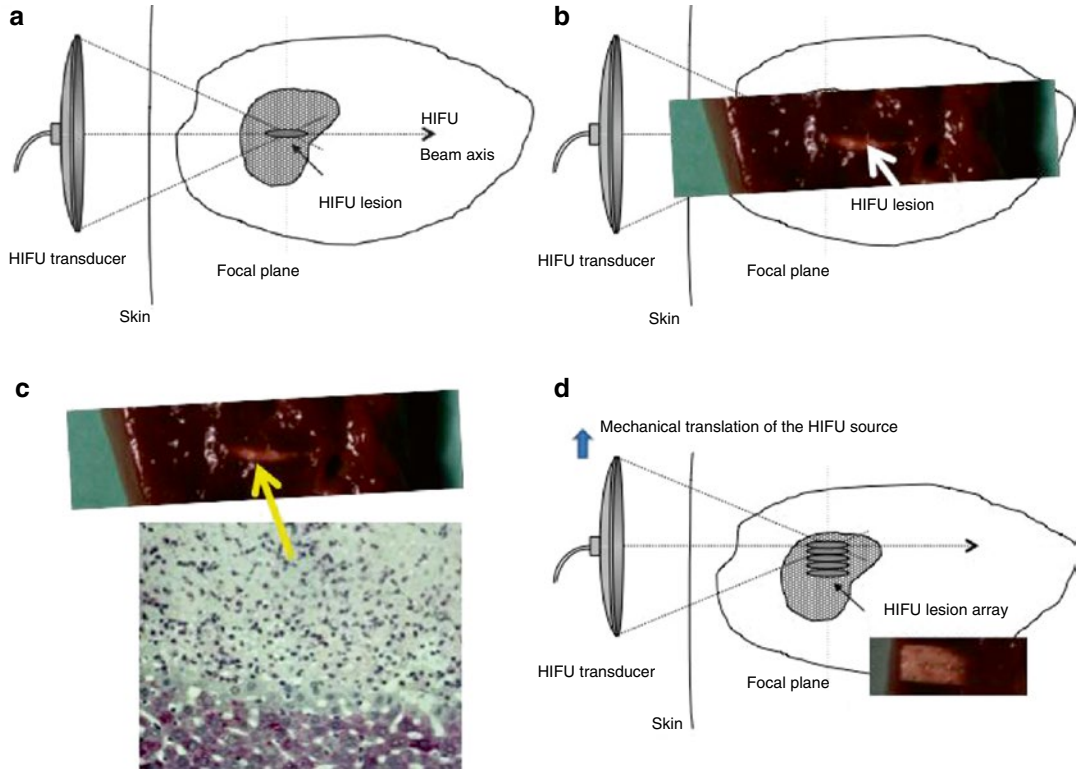

Fig. 1.1 (**a**) Schematic diagram showing the principle of high intensity focused ultrasound (*HIFU*). (**b**) Slice of *ex-vivo* bovine showing a HIFU lesion. (**c**) Histological section showing the sharp demarcation between ablated and unablated cells (Hematoxylin and Eosine staining). (**d**) Schematic diagram showing the formation of confluent regions of ablation

pressure after 1 year (Silverman et al. 1991). Although HIFU showed considerable promise in these, and other, ophthalmological applications, laser surgery has enjoyed wider success and application, presumably because of its apparently simpler technology and application. It is only now that the use of HIFU in the treatment of glaucoma is being revisited, with considerable success (Aptel et al. 2014).

Overview of clinical usage The realization of the full potential of HIFU treatments is only possible now that precise targeting and good treatment follow-up techniques, (with anatomical and functional imaging), are available with modern diagnostic ultrasound scanning and magnetic resonance imaging (MRI) methodologies. The provision of real-time images with excellent spatial resolution and contrast has opened a window of opportunity for HIFU which can only be used to full advantage when the tissue volume to be destroyed can be precisely targeted. Both ultrasound and MRI have been used to guide and monitor HIFU treatments. Each method comes with its advantages and disadvantages. MRI gives anatomical images, and can provide thermometry sequences that allow the tissue temperature to be mapped, thus providing information not only about the success of ablation in the target, but also about the safety of critical regions outside this volume. While ultrasound thermometry has not yet found clinical implementation, this modality offers superior spatial and temporal resolution for imaging. Confirmation of successful ablation under ultrasound guidance relies on the appearance of bright echoes on an ultrasound scan, The ability of HIFU to ablate subcutaneous tissue volumes non-invasively has made it an

attractive potential therapy for deep-seated soft tissue tumors. Malignant tumors of the liver, kidney, breast and pancreas have been successfully targeted (Al-Bataineh et al. 2012; Orsi et al. 2010; Wu et al. 2004, 2005a, b). While ultrasound does not significantly penetrate bone, many osteosarcomas break through the bone cortex, and thus are also good candidates for HIFU treatment (Li et al. 2010; Chen and Zhou 2005). The successful palliation of pain resulting from bone tumors has also been reported, with the treatment here being aimed at destroying the nerves lying on the peri-osteum (Liberman et al. 2009; Hurwitz et al. 2014). Care must be exercised to avoid bowel gas that lies in the propagation path. In some treatment orientations this gas may be successfully displaced by applying pressure from a water balloon placed against the abdomen. HIFU has proved to be an attractive technique for the treatment of uterine fibroids. These may be clearly visualized on either MR or Ultrasound images (Froeling et al. 2013; Hesley et al. 2013; Quinn et al. 2015).

Trans-rectal HIFU treatment of prostate tumors has also been widely investigated. Both benign prostate hyperplasia (BPH) and prostate cancer have been targeted (Crouzet et al. 2015; Thüroff and Chaussy 2015). Initial results from clinical trials for treatment of BPH (Gelet et al. 1993; Sullivan et al. 1997) were encouraging, with increase in flow rate and decreases in post-void residual volume. However, the long-term results of Madersbacher et al. (2000) were disappointing, with 44 % of patients requiring a salvage trans-urethral resection of the prostate (TURP) within 4 years. HIFU has thus not proved to be significantly better than the "gold standard" treatment (TURP). Treatment of cancer in the prostate presents different problems from those associated with the treatment of BPH (Crouzet et al. 2015; Thüroff and Chaussy 2015). Prostate cancer is a multi-focal disease, the foci of which are difficult to detect with diagnostic ultrasound. It is important for its control that all foci are destroyed. Initially HIFU treatments were aimed at ablation of the whole gland (Chaussy et al. 2001; Dickinson et al. 2013). More recently, there has been a move towards partial ablation, with either hemi-ablation, or focal ablations (Crouzet et al. 2014; Baco et al. 2014; Valerio et al. 2014). There is little in the way of conventional therapy to offer patients whose prostate cancer recurs after radiation therapy. High intensity focused ultrasound may be able to fulfill this role as it offers selective tissue destruction without side effect. Early trials for this application have shown encouraging results (Ahmed et al. 2012; Gelet et al. 2004).

1.4 Exposure Dosimetry

In imaging and therapies that use ionizing radiation, a distinction is clearly made between "exposure" and "dose", with exposure for these energy forms being the amount of ionization produced in air by X- or γ-rays. The unit of exposure is the Roentgen, R. Exposure describes the amount of radiation that reaches the body, but does not describe the fraction of that incident energy that is absorbed within tissue. A second parameter is used for this, the "absorbed dose" (commonly referred to as "dose"). Dose characterizes the amount of energy deposited per kilogram and has units of the gray (Gy) and the rad, where 1 rad = 100 Gy. A weighting factor (relative biological effect, RBE) is used in an attempt to compare the biological effects of different forms of ionizing radiation. This leads to a "dose equivalent" parameter, whose units are the rem or Sievert, Sv, (1 rem = 100 Sv). These parameters are related by the equation: Dose equivalent (Sv) = dose (Gy)x RBE. X-rays, γ-rays and ß particles have an RBE of 1.0, whereas α particles have an RBE of 20.

The terms "exposure" and "dose" are used interchangeably in medical ultrasound, although a convincing case for drawing the distinction can be made. Different biological effects result from different modes of ultrasonic energy delivery. For example, two exposures that use the same total acoustic energy over an identical time span, where one is delivered in continuous mode, and the other in short pulses at low repetition rate and high amplitude may result in very different effects in tissue. The first is more likely to induce

thermal effects, while the second may stimulate cavitation activity and its associated characteristic cell damage (ter Haar 2010).

Ultrasound exposures are most usually characterized in terms of the acoustic field determined under "free field conditions" in water. Here, "free field" is taken to describe the conditions in which the ultrasound beam propagates freely, without influence from boundaries or other obstacles. A full description of HIFU exposures requires knowledge of frequency, exposure time, transducer characteristics, total power, acoustic pressure and/or intensity (energy flux in Watts.cm^{-2}) and mode of energy delivery (single shots, scanned exposures, *etc.*) (ter Haar et al. 2011).

In order to make the transition from exposure to dose in an ultrasound field, it is necessary to know the acoustic characteristics of the propagation medium. The parameters of most importance are the attenuation and absorption coefficients, the speed of sound and the nonlinearity parameter B/A. There are large gaps in knowledge about these parameters for both normal and malignant human tissues, although many have been tabulated (Goss et al. 1980; Duck 2013). Generally HIFU exposures are described in terms of free field water measurements, but in some cases, an attempt is made to calculate an *in-situ* intensity by estimating the total attenuation in the beam path. Spatial peak (focal peak) intensities and spatially averaged intensities are also sometimes quoted.

Two dose parameters related solely to thermal effects have been proposed. Sapareto and Dewey (1984) proposed a thermal dose parameter. This has been used extensively to describe hyperthermic cancer treatments. The temperature-time history for a particular tissue volume is integrated and reduced to a biologically equivalent exposure time at 43 °C, t_{43}. This equivalent time is given by the equation:

$$t_{43} = R^{(T-43)}\Delta t \tag{1.1}$$

where R is 0.5 above 43 °C and 0.25 below 42 °C, and T is the average temperature over a time Δt.

This has been shown to be valid up to about 50 °C, but is difficult to validate experimentally for the short times required above this temperature, since very fast heating and cooling rates are required. An alternative parameter related to the heating potential of the HIFU beam is the product of intensity and time (a measure of the total energy), but this concept has not gained widespread acceptance in the therapy ultrasound literature. Clinically, a t_{43} of 240 min is used as the threshold for successful thermal ablation (MacDannold et al. 2006). It is now well accepted that cavitation can enhance the heating in a HIFU field (Holt and Roy 2001; Khokhlova et al. 2006). However, there is, as yet, no validated method of quantifying cavitation activity, nor accepted method for defining "cavitation dose" (Chen et al. 2003; Hwang et al. 2006).

1.5 HIFU Treatment Delivery

The devices used to deliver HIFU clinically are broadly divided into two classes, extra-corporeal and interstitial. The basic components however, do not differ much, comprising as they do, the transducer, a signal generator, amplifier, matching circuitry to maximize the electro-acoustic efficiency, a power meter, and in some cases a method of cooling the transducer. These are connected to an operator console that allows movement and positioning of the source, and also provides a means of monitoring the treatment.

The focusing required for HIFU treatments can be achieved in a number of ways. The simplest is to use a single element transducer: most commonly, either in the form of a planar disc fronted by a lens, or shaped as a spherical bowl. Such transducers are limited in that they can only provide a fixed focus, and if clinically relevant volumes are to be treated, the whole transducer assembly must be physically moved in order to place lesions side by side (Fig. 1.1d). The more common alternative is to use multi-element transducer arrays. Electronic phasing of the signal to individual elements allows both flexibility in shaping the focal volume, and some dynamic control of its position, both axially and transaxially (Gavrilov et al. 2000; Gavrilov and Hand 2000; Daum and Hynynen 1999). The geometry

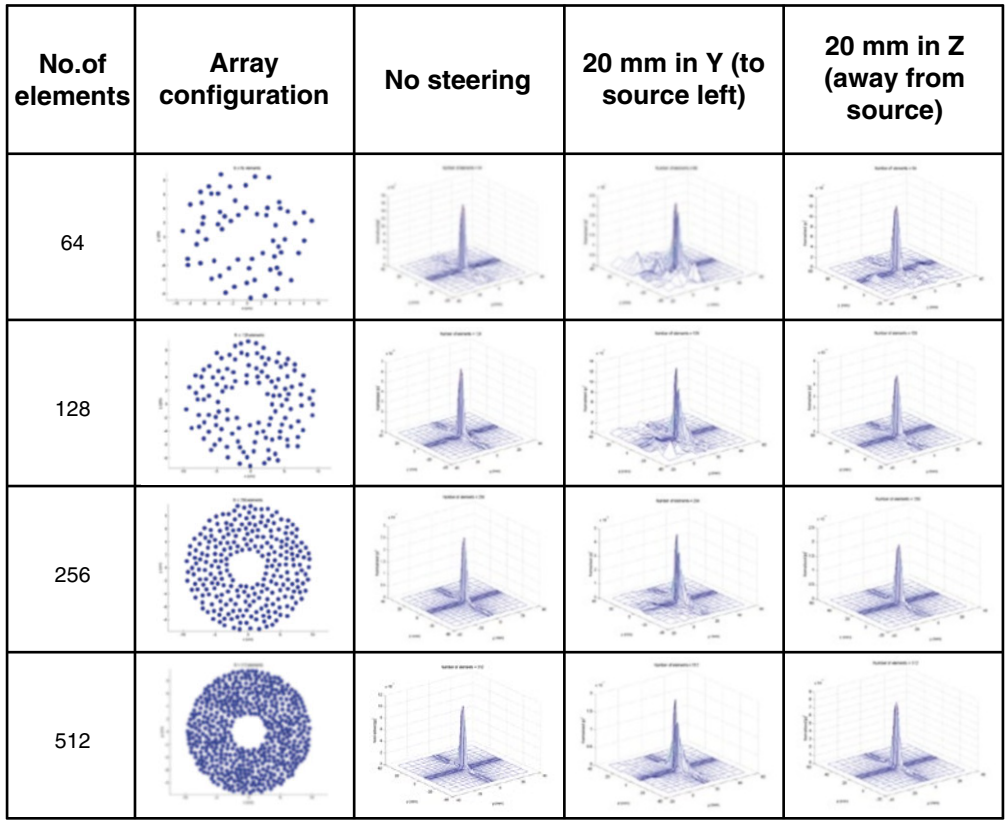

Fig. 1.2 Effect of changing number of elements. 20 cm radius of curvature, 20 cm diameter, 1.7 MHz, 5 cm diameter central aperture

of the elements determines its capabilities. For example, if the array is comprised of concentric elements (an annular array) it is only possible to move the focus electronically to different positions along the beam axis (Hynynen et al. 1996; Dupenloup et al. 1996).

When the individual elements are placed on a spherical shell, focusing is achieved using both the transducer's geometry, and dynamic control of phase and amplitude. For the safe application of HIFU it is important to minimize the grating lobes that can occur when elements are uniformly spaced. These, and other secondary maxima that can be present in the acoustic field, may lead to unwanted local heating in tissue away from the target volume. A number of solutions for reducing grating lobes have been suggested. In the main, these involve destroying the regular periodicity of the element spacing, and introducing randomness and sparsity into their arrangement (Hutchinson et al. 1996; Goss et al. 1996; Gavrilov et al. 1997; Filonenko et al. 2004; Hand et al. 2009). Random arrays typically allow lateral movement in the focal plane by distances of ~10 % of the geometric focal length. Pernot et al. (2003) compared the steering capabilities and appearance of side lobes at a frequency of 0.9 MHz for three sparse array geometries (hexagonal, annular and quasi-random), each with 52 % coverage of the 180 mm diameter, 120 mm geometrical focal length spherical surface on which they were mounted. They showed by simulation that the quasi-random design gave the best beam steering capability while maintaining sufficient peak pressure amplitude. Their results were validated by experiment. In Figs. 1.2, 1.3 and 1.4, field simulations for a 256 element random array are displayed, showing the influence

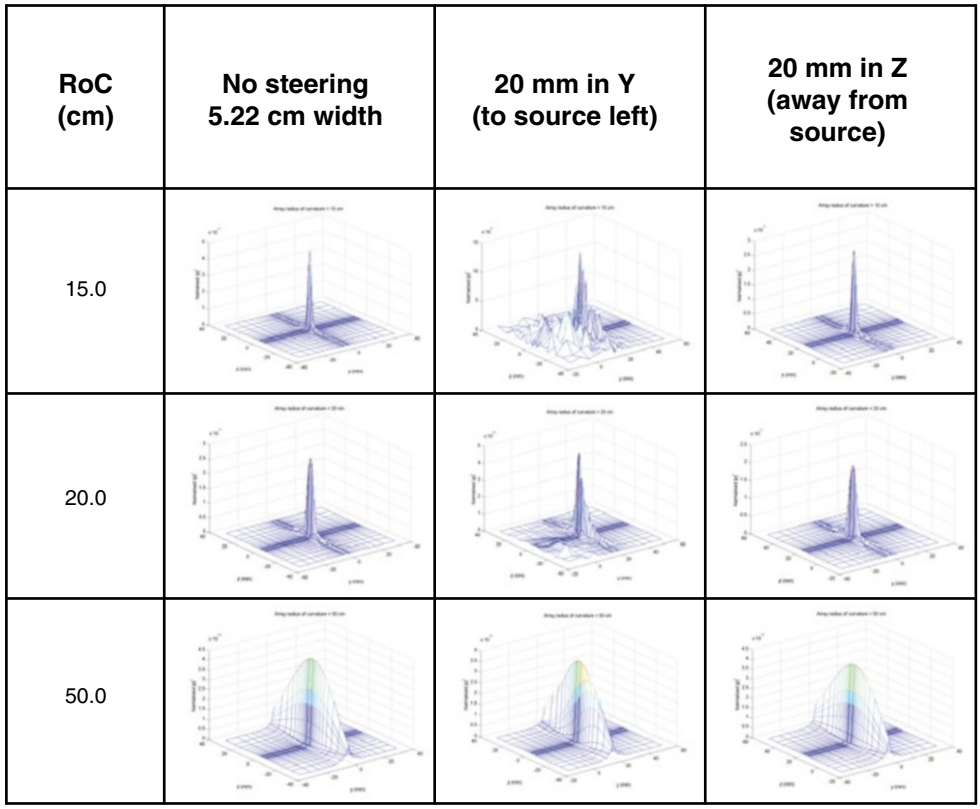

Fig. 1.3 Effect of changing radius of curvature (RoC). 256 elements, 20 cm diameter, 1.7 MHz, 5 cm diameter central aperture

of the beam pattern of the number of array elements (Fig. 1.2), the radius of curvature of the bowl on which they are placed (Fig. 1.3), and the drive frequency (Fig. 1.4).

A disadvantage of the sparse array is that energy is deposited incoherently in the near field (Payne et al. 2011). This leads to a low level of heating that becomes problematic when focal lesions are to be placed side by side (to gain confluent ablation volumes) with their near fields overlapping, since the temperature may rise to biologically significant levels. This is avoided by introducing a cooling time between "shots", but this in turn lengthens the treatment time. In order to reduce these problems, a 500 kHz flat phased array with elements space λ/2 apart has been proposed (Ellens et al. 2015). While this reduces the effects of near field heating, and avoids the problem of grating lobes, this lower frequency (necessary if the λ/2 separation is to be achieved), results in a lower spatial resolution and cavitation threshold, and increases the probability of heating post-focally. At this lower frequency, the ultrasound absorption is reduced, and more acoustic power is required to achieve the desired temperatures than for the 1–3 MHz frequency range that is more commonly used. This illustrates the necessity, common to all designs, of making trade offs and compromises Hill et al. 1994.

It is not possible here to describe in detail the many different transducer geometries available, but Table 1.1 summarizes the many different designs, their steering capabilities, and their advantages and disadvantages.

When tissue targets lie behind the ribcage (such as those in liver, kidney or pancreas) or under the skull, approaches that avoid overheating the bone surface are required if an acoustic window is not to be created by surgical removal of some skull or ribs. For the rib cage, simple ray

Freq. (MHz)	No steering	20 mm in Y (to source left)	20 mm in Z (away from source)
0.50	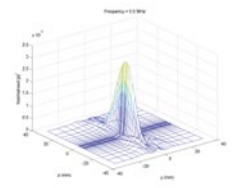	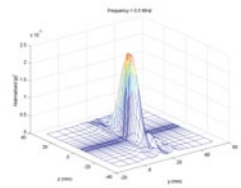	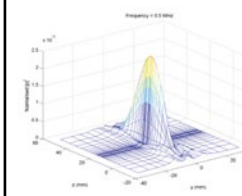
1.00	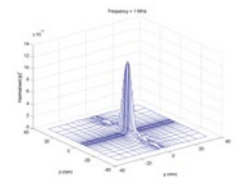	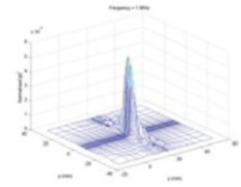	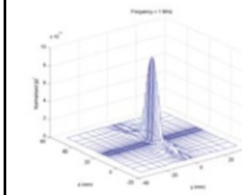
1.50	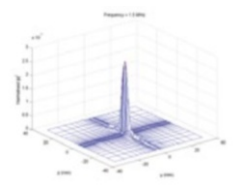	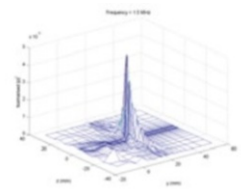	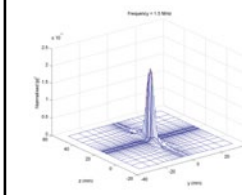
1.75	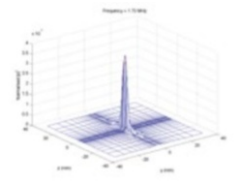	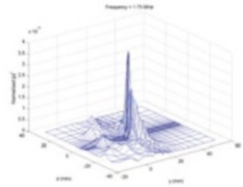	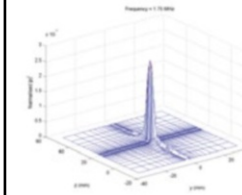
2.00	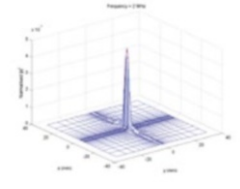	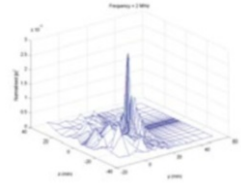	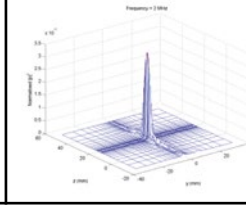

Fig. 1.4 Effect of changing frequency. 256 elements, 20 cm radius of curvature, 20 cm diameter, 5 cm diameter central aperture

tracing may be used to "turn off" elements whose beam impinges on the bone (Civale et al. 2006) or, more sophisticatedly, time reversal or adaptive focusing techniques are used (Pernot et al. 2003; Tanter et al. 1998, 2001; Thomas and Fink 1996; Clement and Hynynen 2002a, b; Aubry et al. 2008). Using these techniques, selective regions lying behind bone can be targeted, and clinically, they have been used successfully in the treatment of essential tremor and other neurological problems (Medel et al. 2012; Martin et al. 2009; Elias et al. 2013). The ultrasound field is severely distorted in amplitude and phase by passage through the skull. Time reversal can correct the phase

Table 1.1 Summary of available transducer geometries, their advantages and disadvantages

Transducer geometry/ composition	Steering capability	Significant grating lobes?	Cover (packing fraction)	Capable of bone sparing	Application	References
Single element Planar + lens Spherical bowl Toroid Cylinder	None, mechanical translational only	No	100 %	No	Abdomen, breast, prostate Abdomen, breast, prostate Liver – intra-operative Ophthalmology – glaucoma	Chan et al. (2002), Fjeld et al. (1999), Couppis et al. (2012), Fry (1958), Rivens et al. (1996), ter Haar and Coussios (2007), Melodelima et al. (2009), Aptel et al. (2011)
Multi-element Annular array	Only in axial direction	No	≈100 %	No	Abdomen, breast	Hynynen et al. (1996), Dupenloup et al. (1996)
Multi-element Toroid array	Limited	No	≈100 %	No	Liver – intra-operative	Vincenot et al. (2013)
Multi-element Periodic array	Limited	Yes	High	Yes	Abdomen, breast, prostate	Pernot et al. (2003), Filonenko et al. (2004)
Multi-element Periodic array λ/2 spacing	Yes, limited	No	Variable	Yes	Abdomen, breast, prostate	Ellens et al. (2015)
1.5^{D} array	Only in lateral direction	Depends on element spacing	High (variable)	(Yes)	Abdomen, breast, prostate	Chen et al. (2012), Urban et al. (2013)
Multi-element Aperiodic, random, sparse array	Yes ≈10 % focal length laterally	No	Reduced	Yes	Abdomen, breast, prostate, brain	Filonenko et al. (2004), Hand et al. (2009), Gavrilov et al. (2000)
Multi-element Randomly sized elements (including sector arrays, strip arrays)	Yes	No	Variable	(Yes)	Abdomen, breast, prostate	Civale et al. (2006), Lafon et al. (2000), Melodelima et al. (2003)

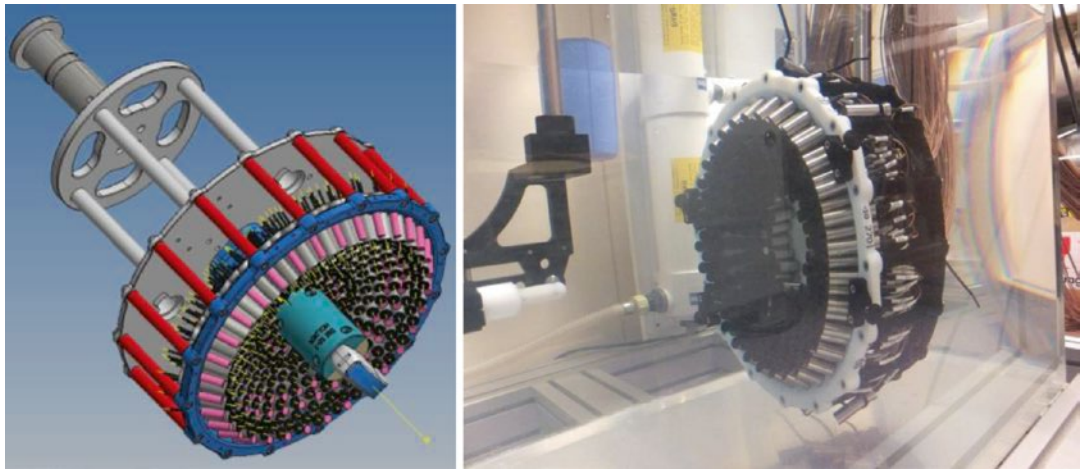

Fig. 1.5 Multi-element pseudo-random array composed of 256 individual elements mounted in 3^D printed shell

aberrations induced by the skull bone, and when combined with amplitude correction, is used to restore the desired focus at the brain target. The time reversal technique relies on the reciprocity property of the wave equation, and requires the presence of a sensor at the anticipated focal point in the brain to record the aberrations, which disrupt the focus. The implantation of such a sensor is clinically unrealistic, but it has been shown that it is possible to perform the required phase and amplitude corrections using either magnetic resonance (MR) or computed tomography (CT) images of the skull to model its ultrasonic properties for use in numerical modeling of the wave front distortion (Hynynen and Sun 1999; Aubry et al. 2003). This allows the propagation of a wave front emanating from a virtual point-like source in the brain (the intended "target") through the skull to be simulated and recorded by a set of virtual receivers outside the head. This wave front can be time reversed, and emitted by a real transducer array. This, along with amplitude correction made possible by knowledge of the porosity of the bone obtained from the CT scan, results in a focused beam at the brain "target" (Aubry et al. 2003).

1.5.1 Transducer Materials

There are a number of constraints that must be considered in the design of a therapy ultrasound transducer. Apart from the obvious necessity of the ability to produce high powers at frequencies in the range 0.25–10 MHz (requiring high electro-acoustic conversion efficiency), they must be reliable, able to deliver energy in pulsed or continuous wave form, and be physically compatible with the chosen imaging methods. Compatibility with the high magnetic fields present during MR guided HIFU is clearly a technological challenge. When ultrasound is the monitoring modality of choice, a central aperture is usually required in the therapy transducer, into which an imaging probe can be inserted. There is increasingly a call for transducer elements that are dual mode, that is, are capable of operating both as therapy sources at high power, and of being used in short pulse, imaging mode (Ebbini et al. 2006; Owen et al. 2010; Mari et al. 2013; Casper et al. 2013).

Multi-element arrays are most commonly constructed in one of two ways. Individual elements can be cased in separate housings and then mounted individually on a shell of the required geometry. This allows easy replacement of failing elements and gives flexibility in their arrangement, but only allows for sparse arrays. An example of such a multi-element array is shown in Fig. 1.5. The alternative is to create an array by, for example, cutting deep grooves into a single piezo-ceramic sheet. This allows for denser packing of the elements, but can create a fragile

array when larger sizes are required. Hybrid combinations of these two methods are also possible.

With few exceptions (most notably for lithotripsy), medical ultrasound transducers are made from piezo-electric materials. Early pioneers in this area used the naturally occurring material, quartz (Fry 1953, 1977; Fry et al. 1954). Piezo-electricity was first discovered by Pierre and Jacques Curie in the 1880s, and is the name given to the property of a crystalline material that develops a charge when it is subjected to mechanical stress. The inverse effect is that when an electrical charge is applied to such a material, it will change its shape. An alternating current applied across a piezo-electric disc will cause rapid movement of its faces, creating a pressure wave in the medium in which it sits. Naturally occurring piezo-electric materials other than quartz include sucrose, tourmaline, lead titanate and dry bone.

In medical ultrasound, the most commonly used piezo-electric material is now lead zirconate titanate ($Pb[Zr_xTi_{1-x}]O_3$, PZT). Low loss PZT ceramic is cut into discs, the thickness of which determines the resonant frequency, the higher the frequency, the thinner the disc. In order to reduce fragility it is often convenient to drive these transducers at their third harmonic. For high power applications, PZT ceramic transducers are commonly air backed, to allow cooling and to reduce damping of the pressure wave. While high-density arrays can be made from simple piezo-electric materials, they operate in a narrow bandwidth, and it is necessary to avoid cross talk between adjacent elements of the array.

An alternative to using the piezo-ceramic crystals on their own is to incorporate them into a piezo-composite structure (Chapelon et al. 2000). Here, pillars of piezo-ceramic material are embedded in a polymer. The presence of the polymer enhances the vibration in the thickness mode used to generate the ultrasound wave, and reduces cross talk between the elements. The transducer shell can be shaped, and a solid backing material can be used, rendering the transducer less fragile. A common geometry for piezo-composites used in therapy ultrasound is 1–3. This describes the continuity of the piezo-ceramic in one dimension (a pillar) and the 3^D continuity of the embedding polymer.

Polyvinylidene fluoride (PVDF) is another commonly used piezo-electric material used in medical ultrasound applications. This may be manufactured as a thin (acoustically transparent) membrane, and can be electroded to act as either a sensor or a low power source. PVDF membrane hydrophones are in common use as they only minimally distort the acoustic field during pressure measurement (Shotton et al. 1980; Bacon 1982; Bailey et al. 2011; Wear et al. 2014).

Capacitive micromachined ultrasonic transducers (CMUTs) have until now not been thought to be capable of producing sufficient power for HIFU applications, but recent publications indicate that this limitation may be overcome (Wong et al. 2010; Khuri-Yakub and Oralkan 2011; Yamaner et al. 2012; Lee et al. 2013).

1.6 Clinical Devices

The characteristics of transducers currently in clinical use are shown in Table 1.2. This is necessarily not a completely comprehensive list. The aim for most systems is to deliver an *in-situ* intensity greater than 10^3 W.cm^{-2} at the focus. For extra-corporeal sources with long focal length, this is achieved using a high power wide aperture source. Wide aperture sources have the advantage of distributing the incident energy over a large skin area, thus reducing the possibility of skin burn. Trans-rectal and intra-cavitary sources operate at lower powers and higher frequencies as they can be placed close to the target volume.

1.6.1 Extracorporeal Devices

Tissue targets lying within the breast, abdomen, brain or limbs are usually treated using an extracorporeal HIFU source. This necessitates a suitable acoustic window on the skin that allows access to the treatment site that is free of gas or bone in the propagation path. It must also be possible to couple the ultrasound energy to the skin surface using coupling gel, a water balloon or

Table 1.2 Summary of devices currently in use clinically

Device	Application	Guidance	Freq. (MHz)	Transducer aperture (cm)	Focal length (mm)	Acoustic power (W)	Intensity ($W.cm^{-2}$)	References
E/C	Liver cancer	US	0.8/1.6	12	135	–	$5–20·10^3$	Wu et al. (2005a)
E/C	Kidney cancer	US	0.8/1.6	12	13.5	<300	–	Illing et al. (2005)
E/C	Breast cancer	US	1.6	12	90	–	$5–15·10^3$	Wu et al. (2005a, b)
E/C	Uterine fibroid	MR	0.96–1.14	12	Variable	100–140	–	Tempany et al. (2003)
E/C	Osteosarcoma	US	0.8	12	135	80–160	$2–8·10^3$	Chen et al. (2002)
E/C	Pancreatic cancer	US	0.8	12	135	<300	$5–10·10^3$	Wu et al. (2005b)
T/R	Prostate BPH	US	4	3.0×2.2	30–40	–	$1.3–2·10^3$	Sanghvi et al. (1999)
T/R	Prostate cancer	US	4	–	30–50	–	$1.3–2.2·10^3$	Dickinson et al. (2013)
T/R	Prostate cancer	US	3	6.1×3.9	45	26–35	–	Chaussy et al. (2001)
I-C	Rhinitis	None	5–8	0.5	2–3	10–20	–	
I-C	Biliary duct cancer	US	10	0.3×1.0	n/a		14	Prat et al. (1999)
H/H	Gynaecology	None	5–8	1.2	5	10–30	–	Li et al. (2004)
E/C	Ophthalmology	Visual	21	6×cylindrical segment, 10.2 mm radius, 4.5 mm width and a 7 mm length	10.2	2	–	Aptel et al. (2011)
I/O	Liver metastases	US	3	Toroid 70 mm	70, 86	–	–	Dupré et al. (2015)
E/C	Breast, thyroid	US	3	–	–	125	–	Kovatcheva et al. (2014, 2015)

E/C extra-corporeal, *T/R* trans-rectal, *H/H* hand held, *I/O* intra-operative, (–) signifies that information in not available

other suitable path of a material of similar acoustic impedance to that of the skin. Extracorporeal HIFU treatments are guided using either US or MRI. These methods have been reviewed by Rivens et al. (2007). When treatments are carried out under MR guidance, care must be taken about the magnetic compatibility of the treatment head. PZT contains Nickel, which helps with the high levels of electrical excitation and mechanical stress induced. Nickel causes magnetic field distortion, and eddy currents may be set up when the transducers are given a conductive silver coating. These eddy currents may cause local magnetic field inhomogeneities, and significant image artifacts. It is possible to reduce these currents by segmenting the transducer face into a number of areas (Wharton et al. 2007). The piezo-composite materials discussed above reduce these problems, and have been used by the commercial clinical systems now available.

MR guidance has the advantage that thermometry sequences are available that allow temperature mapping in soft tissue. This enables the superimposition of either the temperature, or the calculated thermal dose, on the anatomical MR image. Using this type of display, the entire target region can be "painted" out during treatment. The two most commonly used MR guided clinical HIFU systems achieve volume ablation in different ways. Both systems aim to minimize treatment times. In one, the focus is swept electronically in concentric circles, with the user able to choose the maximum diameter of this sweep, and in the other, the phase and amplitude applied to the multi-element array is designed to produce multiple focal peaks in the focal plane.

Where US is used to guide and monitor HIFU treatments, the diagnostic transducer is incorporated into the treatment head. This allows real time imaging of the ablation process. The thermally ablated region is not visible on standard B-mode images in the absence of contrast media, unless gas bubbles have been induced. HIFU exposures levels are therefore often adjusted until a hyperechoic region is seen on the US image, indicating that bubbles are present in this region. These are generated by thermal exsolution of tissue gas. The stiffness of tissue is altered by the ablation process, and so elastographic techniques should allow treatments to be monitored in real time, although this technique has not yet achieved widespread clinical use.

1.6.2 Trans-rectal Devices

Trans-rectal devices have been developed for the treatment of benign and malignant prostate disease. These have probes that can be inserted per rectum and which incorporate both imaging and therapy transducers in one unit. The clinical acceptance of these devices was made easier by trans-rectal ultrasound imaging (TRUS) being the diagnostic investigation of choice for many urologists. There are two commercially available devices, which are very similar in concept. In both systems the therapy transducer takes the form of a truncated spherical bowl.

1.6.3 Interstitial Devices

There has been some interest in the development of high intensity ultrasound probes for interstitial use. In the main, these use plane transducers rather than focusing elements, and volume destruction is obtained by rotation of the probe. Prat et al. (1999) have described a probe designed for the intra-ductal treatment of biliary tumors. A 3×10 mm 10 MHz plane transducer is mounted on a stainless steel shaft that is passed through a jumbo fiberduodenoscope. The probe can be positioned under fluoroscopic guidance. An ultrasound intensity at the transducer face of 14 Wcm^{-2} is used for 10–20 s bursts. Circumferential ablation is achieved by rotation of the flexible probe. The transducer is rotated by 18° after each "shot". Once 360° of damage has been achieved, the probe is repositioned under fluoroscopic guidance to create adjacent rings. This has been used clinically with some encouraging results (Prat et al. 2001). An MR compatible device working on similar principles has been created for the treatment of esophageal tumors (Melodelima et al. 2005).

While the main clinical route for the HIFU treatment of the prostate is trans-rectal, the trans-urethral route has also been explored under ultrasound and MR guidance (Sommers et al. 2013; Siddiqui et al. 2010). This route reduces the risk of damaging the rectal wall.

1.7 Summary

Modern medicine concentrates on developing personalized treatments and techniques that minimize intervention to the patient and length of hospital stay. HIFU fits excellently into this philosophy. Thermal ablation therapies in general provide a minimally invasive approach to cancer therapy that is gaining rapid clinical acceptance. HIFU is the least invasive of the available ablative techniques, and as such should be the most attractive. However, there remain outstanding technical and treatment delivery questions to be addressed. The growing use of multi-element phased array sources has increased the flexibility of HIFU delivery, and shortened treatment times. Integration of therapy and diagnostic technique has improved treatment targeting and monitoring, thus rendering HIFU both safer and more effective. It seems probable that, as the evidence base for the clinical efficacy of HIFU improves, there will be a move towards more application specific devices, as already seen for treatments in the brain, eye and thyroid.

Acknowledgements I should like to thank my team at the ICR for providing me with photographs and figures, most especially Drs Ian Rivens, John Civale, David Sinden and Pierre Gelat.

References

Al-Bataineh O, Jenne J, Huber P (2012) Clinical and future applications of high intensity focused ultrasound in cancer. Cancer Treat Rev 38:346–353

Aptel F, Charrel T, Lafon C, Romano F, Chapelon JY, Blumen-Ohana E, Denis P (2011) Miniaturized high-intensity focused ultrasound device in patients with glaucoma: a clinical pilot study. Investig Ophthalmol Vis Sci 52:8747–8753

Aptel F, Dupuy C, Rouland JF (2014) Treatment of refractory open-angle glaucoma using ultrasonic circular cyclocoagulation: a prospective case series. Curr Med Res Opin 30:1599–1605

Aubry JF, Pernot M, Marquet F, Tanter M, Fink M (2008) Transcostal high-intensity-focused ultrasound: ex vivo adaptive focusing feasibility study. Phys Med Biol 53:2937–2951

Aubry JF, Tanter M, Pernot M, Thomas JL, Fink M (2003) Experimental demonstration of noninvasive transskull adaptive focusing based on prior computed tomography scans. J Acoust Soc Am 113:84–93

Baco E, Gelet A, Crouzet S, Rud E, Rouvière O, Tonoli-Catez H, Eggesbø HB (2014) Hemi salvage high-intensity focused ultrasound (HIFU) in unilateral radiorecurrent prostate cancer: a prospective two-centre study. BJU Int 114:532–540

Bacon DR (1982) Characteristics of a PVDF membrane hydrophone for use in the range 1–100 MHz. IEEE Trans Sonics Ultrasonics 29:18–25

Bailey MR, Maxwell AD, Pishchalnikov YA, Sapozhnikov OA (2011) Polyvinylidene fluoride membrane hydrophone low-frequency response to medical shockwaves. J Acoust Soc Am 129:2677–2677

Ballantine HT, Bell E, Manlapaz J (1960) Progress and problems in the neurological application of focused ultrasound. J Neurosurg 17:858–876

Casper AJ, Liu D, Ballard JR, Ebbini ES (2013) Real-time implementation of a dual-mode ultrasound array system: *in vivo* results. IEEE Trans Biomed Eng 60: 2751–2759

Chan AH, Fujimoto VY, Moore DE, Martin RW, Vaezy S (2002) An image-guided high intensity focused ultrasound device for uterine fibroids treatment. Med Phys 29:2611–2620

Chapelon JY, Cathignol D, Cain C, Ebbini E, Kluiwstra JU, Sapozhnikov OA, Guey JL (2000) New piezoelectric transducers for therapeutic ultrasound. Ultrasound Med Biol 26:153–159

Chaussy C, Thuroff S, de la Rosette JJMC (2001) Results and side effects of high-intensity focused ultrasound in localized prostate cancer. J Endourol 15:437–440

Chen W, Wang Z, Wu F, Zhu H, Zou J, Bai J, Li K, Xie F (2002) High intensity focused ultrasound in the treatment of primary malignant bone tumor. Zhonghua Zhong Liu Za Zhi 24:612–615

Chen WS, Brayman AA, Matula TJ, Crum LA (2003) Inertial cavitation dose and hemolysis produced in vitro with or without Optison®. Ultrasound Med Biol 29:725–737

Chen W, Zhou K (2005) High-intensity focused ultrasound ablation: a new strategy to manage primary bone tumors. Curr Opin Orthop 16:494–500

Chen GS, Lin CY, Jeong JS, Cannata JM, Lin WL, Chang H, Shung KK (2012) Design and characterization of dual-curvature 1.5-dimensional high-intensity focused ultrasound phased-array transducer. IEEE Trans Ultrason Ferroelectr Freq Control 59:150–155

Civale J, Clarke RL, Rivens IH, ter Haar GR (2006) The use of a segmented transducer for rib sparing in HIFU treatments. Ultrasound Med Biol 32:1753–1761

Clement GT, Hynynen K (2002a) Micro-receiver guided transcranial beam steering. IEEE Trans Ultrason Ferroelectr Freq Control 49:447–453

Clement GT, Hynynen K (2002b) A non-invasive method for focusing ultrasound through the skull. Phys Med Biol 47:1219–1236

Coleman DJ, Lizzi FL, El-Mofty AAM, Driller J, Franzen LA (1980) Ultrasonically accelerated absorption of vitreous membranes. Am J Ophthalmol 89:490–499

Coleman DJ, Lizzi FL, Torpey JH, Burgess SEP, Driller J, Rosado A, Nguyen HT (1985a) Treatment of experimental lens capsular tears with intense focused ultrasound. Br J Ophthalmol 69:645–649

Coleman DJ, Lizzi FL, Driller J, Rosado AL, Burgess SEP, Torpey JH, Smith ME, Silverman RH, Yablonski ME, Chang S et al (1985b) Therapeutic ultrasound in the treatment of Glaucoma – II Clinical Applications. Ophthalmol 92:347–353

Couppis A, Damianou C, Kyriacou P, Lafon C, Chavrier F, Chapelon JY, Birer A (2012) Heart ablation using a planar rectangular high intensity ultrasound transducer and MRI guidance. Ultrasonics 52:821–829

Crouzet S, Rouvière O, Lafon C, Chapelon JY, Gelet A (2015) Focal High-Intensity Focused Ultrasound (HIFU). In: Technical aspects of focal therapy in localized prostate cancer. Springer, Paris, pp 137–151

Crouzet S, Rouviere O, Martin X, Gelet A (2014) High-intensity focused ultrasound as focal therapy of prostate cancer. Curr Opin Urol 24:225–230

Daum DR, Hynynen K (1999) A 256-element ultrasonic phased array system for the treatment of large volumes of deep seated tissue. IEEE Trans Ultrason Ferroelectr Freq Control 46:1254–1268

Dickinson L, Ahmed H, McCartan N, Weir S, Hindley R, Lewi H, Cornaby A et al (2013) 553 Five year oncological outcomes following whole gland primary HIFU from the UK independent HIFU registry. J Urol 189, e227

Duck FA (2013) Physical properties of tissues: a comprehensive reference book. Academic press, London

Dupenloup F, Chapelon J-Y, Cathignol DJ, Sapozhnikov OA (1996) Reduction of the grating lobes of annular arrays used in focused ultrasound surgery. IEEE Trans Ultrason Ferroelectr Freq Control 43:991–998

Dupré A, Melodelima D, Pérol D, Chen Y, Vincenot J, Chapelon JY, Rivoire M (2015) First clinical experience of intra-operative high intensity focused ultrasound in patients with colorectal liver metastases: a phase I-IIa study. PLoS One 10, e0118212

Ebbini ES, Yao H, Shrestha A (2006) Dual-mode ultrasound phased arrays for image-guided surgery. Ultrason Imaging 28:65–82

Elias WJ, Huss D, Voss T, Loomba J, Khaled M, Zadicario E, Frysinger RC, Sperling SA, Wylie S, Monteith SJ, Druzgal J, Shah BB, Harrison M, Wintermark M (2013) A pilot study of focused ultrasound thalamotomy for essential tremor. N Engl J Med 369:640–648

Ellens N, Lucht BBC, Gunaseelan ST, Hudson JM, Hynynen KH (2015) A novel, flat, electronically-steered phased array transducer for tissue ablation:preliminary results. Phys Med Biol 60:2195–2215

Filonenko EA, Gavrilov LR, Khokhlova VA, Hand JW (2004) Heating of biological tissues by two-dimensional phased arrays with random and regular element distributions. Acoust Phys 50:222–231

Fjield T, Silcox CE, Hynynen K (1999) Low-profile lenses for ultrasound surgery. Phys Med Biol 44:1803–1813

Froeling VK, Meckelburg NF, Schreiter C, Scheurig-Muenkler J, Kamp MH, Maurer A, Beck A, Hamm B, Kroencke TJ (2013) Outcome of uterine artery embolization versus MR-guided high-intensity focused ultrasound treatment for uterine fibroids: long-term results. Eur J Radiol 82:2265–2269

Fry WJ (1953) Action of ultrasound on nerve tissue—a review. J Acoust Soc Am 25:1–5

Fry FJ (1958) Precision high intensity focused ultrasonic machines for surgery. Am J Phys Med 37:152–156

Fry FJ (1977) Transkull transmission of an intense focused ultrasonic beam. Ultrasound Med Biol 3:179–189

Fry WJ, Mosberg WH, Barnard JW, Fry FJ (1954) Production of focal destructive lesions in the central nervous system with ultrasound. J Neurosurg 11: 471–478

Fry FJ, Ades HW, Fry WJ (1958) Production of reversible changes in the central nervous system by ultrasound. Science 127:83–84

Fry WJ, Fry FJ (1960) Fundamental neurological research and human neurosurgery using intense ultrasound. IRE Trans Med Electron ME-7:166–181

Gavrilov LR, Hand JW (2000) Two-dimensional phased arrays for surgery: movement of a single focus. Acoust Phys 46:390–399

Gavrilov LR, Hand JW, Abel P, Cain CA (1997) A method of reducing grating lobes associated with an ultrasound linear phased array intended for transrectal thermotherapy. IEEE Trans Ultrason Ferroelectr Freq Control 44:1010–1017

Gavrilov LR, Hand JW, Yushina IG (2000) Two-dimensional phased arrays for application in surgery: scanning by several focuses. Acoust Phys 46:551–558

Gelet A, Chapelon JY, Margonari J, Theilliere Y, Gorry F, Souchon R, Bouvier R (1993) High-intensity focused ultrasound experimentation on human benign prostatic hypertrophy. Eur Urol 23:44–47

Gelet A et al (2004) Local recurrence of prostate cancer after external beam radiotherapy: early experience of salvage therapy using high-intensity focused ultrasonography. Urology 63:625–629

Goss SA, Johnston RL, Dunn F (1980) Compilation of empirical ultrasonic properties of mammalian tissues. II. J Acoust Soc Am 68:93–108

Goss SA, Frizell LA, Kouzmanoff JT, Barich JM, Yang JM (1996) Sparse random ultrasound phased array for focal surgery. IEEE Trans Ultrason Ferroelectr Freq Control 43:1111–1121

ter Haar GR, Coussios CC (2007) HIFU physical principles & devices. Int J Hyperthermia 23:89–104

ter Haar G (2010) Ultrasound bioeffects and safety. Proc Inst Mech Eng H 224:363–373

ter Haar G, Shaw A, Pye S, Ward B, Bottomley F, Nolan R, Coady AM (2011) Guidance on reporting ultra-

sound exposure conditions for bioeffects studies. Ultrasound Med Biol 37:177–183

Hand JW, Shaw A, Sadhoo N, Rajagopal S, Dickinson RJ, Gavrilov LR (2009) A random phased array device for delivery of high intensity focused ultrasound. Phys Med Biol 54:5675–5693

Hesley GK, Gorny KR, Woodrum DA (2013) MR-guided focused ultrasound for the treatment of uterine fibroids. Cardiovasc Intervent Radiol 36:5–13

Hill CR, Rivens IH, Vaughan MG, ter Haar GR (1994) Lesion development in focused ultrasound surgery: a general model. Ultrasound Med Biol 20:259–269

Holt RG, Roy RA (2001) Measurements of bubble-enhanced heating from focused, MHz-frequency ultrasound in a tissue-mimicking material. Ultrasound Med Biol 27:1399–1412

Hwang JH, Tu J, Brayman AA, Matula TJ, Crum LA (2006) Correlation between inertial cavitation dose and endothelial cell damage in vivo. Ultrasound Med Biol 32:1611–1619

Hurwitz MD, Ghanouni P, Kanaev SV, Iozeffi D, Gianfelice D, Fennessy FM, Kuten A, Meyer JE, LeBlang SD, Roberts A, Choi J, Larner JM, Napoli A, Turkevich VG, Inbar Y, Tempany CM, Pfeller RM (2014) Magnetic resonance-guided focused ultrasound for patients with painful bone metastases: phase III trial results. J Natl Cancer Inst 106:1–9

Hutchinson EB, Buchanan MT, Hynynen K (1996) Design and optimization of an aperiodic ultrasound phased array for intracavitary prostate thermal therapies. Med Phys 23:767–776

Hynynen K, Chung A, Fjield T, Buchanan M, Daum D, Colucci V, Lopath P, Jolesz F (1996) Feasibility of using ultrasound phased arrays for MRI monitored noninvasive surgery. IEEE Trans Ultrason Ferroelectr Freq Control 43:1043–1053

Hynynen K, Sun J (1999) Transskull ultrasound therapy: The feasibility of using image derived skull thickness information to correct the phase distortion. IEEE Trans Ultrason Ferroelectr Freq Control 46:752–755

Illing RO, Kennedy JE, Wu F, ter Haar GR, Protheroe AS, Friend PJ, Gleeson FV, Cranston DW, Philips RR, Middleton MR (2005) The safety and feasibility of extracorporeal high-intensity focused ultrasound (HIFU) for the treatment of liver and kidney tumours in a Western population. Br J Cancer 93:890–895

Khokhlova VA, Bailey MR, Reed JA, Cunitz BW, Kaczkowski PJ, Crum LA (2006) Effects of nonlinear propagation, cavitation, and boiling in lesion formation by high intensity focused ultrasound in a gel phantom. J Acoust Soc Am 119:1834–1848

Khuri-Yakub BT, Oralkan Ö (2011) Capacitive micromachined ultrasonic transducers for medical imaging and therapy. J Micromech Microeng 21:054004

Kovatcheva R, Vlahov J, Stoinov J, Lacoste F, Ortuno C, Zaletel K (2014) US-guided high-intensity focused ultrasound as a promising non-invasive method for treatment of primary hyperparathyroidism. Eur Radiol 24:2052–2058

Kovatcheva R, Guglielmina JN, Abehsera M, Boulanger L, Laurent N, Poncelet E (2015) Ultrasound-guided high-intensity focused ultrasound treatment of breast fibroadenoma—a multicenter experience. J Ther Ultrasound 3:1

Lafon C, Theillere Y, Prat F, Arefiev A, Chapelon J, Cathignol D (2000) Development of an interstitial ultrasound applicator for endoscopic procedures: animal experimentation. Ultrasound Med Biol 26:669–675

Lavine O, Langenstrass K, Bowyer C, Fox F, Griffing V, Thaler W (1952) Effects of ultrasonic waves on the refractive media of the eye. Arch Ophthalmol 47:204–209

Lee BC, Nikoozadeh A, Park KK, Khuri-Yakub BPT (2013) Fabrication of CMUTs with substrate-embedded springs. In: Proceeding IEEE Ultrasonics Symposium, Czech Republic, Prague, pp 1733–1736

Li C, Bian D, Chen W, Zhao C, Yin N, Wang Z (2004) Focused ultrasound therapy of vulvar dystrophies: a feasibility study. Obstet Gynecol 104:915–921

Li C, Zhang W, Fan W, Huang J, Zhang F, Wu P (2010) Noninvasive treatment of malignant bone tumors using high-intensity focused ultrasound. Cancer 116: 3934–3942

Liberman B, Gianfelice D, Inbar Y, Beck A, Rabin T, Shabshin N, Chander G, Hengst S, Pfeller R, Chechick A, Hanannel A, Dogadkin O, Catane R (2009) Pain palliation in patients with bone metastases using MR-guided focused ultrasound surgery: a multicenter study. Ann Surg Oncol 16:140–146

Lizzi FL, Coleman DJ, Driller J, Franzen LA, Jackobiec FA (1978) Experimental ultrasonically induced lesions in the retina, choroid, and sclera. Invest Ophthalmol 17:350–360

Lynn JG, Zwemer RL, Chick AJ, Miller AE (1942) A new method for the generation and use of focused ultrasound in experimental biology. J Gen Physiol 26:179–192

McDannold N, Tempany CM, Fennessy FM, So MJ, Rybicki FJ, Stewart EA, Hynynen K (2006) Uterine leiomyomas: MR imaging–based thermometry and thermal dosimetry during focused ultrasound thermal ablation 1. Radiol 240:263–272

Madersbacher S, Schatzl G, Djavan B, Stulnig T, Marberger M (2000) Long-term outcome of transrectal high- intensity focused ultrasound therapy for benign prostatic hyperplasia. Eur Urol 37:687–694

Mari JM, Bouchoux G, Dillenseger JL, Gimonet S, Birer A, Garnier C, Brasset L, Ke W, Guey JL, Fleury G (2013) Study of a dual-mode array integrated in a multi-element transducer for imaging and therapy of prostate cancer. IRBM 34:147–158

Martin E, Jeanmonod D, Morel A, Zadicario E, Werner B (2009) High-intensity focused ultrasound for noninvasive functional neurosurgery. Ann Neurol 66:858–861

Medel R, Monteith SJ, Elias WJ, Eames M, Snell J, Sheehan JP, Wintermark M, Jolesz FA, Kassell NF (2012) Magnetic resonance guided focused ultrasound surgery: part 2 – a review of current and future applications. Neurosurgery 71:755–763

Melodelima D, Lafon C, Prat F, Theillère Y, Arefiev A, Cathignol D (2003) Transoesophageal ultrasound appli-

cator for sector-based thermal ablation: first in vivo experiments. Ultrasound Med Biol 29:285–291

Melodelima D, Salomir R, Chapelon JY, Theillère Y, Moonen C, Cathignol D (2005) Intraluminal high intensity ultrasound treatment in the esophagus under fast MR temperature mapping: in vivo studies. Magn Reson Med 54:975–982

Melodelima D, N'Djin WA, Parmentier H, Chesnais S, Rivoire M, Chapelon JY (2009) Thermal ablation by high-intensity-focused ultrasound using a toroid transducer increases the coagulated volume. Results of animal experiments. Ultrasound Med Biol 35:425–435

Orsi F, Arnone P, Chen W, Zhang L (2010) High intensity focused ultrasound ablation: a new therapeutic option for solid tumors. J Cancer Res Ther 6:414–420

Owen NR, Chapelon JY, Bouchoux G, Berriet R, Fleury G, Lafon C (2010) Dual-mode transducers for ultrasound imaging and thermal therapy. Ultrasonics 50:216–220

Payne A, Vyas U, Todd N, de Bever J, Christensen DA, Parker DL (2011) The effect of electronically steering a phased array ultrasound transducer on nearfield tissue heating. Med Phys 38:4971–4981

Pernot M, Aubry JF, Tanter M, Thomas JL, Fink M (2003) High power transcranial beam steering for ultrasonic brain therapy. Phys Med Biol 48:2577–2589

Prat F, Lafon C, Margonari J, Gorry F, Theillere Y, Chapelon JY, Cathignol D (1999) A high-intensity US probe designed for intraductal tumor destruction: experimental results. Gastrointest Endosc 50:388–392

Prat F, Lafon C, Theillere JY, Fritsch J, Choury AD, Lorand I, Cathignol D (2001) Destruction of bile duct carcinoma by intraductal high intensity ultrasound during ERCP. Gastrointest Endosc 53:797–800

Quinn SD, Gedroye WM (2015) Thermal ablation treatment of uterine fibroids. Int J Hyperthermia 31: 272–279

Rivens IH, Clarke RL, ter Haar GR (1996) Design of focused ultrasound surgery transducers. IEEE Trans Ultrason Ferroelectr Freq Control 43:1023–1031

Rivens I, Shaw A, Civale J, Morris H (2007) Treatment monitoring and thermometry for therapeutic focused ultrasound. Int J Hyperthermia 23:121–139

Rosenberg RS, Purnell E (1967) Effects of ultrasonic radiation on the ciliary body. Am J Ophthalmol 63: 403–409

Sanghvi NT, Foster RS, Bihrle R, Casey R, Uchida T, Phillips MH, Syrus J, Zaitsev AV, Marich KW, Fry FJ (1999) Noninvasive surgery of prostate tissue by high intensity focused ultrasound: an updated report. Eur J Ultrasound 9:19–29

Sapareto SA, Dewey WC (1984) Thermal dose determination in cancer therapy. Int J Radiat Oncol Biol Phys 10:787–800

Shotton KC, Bacon DR, Quilliam RM (1980) A PVDF membrane hydrophone for operation in the range 0.5 MHz to 15 MHz. Ultrasonics 18:123–126

Siddiqui K, Chopra R, Vedula S, Sugar L, Haider M, Boyes A, Klotz L (2010) MRI-guided transurethral ultrasound therapy of the prostate gland using real-time thermal mapping: initial studies. Urology 76:1506–1511

Silverman RH, Vogelsang B, Rondeau MJ, Coleman DJ (1991) Therapeutic ultrasound for the treatment of glaucoma. Am J Ophthalmol 111:327–337

Sommer G, Pauly KB, Holbrook A, Plata J, Daniel B, Bouley D, Diederich C (2013) Applicators for MR-guided ultrasonic ablation of BPH. Invest Radiol 48:387–394

Sullivan LD, McLoughlin MG, Goldenberg LG, Gleave ME, Marich KW (1997) Early experience with high-intensity focused ultrasound for the treatment of benign prostatic hypertrophy. Br J Urol 79:172–176

Tanter M, Thomas JL, Fink M (1998) Focusing and steering through absorbing and aberrating layers: application to ultrasonic propagation through the skull. J Acoust Soc Am 103:2403–2410

Tanter M, Aubry JF, Gerber J, Thomas JL, Fink M (2001) Optimal focusing by spatio-temporal inverse filter: part I. Basic principles. J Acoust Soc Am 101:37–47

Tempany CM, Stewart EA, McDannold N, Quade BJ, Jolesz FA, Hynynen K (2003) MR imaging-guided focused ultrasound surgery of uterine leiomyomas: a feasibility study. Radiol 226:897–905

Thomas JL, Fink M (1996) Ultrasonic beam focusing through tissue inhomogeneities with a time reversal mirror: application to transskull therapy. IEEE Trans Ultrason Ferroelectr Freq Control 43:1122–1129

Thüroff S, Chaussy CG (2015) Transrectal prostate cancer ablation by robotic High-Intensity Focused Ultrasound (HIFU) at 3 MHz: 18 years clinical experiences. In: Focal therapy of prostate cancer, Springer International Publishing, Switzerland, pp 105–133

Uddin Ahmed H, Cathcart P, Chalasani V, Williams A, McCartan N, Freeman A, Emberton M (2012) Whole-gland salvage high-intensity focused ultrasound therapy for localized prostate cancer recurrence after external beam radiation therapy. Cancer 118:3071–3078

Urban MW, Chalek C, Haider B, Thomenius KE, Fatemi M, Alizad A (2013) A beamforming study for implementation of vibro-acoustography with a 1.75-D array transducer. IEEE Trans Ultrason Ferroelectr Freq Control 60:535–551

Valerio M, Ahmed HU, Emberton M, Lawrentschuk N, Lazzeri M, Montironi R, Polascik TJ (2014) The role of focal therapy in the management of localised prostate cancer: a systematic review. Eur Urol 66:732–751

Vincenot J, Melodelima D, Chavrier F, Vignot A, Kocot A, Chapelon JY (2013) Electronic beam steering used with a toroidal HIFU transducer substantially increases the coagulated volume. Ultrasound Med Biol 39:1241–1254

Wear K, Gammell P, Maruvada S, Liu Y, Harris G (2014) Improved measurement of acoustic output using complex deconvolution of hydrophone sensitivity. IEEE Trans Ultrason Ferroelectr Freq Control 61:62–75

Wong SH, Kupnik M, Watkins RD, Butts-Pauly K, Khuri-Yakub BT (2010) Capacitive micromachined ultrasonic transducers for therapeutic ultrasound applications. IEEE Trans Biomed Eng 57:114–123

Wharton IP, Rivens IH, ter Haar GR, Gilderdale DJ, Collins DJ, Hand JW, Desouza NM (2007) Design and development of a prototype endocavitary probe for high-intensity focused ultrasound delivery with integrated magnetic resonance imaging. J Magn Reson Imaging 25:548–556

Wu F, Wang ZB, Chen WZ, Wang W, Gui Y, Zhang M, Feng R (2004) Extracorporeal high intensity focused ultrasound ablation in the treatment of 1038 patients with solid carcinomas in China: an overview. Ultrason Sonochem 11:149–154

Wu F, Wang ZB, Chen WZ, Zou JZ, Bai J, Zhu H, Li KQ, Jin CB, Xie FL, Su HB (2005a) Advanced hepatocellular carcinoma: treatment with high-intensity focused ultrasound ablation combined with transcatheter arterial embolization. Radiology 235: 659–667

Wu F, Wang ZB, Zhu H, Chen WZ, Zou JZ, Bai J, Li KQ, Jin CB, Xie FL, Su HB (2005b) Feasibility of US-guided high-intensity focused ultrasound treatment in patients with advanced pancreatic cancer: initial experience. Radiol 236:1034–1040

Yamaner FY, Olcum S, Oguz HK, Bozkurt A, Koymen H, Atalar A (2012) High-power CMUTs: design and experimental verification. IEEE Trans Ultrason Ferroelectr Freq Control 59:1276–1284

Prostate Focused Ultrasound Therapy

2

Jean-Yves Chapelon, Olivier Rouvière, Sébastien Crouzet, and Albert Gelet

Abstract

The tremendous progress in engineering and computing power coupled with ultrasound transducer technology and imaging modalities over the past 20 years have encouraged a revival of clinical interest in ultrasound therapy, mainly in High-Intensity Focused Ultrasound (HIFU). So far, the most extensive results from HIFU obtained in urology involve transrectal prostate ablation, which appears to be an effective therapeutic alternative for patients with malignant prostate tumors. Prostate cancer (PCa) is one of the most frequently diagnosed cancers in men. Several treatment options with different therapeutic approaches exist, including HIFU for localized PCa that has been in use for over 15 years. Since the early 2000s, two systems have been marketed for this application, and other devices are currently in clinical trials. HIFU treatment can be used either alone or in combination with (before- or after-) external beam radiotherapy (EBRT) (before or after HIFU) and can be repeated multiple times. HIFU treatment is performed under real-time monitoring with ultrasound or guided by MRI. Two indications are validated today: Primary care treatment and EBRT failure. The results of HIFU for primary care treatment are similar to standard conformal EBRT, even though no randomized comparative studies have been performed and no 10-year follow up data is yet available

J.-Y. Chapelon (✉)
INSERM, U1032, Lyon F-69003, France

Laboratory of Therapeutic Applications of Ultrasound, Université Lyon 1, Lyon, France
e-mail: jean-yves.chapelon@inserm.fr

O. Rouvière
INSERM, U1032, Lyon F-69003, France

Laboratory of Therapeutic Applications of Ultrasound, Université Lyon 1, Lyon, France

Department of Radiology, Hospices Civils de Lyon, Edouard Herriot Hospital, Lyon, France

S. Crouzet • A. Gelet
INSERM, U1032, Lyon F-69003, France

Laboratory of Therapeutic Applications of Ultrasound, Université Lyon 1, Lyon, France

Department of Urology, Hospices Civils de Lyon, Edouard Herriot Hospital, Lyon, France

© Springer International Publishing Switzerland 2016

J.-M. Escoffre, A. Bouakaz (eds.), *Therapeutic Ultrasound*, Advances in Experimental Medicine and Biology, Vol. 880, DOI 10.1007/978-3-319-22536-4_2

for HIFU. Salvage HIFU after EBRT failure is increasing with oncological outcomes, similar to those achieved with surgery but with the advantage of fewer adverse effects. HIFU is an evolving technology perfectly adapted for focal treatment. Thus, HIFU focal therapy is another pathway that must be explored when considering the accuracy and reliability for PCa mapping techniques. HIFU would be particularly suited for such a therapy since it is clear that HIFU outcomes and toxicity are relative to the volume of prostate treated.

Keywords
HIFU • Prostate cancer

2.1 Introduction

PCa (Prostate Cancer) is the most common male cancer after the age of 60. The American Cancer Society's estimates for PCa in the United States for 2014 are that 233,000 new cases of PCa will be diagnosed and 29,480 men will die of PCa.[1] In the absence of large randomized trials, it is often difficult to define the therapeutic strategy for clinically localized or locally advanced PCa disease detected in elderly patients. The latest results of the Scandinavian randomized study comparing radical surgery versus watchful waiting concluded that there was no benefit from radical prostatectomy in terms of metastasis-free survival and disease-specific survival in patients over 65 years old (Bill-Axelson et al. 2008). Note, however, that in this study patients were not subjected to prostate specific antigen (PSA) monitoring.

The three main strategies for PCa treatment of elderly patients are conformal radiotherapy, brachytherapy and active watchful waiting. Recent studies have demonstrated that local control of the disease would be obtained in only 68 % of patients after treatment with external conformal radiotherapy. For patients with one positive control biopsy, the biochemical control at 10 years is 5 % and the metastasis-free survival rate is 69 % (Zelefsky et al. 2008). The results of long-term active surveillance have recently been published by Klotz et al. (2010): At 10 years 38 % of patients had left active surveillance and had been treated with surgery or external beam radiation; 50 % of them were biological failures at 5 years. Treatment of PCa by High Intensity Focused Ultrasound (HIFU) is a new therapeutic modality in use in clinics since 2000 for first-line treatment of PCa (Crouzet et al. 2010b) and for patients with local recurrence after external radiotherapy (Murat et al. 2009). HIFU treatment is a potential treatment option whose place remains to be defined. The tremendous progress in engineering and sciences coupled with ultrasound transducer technology and imaging modalities during the past 20 years, together with better understanding of PCa natural history, offer new opportunities to change the terms of support with a wider area devoted to the use of HIFU.[2]

2.2 History and Principle of PCa Treatment by HIFU

HIFU is a non-ionizing and non-surgical physical therapy that produces biological effects by thermal and mechanical means. Heating tissue denatures proteins and leads to cell death, regardless of whether they are normal or abnormal, whereas mechanical effects disrupt cells by the collapse of

[1] http://www.cancer.org/cancer/prostatecancer/detailedguide/prostate-cancer-key-statistics

[2] The authors published some materials of this book chapter in 2012 in Chapter 6 of "Management of Prostate, A Multidisciplinary Approach". Springer, Bolla, Michel, van Poppel, Hendrik (Eds.), 2012, pp.191–212.

microbubbles generated by cavitation. In most applications, spherically shaped power transducers are used to focus the ultrasound energy onto a target point deep within the body. This results in thermal tissue coagulation necrosis, cavitation and heat shock. Each sonication heats only a small focal target, creating an elementary lesion with extreme precision and accuracy. Subsequently, multiple sonications are necessary to create, side-by-side and layer after layer, a volume of lesions covering the entire target volume to be ablated. The main sonication parameters are acoustic intensity, duration of exposure, on/off ratio, the distance between 2 elementary lesions and the displacement path when multiple lesions are made.

The first description of HIFU was made in 1942 and the ability to destroy tissue established in 1944 (Lynn et al. 1942; Lynn and Putnam 1944). However, the general technology remained in an experimental setting for over 50 years, and only recently has this technology been employed for approved clinical applications. Indeed, the tremendous progress in engineering and sciences coupled with ultrasound transducer technology and imaging modalities during the past 20 years has encouraged a revival of clinical interest in HIFU. It is currently used to non-invasively treat a variety of clinical conditions including: Symptomatic uterine fibroids, tumors in the prostate, breast, liver low back pain and brain disorders, such as essential tremor, Parkinson's disease and epilepsy.

The first experiments on the prostate were made in the early 90s. It was first demonstrated with the adenocarcinoma of a prostate experimentally implanted in rats (R 3327 AT2 Dunning tumor) that HIFU could be used to ablate tumors and cure cancer without causing metastases (Chapelon et al. 1992). It was next established that it was possible to induce regions of irreversible coagulation necrosis in canine prostates without damaging the rectal wall (Gelet et al. 1993b). The first treatments in men were performed in 1992 on benign prostate hyperplasia (Madersbacher et al. 1993; Gelet et al. 1993a, b). The results of a pilot study on PCa treatments were published in 1996 and the preliminary results from the first 50 patients in 1999 (Gelet et al. 1996, 1999). The main results of these studies were that histological analysis of prostate biopsies performed 48 h after HIFU treatment showed significant inflammation and lesions of coagulation necrosis, which hamper the identification of viable cancer cells. At 3 months, prostate biopsies were the seat of intense well-circumscribed fibrous reactions, making it possible to easily identify any residual cancer cells.

The main advantages of HIFU treatment are:

- The lack of induction of apoptosis avoiding late complications of treatment. No late rectal or bladder toxicity has been reported.
- A PSA nadir obtained in the first 8 weeks following tissue damage immediately allows one to conclude that treatment has been effective. PSA nadir is also an independent predictor of treatment success (Beerlage et al. 1999; Kennedy et al. 2003; Chaussy et al. 2005).
- A lack of cumulative effect with the possibility of repeating treatment.

By combining accurate control of the position of the transducer within the rectum and active cooling of the rectal mucosa, the risk of rectal injury is minimized. This technique offers the advantage of a transrectal treatment to ablate prostate tissue while sparing the rectum itself (Gelet et al. 1999).

2.3 HIFU Devices Dedicated to PCa Treatment

Since the early 2000s, two HIFU devices have been commercially available for the treatment of PCa: Ablatherm® (EDAP TMS, Vaulx-en-Velin, France) and Sonablate® (SonaCare Medical LLC, Charlotte, NC, USA). Both devices operate transrectally under ultrasound guidance and are approved for commercial distribution in the European Union, Canada, South Korea, Japan and Russia. The most important difference in the two devices is in their patient positioning.

2.3.1 Ablatherm® with Ultrasound Integrated Imaging

The Ablatherm II® (EDAP TMS, Vaulx-en-Velin, France) integrates both the imaging transducer (7.5 MHz) and the therapeutic transducer (3 MHz) in a single endorectal probe focused at 40 mm. The probe is covered by a latex condom filled with a coupling and refrigerant liquid to thermally protect the rectal wall. The probe is mounted on a computer-controlled motorized holder that allows movements in three spatial directions. The Ablatherm II® requires a special bed with the patient in a lateral position (Fig. 2.1).

The lateral position of the treatment allows gas bubbles produced in the coupling liquid during heating of the prostate to rise by buoyancy to a position outside the field of view of the imaging probe, and therefore of the therapy transducer. The Ablatherm II® software includes four treatment protocols with specially designed treatment parameters depending on the clinical use: Primary care (standard), retreatment, radiation failure and post brachytherapy. The treatment plan involves setting up the probes to target the thermal lesion within the prostate. The operator defines the boundaries of the target area using the US scanner. The Ablatherm II® is then switched to treatment mode and the computer-driven module induces lesions using the HIFU transducer. To treat the entire target area, several sonications are made side-by-side, first moving the head following the transverse plane (right-left), and then following the longitudinal plane (perpendicularly to the transverse plane). The lesion height may be adjusted between 19 and 24 mm to match the size of the target area. The device offers real-time ultrasonic monitoring of the treatment because HIFU-induced lesions are visible using standard ultrasound as hyper-echoic areas, but their extent is not always accurately defined. However, at the end of the procedure contrast-enhanced ultrasound with Sonovue® (Bracco Imaging, Switzerland) may be implemented to validate treated volumes and to define areas for treatment completion.

Fig. 2.1 Ablatherm® integrated imaging device

2.3.2 Sonoblate 500

The Sonablate 500® (SonaCare Medical LLC, Charlotte, NC, USA) is based on a console, a fully integrated probe (Fig. 2.2) and a module for degassing and circulating chilled water in the probe tip. The console consists of a portable system with a display monitor, an articulating arm with reliable probe holding capabilities and a stepper motor with 3-axes of precise movement. The transrectal probe uses double-sided and dual-mode transducers for imaging (6.3 MHz) and treatment (4 MHz). The double-sided transducer is available with two focal lengths (30–40 mm) that move robotically to follow the precise treatment plan devised by the physician. The size of an elementary thermal lesion is 10–12 mm long and 3 mm in diameter. The treatment is performed in the supine position. The system uses a treatment protocol allowing adjustable power settings for customizable treatment by the physician. The treatment is carried out in two or three consecutive layers (based on anterior-posterior dimensions of the prostate), beginning with the anterior portion of the prostate and moving to the posterior part by changing the focal length during the procedure. The choice of the focal length depends on the size of the prostate. The maximum prostate size that can be treated is 40 mm AP dimension. The latest version of the device uses a pulse echo back-scattered ultrasound (RF signals) -processing algorithm called TCM™ (Tissue Change Monitoring) to check in real-time whether the treatment was sufficient. A pulse echo RF signal is sent to the treatment site prior to delivery of HIFU energy, and then the second signal is sent post HIFU delivery to the same treatment site. The TCM™ algorithm, in real time, calculates and quantifies the tissue change that takes place in the treatment site and displays the degree of HIFU lesion completeness on the screen. This feedback allows the physician to re-treat the sites that were not treated optimally. For more details on the Sonablate 500® see Chap. 6 of "Therapeutic Ultrasound: Mechanisms to Applications" (Tavakkoli and Sanghvi 2011).

Fig. 2.2 Sonoblate® device

2.3.3 Focal One

A new device, FocalOne® (EDAP TMS, Vaulx-en-Velin, France), has recently been developed by EDAP to deliver HIFU treatment by combining all the latest technologies in imaging and treatment for an ideal PCa therapy: Accurate and MRUS-based fusion imaging guidance, a non-invasive surgical approach, precise and efficient therapeutic energy and end-of-treatment validation imaging.

In contrast to Ablatherm II®, the FocalOne® does not use a special bed and consists of a single module (Fig. 2.3). The treatment sequence now includes a pre-treatment step in which MR prostate images of the patient are imported from PACS or CD and elastic fusion is automatically performed to match the 3D contours of the prostate on the MRI and ultrasound images. For the pre-treatment step, the 3D MR target is automatically displayed on live ultrasound, and the software makes it possible to design a precise target area with accuracy better than 1 mm. A second screen displays the conformational treatment with an ultrasound image of the prostate and the target area defined in the prostate. The software can be used to modify in real-time the shape and size of the treatment area; this was not possible with the Ablatherm II®. Finally, in post-treatment sessions, contrast-enhanced Ultrasound with Sonovue® is used to validate treated areas and to define the areas for treatment completion. In the days following the procedure, review of treatment images is available for comparison with MR follow-up images.

A new probe based on the technology of "dynamic focusing" (beam steering) has been developed to deliver localized thermal therapy to the areas of the prostate gland via the transrectal approach. The probe has the same ergonomic design and the same ultrasound imaging transducer as that of the Ablatherm II® (Fig. 2.3). The HIFU transducer consists of an annular array with 16 individual concentric rings. All of the rings have the same surface area and are fed through their own amplifier channel (16 channels). The geometric focal point of the firing head is located at 60 mm from the front face, instead of 40 mm for that of the Ablatherm II®. The annular array makes it possible to steer the ultrasound beam at different depths and to adjust the treatment according to the thickness of the prostatic

Fig. 2.3 Focal One® device

tissues to be treated. In particular, it is possible to focus the ultrasound beam at a depth other than the natural radius of curvature of the transducer. The objective is to fit the treated volume as closely as possible to the geometry of the prostate, approaching a model of lesions formed "point by point" with short sub-sonications performed at different depths. For this, a phase shift is performed electronically on each ring to steer the HIFU beam along the axis of penetration, allowing enough depth to be reached to treat large prostates.

The advantage of this new probe is that it allows for a correction of the major disadvantages associated with the use of a fixed focus transducer. The 16 annular elements activated by a multichannel generator are used to split each sonication into sequences of one-second sub-sonications. Each sub-sonication ablates an ellipsoidal volume of 5 mm in height. The lesion consists of a small region of coagulation necrosis with reduced cavitation effects and concentrated thermal diffusion. The device makes it possible to add dynamic focusing sub-sonications along the axis of penetration of the ultrasound beam. It is therefore possible to obtain small necrotic lesions of 5 mm long with a shot of 1 s. Although the damage obtained with a single shot is small, large treatment zones can be obtained up to 40 mm in length, by adding 8 successive sub-sonications of 5 mm each. The fact that the height of the lesions can be varied between 5 and 40 mm allows for better matching of the treated area to the morphology of the prostate, as the focal point being always inside the prostate. The thermal dose delivered to the prostate is theoretically homogeneous, with fewer thermal diffusion phenomena, laterally towards the neurovascular bundles and vertically toward the striated sphincter. The anatomical distribution and homogeneous thermal dose throughout the prostate gland is expected to achieve better oncological results regardless of the size of the prostate. Furthermore, the absence of thermal diffusion should provide a significant reduction in side effects, such as incontinence and impotence. This new probe can be used to treat many, very small prostates with a focal point that will always be maintained within the gland, as well as large prostates with antero-posterior distances of up to 35 mm, which corresponds to prostates of about 50 cc. This is an improvement over the fixed focus transducer that could only treat prostates with a maximum antero-posterior distance of 26 mm, which corresponded to prostates with a maximum of 30 cc. Finally, it is possible to shorten the duration of treatment for a given treated volume. In fact, the shots fired at shallow depth will be associated with reduced firing power. Rest periods, with the aim of limiting the temperature rise in the rectal wall, could therefore be shortened.

2.3.4 MRgFUS Devices

Magnetic resonance guided focused ultrasound surgery (MRgFUS) was recently presented as a method for ablation with focused ultrasound under magnetic resonance imaging guidance. This approach has the advantage of improved targeting and real-time temperature monitoring. To date, two different approaches have been used for MRgFUS of the prostate: One with a transrectal probe compatible with the ExAblate® system (InSightec, Haifa, Israel) under a 1.5 T GE MRI, and another with a MRI-compatible ultrasound applicator to deliver controlled thermal therapy to the regions of the prostate gland via a transurethral approach (Profound Medical Inc., Toronto, Canada). The potential of both technologies is currently being demonstrated in Phase I clinical trials, but only a few studies have been conducted in therapy of PCa with human patients (Zini et al. 2012; Chopra et al. 2012), and most of the currently available literature on MRgFUS for prostate uses a canine model for research (Siddiqui et al. 2010; Chopra et al. 2009).

2.4 Long-Term Outcomes of HIFU in PCa Treatment

This section gives an extensive review of clinical outcomes in all uses of HIFU technology for treatment of localized PCa.

2.4.1 HIFU as Primary Care Treatment

The recommendations and updated guidelines on the use of HIFU for PCa as a primary treatment concern patients with localized PCa (clinical T1-T2 stage Nx/0 M0 PCa) for whom radical prostatectomies are not an option for one of the following reasons: Age >70 years old, life expectancy ≤10 years, major co-morbidities which preclude surgery or the simple refusal on the part of the patient to undergo surgery (Rebillard et al. 2003; AURO 2009). Among the publications on HIFU as a primary therapy for PCa, 16 studies report on a series of at least 50 patients (Uchida et al. 2006a, b, 2009; Crouzet et al. 2010a, b, c; Lee et al. 2007; Poissonier et al. 2007; Ahmed et al. 2009; Blana et al. 2008a, b, 2009; Mearini et al. 2009; Misrai et al. 2008; Ganzer et al. 2008; Turoff et al. 2003; Chaussy and Thuroff 2001; Gelet et al. 2000), while the others report on fewer patients (Ficarra et al. 2006; Challacombe et al. 2009; Maestroni et al. 2008; Koch et al. 2007). Follow-up varies significantly between series (range: 6 months to 6.4 years). In most cases, the PSA nadir was reached 3–4 months after treatment by HIFU, and was = 0.05 ng/mL in 55–91 % of the cases. Many studies have demonstrated that the PSA nadir was a significant predictor of HIFU failure. Patients with a PSA nadir over 0.5 ng/mL must be carefully monitored (Lee et al. 2007; Ganzer et al. 2008). A PSA nadir >0.2 ng/mL after HIFU has been associated with a four times greater risk of treatment failure, which is defined as a positive biopsy after HIFU treatment (Uchida et al. 2006a).

The 7-year disease-free survival rate in the longest follow-up multicenter studies was 75 %, 63 % and 62 % for low, intermediate and high-risk patients, respectively, and the 8-year cancer-specific survival rate was 99 % (Crouzet et al. 2010a, b, c). Complication rates are low with sloughing occurring in 0.3–8.6 %. Impotence occurs in 20–77 % of patients and bladder outlet obstruction in 12–22 %. The incontinence rates reported in a recent study were grade I (4–17.5 %) and grade II and III (0–5 %) (Chaussy et al. 2005; Crouzet et al. 2011). In our institution, we have recently reviewed the results of 880 patients. The mean age was 70 years old. Stratification according to d'Amico's risk group was low, intermediate and high in 36 %, 48 % and 16 %, respectively. Median follow-up was 41 months. Median PSA nadir was 0.1 ng/mL. The overall and cancer-specific survival rates at 7 years were 90 and 98 %, respectively. The metastasis-free survival rate at 7 years was 96 %. The 5- and 7-year disease-free survival rates were 75–62 %, 59–50 % and 45–39 % for low, intermediate and high risk patients, respectively ($p = 0.0001$) (Crouzet et al. 2010a, b, c). Recent articles published in 2013 from three European urology departments confirm the long-term efficacy of HIFU treatment (Crouzet et al. 2014; Thüroff and Chaussy 2013; Ganzer et al. 2013).

In a study from a prospective database, Shoji et al. included 326 patients who filled in self-administered questionnaires on urinary function, QOL and sexual assessment (Shoji et al. 2010). The FACT G, FACT-prostate and IIEF 5 were used. Maximum flow rate and residual urine volume were significantly impaired at 6 months ($p = 0.010$) after HIFU, even though they returned to baseline values at 12 or 24 months after HIFU. The total FACT-G score significantly improved at 24 months ($p = 0.027$) after HIFU. At 6, 12 and 24 months after HIFU, 52 %, 63 % and 78 %, respectively, of the patients who had not received neoadjuvant hormonal therapy were potent.

In a prospective study, Li et al. compared the IIEF score, penile colour Doppler ultrasound, penile length and circumference on patients treated for PCa with HIFU or cryoablation (Li et al. 2010). A total of 55 patients in the HIFU group and 47 in the cryoablation group were included. At 36 months, cryoablation patients experienced a lower erectile function recovery rate compared to HIFU patients (Cryoablation = 46.8 %; HIFU = 65.5 %; $p = 0.021$). No significant decreases in penile length and circumference were found in the two groups (all p-values ≥0.05). Finally, HIFU treatment seems to be standardized with similar outcomes between centers (Rebillard et al. 2003).

2.4.2 Salvage After HIFU Failure

2.4.2.1 HIFU Retreatment

One of the potential interests of HIFU, especially compared to radiotherapy, is the fact that treatment can be repeated. Unlike radiation, there is no dose limitation and no limited number of sessions. In case of incomplete treatment or treatment failure, HIFU does not result in a therapeutic impasse. The re-treatment rate is estimated in the literature to be between 1.2 and 1.47 % (Uchida et al. 2006a, b, c; Crouzet et al. 2010a, b, c; Thuroff et al. 2003; Blana et al. 2006). Morbidity related to repeat HIFU treatment for localized PCa has been studied on 223 patients with a re-treatment rate of 22 %. While urinary infection, bladder outlet obstruction and chronic pelvic pain did not significantly differ after one or more sessions; a significant increase was observed for urinary incontinence and impotence in the group, which required retreatment (Blana et al. 2006).

2.4.2.2 External Radiation Therapy (ERBT)

EBRT is feasible after HIFU. In a retrospective study, Pasticier et al. (2010) included patients treated with salvage radiation after HIFU. A total of 100 patients were included with a median follow-up of 33 months. Mean doses of radiation were 71.9 ± 2.38 Gys. 83 patients underwent radiation treatment only and 17 patients underwent radio-hormonal treatment. The mean time between HIFU and ERBT was 14.9 ± 11.8 months. Mean PSA before salvage ERBT was 2.1 ± 1.8 ng/mL and the nadir PSA after ERBT was 0.28 ± 0.76 ng/mL, with 17.4 ± 10.8 months to reach nadir. The incontinence rate was the same both before and 1 year after salvage ERBT. The progression-free survival rate was 76.6 % at 5 years, and was 93, 70 and 57.5 % for low, intermediate and high-risk groups, respectively. The predicting factors of failure were the PSA nadir after salvage ERBT and the time to reach nadir after ERBT. Recently, similar results were published by Ripert et al. (2011) which reported the disease free survival rate after HIFU was 3 % at 36.5 months (Phoenix criteria) and there was no major EBRT related toxicity at 12 or 24 months.

2.4.2.3 Salvage Surgery

Salvage surgery is feasible after HIFU but with higher morbidity than after primary surgery. Lawrentschuk et al. (2011) reported the results in 15 men with a rising PSA and biopsy-verified PCa after HIFU treatment. Perioperative morbidity was limited to one transfusion in a patient with a rectal injury. Pathological extensive periprostatic fibrosis was found in all patients. Postoperative PSA value was undetectable in 14 patients (93.3 %). Six out of 10 patients experienced no postoperative incontinence at 12 months, but with uniformly poor erectile function. Salvage surgery after HIFU is difficult to perform due to fibrotic reaction. In selected patients with a long life expectancy, only experienced surgeons should perform salvage surgery after HIFU.

2.4.3 Salvage HIFU After ERBT or Brachytherapy

External radiation therapy (ERBT), or brachytherapy, is used as a curative treatment of localized PCa. Several studies have shown that tumor destruction is not complete (Kirkham et al. 2008). Given these tumor recurrences, there is no clear consensus on selecting optimal therapeutic management. Most often a hormonal treatment is implemented to delay the onset of metastasis. Recovery techniques exist, including radical prostatectomy, cryotherapy and brachytherapy, but they are technically difficult and induce significant side effects. The efficacy of HIFU was evaluated as salvage treatment following radiotherapy failure to identify pre-operative predictive factors of success.

2.4.3.1 ERBT Failure

The rate of positive biopsy after External Beam Radio Therapy (ERBT) for PCa in the literature is between 25 and 32 % (Borghede et al. 1997; Zelefsky et al. 2001). There appears to be curative intents for salvage HIFU therapy for patients with a locally proven recurrence after external-beam radiation therapy (patients presenting no metastases) and for patients that are usually treated with

androgen deprivation (AD). Local control was achieved with negative biopsies in 73 % of cases, with a median PSA nadir of 0.19 ng/mL (Murat et al. 2009). A mean follow-up of 18.1 (3–122) months was reported, the overall actual 5-year specific survival rate being 84 %. The actual 3-year progression-free survival (PSA greater than nadir + 2 ng/mL, positive biopsy or salvage treatment requirement) was 53, 43 and 25 % for low- and intermediate-risk patients, respectively, according to D'Amico's risk groups. Disease progression was inversely related to pre-HIFU PSA and the use of AD during PCa management. In a recent study, we examined the outcomes of salvage HIFU in 290 consecutive patients (Crouzet et al. 2012). The mean PSA nadir post-HIFU was 1.54 ± 3.38 ng/mL (median 0.14). The estimated cancer-specific and metastasis free survival rates at 5 and 7 years were 80 % (95 % CI 72.7–88.5 %) and 79.6 % (95 % CI 73.5–86.2 %), respectively. In the multivariate analysis three factors were significantly linked to disease progression. The increase of the Progression Free Survival Rate (PFSR) with the pre-HIFU PSA level was statistically significant ($p = 0.0002$). Previous AD treatment increased the PFSR by a factor of 1.3 ($p = 0.01$), and a Gleason score over or equal to 8 increased it by a factor of 1.2 ($p = 0.01$), compared to a Gleason score of less than or equal to 6. While the technique offers promising results, it has to be weighed against the side effects. Since 2002, the Ablatherm® device has included specific acoustic parameters for salvage HIFU. The acoustic dose was adapted to the low blood flow inside the gland fibrosis induced by radiation. Concerning incontinence, 54 % of the patients had no incontinence after salvage HIFU, whereas 25 % had a grade I incontinence (no pads + grade I = 79 %). The risk of urethrorectal fistulas (URF) was only 0.4 % with the introduction of a specific treatment algorithm designed for radiation failure. The impotence rate increased from 36.9 % before salvage HIFU to 58.7 % after treatment (Berge et al. 2010). With the Sonablate®, the biochemical survival rate was 71 % at 9 month (Zaracharakis et al. 2008) and 52 % at 5 years (Uchida et al. 2010). Nevertheless, the risk–benefit ratio of salvage HIFU compares favourably with those of the other available techniques and with less morbidity and similar oncological outcomes. In this context, HIFU appears to be an effective curative treatment option for local recurrence after radiation failure.

2.4.3.2 Brachytherapy Failure

Sylvester et al. (2010) reported a 15-year biochemical relapse-free survival rate and cause-specific survival following Iodine-125 prostate brachytherapy in 215 patients: 15-year biochemical relapse free survival (BRFS) for the entire cohort was 80.4 % and the cancer specific survival rate was 84 %. There was no significant difference between the low and intermediate risk groups. Salvage surgery is a challenging procedure after Brachytherapy (Heidenreich et al. 2010). A study with the Ablatherm® device is currently being conducted in Lyon and includes 26 patients (mean age 67 years) with MRI and biopsy-proven recurrence after brachytherapy (non-published data). Nineteen of them underwent whole gland ablation and 7 underwent focal therapy (hemiablation). The mean follow-up was 19 months. The mean PSA before HIFU was 5.02 ± 4.8 ng/mL, (median PSA 0.35 ng/mL). Nine patients have undetectable PSA with no hormonal deprivation treatment, 8 needed hormonal deprivation treatment for a rising PSA and 9 are recent cases with a very short follow-up. The complication rate was high in the first 9 cases with 3 urinary incontinences (grade 3) and 1 urethrorectal fistula. For these first patients, we used the treatment acoustic parameters defined for radiation failure. Due to the high rates of rectal injury and severe incontinence, new specifically designed treatment parameters for brachytherapy failure were developed with a decrease in the acoustic dose according to the intense prostate fibrosis. Since the introduction of these new parameters, no urethrorectal fistula occurred and no rectal lesion was seen on control MRI, all while maintaining same treatment efficacy.

2.5 Focal Therapy with HIFU

Standard treatment for PCa has long been "whole-gland" therapy or radiation therapy of the entire prostate. It would be interesting, however, to destroy only the cancer foci in order to decrease

the treatment morbidity while maintaining its oncologic efficacy. This so-called 'focal therapy' can be performed using several techniques: Cryotherapy, HIFU, Brachytherapy and Interstitial Laser Therapy, either with or without photodynamic therapy (PDT). HIFU might be one of the best techniques for focal therapy because it is performed under real-time control using ultrasound or MRI. Immediate control of the necrotic area boundaries is possible using contrast agents, either with ultrasound or MRI. HIFU can also be repeated if necessary. Finally, several salvage standard curative therapies are feasible after focal HIFU.

The first condition for 'focal therapy' is to precisely determine the size and position of the different tumor foci within the gland before the ablation. Standard biopsy protocols cannot provide an accurate detection of all tumor foci. Transperineal template biopsies may increase cancer detection. However, the precision of the location within the gland of the cancers detected with this method remains difficult to assess. Additionally, template biopsy requires general anaesthesia or heavy sedation and is associated with increased morbidity, with at least 10 % of urinary retention due to oedema and bleeding (Rouviere et al. 2012a). Ideally, the simplest way to select patients for focal therapy would be to use imaging. Imaging could also be used to assess whether the target area has been correctly destroyed and to detect for local recurrences. Nonetheless, its role in focal therapy remains under debate.

2.5.1 The Current Role of Imaging in PCa Focal Therapy

In theory, imaging could be used in three different fields: To detect and localize PCa within the gland, to assess tissue destruction after HIFU ablation and to detect post-HIFU cancer recurrence.

2.5.1.1 Patient Selection and Treatment Planning: The Need for Better PCa Mapping

For many years, prostate imaging has yielded suboptimal results in PCa detection and localization, and the results of US-based techniques have been particularly disappointing (Rouvière et al. 2007).

Nevertheless, excellent results have recently been published with MRI, especially since dynamic contrast-enhanced (DCE) and diffusion-weighted (Dw) sequences have been used in addition to the classical T2-weighted (T2w) imaging. There is now a large and concordant body of literature showing that this so-called prostate 'multiparametric MRI' (mp-MRI) allows for good detection of high-grade PCas (Gleason score ≥7), with an excellent negative predictive value in candidates undergoing radical prostatectomy (Girouin et al. 2007; Villers et al. 2006; Turkbey et al. 2010; Bratan et al. 2013), but also in the more challenging population of candidates undergoing prostate biopsy (Cheikh et al. 2009; Habchi et al. 2014) (Fig. 2.4).

The detection of anterior tumors, which are usually missed by random biopsies, is also excellent (Lemaitre et al. 2009). A recent study reported the results of precise radiopathological correlations in 175 patients treated by radical prostatectomy following preoperative mp-MRI (CLARA-P database). MR detection rates for tumors of <0.5 cc, 0.5–2 cc and >2 cc were respectively 21–29 %, 43–54 % and 67–75 % for Gleason ≤6 cancers, 63 %, 82–88 % and 97 % for Gleason 7 cancers, and 80 %, 93 % and 100 % for Gleason ≥8 cancers (Bratan et al. 2013). These results suggest that mp-MRI is an excellent screening tool, with a good negative predictive value for Gleason ≥7 tumors. However, the detection of Gleason ≤6 tumors remains limited.

In addition, mp-MRI specificity needs to be improved since up to 40 % of MR abnormalities are benign (Bratan et al. 2013; Cheikh et al. 2009; Habchi et al. 2014; Lemaitre et al. 2009; Rouviere et al. 2012a, b). To improve the characterization (benign/malignant) of focal lesions detected by mp-MRI, it has been suggested that a five-level Likert score (1, definitely benign; 2, likely benign; 3, indeterminate; 4, likely malignant; 5, definitely malignant) be used. Although subjective and entirely based on the radiologist's experience, this score has been proved to significantly stratify the likelihood of malignancy of MR lesions. In the CLARA-P database, the per-

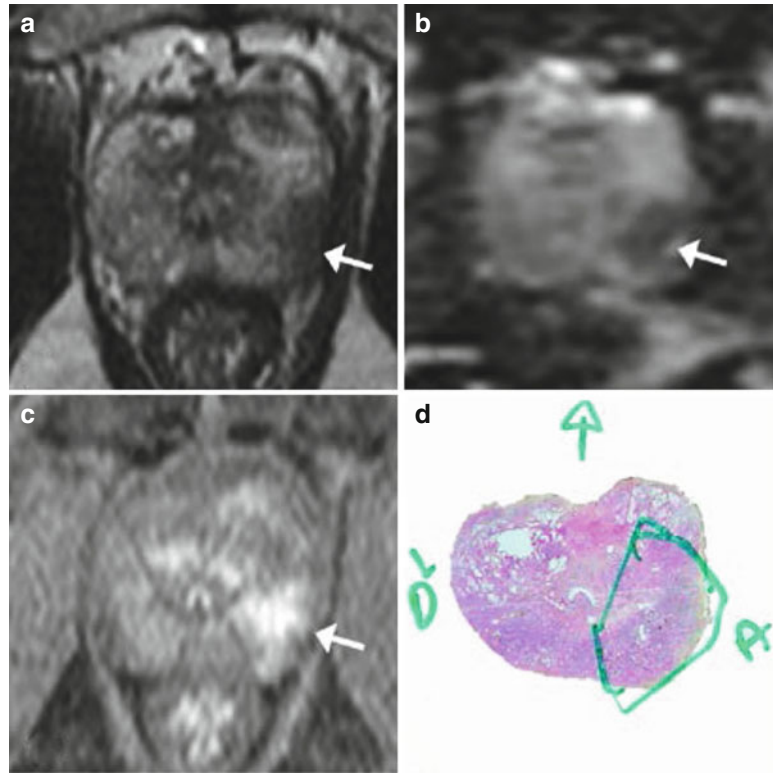

Fig. 2.4 MRI: Multiparametric MRI obtained in a 59-year old patient with a PSA level of 6 ng/mL presenting a suspicious lesion in the peripheral zone of the left mid-gland, with marked hyposignal on the T2-weighted imaging (**a**, *arrow*). Apparent Diffusion Coefficient map (**b**, *arrow*) and early and marked enhancement on Dynamic Contrast-Enhanced imaging (**c**, *arrow*). Radical prostatectomy confirmed the presence of a Gleason 8 (4+4) cancer (**d**)

centage of malignant lesions was 7–26 %, 27–41 %, 61–72 % and 97–98 % in MR lesions with a Likert score of 2/5, 3/5, 4/5 and 5/5, respectively (Bratan et al. 2013). Semi-objective scores based on more precise features have been described recently (Rouviere et al. 2012a, b; Barentsz et al. 2012; Puech et al. 2013). Particularly, the European Society of Urogenital Radiology (ESUR) endorsed the Prostate Imaging Reporting and Data System (PIRADS) that assigns a score ranging from 3 to 15 based on T2w, Dw and DCE imaging (Barentsz et al. 2012). However, it remains unclear whether these semi-objective scores perform better than the subjective Likert score. Two recent studies have even shown that, paradoxically, the Likert score yielded better inter-observer agreement than the PIRADS score (Rosenkrantz et al. 2013; Vache et al. 2014). Thus, new scores will probably be defined in the future to improve the characterization of MR abnormalities seen at mp-MRI. Some authors also used computer-aided diagnostic systems with interesting results on preliminary studies (Hambrock et al. 2013; Niaf et al. 2014).

Focal ablation also requires a good evaluation of the tumor volume. Little has been published on mp-MRI accuracy in assessing tumor volume. Several studies have, however, pointed out that mp-MRI had a tendency to underestimate tumor volume (Cornud et al. 2014; Le Nobin et al. 2014). The optimal safety margin to use around malignant lesions seen on mp-MRI remains to be determined.

After radiation therapy, mp-MRI showed excellent results in detecting and localizing local recurrences (Cornud et al. 2014; Le Nobin et al. 2014; Rouvière et al. 2004; Haider et al. 2008; Donati et al. 2013; Roy et al. 2013). Tumor detection appears easier than in untreated prostates because of the favourable contrast between recurrent cancer and post-radiation fibrosis on DCE and Dw imaging (Fig. 2.5).

In conclusion, mp-MRI is an interesting tool for detecting and localizing Gleason ≥7 PCas. Targeted biopsies of MR abnormalities remain

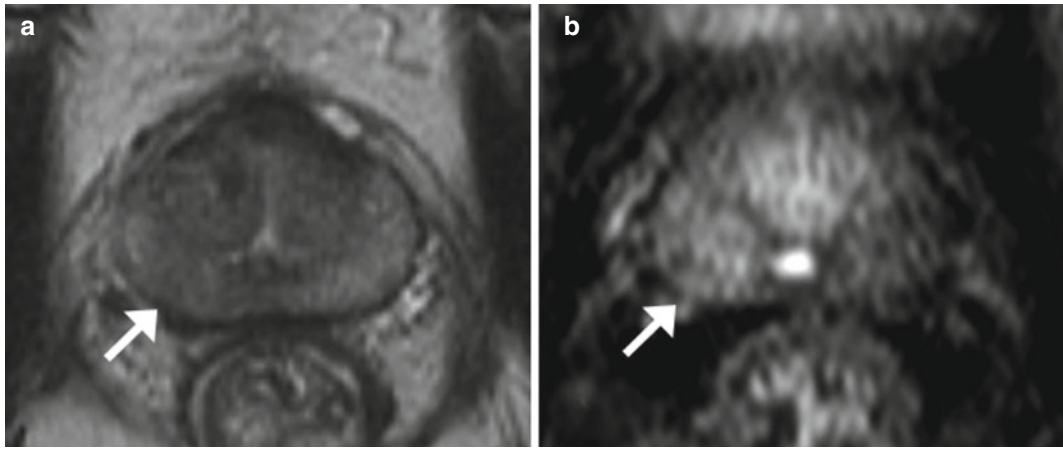

Fig. 2.5 Post-EBRT recurrence. MRI obtained in a 66-year old patient with history of external-beam radiation therapy for a Gleason 6 PCa 5 years earlier. MRI shows recurrent cancer in the right mid gland appearing as slightly hypointense on T2-weighted imaging (**a**, *arrow*) with a marked enhancement on Dynamic Contrast-Enhanced imaging (**b**, *arrow*). Targeted biopsy confirmed Gleason 7 (3 + 4) recurrent cancer in the right mid-gland

mandatory because of the lack of specificity of mp-MRI. Random biopsies of areas negative at mp-MRI are also necessary to detect less aggressive Gleason ≤6 tumors that may have been missed by mp-MRI.

2.5.1.2 Postoperative Evaluation of the Ablated Area

Ideally, imaging should indicate the amount of prostate volume destroyed at the end of the HIFU ablation session so that in the event of unsatisfactory results, additional HIFU ablation can be immediately performed. Unfortunately, transrectal ultrasound, which is used to guide the HIFU treatment, is not sufficiently accurate to indicate the post-treatment zone of tissue ablation (Rouvière et al. 2007). Gadolinium-enhanced (non-dynamic) MRI clearly reveals the treated volume as a devascularised zone (corresponding to the central core of the coagulation necrosis) surrounded by a peripheral rim of enhancement (corresponding to oedema). However, MRI cannot be obtained in the operating room (Rouvière et al. 2001; Kirkham et al. 2008).

Contrast-enhanced ultrasound (CEUS), using Sonovue™ as a contrast agent, can indicate the ablated volume immediately at the end of the treatment with an excellent correlation with MR and biopsy findings. All prostate sectors showing no enhancement of CEUS at the end of HIFU ablation can be safely considered to have been entirely destroyed. On the other hand, prostate sectors showing any degree of enhancement can be considered to contain living (benign or malignant) tissue (Rouvière et al. 2001a) (Fig. 2.6). These results should lead to immediate retreatment of the parts of the gland showing residual enhancement and that are within the range of the transducer.

2.5.1.3 Detection of Post-HIFU Local Recurrences

After focal HIFU ablation, the residual prostate is composed of scarred fibrosis and benign prostate tissue. Given that local recurrences (or residual cancers) after HIFU ablation can be treated by a second session of HIFU ablation or by radiation therapy (Rivière et al. 2010), it is imperative that they be detected early. The precise location of these recurrences can also help in selecting the salvage treatment (*e.g.,* anterior recurrences, which are more difficult to treat using HIFU may be better treated by radiation therapy or cryotherapy). Even though Colour Doppler can sensitize transrectal ultrasound (TRUS) (Rouvière et al. 2006), US-based techniques are not accurate enough to detect early local recurrences and guide the biopsy.

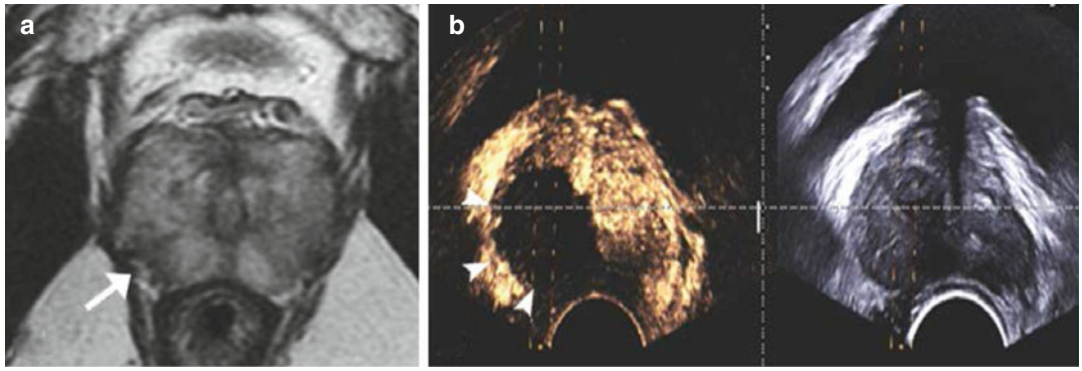

Fig. 2.6 CEUS. Images obtained in a 62-year old patient referred for focal HIFU ablation of a Gleason 6 PCa of the right mid-gland. The tumor was well visible on T2-weighted imaging (**a**, *arrow*). Contrast-enhanced Ultrasound performed after focal HIFU ablation showed a large devascularized area within the right lobe around the tumor area (**b**, *arrowheads*)

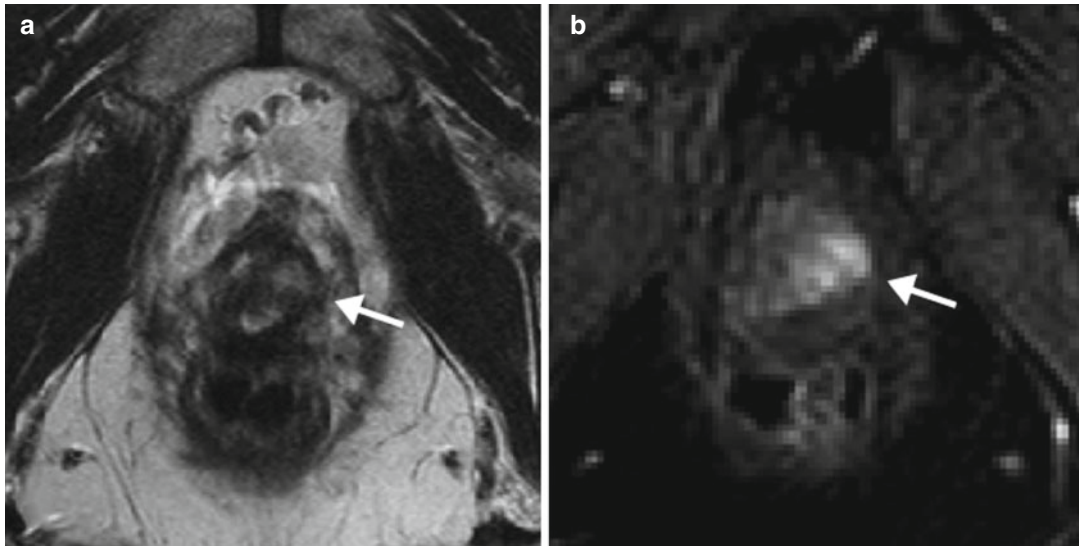

Fig. 2.7 Post-HIFU recurrence. MRI obtained in a 70-year old patient with a history of whole-gland HIFU for a Gleason 6 PCa 4 years earlier. MRI indicates early and marked enhancement in the left base of the residual gland (**b**, *arrow*). This area is difficult to analyze on T2-weighted imaging (**a**, *arrow*) because the gland appears as diffusely heterogeneous. Targeted biopsy confirmed Gleason 6 recurrent cancer in the left base

MRI, in particularly DCE MRI, seems to provide early detection and accurate localization of recurrent cancers that enhance earlier and more than post-HIFU fibrosis (Ben Cheikh et al. 2008, Rouvière et al. 2010) (Fig. 2.7). However, DCE MRI lacks specificity. It is indeed difficult to distinguish recurrent cancer from residual benign prostatic hyperplasia (BPH) tissue. In a retrospective study of 65 patients with biochemical recurrence after HIFU ablation performed at our institution, neither the enhancement pattern nor the apparent diffusion coefficient (ADC) was able to significantly distinguish BPH nodules from recurrent cancers. This was even though cancer tissues had, on average, higher wash-in rates, lower wash-out rates and lower ADCs (unpublished results). So to date, all patients with rising PSA after HIFU ablation should undergo

prostate MRI, and all areas with early and intense enhancement should be biopsied to distinguish cancers from residual BPH tissue.

2.5.2 Outcomes of HIFU Focal Therapy

2.5.2.1 Sub-total HIFU Strategy

In 2008, Muto et al. (2008) reported the outcomes of 29 patients treated with the Sonablate® device. In selected patients whose cancer was confined to only one lobe by multi regional biopsies, the total peripheral zone and half a portion of the transitional zone were ablated. The prostate volume decreased from 35.8 to 30.3 cc, and the PSA level decreased from 5.36 ± 5.89 ng/mL to 1.52 ± 0.92 at 36 months. Twenty-eight patients underwent control biopsies 6 months after the procedure: Residual cancer foci were found in 3 patients (10.7 %). Seventeen patients underwent control biopsies 12 months after the procedure: Residual cancer foci were found in 4 patients (23.5 %); only one patient had urethral stricture. No significant differences were noted in the 2 years. Disease-free survival rates at 2 years for low and intermediate risk patients treated with this focal therapy strategy were 83.3 % and 53.6 %, respectively. The frequency of urethral stricture and symptomatic tract infection were 4 % and 4 %, respectively. No significant change was found on IPSS score and Maximal Flow Rate before and 12 months after the procedure. No information was provided about potency.

2.5.2.2 Hemi-Ablation Strategy (UK Experience)

A short series of prostate hemi-ablations with HIFU using the Sonablate® device was published (Ahmed et al. 2011). Inclusion criteria were men with low-moderate risk (Gleason = 7, PSA = 15 μg/mL), unilateral PCa (= T2bN0M0) on TRUS biopsy. All were treated using transrectal HIFU incorporating the entire positive hemi-prostate up to the urethra. A total of 20 patients (mean age 60.4 years) were treated. Regarding the cohort, 25 % had low risk and 75 % had intermediate risk cancer. The mean PSA pre-HIFU was 7.3 ng/mL. 95 % were pad-free. Erection sufficient for penetrative sex occurred in 95 % of the patients. Mean PSA decreased to 1.5 ± 1.3 ng/mL at 12 months. A total of 89 % of the patients had no histological evidence of any cancer. Two patients (11.1 %) had positive protocol biopsy at 6 months with residual 1 mm Gleason 3 + 3: One elected for retreatment and the other active surveillance. Eighty-nine% achieved the trifecta status.

2.5.2.3 Zonal Treatment (Belgium Experience)

Van Velthoven et al. (2014) reported long-term results of 31 patients with unilateral organ-confined PCa treated by "Zonal" HIFU from January 2007 to June 2011. The biochemical recurrence-free survival rate at 3 years was 82.7 % (Phoenix criteria). All patients were continent and 55 % had erectile function sufficient for penetration.

2.5.2.4 Hemi-ablation Strategy (French Experience)

The French Urological Association (AFU) has started a multi-institutional study to evaluate hemi-ablation with HIFU as a primary treatment for patients >50 years, T1C or T2A, PSA <10 ng/mL, Gleason 6 or 7 (3 + 4), with no more than 2 contiguous biopsies in no more than one lobe after MRI (random and targeted biopsies). To be included the tumor must be >6 mm from the apex and >5 mm from the midline. Only one prostatic lobe is treated. Preliminary results are available (AFU Congress 2014, Las Vegas, USA): 110 patients were treated; mean age 64.8 years {50–78}, mean PSA value 5.42 ± 3 ng/mL, mean prostate volume 39 ± 17 cc. The Glean sum was ≤ 6 in 78 patients (71 %) and = 7 in 32 patients (29 %). The PSA nadir value was 1.93 ± 1.62 ng/mL and the PSA at 12 months was 2.42 ± 2.08 ng/mL (78 patients). Control biopsies were performed in 91 patients. Biopsies were negative in 57 patients (63 %). Recurrence was found in 34 patients (37 %): Only in 13 patients in the treated lobe (14 %), 20 patients in the contralateral lobe (22 %) and 1 patient in both lobes (1 %). The Gleason sum of recurrence was 6 (24 patients), 7 (8 patients) and not determined in 1 patient. The additional therapies were: Redo-HIFU (9

patients), active surveillance (18 patients), external beam radiation therapy (4 patients), radical surgery (4 patients) and AD (1 patient). Grade 1 incontinence occurred in 2 patients (2 %) and erectile dysfunction (partial loss of potency with IIEF5 score <17) was observed in 13 patients out of 53 patients, with an IIEF5 score ≥17 before HIFU (24 %).

2.5.2.5 Focal Therapy (Uni- and Multi-focal Strategy: UK Experience)

(Ahmed et al. 2012b) reported preliminary results from selective focal ablation of single-focal and multi-focal cancer in 42 patients (45–80 years) eligible for a prospective development study. Eligibility entailed: Low-risk to high-risk localized PCa, PSA ≤15 ng/mL, Gleason score ≤4 + 3, stage ≤ T2, no previous AD or PCa treatment, ability to safely undergo multi-parametric MRI focal therapy using high-intensity focused ultrasound (HIFU). HIFU was then delivered to all known cancer lesions, including a margin of normal tissue, identified on multi-parametric MRI template prostate-mapping. No histological evidence of cancer was identified in 30 of 39 men biopsied at 6 months (77 %); 36 (92 %) were free of clinically significant cancer. After retreatment in four men, 39 of 41 (95 %) had no evidence of disease on multi-parametric MRI at 12 months. All 40 men that were pad-free at baseline were still pad-free by 3 months, and they maintained pad-free continence at 12 months. Of the 35 men with good baseline function, 31 (89 %, 95 % CI 73–97) had erections sufficient for penetration 12 months after focal therapy. For the authors, this study demonstrated that focal therapy of individual PCa lesions, whether multifocal or single-focal, leads to a low rate of genitourinary side effects and an encouraging rate of early absence of clinically significant PCa.

2.5.2.6 Focal Therapy (Edouard Herriot Experience)

Ten patients with mono-focal PCa were treated between March 2013 and January 2014. The HIFU treatment process was performed with the Focal One device using a 6 mm safety margin around the tumor. Contrast-enhanced MRI was performed at day 2 after HIFU, and control biopsies guided with contrast-enhanced ultrasound imaging were performed 1 month after HIFU inside and on the edge of the treated area. The mean age of patients was 65.8 ± 5.5 years. The clinical stage was T1 for 9 patients and T2a for 1 patient. The Gleason sum was 6 for 7 patients and 7 (3 + 4) for 3 patients. The PSA value was 4.47 ± 3.7 ng/mL and the mean Prostate Volume was 50 ± 23 cc. The mean treated volume was 14 cc (7.3–20.4) 28 % of prostate gland. The mean nadir PSA value was 3.46 ± 2 ng/mL. In all patients, targeted biopsies inside the treated area performed on day 30 after the HIFU session demonstrated a complete destruction of the targeted tumor. No incontinence was observed. A partial loss of potency (IIEF <17) occurred in 2 patients (20 %). The Focal One device is able to achieve complete destruction of small PCa using an elastic magnetic resonance-ultrasound (MR-US) registration system for tumor location and HIFU treatment planning. A multicenter trial is in progress (30 patients).

2.5.2.7 Hemi-Salvage HIFU for Radio-Recurrent PCa

Whole gland salvage HIFU treatment offers acceptable cancer control, but carries a risk of severe urinary incontinence in at least 20 % of cases and reduction of Quality of Life (QoL). In patients with unilateral local relapse, focal HIFU is feasible. Two studies reported favourable outcomes in selected patients. The results from these studies indicated that focal salvage therapy is a potential strategy for unilateral recurrence after radiotherapy that may reduce the side effects resulting from whole-gland salvage therapies.

2.5.2.7.1 UK Pilot Study (Ahmed et al. 2012a, b)

Thirty-nine patients received focal salvage therapy for localized recurrence after external beam radiotherapy. Multi-parametric magnetic resonance imaging studies, combined with transperineal template prostate mapping biopsies or transrectal biopsies, were used to localize disease. Hemi-Salvage HIFU (HSH) was performed under spinal

or general anaesthesia using the Sonablate 500® device. The mean pre-HIFU PSA level was 4.6 ng/mL. The median follow-up was 17 months. The actuarial progression-free survival rate was 49 % at 2 years according to the Phoenix criteria. Index of Erectile Function-5 scores decreased from a median of 18 ± 16 to 13 ± 21 at 6 months, demonstrating worsening deterioration in function. The pad-free, leak-free continence status was 64 %, and the pad-free rate was 87.2 % at last follow-up. One recto-urethral fistula occurred and spontaneously resolved with urinary and bowel diversion.

2.5.2.7.2 Multicenter Study (Baco et al. 2014)

Between 2009 and 2012, 48 patients were prospectively enrolled in two European centers. Inclusion criteria included biochemical recurrence following primary radiotherapy positive magnetic resonance imaging, and ≥1 positive biopsy in only one lobe. HemiSalvage HIFU (HSH) was performed under spinal or general anaesthesia using the Ablatherm® Integrated Imaging device. Patients with obstructive voiding symptoms at the time of treatment underwent an endoscopic bladder neck resection or incision under the same anaesthesia to prevent the risk of post-operative obstruction.

Post HSH PSA nadir was (mean ± SD) 0.69 ± 0.83 ng/mL. Disease progression occurred in 16/48 (33 %). Of these, 4 had local recurrence in the untreated lobe and 4 bilaterally; 6 developed metastases, and 2 had rising PSA without local recurrence or radiologically proven metastasis. Progression-free survival rates (PFSR) at 12, 18, and 24 months were 83 %, 64 %, and 52 %, respectively. Severe incontinence occurred in 4/48 (8 %), with 8/48 (17 %) requiring one pad a day, and 36/48 (75 %) were pad-free. The IIEF-5 score significantly decreased ($p < 0.001$) from 11.2 ± 8.6 to 7.0 ± 5.8. Osteitis occurred in two patients.

Conclusion

HIFU is now used to treat PCa in clinical practice and in different clinical situations. The strengths and weaknesses of the technique have now been identified. The outcomes achieved for primary care patients seem close to those obtained by radiation therapy. HIFU does not represent a therapeutic impasse: EBRT is a safe salvage option after HIFU failure and salvage surgery is possible in young and motivated patients. On the other hand, HIFU has a considerable potential for local recurrence after radiation failure. Recently, some early experiences with focal therapy suggest that HIFU provides an excellent opportunity to achieve local control of the disease in low-risk PCa and in early-identified local relapse after EBRT.

References

Ahmed HU, Cathcart P, McCartan N, Kirkham A, Allen C, Freeman A, Emberton M (2012a) Focal salvage therapy for localized prostate cancer recurrence after external beam radiotherapy: a pilot study. Cancer 118:4148–4155

Ahmed HU, Hindley RG, Dickinson L, Freeman A, Kirkham AP, Sahu M, Scott R, Allen C, Van der Meulen J, Emberton M (2012b) Focal therapy for localised unifocal and multifocal prostate cancer: a prospective development study. Lancet Oncol 13: 622–632

Ahmed HU, Zacharakis E, Dudderidge T, Armitage JN, Scott R, Calleary J, Illing R, Kirkham A, Freeman A, Ogden C, Allen C, Emberton M (2009) High-intensity-focused ultrasound in the treatment of primary prostate cancer: the first UK series. Br J Cancer 101:19–26

AURO (2009) The association of italian urologists: guidelines, Prostate Cancer PCa

Baco E, Gelet A, Crouzet S, Rud E, Rouvière O, Tonoli-Catez H, Berge V, Chapelon JY, Eggesbø HB (2014) Hemi salvage high-intensity focused ultrasound (HIFU) in unilateral radiorecurrent prostate cancer PCa: a prospective two-centre study. BJU Int 114: 532–540

Barentsz JO, Richenberg J, Clements R, Choyke P, Verma S, Villeirs G, Rouviere O, Logager V, Futterer JJ (2012) ESUR prostate MR guidelines 2012. Eur Radiol 22:746–757

Beerlage HP, van Leenders GJ, Oosterhof GO, Witjes JA, Ruijter ET, van de Kaa CA, Debruyne FM, de la Rosette JJ (1999) High-intensity focused ultrasound (HIFU) followed after one to two weeks by radical retropubic prostatectomy: results of a prospective study. Prostate 39:41–46

Ben Cheikh A, Girouin N, Ryon-Taponnier P, Mège-Lechevallier F, Gelet A, Chapelon JY, Lyonnet D, Rouvière O (2008) MR detection of local prostate cancerPCa recurrence after transrectal high-intensity focused US treatment: preliminary results. J Radiol 89:571–577

Berge V, Baco E, Karlsen SJ (2010) A prospective study of salvage high-intensity focused ultrasound for locally radiorecurrent prostate cancer: early results. Scand J Urol Nephrol 44:223–227

Bill-Axelson A, Holmberg L, Filen F, Ruutu M, Garmo H, Busch C, Haggman M, Andersson SO, Bratell S, Spangberg A, Palmgren J, Adami HO, Johansson JE (2008) Radical prostatectomy versus watchful waiting in localized prostate cancer: the Scandinavian prostate cancer group-4 randomized trial. J Natl Cancer Inst 100:1144–1154

Blana A, Brown SCW, Chaussy C, Conti GN, Eastham JA, Ganzer R, Murat FJ, Rebillard X, Rewcastle JC, Robertson CN, Tueroff S, Ward JF, Gelet A (2009) Primary prostate HIFU without pretreatment hormone therapy: biochemical survival of 468 patients tracked with the @-registry. J Urol 181:227

Blana A, Murat FJ, Walter B, Thuroff S, Wieland WF, Chaussy C, Gelet A (2008a) First analysis of the long-term results with transrectal HIFU in patients with localised prostate cancer. Eur Urol 53:1194–1201

Blana A, Rogenhofer S, Ganzer R, Lunz JC, Schostak M, Wieland WF, Walter B (2008b) Eight years' experience with high-intensity focused ultrasonography for treatment of localized prostate cancer. Urology 72:1329–1333; discussion 1333–13334

Blana A, Rogenhofer S, Ganzer R, Wild PJ, Wieland WF, Walter B (2006) Morbidity associated with repeated transrectal high-intensity focused ultrasound treatment of localized prostate cancer. World J Urol 24: 585–590

Borghede G, Aldenborg F, Wurzinger E, Johansson KA, Hedelin H (1997) Analysis of the local control in lymph-node staged localized prostate cancer treated by external beam radiotherapy, assessed by digital rectal examination, serum prostate-specific antigen and biopsy. Br J Urol 80:247–255

Bratan F, Niaf E, Melodelima C, Chesnais AL, Souchon R, Mège-Lechevallier F, Colombel M, Rouvière O (2013) Influence of imaging and histological factors on prostate cancer detection and localisation on multiparametric MRI: a prospective study. Eur Radiol 23:2019–2029

Challacombe BJ, Murphy DG, Zakri R, Cahill DJ (2009) High-intensity focused ultrasound for localized prostate cancer: initial experience with a 2-year follow-up. BJU Int 104:200–204

Chapelon JY, Margonari J, Vernier F, Gorry F, Ecochard R, Gelet A (1992) In vivo effects of high-intensity ultrasound on prostatic adenocarcinoma Dunning R3327. Cancer Res 52:6353–6357

Chaussy C, Thuroff S, Rebillard X, Gelet A (2005) Technology insight: high-intensity focused ultrasound for urologic cancers. Nat Clin Pract Urol 2:191–198

Chaussy C, Thuroff S (2001) Results and side effects of high-intensity focused ultrasound in localized prostate cancer. J Endourol 15:437–440; discussion 47–48

Cheikh AB, Girouin N, Colombel M, Maréchal JM, Gelet A, Bissery A, Rabilloud M, Lyonnet D, Rouvièrre O (2009) Evaluation of T2-weighted and dynamic contrast-enhanced MRI in localizing prostate cancer before repeat biopsy. Eur Radiol 19:770–778

Chopra R, Tang K, Burtnyk M, Boyes A, Sugar L, Appu S, Klotz L, Bronskill M (2009) Analysis of the spatial and temporal accuracy of heating in the prostate gland using transurethral ultrasound therapy and active MR temperature feedback. Phys Med Biol 54:2615–2633

Chopra R, Colquhoun A, Burtnyk M, N'djin WA, Kobelevskiy I, Boyes A, Siddiqui L, Foster H, Sugar L, Haider MA, Bronskill M, Klotz L (2012) MR imaging-controlled transurethral ultrasound therapy for conformal treatment of prostate tissue: initial feasibility in humans. Radiology 265:303–313

Cornud F, Khoury G, Bouazza N, Beuvon F, Peyromaure M, Flam T, Zerbib M, Legmann P, Delongchamps NB (2014) Tumor target volume for focal therapy of prostate cancer: does multiparametric MRI allow for a reliable estimation? J Urol 191:1272–1279

Crouzet S, Chapelon JY, Rouvière O, Mege-Lechevallier F, Colombel M, Tonoli-Catez H, Martin X, Gelet A (2014) Whole-gland ablation of localized prostate cancer with high-intensity focused ultrasound: oncologic outcomes and morbidity in 1002 patients. Eur Urol 65:907–914

Crouzet S, Murat FJ, Pasticier G, Cassier P, Chapelon JY, Gelet A (2010a) High intensity focused ultrasound (HIFU) for prostate cancer: current clinical status, outcomes and future perspectives. Int J Hyperthermia 26:796–803

Crouzet S, Murat FJ, Pommier P, Poissonnier L, Pasticier G, Rouviere O, Chapelon JY, Rabilloud M, Belot A, Mège-Lechevallier F, Tonoli-Catez H, Martin X, Gelet A (2012) Locally recurrent prostate cancer after initial radiation therapy: early salvage high-intensity focused ultrasound improves oncologic outcomes. Radiother Oncol 105:198–202

Crouzet S, Murat FJ, Rouviere O, Poissonnier L, Martin X, Colombel M et al (2010b) Oncological outcomes of HIFU for localized prostate cancer in 880 consecutive patients. BJU Int 58:559–566

Crouzet S, Poissonnier L, Murat FJ, Pasticier G, Rouviere O, Mege-Lechevallier F, Chapelon JY, Martin X, Gelet A (2011) Outcomes of HIFU for localised prostate cancer using the Ablatherm Integrate Imaging® device. Prog Urol 21:191–197

Crouzet S, Rebillard X, Chevallier D, Rischmann P, Pasticier G, Garcia G, Rouvière O, Chapelon JY, Gelet A (2010c) Multicentric oncologic outcomes of high-intensity focused ultrasound for localized prostate cancer in 803 patients. Eur Urol 58:559–566

Donati OF, Jung SI, Vargas HA, Gultekin DH, Zheng J, Moskowitz CS, Hricak H, Zelefsky MJ, Akin O (2013) Multiparametric prostate MR imaging with T2-weighted, diffusion-weighted, and dynamic contrast-enhanced sequences: are all pulse sequences necessary to detect locally recurrent prostate cancer after radiation therapy? Radiology 268:440–450

Ficarra V, Antoniolli SZ, Novara G, Parisi A, Fracalanza S, Martignoni G, Artibani W (2006) Short-term outcome after high-intensity focused ultrasound in the

treatment of patients with high-risk prostate cancer. BJU Int 98:1193–1198

Ahmed HU, Freeman A, Kirkham A, Sahu M, Scott R, Allen C, Van der Meulen J, Emberton M (2011) Focal therapy for localized prostate cancer: a phase I/II trial. J Urol 185:1246–1254

Ganzer R, Fritsche HM, Brandtner A, Bründl J, Koch D, Wieland WF, Blana A (2013) Fourteen-year oncological and functional outcomes of high-intensity focused ultrasound in localized prostate cancer. BJU Int 112:322–329

Ganzer R, Rogenhofer S, Walter B, Lunz JC, Schostak M, Wieland WF, Blana A (2008) PSA nadir is a significant predictor of treatment failure after high-intensity focussed ultrasound (HIFU) treatment of localised prostate cancer. Eur Urol 53:547–553

Gelet A, Chapelon JY, Bouvier R, Pangaud C, Lasne Y (1999) Local control of prostate cancer by transrectal high intensity focused ultrasound therapy: preliminary results. J Urol 161:156–162

Gelet A, Chapelon JY, Bouvier R, Rouviere O, Lasne Y, Lyonnet D, Dubernard JM (2000) Transrectal high-intensity focused ultrasound: minimally invasive therapy of localized prostate cancer. J Endourol 14: 519–528

Gelet A, Chapelon JY, Bouvier R, Souchon R, Pangaud C, Abdelrahim AF, Cathignol D, Dubernard JM (1996) Treatment of prostate cancer with transrectal focused ultrasound: early clinical experience. Eur Urol 29:174–183

Gelet A, Chapelon JY, Margonari J, Theillere Y, Gorry F, Cathignol D, Blanc E (1993a) Prostatic tissue destruction by high-intensity focused ultrasound: experimentation on canine prostate. J Endourol 7:249–253

Gelet A, Chapelon JY, Margonari J, Theillere Y, Gorry F, Souchon R, Bouvier R (1993b) High-intensity focused ultrasound experimentation on human benign prostatic hypertrophy. Eur Urol 23(Suppl 1):44–47

Girouin N, Mege-Lechevallier F, Tonina Senes A, Bissery A, Rabilloud M, Maréchal JM, Colombel M, Lyonnet D, Rouvière O (2007) Prostate dynamic contrast-enhanced MRI with simple visual diagnostic criteria: is it reasonable? Eur Radiol 17:1498–1509

Habchi H, Bratan F, Paye A, Pagnoux G, Sanzalone T, Mège-Lechevallier F, Crouzet S, Colombel M, Rabilloud M, Rouvière O (2014) Value of prostate multiparametric magnetic resonance imaging for predicting biopsy results in first or repeat biopsy. Clin Radiol 69:e120–128

Haider MA, Chung P, Sweet J, Toi A, Jhaveri K, Ménard C, Warde P, Trachtenberg J, Lockwood G, Milosevic M (2008) Dynamic contrast-enhanced magnetic resonance imaging for localization of recurrent prostate cancer after external beam radiotherapy. Int J Radiat Oncol Biol Phys 70:425–430

Hambrock T, Vos PC, Hulsbergen-van de Kaa CA, Barentsz JO, Huisman HJ (2013) Prostate cancer: computer-aided diagnosis with multiparametric 3-T MR imaging – effect on observer performance. Radiology 266:521–530

Heidenreich A, Richter S, Thuer D, Pfister D (2010) Prognostic parameters, complications, and oncologic and functional outcome of salvage radical prostatectomy for locally recurrent prostate cancer after 21st-century radiotherapy. Eur Urol 57:437–443

Kennedy JE, Ter Haar GR, Cranston D (2003) High intensity focused ultrasound: surgery of the future? Br J Radiol 76:590–599

Kirkham AP, Emberton M, Hoh IM, Illing RO, Freeman AA, Allen C (2008) MR imaging of prostate after treatment with high-intensity focused ultrasound. Radiology 246:833–844

Klotz L, Zhang L, Lam A, Nam R, Mamedov A, Loblaw A (2010) Clinical results of long-term follow-up of a large, active surveillance cohort with localized prostate cancer. J Clin Oncol 28:126–131

Koch MO, Gardner T, Cheng L, Fedewa RJ, Seip R, Sanghvi NT (2007) Phase I/II trial of high intensity focused ultrasound for the treatment of previously untreated localized prostate cancer. J Urol 178:2366–2370; discussion 70–71

Lawrentschuk N, Finelli A, Van der Kwast TH, Ryan P, Bolton DM, Fleshner NE, Trachtenberg J, Klotz L, Robinette M, Woo H (2011) Salvage radical prostatectomy following primary high intensity focused ultrasound for treatment of prostate cancer. J Urol 185: 862–868

Le Nobin J, Orczyk C, Deng FM, Melamed J, Rusinek H, Taneja SS, Rosenkrantz AB (2014) Prostate tumor volumes: agreement between MRI and histology using novel co-registration software. BJU Int 114(6b): E105–12

Lee HM, Hong JH, Choi HY (2007) High-intensity focused ultrasound therapy for clinically localized prostate cancer. Prostate Cancer Prostatic Dis 9:439–443

Lemaitre L, Puech P, Poncelet E, Bouyé S, Leroy X, Biserte J, Villers A (2009) Dynamic contrast-enhanced MRI of anterior prostate cancer: morphometric assessment and correlation with radical prostatectomy findings. Eur Radiol 19:470–480

Li LY, Lin Z, Yang M, Gao X, Xia TL, Ding T (2010) Comparison of penile size and erectile function after high-intensity focused ultrasound and targeted cryoablation for localized prostate cancer: a prospective pilot study. J Sex Med 7:3135–3142

Lynn JG, Putnam TJ (1944) Histology of cerebral lesions produced by focused ultrasound. Am J Pathol 20: 637–649

Lynn JG, Zwemer RL, Chick AJ, Miller AE (1942) A new method for the generation and use of focused ultrasound in experimental biology. J Gen Physiol 26:179–193

Madersbacher S, Kratzik C, Szabo N, Susani M, Vingers L, Marberger M (1993) Tissue ablation in benign prostatic hyperplasia with high-intensity focused ultrasound. Eur Urol 23(Suppl 1):39–43

Maestroni U, Ziveri M, Azzolini N, Dinale F, Ziglioli F, Campaniello G, Frattini A, Ferretti S (2008) High Intensity Focused Ultrasound (HIFU): a useful alternative choice in prostate cancer treatment. Preliminary results. Acta Biomed 79:211–216

Mearini L, D'Urso L, Collura D, Zucchi A, Costantini E, Formiconi A, Bini V, Muto G, Porena M (2009) Visually directed transrectal high intensity focused ultrasound for the treatment of prostate cancer: a preliminary report on the Italian experience. J Urol 181:105–111; discussion 11-2

Misrai V, Roupret M, Chartier-Kastler E, Comperat E, Renard-Penna R, Haertig A, Bitker MO, Richard F, Conort P (2008) Oncologic control provided by HIFU therapy as single treatment in men with clinically localized prostate cancer. World J Urol 26:481–485

Murat FJ, Poissonnier L, Rabilloud M, Belot A, Bouvier R, Rouviere O, Chapelon JY, Gelet A (2009) Mid-term results demonstrate salvage high-intensity focused ultrasound (HIFU) as an effective and acceptably morbid salvage treatment option for locally radiorecurrent prostate cancer. Eur Urol 55:640–647

Muto S, Yoshii T, Saito K, Kamiyama Y, Ide H, Horie S (2008) Focal therapy with high-intensity-focused ultrasound in the treatment of localized prostate cancer. Jpn J Clin Oncol 38:192–199

Niaf E, Lartizien C, Bratan F, Roche L, Rabilloud M, Miège-Lechevallier F, Rouvière O (2014) Prostate focal peripheral zone lesions: characterization at multiparametric MR imaging – influence of a computer-aided diagnosis system. Radiology 271:761–769

Pasticier G, Riviere J, Wallerand H, Robert G, Bernhard JC, Ferriere JM, Ballanger P, Richaud P, Maire J, Chapet O, Gelet A (2010) Salvage Radiotherapy (SRT) for local recurrence of prostate adenocarcinoma after primary treatment with High Intensity Focused Ultrasound (HIFU): first series of 100 patients. ASCO Genitourinary Cancer Symposium San Francisco, California 2010;5–7

Poissonnier L, Chapelon JY, Rouviere O, Curiel L, Bouvier R, Martin X, Dubernard JM, Gelet A (2007) Control of prostate cancer by transrectal HIFU in 227 patients. Eur Urol 51:381–387

Puech P, Rouviere O, Renard-Penna R, Villers A, Devos P, Colombel M, Bitker MO, Leroy X, Mège-Lechevallier F, Comperat E, Ouzzane A, Lemaitre L (2013) Prostate cancer diagnosis: multiparametric MR-targeted biopsy with cognitive and transrectal US-MR fusion guidance versus systematic biopsy – prospective multicenter study. Radiology 268:461–469

Rebillard X, Davin JL, Soulie M (2003) Treatment by HIFU of prostate cancer: survey of literature and treatment indications. Prog Urol 13:1428–1456

Ripert T, Bayoud Y, Messaoudi R, Menard J, Azemar MD, Duval F, Nguyen TD, Staerman F (2011) Salvage radiotherapy after high-intensity focused ultrasound treatment for localized prostate cancer: feasibility, tolerance and efficacy. Can Urol Assoc J 1:1–5

Riviere J, Bernhard JC, Robert G, Wallerand H, Deti E, Maurice-Tison S, Ardiet JM, Maire JP, Richaud P, Ferriere JM, Ballanger P, Gelet A, Pasticier G (2010) Salvage radiotherapy after high-intensity focussed ultrasound for recurrent localised prostate cancer. Eur Urol 58:567–573

Rosenkrantz AB, Kim S, Lim RP, Hindman N, Deng FM, Babb JS, Taneja SS (2013) Prostate cancer localization using multiparametric MR imaging: comparison of prostate imaging reporting and data system (PI-RADS) and likert scales. Radiology 269:482–492

Rouviere O, Gelet A, Crouzet S, Chapelon JY (2012a) Prostate focused ultrasound focal therapy – imaging for the future. Nat Rev Clin Oncol 9:721–727

Rouviere O, Girouin N, Glas L, Ben Cheikh A, Gelet A, Mège-Lechevallier F, Rabilloud M, Chapelon JY, Lyonnet D (2010) Prostate cancer transrectal HIFU ablation: detection of local recurrences using T2-weighted and dynamic contrast-enhanced MRI. Eur Radiol 20:48–55

Rouvière O, Glas L, Girouin N, Mège-Lechevallier F, Gelet A, Dantony E, Rabilloud M, Chapelon JY, Lyonnet D (2001a) Transrectal HIFU ablation of prostate cancer: assessment of tissue destruction with contrast-enhanced ultrasound. Radiology 259:583–591

Rouvière O, Lyonnet D, Raudrant A, Colin-Pangaud C, Chapelon JY, Bouvier R, Dubernard JM, Gelet A (2001b) MRI appearance of prostate following transrectal HIFU ablation of localized cancer. Eur Urol 40:265–274

Rouviere O, Mège-Lechevallier F, Chapelon JY, Gelet A, Bouvier R, Boutitite F, Lyonnet D (2006) Evaluation of color doppler in guiding prostate biopsy after HIFU ablation. Eur Urol 50:490–497

Rouviere O, Papillard M, Girouin N, Boutier R, Rabilloud M, Riche B, Mège-Lechevallier F, Colombel M, Gelet A (2012b) Is it possible to model the risk of malignancy of focal abnormalities found at prostate multiparametric MRI? Eur Radiol 22:1149–1157

Rouviere O, Souchon R, Salomir R, Gelet A, Chapelon JY, Lyonnet D (2007) Transrectal high-intensity focused ultrasound ablation of prostate cancer: Effective treatment requiring accurate imaging. Eur J Radiol 63:317–327

Rouviere O, Valette O, Grivolat S, Colin-Pangaud C, Bouvier R, Chalepon JY, Gelet A, Lyonnet D (2004) Recurrent prostate cancer after external beam radiotherapy: value of contrast-enhanced dynamic MRI in localizing intraprostatic tumor – correlation with biopsy findings. Urology 63:922–927

Roy C, Foudi F, Charton J, Jung M, Lang H, Saussine C, Jacqmin D (2013) Comparative sensitivities of functional MRI sequences in detection of local recurrence of prostate carcinoma after radical prostatectomy or external-beam radiotherapy. AJR Am J Roentgenol 200:W361–368

Shoji S, Nakano M, Nagata Y, Usui Y, Terachi T, Uchida T (2010) Quality of life following high-intensity focused ultrasound for the treatment of localized prostate cancer: a prospective study. Int J Urol 17:715–719

Siddiqui K, Chopra R, Vedula S, Sugar L, Haider M, Boyes A, Musquera M, Bronskill M, Klotz L (2010) MRIguided transurethral ultrasound therapy of the prostate gland using real-time thermal mapping: initial studies. Urology 76:1506–1551

Sylvester JE, Grimm PD, Wong J, Galbreath RW, Merrick G, Blasko JC (2010) Fifteen-year biochemical relapse-free survival, cause-specific survival, and overall survival following I(125) prostate brachytherapy in clinically localized prostate cancer: Seattle experience. Int J Radiat Oncol Biol Phys 81:376–381

Tavakkoli J, Sanghvi NT (2011) Ultrasound-guided HIFU and thermal ablation. In: Frenkel V (ed) Therapeutic ultrasound: mechanisms to applications, Chapter 6. Nova Science Publishers, Hauppauge, pp 137–161

Thuroff S, Chaussy C, Vallancien G, Wieland W, Kiel HJ, Le Duc A, Desgrandchamps F, De La Rosette JJ, Gelet A (2003) High-intensity focused ultrasound and localized prostate cancer: efficacy results from the European multicentric study. J Endourol 17:673–677

Thüroff S, Chaussy C (2013) Evolution and outcomes of 3 MHz high intensity focused ultrasound therapy for localized prostate cancer during 15 years. J Urol 190: 702–710

Turkbey B, Pinto PA, Mani H, Bernardo M, Pang Y, McKinney YL, Khurana K, Ravizzini GC, Albert PS, Merino MJ, Choyke PL (2010) Prostate cancer: value of multiparametric MR imaging at 3 T for detection – histopathologic correlation. Radiology 255:89–99

Uchida T, Illing RO, Cathcart PJ, Emberton M (2006a) To what extent does the prostate-specific antigen nadir predict subsequent treatment failure after transrectal high-intensity focused ultrasound therapy for presumed localized adenocarcinoma of the prostate? BJU Int 98:537–539

Uchida T, Nakano M, Shoji S, Omaat T, Harano H, Nagata Y et al (2009) Ten Year Biochemical disease free survival after high intensity focused ultrasound (HIFU) for localised prostate cancer: comparison with three different generation devices. Conference: 104th Annual Meeting of the American-Urological-Association Location: Chicago, IL Date: APR 25–30, 2009. J Urol 181:228–228

Uchida T, Ohkusa H, Nagata Y, Hyodo T, Satoh T, Irie A (2006b) Treatment of localized prostate cancer using high-intensity focused ultrasound. BJU Int 97:56–61

Uchida T, Ohkusa H, Yamashita H, Shoji S, Nagata Y, Hyodo T, Satoh T (2006c) Five years experience of transrectal high-intensity focused ultrasound using the Sonablate device in the treatment of localized prostate cancer. Int J Urol 13:228–233

Uchida T, Shoji S, Nakano M, Hongo S, Nitta M, Usui Y, Nagata Y (2010) High-intensity focused ultrasound as salvage therapy for patients with recurrent prostate cancer after external beam radiation, brachytherapy or proton therapy. BJU Int 107:378–382

Vache T, Bratan F, Mege-Lechevallier F, Roche S, Rabilloud M, Rouviere O (2014) Characterization of prostate lesions as benign or malignant at multiparametric MR imaging: comparison of three scoring systems in patients treated with radical prostatectomy. Radiology 272:446–455

Van Velthoven R, Aoun F, Limani K, Narahari K, Lemort M, Peltier A (2014) Primary zonal high intensity focused ultrasound for prostate cancer: results of a Prospective Phase IIa Feasibility Study. Prostate Cancer 2014:756189

Villers A, Puech P, Mouton D, Leroy X, Ballereau C, Lemaitre L (2006) Dynamic contrast enhanced, pelvic phased array magnetic resonance imaging of localized prostate cancer for predicting tumor volume: correlation with radical prostatectomy findings. J Urol 176: 2432–2437

Zacharakis E, Ahmed HU, Ishaq A, Scott R, Illing R, Freeman A, Allen C, Emberton M (2008) The feasibility and safety of high-intensity focused ultrasound as salvage therapy for recurrent prostate cancer following external beam radiotherapy. BJU Int 102:786–792

Zelefsky MJ, Fuks Z, Hunt M, Lee HJ, Lombardi D, Ling CC, Reuter VE, Venkatraman ES, Leibel SA (2001) High dose radiation delivered by intensity modulated conformal radiotherapy improves the outcome of localized prostate cancer. J Urol 166:876–881

Zelefsky MJ, Reuter VE, Fuks Z, Scardino P, Shippy A (2008) Influence of local tumor control on distant metastases and cancer related mortality after external beam radiotherapy for prostate cancer. J Urol 179: 1368–1373; discussion 73

Zini C, Hipp E, Thomas S, Napoli A, Catalano C, Oto A (2012) Ultrasound- and MR-guided focused ultrasound surgery for prostate cancer. World J Radiol 4:247–252

MRI-Guided HIFU Methods for the Ablation of Liver and Renal Cancers

3

Baudouin Denis de Senneville, Chrit Moonen, and Mario Ries

Abstract

MRI-guided High Intensity Focused Ultrasound (MRI-HIFU) is a promising method for the non-invasive ablation of pathological tissue in many organs, including mobile organs such as liver and kidney. The possibility to locally deposit thermal energy in a non-invasive way opens a path towards new therapeutic strategies with improved reliability and reduced associated trauma, leading to improved efficacy, reduced hospitalization and costs. Liver and kidney tumors represent a major health problem because not all patients are suitable for curative treatment with surgery. Currently, radio-frequency is the most used method for percutaneous ablation. The development of a completely non-invasive method based on MR guided high intensity focused ultrasound (HIFU) treatments is of particular interest due to the associated reduced burden for the patient, treatment related patient morbidity and complication rate. The objective of MR-guidance is hereby to control heat deposition with HIFU within the targeted pathological area, despite the physiological motion of these organs, in order to provide an effective treatment with a reduced duration and an increased level of patient safety. Regarding this, several technological challenges have to be addressed: Firstly, the anatomical location of both organs within the thoracic cage requires inter-costal ablation strategies, which preserve the therapeutic efficiency, but prevent undesired

B. Denis de Senneville (✉)
Imaging Division, Department of UMCU, University Medical Center Utrecht, Utrecht, Netherlands

Mathematical Institute of Bordeaux, Department of CNRS, UMR 5251 CNRS/University of Bordeaux, Talence 33400, France
e-mail: b.desenneville@umcutrecht.nl

C. Moonen • M. Ries
Imaging Division, Department of UMCU, University Medical Center Utrecht, Utrecht, Netherlands
e-mail: c.moonen@umcutrecht.nl; m.ries@umcutrecht.nl

© Springer International Publishing Switzerland 2016
J.-M. Escoffre, A. Bouakaz (eds.), *Therapeutic Ultrasound*, Advances in Experimental Medicine and Biology, Vol. 880, DOI 10.1007/978-3-319-22536-4_3

tissue damage to the ribs and the intercostal muscle. Secondly, both therapy guidance and energy deposition have to be rendered compatible with the continuous physiological motion of the abdomen.

Keywords
Real-time • MRI HIFU • Tumor ablation

3.1 Introduction

Hepatic and renal cancers account for 700,000 and 115,000 deaths per year in the word, respectively (Ferlay et al. 2010). Worldwide, liver cancer is the fifth most frequent cancer in the male population and the seventh in the female. In East and Southeast Asia, and in West and Central Africa, primary liver cancer is the most common form of liver cancer (American Cancer Society 2011). Primary liver cancer is most frequently the result of a chronically damaged liver, with viral hepatitis, alcohol abuse and obesity as the predominant contributing factors (American Cancer Society 2011). To date, treatment options for primary liver cancer include liver transplantation, resection and ablation. However, only about 25 % of primary liver cancer patients are eligible candidates for these curative therapies. The most frequent counter indications include the tumor size and location, underlying parenchymal disease or multi-focal lesions. This translated into a growing interest in mini-invasive local therapy, such as Radio Frequency-ablation (Gellermann et al. 2005; Lepetit-Coiffe et al. 2006), which the American Association for the Study of Liver Disease recommends for patients with less than three primary tumors with a diameter less than 3 cm. For more advanced disease, transarterial chemo-embolization (TACE), radio-embolization and systemic chemotherapy are frequently offered as palliative measures.

In Europe and North America, metastatic liver tumors are the most common form of liver cancer (American Cancer Society 2011), whereby the majority of the primary tumors are located in the breast, lung, colon, prostate and rectum. In particular, colorectal cancer (CRC) has over 400,000 cases per year, the second largest diagnosed cancer, of which about 70 % develop metastatic disease in the liver (Ruers and Bleichrodt 2003). The occurrence of metastatic disease in the liver means that the primary cancer has reached stage IV and requires systemic therapy. Therapy for metastatic disease in the liver originating from CRC is flanking the curative therapy of the primary cancer. Similarly to primary liver cancer, the most frequently offered therapeutic approaches are surgical resection. However, similar to primary liver cancer, only about 20–25 % of the metastatic disease is resectable, translating into a growing interest for mini-invasive local therapies, such as radiofrequency and laser induced ablation, cryotherapy or local embolization (Goldberg et al. 2009). These are less limited with respect to patient selection.

Since local ablative therapy has become of increasing importance for both primary liver and metastatic liver cancer, the possibility to target and ablate in a single session primary and metastatic cancer deep in the liver and kidneys in a non-invasive way has considerably amplified HIFU clinical interest in recent years. Due to the associated reduced burden for the patient, treatment related patient morbidity and complication rate, HIFU represents a potential therapeutic alternative to patient that are currently not eligible for invasive or mini-invasive therapy.

From a historical point of view, the possibility to employ HIFU as an external energy source for non-invasive tissue ablation has been described by Lynn et al. (1942). Nevertheless, the first clinical experiments with HIFU were conducted in the field of neuro-surgery 16 years later by Fry (1958). One of the many technical limitations that hampered clinical adoption of this methodology at this point in time was the lack of a non-invasive method for interventional planning and guidance. As a consequence, the widespread introduction of ultrasound imaging systems with

b-mode capabilities during the 1980s renewed the interest in this non-invasive therapeutic modality. The feasibility of HIFU ablations with an extracorporeal device under ultrasound guidance in the liver was demonstrated by Vallancien and coworkers (1992). The first larger clinical studies were conducted by Wu and colleagues (Wu et al. 1999; Wu et al. 2004; Kennedy et al. 2004) using ultrasound imaging with a JC ablation device from Chongqung Haifu (Chongqung, China) between 1997 and 2003.

In parallel, Cline et al. (1992) had already suggested in 1992 the concept of MR-guided HIFU interventions. This was followed up upon by several prototype HIFU systems that were fully integrated in whole body MRI systems (Cline et al. 1995; Hynynen et al. 1997; Jolesz and Hynynen 2008). Although these first systems were originally designed for MR-guided HIFU therapy of uterine fibroids, modifications to cope with the respiratory motion of the liver enabled first clinical studies using a modified ExAblate 2000 system (InSightec, Israel) by Okada et al. (2006) and Kopelman et al. (2006).

With respect to the kidney, the first pre-clinical application of HIFU with an extracorporeal transducer on the kidney in an animal model was demonstrated by Chapelon and coworkers (1992) using ultrasound guidance. Nevertheless, it took another 13 years until the first clinical studies of HIFU ablations for renal masses under ultrasound guidance were reported in the same year by Hacker et al. (2005) and Illing et al. (2005). More recent clinical studies explored the benefit of laparoscopic HIFU transducers (Klingler et al. 2008) under ultrasound guidance.

MR-guided HIFU interventions in the kidney have so far been investigated only in preclinical experiments by Ries et al. (2010) and Quesson et al. (2011) and demonstrated that MR-based real-time monitoring of temperature evolution and real-time motion compensation strategies, such as respiratory gating and beam steering, are feasible.

In particular the integration of HIFU-systems in clinical magnetic resonance imaging systems offers several compelling advantages (Okada et al. 2006; Kopelman et al. 2006). First, MRI allows acquiring high-resolution 3D images with an anatomical contrast similar to diagnostic imaging, while the patient is in place on the therapeutic ablation system. This allows depicting both the lesion and organs at risk (OAR) directly before therapy, and thus takes directly into account recent physiological changes, such as tumor growth (or regression), and liver position modifications due to patient positioning on the ablation system. Furthermore, MRI allows non-invasive measurement of the local tissue temperature with a high precision and spatio-temporal resolution (for an extensive overview, see Denis de Senneville et al. 2005; Rieke and Butts Pauly 2008). As a consequence, MR-Thermometry allows direct and continuous monitoring of energy delivery, and thus therapy progression (Hynynen et al. 2006; Gellermann et al. 2005; Denis de Senneville et al. 2007a, b). Furthermore, temporal evolution of temperature allows calculation of the thermal dose delivered (hereafter referred to as MR-dosimetry), which has been demonstrated as an empirical estimator of induced necrosis (Sapareto and Dewey 1984). This is also applicable for the liver and kidney (Quesson et al. 2011). Of particular importance here is the ability of monitoring not only the temperature in the target area, but also in the OAR and in the propagation part of the acoustic beam (Mougenot et al. 2011; Baron et al. 2013). Finally, dynamic contrast enhanced T1-weighted imaging (DCE-T_1wMRI) allows mapping the non-perfused volume (NPV) immediately after therapy, and thus validates the therapeutic endpoint on the fly.

In order to exploit these intriguing possibilities of MRI-guided HIFU for the ablation of liver and renal cancers, compared to other clinical HIFU applications two principal problems have to be overcome: The necessity to deposit the acoustic energy across the thoracic cage, and the necessity to render the targeting, energy deposition and interventional guidance compatible with the continuous physiological motion of the abdominal area.

3.2 Obstruction of the Ultrasonic Beam Path by the Thoracic Cage

As shown in Fig. 3.1, an important challenge for HIFU ablations in the liver and the kidney is obstruction of the acoustic beam path by the thoracic cage. For sonications in the cranial and

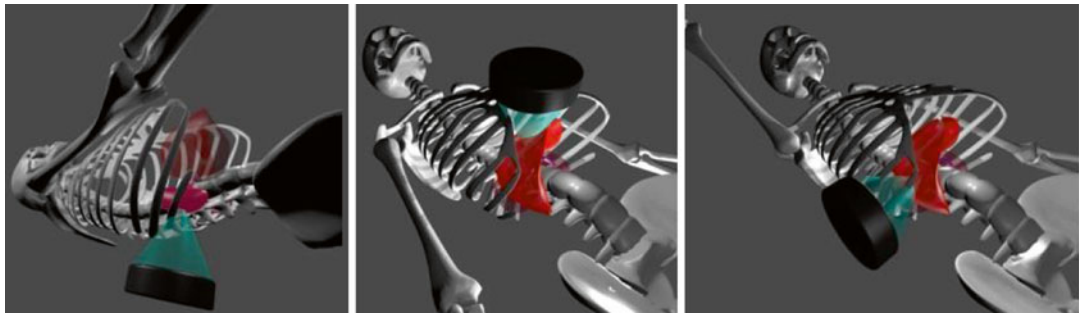

Fig. 3.1 Obstruction of the acoustic beam path by the thoracic cage. As the left illustration displays, only the caudal part of the kidneys can be reached by an extracorporeal transducer from dorsal direction, without parts of the propagation path being partially obstructed by the first and second floating rib. In particular the more cranially located left kidney is often only reachable by an intercostal sonication. With respect to the liver, only lesions in segments 4b and 5 can be reached by an extracorporeal transducer from a ventral position without any obstruction by the costal cartilage or the ribs, as shown in the center illustration. Therapy in segments 1, 2, 3, 4a requires angulated sonications. These partially interfere with the costal cartilage or the sternum. HIFU therapy in segments 6 and 7 of the liver generally require an intercostal sonication through the last two false ribs (9 and 10) from a lateral position, as shown in the right illustration. Otherwise, therapy in segment 8 is obstructed by both the false ribs and the costal cartilage (Image courtesy of Dr. Mario Ries, UMC Utrecht)

lateral part of both organs, the ribs and the costal cartilage block part of the acoustic energy that is delivered by the ultrasound beam. This, in turn, leads to two principal problems:

Firstly, the high ultrasound absorption coefficient of the bone (Goss et al. 1979) reduces the available acoustic beam power in the focal area. Moreover, the thoracic cage acts as an aberration, decreasing the focusing quality of the ultrasonic beam (Liu et al. 2007; Bobkova et al. 2010). Due to such beam aberrations, the required temperature increase in the target area may be significantly reduced (Liu et al. 2005). This leads to either a significantly reduced volumetric ablation rate, or, if compensated for by an increased total emitted power of the transducer, to an increased risk of undesired near-field damage due to high acoustic power densities in the intercostal and/or abdominal muscle and ribs.

Secondly, the high acoustic absorption in the ribs and the cartilage can lead to local hyperthermia in the cortical bone, the bone marrow and the adjacent intercostal muscle. During energy delivery, temperature elevations directly adjacent to the ribs have been reported that were up to five times higher than the temperature in the intercostal space (Daum et al. 1999). Such high local temperature elevations can lead to adverse effects, such as skin burns and intercostal tissue necrosis, which have been frequently reported in clinical studies (Wu et al. 2004; Li et al. 2007). Jung et al. (2011) reported rib necrosis and diaphragmatic ruptures as the most frequent complications for HIFU treatments of hepatic tumors.

Several measures have been proposed to reduce or to avoid these adverse effects. In some cases, surgical removal of the part of the ribs that intersect with the acoustic propagation path has been applied to selectively perform HIFU treatment (Wu et al. 2004). However, this negates the non-invasive nature of HIFU interventions and is likely to introduce new sources of adverse effects such as scar tissue, which in turn can lead to skin-burns.

The currently most commonly proposed method to mitigate excessive rib heating and restore focal point heating is beam shaping. Ibbini et al. (1990) proposed a HIFU transducer design in form of a sparse spherical phased array. The main motivation of the use of spherical phased arrays is the combination of a geometric focus with the possibility to deflect the beam by modulating the phase of each individual transducer element. For intercostal sonications, this

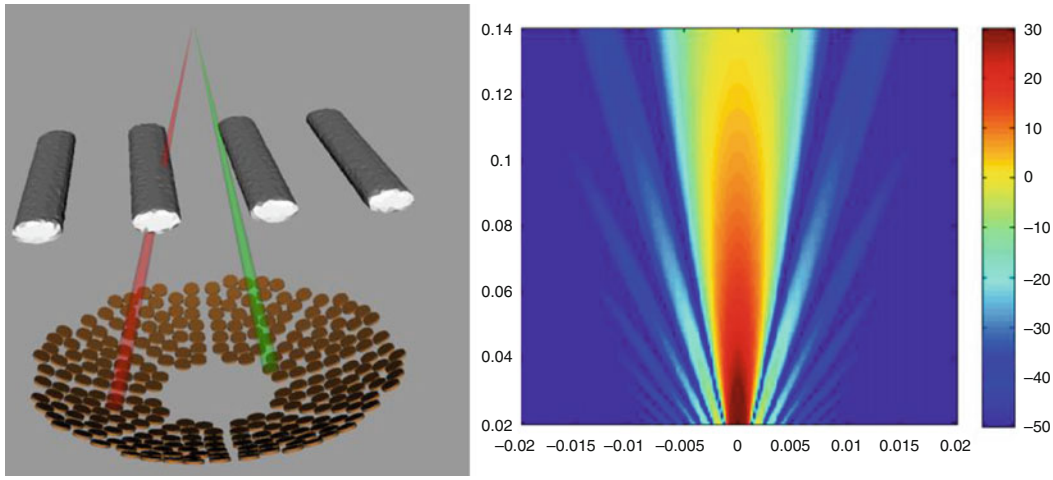

Fig. 3.2 Binarized apodization approach for the compensation of the obstruction of the ultrasonic beam path by the thoracic cage. The true acoustic emission profile of an individual cylindrical phased array element (shown in the *right image*) is approximated by a geometric ray in the normal direction of each element (shown on the *left*). Each ray is tested for intersections with scattering/attenuating anatomical structures, and obstructed elements (*red*) are selectively deactivated, while unobstructed elements (*green*) are amplified to partially compensate for the lost acoustic power (Image courtesy of Dr. Martijn de Greef, UMC Utrecht)

type of transducer design offers the additional possibility to selectively attenuate, or even deactivate, parts of the transducer surface. This has been demonstrated by McGough et al. (1996) and Botros et al. (1997) who proposed in theoretical design studies to adjust the amplitudes and phases of the voltage signals driving the individual phased array elements to limit rib exposure, while preserving the focal point intensity.

Civale and coworkers (2006) investigated the use of a linearly segmented transducer for intercostal sonications. He validated in both simulations and experiments the earlier prediction that the deactivation of edge segments leads to a significant reduction of the acoustic intensity on the ribs.

Since these early years, several refined methods to derive efficient beam shaping for intercostal sonications have been suggested. They fall into two families: Approaches that use anatomical information in conjunction with acoustic simulations to derive the aperture function, and methods that directly use the therapeutic transducer for the detection of attenuating/scattering structures.

3.2.1 Apodization Methods Based on an Anatomical Model of the Thoracic Cage Using Binarized Apodization Based on Geometric Ray-Tracing

One of the first methods relying on anatomical information was proposed by Liu and coworkers (2007). Their method is based on geometric ray-tracing using CT images of the thoracic cage. In this approach, obstructed elements of a 2D phased array are identified by testing whether the normal vector of each element intersects with parts of the thoracic cage, as shown in Fig. 3.2 on the left.

A subsequent selective deactivation of the obstructed elements (Fig. 3.2, red) and an amplification of unobstructed elements (Fig. 3.2, green) leads to a binarized apodization function, which can substantially reduce undesired heating of the ribs, while maintaining sufficient energy deposition at the target area. Quesson and coworkers (2010) demonstrated the effectiveness of this approach both *ex-vivo* and *in-vivo* by using anatomical data derived from MR-images. The advantage of using MR-images in the context of

MR-HIFU is that the anatomical information can be obtained with the patient in therapeutic position, thus taking local deformations and shifts of the organ vs. the thoracic cage directly into account.

Furthermore, this method requires only a model of the thoracic cage with a moderate spatial resolution ($<1.5\times1.5\times1.5$ mm^3), which can be obtained in a clinically relevant time frame. This approach is computationally efficient enough to be potentially feasible in a clinical workflow. The main drawback however is the coarse approximation of the true acoustic emission profile of an individual cylindrical phased array element (Fig. 3.2, right), which is in the form of a much more complex Bessel-function with the pointing vector of a plane wave. This neglects both the substantial off-axis energy emission of each element, which also contributes to undesired heating of the thoracic cage and diffractive effect of the ribs on the remaining acoustic field. Nevertheless, despite its limitations, this approach has been shown in several preclinical studies as quite effective (Bobkova et al. 2010; de Greef et al. 2015; Gélat et al. 2014).

3.2.1.1 Phase Conjugation

Phase conjugation is a more advanced beam shaping method introduced by Aubry and coworkers (2008), which in turn is based on the principle of time-reversal (Fink 1997; Fink et al. 2003). In this approach, a point source is placed in the focus and the acoustic wave is propagated towards the transducer. Subsequently, the received signal in each individual transducer element is recorded. By emitting these recorded signals in a time-reversed fashion, a focus will be created at the target location under minimal exposure of the ribs, as most of the incident energy on the ribs will not be incident on the transducer. This approach relies on the linearity and the reciprocity of the wave equation in a non-dispersive medium. If both assumptions are fulfilled, the time-reversal process represents a spatio-temporally matched filter of the wave propagation operator (Tanter et al. 2007). In its original implementation, this approach required a physical acoustic point source in the focus, and was therefore as an invasive technique clinically not feasible. However, if a high-resolution 3D representation of the tissue stack is combined with the appropriate acoustic impedance values of the tissues, the *phase conjugation* approach can be carried out virtually, i.e. in a simulation environment (Aubry et al. 2008). Compared to binarized apodization, this approach performs a (full) phase-amplitude optimization for each transducer element. Furthermore, it has been shown to be among the most effective approaches to further reduce the energy exposure to the ribs, while maintaining the acoustic intensity in the focal point (Gélat et al. 2014).

One of the drawbacks is that these methods are for computational reasons approximative and lengthy due to the fact the wave front is sampled with a sampling distance corresponding to several wavelengths, causing a mismatch between the forward and reverse acoustic field (Tanter et al. 2001). Furthermore, this approach requires a large dynamic amplitude range of the transducer elements, which in-turn leads to a heterogeneous distribution of element power, thus local near-field overheating becomes an even larger risk, as well as overheating of individual transducer elements. In addition, this approach requires a complete and precise segmentation of the heterogeneous tissue stack between the HIFU transducer and target location. As a consequence, practical limitations with respect to the resolution and spatial fidelity of the acquired 3D model, and deviations from the assumed tissue properties will render the calculated solutions in practice sub-optimal.

3.2.1.2 Constrained Optimization Using the Boundary Element Method (BEM)

One of the limitations of binarized apodization based on geometric ray-tracing is that the effect of the apodization on the focus quality is not taken into account. This means that, although undesired heating of the thoracic cage is prevented, the impact of the element deactivation on the focal point amplitude might lead to a configuration that is therapeutically ineffective in the focus. This motivated Gélat and colleagues

(2014) to formulate the problem of focusing the field of a multi-element HIFU array inside the thoracic cage with an optimal apodization as an inverse problem using the boundary element method (BEM). The underlying physical model of this approach takes into account physical effects such as scattering and diffraction and requires segmented 3D anatomical data together with the corresponding acoustic impedances as a description of the acoustic environment (Gélat et al. 2011). While a first preclinical study (Gélat et al. 2014) suggests considerable potential of this approach, its current formulation is computationally extensive and requires a precise anatomical 3D model of each shot position for optimal results. Similar to the *phase conjugation* method, *constrained optimization* also requires a large transducer element dynamic amplitude range for it to be effective. As a consequence, future studies will have to investigate if this concept can be exploited for clinical applications.

3.2.1.3 Apodization Methods Based on Direct Detection of Scattering or Attenuating Structures

One of the major drawbacks of intercostal apodization methods, which rely on an anatomical 3D model, is the requirement to rapidly and non-invasively map the anatomy between the energy source and the ablation area, and then to transform this anatomical data into a valid acoustic 3D model. If CT is chosen as the imaging modality on which the anatomical 3D model is based, then the anatomical 3D images are generally not acquired with the patient in the final therapeutic treatment position. Therefore, local anatomy deformations due to different patient positions and shifts of the organs vs. the thoracic cage that occur during transfer, limit the validity of the anatomic model. For MR-HIFU this can be omitted by using 3D MRI itself to derive an accurate spatial representation of the target anatomy and the scattering/attenuating structures. Nevertheless, this approach requires considerable image acquisition time, and a lengthy segmentation process that transforms the anatomical map into an acoustic model before the acoustic optimization of the transducer apodization can even begin.

Although each of the required steps is well understood, the ensemble is in practice often laborious, time consuming and error prone, requiring frequent user intervention for error correction and quality control. This complicates the clinical workflow of HIFU intervention. As a consequence, there has been a growing interest in developing methods that can directly detect scatterers and/or attenuating structures without an additional imaging modality and preferably without user intervention.

3.2.2 Decomposition of the Time-Reversal Operator

One of the first methods of this type for intercostal HIFU was suggested by Cochard and coworkers (2009), for 1D linear phased arrays, and has subsequently extended for sparse 2D arrays (Cochard et al. 2011). The method was derived from the initial decomposition of the time-reversal operator (DORT) selective focusing method from Prada (2002). In its original implementation, the DORT method was developed for adaptive focusing of ultrasonic arrays on strong back-scatterers. DORT relies on the acquisition of the backscatter matrix (i.e., the columns of this matrix relate the scattered signal received by all transducer elements from an excitation event of each transducer element). A singular value decomposition of this matrix leads to a set of eigenvectors that represent amplitude/phase combinations, which focus the beam on the individual scattering structures. Since the corresponding eigenvalues to the obtained eigenvectors allow their classification by their scattering magnitude, a linear combination of the eigenvectors can be computed. This combination represents a phase/amplitude combination for each transducer element that focuses the beam on several selected scattering structures simultaneously. For optimal intercostal HIFU, Cochard et al. (2009) proposed to reverse this principle and to compose an amplitude/phase vector from the eigenvectors with the lowest eigenvalues, i.e. eigenvectors that focus the beam on acoustically transparent (i.e., unobstructed) areas in the beam path.

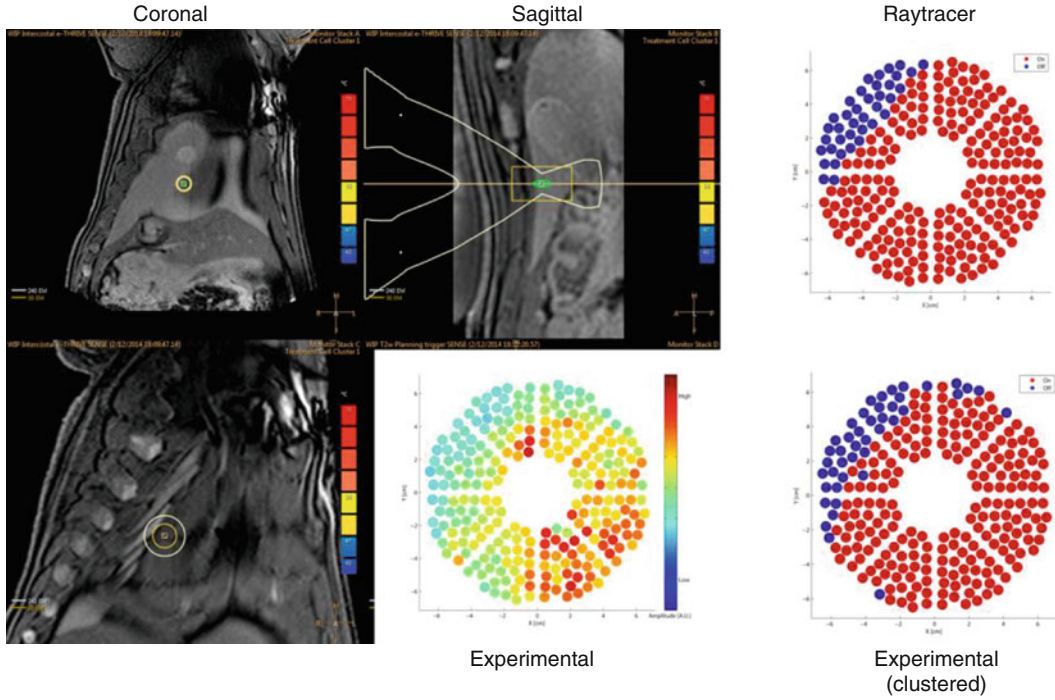

Fig. 3.3 Automatic detection of beam obstruction by the thoracic cage during liver ablation in an *in-vivo* experiment. The focus is placed in segment 4 of a porcine liver, as shown in the coronal (*top left*) and the sagittal (*top center*) T_1 weighted image. As indicated in the coronal image on the level of the sternum (*bottom left*), the beam cone intersects with parts of the costal cartilage. In this example, the binarized apodization based on geometric raytracing (*top right*) is based on a semi-automatic segmentation of a 3D T_1–weighted MRI of the costal cartilage, resulting in a selective deactivation of obstructed transducer elements. The binarized apodization based on cavitation enhanced back projection (*bottom right*) leads to comparable results, but requires only a fraction of the acquisition and processing time (<1 s vs. 5.3 min). In addition, this approach provides an estimate of the relative attenuation between focus and transducer for each element (*bottom middle*) (Image courtesy of Pascal Ramaekers, UMC Utrecht)

The main advantages of this approach are that it uses the HIFU transducer itself as the detector and allows performing the required acquisitions and calculations in not only a very short time frame, but also non-invasively. This allows potential adaptation of the apodization of the phased array elements for optimal intercostal sonications, even under the limitations of a clinically feasible and repetitive workflow for every different transducer position on the fly.

The main disadvantage of the DORT method is that it relies on the presence of strong scatterers and works best with well-resolved point-like scatterers. Although cortical bone represents such a strong scatterer, the complex shape of the ribs is not well represented by a low number of point sources. Furthermore, as Fig. 3.3 illustrates, the ultrasonic propagation path is also frequently obstructed by attenuating structures, such as costal cartilage, which are not well suited for this detection method.

As a result, a comparison of the DORT method in simulated experiments with other approaches (binarized apodization based on geometric raytracing, phase conjugation and constrained optimization as previously proposed (Gélat et al. 2012) (see below)), indicated that although the DORT method results in an apodization which spares the thoracic cage from undesired acoustic intensity, this is more at the expense of the focal point pressure. In summary, although the DORT approach is conceptually very promising, *in-vivo* studies that validate the efficiency of the approach are to date still pending.

3.2.2.1 Pulse-Echo Detection

A much simpler approach was suggested by Marquet and colleagues (2011) that exploits the A-mode imaging capabilities of the HIFU transducer directly in order to detect obstructed parts of the transducer. Similar to DORT, this approach exploits the strong backscattering of an emitted acoustic pulse from the thoracic cage. Here, the transducer channels are ordered according to the amplitude strength of their back reflected signal and clustered into obstructed and unobstructed elements. This approach has the advantage to be both very fast and comparably simple, thus having the potential to be compatible with a clinical workflow. The main drawbacks are that although cortical bone represents a strong acoustic reflector, cartilage signal reflection is much harder to differentiate from reflections from the adipose-muscle and muscle-liver/kidney tissue boundaries. This is further complicated by the fact that most HIFU transducers are designed as narrow-band systems at lower frequencies (0.75–1.5 MHz), thus being limited in their A-mode imaging quality.

3.2.2.2 Cavitation-Enhanced Back-Projection

The original implementation of the *phase conjugation approach* requires a point source in the focus, which emits a spherical acoustic wave that is subsequently received by all transducer elements. As Tanter et al. (2001) have shown, the time-reversal of this received amplitude/phase vector represents a spatially and temporally matched filter of the propagation operator through the heterogeneous medium. The drawback of this approach is that it is invasive, and thus for clinical applications unfeasible. The aim of subsequent work for intercostal HIFU with a transducer apodization based on time-reversal was aimed to circumvent this limitation: Aubry et al. (2008) virtualized the physical time-reversal measurement with model based solutions (see Sect. 3.2.1), while Cochard and coworkers (2009) recorded the complementary information, i.e. the backscatter from the ribs.

The key idea of *cavitation-enhanced back-projection* is to replace the time-reversal experiment (i.e., using the propagation of a spherical wave from the focus to the transducer in order to derive the transmit apodization of the transducer) with a true pulse echo experiment between the transducer and a point scatterer in the focus. However, this requires placing a sufficiently large point scatterer in the focus of the transducer in a non-invasive way. This is achieved by emitting a first short pulse of ultrasonic energy through all transducer elements simultaneously, which are used to create a sufficient peak negative pressure in the focus to induce non-inertial cavitation. The resulting bubble cloud in the focal area represents a spatially confined cloud of point scatterer. As a result, consecutive ultrasonic waves are then reflected by the cavitation bubbles back onto the transducer.

The relative signal strength received from the back-reflected wave by each transducer element represents a measurement of the relative attenuation between the focus and each individual transducer element. In order to suppress undesired echoes other than those originating from the cavitation bubble cloud, a pulse inversion sequence was used. Using such a sequence, the majority of the received signal originates from the reflections of the cavitation bubbles.

This proposed method allows rapid mapping of any aberrating structures in each of the individual beam paths of the transducer elements before a HIFU sonication is started, and consecutively calculates the appropriate apodization law. Similar to the invasive *phase conjugation* method, this approach takes both absorbing and scatterering structures in the beam into account, whereby the acquisition and processing times are comparable with the DORT approach (<1 s), and thus entirely compatible with the clinical workflow.

The principal disadvantage of *cavitation-enhanced back-projection* is the requirement to induce stable cavitation. Stable cavitation requires, in particular in deeper tissue layers, transducer and generator systems, which can deliver large peak acoustic pressures. While this increases the complexity and the cost of the HIFU system, it also increases the risks of adverse effects. Power control of non-linear energy deposition is challenging and pulses in the

3–6.5 MPa pressure regime also increases the probability of potentially harmful inertial cavitation events, which in turn can lead to undesired tissue damage (Hwang et al. 2006; Miller 2007).

3.3 Challenges Associated with Physiological Motion of the Liver and Kidney

Besides the necessity to deposit the acoustic energy across the thoracic cage, the second major challenge for non-invasive HIFU therapy in liver and kidney, with respect to both energy delivery and therapy guidance, is physiological motion. It is therefore important to differentiate between the sources and the time-scale of the different types of physiological motion and the adequate measures in more details:

Respiratory motion The liver and the kidney of an adult patient move under free-breathing conditions with a periodicity of around 3–5 s, and a motion amplitude of 10–20 mm, as shown in Fig. 3.4. While the motion pattern of free-breathing patients is over longer episodes (<30–45 s) periodic, it is frequently subject to changes in amplitude, phase and frequency before a new stable breathing rhythm is reached. In particular, the occurrence of involuntary spontaneous motion events, such as swallowing, coughing or muscle spasms, is hard to predict and interrupts a regular breathing pattern.

As a consequence, there is a growing trend to perform non- and minimally invasive therapy under deep sedation. Deep sedation is induced by an intravenous infusion of a hypnotic/amnestic agent, such as propofol or sodium thiopental, to reduce the probability of involuntary spontaneous motion events.

The additional use of analgesic drugs, in particular analgesics based on opioids, lead to respiratory depression, sometimes used to reduce in addition both the respiratory frequency and amplitude. Although the patient still displays spontaneous respiration, this measure can significantly increase the time fraction during which the abdomen is not subject to respiratory motion.

The next step from this intermediate regime is to induce complete respiratory depression and to control the respiratory cycle by an external mechanical ventilator. This approach leads to repetitive and stable respiratory motion over long durations, whereby the amplitude and the frequency can be adjusted within the boundaries

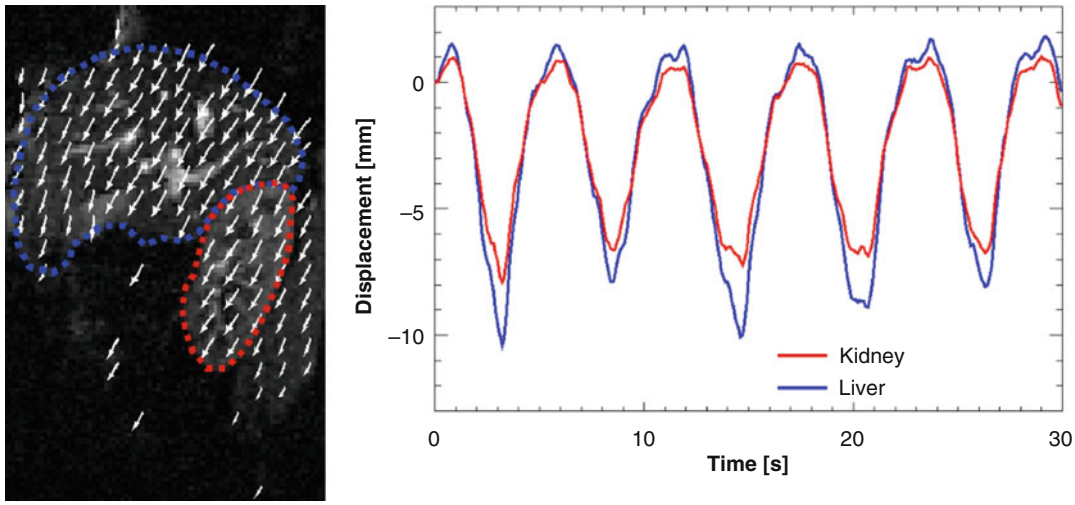

Fig. 3.4 Proof of concept of the motion estimation process performed on-line in the abdomen of a healthy volunteer for liver (*inside blue contour*) and kidney (*inside red contour*). The estimation of organ motion is performed using real-time optical-flow algorithm as described in (Denis de Senneville et al. 2011) with the sagittal anatomical images reported on the left. The vertical component of the estimated motion is reported on the right in the liver and the kidney (Image courtesy of Baudouin Denis de Senneville, CNRS/UMC Utrecht)

of sufficient blood-oxygen saturation according to the required interventional workflow.

Peristaltic motion A second important source of physiological motion is induced by peristaltic and digestive activity in the digestive tract. Although the time-scale of peristaltic motion events depends on the particular source, such as bladder filling with urine, the development of digestive gases or the passage of digestive products in the gastrointestinal tract, the resulting abdominal organ position shifts usually occur on a scale of several minutes (Mirabell et al. 1998; Langen et al. 2008). Although peristaltic motion is with respect to both amplitude and speed a magnitude below respiratory induced displacements, it is generally non-reversible and a-periodic. Peristaltic motion can clinically be moderated by several measures: Peristaltic bowel motion and the development of peristaltic gases can be reduced by adjusting the diet of the patient prior to the intervention (Smitmans et al. 2008). Similarly, administration of Butylscopolamine, which represents a peripherally acting antimuscarinic and anticholinergic agent used as an abdominal-specific antispasmodic (Emmott et al. 2008). Furthermore, shifts in the lower abdomen due to bladder filling can be reduced by the use of Foley catheters (Mirabell et al. 1998).

Spontaneous motion Finally, spontaneous motion is considered one of the most challenging types of physiological motion since it occurs infrequently, on a very short time-scale and is in general irreversible. It is particularly problematic for long interventions that require the patient to remain in an uncomfortable position. In the past, this problem has been alleviated in the field of external beam therapy by using either restraints, such as molds or casts (Verhey 1995), by sedating the patient (Zhang et al. 2010), or by introducing general anesthesia (GA).

3.3.1 Motion Compensation Strategies for HIFU Ablation on Abdominal Organs

As shown in Fig. 3.5 the typical workflow of an MRI-guided HIFU intervention starts with an initial planning (5–15 min), followed with a sequential set of energy depositions (5–60 s each) together with the associated cool down delay (30–180 s, depending on the energy density in the near-field).

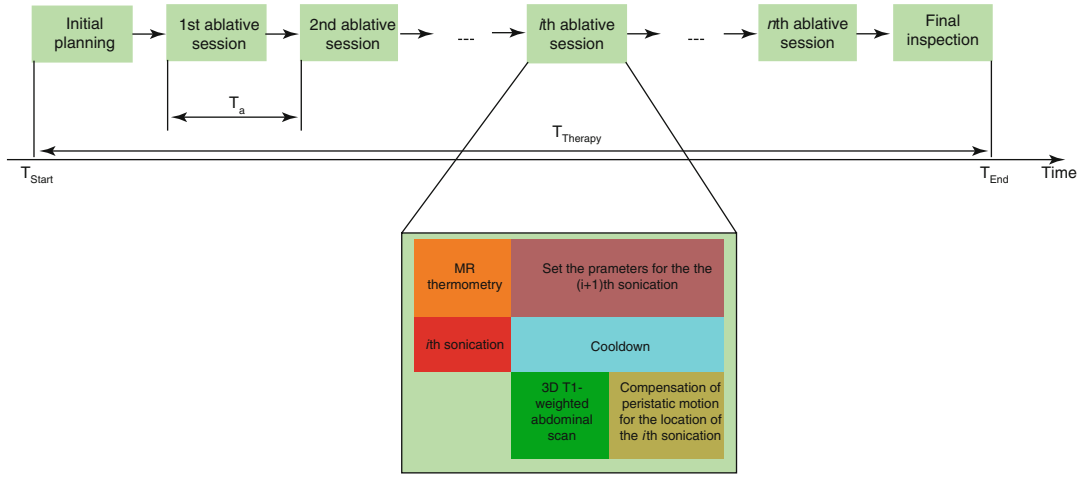

Fig. 3.5 Typical workflow of an MR-guided HIFU intervention. During the initial planning a set of anatomical images is obtained on which the planning target volume (PTV) around the tumor is delineated. In general, the PTV is ablated in smaller subvolumes, which allows intermediate tissue layers to cool down during the intervention. At the end of the intervention a dynamic contrast enhanced 3D MRI validates the therapeutic endpoint (Image courtesy of Cornel Zachiu, UMC Utrecht)

This therapeutic phase can have duration of up to 3 h. It is concluded with a set of physiological and functional MRI datasets, which validate the therapeutic endpoint. As Fig 3.5 displays, while peristaltic motion is during the short duration of each of these episodes not a major problem, these shifts can become challenging when considered at the time scale of the entire intervention.

The influence of respiratory motion during the initial and the final phases of the intervention are generally addressed with the established measures of diagnostic MRI: Either respiratory gating or breath holding. During the therapeutic phase, both for MR-guidance and energy delivery, respiratory induced motion needs to be addressed individually. Several approaches have been investigated to achieve this:

Induced Apneas The most simple and efficient way to prevent undesired respiratory motion of abdominal organs is to temporary interrupt the respiratory cycle. This is generally achieved by inducing general anesthesia with hypnotic/amnestic agents, which are given in conjunction with analgesics based on opioids to achieve a full respiratory depression. This allows controlling the respiratory cycle entirely by mechanical ventilation, which in turn can be synchronized with the therapeutic energy delivery. Several clinical studies have demonstrated the feasibility of this approach: Both Gedroyc (2006) and Kopelman et al. (2006) have successfully ablated Hepatic tumors by repetitive induced apneas. The main advantage of energy delivery during induced apneas is that this approach is compatible with any type of clinical HIFU equipment and does not require major modifications with respect to beam steering capabilities or beam amplitude modulation capabilities. The main drawback of this approach is that it reduces the non-invasive nature of MR-guided focused ultrasound interventions. While for primary tumor therapy of patients with a good general condition, an intervention under sustained general anesthesia of 2–3 h is generally considered clinically acceptable, the situation is more complicated when metastatic disease or patients in a poor general state are considered. In particular, for the case of metastatic disease, where local HIFU therapy represents only one aspect out of a combination of systemic and local therapy measures, an increased invasiveness of HIFU therapy is likely to reduce both the therapeutic possibilities and patient eligibility.

Gating Strategies As an alternative to induced apneas, respiratory-gated energy delivery strategies also allow the addressal of respiratory motion. As shown in Fig. 3.4, the respiratory cycle of an adult patient under resting conditions displays typically a time-window of 1–3 s when the diaphragm remains stationary. Therefore, a time synchronous amplitude modulation of a spatially stationary HIFU beam allows depositing the entire acoustic energy in a precise location despite the periodic displacements of the target. However, the required HIFU amplitude modulation leads to a significant reduction of the duty cycle of the ablation process. Since both kidney and liver display a high perfusion rate and consequently heat evacuation, a respiratory-gated energy delivery significantly reduces the achievable temperatures for larger sonication volumes (Cornelis et al. 2011). The situation is further complicated by the tendency of the respiratory cycle to be under free-breathing, only periodic/stable for shorter durations (10–30 s), and by slow drifts of the diaphragm resting position of 8–9 mm/h.

A gated energy delivery is considerably more favorable for patients under full anesthesia, where analgesic drugs allow the induction of full respiratory depression, and both breathing frequency and volume are adjusted by an external mechanical ventilator. Mechanical ventilation allows the maintenance of an entirely periodic breathing pattern that allows gated HIFU energy delivery with a duty cycle of up to 80 % for extended durations of several hours.

The clinical feasibility of this approach has been demonstrated by Okada and coworkers (2006) for the treatment of hepatocellular carcinoma. More recent preclinical work introduced several methodological improvements, such as MR pencil-beam navigators (Wijlemans et al. 2015a) and optical tracking as the gating source

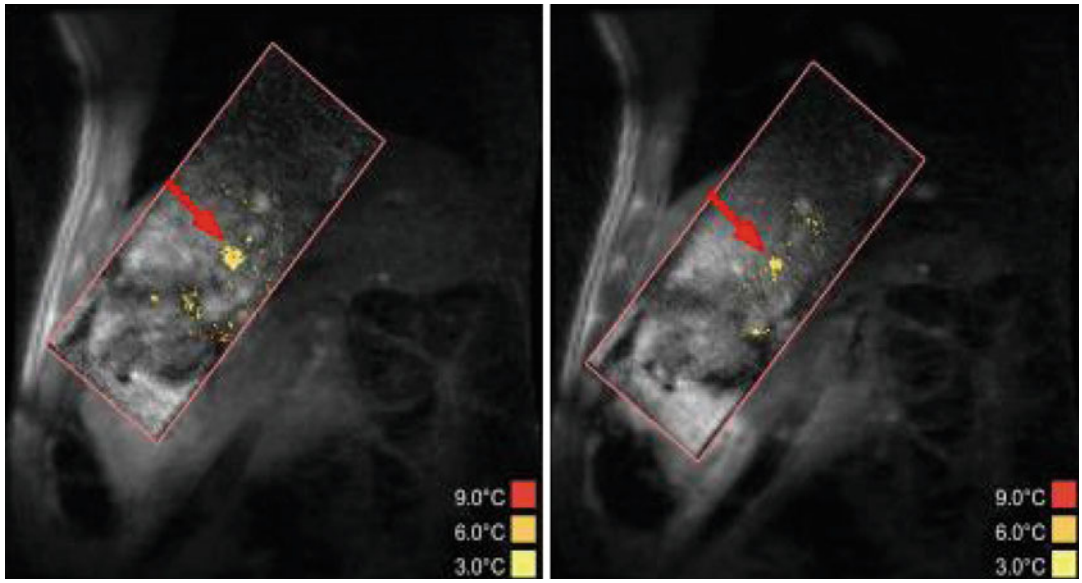

Fig. 3.6 *In-vivo* HIFU steered and breath-hold ablations. The *red arrows* indicate the location of the heated regions. These two images show representative images of a steered (*left*) and breath-hold (*right*) ablation *in-vivo* at the time point when the maximum temperature reached 10 °C above baseline. The steered ablation took 31.2 s to reach this point, whereas the breath-hold ablation took 26.7 s. The steered ablation required 16.7 % more energy than the breath-hold case (Reproduced with permission from Holbrook et al. (2014))

(Auboiroux et al. 2014), and additional motion correction strategies to account for peristalsis and slow target drifts.

As a consequence, for patients under full anesthesia, respiratory gating represents an interesting alternative to induced apnea, allowing a more continuous workflow compared to the cyclic apnea/re-oxygenation workflow of the later. In particular, recent work (Wijlemans et al. 2015b) to evaluate the compatibility of respiratory-gated sonications under Procedural Sedation and Analgesia (PSA), instead of general anesthesia, is likely to reduce the risk of complications and to shorten patient recovery.

Beam Steering Strategies The most promising approach to render ablations under free-breathing conditions compatible with an efficient energy delivery is to exploit the beam steering capabilities of modern phased array-transducers to continuously reposition the focus on the current position of the target (see Fig. 3.6). Contrary to amplitude modulated delivery schemes, such as gating, beam steering allows the continuous deposition of acoustic energy over periods of time that exceed the duration of the respiratory cycle. This is of particular importance in tissues, which display high perfusion rates, such as the kidney and liver (typical liver perfusion 65–100 mL/min/100 mL, kidney perfusion 287–379 mL/min/100 mg (Koh et al. 2008)).

MR-based tracking In the context of real-time guidance of hyperthermia, MR-navigator echoes have initially been proposed to provide motion information in combination with MR images (de Zwart et al. 2001). These techniques are however inadequate to estimate complex organ deformation because the motion estimate is generally restricted to translational displacement. Since modern MRI acquisition methods now allow the rapid acquisition of large data volumes, combined with an excellent tissue contrast and high spatial resolution, image-registration techniques (Sotiras et al. 2013) were recently employed to estimate on-line organ displacements from ana-

tomical images. Complex deformations can for example be estimated on a voxel-by-voxel basis using optical flow based approaches (Barron et al. 1994), which assume a conservation of local pixel intensities along the target displacement. The potential of such techniques for real-time MR-guided HIFU on mobile targets was first demonstrated in 2007 (Denis de Senneville et al. 2007a, b). However, this approach faces the following challenges:

First, both the update rate and latency of measured displacement information may hamper steering accuracy. While the image sampling frequency is limited by the MR-acquisition time, the latency is determined by the remaining acquisition time after echo-formation, the image processing time, the switching time of the HIFU-generator and the required data transport. For typical abdominal organ motion, the delay between the actual time of displacement and when motion information is available must remain below 100 ms (Ries et al. 2010). The image registration task is however highly computationally intensive and recent approaches take benefit of a combined CPU/GPU (Central Processing Unit/Graphical Processing Unit) architecture by offloading computational intensive calculations to the GPU, thus freeing the CPU for pipeline management and data preparation. That way, the image registration step can be dedicated to the GPU, which allows completing all calculations on a typical image size of 128×128 voxels in about 100 ms, as shown in (Roujol et al. 2010, 2011).

Secondly, optical-flow based algorithms rely on the assumption of conservation of local intensity along the trajectory which can be violated during thermotherapy because rapid MR-imaging is in general associated with low SNR (Signal-to-Noise Ratio). In addition, since the tissue is heated, several MR relevant tissue properties; such as T_1, T_2 and T_2^* relaxation times, are subject to change during imaging (Graham et al. 1998). This leads to local intensity variations, which in turn can be misinterpreted by optical-flow based algorithms as "false motion". A PCA (Principal Component Analysis)-based motion descriptor was thus recently introduced in order to characterize in real-time complex organ deformation (Denis de Senneville et al. 2011). PCA was used to detect, in a preparative learning step, spatio-temporal coherences in the motion of the targeted organ. Then, during hyperthermia, incoherent motion patterns could be discarded. This method allowed maintenance of only the physiological components of estimated motion in the registration process, permitting reduction in the noise of the estimated displacement. In addition, the PCA-based motion descriptor provides a flow field that is consistent with the learned model. It is also robust under the assumption of global brightness constancy, but allows local intensity variations.

Finally, although it is well established that MR-imaging can provide motion estimates with a high spatial resolution, it is difficult in practice to acquire on-line 3D isotropic images due to technical limitations, spatial and temporal resolution trade-offs and low SNR associated with fast 3D acquisition sequences. Real-time target tracking of abdominal organs depends on high frame-rate imaging; therefore it is not compatible with methods, such as respiratory gating or the acquisition of extended 3D volumes. In practice this limits MR-imaging to the acquisition of 1–3 slices, with modest spatial resolution in the slice direction. One approach consists of aligning the normal vector of the slice orthogonal to the motion vector, and thus to contain the entire motion cycle within a 2D imaging slice, as suggested in one report (Denis de Senneville et al. 2007a, b). This, however, imposes severe constraints on the imaging geometry, which might be for anatomical or diagnostic reasons unfavorable. It is often not possible to ensure that the target area remains observable during the entire motion cycle by a single static image slice. Furthermore, although the motion trajectory of the kidney and the lower part of the liver can be approximated by a linear shift, the true trajectory has a shape in 3D space. In particular, the upper part of the liver, which is subject to an elastic deformation, is hard to contain in a static 2D imaging slice during the entire respiratory cycle. Since extensive 3D-volume imaging is in practice hard to achieve with sub-second resolution, alternative

approaches that dynamically adapt the image location to the current target location, have been proposed as a possible solution. The slice position is hereby continuously adjusted to the current target location using fast pencil beam navigator echoes (Ries et al. 2010; Köhler et al. 2011) or ultrasound echoes (Günther and Feinberg 2004; Feinberg et al. 2010). In addition, a real-time image-based motion estimation algorithm applied on the image stream allows obtaining the in-plane target position sub-voxel precision. This, in combination with the retained slice tracking position, may describe the complete target position in 3D space, which can be conveniently employed to adjust the beam position (Ries et al. 2010). Alternative strategies are under active investigation that consists in estimating the 3D motion from 2D real-time MRI, using for example one or several volumetric scans obtained before the intervention (Arnold et al. 2011; Brix et al. 2014; Stemkens et al. 2014; Stemkens et al. 2015). These techniques however must still be validated in combination with MR-HIFU.

US-based tracking The simultaneous use of US imaging and HIFU is difficult because of their mutual interferences. However, the combination of the two devices represents a promising approach to operate thermometry/dosimetry and beam steering tasks, independently and with different temporal resolutions. The acquisition of US signal and HIFU sonication must be interleaved. In the context of real-time guidance of hyperthermia, ultrasonic echoes have been used in the past to provide motion information with high temporal resolution in conjunction with MR images. Pernot and coworkers (2003) used 4 pulse receivers to estimate the 3D displacement of the targeted organ (3 transducers were required to estimate the displacement, and another one was added to increase the robustness of the process). In the context of real-time guidance of hyperthermia, 1D ultrasonic echoes have been used in the past to provide motion information with high temporal resolution in conjunction with MR-thermometry in (Lorenço de Oliveira et al. 2010). However, using these techniques the estimated motion information is restricted to knowledge outside the heated zone because of the echo perturbation induced by the temperature rises with ultrasonic echoes. In addition, the challenge of US echoes increases when US waves are obstructed by ribs and/or air in the beam path. Consequently, it has been recently proposed to use 2D ultrasound echography as an additional imaging modality for continuous target tracking under MR-HIFU environment (Günther and Feinberg 2004; Feinberg et al. 2010; Ries et al. 2012; Auboiroux et al. 2012; Denis de Senneville et al. 2014; Denis de Senneville et al. 2015).

3.3.2 MR Guided Thermometry and Dosimetry in Abdominal Organs

One of the most intriguing possibilities of MRI-HIFU is the possibility to real-time monitor temperature changes during an HIFU sonication non-invasively. Initial approaches focused on the temperature dependence of several MR observable tissue properties (such as T_1 and T_2 relaxation time of water protons, molecular diffusion constant of water…), which have been intensively studied in the literature. The associated thermometric MR-methods are reviewed elsewhere (Denis de Senneville et al. 2005; Rieke and Butts Pauly 2008). The most promising candidate is real-time MR-thermometry based on the water proton resonance frequency (PRF), mainly because of its near-independence on tissue composition. Tissue necrosis can also be empirically estimated during the interventional procedure using the calculation of the accumulated thermal dose based on dynamic MR thermometry (Sapareto and Dewey 1984). MR-thermometry/dosimetry is thus a promising candidate to assess an on-line retroactive control of therapy and ensure an accurate thermal energy delivery with HIFU.

Nevertheless, artifacts in the temperature measurements have a large impact on the precision of the thermal dose estimate due to its exponential dependence on the temperature, and will accumulate during the intervention due to the integration. A first challenge arises because the MR-thermometry based on the PRF shift of mov-

ing targets, such as the abdominal organs, is complicated by the continuous target motion through an inhomogeneous and time-variant magnetic field (Peters and Henkelman 2000). Respiration or cardiac-induced organ displacement and deformation will modify the local demagnetization field, and thus also the local magnetic field, experienced by the target organ. This will in turns result in temperature artifacts (De Poorter et al. 1994; Young et al. 1996). A second challenge rises from the fact that MR-thermometry is limited by the available SNR. An inherent trade-off exists between spatial resolution, volume coverage and scan time. It is therefore currently difficult to acquire in real-time 3D isotropic thermal maps of a large field-of-view.

3.3.2.1 Compensation of Motion Related Errors in Thermal Maps

Several strategies have been proposed to reduce the impact of breathing activity on MR thermometry in abdominal organs:

Gated strategy Using respiratory-gated strategies, MR acquisition is synchronized to a stable period of breathing activity. To this end, a temporal window of 1 s is employed during the exhalation phase of the respiratory cycle. The breathing motion pattern can be assessed on-line using various types of qualitative sensors, such as breathing belt (Morikawa et al. 2004) or quantitative surrogates, such as MR navigators (Vigen et al. 2003). This way, motion artifacts on thermal maps can be reduced, limiting however the temporal resolution to the respiratory frequency (Weidensteiner et al. 2004).

Non-gated strategy Non-gated strategies have been recently proposed to provide continuous and regular temperature updates with a high temporal frequency during the entire respiratory cycle. However, precise modeling of the inhomogeneous magnetic field *in-vivo* and under real-time conditions is difficult to achieve, and consequently several alternative simplified strategies have been proposed to allow correcting motion related errors in PRF-based MR thermometry. For this purpose, two approaches emerged as promising candidates to enable continuous MR-thermometry of abdominal organs under free-breathing conditions: "Referenced" and "Referenceless" MR thermometry.

Referenced MR thermometry consists of analyzing phase artifacts with motion during a pre-treatment step performed prior to the intervention. A reference data-set of magnitude and phase images is recorded during the motion cycle of the organ. For this intention, the motion cycle must be sampled with a sufficient density in order to avoid discretization errors. With typical imaging frame-rates of 5–10 images per second, and a respiration frequency of 3–5 s, this pre-treatment step can be completed in a relatively short duration of 10–20 s. Phase artifacts, due to the periodical motion of the respiration cycle, are then addressed either by a multi-baseline strategy (Vigen et al. 2003; Denis de Senneville et al. 2007a, b; Quesson et al. 2011), or alternatively by applying a phase correction based on a model of the phase variation in dependence of the estimated target motion (Hey et al. 2009; Denis de Senneville et al. 2011).

Using referenceless MR thermometry, a background phase is estimated by fitting a polynomial function to the measured phase obtained from a region of interest (ROI) outside the treatment area, which is assumed to remain at body temperature as described by (Rieke et al. 2004; McDannold et al. 2008; Holbrook et al. 2010). Recent updates of this approach aim at avoiding fitting problems due to spatial phase wraps, as well as determining the appropriate size and location of the ROI, and the optimal polynomial order for the phase fit can be determined before heating (Kuroda et al. 2006; Zou et al. 2013). In particular, the computation of background phase using dipole-based filtering (Liu et al. 2011) or harmonic interpolation (Schweser et al. 2010; Salomir et al. 2012) have also been investigated to further improve the performance of this approach.

A hybrid of both the multi-baseline and the referenceless methods has also been investigated: A direct combination of both techniques to compute each temperature map has been proposed by (Grissom et al. 2010), as well as a

temporal switch method (Denis de Senneville et al. 2010). The latter initially employs the multi-baseline algorithm to continuously provide temperature maps across the entire field of view. In case of spontaneous movement during the intervention, for which no reference phase is pre-recorded, the correction strategy is updated dynamically from "referenced" to "referenceless" MR-Thermometry.

3.3.2.2 Challenges Associated with Real-Time Volumetric MR-Temperature Imaging

Finally, 3D isotropic MR-Thermometry in a large field-of-view is a prerequisite to achieve an accurate monitoring of the thermal dose measured in the targeted area, as well as the collateral damages (such as edema induced in the near field close to the skin or due to heating of the bone by absorption of the acoustic energy). Several MR acquisition/reconstruction techniques have been employed to reduce the scan time of PRF sequences (Tsao et al. 2003). In a study by Quesson et al. (2011), volumetric MRI thermometry in pig livers was achieved with an update rate of 400 ms on a volume of five slices, together with a relatively high temperature precision of 2 °C. More recently, post-processing techniques have been also introduced to compute 3D MR-temperature maps in real-time using sparse sampling or Kalman filtering approaches (Todd et al. 2014; Roujol et al. 2012; Denis de Senneville et al. 2013).

Conclusion

Since the introduction of the concept of MRI-guided HIFU for interventional oncology 20 years ago, a considerable interest has been directed towards ablation methods for liver and renal malignancies. In particular in the last decade, extensive preclinical research has meanwhile identified several clinically feasible solutions for the most challenging problems and several clinical pilot trial studies have been conducted.

Nevertheless, the substantial progress in both MR-guidance and refined acoustic energy delivery has so far not led to widespread clinical acceptance. The main reason is a lack of dedicated MRI-HIFU equipment, which must still be optimized for liver and kidney cancer therapy. The currently employed equipment and its associated methodology leads to many compromises, such as low volumetric ablation rates, or requirements such as general anesthesia, which renders this approach on par with other already clinically established minimally invasive techniques, such as RF-ablation.

However, recently we have seen a rapid development of cancer screening modalities, which in turn has meanwhile resulted in an increasing number of patients where the primary tumor is detected at an earlier stage. As a consequence, the demand for non-invasive local therapy with non-ionizing radiation is likely to increase in the future.

References

American Cancer Society (2011) Global cancer facts and figures, 2nd edn. American Cancer Society, Atlanta

Arnold P, Preiswerk F, Fasel B, Salomir R, Scheer K, Cattin PC (2011) 3D organ motion prediction for MR-guided high intensity focused ultrasound. Med Image Comput Comput Assist Interv 14:623–630

Auboiroux V, Petrusca L, Viallon M, Goget T, Becker CD, Salomir R (2012) Ultrasonography-based 2D motion-compensated HIFU sonication integrated with reference-free MR temperature monitoring: a feasibility study ex vivo. Phys Med Biol 57:N159–N171

Auboiroux V, Petrusca L, Viallon M, Muller A, Terraz S, Breguet R, Montet X, Becker CD, Salomir R (2014) Respiratory-gated MRgHIFU in upper abdomen using an MR-compatible in-bore digital camera. BioMed Res Int 2014:421726

Aubry JF, Pernot M, Marquet F, Tanter M, Fink M (2008) Transcostal high-intensity-focused ultrasound: ex vivo adaptive focusing feasibility study. Phys Med Biol 53:2937–2951

Baron P, Ries M, Deckers R, de Greef M, Tanttu J, Köhler M, Viergever MA, Moonen CT, Bartels LW (2013) In vivo T2-based MR thermometry in adipose tissue layers for high-intensity focused ultrasound near-field monitoring. Magn Reson Med 72:1057–1064

Barron JL, Fleet DJ, Beauchemin SS (1994) Performance of optical flow techniques. Int J Comput Vis 12: 43–77

Bobkova S, Gavrilov L, Khoklova V, Shaw A, Hand J (2010) Focusing of high intensity ultrasound through the rib cage using a therapeutic random phased array. Ultrasound Med Biol 366:888–906

Botros YY, Volakis JL, VanBaren P, Ebbini ES (1997) A hybrid computational model for ultrasound phased-array heating in presence of strongly scattering obstacles. IEEE Trans Biomed Eng 44:1039–1050

Brix L, Ringgaard S, Sorensen TS, Poulsen PR (2014) Three-dimensional liver motion tracking using real-time two-dimensional MRI. Med Phys 41:042302

Chapelon JY, Margonari J, Theillère Y, Gorry F, Vernier F, Blanc E, Gelet A (1992) Effects of high-energy focused ultrasound on kidney tissue in the rat and the dog. Eur Urol 22:147–152

Civale J, Clarke R, Rivens I, ter Haar G (2006) The use of a segmented transducer for rib sparing in HIFU treatments. Ultrasound Med Biol 32:1753–1761

Cline HE, Schenck JF, Hynynen K, Watkins RD, Souza SP, Jolesz FA (1992) MR-guided focused ultrasound surgery. J Comput Assist Tomogr 16:956–965

Cline HE, Hynynen K, Watkins RD, Adams WJ, Schenck JF, Ettinger RH, Freund WR, Vetro JP, Jolesz FA (1995) Focused US system for MR imaging-guided tumor ablation. Radiology 194:731–737

Cochard E, Prada C, Aubry JF, Fink M (2009) Ultrasonic focusing through the ribs using the DORT method. Med Phys 36:3495–3503

Cochard E, Aubry JF, Tanter M, Prada C (2011) Adaptive projection method applied to three-dimensional ultrasonic focusing and steering through the ribs. J Acoust Soc Am 130:716–723

Cornelis F, Grenier N, Moonen CT, Quesson B (2011) In vivo characterization of tissue thermal properties of the kidney during local hyperthermia induced by MR-guided high-intensity focused ultrasound. NMR Biomed 24:799–806

Daum D, Smith N, King R, Hynynen K (1999) In vivo demonstration of noninvasive thermal surgery of the liver and kidney using an ultrasonic phased array. Ultrasound Med Biol 257:1087–1098

De Greef M, Schubert G, Wijlemans JW, Koskela J, Bartels LW, Moonen CTW, Ries M (2015) Intercostal high intensity focused ultrasound for liver ablation: the influence of beam shaping on sonication efficacy and near-field risks. 42(8):4685

De Poorter J, De Wagter C, De Deene Y, Thomson C, Stahlberg F, Achten E (1994) The proton resonance frequency shift method compared with molecular diffusion for quantitative measurement of two dimensional time dependent temperature distribution in phantom. J Magn Reson Imaging 103:234–241

de Zwart JA, Vimeux FC, Palussiere J, Salomir R, Quesson B, Delalande C, Moonen CTW (2001) On-line correction and visualization of motion during MRI-controlled hyperthermia. Mag Reson Med 45: 128–137

Denis de Senneville B, Quesson B, Moonen CTW (2005) Magnetic resonance temperature imaging. Int J Hyperthermia 21:515–531

Denis de Senneville B, Mougenot C, Moonen CTW (2007a) Real-time adaptive methods for treatment of mobile organs by MRI-controlled high-intensity focused ultrasound. Mag Reson Med 57:319–330

Denis de Senneville B, Mougenot C, Quesson B, Dragonu I, Grenier N, Moonen CTW (2007b) MR-thermometry for monitoring tumor ablation. Eur Radiol 17: 2401–2410

Denis de Senneville B, Roujol S, Moonen CTW, Ries M (2010) Motion correction in MR thermometry of abdominal organs: a comparison of the referenceless vs the multi-baseline approach. Magn Reson Med 64:1373–1381

Denis de Senneville B, Ries M, Maclair G, Moonen CTW (2011) MR-guided thermotherapy of abdominal organs using a robust PCA-based motion descriptor. IEEE Trans Med Imaging 30:1987–1995

Denis de Senneville B, Roujol S, Hey S, Moonen CTW, Ries M (2013) Extended Kalman filtering for continuous volumetric MR-temperature imaging. IEEE Trans Med Imaging 32:711–718

Denis de Senneville B, Regard Y, Moonen CTW, Ries M (2014) Combined magnetic resonance and ultrasound echography guidance for direct and indirect motion tracking. 11th IEEE International Symposium on Biomedical Imaging (ISBI), Beijing

Denis de Senneville B, El Hamidi A, Moonen C (2015) A direct PCA-based approach for real-time description of physiological organ deformations. IEEE Trans Med Imaging 34(4):974–982

Emmott J, Sanghera B, Chambers J, Wong WL (2008) The effects of n-butylscopolamine on bowel uptake: an F-FDG PET study. Nuc Med Commun 29:11–16

Feinberg DA, Giese D, Bongers DA, Ramanna S, Zaitsev M, Markl M, Günther M (2010) Hybrid ultrasound MRI for improved cardiac imaging and real-time respiration control. Mag Reson Med 63:290–296

Ferlay J, Shin HR, Bray F, Forman D, Mathers C, Parkin DM (2010) Estimates of worldwide burden of cancer in 2008. Int J Cancer 127:2893–2917

Fink M (1997) Time reversed acoustics. Physics Today 50:34–40

Fink M, Montaldo G, Tanter M (2003) Time reversal acoustics in biomedical engineering. Ann Rev Biomed Eng 5:465–497

Fry FJ (1958) Precision high intensity focusing ultrasonic machines for surgery. Am J Phys Med 37:152–156

Gedroyc WM (2006) New clinical applications of magnetic resonance-guided focused ultrasound. Top Magn Reson Imaging 17:189–194

Gélat P, Ter Haar G, Saffari N (2011) Modelling of the acoustic field of a multi-element HIFU array scattered by human ribs. Phys Med Biol 56:5553–5581

Gélat P, ter Haar G, Saffari N (2012) The optimization of acoustic fields for ablative therapies of tumours in the upper abdomen. Phys Med Biol 57:8471–8497

Gélat P, Ter Haar G, Saffari N (2014) A comparison of methods for focusing the field of a HIFU array transducer through human ribs. Phys Med Biol 59:3139–3171

Gellermann J, Wlodarczyk W, Feussner A, Fahling H, Nadobny J, Hildebrandt B, Felix R, Wust P (2005) Methods and potentials of magnetic resonance imaging for monitoring radiofrequency hyperthermia in a hybrid system. Int J Hyperthermia 21(6):497–513

Goldberg SN, Grassi CJ, Cardella JF, Charboneau JW, Dodd GD III, Dupuy DE, Gervais DA, Gillams AR, Kane RA, Lee FT Jr, Livraghi T, McGahan J, Phillips DA, Rhim H, Silverman SG, Solbiati L, Vogl TJ, Wood BJ, Vedantham S, Sacks D (2009) Image-guided tumor ablation: standardization of terminology and reporting criteria. J Vasc Interv Radiol 20:S377–S390

Goss S, Frizzell L, Dunn F (1979) Ultrasonic absorption and attenuation in mammalian tissues. Ultrasound Med Biol 5:181–186

Graham SJ, Bronskill MJ, Henkelman RM (1998) Time and temperature dependence of MR parameters during thermal coagulation of ex vivo rabbit muscle. Mag Reson Med 39:198–203

Grissom WA, Rieke V, Holbrook AB, Medan Y, Lustig M, Santos J, McConnell MV, Pauly KB (2010) Hybrid referenceless and multibaseline subtraction MR thermometry for monitoring thermal therapies in moving organs. Med Phys 37:5014–5026

Günther M, Feinberg DA (2004) Ultrasound-guided MRI: preliminary results using a motion phantom. Mag Reson Med 52:27–32

Hacker A, Michel MS, Marlinghaus E, Kohrmann KU, Alken P (2005) Clinical study with extracorporeal transducer ultrasound guidance 2005: extracorporeally induced ablation of renal tissue by high-intensity focused ultrasound. BJU Int 97:779–785

Hey S, Maclair G, Denis de Senneville B, Lepetit-Coiffe M, Berber Y, Köhler MO, Quesson B, Moonen CT, Ries M (2009) Online correction of respiratory-induced field disturbances for continuous MR-thermometry in the breast. Magn Reson Med 61:1494–1499

Holbrook AB, Santos JM, Kaye E, Rieke V, Pauly KB (2010) Real-time MR thermometry for monitoring HIFU ablations of the liver. Magn Reson Med 63:365–373

Holbrook AB, Ghanouni P, Santos JM, Dumoulin C, Medan Y, Pauly KB (2014) Respiration based steering for high intensity focused ultrasound liver ablation. Mag Reson Med 71:797–806

Hwang JH, Tu J, Brayman AA, Matula TJ, Crum LA (2006) Correlation between inertial cavitation dose and endothelial cell damage in vivo. Ultrasound Med Biol 32:1611–1619

Hynynen K, Vykhodtseva NI, Chung AH, Sorrentino V, Colucci V, Jolesz FA (1997) Thermal effects of focused ultrasound on the brain: determination with MR imaging. Radiology 204:247–253

Hynynen K, McDannold N, Clement G, Jolesz FA, Zadicario E, Killiany R, Moore T, Rosen D (2006) Pre-clinical testing of a phased array ultrasound system for MRI-guided noninvasive surgery of the brain – a primate study. Eur J Radiol 59:149–156

Ibbini MS, Ebbini ES, Cain CA (1990) NxN square-element ultrasound phased-array applicator: simulated temperature distributions associated with directly synthesized heating patterns. IEEE Trans Ultrason Ferroelectr Freq Control 37:491–500

Illing RO, Kennedy JE, Wu F, ter Haar GR, Protheroe AS, Friend PJ, Gleeson FV, Cranston DW, Phillips RR, Middleton MR (2005) The safety and feasibility of extracorporeal high-intensity focused ultrasound (HIFU) for the treatment of liver and kidney tumours in a Western population. Br J Cancer 93:890–985

Jolesz FA, Hynynen K (2008) Magnetic resonance image-guided focused ultrasound surgery. Cancer J 8:S100–S112

Jung SE, Cho SH, Jang JH, Han JY (2011) High-intensity focused ultrasound ablation in hepatic and pancreatic cancer: complications. Abdom Imaging 362:185–195

Kennedy JE, Wu F, ter Haar GR, Gleeson FV, Phillips RR, Middleton MR, Cranston D (2004) High-intensity focused ultrasound for the treatment of liver tumours. Ultrasonics 42:931–935

Klingler HC, Susani M, Seip R, Mauermann J, Sanghvi N, Marberger MJ (2008) A novel approach to energy ablative therapy of small renal tumours: laparoscopic high-intensity focused ultrasound. Eur Urol 53:810–816

Koh TS, Thng CH, Lee PS, Hartono S, Rumpel H, Goh BC, Bisdas S (2008) Hepatic metastases: in vivo assessment of perfusion parameters at dynamic contrast-enhanced MR imaging with dual-input two-compartment tracer kinetics model. Radiology 249:307–320

Köhler M, Denis de Senneville B, Quesson B, Moonen CTW, Ries M (2011) Spectrally selective pencil-beam navigator for motion compensation of MR-guided high-intensity focused ultrasound therapy of abdominal organs. Mag Reson Med 66:102–111

Kopelman D, Inbar Y, Hananel A, Freundlich D, Castel D, Perel A, Greenfeld A, Salamon T, Sareli M, Valeanu A, Papa M (2006) Magnetic resonance-guided focused ultrasound surgery (MRgFUS): ablation of liver tissue in a porcine model. Eur J Radiol 59:157–162

Kuroda K, Kokuryo D, Kumamoto E, Suzuki K, Matsuoka Y, Keserci B (2006) Optimization of self-reference thermometry using complex field estimation. Magn Reson Med 56:835–843

Langen KM, Willoughby TR, Meeks SL, Santhanam A, Cunningham A, Levine L, Kupelian PA (2008) Observations on real-time prostate gland motion using electromagnetic tracking. Int J Radiat Oncol Biol Phys 71:1084–1090

Lepetit-Coiffe M, Quesson B, Seror O, Dumont E, Le Bail B, Moonen CTW, Trillaud H (2006) Real-time monitoring of radiofrequency ablation of rabbit liver by respiratory-gated quantitative temperature MRI. J Magn Reson Imaging 24(1):152–159

Li J, Xu G, Gu M, Luo G, Rong Z, Wu P, Xia J (2007) Complications of high intensity focused ultrasound in patients with recurrent and metastatic abdominal tumors. World J Astroenterol 13:2747–2751

Liu H, McDannold N, Hynynen K (2005) Focal beam distortion and treatment planning in abdominal focused ultrasound surgery. Med Phys 325:1270–1280

Liu HL, Chang H, Chen WS, Shih TC, Hsiao JK, Lin WL (2007) Feasibility of transrib focused ultrasound thermal ablation for liver tumors using a spherically curved 2D array: a numerical study. Med Phys 349: 3436–3448

Liu T, Khalidov I, de Rochefort L, Spincemaille P, Liu J, Tsiouris AJ, Wang Y (2011) A novel background field

removal method for MRI using projection onto dipole fields (PDF). NMR Biomed 24:1129–1136

Lorenço de Oliveira P, Denis de Senneville B, Dragonu I, Moonen CTW (2010) Rapid motion correction in MR-guided high-intensity focused ultrasound heating using real-time ultrasound echo information. NMR Biomed 23:1103–1108

Lynn JG, Zwemer RL, Chick AJ, Miller A (1942) A new method for the generation and use of focused ultrasound in experimental biology. J Gen Physiol 26:179–193

Marquet F, Aubry J, Pernot M, Fink M, Tanter M (2011) Optimal transcostal high-intensity focused ultrasound with combined real-time 3D movement tracking and correction. Phys Med Biol 56:7061–7068

McDannold N, Tempany CM, Jolesz FA, Hynynen K (2008) Evaluation of referenceless thermometry in MRI-guided focused ultrasound surgery of uterine fibroids. J Magn Reson Imaging 228:1026–1032

McGough RJ, Kessler ML, Ebbini ES, Cain CA (1996) Treatment planning for hyperthermia with ultrasound phased arrays. IEEE Trans Ultrason Ferroelectr Freq Control 43:1074–1084

Miller DL (2007) Overview of experimental studies of biological effects of medical ultrasound caused by gas body activation and inertial cavitation. Prog Biophys Mol Biol 9:314–330

Mirabell R, Nouet P, Rouzaud M, Bardina A, Heijira N, Schneider D (1998) Radiotherapy of bladder cancer: relevance of bladder volume changes in planning boost treatment. Int J Radiat Oncol Biol Phys 41: 741–746

Morikawa S, Inubushi T, Kurumi Y, Naka S, Sato K, Demura K, Tani T, Haque HA (2004) Feasibility of respiratory triggering for MR-guided microwave ablation of liver tumors under general anesthesia. Cardiovasc Intervent Radiol 27:370–373

Mougenot C, Köhler MO, Enholm J, Quesson B, Moonen CTW (2011) Quantification of near-field heating during volumetric MR-HIFU ablation. Med Phys 38: 272–282

Okada A, Murakami T, Mikami K, Onishi H, Tanigawa N, Marukawa T, Nakamura H (2006) A case of hepatocellular carcinoma treated by MR-guided focused ultrasound ablation with respiratory gating. Magn Reson Med Sci 5:167–171

Pernot M, Aubry JF, Tanter M, Thomas JL, Fink M (2003) High power transcranial beam steering for ultrasonic brain therapy. Phys Med Biol 48:2577–2589

Peters RD, Henkelman RM (2000) Proton-resonance frequency shift MR thermometry is affected by changes in the electrical conductivity of tissue. Magn Reson Med 43:62–71

Prada C (2002) Detection and imaging in complex media with the DORT method. Top Appl Phys 84:107–133

Quesson B, Merle M, Kohler M, Mougenot C, Roujol S, Denis de Senneville B, Moonen CTW (2010) A method for MRI guidance of intercostal high intensity focused ultrasound ablation in the liver. Med Phys 376:2533–2540

Quesson B, Laurent C, Maclair G, Denis de Senneville B, Mougenot C, Ries M, Carteret T, Rullier A, Moonen CTW (2011) Real-time volumetric MRI thermometry of focused ultrasound ablation in vivo: a feasibility study in pig liver and kidney. NMR Biomed 24:145–153

Rieke V, Butts Pauly K (2008) MR thermometry. J Magn Reson Imaging 27:376–390

Rieke V, Vigen KK, Sommer G, Daniel BL, Pauly JM, Butts K (2004) Referenceless PRF shift thermometry. Magn Reson Med 51:1223–1231

Ries M, Denis de Senneville B, Roujol S, Berber Y, Quesson B, Moonen CTW (2010) Real-time 3D target tracking in MRI-guided focused ultrasound ablations in moving tissues. Mag Reson Med 64:1704–1712

Ries M, Denis de Senneville B, Regard Y, Moonen CTW (2012) Combined magnetic resonance imaging and ultrasound echography guidance for motion compensated HIFU interventions. 12th international symposium on therapeutic ultrasound. AIP Publishing, pp 202–206

Roujol S, Ries M, Quesson B, Moonen CTW, Denis de Senneville B (2010) Real-time MR-thermometry and dosimetry for interventional guidance on abdominal organs. Mag Reson Med 63:1080–1087

Roujol S, Ries M, Moonen CTW, Denis de Senneville B (2011) Automatic nonrigid calibration of image registration for real time MR-guided HIFU ablations of mobile organs. IEEE Trans Med Imaging 30:1737–1745

Roujol S, Denis de Senneville B, Hey S, Moonen CTW, Ries M (2012) Robust adaptive extended Kalman filtering for real time MR-thermometry guided HIFU interventions. IEEE Trans Med Imaging 31:533–542

Ruers T, Bleichrodt RP (2003) Treatment of liver metastases, an update on the possibilities and results. Eur J Cancer 238:1023–1033

Salomir R, Viallon M, Kickhefel A, Roland J, Morel DR, Petrusca L, Auboiroux V, Goget T, Terraz S, Becker CD, Gross P (2012) Reference-free PRFS MR-thermometry using near-harmonic 2-D reconstruction of the background phase. IEEE Trans Med Imaging 31:287–301

Sapareto SA, Dewey WC (1984) Thermal dose determination in cancer therapy. Int J Radiat Oncol Biol Phys 10:787–800

Schweser F, Lehr BW, Deistung A, Reichenbach JR (2010) A novel approach for separation of background phase in SWI phase data utilizing the harmonic function mean value property. Proceedings to the 18th meeting of the International Society for Magnetic Resonance in Medicine, Stockholm

Smitmans MHP, Pos FJ, de Bois J, Heemsbergen WD, Sonke J-J, Lebesque JV, van Herk M (2008) The influence of a dietary protocol on a cone beam CT-guided radiotherapy for prostate cancer patients. Int J Radiat Oncol Biol Phys 71:1279–1286

Sotiras A, Davatzikos C, Paragios N (2013) Deformable medical image registration: a survey. IEEE Trans Med Imaging 32:1153–1190

Stemkens B, Tijssen R, Denis de Senneville B, Lagendijk J, van den Berg C (2014) Retrospective reconstruction of 3D radial MRI data to evaluate the effect of abdominal compression on 4D abdominal organ motion. Med Phys 41(6):538

Stemkens B, Tijssen R, Denis de Senneville B, Heerkens HD, van Vulpen M, Lagendijk J, van den Berg C (2015) Optimizing 4D-MRI data sampling for respiratory motion analysis of pancreatic tumors. Int J Radiat Oncol Biol Phys 91(3):571–578

Tanter M, Aubry JF, Gerber J, Thomas JL, Fink M (2001) Optimal focusing by spatio-temporal inverse filter. I. Basic principles. J Acoust Soc Am 110:37–47

Tanter M, Pernot M, Aubry J-F, Montaldo G, Marquet F, Fink M (2007) Compensating for bone interfaces and respiratory motion in high intensity focused ultrasound. Int J Hyperthermia 23:141–151

Todd N, Prakash J, Odéen H, de Bever J, Payne A, Yalavarthy P, Parker DL (2014) Toward real-time availability of 3D temperature maps created with temporally constrained reconstruction. Magn Reson Med 71:1394–1404

Tsao J, Boesiger P, Pruessmann KP (2003) k-t BLAST and k-t SENSE: dynamic MRI with high frame rate exploiting spatiotemporal correlations. Magn Reson Med 50:1031–1042

Vallancien G, Harouni M, Veillon B, Mombet A, Praponitch D, Brisset JM, Bougaran J (1992) Focused extracorporeal pyrotherapy: feasibility study in man. J Endourol 6:173–181

Verhey LJ (1995) Immobilizing and positioning patients for radiotherapy. Sem Radiat Oncol 5:100–114

Vigen KK, Daniel BL, Pauly JM, Butts K (2003) Triggered, navigated, multi-baseline method for proton resonance frequency temperature mapping with respiratory motion. Magn Reson Med 50:1003–1010

Weidensteiner C, Kerioui N, Quesson B, Denis de Senneville B, Trillaud H, Moonen CTW (2004) Stability of real-time MR temperature mapping in healthy and diseased human liver. J Magn Reson Imaging 19:438–446

Wijlemans JW, de Greef M, Schubert G, Bartels LW, Moonen CTW, van den Bosch MAAJ, Ries M (2015a) A clinically feasible treatment protocol for MR-guided HIFU ablation in the liver. Invest Radiol 50(1):24–31

Wijlemans JW, van Breugel JMM, de Greef M, Moonen CTW, van den Bosch MAAJ, Ries M (2015b) Spontaneous breathing vs mechanical ventilation for respiratory-gated MR-HIFU ablation in the liver. J Ther Ultrasound 3(Suppl 1)

Wu F, Chen WZ, Bai J (1999) Effect of high-intensity focused ultrasound on the patients with hepatocellular carcinoma: preliminary report. Chin J Ultrasonogr 8:213–216

Wu F, Wang ZB, Chen WZ, Zhu H, Bai J, Zou JZ, Li KQ, Jin CB, Xie FL, Su HB (2004) Extracorporeal high intensity focused ultrasound ablation in the treatment of patients with large hepatocellular carcinoma. Ann Surg Oncol 1:1061–1069

Young IR, Hajnal JV, Roberts IG, Ling JX, Hill-Cottingham RJ, Oatridge A, Wilson JA (1996) An evaluation of the effects of susceptibility changes on the water chemical shift method of temperature measurement in human peripheral muscle. Magn Reson Med 36:366–374

Zhang L, Chen WZ, Liu YJ, Hu X, Zhou K, Chen S, Peng L, Zhu H, Zou HL, Bai J, Wang ZB (2010) Feasibility of magnetic resonance imaging-guided high intensity focused ultrasound therapy for ablating uterine fibroids in patients with bowel lies anterior to uterus. Eur J Radiol 73:396–403

Zou C, Shen H, He M, Tie C, Chung YC, Liu X (2013) A fast referenceless PRFS-based MR thermometry by phase finite difference. Phys Med Biol 58:5735–5751

Magnetic Resonance-Guided High Intensity Focused Ultrasound Ablation of Breast Cancer

4

Floortje M. Knuttel and Maurice A.A.J. van den Bosch

Abstract

This chapter describes several aspects of MR-HIFU treatment for breast cancer. The current and future applications, technical developments and clinical results are discussed. MR-HIFU ablation is under investigation for the treatment of breast cancer, but is not yet ready for clinical implementation. Firstly, the efficacy of MR-HIFU ablation should be investigated in large trials. The existing literature shows that results of initial, small studies are moderate, but opportunities for improvement are available. Careful patient selection, taking treatment margins into account and using a dedicated breast system might improve treatment outcomes. MRI-guidance has proven to be beneficial for the accuracy and safety of HIFU treatments because of its usefulness before, during and after treatments. In conclusion, MR-HIFU is promising for the treatment of breast cancer and might lead to a change in breast cancer care in the future.

Keywords

Breast cancer • Magnetic resonance imaging • High-intensity focused ultrasound

4.1 Introduction

Breast cancer is the second most diagnosed cancer worldwide. Estimates of worldwide burden of cancer in 2012 showed that 14.1 million cases of newly diagnosed cancer occurred, of which 1.67 million were breast cancer (25 % of cancer cases in women) (International Agency for Research on Cancer 2012). Due to the worldwide disease burden caused by breast cancer, improving the diagnostic process and treatment efficacy are important

F.M. Knuttel (✉) • M.A.A.J. van den Bosch (✉)
Department of Radiology,
University Medical Center Utrecht,
Utrecht, The Netherlands
e-mail: f.m.knuttel@umcutrecht.nl;
mbosch@umcutrecht.nl

© Springer International Publishing Switzerland 2016

J.-M. Escoffre, A. Bouakaz (eds.), *Therapeutic Ultrasound*, Advances in Experimental Medicine and Biology, Vol. 880, DOI 10.1007/978-3-319-22536-4_4

research goals. The primary treatment modality for breast cancer is surgery, which has evolved from radical Halsted mastectomy to breast-conserving surgery during the last decades (Halsted 1907). Local control of breast cancer is achieved in most patients, making surgery a very effective treatment. Radiotherapy has an important role in breast-conserving therapy; large randomized trials have shown that the recurrence rate is reduced and survival is increased after radiotherapy (Darby et al. 2011; Fisher et al. 2002). However, unless breast-conserving therapy yields very favorable results with respect to recurrence and survival, the risk of complications exists and cosmetic results are not always satisfying.

For this reason, current research is increasingly aimed at investigating new treatment techniques, such as the use of Magnetic Resonance-guided High Intensity Focused Ultrasound (MR-HIFU) for tumor destruction (Kaiser et al. 2008). Introducing this new completely non-invasive technique will probably change breast cancer care in the near future (Jolesz 2009). The most important benefit of HIFU treatment is non-invasiveness, potentially resulting in a decreased risk of complications and improved cosmetic outcomes. Additionally, the breast is a suitable body part for HIFU treatment because of its peripheral location. MRI-guidance enables safe and precise HIFU treatments since it is the most sensitive imaging method for tumor delineation and provides temperature feedback for treatment monitoring and imaging for evaluation of treatment results (Merckel et al. 2013).

This chapter focuses on MR-HIFU ablation of breast cancer. A complete overview of technical and clinical challenges and previous research is given, combined with an insight into future possibilities for the use of MR-HIFU in breast cancer patients.

4.2 Role of MR Imaging in HIFU Ablation of Breast Lesions

4.2.1 Imaging of Breast Cancer

Mammography and ultrasound are currently most widely used for the detection and staging of breast cancer. The sensitivity and specificity of mammography vary from 75.8 % to 85.8 % and 87.7 % to 97 %, respectively. Ultrasound has a sensitivity of 70.8–92.4 % with a specificity of 72.6–76.4 %. When mammography and ultrasound are combined, sensitivity and specificity increase to 91 % and 98 %, respectively (Zonderland et al. 1999; Houssami et al. 2003; Bruening et al. 2012; Barlow et al. 2002). The sensitivity of breast MRI ranges from 90 to 95 %, with a specificity of 72 to 77.5 % (Peters et al. 2008; Bruening et al. 2012; Hrung et al. 1999). Although it has a comparable diagnostic accuracy, MRI performs better in determining lesion size when compared to conventional imaging methods (Fig. 4.1) (Blair et al.

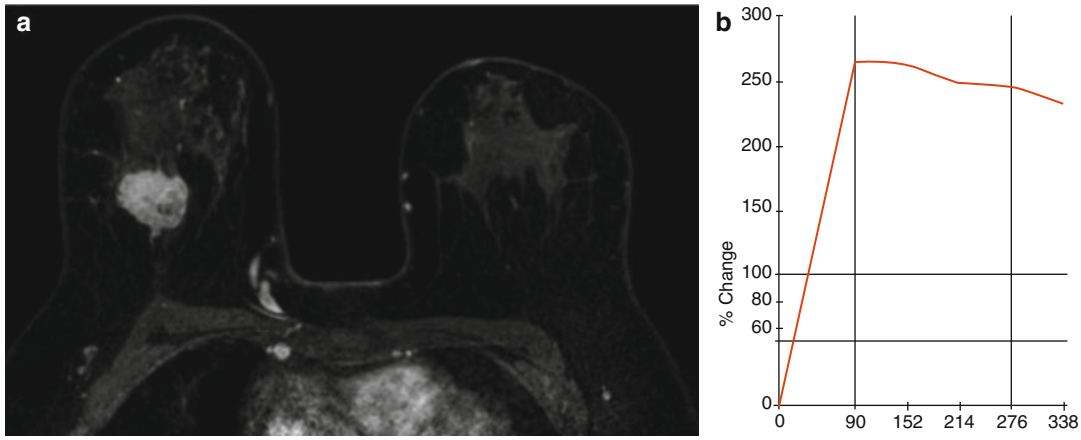

Fig. 4.1 Dynamic contrast-enhanced bilateral 3 T MRI with fat suppression showing a mass in the right breast with an irregular enhancement pattern (**a**). The lesion has suspect enhancement kinetics with rapid wash-in followed by washout in the delayed phase (**b**)

2006; Shin et al. 2012). There is a lot of controversy about whether MRI should be performed in all breast cancer patients. Its moderate specificity results in false-positive findings and clinical trials have not (yet) proven that MRI improves the long-term outcome of breast cancer patients (Turnbull et al. 2010; Peters et al. 2011). MRI is known, however, to be of added value in certain patient groups (Knuttel et al. 2014). For example, patients with invasive lobular carcinoma benefit from MRI because it has a diffuse growth pattern, which makes it harder to accurately determine disease extent by conventional imaging (Mann et al. 2008, 2010). Patients with an increased risk of developing breast cancer also benefit from breast MRI (screening) as they tend to develop breast cancer at a younger age when breast density is still high, which impairs the sensitivity of mammography. Besides, high-risk patients more often present with multifocal/multicentric and contralateral disease, not detected by conventional imaging (Kuhl et al. 2005; Warner et al. 2004). Lastly, MRI is useful in finding the primary breast tumor in patients with axillary lymphatic metastases in whom primary tumors could not otherwise be found (de Bresser et al. 2010).

4.2.2 MRI for Guidance of HIFU Treatment

MRI has different roles with regard to treatment. Firstly, it is a tool for patient selection. The size of the tumor, the distance to the skin and pectoral muscle and the position in the breast can be accurately determined (Peters et al. 2008; Blair et al. 2006). These factors should be investigated beforehand to assess whether a patient is eligible for MR-HIFU treatment. Besides, MRI frequently detects additional lesions that are occult on conventional imaging, altering the eligibility for MR-HIFU treatment and possibly even changing the surgical therapy (Houssami et al. 2008).

Secondly, MRI is useful for guidance during HIFU treatment for several reasons. Foremost, it provides accurate anatomic details of the tumor and surrounding tissue, enabling precise treatment planning. Additionally, MRI provides real-time temperature maps. Monitoring the temperature in the breast during HIFU treatments is of utmost importance as it shows whether the target temperature of more than 60 °C is reached at the treatment site. Consequently, treatments can be adjusted when necessary. The most widely used thermometry method is proton resonance frequency shift (PRFS) (Zippel and Papa 2005; Furusawa et al. 2006). This technique is discussed in Sect. 5.5.2.

Lastly, MRI can be used after treatment for the assessment of treatment results. Since MR-HIFU ablation is a non-invasive technique, reliable imaging methods are a prerequisite for clinical implementation of MR-HIFU ablation in order to detect eventual residual disease. MRI can accurately depict the amount of coagulated tissue (Hynynen 2010). The most reliable method is T1-weighted contrast-enhanced MR imaging. The coagulated area is seen as a hypointense mass due to the cessation of blood perfusion (McDannold et al. 1998). Gianfelice and Khiat et al. investigated the value of three dynamic contrast enhanced-MRI (DCE-MRI) parameters and found correlations with the percentage of residual tumor. These correlations are most likely based on the decrease of microvessel density after ablation. The reliability of DCE-MRI was dependent on the time-interval between MR-HIFU and imaging, correlation coefficients clearly improved after 7 days when compared to imaging directly after treatment (Gianfelice et al. 2003a; Khiat et al. 2006).

4.3 High Intensity Focused Ultrasound of the Breast

4.3.1 Technique

The HIFU technique is already described in detail in Chap. 1 of this book. In summary, MR-HIFU ablation is an entirely non-invasive technique which makes use of ultrasound beams that are focused in a focal point. Due to the high intensity of the focused ultrasound beam, the temperature in the focal point increases rapidly. The amount of heating depends mainly on the applied power and the perfusion of the targeted tissue. The more perfusion, the less heating will

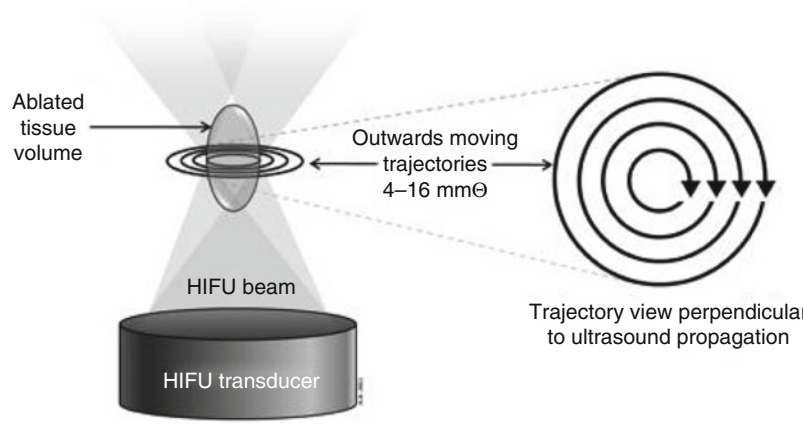

Fig. 4.2 Schematic outline of the volumetric ablation technique

occur as the blood flow distributes the heat away from the focal point. Due to the precise targeting with MRI-guidance, the adjacent healthy tissue and the skin remain unaffected. If a temperature of at least 57–60 °C is reached for a few seconds, protein denaturation occurs, leading to tissue necrosis. Lower temperatures for a longer period of time can also induce tissue necrosis (Jenne et al. 2012; Jolesz 2009; Hynynen 2010).

The size of the focal point depends on characteristics of the transducer that produces the ultrasound beams. The focal point is usually too small to totally ablate a tumor in one sonication (Haar and Coussios 2007). Ablation of large volumes is either done by "the point-by-point method" or by a "volumetric heating method" (Voogt et al. 2012; Kohler et al. 2009). With the point-by-point method, separate points are consecutively heated forming a grid of ablations. A limitation of this technique is the cooling time between the separate sonications that has to be taken into account, enabling diffusion of deposited energy. This makes MR-HIFU treatments relatively time consuming. Volumetric heating is performed by steering the focal point along outward moving trajectories, using the previous heat buildup in the center of the tumor. A larger tissue volume is ablated per sonication, resulting in shorter treatment durations (Fig. 4.2) (Kohler et al. 2009; Salomir et al. 2000; Voogt et al. 2012).

4.3.2 HIFU Breast Systems

Two different types of MR-HIFU systems exist. The most important difference between both systems is the targeting approach. The "fibroid platform", or "generic" approach, is currently most widely used. With this type of system, the breast is targeted from an anterior direction (Fig. 4.3a).

The transducer is immersed in a water bath, which is embedded in an MRI tabletop. The shape of the transducer is spherical to enable focusing of the ultrasound beam. In most centers that perform clinical studies MR-HIFU breast studies, the ExAblate 2000, produced by InSightec (Haifa, Israel) has been used (Gianfelice et al. 2003b; Furusawa et al. 2006). Another system that provides anterior sonications has also been used (Hynynen et al. 2001; Cline et al. 1995).

More recently, systems using a "dedicated approach" have been developed. The main difference with the generic approach is the direction of the HIFU beam. The ultrasound transducers are positioned around the breast, allowing for lateral sonications (Fig. 4.3b). In 2001, the first patient was treated with a dedicated breast system in a feasibility study (Huber et al. 2001). Other breast-specific systems have been developed by different research groups. Payne et al. introduced a 256-element phased-array transducer, which can be moved around the breast (Payne et al. 2012). In-vivo experiments in a goat udder model

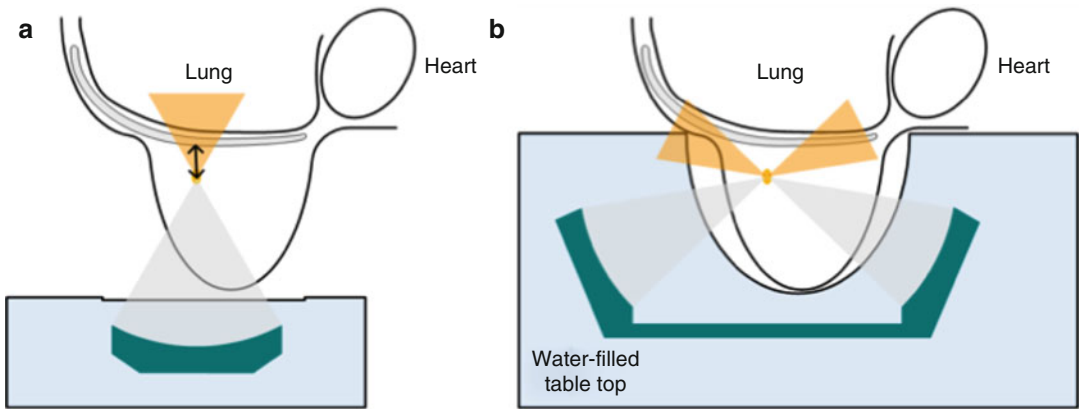

Fig. 4.3 Two approaches of HIFU ablation of the breast. Generic approach (**a**), Dedicated approach (**b**)

demonstrated that this MR-HIFU system was able to effectively and safely perform ablations (Payne et al. 2013). Currently, a dedicated breast system (Sonalleve, Philips Healthcare, Vantaa, Finland) is used in clinical feasibility and efficacy studies in the University Medical Center of Utrecht, the Netherlands (see Sect. 4.6). The transducer of this system consists of eight modules with 32 elements each, submerged in degassed water. The transducer is circumferentially positioned around a breast cup, which is positioned in the middle of an MRI tabletop (Fig. 4.4) (Moonen and Mougenot 2006; Merckel et al. 2013).

An important benefit of the dedicated, lateral approach is the distance between the focus and the rib cage and heart and lungs. The area behind the focal point, where the ultrasound beam diverges, is called the far field of the beam path. During MR-HIFU treatments, a risk of overheating is caused by energy deposition of the far-field beam in the rib cage, heart and lungs. The effective distance between the focal point and the structures in the far field is larger with the dedicated approach when compared to the anterior approach. Besides, not the entire far-field beam will reach the ribcage, heart and lungs because it leaves the breast on the opposite side of the transducer due to its horizontal orientation. As a result, the risk of overheating the far field is reduced. Furthermore, the aforementioned dedicated breast system contains eight transducer modules which all reach the breast from a slightly different direction. The energy density at the skin level is therefore decreased compared to systems with a single transducer, reducing the risk of skin burns (Merckel et al. 2013). A possible disadvantage of this wide aperture system is focus aberration due to heterogeneous breast tissue. The breast contains fibroglandular and adipose tissue in which the speed of sound is different. The ultrasound beams from different directions therefore have different acoustic paths. In very large, heterogeneous breasts this might lead to clinically relevant focus aberration. Mougenot et al. have investigated a correction method to mitigate distortion of the focal point during treatments (Mougenot et al. 2012).

4.4 Clinical Studies

4.4.1 Benign Lesions

In 2001, the first application for MR-HIFU ablation of benign lesions in the breast was reported. Nine patients with 11 fibroadenomas underwent MR-HIFU ablation in a feasibility study. They received local anesthesia injected behind the fibroadenoma. Eight tumors showed partial (50–90 %) or complete (>90 %) response, indicated by the size of non-perfused volumes on MRI. Follow-up MRI scans at 6 months showed a significant decrease in tumor volume of 0.6 cm^3

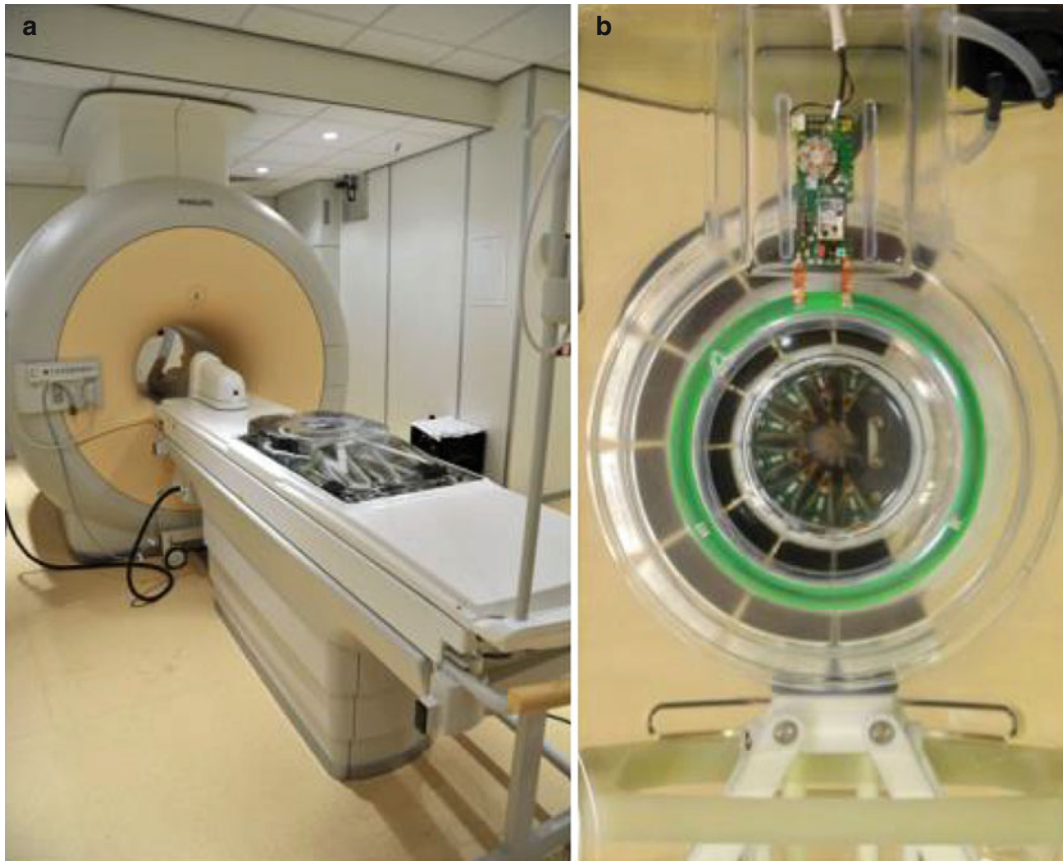

Fig. 4.4 Dedicated breast system with tabletop integrated in 1.5 T MRI scanner (**a**) and a close-up of the breast cup with eight circumferentially positioned transducers (**b**)

on average. The lesions felt softer on physical examination, which was also reported by the patients. Non-effectiveness of MR-HIFU ablation was attributed to insufficient energy deposition in the tumor in one patient, and to patient movements in two other patients. In one patient, an analgesic was injected in front of the fibroadenoma, causing scattering of the ultrasound and therefore no sufficient heating of the tumor. This study also showed a number of side effects that are known to occur after HIFU ablation. One patient had post-procedural edema in the pectoral muscle. However, no clinical consequences were observed and the edema disappeared within 14 days. One patient developed a bruise on the skin. Four patients experienced mild pain during treatment, two patients moderate pain and one patient severe pain. Breast tenderness lasted up to 10 days in some cases. Finally, transient moderate swelling of the treated breast was observed. No long-term side effects occurred (Hynynen et al. 2001).

4.4.2 Invasive Breast Cancer with Resection

The first-in-man study in patients with benign tumors was followed by various studies in patients with invasive breast cancer. The majority of MR-HIFU breast studies were performed according to a treat-and-resect protocol to facilitate histologic evaluation of the treatment response. Huber et al. reported the first results of MR-HIFU ablation of invasive breast cancer. They treated one patient who underwent breast-conserving surgery 5 days later. Post-therapeutic

MR imaging showed a lack of contrast uptake in the treated region, indicating that the tumor was successfully ablated. Furthermore, a hyperintense rim surrounding the tumor was seen. Histopathology demonstrated sublethal and lethal thermal damage in the tumor (Huber et al. 2001). Gianfelice et al. performed MR-HIFU ablation in 12 patients. Only in two patients complete necrosis of the tumorous tissue was achieved. They used two different focused US systems, of which the second performed better. An average of 43.3 % of malignant tissue was ablated with the first system in three patients. The second system provided tumor necrosis in 88.3 % in nine patients. All patients experienced slight to moderate pain during the treatments, despite administration of analgesics (fentanyl citrate) and sedatives (midazolam) in variable doses. The pain or discomfort was transient in all cases. The most important side effects were second-degree skin burns in two patients (Gianfelice et al. 2003b). In the same year, Gianfelice et al. reported results of 17 breast cancer patients treated with MR-HIFU, also partly included in their previous paper (Gianfelice et al. 2003b). This study was designed to investigate the role of DCE-MRI in assessing the amount of residual disease after MR-HIFU. In four patients, total tumor necrosis was found under histopathological evaluation, more than 90 % of the tumor was ablated in nine patients and four patients had necrotic volumes ranging from 25 to 70 % (Gianfelice et al. 2003a). Khiat et al. used the same patient population and added extra patients; they reported the results of the treatments of 25 women in total. The focus of this paper was the effect of the duration between HIFU treatment and MRI performance on MRI parameters that are used to assess the presence of residual tumor. A total of 26 tumors were treated, of which seven were found to be totally ablated. Another seven tumors were 10–80 % ablated, the remaining tumors showed less than 10 % residual disease. Contrast-enhanced MRI parameters were most reliable when assessed after 7 or more days after HIFU. When MRI was performed directly after treatment, no conclusions about treatment efficacy could be drawn (Khiat et al. 2006). In 2005, another phase one trial was conducted in ten patients with early stage breast cancer. MR-HIFU ablation was 100 % effective in two patients. The amount of residual disease in the other eight patients ranged from 30 % to only microscopic foci (Zippel and Papa 2005). Furusawa et al. treated 30 breast cancer patients with MR-HIFU ablation. Complete necrosis of the tumor was seen in 15 of 30 patients (50 %). The amount of necrotic tumor exceeded 85 % in 28 patients (Furusawa et al. 2006). Finally, an Italian MR-HIFU study is currently being performed. Preliminary results from 2013 show that in nine out of 10 treated patients, complete tumor necrosis, including a margin of 5 mm, was achieved (Napoli et al. 2013).

Adverse events occurred in many patients, but were usually mild. The majority of patients experienced mild pain, discomfort or a pressure sensation during the treatments (Huber et al. 2001; Furusawa et al. 2006; Zippel and Papa 2005). In some cases, some breast tenderness lasted for a few days (Gianfelice et al. 2003b). Another common side effect is skin burns, which were reported in four patients in three studies. One of these patients had a third-degree skin burn, the only reported major adverse event (Furusawa et al. 2006; Gianfelice et al. 2003b; Zippel and Papa 2005). The occurrence of long-term side effects could not be investigated in these studies as a result of subsequent surgical resection of the treated tumors. Generally, few complications occur after MR-HIFU treatment, especially when safety margins are taken into account.

MR-HIFU ablation was not equally successful in all patients. Several reasons for treatment failure have been mentioned. In most cases, insufficient power was delivered to the tumor. In one patient, the skin absorbed an abnormal amount of energy, hampering lethal heating of the tumor (Furusawa et al. 2006). In some studies, patients received local anesthesia that was injected behind the tumor (Furusawa et al. 2006). Another anesthesia method was intravenous administration of an opioid with a sedative (Gianfelice et al. 2003b) or just an oral sedative (Huber et al. 2001). Generally it seems that local analgesia or conscious sedation is not always sufficient during

MR-HIFU treatments. Patients still experience pain or move, which makes accurate targeting difficult. Tumor targeting was often poor, indicating that careful patient selection is important and that technical problems still have to be solved (Gianfelice et al. 2003b). Furthermore, a large enough margin around the tumor should be taken into account (Gianfelice et al. 2003b).

4.4.3 Invasive Breast Cancer Without Resection

Gianfelice et al. also assessed the feasibility and efficacy of MR-HIFU ablation in breast cancer patients who did not undergo surgical excision after HIFU treatment. These patients were either at high risk for surgical complications or refused surgery. Twenty-four patients with biopsy-proven breast cancer received Tamoxifen as a primary treatment and underwent 'adjuvant' MR-HIFU ablation. All patients were free of metastases at the start of the study. The effectiveness of MR-HIFU ablation was assessed by multiple biopsies in different areas of the tumor after one or two treatments. After the first treatment, core biopsies were negative in 58.3 % (14 patients). A second MR-HIFU procedure yielded five more tumor free patients, increasing the total number of successful treatments to 19 (79 %). No patients developed metastases during a mean follow-up of 20.2 months (range 12–39 months). All patients reported mild to moderate pain during treatment and one patient was found to have a second-degree skin burn after treatment. It should be mentioned that patients undergoing MR-HIFU ablation had already been receiving Tamoxifen therapy for variable periods of time. Therefore, the treatment results cannot be entirely attributed to MR-HIFU ablation (Gianfelice et al. 2003c).

The most recently published MR-HIFU study was performed by Furusawa et al. Twenty-one patients were treated with MR-HIFU ablation without subsequent surgery and radiotherapy. Four patients were treated twice to ensure ablation of the entire tumor volume. During a mean follow-up period of 15 months (range 3–26 months), one recurrence was observed. This was attributed to insufficient heating during treatment, which was determined retrospectively. Skin burns were observed in two patients, one third-degree and one second-degree (Furusawa et al. 2007). Furusawa et al. are continuing this MR-HIFU study without resection, no additional results have been published so far (Furusawa 2012). An overview of the existing literature is presented in Table 4.1.

4.5 Clinical and Technical Challenges

4.5.1 Challenges for Improvement

4.5.1.1 Patient Selection

As shown in the previous section, the MR-HIFU ablation clinical results are variable. The minority of MR-HIFU treatments resulted in total tumor ablation, indicating that the technique is not yet ready for clinical practice. Adequate patient selection proved to be very important for successful MR-HIFU treatments, since not all patients are candidates for MR-HIFU ablation. Ideal candidates for MR-HIFU ablation have a unifocal, small tumor with a maximum diameter of around 2 cm, without ductal carcinoma *in-situ* (DCIS). If MR-HIFU ablation was to be the primary treatment of breast cancer, the margin status would not be able to be assessed since the tumor is not surgically removed. Consequently, it would be very important to minimize the risk of leaving residual disease behind. This could be achieved by selecting patients with "breast cancer of limited extent", in whom no *in-situ* or invasive disease is present outside a margin of 10 mm around the index tumor (Faverly et al. 2001).

According to Schmitz et al., who investigated the presence of additional disease in a 10 mm margin around the tumor visualized by MRI, these tumors more frequently show persistent enhancement (plateau) on DCE-MRI and are smaller. A larger quantity of DCIS in the primary tumor was also associated with the presence of disease outside a 10 mm margin (Schmitz et al. 2012). Another reason to exclude patients with DCIS is that MRI cannot reliably assess its size and it may therefore

Table 4.1 Overview of clinical MR-HIFU breast studies

Reference	Patients	Tumors	Protocol	Lesion size	HIFU device	Results	Side effects
Furusawa et al. (2006)	30	28 invasive BC 2 DCIS	Treat and resect	∅ 13 mm (5–25 mm)	ExAblate 2000	15–100 % necrosis Mean: 96.9 % necrosis	One 3rd degree skin burn 5 minor adverse events (1 severe, 1 moderate and 3 mild pains)
Furusawa et al. (2007)	21	21 invasive and non-invasive DC	HIFU with follow-up	∅ 15 mm (5–50 mm)	ExAblate 2000	Mean follow-up 14 months 1 Recurrence	2 skin burns (One 3rd degree)
Gianfelice et al. (2003b)	12	12 invasive BC	Treat and resect	0.11–8.8 cm^3	ExAblate 2000	Mean necrosed volume: Patients 1–3: 43.3 %; Patients 4–12 88.3 %	8 moderate and 4 slight pains during therapy All patients mild discomfort in treated for 24–36 h Two 2nd degree skin burn
Gianfelice et al. (2003a)	17	17 invasive BC	Treat and resect	0.11–8.8 cm^3	ExAblate 2000	4: 100 % necrosis 9: <10 % residual disease 4:30–75 % residual disease	NR
Gianfelice et al. (2003c)	24	24 invasive BC	HIFU + Tamoxifen with follow-up	∅ 15.1 mm (6–25 mm)	ExAblate 2000	19: biopsy negative Mean follow-up: 20.2 months: 22 no change, 2 lesions not visible anymore	14 moderate and 10 light pains during therapy One 2nd degree skin burn
Huber et al. (2001)	1	1 invasive DC	Treat and resect	3.08 cm^3	Single element transducer integrated in 1.5 T MRI	(Sub)lethal thermal damage	None

(continued)

Table 4.1 (continued)

Reference	Patients	Tumors	Protocol	Lesion size	HIFU device	Results	Side effects
Hynynen et al. (2001)	9	11 fibroadenomas	HIFU with follow-up	1.9 cm^3 (0.7–6.5 cm^3)	Single element transducer integrated in 1.5 T MRI	8 (73 %) totally or partially ablated 0.6 cm^3 decreased at 6 months	1 severe, 2 moderate and 4 light pains during therapy Edema pectoral muscle Swelling breast Tenderness treatment area, max. 10 days
Khiat et al. (2006)	25	25 invasive DC 1 invasive LC	Treat and resect	0.11–11.2 cm^3	ExAblate 2000	8: 100 % necrosis 11: <10 % residual disease 7: 20–90 % residual disease	NR
Zippel and Papa (2005)	10	10 invasive BC	Treat and resect	∅ 22 mm	ExAblate 2000	2: 100 % necrosis 2: residual microscopic foci 3: 10 % residual disease 3: 10–30 % residual disease	Pain during therapy One 2nd degree skin burn

BC breast carcinoma *DCIS* ductal carcinoma *in-situ*, *DC* ductal carcinoma, *NR* not reported, *LC* lobular carcinoma

partly be missed during treatment (Kropcho et al. 2012; Kuhl et al. 2007). Furthermore, patients with an invasive lobular carcinoma (ILC) are often not eligible. ILC has a diffuse growth pattern, hampering reliable visualization of the tumor boundaries by MRI, and as a consequence accurate treatment (Menezes et al. 2013).

4.5.1.2 Treatment Margins

As with surgical therapy, treating a margin around the tumor is important to eradicate all cancer cells. The size of this margin has not been established with certainty. In general, a margin of 5 mm is considered to be safe (Furusawa et al. 2006). By others, one centimeter is deemed necessary (Gianfelice et al. 2003b). Ablating a margin of 0.5–1 cm is comparable to the current surgical treatment of breast cancer, which aims for gross resection margins of 0.5–2 cm (Rutgers and EUSOMA Consensus Group 2001; Parvez et al. 2014). However, surgery may be less precise than image-guided treatment techniques, especially in non-palpable breast lesions where the surgeon cannot see or feel the lesion and has to rely on a needle-wire for guidance of the excision. Based on the surgical literature and the precision of image-guided treatments, we propose a treatment margin of 5 mm for MR-HIFU treatments of breast cancer. A limitation of MR-HIFU is the safety margin of 1 cm from the skin and rib cage that has to be taken into account (Furusawa et al. 2006). As a result, a proportion of patients would not be eligible for MR-HIFU treatment. If a treatment margin of 5 mm, with a safety margin of 10 mm to both the skin and the pectoral muscle is taken into account, approximately 46 % of patients with early stage breast cancer would not be eligible for MR-HIFU treatment (unpublished data from our group).

When considering treatment efficacy and use of margins, radiotherapy should also be taken into account. Not all malignant cells might be ablated, but lumpectomy might also not ensure total removal of all tumor cells. In a pathology study of 282 patients who underwent mastectomy but were eligible for breast-conserving surgery, additional foci within a 2 cm margin were found in 20 %. In 43 %, tumor foci were found at a distance of more than 2 cm from the primary tumor (Holland et al. 1985). Schmitz et al. reported the presence of tumor foci at a distance of more than 1 cm from the tumor in 52 % of patients (Schmitz et al. 2010). These findings illustrate the importance of radiotherapy following breast-conserving surgery or ablation. Adding radiotherapy to breast-conserving surgery lowers the risk of recurrence by 15.7 % within 10 years, and reduces the 15-year mortality by 3.8 % (Darby et al. 2011). Combining MR-HIFU ablation with radiotherapy in the future will probably result in more effective treatment and tumor control as occult residual disease after ablation will be treated by irradiation. The role of radiotherapy should be investigated once MR-HIFU technique is sufficiently improved for gross tumor ablation in the majority of patients.

4.5.2 Thermometry

An advantage of MRI-guidance of HIFU treatments is the ability of real-time treatment monitoring based on temperature maps. Various methods for non-invasive MR thermometry exist where proton resonance frequency shift (PRFS) is most widely used. This technique is based on the temperature dependent electron screening of hydrogen nuclei in water, causing a resonance frequency shift in water protons that is proportional to changes of tissue temperature. The linear temperature dependence makes PRFS a very suitable thermometry method. PRFS-based temperature maps can be constructed by MRI and utilized for real-time treatment control (Rieke and Butts Pauly 2008; Quesson et al. 2000).

Nonetheless, the PRFS method is only suitable for aqueous tissues, that is, the tumor and the glandular tissue. The temperature in adipose tissue cannot be measured using PRFS. Most tumor margins partly consist of adipose tissue, in which the temperature, and thus treatment efficacy, cannot be monitored. This could hamper total ablation of the tumor margins. The radiologist would not be capable of determining if high enough temperatures are reached, risking under treatment. Besides, being unable to monitor the temperature

in the adipose tissue of the near field might lead to an increased risk of overheating (sub)cutaneous tissue. To mitigate the risk of overheating the near field, a cool down period after every sonication is required. The ideal cool down duration varies between patients due to different breast compositions. Therefore, cool down times are chosen conservatively long, possibly unnecessarily prolonging HIFU treatments. Thermometry in adipose tissue is indispensable to optimize HIFU treatments. Methods to do so exist, but have not yet been implemented in clinical studies. Temperature mapping based on T_2 relaxation times is a suitable thermometry method for adipose tissue, as T_2 changes linearly with temperature. On the contrary, in aqueous tissues temperature dependence is not linear and nonreversible, making T_2 thermometry inappropriate for aqueous tissues (Baron et al. 2013). The ideal approach would be a combination of two methods to enable simultaneous thermometry in glandular, as well as in adipose tissue. A hybrid method has been developed using a combination of T_1 and PRFS. For T_1 thermometry, a variable flip angle method is employed. The two techniques are combined, allowing for real-time simultaneous temperature mapping in both types of tissues (Todd et al. 2013a, b; Diakite et al. 2014). This method is not yet applied in MR-HIFU treatments of the breast, but is promising for obtaining better treatment results in the future.

PRFS is very sensitive to patient movement (Rieke and Butts Pauly 2008). Besides, cardiac motion and breathing induce temperature errors, impeding treatment monitoring. On average, cardiac motion and breathing result in temperature errors of 13 °C, greatly decreasing the precision of temperature maps (Peters et al. 2009). A correction method should be applied to provide adequate temperature monitoring. Possible correction methods are spectroscopic imaging for internally-referenced temperature changes (Rieke and Butts Pauly 2008; Kuroda 2005), and a look-up table based multibaseline approach or model based approach (Vigen et al. 2003; Hey et al. 2009). In most MR-HIFU studies, patients receive local anesthesia, which is injected behind the tumor, or light sedation. The long treatment duration and possibly pain sensation result in reduced patient comfort, which is likely to cause motion in patients who are not fully sedated (Hynynen et al. 2001). Applying deep sedation could result in improved temperature measurements because patients receiving deep sedation have a more regular breathing pattern and are immobilized.

4.5.3 Pathology

Surgical removal of breast cancer enables pathologists to determine tumor size, receptor status and tumor grade. These characteristics are necessary for the selection of adjuvant systemic therapy. In patients who undergo MR-HIFU, the aim of the treatment is to destroy all malignant tissue. No viable tissue will be available for the pathologist. Therefore, tumor size, receptor status and tumor grade have to be determined before MR-HIFU ablation takes place. Tumor size can be determined reliably by contrast-enhanced MRI, thus the excision specimen is not required for tumor size assessment (Shin et al. 2012). Vacuum-assisted or large core needle biopsy may be used to obtain tissue for assessment of receptor status and tumor grade prior to MR-HIFU treatment (Chen et al. 2012; Park et al. 2009). For tumor grade, the correlation between core needle biopsy and surgical excision specimens is somewhat lower than for receptor status, which is the result of undersampling. However, the correlation is best in small tumors, in which MR-HIFU treatment is mainly performed (Zheng et al. 2013; Harris et al. 2003; Badoual et al. 2005). Also, experienced pathologists should assess the core biopsies and the risk of erroneously determining indications for adjuvant therapy should be kept in mind and discussed with the patient (Schmitz et al. 2014).

4.5.4 Sentinel Lymph Node Procedure

The sentinel node is the first lymph node to which the tumor drains. In case of metastatic disease,

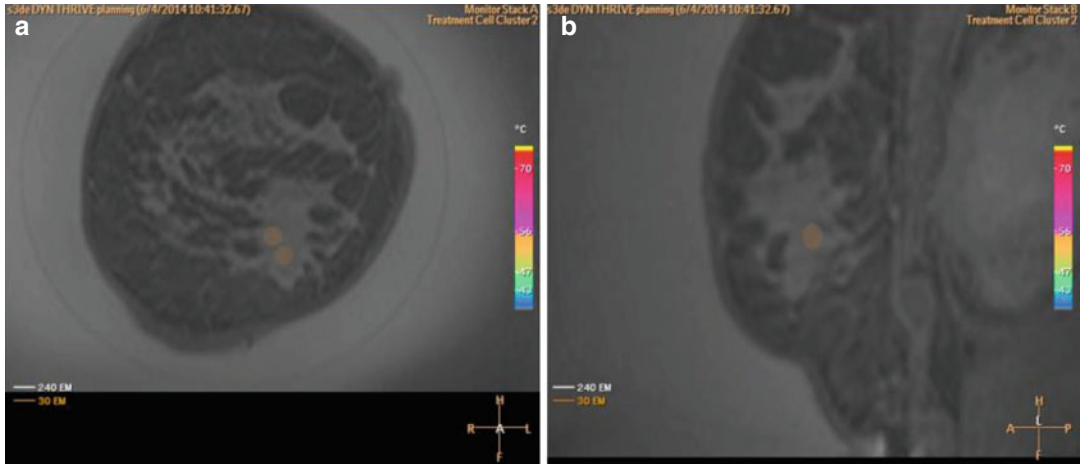

Fig. 4.5 Treatment planning on coronal and sagittal images. Two treatment cells of 6 mm are positioned in the tumor. (**a**) coronal view. (**b**) sagittal view. (*red dots*)

this node is the first location to contain tumor cells. Excision of the sentinel lymph node (sentinel lymph node biopsy, SLNB) should always be performed in patients with breast cancer to determine the need for complete axillary lymph node dissection (Lyman et al. 2005). This procedure should also be performed in patients who undergo MR-HIFU ablation. Concerns exist that HIFU might alter lymphatic anatomy, causing difficulties in finding the sentinel lymph node. Whether this is true is currently unknown. No problems with identifying the sentinel lymph node have been described so far (Zippel and Papa 2005). In case of doubt, the SLNB could be performed before MR-HIFU treatment.

4.6 Experience with the Dedicated Breast System

Currently, the feasibility and safety of a dedicated breast system (Sonalleve, Philips Healthcare, Vantaa, Finland) is assessed in a clinical study in the University Medical Center of Utrecht, the Netherlands (Fig. 4.4) (Merckel et al. 2013). One of the aims of this study is to overcome technical challenges, which are always present when a treatment is used for the first time. Furthermore, the accuracy and safety of MR-HIFU ablation with the dedicated breast system are investigated.

A total of 10 patients have been treated with the dedicated breast system. Patients were positioned in the MRI in prone position, with the affected breast in the breast cup (Fig. 4.4b). After positioning, a contrast-enhanced MRI scan was performed for treatment planning. These breast cancer patients underwent partial tumor ablation, meaning that only a few sonications per tumor were performed (Fig. 4.5).

Only treatment cells with a diameter of 6 mm were used to ensure comparability. Accuracy was measured by comparing the location of the actual focal point and the planned focal point during treatments, as measured by thermometry. Furthermore, the size and location of thermal damage at pathologic examination indicated whether the ablations were accurate. Results will soon be reported (Fig. 4.6).

4.7 Future Directions

MR-HIFU ablation is currently not ready for clinical implementation. Possibly, the availability and use of a dedicated breast system might improve treatment results. The efficacy of a dedicated breast system for tumor ablation is currently assessed in a phase 2 clinical trial at the

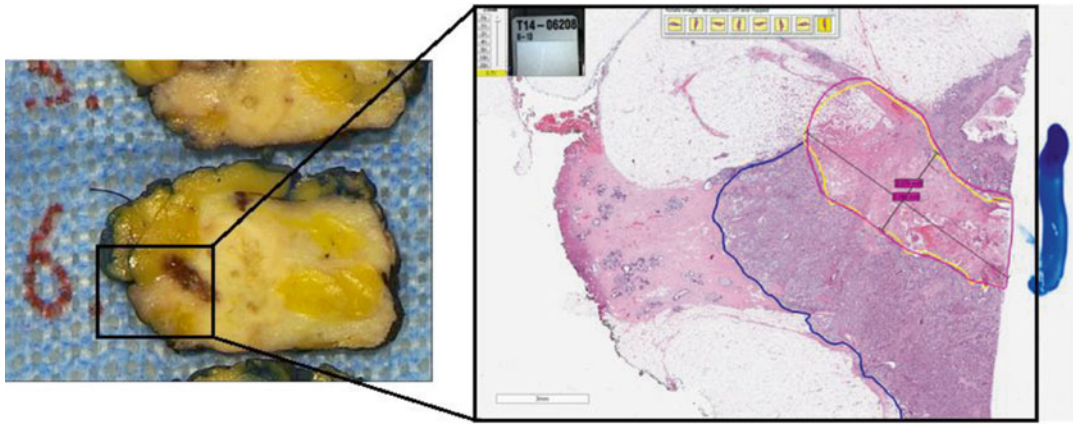

Fig. 4.6 Histopathologic result of a 6 mm treatment cell using the dedicated breast system. The size of thermal damage is measured to assess accuracy and precision

University Medical Center of Utrecht, the Netherlands.

Another potential application of MR-HIFU in the breast is the use of hyperthermia for enhanced local drug delivery in patients with an indication for neo-adjuvant chemotherapy. MR-HIFU has the potential to create mild hyperthermia (temperatures of 41–45 °C) (Diederich and Hynynen 1999). Thermo-sensitive liposomes that accelerate the release of their contents above a threshold temperature have been developed. Intravenously injecting these liposomes, while providing mild hyperthermia in the breast tumor, could potentially enhance the local release of cytostatic drug from the thermo-sensitive liposomes in the tumor microenvironment. Consequently, this would result in substantially higher local cytostatic concentrations in the tumor than in the rest of the body (Deckers and Moonen 2010; van Elk et al. 2014). This combination therapy could potentially be used as a neo-adjuvant therapy to downstage tumor prior to surgical resection.

Conclusion

MR-HIFU ablation is an interesting technique for the treatment of breast cancer and is still in an early stage of development. The possibility of treating breast cancer without affecting the integrity of the breast is appealing. Additionally, the breast is a very suitable organ for MR-HIFU ablation due to its peripheral location and thus easy targeting. More research is needed to find solutions for existing technical challenges and to determine which patient groups would benefit most from this treatment.

References

Badoual C, Maruani A, Ghorra C, Lebas P, Avigdor S, Michenet P (2005) Pathological prognostic factors of invasive breast carcinoma in ultrasound-guided large core biopsies-correlation with subsequent surgical excisions. Breast 14:22–27

Barlow WE, Lehman CD, Zheng Y, Ballard-Barbash R, Yankaskas BC, Cutter GR, Carney PA, Geller BM, Rosenberg R, Kerlikowske K, Weaver DL, Taplin SH (2002) Performance of diagnostic mammography for women with signs or symptoms of breast cancer. J Natl Cancer Inst 94:1151–1159

Baron P, Ries M, Deckers R, de Greef M, Tanttu J, Kohler M, Viergever MA, Moonen CT, Bartels LW (2013) In vivo T2-based MR thermometry in adipose tissue layers for high-intensity focused ultrasound near-field monitoring. Magn Reson Med 72: 1057–1064

Blair S, McElroy M, Middleton MS, Comstock C, Wolfson T, Kamrava M, Wallace A, Mortimer J (2006) The efficacy of breast MRI in predicting breast conservation therapy. J Surg Oncol 94:220–225

Bruening W, Uhl S, Fontanarosa J, Reston J, Treadwell J, Schoelles K (2012) Noninvasive Diagnostic Tests for Breast Abnormalities: Update of a 2006 Review. Comparative Effectiveness Review No. 47. (Prepared by the ECRI Institute Evidence-based Practice Center under Contract No. 290- 02-0019.) AHRQ Publication No. 12-EHC014-EF. Rockville, MD: Agency for Healthcare Research and Quality. www.effectivehealthcare.ahrq.gov/reports/final.cfm

Chen X, Yuan Y, Gu Z, Shen K (2012) Accuracy of estrogen receptor, progesterone receptor, and HER2 status between core needle and open excision biopsy in breast cancer: a meta-analysis. Breast Cancer Res Treat 134:957–967

Cline HE, Hynynen K, Watkins RD, Adams WJ, Schenck JF, Ettinger RH, Freund WR, Vetro JP, Jolesz FA (1995) Focused US system for MR imaging-guided tumor ablation. Radiology 194:731–737

Darby S, McGale P, Correa C, Taylor C, Arriagada R, Clarke M, Cutter D, Davies C, Ewertz M, Godwin J, Gray R, Pierce L, Whelan T, Wang Y, Peto R (2011) Effect of radiotherapy after breast-conserving surgery on 10-year recurrence and 15-year breast cancer death: meta-analysis of individual patient data for 10,801 women in 17 randomised trials. Lancet 378:1707–1716

de Bresser J, de Vos B, van der Ent F, Hulsewe K (2010) Breast MRI in clinically and mammographically occult breast cancer presenting with an axillary metastasis: a systematic review. Eur J Surg Oncol 36:114–119

Deckers R, Moonen CT (2010) Ultrasound triggered, image guided, local drug delivery. J Control Release 148:25–33

Diakite M, Odeen H, Todd N, Payne A, Parker DL (2014) Toward real-time temperature monitoring in fat and aqueous tissue during magnetic resonance-guided high-intensity focused ultrasound using a three-dimensional proton resonance frequency T method. Magn Reson Med 72:178–187

Diederich CJ, Hynynen K (1999) Ultrasound technology for hyperthermia. Ultrasound Med Biol 25:871–887

Faverly DR, Hendriks JH, Holland R (2001) Breast carcinomas of limited extent: frequency, radiologic-pathologic characteristics, and surgical margin requirements. Cancer 91:647–659

Fisher B, Anderson S, Bryant J, Margolese RG, Deutsch M, Fisher ER, Jeong JH, Wolmark N (2002) Twenty-year follow-up of a randomized trial comparing total mastectomy, lumpectomy, and lumpectomy plus irradiation for the treatment of invasive breast cancer. N Engl J Med 347:1233–1241

Furusawa H (2012) MRgFUS of breast cancer: its efficacy and safety in the clinical studies. In: 3th international focused ultrasound symposium, Washington, DC

Furusawa H, Namba K, Thomsen S, Akiyama F, Bendet A, Tanaka C, Yasuda Y, Nakahara H (2006) Magnetic resonance-guided focused ultrasound surgery of breast cancer: reliability and effectiveness. J Am Coll Surg 203:54–63

Furusawa H, Namba K, Nakahara H, Tanaka C, Yasuda Y, Hirabara E, Imahariyama M, Komaki K (2007) The evolving non-surgical ablation of breast cancer: MR guided focused ultrasound (MRgFUS). Breast Cancer 14:55–58

Gianfelice D, Khiat A, Amara M, Belblidia A, Boulanger Y (2003a) MR imaging-guided focused ultrasound surgery of breast cancer: correlation of dynamic contrast-enhanced MRI with histopathologic findings. Breast Cancer Res Treat 82:93–101

Gianfelice D, Khiat A, Amara M, Belblidia A, Boulanger Y (2003b) MR imaging-guided focused US ablation of breast cancer: histopathologic assessment of effectiveness–initial experience. Radiology 227:849–855

Gianfelice D, Khiat A, Boulanger Y, Amara M, Belblidia A (2003c) Feasibility of magnetic resonance imaging-guided focused ultrasound surgery as an adjunct to tamoxifen therapy in high-risk surgical patients with breast carcinoma. J Vasc Interv Radiol 14:1275–1282

Haar GT, Coussios C (2007) High intensity focused ultrasound: physical principles and devices. Int J Hyperthermia 23:89–104

Halsted WS (1907) I. The results of radical operations for the cure of carcinoma of the breast. Ann Surg 46:1–19

Harris GC, Denley HE, Pinder SE, Lee AH, Ellis IO, Elston CW, Evans A (2003) Correlation of histologic prognostic factors in core biopsies and therapeutic excisions of invasive breast carcinoma. Am J Surg Pathol 27:11–15

Hey S, Maclair G, de Senneville BD, Lepetit-Coiffe M, Berber Y, Kohler MO, Quesson B, Moonen CT, Ries M (2009) Online correction of respiratory-induced field disturbances for continuous MR-thermometry in the breast. Magn Reson Med 61:1494–1499

Holland R, Veling SH, Mravunac M, Hendriks JH (1985) Histologic multifocality of Tis, T1-2 breast carcinomas. Implications for clinical trials of breast-conserving surgery. Cancer 56:979–990

Houssami N, Irwig L, Simpson JM, McKessar M, Blome S, Noakes J (2003) Sydney Breast Imaging Accuracy Study: comparative sensitivity and specificity of mammography and sonography in young women with symptoms. AJR Am J Roentgenol 180:935–940

Houssami N, Ciatto S, Macaskill P, Lord SJ, Warren RM, Dixon JM, Irwig L (2008) Accuracy and surgical impact of magnetic resonance imaging in breast cancer staging: systematic review and meta-analysis in detection of multifocal and multicentric cancer. J Clin Oncol 26:3248–3258

Hrung JM, Sonnad SS, Schwartz JS, Langlotz CP (1999) Accuracy of MR imaging in the work-up of suspicious breast lesions: a diagnostic meta-analysis. Acad Radiol 6:387–397

Huber PE, Jenne JW, Rastert R, Simiantonakis I, Sinn HP, Strittmatter HJ, von Fournier D, Wannenmacher MF, Debus J (2001) A new noninvasive approach in breast cancer therapy using magnetic resonance imaging-guided focused ultrasound surgery. Cancer Res 61:8441–8447

Hynynen K (2010) MRI-guided focused ultrasound treatments. Ultrasonics 50:221–229

Hynynen K, Pomeroy O, Smith DN, Huber PE, McDannold NJ, Kettenbach J, Baum J, Singer S, Jolesz FA (2001) MR imaging-guided focused ultrasound surgery of fibroadenomas in the breast: a feasibility study. Radiology 219:176–185

International Agency for Research on Cancer (2012) GLOBOCAN 2012: estimated cancer incidence, mortality and prevalence worldwide in 2012. http://globocan.iarc.fr/Pages/fact_sheets_cancer.aspx?cancer=breast. Accessed 22 July 2014

Jenne JW, Preusser T, Gunther M (2012) High-intensity focused ultrasound: principles, therapy guidance, simulations and applications. Z Med Phys 22:311–322

Jolesz FA (2009) MRI-guided focused ultrasound surgery. Annu Rev Med 60:417–430

Kaiser WA, Pfleiderer SO, Baltzer PA (2008) MRI-guided interventions of the breast. J Magn Reson Imaging 27:347–355

Khiat A, Gianfelice D, Amara M, Boulanger Y (2006) Influence of post-treatment delay on the evaluation of the response to focused ultrasound surgery of breast cancer by dynamic contrast enhanced MRI. Br J Radiol 79:308–314

Knuttel FM, Menezes GL, van den Bosch MA, Gilhuijs KG, Peters NH (2014) Current clinical indications for magnetic resonance imaging of the breast. J Surg Oncol 110:26–31

Kohler MO, Mougenot C, Quesson B, Enholm J, Le Bail B, Laurent C, Moonen CT, Ehnholm GJ (2009) Volumetric HIFU ablation under 3D guidance of rapid MRI thermometry. Med Phys 36:3521–3535

Kropcho LC, Steen ST, Chung AP, Sim MS, Kirsch DL, Giuliano AE (2012) Preoperative breast MRI in the surgical treatment of ductal carcinoma in situ. Breast J 18:151–156

Kuhl CK, Schrading S, Leutner CC, Morakkabati-Spitz N, Wardelmann E, Fimmers R, Kuhn W, Schild HH (2005) Mammography, breast ultrasound, and magnetic resonance imaging for surveillance of women at high familial risk for breast cancer. J Clin Oncol 23:8469–8476

Kuhl CK, Schrading S, Bieling HB, Wardelmann E, Leutner CC, Koenig R, Kuhn W, Schild HH (2007) MRI for diagnosis of pure ductal carcinoma in situ: a prospective observational study. Lancet 370:485–492

Kuroda K (2005) Non-invasive MR thermography using the water proton chemical shift. Int J Hyperthermia 21:547–560

Lyman GH, Giuliano AE, Somerfield MR, Benson AB 3rd, Bodurka DC, Burstein HJ, Cochran AJ, Cody HS 3rd, Edge SB, Galper S, Hayman JA, Kim TY, Perkins CL, Podoloff DA, Sivasubramaniam VH, Turner RR, Wahl R, Weaver DL, Wolff AC, Winer EP (2005) American Society of Clinical Oncology guideline recommendations for sentinel lymph node biopsy in early-stage breast cancer. J Clin Oncol 23: 7703–7720

Mann RM, Hoogeveen YL, Blickman JG, Boetes C (2008) MRI compared to conventional diagnostic work-up in the detection and evaluation of invasive lobular carcinoma of the breast: a review of existing literature. Breast Cancer Res Treat 107:1–14

Mann RM, Loo CE, Wobbes T, Bult P, Barentsz JO, Gilhuijs KG, Boetes C (2010) The impact of preoperative breast MRI on the re-excision rate in invasive lobular carcinoma of the breast. Breast Cancer Res Treat 119:415–422

McDannold HK, Wolf D, Wolf G, Jolesz F (1998) MRI evaluation of thermal ablation of tumors with focused ultrasound. J Magn Reson Imaging 8:91–100

Menezes GL, van den Bosch MA, Postma EL, El Sharouni MA, Verkooijen HM, van Diest PJ, Pijnappel RM (2013) Invasive ductolobular carcinoma of the breast: spectrum of mammographic, ultrasound and magnetic resonance imaging findings correlated with proportion of the lobular component. SpringerPlus 2:621

Merckel LG, Bartels LW, Kohler MO, van den Bongard HJ, Deckers R, Mali WP, Binkert CA, Moonen CT, Gilhuijs KG, van den Bosch MA (2013) MR-guided high-intensity focused ultrasound ablation of breast cancer with a dedicated breast platform. Cardiovasc Intervent Radiol 36:292–301

Moonen CTW, Mougenot C (2006) MRI-guided focused ultrasound, apparatus for novel treatment of breast cancer. In: Philips research book series vol 6. Springer, New York, pp 183–200

Mougenot C, Tillander M, Koskela J, Kohler MO, Moonen C, Ries M (2012) High intensity focused ultrasound with large aperture transducers: a MRI based focal point correction for tissue heterogeneity. Med Phys 39:1936–1945

Napoli A, Anzidei M, Ciolina F, Marotta E, Cavallo Marincola B, Brachetti G, Di Mare L, Cartocci G, Boni F, Noce V, Bertaccini L, Catalano C (2013) MR-guided high-intensity focused ultrasound: current status of an emerging technology. Cardiovasc Intervent Radiol 36:1190–1203

Park SY, Kim KS, Lee TG, Park SS, Kim SM, Han W, Noh DY, Kim SW (2009) The accuracy of preoperative core biopsy in determining histologic grade, hormone receptors, and human epidermal growth factor receptor 2 status in invasive breast cancer. Am J Surg 197:266–269

Parvez E, Hodgson N, Cornacchi SD, Ramsaroop A, Gordon M, Farrokhyar F, Porter G, Quan ML, Wright F, Lovrics PJ (2014) Survey of American and Canadian general surgeons' perceptions of margin status and practice patterns for breast conserving surgery. Breast J 20:481–488

Payne A, Merrill R, Minalga E, Vyas U, de Bever J, Todd N, Hadley R, Dumont E, Neumayer L, Christensen D, Roemer R, Parker D (2012) Design and characterization of a laterally mounted phased-array transducer breast-specific MRgHIFU device with integrated 11-channel receiver array. Med Phys 39:1552–1560

Payne A, Todd N, Minalga E, Wang Y, Diakite M, Hadley R, Merrill R, Factor R, Neumayer L, Parker DL (2013) In vivo evaluation of a breast-specific magnetic resonance guided focused ultrasound system in a goat udder model. Med Phys 40:073302

Peters NH, Borel Rinkes IH, Zuithoff NP, Mali WP, Moons KG, Peeters PH (2008) Meta-analysis of MR imaging in the diagnosis of breast lesions. Radiology 246:116–124

Peters NH, Bartels LW, Sprinkhuizen SM, Vincken KL, Bakker CJ (2009) Do respiration and cardiac motion induce magnetic field fluctuations in the breast and are there implications for MR thermometry? J Magn Reson Imaging 29:731–735

Peters NH, van Esser S, van den Bosch MA, Storm RK, Plaisier PW, van Dalen T, Diepstraten SC, Weits T, Westenend PJ, Stapper G, Fernandez-Gallardo MA, Borel Rinkes IH, van Hillegersberg R, Mali WP, Peeters PH (2011) Preoperative MRI and surgical management in patients with nonpalpable breast cancer: the MONET – randomised controlled trial. Eur J Cancer 47:879–886

Quesson B, de Zwart JA, Moonen CT (2000) Magnetic resonance temperature imaging for guidance of thermotherapy. J Magn Reson Imaging 12:525–533

Rieke V, Butts Pauly K (2008) MR thermometry. J Magn Reson Imaging 27:376–390

Rutgers EJ, EUSOMA Consensus Group (2001) Quality control in the locoregional treatment of breast cancer. Eur J Cancer 37:447–453

Salomir R, Palussiere J, Vimeux FC, de Zwart JA, Quesson B, Gauchet M, Lelong P, Pergrale J, Grenier N, Moonen CT (2000) Local hyperthermia with MR-guided focused ultrasound: spiral trajectory of the focal point optimized for temperature uniformity in the target region. J Magn Reson Imaging 12:571–583

Schmitz AC, van den Bosch MA, Loo CE, Mali WP, Bartelink H, Gertenbach M, Holland R, Peterse JL, Rutgers EJ, Gilhuijs KG (2010) Precise correlation between MRI and histopathology – exploring treatment margins for MRI-guided localized breast cancer therapy. Radiother Oncol 97:225–232

Schmitz AC, Pengel KE, Loo CE, van den Bosch MA, Wesseling J, Gertenbach M, Alderliesten T, Mali WP, Rutgers EJ, Bartelink H, Gilhuijs KG (2012) Pre-treatment imaging and pathology characteristics of invasive breast cancers of limited extent: potential relevance for MRI-guided localized therapy. Radiother Oncol 104:11–18

Schmitz AM, Oudejans JJ, Gilhuijs KG (2014) Agreement on indication for systemic therapy between biopsied tissue and surgical excision specimens in breast cancer patients. PLoS One 9:e91439

Shin HC, Han W, Moon HG, Yom CK, Ahn SK, You JM, Kim JS, Chang JM, Cho N, Moon WK, Park IA, Noh DY (2012) Limited value and utility of breast MRI in patients undergoing breast-conserving cancer surgery. Ann Surg Oncol 19:2572–2579

Todd N, Diakite M, Payne A, Parker DL (2013a) Hybrid proton resonance frequency/T1 technique for simultaneous temperature monitoring in adipose and aqueous tissues. Magn Reson Med 69:62–70

Todd N, Diakite M, Payne A, Parker DL (2013b) In vivo evaluation of multi-echo hybrid PRF/T1 approach for temperature monitoring during breast MR-guided focused ultrasound surgery treatments. Magn Reson Med 72:793–799

Turnbull L, Brown S, Harvey I, Olivier C, Drew P, Napp V, Hanby A, Brown J (2010) Comparative effectiveness of MRI in breast cancer (COMICE) trial: a randomised controlled trial. Lancet 375:563–571

van Elk M, Deckers R, Oerlemans C, Shi Y, Storm G, Vermonden T, Hennink WE (2014) Triggered release of doxorubicin from temperature-sensitive poly(N-(2-hydroxypropyl)-methacrylamide mono/dilactate) grafted liposomes. Biomacromolecules 15:1002–1009

Vigen KK, Daniel BL, Pauly JM, Butts K (2003) Triggered, navigated, multi-baseline method for proton resonance frequency temperature mapping with respiratory motion. Magn Reson Med 50:1003–1010

Voogt MJ, Trillaud H, Kim YS, Mali WP, Barkhausen J, Bartels LW, Deckers R, Frulio N, Rhim H, Lim HK, Eckey T, Nieminen HJ, Mougenot C, Keserci B, Soini J, Vaara T, Kohler MO, Sokka S, van den Bosch MA (2012) Volumetric feedback ablation of uterine fibroids using magnetic resonance-guided high intensity focused ultrasound therapy. Eur Radiol 22:411–417

Warner E, Plewes DB, Hill KA, Causer PA, Zubovits JT, Jong RA, Cutrara MR, DeBoer G, Yaffe MJ, Messner SJ, Meschino WS, Piron CA, Narod SA (2004) Surveillance of BRCA1 and BRCA2 mutation carriers with magnetic resonance imaging, ultrasound, mammography, and clinical breast examination. JAMA 292:1317–1325

Zheng J, Alsaadi T, Blaichman J, Xie X, Omeroglu A, Meterissian S, Mesurolle B (2013) Invasive ductal carcinoma of the breast: correlation between tumor grade determined by ultrasound-guided core biopsy and surgical pathology. AJR Am J Roentgenol 200:W71–W74

Zippel DB, Papa MZ (2005) The use of MR imaging guided focused ultrasound in breast cancer patients; a preliminary phase one study and review. Breast Cancer 12:32–38

Zonderland HM, Coerkamp EG, Hermans J, van de Vijver MJ, van Voorthuisen AE (1999) Diagnosis of breast cancer: contribution of US as an adjunct to mammography. Radiology 213:413–422

HIFU for Palliative Treatment of Pancreatic Cancer

5

Tatiana D. Khokhlova and Joo Ha Hwang

Abstract

Pancreatic cancer is one of the deadliest malignancies, with only a 6 % 5-year survival rate and over 50 % of patients being diagnosed at the advanced stage. Current therapies are ineffective, and the treatment of patients with advanced disease is palliative. In the past decade, HIFU ablation has emerged as a modality for palliative treatment of pancreatic tumors. Multiple preclinical and non-randomized clinical trials have been performed to evaluate the safety and efficacy of this procedure. Substantial tumor-related pain reduction was achieved in most cases after HIFU treatment and few significant side effects were observed. In addition, some studies indicate that combination of HIFU ablation with chemotherapy may provide a survival benefit. This chapter summarizes the pre-clinical and clinical experience obtained to date in HIFU treatment of pancreatic tumors and discusses the challenges, limitations and new approaches in this modality.

Keywords

HIFU • Pancreatic cancer

5.1 Clinical Management of Pancreatic Cancer

Pancreatic ductal adenocarcinoma (PDA), also known as pancreatic cancer, is the 10th most common cancer diagnosis among men and the 9th most common among women in the United States. It is also the deadliest cancer; it has a 5-year survival rate of only 6 %, which has not substantially improved in the last 40 years (American Cancer 2013). According to the 2013 Cancer Statistics report, the median survival ranges from 4.5 months for stage IV disease, and 24.1 months for stage I disease. There are a number of characteristics of pancreatic cancer that make it resistant to therapy; most importantly the formation of a dense stroma. This results from a desmoplastic reaction that creates a barrier

T.D. Khokhlova (✉) • J.H. Hwang
Division of Gastroenterology,
Department of Medicine, University of Washington,
Seattle, WA 98195, USA
e-mail: tdk7@uw.edu

© Springer International Publishing Switzerland 2016
J.-M. Escoffre, A. Bouakaz (eds.), *Therapeutic Ultrasound*, Advances in Experimental Medicine and Biology, Vol. 880, DOI 10.1007/978-3-319-22536-4_5

Table 5.1 TNM staging system for pancreatic cancer (Edge et al. 2010; Bilimoria et al. 2007)

Stage	T	N	M	Median Survival, months	Description
IA	T1	N0	M0	24.1	Tumor limited to the pancreas, ≤2 cm in greatest dimension, resectable
IB	T2	N0	M0	20.6	Tumor limited to the pancreas, >2 cm in greatest dimension, resectable
IIA	T3	N0	M0	15.4	Tumor extends beyond the pancreas, but does not involve the celiac axis or superior mesenteric artery, resectable
IIB	T1, T2 or T3	N1	M0	12.7	Regional lymph node metastasis
III	T4	N0, N1	M0	10.6	Tumor involves the celiac axis and superior mesenteric artery, unresectable
IV	any T	N0, N1	M1	4.5	Distant metastasis

T describes the size of the primary tumor and whether it has invaded nearby tissue; N describes the degree of spread to regional lymph nodes; M denotes the presence of distant metastases

between cancer cells and blood vessels (Hidalgo 2010). The stroma is not just a mechanical barrier; rather, it constitutes a dynamic compartment that is critically involved in the process of tumor formation, progression, invasion and metastasis (Chu et al. 2007; Mahadevan and Von Hoff 2007). Stromal cells express multiple proteins, such as vascular endothelial growth factor, which have been associated with a poor prognosis and resistance to treatment. In addition, a subgroup of tumor cancer cells with cancer stem cell properties, such as tumor initiation, has been identified. Pancreatic cancer stem cells are resistant to chemotherapy and radiation therapy. This may explain why these treatments are not very effective. High interstitial pressure within pancreatic tumors, as well as poor vascularization, further contributes to drug resistance.

Early stage pancreatic cancer usually has no symptoms. When symptoms do occur, the tumor has usually spread to surrounding tissues or distant organs. Common pancreatic cancer symptoms include mild abdominal discomfort, dull and deep upper abdominal pain, jaundice (yellowing of the skin or whites of the eyes) and weight loss. Nausea and vomiting may occur among patients with more advanced disease. If pancreatic cancer is suspected in a patient, further evaluation is focused on the diagnosis and staging of the disease, as well as assessment of tumor resectability. Multiphase, multidetector helical computed tomography (CT) with intravenous administration of contrast material is the imaging procedure of choice for initial evaluation (Miura et al. 2006). This technique allows visualization of the primary tumor in relation to the major arteries, and also in relation to distant organs. In general, contrast-enhanced CT is sufficient to confirm a suspected pancreatic mass, and can be used to predict surgical resectability with 80–90 % accuracy (Karmazanovsky et al. 2005). Positron-emission tomography and endoscopic ultrasonography are also used if the CT findings are ambiguous. In addition, serum level of CA 19–9 biomarker is commonly used for therapeutic monitoring and early detection of recurrent disease after treatment. The important limitation of CA 19–9, however, is that it is not specific for pancreatic cancer and may be elevated in other conditions, such as choleostasis. Therefore, CA 19–9 is only used in patients with known pancreatic cancer (Hidalgo 2010).

Pancreatic cancer staging is based primarily on assessment of resectability obtained by helical CT (Edge et al. 2010). T1, T2 and T3 tumors are potentially resectable, whereas T4 tumors, which involve the superior mesenteric artery or celiac axis, are unresectable (Table 5.1) (Bilimoria et al. 2007). For patients with resectable disease, surgery remains the treatment of choice (Shaib et al. 2007). Depending on the location of the tumor, the operative procedures may involve cephalic pancreatoduodenectomy (the Whipple procedure), distal pancreatectomy or total pancreatectomy.

A minimum of 12–15 lymph nodes should be resected, and every attempt should be made to obtain a tumor-free margin. Unfortunately, even if the tumor is fully resected, the outcome in patients with early pancreatic cancer is disappointing, with a median survival of 20–22 months. Postoperative treatment with gemcitabine alone-, or gemcitabine in combination with fluorouracil-, based chemoradiation has demonstrated improved survival in these patients. This has been one of the most important advances made in the management of pancreatic cancer.

If the tumor is obstructing the bile duct, a stent can be placed to relieve the blockage using non-surgical approaches. If a patient develops gastric-outlet obstruction, treatment may include duodenal wall stents or percutaneous endoscopic gastrostomy placement for decompression. Occasionally, a patient may need surgery to create a bypass (biliary bypass or gastric bypass) to manage obstructive jaundice and gastric outlet obstruction.

In the US, only about 15–20 % of pancreatic cancer cases are diagnosed early enough to be eligible for surgery. The majority of patients diagnosed with pancreatic cancer already present metastatic disease or they later develop metastatic disease. This is mainly in the liver and peritoneal cavity. The treatment of these patients remains palliative, and pain management is one of the most important aspects of care, with pancreatic cancer causing severe pain in 50–70 % of patients. This type of pain is multi-factorial and may be caused by infiltration of nerve sheaths and neural ganglia, increased ductal and interstitial pressure, and gland inflammation (Staatas et al. 2001). The current management of pancreatic pain starts with non-opioid analgesics, such as nonsteroidal anti-inflammatory drugs (NSAIDs), and progresses to increasing doses of opioid analgesics. For pain that does not respond to drugs, or when oral or topical medication leads to unacceptable side effects, a nerve block may be performed by injecting alcohol under endoscopic ultrasound or CT guidance into the nerves (celiac plexus) that carry painful stimuli from the diseased pancreas to the brain (Arcidiacono et al. 2011). This procedure, known as celiac plexus neurolysis, does provide temporary pain relief, but the benefit is limited and continued use of analgesics is often still necessary.

Thus, based on the current standard of care described above, new treatment approaches that would offer both local tumor control and palliation of symptoms would be beneficial to advanced pancreatic cancer patients. HIFU was introduced relatively recently as a modality for ablation of unresectable pancreatic tumors to reduce the tumor size and achieve pain relief. The first clinical trials were performed in China and have been reported in Chinese literature since 2001 (Jang et al. 2010), with the first publication in English literature in 2005 by Wu et al. Currently, HIFU treatment of advanced pancreatic cancer is still widely available in China, with limited availability in South Korea, Japan and Europe.

5.2 Devices and Methods

There are three US-guided HIFU devices that are commercially available outside of China for treatment of pancreatic tumors, all manufactured in China: The FEP-BY-02 HIFU tumor therapy device (Yuande Biomedical Engineering Limited Corporation, Beijing, China), HAIFU (Chongqing Haifu Technology Co.,) and HIFUNIT-9000 (Shanghai A&S Sci-Tech Co., Ltd, Shanghai, China). All devices operate at similar ultrasound frequencies (0.8–1.6 MHz) and similar acoustic powers (up to 300 W). In all three devices, an ultrasound imaging probe is inserted into the opening at the center of the HIFU transducer. B-mode ultrasound serves three purposes in these devices: visualization of the target, monitoring tissue changes during treatment and assessment of the treatment outcome. Unfortunately, to date, B-mode ultrasound imaging can neither provide a direct map of the thermally ablated region, nor does it have the capability of performing tissue thermometry. However, it does provide real-time imaging using the same energy modality as HIFU. This is a significant benefit because: 1. adequate ultrasound imaging of the target suggests that there is no obstruction (*e.g.,* bowel gas or bone) to ultrasound energy reaching the target, and: 2. the risk of causing thermal

injury to unintended tissue is minimized. The appearance of a hyperechoic region on the ultrasound image during treatment is one method often used for confirmation of general targeting accuracy and prediction of ablation efficacy. This region has been shown to correspond to the formation of boiling bubbles at the focal region when tissue temperature reaches 100 °C (Khokhlova et al. 2011).

Two recent studies attempted to evaluate the ultrasound reflectance change during HIFU therapy of pancreatic neoplasms and to correlate the change with the degree of tumor ablation (Wang et al. 2012; Ge et al. 2013). Wang et al. (2012) found a strong correlation between the appearance of a bright hyperechoic region and the increase in both average ultrasound power and total ultrasound energy delivered to the target. This was consistent with the hypothesized formation of boiling bubbles at the focus. However, the local response measured by CT in terms of tumor size 1-month post treatment in 136 patients enrolled in the study did not correlate with the change in reflectance. This lack of correlation may be related to the assessment criteria for local response: the change in tumor size would not accurately reflect the effects of HIFU ablation due to tissue swelling and imperfections in the CT evaluation. In the study by Ge et al. (2013), the extent of tumor ablation effects following HIFU in 31 patients was assessed by enhanced CT. A good positive correlation was found between the variation of ultrasound reflection and tumor ablation ratio.

The operation characteristics of the two most widely used treatment systems - FEB-BY-02 and Haifu – are very similar, but there are some notable differences. The FEB-BY-02 system uses a 1 MHz transducer (aperture of 37 cm and a focal distance of 25.5 cm) consisting of 251 elements, all of which are driven in phase. The focal area has a width of 3 mm and axial length of 10 mm at −6 dB level. The change in the focus position in tissue is achieved by mechanical scanning of the transducer array in 3D from one treatment spot to the next. The treatment spots are placed in overlapping fashion: The interval spacing in the lateral dimension is 4–5 mm, in the axial direction – 6–8 mm. The system has two identical transducers for two patient positioning options. One transducer is located below the treatment table, in a water bath, and the patient is positioned prone on the table. The other transducer is located above the treatment table, and the patient is positioned supine. Acoustic coupling in this case is achieved by pressing a water-filled balloon onto the patient's abdomen. This position was shown to be beneficial as it allows compression of the bowel and intestinal loops, as well as reducing the amount of gas in the acoustic pathway. The sonications are usually pulsed to allow ultrasound imaging between HIFU pulses, with pulse lengths of 150–1000 ms, duty factors of 33–60 % and 50–80 pulses per spot. For treatment planning an *in-situ* target acoustic energy dose (in J per spot) is set at 500–1250 J, taking into account the attenuation of the intervening tissues at each focal depth. The required output electric power is then calculated accordingly, and the treatment is delivered automatically spot by spot. In most studies, therapy is divided into several 60-min long sessions and performed without sedation or anesthesia (Xiong et al. 2009; Hwang et al. 2009; Zhao et al. 2010).

The HAIFU system offers the choice of three single-element HIFU transducers with 12 cm aperture, with different focal distances (9 cm, 13 cm or 16 cm) and different frequencies (0.8–1.6 MHz) for tumors located at different depths. The target tissue is exposed to focal peak intensities from 5000 to 20,000 W cm^{-2}, depending on the focal depth (Wu et al. 2004). The transducers are located below the treatment table in a water bath, with an expandable water balloon on top for compression; the patient is positioned prone for HIFU exposures. The treatment planning and pulsing is performed differently to that by the FEB-BY device; using US images of the tumor, it is divided into several slices with 5-mm separation. The transducer is then continuously powered as the HIFU beam is scanned at the speed of 0.5–3 mm/s in successive sweeps from the deep to shallow regions of the tumor. After each sweep the HIFU transducer is turned off and the changes in tissue reflectivity are evaluated; if the increase in hyperechogenicity is not observed, the sweep is repeated until the tissue is considered

completely ablated. The major procedural difference compared to the operation of the FEB-BY-02 device is that the ablation is usually performed in a single session, under sedation or general anesthesia. Sedation is performed to avoid deep visceral-type pain that is experienced during treatment by this device, most probably due to the higher rate of energy deposition compared to FEB-BY-02 (continuous sonication *vs* pulsed sonication), and for immobilization purposes.

Recently, an MR-guided HIFU system ExAblate (InSightec, Israel) was used to treat a limited cohort of locally advanced stage pancreatic cancer patients in Italy (Anzidei et al. 2014). The transducer used in ExAblate system is a 1.1 MHz 206-element annular phased array (aperture 12 cm, radius of curvature 16 cm) that allows electronic beam steering in the axial direction (focal distance 60–200 cm). The transducer is positioned below the treatment table, the patient is positioned prone and a convex gel pad is used to compress the abdominal wall. A 3 T medical MR scanner (GE Medical Systems) is used for treatment planning, as well as real-time measurement of tissue temperature during treatment using the proton chemical shift method (Jolesz et al. 2005). Sonications are administered to a given spot until the thermal ablation temperature threshold (65 °C) is reached in the focal area according to the temperature maps. Follow-up evaluation is performed by contrast-enhanced MRI, allowing measurement of the non-perfused volume of the tumor – likely a more accurate method of measuring long-term local response compared to tumor volume measurement.

5.3 Preclinical Studies

The first preclinical *in-vivo* studies of HIFU ablation of the pancreas utilized the swine model because of its size and similarity to human anatomy (Hwang et al. 2009; Xie et al. 2010; Liu et al. 2011). The animals did not bear tumors in the pancreas, therefore it was not possible to evaluate HIFU therapy survival; however, the main goal of these studies was to systematically evaluate the safety and efficacy of HIFU ablation of the pancreas. In the earliest study the pancreas of 12 common swine was successfully treated *in-vivo* using the FEP-BY02 device. No significant adverse effects, such as skin burns or evidence of pancreatitis, were observed during the 7-day post-treatment observation period (Hwang et al. 2009). Three *in-situ* total acoustic energy doses were tested – 750 J, 1000 J and 1250 J. Only the two higher doses resulted in macroscopic ablation of the pancreas. The highest dose resulted in a greater degree of ablation, but was also associated with greater collateral damage; minor skin burns, abdominal wall injuries and bowel ulceration.

A subsequent study by another group also in swine used the HAIFU device. They used both light microscopy and electron microscopy to confirm that complete necrosis is confined to the target regions, with clear boundaries and no damage to adjacent tissues (Xie et al. 2010). Pancreatitis was an important safety concern because the mechanical effects of HIFU can cause cell lysis and release of pancreatic enzymes. Although the cavitation, or boiling bubble activity, during HIFU was confirmed by electron microscopic examination (intercellular space widening and formation of numerous vacuoles of different sizes in the cytoplasm), pancreatitis was not observed, thus confirming the safety of the treatment protocol. Another preclinical study showed that a combined treatment of HIFU ablation followed by radiation therapy may be a promising method. The injury to the targeted pancreas was increased compared to either modality alone, without additional injury outside of the targeted region (Liu et al. 2011).

One other important safety consideration for HIFU ablation of pancreatic neoplasms is maintaining the endocrine and exocrine functions of the pancreas. These both play an important role in metabolism of glucose, fat and protein. A recent study in felines (Mao et al. 2014) addressed this concern by monitoring serum glucose and amylase levels after HIFU ablation of 25 % and 50 % of pancreatic tissue for 21 days. Both serum amylase and glucose levels had a short peak after the treatment, but returned to normal 14 days and 3 days after the treatment, respectively, thus not presenting a threat to the patient's health. Histopathological study also revealed that new

pancreatic ducts formed on the 7th day, and fibrous tissue completely substituted destroyed parenchyma by the 21st day.

In order to evaluate the effect of HIFU on pancreatic tumor and the benefit in survival, a study in a small animal tumor model was performed (Jiang et al. 2013). Jiang et al. used a nude mouse model subcutaneously injected with SW1990 human pancreatic cancer cells. The tumors were ablated with US-guided HIFU, and the success of treatment was confirmed by the increase in tissue reflectivity in the ultrasound images. Following HIFU, a 100 % reduction in tumor volume was observed within 28 days after treatment. The limitation of this study, however, was that the mouse model did not exhibit metastatic disease, the primary concern in most pancreatic cancer patients.

5.4 Ultrasound-guided HIFU System Clinical Trials

HIFU was first used for the palliative treatment of pancreatic cancer in an open-label study in China in 251 patients with advanced pancreatic cancer (TNM stages II–IV) (He and Wang 2002). HIFU therapy resulted in significant pain relief in 84 % of the patients. In some cases, significant reduction of tumor volume was achieved without any significant adverse effects or pancreatitis, which appeared to prolong survival. Multiple nonrandomized studies followed; they were reported in the Chinese literature (Wang and Sun 2002; Xie et al. 2003; Xiong et al. 2005; Xu et al. 2003; Yuan et al. 2003), and later in English literature (Wu et al. 2005; Xiong et al. 2009; Orsi et al. 2010; Wang et al. 2011; Sung et al. 2011). These studies provided additional evidence showing that HIFU does provide palliation of tumor-related pain, and also achieves local disease control in some cases, but does not cause adverse effects. These trials are discussed in more detail below.

The general patient inclusion criteria were similar in all trials: Diagnosis of unresectable stage III-IV pancreatic cancer and adequate physical condition to undergo the treatment. Before the treatment, bowel preparation was performed which included preoperative fasting and catharsis. In some cases, placement of a nasogastric tube to evacuate the gas from the stomach and colon was required. These preparations are of great importance to the success of treatment as gas and food debris harboring bubbles are known to reflect and redistribute HIFU energy, preventing it from reaching the target, also causing adverse effects such as burns and bowel perforation. To further eliminate the bowel gas from the acoustic pathway, expandable water balloons were used in all studies to compress the bowel and the intestinal loops. Figure 5.1 illustrates

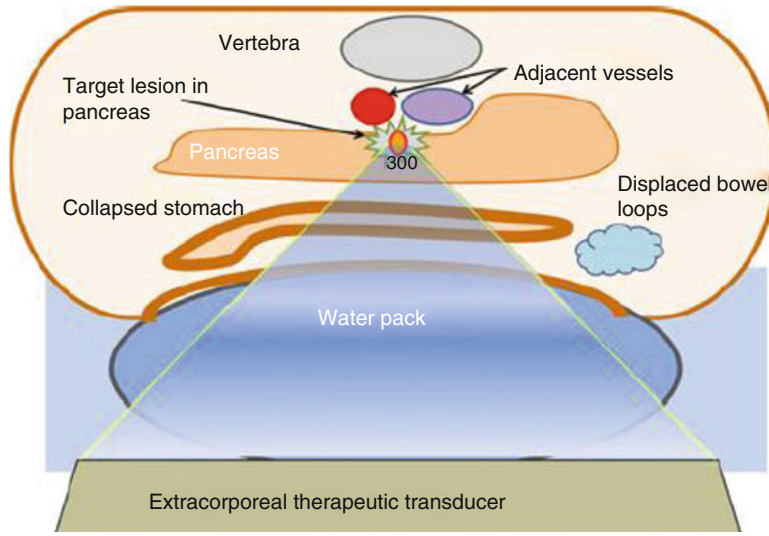

Fig. 5.1 A schematic representation of patient positioning for HIFU ablation of pancreatic neoplasms. Evacuation of gas and food debris from the acoustic pathway is achieved by bowel preparation (fasting, catharsis) and water balloon placement (Reproduced with kind permission from Springer Science + Business media from Jung et al. 2011)

patient positioning during HIFU procedure. In some studies (Wu et al. 2005; Wang et al. 2011), to reduce the likelihood of pancreatitis, 14-peptide somatostatin, a strong inhibitor of pancreas exocrine secretion, was administered before the HIFU treatment.

The treatment outcome was measured in terms of pain palliation, using a numerical rating scale from 0 to 10 (0: no pain, 10: worst pain imaginable), as well as local tumor response, using contrast-enhanced CT or MRI to measure unperfused volume of the tumor, and finally survival. Table 5.2 summarizes the findings of these studies. Notably, pain relief was achieved in most patients immediately after or within 24–48 h after HIFU ablation, and the response was long-lasting. Some studies reported complete remission of pain for the entire follow-up period of several months (Wu et al. 2005), in others, pain relief lasted for an average of 10 weeks (Wang et al. 2011). For comparison, celiac plexus block usually provides pain relief for 3–4 months, but carries a higher risk of complications (Rykowski and Hilgier 2000). As mentioned previously, the mechanism for pain relief remains unknown, but it is hypothesized to be related to the ablation of the nerve fibers in the tumor, and possibly thermal injury to the celiac plexus. Interestingly, as noted in the study by Xiong et al. (2009), pain relief was observed both in patients who had local tumor response (unperfused areas on contrast-enhanced CT after HIFU ablation) and in those who did not, which suggests that nerve fibers may be more susceptible to damage by HIFU.

All the studies report at least partial local response of the tumor (14–100 %), and some even suggest survival benefit, although this is difficult to determine since the studies were not designed to assess this outcome. The method used to evaluate local response is the subject of further debate. Several reports in the literature suggest that contrast-enhanced MRI or CT are appropriate methods to evaluate the efficacy of thermal ablation (Damianou et al. 2004; Lu et al. 2007). However, contrast enhanced-CT scan or MRI can only assess for change in tumor size and possible necrosis by noting the absence of vascularity within the tumor. However, these methods are not able to assess for tumor viability. PET or PET-CT can be a useful adjunctive imaging method for diagnosing and staging of pancreatic cancer, as well as for evaluating response to treatment (Balci and Semelka 2001; Bang et al. 2006; Mertz et al. 2000). Xiong et al. (2009) and Wang

Table 5.2 Clinical trials of ultrasound-guided HIFU ablation for palliative treatment of pancreatic cancer

Author	N	HIFU device	Pain reduction	Local tumor response	Median survival, months
Wu (2005)	8	Haifu, 1–2 sessions	Complete: 8 (100 %)	Full/Partial: 8(100 %)	11.2
Xiong (2009)	89	FEB-BY-02, 4–10 sessions	Complete: 21 (31.3 %) Partial: 33 (49 %) None: 13 (19.4 %)	Partial: 13(14.6 %) No change: 51(57 %) Progressive disease: 25(28.1 %)	11.2 (stage III) 5.4 (stage IV) 8.6 (overall)
Orsi (2010)	7	Haifu, once	Partial: 6 (85 %) None: 1 (15 %)	Not reported	7
Wang (2011)	40	Haifu, once	Complete: 9 (22.5 %) Partial: 26 (65 %) None: 5 (12.5 %)	Partial: 7(17.5 %) No change: 28(70 %) Progressive disease: 5(12.5 %)	10 (stage III) 6 (stage IV) 8 (overall)
Sung (2011)	46	Haifu, once	Complete/partial: 24 (52 %) Average pain score: before HIFU: 4.9 ± 1.1 after HIFU: 2.1 ± 1.1	Full: 38(77.5 %) Partial: 11(24 %) None: 0 %	7

N denotes the number of patients in the study

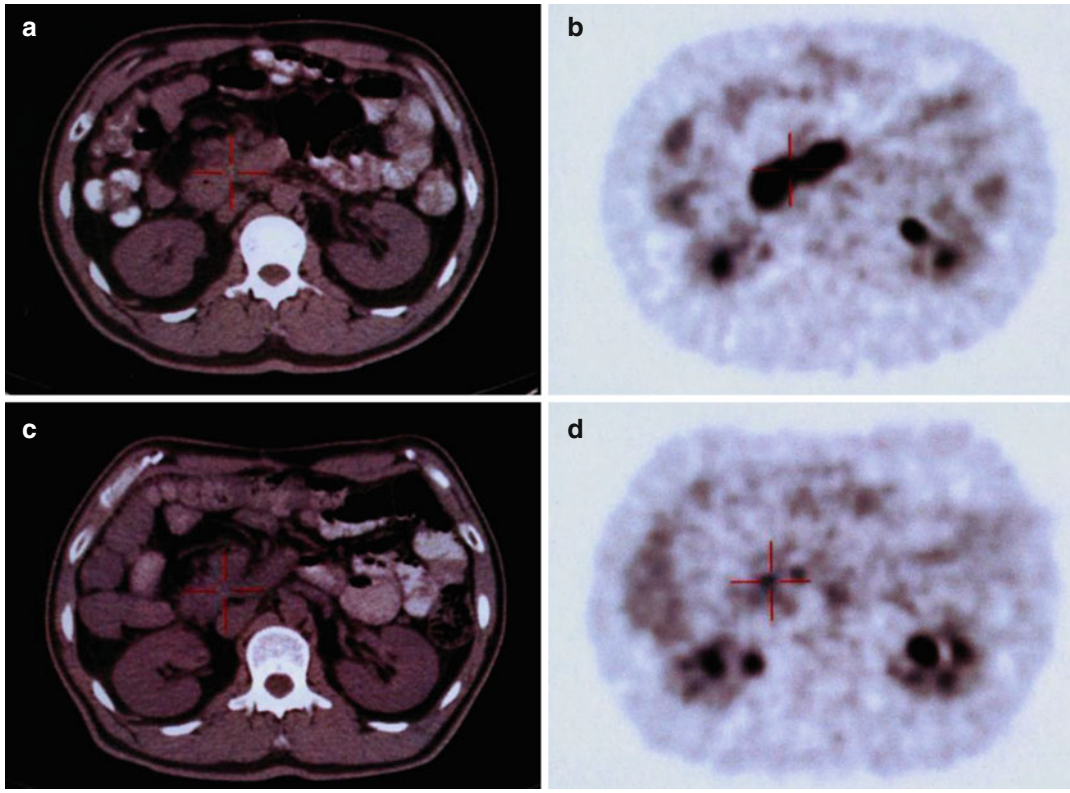

Fig. 5.2 (**a**) A contrast-enhanced CT scan performed before HIFU demonstrating a tumor in the head of the pancreas. (**b**) A PET-CT scan performed before HIFU demonstrating a maximum standardized uptake value (SUV_{max}) of 9.1 g/mL. (**c**) A contrast-enhanced CT scan demonstrating no change 1 month after HIFU. (**d**) The PET-CT scan performed 1 month after HIFU demonstrated that SUV_{max} value decreased to 3.1 g/mL. All four images were taken from the same patient (Reproduced with permission from Xiong et al. 2009)

et al. (2011) used PET-CT to assess the efficacy of HIFU therapy in a limited subset of patients (Fig. 5.2). The results demonstrate that the maximum and mean standard uptake values of the treated pancreatic cancer decreased after HIFU treatment, even if contrast enhanced-CT imaging did not demonstrate necrosis or decreased tumor volume. PET-CT scan may thus potentially be a better imaging method to evaluate the effect of HIFU treatment in pancreatic cancer.

Ge et al. (2014) performed a retrospective analysis of the different factors that may influence the degree of tumor ablation by HIFU in 136 patients. The major factor that was found to be negatively correlated with tumor ablation was posterior tumor depth, and the posterior depth of 7 cm was considered a critical value for the procedure: Tumor ablation rate of 30 % was almost 10 times better in tumors at <7 cm depth than the tumors at >7 cm depth. This finding may be well explained by the increase in the ultrasound attenuation losses as the target depth increases, and by the increased probability of encountering obstacles in the acoustic pathway that may refract, reflect or absorb the ultrasound energy. Acoustic attenuation is partly accounted for during treatment planning; however, the operator relies on a certain "average" attenuation value, which in reality may vary in a wide margin depending on the tissue type and between patients.

HIFU ablation is generally considered to be non-invasive and safe, and most studies do not report any adverse effects. However, some studies report frequent minor complications which quickly subside without any special treatment, such as nausea, mild abdominal pain, first and

second degree skin and abdominal wall burns, vertebral body necrosis (asymptomatic) and transient pancreatitis (Xiong et al. 2009; Sung et al. 2011; Jung et al. 2011). More serious but infrequent complications included third-degree burns (in 1 patient), pancreaticoduodenal fistula (2 patients) and deep vein thrombosis (1 patient) (Orsi et al., Sung et al. 2011; Jung et al. 2011). A separate study by Jung et al. (2011) analyzed the reasons for the complications in the patients enrolled in the previously reported study by Sung et al. (2011). The third degree skin burn case was related to inadequate acoustic coupling and improper positioning of the water balloon, which once again enhances the importance of pretreatment preparation of the acoustic pathway. Both cases of the pancreaticoduodenal fistula were potentially related to the presence of a metallic stent in the acoustic pathway. Metallic stent is highly reflective and therefore may efficiently redistribute ultrasound energy around it causing collateral damage. Therefore, tumors adjacent to a bowel loop with a stent may be a contraindication for HIFU.

5.5 MR-guided HIFU System Clinical Trials

The clinical experience with MR-guided ablation of pancreatic tumors to date is very limited but encouraging. A recent report from Italy (Anzidei et al. 2014) describes the treatment of two patients with unresectable pancreatic adenocarcinoma with the MR-guided system Insightech. Treatments were performed on a 3 T scanner under general anesthesia and controlled respiration to avoid respiratory motion of the target during treatment. Both the lesions (24 and 37 mm in size) and 4–5 mm tumor-free margin were ablated, as evidenced by the MR-controlled temperature maps (temperature over 62°). The procedures took approximately 70 min, and the patients were discharged uneventfully the next day. Contrast-enhanced MR follow-up was performed immediately post treatment and then at 1, 3 and 6 months to evaluate the non-perfused volume of the tumor. Pain was also evaluated on a numeric scale of 1–10. Immediate post-treatment MR evaluation and 1-month follow-up confirmed almost complete ablation of both pancreatic lesions, with a non-perfused volume respectively of 80 and 85 %. Due to accurate, MR-aided planning, no signs of damage to adjacent structures were observed, and little regrowth of tumor tissue along the ablation margins was demonstrated at the 3- and 6-month MR follow-up in both cases (non-perfused volumes of 70 and 80 % respectively). The mean pain score decreased from 6.7 ± 5 at baseline, to 2.0 ± 2 at 1 month, and then increased slightly to 2.3 ± 2 at 3 months and 3.0 ± 2 at 6 months. One of the patients died at 13 months post treatment from metastatic disease (pain score of 2 at the time of death), and the other was still alive at 8 months post treatment with a pain score of 4. Therefore, adequate local tumor control and pain relief were achieved in this study with no side effects.

5.6 Clinical Experience with HIFU Treatment of Neuroendocrine Tumors

Pancreatic neuroendocrine tumors (PNETs) form in the islet cells that control hormone production (*e.g.,* insulin, glucagon, gastrin) and remain quite rare; they represent only 2 % of all pancreatic neoplasms (Delaunoit et al. 2008). Although PNETs have a better prognosis compared to pancreatic cancer, most of them are functional, *i.e.,* make extra amounts of hormones. Different patient symptoms occur depending on the hormone produced. For example, insulinomas produce increased amounts of insulin and may cause hypoglycaemia, and gastrinomas may cause abdominal pain, stomach ulcers and diarrhea. Non-functioning PNETs are usually malignant. The therapy of choice for patients with PNETs is surgical resection. This is associated with an 80 % 5-year survival rate in nonfunctioning PNET cases (Hellman et al. 2000), and was reported to be curative in 75–98 % of the patients with functioning insulinomas (Tucker et al. 2006). In the case of inoperability, there is no standard care for patients with advanced

pancreatic endocrine tumors, and HIFU ablation may represent a viable solution for local tumor control and symptom management.

To date, HIFU ablation of PNETs has been reported in two case studies. In the first study from Italy, two inoperable young female patients with insulinomas that were not responding to medical treatment were treated using the HAIFU system under general anesthesia (Orgera et al. 2011). Similarly to the previous studies, echogenicity changes were used as an indication of successful ablation, and according to the post-operative CT scans, the tumor was 70 % and 100 % ablated in the two patients, correspondingly. Both patients suffered from severe episodes of hypoglycemia before the treatment, but the symptoms disappeared completely immediately after the treatment. The patients remained symptom-free for the 9-month follow up period and no complications were noted. In the second study from China, an 80-year old man with a large non-functioning PNET underwent 3 sessions of HIFU ablation (every 2–3 months) to achieve the analgesic effect and local control of the lesion (Chen et al. 2013). The ablation was performed using the HAIFU system under general anesthesia with no complications. Encouragingly, after three sessions of treatment the abdominal pain significantly reduced (pain score decreased from 8 to 1 out of 10) during the follow up period of 25 months, and the tumor remained stable, with no distant metastases detected. Both of these studies indicate that HIFU represents both a palliative and a curative treatment option for unresectable PNETs, however more studies are needed to confirm this observation.

5.7 Concurrent Gemcitabine and HIFU Therapy

Several large clinical trials have shown that in patients with resectable disease, postoperative administration of systemic chemotherapy improves progression and overall survival (Hidalgo 2010). Since HIFU ablation may be considered a substitute to surgical resection in inoperable patients, with an added benefit of pain palliation, concurrent administration of chemotherapy seems like a viable strategy to improve survival. The survival benefit of this strategy was investigated in two studies where HIFU ablation was used in combination with gemcitabine. In the first study from China (Zhao et al. 2010), 37 patients with locally advanced pancreatic cancer (stages II-III) were treated with multiple (1–8) cycles of chemotherapy (1000 mg/m^2 gemcitabine, administered on days 1, 8 and 15) and concurrent HIFU ablation (performed on days 1, 3 and 5) using the HIFUNIT system. The treatment was performed every 28 days until patient refusal or disease progression. The median time for progression for all patients was 8.4 months, and the estimated median survival time was 12.6 months. The 1-year overall survival rate in this study was 50.6 %, which is comparable with recently published phase II trials on chemoradiotherapy in locally advanced pancreatic cancer - 40–63 % (Haddock et al. 2007; Hong et al. 2008). Chemoradiotherapy is limited by the total radiation dose, whereas HIFU has no exposure limitation. In addition, consistent with previous studies of HIFU treatment alone, pain was relieved in 78 % of patients.

In a more recent report from Korea, 12 patients with stage III-IV pancreatic cancer were treated with several weekly rounds of concurrent chemotherapy and HIFU using the FEB-BY system (Lee et al. 2011). The major difference from the first study was that HIFU was performed no more than 24 h after the administration of gemcitabine. Unfortunately, only three of twelve patients were able to complete at least three full cycles of concurrent therapy due to adverse reactions to chemotherapy. The survival times of these three patients were 11, 21 and 26 months, with excellent physical conditions and no complications. These results were even better than the previous study results, possibly due to the small time interval between HIFU ablation and chemotherapy infusion, meaning the two treatments could work synergistically. HIFU not only causes tissue heating, and therefore increased blood supply, but also causes additional mechanical effects (primarily acoustic cavitation). In combination, these may make the tumor more permeable for

chemotherapy. According to the measured CA 19–9 level and the CT findings, the growth inhibition period appeared to extend beyond 8 months from the time of initiating chemotherapeutic agents in all three patients. This is likely to have contributed to their prolonged survival times. In conclusion, although the number of cases was small in this study, the improved survival times achieved by the patients suggest that concurrent chemotherapy and HIFU therapy has potential to become an effective and safe modality for treating unresectable pancreatic cancer.

Conclusions

HIFU ablation has been shown to be a promising method for palliative treatment of pancreatic tumors, which, in combination with systemic chemotherapy may offer a survival benefit in addition to palliation of pain. As the design of HIFU devices is improved over time, and physicians become more comfortable and experienced with the procedure, fewer complications are being observed. In addition, the rate of successful ablations is increasing with enhanced targeting and treatment planning methods (Anzidei et al. 2014). Further clinical trials will help to define the future role of HIFU in the treatment of patients with pancreatic cancer.

References

Anzidei M, Napoli A, Sandolo F, Marincola BC, Di Martino M, Berloco P, Bosco S, Bezzi M, Catalano C (2014) Magnetic resonance-guided focused ultrasound ablation in abdominal moving organs: a feasibility study in selected cases of pancreatic and liver cancer. Cardiovasc Intervent Radiol 37:1611–1617

Arcidiacono PG, Calori G, Carrara S, McNicol ED and Testoni PA (2011) Celiac plexus block for pancreatic cancer pain in adults. Cochrane Database Syst Rev (3):CD007519

Balci NC, Semelka RC (2001) Radiologic diagnosis and staging of pancreatic ductal adenocarcinoma. Eur J Radiol 38:105–112

Bang S, Chung HW, Park SW, Chung JB, Yun M, Lee JD, Song SY (2006) The clinical usefulness of 18-fluorodeoxyglucose positron emission tomography in the differential diagnosis, staging, and response evaluation after concurrent chemoradiotherapy for pancreatic cancer. J Clin Gastroenterol 40:923–929

Bilimoria KY, Bentrem DJ, Ko CY, Ritchey J, Stewart AK, Winchester DP, Talamonti MS (2007) Validation of the 6th edition AJCC pancreatic cancer staging system: report from the National Cancer Database. Cancer 110:738–744

Chen Q, Zhu X, Chen Q, Wang K, Meng Z (2013) Unresectable giant pancreatic neuroendocrine tumor effectively treated by high-intensity focused ultrasound: a case report and review of the literature. Pancreatology 13(6):634–638

Chu GC, Kimmelman AC, Hezel AF, DePinho RA (2007) Stromal biology of pancreatic cancer. J Cell Biochem 101:887–907

Damianou C, Pavlou M, Velev O, Kyriakou K, Trimikliniotis M (2004) High intensity focused ultrasound ablation of kidney guided by MRI. Ultrasound Med Biol 30:397–404

Delaunoit T, Neczyporenko F, Rubin J, Erlichman C, Hobday TJ (2008) Medical management of pancreatic neuroendocrine tumors. Am J Gastroenterol 103:475–484

Edge SB, Byrd DR, Compton CC, Fritz AG, Greene FL, Trotti A (eds) (2010) AJCC cancer staging manual, 7th edn. Springer, New York

Ge HY, Miao LY, Wang JR, Xiong LL, Yan F, Zheng CS, Jia JW, Cui LG, Chen W (2013) Correlation between ultrasound reflection intensity and tumor ablation ratio of late-stage pancreatic carcinoma in HIFU therapy: dynamic observation on ultrasound reflection intensity. Scientific World Journal 2013:852874

Ge HY, Miao LY, Xiong LL, Yan F, Zheng C, Wang JR, Jia JW, Cui LG, Chen W (2014) High-intensity focused ultrasound treatment of late-stage pancreatic body carcinoma: optimal tumor depth for safe ablation. Ultrasound Med Biol 40:947–955

Haddock MG, Swaminathan R, Foster NR, Huage MD, Martenson JA, Camariano JK, Stella PJ, Tenglin RC, Schaefer PL, Moore DR Jr, Alberts SR (2007) Gemcitabine, cisplatin, and radiotherapy for patients with locally advanced pancreatic adenocarcinoma: results of the North Central Cancer Treatment Group Phase II Study N9942. J Clin Oncol 25:2567–2572

He SX and Wang GM (2002) The noninvasive treatment of 251 cases of advanced pancreatic cancer with focused ultrasound surgery. In: Proceedings of 2nd international symposium on therapeutic ultrasound, Seattle

Hellman P, Andersson M, Rastad J, Juhlin C, Karacagil S, Eriksson B, Skogseid B, Akerstrom G (2000) Surgical strategy for large or malignant endocrine pancreatic tumors. World J Surg 24:1353e60

Hidalgo M (2010) Pancreatic cancer. N Engl J Med 362:1605–1617

Hong SP, Park JY, Jeon TJ, Bang S, Park SW, Chung JB, Park MS, Seong J, Lee WJ, Song SY (2008) Weekly full-dose gemcitabine and single-dose cisplatin with concurrent radiotherapy in patients with locally advanced pancreatic cancer. Br J Cancer 98:881–887

Hwang JH, Wang YN, Warren C, Upton MP, Starr F, Zhou Y, Mitchell SB (2009) Preclinical *in vivo* evaluation of an extracorporeal HIFU device for ablation of pancreatic tumors. Ultrasound Med Biol 35:967–975

Jang HJ, Lee JY, Lee DH, Kim WH, Hwang JH (2010) Current and future clinical applications of high-intensity focused ultrasound (HIFU) for pancreatic cancer. Gut Liver 1(Supp l):S57–S61

Jiang L, Hu B, Guo Q, Chen L (2013) Treatment of pancreatic cancer in a nude mouse model using high-intensity focused ultrasound. Exp Ther Med 5:39–44

Jolesz FA, Hynynen K, McDannold N, Tempany C (2005) MR imaging-controlled focused ultrasound ablation: a noninvasive image-guided surgery. Magn Reson Imaging Clin N Am 13:545–560

Jung SE, Cho SH, Jang JH, Han JY (2011) High-intensity focused ultrasound ablation in hepatic and pancreatic cancer: complications. Abdom Imaging 36:185–195

Karmazanovsky G, Fedorov V, Kubyshkin V, Kotchatkov A (2005) Pancreatic head cancer: accuracy of CT in determination of resectability. Abdom Imaging 30:488–500

Khokhlova TD, Canney MS, Khokhlova VA, Sapozhnikov OA, Crum LA, Bailey MR (2011) Controlled tissue emulsification produced by high intensity focused ultrasound shock waves and millisecond boiling. J Acoust Soc Am 130:3498–3510

Lee JY, Choi BI, Ryu JK, Kim YT, Hwang JH, Kim SH, Han JK (2011) Concurrent chemotherapy and pulsed high-intensity focused ultrasound therapy for the treatment of unresectable pancreatic cancer: initial experiences. Korean J Radiol 12:176–186

Liu CX, Gao XS, Xiong LL, Ge HY, He XY, Li T, Zhang HJ, Bai HZ, Lin Q, Zhang M, Zhao J, Xiong W, Bai Y, Asaumi J (2011) A preclinical in vivo investigation of high-intensity focused ultrasound combined with radiotherapy. Ultrasound Med Biol 37:69–77

Lu MD, Yu XL, Li AH, Jiang TA, Chen MH, Zhao BZ, Zhou XD, Wang JR (2007) Comparison of contrast enhanced ultrasound and contrast enhanced CT or MRI in monitoring percutaneous thermal ablation procedure in patients with hepatocellular carcinoma: a multi-center study in China. Ultrasound Med Biol 33:1736–1749

Mahadevan D, Von Hoff DD (2007) Tumor-stroma interactions in pancreatic ductal adenocarcinoma. Mol Cancer Ther 6:1186–1197

Mao Y, Fang L, Ai L, Li C, Wang Z, Wu J, Bai J, Li F (2014) An in vivo study of the effects on serum glucose, amylase and histopathology of the feline pancreatic tissue treated by focused ultrasound. PLoS One 9(2), e88815

Mertz HR, Sechopoulos P, Delbeke D, Leach SD (2000) EUS, PET, and CT scanning for evaluation of pancreatic adenocarcinoma. Gastrointest Endosc 52:367–371

Miura F, Takada T, Amano H, Yoshida M, Furui S, Takeshita K (2006) Diagnosis of pancreatic cancer. HPB (Oxford) 8:337–342

Orgera G, Krokidis M, Monfardini L, Bonomo G, Della Vigna P, Fazio N, Orsi F (2011) High intensity focused ultrasound ablation of pancreatic neuroendocrine tumours: report of two cases. Cardiovasc Intervent Radiol 34:419–423

Orsi F, Zhang L, Arnone P, Orgera G, Bonomo G, Vigna PD, Monfardini L, Zhou K, Chen W, Wang Z, Veronesi U (2010) High intensity focused ultrasound (HIFU) ablation: effective and safe therapy for solid tumors at difficult locations. Am J Roentgenol 195:W245–W252

Rykowski JJ, Hilgier M (2000) Efficacy of neurolytic celiac plexus block in varying locations of pancreatic cancer. Anesthesiology 92:347–354

Shaib Y, Davila J, Naumann C, El-Serag H (2007) The impact of curative intent surgery on the survival of pancreatic cancer patients: a U.S. population-based study. Am J Gastroenterol 102:1377–1382

American Cancer Society (2013) Cancer Facts & Figures (2013) Available at http://www.cancer.org/research/cancerfactsfigures/cancerfactsfigures/cancer-facts-figures-2013. Accessed 15 Aug 2014

Staatas PS, Hekmat H, Sauter P, Lillemoe K (2001) The effects of alcohol celiac block, pain, and mood on longevity in patients with unresectable pancreatic pain: a double blind, randomised, placebo-controlled study. Pain Med 2:28–34

Sung HY, Jung SE, Cho SH, Zhou K, Han JY, Han ST, Kim JI, Kim JK, Choi JY, Yoon SK, Yang JM, Han CW, Lee YS (2011) Long-term outcome of high-intensity focused ultrasound in advanced pancreatic cancer. Pancreas 40:1080–1086

Tucker ON, Crotty PL, Conlin KC (2006) The management of insulinoma. Br J Surg 93:264–275

Wang K, Chen L, Meng Z, Lin J, Zhou Z, Wang P, Chen Z (2012) High intensity focused ultrasound treatment for patients with advanced pancreatic cancer: a preliminary dosimetric analysis. Int J Hyperthermia 28:645–652

Wang K, Chen Z, Meng Z, Lin J, Zhou Z, Wang P, Chen L, Liu L (2011) Analgesic effect of high intensity focused ultrasound therapy for unresectable pancreatic cancer. Int J Hyperthermia 27:101–107

Wang X, Sun JZ (2002) Preliminary study of high intensity focused ultrasound in treating patients with advanced pancreatic carcinoma. Chin J Gen Surg 17:654–655

Wu F, Wang ZB, Chen WZ, Zou JZ, Bai J, Zhu H, Li KQ, Xie FL, Jin CB, Su HB, Gao GW (2004) Extracorporeal focused ultrasound surgery for treatment of human solid carcinomas: early Chinese clinical experience. Ultrasound Med Biol 30:245–260

Wu F, Wang ZB, Zhu H, Chen WZ, Zou JZ, Bai J, Li KQ, Jin CB, Xie FL, Su HB (2005) Feasibility of US-guided high-intensity focused ultrasound treatment in patients with advanced pancreatic cancer: initial experience. Radiology 236:1034–1040

Xie B, Li YY, Jia L, Nie YQ, Du H, Jiang SM (2010) Experimental ablation of the pancreas with high intensity focused ultrasound (HIFU) in a porcine model. Int J Med Sci 8:9–15

Xie DR, Chen D, Teng H (2003) A multicenter non-randomized clinical study of high intensity focused ultrasound in treating patients with local advanced pancreatic carcinoma. Chin J Clin Oncol 30:630–634

Xiong LL, He CJ, Yao SS, Zeng JQ, Zhang GX, Huang K, He SX (2005) The preliminary clinical results of the treatment for advanced pancreatic carcinoma by high intensity focused ultrasound. Chin J Gen Surg 16: 345–347

Xiong LL, Hwang JH, Huang XB, Yao SS, He CJ, Ge XH, Ge HY, Wang XF (2009) Early clinical experience using high intensity focused ultrasound for palliation of inoperable pancreatic cancer. JOP 10:123–129

Xu YQ, Wang GM, Gu YZ, Zhang HF (2003) The acesodyne effect of high intensity focused ultrasound on the treatment of advanced pancreatic carcinoma. Clin Med J China 10:322–323

Yuan C, Yang L, Yao C (2003) Observation of high intensity focused ultrasound treating 40 cases of pancreatic cancer. Chin J Clin Hep 19:145

Zhao H, Yang G, Wang D, Yu X, Zhang Y, Zhu J, Ji Y, Zhong B, Zhao W, Yang Z, Aziz F (2010) Concurrent gemcitabine and high-intensity focused ultrasound therapy in patients with locally advanced pancreatic cancer. Anticancer Drugs 21:447–452

MR-Guided Transcranial Focused Ultrasound

6

Jean-François Aubry and Mickael Tanter

Abstract

Previous chapters introduced the ability of using focused ultrasound to ablate tissues. It has led to various clinical applications in the treatment of uterine fibroid, prostate or liver cancers. Nevertheless, treating the brain non-invasively with focused ultrasound has been considered beyond reach for almost a century: The skull bone protects the brain from mechanical injuries, but it also reflects and refracts ultrasound, making it difficult to target the brain with focused ultrasound. Fortunately, aberration correction techniques have been developed recently and thermal lesioning in the thalamus has been achieved clinically. This chapter introduces the aberration effect of the skull bone and how it can be corrected non-invasively. It also presents the latest clinical results obtained with thermal ablation and introduces novel non-thermal approaches that could revolutionize brain therapy in the future.

Keywords

Skull aberration • Thalomotomy • Mechanical ablation • BBB opening • Neuromodulation

6.1 Influence of the Skull Bone

For many different reasons, the influence of the skull bone is the major issue for transcranial brain HIFU. First of all, its acoustic properties (local density and sound speed) strongly differ from soft tissues and present strong spatial variations. All ultrasound imaging devices perform hundreds of thousands of sonographic exams all over the world every day, based on the correct assumption that soft tissue is an almost

J.-F. Aubry (✉)
Institut Langevin, ESPCI ParisTech,
CNRS UMR 7587, INSERM U979, Paris, France

Department of Radiation Oncology,
University of Virginia, Charlottesville, VA, USA
e-mail: jean-francois.aubry@espci.fr

M. Tanter (✉)
Institut Langevin, ESPCI ParisTech,
CNRS UMR 7587, INSERM U979, Paris, France
e-mail: mickael.tanter@espci.fr

© Springer International Publishing Switzerland 2016
J.-M. Escoffre, A. Bouakaz (eds.), *Therapeutic Ultrasound*, Advances in Experimental Medicine and Biology, Vol. 880, DOI 10.1007/978-3-319-22536-4_6

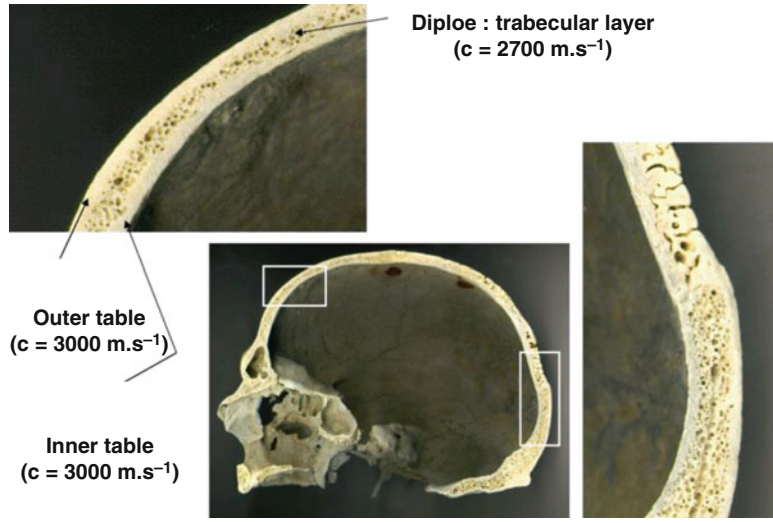

Fig. 6.1 The skull bone. A complex medium for transcranial ultrasonic propagation

homogeneous medium. Unfortunately, this assumption becomes irrelevant for the particular case of transcranial focusing. The large discrepancy in acoustic velocities between brain tissue and skull tissue (about 1500 m.s^{-1} versus 3000 m.s^{-1} respectively) and the severe attenuation of ultrasound in the skull bone strongly degrade the beam shape and consequently reduce the diagnostic and therapeutic performances. This problem was first discovered by (White et al. 1968) during investigation of brain imaging.

Secondly, the human skull bone itself comprises strong speed of sound and absorption heterogeneities. It is made of three successive layers of very different porosities. Two cortical dense bones (inner and outer tables) surround a trabecular porous region named diploe, see Fig. 6.1. Moreover, the acoustic impedance mismatch at skin/bone and bone/dura mater interfaces is very high and limits the acoustic transmission. In Fry and Barger 1978 published extensive experimental work on not only the acoustic scattering properties of the trabecular component of the skull (diploe), but also on the sound velocity, dispersion and attenuation in both cortical and trabecular components (Fry and Barger 1978). This pioneering work remains today a benchmark, giving access to experimental acoustic parameters of the human skull bone.

Sound speed within the skull bone ranges between 1500 m/s in the liquid phase of porous regions, and 3000 m/s in dense cortical regions (Fry and Barger 1978). Local density in the skull ranges between 1000 kg/m^3 in the liquid phase of porous regions and 2200 kg/m^3 in dense cortical regions. The speed of sound spatial heterogeneities strongly varies from one region to another and from one individual to another. A major reason for this high variability is the micro-structured architecture of the skull bone.

The inner and outer tables are defined by a very low porosity with a pore size ranging between 50 and 100 µm. For typical HIFU frequencies (500 kHz to 1.5 MHz), this pore size is very small compared to the ultrasonic wavelength in the bone (~3 mm at 1 MHz) and these cortical layers can be considered as a relatively homogeneous medium. On the contrary, the pore size is much larger in the trabecular layer (diploe) and is not negligible compared to the ultrasonic wavelength. Consequently, the acoustic propagation is influenced by the inner geometry of the skull bone (Aubry et al. 2003). Mode conversion and acoustic diffusion are more significant in the diploe than in inner and outer layers. This leads to a much higher attenuation of the ultrasonic beam in this inner region of the skull. In the classical frequency domain of transcranial HIFU (300 kHz to 1 MHz), the skull attenuation is due to both acoustic diffusion (reversible phenomenon) and absorption (irreversible phenomenon). The part of ultrasonic attenuation resulting from acoustic

diffusion is more significant than that resulting from absorption (Fry and Barger 1978; Pinton et al. 2012a).

This complex medium introduces both strong phase aberrations and attenuation on the ultrasonic beam during its transcranial propagation. These aberrations have been extensively explained by Fry and Barger, but have remained a bottleneck for non-invasive transcranial therapy for several decades. To compensate for these distortions, Phillips et al. (1975) introduced for diagnostic applications the idea of adaptive focusing by applying a correcting phase on the transmit signal of each element of the ultrasonic array. This concept has been adapted for therapeutic applications, as presented in the following section.

6.2 Skull Aberration Correction Techniques

6.2.1 Minimally Invasive Correction

In 1996, Thomas and coauthors introduced the concept of time reversal mirror for transcranial HIFU therapy (Tanter et al. 1996; Thomas and Fink 1996). They proposed embedding a miniature hydrophone on the surgeon's catheter used during the biopsy. Then by spatial reciprocity they recorded the signal transmitted from a point located close to the targeted area (tumor) to the HIFU array. At the end of the minimally invasive biopsy exam and after removing the catheter, the HIFU device would be used if the tumor malignancy was confirmed. In order to perform adaptive focusing of the ultrasonic therapeutic beam, the HIFU system would emit the time-reversed version of the initial experimental signals acquired during the biopsy. In conjunction with the phase aberration correction performed by the time reversal process, an amplitude compensation was also proposed in order to correct for both speed of sound and absorption aberrations caused by the skull. Using this time reversal focusing concept, they demonstrated both a 10 dB improvement of the focusing quality, and the ability to focus at the initial target location, thus cancelling the shifts induced by the skull. Initially limited to ultrasonic adaptive focusing at the sole location of the initial miniaturized hydrophone, this concept was extended in 1998 by Tanter et al. to adaptive focusing in large regions around the initial autofocus point (Thomas and Fink 1996; Tanter et al. 1998). In order to electronically steer the beam and heat the whole target spot by spot without moving the therapeutic array, the authors proposed combining the time reversal process with a numerical back-propagation and steering algorithm. They experimentally demonstrated the feasibility of this approach on *ex-vivo* human skull bones.

In 1998, Hynynen and Sun numerically modeled a phase conjugation technique (equivalent to the time reversal process for phase aberration correction of monochromatic signals) with a high intensity ultrasound system (Sun and Hynynen 1998). In 2000 and 2002, Clement et al. evaluated this phase conjugation technique from a single point location and extended the sonication regions around the initial focus by using a steering technique equivalent to the one introduced by Tanter et al. Clement et al. validated this approach at high power by performing *in-vitro* necrosis at the geometrical center of a spherical transducer array using a therapeutic beam steered from an implantable hydrophone located 1 cm away from geometrical focus (Clement and Hynynen 2002b). In 2004, Pernot et al. performed a first preclinical trial on 20 sheep using the time reversal focusing concept (Pernot et al. 2004, 2007). Transcranial adaptive focusing was achieved using a 300-element HIFU array driven by a fully programmable system with 300 independent electronic channels. The histological examination confirmed that thermal necrosis had been induced in the targeted area and that no skin and skull burns occurred.

6.2.2 Non Invasive Correction

Some years later, the possibility to assess the acoustic properties of each patient skull from MRI (Clement and Hynynen 2002a, b) or CT images (Aubry et al. 2003) raised new hopes for fully noninvasive brain therapy. Thus, the

minimally invasive procedures described in (Tanter et al. 1998, Clement and Hynynen 2002) were replaced by a totally non-invasive method guided by imaging modalities to predict skull aberrations. Hynynen et al. proposed MRI guidance (Clement and Hynynen 2002a, b) for extracting the skull profile without information on internal heterogeneities. Although this simplified model improves the focusing beam quality, it is not sufficient to completely model the phase aberrations induced by the skull. Heterogeneous speed of sound and density maps can be extracted from high-resolution CT images. For this reason, CT imaging is more suited for modeling the ultrasonic properties of the skull (Pernot et al. 2003; Marquet et al. 2006).

Aubry et al. (2003) suggested and validated a way to extract local acoustic properties of the skull from 3D CT scans and then used these parameters in a numerical model of the wave propagation based on three-dimensional finite differences. By taking into account the internal bone structure (heterogeneities in density, speed of sound and ultrasonic absorption coefficient), this finite difference simulation models all the defocusing effects first highlighted by White et al. (1968). The feasibility of such transcranial ultrasound therapy based on the prior acquisition and guidance of 3D CT-scans was confirmed *in-vitro*, and the performances of the fully adaptive focusing protocol was studied by Marquet et al. (2006). They demonstrated that this focusing approach based on 3D CT scans and numerical modeling was reaching an excellent focus localization with a spatial variance of the focal spot being of the order of 1 mm (*i.e.* comparable to the CT scan voxel size). The same system was used to perform preclinical demonstration of such noninvasive CT-based HIFU treatment on 5 monkeys (Tanter et al. 2007; Marquet et al. 2013). Monkeys were sacrificed 2 weeks after the treatment and no skin burn was reported. The histological examination confirmed thermal acidophilic necrosis in the area treated with the CT based time reversal correction, whereas no necrosis was induced in regions without adaptive focusing. The first clinical application of CT-based adaptive focusing of ultrasonic therapeutic beams was performed on 11 patients suffering from chronic therapy-resistant neuropathic pain during TcMRgFUS-induced thalamotomy (Martin et al. 2009).

In conclusion, adaptive focusing techniques for transcranial ultrasonic therapy are based on time-reversal processing (Thomas and Fink 1996; Tanter et al. 1998) or phase conjugation focusing (Sun and Hynynen 1998; Clement and Hynynen 2002a, b), and have been shown to restore a good focusing quality down to 20 dB, which is known to be sufficient for ultrasonic therapy. Two kinds of correction algorithms are used: 3D finite difference simulations of the full propagation through the skull bone structure for the time reversal approach (Aubry et al. 2003), and a layered wave-vector-frequency estimation for the phase conjugation technique (Clement and Hynynen Clement and Hynynen 2002a, b). The focusing quality was further improved down to 40 dB by correcting both phase and amplitude thanks to spatio-temporal inverse filtering (Tanter et al. 2000; Aubry et al. 2001; Tanter et al. 2001; Vignon et al. 2006) for future optimal transcranial brain imaging.

Recently, another adaptive focusing approach was proposed that does not require the use of numerical modeling (Herbert et al. 2009; Larrat et al. 2010). Correction of the therapeutic beam is performed by maximizing the local displacement induced at the targeted location by the radiation force of transmitted ultrasonic signals, as imaged by MR-Acoustic Radiation Force Imaging (Hertzberg et al. 2010; Larrat et al. 2010; Kaye et al. 2011; Marsac et al. 2012). To date, this approach was validated only in human cadaver heads (Marsac et al. 2012) and further clinical translation requires further developments. If successful, this approach could be of great interest, as it does not rely on any numerical modeling of transcranial propagation, but rather on the direct observation and optimization of acoustic beam intensity using MRI.

6.3 Thermal Therapy

The technological developments presented in previous sections have led to the development of two brain therapy devices. The devices have been first tested on cadaver (Marsac et al. 2012; Chauvet

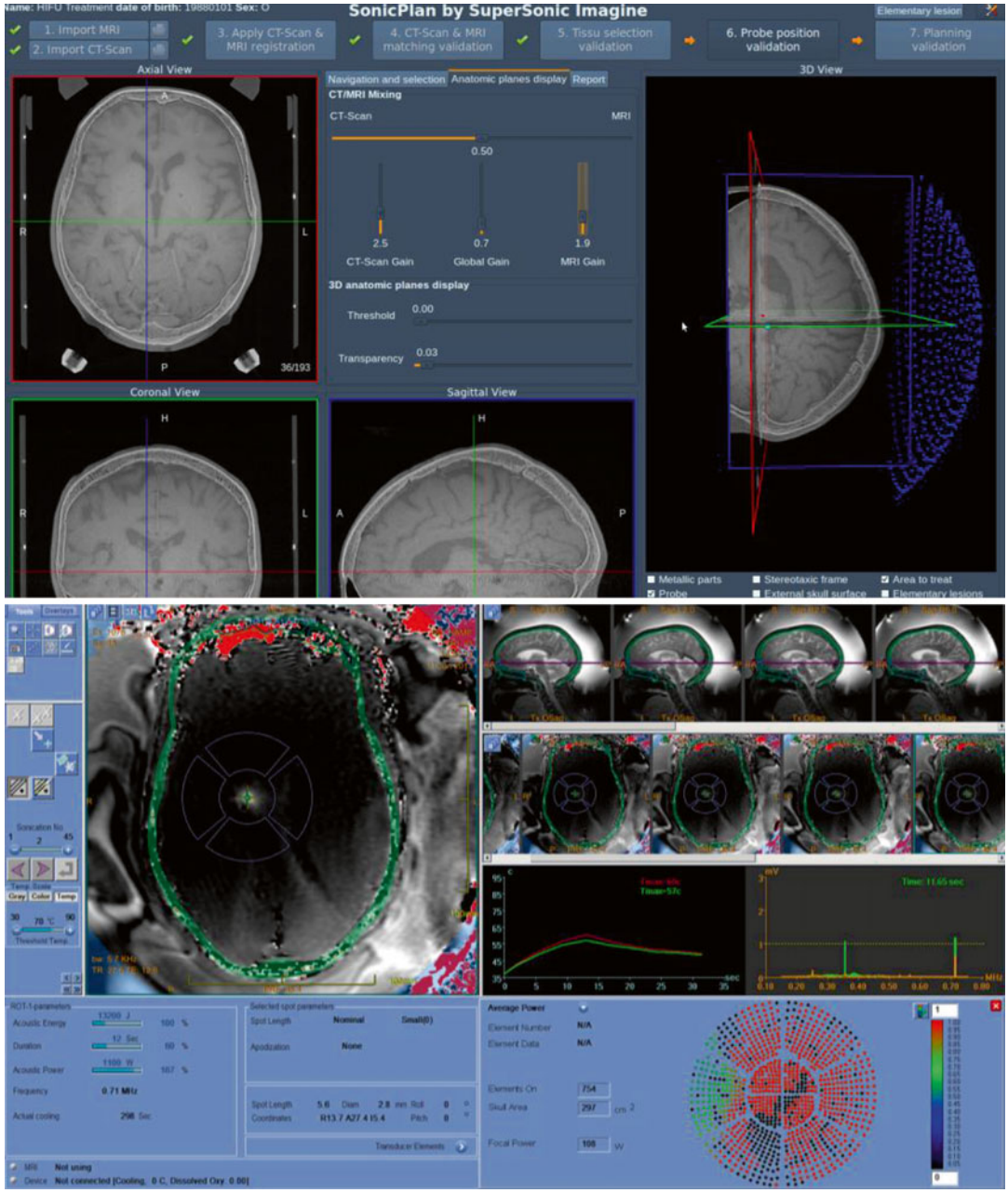

Fig. 6.2 SuperSonic Imagine (*Top*) and Insightec (*Bottom*) planning and monitoring software during planning (*Top*) and monitoring (*Bottom*) phase of human cadaver experiments

et al. 2013; Monteith et al. 2013b), as illustrated in Fig. 6.2, and have been recently translated into clinics for non-invasive TcMRgFUS thalamotomy (see next section). Current research focuses on expanding the treatment envelope to other areas of the brain, as presented later in this chapter.

6.3.1 Thalamotomy

The thalamus is a neurological relay that plays a major role in many movement disorders such as Essential Tremor, Parkinsonian tremor or Dyskinesia, but also in neuropathic pain. It is

deeply seated in a central area of the brain and is thus an ideal candidate for TcMRgFUS from an ultrasonic point of view given it allows a high antenna gain (ratio between the surface of the beam intercepting the skull and the transverse surface of the beam in the focal plane).

Surgical intervention was proposed in the 70s to address tremor with radiofrequency lesioning or electrical stimulation of the ventralis intermediate nucleus of the thalamus (Tasker 1998). Radiofrequency ablation in the medial thalamus also showed long term reduction of neurogenic pain (Jeanmonod et al. 2001). Nevertheless, in both cases patients are reluctant to undergo such invasive surgeries. Targeting the thalamus with focused ultrasound is thus of great potential. This was actually demonstrated *in-vivo* in pigs (Elias et al. 2013b). This study showed that long sonication (typically 10–30 s) of high power focused ultrasound (typically 1 kW/cm^2 at focus) can locally increase the temperature and induce thermal necrosis that evolves similarly to radiofrequency lesions, as assessed by MRI, histology and theoretical modeling (Elias et al. 2013a, b).

Example – Neuropathic pain

The first TcMRgFUS-induced thalamotomy was performed in Zurich on 11 patients suffering from chronic therapy-resistant neuropathic pain. Short term outcomes of the first 9 patients were reported in a preliminary paper (Martin et al. 2009) and a complete report was published with two additional patients (Jeanmonod et al. 2012). Peak temperatures of 51 and 53 °C were achieved in the first two patients in the posterior part of the central lateral thalamic nucleus, as measured by MR-based temperature mapping. The acoustic power was increased for patients 3–9, and the peak temperature ranged between 51 and 60 °C. Power was further increased and a peak temperature of 64 °C was achieved in the last two patients. All patients experienced somatosensory and vestibular manifestations during sonication, but only six patients experienced immediate and persisting somatosensory improvements. Sensory improvements were not correlated to the peak temperature at focus (Table 6.1). The precision of the targeting was further investigated in (Moser et al. 2012). The authors computed the global accuracy as the difference between the coordinates of the center of the lesion as seen on post-operative MR images and the coordinates of the target as defined on the pre-treatment MR coordinates of the target. The mean global error was 0.54 ± 0.34 mm in the antero-posterior direction, 0.72 ± 0.42 mm in the medio-lateral direction and 0.72 ± 0.39 mm in the dorso-ventral direction. In 45 % of the patients (patients #1, #2, #3, #7 and #11) the error along one axis exceeded 1 mm. Thus, lack of sensory improvement does not correlate with largest targeting errors.

Table 6.1 Summary of thalamotomy treatments using focused ultrasound for neuropathic pain

Case number	Max temperature at target (°C)	Sensory improvements	Side effects
1	53	+	
2	51	+	
3	57	+	
4	59	–	
5	55	+	
6	58	+	
7	57	–	
8	55	–	
9	60	–	
10	64	+	
11	64	–	[a]
Overall	57.5		

Adapted from Jeanmonod et al. (2012)

[a]Right-sided motor hemineglect associated with bleeding centered in the targeted thalamic central lateral nucleus

Right after the last sonication of the treatment, patient #11 suffered an acute appearance of right-sided motor hemineglect with dysmetria of the arm and leg and dysarthria (Jeanmonod et al. 2012). Post-treatment MR images showed a 10 mm bleed centered in the targeted thalamic central lateral nucleus, as well as ischemic changes in the posterior part of the thalamic motor ventral lateral nucleus. An 80 % reduction in the motor symptoms were reported over the next 24 h and dysmetric manifestations almost disappeared, except during activation of the finer functions of speaking and writing.

Bleeding can be induced by the violent collapse of ultrasound-induced bubbles created

during sonication by a process called acoustic cavitation (Leighton 1994). The brain is very sensitive to such collapse and hemorrhagic effects have been reported in dog brains by Fry et al. (1995) at the cortical gray and subcortical white matter interface when multiple adjacent focal sites where exposed to ultrasound. Acoustic emission induced by the collapse of cavitation bubbles can be detected by passive cavitation detectors and passive mapping can be sensitive up to single cavitation events (Gateau et al. 2011a). Passive cavitation detection can thus be used to trigger a shutdown of the system at the early onset of cavitation (Gyongy and Coussios 2009). Following the adverse event reported in (Jeanmonod et al. 2012), passive cavitation detection was implemented on the Exablate 4000 system for upcoming clinical trials.

Example – Essential Tremor

Between 2011 and 2012, 15 drug-resistant patients participated in a phase I study on essential tremor with the Exablate 4000 system at the University of Virginia (Elias et al. 2013a, b). The treatment consisted of a controlateral thalomotomy of the ventralis intermediate nucleus (VIM). A series of low-power sonications were delivered to the intended target to validate the location of the target. Once verified, thermal rise was achieved until the measured thermal dose was higher than 240 cumulative equivalent minutes (CEM). The maximum temperatures reached ranged between 55 and 63 °C. The results showed an average decrease of the tremor of 67 % 1 year after treatment, resulting in a reduction of disability of 83 %. However, a mild facial paralysis and numbness of the fingers were observed in some cases (transiently for 9 patients, and persistent after 1 year for 4 patients). At the end of 2012, four patients with essential tremor of the hand were also treated in Toronto (Lipsman et al. 2013). The targets were in the VIM opposite to the most affected hand. The focus was verified by moderate heating and adapted so as not to affect the adjacent sensory areas. The lesions were gradually extended by increasing the power or duration of emissions (between 12 and 29 times in increments between 0 and 2 °C and between 10 and 25 s) until the disappearance of tremor or occurrence of adverse effects. Temperatures between 56 and 63 °C were reached. The tremors decreased significantly during treatment and after 3 months. However, paresthesia at the tip of the thumb occurred in one patient during treatment, still persisting after 3 months. Another patient had a deep vein thrombosis, which, according to the authors, was potentially linked to the duration of treatment. More recently, 11 patients were treated at Yonsei University College of Medicine, Seoul, Korea (Chang et al. 2014), showing an overall significant decrease in tremor symptoms (Table 6.2), but treatment was not possible for three patients: The maximum temperature at target was less than 42 °C, even with up to 24 000 acoustic joules emitted by the transducer (1200 W during 20 s).

Improvement of the tremor was significant for the three clinical trials summarized in Table 6.2. All studies also reported adverse effects, mostly paresthesia. (Chang et al. 2014) reported minimal adverse effects. In (Lipsman et al. 2013), two out of three patients developed paresthesias during sonication; paresthesias in the tips of the thumb and index finger persisted at the 3-month follow-up for one patient. (Elias et al. 2013a, b) reported a detailed list of transient and one-year lasting adverse effect observed in the 15 patients treated; three paresthesias were reported, but the only serious adverse effect was dysesthesia in one patient.

6.3.2 Expansion of Treatment Envelope

The non-invasive, radiation-free and precise properties of tcMRgFUS would make it an ideal candidate for many other brain indications outside of the thalamus, such as trigeminal neuralgia, epilepsy, cingulotomy or brain tumors (Monteith et al. 2013a, b). Nevertheless, transcranial focused ultrasound therapy becomes challenging when the target is in proximity of bony structures. The ratio between the acoustic intensity at focus and on the skull decreases indeed as the target approaches the skull, as illustrated in Fig. 6.3 (top row compared to bottom row). As the ultrasonic absorption coefficient of the bone

Table 6.2 Summary of essential tremor treatments with focused ultrasound

Reference	Case number	Max temperature at target (°C)	Sensory improvements	
			Baseline CRST (total)	*3 months CRST (total)*
Lipsman et al. (2013)	1	56	63	28
	2	63	82	42
	3	59	47	24
	4	59	91	47
	Overall Mean	59.25	70.75	35.25
Elias et al. (2013a, b)	1	N/A (55–63)	N/A average: 55	N/A average: 25
	2	N/A (55–63)	N/A average: 55	N/A average: 25
	3	N/A (55–63)	N/A average: 55	N/A average: 25
	4	N/A (55–63)	N/A average: 55	N/A average: 25
	5	N/A (55–63)	N/A average: 55	N/A average: 25
	6	N/A (55–63)	N/A average: 55	N/A average: 25
	7	N/A (55–63)	N/A average: 55	N/A average: 25
	8	N/A (55–63)	N/A average: 55	N/A average: 25
	9	N/A (55–63)	N/A average: 55	N/A average: 25
	10	N/A (55–63)	N/A average: 55	N/A average: 25
	11	N/A (55–63)	N/A average: 55	N/A average: 25
			Baseline CRST (A + B + C)	*6 months CRST (A + B + C)*
Chang et al. (2014)	1	N/A (48–61)	34	8
	2	N/A (48–61)	22	1
	3	N/A (48–61)	36	18
	4	<42	N/A	N/A
	5	N/A (48–61)	29	7
	6	N/A (48–61)	27	0
	7	<42	N/A	N/A
	8	<42	N/A	N/A
	9	N/A (48–61)	40	19
	10	N/A (48–61)	24	0
	11	N/A (48–61)	40	1
	Overall mean		31.5	6.75

is higher than in soft tissue (White and Hanna 1974; Pinton et al. 2012a, b), maximum temperature in the brain can be higher at the outer surface of the brain than at the targeted location. Several approaches have been proposed to expand the treatment envelope to off-center parts of the brain.

6.3.2.1 Improvements in Aberration Correction

As mentioned in previous sections, central locations of the brain are particularly suited for focused ultrasound and early developments of transcranial focused ultrasound took advantage of the geometry of the skull: For thalamic targets the ultrasonic beam crosses the skull almost perpendicularly to the skull surface. In this case, transcranial propagation is composed of longitudinal waves: Mode conversion from longitudinal to transverse waves can be neglected and the skull can be modeled as a fluid in aberration correction algorithms. This remains valid for incident beam angles lower than the critical angle (approximately 25° at the skin/skull interface),

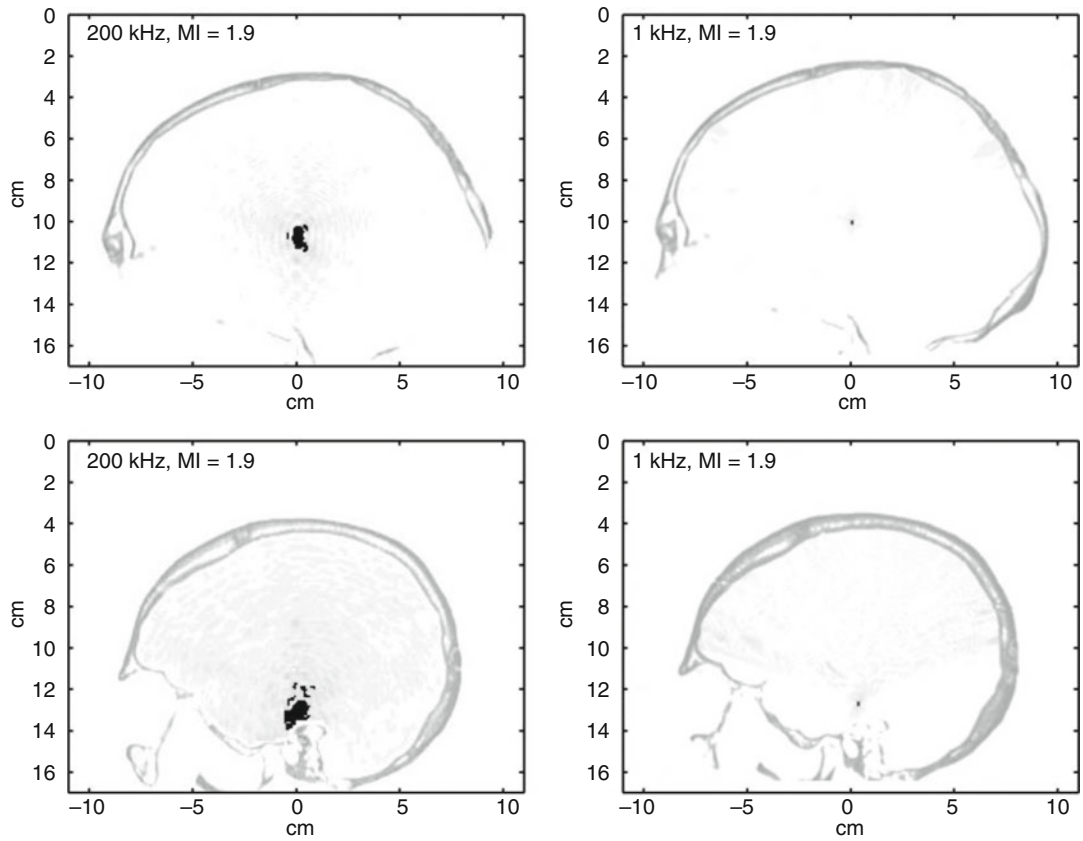

Fig. 6.3 Numerical modeling of the mechanical index distribution in the head using 3D finite differences computing at 220 kHz (*Left column*) and 1 MHz (*Right column*). Top row: Target located in the thalamus. Bottom row: Target located at the skull base (Extracted from Pinton et al. 2012a, b)

but does not hold anymore when the focus is directed at the periphery of the brain. Advanced numerical models of transcranial wave propagation in solid structures have thus been introduced to take into account mode conversion (Pinton et al. 2010; Pulkkinen et al. 2011).

6.3.2.2 Choice of the Frequency

Low frequency ultrasound beams are less distorted than higher frequency ones when crossing the skull bone. For this reason, a low frequency brain device operating at 220 kHz was constructed to expand the treatment envelope (Xu et al. 2014). However, low frequency ultrasound is likely to induce acoustical cavitation in the brain, which can lead to massive hemorrhage (Daffertshofer et al. 2005; Baron et al. 2009). For this reason, cavitation detectors have been added to brain devices to automatically shut down the system if cavitation occurs (Clark et al. 1971; Jeanmonod et al. 2012). On the opposite range of frequency, it has been shown that high frequency waves can take advantage of a smaller size of the focal spot to reach targets close to the skull base (Pinton et al. 2010), as illustrated in Fig. 6.1 (bottom row). Low frequency ultrasound could thus expand the treatment envelope toward the skull vault, whereas high frequency ultrasound could expand the treatment envelope toward the skull base.

6.3.2.3 Cavitation-Enhanced Heating

The absorption coefficient of ultrasound in tissues increases linearly with frequency (White and Hanna 1974). Heat transfer is thus more efficient at higher frequencies. Stable and inertial cavitation are known to generate high ultrasonic frequencies

(Leighton 1994) and can thus lead to cavitation-enhanced tissue heating. For brain therapy, the non-linear response of the bubbles advantageously enhances the effects of the slight difference in pressure levels between the target and the outer surface of the brain when the target gets close to the skull. Cavitation activity has been so far either triggered by ultrasound pulses of high intensity (Kieran et al. 2007; Gateau et al. 2010) or facilitated by injection of microbubbles (Zhang et al. 2011) or nanoemulsions (Jenkins and White 1972).

6.4 Non Thermal Therapy

6.4.1 Mechanical Ablation

Ultrasound interacts with biological tissues via two major mechanisms: Thermal and mechanical mechanisms. Previous sections discussed the use of thermal effects in the brain, but mechanical effects can also be taken advantage of. Mechanical effects are of several types. Acoustic cavitation (Leighton 1994) is the most violent and most effective (Xu et al. 2010), corresponding to the stable or inertial oscillation of microbubbles (either injected or generated spontaneously).

Example – Mechanical ablation by ultrasonic cavitation

Alkins et al. performed cavitation-enhanced noninvasive third ventriculostomy in live pigs at 650 and 230 kHz (Alkins et al. 2013). Ventriculostomy was achieved by tissue fractionation. Two sets of experiments were performed on craniectomized animals: With and without a human skull inserted between the transducer and the animal's head. At 650 kHz, a peak pressure higher than 22.7 MPa was needed at focus for 1 s to reliably create a ventriculostomy. Transcranially at this frequency the ExAblate 4000 was unable to generate the required intensity to fractionate tissue, although cavitation was initiated. This is consistent with previous observations that pressure levels higher than 18 MPa were needed to nucleate cavitation in living sheep brains (Gateau et al. 2011b). At 230 kHz, ventriculostomy was successful through the skull with a peak pressure of 8.8 MPa.

Example – Optic nerve sparing by microbubble enhanced low-intensity low-duty-cycle sonication

McDannold et al. used a 525 kHz single-element focused transducer in 29 rats to ablate tissue structures close to the optic tract at the skull base. Intravenous injection of a contrast agent (Definity, Lantheus Medical Imaging Inc.) was first performed. Low-intensity, low-duty-cycle ultrasound sonications were then applied for 5 min. Lesions were induced in the gray matter, while the adjacent optic tract and white matter tracts suffered no damage, or little damage (no significant changes were found in the magnitude or latency of visual evoked potential recordings). The enhancing therapeutic effect of the microbubbles helped in the production of sharp lesions with optic nerve sparing. The authors hypothesize that lesions were produced via non-thermal destruction of the vasculature and subsequent ischemia in downstream tissues.

6.4.2 BBB Opening

Hynynen et al. (2001) demonstrated that the use of low power focused ultrasound combined with a systemic injection of lipid- (or polymer-) shelled microbubbles enabled noninvasive, local and transient disruption of the BBB. Following this pioneering study, extensive literature established optimal ultrasound parameters leading to required brain tissue penetration without causing tissue damage (Hynynen et al. 2005; Choi et al. 2007; Sheikov et al. 2008; O'Reilly et al. 2011; O'Reilly et al. 2011; O'Reilly and Hynynen 2012). Other groups quantified the permeability of the disrupted brain tissue (Vlachos et al. 2010; Vlachos et al. 2011) and the dynamics of BBB closure after its disruption using low power focused ultrasound (Marty et al. 2012). The potential of BBB opening using low power focused ultrasound was studied in preclinical models for a large variety of pathologies including tumors (Treat et al. 2007; Chen et al. 2010; Liu et al. 2010) and Alzheimer's disease (Raymond et al. 2008; Jordao et al. 2010). For a more detailed description of ultrasound BBB opening, the reader should refer to the chapter dedicated to this application.

6.4.3 Neuromodulation

In 1958, Fry and co-authors (Fry et al. 1958) demonstrated that transmission of ultrasound waves to the lateral geniculate nucleus suppresses the induced response in the primary visual cortex in cats, as evidenced by electroencephalogram recordings (EEG). In 1976, Gavrilov and colleagues (Gavrilov et al. 1976) demonstrated that focused ultrasound was a powerful tool for stimulating nerve structures and produced different thermal, tactile and pain responses to ultrasound beams focused in the human arm. More recently, Tyler and colleagues (Tyler et al. 2008; Tufail et al. 2010) proved the ability of low-frequency, low-intensity ultrasound waves to induce motor stimulation without producing damage to brain tissue. Yoo et al. (2011) obtained similar results in rabbits in 2010 and used an MR-compatible transducer to visualize the activation of the motor cortex using functional MRI. As shown in previous sections, ultrasound can be focused through the intact human skull using multi-element transducers and phase correction, thus making it possible to translate these animal studies to humans.

Compared to current non-ultrasonic neurostimulation techniques, such as transcranial direct current stimulation (tDCS) (Nitsche et al. 2008), implanted electrodes (Ressler and Mayberg 2007), Transcranial Magnetic Stimulation (TMS) (Hallett 2000) or optogenetics (Szobota et al. 2007; Zhang et al. 2007), transcranial ultrasonic neuromodulation offers a unique combination of high resolution in space (a few millimeters) and time (few hundreds of milliseconds). This is also together with access to deep brain structures and non-invasiveness. Transcranial ultrasound neuromodulation could thus open the door to unique high resolution and non-invasive neuromodulation applications. Recent results confirm this potential, as focused ultrasound was shown to be able to modulate the level of cortical neurotransmitters (Yang et al. 2012) and thus, may have diagnostic as well as therapeutic implications for psychiatric disorders.

Important questions on the mechanisms behind ultrasound neuromodulation remain. On the physiological scale, different hypotheses have been proposed from the ultrasound-induced release of neurotransmitters inside the synaptic cleft (Borrelli et al. 1981) to the ultrasound-induced opening of mechano-sensitive channels on the membrane (Krasovitski et al. 2011; Plaksin et al. 2014) that would then trigger action potentials (Tyler et al. 2008). However, the existence of a lower bound acoustic threshold for the effect has been questioned as, interestingly, Tufail et al. (2010) reported higher electromyography (EMG) responses when lower acoustic intensities were used. In contrast, King et al. (2013) and Younan et al. (2013) reported an acoustic threshold below which no stimulation was observed for ultrasonic neuromodulation in rats. The stimulation of very specific structures, such as the oculomotor system or single whisker, was observed (Younan et al. 2013), even though the wavelength at 320 kHz is approximately 5 mm. Simulation using a finite-difference-time-domain software and CT scan shown ultrasound reverberations in the head cavity yielding a 1.8-fold increase in the spatial peak - time peak pressure compared to free water, and a 2.3-fold increase in spatial peak, pulse averaged intensity (Younan et al. 2013). At such a low frequency, the acoustic field resulting from the reverberations needs to be carefully taken into account for small animal studies at low frequencies.

More recently, low intensity FUS stimulation has been shown to causally modulate behavior in an awake nonhuman primate brain (Deffieux et al. 2013): The latency of an anti-saccade task was significantly delayed ($p<0.05$) in the presence of ultrasonic beam focused in the Frontal Eye Field. Sham experiments did not show any significant change in the latencies (Deffieux et al. 2013). The activity of primary somatosensory cortex was recently modulated with transcranial ultrasound in humans, as evidenced by Legon et al. (2014).

6.5 Conclusions and Future Prospects

Treating the brain non-invasively with focused ultrasound has long been considered as beyond reach. The first study reporting successful ultrasonic

thermal lesioning of the thalamus was published no more than 5 years ago (Martin et al. 2009), rapidly followed by very promising results on essential tremor (Elias et al. 2013, Lipsman et al. 2013; Chang et al. 2014). Thermal lesioning will continue to ramp up with novel clinical applications, such as treatment of tumors, obsessive-compulsive disorders or parkinsonian tremor and dyskinesia. Additionally, a second breakthrough is already about to occur: Non-thermal treatments of the brain. Reversible opening of the blood brain barrier (to deliver therapeutic agents) and neuromodulation (to modulate brain activity) are on their way to the clinic.

References

Alkins R, Huang Y, Pajek D, Hynynen K (2013) Cavitation-based third ventriculostomy using MRI-guided focused ultrasound: Laboratory investigation. J Neurosurg 119:1520–1529

Aubry JF, Tanter M, Gerber J, Thomas JL, Fink M (2001) Optimal focusing by spatio-temporal inverse filter. II experiments application to focusing through absorbing and reverberating media. J Acoust Soc Am 110:48–58

Aubry JF, Tanter M, Pernot M, Thomas JL, Fink M (2003) Experimental demonstration of noninvasive transskull adaptive focusing based on prior computed tomography scans. J Acoust Soc Am 113:84–93

Baron C, Aubry JF, Tanter M, Meairs S, Fink M (2009) Simulation of intracranial acoustic fields in clinical trials of sonothrombolysis. Ultrasound Med Biol 35:1148–1158

Borrelli M, Bailey K, Dunn F (1981) Early ultrasonic effects upon mammalian CNS structures (chemical synapses). J Acoust Soc Am 69:1514–1516

Chang WS, Jung HH, Kweon EJ, Zadicario E, Rachmilevitch I, Chang JW (2014) Unilateral magnetic resonance guided focused ultrasound thalamotomy for essential tremor: practices and clinicoradiological outcomes. J Neurol Neurosurg Psychiatry 86(3):257

Chauvet D, Marsac L, Pernot M, Boch AL, Guillevin R, Salameh N, Souris L, Darrasse L, Fink M, Tanter M, Aubry JF (2013) Targeting accuracy of transcranial magnetic resonance–guided high-intensity focused ultrasound brain therapy: a fresh cadaver model. J Neurosurg 118:1046–1052

Chen PY, Liu HL, Hua MY, Yang HW, Huang CY, Chu PC, Lyu LA, Tseng IC, Feng LY, Tsai HC, Chen SM, Lu YJ, Wang JJ, Yen TC, Ma YH, Wu T, Chen JP, Chuang JI, Shin JW, Hsueh C, Wei KC (2010) Novel magnetic/ultrasound focusing system enhances nanoparticle drug delivery for glioma treatment. Neuro Oncol 12:1050–1060

Choi JJ, Pernot M, Small SA, Konofagou EE (2007) Noninvasive, transcranial and localized opening of the blood–brain barrier using focused ultrasound in mice. Ultrasound Med Biol 33:95–104

Clark JM, White DN, Curry GR, Stevenson RJ, Campbell JK, Jenkins CO (1971) The measurement of intracranial echo pulsations. Med Biol Eng 9:263–287

Clement G, Hynynen K (2002a) A non-invasive method for focusing ultrasound through the human skull. Phys Med Biol 47:1219–1236

Clement GT, Hynynen K (2002b) Micro-receiver guided transcranial beam steering. IEEE Trans Ultrason Ferroelect Freq Control 49:447–453

Clement GT, Sun J, Giesecke T, Hynynen K (2000) A hemisphere array for non-invasive ultrasound brain therapy and surgery. Phys Med Biol 45:3707–3719

Daffertshofer M, Gass A, Ringleb P, Sitzer M, Sliwka U, Els T, Sedlaczek O, Koroshetz WJ, Hennerici MG (2005) Transcranial low-frequency ultrasound-mediated thrombolysis in brain ischemia: increased risk of hemorrhage with combined ultrasound and tissue plasminogen activator: results of a phase II clinical trial. Stroke 36:1441–1446

Deffieux T, Younan Y, Wattiez N, Tanter M, Pouget P, Aubry JF (2013) Low-intensity focused ultrasound modulates monkey visuomotor behavior. Curr Biol 23:2430–2433

Elias WJ, Huss D, Voss T, Loomba J, Khaled M, Zadicario E, Frysinger RC, Sperling SA, Wylie S, Monteith SJ, Druzgal J, Shah BB, Harrison M, Wintermark M (2013a) A pilot study of focused ultrasound thalamotomy for essential tremor. N Engl J Med 369:640–648

Elias WJ, Khaled M, Hilliard JD, Aubry JF, Frysinger RC, Sheehan JP, Wintermark M, Lopes MB (2013b) A magnetic resonance imaging, histological, and dose modeling comparison of focused ultrasound, radiofrequency, and Gamma Knife radiosurgery lesions in swine thalamus. J Neurosurg 119:307–317

Fry FJ, Barger JE (1978) Acoustical properties of the human skull. J Acoust Soc Am 63:1576–1590

Fry FJ, Ades HW, Fry WJ (1958) Production of reversible changes in the central nervous system by ultrasound. Science 127:83–84

Fry FJ, Sanghvi NT, Foster RS, Bihrle R, Hennige C (1995) Ultrasound and microbubbles: their generation, detection and potential utilization in tissue and organ therapy—experimental. Ultrasound Med Biol 21: 1227–1237

Gateau J, Marsac L, Pernot M, Aubry JF, Tanter M, Fink M (2010) Transcranial ultrasonic therapy based on time reversal of acoustically induced cavitation bubble signature. IEEE Trans Biomed Eng 57:134–144

Gateau J, Aubry JF, Pernot M, Fink M, Tanter M (2011a) Combined passive detection and ultrafast active imaging of cavitation events induced by short pulses of high-intensity ultrasound. IEEE Trans Ultrason Ferroelectr Freq Control 58:517–532

Gateau J, Aubry JF, Chauvet D, Boch A, Fink M, Tanter M (2011b) In vivo bubble nucleation probability in sheep brain tissue. Phys Med Biol 56:7001

Gavrilov L, Gersuni G, Ilyinsky O, Sirotyuk M, Tsirulnikov E, Shchekanov E (1976) The effect of

focused ultrasound on the skin and deep nerve structures of man and animal. Prog Brain Res 43:279–292
Gyongy M, Coussios CC (2009) Passive spatial mapping of inertial cavitation during HIFU exposure. IEEE Trans Biomed Eng 57:48–56
Hallett M (2000) Transcranial magnetic stimulation and the human brain. Nature 406:147–150
Herbert E, Pernot M, Montaldo G, Fink M, Tanter M (2009) Energy-based adaptive focusing of waves: application to noninvasive aberration correction of ultrasonic wavefields. IEEE Trans Ultrason Ferroelectr Freq Control 56:2388–2399
Hertzberg Y, Volovick A, Zur Y, Medan Y, Vitek S, Navon G (2010) Ultrasound focusing using magnetic resonance acoustic radiation force imaging: application to ultrasound transcranial therapy. Med Phys 37:2934–2942
Hynynen K, McDannold N, Vykhodtseva N, Jolesz FA (2001) Noninvasive MR imaging-guided focal opening of the blood–brain barrier in rabbits. Radiology 220:640–646
Hynynen K, McDannold N, Sheikov NA, Jolesz FA, Vykhodtseva N (2005) Local and reversible blood–brain barrier disruption by noninvasive focused ultrasound at frequencies suitable for trans-skull sonications. Neuroimage 24:12–20
Jeanmonod D, Magnin M, Morel A, Siegemund M (2001) Surgical control of the human thalamocortical dysrhythmia: I. Central lateral thalamotomy in neurogenic pain. Thalamus Relat Syst 1:71–79
Jeanmonod D, Werner B, Morel A, Michels L, Zadicario E, Schiff G, Martin E (2012) Transcranial magnetic resonance inaging-guided focused ultrasound: noninvasive central lateral thalamotomy for chronic neuropathic pain. Neurosurg Focus 32:1–11
Jenkins CO, White DN (1972) The rise time of intracranial echo pulsations and intracranial pressure. Acta Neurol Scand 48:115–123
Jordao JF, Ayala-Grosso CA, Markham K, Huang Y, Chopra R, McLaurin J, Hynynen K, Aubert I (2010) Antibodies targeted to the brain with image-guided focused ultrasound reduces amyloid-beta plaque load in the TgCRND8 mouse model of Alzheimer's disease. PLoS One 5, e10549
Kaye EA, Chen J, Pauly KB (2011) Rapid MR-ARFI method for focal spot localization during focused ultrasound therapy. Mag Reson Med 65:738–743
Kieran K, Hall TL, Parsons JE, Wolf JS, Fowlkes JB, Cain CA, Roberts WW (2007) Refining histotripsy: defining the parameter space for the creation of nonthermal lesions with high intensity, pulsed focused ultrasound of the in vitro kidney. J Urol 178:672–676
King RL, Brown JR, Newsome WT, Pauly KB (2013) Effective parameters for ultrasound-induced in vivo neurostimulation. Ultrasound Med Biol 39:312–331
Krasovitski B, Frenkel V, Shoham S, Kimmel E (2011) Intramembrane cavitation as a unifying mechanism for ultrasound-induced bioeffects. Proc Natl Acad Sci U S A 108:3258–3263
Larrat B, Pernot M, Montaldo G, Fink M, Tanter M (2010) MR-guided adaptive focusing of ultrasound. IEEE Trans Ultrason Ferroelectr Freq Control 57: 1734–1747
Legon W, Sato TF, Opitz A, Mueller J, Barbour A, Williams A, Tyler WJ (2014) Transcranial focused ultrasound modulates the activity of primary somatosensory cortex in humans. Nat Neurosci 17:322–329
Leighton T (1994) The acoustic bubble. Academic, London
Lipsman N, Schwartz ML, Huang Y, Lee L, Sankar T, Chapman M, Hynynen K, Lozano AM (2013) MR-guided focused ultrasound thalamotomy for essential tremor: a proof-of-concept study. Lancet Neurol 12:462–468
Liu HL, Hua MY, Chen PY, Chu PC, Pan CH, Yang HW, Huang CY, Wang JJ, Yen TC, Wei KC (2010) Blood–brain barrier disruption with focused ultrasound enhances delivery of chemotherapeutic drugs for glioblastoma treatment. Radiology 255:415–425
Marquet F, Pernot M, Aubry JF, Montaldo G, Tanter M, Fink M (2006) Non-invasive transcranial ultrasound therapy guided by CT-scans. Conf Proc IEEE Eng Med Biol Soc 1:683–687
Marquet F, Boch AL, Pernot M, Montaldo G, Seilhean D, Fink M, Tanter M, Aubry JF (2013) Non-invasive ultrasonic surgery of the brain in non-human primates. J Acoust Soc Am 134:1632–1639
Marsac L, Chauvet D, Larrat B, Pernot M, Robert B, Fink M, Boch AL, Aubry JF, Tanter M (2012) MR-guided adaptive focusing of therapeutic ultrasound beams in the human head. Med Phys 39:1141
Martin E, Jeanmonod D, Morel A, Zadicario E, Werner B (2009) High-intensity focused ultrasound for noninvasive functional neurosurgery. Ann Neurol 66:858–861
Marty B, Larrat B, Van Landeghern M, Robic C, Robert P, Port M, Le Bihan D, Pernot M, Tanter M, Lethimonnier F, Meriaux S (2012) Dynamic study of blood–brain barrier closure after its disruption using ultrasound: a quantitative analysis. J Cereb Blood Flow Metab 32: 1948–1958
Monteith S, Sheehan J, Medel R, Wintermark M, Eames M, Snell J, Kassell NF, Elias WJ (2013a) Potential intracranial applications of magnetic resonance–guided focused ultrasound surgery: a review. J Neurosurg 118: 215–221
Monteith SJ, Harnof S, Medel R, Popp B, Wintermark M, Lopes MBS, Kassell NF, Elias WJ, Snell J, Eames M (2013b) Minimally invasive treatment of intracerebral hemorrhage with magnetic resonance–guided focused ultrasound: laboratory investigation. J Neurosurg 118: 1035–1045
Moser D, Zadicario E, Schiff G, Jeanmonod D (2012) Measurement of targeting accuracy in focused ultrasound functional neurosurgery: technical note. Neurosurg Focus 32, E2
Nitsche MA, Cohen LG, Wassermann EM, Priori A, Lang N, Antal A, Paulus W, Hummel F, Boggio PS, Fregni F (2008) Transcranial direct current stimulation: state of the art 2008. Brain Stimul 1:206–223
O'Reilly MA, Hynynen K (2012) Blood–brain barrier: real-time feedback-controlled focused ultrasound disruption by using an acoustic emissions-based controller. Radiology 263:96–106

O'Reilly MA, Waspe AC, Ganguly M, Hynynen K (2011) Focused-ultrasound disruption of the blood–brain barrier using closely-timed short pulses: influence of sonication parameters and injection rate. Ultrasound Med Biol 37:587–594

Pernot M, Aubry JF, Tanter M, Thomas J, Fink M (2003) High power transcranial beam steering for ultrasonic brain therapy. Phys Med Biol 48:2577–2589

Pernot M, Aubry JF, Tanter M, Boch AL, Kujas M and Fink M (2004) Ultrasonic transcranial brain therapy: First in vivo clinical investigation on 22 sheep using adaptive focusing. 2004 IEEE Ultrasonics Symposium, Vol 1–3. M. P. Yuhas, pp 1013–1016

Pernot M, Aubry JF, Tanter M, Boch AL, Marquet F, Kujas M, Seilhean D, Fink M (2007) In vivo transcranial brain surgery with an ultrasonic time reversal mirror. J Neurosurg 106:1061–1066

Phillips DJ, Smith SW, von Ramm OT and Thurstone FL (1975) Sampled aperture techniques applied to B-Mode echoencephalography. Acoustical Holography. N. Booth, Springer US, pp 103–120

Pinton GF, Aubry JF, Fink M and Tanter M (2010) Numerical prediction of frequency dependent 3D maps of mechanical index thresholds in ultrasonic brain therapy. Ultrasonics Symposium (IUS), 2010 IEEE

Pinton G, Aubry JF, Bossy E, Muller M, Pernot M, Tanter M (2012a) Attenuation, scattering, and absorption of ultrasound in the skull bone. Med Phys 39:299–307

Pinton G, Aubry JF, Fink M, Tanter M (2012b) Numerical prediction of frequency dependent 3D maps of mechanical index thresholds in ultrasonic brain therapy. Med Phys 39:455–467

Plaksin M, Shoham S, Kimmel E (2014) Intramembrane cavitation as a predictive Bio-piezoelectric mechanism for ultrasonic brain stimulation. Phys Rev X 4:011004

Pulkkinen A, Huang Y, Song J, Hynynen K (2011) Simulations and measurements of transcranial low-frequency ultrasound therapy: skull-base heating and effective area of treatment. Phys Med Biol 56:4661

Raymond SB, Treat LH, Dewey JD, McDannold NJ, Hynynen K, Bacskai BJ (2008) Ultrasound enhanced delivery of molecular imaging and therapeutic agents in Alzheimer's disease mouse models. PLoS One 3, e2175

Ressler KJ, Mayberg HS (2007) Targeting abnormal neural circuits in mood and anxiety disorders: from the laboratory to the clinic. Nature Neuroscience 10: 1116–1124

Sheikov N, McDannold N, Sharma S, Hynynen K (2008) Effect of focused ultrasound applied with an ultrasound contrast agent on the tight junctional integrity of the brain microvascular endothelium. Ultrasound Med Biol 34:1093–1104

Sun J, Hynynen K (1998) Focusing of therapeutic ultrasound through a human skull: a numerical study. J Acoust Soc Am 104:1705–1715

Szobota S, Gorostiza P, Del Bene F, Wyart C, Fortin DL, Kolstad KD, Tulyathan O, Volgraf M, Numano R, Aaron HL (2007) Remote control of neuronal activity with a light-gated glutamate receptor. Neuron 54: 535–545

Tanter M, Thomas JL and Fink M (1996) Focusing through skull with time reversal mirrors. Application to hyperthermia. 1996 IEEE Ultrasonics Symposium, Proceedings, Vols 1 and 2. Levy M, Schneider SC and McAvoy BR, pp 1289–1293

Tanter M, Thomas JL, Fink M (1998) Focusing and steering through absorbing and aberrating layers: application to ultrasonic propagation through the skull. J Acoust Soc Am 103:2403–2410

Tanter M, Thomas JL, Fink M (2000) Time reversal and the inverse filter. J Acoust Soc Am 108:223–234

Tanter M, Aubry JF, Gerber J, Thomas JL, Fink M (2001) Optimal focusing by spatio-temporal inverse filter I. Basic principles. J Acoust Soc Am 110:37–47

Tanter M, Pernot M, Aubry JF, Montaldo G, Marquet F, Fink M (2007) Compensating for bone interfaces and respiratory motion in high-intensity focused ultrasound. Int J Hyperthermia 23:141–151

Tasker RR (1998) Deep brain stimulation is preferable to thalamotomy for tremor suppression. Surg Neurol 49:145–153; discussion 153–144

Thomas JL, Fink MA (1996) Ultrasonic beam focusing through tissue inhomogeneities with a time reversal mirror: application to transskull therapy. IEEE Trans Ultrason Ferroelectr Freq Contr 43:1122–1129

Treat LH, McDannold N, Vykhodtseva N, Zhang Y, Tam K, Hynynen K (2007) Targeted delivery of doxorubicin to the rat brain at therapeutic levels using MRI-guided focused ultrasound. Int J Cancer 121:901–907

Tufail Y, Matyushov A, Baldwin N, Tauchmann ML, Georges J, Yoshihiro A, Sih T, Tyler WJ (2010) Transcranial pulsed ultrasound stimulates intact brain circuits. Neuron 66:681–694

Tyler WJ, Tufail Y, Finsterwald M, Tauchmann ML, Olson EJ, Majestic C (2008) Remote excitation of neuronal circuits using low-intensity, low-frequency ultrasound. PLoS One 3, e3511

Vignon F, Aubry JF, Tanter M, Margourn A, Fink M (2006) Adaptive focusing for transcranial ultrasound imaging using dual arrays. J Acoust Soc Am 120: 2737–2745

Vlachos F, Tung YS, Konofagou EE (2010) Permeability assessment of the focused ultrasound-induced blood–brain barrier opening using dynamic contrast-enhanced MRI. Phys Med Biol 55:5451–5466

Vlachos F, Tung YS, Konofagou E (2011) Permeability dependence study of the focused ultrasound-induced blood–brain barrier opening at distinct pressures and microbubble diameters using DCE-MRI. Mag Reson Med 66:821–830

White DN, Hanna LF (1974) Automatic midline echoencephalography. Examination of 3,333 consecutive cases with the automatic midline computer. Neurology 24:80–93

White DN, Clark JM, Chesebrough JN, White MN, Campbell JK (1968) Effect of the skull in degrading

the display of echoencephalographic B and C scans. J Acoust Soc Am 44:1339–1345

Xu Z, Owens G, Gordon D, Cain C, Ludomirsky A (2010) Noninvasive creation of an atrial septal defect by histotripsy in a canine model. Circulation 121:742–749

Xu Z, Carlson C, Beckelman B, Snell J, Eames M, Hanael A, Lopes B, Raghavan P, Lee CC, Yen CP, Schlesinger D, Aubry JF, Sheehan J (2014) Intracranial inertial cavitation threshold and thermal ablation lesion creation using magnetic resonance imaging-guided 220 kHz focused ultrasound surgery. J Neurosurg 7: 1–10

Yang PS, Kim H, Lee W, Bohlke M, Park S, Maher TJ, Yoo SS (2012) Transcranial focused ultrasound to the thalamus is associated with reduced extracellular GABA levels in rats. Neuropsychobiology 65: 153–160

Yoo SS, Bystritsky A, Lee JH, Zhang Y, Fischer K, Min BK, McDannold NJ, Pascual-Leone A, Jolesz FA (2011) Focused ultrasound modulates region-specific brain activity. Neuroimage 56:1267–1275

Younan Y, Deffieux T, Larrat B, Fink M, Tanter M, Aubry JF (2013) Influence of the pressure field distribution in transcranial ultrasonic neurostimulation. Med Phys 40:082902

Zhang F, Aravanis AM, Adamantidis A, de Lecea L, Deisseroth K (2007) Circuit-breakers: optical technologies for probing neural signals and systems. Nat Rev Neurosci 8:577–581

Zhang S, Ding T, Wan M, Jiang H, Yang X, Zhong H, Wang S (2011) Minimizing the thermal losses from perfusion during focused ultrasound exposures with flowing microbubbles. J Acoust Soc Am 129: 2336–2344

Focused Ultrasound and Lithotripsy

7

Teiichiro Ikeda, Shin Yoshizawa, Norihiro Koizumi, Mamoru Mitsuishi, and Yoichiro Matsumoto

Abstract

Shock wave lithotripsy has generally been a first choice for kidney stone removal. The shock wave lithotripter uses an order of microsecond pulse durations and up to a 100 MPa pressure spike triggered at approximately 0.5–2 Hz to fragment kidney stones through mechanical mechanisms. One important mechanism is cavitation. We proposed an alternative type of lithotripsy method that maximizes cavitation activity to disintegrate kidney stones using high-intensity focused ultrasound (HIFU). Here we outline the method according to the previously published literature (Matsumoto et al., Dynamics of bubble cloud in focused ultrasound. Proceedings of the second international symposium on therapeutic ultrasound, pp 290–299, 2002; Ikeda et al., Ultrasound Med Biol 32:1383–1397, 2006; Yoshizawa et al., Med Biol Eng Comput 47:851–860, 2009; Koizumi et al., A control framework for the non-invasive ultrasound the ragnostic system. Proceedings of 2009 IEEE/RSJ International Conference on Intelligent Robotics and Systems (IROS), pp 4511–4516, 2009; Koizumi et al., IEEE Trans Robot 25:522–538, 2009). Cavitation activity is highly unpredictable; thus, a precise control system is needed. The proposed method comprises three steps of control in kidney stone treatment. The first step is control of localized high pressure fluctuation on the stone. The second step is monitoring of cavitation activity and giving feedback on the optimized ultrasound conditions. The third step is stone tracking and precise ultrasound focusing on the stone. For the high pressure control we designed a two-frequency wave (cavitation control (C-C)

T. Ikeda
Central Research Laboratory, Hitachi Ltd., Tokyo, Japan

S. Yoshizawa
Department of Communications Engineering, Tohoku University, Sendai, Miyagi, Japan

N. Koizumi • M. Mitsuishi • Y. Matsumoto (✉)
Department of Mechanical Engineering, The University of Tokyo, Tokyo, Japan
e-mail: ymats@fel.t.u-tokyo.ac.jp

© Springer International Publishing Switzerland 2016
J.-M. Escoffre, A. Bouakaz (eds.), *Therapeutic Ultrasound*, Advances in Experimental Medicine and Biology, Vol. 880, DOI 10.1007/978-3-319-22536-4_7

waveform); a high frequency ultrasound pulse (1–4 MHz) to create a cavitation cloud, and a low frequency trailing pulse (0.5 MHz) following the high frequency pulse to force the cloud into collapse. High speed photography showed cavitation collapse on a kidney stone and shock wave emission from the cloud. We also conducted *in-vitro* erosion tests of model and natural kidney stones. For the model stones, the erosion rate of the C-C waveform showed a distinct advantage with the combined high and low frequency waves over either wave alone. For optimization of the high frequency ultrasound intensity, we investigated the relationship between subharmonic emission from cavitation bubbles and stone erosion volume. For stone tracking we have also developed a non-invasive ultrasound theragnostic system (NIUTS) that compensates for kidney motion. Natural stones were eroded and most of the resulting fragments were less than 1 mm in diameter. The small fragments were small enough to pass through the urethra. The results demonstrate that, with the precise control of cavitation activity, focused ultrasound has the potential to be used to develop a less invasive and more controllable lithotripsy system.

Keywords
Lithotripsy • Focused Ultrasound

7.1 Introduction

Shock wave lithotripsy (SWL) uses an order of microsecond pulse durations and up to a 100 MPa pressure spike triggered at about 0.5–2 Hz to fragment kidney stones through mechanical mechanisms, as shown in Fig. 7.1. One important mechanism is cavitation (Coleman et al. 1987; Crum 1988). Other mechanisms, such as spallation (Chaussy et al. 1980), shear stress (Gracewski et al. 1993) and squeezing (Eisenmenger 2001; Eisenmenger et al. 2002) are also important. A number of studies suggest the importance of cavitation collapse in SWL (Church 1989; Carnel et al. 1993; Philip et al. 1993; Bailey 1997; Cathignol et al. 1998; Sapozhnikov et al. 2002; Pishchalnikov et al. 2003), and cavitation control has been attempted. The goal has been to accelerate comminution while minimizing tissue damage (Zhong et al. 1997; Williams et al. 1999; Bailey et al. 1999; Zhu et al. 2002; Evan et al. 2002). Research has included modifying the shock waveform and the timing between shock waves to control the expansion and collapse of cavitation bubbles (Cleveland et al. 2000a, b; Xi and Zhong 2000; Loske et al. 2002; Sokolov et al. 2001, 2003). Xi and Zhong (2000) attempted to enhance cavitation bubble collapse with two different shock wave generators and observed accelerated stone fragmentation com-

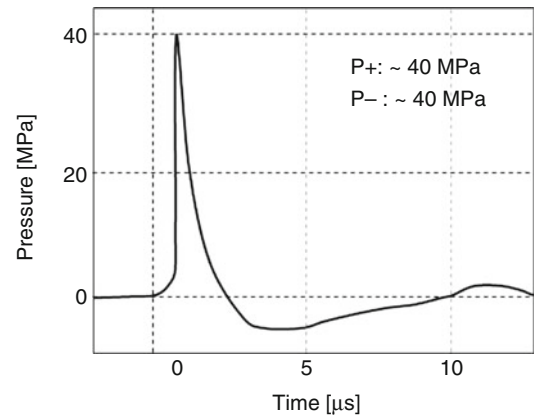

Fig. 7.1 Schematic of a typical shock wave pulse used in SWL. High pressure, which exceeds 40 MPa, is followed by a long tail of negative pressure. The repeated positive and negative pressure yields dynamic stress in the stone. The negative pressure also produces cavitation on the propagating path. Both the shock wave stress and collapse pressure of the cavitation bubble are important mechanisms of stone disintegration

pared to that from a standard forcing scheme. Sokolov et al. (2001, 2003) investigated a dual-pulse lithotripter to localize the cavitation area near the stone and effectively reduced cell lysis and observed accelerated fragmentation. Duryea et al. (2011, 2013) used extremely high-intensity ultrasound pulse (histotripsy pulse) for stone comminution. Maxwell et al. (2015) investigated the characteristics of stone comminution using the burst waves of focused ultrasound.

In this chapter, high-intensity focused ultrasound (HIFU), which has a higher frequency (>500 kHz) than a lithotripsy shock wave, is used to erode kidney stones. Specifically, a tone burst of one frequency is used to generate a cloud cavitation (bubble cloud) at the surface of a kidney stone. A second lower frequency wave is used to collapse the cloud and this erodes the stone (cavitation control (C-C) waveform). We investigated the development and optimization of focused ultrasound lithotripsy using the C-C waveform (Matsumoto et al. 2002; Ikeda et al. 2006; Yoshizawa et al. 2009). Different from a lithotripter shock wave, focused ultrasound has a smaller focal volume. As the cavitation phenomenon is highly unpredictable and destructive, a fine control system is needed. We propose a control method composed of three steps for kidney stone treatment. The first step is control of localized high pressure on the stone. The second step is monitoring of cavitation activity and feedback on the optimized ultrasound conditions (Yoshizawa et al. 2009). The third step is stone tracking and precise ultrasound focusing on the stone, which is altered in accordance with respiration (Koizumi et al. 2009a, b). The three control steps are outlined, and the feasibility of a focused ultrasound lithotripter is discussed in this chapter.

7.2 Localized High Pressure on Kidney Stones

7.2.1 Cavitation Control Waveform (C-C waveform)

The two-frequency ultrasound wave of the C-C waveform used in this study is shown in Fig. 7.2. The acoustic pressure is recorded using a membrane hydrophone (MHB200B, NTR systems, Seattle, WA, United States) placed at the focus of a concave lead zirconium titanate (PZT) transducer.

First, the high frequency ultrasound wave (3.82 MHz, 175 cycles in this case) is transmitted. Immediately after the high frequency wave is stopped, a short pulse of a low-frequency wave (545 kHz, 6 cycles) follows. For the high frequency wave in Fig. 7.2, the focal pressure is the maximum positive pressure $|P+| = 10.0$ MPa, and the maximum negative pressure $|P-| = 6.0$ MPa. For the low frequency part; $|P+| = 16.0$ MPa and $|P-| = 6.5$ MPa. High frequency ultrasound is designed to produce a localized cavitation bubble cloud on a stone, and low frequency ultrasound triggers the bubble cloud into violent collapse.

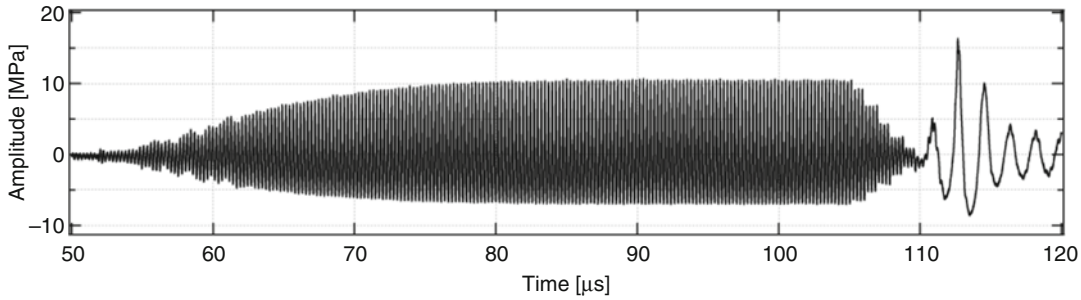

Fig. 7.2 Acoustic pressure of typical cavitation control (C-C) waveform**.** Ultrasound acoustic pressure was measured with a membrane hydrophone located at the focal point. The ultrasound wave is a high frequency one (3.82 MHz, 175 cycles (46 μs)), and a low frequency (545 kHz pulse (6 cycles)) ultrasound follows immediately after the high frequency wave has stopped

Cloud cavitation is a densely populated cluster of cavitation bubbles that has lost the characteristics of individual bubble behavior and the global behavior as a cluster increases. Bubbles are dynamically coupled through fluid motion and acoustic wave propagation inside the cloud (d'Agostino and Brennen 1988, 1989). Cloud collapse has been shown to be more destructive to high speed turbo-pumps and ship propellers than the collapse of individual bubbles. Numerous experimental studies (Knapp 1955; Soyama et al. 1992; Kato et al. 1996; Reisman and Brennen 1996; Reisman et al. 1998; Konno et al. 2002) and analytical/numerical studies (van Wijngaarden 1964; Mørch 1981; Omta 1987; Chahine and Duraiswami 1992; d'Agostino and Brennen 1988, 1989; Wang and Brennen 1995, 1999) have been conducted to investigate the dynamics of cloud collapse and to calculate the pressure generated in a cloud. The indirect experimental measurements of the maximum pressure inside a cloud of up to $O(10^8 \sim 10^9)$ Pa have been reported (Kato et al. 1996; Reisman et al. 1998). Shimada et al. (2000) used a numerical model for a spherical bubble cloud considering the individual oscillating bubbles to investigate the converging shock wave within the cloud. They argued that the shock wave convergence inside the cloud led to a center bubble collapse pressure of $O(10^9)$ Pa, when a bubble cloud with bubbles of radius 20 μm and a cloud radius of 5 mm was subjected to stepwise pressure decrease and increase. Their work has been extended for initial and boundary conditions appropriate for focused ultrasound applications (Yoshizawa et al. 2004; Matsumoto and Yoshizawa 2005), although the model was restricted to lower ultrasound pressure amplitudes than those used clinically. They investigated the behavior of spherical cloud cavitation with uniform bubble size and distribution excited using medical ultrasound. They also showed that a violent cavitation cloud collapse occurs with a frequency range much less than the resonance frequency of the individual bubbles inside the cloud, with a collapse pressure up to 1000 times the ultrasound pressure amplitude, which forces the cloud into strong collapse. They also showed a broadening of the resonance bandwidth when the cloud was subjected to relatively large pressure amplitude. Their results provide the basis for our method for eroding kidney stones. A one-frequency wave is used to generate a cloud of bubbles, and then a lower frequency wave excites the cloud at its broad resonance to create high collapse pressure. Due to the broad resonances of the cloud, the low and high frequencies do not need to be precisely fixed.

7.2.2 Observation of Cavitation on Stones

The cavitation phenomenon at the focus of the focused ultrasound is recorded with a high speed image converter camera, Imacon 200 (DRS Hadland; at present, DRS Data & Imaging Systems, Oakland, NJ, USA). The Imacon 200 can take 8 photographs at a rate of up to 200 million frames/s, with a 5 ns minimum exposure. This is suitable for observing cavitation in the frequency bandwidth of the experiment (0.5–4 MHz), as this corresponds to a comparably shorter exposure time than the ultrasound cycle (250 ns–2 μs) and a faster frequency than ultrasound. Interframe and exposure time are varied by the software control, and the double shutter mode of Imacon 200 can obtain 16 frames with time intervals between frames of greater than 300 μs. An air-backed ultrasound transducer with a concave PZT ceramic element (C-213, Fuji Ceramics, Japan) was fixed in an acrylic water tank. Both the aperture and focal length of the PZT element were 80 mm.

7.2.2.1 High Frequency

Acoustic cloud cavitation in the focus of the focused ultrasound is visualized for the different ultrasound frequencies of 1.08, 1.64, 2.75, 3.27 and 3.82 MHz, after 100–200 μs irradiation. Figure 7.3a–d show the bubble clouds made from four of the five different ultrasound frequencies at the focal point.

After 100–200 μs of ultrasound irradiation, the hemispherical bubble clouds maintained their shape and size. Figure 7.3e shows the measured characteristic lengths of the bubble clouds for different frequencies. This length is the maximum

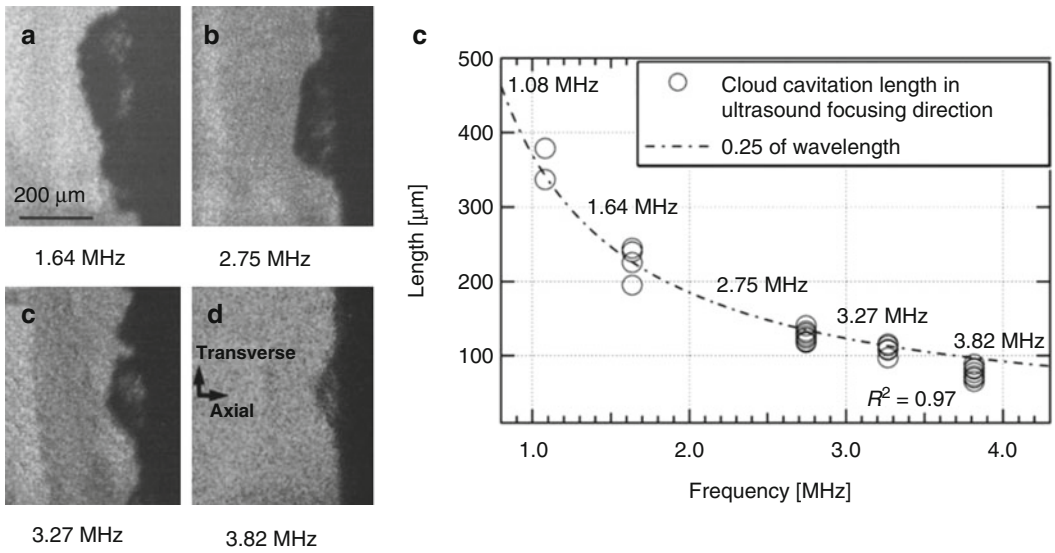

Fig. 7.3 Frequency dependence of cloud cavitation. (**a**–**d**) Cloud cavitation exhibits constant shape and size for different ultrasound frequencies. Ultrasound irradiation duration is from 100 to 200 µs. (**e**) Characteristic length of cloud cavitation: For different frequencies, the length of the acoustic cloud cavitation generated at the surface of the aluminium ball was measured. In every case, the ultrasound irradiation duration was 100–200 µs and the length was measured in the axial direction (parallel to the ultrasound focusing direction). The cloud cavitation length showed strong relationship with 1/4λ the ultrasound wavelength ($R^2 = 0.97$)

length of the cloud cavitation in the axial direction of focused ultrasound, *i.e.,* the horizontal direction in Fig. 7.3a–d. The length of the cloud approximately fits one-quarter of the ultrasound wavelength. The determination coefficient R^2 is 0.97. This is consistent with the distance from the antinode (at the solid surface) to the node of the standing wave created by the incident and reflected ultrasound wave. These results demonstrate that the size of the bubble cloud generated by the focused ultrasound can be controlled with respect to the ultrasound frequency. The cavitation region is within 1 mm (axial direction) when the ultrasound frequency is higher than 1 MHz. Hence, in the focused ultrasound field, the acoustic cavitation at the solid surface can be controlled in space by altering the ultrasound frequency.

7.2.2.2 Low Frequency

The forced collapse of the bubble cloud and the shock wave emission from the cloud were also photographed. The bubble clouds, which were generated using higher frequency focused ultrasound (2.75 and 3.82 MHz, shown in Fig. 7.3), were forced to oscillate due to low frequency ultrasound (545 kHz).

Figure 7.4 shows photographs of the bubble cloud forced into oscillation. Immediately after the 100 µs irradiation of the 2.75 MHz ultrasound was stopped, the 545 kHz pulse ultrasound was focused on the cloud. The interframe and exposure times for the photograph were 325 and 50 ns. In Fig. 7.4, the first to the fifth frames correspond to one cycle of the 545 kHz ultrasound, and the sixth to the tenth frames correspond to the next cycle. In the first frame in Fig. 7.4, a hemispherical cloud cavitation was observed on the solid surface. The cloud was forced to oscillate due to the 545 kHz ultrasound. The bubble cloud shrank during the positive phase of the 545 kHz ultrasound and was forced to collapse, as shown in the fourth frame. In the fifth frame, the bubbles rebounded, and the next collapse occurred at the eighth frame. During the photographic sequence, the boundary of the cloud (the border between the water and the two-phase medium) did not significantly change its position, whereas the image density of bubbles in the bubble cloud drastically changed.

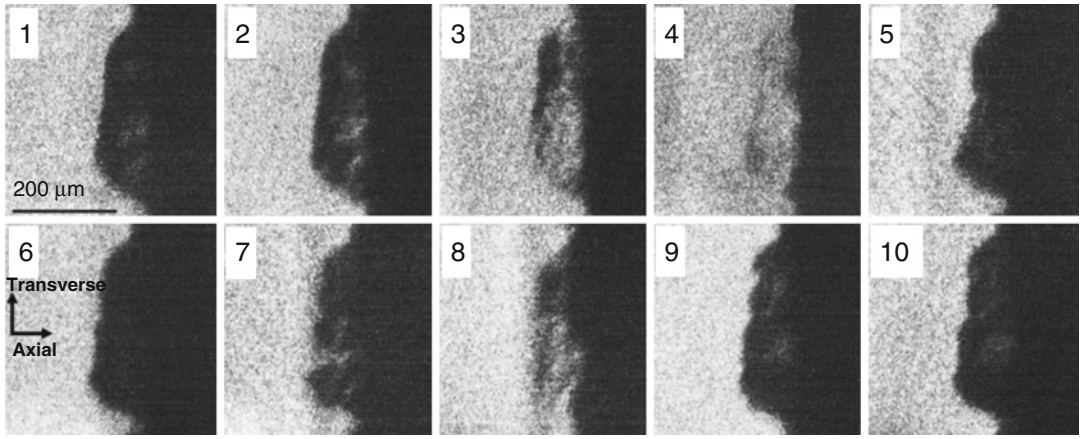

Fig. 7.4 Forced collapse of cloud cavitation: Hemispherical cloud cavitation generated due to 2.75 MHz focused ultrasound (shown in Fig. 7.3) forced into collapse by 545 kHz ultrasound. The camera interframe time was 325 ns with an exposure of 50 ns. During the first frame, the low frequency ultrasound's second positive phase started. During the fourth frame, the bubble cloud collapsed with each bubble radii decreasing in size. At that time, high pressure was hypothesized to be localized at the solid surface. The bubbles rebounded during the fifth frame, and the next collapse occurred during the eighth frame

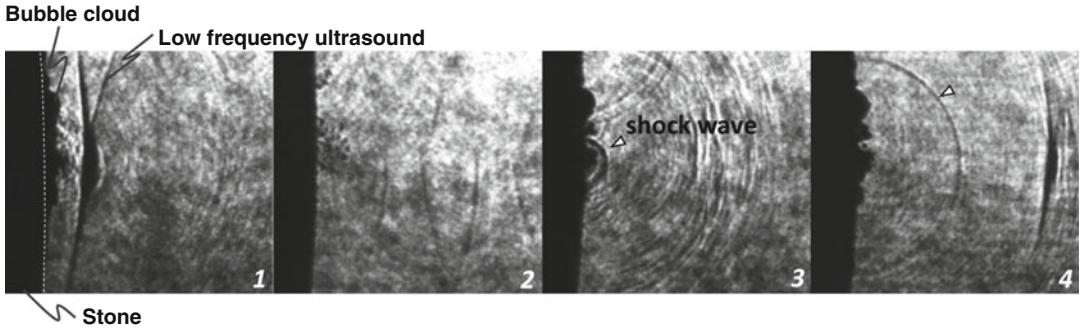

Fig. 7.5 Shock wave emission from cloud cavitation**.** Forcing ultrasound in C-C waveform (Fig. 7.2, high frequency 3.82 MHz, low frequency 545 kHz). The camera interframe time was 105 ns with an exposure of 5 ns. The photograph time corresponds to the low frequency wave immediately focused after the high frequency was stopped. Shortly after the second positive phase of the 545 kHz ultrasound hit the cloud cavitation (first frame), the bubble cloud collapsed in the second frame, then a spherical shock wave propagated outwards from the cloud cavitation (third and fourth frames)

The phenomena exhibited in Fig. 7.4 shows the resonance phenomena as the cloud underwent oscillation. Every bubble in the cloud collapsed at approximately the same time. In the fourth frame of Fig. 7.4, it is thought that the bubbles close to the solid surface, *i.e.,* near the center of the hemispherical bubble cloud, violently collapsed, such that a very high pressure might have occurred at the aluminum ball surface. The boundary of the cloud (interface of bubble flow and water) maintained its position, but the individual bubbles collapsed, decreasing in their respective sizes. Likewise, this result also suggests that the cloud cavitation collapse in Fig. 7.4 is related to the wave propagation of the low frequency part through the bubble flow, rather than the volumetric oscillation of the cloud cavitation region, such that the boundary of the cloud behaved like a wall of single bubbles (collapse of a bubble cloud similar to that reported previously, Pishchalnikov et al. 2003). This cloud cavitation collapsing phenomena occurred almost at the same frame for each test run, indicating the high reproducibility of the phenomena.

Figure 7.5 shows a shadowgraph photograph of the bubble collapse. The shock wave emitted

from cloud cavitation (produced by the C-C waveform) is visualized. The high frequency (3.82 MHz, 175 cycles) wave was immediately followed by the 545 kHz ultrasound. In the first frame of Fig. 7.5, low-frequency ultrasound just reached the bubble clouds on the kidney stone. In the second frame, upon the low frequency hit on the bubbles, the bubbles were simultaneously forced into collapse. The sizes of the bubble in the images are very small (almost disappeared). In the third frame, a strong shock wave shadow, with a high contrast to background, was emitted from the cloud cavitation. In the fourth frame, hemispherical shock wave propagated out of the imaging area. This shock wave emission was photographed in the same frame for different test runs, again demonstrating the reproducibility of the phenomena. These results suggest that the C-C waveform successfully localizes the cavitation bubbles on the stone and controls the high collapse pressure of cloud cavitation acting on the stone surface.

7.2.3 Stone Fragmentation

Stone-erosion tests were conducted to investigate the applicability and efficiency of C-C waveform for lithotripsy applications. The erosion rate was also determined to investigate the efficiency of cavitation erosion in stone disintegration. The model stones are the test materials that were previously developed for research with commercial SWL machines. The U-30 stones were supplied by McAteer et al. (2005). These stones were cylindrical and longer (6.4 ~ 10.1 mm) than the wavelength of ultrasound (0.38 ~ 3.0 mm), and a -6 dB beam width of the focused ultrasound (0.6 ~ 4.0 mm). It took 72 h to completely rehydrate the U-30 stones in the atmospheric pressure (McAteer et al. 2005). Since the trapped gas inside the stone potentially affects the amount of erosion and distorts the acoustic profile, every stone was dipped in a desiccator filled with degassed water maintained at 10 kPa. They were left to stand for more than 48 h until there were no observable gas bubbles rising from the stone surfaces.

The acoustic waves for the stone-erosion tests were designed to demonstrate the advantage of the C-C waveform, which has combined high and low frequency waves. The C-C waveform was compared with waves with only a high or low frequency wave. The test waves for stone erosion were as follows: (a) High frequency alone (3.82 MHz, 175 μs), (b) low frequency alone (545 kHz, 6 cycles), and (c) high frequency and low frequency combined (C-C waveform). The ultrasound wave of the C-C waveform is shown in Fig. 7.2, and was also used in the experiment shown in Fig. 7.5.

In each case, the pulse repetition frequency (PRF) of the waves transmitted from the PZT transducer was fixed at 25 Hz, such that a 39.94 ms interval elapsed before the next pulse of the C-C waveform (c) (39.95 ms for (a) and 39.99 ms for (b)).

The upper graphs in Fig. 7.6 show the measured weight losses of the U-30 stones for each wave. The ultrasound irradiation time was 3, 6, 12, 18 min. Two samples were tested for each wave and irradiation time. The lower photographs correspond to the eroded model stones for each ultrasound irradiation time for the C-C waveform. In this experiment, each stone was moved in an attempt to achieve erosion over the entire stone surface. Two operators moved the stones while monitoring them with a microscope equipped with an ocular ruler with 0.1 mm resolution. In the transverse direction, the operators moved the stone so that the focus entirely covered the whole area of the stone's base circle. The round trip of diameter scanning was maintained at 4 s. In the axial direction, the stones were also moved as the ultrasound focus was maintained on the base circle. This stone-erosion test protocol was applied for every sample (48 samples). The erosion rate was calculated using the least square fit of linear regression between the weight loss and ultrasound irradiation time. The calculated erosion speeds of the C-C waveform, low frequency alone and high frequency alone were 0.3, 2.2 and 5.0 mg/min, respectively. The determination coefficient R^2 between the weight loss and ultrasound irradiation time was 0.66, 0.91 and 0.99, respectively.

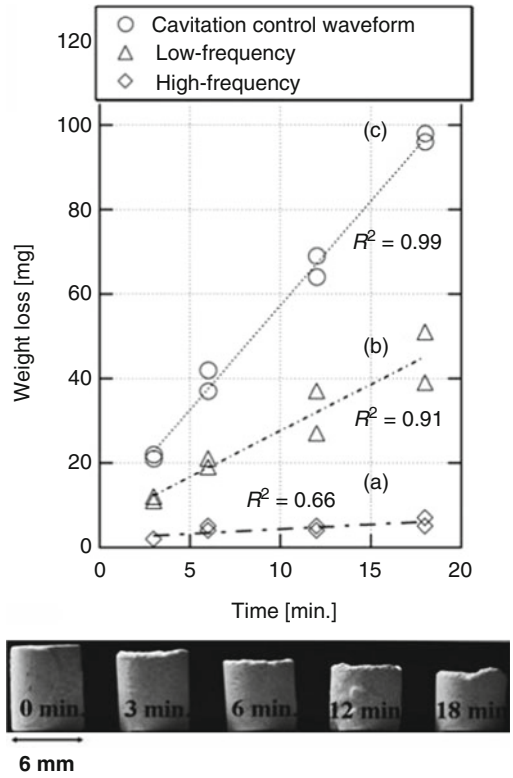

Fig. 7.6 Erosion rate measurement using U-30 model stones**.** The weight losses for different times were measured for different waves; (*a*) high frequency wave (3.82 MHz) alone, (*b*) low frequency wave (545 kHz) alone, and (*c*) C-C waveform. The PRF of each ultrasound wave was 25 Hz. The *lines* in the *upper figures* are the results of the least square fit of linear regression between the weight loss and ultrasound irradiation time (R^2 is also shown). The *lower photographs* correspond to the eroded model stones for each ultrasound irradiation time for the C-C waveform

As shown in Fig. 7.6, the C-C waveform eroded the stones more efficiently compared with the high frequency alone and low frequency alone waves. The calculated erosion rate reveals that the erosion rate of the C-C waveform (c) is double the rate of the sum of the high frequency alone (a) and low frequency alone (b). The high frequency causes localized cloud cavitation on the stone surface, but the amount of erosion is small, possibly because the cloud cavitation shields the stone surface. The low frequency wave alone creates a wider region of cavitation bubbles, so the eroded region is wider than the high frequency alone case. These bubbles collapse independently, such that the maximum pressure is not as high in comparison to the collapse of the cloud cavitation. The C-C waveform, with the high and low frequency in combination, forces the bubble cloud into a violent collapse, and the C-C waveform's advantage might be a result from the controlled cloud cavitation collapse on the stone surface.

Ultrasound irradiation of the C-C waveform was applied to two types of natural kidney stones: Cystine and staghorn. The ultrasound wave was the same as that in Fig. 7.2, and the PRF of the cycle was 25 Hz. The upper photographs in Fig. 7.7 are of the eroded stones and their fragments, (a) cystine stone and (b) staghorn stone.

Erosion holes can be seen in both. The lower figures are the size-frequency of the number-size distribution of the fragment diameter D_p for (a) cystine stone and (b) staghorn stone. The D_p was calculated from the binary processed image of photographed stone fragments. From the area and peripheral length of the fragments, the D_p was calculated for each particle. For the cystine stone, the mean diameter was 0.13 ± 0.070 mm for 756 fragments, and 0.187 ± 0.120 mm for 1393 fragments of the staghorn stone. Every cystine stone particle was less than 0.8 mm. Almost all the staghorn fragments were less than 1.0 mm, although three fragments of $D_p = 1.2$ mm, and one particle of $D_p = 1.5$ mm, were observed. The size distribution for each stone had slightly different characteristics. The staghorn stone fragments had a typical size-frequency distribution of fragments, with a long tail for increasing fragment size. The cystine stone's distribution also had a long tail for the larger fragment sizes, whereas the small fragments did not have a local maximum. This is possibly due to the fact that very small fragments could not be completely collected due to water convection in the tank, so they did not all fall into the beaker placed just beneath the stone.

Almost all the eroded fragments were less than $D_p = 1$ mm, except the three fragments of $D_p = 1.2$–1.5 mm for the staghorn stone. These results show one of the main advantages of using cavitation erosion. Using cavitation erosion, fragmentation is expected to result in small stone

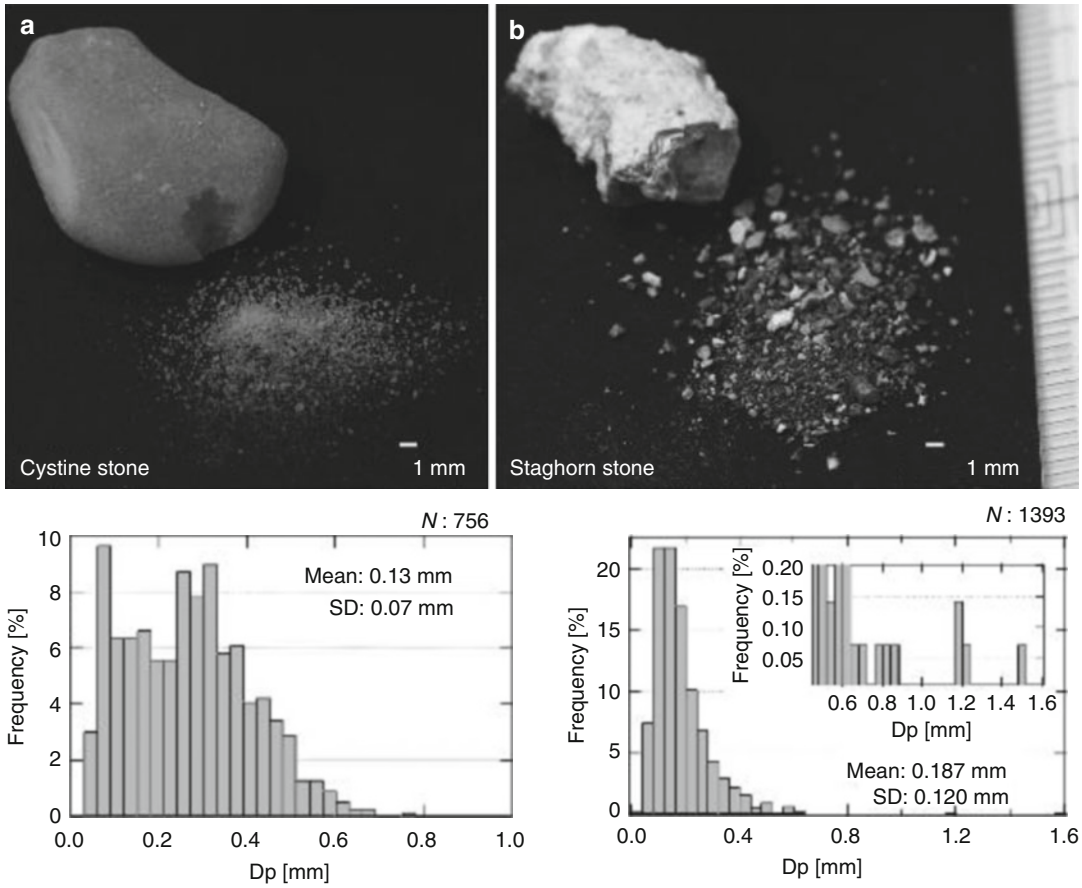

Fig. 7.7 Natural kidney stones and their fragments after irradiation by C-C waveform**.** (**a**) Cystine stone and fragments, (**b**) staghorn stone and fragments. *Upper figures* are photographs of each stone and *lower figures* are the size-frequency of the number-size distribution of fragment diameter D_p. The resulting fragments were typically less than 1 mm in diameter. Three fragments of $D_p = 1.2 \sim 1.5$ mm were calculated for the staghorn stone

fragments (1–2 mm) of clinically passable size from the initial stage of treatment. Cystine stones have been reported to be the most difficult to break by SWL. Zhong et al. (1992) argues that cystine stones are non-breakable due to their ductility in spite of their small surface hardness value. Figure 7.7 shows that the cystine stone was eroded by cavitation from the surface into small fragments of less than 1 mm.

Finally, the estimated acoustic power of the C-C waveform is in the range between the intensity of the Power Doppler (15 W/cm^2) and typical HIFU for the treatment of tumors (500–2000 W/cm^2) (ter Haar 2001; Bailey et al. 2001). Although the intensity was small compared with that of HIFU treatment, and there is the large time interval between C-C waveform pulses, the effect of unwanted tissue heating should be examined through *in-vivo* studies.

7.3 Ultrasound Lithotripsy with Cavitation Monitoring

7.3.1 Experimental Setup and Ultrasound Sequence for Subharmonic Detection

In the experiment discussed in Sect. 7.2, the cavitation activity in the C-C waveform sequence was well visualized and seemed to be well controlled *in-vitro* in degassed and distilled water. Whereas

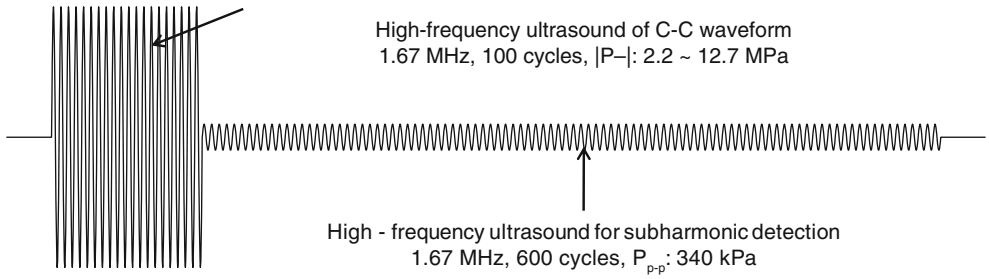

Fig. 7.8 Ultrasound sequence for subharmonic detection. Immediately after 100-cycle (60 μs) exposure to 1.67 MHz ultrasound, much lower intensity ultrasound at the same frequency was used. The subharmonic component of the 1.67 MHz ultrasound was detected during lower intensity ultrasound exposure

in the human body, the cavitation phenomena should be different and unpredictable because the physical property of the medium in which the stone exists is totally different. Thus, specially designed cavitation monitoring is necessary to optimize stone comminution under *in-vivo* conditions.

Passive and active cavitation detection has been investigated through SWL (Coleman et al. 1996; Cleveland et al. 2000a, b; Bailey et al. 2005). In two-frequency ultrasound lithotripsy using the C-C waveform, it is important to detect cavitation generation as stone erosion efficiency by the low frequency ultrasound wave depends on the state of cavitation bubbles induced by the high frequency wave. Cavitation bubbles were generated on a stone in a small region from the high frequency wave, as shown in Fig. 7.3, and acoustic emission intensity from the bubbles during high frequency exposure was much lower than that of the reflected ultrasound from the stone surface. Therefore, a sensitive detection method is required. The subharmonic ultrasound signal is a specific frequency component emitted from highly, nonlinear scatter, such as cavitation bubbles. The subharmonic detection method and the relation between the signal amplitude and stone erosion volume (Yoshizawa et al. 2009) are introduced in this section.

The experimental setup was similar to that discussed in the previous section. An air-backed ultrasound transducer with a concave PZT ceramic element (C-213, Fuji Ceramics, Japan) was fixed in an acrylic water tank. Both the aperture and focal length of the PZT element were 80 mm. The resonance frequency of the transducer was 552 kHz. The resonance frequency was used to generate the low frequency wave of the C-C waveform, and the 3rd harmonics of the transducers, 1.67 MHz, was used to generate the high frequency wave. A function generator (WF1946B, NF Corporation) created the driving signal, which was amplified using a radio-frequency-band amplifier (AG1024, T&C Power Conversion) or a high power pulser receiver (RPR-4000, RITEC Inc.). A model stone was placed at the focus of the ultrasound. The acrylic water tank was filled with degassed and distilled tap water. Continuous filtering through a deionizer activated carbon filtering; a 0.45 μm mesh filter was used. The O_2 concentration was 7 ppm. The temperature of the water was kept at room temperature for every experiment, 19–23 °C. The electroconductivity of the water was kept to less than 5 μS/cm. The focal pressure was measured with a membrane hydrophone (MHB200B, NTR systems) without the solid surface and in the absence of cavitation for the highly degassed (O_2 concentration was less than 1.0 ppm) and distilled (electroconductivity was less than 2 μS/cm) water. A concave focused hydrophone (diameter 12 mm, focal length 42.2 mm, TORAY Engineering) was used to measure the acoustic pressure reflected from the cavitation bubbles.

Figure 7.8 shows the ultrasound sequence for subharmonic detection. In the sequence, 100-cycle ultrasound at a frequency of 1.67 MHz was followed by 600-cycle ultrasound at the same frequency. The 100-cycle ultrasound was the same used for the high frequency wave of the C-C

waveform. The peak negative pressure was 2.2–12.7 MPa. The peak-to-peak pressure of the 600-cycle ultrasound was 0.34 MPa to avoid generating cavitation with ultrasound exposure.

The subharmonic component of the 1.67 MHz ultrasound was detected during lower intensity ultrasound exposure. The detected subharmonic acoustic emission was classified into four groups by its signal amplitude. The subharmonic signal amplitude was calculated by subtracting the amplitude of the frequency components around the subharmonic from the subharmonic amplitude in the FFT spectrum of the acoustic pressure. After the determination of the subharmonic signal level of the stone, the C-C waveform, which consists of high and low frequency waves, was exposed to erode the stone for 600 s. The low frequency wave was 3 cycles, frequency 552 kHz and its peak negative pressure was 9.5 MPa. The PRF of the C-C waveform was 10 Hz, and a total of 19 stones were exposed to the C-C wave. The erosion volume was estimated from 1D measurement of the erosion depth with a laser displacement meter, assuming axial symmetry of the eroded shape.

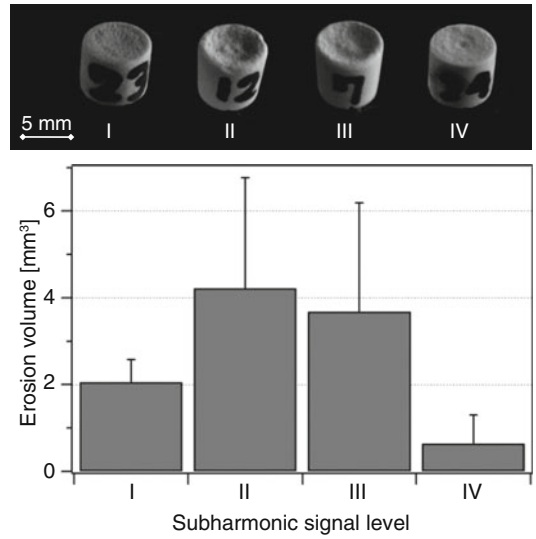

Fig. 7.9 Eroded model stones and erosion volume with various intensities of high frequency ultrasound**.** Each stone was subjected to 10 min ultrasound exposure. The results were divided into four groups using subharmonic signal amplitude measured with a focused hydrophone during the customized ultrasound sequence, as shown in Fig. 7.8 before the C-C waveform was used to fragment the stones. The subharmonic signal was not detected in group (*I*). By increasing the intensity of the high frequency ultrasound, the subharmonic signal was observed in group (*II*). By further increasing the intensity, the subharmonic signal became relatively large, and the n/3, n/4 (n = 1, 2, 3…) signal was often observed in group (*III*). In group (*IV*), the subharmonic signal peak in the spectrum decreased. The peak negative pressure of the high frequency ultrasound was 2.2–3.1 MPa in group (*I*), 4.5–6.4 MPa in group (*II*), 5.7–8.8 MPa in group (*III*) and 11.2–12.7 MPa in group (*IV*)

7.3.2 Subharmonic Signal Level and Stone Erosion Volume

Figure 7.9 shows eroded model stones and the erosion volume of the stones. The intensity of the high frequency ultrasound of the C-C waveform in group (I) was the smallest, and that in group (IV) was the largest. The subharmonic signal was not detected in group (I). The intensity of the subharmonic signal was relatively small in group (II), the intensity of the subharmonic signal was relatively large and the *n*/3, *n*/4 signal was often observed in group (III). In group (IV), the subharmonic signal peak in the spectrum decreased compared with the other frequency components. The peak negative pressure of the high frequency ultrasound was 2.2–3.1 MPa in group (I), 4.5–6.4 MPa in group (II), 5.7–8.8 MPa in group (III) and 11.2–12.7 MPa in group (IV). The number of eroded stones was 3 in group (I), 6 in group (II), 6 in group (III) and 4 in group (IV). Comparing the results of the 4 groups, the erosion volumes in groups (II) and (III) were clearly larger than those in groups (I) and (IV). In many cases, the shape of the eroded stones in groups (II) and (III) were similar, and their eroded depths were comparable. The eroded depths in groups (I) and (IV) were much shallower, and the eroded area in group (IV) was much smaller.

7.3.2.1 Subharmonic Signal Level

These results indicate the importance of the optimization of the C-C waveform. They also show that there is clearly an “optimal condition” for stone erosion. The erosion volume and eroded area in group (IV) were smaller than those in

group (I). This suggests that large cavitation induced by the strong high frequency ultrasound in this experiment had lower resonance frequency than 552 kHz and shielded the stone from the low frequency ultrasound. As a result, efficiency in group (IV) was lower than that not only in groups (II) and (III), but also that in group (I). This means that optimization of the high frequency intensity wave is an important factor in stone erosion with the C-C waveform. For practical use, as optimization depends on many parameters, which vary case by case, a feedback system would be helpful. The subharmonic acoustic pressure is one possible signal for the feedback system. Though the proposed method seems to be a good direction towards optimization, there is still room for improvement in terms of the sensitivity of the subharmonic signal detection. Some stones in groups (II) and (III) had remaining "islands", corresponding to the high frequency focal region, and the erosion shape was sometimes like a doughnut. This suggests that the high frequency ultrasound intensity in groups (II) and (III) was in some cases still too large. Recently, active ultrasound detection using ultrafast plane wave imaging has been used for the detection of cavitation bubbles induced by high-intensity focused ultrasound pulses (Gateau et al. 2011). A method using ultrafast imaging, or the combination of ultrafast imaging and subharmonic detection, would be useful to more precisely optimize parameters of the C-C waveform.

7.4 Motion Compensation System for Ultrasound Lithotripsy

7.4.1 Image-guided Motion Compensation System

A serious problem in removing a kidney stone using ultrasound lithotripsy is the movement of the kidney containing the stone to be treated. Therefore, not only the surrounding healthy tissue may be damaged during the focused ultrasound therapy, but also the stone erosion rate may decrease. To solve this problem, it is necessary to compensate for stone motion. We now review related work on the targeting technology for various kinds of targets in the body.

Nakamura et al. (2001) developed a surgical robot system to compensate for organ motion during surgery by using a 955 fps high speed CCD camera. Ginhoux et al. (2005) proposed a model predictive control and an adaptive observer for the surgical system of a beating heart by using a 500 fps high speed CCD camera. Tuna et al. (2013) developed a heart motion prediction algorithm using an adaptive filter to estimate the future point of interest on the beating heart surface and achieved high tracking performance (0.160–0.350 mm). Among the applications in the field of radio surgery, Cyber Synchrony™, which is a real-time image-guided system of CyberKnife™, uses externally placed optical markers on a patient's skin for target detection and motion compensation (Ozhasoglu et al. 2008). Optical/magnetic position sensors, inertial sensors, ECG signals, *etc*. are used in the system. To and Mahfouz (2013) developed an inertial measurement system for human body motion tracking to satisfy the demand of reliability and high accuracy in biomedical applications. Li et al. (2010) developed an algorithm for real-time volumetric image reconstruction and 3D tumor localization based on a single x-ray projection image for lung cancer radiotherapy. Arnold et al. (2011) developed a 3D organ motion prediction system, called "pencil beam", by using diaphragm motion for MR-guided high-intensity focused ultrasound. Brix et al. (2014) developed a 3D motion tracking system that involves stereo MRI images.

Several guidance methods for ultrasound imaging have been introduced. Abolmaesumi et al. (2002) developed a robot-assisted ultrasound diagnostic system with a visual servo controller. In this system, an operator, robot controller and ultrasound image processor share control over the motion of the robot positioning the ultrasound transducer. Speckle decorrelation change can be used to estimate out-of-plane motion with a single ultrasound plane (Krupa et al. 2009). A spatial probability map of the target body position was introduced to guide surgical tools (Thienphrapa

et al. 2014). The contact force between the ultrasound probe and body surface can be used to obtain proper ultrasound images (Aoki et al. 2010). Mura et al. (2014) developed US-based tracking algorithms for endoluminal devices for cardiovascular surgery. Kubota et al. (2014) proposed an ultrasound-based tracking method by applying a Pyramidal LK method for radiation beam therapy. It consists of multiple templates obtained at the time of the maximum inspiration or expiration of the patient's breathing,.

7.4.2 Body Motion Compensation System for Focused Ultrasound Treatment

The main problem in removing kidney stones is organ movement due to respiration, heartbeat, *etc*. A non-invasive ultrasound theragnostic system (NIUTS) was proposed and developed (Koizumi et al. 2013) to compensate for body movement by using a focal lesion servo (FLS) function by bi-plane ultrasound imaging during HIFU exposure (Fig. 7.10).

Theragnostics is a compound word composed of therapeutics and diagnostics. The NIUTS has a spherical piezoelectric transducer and two ultrasound probes (Fig. 7.10a), one of which is located in the center of the piezoelectric transducer, and the other of which is located on the lateral side of the transducer. In the image taken by the center probe, the long axis of a kidney phantom with an artificial stone is parallel to the body axis. The image plane of the phantom by the lateral probe is perpendicular to the long axis (Fig. 7.10b). These images are then used to identify the 3D positioning data of the focal region and move the focus point of HIFU onto the kidney stone. In the control, the focus point tracks and follows the target kidney stone using the 3D positioning data. It should be noted that servo errors cause ultrasound images to change due to the fluctuation in the viewpoints of the ultrasound probes, which in turn increases the servo error. This negative spiral worsens servo performance. However, if servo performance can be improved by some method that results in a positive spiral, the possibility of dramatically enhancing servo performance increases. We take two approaches to solve the above-mentioned problems: Approach 1; minimize the servo error to reduce the changes in viewpoint, Approach 2; reduce the effect of servo error.

With respect to the first approach, we have developed two solutions to enhance not only servo performance, but also patient safety. One solution is robust extraction, tracking, following and a monitoring method of the focal lesion based on the information in the ultrasound image (Koizumi et al. 2009a, b, 2013, 2014). The second solution is a controller that compensates for the quasi-periodical respiratory motion of the focal lesion (Koizumi et al. 2009a, b). With respect to the second approach, we proposed two solutions. One solution is HIFU irradiation con-

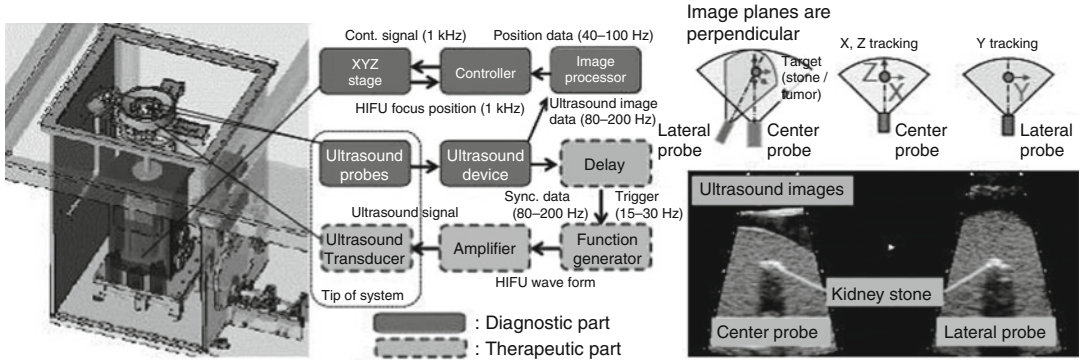

Fig. 7.10 NIUTS system configuration (Koizumi et al. 2013). (**a**) Block diagram of NIUTS and (**b**) Ultrasound bi-plane images

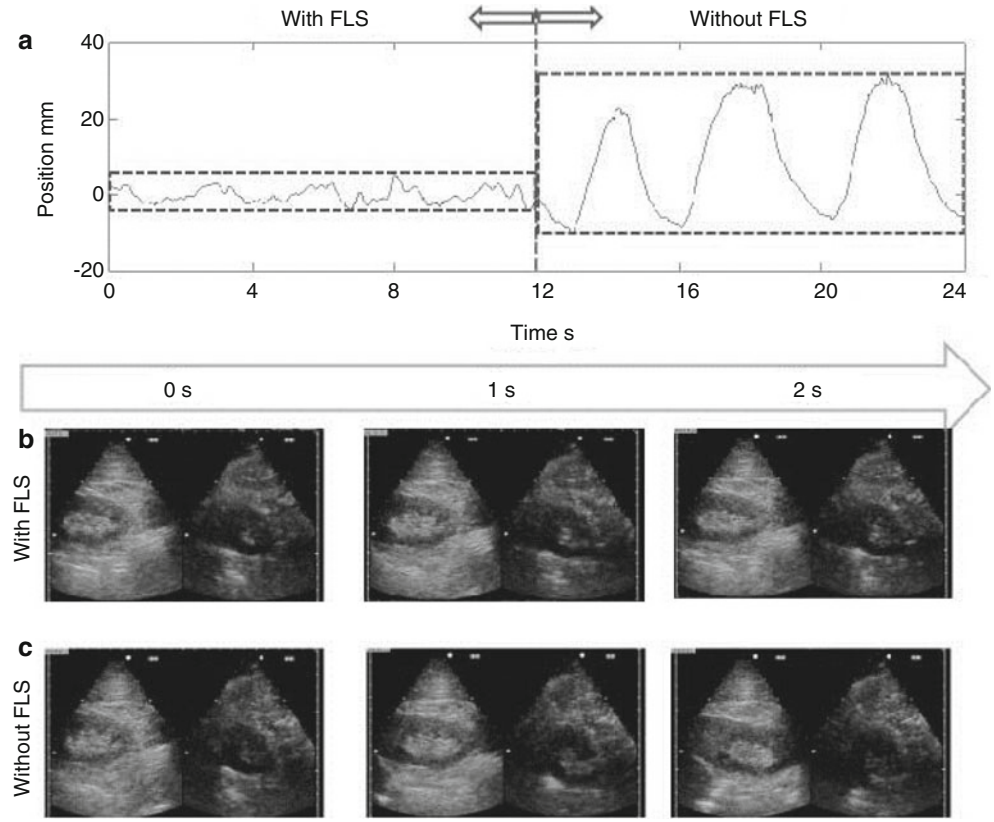

Fig. 7.11 Body motion compensation performance from focal lesion servo (*FLS*) function of NIUTS. (**a**) Trajectory of human kidney movements with/without FLS functions in ultrasound images. (**b**) Kidney looks almost still in ultrasound images with FLS function. (**c**) Kidney moves in accordance with respiration without FLS function

trol, in accordance with the servo error, based on the identified HIFU irradiation pattern (Seo et al. 2010, 2011; Koizumi et al. 2011). The second solution is a recovering algorithm to automatically track the status by using the robust template matching method and 3D positioning sensor data (Koizumi et al. 2014).

As a result, with the NIUTS, tracking performance within 2.5 mm was achieved for a healthy human kidney (Koizumi et al. 2013). Figure 7.11 shows the experimental results showing the effectiveness of the FLS function of NIUTS. Figure 7.11a is the trajectory of the servo target with/without the FLS function. The standard deviation of the position of the servo target was 1.92 mm with FLS, while it was 13.2 mm without FLS. In other words, 86 % of body movement could be compensated for by using NIUTS. Without our NIUTS, the healthy tissue surrounding the focal lesion may be damaged by HIFU irradiation, meaning we cannot take advantage of the localized HIFU therapy with the C-C waveform against the conventional SWL. Our NIUTS with the FLS function can be an effective tool to cancel out kidney motion to remove kidney stones by localized HIFU therapy with C-C waveform, minimizing damage to the surrounding healthy tissues.

Conclusion

Shock wave lithotripsy has been the first choice for removing kidney stones and will continue to be the gold standard. However, the large focal volume of shock wave is probably a side effect and tissue trauma cause. More localized and controlled stone comminution is one possible direction of lithotripsy technology in the future. The use of focused ultrasound may be

an alternative solution for less side effects and more patient-friendly kidney stone treatment because of its shorter wavelength and more localized cavitation volume than conventional shock wave pulses. The aim of ultrasound lithotripsy introduced in this chapter is to maximize cavitation activity to disintegrate kidney stones using high-intensity focused ultrasound (HIFU). Cavitation activity is highly unpredictable; thus, we proposed a method involving three controlled steps in kidney stone treatment. We outlined the method according to our previously published literatures.

The first step is the control of localized high pressure fluctuation on the stone. We proposed a method for disintegrating the stone by acoustic cavitation collapse. The two-frequency combined wave (C-C waveform) was used for controlling cloud cavitation collapse. This cavitation control method efficiently concentrates very high pressure on the stone surface with the localized cavitation region. Stone erosion tests *in-vitro* suggested the stone erosion mechanism attributed mostly to cavitation erosion. Fragmentation of natural and model kidney stones was achieved with small fragment sizes of less than 2 mm, and mostly less than 1 mm, showing one of the advantages of using cavitation for lithotripsy application. The second step is the monitoring of cavitation activity by subharmonic detection. This method seems to be a good direction towards optimization of the C-C waveform in clinical use. The third step is a motion compensation system for stone tracking. The standard deviation of the target position in kidney was less than 2 mm.

We have shown that the cavitation phenomenon has a close relationship with ultrasound frequencies and amplitude. Further optimization of the ultrasound parameters can lead to more efficient stone comminution. Moreover, complementary *in-vivo* studies are needed to investigate the applicability of the C-C waveform with respect to tissue environments. The ultimate goal of this research was the development of a less invasive lithotripsy treatment with minimal tissue damage as the stone is chipped into small fragments.

References

Abolmaesumi P, Salcudean SE, Zhu WH, Sirouspour M, DiMaio S (2002) Image-guided control of a robot for medical ultrasound. IEEE Trans Robot Autom 18:11–23

Aoki Y, Kaneko K, Sakai T, Masuda K (2010) A study of scanning the ultrasound probe on body surface and construction of visual servo system based on echogram. J Robot Mech 22:273–279

Arnold P, Preiswerk F, Fasel B, Salomir R, Scheffler K, Cattin P (2011) 3D organ motion prediction for MR-guided high intensity focused ultrasound. Med Image Comput Comput Assist Interv 14:623–630

Bailey MR (1997) Control of acoustic cavitation with application of lithotripsy. PhD dissertation, University of Texas at Austin, Austin.

Bailey MR, Blackstock DT, Cleveland RO, Crum LA (1999) Comparison of electrohydraulic lithotripters with rigid and pressure-release ellipsoidal reflectors. II Cavitation fields. J Acoust Soc Am 106:1149–1159

Bailey MR, Couret LN, Sapozhnikov OA, Khokhlova VA, ter Haar G, Vaezy S, Shi X, Martin R, Crum LA (2001) Use of overpressure to assess the role of bubbles in focused ultrasound lesion shape in vitro. Ultrasound Med Biol 27:695–708

Bailey MR, Pishchalnikov YA, Sapozhnikov OA, Cleveland RO, McAteer JA, Miller NA, Pishchalnikova IV, Connors BA, Crum LA, Evan AP (2005) Cavitation detection during shock-wave lithotripsy. Ultrasound Med Biol 31:1245–1256

Brix L, Ringgaard S, Sorensen TS, Poulsen PR (2014) Three-dimensional liver motion tracking using real-time two-dimensional MRI. Med Phys 41:042303

Carnel MT, Alcock RD, Emmony DC (1993) Optical imaging of shock waves produced by a high-energy electromagnetic transducer. Phys Med Biol 38:1575–1588

Cathignol D, Tavakkoli J, Birer A, Arefiev A (1998) Comparison between the effects of cavitation induced by two different pressure-time shock waveform pulses. IEEE Trans Ultrason Ferroelectr Freq Control 45: 788–799

Chahine GL, Duraiswami R (1992) Dynamical interactions in a multi-bubble cloud. J Fluids Eng 114:680–686

Chaussy C, Brendel W, Schiemdt E (1980) Extracorporeally induced destruction of kidney stones by shock waves. Lancet 2:1265–1268

Church CC (1989) A theoretical study of cavitation generated by an extracorporeal shock wave lithotripter. J Acoust Soc Am 86:215–227

Cleveland RO, Bailey MR, Fineberg N, Hartenbaum B, Lokhandwalla M, McAteer JA, Sturtevant B (2000a) Design and characterization of a research electrohydraulic lithotripter patterned after the Dornier HM3. Rev Sci Instrum 71:2514–2525

Cleveland RO, Sapozhnikov OA, Bailey MR, Crum LA (2000b) A dual passive cavitation detector for localized detection of lithotripsy-induced cavitation in vitro. J Acoust Soc Am 107:1745–1758

Coleman AJ, Saunders JE, Crum LA, Dyson M (1987) Acoustic cavitation generated by an extracorporeal shockwave lithotripter. Ultrasound Med Biol 13:69–76

Coleman AJ, Choi MJ, Saunders JE (1996) Detection of acoustic emission from cavitation in tissue during clinical extracorporeal lithotripsy. Ultrasound Med Biol 22:1079–1087

Crum LA (1988) Cavitation microjets as a contributory mechanism for renal calculi disintegration in ESWL. J Urol 140:1587–1590

d'Agostino L, Brennen CE (1988) Acoustical absorption and scattering cross sections of spherical bubble clouds. J Acoust Soc Am 84:2126–2134

d'Agostino L, Brennen CE (1989) Linearized dynamics of spherical bubble clouds. J Fluid Mech 199:155–176

Duryea AP, Maxwell AD, Roberts WW, Xu Z, Hall TL, Cain CC (2011) In vitro comminution of model renal calculi using histotripsy. IEEE Trans Ultrason Ferroelectr Freq Control 58:971–980

Duryea AP, Roberts WW, Cain CC, Hall TL (2013) Controlled cavitation to augment SWL stone comminution mechanistic insights in vitro. IEEE Trans Ultrason Ferroelectr Freq Control 60:301–309

Eisenmenger W (2001) The mechanisms of stone fragmentation in ESWL. Ultrasound Med Biol 27:683–693

Eisenmenger W, Du XX, Tang C, Zhao S, Wang Y, Rong F, Dai D, Guan M, Qi A (2002) The first clinical results of "wide-focus and low pressure" ESWL. Ultrasound Med Biol 28:769–774

Evan AP, Lynn R, Willis LR, McAteer JA, Bailey MR, Connors BA, Shao Y, Lingeman JE, Williams JC Jr, Fineberg NS, Crum LA (2002) Kidney damage and renal functional changes are minimized by waveform control that suppresses cavitation in shock wave lithotripsy. J Urol 168:1556–1562

Gateau J, Aubry JF, Pernot M, Fink M, Tanter M (2011) Combined passive detection and ultrafast active imaging of cavitation events induced by short pulses of high-intensity ultrasound. IEEE Trans Ultrason Ferroelectr Freq Control 58:517–532

Ginhoux R, Gangloff J, Mathelin M, Soler L, Sanchez MMA, Marescaux J (2005) Active filtering of physiological motion in robotized surgery using predictive control. IEEE Trans Robot 21:67–79

Gracewski SM, Dahake G, Ding Z, Burns SJ, Everbach EC (1993) Internal stress wave measurements in solids subjected to the lithotripter pulses. J Acoust Soc Am 94:652–661

Ikeda T, Yoshizawa S, Tosaki M, Allen JS, Takagi S, Ohta N, Kitamura T, Matsumoto Y (2006) Cloud cavitation control for lithotripsy using high intensity focused ultrasound. Ultrasound Med Biol 32:1383–1397

Kato H, Konno A, Maeda M, Yamaguchi H (1996) Possibility of quantitative prediction of cavitation erosion without model test. J Fluids Eng 118:582–588

Knapp RT (1955) Recent investigation on the mechanics of cavitation and erosion damage. Trans ASME 77: 1045–1054

Koizumi N, Seo J, Suzuki Y, Lee D, Ota K, Nomiya A, Yoshizawa S, Yoshinaka K, Sugita N, Homma Y, Matsumoto Y, Mitsuishi M (2009a) A control framework for the non-invasive ultrasound theragnostic system. Proceedings of 2009 IEEE/RSJ International Conference on Intelligent Robotics and Systems (IROS), St. Louis, USA, pp 4511–4516

Koizumi N, Warisawa S, Nagoshi M, Hashizume H, Mitsuishi M (2009b) Construction methodology for a remote ultrasound diagnostic system. IEEE Trans Robot 25:522–538

Koizumi N, Seo J, Lee D, Funamoto T, Nomiya A, Yoshinaka K, Sugita N, Homma H, Matsumoto Y, Mitsuishi M (2011) Robust kidney stone tracking for a non-Invasive ultrasound theragnostic system –servoing performance and safety enhancement. Proceedings of the 2011 IEEE International Conference on Robotics and Automation (ICRA), Shanghai, China, pp 2443–2450

Koizumi N, Seo J, Funamoto T, Nomiya A, Ishikawa A, Yoshinaka K, Sugita N, Homma Y, Matsumoto Y, Mitsuishi M (2013) Construction methodology for NIUTS ——Bed servoing system for body targets. J Robot Mech 25:1088–1096

Koizumi N, Funamoto T, Seo J, Lee D, Tsukihara H, Nomiya A, Azuma T, Yoshinaka K, Sugita N, Homma H, Matsumoto Y, Mitsuishi M (2014) A novel robust template matching method to track and follow body targets for NIUTS. Proceedings of the 2014 IEEE International Conference on Robotics and Automation (ICRA), Hong Kong, China, pp 1929–1936

Konno A, Kato H, Yamaguchi H, Maeda M (2002) On the collapsing behavior of cavitation bubble clusters. JSME Int J B 3:631–637

Krupa A, Fichtinger G, Hager G (2009) Real-time motion stabilization with B-mode ultrasound image speckle information and visual servoing. Int J Robot Res 28:1334–1354

Kubota Y, Matsumura A, Fulahori M, Minohara S, Yasuda S, Nagahashi H (2014) A new method for tracking organ motion on diagnostic ultrasound images. Med Phys 41:092901

Li R, Jia X, Lewis JH, Gu X, Folkerts M, Men C, Jiang SB (2010) Real-time volumetric image reconstruction and 3D tumor localization based on a single x-ray projection image for lung cancer radiotherapy. Med Phys Lett 37:2822–2826

Loske AM, Prieto FE, Fernández F, van Cauwelaert J (2002) Tandem shock wave cavitation enhancement for extracororeal lithotripsy. Phys Med Biol 47:3945–3957

Matsumoto Y, Yoshizawa S (2005) Behavior of bubble cluster in an ultrasound field. Int J Numer Methods Fluids 47:591–601

Matsumoto Y, Yoshizawa S, Ikeda T (2002) Dynamics of bubble cloud in focused ultrasound. Proceedings of the second international symposium on therapeutic ultrasound, International Society for Therapeutic Ultrasound (ISTU), Seattle, USA, pp290–299

Maxwell AD, Cunitz BW, Kreider W, Sapozhnikov OA, Hsi RS, Harper JD, Bailey MR, Sorensen MD (2015) Fragmentation of urinary calculi *in vitro* by burst wave lithotripsy. J Urol 193(1):338–344

McAteer JA, Williams JC, Cleveland RO, Van Cauwelaert J, Bailey MR, Lifshitz DA, Evan AP (2005) Ultracal-30

gypsum artificial stones for research on the mechanisms of stone breakage in shock wave lithotripsy. Urol Res 33:429–434

Mørch KA (1981) Cavity cluster dynamics and cavitation erosion. Proceedings of ASME Cavitation polyphase flow forum, ASME, Boulder, Colorado, pp 1–10

Mura M, Ciuti G, Ferrari V, Dario P, Menciassi A (2014) Ultrasound-based tracking strategy for endoluminal devices in cardiovascular surgery. Int J Med Robot, doi: 10.1002/rcs.1603. [Epub ahead of print]

Nakamura Y, Kishi K, Kawakami H (2001) Heartbeat synchronization for robotic cardiac surgery. IEEE Int Conf Robot Autom (ICRA) 2:2014–2019

Omta R (1987) Oscillations of a cloud of bubbles of small and not so small amplitude. J Acoust Soc Am 82: 1018–1033

Ozhasoglu C, Saw CB, Chen H, Burton S, Komanduri K, Yue NJ, Huq SM, Heron DE (2008) Synchrony – cyberknife respiratory compensation technology. Med Dosim 33:117–123

Philip A, Delius M, Scheffczyk C, Vogel A, Lauterborn W (1993) Interaction of lithotripter-generated shock waves with air bubbles. J Acoust Soc Am 93:2496–2509

Pishchalnikov YA, Sapozhnikov OA, Bailey MR, Williams JC Jr, Cleveland RO, Colonius T, Crum LA, Evan AP, McAteer JA (2003) Cavitation bubble cluster activity in the breakage of kidney stones by lithotripter shockwaves. J Endourol 17:435–446

Reisman GE, Brennen CE (1996) Pressure pulses generated by cloud cavitation. ASME FED 236:319–328

Reisman GE, Wang YC, Brennen CE (1998) Observation of shock waves in cloud cavitation. J Fluid Mech 355:255–283

Sapozhnikov OV, Khokhlova VA, Williams JC Jr, McAteer JA, Cleveland RO, Crum LA (2002) Effect of overpressure and pulse repetition frequency on cavitation in shock wave lithotripsy. J Acoust Soc Am 112:1183–1195

Seo J, Koizumi N, Yoshinaka K, Sugita N, Nomiya A, Homma Y, Matsumoto Y, Mitsuishi M (2010) Three-dimensional computer controlled acoustic pressure scanning and quantification of focused ultrasound. IEEE Trans Ultrason Ferroelectr Freq Control 57:883–891

Seo J, Koizumi N, Funamoto T, Sugita N, Yoshinaka K, Nomiya A, Ishikawa A, Homma Y, Matsumoto Y, Mitsuishi M (2011) Visual servoing for a US-guided therapeutic HIFU system by coagulated lesion tracking: a phantom study. Int J Med Robot Comput Assist Surg 7:237–247

Shimada M, Matsumoto Y, Kobayashi T (2000) Influence of the nuclei size distribution on the collapsing behavior of the cloud cavitation. JSME Int J B 43:380–385

Sokolov DL, Bailey MR, Crum LA (2001) Use of a dual-pulse lithotripter to generate a localized and intensified cavitation field. J Acoust Soc Am 110:1685–1695

Sokolov DL, Bailey MR, Crum LA (2003) Dual-pulse lithotripter accelerates stone fragmentation and reduces cell lysis in vitro. Ultrasound Med Biol 29:1045–1052

Soyama H, Kato H, Oba R (1992) Cavitation observations of severely erosive vortex cavitation arising in a centrifugal pump. Proceedings of third IMechE International Conference on Cavitation, IMechE, London, UK, pp 103–110

ter Haar G (2001) Acoustic surgery. Phys Today, 54(12), pp. 29–34

Thienphrapa P, Ramachandran B, Elhawary H, Popovic A, Taylor RH (2014) Guidance of a high dexterity robot under 3d ultrasound for minimally invasive retrieval of foreign bodies from a beating heart. IEEE International Conference on Robotics and Automation (ICRA), Hong Kong, China, pp 4869–4874

To G, Mahfouz MR (2013) Quaternionic attitude estimation for robotic and human motion tracking using sequential Monte Carlo methods with von Mises-Fisher and nonuniform densities simulations. IEEE Trans Biomed Eng 60:3046–3059

Tuna E, Franke T, Bebek O, Shiose A, Fukamachi K, Cavusoglu M (2013) Heart motion prediction based on adaptive estimation algorithms for robotic-assisted beating heart surgery. IEEE Trans Robot 29: 261–276

van Wijngaarden L (1964) On the collective collapse of a large number of gas bubbles in water. Proceedings of 11th International Conference on Applied Mechanics, SpringerVerlag, Berlin, Germany, pp 854–861

Wang YC, Brennen CE (1995) The noise generated by the collapse of a cloud of cavitation bubbles. ASME FED 226. In: Cavitation and gas-liquid flow in fluid machinery devices, ASME, South Carolina, USA, pp 17–29

Wang YC, Brennen CE (1999) Numerical computation of shock waves in a spherical cloud of cavitation bubbles. ASME J Fluids Eng 121:872–880

Williams JC, Stonehill MA, Colmenares K, Evan AP, Andreoli SP, Cleveland RO, Bailey MR, Crum LA, McAteer JA (1999) Effect of macroscopic air bubbles on cell lysis by shock wave lithotripsy in vivo. Ultrasound Med Biol 25:473–479

Xi X, Zhong P (2000) Improvement of stone fragmentation during shock-wave lithotripsy using a combined EH/PEAA shock-wave generator – in vivo experiments. Ultrasound Med Biol 26:457–467

Yoshizawa S, Ikeda T, Takagi S, Matsumoto Y (2004) Nonlinear ultrasound propagation in a spherical bubble cloud. Proceedings of IEEE International ultrasonics symposium 2004, Montreal, Canada, vol 2, pp 886–889

Yoshizawa S, Ikeda T, Ito A, Ota R, Takagi S, Matsumoto Y (2009) High intensity focused ultrasound lithotripsy with cavitating microbubbles. Med Biol Eng Comput 47:851–860

Zhong P, Chuong CJ, Goolsby RD, Preminger GM (1992) Microhardness measurements of renal calculi: regional differences and effects of microstructure. J Biomed Mater Res 26:1117–1130

Zhong P, Cocks FH, Cioanta I, Preminger GM (1997) Controlled, forced collapse of cavitation bubbles for improved stone fragmentation during shock wave lithotripsy. J Urol 158:2323–2328

Zhu S, Cocks FH, Preminger GM, Zhong P (2002) The role of stress waves and cavitation in stone comminution in shock wave lithotripsy. Ultrasound Med Biol 28:661–671

Heat-Based Tumor Ablation: Role of the Immune Response

8

Feng Wu

Abstract

The ideal cancer therapy not only induces the death of all localized tumor cells with less damage to surrounding normal tissue, but also activates a systemic antitumor immunity. Heat-based tumor ablation has the potential to be such a treatment as it can minimal-invasively ablate a targeted tumor below the skin surface, and may subsequently augment host antitumor immunity. This chapter primarily introduces increasing pre-clinical and clinical evidence linking antitumor immune response to thermal tumor ablation, and then discusses the potential mechanisms involved in ablation-enhanced host antitumor immunity. The seminal studies performed so far indicate that although it is not possible to make definite conclusions on the connection between thermal ablation and antitumor immune response, it is nonetheless important to conduct extensive studies on the subject in order to elucidate the processes involved.

Keywords

Heat • Ablation • Neoplasm • Thermal ablation • Immunity • High intensity focused ultrasound • Radiofrequency • Microwave • Laser • Cryoablation • Antigen presenting cell • Cytotoxic T lymphocyte • Tumor infiltrating lymphocyte • Heat shock protein • Tumor vaccine

8.1 Introduction

As an alternative approach to surgical intervention, heat-based tumor ablation with minimally invasive techniques has received increasingly widespread interest in the local management of solid malignancy. It employs various kinds of physical energy for *in-situ* destruction of a targeted tumor, instead of local tumor removal. This

F. Wu
Nuffield Department of Surgical Sciences, HIFU Unit, Churchill Hospital, University of Oxford, Oxford OX3 9 DU, UK

Institute of Ultrasonic Engineering in Medicine, College of Biomedical Engineering, Chongqing Medical University, Chongqing 400016, China
e-mail: mfengwu@yahoo.com; feng.wu@nds.ox.ac.uk

© Springer International Publishing Switzerland 2016
J.-M. Escoffre, A. Bouakaz (eds.), *Therapeutic Ultrasound*, Advances in Experimental Medicine and Biology, Vol. 880, DOI 10.1007/978-3-319-22536-4_8

is achieved by either raising the temperature between 56 and 100 °C, or by using extremely cold temperatures. The main advantage of this alternative is a decrease in less invasiveness versus surgical procedures, resulting in an associated reduction in mortality, morbidity, hospital stay, cost and improved quality of life for cancer patients (Cabibbo et al. 2009; Timmerman et al. 2009; Liapi and Geschwind 2007; Hong et al. 2006; Hafron and Kaouk 2007, Dacadt and Siriwardena 2004). Due to various energy sources, the thermal ablation techniques include high-intensity focused ultrasound (HIFU), radiofrequency, laser, microwave and cryoablation. All of them can selectively destroy a targeted tumor via either percutaneous or extracorporeal approaches. As curative and palliative intentions, they have partially replaced some open surgery procedures in the clinical treatment of patients with solid tumors, including those of the liver, prostate, kidney, lung, breast, pancreas, brain, bone and soft tissues.

It has been observed for a long time that large amounts of tumor debris remain *in-situ* after thermal ablation. As a normal process of the healing response, tumor debris is gradually reabsorbed and then replaced by scar tissue in the patient. It usually takes a period from months to years, which depends on the size of the ablated tumor. However, it is still unclear what kind of biological significance may exist during the absorption period of the ablated tumor. Some studies have recently shown that an active immune response to the treated tumor could be developed after thermal ablation, and the host immune system could become more sensitive to the tumor cells (Wu et al. 2007a, b; Gravante et al. 2009; Fagnoni et al. 2008; Sabel 2009). This may lead to a potential procedure that reduces or perhaps eliminates metastases, thus preventing local recurrence in cancer patients who have had original dysfunction of antitumor immunity before treatment. In this chapter we will introduce the studies that focused on the host immune responses after thermal tumor ablation, and provide experimental and clinical data available to assess whether they could be potential for understanding of this complex phenomenon.

8.2 Methods of Thermal Ablation Technique

Local tumor destruction occurs when physical energy is transmitted into a tumor lesion and all targeted cancer cells can be completely destroyed. Minimally invasive thermal techniques rely on heat as the major mode of tumor ablation. They vary based on the processes involved in heat generation and their delivery. Due to differences in energy sources, these thermal techniques can be classified into five categories as follows: High-intensity focused ultrasound (HIFU) ablation, radiofrequency ablation (RFA), laser ablation (LA), microwave ablation (MWA) and cryoablation. Each method has unique characteristics for tumor ablation with regards to the method of energy delivery through the skin, conduction of energy and length of time required, real-time imaging for targeting/monitoring and a variety of other specific issues. A summary comparing the varied methods is shown in Table 8.1.

8.2.1 High-Intensity Focused Ultrasound Ablation

Concerning all minimally invasive therapies, HIFU ablation is the only non-invasive approach proposed to date (Kennedy 2005). It employs extracorporeal ultrasound energy to ablate a targeted tumor at depth without any needle insertion. Thus, there is no damage to the skin and overlying tissues. Ultrasound is a high frequency pressure wave. It can be brought to a tight focus at a distance from its source while propagating through tissues. If the concentrated energy is sufficient, energy absorption by the living tissue causes measurable temperature rises (56–100 °C), resulting in coagulation necrosis of the tissue solely within the focal volume (Chaussy et al. 2005). In addition, non-thermal effects, such as cavitation, can induce local tissue destruction due to cavitation-induced high pressures and temperatures (Wu 2006). A single exposure ablation zone (1–3 s) is small, ellipsoidal sized, approximately 1.5×15 mm under normal exposure parameters at 1.0 MHz. By placing numerous individual ablation zones side-by-side, conformal confluent ablation

Table 8.1 Comparison of thermal ablation methods for tumors

Methods	Energy conduction	Ablation volume	Energy delivery	Imaging guidance	Ablation time (min)	Ablation expense
HIFU	Heat cavitation	Conformal ablation No tumor size limitation	Transcutaneous No probe insertion	Ultrasound MRI	30–120	Expensive device No probe charge
RFA	Heat	No conformal ablation Tumor size limitation	Percutaneous Electrode probe	Ultrasound CT	10–30	Cheap device Expensive probe
Laser	Heat	Not Conformal ablation Tumor size limitation	Percutaneous Optical fiber	Ultrasound MRI	25–30	Expensive device Probe charge
Microwave	Heat	Not Conformal ablation Tumor size limitation	Percutaneous Electrode Antenna	Ultrasound CT/MRI	20–60	Cheap device Probe charge
Cryoablation	Cold	Not conformal ablation Tumor size limitation	Percutaneous Applicator	Ultrasound CT	15–30	Cheap device Expensive applicator

volumes of clinically relevant size can be achieved (ter Haar 2007). On the other hand, while HIFU ablation only takes 1–3 s per exposure; the total time can be substantial, longer than other minimally invasive therapies.

8.2.2 Radiofrequency Ablation

RFA uses an electromagnetic energy source with frequencies less than 900 kHz to generate heat (Decadt and Siriwardena 2004). An electrode probe is percutaneously placed into a targeted tumor. Through the probe, there is transmission of low voltage alternating current that creates ionic agitation and heating (Lau and Lai 2009). Ablation temperatures reach 50–100 °C, resulting in the coagulation necrosis of the targeted tumor (Curley 2001). While the tissue surrounding the tip of the probe reaches in excess of 100 °C, it will vaporize and char. This decreases the absorption of the energy, and reduces the ablative size of the surrounding tissue (Goldberg et al. 1996).

8.2.3 Laser Ablation

The term LA is also referred to as laser photocoagulation or laser interstitial thermal therapy (Goldberg et al. 2005). LA employs infrared light energy to produce heat and ablate a targeted cancer. The light energy is transmitted through an optical fiber with a bare tip, and thus induces coagulation necrosis of the targeted tumor while it diffuses through the target (Gough-Palmer and Gedroyc 2008). The Nd-YAG (neodymium:yttrium aluminum garnet) laser with a wavelength of 1064 nm, and diode laser with shorter wavelengths (800–980 nm), are the most widely used devices for laser ablation of solid tumors. They can both induce tissue photocoagulation at low power, or vaporization and cavitation at a higher output. The extent of tissue necrosis is typically limited, dependent on the amount of deposited energy. Thus, multiple fiber applicators are necessary in clinical application for ablation of larger lesions (Sabharwal et al. 2009).

8.2.4 Microwave Ablation

MWA employs electromagnetic energy to ablate a targeted tumor via an electrode-antenna placed within the lesion (Carrafiello et al. 2008). While electromagnetic microwaves (900–3,000 kHz) travel through the tissues, they evoke agitation and vibration of ionic molecules, such as water molecules, within cells. The rapid motion of these ionic molecules causes frictional heating, raising the local temperature range from 60–100 °C in the cellular environment, resulting in tissue coagulation necrosis (Simon et al. 2005). Compared to RFA, microwave ablation can actively heat a much larger area, with less effect on the heat sink, but there is no tissue boiling and charring during ablation procedure (Beland et al. 2007).

8.2.5 Cryoablation

Cryoablation is an alternative technique that uses extreme cold to freeze a targeted tumor in the form of an "ice-ball." It is one of the oldest ablation methods, with less peri- and post-procedural pain (Rybak 2009). Cryoablation has recently gained an increased interest due to the use of an argon-gas cryotherapy technique, which induces controlled tissue freezing by inserting a percutaneous applicator into a targeted lesion (Dumot and Greenwald 2008). A typical cryoablation session involves a freeze-thaw-freeze cycle. The argon and helium gases are alternately delivered to achieve extra- and intra-cellular ice crystal formation and tissue osmosis. This process causes protein denaturation, cell membrane rupture and cellular death (Babaian et al. 2008).

8.3 Mechanisms of Thermal Ablation and Immune Response

The absorption of physical energy delivered by thermal ablation technique can result in a measurable temperature elevation in living tissue. The thermal effects on tissue are directly dependent on how heat interacts with the tissue. When temperatures are increased to 42–45 °C for a period of 30–60 min, cells become more subject to damage by other agents such as radiotherapy and chemotherapy (Hill and ter Haar 1995). Increasing the temperature can obviously shorten the exposure time for therapeutic effects. If the temperature is increased a few degrees more to 50–52 °C and maintained for 4–6 min, irreversible cellular damage is induced (Thomsen 1991). Between 60 and 100 °C, instantaneous induction of protein coagulation occurs, resulting in the permanent destruction of key mitochondrial enzymes and nucleic acid-histone complexes (Goldberg et al. 2000). Temperatures greater than 105 °C can cause tissue vaporization and carbonization (Goldberg et al. 1996).

Thermal ablation technique is a different therapy to hyperthermia, which has been applied by physical heating technology to elevate targeted regions to temperatures in the 42–45 °C range. This "conventional" hyperthermia usually maintains uniform temperature distributions in a narrow therapeutic range for a period of 30–60 min, and is applied once or twice a week (Diederich and Hynynen 1999). However, the temperature distributions induced *in-vivo* are usually non-uniform because of tissue cooling by blood flow, and it is extremely difficult to avoid local cold spots that do not reach the required therapeutic temperature level (Lubbe and Bergemann 1994). The efficiency of hyperthermia is highly dependent on the ability to localize and control the successful temperature distributions, which are often influenced by tissue heterogeneities and blood flow. As a result, hyperthermia cannot be used alone in its clinical application, but can be only implemented as an adjuvant method to combine with either radiation therapy or chemotherapy in the treatment of malignant tumors (Dewey 1994). Two types of mechanism are commonly involved to explain the rational for this combined therapy. Heat is a radio-sensitizer that increases radiation damage and prevents subsequent repair. Hyperthermia can also produce biological effects on targeted tumors, including direct cellular toxicity, hypoxia, low pH and indirect blood perfusion deprivation in the tumor (Overgaard 1989).

Thermal ablation can cause direct and indirect damages to a targeted tumor. Direct heat injury occurs during the period of heat deposition, and it is predominately determined by the total energy delivered to the targeted tumor (Nikfarjam et al. 2005a, b, c). Indirect heat injury usually occurs after thermal ablation, which produces a progression in tissue damage. It may involve a balance of several factors, including microvascular damage, cellular apoptosis, Kupffer cell activation and altered cytokine release (Nikfarjam et al. 2005a, b, c). Direct injury is generally better defined than the secondary indirect effects.

8.3.1 Direct Thermal and Non-thermal Effects on Tumor

The effects of thermal ablation on a targeted tumor are determined by increased temperatures, thermal energy deposition, rate of heat removal and the specific thermal sensitivity of the tissue. As the tissue temperature rises, the time required to achieve irreversible cellular damage decreases exponentially. At temperatures between 50 and 55 °C, cellular death occurs instantaneously in cell culture (Wheatley et al. 1989). Protein denaturation, membrane rupture, cell shrinkage, pyknosis and hyperchromasia occur *ex-vitro* between 60 and 100 °C, leading to immediate coagulation necrosis (Wheatley et al. 1989). Additional to this necrosis, tissue vaporization and boiling occur at temperatures greater than 105 °C. Carbonization, charring and smoke generation occur when the temperature is over 300 °C (Heisterkamp et al. 1997).

In addition, acoustic cavitation, one of mechanical effects induced by HIFU ablation, is the most important non-thermal mechanism for tissue disruption in the ultrasound field (Germer et al. 1998a, b). The presence of small gaseous nuclei within subcellular organelles and tissue fluids are the source of cavitation. These bubbles can expand and contract under influence of the acoustic pressure. During the collapse of bubbles, the acoustic pressure is more than several thousand Pascals, and the temperatures reach several thousand degrees Celsius, resulting in the local destruction of the tissue (Maris and Balibar 2000).

Histological changes are evident in tumor tissue after thermal ablation (Clement 2004). In addition to HIFU ablation, four cellular change zones are described in the liver after thermal ablation as follows: Application, central, transition and reference tissue zones (Ozaki et al. 2003a, b; Germer et al. 1998a, b; Ohno et al. 2001). The application zone is where the heat source contacts the tissue. The central zone immediately surrounds the application zone and consists of damaged tissue. The transition zone contains apparently undamaged tissue, but exhibits signs of subacute hemorrhage. The reference zone refers to normal tissue surrounding the transition zone.

8.3.2 Direct Thermal Effects on Tumor Blood Vessels

Structural and functional changes are directly observed in tumor blood vessels after thermal ablation. These changes are not as well described as the thermal effects on tissues, but they do rely on varying temperatures. At temperatures between 40 and 42 °C, there is no significant change in tumor blood flow after 30–60 min exposure (Ozaki et al. 2003a, b). Beyond 42–44 °C, there is an irreversible decrease in tumor blood flow, with vascular stasis and thrombosis resulting in heat trapping and progressive tissue damage (Emami and Song 1984). While temperatures exceed 60 °C, immediate destruction of tumor microvasculature occurs (Tranberg 2004). It cuts the blood supply to the tumor directly through the cauterization of the tumor feeder vessels, leading to nutrient and oxygen deprivation. Thus, tissue destruction can be enhanced by the damage caused by thermal ablation to tumor blood vessels.

8.3.3 Indirect Effects After Thermal Ablation

Indirect injury is a secondary damage to tissue that progresses after the cessation of thermal ablation stimulus (Muralidharan et al. 2004). It is

based on histological evaluation of tissue damage at various time points after thermal ablation (Matsumoto et al. 1992). The full extent of the secondary tissue damage becomes evident 1–7 days after thermal ablation, depending on the model and energy source used (Wiersinga et al. 2003; Benndorf and Bielka 1997). The exact mechanism of this process is still unknown. However, it may represent a balance of several promoting and inhibiting mechanisms, including induction of apoptosis, Kupffer cell activation and cytokine release.

Cellular apoptosis may contribute to progressive tissue injury after thermal ablation. It is well established that apoptosis increases in a temperature-dependent manner, and temperatures between 40 and 45 °C cause inactivation of vital enzymes, thus initiating tumor cell apoptosis (Barry et al. 1990; Hori et al. 1989). Thermal ablation creates a temperature gradient that progressively decreases away from the site of probe insertion. The induction of apoptosis at a distance from the heat source may potentially contribute to the progression of injury. An increased apoptosis rate is observed in the liver 24 h after microwave ablation (Ohno et al. 2001). The stimulation of apoptosis may be directly induced by temperature elevations, alterations in tissue microenvironment and the release of various cytokines after thermal ablation. Kupffer cell activity may be one of the major factors involved in progressive injury after thermal ablation (Heisterkamp et al. 1997). Heat induces Kupffer cell IL-1 (Decker et al. 1989) and tumor necrosis factor-α (TNF-α) (Adams and Hamilton 1984) secretion, which are known to have *in-vivo* antitumor activity and increase cancer cell apoptosis (Hori et al. 1989). Kupffer cells also induce the production of interferon that augments liver-associated natural killer cell activity (Kirn et al. 1982).

Thermal ablation may induce both regional and systemic production of cytokines through activation of inflammatory cells. Compared with controls, the circulating level of IFN-γ and vascular endothelial growth factor levels markedly increase after RFA (Napoletano et al. 2008; Evrard et al. 2007a, b). The increased level of IL-1 and TNF-α is also observed after RFA (Ali et al. 2005). These cytokines may have direct cytotoxic effects, such as inducing tumor endothelial injury and rendering tumor cells more sensitive to heat-induced damage (Watanabe et al. 1988; Isbert et al. 2004). However, contrasting results are obtained for TNF-α levels in two studies (Evrard et al. 2007a, b; Schell et al. 2002) and IL-1 level in one study (Schell et al. 2002), where levels remain unchanged after thermal ablation. Cryoablation may cause pathophysiological changes, which are similar to those observed after endotoxin administration (Chapman et al. 2000a, b, c; Wudel et al. 2003). These changes cause significant increases in capillary permeability in the lung, leading to secondary injury (Washington et al. 2001). It is generally believed that all alterations may be associated with post-cryosurgery activation in the lungs of the nuclear factor-κB factor and derived cytokines, including TNF-α and macrophage inflammatory protein-2, along with an increase in serum thromboxane levels (Seifert et al. 2002; Sadikot et al. 2002).

8.4 Antitumor Immune Response After Thermal Ablation

8.4.1 HIFU Ablation

As shown in Table 8.2, there is increasing evidence from animal studies that indicate that HIFU may modulate host antitumor immunity after tumor ablation. Yang and colleagues (Yang et al. 1992) used HIFU to treat C1300 neuroblastoma implanted in mouse flanks, followed by the re-challenge of the same tumor cells. A significantly slower growth of re-implanted tumors was observed in these mice compared with the controls. After HIFU treatment, the cytotoxicity of cytotoxic T lymphocytes (CTLs) and the number of activated tumor-specific CTLs was significantly increased in the H22 tumor bearing mice treated with HIFU. Adoptive transfer of the activated lymphocytes could provide better long-term survival and lower metastatic rates in the mice re-challenged by the same tumor cells when compared with sham-HIFU and control groups.

Table 8.2 Antitumor Immune Response to HIFU Alone in Animal Studies

References	Tumor cell line/model	HIFU parameters	Endpoint	Results	Additional observations
Yang et al. (1992)	C1300 Neuroblatoma Ajax (A/J) mice	4 MHz 550 W/cm^2	Resistance to rechallenge	Significant inhibition of tumor growth in mice treated with curative HIFU compared to the untreated controls	Single & repeated HIFU could prolong survival rates in the tumor bearing mice
Xia et al. (2012)	H22 Hepatocarcinoma C57BL/6 J mice	9.5 MHz 5 W 180–240 s	Measurement of CTL cytotoxicity & resistance to rechallenge after adoptive transfer of the activated lymphocytes	Significant increase in CTL cytotoxicity Superior protection after adoptive immunotherapy	Significantly increased number of activated tumor-specific CTLs
Xing et al. (2008)	B16F10-LucG5 melanoma C57Bl/6 mice	3.3 MHz	Measurement of CTL cytotoxicity	Significant increase in CTL cytotoxicity in mice treated with curative HIFU compared to the untreated controls	HIFU couldn't increase the risk of distant metastasis
Hu et al. (2007)	MC-38 colon adenocarcinoma C57Bl/6 mice	3.3 MHz	Resistance to rechallenge & cytotoxicity assays of splenic lymphocytes	Superior protection & tumor-specific lymphocyte mediated cytotoxicity after both thermal & mechanical HIFU treatments Antitumor immunity induced by cavitation-based HIFU was stronger compared to thermal HIFU	HIFU could enhance dendritic cell (DC) infiltration in the treated tumor & subsequent migration to draining lymph nodes
Zhang et al. (2010)	H22 hepatocarcinoma C57BL/6 J	9.5 MHz 5 W 180–240 s	Resistance to rechallenge Measurement of DC activation & CTL cytotoxicity after immunization with HIFU-generated tumor vaccine	Significant increase in CTL cytotoxicity & DC activation Superior protection in mice immunized with HIFU-generated tumor vaccine when compared with the controls	HIFU treatment alone could enhance CTL cytotoxicity & resistance to rechallenge
Deng et al. (2010)	H22 Hepatocarcinoma C57BL/6 J mice	9.5 MHz 5 W 180–240 s	Measurement of DC activation & CTL cytotoxicity Resistance to rechallenge after immunization of DCs loaded with HIFU-treated tumor	Significant increase in DC activation & CTL cytotoxicity with inhibition of tumor growth in mice immunized by DCs loaded with HIFU-treated tumor when compared with the controls	

(continued)

Table 8.2 (continued)

References	Tumor cell line/model	HIFU parameters	Endpoint	Results	Additional observations
Hu et al. (2005)	MC-38 mouse colon adenocarcinoma *In-vitro*	1.1 MHz P^+ 12/P^- 6.7 MPa P^+ 31.7/P^- 10.7 MPa DC 30 or 3 % 5 s or 30s	Measurement of endogenous danger signals released from HIFU-treated cells Activation of APCs	Release of ATP and HSP-60 from HIFU-treated tumor cells Activation of DCs & macrophages	
Kruse et al. (2008)	Transgenic reporter mouse for HSP70-Luc2AeGFP	1.5 MHz 53–353 W/cm^2	Skin HSP-70 expression after 1 s HIFU treatment	Upregulated HSP-70 expression after HIFU treatment	
Hundt et al. (2007)	Transfected HSP-70-Luc M21 Melanoma NIH-3 T3 mouse fibroma SCCVII mouse squamous cell carcinoma cells *in-vitro*	1 MHz 28–179 W/cm^2	HSP-70 expression in tumor cells after either thermal stress or HIFU treatment	Increased HSP-70 expression after both thermal stress & HIFU treatment Higher expression observed at HIFU-induced lower temperatures than thermal stress alone	
Liu et al. (2010)	B16 melanoma C57BL/6 mice	3.3 MHz P^+19.5/P^-7.2 MPa 4 s	Measurement of DC infiltration & maturation in HIFU-treated tumor	Significant increase in local DC infiltration & maturation after HIFU treatment compared to the controls	Sparse-scan HIFU was more effective than dense-scan HIFU in enhancing DC infiltration & maturation *in-situ*
Zhou et al. (2007)	H22 hepatocarcinoma Chinese Kun Ming mice	9.5 MHz 5 W 180–240 s	Resistance to rechallenge after immunization with HIFU-treated tumor vaccine	Significant protection in mice immunized with HIFU-treated tumor compared to heat-treated tumor group Activation of DCs and Macrophages	A significant increase in $CD4^+$ levels & $CD4^+/CD8^+$ ratio in both HIFU & thermal groups

This is indicative that HIFU ablation could activate tumor-specific T lymphocytes, thus inducing antitumor cellular immunity in the mice (Xia et al. 2012). Similar results were confirmed in the mice implanted with MC-38 colon adenocarcinoma and melanoma after HIFU ablation.

HIFU treatment could also induce an enhanced CTL activity *in-vivo*, thus providing protection against subsequent tumor re-challenge (Xing et al. 2008). In addition, HIFU could enhance infiltration of dendritic cells (DCs) in the treated tumor and subsequent migration to the draining lymph nodes. Compared to thermal HIFU treatment, antitumor immunity induced by mechanical HIFU treatment (being a pulsed HIFU exposure with no significantly elevated temperature increase in tumor tissue and thermal necrosis) was significantly stronger in terms of DC and CTL activation, and a superior protection against tumor re-challenge was reported (Hu et al. 2007).

After HIFU ablation, large amounts of tumor debris remain *in-situ,* and the host gradually reabsorbs the debris as the normal process of the healing response. Using a murine hepatocellular carcinoma model, Zhang and colleagues (Zhang et al. 2010) demonstrated that the remaining tumor debris induced by HIFU could be immunogenic, thus an effective vaccine to elicit tumor-specific immune responses. In this study, these included induction of CTL cytotoxic activity, enhanced activation of DCs and protection against lethal tumor challenge in naïve mice. When the tumor debris was loaded with immature DCs, it could significantly induce DC maturation, increase cytotoxicity and CTL TNF-α and IFN-γ secretion, thus initiating a host-specific immune response after H22 challenge in the vaccinated mice (Deng et al. 2010). Immediately after HIFU exposure to MC-38 colon adenocarcinoma cells *in-vitro*, the release of endogenous danger signals, including HSP60, was observed from the damaged cells. These signals could subsequently activate antigen-presenting cells (APCs), leading to an increased expression of co-stimulatory molecules and enhanced secretion of IL-12 by DCs and TNF-α by macrophages (Hu et al. 2005). In addition, HIFU could upregulate *in-vitro* and *ex-vitro* molecular expression of HSP70 (Kruse et al. 2008; Hundt et al. 2007). This is an intracellular molecular chaperone that can enhance tumor cell immunogenicity, resulting in potent cellular immune responses.

The potency of DC infiltration and activation following mechanical lysis and sparse-scan HIFU was much stronger than that from thermal necrosis and dense-scan HIFU exposure, suggesting that optimization of a HIFU ablation strategy may help in enhancing immune responses after treatment (Liu et al. 2010). Heat and acoustic cavitation are two major mechanisms involved in HIFU-induced tissue damage, while cavitation is a HIFU-unique effect when compared with other thermal ablation techniques. It causes membranous organelles to collapse, including mitochondria and endoplasmic reticulum, as well as cell and nuclear membranes. This breaks tumor cells up into small pieces, by which the tumor antigens can remain intact, or it may lead to the exposure of an immunogenic moiety that is normally hidden in tumor antigens. Zhou and colleagues (Zhou et al. 2007) used either heat-exposed or HIFU-treated H22 tumor vaccines to inoculate naïve mice. The vaccination times were four sessions once a week for four consecutive weeks, and each mouse was challenged with H22 tumor cells 1 week after the last vaccination. They found that the HIFU-treated tumor vaccine could significantly inhibit tumor growth and increase survival rates in the vaccinated mice, suggesting that acoustic cavitation could play an important role in stimulating the host antitumor immune system.

Emerging clinical results revealed that systemic cellular immune response was observed in cancer patients after HIFU treatment, as shown in Table 8.3. Rosberger and colleagues (Rosberger et al. 1994) reported five consecutive cases of posterior choroidal melanoma treated with HIFU. Three patients had abnormal, and two patients normal $CD4^+/CD8^+$ ratios before treatment. One week after treatment, the ratio in two patients reverted to normal, while another was noted to have a 37 % increase in $CD4^+$ T cells relative to $CD8^+$ cells. Wang and Sun (2002) used multiple-session HIFU to treat 15 patients with late stage pancreatic cancer. Although there was

Table 8.3 Antitumor immune response to HIFU alone in clinical studies

Reference	Tumor/nb. patients	HIFU parameters	Endpoint	Results	Additional observations
Rosberger et al. (1994)	Choroidal melanoma /5	4.6 MHz 2 W/cm^2	Measurement of T cells & subsets in peripheral blood	$CD4^+/CD8^+$ ratio reverted to normal after HIFU in 2 of 3 patients with previously abnormal $CD4^+/CD8^+$ ratio	37 % increase in $CD4^+$ relative to $CD8^+$ in the remaining one patient
Wang and Sun (2002)	Pancreatic cancer/15	0.5–1.6 kW 30–80 s	Measurement of T cells, subsets, NK cell activity in peripheral blood	A significant increase in NK cell activity after HIFU treatment	An increase in $CD3^+$, $CD4^+$ & $CD4^+/CD8^+$ ratios in 10 patients after HIFU treatment, but not statistically significant
Wu et al. (2004)	Osteosarcoma/6 Hepatocarcinoma/5 Renal cell carcinoma/5	0.8 MHz 5–20 kW/cm^2	Measurement of circulating NK, T cells & subsets	A significant increase in $CD4^+$ & $CD4^+/CD8^+$ ratios after HIFU treatment	The abnormal levels of $CD3^+$ returned to normal in 2 patients, $CD4^+/CD8^+$ ratios in 3 patients, $CD19^+$ in 1 patient & NK cells in 1 patient
Zhou et al. (2008)	Liver cancer/13 Sarcoma/3	0.8 MHz 5–20 kW/cm^2	Measurement of serum immunosuppressive cytokines in peripheral blood	A significant decrease in serum VEGF, TGF-β1 & β-2 levels after HIFU treatment	
Madersbacher et al. (1998)	Prostate cancer/5 Bladder cancer/4	4 MHz 1.26–2.2 kW/cm^2	Measurement of HSP-27 expression in HIFU-treated tumor and prostate tissue	A significant increase of HSP-27 expression after HIFU treatment compared to the controls	
Kramer et al. (2004)	Prostate cancer/6	4 MHz 1.26–2.2 kW/cm^2	Measurement of HSP expression & Th1- & Th2-cytokine release from TILs in HIFU-treated tumor	A significant upregulated expression of HSP-72, HSP-73, glucose GRP-75 & GRP-78 Significant increase in TIL-released IL-2, IFN-γ & TNF-α after HIFU treatment	A significant decrease in TIL-released Th2-cytokines (IL-4, -5, -10) after HIFU treatment

Wu et al. (2007a, b)	Breast cancer/23	4 MHz 1.26–2.2 kW/cm^2	Measurement of expression of 13 proteins on tumor cells including HSPs	100 % positive rate of HSP-70 in HIFU-treated cancer cells compared to the control	Varied expressions of ER, PR, CA15-3, VEGF, TGF-β1, TGFβ2, IL-6, IL-10 and EMA in HIFU treated tumor, with no expression of PCNA, MMP-9 and CD44v6
Xu et al. (2009)	Breast cancer/23	4 MHz 1.26–2.2 kW/cm^2	Measurement of APC infiltration & activation in HIFU-treated tumor	A significant increase in local infiltration & activation of DCs & macrophages compared to the control	
Liu et al. (2010)	Breast cancer/23	4 MHz 1.26–2.2 kW/cm^2	Measurement of TIL infiltration & activation in HIFU-treated tumor	A significant decrease in tumor-infiltrating $CD3^+$, $CD4^+$, $CD8^+$, $CD4^+/CD8^+$, B lymphocytes, NK cells, $FasL^+$, $Granzyme^+$ and $perforin^+$ TILs when compared with the control	

an increase in average numbers of NK cells, T lymphocytes and subsets in ten patients after HIFU treatment, a significant statistical difference was only observed in NK cell activity before and after HIFU treatment ($p<0.05$). Wu and colleagues (Wu et al. 2004) observed changes in circulating NK, T lymphocyte and subsets in 16 patients with solid malignancy before and after HIFU treatment. The results showed a significant increase in the $CD4^+$ T lymphocyte population ($p<0.01$) and the ratio of $CD4^+/CD8^+$ cells ($p<0.05$) after HIFU treatment. The abnormal levels of $CD3^+$ lymphocytes returned to normal in two patients, $CD4^+/CD8^+$ ratio in three patients, $CD19^+$ lymphocytes in one patient and NK cells in one patient, in comparison to the values in the control group. In addition, serum levels of immunosuppressive cytokines, including VEGF, TGF-β1 and TGF-β2, were significantly decreased in peripheral blood of cancer patients after HIFU treatment, indicating that HIFU may decrease tumor-induced immunosuppression and renew host antitumor immunity (Zhou et al. 2008).

Clinical evidence suggests that HIFU treatment may also enhance local antitumor immunity in cancer patients. Kramer and colleagues (Madersbacher et al. 1998; Kramer et al. 2004) found that HIFU treatment could alter the presentation of tumor antigens in prostate cancer patients, which was most likely to be stimulatory. Histological examination showed significantly upregulated expression of HSP72, HSP73 and glucose regulated protein (GRP) 75 and 78 at the border zone of HIFU treatment in prostate cancer. Heated prostate cancer cells exhibited increased Th1-cytokine (IL-2, IFN-γ, TNF-α) release, but decreased Th2-cytokine (IL-4, -5, -10) release from tumor infiltrating lymphocytes (TIL). The upregulated expression of HSP70 was confirmed in the tumor debris of breast cancer after HIFU ablation (Wu et al. 2007a, b), indicating that HIFU may modify tumor antigenicity to produce a host immune response.

Xu and colleagues (2009) found the number of tumor-infiltrating APCs, including DCs and macrophages, increased significantly along the margin of HIFU-treated human breast cancer, with an increased expression of HLA-DR, CD80 and CD86 molecules. Activated APCs may take up the HSP-tumor peptide complex, which remains in the tumor debris and present the chaperoned peptides directly to tumor-specific T lymphocytes with high efficiency, resulting in potent cellular immune responses against tumor cells after HIFU treatment.

Furthermore, HIFU could induce significant infiltration of TILs in human breast cancer, including $CD3^+$, $CD4^+$, $CD8^+$, B lymphocytes and NK cells. The number of the activated CTLs expressing $FasL^+$, $granzyme^+$ and $perforin^+$ significantly increased in the HIFU-treated tumor, suggesting that specific cellular antitumor immunity could be locally triggered after HIFU treatment (Lu et al. 2010).

8.4.2 Radiofrequency Ablation

With regards to minimally invasive therapies, RFA is only one technique that has been widely used in the clinical management of solid tumors, particularly in hepatocellular carcinoma (HCC). As coagulative necrosis is immediately induced in a targeted tumor after thermal ablation, necrotic cell death can be recognized by the immune system as a result of dangerous events, according to the "danger" model of immunity by Matzinger (Gallucci et al. 1999; Matzinger 2002). It is also accompanied by the release of "danger signals" from the heat-stressed cells, such as acute phase proteins, pro-inflammatory cytokines and heat shock proteins (HSPs), thus developing a temporary inflammatory stress. This stress may be associated with positive processes similar to the healing of injured tissues, but could also lead to the stimulation of tumor growth (Gravante et al. 2009). After RFA treatment, a moderate and temporary systemic inflammatory response has been observed in cancer patients, as demonstrated by the increase in plasma levels of pro-inflammatory cytokines and acute phase reactants (Evrard et al. 2007a, b; Schell et al. 2002; Meredith et al. 2007; Schueller et al. 2003; Fietta et al. 2009).

HSPs are families of highly conserved proteins involved in mechanisms of cell repair. They

are intracellular molecular chaperones that physiologically bind tumor peptide antigens and enhance tumor cell immunogenicity (Pockley 2003). APCs take up HSP-tumor peptide complex and present the chaperoned peptides directly to tumor-specific T lymphocytes with high efficiency, resulting in potent cellular immune responses against tumor cells (Todryk et al. 2003). Around the necrotic ablated area, RFA produced sub-lethal injury in the zone of transition that showed apoptosis, and increased HSP70 expression in the liver of normal swine (Schueller et al. 2004). Schueller and colleagues found that there was an increased synthesis and cell surface expression of HSPs (HSP70, 90) after RFA in nude rats bearing human hepatocellular carcinoma (Rai et al. 2005). In addition, large amounts of tumor debris could induce local infiltration of activated DCs, the most potent APC for induction of adaptive immunity against cancer (Melief 2008). Activating signals, including necrotic tumor cells and HSPs, could induce the progression of infiltrating DCs from an immature to a mature stage, resulting in the presentation of tumor antigens by mature DCs to naïve T lymphocytes in a MHC-restricted fashion (Lutz and Schuler 2002). Ali and colleagues demonstrated that a transient function of myeloid DCs could be activated in HCC patients 7–14 days after RFA, with an increased ability to stimulate $CD4^+$ T cells (Ali et al. 2005). Up to 7 % of DCs present in the draining lymph nodes contained tumor antigens in the ablated tumor after RFA. Compared to untreated HCC and normal liver tissue, expression of costimulatory molecules, such as CD80 and CD86, was significantly enhanced by incubation with RFA-treated HCC (den Brok et al. 2006). Similar results were also demonstrated by Zerbini and colleagues (2008) in HCC patients; indicative that local tumor ablation could lead to efficient antigen loading, migration and maturation of APCs, including DCs and monocytes. Direct evidence has recently been found that RFA could induce weak tumor-induced immunity in a murine tumor model harboring APC infiltration and amplification, and that enhanced systemic antitumor T cell immune responses and tumor regression was associated with increased infiltration of DCs after subtotal RF ablation (Dromi et al. 2009). These results suggest that the generation of heat-altered tumor antigens, in combination with the "dangerous signals", may help to overcome immune tolerance or allergy towards the remaining tumor.

The effects of RFA on antitumor T cell responses have been studied in animal models. A local influx of immune cells was observed after RFA in tumor-free domestic pigs and in the livers of rabbits implanted with epithelial tumors (Hänsler et al. 2002). The latter was located in the periphery of the coagulated area, and consisted of lymphocytic and plasma cell infiltrates. Concomitantly, a specific T cell proliferative response to the tumor cells was also detected in the peripheral blood of RFA-treated animals (Wissniowski et al. 2003). Den Brok and colleagues (2004) found that a weak, but detectable, immune response was present after RFA in mice bearing ovalbumin-transfected melanoma. This antitumor immunity was mediated by antigen-specific $CD8^+$ T cells, and adoptive transfer of splenocytes could induce partial protection against tumor challenge in syngenic mice. Compared to surgical resection and control groups, RFA could efficiently stimulate activation and proliferation of splenocytes in mice bearing H22 tumor, and the cytotoxicity of splenocytes to tumor cells was significantly enhanced in RFA-treated animals, with an increased secretion of IL-2 and IFN-gamma (Zhang et al. 2006). After *in-situ* RFA of liver tumor, resistance to local and systemic tumor rechallenge was increased in mice bearing CC531 colon carcinoma (van Duijnhoven et al. 2005). However, no inhibitory effect on tumor growth was observed in the nearby untreated liver tumors.

Similar results have been also demonstrated in cancer patients treated with RFA. Zerbini and colleagues (2006) showed convincing evidence that RFA could activate a systemic antitumor T cell response in 20 HCC patients. Using an ELISPOT assay, the reactivity of circulating T cells to autologous HCC lysate was assessed before and after RFA treatment. They found that the specific T cell response was increased in three patients immediately after RFA, compared to no

patients before treatment. Importantly, this boosting effect still persisted at 4 weeks after RFA, and the number of patients showing the same T cell response increased up to nine. These data were confirmed by another study where both HCC and colorectal liver metastasis were treated with RFA (Hänsler et al. 2006). After RFA treatment, both HCC and colorectal cancer cells could significantly stimulate a specific immune response, resulting in an increase of circulating $CD4^+$ and $CD8^+$ T cells and cytotoxic activity. In contrast, one study observed a decrease in circulating $CD3^+$ and $CD4^+$ T cells after RFA treatment in metastatic cancer patients, together with no change in HCC patients. However, RFA induced trafficking of naïve and memory $CD62L^+$ T cells from the circulation to tissues, and enhanced the function of T cells, including *in-vitro* responses to phytohaemagglutinin (PHA) and tumor associated MUC1 antigen (Napoletano et al. 2008).

In order to improve the RFA-induced weak immune response, the combination of RFA with immunotherapy has been investigated in laboratory settings. RFA could be efficiently combined with immune modulation by anti-CTLA-4 antibodies or regulatory T cell depletion. These combination treatments protected mice from the outgrowth of tumor challenges and led to *in-vivo* enhancement of tumor-specific T cell numbers, which produced more IFN-γ upon activation (den Brok et al. 2006). Saji and colleagues (2006) demonstrated that RFA, plus intratumoral injection of naïve DCs, could induce DC migration to regional lymph nodes and induce adoptive antitumor immunity in a mouse tumor model. The combination of RFA with IFN injection could significantly increase antitumor effects in an orthotopic murine model with squamous cell carcinoma, upon comparison with single therapy and control groups (Saito et al. 2005). In this study, the RFA treatment stimulated tumor specific T cells to move to tumor sites, whereas IFN activated DCs and enhanced antigen presentation. All of the mice survived for 50 days in the combined therapy group. Using both neu-overexpressing mouse mammary carcinoma in FVBN202 transgenic mice and 4 T1 tumors in Balb/c mice, RFA treatment was followed by the administration of intratumor IL-7 and IL-15. This induced immune responses against tumors, inhibited tumor development and lung metastasis, and reduced myeloid-derived suppressor cells (Habibi et al. 2009).

8.4.3 Laser Ablation

In addition to local destruction with thermal energy, LA can induce an immunogenic effect on cancer in both animal tumor models and cancer patients. Compared to surgical resection, LA could reduce metastatic liver tumor spread in rats bearing a liver adenocarcinoma (Möller et al. 1998). Furthermore, with HSP70 shifts from the cytoplasm to the nucleus in LA-treated liver cancer cells, an increase in HSP70 immunoreactivity in tumors was observed, leading to increased numbers of tumor-infiltrating macrophages and an increased presence of HSP70 in the membrane and cytoplasm of these macrophages (Ivarsson et al. 2003). LA could also induce a significant increase in HSP70 expression in the colorectal liver metastasis mouse model (Nikfarjam et al. 2005a, b, c) and prostate cancer (Paulus et al. 1993; Rylander et al. 2006). While two independent adenocarcinomas were implanted into both lobes of the liver in rats (one as a control in the right and one treated with LA in the left lobe), the control tumor volumes were significantly smaller in the LA group than those in the hepatic resection group. The expression of CD8 and B7-2 (CD86) was significantly higher in the control tumor after LA (Isbert et al. 2004). Moreover, compared to surgical extirpation, complete eradication of reimplanted tumor, as well as increased local infiltration of ED1 macrophages and CD8 lymphocytes, were observed in the LA group 48 days after tumor challenge (Ivarsson et al. 2005). Overall, this suggests that LA could enhance antitumor immune response to eradicate a challenging tumor, which might be associated with increased numbers of tumor-infiltrating macrophages and CD8+ lymphocytes.

Immunological assays followed by LA procedure for cancer patients are still limited in the clinical setting. An early systemic inflammatory reaction was observed after LA in patients with

malignant liver tumors (Kallio et al. 2006). Serum level of IL-6, TNFRI and CRP increased significantly up to 72 h after LA procedure, while the TNF-α, IL-1β and IL-10 levels remained unchanged. Using an IFN-γ secretion assay and flow cytometry, Vogl and colleagues (2009) studied peripheral T lymphocyte ($CD3^+$, $CD4^+$, $CD8^+$) activation against autologous tumor tissue, and T cell cytotoxicity against allogenic colorectal cancer cells (CaCo). This was carried out before and after LA in patients with liver metastases of colorectal cancer. They found that tumor-specific cytotoxic T cell stimulation was detected after LA treatment, with a significant increase in cytolytic activity against CaCo cells, indicative that LA could trigger T lymphocyte-mediated antitumor immune response against autologous tumor tissue in patients.

8.4.4 Cryoablation

In the early introduction of cryoablation to clinical practice, there were occasional reports of patients with spontaneous regression of tumor metastases after ablation of a primary tumor, suggesting a potential systemic benefit to a local therapy (Sabel 2009). However, the mechanisms behind the existence of a cryo-immunologic response were unclear because immunologic assays were limited at the time of many of these observations. Subsequently, an immune response induced by cryoablation was investigated using a variety of animal tumor models. The results revealed that tumor-specific immunity, as measured by resistance to rechallenge in tumor-bearing animals undergoing cryoablation of primary tumor, was significantly greater in the cryoablation-treated animals when compared with surgical excision or naïve animals (Redondo et al. 2007; den Brok et al. 2006; Sabel et al. 2005). In addition, cryoablation could significantly inhibit the growth of contralateral tumors (Joosten et al. 2001; Shibata et al. 1998), and reduce metastatic deposits in the lung and liver in tumor-bearing animals (Müller et al. 1985; Urano et al. 2003).

On the contrary, some studies found that cryoablation failed to induce antitumor immune responses. There was no significant inhibition on secondary tumor growth after rechallenge in cryotreated rats (Hoffmann et al. 2001). Cryoablation alone couldn't directly cause a tumor-specific CTL response and a protective anti-metastatic impact when compared to cryotherapy combined with subsequent *in-situ* injection of immature DCs (Udagawa et al. 2006; Machlenkin et al. 2005). Moreover, immunosuppressive effects induced by cryoablation on host antitumor immunity were also observed in tumor-bearing animals, resulting in a decreased resistance to a secondary tumor challenge and an increase in pulmonary metastases after cryoablation (Shibata et al. 1998; Hanawa 1993; Miya et al. 1987). This has led to controversy whether a cryo-immunologic response would exist after cryoablation of malignant tissue.

Recently, due to a better understanding of the relationships between the innate and adaptive arms of the immune response, more detailed studies of the mechanism behind cryoimmunology have offered insight into why cryoablation may alternate between immune enhancement and immune suppression. It is evident that several changes induced by cryoablation (cytokine profile, availability of tumor antigens processed by APCs, mechanism of cell death (apoptosis or necrosis)), and the subsets of phagocytic cells (DCs or macrophages) responsible for ablated cell clearance, may either positively or negatively impact the immune response (Sabel 2009). For instance, although apoptosis and necrosis are the primary mechanisms of tumor cell death, they have a significantly different impact on the immune response (Viorritto et al. 2007). Apoptosis results in the uptake of cellular debris without causing inflammation or releasing the intracellular contents. APCs that take up the apoptotic cells do not only not generate an immune response, but also can lead to clonal deletion and anergy (Viorritto et al. 2007; Peng et al. 2007; Savill et al. 2002; Liu et al. 2002). In contrast, necrotic cell death is characterized by cellular breakdown and release of intracellular contents, many of which are danger signals. These signals promote cross-presentation, maturation of DCs and ultimately the activation of antigen-specific T cells (Gallucci et al. 1999; Sauter et al. 2000; Skoberne et al. 2004). As both

necrosis and apoptosis play a role in tumor cell death after cryoablation, the relative contribution of necrosis and apoptosis in the death of the tumor cells may shift the immune response from stimulatory to suppressive. Cryoablative techniques that result in large areas of apoptotic cell death, as opposed to necrosis, may result in immunosuppression. However, some studies have suggested that apoptotic tumor cells may be superior to necrotic cells in stimulating an antitumor immune response (Rock et al. 2006; Scheffer et al. 2003; Schnurr et al. 2002).

In addition to animal models, some clinical studies have recently attempted to reveal how cryoablation has profound effects on the immune system in cancer patients. Osada and colleagues (2007) measured serum levels of IL- 2, IL-4, IL-6, IL-10, TNF-α and IFN-γ in 13 patients with unresectable hepatic tumors before and after cryoablation. Decreased levels of serum tumor markers and local tumor necrosis detected on CT scan were observed in all patients, including five cases who presented evidence of necrosis in metastatic tumors away from the treated lesions. Serum IL-6 level was increased in all patients after cryoablation, but no change in the IL-2 level was observed. There was a significant increase in serum TNF-α level and Th1/Th2 ratios in the patients showing necrosis of secondary tumors. The effects of cryoablation on humoral immune compartments were also analyzed by Ravindranath and colleagues (2002) in 35 patients with liver metastases originated from colon cancer. They found an increase in the production of IgM antibodies against tumor-released gangliosides. Interestingly, these antibodies were not significantly increased in patients undergoing RFA or routine surgery. Si and colleagues (2008) observed a specific cytotoxic T cell response induced by cryoablation in 20 patients with high-risk prostate cancer. Four weeks after cryoablation, there was a significant increase in serum TNF-α and IFN-γ levels, as well as Th1/Th2 ratios, when compared with the values before cryoablation. However, no changes were observed in the serum levels of IL-4 or IL-10. Tumor-specific T cell responses were significantly increased 4 weeks after cryoablation, while peripheral blood mononuclear cells were co-incubated with human prostate cancer cells (LNCaP), indicating that cryoablation could improve tumor-specific cytolytic activity of CTLs in prostate cancer patients. This immune response was only sufficiently maintained for a period of 4 weeks. However, when cryoablation was combined with granulocyte macrophage colony-stimulating factor (GM-CSF) administration to treat metastatic hormone refractory prostate cancer, the response could last for at least 8 weeks (Si et al. 2009).

For the case of freezing large tumors, cryoablation may cause a serious complication known as "cryoshock", a syndrome of coagulopathy, disseminated intravascular coagulation and multiorgan failure (Seifert and Junginger 2004). As it is similar to those observed after endotoxin administration and other systemic inflammatory stimuli, cryoshock is believed to be caused by the systemic release of inflammatory cytokines after cryoablation, including IL-1, IL-6 and TNF-α (Chapman et al. 2000a, b, c; Sadikot et al. 2002; Seifert et al. 2002). This is different from the RFA-treated liver tissue, where there is a coagulative destruction of the hepatocyte organelles within an intact plasma membrane (Chapman et al. 2000a, b, c). Cryoshock remains rare in the cryoablation of renal and prostate tumors, but a more common side effect of hepatic cryoablation.

8.4.5 Microwave Ablation

The effect of microwaves on immune cells was initially investigated in murine B16 melanoma models. Microwave hyperthermia, in combination with ethanol injection, could significantly prolong the survival of the tumor bearing mice with an increased infiltration of T lymphocytes and NK cells in the ablated melanoma (Nakayama et al. 1997a, b). Whole body microwave hyperthermia could cause a significant enhancement in TNF-α secretion in murine peritoneal macrophages and splenic T lymphocytes (Fesenko et al. 1999). Yao and Yang (2007) found that a murine CT-26 tumor treated with microwave ablation could sensitize immature DCs, which subsequently induced *in-vitro* proliferation of T cells and activated CTL cytotoxicity. In addition, the sensitized DCs could significantly inhibit *in-vivo* tumor growth and prolong the survival of the mice.

Clinical studies related to the immune response were initially conducted on prostate cancer treated by microwave energy. A transient, yet significant increase in the $CD4^+/CD8^+$ ratio, PHA and Con-A transformation indices was observed after microwave hyperthermia in 15 prostate cancer patients, and the peak effect of this immune response was noted at 2 months, followed by a subsequent decrease (Szmigielski et al. 1991). Fan and colleagues (1996) treated 58 patients with malignant bone tumors by surgical procedure in combination with microwave hyperthermia and adjuvant immunotherapy. The immune response, including T cell subsets, IL-2 and sIL-2, was monitored 3–38 months (mean 19 months) after the combined therapies. The immune function was significantly improved in the majority of the patients, though oncologic outcome was similar to that obtained by limb-saving procedure.

The MWA-induced immune response was studied in majority by Dr Dong and colleagues in 78 patients with hepatocellular carcinoma. Ultrasound-guided core needle biopsy was performed after treatment for determining the local infiltration of immunocytes within the treated lesion. The results demonstrated a significantly increased infiltration of T lymphocytes, memory T lymphocytes, NK cells and monocytes in the ablated tumor, with no change in B lymphocytes, suggesting that MWA could only enhance cellular immune response in HCC patients (Zhang et al. 2002; Dong et al. 2002, 2003). This response was maximal on the third day after thermal ablation, but persisted to day 30. The extent of infiltration was negatively related to serum α-fetoprotein and tumor size (Dong et al. 2002). However, interestingly, patients with a high degree of immune cell infiltration in the treated tumor had lower recurrence rates than those with low levels of infiltration, and there is a statistically significant correlation between survival outcome and the extent of immunocyte infiltration (Dong et al. 2003). In addition, IL-6 serum levels, IL-1ra and C-reactive protein were significantly elevated 1 day after laparoscopic MWA, and returned to the preoperative levels at day 7 postoperatively (Sadamori et al. 2003). Furthermore, MWA combined with either local injection of staphylococin, or oral uptake of Shenqi (a Chinese herb) mixture, could enhance the cellular immune response once compared with the control group, improving survival time and reducing local recurrence in HCC patients (Lin et al. 2005; Han et al. 2009).

Conclusion

As a minimally invasive therapy, thermal ablation has been increasingly used in clinical practice for the local treatment of solid malignancy. Beyond optimization of technical and physiological parameters, it is clear that thermal ablation should be undertaken when there is precise knowledge not only of the number and location of the lesions, but also of the biological characteristics and natural history of the tumor. The goal of tumor therapy is that all cancer cells should be completely killed in the patient's body. A similar multidisciplinary approach including other modalities is important in the treatment of solid malignancies. For patients with cancer, the therapeutic strategy for the disease should be a multiple treatment plan, which includes local treatments, such as surgery and radiotherapy, and systemic therapy, such as chemotherapy and immunotherapy. Thus, success achieved in the application of thermal ablation is mainly dependent not only on the ablation technique, but also on a better understanding of the natural characteristics of tumors.

A review of the literature strongly supports academic evidence that thermal ablation may elicit a systemic antitumor immune response. It may lead to a post-ablative procedure that reduces, or perhaps eliminates distant disease, and prevents local recurrence through the immune system in cancer patients who have had original dysfunction of antitumor immunity after ablation. Evidence ranges from anecdotal observations in a clinical setting, a variety of animal models and correlative immune studies in patients undergoing thermal ablation. It is not surprising that there is great concern about a close relationship between thermal ablation and antitumor immune response, as thermal ablation may have the potential to be both local and systemic therapies. However, the generation of an antitumor immune response is complex, and

several factors can not only preclude the development of a positive response, but tilt that response towards immunosuppression that is observed in cryoablation. As the clinical use of thermal ablation expands, it becomes increasingly crucial that we better understand the means by which thermal ablation modulates the immune system in cancer patients.

Although the mechanism for ablation-induced immunologic changes is still unclear, several possibilities have been hypothesized based on previous study results. Firstly, host immune suppression, induced by tumor cells, may be decreased or relieved after thermal ablation as the tumor is completely ablated, leading to renewed host antitumor immunity. Secondly, thermal ablation may modify tumor antigenicity and upregulate expression of HSPs, which act as tumor vaccines to produce potent cellular immune responses. Thirdly, cytokines are secreted by immune cells at the inflammatory margin of the ablation-treated region, presenting a milieu for the development of mature CTLs. Finally, large amounts of cellular debris are gradually phagocytized by macrophages and other cells that can function as APCs.

It is increasingly apparent that thermal ablation alone may not be sufficient to generate a clinically relevant immune response and to consistently stimulate the host immune system. A strategy to combine thermal ablation with active immunological stimulation, such as immunoadjuvants, may augment the efficacy of ablation-induced antitumor immunity specifically against the targeted tumors, if the tumor destruction releases tumor antigens or improves tumor immunogenicity. This combined approach may become an important part in the thermal ablation of solid malignancy.

References

Adams DO, Hamilton TA (1984) The cell biology of macrophage activation. Annu Rev Immunol 2:283–318

Ali MY, Grimm CF, Ritter M, Mohr L, Allgaier HP, Weth R, Bocher WO, Endrulat K, Blum HE, Geissler M (2005) Activation of dendritic cells by local ablation of hepatocellular carcinoma. J Hepatol 43:817–822

Babaian RJ, Donnelly B, Bahn D, Baust JG, Dineen M, Ellis D, Katz A, Pisters L, Rukstalis D, Shinohara K, Thrasher JB (2008) Best practice statement on cryosurgery for the treatment of localized prostate cancer. J Urol 180:1993–2004

Barry MA, Behnke CA, Eastman A (1990) Activation of programmed cell death (apoptosis) by cisplatin, other anticancer drugs, toxins and hyperthermia. Biochem Pharmacol 40:2353–2362

Beland M, Mueller PR, Gervais DA (2007) Thermal ablation in interventional oncology. Semin Roentgenol 42:175–190

Benndorf R, Bielka H (1997) Cellular stress response: stress proteins – physiology and implications for cancer. Recent Results Cancer Res 143:129–144

Cabibbo G, Latteri F, Antonucci M, Craxì A (2009) Multimodal approaches to the treatment of hepatocellular carcinoma. Nat Clin Pract Gastroenterol Hepatol 6:159–169

Carrafiello G, Laganà D, Mangini M, Fontana F, Dionigi G, Boni L, Rovera F, Cuffari S, Fugazzola C (2008) Microwave tumors ablation: principles, clinical applications and review of preliminary experiences. Int J Surg 6:S65–S69

Chapman WC, Debelak JP, Blackwell TS, Gainer KA, Christman JW, Pinson CW, Brigham KL, Parker RE (2000a) Hepatic cryoablation, but not radiofrequency ablation, results in lung inflammation. Arch Surg 135:667–672

Chapman WC, Debelak JP, Blackwell TS, Gainer KA, Christman JW, Pinson CW, Brigham KL, Parker RE (2000b) Hepatic cryoablation-induced acute lung injury: pulmonary hemodynamic and permeability effects in a sheep model. Arch Surg 135:667–672

Chapman WC, Debelak JP, Wright Pinson C, Washington MK, Atkinson JB, Venkatakrishnan A, Blackwell TS, Christman JW (2000c) Hepatic cryoablation, but not radiofrequency ablation, results in lung inflammation. Ann Surg 231:752–761

Chaussy C, Thuroff S, Rebillard X, Gelet A (2005) Technology insight: high-intensity focused ultrasound for urologic cancers. Nat Clin Pract Urol 2:191–198

Clement GT (2004) Perspectives in clinical uses of high-intensity focused ultrasound. Ultrasonics 42: 1087–1093

Curley SA (2001) Radiofrequency ablation of malignant liver tumors. Oncologist 6:14–23

Decadt B, Siriwardena AK (2004) Radiofrequency ablation of liver tumours: systematic review. Lancet Oncol 5:550–560

Decker T, Lohmann-Matthes ML, Karck U, Peters T, Decker K (1989) Comparative study of cytotoxicity, tumor necrosis factor, and prostaglandin release after stimulation of rat Kupffer cells, murine Kupffer cells, and murine inflammatory liver macrophages. J Leukoc Biol 45:139–146

den Brok MH, Sutmuller RP, van der Voort R, Bennink EJ, Figdor CG, Ruers TJ, Adema GJ (2004) In situ tumor ablation creates an antigen source for the generation of antitumor immunity. Cancer Res 64:4024–4029

den Brok MH, Sutmuller RP, Nierkens S, Bennink EJ, Frielink C, Toonen LW, Boerman OC, Figdor CG, Ruers TJ, Adema GJ (2006) Efficient loading of dendritic cells following cryo and radiofrequency ablation in combination with immune modulation induces antitumor immunity. Br J Cancer 95:896–905

Deng J, Zhang Y, Feng J, Wu F (2010) Dendritic cells loaded with ultrasound-ablated tumour induce in vivo specific antitumour immune responses. Ultrasound Med Biol 36:441–448

Dewey WC (1994) Arrhenius relationships from the molecule and cell to the clinic. Int J Hyperthermia 10:457–483

Diederich CJ, Hynynen K (1999) Ultrasound technology for hyperthermia. Ultrasound Med Biol 25:871–887

Dong B, Zhang J, Liang P, Yu X, Su L, Yu D, Ji X, Yu G, Yin Z (2002) Influencing factors of local immunocyte infiltration in hepatocellular carcinoma tissues pre-and post-percutaneous microwave coagulation therapy. Zhonghua Yi Xue Za Zhi 82:393–397

Dong BW, Zhang J, Liang P, Yu XL, Su L, Yu DJ, Ji XL, Yu G (2003) Sequential pathological and immunologic of percutaneous microwave coagulation therapy of hepatocellular carcinoma. Int J Hyperthermia 19:119–133

Dromi SA, Walsh MP, Herby S, Traughber B, Xie J, Sharma KV, Sekhar KP, Luk A, Liewehr DJ, Dreher MR, Fry TJ, Wood BJ (2009) Radiofrequency ablation induces antigen-presenting cell infiltration and amplification of weak tumor-induced immunity. Radiology 251:58–66

Dumot JA, Greenwald BD (2008) Argon plasma coagulation, bipolar cautery, and cryotherapy: ABC's of ablative techniques. Endoscopy 40:1026–1032

Emami B, Song CW (1984) Physiological mechanisms in hyperthermia: a review. Int J Radiat Oncol Biol Phys 10:289–298

Evrard S, Menetrier-Caux C, Biota C, Neaud V, Mathoulin-Pélissier S, Blay JY, Rosenbaum J (2007) Cytokines pattern after surgical radiofrequency ablation of liver colorectal metastases. J Gastroenterol Clin Biol 31: 141–145

Fagnoni FF, Zerbini A, Pelosi G, Missale G (2008) Combination of radiofrequency ablation and immunotherapy. Front Biosci 13:369–381

Fan Q, Ma B, Guo A, Li Y, Ye J, Zhou Y, Qiu X (1996) Surgical treatment of bone tumors in conjunction with microwave-induced hyperthermia and adjuvant immunotherapy. A preliminary report. Chin Med J 109:425–431

Fesenko EE, Makar VR, Novoselova EG, Sadovnikov VB (1999) Microwaves and cellular immunity. I. Effect of whole body microwave irradiation on tumor necrosis factor production in mouse cells. Bioelectrochem Bioenerg 49:29–35

Fietta AM, Morosini M, Passadore I, Cascina A, Draghi P, Dore S, Rossi R, Pozzi E, Meloni F (2009) Systemic inflammatory response and downmodulation of peripheral CD25+ Foxp3+ T-regulatory cells in patients undergoing radiofrequency thermal ablation for lung cancer. Hum Immunol 70:477–486

Gallucci S, Lolkema M, Matzinger P (1999) Natural adjuvants: endogenous activators of dendritic cells. Nat Med 5:1249–1255

Germer CT, Roggan A, Ritz JP, Isbert C, Albrecht D, Muller G, Buhr HJ (1998a) Optical properties of native and coagulated human liver tissue and liver metastases in the near infrared range. Lasers Surg Med 23:194–203

Germer C, Isbert CM, Albrecht D, Ritz JP, Schilling A, Roggan A, Wolf KJ, Muller G, Buhr H (1998b) Laser-induced thermotherapy for the treatment of liver metastasis. Correlation of gadolinium-DTPA-enhanced MRI with histomorphologic findings to determine criteria for follow-up monitoring. Surg Endosc 12:1317–1325

Goldberg SN, Gazelle GS, Halpern EF, Rittman WJ, Mueller PR, Rosenthal DI (1996) Radiofrequency tissue ablation: importance of local temperature along the electrode tip exposure in determining lesion shape and size. Acad Radiol 3:212–218

Goldberg SN, Gazelle GS, Mueller PR (2000) Thermal ablation therapy for focal malignancy: a unified approach to underlying principles, techniques, and diagnostic imaging guidance. AJR Am J Roentgenol 174:323–331

Goldberg SN, Grassi CJ, Cardella JF, Charboneau JW, Dodd GD, Dupuy DE, Gervais D, Gillams AR, Kane RA, Lee FT, Livraghi T, McGahan J, Phillips DA, Rhim H, Silverman SG (2005) Image-guided tumor ablation: standardization of terminology and reporting criteria. Radiology 235:728–739

Gough-Palmer AL, Gedroyc WM (2008) Laser ablation of hepatocellular carcinoma – a review. World J Gastroenterol 14:7170–7174

Gravante G, Sconocchia G, Ong SL, Dennison AR, Lloyd DM (2009) Immunoregulatory effects of liver ablation therapies for the treatment of primary and metastatic liver malignancies. Liver Int 29:18–24

Habibi M, Kmieciak M, Graham L, Morales JK, Bear HD, Manjili MH (2009) Radiofrequency thermal ablation of breast tumors combined with intralesional administration of IL-7 and IL-15 augments anti-tumor immune responses and inhibits tumor development and metastasis. Breast Cancer Res Treat 114:423–431

Hafron J, Kaouk JH (2007) Ablative techniques for the management of kidney cancer. Nat Clin Pract Urol 4:261–269

Han XJ, Dong BW, Liang P, Yu XL, Yu DJ (2009) Local cellular immune response induced by ultrasound-guided tumor bed superantigen injection after percutaneous microwave coagulation therapy for liver cancer. Zhonghua Zhong Liu Za Zhi 31:602–606

Hanawa S (1993) An experimental study on the induction of anti-tumor immunological activity after cryosurgery for liver carcinoma, and the effect of concomitant immunotherapy with OK432. Nippon Geka Gakkai Zasshi 94:57–65

Hänsler J, Neureiter D, Strobel D, Müller W, Mutter D, Bernatik T, Hahn EG, Becker D (2002) Cellular and vascular reactions in the liver to radiofrequency thermo-ablation with wet needle applicators. Study on juvenile domestic pigs. Eur Surg Res 34:357–363

Hänsler J, Wissniowski TT, Schuppan D, Witte A, Bernatik T, Hahn EG, Strobel D (2006) Activation and dramatically increased cytolytic activity of tumor specific T lymphocytes after radio-frequency ablation in patients with hepatocellular carcinoma and colorectal liver metastases. World J Gastroenterol 12:3716–3721

Heisterkamp J, van Hillegersberg R, Sinofsky E, Ijzermans JN (1997) Heat-resistant cylindrical diffuser for interstitial laser coagulation: comparison with the bare-tip fiber in a porcine liver model. Lasers Surg Med 20: 304–309

Hill CR, ter Haar GR (1995) Review article: high intensity focused ultrasound – potential for cancer treatment. Br J Radiol 68:1296–1303

Hoffmann NE, Coad JE, Huot CS, Swanlund DJ, Bischof JC (2001) Investigation of the mechanism and the effect of cryoimmunology in the Copenhagen rat. Cryobiology 41:59–68

Hong K, Georgiades CS, Geschwind JF (2006) Technology insight: image-guided therapies for hepatocellular carcinoma—intra-arterial and ablative techniques. Nat Clin Pract Oncol 3:315–324

Hori K, Mihich E, Ehrke MJ (1989) Role of tumor necrosis factor and interleukin 1 in gamma-interferon-promoted activation of mouse tumoricidal macrophages. Cancer Res 49:2606–2614

Hu Z, Yang XY, Liu Y, Morse MA, Lyerly HK, Clay TM, Zhong P (2005) Release of endogenous danger signals from HIFU-treated tumor cells and their stimulatory effects on APCs. Biochem Biophys Res Commun 335:124–131

Hu Z, Yang XY, Liu Y, Sankin GN, Pua EC, Morse MA, Lyerly HK, Clay TM, Zhong P (2007) Investigation of HIFU-induced anti-tumor immunity in a murine tumor model. J Transl Med 5:34

Hundt W, O' Connell-Rodwell CE, Bednarski MD, Steinbach S, Guccione S (2007) In vitro effect of focused ultrasound or thermal stress on HSP70 expression and cell viability in three tumor cell lines. Acad Radiol 14:859–870

Isbert C, Ritz JP, Roggan A, Schuppan D, Ruhl M, Buhr HJ, Germer CT (2004) Enhancement of the immune response to residual intrahepatic tumor tissue by laser-induced thermotherapy (LITT) compared to hepatic resection. Lasers Surg Med 35:284–292

Ivarsson K, Myllymäki L, Jansner K, Bruun A, Stenram U, Tranberg KG (2003) Heat shock protein 70 (HSP70) after laser thermotherapy of an adenocarcinoma transplanted into rat liver. Anticancer Res 23:3703–3712

Ivarsson K, Myllymäki L, Jansner K, Stenram U, Tranberg KG (2005) Resistance to tumor challenge after tumor laser thermotherapy is associated with a cellular immune response. Br J Cancer 93:435–440

Joosten JJ, Muijen GH, Wobbes T, Ruers TJ (2001) In vivo destruction of tumor tissue by cryoablation can induce inhibition of secondary tumor growth: an experimental study. Cryobiology 41:49–58

Kallio R, Sequeiros R, Surcel HM, Ohtonen P, Kiviniemi H, Syrjälä H (2006) Early cytokine responses after percutaneous magnetic resonance imaging guided laser thermoablation of malignant liver tumors. Cytokine 34:278–283

Kennedy JE (2005) High-intensity focused ultrasound in the treatment of solid tumors. Nat Rev Cancer 5:321–327

Kirn A, Bingen A, Steffan AM, Wild MT, Keller F, Cinqualbre J (1982) Endocyticcapacities of Kupffer cells isolated from the human adult liver. Hepatology 2:216–222

Kramer G, Steiner GE, Grobl M, Hrachowitz K, Reithmayr F, Paucz L, Newman M, Madersbacher S, Gruber D, Susani M, Marberger M (2004) Response to sublethal heat treatment of prostatic tumor cells and of prostatic tumor infiltrating T-cells. Prostate 58:109–120

Kruse DE, Mackanos MA, O'Connell-Rodwell CE, Contag CH, Ferrara KW (2008) Short-duration-focused ultrasound stimulation of Hsp70 expression in vivo. Phys Med Biol 53:3641–3660

Lau WY, Lai EC (2009) The current role of radiofrequency ablation in the management of hepatocellular carcinoma: a systematic review. Ann Surg 249:20–25

Liapi E, Geschwind JF (2007) Transcatheter and ablative therapeutic approaches for solid malignancies. J Clin Oncol 25:978–986

Lin JJ, Jin CN, Zheng ML, Ouyang XN, Zeng JX, Dai XH (2005) Clinical study on treatment of primary hepatocelluar carcinoma by Shenqi mixture combined with microwave coagulation. Chin J Integr Med 11:104–110

Liu K, Iyoda T, Saternus M, Kimura Y, Inaba K, Steinman RM (2002) Immune tolerance after delivery of dying cells to dendritic cells in situ. J Exp Med 196:1091–1097

Liu F, Hu Z, Qiu L, Hui C, Li C, Zhong P, Zhang J (2010) Boosting high-intensity focused ultrasound-induced anti-tumor immunity using a sparse-scan strategy that can more effectively promote dendritic cell maturation. J Transl Med 8:7

Lu P, Zhu XQ, Xu ZL, Zhou Q, Zhang J, Wu F (2009) Increased infiltration of activated tumor-infiltrating lymphocytes after high intensity focused ultrasound ablation of human breast cancer. Surgery 145:286–293

Lubbe AS, Bergemann C (1994) Ultrasound therapy for malignant tumors: a conceptual assessment. J Clin Ultrasound 22:113–117

Lutz MB, Schuler G (2002) Immature: semi-mature and fully mature dendritic cells: which signals induce tolerance or immunity? Trends Immunol 23:445–449

Machlenkin A, Goldberger O, Tirosh B, Paz A, Volovitz I, Bar-Haim E, Lee SH, Vadai E, Tzehoval E, Eisenbach L (2005) Combined dendritic cell cryotherapy of tumor induces systemic antimetastatic immunity. Clin Cancer Res 11:4955–4961

Madersbacher S, Gröbl M, Kramer G, Dirnhofer S, Steiner GE, Marberger M (1998) Regulation of heat

shock protein 27 expression of prostatic cells in response to heat treatment. Prostate 37:174–181
Maris H, Balibar S (2000) Negative pressures and cavitation in liquid helium. Phys Today 53:29–32
Matsumoto R, Selig AM, Colucci VM, Jolesz FA (1992) Interstitial Nd:YAG laser ablation in normal rabbit liver: trial to maximize the size of laser-induced lesions. Lasers Surg Med 12:650–658
Matzinger P (2002) The danger model: a renewed sense of self. Science 296:301–305
Melief CJ (2008) Cancer immunotherapy by dendritic cells. Immunity 29:372–383
Meredith K, Haemmerich D, Qi C, Mahvi D (2007) Hepatic resection but not radiofrequency ablation results in tumor growth and increased growth factor expression. Ann Surg 245:771–776
Miya K, Saji S, Morita T, Niwa H, Sakata K (1987) Experimental study on mechanism of absorption of cryonecrotized tumor antigens. Cryobiology 24:135–139
Möller PH, Ivarsson K, Stenram U, Radnell M, Tranberg KG (1998) Comparison between interstitial laser thermotherapy and excision of an adenocarcinoma transplanted into rat liver. Br J Cancer 77:1884–1892
Müller LC, Micksche M, Yamagata S, Kerschbaumer F (1985) Therapeutic effect of cryosurgery of murine osteosarcoma—influence on disease outcome and immune function. Cryobiology 22:77–85
Muralidharan V, Nikfarjam M, Malcontenti-Wilson C, Christophi C (2004) Effect of interstitial laser hyperthermia in a murine model of colorectal liver metastases: scanning electron microscopic study. World J Surg 28:33–37
Nakayama J, Kokuba H, Kobayashi J, Yoshida Y, Hori Y (1997a) Experimental approaches for the treatment of murine B16 melanomas of various sizes. I: local injection of ethanol with a combination of interleukin-2 or microwaval hyperthermia for B16 melanomas with a size of less than 7 mm in diameter. J Dermatol Sci 15:75–81
Nakayama J, Kokuba H, Kobayashi J, Yoshida Y, Hori Y (1997b) Experimental approaches for the treatment of murine B16 melanomas of various sizes. II: injection of ethanol with combinations of beta-interferon and microwaval hyperthermia for B16 melanomas with a size of greater than 10mm in diameter. J Dermatol Sci 15:82–88
Napoletano C, Taurino F, Biffoni M, De Majo A, Coscarella G, Bellati F, Rahimi H, Pauselli S, Pellicciotta I, Burchell JM, Gaspari LA, Ercoli L, Rossi P, Rughetti A (2008) RFA strongly modulates the immune system and anti-tumor immune responses in metastatic liver patients. Int J Oncol 32:481–490
Nikfarjam M, Malcontenti-Wilson C, Christophi C (2005a) Focal hyperthermia produces progressive tumor necrosis independent of the initial thermal effects. J Gastrointest Surg 9:410–417
Nikfarjam M, Muralidharan V, Christophi C (2005b) Mechanisms of focal heat destruction of liver tumors. J Surg Res 127:208–223
Nikfarjam M, Muralidharan V, Su K, Malcontenti-Wilson C, Christophi C (2005c) Patterns of heat shock protein (HSP70) expression and Kupffer cell activity following thermal ablation of liver and colorectal liver metastases. Int J Hyperthermia 21:319–332
Ohno T, Kawano K, Sasaki A, Aramaki M, Yoshida T, Kitano S (2001) Expansion of an ablated site and induction of apoptosis after microwave coagulation therapy in rat liver. J Hepatobiliary Pancreat Surg 8:360–366
Osada S, Imai H, Tomita H, Tokuyama Y, Okumura N, Matsuhashi N, Sakashita F, Nonaka K (2007) Serum cytokine levels in response to hepatic cryoablation. J Surg Oncol 95:491–498
Overgaard J (1989) The current and potential role of hyperthermia in radiotherapy. Int J Radiat Oncol Biol Phys 16:537–549
Ozaki T, Tabuse K, Tsuji T, Nakamura Y, Kakudo K, Mori I (2003a) Microwave cell death: enzyme histochemical evaluation for metastatic carcinoma of the liver. Pathol Int 53:837–845
Ozaki T, Mori I, Nakamura M, Utsunomiya H, Tabuse K, Kakudo K (2003b) Microwave cell death: immunohistochemical and enzyme histochemical evaluation. Pathol Int 53:686–692
Paulus JA, Tucker RD, Flanagan SW, Moseley PL, Loening SA, Park JB (1993) Heat shock protein response in a prostate tumor model to interstitial thermotherapy: implications for clinical treatment. Prostate 23:263–270
Peng Y, Martin DA, Kenkel J, Zhang K, Ogden CA, Elkon KB (2007) Innate and adaptive immune response to apoptotic cells. J Autoimmun 29:303–309
Pockley AG (2003) Heat shock proteins as regulators of the immune response. Lancet 362:469–476
Rai R, Richardson C, Flecknell P, Robertson H, Burt A, Manas DM (2005) Study of apoptosis and heat shock protein (HSP) expression in hepatocytes following radiofrequency ablation (RFA). J Surg Res 129:147–151
Ravindranath MH, Wood TF, Soh D, Gonzales A, Muthugounder S, Perez C, Morton DL, Bilchik AJ (2002) Cryosurgical ablation of liver tumors in colon cancer patients increases the serum total ganglioside level and then selectively augments antiganglioside IgM. Cryobiology 45:10–21
Redondo P, del Olmo J, Lopez-Diaz de Cerio A, Inoges S, Marquina M, Melero I, Bendandi M (2007) Imiquimod enhances the systemic immunity attained by local cryosurgery destruction of melanoma lesions. J Invest Dermatol 127:1673–1680
Rock KL, Hearn A, Chen CJ, Shi Y (2006) Natural endogenous adjuvants. Springer Semin Immunopathol 26: 231–246
Rosberger DF, Coleman DJ, Silverman R, Woods S, Rondeau M, Cunningham-Rundles S (1994) Immunomodulation in choroidal melanoma: reversal of inverted CD4+/CD8+ ratios following treatment with ultrasonic hyperthermia. Biotechnol Ther 5:59–68
Rybak LD (2009) Fire and ice: thermal ablation of musculoskeletal tumors. Radiol Clin North Am 47:455–469
Rylander MN, Feng Y, Zhang Y, Bass J, Stafford RJ, Volgin A, Hazle JD, Diller KR (2006) Optimizing heat

shock protein expression induced by prostate cancer laser therapy through predictive computational models. J Biomed Opt 11:041113
Sabel MS (2009) Cryo-immunology: a review of the literature and proposed mechanisms for stimulatory versus suppressive immune responses. Cryobiology 58:1–11
Sabel MS, Nehs MA, Su G, Lowler KP, Ferrara JL, Chang AE (2005) Immunologic response to cryoablation of breast cancer. Breast Cancer Res Treat 90:97–104
Sabharwal T, Katsanos K, Buy X, Gangi A (2009) Image-guided ablation therapy of bone tumors. Semin Ultrasound CT MR 30:78–90
Sadamori H, Yagi T, Kanaoka Y, Morimoto Y, Inagaki M, Ishikawa T, Matsukawa H, Matsuda H, Iwagaki H, Tanaka N (2003) The analysis of the usefulness of laparoscopic microwave coagulation therapy for hepatocellular carcinoma in patients with poor hepatic reserve by serial measurements of IL-6, cytokine antagonists, and C-reactive protein. Surg Endosc 17:510–514
Sadikot RT, Wudel LJ, Jansen DE, Debelak JP, Yull FE, Christman JW, Blackwell TS, Chapman WC (2002) Hepatic cryoablation-induced multisystem injury: bioluminescent detection of NF-kappaB activation in a transgenic mouse model. J Gastrointest Surg 6:264–270
Saito K, Haas A, Albelda S, Li D, O'Malley BW (2005) Combination of immunotherapy with radiofrequency ablation for head and neck cancer. Otolaryngol Head Neck Surg 133:98–99
Saji H, Song W, Nakamura H, Saijo T, Hosaka M, Hagiwara M, Ogata A, Kawasaki N, Engleman EG, Kato H (2006) A possibility of overcoming local tumor immune tolerance by radiofrequency ablation in combination with intratumoral injection of naïve dendritic cell. Gan To Kagaku Ryoho 33: 1736–1738
Sauter B, Albert ML, Francisco L, Larsson M, Somersan S, Bhardwaj N (2000) Consequences of cell death: exposure to necrotic tumor cells, but not primary tissue cells or apoptotic cells, induces the maturation of immunostimulatory dendritic cells. J Exp Med 191:423–434
Savill J, Dransfield I, Gregory C, Haslett C (2002) A blast from the past: clearance of apoptotic cells regulates immune responses. Nat Rev Immunol 2:965–975
Scheffer SR, Nave H, Korangy F, Schlote K, Pabst R, Jaffee EM, Manns MP, Greten TF (2003) Apoptotic, but not necrotic, tumor cell vaccines induce a potent immune response in vivo. Int J Cancer 103:205–211
Schell SR, Wessels FJ, Abouhamze A, Moldawer LL, Copeland EM (2002) Pro- and antiinflammatory cytokine production after radiofrequency ablation of unresectable hepatic tumors. J Am Coll Surg 195:774–781
Schnurr M, Scholz C, Rothenfusser S, Galambos P, Dauer M, Röbe H, Endres S, Eigler A (2002) Apoptotic pancreatic tumor cells are superior to cell lysates in promoting cross-priming of cytotoxic T-cells and activate NK and gammadelta T cells. Cancer Res 62:2347–2352
Schueller G, Stift A, Friedl J, Dubsky P, Bachleitner-Hofmann T, Benkoe T, Jakesz R, Gnant M (2003) Hyperthermia improves cellular immune response to human hepatocellular carcinoma subsequent to co-culture with tumor lysate pulsed dendritic cells. Int J Oncol 22:1397–1402
Schueller G, Kettenbach J, Sedivy R, Bergmeister H, Stift A, Fried J, Gnant M, Lammer J (2004) Expression of heat shock proteins in human hepatocellular carcinoma after radiofrequency ablation in an animal model. Oncol Rep 12:495–499
Seifert JK, Junginger T (2004) Cryotherapy for liver tumors: current status, perspectives, clinical results, and review of literature. Technol Cancer Res Treat 3:151–163
Seifert JK, France MP, Zhao J, Bolton EJ, Finlay I, Junginger T, Morris DL (2002) Large volume hepatic freezing: association with significant release of the cytokines interleukin-6 and tumor necrosis factor a in a rat model. World J Surg 26:1333–1341
Shibata T, Yamashita T, Suzuki K, Takeichi N, Micallef M, Hosokawa M, Kobayashi H, Murata M, Arisue M (1998) Enhancement of experimental pulmonary metastasis and inhibition of subcutaneously transplanted tumor growth following cryosurgery. Anticancer Res 18:4443–4448
Si T, Guo Z, Hao X (2008) Immunologic response to primary cryoablation of high-risk prostate cancer. Cryobiology 57:66–71
Si T, Guo Z, Hao X (2009) Combined cryoablation and GM-CSF treatment for metastatic hormone refractory prostate cancer. J Immunother 32:86–91
Simon CJ, Dupuy DE, Mayo-Smith WW (2005) Microwave ablation: principles and applications. Radiographics 25:S69–S83
Skoberne M, Beignon AS, Bhardwaj N (2004) Danger signals: a time and space continuum. Trends Mol Med 10:251–257
Szmigielski S, Sobczynski J, Sokolska G, Stawarz B, Zielinski H, Petrovich Z (1991) Effects of local prostatic hyperthermia on human NK and T cell function. Int J Hyperthermia 7:869–880
ter Haar G (2007) Therapeutic applications of ultrasound. Prog Biophys Mol Biol 93:111–129
Thomsen S (1991) Pathologic analysis of photothermal and photomechanical effects of laser-tissue interactions. Photochem Photobiol 53:825–835
Timmerman RD, Bizekis CS, Pass HI, Fong Y, Dupuy DE, Dawson LA, Lu D (2009) Local surgical, ablative, and radiation treatment of metastases. CA Cancer J Clin 59:145–170
Todryk SM, Michael J, Goughy MJ, Pockley AG (2003) Facets of heat shock protein 70 show immunotherapeutic potential. Immunology 110:1–9
Tranberg KG (2004) Percutaneous ablation of liver tumors. Best Pract Res Clin Gastroenterol 18:125–145
Udagawa M, Kudo-Saito C, Hasegawa G, Yano K, Yamamoto A, Yaguchi M, Toda M, Azuma I, Iwai T, Kawakami K (2006) Enhancement of immunologic tumor regression by intratumoral administration of dendritic cells in combination with cryoablative tumor pretreatment and bacillus calmetteguerin cell wall skeleton stimulation. Clin Cancer Res 12:7465–7475
Urano M, Tanaka C, Sugiyama Y, Miya K, Saji S (2003) Antitumor effects of residual tumor after cryoablation:

the combined effect of residual tumor and a protein-bound polysaccharaide on multiple liver metastases in a murine model. Cryobiology 46:238–245

van Duijnhoven FH, Tollenaar RA, Terpstra OT, Kuppen PJ (2005) Locoregional therapies of liver metastases in a rat CC531 coloncarcinoma model results in increased resistance to tumor rechallenge. Clin Exp Metastasis 22:247–253

Viorritto ICB, Nikolov NP, Siegel RM (2007) Autoimmunity versus tolerance: can dying cells tip the balance? Clin Immunol 122:125–134

Vogl TJ, Wissniowski TT, Naguib NN, Hammerstingl RM, Mack MG, Münch S, Ocker M, Strobel D, Hahn EG, Hänsler J (2009) Activation of tumor-specific T lymphocytes after laser-induced thermotherapy in patients with colorectal liver metastases. Cancer Immunol Immunother 58:1557–1563

Wang X, Sun J (2002) High-intensity focused ultrasound in patients with late-stage pancreatic carcinoma. Chin Med J 115:1332–1335

Washington K, Debelak JP, Gobbell C, Sztipanovits DR, Shyr Y, Olson S, Chapman WC (2001) Hepatic cryoablation-induced acute lung injury: histopathologic findings. J Surg Res 95:1–7

Watanabe N, Niitsu Y, Umeno H, Kuriyama H, Neda H, Yamauchi N, Maeda M, Urushizaki I (1988) Toxic effect of tumor necrosis factor on tumor vasculature in mice. Cancer Res 48:2179–2183

Wheatley DN, Kerr C, Gregory DW (1989) Heat-induced damage to HeLa-S3 cells: correlation of viability, permeability, osmosensitivity, phase-contrast light-, scanning electron- and transmission electron-microscopical findings. Int J Hyperthermia 5:145–162

Wiersinga WJ, Jansen MC, Straatsburg IH, Davids PH, Klaase JM, Gouma DJ, van Gulik TM (2003) Lesion progression with time and the effect of vascular occlusion following radiofrequency ablation of the liver. Br J Surg 90:306–312

Wissniowski TT, Hänsler J, Neureiter D, Frieser M, Schaber S, Esslinger B, Voll R, Strobel D, Hahn EG, Schuppan D (2003) Activation of tumorspecific T lymphocytes by radio-frequency ablation of the VX2 hepatoma in rabbits. Cancer Res 63:6496–6500

Wu F (2006) Extracorporeal high intensity focused ultrasound in the treatment of patients with solid malignancy. Minim Invasive Ther Allied Technol 15:26–35

Wu F, Wang ZB, Lu P, Xu ZL, Chen WZ, Zhu H, Jin CB (2004) Activated anti-tumor immunity in cancer patients after high intensity focused ultrasound ablation. Ultrasound Med Biol 30:1217–1222

Wu F, Zhou L, Chen WR (2007a) Host antitumour immune responses to HIFU ablation. Int J Hyperthermia 23:165–171

Wu F, Wang ZB, Cao YD, Zhou Q, Zhang J, Xu ZL, Zhu XQ (2007b) Expression of tumor antigens and heat-shock protein 70 in breast cancer cells after high-intensity focused ultrasound ablation. Ann Surg Oncol 14:1237–1242

Wudel LJ, Allos TM, Washington MK, Sheller JR, Chapman WC (2003) Multi-organ inflammation after hepatic cryoablation in BALB/c mice. J Surg Res 112:131–137

Xia JZ, Xie FL, Ran LF, Xie XP, Fan YM, Wu F (2012) High-intensity focused ultrasound tumor ablation activates autologous tumor-specific cytotoxic T lymphocytes. Ultrasound Med Biol 38:1363–1371

Xing Y, Lu X, Pua EC, Zhong P (2008) The effect of high intensity focused ultrasound treatment on metastases in a murine melanoma model. Biochem Biophys Res Commun 375:645–650

Xu ZL, Zhu XQ, Lu P, Zhou Q, Zhang J, Wu F (2009) Activation of tumor-infiltrating antigen presenting cells by high intensity focused ultrasound ablation of human breast cancer. Ultrasound Med Biol 35:50–57

Yang R, Reilly CR, Rescorla FJ, Sanghvi NT, Fry FJ, Franklin TD, Grosfeld JL (1992) Effects of high-intensity focused ultrasound in the treatment of experimental neuroblastoma. J Pediatr Surg 27:246–250

Yao LC, Yang RL (2007) Immunotherapy against tumor with dendritic cell sensitized by necrotic tumor tissue after microwave coagulation therapy. Zhonghua Yi Xue Za Zhi 87:2552–2556

Zerbini A, Pilli M, Penna A, Pelosi G, Schianchi C, Molinari A, Schivazappa S, Zibera C, Fagnoni FF, Ferrari C, Missale G (2006) Radiofrequency thermal ablation of hepatocellular carcinoma liver nodules can activate and enhance tumor-specific T-cell responses. Cancer Res 66:1139–1146

Zerbini A, Pilli M, Fagnoni F, Pelosi G, Pizzi MG, Schivazappa S, Laccabue D, Cavallo C, Schianchi C, Ferrari C, Missale G (2008) Increased immunostimulatory activity conferred to antigen-presenting cells by exposure to antigen extract from hepatocellular carcinoma after radiofrequency thermal ablation. J Immunother 31:271–282

Zhang J, Dong B, Liang P, Yu X, Su L, Yu D, Ji X, Yu G (2002) Significance of changes in local immunity in patients with hepatocellular carcinoma after percutaneous microwave coagulation therapy. Chin Med J 115:1367–1371

Zhang JP, Pan HM, Huang LP, Huang LP, Wu JM (2006) Impact of radiofrequency on splenocyte immunity of mice bearing H22 liver cancer. Ai Zheng 25:34–39

Zhang Y, Deng J, Feng J, Wu F (2010) Enhancement of antitumor vaccine in ablated hepatocellular carcinoma by high-intensity focused ultrasound: a preliminary report. World J Gastroenterol 16:3584–3591

Zhou P, Fu M, Bai J, Wang Z, Wu F (2007) Immune response after high-intensity focused ultrasound ablation for H22 tumor. J Clin Oncol 25:21169

Zhou Q, Zhu XQ, Zhang J, Xu ZL, Lu P, Wu F (2008) Changes in circulating immunosuppressive cytokine levels of cancer patients after high intensity focused ultrasound treatment. Ultrasound Med Biol 34:81–88

Part II

Drug and Gene Delivery Using Bubble-Assisted Ultrasound

Droplets, Bubbles and Ultrasound Interactions

9

Oleksandr Shpak, Martin Verweij, Nico de Jong, and Michel Versluis

Abstract

The interaction of droplets and bubbles with ultrasound has been studied extensively in the last 25 years. Microbubbles are broadly used in diagnostic and therapeutic medical applications, for instance, as ultrasound contrast agents. They have a similar size as red blood cells, and thus are able to circulate within blood vessels. Perfluorocarbon liquid droplets can be a potential new generation of microbubble agents as ultrasound can trigger their conversion into gas bubbles. Prior to activation, they are at least five times smaller in diameter than the resulting bubbles. Together with the violent nature of the phase-transition, the droplets can be used for local drug delivery, embolotherapy, HIFU enhancement and tumor imaging. Here we explain the basics of bubble dynamics, described by the Rayleigh-Plesset equation, bubble resonance frequency, damping and quality factor. We show the elegant calculation of the above characteristics for the case of small amplitude oscillations by linearizing the equations. The effect and importance of a bubble coating and effective surface tension are also discussed. We give the main characteristics of the power spectrum of bubble oscillations. Preceding bubble dynamics, ultrasound propagation is introduced. We explain the speed of sound, nonlinearity and attenuation terms. We examine bubble ultrasound scattering and how it depends on the wave-shape of the incident wave. Finally, we introduce droplet

O. Shpak • M. Versluis (✉)
Physics of Fluids Group,
MIRA Institute for Biomedical Technology and Technical Medicine, University of Twente,
P.O. Box 217, Enschede 7500 AE, The Netherlands
e-mail: m.versluis@utwente.nl

M. Verweij
Acoustic Wavefield Imaging, Delft University of Technology, Delft 2600 GA, The Netherlands

N. de Jong
Acoustic Wavefield Imaging,
Delft University of Technology, Delft 2600 GA,
The Netherlands

Biomedical Engineering,
Erasmus MC University Medical Center Rotterdam,
Rotterdam 3000 CA, The Netherlands

© Springer International Publishing Switzerland 2016

J.-M. Escoffre, A. Bouakaz (eds.), *Therapeutic Ultrasound*, Advances in Experimental Medicine and Biology, Vol. 880, DOI 10.1007/978-3-319-22536-4_9

interaction with ultrasound. We elucidate the ultrasound-focusing concept within a droplets sphere, droplet shaking due to media compressibility and droplet phase-conversion dynamics.

Keyword
Droplet • Microbubble • Ultrasound

9.1 Introduction

Medical ultrasound is widely used for imaging purposes (Szabo 2004). It is an effective, mobile, inexpensive method and has the ability to provide high-resolution real-time images of tissue (Shung 2006). Ultrasound imaging is performed by propagating waves through tissue and evaluating the echo that is returned. Due to the different scattering properties of the different tissues, the ultrasound receiver can evaluate the echo and construct an acoustic image.

The ultrasound wave is transmitted by an ultrasound transducer. It consists of piezoelectric crystals, which have the property of changing their volume when a voltage is applied. Applying an alternating current across piezoelectric crystals causes them to volumetrically oscillate at frequencies (~MHz) that cause mechanical stress on the surrounding medium, thereby converting electric energy into a mechanical wave, which is then transmitted into the body. Analogously, upon receiving the echo the transducer turns the mechanical sound waves back into electrical energy, which can be measured and displayed. The transmit signal consists of a short ultrasound burst. After each burst, the electronics measure the return signal within a small window of time corresponding to the time it takes for the energy to pass through the tissue.

Blood is a poor ultrasound scatterer and individual blood vessels are almost invisible to ultrasound. To increase the contrast of the blood pool, microbubbles can be injected into the bloodstream. The microbubbles scatter ultrasound much more efficiently, allowing very good contrast on the echo image. The contrast ability was discovered accidentally more than 40 years ago during an intravenous injection of a saline solution (Gramiak and Shah 1968). Saline, when injected intravenously, generates tiny microbubbles within the patient's blood vessels, thus creating an echo on the acoustic image. Since then, the second and third generations of ultrasound contrast agents were developed. Nowadays, commercially available microbubbles are small spheres (typically 1–5 μm in diameter) of gas encapsulated in a biocompatible shell. This size is similar to that of red blood cells, allowing them to circulate inside the bloodstream. The resonance frequency is directly related to the size of the bubbles (1–10 μm diameter) and coincides with the optimum imaging frequencies used in medical ultrasound imaging, 1–10 MHz.

Microbubbles are also widely used for therapy. They can enhance high intensity focused ultrasound (HIFU) therapy (Unger et al. 2004). The bubbles increase heat uptake by the tissue and can reduce the time necessary for an ultrasound therapeutic procedure. They are sufficiently stable for time periods of approximately 15 min following injection (Klibanov 2006). Bubble oscillations and disruptions close to cells create reversible pores within the cell membrane that can enhance drug uptake (Karshafian et al. 2009). Microbubbles may also be used as potential carriers for selective drug delivery (Unger et al. 2009) and for non-invasive molecular imaging (Lindner 2004; Klibanov 2006). They can be covered with targeting ligands, such as antibodies, which bind specifically to target cells at the blood vessel wall.

A novel approach is the use of liquid-based agents rather than gas bubbles. Ultrasound can be used to phase-transition these liquid droplets into gas bubbles; a process known as acoustic droplet vaporization (ADV). Droplets are composed of a volatile perfluorocarbon (PFC), such as perfluoropentane (PFP, 29 °C boiling point). A PFP emulsion does not spontaneously vaporize

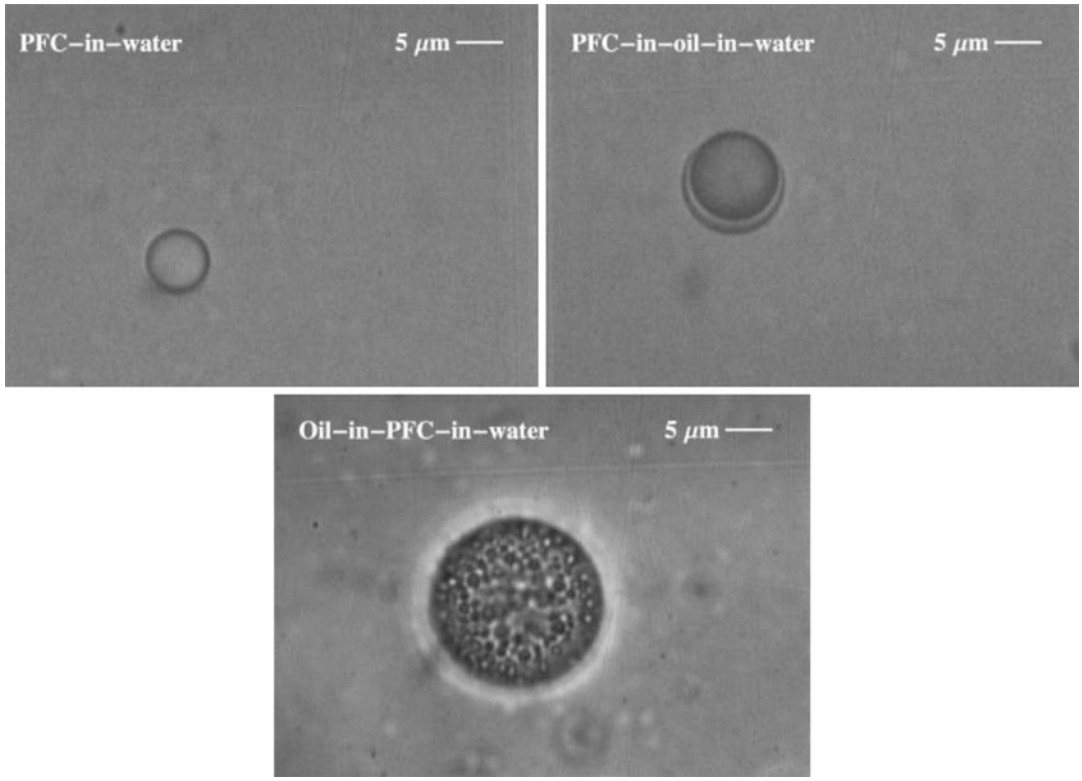

Fig. 9.1 PFC-in-water, PFC-in-oil-in-water and oil-in-PFC-in-water emulsions under the microscope

when injected *in-vivo* at 37 °C. However, upon exposure to ultrasound above certain acoustic pressure amplitudes, the PFP within the emulsion is vaporized. This opens up possibilities in a wide variety of diagnostic and therapeutic applications, such as embolotherapy (Zhang et al. 2010), aberration correction (Carneal et al. 2011) and drug delivery (Fabiilli et al. 2010a, b). Single and double emulsions of PFC-in-water and oil-in-PFC-in-water can be prepared, for instance, to encapsulate oil soluble drugs (Fig. 9.1).

PFC liquids are known for their use in medicine due to their biocompatibility and inertness (Biro et al. 1987). PFC nanodroplet emulsions can be utilized for selective extravasation in tumor regions (Long et al. 1978). Due to their biocompatibility and suggested ability to passively target regions of cancer growth, PFC droplets represent an attractive tool for cancer diagnosis. PFC droplets may also extravasate and be retained in the extravascular space due to the enhanced permeability and retention effect in tumors (Rapoport et al. 2007; Zhang and Porter 2010). Extravasated droplets may be acoustically converted into gas bubbles allowing for ultrasound tumor imaging. At the same time PFC droplets are rich in fluorine, which makes them potential candidates as a contrast agent for MRI imaging. The availability of both intravascular contrast agents (microbubbles), and tumor-specific extravascular contrast agents (nanodroplets), would significantly increase diagnostic and therapeutic capabilities. Moreover, the droplets may be used to deliver chemotherapeutic agents to tumor regions, and locally release them upon exposure to triggered ultrasound (Rapoport et al. 2009).

9.2 Nonlinear Propagation

The amplitude of the acoustic pressure that is required to nucleate droplets in ADV turns out to be very high (Kripfgans et al. 2000). To obtain a

sufficiently high pressure, a focused ultrasound transducer is applied and the droplet is placed in the focal area of the emitted beam. Moreover, the frequency of the emitted ultrasound wave is several MHz. In a typical ADV experiment, the ultrasound wave travels a few centimeters (Kripfgans et al. 2000; Reznik et al. 2013; Shpak et al. 2013a, b; Giesecke and Hynynen 2003; Schad and Hynynen 2010; Williams et al. 2013) before impinging on the droplet. The high pressure, high frequency, applied focusing and long propagation distances are all factors that strengthen the nonlinear behavior of the ultrasound wave (Blackstock 1964; Bacon 1984). As a result, the wave that impinges on the droplet will be a highly deformed version of the one that is emitted by the transducer (Fig. 9.2). This has important consequences for the focusing inside the droplet, as will be demonstrated in Sect. 9.4.2.2.

9.2.1 Basic Equations for the Nonlinear Ultrasound Beam

Similar to most cases involving nonlinear medical ultrasound, the description of the beam that hits the droplet can be based on the Westervelt equation (Westervelt 1963; Hamilton and Morfey 2008):

$$\nabla^2 p - \frac{1}{c_0^2}\frac{\partial^2 p}{\partial t^2} + \frac{d}{c_0^4}\frac{\partial^3 p}{\partial t^3} = -\frac{b}{r_0 c_0^4}\frac{\partial^2 p^2}{\partial t^2} \tag{9.1}$$

where $\nabla^2 = \partial^2/\partial x^2 + \partial^2/\partial y^2 + \partial^2/\partial z^2$ is the Laplace operator and $p = p(x,y,z,t)$ denotes the acoustic pressure. The medium in which the ultrasound wave propagates is characterized by the ambient speed of sound c_0, the ambient density of mass ρ_0, the diffusivity of sound δ and

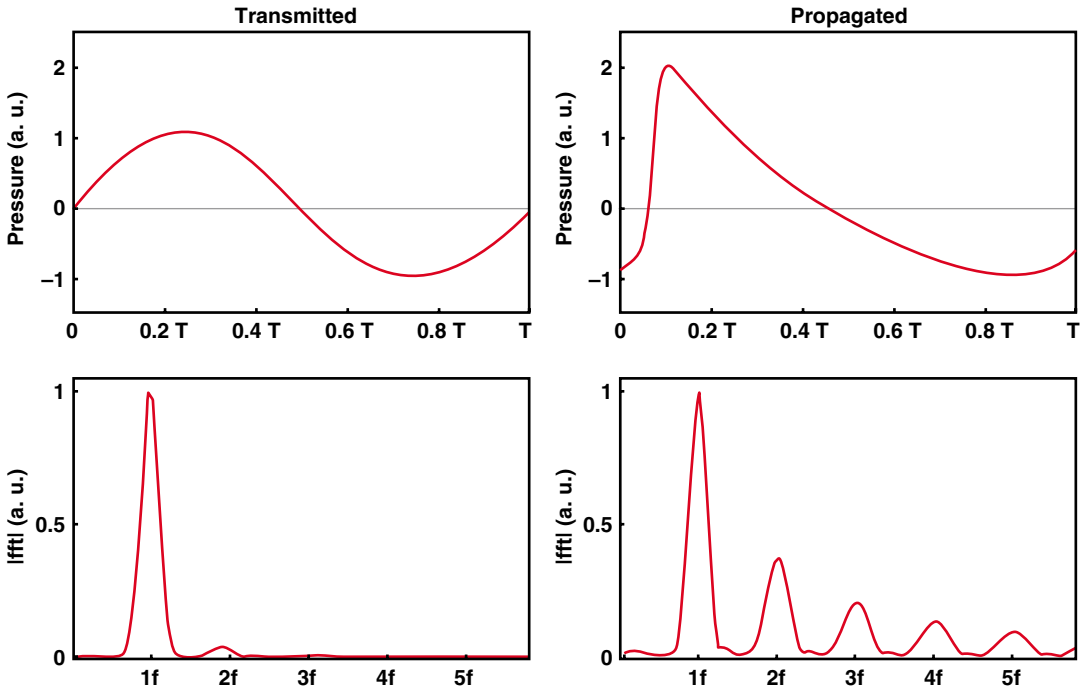

Fig. 9.2 Schematics of nonlinear propagation of an ultrasound wave. *T* and *f* are the period of oscillation and frequency of an ultrasound wave, respectively. Two upper plots are the transmitted and propagated wave, and two lower plots are their frequency domains. *–fft–* stands for the Fast Fourier Transform

the coefficient of nonlinearity β. Unfortunately, closed-form analytical solutions of this equation do not exist and its numerical solution generally requires considerable computational effort. However, in the present case of a narrow, focused beam and a homogeneous medium, some simplifying assumptions can be made. Firstly, it may be assumed that the predominant direction of propagation is along the transducer axis, which is taken in the z-direction. In this case, we can replace the ordinary time coordinate t by the retarded time coordinate $\tau = (t - t_0) - (z - z_0)/c_0$, which keeps the same value when traveling along with the wave. Here, t_0 is the time at which the transducer emits the pressure wave, and z_0 is the axial position of the transducer. The equivalent of Eq. 9.1 in the co-moving time frame is:

$$\nabla^2 \bar{p} - \frac{2}{c_0}\frac{\partial^2 \bar{p}}{\partial z \partial \tau} + \frac{\delta}{c_0^3}\frac{\partial^3 \bar{p}}{\partial \tau^3} = -\frac{\beta}{\rho_0 c_0^4}\frac{\partial^2 \bar{p}^2}{\partial \tau^2} \qquad (9.2)$$

with $\bar{p} = \bar{p}(x, y, z, \tau)$ denoting the acoustic pressure in the co-moving time frame. Secondly, it may be assumed that in the retarded time frame the axial derivative $\partial^2 \bar{p}/\partial z^2$ is much smaller than the lateral derivatives $\partial^2 \bar{p}/\partial x^2$ and $\partial^2 \bar{p}/\partial y^2$. This motivates the use of the parabolic approximation $\nabla^2 \bar{p} \approx \nabla_\perp^2 \bar{p}$, where $\nabla_\perp^2 = \partial^2/\partial x^2 + \partial^2/\partial y^2$ is the Laplace operator in the lateral plane. This approximation is valid for waves propagating under at most 20° of the transducer axis (Lee and Pierce 1995). Applying the parabolic approximation to Eq. 9.2 and rearranging terms results in the Khokhlov-Zabolotskaya-Kuznetsov (KZK) equation (Zabolotskaya and Khokhlov 1969; Kuznetsov 1971):

$$\frac{\partial^2 \bar{p}}{\partial z \partial \tau} = \frac{c_0}{2}\nabla_\perp^2 \bar{p} + \frac{\delta}{2c_0^3}\frac{\partial^3 \bar{p}}{\partial \tau^3} + \frac{\beta}{2\rho_0 c_0^3}\frac{\partial^2 \bar{p}^2}{\partial \tau^2} \qquad (9.3)$$

Dedicated coordinate transformations may be applied to improve the numerical solution in the far field (Hamilton et al. 1985; Hart and Hamilton 1988) or to adapt to specific forms of focused beams (Kamakura et al. 2000), but these will not be discussed here.

9.2.2 Numerical Solution for the Nonlinear Ultrasound Beam

We will follow a well-known numerical solution strategy (Lee and Hamilton 1995; Cleveland et al. 1996) that is based on the time integrated version of Eq. 9.3:

$$\frac{\partial \bar{p}}{\partial z} = \frac{c_0}{2}\int_{-\infty}^{\tau} \nabla_\perp^2 \bar{p}(\tau')\, d\tau' + \frac{\delta}{2c_0^3}\frac{\partial^2 \bar{p}}{\partial \tau^2} + \frac{\beta \bar{p}}{\rho_0 c_0^3}\frac{\partial \bar{p}}{\partial \tau} \qquad (9.4)$$

The first term at the right-hand side of this equation accounts for the diffraction of the beam, the second term for its attenuation, and the third term for its nonlinear distortion. Further, the solution strategy is based on the split-step approach. This means that the field $\bar{p}$ is stepped forward over a succession of parallel planes with mutual distance Δz, where the field $\bar{p}(x, y, z_0, \tau)$ in the transducer plane acts as the starting plane. The stepsize Δz is taken sufficiently small, allowing that each of the above phenomena may be accounted for in separate sub steps (Varslot and Taraldsen 2005). Therefore, the total step $z \to z + \Delta z$ involves the numerical solution of the separate equations:

$$\frac{\partial \bar{p}}{\partial z} = \frac{c_0}{2}\int_{-\infty}^{\tau} \nabla_\perp^2 \bar{p}(\tau')\, d\tau' \qquad (9.5)$$

$$\frac{\partial \bar{p}}{\partial z} = \frac{\delta}{2c_0^3}\frac{\partial^2 \bar{p}}{\partial \tau^2} \qquad (9.6)$$

$$\frac{\partial \bar{p}}{\partial z} = \frac{\beta \bar{p}}{\rho_0 c_0^3}\frac{\partial \bar{p}}{\partial \tau} \qquad (9.7)$$

over the same interval, where the result of solving one equation is used as the input for solving the next one. A numerical implementation of the above process is used to step the acoustic pressure from the transducer to the focus of the beam, i.e. the location of the droplet. For convenience, it is now assumed that the droplet is located at the origin of the coordinate system and that the source emits the pressure wave at $t_0 = z_0/c_0$. This

makes $\tau = t$ at the position of the droplet. For ease of notation, the bar and the coordinates of the droplet will be suppressed, and the pressure at the droplet position, as obtained from the numerical solution of the KZK-equation, will simply be indicated by $p_{\mathrm{KZK}}(t)$.

9.2.3 Nonlinear Pressure Field at the Focus of the Beam

The nonlinear pressure field at the focus of the beam can be expanded in a Fourier series:

$$p_{\mathrm{KZK}}(t) = \sum_{n=0}^{\infty} a_n \cos(n\omega t + \phi_n) = \mathrm{Re}\left[\sum_{n=0}^{\infty} a_n e^{i(n\omega t + \phi_n)}\right] \tag{9.8}$$

where a_n and ϕ_n are the amplitudes and the phases of the $n-th$ harmonic component of the ultrasound wave. For convenience, all the subsequent derivations will be given in the complex representation, so we will omit taking the real part and simply write:

$$p_{\mathrm{KZK}}(t) = \sum_{n=0}^{\infty} a_n e^{i(n\omega t + \phi_n)} \tag{9.9}$$

Given that nonlinear deformation of the waveform builds up over distance and the droplet is four orders of magnitude smaller in size than the distance to the transducer, the additional nonlinear distortion inside the droplet is neglected. This implies that wave propagation inside the droplet is considered linear, so the superposition theorem holds, and the focusing of each harmonic component in the droplet may be analyzed on an individual basis, as will be done in Sect. 9.4.2.2.

9.3 Bubble Dynamics

9.3.1 Dynamics of a Gas Bubble

Bubble radial oscillations are governed by the Rayleigh-Plesset equation:

$$\ddot{R}R + \frac{3}{2}\dot{R}^2 = \frac{\Delta P}{\rho} \tag{9.10}$$

where R, $\dot{R}$, and $\ddot{R}$ are the radius, the velocity and the acceleration of the bubble wall, respectively, and ρ is the density of the liquid. $\Delta P = P_L(R) - P_\infty$ is the pressure difference between the liquid at the bubble wall $P_L(R)$ and the external pressure infinitely far from the bubble p_∞. Equation 9.10 was first described by Lord Rayleigh (1917) for the case $\Delta P = 0$ and was later refined (Plesset 1949; Noltingk and Neppiras 1950; Neppiras and Noltingk 1951; Poritsky 1952). It is derived for a spherically symmetric bubble, and follows from the Bernoulli's equation and the continuity equation (Leighton 1994). Equation 9.10 assumes spherical symmetry of the bubble, and the motion of the liquid around the bubbles is considered to be spherically symmetric. The liquid is incompressible.

The bubble is assumed to be much smaller than the acoustic wavelength, such that acoustic pressure is considered to be uniform. Thus, the pressure at infinity is the sum of the acoustic forcing $P(t)$ and the ambient pressure P_0:

$$p_\infty = P(t) + P_0 \tag{9.11}$$

The interfacial pressure acting on the liquid at the bubble wall consists of the Laplace pressure $2\sigma / R_0$, viscous pressure $4\mu\dot{R}/R$ and the gas pressure P_g. Neglecting the vapor pressure of the liquid, the gas pressure inside the bubble as a function of the bubble radius R can be described by the ideal gas relation $P_g V^\gamma = const$, where γ is the polytropic constant and $V \propto R^3$ is the bubble volume. For this derivation we first neglect the gas diffusion. Thus, the total number of gas molecules inside the bubble is constant. In equilibrium, the pressure inside the bubble P_{eq} is equal to the sum of the ambient pressure P_0 and the Laplace pressure:

$$P_{eq} = P_0 + \frac{2\sigma}{R_0} \tag{9.12}$$

where σ and R_0 are the surface tension and the equilibrium radius, respectively. In combination with the ideal gas law, the dependence of the gas pressure as a function of the bubble radius can be

written as $P_g = \left(P_0 + \frac{2\sigma}{R_0}\right)\left(\frac{R_0}{R}\right)^{3\gamma}$. The right-hand side of Eq. 9.10 can then be written as:

$$\Delta P = \left(P_0 + \frac{2\sigma}{R_0}\right)\left(\frac{R_0}{R}\right)^{3\gamma} - P_0 - \frac{2\sigma}{R} - 4\mu\frac{\dot{R}}{R} - P(t) \tag{9.13}$$

which gives the final form of the bubble dynamic equation:

$$\rho\left(\ddot{R}R + \frac{3}{2}\dot{R}^2\right) = \left(P_0 + \frac{2\sigma}{R_0}\right)\left(\frac{R_0}{R}\right)^{3\gamma} - P_0 - \frac{2\sigma}{R} - 4\mu\frac{\dot{R}}{R} - P(t) \tag{9.14}$$

The microbubbles in the ultrasound contrast agents can be encapsulated with a phospholipid, protein or polymer coating, thus preventing bubbles from dissolution. For more details please see (Marmottant et al. 2005; de Jong et al. 2007; Church 1995). The viscoelastic coating also contributes to an increased stiffness and to additional viscous damping (Overvelde et al. 2010).

9.3.2 Linearization

The acoustic pressure typically has the form of a sinusoidal oscillation $P(t) = P_A \sin(\omega t)$, with P_A being the driving pressure amplitude, and ω the driving pressure angular frequency. With relatively small oscillation amplitudes Eq. 9.10 can be linearized. To rewrite Eq. 9.10 in linear terms we express the bubble radius R as:

$$R = R_0(1 + x) \tag{9.15}$$

with R_0 the equilibrium radius, as before, and $x \ll 1$ a small dimensionless perturbation to the radius. Substituting Eq. 9.15 into Eq. 9.10 and retaining only first-order terms, x, $\dot{x}$ and $\ddot{x}$ gives:

$$\ddot{x} + 2\beta\dot{x} + \omega_0^2 x = \frac{P_A}{\rho R_0^2}\sin(\omega t) \tag{9.16}$$

where

$$\omega_0 = \sqrt{\frac{1}{\rho R_0^2}\left[3\gamma\left(P_0 + \frac{2\sigma}{R_0}\right) - \frac{2\sigma}{R_0}\right]} \tag{9.17}$$

the eigenfrequency of bubble oscillations, and:

$$\beta = \frac{2\mu}{\rho R_0^2} \tag{9.18}$$

the damping due to viscosity. The damping has the dimensions of the reversed time $\left[s^{-1}\right]$ and represents how fast the amplitude of oscillations is decaying in time due to the energy loss.

The solution to the equation Eq. 9.16 is:

$$x(t) = X_t e^{-\beta t}\cos(\omega_1 t) + X_s \cos(\omega t + \phi_1) \tag{9.19}$$

with the ϕ_1 being the phase shift between the two terms:

$$\phi_1 = \arctan\left(\frac{\omega_0^2 - \omega^2}{2\beta\omega}\right) \tag{9.20}$$

The first term of Eq. 9.19 is the transient solution. Its amplitude dampens out in time as $X_t e^{-\beta t}$, where X_t is the amplitude of transient oscillations at time $t_0 = 0$. Not only the viscosity of water can contribute to the damping, but also the acoustic reradiation and the viscosity of the coating shell and thermal damping. For more details please see (Overvelde et al. 2010). The frequency of the transient solution is equal to $\omega_1 = \sqrt{\omega_0^2 - \beta^2}$. The amplitude of the transient solution X_t depends strongly on the initial conditions.

The second term of Eq. 9.19 is the steady-state solution. The amplitude of the steady-state response depends on the driving frequency as:

$$X_s = \frac{P_A}{\rho R_0^2}\frac{1}{\sqrt{\left(\omega_0^2 - \omega^2\right)^2 + 4\omega^2\beta^2}} \tag{9.21}$$

The resonance frequency ω_{res} of the system, by definition, corresponds to the maximal amplitude of the steady-state solution. X_s is at maximum, when the denominator in the Eq. 9.21 is at minimum. Thus, the resonance frequency relates to the eigenfrequency ω_0 as:

$$\omega_{\text{res}} = \sqrt{\omega_0^2 - 2\beta^2} \tag{9.22}$$

The smaller the damping β, the closer the resonance frequency to the eigenfrequency of the bubble oscillations. Additionally, for large bubbles, when the Laplace pressure is small compared to the ambient pressure Eq. 9.17 simplifies to:

$$\omega_M = 2\pi f_M = \sqrt{3\gamma \frac{P_0}{\rho R_0^2}} \tag{9.23}$$

with f_M the Minnaert eigenfrequency, resonance frequency of the bubble (Minnaert 1933). Relation Eq. 9.23 tells us that the resonance frequency can be estimated directly from the bubble radius R_0. For a bubble in water at standard pressure ($P_0 = 100\text{kPa}$, $\rho = 1000\text{kg/m}^3$), the equation becomes $f_M R_0 \approx 3.26\,\mu\text{m.MHz}$. The smaller the bubble radius, the higher the resonance frequency becomes.

It is insightful to make the analogy to the classical mass-spring system. The dynamics of the classical mass spring system is governed by the equation:

$$\ddot{x} + 2\frac{\beta'}{m}\dot{x} + \omega_0'^2 x = \frac{F_0}{m}\sin(\omega t) \tag{9.24}$$

where $\omega'_0 = \sqrt{k/m}$ is the eigenfrequency, β' is the damping constant, k is the spring stiffness, F_0 is the driving force and m is the mass. Equation 9.24 has the same form as Eq. 9.16. Thus, a gas inside the bubble, represented by the polytropic constant γ, acts as the restoring force, the liquid around the bubble acts as a mass $\left(4\pi R_0^3 \rho\right)$, and ultrasound is acting as a driving force $\left(12\pi\gamma R_0 P_0\right)$.

9.3.3 Pressure Emitted by the Bubble

Far from the bubble wall, at a distance r, the velocity of the liquid v_r can be calculated from the continuity equation (Prosperetti 2011):

$$4\pi r^2 v_r = 4\pi R^2 \dot{R} \tag{9.25}$$

$$v_r = \frac{R^2}{r^2}\dot{R} \tag{9.26}$$

The liquid is incompressible and the bubble wall and the liquid motion around the bubble are spherically symmetric. $\dot{R}$ is the velocity of the bubble wall in the radial direction, as before.

The pressure field, generated by the radial bubble wall oscillations, can be calculated from the Euler equation (Prosperetti 2011):

$$\rho\frac{\partial v}{\partial t} + \frac{\partial p}{\partial r} = 0 \tag{9.27}$$

where p is the pressure emitted by the bubble. In Eq. 9.27 we omit the nonlinear convective term. Substituting the expression of the velocity field (Eq. 9.26) into Eq. 9.27 gives the pressure gradient:

$$\frac{\partial p}{\partial r} = -\frac{\rho}{r^2}\frac{d}{dt}\left(R^2\dot{R}\right) \tag{9.28}$$

and the pressure emitted by the bubble:

$$p = \frac{\rho}{r}\frac{d}{dt}\left(R^2\dot{R}\right) = \rho\left(\frac{R^2\ddot{R} + 2R\dot{R}^2}{r}\right) \tag{9.29}$$

9.3.4 Secondary Bjerknes Force

Let us now consider two interacting gas bubbles, separated by a distance l. The distance between the bubbles 1 and 2 is much larger that their radii $R_1(t)$ and $R_2(t)$. Thus, we can consider the motion of the liquid around the bubbles to be spherically symmetric. Bubble 2 with volume $V_2 = \frac{4}{3}\pi R_2^3$ experiences a force F_{12} as a result of the pressure emitted by bubble 1, p_1 (Leighton 1994):

$$F_{12} = -V_2 \nabla p_1 \tag{9.30}$$

The force is directed along the line, which connects the centers of the two interacting bubbles. Substitution of Eq. 9.28 (expression for the pressure gradient generated by the first bubble) into Eq. 9.30 yields the force of the first bubble on the second one at a distance l:

$$F_{12} = -V_2 \left.\frac{\partial p_1}{\partial r}\right|_{r=l} = V_2 \frac{\rho}{l^2}\frac{d}{dt}\left(R_1^2 \dot{R}_1\right) = \frac{\rho}{4\pi l^2} V_2 \frac{d^2 V_1}{dt^2} \tag{9.31}$$

where $V_1 = \frac{4}{3}\pi R_1^3$ the volume of bubble 1.

The net radiation force acting on a neighboring bubble is called the secondary Bjerknes force F_B after Bjerknes (Bjerknes 1906). The time averaged equation $\langle F_{12} \rangle$ is obtained by integrating Eq. 9.31 over the period of volume oscillations by partial integration:

$$F_B = \langle F_{12} \rangle = -\frac{\rho}{4\pi d^2}\langle \dot{V}_1 \dot{V}_2 \rangle \tag{9.32}$$

A positive value of $\langle \dot{V}_1 \dot{V}_2 \rangle$ corresponds to attraction of the bubbles, and a negative value to repulsion. This means that the bubbles that oscillate with the same phase will attract each other. Note also the symmetry of Eq. 9.32. To calculate the force of the second bubble on the first one $\langle F_{21} \rangle$, one just needs to exchange indexes $1 \leftrightarrow 2$. $\langle F_{21} \rangle$ has the same magnitude, but an opposite direction as $\langle F_{12} \rangle$.

9.4 Droplet Dynamics

9.4.1 Oscillatory Translations

The typical pressure amplitudes, which are used to activate perfluorocarbon droplets, are two orders of magnitude higher that those used to drive ultrasound contrast agents. Water itself always experiences periodic compression as a result of ultrasound forcing (Leighton 1994). Let us express such oscillations as:

$$\epsilon = \epsilon_0 \sin(\omega t - kx) \tag{9.33}$$

where ϵ is the fluid particle displacement. The acoustic impedance, by definition, is the ratio of the driving pressure to the fluid particle velocity (Leighton 1994):

$$Z = P_A / \dot{\epsilon}_0 \tag{9.34}$$

where $\dot{\epsilon}_0$ is the particle displacement velocity amplitude, and P_A is the acoustic pressure amplitude. The $\dot{\epsilon}_0$ particle velocity amplitude relates to the particle displacement amplitude ϵ_0 as $\dot{\epsilon}_0 = \omega \epsilon_0$, which follows from Eq. 9.33 by taking its time derivative. The dP pressure change with respect to the equilibrium value is related to a dV volume change by the bulk modulus B, defined by (Leighton 1994):

$$dP = -B\frac{dV}{V} \tag{9.35}$$

Equation 9.35 can be used to calculate the acoustic pressure P at any given spatial point x_0 as $P(x_0) = -B\left.\frac{\partial \epsilon}{\partial x}\right|_{x=x_0}$. Applying this relation to Eq. 9.33 gives $P_A = Bk\epsilon_0$, or $P_A = B\frac{k}{\omega}\dot{\epsilon}_0$. The acoustic impedance Eq. 9.34 can then be written as:

$$Z = B\frac{k}{\omega} \tag{9.36}$$

or by using the equation for the wave speed $c = \omega / k = \sqrt{B/\rho}$:

$$Z = \rho c \tag{9.37}$$

With the relations given above, one can now estimate the oscillatory translational amplitude. For the case of $f = 3.5\text{MHz}$, $P_A = 8\text{MPa}$ and $c_\omega = 1522\text{m/s}$, the speed of sound in water at 37 °C, the amplitude is $\epsilon_0 = P_A / 2\pi\rho f c_\omega = 210\text{nm}$.

The acoustic impedance $Z = \rho c$ has the analogy with a refractive index n in optics. The ultrasound wave at the interface of two substances with different acoustic impedances Z_1 and Z_2 will experience a reflection and a refraction, similarly as light would experience at the interface with two different refractive indexes n_1 and n_1.

Let us now denote θ_I, θ_R, and θ_T the incident, the translated and the reflected angles, respectively (Fig. 9.3). One can derive the relation between these angles by considering continuity of the normal displacement at the interface.

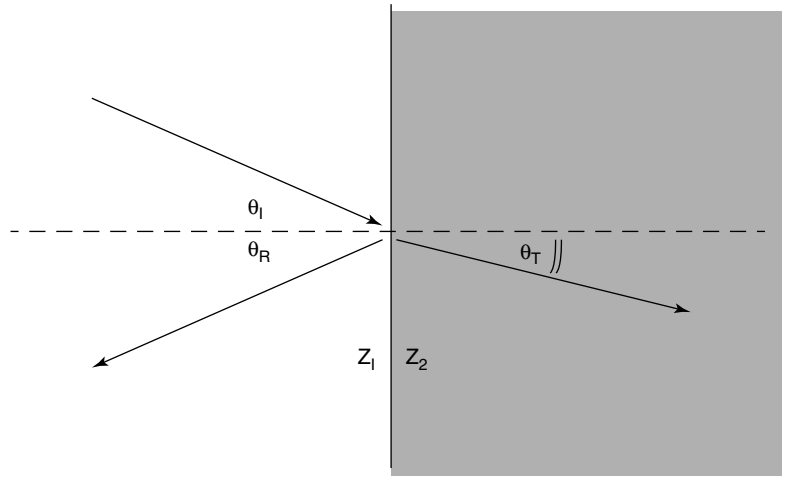

Fig. 9.3 Schematics of reflection and transmission of a wave of displacement

This gives Snell's reflection law $\sin(\theta_I) = \sin\theta_R$ and $c_2 \sin\theta_I = c_1 \sin\theta_T$, where c_1 and c_2 are the speed of sound of the first and the second medium, respectively (Leighton 1994).

9.4.2 Focusing inside a Spherical Droplet

When an interface between two acoustic media has a finite curvature R, as in the case of a spherical droplet, acoustic focusing is observed. This is a similar effect as the focusing of light by an optical lens. First, the case of large droplets is considered, i.e. when the acoustic wavelength λ is much smaller than the droplet radius R. Next, the case where λ is of the order of R, or even larger, is considered.

9.4.2.1 Case 1: Droplets much Larger in Size than the Wavelength

When $\lambda \ll R$, the refraction formulas provided by the theory of geometrical scattering apply. When a parallel beam of light travels in a medium with refractive index n_1 and encounters a spherical interface between this medium and a second medium with refractive index n_2, either the transmitted or the reflected wave focuses in a point at a distance:

$$f = R\frac{n_2}{n_2 - n_1} \tag{9.38}$$

This distance is measured from the intersection point of the interface and the beam axis, which crosses the center of the curvature (Fig. 9.4).

In analogy with the optical focus, an acoustic focus can be calculated for the case $\lambda \ll R$ by simply replacing n_1 / n_2 with c_1 / c_2 in the equation above. This gives:

$$f = R\frac{c_1}{c_1 - c_2} \tag{9.39}$$

For instance, when a large spherical perfluoropentane droplet with $c_2 = 406\,\mathrm{m/s}$ is immersed in water with $c_1 = 1522\,\mathrm{m/s}$ (at 37 °C), the acoustic focus is at $f = 1.36R$. This means that the acoustic wave focuses on a distal side, $0.36R$ away from the geometrical droplet center.

9.4.2.2 Case 2: Droplets Similar or Smaller in Size than the Wavelength

The situation complicates when the radius of the droplet is of the same order of magnitude as the wavelength, or even smaller, i.e. when $\lambda \sim R or \lambda \gg R$. Experimental data obtained with small droplets shows that the ultrasound beam focuses on the proximal side of the droplet, which is not in agreement with the prediction above. Obviously, in this case geometrical considerations can no longer be applied, and a full wave theory must be applied. Figure 9.5 shows the configuration of the acoustic

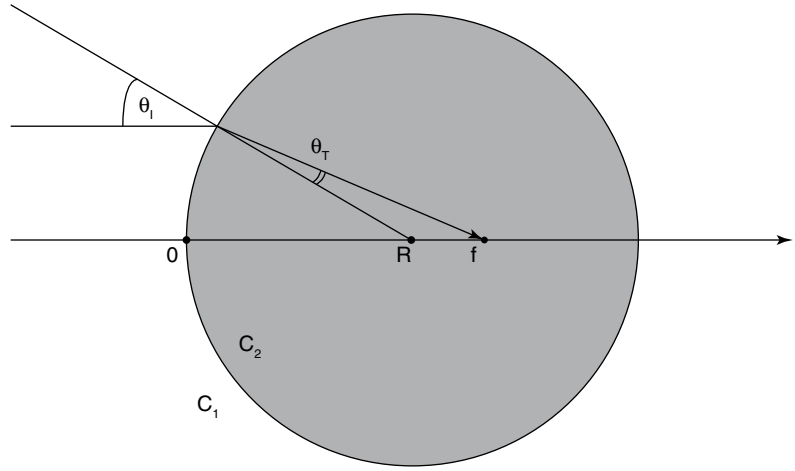

Fig. 9.4 Schematics of the focusing of an acoustic wave on the droplet sphere when the acoustic wavelength is much larger than the droplet radius

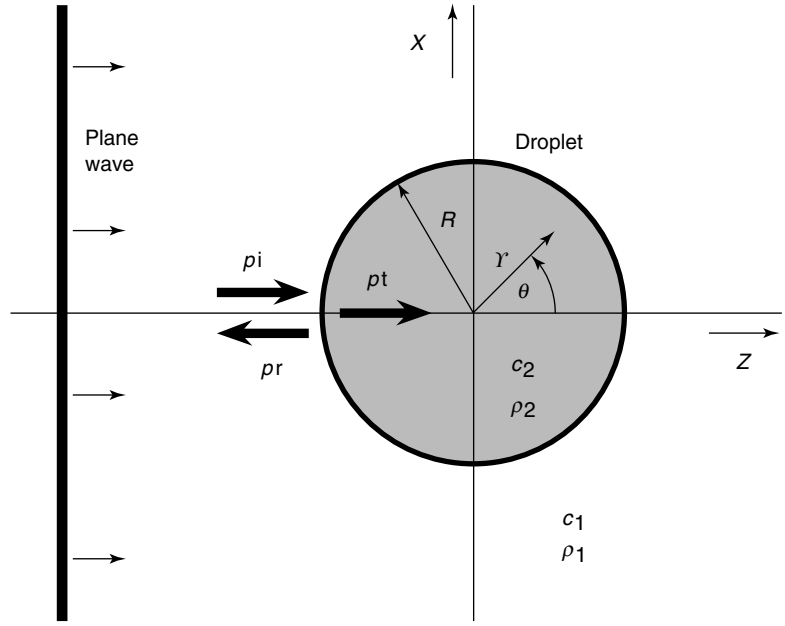

Fig. 9.5 Configuration of the droplet and the incident, transmitted, reflected ultrasound waves

diffraction problem that will be solved here. Throughout the derivations, the parameters of the surrounding medium are labeled with a subscript 1, and the parameters of the medium inside the droplet are labeled with a subscript 2.

At the location of the droplet, the incident ultrasound wave is considered to be planar. In view of Eq. 9.9, it is written as:

$$p_i\left(x,y,z,t\right)=\sum_{n=0}^{\infty}a_n e^{i\left(n\omega t-nk_1 z+\phi_n\right)} \qquad (9.40)$$

where $k_1=\omega/c_1$ is the wave number outside the droplet. To keep the derivations simple, the diffraction problem will first be solved for one spectral component:

$$p_i\left(x,y,z,t\right)=ae^{i\left(\omega t-k_1 z+\phi\right)} \qquad (9.41)$$

In view of the spherical symmetry of the configuration, it is convenient to apply a coordinate transformation from cartesian coordinates $\left(x,y,z\right)$ to spherical coordinates $\left(r,\theta,\phi\right)$, where ϕ is the azimuthal angle measured with respect to the positive z-axis, and ϕ is the elevation angle in the xy-plane. Due to the waves having rotational symmetry with respect to the z-axis, there will be no dependence on ϕ, and this coordinate will be omitted. In spherical coordinates,

the incident pressure wave can be written as a summation of spherical harmonics:

$$p_i(r,\theta,t) = ae^{i(\omega t+\phi)}\sum_{m=0}^{\infty}\gamma_m j_m(k_1 r)P_m(\cos\theta) \tag{9.42}$$

Here, $\gamma_m = (2m+1)(-i)^m$, j_m is the spherical Bessel function of the first kind and order m, and P_m is the $m-$th order Legendre polynomial. The spherical Bessel function j_m is related to the ordinary Bessel function J_m according to $j_m(x) = \sqrt{(\pi/2x)}J_{m+1/2}(x)$.

When the incident wave encounters the droplet, it gives rise to a transmitted wave inside the droplet:

$$p_t(r,\theta,t) = ae^{i(\omega t+\phi)}\alpha_m j_m(k_2 r)P_m(\cos\theta) \tag{9.43}$$

and a reflected wave outside the droplet:

$$p_r(r,\theta,t) = ae^{i(\omega t+\phi)}\beta_m h_m^{(2)}(k_1 r)P_m(\cos\theta) \tag{9.44}$$

In these equations, $k_2 = \omega/c_2$ is the wave number inside the droplet, and $h_m^{(2)}$ is the spherical Hankel function of the second kind and order m. The spherical Hankel function $h_m^{(2)}$ is related to the ordinary Hankel function $H_m^{(2)}$ following $h_m^{(2)}(x) = \sqrt{(\pi/2x)}H_{m+1/2}^{(2)}(x)$. At the spherical interface between the outside and the inside of the droplet, the pressure and the radial particle velocity should be continuous. The latter requirement can be translated into a condition on the radial derivative of the pressure. In mathematical form, the boundary conditions at the interface are:

$$\lim_{r\downarrow R}\left[p_i(r,\theta,t)+p_r(r,\theta,t)\right] = \lim_{r\uparrow R}p_t(r,\theta,t) \tag{9.45}$$

$$\lim_{r\downarrow R}\frac{1}{\rho_1}\frac{\partial}{\partial r}\left[p_i(r,\theta,t)+p_r(r,\theta,t)\right] = \lim_{r\uparrow R}\frac{1}{\rho_2}\frac{\partial}{\partial r}p_t(r,\theta,t) \tag{9.46}$$

which should hold for all θ and t. Substitution of Eqs. 9.42, 9.43, and 9.44 into these boundary conditions results in a system of two equations for α_m and β_m. Solution of this system yields:

$$\alpha_m = \gamma_m\frac{Z_2 j_m(k_1R)h_m^{(2)\prime}(k_1R) - Z_2 h_m^{(2)}(k_1R)j'_m(k_1R)}{Z_2 j_m(k_2R)h_m^{(2)\prime}(k_1R) - Z_1 h_m^{(2)}(k_1R)j'_m(k_2R)} \tag{9.47}$$

$$\beta_m = \gamma_m\frac{Z_1 j_m(k_1R)j'_m(k_2R) - Z_2 j_m(k_2R)j'_m(k_1R)}{Z_2 j_m(k_2R)h_m^{(2)\prime}(k_1R) - Z_1 h_m^{(2)}(k_1R)j'_m(k_2R)} \tag{9.48}$$

where $Z_1 = \rho_1 c_1$ and $Z_2 = \rho_2 c_2$ are the acoustic impedances of the media outside and inside the droplet, respectively. The prime indicates the derivative of a function. The constant α_m can be considered as the transmission coefficient of the droplet interface for spherical harmonics of order m, and the constant β_m can be considered as the corresponding reflection coefficient. At this stage, the problem of finding the wave inside the droplet due to a single sinusoidal component of the incident wave is solved.

To find the wave that is formed inside the droplet by the nonlinear incident wave, all the transmitted waves caused by the individual components of the incident wave must be added. The result is:

$$p_{inside}(r,\theta,t) = p_t(r,\theta,t) = \sum_{n=0}^{\infty}\sum_{m=0}^{\infty}a_n e^{i(n\omega t+\phi_n)}\alpha_{n,m}j_m(nk_1 r)P_m(\cos\theta) \tag{9.49}$$

where $\alpha_{m,n}$ follows from Eq. 9.47 by replacing k_1 by nk_1 and k_2 by nk_2. This equation can be used to calculate the pressure in any position (r,θ,φ) at any time t. Numerical implementation

requires that both summations involve a finite number of terms. This forms no significant limitation, because in practice only a limited number of N harmonics will give a significant contribution to the ultrasound field inside the droplet, and only a limited number of M spherical harmonics is required to accurately represent this field. However, another numerical issue arises when the radius of the droplet is much smaller than the wavelength. In this case, the numerical results for the spherical Bessel and Hankel functions may contain large errors. This problem may be eliminated by first approximating these functions by their series expansion around zero. With the full pressure field determined both in space and time we can now find the local maximum of pressure - the focus.

The pressure amplification factor in the focusing spot, as well as its location, depend on the input parameter values, i.e. the pressure amplitude, the frequency and the transducer geometry and size, which prescribe the focusing strength and the propagation distance to the focal point. For instance, in case of a $R = 10\,\mu\text{m}$ perfluoropentane droplet immersed in water and insonified with an incoming ultrasound wave with a peak negative pressure $P_i^- = -4.5\text{MPa}$ and frequency $f = 3.5\text{MHz}$ ($\lambda = 430\,\mu\text{m}$ in water at 37 °C) coming from a transducer with a 3.81 cm focal distance, a focused peak negative pressure of $P_{\text{inside}}^- = -26\text{MPa}$ is achieved within the droplet (Fig. 9.6). Thus, a near six-fold increase in the peak negative pressure amplitude is observed in a concentrated region on the proximal side around z = −0.4R.

From Eq. 9.47 it follows that the pressure inside the droplet, due to a single incident wave component, depends on the dimensionless product ωR. When for two droplets with different radii R_1 and R_2 the relation $\omega_1 R_1 = \omega_2 R_2$ holds, an incident wave with frequency f_1 encountering a droplet with radius R_1 is focused at the same relative position within the droplet as an incident wave with frequency f_2 that hits a droplet with radius R_2. This implies that when larger droplets turn out to vaporize more easily than smaller droplets at the same frequency, it also follows that for the same radius droplets are easier to evaporate at high frequencies than at low frequencies, and vice-versa.

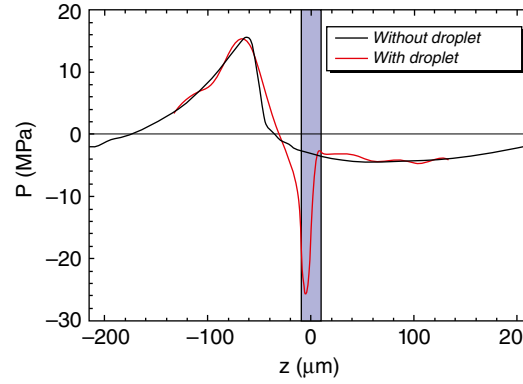

Fig. 9.6 Schematics of the superharmonic focusing effect within a perfluoropentane spherical droplet. The *black line* represents the acoustic pressure waveform on the axis of symmetry (θ = 0) as a function of the z-coordinate in the absence of a droplet. The *red solid line* is the focused pressure in presence of the droplet. The snapshot represents the moment of minimum focused pressure both in time and space. The *blue shaded* region depicts the position of the droplet

However, nonlinear propagation makes this picture more complex. First, the higher the acoustic pressure amplitude, the more nonlinear the wave becomes as the amplitudes of the higher harmonics build up roughly as $\left(P_{surface}\right)^{n-1}$, where $P_{surface}$ is the pressure amplitude at the transducer surface and n is the number of the particular harmonic. Second, the nonlinear propagation depends on the frequency. Additionally, of course, the nonlinear beam is focused differently from the linear one, with different pressure amplification factors and focusing positions for each harmonic. Finally, the shape of the nonlinearly distorted wave is strongly dependent on the parameters of the propagating media. For human tissue the Goldberg ratio is lower than for water (Szabo et al. 1999). This indicates that nonlinear distortion is easier to achieve in water compared to tissue. Therefore the experiments performed *in-vivo* are expected to have different nucleation patterns, with a higher nucleation threshold compared to the *in-vitro* experiments.

Knowledge of the physics of acoustic focusing in small droplets is important for the optimization of acoustic droplet vaporization for therapeutic applications. This is particularly the

case for attaining activation at low acoustic pressures, thereby minimizing the negative bioeffects associated with the use of high-intensity ultrasound. Moreover, it helps in the design of droplets: by mixing liquids with different physical properties, the acoustic impedance may be tuned through a change of the density of mass and/or the speed of sound. Using dedicated waveforms, the amplitudes and phases of the nonlinear wave at the focus of the beam can be optimized to obtain maximal constructive interference within the droplets and obtain maximal focusing strength at any particular acoustic input pressure. Moreover, the knowledge of consecutive droplet vaporization dynamics is important because it affects the surrounding tissue and may cause damage. It is not only the acoustic impedance mismatch between the droplet and the surrounding media that determines the interior pressure, but also the exterior of the droplet. Here we have only considered single droplets, but clouds of droplets may cause complicated pressure scattering patterns and may lead to different focusing spots. One can also think of periodic arrangements of monodisperse droplets to observe similar diffraction relations as we have with light passing through crystals.

9.4.3 Radial Vapor Bubble Expansion

There are three main physical mechanisms that govern the vapor bubble growth process: phase-change, heat transfer and inertia. There are also two phenomena, which can limit vapor bubble growth. Firstly, the vapor bubble pushes the surrounding liquid as it grows. The force by which the liquid is pushed is determined by the pressure which acts on the bubble wall. The surrounding liquid has inertia, and the vapor bubble growth rate will be limited by this inertia. Secondly, the phase-change from liquid to vapor is an endothermic process, requiring heat absorption. The required heat for vaporization is transferred from the liquid around the bubble by cooling the surroundings. The rate of this process is limited by heat transfer.

Let us now first have a closer look at inertial growth limitation. Here we assume that the heat transfer is high enough to supply the required energy for the endothermic phase-transition. In this case the Rayleigh-Plesset equation can be written as:

$$\ddot{R}R + \frac{3}{2}\dot{R}^2 = \frac{P_v - P_\infty}{\rho} \tag{9.50}$$

where P_v is the vapor pressure and P_∞ is the pressure far away from the bubble wall. We disregard the surface tension, the sound reradiation and the viscosity. The boiling temperature of the liquid is T_b and the ambient temperature is T_∞. The liquid is superheated ($T_\infty > T_b$) so that $P_v > P_\infty$. The vapor pressure P_v is a function of the temperature and assumed to be constant during vapor bubble growth. Initially the velocity of the bubble wall $\dot{R}$ is small, and the first term on the left hand side of Eq. 9.50 is dominant. After approximately a few nanoseconds at $P_v = 1.4P_\infty$, the bubble wall velocity reaches its terminal value and the second term on the right hand side of Eq. 9.50 becomes dominant.

Terminal velocity is reached at the condition $\ddot{R} \to 0$. Substituting this into Eq. 9.50 and integrating with the initial condition $R(t=0)=0$ gives the radius-time dependency of the inertially limited vapor bubble growth:

$$R(t) = \left(\frac{2}{3}\frac{(P_v - P_\infty)}{\rho}\right)^{1/2} t \tag{9.51}$$

Equation 9.51 is linear with time and is faster for higher vapor pressures P_v, thus at higher ambient temperatures T_∞.

Let us now have a look at the second case, where we focus on heat transfer and where inertial limitations are neglected. Contrary to the solution of the inertial problem, the heat transfer is complicated by the temperature distribution outside the vapor bubble (Fig. 9.7).

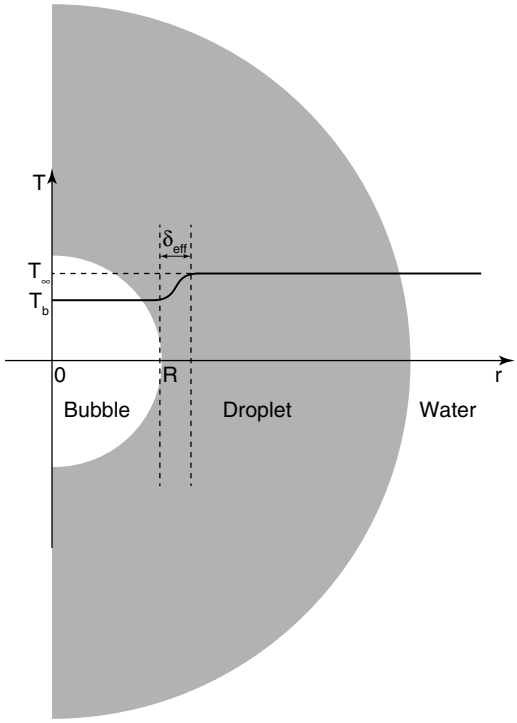

Fig. 9.7 Schematics of temperature distribution during the vaporization of a superheated perfluorocarbon droplet immersed in water. T_b is boiling temperature of perfluorocarbon, T_∞ is ambient temperature and δ_{eff} is effective thermal boundary layer around the vapor bubble of the radius R

The temperature distribution changes with time due to thermal diffusion. In addition, it is also affected by the expansion of the bubble, as described by the continuity equation. The effective thermal boundary layer around the vapor bubble is determined by (Prosperetti 2011):

$$\delta_{\text{eff}} = \sqrt{Dt} \tag{9.52}$$

where D is the thermal diffusivity of the liquid. This estimation follows from the thermal diffusion equation and shows that the thermal boundary layer diffuses with time as $\sqrt{t}$. On the vapor side of the thermal boundary layer the temperature is T_b, and on the liquid side of the thermal boundary layer the temperature is T_∞. The effective temperature gradient over the thermal boundary layer is $\Delta T / \delta_{eff}$, where $\Delta T = T_\infty - T_b$ is the temperature difference. The heat flow W_1 inside the vapor bubble from the surrounding liquid caused by the temperature mismatch can be estimated as follows:

$$W_1 = 4\pi R^2 k \frac{\Delta T}{\sqrt{Dt}} \tag{9.53}$$

where k is the heat transfer coefficient and $4\pi R^2$ is the interfacial area.

The latent heat energy per unit time W_2 required to supply the vapor bubble growth is:

$$W_2 = 4\pi R^2 L \rho_v \frac{dR}{dt} \tag{9.54}$$

with L the latent heat, and $4\pi R^2 \rho_v \frac{dR}{dt}$ the derivative of the mass, with ρ_v the density of the vapor. Equalizing Eqs. 9.53 and 9.54, and integrating with the initial condition $R(t=0)=0$, gives the radial dynamics of the heat transfer limited vapor bubble growth:

$$R(t) = 2\frac{k\Delta T}{L\rho_v\sqrt{D}}\sqrt{t} \tag{9.55}$$

It is dependent on time t following a square root behavior, and eventually will become slower than the inertia limited vapor bubble growth expressed by the linear dependence by Eq. 9.51. Thus, initially the vapor bubble growth is limited by the inertia, and then the vapor bubble growth becomes limited by the heat transfer. One can estimate the radius and the time when the transition of the two regimes occurs by calculating the intersection of the two curves expressed by the Eqs. 9.51 and 9.55. For typical parameters of acoustic perfluorocarbon droplet vaporization, the vapor bubble growth is heat transfer limited for a typical timescale longer than 1 microsecond (Fig. 9.8).

When the bubble growth is accompanied by bubble oscillations due to the ultrasound forcing, one can observe a phenomenon called rectified heat transfer. Rectified heat transfer is the net effect of the decrease of the heat transfer during the ultrasound half cycle when the vapor bubble surface contracts, and which is lower than the

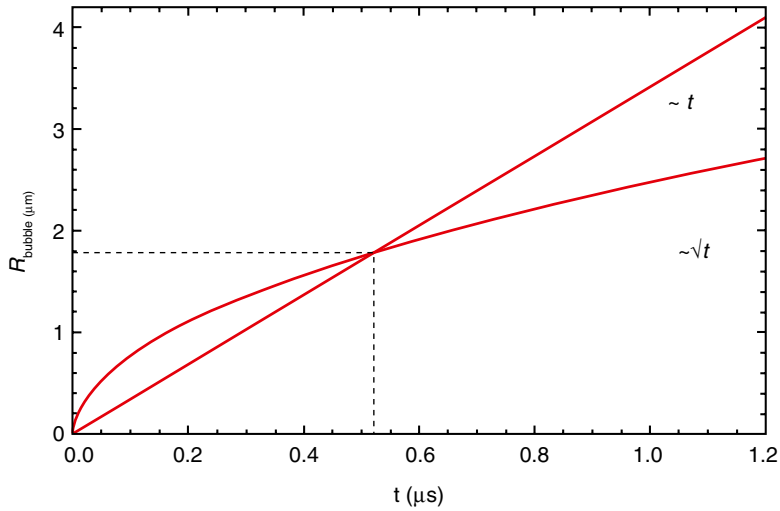

Fig. 9.8 Radius time dynamics of the inertial and the heat transfer limited vapor bubble growth in superheated liquid. The *curves* are calculated for perfluoropentane liquid (Boiling point $T_b = 29$ °C) at 35 °C ambient temperature employing the Eqs. 9.51 and 9.55. At $t = 0.52$ µs, the growth becomes limited by the heat transfer as it becomes slower than the growth limited by the inertia

increase of the heat transfer during the second half cycle when the surface expands. Here, two effects come into play; the increment of the bubble wall area during the expansion cycle, and the increment of the temperature gradient. The increment of the temperature gradient can be understood in the following way. Let us consider that the radius of the vapor bubble changes from R_0 to R. The change of the thin thermal boundary layer from δ_0 to δ is then calculated from continuity: $4\pi R^2\delta = 4\pi R_0^2\delta_0$. This gives (Prosperetti 2011):

$$\delta = \delta_0 \frac{R_0^2}{R^2} \tag{9.56}$$

and from the reciprocal relation for the temperature gradient:

$$\frac{\Delta T}{\delta} = \frac{\Delta T}{\delta_0}\frac{R^2}{R_0^2} \tag{9.57}$$

it can be seen that the temperature gradient increases with the radius squared, R^2, i.e. with the bubble wall area $4\pi R^2$. Thus, the bubble wall area and the temperature gradient will both decrease with R^2 when the radius decreases. However, the net effect is typically positive, meaning that bubble wall oscillations due to the interaction with ultrasound will pump additional heat into the bubble, thereby promoting the phase-conversion process; the larger the bubble oscillation amplitude, the stronger the pumping of additional heat.

9.4.4 Activation Below Boiling Point

After the initiation of droplet vaporization by the focused ultrasound pulse, gas diffuses into the nucleus/vapor bubble during vapor bubble growth as perfluorocarbon droplets dissolve air by an order of magnitude more than water. As was shown before, vapor bubble growth strongly depends on temperature. From both Eq. 9.51 and Eq. 9.55 it follows that the vapor bubble growth is slower when the ambient temperature is lower, whereas the dependence of air diffusion on the temperature is much less pronounced. This means that at low ambient temperatures ($T_\infty \le T_b$), the air diffusion dynamics becomes comparable to the evaporation processes.

Here, for simplicity, we only show the bubble growth dynamics due to gas diffusion, disregarding the evaporation processes and oscillations of the bubble due to ultrasound forcing. The partial pressure of gas P_g which is in equilibrium with the saturated gas concentration c_s dissolved in the liquid is given by Henry's law:

$$P_g = Hc_s \tag{9.58}$$

We assume that the liquid is at a uniform supersaturated concentration i. The mass flow of gas into the bubble per unit time is:

$$\frac{dm}{dt} = 4\pi R^2 \kappa \left.\frac{\partial c}{\partial r}\right|_{r=R} \tag{9.59}$$

where κ is the coefficient of diffusivity of the gas in the liquid. If ρ_g is the density of the gas in the bubble, the mass flow can be written as follows:

$$\frac{dm}{dt} = 4\pi R^2 \rho \frac{dR}{dt} \tag{9.60}$$

One can use the reasonable physical approximation to calculate the gradient of the concentration for a bubble interface, which changes in time by diffusion (Epstein and Plesset 1950):

$$\left.\frac{\partial c}{\partial r}\right|_{r=R} = \left(c_i - c_s\right)\left(\frac{1}{R} + \frac{1}{\sqrt{\pi\kappa t}}\right) \tag{9.61}$$

Substitution of Eqs. 9.60 and 9.61 into Eq. 9.59 gives the radial time dynamics equation for the gas diffusion:

$$\frac{dR}{dt} = \frac{\kappa\left(c_i - c_s\right)}{\rho}\left(\frac{1}{R} + \frac{1}{\sqrt{\pi\kappa t}}\right) \tag{9.62}$$

The gas bubble shrinks when $c_i < c_s$, and grows when $c_i > c_s$. Similar to the rectified heat transfer problem, gas diffusion into the bubble can be promoted due to interaction with ultrasound. This phenomenon is called rectified diffusion and similar relations can be derived as was shown in the previous subsection.

References

Bacon DR (1984) Finite amplitude distortion of the pulsed fields used in diagnostic ultrasound. Ultrasound Med Biol 10:189–195

Biro GP, Blais P, Rosen AL (1987) Peruorocarbon blood substitutes. CRC Critic Rev Oncol Hematol 6:311–374

Bjerknes VFK (1906) Fields of force. Columbia University Press, New York

Blackstock DT (1964) On plane, spherical and cylindrical sound waves of finite amplitude in loss less fluids. J Acoust Soc Am 36:217–219

Carneal CM, Kripfgans OD, Krucker J, Carson PL, Fowlkes JB (2011) A tissue mimicking ultrasound test object using droplet vaporization to create point targets. Pharm Res 58:2013–2025

Church CC (1995) The effects of an elastic solid surface layer on the radial pulsations of gas bubbles. J Acoust Soc Am 97:1510–1521

Cleveland R, Hamilton M, Blackstock DT (1996) Time-domain modeling of finite amplitude sound in relaxing fluids. J Acoust Soc Am 99:3312–3318

de Jong N, Emmer M, Chin CT, Bouakaz A, Mastik F, Lohse D, Versluis M (2007) Compression-only behavior of phospholipid-coated contrast bubbles. Ultrasound Med Biol 33:653–656

Epstein PS, Plesset MS (1950) On the stability of gas bubbles in liquid-gas solutions. J Chem Phys 18:1505–1509

Fabiilli ML, Haworth KJ, Sebastian IE, Kripfgans OD, Carson PL, Fowlkes JB (2010a) Delivery of chlorambucil using an acoustically-triggered perfluoropentane emulsion. Ultrasound Med Biol 36: 1364–1375

Fabiilli ML, Lee JA, Kripfgans OD, Carson PL, Fowlkes JB (2010b) Delivery of water-soluble drugs using acoustically triggered perfluorocarbon double emulsions. Ultrasound Med Biol 27:2753–2765

Giesecke T, Hynynen K (2003) Ultrasound-mediated cavitation thresholds of liquid perfluorocarbon droplets in vitro. Ultrasound Med Biol 29:1359–1365

Gramiak R, Shah PM (1968) Echocardiography of the aortic root. Invest Radiol 3:356–366

Hamilton M, Morfey C (2008) Model equations. In: Hamilton MF, Blackstock DT (eds) Nonlinear acoustics. Acoustical Society of America, Melville, pp 41–63

Hamilton M, Tjotta JN, Tjotta S (1985) Nonlinear effects in the farfield of a directive sound source. J Acoust Soc Am 78:202–216

Hart TS, Hamilton MF (1988) Nonlinear effects in focused sound beams. J Acoust Soc Am 84:1488–1496

Kamakura T, Ishiwata T, Matsuda K (2000) Model equation for strongly focused finite amplitude sound beams. J Acoust Soc Am 107:3035–3046

Karshafian R, Bevan PD, Williams R, Samac S, Burns PN (2009) Sonoporation by ultrasound-activated microbubble contrast agents: effect of acoustic exposure parameters on cell membrane permeability and cell viability. Ultrasound Med Biol 35:847–860

Klibanov AL (2006) Microbubble contrast agents: targeted ultrasound imaging and ultrasound-assisted drug-delivery applications. Invest Radiol 41:354–362

Kripfgans OD, Fowlkes JB, Miller DL, Eldevik OP, Carson PL (2000) Acoustic droplet vaporization for therapeutic and diagnostic applications. Ultrasound Med Biol 26:1177–1189

Kuznetsov VP (1971) Equation of nonlinear acoustics. Sov Phys Acoust 16:467–470

Lee YS, Hamilton MF (1995) Time-domain modeling of pulsed finite-amplitude sound beams. J Acoust Soc Am 97:906–917

Lee D, Pierce A (1995) Parabolic equation development in recent decade. J Comput Acoust 3:95–173

Leighton TG (1994) The acoustic bubble. Academic, London

Lindner JR (2004) Microbubbles in medical imaging: current applications and future directions. Nat Rev Drug Discov 35:527–533

Long DM, Multer FK, Greenburg AG, Peskin GW, Lasser EC, Wickham WG, Sharts CM (1978) Tumor imaging with x-rays using macrophage uptake of radiopâque fluorocarbon emulsions. Surgery 84:104–112

Marmottant P, van der Meer SM, Emmer M, Versluis M, de Jong N, Hilgenfeldt S, Lohse D (2005) A model for large amplitude oscillations of coated bubbles accounting for buckling and rupture. J Acoust Soc Am 118:3499–3505

Minnaert M (1933) On musical air-bubbles and sounds of running water. Philos Mag 16:235–248

Neppiras EA, Noltingk BE (1951) Cavitation produced by ultrasonics: theoretical conditions for the onset of cavitation. Proc Phys Soc B 64:1032–1038

Noltingk BE, Neppiras EA (1950) Cavitation produced by ultrasonics. Proc Phys Soc B 63:674–685

Overvelde M (2010) Ultrasound contrast agents: dynamics of coated bubbles. PhD thesis, University of Twente

Overvelde M, Garbin V, Sijl J, Dollet B, de Jong N, Lohse D, Versluis M (2010) Nonlinear shell behavior of phospholipid-coated microbubbles. Ultrasound Med Biol 36:2080–2092

Plesset MS (1949) The dynamics of cavitation bubbles. J Appl Phys 16:277–282

Poritsky H (1952) The collapse or growth of a spherical bubble or cavity in a viscous fluid. Proceedings of the first US National Congress on Applied Mechanics, ASME, New York, pp 813–821

Prosperetti A (2011) Advanced mathematics for applications. Cambridge University Press, Cambridge, UK/New York

Rapoport NY, Gao Z, Kennedy A (2007) Multifunctional nanoparticles for combining ultrasonic tumor imaging and targeted chemotherapy. J Natl Cancer Inst 99:1095–1106

Rapoport NY, Kennedy AM, Shea JE, Scaife CL, Nam KH (2009) Controlled and targeted tumor chemotherapy by ultrasound-activated nanoemulsions/microbubbles. J Control Release 138:268–276

Rayleigh L (1917) On the pressure development in a liquid during the collapse of a spherical cavity. Philos Mag 32:94–98

Reznik N, Shpak O, Gelderblom E, Williams R, de Jong N, Versluis M, Burns P (2013) The efficiency and stability of bubble formation by acoustic vaporization of submicron perfluorocarbon droplets. Ultrasonics 53:1368–1376

Schad KC, Hynynen K (2010) In vitro characterization of perfluorocarbon droplets for focused ultrasound therapy. Phys Med Biol 55:4933–4947

Shpak O, Kokhuis T, Luan Y, Lohse D, de Jong N, Fowlkes B, Fabiilli M, Versluis M (2013a) Ultrafast dynamics of the acoustic vaporization of phase-change microdroplets. J Acoust Soc Am 134:1610–1621

Shpak O, Stricker L, Versluis M, Lohse D (2013b) The role of gas in ultrasonically driven vapor bubble growth. Phys Med Biol 58:2523–2535

Shung KK (2006) Diagnostic ultrasound: imaging and blood flow measurements. CRC Press, Boca Raton

Szabo TL (2004) Diagnostic ultrasound, imaging, inside out. Academic, New York

Szabo TL, Clougherty F, Grossman C (1999) Effects on nonlinearity on the estimation of in situ values of acoustic output parameters. Ultrasound Med Biol 18:33–42

Unger EC, Porter T, Culp W, Labell R, Matsunaga T, Zutshi R (2004) Therapeutic applications of lipid-coated microbubbles. Adv Drug Deliv Rev 59:1291–1314

Unger EC, Hersh E, Vannan M, Matsunaga TO, McCreery T (2009) Local drug and gene delivery through microbubbles. Prog Cardiovasc Dis 41:45–54

Varslot T, Taraldsen G (2005) Computer simulation of forward wave propagation in soft tissue. IEEE Trans Ultrason Ferroelectr Freq Control 52:1473–1482

Westervelt P (1963) Parametric acoustic array. J Acoust Soc Am 52:535–537

Williams R, Wright C, Cherin E, Reznik N, Lee M, Gorelikov I, Foster FS, Matsuura N, Burns PN (2013) Characterization of submicron phase-change perfluorocarbon droplets for extravascular ultrasound imaging of cancer. Phys Med Biol 39:475–489

Zabolotskaya EA, Khokhlov RV (1969) Quasi-plane waves in the nonlinear acoustics of confined beams. Sov Phys Acoust 15:35–40

Zhang P, Porter T (2010) An in vitro study of a phase-shift nanoemulsion: a potential nucleation agent for bubble-enhanced HIFU tumor ablation. Ultrasound Med Biol 36:1856–1866

Zhang M, Fabiilli ML, Haworth KJ, Fowlkes JB, Kripfgans OD, Roberts WW, Ives KA, Carson PL (2010) Initial investigation of acoustic droplet vaporization for occlusion in canine kidney. Ultrasound Med Biol 36:1691–1703

Sonoporation: Concept and Mechanisms

10

Ayache Bouakaz, Aya Zeghimi, and Alexander A. Doinikov

Abstract

Contrast agents for ultrasound are now routinely used for diagnosis and imaging. In recent years, new promising possibilities for targeted drug delivery have been proposed that can be realized by using the microbubble composing ultrasound contrast agents (UCAs). The microbubbles can carry drugs and selectively adhere to specific sites in the human body. This capability, in combination with the effect known as sonoporation, provides great possibilities for localized drug delivery. Sonoporation is a process in which ultrasonically activated UCAs, pulsating nearby biological barriers (cell membrane or endothelial layer), increase their permeability and thereby enhance the extravasation of external substances. In this way drugs and genes can be delivered inside individual cells without serious consequences for the cell viability. Sonoporation has been validated both *in-vitro* using cell cultures and *in-vivo* in preclinical studies. However, today, the mechanisms by which molecules cross the biological barriers remain unrevealed despite a number of proposed theories. This chapter will provide a survey of the current studies on various hypotheses regarding the routes by which drugs are incorporated into cells or across the endothelial layer and possible associated microbubble acoustic phenomena.

Keywords

Sonoporation • Ultrasound • Microbubble • Mechanisms

10.1 Introduction

Targeted drug delivery is one of the most important goals of modern pharmacology and therapy. The strict localization of the pharmacological activity of a drug to the site of action would result in a significant reduction in drug toxicity,

A. Bouakaz (✉) • A. Zeghimi • A.A. Doinikov
Inserm Imaging and Ultrasound,
INSERM U930, Imagerie et Cerveau,
Université François-Rabelais de Tours, Tours, France
e-mail: ayache.bouakaz@univ-tours.fr

© Springer International Publishing Switzerland 2016

J.-M. Escoffre, A. Bouakaz (eds.), *Therapeutic Ultrasound*, Advances in Experimental Medicine and Biology, Vol. 880, DOI 10.1007/978-3-319-22536-4_10

reduction of the drug dose, and increased treatment efficacy. Currently a great amount of work is concentrated worldwide on the research of various targeted drug delivery systems. However, this goal still remains unachievable.

In recent years, new promising possibilities for targeted drug and gene delivery have been discovered that can be realized by using ultrasound contrast agents (UCAs). Ultrasound contrast agents are micron-sized encapsulated gas bubbles, which are produced by pharmaceutical companies for medical ultrasound applications (Goldberg et al. 2001; Szabo 2004). The encapsulation is necessary to prevent the microbubbles from fast dissolution in blood and from coalescence. Currently, contrast agents are used in ultrasonic diagnostics. In this case, they are injected into the bloodstream of the patient in order to increase the contrast between blood (microcirculation) and tissue during an ultrasonic examination and thereby to improve the quality of ultrasonic images and diagnosis confidence. Recently, specific contrast agents have been designed, which are capable of selectively adhering to desired target sites in the human body (Bloch et al. 2004; Klibanov 2006). Adhering to specific sites or tissues, such targeted agents can enhance the acoustic differences between normal and abnormal parts of organs and thereby improve the detectability of abnormalities, such as lesions, inflammatory processes and thrombi. Moreover, targeted contrast agents can carry drugs or genes on the encapsulating shell. This capability, in combination with the phenomenon known as sonoporation, provides unprecedented possibilities for a highly selective therapeutic action. The term sonoporation denotes a process in which ultrasonically activated contrast microbubbles, pulsating nearby cells or biological barriers, increase their permeability and thereby enhance the penetration and the extravasation of external substances (Ferrara et al. 2007; Kaddur et al. 2007). This leads to an increase in vascular permeability, thus facilitating the extravasation of drugs into targeted tissue and hence an augmented drug bioavailability without serious consequences for the cell viability (Fig. 10.1). In addition, this delivery system promises to be a low-cost technology, which is a notable feature of all ultrasound technologies.

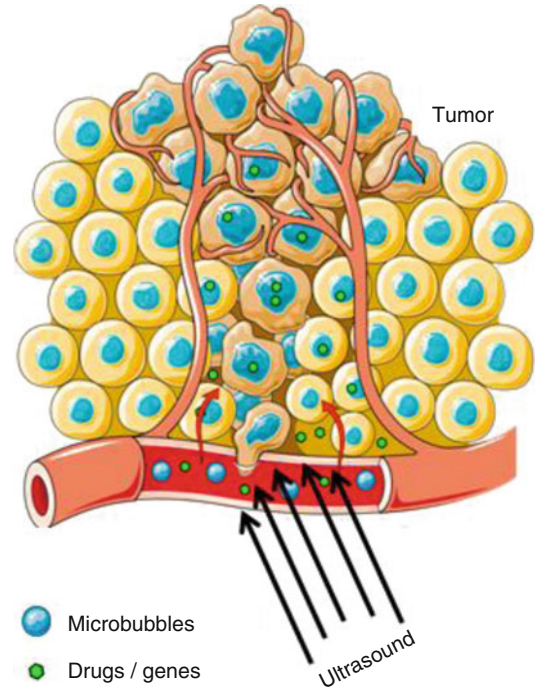

Fig. 10.1 Pictographic essay of sonoporation for drug and gene delivery (Adapted from Servier Medical Art, www.servier.fr)

The first experiments on sonoporation date back to the 1980s, where various ultrasound (US) exposure conditions were tested blindly at frequencies ranging from the kHz to the MHz (Ferrara et al. 2007; Escoffre et al. 2013). Sonoporation has also been evaluated using high-pressure amplitude US waves. Since then and with the recent introduction of contrast agents, higher frequency US in conjunction with cavitation has been called on to induce a range of effects on cells. Extensive examinations have been carried out to evaluate the efficiency of US in combination with contrast microbubbles for inducing cellular uptake. Although these results and findings were achieved in a controlled *in-vitro* environment, diagnostic US scanners were also useful for therapeutic applications of sonoporation, particularly with the guidance of treatment afforded by the imaging mode.

One of the first papers that described the use of sonoporation with ultrasound and UCAs dates back to 1997 (Bao et al. 1997). Since then, several studies have been reported on this topic, but so far the exact mechanism of sonoporation responsible for permeabilization remains unrevealed. Available hypotheses suggest that acoustic phenomena, such as stable and inertial cavitation, microstreaming, microjets, and shock waves are involved in the observed permeabilization sequences. All these acoustic phenomena are induced by the oscillations or destructions of microbubbles activated by US waves. Although the results obtained from these studies demonstrate the potential of sonoporation as a therapeutic strategy, they still provide conflicting conclusions. Some studies show that inertial cavitation is required for the induction of drug uptake; whilst others show that stable cavitation is sufficient. Microbubble jetting has been observed near a cell layer, but its effect on drug uptake was not really studied. The influence of microstreaming has rarely been studied in experiments using encapsulated contrast microbubbles, but there are various theoretical approaches. Other studies show that standing waves are required for drug uptake. A few recent reports have shown that oscillating microbubbles can deform cells, which could be a trigger for drug uptake. This suggests that drug uptake can be induced by several acoustic mechanisms. It has been reported that the conclusions about the mechanisms of cell membrane permeabilization are not straightforward despite numerous papers using various cell line models, ultrasound systems and experimental environments. Current investigations report only on drug uptake, electron microscopy observations, or cell electrophysiological measurements but do not address the relationship between microbubble acoustic behavior and drug uptake.

In this chapter, firstly we will present various acoustic phenomena that originate from the interaction of ultrasound waves and microbubbles and that are likely to be involved in the permeabilization of the cell membrane. In the second part, various assumed mechanisms by which molecules or drugs extravsate through the cell membrane and enter into the cytoplasm after sonoporation will be discussed. Finally, we will give a number of examples of *in-vivo* applications of sonoporation.

10.2 Mechanisms of Barrier Permeabilization and Molecular Delivery

Sonoporation was first demonstrated in the late 80s where kHz frequency ultrasound was evaluated for molecular uptake. This finding was original, although the efficiency of this approach was not fully proved. Following the introduction of ultrasound contrast agents in the late 90s, microbubbles were thought to be associated with a higher molecular uptake. Indeed, microbubbles, which are known to be a pure intravascular tracer, do not cross the endothelial barrier. However, their oscillations next to the endothelial layer might induce the permeabilization of the vessel wall. At the cellular level, microbubble oscillations increase the cell membrane permeability transiently. The availability of different contrasts and various protocols led to a large diversity of results on molecular uptake and efficiency rendering the comparison between them nearly impossible. It is believed that contrast microbubbles can be used as a nuclei trigger to enhance the delivery of drugs and molecules through the biological barriers. Nevertheless, the diversity of the insonation parameters did not allow providing precise conclusions and comparisons between various experimental conditions.

Although the sonoporation efficiency in permeabilizing the cell membrane was demonstrated, mechanisms behind the action of ultrasound and microbubbles were not clearly identified. Therefore several groups were engaged in elucidating the mechanisms responsible for cell membrane permeabilization caused by ultrasound and microbubble insonation. Current investigations report only on drug uptake, electron microscopy observations, or cell electrophysiological measurements but do not address the relationship between microbubble acoustic behavior and drug uptake.

10.2.1 Acoustical Phenomena

Various microbubble acoustic phenomena have been explored and studied to determine their involvement in the sonoporation mechanisms. Microstreaming, microjets, stable and inertial cavitations have been proposed as possible candidates in the transient or permanent permeabilization of the cell membrane. All these acoustic phenomena are induced by the oscillations or destructions of microbubbles activated by US waves.

One of acoustic phenomena that might impact mechanically on the cell membrane to make it permeable is acoustic microstreaming. When a bubble is driven acoustically, it is known to generate steady vortical flows in the surrounding liquid. It has been suggested that this phenomenon, called acoustic microstreaming, plays an important role in various biological effects of ultrasound, such as hemolysis, sonothrombolysis and sonoporation. Early experimental investigations into this phenomenon go back to the work of Kolb and Nyborg (1956) and Elder (1959), where the dependence of acoustic microstreaming on certain parameters (*e.g.,* amplitude of sound) was determined and observations of microstreaming patterns for various amplitudes and viscosities were made. Hughes and Nyborg (1962) were the first to show that bubble-induced vortex streaming can be used for disruption of cells in suspension. Pritchard et al. (1966) established that the number of breaks occurring in DNA molecules was directly related to velocity gradients of acoustic microstreaming. These effects were attributed to shear stresses exerted on cells and large molecules by the microstreaming. Further insights into this mechanism were given by experiments of Rooney (1970, 1972) on hemolysis produced by a single air bubble in an erythrocyte suspension.

The progress of experimental studies on microstreaming can be traced in works by Nyborg (1978), Liu et al. (2002), Tho et al. (2007), Wu and Nyborg (2008), Collis et al. (2010) and Wang et al. (2012). Wu et al. (2002) used a Mason horn with a 0.4 mm probe tip vibrating at 21.4 kHz. The transverse displacement amplitudes were

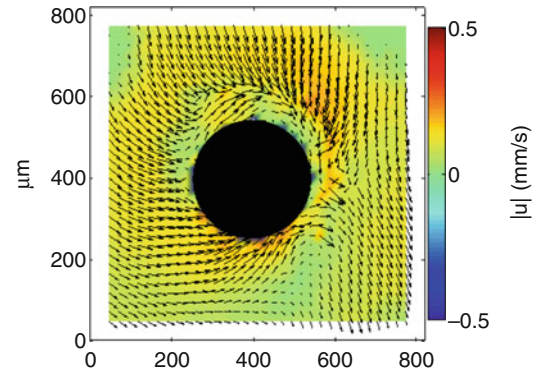

Fig. 10.2 Acoustic microstreaming around an air bubble as recorded with PIV using ultrasound at 28 kHz and 7 kPa

greater than 7.8 µm and produced shear stresses on the Jurkat cell suspension due to microstreaming. The authors believe that the generated microstreaming around the probe tip was the main reason for the cell reparable sonoporation, inducing the uptake of fluorescent dextran molecules. The threshold was estimated to be 12 Pa for an exposure time of up to 7 min (Ross et al. 2002).

Shear stresses generated by relatively large bubbles have been recorded using a particle imaging velocity (PIV) system. The PIV measurements were performed for bubbles of different sizes ranging from 200 to 400 µm (Novell et al. 2011). The results showed that the flow velocity exhibited a first peak near the bubble resonance. For this bubble, the shear stress is also maximal. The experimental measurements also revealed a second peak for bubbles larger than the resonance size but with lower amplitude. Figure 10.2 demonstrates an example of PIV images showing the microstreaming generated around a bubble of 200 µm in diameter at 28 kHz and an acoustic pressure of 7 kPa.

First theoretical studies on bubble-induced microstreaming were performed by Nyborg (1958). In particular, his theory gives a formula for shear stresses exerted on a rigid plane by a pulsating hemispherical bubble resting on this plane. This formula was used by Rooney (1972) for estimating shear stresses experienced by cells near a pulsating bubble. To apply Nyborg's formula to nonlinear bubble oscillations, Lewin and Bjørnø (1982) suggested combining

Nyborg's formula with the Rayleigh-Plesset equation. The combination of Nyborg's formula with the de Jong shell model was used by Wu (2002) to estimate shear stresses generated by contrast agent microbubbles. It was pointed out by Doinikov and Bouakaz (2010c) that the use of Nyborg's formula, which was derived for a hemispherical bubble, is not correct in the case of an encapsulated bubble. To solve this problem, they recalculated Nyborg's formula for the case of a spherical bubble being at a distance from a rigid plane. The same result, in a simplified formulation, was obtained by Yu and Chen (2014). Numerical simulations of shear stresses produced by free and encapsulated bubbles on a rigid wall were performed by Krasovitski and Kimmel (2004) using the boundary integral method. They came to the conclusion that the bubble-induced stress is several orders of magnitude greater than the physiological stress induced on the vessel wall by the flowing blood.

There are a number of theoretical models for the velocity and stress fields of acoustic microstreaming that is developed around a bubble in an unbounded liquid. Davidson and Riley (1971) derived equations for microstreaming generated by a bubble undergoing translational harmonic oscillations. Wu and Du (1997) and Longuet-Higgins (1998) considered the case of a bubble undergoing translational and radial oscillations. Maksimov (2007) extended the result of Longuet-Higgins (1998) so as to include the effect of parametrically excited surface modes of high order. Liu and Wu (2009) applied the approach of Wu and Du (1997) to calculate microstreaming produced by an encapsulated bubble. Doinikov and Bouakaz (2010a, b) extended the results of Wu and Du (1997) and Liu and Wu (2009) by taking into account shape oscillations and removing restrictions such as the assumption that the thickness of the viscous boundary layer surrounding the bubble is much smaller than the radius of the bubble. Doinikov and Bouakaz (2010b) also derived equations for acoustic microstreaming generated by a bubble in the presence of a distant rigid wall. They showed that the presence of the wall can change the amplitude and the phase of the bubble oscillations in such a way that the intensity of acoustic microstreaming is increased considerably as compared to that generated by the same bubble in an infinite liquid.

The shear mechanism has also been investigated optically. The interaction of an oscillating microbubble with cells has been observed with a high-speed camera (van Wamel et al. 2004). The observations with the use of endothelial cells revealed a strong mechanical action of SonoVue microbubbles insonified with a single ultrasound burst at 1 MHz and 0.9 MPa acoustic pressure. This action induces oscillatory stresses that pull and push the cell membrane, termed here cellular massage, and likely trigger various cellular and intracellular responses.

Besides microstreaming and shear stresses, other acoustic phenomena related to microbubble oscillations have been regarded as possibly responsible for or involved in the sonoporation mechanisms and effective in permeabilizing the cell membrane at megahertz frequencies and at acoustic pressures as low as a few MPa. Shock waves and liquid microjets generated in the course of inertial cavitation are among such phenomena.

Although the dominant hypothesis is now that sonoporation is caused by shear stresses exerted on the cell membrane by acoustic microstreaming, there are suggestions that pressure shock waves and liquid microjets generated by cavitating bubbles make a contribution as well. Interest in the above phenomena goes back to applied hydrodynamic problems such as cavitation damage of ship propellers and hydraulic turbine blades and ultrasonic cleaning of contaminated surfaces. The literature on the subject is very expensive. There are a number of reviews, written in different years, that describe at length available experimental observations: Plesset and Prosperetti (1977), Mørch (1979), Blake and Gibson (1987), Leighton (1994), Brennen (1995) and Lauterborn and Kurz (2010). Experimental estimates show that the spherical shock wave produced by a collapsing bubble may have an amplitude of up to 1 GPa but this shock so rapidly dies down that its impact may be significant only at distances of about the initial bubble radius. However, in a concentrated bubble cluster, the combined shocks from many collapsing bubbles

can cause damage at much greater distances. The feasibility of this process was supported by the experimental observations of Brunton (1967), Vyas and Preece (1976) and Shima et al. (1983).

A hypothesis that the asymmetric collapse of a bubble might generate a liquid microjet was first put forward by Kornfeld and Suvorov (1944). The first experimental and theoretical evidence of this phenomenon was provided by Naudé and Ellis (1961) and later Benjamin and Ellis (1966). Modern experimental techniques reached the stage where collapsing bubbles can be filmed at framing rates of up to 100 million frames per second: see Lauterborn (1972), Vogel et al. (1989), Field (1991), Ohl et al. (1999) and Lindau and Lauterborn (2003). Particularly impressive experiments were performed by Lindau and Lauterborn (2003). They observed the bubble jetting and shock wave emissions using high-speed cinematography of laser-produced cavitation bubbles near a rigid boundary. Experiments in which the effect of a compliant elastic boundary on the bubble collapse is investigated are reported by Brujan et al. (2001a, b). In particular, Brujan et al. observed that the interaction of a collapsing bubble with a boundary consisting of a polyacrylamide gel with 80 % water concentration could lead to, depending on conditions, bubble splitting, formation of liquid jets away from and towards the boundary, and jet-like ejection of the boundary material into the surrounding liquid.

Much work has been done on numerical modeling of bubble collapse and jet formation. Most numerical studies are based on various modifications of the boundary integral method and focus on modeling the aspherical collapse of a bubble near a rigid boundary with the formation of a liquid jet. Comparisons of measured and simulated results, for example, those made by Lauterborn and Bolle (1972) for the bubble shape at the initial stages of the collapse and Vogel et al. (1989) for liquid flow velocities during the jetting process, demonstrate good agreement.

Biomedical applications have given new impetus to studies on shock waves and microjets generated by cavitating bubbles. Kudo et al. (2009) reported that the generation of liquid microjets caused cell membrane perforation. Similar results were reported previously by Ohl et al. (2006). They investigated experimentally the interaction of a cell monolayer in the culture dish with ultrasound at high peak negative acoustic pressures (4 MPa) and observed that the high intensity ultrasound caused the detachment of cells at the focal depth. Using optical observations, they observed cell removal and showed the cells at the edge of the area became permanently porated and the surrounding cells incorporated the fluorescent marker, calcein. These observations were associated with the collapse of large cavities, which generated a strong fluid flow field. In a separate study, these cavities were assumed to be of the order of tens of micrometers as described by Le Gac et al. (2007).

Koshiyama et al. (2006, 2008) conducted a series of full atomistic molecular dynamics simulations of cell membrane models (lipid bilayers) subject to shock waves. They observed that shock impulses caused the compression and the rebound of the lipid bilayer in the course of which water molecules penetrated inside the hydrophobic core of the membrane. However, in none of these simulations, the formation of transient hydrophilic pores in the membrane occurred. It remained unclear if this was due to a rather small size of the patches considered in the simulations but in a more recent study, Koshiyama et al. (2010) have shown that such pores could form during the reorganization of a bilayer soaked with water. This effect was suggested as a possible mechanism of sonoporation, provided that shock waves lead to fast (subnanosecond) penetration of a huge quantity of water into the lipid hydrophobic region. However, it should be mentioned that their simulations did not consider the presence of gas microbubbles.

10.2.2 Hypothesized Impacts of Acoustic Phenomena on Cell Membrane and Molecular Uptake

The mechanisms involved in the sonoporation process and the cell membrane permeabilization remain poorly identified. Although no consensus

has been reached, several scenarios have been hypothesized, such as the formation of pores, further stimulation of endocytotic pathways and the occurrence of membrane wounds. Elucidating the mechanisms responsible for the delivery of compounds to cells and the kinetics of permeabilization is essential for improving and controlling this therapeutic strategy.

10.2.2.1 Pore Formation

One of the earliest reports on the formation of pores on the cell membrane after ultrasound insonation dates to (1999). The study showed that applying ultrasound at 255 kHz to a suspension of HL-69 cells in presence of photosensitive drug induced cell porosity where craters were observed on the cell membrane. The authors concluded that such holes or craters are responsible for cell killing.

In 2005, the group from Bracco reported the formation of small pores in the nanometer range on MAT B III cells (2005). Using dextran markers of various sizes as drug mimics, they concluded that molecules of a diameter ranging from 11 to 37 nm crossed the membrane and entered in the cell through the formation of small pores. The group from Gent University (Geers et al. 2011) studied the transduction of cells by means of adeno-associated-virus (AAV) as a vector, which totally relies on the receptor-mediated endocytosis to successfully transducer the cells using BLM melanoma cells. They made the use of pegylated AAV, which reduces strongly the endocytosis of AAV. The cells were then tranducted using the BacMam™ 2.0 technique (GFP-reporter gene targeting the Rab5a). They observed no significant colocalization of these red-labeled vectors with the green-labeled endosomes, as no merged green and red (orange) signals could be observed inside the cells meaning that molecules ranging from 20 to 30 nm entered through pores only. These results are in contradiction with those reported earlier by the Dutch team (Meijering et al. 2009). By studying the cellular localization of fluorescent dextrans after sonoporation, they found that the smaller dextran molecules of 4.4 and 70 kDa were homogeneously distributed throughout the cytosol. This is similar to the cellular distribution found after the microinjection of dextran molecules from 3 to 70 kDa (3–8 nm) into the cytosol indicating that during sonoporation, the small dextran molecules enter cells via transient pores in the cell membrane. In contrast, dextran molecules of 155 and 500 kDa (>17 nm) were mainly localized in vesicle-like structures after sonoporation, indicating that the larger dextrans might be taken up via endocytosis. When these dextran molecules had entered via pores, a homogeneous cytosolic distribution would be expected, comparable to the distribution of these dextran molecules after microinjection. They concluded that molecules of a size less than 17 nm entered through pores while molecules larger than 17 nm entered through endocytosis pathways. Nevertheless, they did not indicate which endocytosis pathways might be involved.

Zhou et al. (2012) used controlled manipulation techniques to correlate the ultrasound-generated bubble activities with the cell membrane poration using Xenopus oocyte. They attributed the change in membrane permeability to a submicrometer pore caused by a local membrane rupture formed by bubble collapse or bubble compression depending on ultrasound amplitude and duration. The study was extended to investigate the sonoporation and to quantify the size and the resealing rate of the pores on a single cell using cell-attached microbubbles (2012).

Recently, Hu et al. (2013) have shown by using a cell/microbubble ratio of 1:1 that a localized perforation of the cell membrane occurs immediately upon application of a 10-cycle ultrasound pulse. It was also demonstrated that the pore creation (5.3 μm long axis diameter) was synchronized with the time of bubble collapse. This membrane disruption is transient as membrane releasing commenced within 5 s after the incidence of sonoporation, and took between 6 and 20 s to be fully restored. In contrast, large pores (12–32.6 μm) appeared following sonoporation, but did not reseal.

10.2.2.2 Endocytosis

Endocytosis pathways have been hypothesized as a mechanism of a potential plausible route for

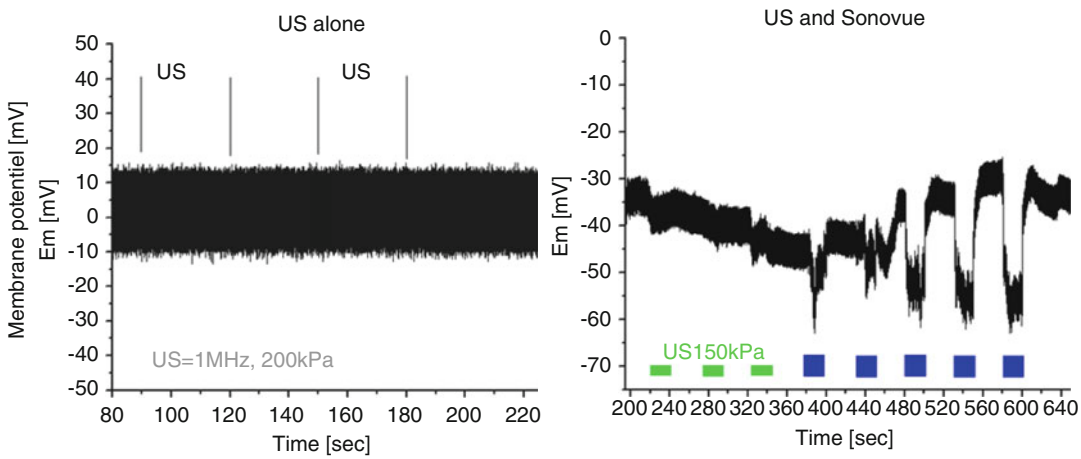

Fig. 10.3 Cell membrane potential after ultrasound insonation (*left*) and ultrasound and SonoVue microbubbles (*right*)

molecule incorporation into cells after sonoporation. A number of cellular reactions observed after ultrasound activation were attributed to molecular uptake, including ion exchange, hydrogen peroxide and cell intracellular calcium concentration.

Fluorescence (Lionetti et al. 2009; Meijering et al. 2009; Paula et al. 2011) and electron microscopy (Saito et al. 1999; Mehier-Humbert et al. 2005; Duvshani-Eshet et al. 2006; Yang et al. 2008; Hauser et al. 2009) studies showed an exceedingly high amount of endocytic vesicles and clathrin coated pits in sonicated cells group, while control cell sections showed single endocytic vesicles. It is believed that Ca^{2+} controls the uncoating of clathrin-coated pits, thus high concentrations of calcium in the cytosol are thought to trigger the uncoating of endocytic vesicles. Therefore, calcium presumably plays a crucial role in the turnover of clathrin-coated vesicles (Hauser et al. 2009).

Tran et al. (2007) investigated the implication of endocytosis routes in the sonoporation mechanisms. Ruptured-patch clamp whole-cell technique was used to measure membrane potential variations of a single cell in the presence of SonoVue microbubbles after application of ultrasound waves at 1 MHz. Microbubbles and cells were simultaneously video monitored during ultrasound exposure. The results displayed in Fig. 10.3 showed that, during sonoporation, a marked cell membrane hyperpolarization occurs at negative pressure amplitudes above 150 kPa, indicating the activation of specific ion channels, while the cell and the microbubbles remain viable. The hyperpolarization was sustained for as long as the microbubbles were in a direct contact with the cell and the ultrasound waves were transmitted. Smaller acoustic amplitudes induced only mild hyperpolarization, whereas shutting off the ultrasound brought the cell membrane potential to its resting value. However, ultrasound alone did not affect the cell membrane potential.

A similar hyperpolarization of the cell membrane was observed when mechanical pressure was applied to the cell through a glass probe (Fig. 10.4). The change in cell membrane potential indicates the activation of specific ion channels and depends on the quality of microbubble adhesion to the cell membrane. The use of IbTx showed that microbubbles induced a mechanical stretch activating BK_{Ca} channels. Simultaneous Ca^{2+} measurements indicate a slow and progressive Ca^{2+} increase, which is likely to be a consequence of BK_{Ca} channels opening but not a cause. In conclusion, these results demonstrate that microbubble oscillations under ultrasound activation entail the modulation of cellular function and signaling by triggering the modulation of ionic transports through the cell membrane. Cell response to the mechanical stretch caused by gentle microbubble oscillations is characterized

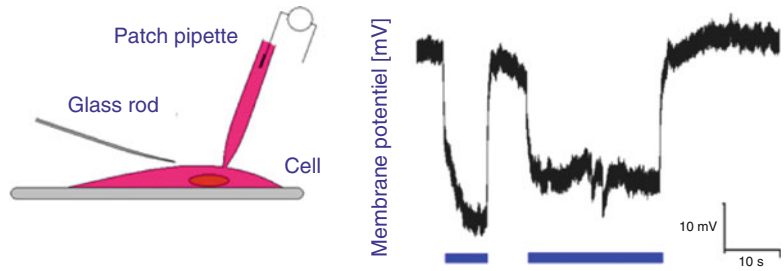

Fig. 10.4 Cell membrane potential after the application of manual mechanical pressure

by the opening of BK_{Ca} stretch channels and a Ca^{2+} flux, which might potentially trigger other cellular reactions responsible for membrane sonopermeabilization.

Juffermans et al. (2006) have observed chemical stress by inducing the formation of free radicals. A significant increase in the production of H_2O_2 after ultrasound-exposed MBs compared with US alone, inducing Ca^{2+} influxes and thus cell membrane permeabilization. At physiological $[Ca^{2+}]_0$, ultrasound application caused immediate $[Ca^{2+}]_i$ transients in some cells, followed by delayed initiation of $[Ca^{2+}]_i$ transients in other surrounding cells (Kumon et al. 2009; Fan et al. 2010). The delay time can be up to 1 min or more. In addition, significant calcium transients and waves were distinctly correlated spatially and temporally with the application of ultrasound and only occurred in the presence of microbubbles. Furthermore, cell-to-cell contact is not always necessary for calcium waves to occur (Sauer et al. 2000).

Similar results have been reported by Juffermans et al. (2008), in which they demonstrated that US-exposed microbubbles caused an influx of calcium ions and local hyperpolarization of the cell membrane in rat cardiomyoblast cells. The same group reported in 2009 (Juffermans et al. 2009), using the same cells, the effect of oscillating microbubbles on a number of cellular parameters. They demonstrated increased membrane permeability for calcium ions, with an important role of hydrogen peroxide (H_2O_2). Further changes in ROS homeostasis involved an increase in intracellular H_2O_2 levels, protein nitrosylation and a decrease in total endogenous glutathione levels.

It has long been reported that during microbubble collapse, extremely high pressures on the order of hundreds of atmospheres and extremely high temperatures on the order of thousands of degrees Kelvin are generated in the vapor phase inside the bubble. These processes were shown to produce under certain conditions highly reactive free radicals. The results of spin-trapping and electron spin resonance studies provided evidence for the formation of hydroxyl radicals $OH^{\bullet}$ and hydrogen atoms $H^{\bullet}$ during the sonolysis of aqueous solutions (Makino et al. 1982; Didenko and Suslick 2002). Sonochemistry reports in fact several primary reaction mechanisms that are believed to occur during sonication:

$$H_2O \Leftrightarrow H^{\bullet} + OH^{\bullet}$$
$$H^{\bullet} + H^{\bullet} \Leftrightarrow H_2$$
$$OH^{\bullet} + OH^{\bullet} \Leftrightarrow H_2O_2$$
$$H^{\bullet} + O_2 \Leftrightarrow HO_2^{\bullet}$$
$$H^{\bullet} + HO_2 \Leftrightarrow H_2O_2$$
$$HO_2^{\bullet} + HO_2^{\bullet} \Leftrightarrow H_2O_2 + O_2$$
$$H_2O^{\bullet} + OH^{\bullet} \Leftrightarrow H_2O_2 + H^{\bullet}$$

These reactions have been considered in sophisticated models to explain experimentally observed sonochemical phenomena (Didenko and Suslick 2002). Comparing three clinically used US contrast agents, Hassan et al. (2010) showed that both shell elasticity and reactivity played a role in modulating the extent of ultrasound-induced free-radical formation. The role of free radicals in the phenomenon of cell membrane permeabilization was also assessed using ultrasound alone (Lionetti et al. 2009). The authors showed that ultrasound at high intensities (mechanical index >1) was able to enhance endothelial caveolar internalization of recombinant EGFP fusion protein, while free-radical

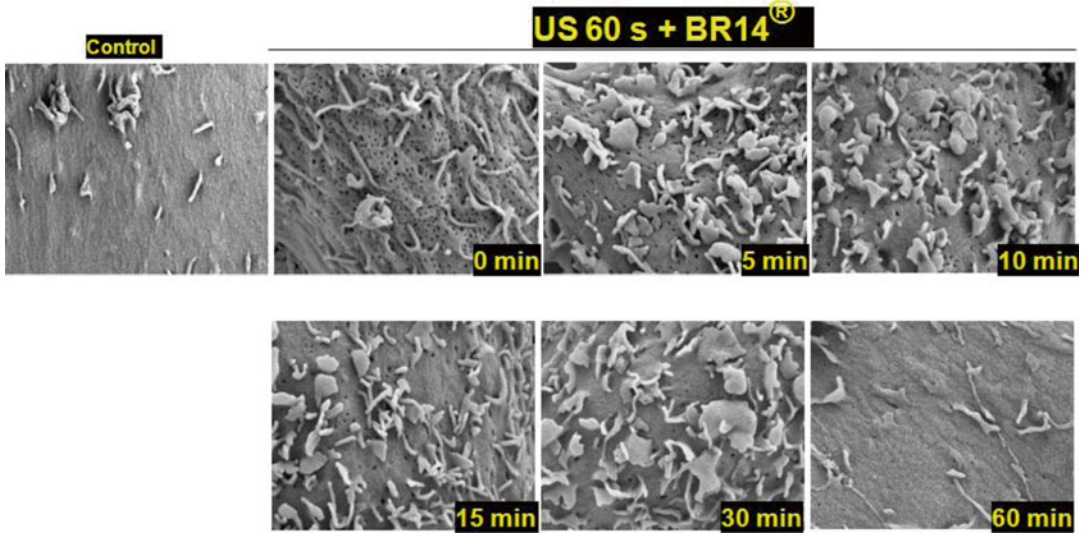

Fig. 10.5 SEM Observations of U-87 MG cells insonified with ultrasound in the presence of BR14 microbubbles. The cells were fixed immediately, and then at different time points after sonoporation

generation inhibitors, such as catalase and superoxide dismutase, reduced the induced internalization by a 49.29 % factor.

Taken together, these results indicate that sonoporation induces an activation of ionic channels, formation of hydrogen peroxide and influx of calcium ions. These cellular reactions are known to be directly related to endocytosis. More recently, the implication of caveole-endocytosis pathways in the mechanisms of cell membrane permeabilization using ultrasound and microbubbles has been hypothesized. In this study, scanning electron microscopy (SEM) was used to investigate the dynamic ultra-structural modifications of cell membranes, induced by sonoporation (Zeghimi et al. 2012). The study showed that sonoporation in the presence of microbubbles induced the formation of a significant number of permeant structures (TPS) at the membrane level. These structures were transient with a half-life of 15 min and had a heterogeneous size distribution ranging from a few nanometers to 150 nm (Fig. 10.5). The number and the size of these structures were positively correlated with the enhanced intracellular uptake of non-permeant molecules (Sytox Green).

Transmission electron microscopy (TEM) images showed a large number of uncoated pits at the plasma membrane level of the cells, which suggests that sonoporation probably increases the native permeability of plasma membranes through caveolae-dependent endocytosis pathways (Fig. 10.6a, b). This was confirmed when the cells were incubated with Genistein, a specific inhibitor of caveolae-endocytosis pathway. The number of uncoated pits for sonoporated cells pre-treated with genistein decreased significantly as compared to sonoporated cells without genistein incubation, thus suggesting that sonoporation stimulated the caveolae-dependent endocytosis.

10.2.2.3 Membrane Wounds

Tachibana et al. (1999) studied the structure of the cell surface with scanning electron microscopy after exposure to continuous wave ultrasound at low frequency (255 kHz). They showed that the cytoplasm of sonicated cells in the presence of a photosensitive drug appeared to get squeezed out through the cell surface, probably due to extensive cell membrane disruptions. These cells seemed to be non viable anymore.

Other studies using microscopic imaging and physical methods, such as shear forces, mechanically created wounds of sub-micrometer radius in the plasma membrane, through which

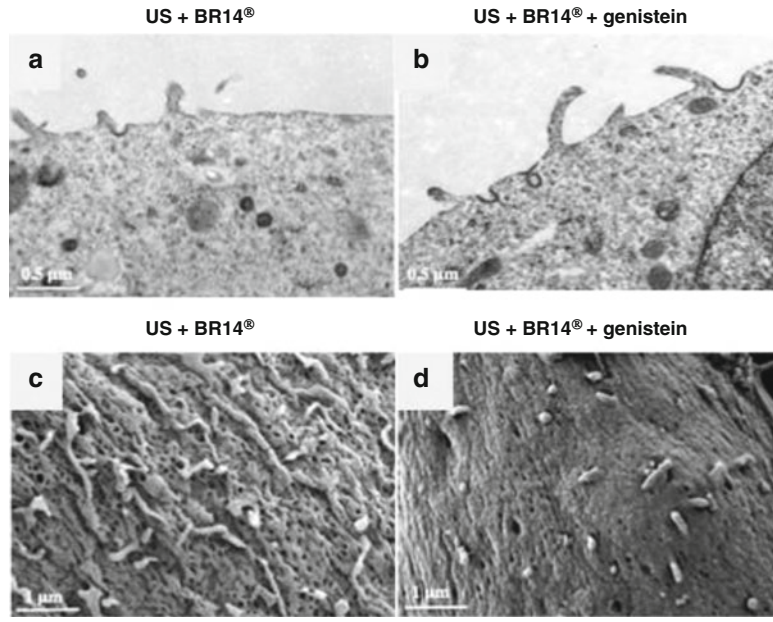

Fig. 10.6 Transmission electron microscopy images (**a**, **b**) and scanning electron microscopy images (**c**, **d**) of U-87 MG cells after sonoporation: (**a**, **c**) without genistein incubation; (**b**, **d**) with genistein incubation

molecules loading occurred (Fechheimer et al. 1987; Zarnitsyn et al. 2008). These wounds are resealed in time by the aggregation and the fusion of lipid vesicles trafficked to the wound site using an active cellular repair processes (McNeil and Terasaki 2001). Theoretical modeling predicted that membrane wounds would have a 300 nm radius initially, then they would shrink, with a half-life of 20–50 s, and then they are completely resealed in 900 s after sonication (Zarnitsyn et al. 2008). They assumed that (i) after the first second of cell wounding, the only mechanism governing the transport on the scale of seconds and minutes is passive diffusion through long-lived wounds in the plasma membrane, (ii) a "sufficiently large" number of nanopores are present in the wound, and (iii) the transport to and from the wound surface is rate-limiting; it is relatively fast because diffusion through the 5-nm-thick nanopores should be fast relative to diffusion between the bulk solution and the wound area.

Furthermore, Schlicher et al. (2010), using SEM, Cryo-SEM and LSCM (Laser Scanning Confocal Microscopy) on DU145 prostate-cancer cells, have reported that wounded cells produced spherically protruding "balloons" and "blister" blebs which pinched off into the extracellular environment at the sites of plasma membrane disruption. The balloon blebs might contain small round lipid vesicles derived from endoplasmic reticulum, indicating that the blebs accessed the cytosol, while the "blister" blebs were created by lipids integrated with the plasma membrane and filled with clear fluid. Moreover, a loss or disruption of actin at sites of blebs formation was observed. In addition, this study reports that acoustic cavitation can also lead to multiple types of membrane blebbing, formation of perikarya, nuclear ejection and instant cell lysis, depending on the degree of wounding incurred.

Most of cells are able to reseal their membrane wounds, despite the damages of their plasma membrane (Andrew et al. 1999; Wu et al. 2002). The resealing of large wounds is similar to resealing processes to repair membrane patches damaged by micropipette insertion into a cell (McNeil and Steinhardt 2003). The repair of these wounds requires the recruitment of intracellular vesicles to the site of disruption and this process is ATP-dependent (Zarnitsyn et al. 2008). Also, it has been reported that the cell recovery after wounding might be related to bleb formation (Schlicher et al. 2010).

Conclusions

Sonoporation of cells and tissues by ultrasonically activated microbubbles is a fascinating phenomenon, which has intrigued many research laboratories worldwide in the last 15 years. More than 150 papers have been published on sonoporation *in-vitro*. Sonoporation was achieved using low frequency ultrasound (of the order of tens of kHz), shockwave lithotripters, medical therapeutic or even diagnostic ultrasound systems and various purpose built laboratory systems in the low MHz frequency range. The sonoporation activity can be generated by pre-existing cavitation nuclei, but better control of the process is achievable by adding stabilized microbubbles to the medium, such as ultrasound contrast agents.

The interaction of ultrasound and cells in the presence of contrast microbubbles induces a modulation of cell membrane permeability and as a result, molecules, which normally do not cross the barrier (cell membrane, endothelial layer), do penetrate into the cell. The transfer of these molecules seems to occur in association with various acoustic phenomena such as microstreaming, shear stress, shockwaves and microjets or a combination of them.

Despite a significant scientific progress during the last few years in the understanding of the cell-ultrasound and microbubble interaction, the mechanisms by which the molecules cross the biological barrier and enter into the cell cytoplasm after sonoporation are still not reasonably understood and no consensus is reached yet. Today, various hypotheses, including (i) non-selective poration of the cell membrane, (ii) endocytosis stimulation and (iii) formation of large cell membrane wounds, have been proposed. Moreover, there are various diverging reports on the duration of the permeabilization process after sonoporation. Some studies indicate transient permeabilizaation of a few seconds to minutes while other reports mention much longer permeabilization durations of up to 24 h.

A number of molecules have transferred into cells with sonoporation including Different molecules have been transferred into cells using sonoporation, including small fluorescent molecules, RNA, plasmid DNA, plasmid lipoplexes, nanoparticles, anti-cancer drugs, anti-bodies and viruses. The types of sonoporated cells vary from primary cells in suspension or adherent configurations to bacteria and cancer cells. Sonoporation has been evaluated in various applications for gene and drug delivery and, as a result, many organs have been targeted with most of the applications directed to tumor, heart, brain and skeletal muscle.

In conclusion, although sonoporation has been extensively investigated with the aim of delivering therapeutic compounds and treating a number of pathologies, it is prudent to consider that the interaction of ultrasound and gaseous microbubbles with cells involves a degree of randomness and can sometimes engender lethal effects. It has been shown that sonoporated cells might undergo apoptosis, have poor cloning efficiency or can suffer from malfunction. Therefore, safety remains an important factor to be addressed before implementing the current results and the technology into the clinic.

References

Andrew A, Brayman ML, Coppage S, Vaidya MWM (1999) Transient poration and cell surface receptor removal from human lumphocytes in vtro by 1 MHz ultrasound. Ultrasound Med Biol 25:999–1008

Bao S, Thrall BD, Miller DL (1997) Transfection of a reporter plasmid into cultured cells by sonoporation in vitro. Ultrasound Med Biol 23:953–959

Benjamin TB, Ellis AT (1966) The collapse of cavitation bubbles and the pressures thereby produced against solid boundaries. Philos Trans R Soc A 260:221–240

Blake JR, Gibson DC (1987) Cavitation bubbles near boundaries. Annu Rev Fluid Mech 19:99–123

Bloch SH, Dayton PA, Ferrara KW (2004) Targeted imaging using ultrasound contrast agents: progress and opportunities for clinical and research applications. IEEE Eng Med Biol Mag 23:18–29

Brennen CE (1995) Cavitation and bubble dynamics. Oxford University Press, Oxford, pp 79–111

Brujan EA, Nahen K, Schmidt P, Vogel A (2001a) Dynamics of laser-induced cavitation bubbles near an elastic boundary. J Fluid Mech 433:251–281

Brujan EA, Nahen K, Schmidt P, Vogel A (2001b) Dynamics of laser-induced cavitation bubbles near

elastic boundaries: influence of the elastic modulus. J Fluid Mech 433:283–314
Brunton JH (1967) Erosion by liquid shock. In: Fyall AA, King RB (eds) Proceedings of the 2nd international conference on rain erosion and allied phenomena. Royal Aircraft Establishment, Farnborough, pp 291–309
Collis J, Manasseh R, Liovic P, Tho P, Ooi A, Petkovic-Duran K, Zhu Y (2010) Cavitation microstreaming and stress fields created by microbubbles. Ultrasonics 50:273–279
Davidson BJ, Riley N (1971) Cavitation microstreaming. J Sound Vib 15:217–233
Didenko Y, Suslick KS (2002) The energy efficiency of formation of photons, radicals, and ions during single bubble cavitation. Nature 418:394–397
Doinikov AA, Bouakaz A (2010a) Acoustic microstreaming around a gas bubble. J Acoust Soc Am 127:703–709
Doinikov AA, Bouakaz A (2010b) Acoustic microstreaming around an encapsulated particle. J Acoust Soc Am 127:1218–1227
Doinikov AA, Bouakaz A (2010c) Theoretical investigation of shear stress generated by a contrast microbubble on the cell membrane as a mechanism for sonoporation. J Acoust Soc Am 128:11–19
Duvshani-Eshet M, Baruch L, Kesselman E, Shimoni E, Machluf M (2006) Therapeutic ultrasound-mediated DNA to cell and nucleus: bioeffects revealed by confocal and atomic force microscopy. Gene Ther 13:163–172
Elder SA (1959) Cavitation microstreaming. J Acoust Soc Am 31:54–64
Escoffre JM, Zeghimi A, Novell A, Bouakaz A (2013) In-vivo gene delivery by sonoporation: recent progress and prospects. Curr Gene Ther 13:2–14
Fan Z, Kumon R, Park J, Deng CX (2010) Intracellular delivery and calcium transients generated in sonoporation facilitated by microbubbles. J Control Release 142:31–39
Fechheimer M, Boylan JF, Parker S, Sisken JE, Patel GL, Zimmer SG (1987) Transfection of mammalian cells with plasmid DNA by scrape loading and sonication loading. Proc Natl Acad Sci U S A 84:8463–8467
Ferrara K, Pollard R, Borden M (2007) Ultrasound microbubble contrast agents: Fundamentals and application to gene and drug delivery. Annu Rev Biomed Eng 9:415–447
Field JE (1991) The physics of liquid impact, shock wave interactions with cavities, and the implications to shock-wave lithotripsy. Phys Med Biol 36:1475–1484
Gac SL, Zwaan E, van den Berg A, Ohl CD (2007) Sonoporation of suspension cells with a single cavitation bubble in a microfluidic confinement. Lab Chip 7:1666–1672
Geers B, Lentacker I, Alonso A, Sanders NN, Demeester J, Meairs S, De Smedt SC (2011) Elucidating the mechanisms behind sonoporation with adeno-associated virus-loaded microbubbles. Mol Pharm 8:2244–2251
Goldberg BB, Raichlen JS, Forsberg F (2001) Ultrasound contrast agents: basic principles and clinical applications. Martin Dunitz, London
Hassan MA, Feril LB Jr, Kudo N, Tachibana K, Kondo T, Riesz P (2010) The sonochemical and biological effects of three clinically-used contrast agents. Jpn J Appl Phys 49:1347
Hauser J, Ellisman M, Steinau HU, Stefan Dudda M, Hauser M (2009) Ultrasound enhanced endocytotic activity of human fibroblasts. Ultrasound Med Biol 35:2084–2092
Hughes DE, Nyborg WL (1962) Cell disruption by ultrasound. Science 138:108–114
Hu Y, Wan JM, Yu AC (2013) Membrane perforation and recovery dynamics in microbubble-mediated sonoporation. Ultrasound Med Biol 39:2393–2405
Juffermans LJM, van Dijk A, Jongenelen CA, Drukarch B, Reijerkerk A, de Vries HE, Kamp O, Musters RJ (2009) Ultrasound and microbubble-induced intra- and intercellular bioeffects in primary endothelial cells. Ultrasound Med Biol 35:1917–1927
Juffermans LJM, Dijkmans PA, Musters RJP, Visser CA, Kamp O (2006) Transient permeabilization of cell membranes by ultrasound-exposed microbubbles is related to formation of hydrogen peroxide. Am J Physiol Heart Circ Physiol 291:H1595–H1601
Juffermans LJM, Kamp O, Dijkmans PA, Visser CA, Musters RJ (2008) Low-intensity ultrasound-exposed microbubbles provoke local hyperpolarization of the cell membrane via activation of BK(Ca) channels. Ultrasound Med Biol 34:502–598
Kaddur K, Palanchon P, Tranquart F, Pichon C, Bouakaz A (2007) Sonopermeabilization: Therapeutic alternative with ultrasound and microbubbles. J Radiol 88:1777–1786
Klibanov AL (2006) Microbubble contrast agents: Targeted ultrasound imaging and ultrasound-assisted drug-delivery applications. Invest Radiol 41:354–362
Kolb J, Nyborg W (1956) Small-scale acoustic streaming in liquids. J Acoust Soc Am 28:1237–1242
Kornfeld M, Suvorov L (1944) On the destructive action of cavitation. J Appl Phys 15:495–506
Koshiyama K, Kodama T, Yano T, Fujikawa S (2006) Structural change in lipid bilayers and water penetration induced by shock waves: molecular dynamics simulations. Biophys J 91:2198–2205
Koshiyama K, Kodama T, Yano T, Fujikawa S (2008) Molecular dynamics simulation of structural changes of lipid bilayers induced by shock waves: effects of incident angles. Biochim Biophys Acta 1778: 1423–1428
Koshiyama K, Yano T, Kodama T (2010) Self-organization of a stable pore structure in a phospholipid bilayer. Phys Rev Lett 105:018105
Krasovitski B, Kimmel E (2004) Shear stress induced by a gas bubble pulsating in an ultrasonic field near a wall. IEEE Trans Ultrason Ferroelectr Freq Control 51:973–979
Kudo N, Okada K, Yamamoto K (2009) Sonoporation by single-shot pulsed ultrasound with microbubbles adjacent to cells. Biophys J 96:4866–4876
Kumon RE, Aehle M, Sabens D, Parikh P, Han YW, Kourennyi D, Deng CX (2009) Spatiotemporal effects of sonoporation measured by real-time calcium imaging. Ultrasound Med Biol 35:494–506

Lauterborn W (1972) High-speed photography of laser-induced breakdown in liquids. Appl Phys Lett 21:27–29
Lauterborn W, Bolle H (1972) Experimental investigations of cavitation-bubble collapse in the neighbourhood of a solid boundary. J Fluid Mech 72:391–399
Lauterborn W, Kurz T (2010) Physics of bubble oscillations. Rep Prog Phys 73:106501
Leighton TG (1994) The acoustic bubble. Academic, London, pp 531–550
Lewin PA, Bjørnø L (1982) Acoustically induced shear stresses in the vicinity of microbubbles in tissue. J Acoust Soc Am 71:728–734
Lindau O, Lauterborn W (2003) Cinematographic observation of the collapse and rebound of a laser-produced cavitation bubble near a wall. J Fluid Mech 479:327–348
Lionetti V, Fittipaldi A, Agostini S, Giacca M, Rechhia FA, Picano E (2009) Enhanced caveolae-mediated endocytosis by diagnostic ultrasound in vitro. Ultrasound Med Biol 35:136–143
Liu RH, Yang J, Pindera MZ, Athavale M, Grodzinski P (2002) Bubble-induced acoustic micromixing. Lab Chip 2:151–157
Liu X, Wu J (2009) Acoustic microstreaming around an isolated encapsulated microbubble. J Acoust Soc Am 125:1319–1330
Longuet-Higgins MS (1998) Viscous streaming from an oscillating spherical bubble. Proc R Soc Lond A 454:725–742
Makino K, Mossoba MM, Riesz P (1982) Chemical effects of ultrasound on aqueous solutions. Evidence for hydroxyl and hydrogen free radicals (.cntdot.OH and.cntdot.H) by spin trapping. J Am Chem Soc 104:3537–3539
Maksimov AO (2007) Viscous streaming from surface waves on the wall of acoustically-driven gas bubbles. Eur J Mech B Fluids 26:28–42
McNeil PL, Steinhardt RA (2003) Plasma membrane disruption: repair, prevention, adaptation. Annu Rev Cell Dev Biol 19:697–731
McNeil PL, Terasaki M (2001) Coping with the inevitable: how cells repair a torn surface membrane. Nat Cell Biol 3:E124–E129
Mehier-Humbert S, Bettinger T, Yan F, Guy RH (2005) Plasma membrane poration induced by ultrasound exposure: implication for drug delivery. J Control Release 104:213–222
Meijering BDM, Juffermans LJM, van Wamel A et al (2009) Ultrasound and microbubble-targeted delivery of macromolecules is regulated by induction of endocytosis and pore formation. Circ Res 104:679–687
Mørch KA (1979) Dynamics of cavitation bubbles and cavitation liquids. In: Preece CM (ed) Erosion. Academic, London, pp 309–353
Naudé CF, Ellis AT (1961) On the mechanism of cavitation damage by nonhemispherical cavities collapsing in contact with a solid boundary. Trans ASME D: J Basic Eng 83:648–656
Novell A, Collis J, Doinikov A, Ooi A, Manasseh R, Bouakaz A (2011) Theoretical and experimental evaluation of microstreaming created by a single microbubble: application to sonoporation. Book Series: IEEE International Ultrasonics Symposium, Orlando, USA pp 482–1485
Nyborg WL (1958) Acoustic streaming near a boundary. J Acoust Soc Am 30:329–339
Nyborg WL (1978) Physical principles of ultrasound. In: Fry FJ (ed) Ultrasound: its applications in medicine and biology, Part I. Elsevier, New York, USA pp 1–75
Ohl CD, Arora M, Ikink R, de Jong N, Versluis M, Delius M, Lohse D (2006) Sonoporation from jetting cavitation bubbles. Biophys J 91:4285–4295
Ohl CD, Kurz T, Geisler R, Lindau O, Lauterborn W (1999) Bubble dynamics, shock waves and sonoluminescence. Phil Trans R Soc Lond A 357:269–294
Paula DMB, Valero-Lapchik VB, Paredes-Gamero EJ, Han SW (2011) Therapeutic ultrasound promotes plasmid DNA uptake by clathrin-mediated endocytosis. J Gene Med 13:392–401
Plesset MS, Prosperetti A (1977) Bubble dynamics and cavitation. Annu Rev Fluid Mech 9:145–185
Pritchard NJ, Hughes DE, Peacocke AR (1966) The ultrasonic degradation of biological macromolecules under conditions of stable cavitation. I. Theory, methods and application to deoxyribonucleic acid. Biopolymers 4:259–273
Rooney JA (1970) Hemolysis near an ultrasonically pulsating gas bubble. Science 169:869–871
Rooney JA (1972) Shear as a mechanism for sonically induced biological effects. J Acoust Soc Am 52: 1718–1724
Ross JP, Cai X, Chiu JF, Yang J, Wu J (2002) Optical and atomic force microscopic studies on sonoporation. J Acoust Soc Am 111:1161–1164
Saito K, Miyake K, McNeil PL, Kato K, Yago K, Sugai N (1999) Plasma membrane disruption underlies injury of the corneal endothelium by ultrasound. Exp Eye Res 68:431–437
Sauer H, Hescheler J, Wartenberg M (2000) Mechanical strain-induced Ca^{2+} waves are propagated via ATP release and purinergic receptor activation. Am J Physiol Cell Physiol 279:C295–C307
Schlicher RK, Hutcheson JD, Radhakrishna H, Apakarian RP, Prausnitz MR (2010) Changes in cell morphology due to plasma membrane wounding by acoustic cavitation. Ultrasound Med Biol 36:677–692
Shima A, Takayama K, Tomita Y, Ohsawa N (1983) Mechanism of impact pressure generation from spark-generated bubble collapse near a wall. AIAA J 21:55–59
Szabo T (2004) Diagnostic ultrasound imaging: inside out. Academic, New York
Tachibana K, Uchida T, Ogawa K, Yamashita N, Tamura K (1999) Induction of cell-membrane porosity by ultrasound. Lancet 353:1409
Tho P, Manasseh R, Ooi A (2007) Cavitation microstreaming in single and multiple bubble systems. J Fluid Mech 576:191–233
Tran TA, Roger S, Le Guennec JY, Tranquart F, Bouakaz A (2007) Effect of ultrasound-activated microbubbles on the cell electrophysiological properties. Ultrasound Med Biol 33:158–163

van Wamel A, Bouakaz A, Versluis M, de Jong N (2004) Micromanipulation of endothelial cells: ultrasound-microbubbles-cell interaction. Ultrasound Med Biol 30:1255–1258

Vogel A, Lauterborn W, Timm R (1989) Optical and acoustic investigations of the dynamics of laser-produced cavitation bubbles near a solid boundary. J Fluid Mech 206:299–338

Vyas B, Preece CM (1976) Stress produced in a solid by cavitation. J Appl Phys 47:5133–5138

Wang C, Jalikop SV, Hilgenfeldt S (2012) Efficient manipulation of microparticles in bubble streaming flows. Biomicrofluidics 6:012801

Wu J (2002) Theoretical study on shear stress generated by microstreaming surrounding contrast agents attached to living cells. Ultrasound Med Biol 28: 125–129

Wu J, Du G (1997) Streaming generated by a bubble in an ultrasound field. J Acoust Soc Am 101:1899–1907

Wu J, Nyborg WL (2008) Ultrasound, cavitation bubbles and their interaction with cells. Adv Drug Deliv Rev 60:1103–1116

Wu J, Ross JP, Chiu JF (2002) Reparable sonoporation generated by microstreaming. J Acoust Soc Am 111:1460

Yang F, Gu N, Chen D, Xi X, Zhang D, Li Y, Wu J (2008) Experimental study on cell self-sealing during sonoporation. J Control Release 131:205–210

Yu H, Chen S (2014) A model to calculate microstreaming-shear stress generated by oscillating microbubbles on the cell membrane in sonoporation. Biomed Mater Eng 24:861–868

Zarnitsyn V, Rostad CA, Prausnitz MR (2008) Modeling transmembrane transport through cell membrane wounds created by acoustic cavitation. Biophys J 95: 4124–4138

Zeghimi A, Uzbekov R, Escoffre JM, Arbeille B, Bouakaz (2012) Ultrastructural modifications of cell membranes and organelles induced by sonoporation. Book Series: IEEE International Ultrasonics Symposium, Dresden, Germany pp 2045–2048

Zhou Y, Yang K, Cui J, Ye JY, Deng CX (2012) Controlled permeation of cell membrane by single bubble acoustic cavitation. J Control Release 157:103–111

Design of Microbubbles for Gene/Drug Delivery

11

Thierry Bettinger and François Tranquart

Abstract

The role of ultrasound contrast agents (UCA) initially designed for diagnosis has evolved towards a therapeutic use. Ultrasound (US) for triggered drug delivery has many advantages. In particular, it enables a high spatial control of drug release, thus potentially allowing activation of drug delivery only in the targeted region, and not in surrounding healthy tissue. Moreover, UCA imaging can also be used firstly to precisely locate the target region to, and then used to monitor the drug delivery process by tracking the location of release occurrence. All these features make UCA and ultrasound attractive means to mediate drug delivery. The three main potential clinical indications for drug/gene US delivery are (i) the cardiovascular system, (ii) the central nervous system for small molecule delivery, and (iii) tumor therapy using cytotoxic drugs. Although promising results have been achieved in preclinical studies in various animal models, still very few examples of clinical use have been reported. In this chapter will be addressed the aspects pertaining to UCA formulation (chemical composition, mode of preparation, analytical methods…) and the requirement for a potential translation into the clinic following approval by regulatory authorities.

Keywords

Microbubbles • Gene and Drug Delivery

11.1 Introduction

Gas microbubbles have long been used as ultrasound contrast agents (UCA). These can be made of phospholipids, albumin, surfactant or synthetic polymer shells filled with gas displaying low aqueous solubility, such as fluorinated gases

T. Bettinger (✉)
Novel agents Department, Bracco Suisse SA, Plan-Les-Ouates, Switzerland
e-mail: thierry.bettinger@bracco.com

F. Tranquart
Bracco Suisse SA, Plan-Les-Ouates, Switzerland

© Springer International Publishing Switzerland 2016
J.-M. Escoffre, A. Bouakaz (eds.), *Therapeutic Ultrasound*, Advances in Experimental Medicine and Biology, Vol. 880, DOI 10.1007/978-3-319-22536-4_11

(*e.g.,* sulfurhexafluoride or perfluorobutane). Their size ranges typically between 2–8 μm (*i.e.,* below red blood size diameter), and thus are considered as pure blood pool agent. These stabilized gas bubbles proved to be useful in many different clinical contexts where imaging of perfusion is desired, such as for the characterization of liver diseases (Burns et al. 2000; Tranquart et al. 2008), left ventricular opacification (Senior et al. 2000; Kitzman et al. 2000) or response of malignant tumors to therapy (Lassau et al. 2007).

In recent years, the role of these microbubbles has expanded beyond their primary role in diagnostics to potentially provide new options for therapeutic purposes. The three main clinical indications for drug/gene US delivery are (i) the cardiovascular system (Unger et al. 2014), (ii) the central nervous system for small molecule delivery (Aryal et al. 2014; Liu et al. 2014), and (iii) tumor therapy using cytotoxic drugs (Ibsen et al. 2013a). All these applications rely on the mechanical properties of UCA when exposed to ultrasound. Indeed, when insonified under specific ultrasound regimen, UCA undergo oscillations inducing acoustic cavitation, allowing an increase in cell membrane permeability in the close vicinity of the UCA. This enables drugs to cross the membrane, thus penetrating into cells and ultimately inducing a therapeutic effect. On the same principle, UCA can also act on vessel permeability for promoting drug access to the extracellular space. Recent promising studies exploiting this property showed that UCA were able to transiently open the blood brain barrier (BBB) for drug delivery to the brain (Liu et al. 2014). Another emerging application is sonothrombolysis (STL), where UCA are used to promote blood clot lysis, leading to recanalization of previously occluded vessels and ultimately improved long-term outcome. This could become of a major clinical interest in the context of ischemic stroke or myocardial ischemia.

Besides UCA, use of ultrasound (US) for triggered drug delivery has many advantages. In particular, it enables a high spatial control of drug release; since the US beam can be focused as such that it represents only a few cubic millimeters of volume. Thus, it potentially allows activation of the drug delivery only in the targeted region, and not in the surrounding healthy tissue. Moreover, imaging of UCA can be used to firstly precisely locate the target region, and then used to monitor the drug delivery process by tracking the location of release occurrence. All these features make UCA and ultrasound an attractive means to mediate drug delivery.

In the course of all these developments, it appeared obvious that requirement for an efficient therapeutic agent based on UCA could be different than what is needed for an imaging agent. In particular, known limitations of UCA are limited payload, short half-life, size restraining their action exclusively to the vascular bed and poor response to ultrasound exposure due to a polydisperse diameter. Whereas these features are typically less critical for imaging purposes due to the exquisite sensitivity of imaging systems, they are prone to affecting the potency of UCA for drug/gene delivery. This has prompted different groups to focus on the design of UCA for therapeutic use. The topic of drug delivery using microbubble-assisted ultrasound has been addressed in several recent reviews (Lentacker et al. 2014; Sirsi and Borden 2014; Rychak and Klibanov 2014). This is also addressed in detail in different chapters of this book.

The purpose of this chapter is more to focus on the aspects of UCA formulation (chemical composition, mode of preparation, analytical methods…) and the requirement for a potential translation into the clinic following approval by regulatory authorities.

11.2 Formulation

11.2.1 General Consideration

11.2.1.1 Shell Components

Shell component selection is important. Semi-synthetic lipids will be favored because of their non-animal origin. Addition of a lipopolymer molecule (*e.g.*, PEGylated lipids) will improve blood circulation lifetime, but will potentially also impair drug loading mediated through non-covalent adsorption, such as hydrophobic or electrostatic

associations. Of interest, manufacturing process and nature of the shell components can also impact the shell membrane homogeneity. Indeed, this was nicely illustrated when microdomain, resulting from sequestration of some lipids, could promote heterogeneity in the UCA shell (Kim et al. 2003). In the same trend, it was recently demonstrated that replacing distearoylphosphatidylcholine (DSPC) by diphosphorylphosphatidylcholine (DPPC) in DSPE-PEG2000-biotin microbubbles yielded a more homogenous distribution of biotin ligands, as probed with fluorescently labeled streptavidin (Kooiman et al. 2014). As a consequence, this could affect the actual loading efficiency of the prepared UCA by restraining drug loading to a limited surface area at the UCA surface. Specific lipid mixtures or manufacturing conditions (heating) could be investigated in order to alter this heterogeneity.

11.2.1.2 UCA Stability and Lifetime

UCA bloodstream lifetime has considerably improved over the past years, now providing good imaging time frames in the range of a few minutes. However, for drug delivery this lifetime might not be optimal to allow release of the therapeutic agent, and thus to mediate the desired biological effect. In that sense, polymeric UCA may provide improved circulation time, but conversely, release of drug load from the polymeric shell must be carefully assessed. Indeed, upon destruction most of the shell remains intact (see below for details). Moreover, UCA with thick and rigid shells (such as protein or polymer-shelled) usually display poor oscillation behavior, unlike lipid-shelled UCA. This will likely have an impact on the cavitation effect induced by ultrasound, and thus their potency to promote a therapeutic effect. It has also been shown that these thick shelled-agents might display a higher loading capacity compared to soft shell agent.

Gas nature is an important player for the lifetime and stability, and a mixture of perfluorocarbon and nitrogen could be preferable to limit the risks of UCA size modification resulting from exchange with soluble nitrogen present in biological fluids. As such, these size changes might induce different responses to the same driven acoustic frequency, and thus might become less sensitive to ultrasound activation.

Since multiple passages are necessary to allow destruction of sufficient UCA for increasing accumulation of the therapeutic agent, the mode of administration might be considered. As an example, using continuous infusion in place of bolus injection of UCA would help in maintaining a constant concentration for a longer time, even at a lower range than that obtained with a bolus. The combination of UCA amount and US pulse characteristics should be carefully tuned according to the selected indication. This could require a high concentration for an instant, or a lower concentration for a longer time. This can significantly enhance drug delivery efficacy, while addressing possible safety issues.

11.2.2 Conditions Allowing Drug Delivery

Generally, UCA loaded with drug or in combination with circulating therapeutic agent can be activated in two manners for delivery: stable cavitation or inertial cavitation. Stable cavitation is usually achieved at relatively low acoustic pressure and is generated when UCA undergo repetitive oscillation. These expansions and contractions generate shear stress to cell membranes, affecting their permeability (van Bavel 2007). In contrast, inertial cavitation is obtained at higher acoustic pressure and results from violent UCA destruction, causing strong biophysical effects, microjets and microstreaming in the immediate surrounding environment (Husseini et al. 2005). This behavior is valid for soft-shelled UCA. In the case of hard shell agents, higher levels of energy are required to generate cavitation due to their inherent shell stiffness. Thus, under these high acoustic pressures, these UCA undergo violent rupture releasing free gas microbubbles through small defects in the shell, or so-called ‘sonic cracks’ (Bloch et al. 2003) (see Fig. 11.1 for illustration). This complex interaction between ultrasound waves, microbubbles and tissue will not be described in detail in the present chapter, but it is the object of a different dedicated chapter (see Chap. 9).

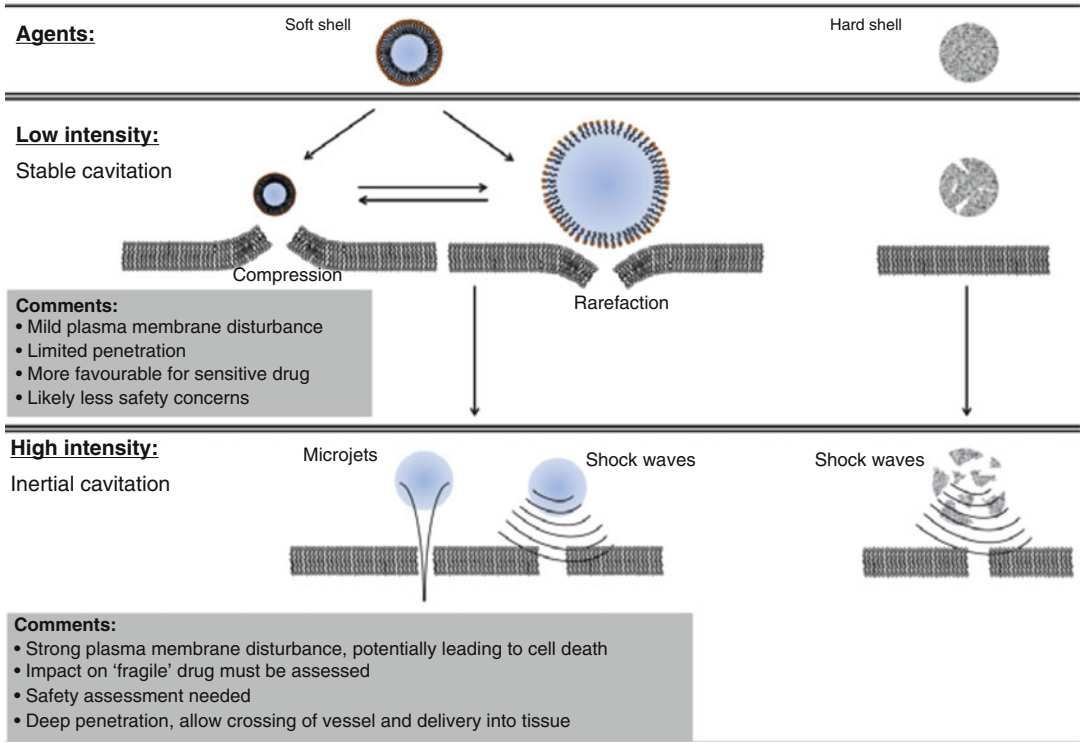

Fig. 11.1 Illustration of the physical mechanisms underlying the biological effect of soft or hard shell Ultrasound Contrast Agents (Adapted from Kiessling et al. 2014)

11.2.3 Drug Delivery with UCA and Ultrasound

11.2.3.1 Plain UCA with Free Drug

There are several reports describing the use of a mixture of UCA and drug for therapeutic purposes. This is a very convenient approach due to the immediate availability of both microbubbles and drug agents. It is also seen as a straightforward continuation of the current diagnostic use of clinically approved agents. Thus, many of these reports have used marketed UCA (Definity®, SonoVue®, Optison®…), and most advanced clinical studies have been conducted for the purpose of clot lysis, so-called sonothrombolysis (de Saint Victor et al. 2014), and more recently for pancreatic cancer (Kotopoulis et al. 2014). Conditions described were in presence or absence of fibrinolytic agent r-tPa, and under the regime of various ultrasound settings (various frequencies, acoustic pressure, pulse repetition frequency…). Some clinical trials have shown the potency of this approach to treat patients suffering from stroke by enabling faster and more complete recanalization (Molina et al. 2006). However, current trials did not provide significant improvement in patient conditions at 3 months post-treatment, partially due to the limited number of patients enrolled. Moreover, one of the main lessons to retrieve from these studies is that still little is known of the mechanism underlying UCA-enhanced sonothrombolysis (STL), and in some cases, lack of control of the biological effects of this new therapeutic approach has triggered some safety concerns. It is thought that design of UCA specific for STL indication has the potential to further improve not only their effect as treatment enhancers, but also their safety profile.

The approach of administering a mixture of UCA and drug has also been exploited for other therapeutic applications, such as delivery of cytotoxic drug (Ibsen et al. 2013a; Escoffre et al. 2013), BBB opening (Aryal et al. 2014) or gene delivery

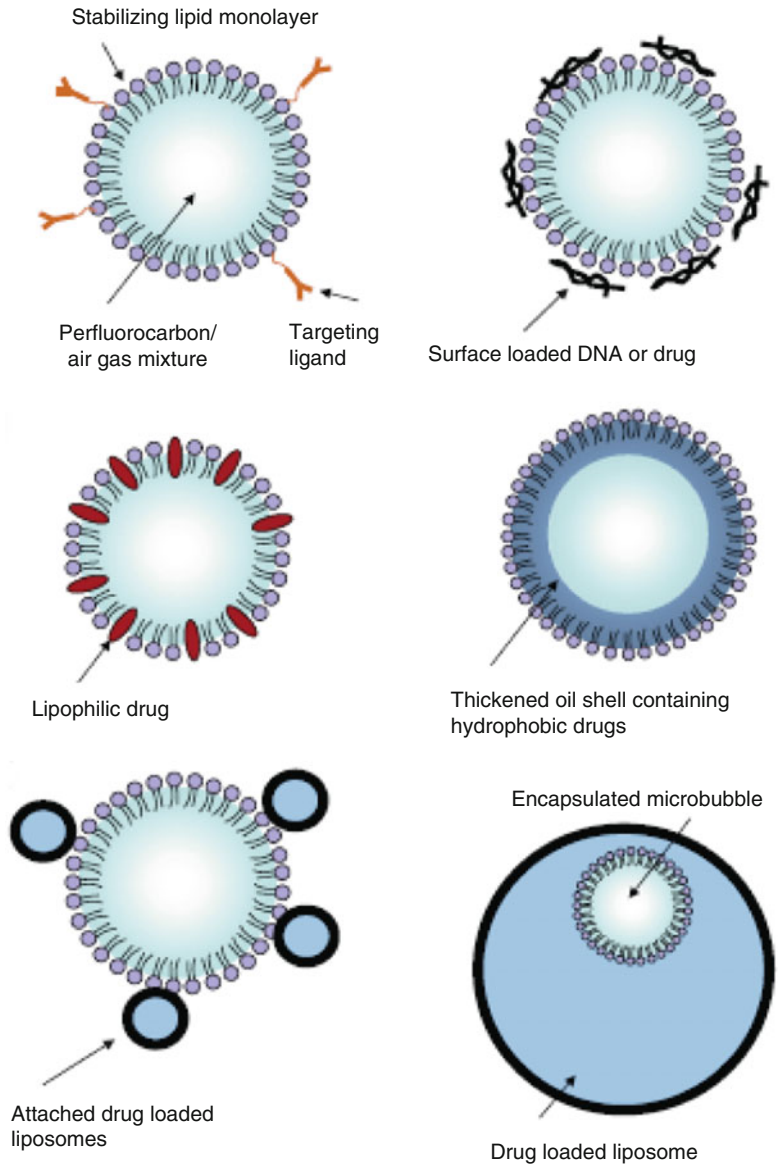

Fig. 11.2 Various options for the design of drug-loaded ultrasound contrast agent. (**a**) The basic microbubble design with a lipid monolayer stabilizing the gas core. Targeting ligands can be conjugated to the surface to help facilitate accumulation of the microbubble in desired tissues. These ligands can be antibodies or short peptide sequences. (**b**) The microbubble itself can be a vehicle by attaching drugs and even DNA to the surface through the use of electrostatic attractions. (**c**) Lipophilic drugs can be incorporated into the lipid monolayer shell of the microbubble. (**d**) The stabilizing shell can be thickened with an oil layer, allowing hydrophobic drugs to be carried within it. (**e**) Drug-filled liposomes can be attached to the surface of the microbubble. When the microbubble is exposed to ultrasound, the liposomes are disrupted by the mechanical actuation of drug release. (**f**) The microbubble can be encapsulated within a liposome along with the drug. When exposed to ultrasound, the microbubble ruptures the outer liposome, releasing the payload (Reproduced from Ibsen et al. 2013a)

(Rychak and Klibanov 2014; Newman and Bettinger 2007). The recent report of a successful chemotherapy improvement by using both ultrasound and UCA to treat pancreatic cancer has highlighted the clinical feasibility of such an approach, even though this has only been done on a limited number of patients (Kotopoulis et al. 2013).

In parallel to the co-administration approach of free drug and UCA, several groups have also investigated the potential of co-localization of drug and cavitational activity on therapeutic efficiency by preparing drug-loaded UCA. Indeed, it is speculated that incorporation of therapeutic agent close to the UCA shell would be more favorable since cavitation will likely drive delivery.

11.2.3.2 Drug-Loaded UCA

Drug loaded UCA have been formulated using different approaches, as illustrated in Fig. 11.2. Several strategies have been employed to incorporate therapeutic agent in UCA, such as chemical conjugation, electrostatic adsorption at the

outer surface and embedding in the shell. The choice for the best method of loading depends mainly on the nature of the drug.

One additional advantage of loading UCA with therapeutics is that it can act as a protective drug carrier. Thus, unstable drugs can be protected from degradation in biological fluids, thus prolonging their half-life. This was nicely illustrated by DNA molecules, for which enhanced resistance to nuclease degradation was measured (Lentacker et al. 2006). On top of that, the limited release outside the insonified area due to the relatively low peripheral microbubble destruction could help in preventing major adverse events related to the drug itself.

11.2.3.2.1 Drug in/on the Shell

Some studies have demonstrated that covalent attachment of the drug is more favorable to elicit a therapeutic effect. For example, conjugation of rose bengal onto UCA was proven to be more cytotoxic compared to un-conjugated sonosensitizer (Nomikou et al. 2012); so-called sonodynamic therapy (SDT). This approach could be of interest for the treatment of cancer lesions, and thanks to a relative good US tissue penetration, it appears better than typical light excitation used in photodynamic therapy (PDT).

However, careful evaluations are warranted to measure the impact of the loading on the actual drug activity. For example, r-tPA proved to be a quite complex molecule to formulate with the need to use specific conditions to maintain biological activity (risk of aggregation of the native protein, personal results). In addition, if chemical conjugation is employed, careful control of the conjugation process is needed to ensure that biological activity of the drug is not altered. Moreover, loading procedure could also impact the actual bioavailability of the drug. Thus, even though drug loading efficiency is obviously important, formula optimization should equally be considered to ensure a proper delivery of the active drug to the site of treatment.

Being inspired by cationic lipids or polymers used for non-viral gene delivery (so-called lipoplexes and polyplexes, respectively), some investigators have prepared UCA bearing cationic charges at the shell surface. For phospholipidic shells, this can be achieved by inserting cationic lipids (*e.g.*, DSTAP) to trigger a positive zeta potential of the microbubbles. This significantly increases the loading of nucleic acids, and several reports have demonstrated usefulness of these UCA constructs to promote gene delivery *in-vitro* and *in-vivo* (Wang et al. 2012; Rychak and Klibanov 2014).

Due to the effective loading capacity being restricted to the UCA shell, drug-loading vehicles have mainly been developed with highly potent drugs, such as nucleic acid, known to be active in the μg range. It was estimated, on average, that loading capacity of UCA for nucleic acid complexation is typically in the range of 0.01 pg/μm^2. For a 2 μm UCA diameter, this corresponds to ca. 0.12 pg/microbubble. Thus, almost 10 million UCA are required to carry 1 μg of nucleic acid, illustrating the limited loading capacity of regular cationic UCA. As an example, the situation is similar for drugs when compared to usual circulating drug concentration during chemotherapy. This is why some groups have used the approach of pre-loading drug into nanoparticles prior to coupling them onto the UCA shell surface (Mullin et al. 2013).

11.2.3.2.2 Nanoparticles on UCA

These nanoparticles can be of different natures, such as liposomes (Kheirolomoom et al. 2007) or poly(lactic-co-glycolic acid) (PLGA) (Chappell et al. 2008). In particular, liposomal preparations of Doxorubicin are quite popular thanks to the availability of FDA approved products (*e.g.,* Doxil®). Properties of the drug to be formulated are of course very important, as it will have a direct impact on the loading efficiency. For example, highly hydrophilic drugs would be difficult to embed into the shell. Most importantly, impact of the drug loading on the UCA ultrasound responsiveness must be evaluated since modifications in UCA stability, risk of aggregation and shell properties (increase in stiffness) can be observed under certain conditions.

There are numerous possible approaches to associate the nanoparticles to the UCA. This can be achieved by biotin-avidin interaction, but this

approach is only valid for research or pre-clinical evaluation due to potential immune reaction with this protein (Chinol et al. 1998). An alternative mean to enable strong association relies on the use of chemical conjugation, such as amide, disulfide or thioether bond formation. Electrostatic attachment is another possibility leading to an easy preparation, but it does carry the risk of lack of reproducibility and lack of association control, impeding further development of this method towards clinical use.

11.2.3.2.3 UCA in Drug-Loaded Liposomes

Interestingly, a recent procedure has been described to increase UCA drug loading. This was accomplished by encapsulating the UCA within the internal aqueous space of a drug-loaded liposome (Ibsen et al. 2011). This rather unusual construct must be evaluated to assess not only the drug delivery potential compared to regular nanoparticle-loaded UCA, but also the US-responsiveness of the encapsulated UCA.

11.2.3.2.4 Hard Shell

In addition to the use of drug pre-formulated in nanoparticles, thick shelled UCA could also be a means to improve drug payload (Lensen et al. 2011). These agents are usually made of polymers and have shells of 20–100 nm thickness. Shell stiffness of these agents requires specific insonation parameters to mediate delivery. Indeed as these agents will not oscillate at low acoustic pressure, but require higher pressure to be activated leading to rupture and gas escape. For this reason, the potential issue that can be faced with this formulation is the drug release from the polymer shell; the shells remain in majority intact as only cracks are observed. Modification of shell properties, by altering shell thickness and composition, could improve both behaviors under US exposure and drug delivery efficiency. In addition, the nature of the polymer must be taken into consideration, particularly when dealing with safety linked to the biocomptability. In the same trend, it has been speculated that use of UCA composed of components with different shell properties can release a drug in a stepwise manner.

11.2.3.2.5 Nanoemulsion

Another possible approach is the use of drug-loaded nanoemulsion (Rapoport et al. 2009). These nanoparticles are made of liquid perfluorocarbon (*e.g.,* perfluoropentane). US exposure triggered heating causes a droplet-to-bubble phase shift, resulting in the *in-situ* formation of drug loaded UCA that can be further activated by distinct US conditions. The impact of phase shift has to be addressed in detail since it can alter the chemical integrity of the loaded drug. These particles display a particularly long circulation time, with up to 50 % of the injected dose still remaining in the circulation 2 h after administration (Rapoport et al. 2011). Moreover, thanks to their relatively small size (200–500 nm), they also have the opportunity to reach compartments not normally accessible to UCA. This is by escaping the blood space, so-called extravasation. Due to the narrow temperature range required for this transition phase, the treatment could be precisely tuned by modulating this temperature increase when focusing the ultrasound beam in the specified location. This will be extensively described in another chapter of this book (see Chap. 14).

11.2.3.2.6 Monosize

Recently, a new way to formulate drug in UCA relying on the use of microfluidics technology was described. Indeed, successful preparation of multilayer gas lipospheres was reported using flow-focusing geometry (Hettiarachchi et al. 2009). These rather complex constructs are composed of a phospholipid shell, an oil layer comprising cytotoxic drug doxorubicin, and an inner gas core. Moreover, this technology can address one additional critical parameter for an efficient drug delivery; control of UCA size so that it nicely matches the selected US frequency. Thus, devices allowing UCA preparation displaying a narrow size distribution were specifically designed. These developments will likely prove to be important for further improvement of drug delivery by ensuring that all the UCA exposed to US will be activated at a defined frequency, maximizing the delivery of the loaded drug. Use of monodisperse UCA may also improve the efficacy/safety balance by allowing use of lower

acoustic energy to elicit drug release, knowing that all UCA will eventually respond to US exposure at the selected frequency.

Use of UCA for BBB opening has been described in several reports (Liu et al. 2014; Choi et al. 2010), most of the tested agents being approved UCA. However, UCA formulation with a defined diameter may improve drug delivery to the brain since it was shown that 4–5 μm size was more effective than 1–2 μm UCA, under tested conditions (Choi et al. 2010). This reinforces again the need to develop manufacturing processes allowing preparation of monodisperse UCA. However, currently the main limitation is the yield of such manufacturing which does not allow a high amount of UCA preparation, meaning that acoustic characterization and *in-vivo* tests are still challenging.

11.2.4 Optimization of Drug Delivery

Close contact between UCA and the target tissue should intuitively favor drug delivery, vessel permeability or clot lysis. Thus, a clever way to further improve drug delivery efficiency could be the use of targeting strategies such as either passive or active accumulation. Passive targeting can result from interaction of some shell components with the specific particle's clearance system. This is clearly illustrated by phosphatidylserine-containing UCA (*e.g.,* Sonazoid®), reported as being efficiently taken up by Kupffer cells.

The specificity of this UCA might be increased by adopting a specific targeting strategy for it. These UCA differ from those initially developed for blood pool imaging by the presence of a targeting moiety able to link the bubble to a selected cell biomarker. The general strategy is to link molecular entities to the phospholipid-stabilizing monolayer, allowing the bubbles to remain attached to selected sites in the vascular compartment. Once attached, these bubbles act as echo-enhancers, similarly to blood pool agents, since the signal is generated by the bubble itself and not the ligand. This raised important points.

As the bubbles remain strictly within the vascular compartment, targets must be selected that are accessible to them *i.e.* on the luminal side of endothelial cells (Bettinger et al. 2012; Pochon et al. 2010). Two application areas are well characterized: neoangiogenesis and inflammation, since both involve endothelial cells. Tumoral neoangiogenesis (Deshpande et al. 2010; Willmann et al. 2010), *i.e.,* the formation of new blood vessels, is a fundamental process occurring during tumor progression and is triggered by hypoxia. In the course of the inflammatory process, various cell surface markers are expressed or up-regulated on the endothelial luminal side, and are therefore accessible to targeted microbubbles. Site targeted microbubbles can also be used for the visualization of thrombi associated with stroke.

The attachment of bubbles to the surface of endothelial cells must be strong enough to withstand vascular areas where shear stress is high due to high blood velocity and viscosity. The attachment could be enhanced by adding radiation force. This improves the interactions between microbubbles themselves and their interactions with endothelial cells. Otherwise, incorporation of magnetic particles within the shell of the core could enhance attachment. By adopting such a strategy, we not only have access to highly specific areas to drive the desired therapeutic effect, but we can also significantly limit adverse events by limiting interaction with non-affected regions.

Efficient ligand-target interaction can be achieved by either using flexible spacers to present the targeting ligand in the most effective way, or by fine-tuning the ligand density at the UCA surface. To improve circulation time and binding specificity, a clever approach of a 'buried ligand' has also been recently proposed (Borden et al. 2006, 2008). Active accumulation could also be achieved by physical means, such as acoustic radiation force (Kheirolomoom et al. 2007; Frinking et al. 2012) or magnetic force to concentrate UCA at the site of treatment (Stride et al. 2009).

11.2.5 Characterization of UCA

An important aspect of UCA preparation is the quality control assessment (Fig. 11.3). This is

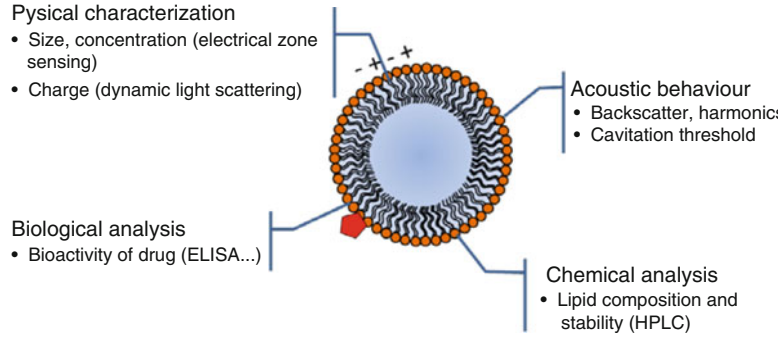

Fig. 11.3 Methods available for the quality control assessment of UCA (Red pentagon represents a drug molecule)

even more acute in the case of these rather complex UCA-drug constructs. As for regular UCA, size can be determined by electrical zone sensing, using the so-called Coulter Counter. This is a fast and accurate method to measure at the same time UCA concentration, gas volume, size distribution (in volume and number) and UCA surface. Other methods exist, but so far they have proven less suitable than electrical zone sensing due to technical limitation from the natural buoyancy behavior of UCA in liquid.

Zeta potential is also an important parameter to assess as it provides information on UCA surface charge. It relies on electrophoretic light scattering technology. The magnitude of the zeta potential gives an indication of the potential stability of the formed UCA. If all the UCA particles in suspension have a large negative or positive zeta potential, then they will tend to repel each other. On the other hand, if UCA particles display low zeta potential values, there will be a tendency for the particles to come together, promoting aggregation behavior. This measure could also be useful to monitor adsorption of nucleic acid molecules on positively charged UCA.

In addition to these physical characterizations, chemical analysis of the shell lipid content is mandatory to ensure that the process of UCA preparation is robust and reproducible. For this purpose, specific analytical methods must be developed to allow titration of each UCA component, as well as the loaded drug. These methods mostly rely on reverse phase High-Performance Liquid Chromatography (RP-HPLC). For native lipids (not derivatized), the Evaporative Light-Scattering Detector (ELSD) is far more useful for lipid titration than the commonly used ultraviolet (UV) detector. Knowing the minute amount of material required for the formation of these stabilized gas microbubbles, this can be a challenging task, and usually requires extensive developments with robust and validated analytical methods. These methods will also be useful for controlling if loaded drug is affected by the manufacturing process. Indeed, drugs could be sensitive toward specific formulation conditions, such as heating and agitation (particularly for the case of probe sonication technique). This is why it is also important to assess whether biological activity of the drug remains unaffected by the formulation process. This is done using specific methods such as enzyme-linked immunosorbent assay (ELISA), or chromogenic assay for drugs with enzymatic activity (*e.g.,* r-tPa).

Besides these physico-chemical analyses, acoustic characterization is warranted to ensure that formulated UCA (with or without drug) are US-responsive. This can be achieved by performing backscatter measurement or determining cavitation threshold. In addition, some of these methods will also be useful to study the stability of UCA formulation. For example, evaluating the impact of long-term storage under stress conditions, such as temperature can be assessed on UCA concentration, chemical integrity of shell components, drug bioactivity and acoustic properties.

Finally, for the screening of drug-loaded UCA formulations in pre-clinical studies, development of analytical methods for assessing efficiency of drug delivery is required. In this trend, a recent report described a LC-MS/MS analysis method that allowed titration of doxorubicin in tumor

tissue extracts with a limit of detection of 7.8 pg (Ibsen et al. 2013b). Further to all these considerations and speculation, there is still some controversy about the relative advantage of administering (i) a mixture of drug and UCA or (ii) drug loaded-UCA. The second approach might prove easier, particularly when moving toward preparation of a Chemistry, Manufacturing and Controls (CMC) dossier for submission to regulatory authorities. This will be addressed in more detail in the last paragraph of this chapter.

11.3 Clinical Translation and Regulatory Issues

A major advantage of UCA is their capability to enable site-specific delivery of the drug by selective destruction of UCA with a non-invasive ultrasonic stimulus. However, this technique still presents many obstacles that need to be addressed and solved before moving into the clinic.

Firstly, a better understanding of the underlying mechanism of this approach is warranted to ensure safe delivery into patients. This is presented in another chapter (see Chap. 9), but so far, many concurrent or challenging hypotheses have been proposed without a unique theory. Even though it is not a pre-requisite to perform *in-vitro* or preclinical tests, the absence of a clear mechanism is a significant barrier for health authorities. This is reinforced by the observation of possible adverse events due to the UCA, the drug or the US beam, meaning that the contribution of each component is clarified. It is a prime importance since bioeffects have been observed in some studies (Vancraeynest et al. 2006). Safety assessment for the therapeutic application must be considered differently than for the diagnostic application. Indeed, whereas for diagnostic purposes, absence of or a few bioeffects is mandatory, it is however likely to be different for therapy to a certain extent. Secondly, one of the main limitations of UCA is their relatively low circulation time, typically ranging from 5–15 min, thus limiting their delivery potential. Thirdly, UCA are efficiently captured by organs, such as liver and spleen, raising the issue of unwanted accumulation in non-targeted organs/tissues that could become detrimental to the patient.

Preparing UCA loaded with a therapeutic agent, and possibly a ligand, for targeting can prove to be complex to manage for CMC dossier preparation. In particular, it is difficult to precisely measure the amount of drug loaded onto UCA, and to develop a process allowing reproducible preparation of such drug-loaded UCA. In that sense, a thorough evaluation of the advantage of loading drug onto UCA over co-injecting of free drug and UCA must be done. Preparation of drug-loaded UCA will lead to a new chemical entity, implying development of a complete process of manufacturing complying with GMP regulations. In contrast, use of approved drug and UCA could present some advantages in terms of development time and cost, if efficacy compared to drug-UCA complex is demonstrated in pre-clinical studies. However, it is also important to obtain authorities guidance on this approach since the use of targeting procedures for increasing local delivery will modify the natural metabolism of the approved drug. Therefore, this point must be carefully addressed during the course of the development of this new therapeutic method in terms of local and circulating concentration, changes in metabolic pathways and therapeutic dose.

In terms of quality control of drug-loaded UCA for chemical conjugation, it will be easier if conjugation occurs prior to UCA preparation. This will enable thorough chemical characterization of the conjugate, and ensure that the conjugation process did not alter biological activity of the therapeutic agent. One advantage of co-administrating the therapeutic agent and UCA is that there is no limitation in terms of drug dose, unlike what can be experienced with drug-loaded UCA.

From a regulatory point of view, the gas microbubble is considered as the active entity, meaning that each of the microbubble components should be fully characterized. Furthermore, the manufacture of clinical materials should be carried out in compliance with the Good Manufacturing Practice. With respect to the formulation characteristics, the selection of the ingredients is of outmost importance since the use of specific components should be validated for these new drug delivery systems for parenteral administration. In that perspective,

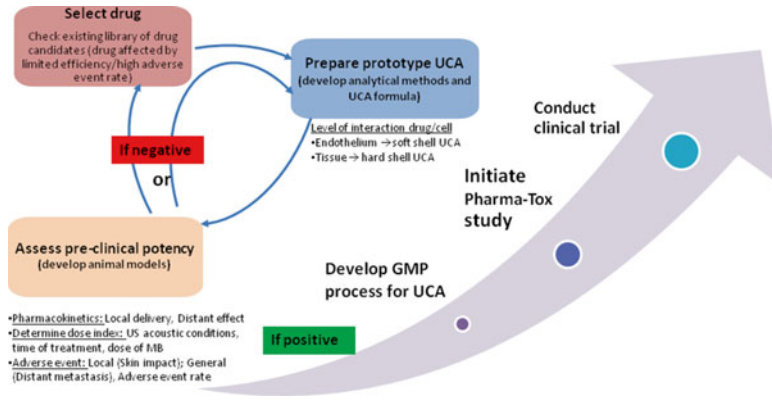

Fig. 11.4 Pre-clinical steps towards UCA clinical development for therapeutic use

the retained formulation for clinical trials must be challenged before finalization, as changing any of the components at a later stage could be difficult, even impossible, and costly.

Once the formulation is finalized, many steps must be accomplished before any clinical use: robustness of the manufacturing process, stability of the product and validation of the test methods. An additional requirement is a pharma-toxicology package that follows the International Conference on Harmonization (ICH) guidelines. Even though adverse events cannot be considered as a limiting factor for the use of UCA in ultrasound imaging, the introduction of therapeutic drugs in addition of other materials in the bubble requires specific toxicology assessment. For conventional agents, it is generally admitted that the rate of these events (around 0.01 % for serious adverse events based on post-marketing safety data, with no significant differences between agents) is below what is reported for iodinated compounds and MR agents. Even though the therapeutic field is exposed to higher rates of adverse events in relation to the intrinsic nature of the interaction with tissues, it is essential to demonstrate that the risk/benefit ratio remains positive and higher than without the introduction of UCA and US. Some key points need to be investigated, such as allergic reactions to foreign materials, maximal tolerable dose in animals to determine the maximal dose to be used in patients, and the absence of compromised blood flow after injection due to sticking of UCA to endothelial cells outside the therapeutic area. These different steps are time-consuming and expensive, and can be summarized as illustrated in Fig. 11.4.

Finally, when the steps above have been completed, the agent is suitable for clinical testing pending Investigational New Drug Application and Institutional Review Board (IRB) or ethical committee approval for the selected indication. Regulatory approval must be carefully considered since three components are closely interacting; the microbubble, the therapeutic drug and ultrasound waves. Whether we can precisely characterize the microbubble constituents and the acoustic parameters, the use of various therapeutic drugs is still a barrier. Indeed, do we need to get an approval of this device whatever the drug is, this being valid for the injection of free drug only, or do we need to get an approval for each individual drug to be used? The use of drug-loaded systems should expose us to a different regulatory pathway, which must be drug-specific.

A key component, which is not discussed in the present chapter, is the acoustic contribution to the desired effect. As such, there is a need to adapt the machines to this new modality, but in the same this is changing the nature of the equipment, which is moving from a pure diagnostic field to the therapeutic field. This means different requirements and higher regulatory constraints. In that perspective, a strong partnership is needed to exploit the potential of this therapeutic approach, and to strengthen the place of UCA in the diagnostic palette so they can be used by physicians according to their specific demand.

Conclusion

Drug delivery mediated using microbubble-assisted ultrasound is a promising therapeutic approach. The fact that ultrasound is a non-invasive technique, that can transmit energy deep into a discrete region of tissue or organ, is a key feature for enabling local drug delivery. In addition to the drug-delivery capabilities, one must bear in mind that UCA are also imaging agents, giving rise to the concept of therapy and diagnostics with one single agent, so-called 'theranostics'.

Future improvements are warranted to pave the way for a clinical translation of this innovative therapeutic approach; (i) manufacture of UCA for longer circulation time and higher loading capacity, (ii) development of specific US protocols and (iii) tackling regulatory hurdles for clinical use in safe conditions. This requires a multi-disciplinary approach, with a close collaboration with ultrasound and drug pharma companies in order to sequentially address the different challenges with a clinical objective. The limited number of drugs tested in these conditions, together with the absence of clinical results, represents a significant drawback, indicating that clinical approval of this method will require at least 5 additional years. Emerging formulation based on microfluidics could become a disruptive technology, by allowing the manufacturing of UCA on spot, using FDA-approved devices. This will completely change the game in the field of UCA, since some features considered as important when using regular manufacturing processes could be obsolete for microfluidics-based preparation (*e.g.,* long-term stability).

References

Aryal M, Arvanitis CD, Alexander PM, McDannold N (2014) Ultrasound-mediated blood-brain barrier disruption for targeted drug delivery in the central nervous system. Adv Drug Deliv Rev 72:94–109

Bettinger T, Bussat P, Tardy I, Pochon S, Hyvelin JM, Emmel P, Henrioud S, Biolluz N, Willmann JK, Schneider M, Tranquart F (2012) Ultrasound molecular imaging contrast agent binding to both E- and P-selectin in different species. Invest Radiol 47: 516–523

Bloch SH, Wan M, Dayton P, Ferrara KW (2003) Optical observation of lipid- and polymer-shelled ultrasound microbubble contrast agents. Appl Phys Lett 84:631–633

Borden MA, Sarantos MR, Stieger SM, Simon SI, Ferrara KW, Dayton PA (2006) Ultrasound radiation force modulates ligand availability on targeted contrast agents. Mol Imaging 5:139–147

Borden MA, Zhang H, Gillies RJ, Dayton PA, Ferrara KW (2008) A stimulus-responsive contrast agent for ultrasound molecular imaging. Biomaterials 29: 597–606

Burns PN, Wilson SR, Simpson DH (2000) Pulse inversion imaging of liver blood flow: improved method for characterizing focal masses with microbubble contrast. Invest Radiol 35:58–71

Chappell JC, Song J, Burke CW, Klibanov AL, Price RJ (2008) Targeted delivery of nanoparticles bearing fibroblast growth factor-2 by ultrasonic microbubble destruction for therapeutic arteriogenesis. Small 4:1769–1777

Chinol M, Casalini P, Maggiolo M, Canevari S, Omodeo ES, Caliceti P, Veronese FM, Cremonesi M, Chiolerio F, Nardone E, Siccardi AG, Paganelli G (1998) Biochemical modifications of avidin improve pharmacokinetics and biodistribution, and reduce immunogenicity. Br J Cancer 78:189–197

Choi JJ, Feshitan JA, Baseri B, Wang S, Tung YS, Borden MA, Konofagou EE (2010) Microbubble-size dependence of focused ultrasound-induced blood-brain barrier opening in mice in vivo. IEEE Trans Biomed Eng 57:145–154

De Saint Victor V, Crake C, Coussios CC, Stride E (2014) Properties, characteristics and applications of microbubbles for sonothrombolysis. Expert Opin Drug Deliv 11:187–209

Deshpande N, Pysz MA, Willmann JK (2010) Molecular ultrasound assessment of tumor angiogenesis. Angiogenesis 13:175–188

Escoffre JM, Novell A, Serriere S, Lecomte T, Bouakaz A (2013) Irinotecan delivery by microbubble-assisted ultrasound: in vitro validation and a pilot preclinical study. Mol Pharm 10:2667–2675

Frinking PJ, Tardy I, Theraulaz M, Arditi M, Powers J, Pochon S, Tranquart F (2012) Effects of acoustic radiation force on the binding efficiency of BR55, a VEGFR2-specific ultrasound contrast agent. Ultrasound Med Biol 38:1460–1469

Hettiarachchi K, Zhang S, Feingold S, Lee AP, Dayton PA (2009) Controllable microfluidic synthesis of multiphase drug-carrying lipospheres for site-targeted therapy. Biotechnol Prog 25:938–945

Husseini GA, Diaz de la Rosa MA, Richardson ES, Christensen DA, Pitt WG (2005) The role of cavitation in acoustically activated drug delivery. J Control Release 107:253–261

Ibsen S, Benchimol M, Simberg D, Schutt C, Steiner J, Esener S (2011) A novel nested liposome drug delivery vehicle capable of ultrasound triggered release of its payload. J Control Release 155:358–366

Ibsen S, Schutt CE, Esener S (2013a) Microbubble-mediated ultrasound therapy: a review of its potential in cancer treatment. Drug Des Devel Ther 7:375–388

Ibsen S, Su Y, Norton J, Zahavy E, Hayashi T, Adams S, Wrasidio W, Esener S (2013b) Extraction protocol and mass spectrometry method for quantification of doxorubicin released locally from prodrugs in tumor tissue. J Mass Spectrom 48:768–773

Kheirolomoom A, Dayton PA, Lum AF, Little E, Paoli EE, Zheng H, Ferrara KW (2007) Acoustically-active microbubbles conjugated to liposomes: characterization of a proposed drug delivery vehicle. J Control Release 118:275–284

Kiessling F, Fokong S, Bzyl J, Lederle W, Palmowski M, Lammers T (2014) Recent advances in molecules, multimodal and theranostic ultrasound imaging. Adv Drug Deliv Rev 72:15–27

Kim DH, Costello MJ, Duncan PB, Needham D (2003) Mechanical properties and microstructure of polycrystalline phospholipid monolayer shells: novel solid microparticles. Langmuir 19:8455–8466

Kitzman DW, Goldman ME, Gillam LD, Cohen JL, Aurigemma GP, Gottdiener JS (2000) Efficacy and safety of the novel ultrasound contrast agent perflutren (definity) in patients with suboptimal baseline left ventricular echocardiographic images. Am J Cardiol 86:669–674

Kooiman K, Kokhuis TJA, van Rooij T, Skachkov I, Nigg A, Bosch JG, van der Steen AFW, van Cappellen WA, de Jong N (2014) DSPC or DPPC as main shell component influences ligand distribution and binding area of lipid-coated targeted microbubbles. Eur J Lipid Sci Technol 116:1217–1227

Kotopoulis S, Delalande A, Popa M, Mamaeva V, Dimcevski G, Gilja OH, Postema M, Gjertsen BT, McCormack E (2014) Sonoporation-enhanced chemotherapy significantly reduces primary tumour burden in an orthotopic pancreatic cancer xenograft. Mol Imaging Biol 16:53–62

Kotopoulis S, Dimcevski G, Gilja OH, Hoem D, Postema M (2013) Treatment of human pancreatic cancer using combined ultrasound, microbubbles, and gemcitabine: a clinical case study. Med Phys 40:072902

Lassau N, Chami L, Benatsou B, Peronneau P, Roche A (2007) Dynamic contrast-enhanced ultrasonography (DCE-US) with quantification of tumor perfusion: a new diagnostic tool to evaluate the early effects of antiangiogenic treatment. Eur Radiol 17(Suppl 6):F89–F98

Lensen D, Gelderblom EC, Vriezema DM, Marmottant P, Verdonschot N, Versluis M, de Jong N, van Hest JCM (2011) Biodegradable polymeric microcapsules for selective ultrasound-triggered drug release. Soft Matter 7:5417–5422

Lentacker I, De Geest BG, Vandenbroucke RE, Peeters L, Demeester J, De Smedt SC, Sanders NN (2006) Ultrasound-responsive polymer-coated microbubbles that bind and protect DNA. Langmuir 22: 7273–7278

Lentacker I, De Cock I, Deckers R, De Smedt SC, Moonen CT (2014) Understanding ultrasound induced sonoporation: definitions and underlying mechanisms. Adv Drug Deliv Rev 72C:49–64

Liu HL, Fan CH, Ting CY, Yeh CK (2014) Combining microbubbles and ultrasound for drug delivery to brain tumors: current progress and overview. Theranostics 4:432–444

Molina CA, Ribo M, Rubiera M, Montaner J, Santamarina E, Delgado-Mederos R, Arenillas JF, Huertas R, Purroy F, Delgado P, Alvarez-Sabin J (2006) Microbubble administration accelerates clot lysis during continuous 2-MHz ultrasound monitoring in stroke patients treated with intravenous tissue plasminogen activator. Stroke 37: 425–429

Mullin LB, Phillips LC, Dayton PA (2013) Nanoparticle delivery enhancement with acoustically activated microbubbles. IEEE Trans Ultrason Ferroelectr Freq Control 60:65–77

Newman CM, Bettinger T (2007) Gene therapy progress and prospects: ultrasound for gene transfer. Gene Ther 14:465–475

Nomikou N, Fowley C, Byrne NM, McCaughan B, McHale AP, Callan JF (2012) Microbubble-sonosensitiser conjugates as therapeutics in sonodynamic therapy. Chem Commun (Camb) 48: 8332–8334

Pochon S, Tardy I, Bussat P, Bettinger T, Brochot J, von Wronski M, Passantino L, Schneider M (2010) BR55: a lipopeptide-based VEGFR2-targeted ultrasound contrast agent for molecular imaging of angiogenesis. Invest Radiol 45:89–95

Rapoport N, Nam KH, Gupta R, Nam KH, Gupta R, Gao Z, Mohan P, Payne A, Todd N, Liu X, Kim T, Shea J, Scaife C, Parker DL, Jeong EK, Kennedy AM (2011) Ultrasound-mediated tumor imaging and nanotherapy using drug loaded, block copolymer stabilized perfluorocarbon nanoemulsions. J Control Release 153:4–15

Rapoport NY, Kennedy AM, Shea JE, Scaife CL, Nam KH (2009) Controlled and targeted tumor chemotherapy by ultrasound-activated nanoemulsions/microbubbles. J Control Release 138:268–276

Rychak JJ, Klibanov AL (2014) Nucleic acid delivery with microbubbles and ultrasound. Adv Drug Deliv Rev 72C:82–93

Senior R, Andersson O, Caidahl K, Carlen P, Herregods MC, Jenni R, Kenny A, Melcher A, Svedenhag J, Vanoverschelde JL, Wandt B, Widgren BR, Williams G, Guerret P, la Rosee K, Agati L, Bezante G (2000) Enhanced left ventricular endocardial border delineation with an intravenous injection of SonoVue, a new echocardiographic contrast agent: a european multicenter study. Echocardiography 17:705–711

Sirsi SR, Borden MA (2014) State-of-the-art materials for ultrasound-triggered drug delivery. Adv Drug Deliv Rev 72C:3–14

Stride E, Porter C, Prieto AG, Pankhurst Q (2009) Enhancement of microbubble mediated gene delivery by simultaneous exposure to ultrasonic and magnetic fields. Ultrasound Med Biol 35:861–868

Tranquart F, Le Gouge A, Correas JM, Ladam Marcu V, Manzoni P, Vilgrain V, Aube C, Bellin MF, Chami L,

Claudon M, Cuilleron M, Drouillard J, Gallix B, Lucidarme O, Marion D, Rode A, Tasu JP, Trillaud H, Fayault A, Rusch E, Giraudeau B (2008) Role of contrast-enhanced ultrasound in the blinded assessment of focal liver lesions in comparison with MDCT and CEMRI: results from a multicentre clinical trial. Eur J Cancer Suppl 6:9–15

Unger E, Porter T, Lindner J, Grayburn P (2014) Cardiovascular drug delivery with ultrasound and microbubbles. Adv Drug Deliv Rev 72C: 110–126

VanBavel E (2007) Effects of shear stress on endothelial cells: possible relevance for ultrasound applications. Prog Biophys Mol Biol 93:374–383

Vancraeynest D, Havaux X, Pouleur AC, Pasquet A, Gerber B, Beauloye C, Rafter P, Bertrand L, Vanoverschelde JL (2006) Myocardial delivery of colloid nanoparticles using ultrasound-targeted microbubble destruction. Eur Heart J 27:237–245

Wang DS, Panje C, Pysz MA, Paulmurugan R, Rosenberg J, Gambhir SS, Schneider M, Willman JK (2012) Cationic versus neutral microbubbles for ultrasound-mediated gene delivery in cancer. Radiology 264:721–732

Willmann JK, Kimura RH, Deshpande N, Lutz AM, Cochran JR, Gambhir SS (2010) Targeted contrast-enhanced ultrasound imaging of tumor angiogenesis with contrast microbubbles conjugated to integrin-binding knottin peptides. J Nucl Med 51:433–440

12 Co-administration of Microbubbles and Drugs in Ultrasound-Assisted Drug Delivery: Comparison with Drug-Carrying Particles

Ryo Suzuki and Alexander L. Klibanov

Abstract

There are two alternative approaches to ultrasound-assisted drug delivery. First, the drug can be entrapped into or attached onto the ultrasound-responsive particles and administered in the vasculature, to achieve ultrasound-triggered drug release from the particles and localized tissue deposition in response to ultrasound treatment of the target zone. Second, the drug can be co-administered with the microbubbles or other sonosensitive particles. In this case, the action of ultrasound on the particles (which act as cavitation nuclei) results in the transient improvement of permeability of the physiological barriers, so that the circulating drug can exit the bloodstream and get into the target tissues and cells. We discuss and compare both of these approaches, their characteristic advantages and disadvantages for the specific drug delivery scenarios. Clearly, the system based on the off-label use of the existing approved microbubbles and drugs (or drug carriers) will have a chance of getting to clinical trials faster and with lesser resources spent. However, if a superior curative potential of a sonosensitive drug carrier is proven, and formulation stability problems are addressed properly, this approach may find its way to practical use, especially for nucleic acid delivery scenarios.

Keywords

Co-administration of microbubbles • Drug-carrying particles • Drug delivery • Ultrasound

R. Suzuki
Cardiovascular Division,
Robert M Berne Cardiovascular Research Center,
University of Virginia, 801394, Charlottesville,
VA 22908, USA

Department of Drug and Gene Delivery System,
Faculty of Pharma-Sciences, Teikyo University,
Tokyo, Japan

A.L. Klibanov (✉)
Cardiovascular Division,
Robert M Berne Cardiovascular Research Center,
University of Virginia, 801394, Charlottesville,
VA 22908, USA
e-mail: sasha@virginia.edu

© Springer International Publishing Switzerland 2016

J.-M. Escoffre, A. Bouakaz (eds.), *Therapeutic Ultrasound*, Advances in Experimental Medicine and Biology, Vol. 880, DOI 10.1007/978-3-319-22536-4_12

12.1 Introduction

Ultrasound-assisted drug delivery field has been making steady progress towards the clinic. There are two competing strategies applied. One focuses on the design of a sonosensitive drug carrier particle that would release the drug upon ultrasound action, and assist drug delivery to the target tissues and cells, across the physiological barriers. The other approach is to simply co-administer the drug and gas microbubbles and perform ultrasound treatment, with the expectation that local energy deposition due to microbubble compression and expansion in the ultrasound pressure field will assist drug delivery. The purpose of this "debate" chapter is to evaluate and compare the advantages and disadvantages for both approaches. In a short review we cannot assess the literature fully; the provided references are used as examples of the trends. Due to the focus of our research interests, we do not discuss thermosensitive liposomes: after all, these particles are not directly ultrasound-sensitive. The general intent is to show which of the techniques is the most efficient and useful for the success of the overarching task of drug delivery, i.e., improvement of therapeutic index.

12.2 Co-administration Approach: Microbubbles that Do Not Carry the Drug

Drugs cannot always efficiently penetrate across the multiplicity of physical and physiological barriers that exist between the drug and its target. This is a major problem of drug delivery, and it can be addressed by local energy deposition via controlled targeted ultrasound field action, augmented by cavitation of gas bodies at the barrier of drug entry.

12.2.1 Cell Membrane as a Barrier to Cross

Co-administration of microbubbles with drug substances (including nucleic acid material) has been historically the first approach evaluated for ultrasound-assisted intracellular delivery (which is not surprising given the complexity of the formulation of the actual drug carrier systems, especially the microbubble-based particles) (Greenleaf et al. 1998; Unger et al. 1997). General initial idea was to use the focal energy deposition due to microbubble vibration (and/or inertial cavitation) to create pores in the membranes, to allow penetration of the drug into the cell, especially advantageous if the drug itself cannot get across the cell membrane. That idea proved to be quite fruitful: numerous subsequent studies explored delivery of model drugs (mostly fluorescent dyes) into cells *in-vitro* (especially useful for the mechanistic studies), and eventually moved into the tissues *in-vivo*.

Nucleic acid is one example of a drug tested in those early studies – thus, ultrasound-assisted transfection has been proposed, initially as a tool for cell culture gene delivery, and eventually as an *in-vivo* ultrasound-assisted transfection tool. One concern with microbubble not carrying the nucleic acid directly has become apparent: if it is not attached to the bubble, nucleic acid is not protected from the degradation by nucleases (Wang et al. 2012) - thus transfection might not be as efficient as desired. Alternative is not to leave nucleic acid unprotected and have it complexed to a traditional, non-microbubble transfection reagent (Unger et al. 1997; Burke et al. 2012) or even packaged as a virus (Muller et al. 2008), so that microbubble cavitation by ultrasound will do what it does best – create the transient pores in the cell membrane that allow material transfer into the cells and tissues.

Thus, the general idea of using microbubble cavitation in the ultrasound field to assist drug penetration across the barrier comes from the early *in-vitro* experiments on ultrasound-assisted intracellular delivery (Greenleaf et al. 1998; Unger et al. 1997). The pores created by microbubble cavitation should not be too large (if over 30 um^2, would not seal easily, which may be detrimental for the sonoporated cells) – and the narrow pores seal rapidly, within 20–30 s (Hu et al. 2013). Therefore, the cell poration will not likely get the drug loaded across the plasma membrane very efficiently – the transient pores make up only a small fraction of the total cell surface, so the diffusion of the drug into the cell from the outside is not going to be efficient. So, for

intracellular delivery a microbubble-based drug carrier system might become more efficient in comparison with the co-administration of drug and bubbles, because ultrasound-triggered action is taking place exactly where the drug-loaded particle is present, and it can be especially efficient if the complex is adhered to the target cell surface, electrostatically (Panje et al. 2012; Wang et al. 2012; Tlaxca et al. 2010; McCreery et al. 2004) or by ligand-mediated targeting (Tlaxca et al. 2013; Phillips et al. 2012). There are also indications of the alternative mechanisms for the ultrasound/microbubble enhancement of intracellular delivery, different from the pore formation, such as activation of endocytosis (Meijering et al. 2009; De Cock et al. 2015). Recently, this alternative mechanism is being assessed as a tool that provides intracellular delivery for up to several hours from the ultrasound/microbubble treatment of cultured cells, and is cell type dependent (Lammertink et al. 2014).

Fig. 12.1 Ultrasound-assisted opening of blood-brain barrier in a rat model. One megahertz focused ultrasound (IGT, 1 Hz, 20 ms pulses, 1–2 min) treatment of rat brain following intravenous administration of decafluorobutane microbubbles (DSPC/PEG stearate shell). Imaging of focal areas 1–6 observed as T1 MRI contrast with Gd-DTPA extravasation and accumulation (UVA Molecular Imaging Center (7 T MRI Clinscan, Bruker/Siemens) © Max Wintermark, 2014, with permission)

12.2.2 Vessel Wall: The First In-Vivo Barrier for Drug Delivery from the Bloodstream

Cell membrane is not the only barrier to overcome to achieve drug delivery, and microbubble cavitation (stable or inertial) may play a significant role in the delivery enhancement. In most of the tissues endothelial lining is dense, and does not permit rapid exchange of materials (including drugs) between the blood and the interstitial space (see also Sect. 12.3.2.1). Transcytosis through endothelial lining of the blood vessels is an important mechanism for proper control and sequestration of delivery of nutrients to the tissues and cells located outside of the vasculature. Respectively, drug delivery may not be efficient if endothelium does not allow transfer of the particular drug. Initially, interaction of ultrasound with microbubbles in the microvasculature was observed in a rather abrupt mode: destructive cavitation of microbubbles in the ultrasound field led to microvessel rupture and exit of RBCs from the bloodstream into the interstitial space (Skyba et al. 1998). Formation of transient petechial hemorrhages upon ultrasound action on microbubbles in the kidney vasculature was also observed, as a sign of large entities (RBC) extravasation (Wible et al. 2002). It has been suggested that this approach could lead to enhancement of drug delivery into the tissues (Skyba et al. 1998); later this suggestion has been confirmed by intravital microscopy observation of the interstitial delivery of fluorescent nanoparticles (Price et al. 1998): when ultrasound of sufficient acoustic pressure (e.g., MI 0.7) was applied to the tissue following intravenous administration of microbubbles and nanoparticles, particles could be detected in the interstitial space, along with red blood cells. Relatively quickly (Hynynen et al. 2003) a more "gentle", lower-energy approach was proposed: stable (nondestructive) cavitation of microbubbles in the vasculature resulted in the "softening" of the strongest endothelial lining barrier of the body, blood-brain barrier (BBB), leading to the ability of small (Hynynen et al. 2006) (Fig. 12.1) and large (Hynynen et al. 2005; Raymond

et al. 2008) molecules, and even nanoparticles (Treat et al. 2012) cross the barrier and accumulate in the interstitial space. Unlike cell membrane sonoporation (cell membrane pores have been reported to stay open for under a minute (Hu et al. 2013), BBB may stay open for many hours following ultrasound treatment (Samiotaki and Konofagou 2013). This approach should be easier to bring to clinical translation, because it implies combining intravascular administration of the drug with the (off-label) use of existing clinical microbubble formulation, and thus does not require the complicated, lengthy and costly approval process for the new drug entity, such as a microbubble that carries the drug. In a glioma brain tumor rodent model, combining intravascular microbubbles and doxorubicin-loaded long-circulating liposomes (Doxil) with focused ultrasound treatment resulted in long-term (up to 140 days) cure of a significant fraction of experimental animals (Aryal et al. 2013) – a remarkable achievement.

This approach has been expanded from BBB opening to enhancing delivery across the vessel wall in other tissues, e.g., hindleg muscle and tumor (Bohmer et al. 2010), from dyes to viruses (Muller et al. 2008); with multiple uses for improvement of tissue delivery of a wide range of drugs. Even more exciting is the ability to enhance tissue delivery specifically in the ultrasound treated areas, while minimizing drug deposition in the normal non-diseased tissues. Exact mechanism of this prolonged vascular permeability enhancement is still debated: from the transient gap junction degradation (Alonso et al. 2010) to enhancement of endocytosis (De Cock et al. 2015) and transcytosis (Sheikov et al. 2004).

An exciting example of an early stage clinical trial for co-administration approach has been reported already (Kotopoulis et al. 2013), in a pancreatic cancer primary tumor setting. Pancreatic cancer is known to have generally low vascularity (Rodallec et al. 2006), so drug delivery from the bloodstream into the tumor mass is restricted. Drug of choice, gemcitabine, stays in the bloodstream for at least an hour following intravenous administration (Gemzar 1996); thus,

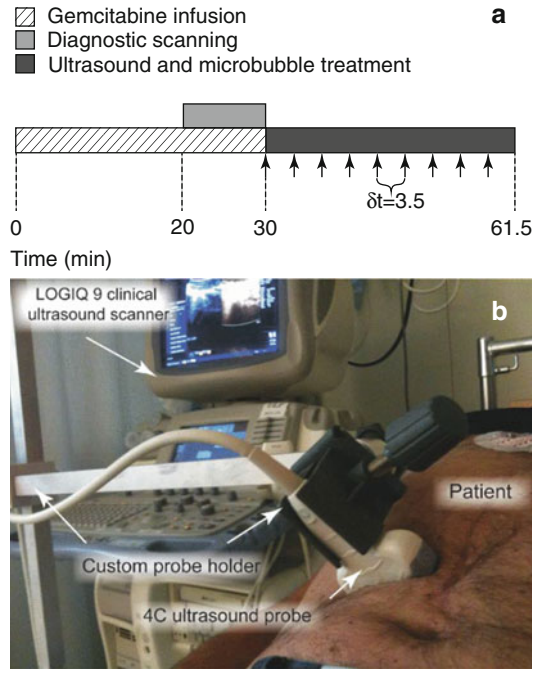

Fig. 12.2 Time frame of each chemotherapy cycle [panel (**a**)] and photograph of probe and custom-made probe holder during patient treatment using microbubble sonoporation for pancreatic cancer [panel (**b**)]. Panel (**a**) shows the time frame for each treatment cycle from the start of the gemcitabine infusion. Arrows indicate intravenous injection time of 0.5 ml SonoVue followed by a 5-ml intravenous injection of saline. Time between each injection (δt) is 3.5 min © American Association of Physicists in Medicine, 2013 (Reprinted with permission from Kotopoulis et al. (2013))

when ultrasound imaging of pancreas and the cancer nodule is performed, repeatedly, with multiple injections of SonoVue microbubbles and corresponding imaging/insonation cycles (Fig. 12.2), the vascular barrier to drug delivery into the tumor tissue is "softened".

Consequently, recirculating drug may have much better chances to enter the tumor from the bloodstream, providing therapy; slowing down tumor growth in patients who did receive ultrasound and microbubbles in comparison with a historical cohort of the standard-of-care patients was demonstrated in this first-in-human trial (Fig. 12.3). A continued expanded study from the same group of authors may point towards an exciting evidence of life extension (Dimcevski et al., manuscript in submission).

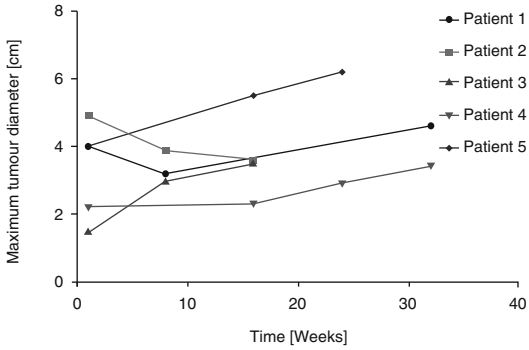

Fig. 12.3 Change in tumor diameter over time measured from CT images in patients with pancreatic malignancy © American Association of Physicists in Medicine, 2013 (Reprinted with permission from Kotopoulis et al. (2013))

12.2.3 Tissue Geometry, Mechanics and Distance as Barriers to Drug Delivery

We have already discussed above that inertial (destructive) as well as stable cavitation of microbubbles in the ultrasound field enhance delivery into the cells and across the endothelial lining. However, there are numerous other barriers that the drug may have to cross, beyond the cell membrane and endothelium. First, there is a layer of pericytes on the outside of endothelial lining, wrapping around capillaries and post-capillary venules. In larger vessels, there are layers of smooth muscle cells; large vessels are quite thick, with distinguished layers of mechanically robust intima, media, and adventitia. Mechanical properties of the vessel wall may limit drug passage, even after endothelial lining "softening" by ultrasound, so in large vessels one may prefer to deliver the drug just to the intima, e.g., an anti-restenosis drug (Phillips et al. 2011). If the drug should be delivered to the bulk interstitial space, perhaps ultrasound-assisted delivery across the vessel wall at the capillary or post-capillary level may be more efficient. Next barrier is the tissue itself: the space from the vessel into the bulk of tissue may extend beyond tens of microns which makes it difficult for the drug molecule to penetrate by diffusion through the crowded interstitial space. Specialized drug or nucleic acid carrier systems can be then applied – e.g., highly pegylated nanoparticles that can penetrate through the tissue rapidly, as proposed by Hanes et al. (Nance et al. 2014b). Combination of focused ultrasound and intravenous microbubbles with PEG-PEI-plasmid resulted in an excellent delivery and transfection efficacy (Burke et al. 2012) as well as deep tissue penetration (Nance et al. 2014a). Acoustic radiation force action on microbubbles may also be of assistance: ultrasound field can improve microbubble delivery to the target surface from the bulk of blood vessels, reducing the required microbubble dose (Dayton et al. 1999); ultrasound-induced microstreaming may also assist drug delivery.

12.3 Drug-Carrying Sonosensitive Particles

12.3.1 Drug-Loaded Nano/Microbubbles

The driving force of drug delivery by sonoporation with nano/microbubbles is stable (or inertial) cavitation, which leads to release of sequestered drug from the particle, as well as increase of permeability of adjacent cell membranes. For efficient delivery, the drug should be present while a bubble is acting on the cell membrane. This is where drug-loaded bubbles may prove beneficial.

Recently, numerous research groups have been developing drug-carrying bubbles, including drug complexes with microbubbles, nanobubbles, nanodropletes, liposomes, emulsions and micelles. The range of tested drugs is quite broad, from small to large molecules, from inorganic to organic to biomolecules. Various types of drugs have been already associated with bubbles, from anti-cancer agents (Gao et al. 2008; Rapoport et al. 2009a), small interfering RNA (Negishi et al. 2008; Endo-Takahashi et al. 2012), micro-RNA (Hatakeyama et al. 2014; Endo-Takahashi et al. 2014), antisense oligonucleotides (Koebis et al. 2013), plasmid DNA (Endo-Takahashi et al. 2013), to proteins (Bioley et al. 2012a, b, 2013). This chapter section focuses on the advances of drug-loaded ultrasound-sensitive particles, discusses their formulation, properties, issues and prospects toward future clinical use.

12.3.2 Formulations and Properties

Formulations are usually based on a perfluorocarbon (PFC) core (gas or liquid), stabilized by a shell. PFCs are hydrophobic. To suspend and stabilize them in physiological media such as saline or isotonic sugar solution (e.g., 5 % glucose) we need to use the shells made of amphipathic material, which could be a protein, surfactant and/or lipid. In the commercially available microbubbles, albumin or lipids are utilized as the shell stabilizers. These molecules have hydrophobic and hydrophilic groups in their structure. Hydrophobic groups (e.g., exposed core of denatured albumin) face the PFC (gas or liquid) core, and hydrophilic groups face the aqueous phase to inhibit particle aggregation and fusion. Gas-filled particles with amphipathic polymer shell have also been studied. In the early phase of drug loading experiments, hydrophobic drugs were selected and loaded in the bubble shell via hydrophobic interaction. Bubble shell surface charge can be modified to attach the drugs (mostly nucleic acids) via electrostatic interaction. As an option to improve drug load, the drug could be covalently attached to the microbubble shell. Lately, newer types of bubbles have been developed, in which nanobubble was encapsulated inside liposomes (Suzuki et al. 2007; Javadi et al. 2012). These liposomal bubbles may co-encapsulate the drug in the inner aqueous phase of liposomes. In this section, we introduce the formulations of drug-loaded bubbles.

12.3.2.1 Drug-Particle Formulations Via Hydrophobic Interaction (Non-covalent Binding)

During the past decade many research groups have reported drug-loaded microbubble formulations. Initially, a hydrophobic anti-tumor agent, paclitaxel, was tested for its ability to associate and retain with the microbubbles shell (Unger et al. 1998; Tartis et al. 2006). Hydrophobic drugs are simply mixed with microbubble shell material and associate with the hydrophobic layer of the shell (Scheme Fig. 12.4a). These drugs are released, possibly in combination with shell fragments, when ultrasound is applied and bubbles are destroyed. Just as traditional ultrasound contrast microbubbles, drug-loaded microbubbles may be visualized with ultrasound imaging, which can provide additional information in the image-guided drug delivery applications.

The endothelial gap junction pores in the normal tissue vasculature are less than 7 nm (Rapoport et al. 2009b), which may limit delivery of nanoparticles and biopharmaceuticals out of the vasculature. In the tumor tissues blood vessels are defective and leaky. In addition, lymphatic drainage in tumor tissue is poor as compared to normal tissues (Matsumura and Maeda 1986). These features allow so-called "passive targeting" to achieve drug and gene delivery and accumulation in the tumors. This phenomenon is known as the enhanced permeability and retention (EPR) effect (Matsumura and Maeda 1986). Microbubbles, with their micrometer dimensions, are optimal as

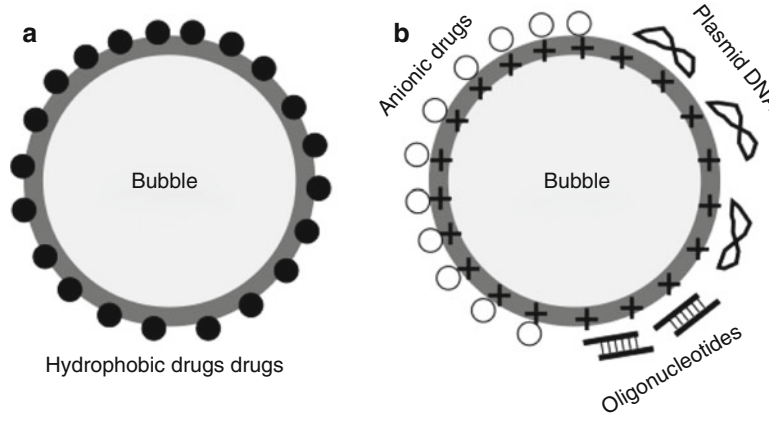

Fig. 12.4 Structure of drug-loaded microbubbles. (**a**) Drug retained within the bubble shell via hydrophobic interaction. (**b**) Drug and nucleic acids attached to the bubble shell via electrostatic interaction

intravascular imaging agents, but their size is too large to penetrate through the vascular endothelial lining in tumors: typically, particles have to be significantly less than 1 μm in diameter to extravasate into the tumor interstitial space (Yuan et al. 1995). Therefore, to deliver drugs to the tissues outside of the vascular bed, nanobubbles (with gas core) and nanodroplets (with liquid core), which are less than 1 μm have been developed. These are generally prepared with sonication. In brief, aqueous solution or nano-dispersion (e.g., micelles) of shell material is sonicated in the presence of perfluorocarbon gas or liquid. Hydrophobic drugs can be loaded in the shell of these particles by hydrophobic interaction. Nanodroplets are usually prepared from liquid perfluoropentane and perfluorohexane and stabilized with a polymer coat or a lipid monolayer shell (Rapoport et al. 2009a, 2011; Mohan and Rapoport 2010). With submicron size, nanodroplets can exit tumor vasculature after intravenous injection and accumulate in the tumor interstitium via EPR mechanism. The boiling points of perfluoropentane and perfluorohexane, which are utilized as liquid core in nanodroplet, are 29 °C and 56 °C, respectively. Due to surface tension, perfluoropentane nanodroplets may remain liquid even at 37 °C, in "superheated" state. However, they can rapidly convert (shift) to gas bubbles in response to ultrasound (Fig. 12.5).

Therefore, these particles are sometimes called phase-shift nanodroplets or nanoemulsion (Marin et al. 2001). This phase shift can be induced by targeted focused ultrasound *in-vivo*, for example, to convert the nanodroplets that have accumulated in the tumor tissue by EPR effect after intravenous injection. As a result, drug can be released from the particles only at the site of their phase shift by ultrasound exposure. Resulting gas microbubbles can be observed by ultrasound imaging. Therefore, this system might be useful for imaging control of triggered drug delivery.

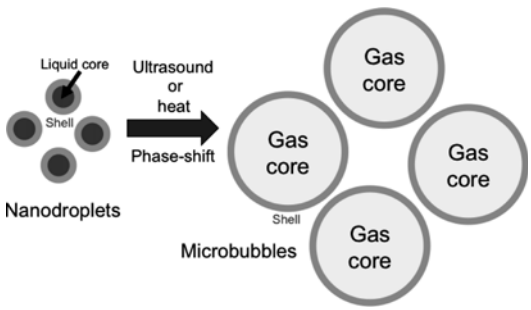

Fig. 12.5 Structure of nanodroplets and their phase-shift conversion to microbubbles. Nanodroplets contain liquid perfluorocarbon core (e.g., C_5F_{12}), stabilized with a lipid or polymer shell. Stimulation with ultrasound irradiation and/or heating results in conversion of the liquid core phase to gas phase, with microbubble formation

Gas-core micro- and nanobubbles and liquid-core nanodroplets usually exhibit a relatively short *in-vivo* lifetime due to core loss (Shiraishi et al. 2011). Lower molecular weight PFCs (usually gases) are better soluble in water and blood; PFC core is lost from the shell and particles become insensitive to ultrasound. Behavior of nanobubbles and nanodroplets under ultrasound exposure (inertial cavitation with rapid collapse) may become uncontrolled. Consequently, damage to cells and tissues might be induced if acoustic pressure is above the mandated ultrasound contrast imaging Mechanical Index (MI) limits. As a "softer" alternative, Zhang et al. (2014) developed an interesting phase shift "solid–liquid-gas" tri-phase transition particle. It is based on a natural "solid–liquid-gas" tri-phase transition medium, L-menthol as an inner core; hollow mesoporous silica is used as the outer shell. The nanoparticle can continuously generate volatile gas in a relatively mild manner, rather than the conventionally abrupt phase transition induced by boiling of superheated PFC liquid. This controllable solid–liquid-gas tri-phase transition of L-menthol can be attributed to the gradual liquid to volatile gas phase-transition at far below its boiling point (212 °C). The generation of L-menthol gas permits extended enhancement of drug delivery following a single bolus injection. In this paper, they reported prolonged blood circulation time ($T_{1/2} = 130$ min) and continuous accumulation in the tumor during 24 h period. These particles have porous structure, so they can be loaded with hydrophobic and hydrophilic drugs at the same time. Synergistic effects of high intensity focused ultrasound therapy and chemotherapy with these particles could be expected.

12.3.2.2 Electrostatic Complexes

This loading style is mostly applied for negatively charged molecules such as nucleic acids and some proteins. Microbubbles or nanobubbles with cationic shells (cationic lipids or polymers) are used. This approach has been applied for almost three decades to prepare liposome-nucleic acid complexes for lipofection. Particles are simply mixed with negatively charged molecules (e.g., plasmid DNA, or oligonucleotides) in low or moderate ionic strength media and complexes are formed by electrostatic interaction (Fig. 12.4b). Electrostatic adsorption onto the bubble shell has been shown to protect nucleic acid from degradation by nucleases, as well as enhance loading efficiency. Net positive charge of the complexes also helps attach the bubbles to cell membrane, and further improve delivery efficiency. This design was first reported by (Unger et al. 1997) who prepared positively charged microbubbles as a modification of MRX-115 microbubbles (lipid shell of that parent formulation is based on zwitterionic dipalmitoyl phosphatidylcholine). In the microbubbles intended for gene delivery, a 1:1 mixture of positively charged dipalmitoyl ethylphosphatidylcholine (DPEPC) and zwitterionic dioleoyl phosphatidylethanolamine was utilized. These microbubbles bound plasmid DNA encoding chloramphenicol acetyl transferase, and could enhance transfection of plasmid DNA into cultured cells when 1 MHz continuous wave ultrasound was applied for 5–30 s.

Many research groups have been utilizing electrostatic binding not only for plasmid DNA but also for oligonucleotides such as antisense, small interfering RNA (siRNA), microRNA, mRNA and minicircles. Various compositions of microbubbles and nanobubbles have been developed and tested as gene delivery systems *in-vitro* and *in-vivo*. To improve stability of microbubble formulations, use of longer-chain lipids with higher phase transition temperature was suggested (Christiansen et al. 2003). In that study, a mixture of cationic distearoyl trimethylammonium propane (DSTAP) and neutral distearoyl phosphatidylcholine (DSPC) and poly(ethylene glycol) stearate, with longer-chain stearoyl (C_{18} acyl) groups, was used for bubble preparation. The resulting shell served as an effective stabilizer for micrometer- size perfluorobutane gas core. Refrigerated storage of these microbubbles for many months in sealed vials under perfluorobutane atmosphere was reported. After complexing with plasmid, they have provided efficient transfection in the insonated skeletal muscle or myocardium *in-vivo* (Christiansen et al. 2003). Stability of microbubble formulations may be a major factor for gene delivery efficiency (Alter et al. 2009).

The type of cationic molecules is important for efficient transfection, as is the ratio between cationic lipids and nucleic acids. The latter is usually described as N/P ratio. N represents total number of aminogroups (nitrogen atom, positive charge) derived from lipid in bubbles; P represents total number of phosphate groups (phosphorus atom, negative charge) derived from nucleic acids. Optimization of N/P ratio is as important for sonoporation as it is for conventional gene delivery methods based on cationic molecules such as lipofection or polyplex. Takahashi et al. reported that distearoyl dimetylammonium propane (DSDAP)-based cationic liposomal nanobubbles had the highest gene delivery efficiency in comparison with other cationic lipid formulations, such as DSTAP or dimethyldioctadecylammonium bromide (DDAB) (Endo-Takahashi et al. 2013). DSDAP-based plasmid DNA-loaded nanobubbles achieved therapeutic effect in mice with hindlimb ischemia by bFGF gene transfer with ultrasound. Lately, nucleic acid delivery is focused on siRNA and microRNA, the novel gene therapy technologies. For gene silencing, siRNA molecules should be delivered into the most of target cells to inhibit expression of a desired gene. However, a simple co-injection of microbubbles and free nucleic acids results in very low transfection efficiency. Yet even sonoporation with nucleic acid-loaded bubbles would not be sufficient to achieve the desired transfection levels. To overcome this problem, Un et al. (2010a, b, 2011) developed active targeting of nucleic acid-loaded nanobubbles, mannose-modified cationic liposomal bubbles, which utilized mannose-modified PEG-lipids for macrophage targeting. In their initial reports, plasmid DNA-loaded mannose-modified liposomal bubbles provided

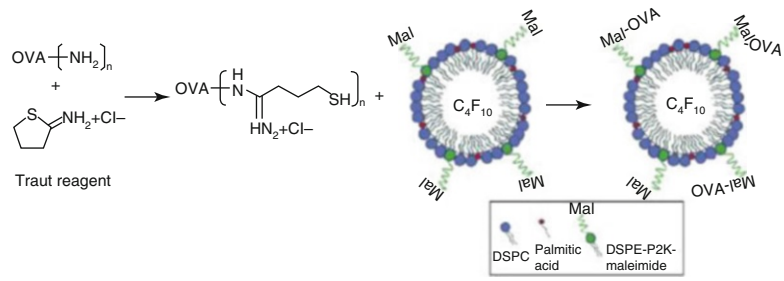

Fig. 12.6 Schematic representation of thiolated OVA linkage to microbubble via maleimide-lipid anchored to the microbubble shell. © Elsevier Ltd, 2012 (Reprinted with permission from Bioley et al. (2012b))

higher transfection efficiency than non-targeted liposomal bubble (Un et al. 2010a, b). Similar mannosylated sonosensitive siRNA lipoplexes targeted to hepatic endothelium suppressed intracellular adhesion molecule-1 (ICAM-1) expression (Un et al. 2012). Moreover, this group has reported lipopolyplex bubbles, prepared as electrostatic complexes of plasmid DNA and cationic polymer with anionic liposomal nanobubbles (Kurosaki et al. 2014). These bubble lipopolyplexes could reduce cytotoxicity, aggregation with erythrocytes and inflammatory response, the usual problems of cationic gene delivery tools. There is another elegant gene delivery system. Chen et al. developed beta cell-specific gene expression system in pancreatic islets by the combination of ultrasound and plasmid DNA-loaded microbubbles (Chen et al. 2006; Chai et al. 2009). In this study, rat insulin promoter-driven human insulin plasmid DNA and lipofectamine 2000 (commercially available cationic liposomes for gene delivery) were mixed, and the electrostatic complexes were added to phospholipids suspension in the perfluoropropane gas-filled sealed vial and shaken in an amalgamator to prepare microbubbles. Following intravenous infusion of these microbubble-lipofectamine-plasmid complexes, ultrasound was directed at the pancreas to destroy microbubbles within the pancreatic microcirculation, and islet-specific transgene expression in pancreas was observed. Expression peaked at day 4 and then decayed steadily over 4 weeks following a single treatment. Later, these researchers have expanded their studies to sonoporation gene delivery regeneration therapy (Chen et al. 2007, 2012, 2014). Overall, electrostatic drug-microbubble complexes play an important role in the development of nucleic acid sonoporation delivery systems.

12.3.2.3 Covalent Coupling of Drug Substances onto Microbubbles

There are other drug loading methods, based on covalent coupling between the drug and the bubble. Covalent coupling of biomolecules to microbubbles has been assessed and optimized for targeted molecular ultrasound imaging for almost two decades, as described and reviewed elsewhere (Villanueva et al. 1998; Klibanov 2005). For therapeutic protein delivery applications (Fig. 12.6), Bioley et al. developed antigen-decorated microbubble formulations (Bioley et al. 2012a, b, 2013), and demonstrated that microbubbles can serve as an efficient antigen delivery system to promote phagocytosis of the model antigen ovalbumin (OVA) even without ultrasound exposure: *in-vivo* administration of OVA-loaded microbubbles in mice resulted in the induction of OVA specific antibody and T cell responses.

12.3.2.4 Particle-Decorated Microbubbles

There are specialized loading methods to protect nucleic acid from nuclease and improve per-particle loading efficiency. Positively charged liposomes, lipoplexes and polyplexes that entrapped and/or stabilize nucleic acids or drug-loaded nanoparticles, can be placed on the surface of the microbubbles, either via streptavidin-biotin bonds (Vandenbroucke et al. 2008; Yang et al. 2013), or by covalent coupling (Sirsi et al. 2012). In addition, there are reports that describe virus-coated microbubbles. Porter, Bamber et al. (Taylor et al. 2007) developed a microbubble complex with an entry-deficient retrovirus, where positively charged microbubbles carried viral particles attached electrostatically. As mentioned above, these

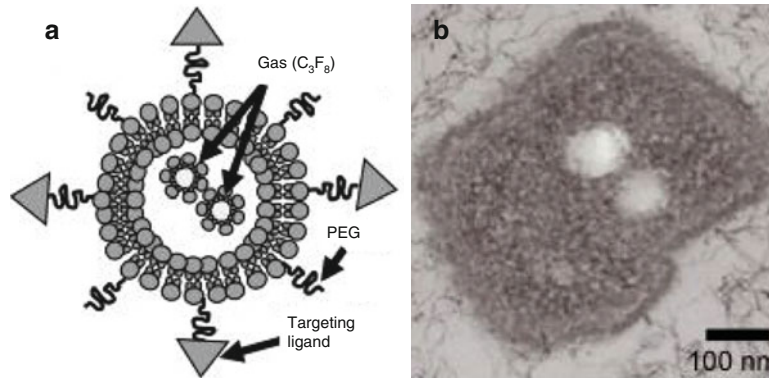

Fig. 12.7 Structure of Bubble liposome. (**a**) Cartoon of Bubble liposome, (**b**) Transmission electron microscopy of Bubble liposome. Original magnification, ×50,000. JEOL JEM2000EX operated at 100 kV. © Elsevier B.V. (Reprinted with permission from Suzuki et al. (2008))

particle-loaded microbubbles were formed by combining pre-formulated microbubbles with particles. Alternative approach is also possible: Bekeredjian et al. prepared adeno-associated virus (AAV) vector-loaded microbubbles by co-amalgamation of viral particles with lipids in water-glycerol solution, by a rapid (45 s) mechanical activation with a Capmix/Vialmix amalgamator and succeeded to develop an ultrasound gene delivery system in a cardiac setting (Muller et al. 2008). Lentacker and colleagues (Geers et al. 2011) developed an *in-situ* microbubble-liposome complex preparation method, where drug-loaded liposomes (Doxil) were added to glycerol:propyleneglycol:water media containing DSPE-PEG-maleimide, dipalmitoyl phosphatidylcholine (DPPC) and distearoyl-sn-glycero-3-phosphoethanolamine-N-[PDP (polyethylene glycol)-2000] (DSPE-PEG-PDP) in sealed vials with decafluorobutane headspace, followed by the same amalgamation step. This mechanical activation gives rise to C_4F_{10} lipid-shelled microbubbles decorated with liposomes. The liposomes are attached to the microbubble shell via covalent thiol-maleimide linkages; respective DSPE lipid anchors on the termini of the conjugate are embedded in the liposome bilayer and bubble monolayer shell. Finally, it was reported that doxorubicin-liposome-microbubbles allowed ultrasound-triggered killing of melanoma cells *in-vitro* even at very low doses of doxorubicin (Escoffre et al. 2013). The advantage of this approach is in the small size, low price and availability of amalgamators. Ease of use and short time of the preparation ensure ability to generate sterile microbubble-particle complex at the bedside.

12.3.2.5 Liposomal Bubbles

Liposome is an intelligent drug/gene delivery tool because of its biocompatibility, flexible composition and ease of loading of various types of drugs (including nucleic acids) inside and outside of the particle. Targeting molecules can be placed on the liposome surface for selective drug delivery to receptor-carrying cells and surfaces. Recently, liposome-based nanobubbles were developed. Suzuki, Maruyama and Negishi et al. reported a sonosensitive liposome particle encapsulating a perfluoropropane nanobubble inside it (Fig. 12.7). This liposomal bubble was termed "Bubble liposome" (Suzuki et al. 2007, 2008; Kodama et al. 2010). For plasmid DNA, siRNA and miRNA delivery, they utilized cationic Bubble liposomes loaded with these nucleic acids. As an alternative siRNA-loading method, they used hydrophobic anchor, cholesterol modified siRNA (Negishi et al. 2011). Targeting of Bubble liposomes with specific ligands further enhanced gene delivery efficiency.

A similar formulation with a similar structure, named "eLiposome" was developed recently by Pitt et al. (Fig. 12.8). This particle entrapped perfluoropentane and/or perfluorohexane nanodroplet inside a liposome (Javadi et al. 2012; Lattin et al. 2012a). First, nanoemulsion of perfluoropentane and/or perfluorohexane was prepared. Then nanodroplets were encapsulated in liposomes by co-sonication for the mixture of nanodroplets and liposomes, or by hydration of dry lipid film with the aqueous dispersion of nanodroplets. Finally, nanodroplet encapsulated liposome was purified with step-wise density gradient centrifugation (Javadi et al. 2012). This eLiposome particles were

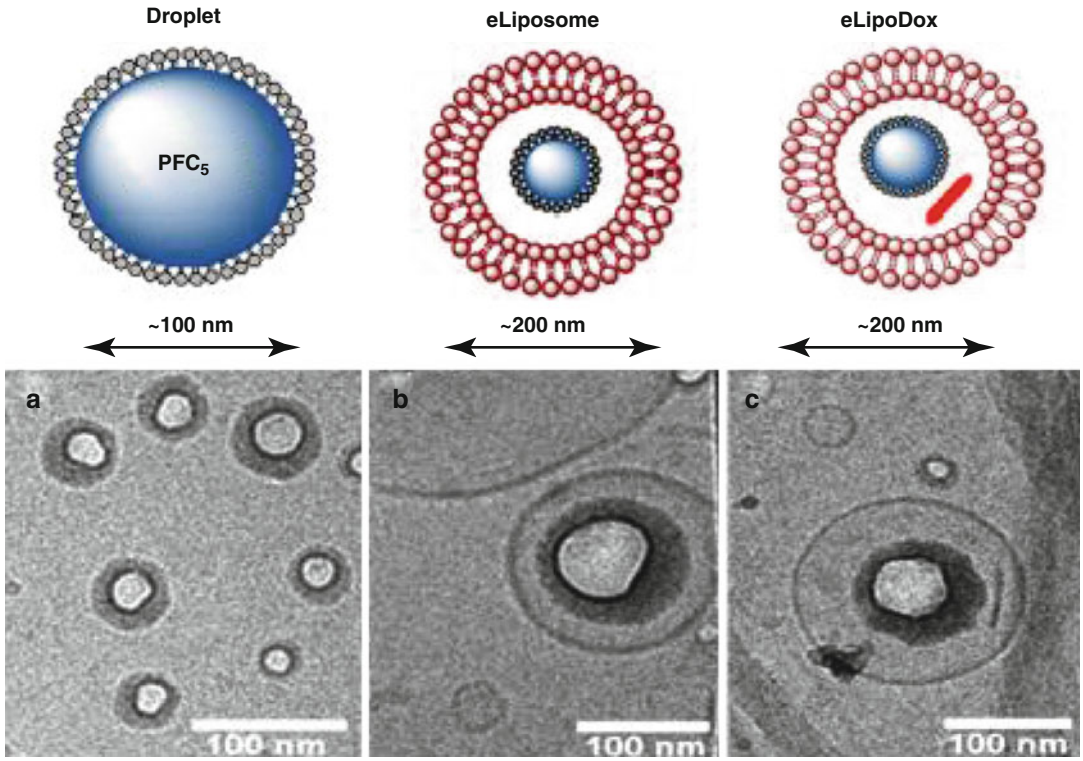

Fig. 12.8 Cryo-TEM and illustrations of the liposome nanoparticles used in this study. Examples of C5F12 nanodroplet (**a**), eLiposome (**b**), and eLipoDox (**c**). © Elsevier, Inc, 2014 (Reprinted with permission from Lin et al. (2014)

sensitive to ultrasound exposure: co-entrapped calcein release was demonstrated (Lattin et al. 2012b). It is suggested that ultrasound helps convert liquid fluorocarbon to gas, leading to a drastic increase of volume and rupture of the surrounding membrane. Targeted, folate modified eLiposome was developed and demonstrated targeted enhanced delivery of calcein and plasmid DNA into HeLa cells with ultrasound (Javadi et al. 2013). Likewise, folate-modified doxorubicin encapsulated eLiposome was also developed; it could effectively deliver doxorubicin into HeLa cells and provided cytotoxicity enhancement (Lin et al. 2014).

12.3.3 Problems to be Addressed: Formulation and Stability of Drug-Carrier Particles

Drug carrier liposome formulations are well known for their excellent stability profile, e.g., as demonstrated by Doxil. However, stability may become an issue for more complex sonosensitive drug carrier formulations (Shiraishi et al. 2011). While microbubbles demonstrate reasonable stability, nanobubbles are not very stable on storage, especially when compared to traditional drugs. Some of the commercially available microbubbles (ultrasound imaging contrast agents) are supplied as freeze-dried formulations, or prepared by sealed vial amalgamation mixing immediately before use. As discussed in the previous section, Geers et al. (2011) prepared microbubble-liposome-doxorubicin complexes by a Vialmix/Capmix amalgamator (same as used for Definity/Luminity clinical bubble formulation) – with the intent of finalizing the preparation at the bedside, immediately prior to use. Extended stability of the preformulated nanobubble/nanodroplet complexes may also be limited, and lyophilization may not be helpful, obviously. Returning perfluorocarbon nanodroplet aqueous emulsion to the

lyophilized particle precursor cake and expecting a uniform formulation after reconstitution may be too optimistic. An example of perflenapent (Echogen) a perfluoropentane/Zonyl nanoparticle emulsion, also suggests a cautionary approach: this formulation was approved by EMEA, yet it was withdrawn from the market without reaching wide clinical use. Overall, optimization of the nanodroplet-based formulations for their stability on storage and *in-vivo* is a critically important point to be addressed before clinical use can be considered.

12.4 Selection of the Best Technique: Optimal Approaches for Particular Tasks

Overall, significant efforts, with dozens of published manuscripts have been dedicated to both ultrasound drug delivery approaches: microbubble drug carrier particles, and co-administration of drug and bubbles. We cannot make a final judgment for the "winner" strategy at this point, but general considerations for the advantages and disadvantages for the particular task can be provided based on the above analysis.

Main reason for any drug delivery project is to improve therapeutic index, i.e., the ratio of the therapeutic dose to the dose of the drug at which the drug becomes toxic. Thus, if the drug is nontoxic and can easily get to the target tissues, onto and into the target cells, there should be no reason to attach the drug to a microbubble, or even to enhance the drug extravasation or intracellular delivery. However, if the drug has low toxicity (e.g., nucleic acid material) yet not active (nor toxic) unless it gets into the desired tissues, cells and even particular intracellular compartments, then enhanced drug delivery (e.g., via sonoporation) into the target is required for any drug efficacy. A more "traditional" is a scenario, when the drug is especially toxic in a particular critical organ or tissue (e.g., doxorubicin in the heart and bone marrow). In this case, entrapment of the drug in a pharmaceutical carrier will minimize drug deposition in the critical toxicity tissue, and selective insonation of the target tissue will enhance drug delivery and deposition into that organ. Obviously, both co-injection of microbubbles with drug-carrier liposomes (e.g., as in (Aryal et al. 2013)) as well as the administration of an ultrasound-responsive drug carrier particles (e.g., liposome-decorated microbubbles (Klibanov et al. 2010; Geers et al. 2011; Yan et al. 2013) can be applied, but the efficiency may vary.

Pharmacokinetic parameters of the carrier and of the drug itself play a major role in the therapeutic index improvement. If a drug (e.g., gemcitabine) or a drug carrier (e.g., a pegylated liposome) stays in the bloodstream for many hours, the recirculating drug has a much better chance to enter the tissue of interest following "softening" endothelial lining barrier by ultrasound treatment, e.g., BBB (Treat et al. 2012), than for the drug carrier bubbles, which lose gas after several minutes in the bloodstream. Therefore, one can expect a higher fraction of the drug (e.g., doxorubicin) accumulated in the insonated tissue in case of longer circulating drug carrier, especially that following the ultrasound/microbubble treatment the barrier stays open for hours, and allows efficient drug delivery into the interstitial space. However, if the desired drug target is the endothelium itself, and the drug cannot enter the target cells unless sonoporation is applied (e.g., nucleic acid), proximity of the drug to the surface of the cell during the ultrasound treatment may provide a significant benefit – and a combined drug/bubble carrier offers such proximity (Christiansen et al. 2003; Panje et al. 2012), especially if the particle is targeted to the endothelium by a specific ligand, e.g., an antibody (Tlaxca et al. 2013).

From the practical consideration standpoint, a combination of ultrasound action with the existing drugs (e.g., microbubbles approved for diagnostic imaging, drug-loaded liposomes or just a free long-circulating drug) would gain approval for clinical trials (e.g., Kotopoulis et al. 2013) easier than for any novel ultrasound-triggered formulation drug carrier systems – the latter will obviously get significant scrutiny from the regulatory agencies.

Conclusion

Both approaches to ultrasound-triggered drug delivery are being actively assessed *in-vitro* and in preclinical animal testing *in-vivo*. Ultrasound-sensitive carrier particle approach is going to be

slower to reach clinical trial stage, which has already begun for the co-injection approach of microbubbles and the drug. Both approaches have their respective advantages and disadvantages. Development cost for the novel drug carrier particles is going to be an important factor (especially that microbubbles and separate drug carrier systems are already available for clinical use worldwide). However, if a novel ultrasound-sensitive drug carrier particle will offer an advantage, such as curative potential with minimal side effects, there will be strong reason for bringing that particle formulation into development and eventually towards the clinical practice.

Acknowledgments This study was supported in part via NIH R21 EB016752.

References

Alonso A, Reinz E, Jenne JW, Fatar M, Schmidt-Glenewinkel H, Hennerici MG, Meairs S (2010) Reorganization of gap junctions after focused ultrasound blood-brain barrier opening in the rat brain. J Cerebr Blood Flow Metabol 30:1394–1402

Alter J, Sennoga CA, Lopes DM, Eckersley RJ, Wells DJ (2009) Microbubble stability is a major determinant of the efficiency of ultrasound and microbubble mediated in vivo gene transfer. Ultrasound Med Biol 35:976–984

Aryal M, Vykhodtseva N, Zhang YZ, Park J, McDannold N (2013) Multiple treatments with liposomal doxorubicin and ultrasound-induced disruption of blood-tumor and blood-brain barriers improve outcomes in a rat glioma model. J Control Release 169:103–111

Bioley G, Bussat P, Lassus A, Schneider M, Terrettaz J, Corthesy B (2012a) The phagocytosis of gas-filled microbubbles by human and murine antigen-presenting cells. Biomaterials 33:333–342

Bioley G, Lassus A, Bussat P, Terrettaz J, Tranquart F, Corthesy B (2012b) Gas-filled microbubble-mediated delivery of antigen and the induction of immune responses. Biomaterials 33:5935–5946

Bioley G, Zehn D, Lassus A, Terrettaz J, Tranquart F, Corthesy B (2013) The effect of vaccines based on ovalbumin coupled to gas-filled microbubbles for reducing infection by ovalbumin-expressing Listeria monocytogenes. Biomaterials 34:5423–5430

Bohmer MR, Chlon CH, Raju BI, Chin CT, Shevchenko T, Klibanov AL (2010) Focused ultrasound and microbubbles for enhanced extravasation. J Control Release 148:18–24

Burke CW, Suk JS, Kim AJ, Hsiang YH, Klibanov AL, Hanes J, Price RJ (2012) Markedly enhanced skeletal muscle transfection achieved by the ultrasound-targeted delivery of non-viral gene nanocarriers with microbubbles. J Control Release 162:414–421

Chai R, Chen S, Ding J, Grayburn PA (2009) Efficient, glucose responsive and islet-specific transgene expression by a modified rat insulin promoter. Gene Ther 16:1202–1209

Chen S, Ding JH, Bekeredjian R, Yang BZ, Shohet RV, Johnston SA, Hohmeier HE, Newgard CB, Grayburn PA (2006) Efficient gene delivery to pancreatic islets with ultrasonic microbubble destruction technology. Proc Natl Acad Sci U S A 103:8469–8474

Chen S, Ding J, Yu C, Yang B, Wood DR, Grayburn PA (2007) Reversal of streptozotocin-induced diabetes in rats by gene therapy with betacellulin and pancreatic duodenal homeobox-1. Gene Ther 14:1102–1110

Chen S, Shimoda M, Chen J, Matsumoto S, Grayburn PA (2012) Transient overexpression of cyclin D2/CDK4/GLP1 genes induces proliferation and differentiation of adult pancreatic progenitors and mediates islet regeneration. Cell Cycle 11:695–705

Chen S, Bastarrachea RA, Roberts BJ, Voruganti VS, Frost PA, Nava-Gonzalez EJ, Arriaga-Cazares HE, Chen J, Huang P, DeFronzo RA, Comuzzie AG, Grayburn PA (2014) Successful beta cells islet regeneration in streptozotocin-induced diabetic baboons using ultrasound-targeted microbubble gene therapy with cyclinD2/CDK4/GLP1. Cell Cycle 13:1145–1151

Christiansen JP, French BA, Klibanov AL, Kaul S, Lindner JR (2003) Targeted tissue transfection with ultrasound destruction of plasmid-bearing cationic microbubbles. Ultrasound Med Biol 29:1759–1767

Dayton P, Klibanov A, Brandenburger G, Ferrara K (1999) Acoustic radiation force in vivo: a mechanism to assist targeting of microbubbles. Ultrasound Med Biol 25:1195–1201

De Cock I, Zagato E, Braeckmans K, Luan Y, de Jong N, De Smedt SC, Lentacker I (2015) Ultrasound and microbubble mediated drug delivery: acoustic pressure as determinant for uptake via membrane pores or endocytosis. J Control Release 197:20–28

Endo-Takahashi Y, Negishi Y, Kato Y, Suzuki R, Maruyama K, Aramaki Y (2012) Efficient siRNA delivery using novel siRNA-loaded Bubble liposomes and ultrasound. Int J Pharm 422:504–509

Endo-Takahashi Y, Negishi Y, Nakamura A, Suzuki D, Ukai S, Sugimoto K, Moriyasu F, Takagi N, Suzuki R, Maruyama K, Aramaki Y (2013) pDNA-loaded Bubble liposomes as potential ultrasound imaging and gene delivery agents. Biomaterials 34:2807–2813

Endo-Takahashi Y, Negishi Y, Nakamura A, Ukai S, Ooaku K, Oda Y, Sugimoto K, Moriyasu F, Takagi N, Suzuki R, Maruyama K, Aramaki Y (2014) Systemic delivery of miR-126 by miRNA-loaded Bubble liposomes for the treatment of hindlimb ischemia. Sci Rep 4:3883

Escoffre JM, Mannaris C, Geers B, Novell A, Lentacker I, Averkiou M, Bouakaz A (2013) Doxorubicin liposome-loaded microbubbles for contrast imaging and ultrasound-triggered drug delivery. IEEE Trans Ultrason Ferroelectr Freq Control 60:78–87

Gao Z, Kennedy AM, Christensen DA, Rapoport NY (2008) Drug-loaded nano/microbubbles for combining ultrasonography and targeted chemotherapy. Ultrasonics 48:260–270

Geers B, Lentacker I, Sanders NN, Demeester J, Meairs S, De Smedt SC (2011) Self-assembled liposome-loaded microbubbles: the missing link for safe and efficient ultrasound triggered drug-delivery. J Control Release 152:249–256

Gemzar (1996) Prescribing information: http://pi.lilly.com/us/gemzar.pdf. Accessed 10 Jan 2015

Greenleaf WJ, Bolander ME, Sarkar G, Goldring MB, Greenleaf JF (1998) Artificial cavitation nuclei significantly enhance acoustically induced cell transfection. Ultrasound Med Biol 24:587–595

Hatakeyama H, Murata M, Sato Y, Takahashi M, Minakawa N, Matsuda A, Harashima H (2014) The systemic administration of an anti-miRNA oligonucleotide encapsulated pH-sensitive liposome results in reduced level of hepatic microRNA-122 in mice. J Control Release 173:43–50

Hu Y, Wan JM, Yu AC (2013) Membrane perforation and recovery dynamics in microbubble-mediated sonoporation. Ultrasound Med Biol 39:2393–2405

Hynynen K, McDannold N, Vykhodtseva N, Jolesz FA (2003) Non-invasive opening of BBB by focused ultrasound. Acta Neurochir Suppl 86:555–558

Hynynen K, McDannold N, Sheikov NA, Jolesz FA, Vykhodtseva N (2005) Local and reversible blood-brain barrier disruption by noninvasive focused ultrasound at frequencies suitable for trans-skull sonications. Neuroimage 24:12–20

Hynynen K, McDannold N, Vykhodtseva N, Raymond S, Weissleder R, Jolesz FA, Sheikov N (2006) Focal disruption of the blood-brain barrier due to 260-kHz ultrasound bursts: a method for molecular imaging and targeted drug delivery. J Neurosurg 105:445–454

Javadi M, Pitt WG, Belnap DM, Tsosie NH, Hartley JM (2012) Encapsulating nanoemulsions inside eLiposomes for ultrasonic drug delivery. Langmuir 28:14720–14729

Javadi M, Pitt WG, Tracy CM, Barrow JR, Willardson BM, Hartley JM, Tsosie NH (2013) Ultrasonic gene and drug delivery using eLiposomes. J Control Release 167:92–100

Klibanov AL (2005) Ligand-carrying gas-filled microbubbles: ultrasound contrast agents for targeted molecular imaging. Bioconjug Chem 16:9–17

Klibanov AL, Shevchenko TI, Raju BI, Seip R, Chin CT (2010) Ultrasound-triggered release of materials entrapped in microbubble-liposome constructs: a tool for targeted drug delivery. J Control Release 148:13–17

Kodama T, Tomita N, Horie S, Sax N, Iwasaki H, Suzuki R, Maruyama K, Mori S, Manabu F (2010) Morphological study of acoustic liposomes using transmission electron microscopy. J Electron Microsc 59:187–196

Koebis M, Kiyatake T, Yamaura H, Nagano K, Higashihara M, Sonoo M, Hayashi Y, Negishi Y, Endo-Takahashi Y, Yanagihara D, Matsuda R, Takahashi MP, Nishino I, Ishiura S (2013) Ultrasound-enhanced delivery of morpholino with Bubble liposomes ameliorates the myotonia of myotonic dystrophy model mice. Sci Rep 3:2242

Kotopoulis S, Dimcevski G, Gilja OH, Hoem D, Postema M (2013) Treatment of human pancreatic cancer using combined ultrasound, microbubbles, and gemcitabine: a clinical case study. Med Phys 40:072902

Kurosaki T, Kawakami S, Higuchi Y, Suzuki R, Maruyama K, Sasaki H, Yamashita F, Hashida M (2014) Development of anionic bubble lipopolyplexes for efficient and safe gene transfection with ultrasound exposure in mice. J Control Release 176:24–34

Lammertink B, Deckers R, Storm G, Moonen C, Bos C (2014) Duration of ultrasound-mediated enhanced plasma membrane permeability. Int J Pharm 482(1–2):92–8

Lattin JR, Belnap DM, Pitt WG (2012a) Formation of eLiposomes as a drug delivery vehicle. Colloids Surf B Biointerfaces 89:93–100

Lattin JR, Pitt WG, Belnap DM, Husseini GA (2012b) Ultrasound-induced calcein release from eLiposomes. Ultrasound Med Biol 38:2163–2173

Lin CY, Javadi M, Belnap DM, Barrow JR, Pitt WG (2014) Ultrasound sensitive eLiposomes containing doxorubicin for drug targeting therapy. Nanomedicine 10:67–76

Marin A, Muniruzzaman M, Rapoport N (2001) Acoustic activation of drug delivery from polymeric micelles: effect of pulsed ultrasound. J Control Release 71:239–249

Matsumura Y, Maeda H (1986) A new concept for macromolecular therapeutics in cancer chemotherapy: mechanism of tumoritropic accumulation of proteins and the antitumor agent smancs. Cancer Res 46:6387–6392

McCreery TP, Sweitzer RH, Unger EC (2004) DNA delivery to cells in culture using ultrasound. Methods Mol Biol 245:287–292

Meijering BD, Juffermans LJ, van Wamel A, Henning RH, Zuhorn IS, Emmer M, Versteilen AM, Paulus WJ, van Gilst WH, Kooiman K, de Jong N, Musters RJ, Deelman LE, Kamp O (2009) Ultrasound and microbubble-targeted delivery of macromolecules is regulated by induction of endocytosis and pore formation. Circ Res 104:679–687

Mohan P, Rapoport N (2010) Doxorubicin as a molecular nanotheranostic agent: effect of doxorubicin encapsulation in micelles or nanoemulsions on the ultrasound-mediated intracellular delivery and nuclear trafficking. Mol Pharm 7:1959–1973

Muller OJ, Schinkel S, Kleinschmidt JA, Katus HA, Bekeredjian R (2008) Augmentation of AAV-mediated cardiac gene transfer after systemic administration in adult rats. Gene Ther 15:1558–1565

Nance E, Timbie K, Miller GW, Song J, Louttit C, Klibanov AL, Shih TY, Swaminathan G, Tamargo RJ, Woodworth GF, Hanes J, Price RJ (2014a) Non-invasive delivery of stealth, brain-penetrating nanoparticles across the blood-brain barrier using MRI-guided focused ultrasound. J Control Release 189:123–132

Nance E, Zhang C, Shih TY, Xu Q, Schuster BS, Hanes J (2014b) Brain-penetrating nanoparticles improve

paclitaxel efficacy in malignant glioma following local administration. ACS Nano 8:10655–10664

Negishi Y, Endo Y, Fukuyama T, Suzuki R, Takizawa T, Omata D, Maruyama K, Aramaki Y (2008) Delivery of siRNA into the cytoplasm by liposomal bubbles and ultrasound. J Control Release 132:124–130

Negishi Y, Endo-Takahashi Y, Ishii K, Suzuki R, Oguri Y, Murakami T, Maruyama K, Aramaki Y (2011) Development of novel nucleic acid-loaded Bubble liposomes using cholesterol-conjugated siRNA. J Drug Target 19:830–836

Panje CM, Wang DS, Pysz MA, Paulmurugan R, Ren Y, Tranquart F, Tian L, Willmann JK (2012) Ultrasound-mediated gene delivery with cationic versus neutral microbubbles: effect of DNA and microbubble dose on in vivo transfection efficiency. Theranostics 2: 1078–1091

Phillips LC, Dhanaliwala AH, Klibanov AL, Hossack JA, Wamhoff BR (2011) Focused ultrasound-mediated drug delivery from microbubbles reduces drug dose necessary for therapeutic effect on neointima formation--brief report. Arterioscler Thromb Vasc Biol 31:2853–2855

Phillips LC, Klibanov AL, Wamhoff BR, Hossack JA (2012) Intravascular ultrasound detection and delivery of molecularly targeted microbubbles for gene delivery. IEEE Trans Ultrason Ferroelectr Freq Control 59:1596–1601

Price RJ, Skyba DM, Kaul S, Skalak TC (1998) Delivery of colloidal particles and red blood cells to tissue through microvessel ruptures created by targeted microbubble destruction with ultrasound. Circulation 98:1264–1267

Rapoport NY, Kennedy AM, Shea JE, Scaife CL, Nam KH (2009a) Controlled and targeted tumor chemotherapy by ultrasound-activated nanoemulsions/microbubbles. J Control Release 138:268–276

Rapoport NY, Nam KH, Gao Z, Kennedy A (2009b) Application of ultrasound for targeted nanotherapy of malignant tumors. Acoust Phys 55:594–601

Rapoport N, Nam KH, Gupta R, Gao Z, Mohan P, Payne A, Todd N, Liu X, Kim T, Shea J, Scaife C, Parker DL, Jeong EK, Kennedy AM (2011) Ultrasound-mediated tumor imaging and nanotherapy using drug loaded, block copolymer stabilized perfluorocarbon nanoemulsions. J Control Release 153:4–15

Raymond SB, Treat LH, Dewey JD, McDannold NJ, Hynynen K, Bacskai BJ (2008) Ultrasound enhanced delivery of molecular imaging and therapeutic agents in Alzheimer's disease mouse models. PLoS One 3:e2175

Rodallec M, Vilgrain V, Couvelard A, Rufat P, O'Toole D, Barrau V, Sauvanet A, Ruszniewski P, Menu Y (2006) Endocrine pancreatic tumours and helical CT: contrast enhancement is correlated with microvascular density, histoprognostic factors and survival. Pancreatology 6:77–85

Samiotaki G, Konofagou EE (2013) Dependence of the reversibility of focused- ultrasound-induced blood-brain barrier opening on pressure and pulse length in vivo. IEEE Trans Ultrason Ferroelectr Freq Control 60:2257–2265

Sheikov N, McDannold N, Vykhodtseva N, Jolesz F, Hynynen K (2004) Cellular mechanisms of the blood-brain barrier opening induced by ultrasound in presence of microbubbles. Ultrasound Med Biol 30: 979–989

Shiraishi K, Endoh R, Furuhata H, Nishihara M, Suzuki R, Maruyama K, Oda Y, Jo J, Tabata Y, Yamamoto J, Yokoyama M (2011) A facile preparation method of a PFC-containing nano-sized emulsion for theranostics of solid tumors. Int J Pharm 421:379–387

Sirsi SR, Hernandez SL, Zielinski L, Blomback H, Koubaa A, Synder M, Homma S, Kandel JJ, Yamashiro DJ, Borden MA (2012) Polyplex-microbubble hybrids for ultrasound-guided plasmid DNA delivery to solid tumors. J Control Release 157(2):224–234. doi:10.1016/j.jconrel.2011.09.071

Skyba DM, Price RJ, Linka AZ, Skalak TC, Kaul S (1998) Direct in vivo visualization of intravascular destruction of microbubbles by ultrasound and its local effects on tissue. Circulation 98:290–293

Suzuki R, Takizawa T, Negishi Y, Hagisawa K, Tanaka K, Sawamura K, Utoguchi N, Nishioka T, Maruyama K (2007) Gene delivery by combination of novel liposomal bubbles with perfluoropropane and ultrasound. J Control Release 117:130–136

Suzuki R, Takizawa T, Negishi Y, Utoguchi N, Sawamura K, Tanaka K, Namai E, Oda Y, Matsumura Y, Maruyama K (2008) Tumor specific ultrasound enhanced gene transfer in vivo with novel liposomal bubbles. J Control Release 125:137–144

Tartis MS, McCallan J, Lum AF, LaBell R, Stieger SM, Matsunaga TO, Ferrara KW (2006) Therapeutic effects of paclitaxel-containing ultrasound contrast agents. Ultrasound Med Biol 32:1771–1780

Taylor SL, Rahim AA, Bush NL, Bamber JC, Porter CD (2007) Targeted retroviral gene delivery using ultrasound. J Gene Med 9:77–87

Tlaxca JL, Anderson CR, Klibanov AL, Lowrey B, Hossack JA, Alexander JS, Lawrence MB, Rychak JJ (2010) Analysis of in vitro transfection by sonoporation using cationic and neutral microbubbles. Ultrasound Med Biol 36:1907–1918

Tlaxca JL, Rychak JJ, Ernst PB, Konkalmatt PR, Shevchenko TI, Pizarro TT, Rivera-Nieves J, Klibanov AL, Lawrence MB (2013) Ultrasound-based molecular imaging and specific gene delivery to mesenteric vasculature by endothelial adhesion molecule targeted microbubbles in a mouse model of Crohn's disease. J Control Release 165:216–225

Treat LH, McDannold N, Zhang Y, Vykhodtseva N, Hynynen K (2012) Improved anti-tumor effect of liposomal doxorubicin after targeted blood-brain barrier disruption by MRI-guided focused ultrasound in rat glioma. Ultrasound Med Biol 38:1716–1725

Un K, Kawakami S, Suzuki R, Maruyama K, Yamashita F, Hashida M (2010a) Development of an ultrasound-responsive and mannose-modified gene carrier for DNA vaccine therapy. Biomaterials 31:7813–7826

Un K, Kawakami S, Suzuki R, Maruyama K, Yamashita F, Hashida M (2010b) Enhanced transfection efficiency into macrophages and dendritic cells by a combination method

using mannosylated lipoplexes and bubble liposomes with ultrasound exposure. Hum Gene Ther 21:65–74

Un K, Kawakami S, Suzuki R, Maruyama K, Yamashita F, Hashida M (2011) Suppression of melanoma growth and metastasis by DNA vaccination using an ultrasound-responsive and mannose-modified gene carrier. Mol Pharm 8:543–554

Un K, Kawakami S, Yoshida M, Higuchi Y, Suzuki R, Maruyama K, Yamashita F, Hashida M (2012) Efficient suppression of murine intracellular adhesion molecule-1 using ultrasound-responsive and mannose-modified lipoplexes inhibits acute hepatic inflammation. Hepatology 56:259–269

Unger EC, McCreery TP, Sweitzer RH (1997) Ultrasound enhances gene expression of liposomal transfection. Invest Radiol 32:723–727

Unger EC, McCreery TP, Sweitzer RH, Caldwell VE, Wu Y (1998) Acoustically active lipospheres containing paclitaxel: a new therapeutic ultrasound contrast agent. Invest Radiol 33:886–892

Vandenbroucke RE, Lentacker I, Demeester J, De Smedt SC, Sanders NN (2008) Ultrasound assisted siRNA delivery using PEG-siPlex loaded microbubbles. J Control Release 126:265–273

Villanueva FS, Jankowski RJ, Klibanov S, Pina ML, Alber SM, Watkins SC, Brandenburger GH, Wagner WR (1998) Microbubbles targeted to intercellular adhesion molecule-1 bind to activated coronary artery endothelial cells. Circulation 98:1–5

Wang DS, Panje C, Pysz MA, Paulmurugan R, Rosenberg J, Gambhir SS, Schneider M, Willmann JK (2012) Cationic versus neutral microbubbles for ultrasound-mediated gene delivery in cancer. Radiology 264: 721–732

Wible JH Jr, Galen KP, Wojdyla JK, Hughes MS, Klibanov AL, Brandenburger GH (2002) Microbubbles induce renal hemorrhage when exposed to diagnostic ultrasound in anesthetized rats. Ultrasound Med Biol 28: 1535–1546

Yan F, Li L, Deng Z, Jin Q, Chen J, Yang W, Yeh CK, Wu J, Shandas R, Liu X, Zheng H (2013) Paclitaxel-liposome-microbubble complexes as ultrasound-triggered therapeutic drug delivery carriers. J Control Release 166:246–255

Yang D, Gao YH, Tan KB, Zuo ZX, Yang WX, Hua X, Li PJ, Zhang Y, Wang G (2013) Inhibition of hepatic fibrosis with artificial microRNA using ultrasound and cationic liposome-bearing microbubbles. Gene Ther 20:1140–1148

Yuan F, Dellian M, Fukumura D, Leunig M, Berk DA, Torchilin VP, Jain RK (1995) Vascular permeability in a human tumor xenograft: molecular size dependence and cutoff size. Cancer Res 55:3752–3756

Zhang K, Chen H, Li F, Wang Q, Zheng S, Xu H, Ma M, Jia X, Chen Y, Mou J, Wang X, Shi J (2014) A continuous tri-phase transition effect for HIFU-mediated intravenous drug delivery. Biomaterials 35: 5875–5885

Drug-Loaded Perfluorocarbon Nanodroplets for Ultrasound-Mediated Drug Delivery

13

Natalya Rapoport

Abstract

The interaction of nanoparticles with directed energy is a novel application in targeted drug delivery. This chapter focuses on perfluorocarbon nanoemulsions, whose action in drug delivery depends on the ultrasound-triggered phase shift from liquid to gaseous state. These nanoemulsions have great potential for unloading encapsulated drugs at a desired time and location in the body in response to directed ultrasound. In addition, they actively alter their nano-environment for enhancing drug transport through various biological barriers to sites of action, which significantly enhances therapeutic outcome.

Keywords

Perfluorocarbon nanodroplet • Ultrasound • Drug delivery

13.1 Introduction

Chemotherapy remains the treatment choice for many types of cancer. However, the dream of a "magic bullet" that exclusively targets tumors while avoiding normal tissues has remained elusive and inspired extensive research. During the last decade, progress in nanomedicine has enabled tumor-targeted delivery of anticancer drugs, which has decreased side effects and increased drug concentration in tumor tissue. Advances in nanotechnology have allowed combining various functionalities in molecular or supramolecular constructs, *i.e.* nanoparticles. The family of nanoparticles includes polymeric micelles, liposomes, nano- or microemulsion droplets, polymerosomes, hollow particles, *etc.* Various chemotherapeutic drugs, imaging agents and targeting moieties may be encapsulated in the same nanocontainer. Drug encapsulation in nanocarriers has a number of additional advantages. First, it may dramatically increase the effective aqueous solubility of highly potent compounds formerly abandoned due to low solubility. Encapsulation also prevents drug

N. Rapoport
Department of Bioengineering, University of Utah,
36 South Wasatch Drive, Room, 3100,
Salt Lake City, UT 84112, USA
e-mail: natasha.rapoport@utah.edu

© Springer International Publishing Switzerland 2016

J.-M. Escoffre, A. Bouakaz (eds.), *Therapeutic Ultrasound*, Advances in Experimental Medicine and Biology, Vol. 880, DOI 10.1007/978-3-319-22536-4_13

degradation resulting from body fluid action, reduces side effects and allows drug transport towards desired targets. However, after encapsulated drug reaches its site of action, it should be released from carrier. This can be achieved by developing stimuli responsive drug carriers. After tumor accumulation, local release of an encapsulated drug into tumor tissue may be triggered by various internal (*i.e.* pH, hypoxia, enzymatic degradation) or external physical stimuli, *e.g.* ultrasound or light (Rapoport 2007). The application of ultrasound for targeted drug delivery is discussed below, with special emphasis on the role of triggered phase-shift transition inside injected nanoparticles.

Ultrasound has a number of advantages when compared with other physical methods used in tumor therapy. Ultrasound is the most cost effective and accessible, and does not use ionizing radiation. Ultrasound can be directed toward deeply located body sites, and tumor sonication with millimeter precision is feasible. Sonication may be performed non-invasively or minimally invasively through intraluminal, laparoscopic or percutaneous means. For extracorporeal sonication, the transducer is placed in contact with a water-based gel or a water layer on the skin, and no insertion or surgery is required. Ultrasound has both thermal (*i.e.* local heating of tissue to hyperthermia or ablative temperatures) and non-thermal mechanisms (*i.e.* cavitation and radiation force). These mechanisms are expected to work synergistically to trigger drug release from carrier, increase extravasation and internalization of carrier and drug, and increase drug diffusion in tumor tissue, which ultimately results in enhanced treatment outcome. Moreover, development of real-time imaging methods, such as magnetic resonance imaging (MRI) or ultrasound imaging, allows precise spatiotemporal control of focused ultrasound (FUS)-mediated drug delivery. Indeed, imaging assists in identification of the target, guidance of ultrasound action and evaluation of therapeutic efficacy. In addition, real-time temperature measurements during treatment using MRI thermometry provide data that can be used in a feedback controller to enable greater control of the energy delivery. Ultrasound has been widely used for decades as an imaging modality. During the last two decades therapeutic application of ultrasound has evolved with the development of tumor ablation technique (Lubner et al. 2010; Manthe et al. 2010; McWilliams et al. 2010).

Tumors are usually highly heterogeneous formations, with necrotic cores and perfused shells. While the heat-induced ablation of a core is relatively effective, that of a shell is problematic since circulating blood carries the heat away. However, enhanced perfusion that hampers ablation favors drug delivery to the tumor periphery, which is an area of active tumor growth. As shown below, at non-ablative energies, ultrasound can enhance tumor-directed drug delivery and overall therapeutic response.

Tumor tissue is characterized by poorly organized vascular architecture, irregular blood flow and reduced lymphatic drainage. Leaky blood vessels and the lack of a lymphatic system result in an increased interstitial fluid pressure, which hinders convectional transport of drug carriers across blood vessel walls. Still, nanoparticles of appropriate size accumulate in tumor tissue via the enhanced permeability and retention (EPR) effect (Iyer et al. 2006) based on defective tumor microvasculature. A characteristic pore cutoff size range between 380 and 780 nm has been shown in a variety of tumors; although in some tumors the size may increase up to 2 μm. This allows extravasation of drug-loaded nanoparticles through large inter-endothelial gaps (Campbell 2006; Hobbs et al. 1998; Iyer et al. 2006), while the poor lymphatic drainage of tumors results in longer retention of extravasated particles in tumor tissue. In contrast to tumors, blood vessels in normal tissues have tight inter-endothelial junctions, which do not allow extravasation of nanoparticles (Fig. 13.1). Effective tumor accumulation of nanoparticles via the EPR effect requires sufficient particle residence time in circulation; to provide for this, nanoparticles are commonly coated with poly(ethylene oxide) chains that decrease blood protein adsorption and particle recognition by the cells of the reticuloendothelial system.

Ultrasound as a component of a drug delivery system may be coupled with a variety of drug

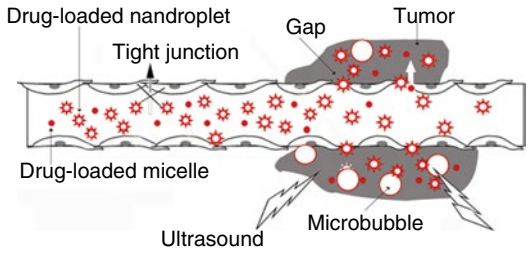

Fig. 13.1 Schematic representation of the EPR effect. Nanoparticles cannot cross tight junctions in normal tissues, but extravasate into tumor tissue through large inter-endothelial gaps in the defective tumor microvasculature

carriers. An ideal drug carrier for ultrasound-mediated drug delivery should satisfy a number of requirements: stability in circulation; drug retention until activated; size that allows extravasation through defective tumor vasculature; ultrasound responsiveness.

13.2 Ultrasound Effects in Drug Delivery: Anticipated Mechanisms

Several mechanisms of ultrasound action in drug delivery have been discussed (Dalecki 2004; Deckers and Moonen 2010; Ferrara 2008; Frulio et al. 2010; Miller et al. 1996; Rapoport et al. 2009a, b, Rapoport et al. 2011, 2013); both ultrasound-triggered localized drug release from carriers and effects of ultrasound on biological tissue should be considered.

13.2.1 Thermal Effects

Ultrasound produces localized tissue heating. Tissue heating depends on the tissue absorption of energy and rates of thermal diffusion and convection. Absorption of ultrasound energy is frequency dependent and increases monotonically with frequency. Even a moderate temperature increase may have serious biological consequences, *e.g.* significantly increase permeability of blood capillaries (Dreher et al. 2006; Kong et al. 2000b, 2001) and/or lead to cell membrane fluidization (Hayat and Friedberg 1986; Krupka et al. 2009). Thermal effects of ultrasound have been used with temperature-sensitive liposomes that rapidly release their contents at physiologically tolerated tissue temperatures (Dewhirst et al. 2005; Gaber et al. 1996; Hauck et al. 2006; Kong et al. 2000a, b; Kong and Dewhirst 1999; Needham et al. 2000; Negussie et al. 2011; Vujaskovic et al. 2010; Yarmolenko et al. 2010). Heating produces a gel-to-fluid phase transition in the phospholipid membrane that enhances release and diffusion of drug in the target region. Doxorubicin-loaded liposomes have been commercialized (ThermoDox®, Celsion Corp.) and are undergoing clinical trials in combination with radiofrequency (RF) thermal ablation (Hauck et al. 2006; Poon and Borys 2009). Ultrasound as a heating modality has also been studied for release of drugs from loaded liposomes, and other similar temperature-sensitive liposomes (Deckers and Moonen 2010; Dromi et al. 2007; Negussie et al. 2011; Staruch et al. 2011; Stone et al. 2007).

13.2.2 Mechanical Action of Ultrasound: Cavitation

Cavitation phenomena may exert substantial effects on biological tissues and drug carriers. Cavitation can be enhanced by the introduction of gas-filled microbubbles. In current clinical practice, microbubbles have been used as ultrasound contrast agents for cardiovascular imaging (Becher and Burns 2000; Becher et al. 2005) and for molecular imaging (Klibanov 2007). During the last decade, microbubbles have attracted attention as drug carriers and enhancers of drug and gene delivery (See Chap. 11). In the ultrasound field, microbubbles grow and collapse in a process of inertial cavitation. Inertial cavitation of microbubbles creates microjets and shock waves that can create holes in blood vessels and cell membranes (sonoporation), thus increasing permeability of biological barriers for drugs, genes and their carriers (see Chaps. 9 and 10). At ultrasound energies that don't induce inertial cavitation, microbubbles stably oscillate in the ultrasound field. Stable cavitation of systemically injected microbubbles can induce alternating

invagination and distention of blood vessel walls, which in turn can damage the endothelial lining and temporarily increase blood vessel permeability (Chen et al. 2010; Chen et al. 2011; Gaitan et al. 2010; Matula and Guan 2011). For blood vessels that are large in comparison to microbubble sizes, invagination appears to be a major vessel damaging factor; for small blood capillaries, both invagination and distension results in endothelial damage and increased permeability (Chen et al. 2011).

Several research groups have concentrated their efforts on developing microbubble-based drug delivery systems (see Chaps. 11 and 12). Microbubble cavitation has been used for enhancing drug delivery from liposomes (Frulio et al. 2010; Hernot and Klibanov 2008; Klibanov et al. 2010). The efficient therapeutic action of microbubbles combined with low duty cycle ultrasound on subcutaneously grown glioma xenografts was reported (Burke et al. 2011).

Microbubble cavitation was successfully used for opening the blood–brain barrier to allow effective delivery of drugs to the brain (see Chap. 16). Drug-loaded microbubbles have also been developed for targeting intravascular targets (see Chaps. 18 and 19), and tissue plasminogen activator (tPA)-loaded microbubbles combined with ultrasound have been developed for thrombolysis (Hitchcock and Holland 2010; Hitchcock et al. 2011; Laing et al. 2011; Shaw et al. 2009; Smith et al. 2010; Sutton et al. 2013a, b). The biological effects of microbubbles are based on the enhanced penetration of various nanoscaled particles or drugs through biological barriers (Mohan and Rapoport 2010; Thakkar et al. 2013).

13.2.3 Mechanical Action of Ultrasound in the Absence of Cavitation

The most frequently discussed non-thermal and non-cavitation mechanism of ultrasound is related to acoustic streaming and ultrasound radiation force. Sound propagating through a medium produces a force upon the medium (acoustic streaming) and the particles suspended in the medium (radiation force) (Dayton et al. 1999, 2006). Acoustic streaming and radiation force each produce particle translation in the acoustic field, and their effects may be combined. It was demonstrated that acoustic streaming and/or radiation force present a means to localize and concentrate particles near a vessel wall, which may assist the delivery of targeted agents. The radiation force pulses can bring a drug carrier into proximity to a cell, which would facilitate adhesion of the carrier or its fragments to cell membranes (Shortencarier et al. 2004). This would be especially effective for enhancing active targeting that is based on ligand/receptor interaction. Actively targeted acoustically active lipospheres were used to deliver paclitaxel (PTX) to HUVEC cells overexpressing $\alpha_v\beta_3$-integrins (Tartis et al. 2006). Circulating drug-loaded particles were first deflected by radiation force to a vessel wall and were subsequently fragmented by stronger pulses (Dayton et al. 1999). A similar strategy was used for enhancing the cellular interaction of targeted lipid-coated perfluorooctylbromide (PFOB) nanoparticles with melanoma cells (Soman et al. 2006). The authors hypothesized that the ultrasound facilitated drug transport from the perfluorocarbon nanoparticles into cells due to direct cell/nanoparticle interaction that stimulated lipid exchange and drug delivery. Acoustic streaming appears to dominate in large blood vessels (with hundreds micrometers per second for particle displacement), while radiation force is expected to dominate in the microvasculature because acoustic streaming decreases with decreasing vessel diameter (Dayton et al. 2006). Acoustic streaming and radiation force can push nanoparticles through blood capillary walls, thus enhancing extravasation of drug carriers or macromolecular drugs (Dayton et al. 1999, 2006; Ferrara 2008; Holland and McPherson 2009; Stieger et al. 2007; Thakkar et al. 2013).

In addition to cavitation, non-cavitation mechanisms may be effective for microbubble action. For perfluorocarbon microbubbles, the mismatch between acoustic impedances of water or tissue (1.4 MRayl) and perfluorocarbon (approx. 0.3 MRayl) may promote generation of shear stresses. This in turn would increase

inter-endothelial gaps and extra-cellular spaces, resulting in increased extravasation and diffusion of drug carriers and drugs in sonicated tissues (Frenkel et al. 2000a, b, 2006; Hancock et al. 2009a, b; O'Neill et al. 2009; Yuh et al. 2005). In an interesting novel application, ultrasound radiation force was used to modulate ligand exposure on the surface of actively targeted contrast agents (Lum et al. 2006).

Ultrasound-triggered localized drug release may be activated using carriers that are sensitive to either mechanical factors, thermal factors, or both (Borden et al. 2005, 2008; Dayton et al. 2006; Ferrara et al. 2007; Ferrara 2008; Gao et al. 2004; Kheirolomoom et al. 2007, 2010; O'Neill and Rapoport 2011; Qin et al. 2009; Rapoport 2012a, b; Schroeder et al. 2007; Schroeder et al. 2009; Unger et al. 2004; Wheatley et al. 2006; Zheng et al. 2008). Ultimately, the combined thermal and mechanical actions of ultrasound on drug carriers and biological tissues enhance perfusion, increase extravasation of drug carriers and drugs, and facilitate drug penetration through other biological barriers. Consequently, this enhances drug diffusion throughout tumor tissue, resulting in significantly enhanced therapeutic efficacy of conventional drugs (see below) (McDannold et al. 2008; McDannold et al. 2006; Rapoport et al. 2009b, 2010b, 2011; Treat et al. 2007; Vykhodtseva et al. 2006, 2008).

The most straightforward and cost-effective way to develop microbubble-based drug delivery systems would be to load drugs into the FDA approved ultrasound contrast agents, such as Optison® (Amersham Inc.) or Definity® (Lanteus Medical Imaging Inc.). While this approach may be very beneficial for targeting intravascular targets, currently used ultrasound contrast agents present a number of inherent problems as interstitial-targeted drug carriers. A very short circulation time (minutes) of commercially available microbubbles, and their large size (2–10 microns), do not allow effective extravasation into tumor tissue, thus preventing effective drug targeting. This problem may be solved by developing nanoscaled phase-shift microbubble precursors, which convert into microbubbles under ultrasound action as discussed below.

13.3 Phase-shift Perfluorocarbon Nanoemulsions as Drug Carriers for Ultrasound-mediated Drug Delivery

As mentioned above, microbubbles as drug carriers present inherent problems for interstitial delivery to tumors. To solve this problem, drug-loaded nanoscaled microbubble precursors that accumulate in tumors via passive or active targeting, which then convert into microbubble *in-situ* under the action of ultrasound have been developed. The microbubble precursors are perfluorocarbon (PFC) nanoemulsions.

13.3.1 Generation of Perfluorocarbon Nanoemulsions

13.3.1.1 General Approach

Perfluorocarbon micro- and nanodroplets are manufactured by emulsification of a water/surfactant/perfluorocarbon mixture. Various surfactants, perfluorocarbons and emulsification means have been explored. In the works by Fowlkes's group, dodecafluoropentane (also called perfluoropentane, PFP) was used as a droplet core, with albumin used as a droplet shell; emulsification was performed in a high-speed shaker (Kripfgans et al. 2000). PFP mixtures with a higher boiling temperature than PFC were used by the Ferrara group, with a lipid mixture used for droplet stabilization (Dayton et al. 2006). For preparing polymer-coated perfluorooctyl bromide (PFOB) "nanocapsules", a poly(lactic-glycolic acid) copolymer was co-dissolved with PFOB in an organic solvent. The mixture was then pre-emulsified in a high-speed shaker and additionally emulsified by ultrasound; organic solvent was removed by evaporation (Reznik et al. 2011). Acoustic characterization of these nanodroplets suggested that vaporization may be induced by diagnostic 7.5 MHz ultrasound at a mechanical index in the diagnostic range (MI<1) (Reznik et al. 2011). In order to decrease droplet sizes, crude emulsions are usually additionally processed through a microfluidizer (Reznik et al. 2014). For delivering

water soluble compounds (fluorescein or thrombin), a double emulsion technique has been developed (Fabiilli et al. 2010b).

A new approach for the generation of highly acoustically active perfluorocarbon droplets was recently suggested (Matsunaga et al. 2012; Sheeran et al. 2011). The authors formulated nanodroplets from highly volatile decafluorobutane (DFB) (boiling point about −2 °C). Nanodroplets were stable at physiological temperatures, but were activated by ultrasound *in-vivo* using pressures within the FDA guidelines for diagnostic imaging (Matsunaga et al. 2012). A different approach to generation of drug-loaded PFC nanodroplets was suggested in the works by Rapoport's group. Here, drug-loaded polymeric micelles were used as a starting point for generating nanoemulsions (Gao et al. 2008; Rapoport et al. 2010a; Rapoport et al. 2007, Rapoport et al. 2009a, b, 2007, 2010b, 2011). Manufacture simplicity, absence of toxic solvents and increased drug loading capacity are attractive features of this technology. In addition, amphiphilic block copolymer micelles (if they are preserved in a formulation) may exert extremely important biological effects by preventing development of drug resistance (Alakhov et al. 1996; Alakhova et al. 2010; Batrakova et al. 1999, 2001, 2003).

13.3.1.2 Polymeric Micelles as a Starting Point for Generation of Drug-loaded PFC Nanodroplets

Polymeric micelles are formed by self-assembly of individual amphiphilic block copolymer molecules (unimers) in aqueous milieu. Hydrophobic blocks form micelle cores, while hydrophilic blocks (usually PEG) form micelle corona (or shells). PEG shells are important for suppression of nanodroplet uptake by reticuloendothelial system cells. Lipophilic drugs are solubilized in micelle cores. Many different polymeric micelle systems have been designed. The application of biodegradable, pH-sensitive micelles, like those of poly(ethylene oxide)-co-poly(D,L-lactide) (PEG-PDLA) or poly(ethylene oxide)-co-poly(caprolactone) (PEG-PCL), are especially appealing. When internalized by tumor cells via endocytosis, the micelles move to the acidic environment of endosomes and lysosomes, where their hydrolysis at low pH results in drug release. The amphiphilic character of block copolymer micelles, their size (between 20 nm and about 100 nm) and surface properties provide a relatively high drug loading capacity and long circulation time in the vascular system, which is important for effective tumor targeting. However, micelles manifest substantial shortcomings as drug carriers. Micelle formation is thermodynamically driven, meaning micelles dissociate into unimers when copolymer concentration drops below a critical value called the critical micelle concentration (CMC). Systemic injections of micellar formulations are associated with substantial dilutions in the circulatory system. This may result in a premature drug release into circulation before the drug reaches its target, which has presumably occurred in clinical trials. Polymeric micelles as drug carriers are either too unstable, thus prematurely releasing their drug load, or on the contrary too stable, therefore incapable of providing adequate drug release at the tumor site.

A feasible approach to overcoming these complications consists in developing stable micellar systems that could be activated using external triggers (*e.g.* ultrasound), inducing drug release at a desired body location (Rapoport 2007). This may be done via introduction of some oil, *e.g.* a PFC compound. At a suitable PFC/copolymer ratio, PFC nanodroplets are formed. Nanodroplets are much more stable against dilution than micelles, and have other important advantages for ultrasound-mediated drug delivery (see below). To produce nanodroplets, a PFC compound was introduced into a micellar solution formed by an amphiphilic block copolymer (*i.e.* poly(ethylene oxide)-co-poly(L-lactide) (PEG-PLLA), poly(ethylene oxide)-co-poly(D,L-lactide) (PEG-PDLA), or poly(ethylene oxide-co-polycaprolactone (PEG-PCL). The mixture was emulsified on ice under low-frequency ultrasound. A chemotherapeutic drug (Doxorubicin (DOX) or paclitaxel (PTX)) was pre-introduced into a micellar solution (Gao et al. 2008; Rapoport et al. 2007, 2009b, 2011).

Perfluorocarbon compounds tested were PFP or perfluoro-15-crown-5-ether (PFCE), however any PFC compound or their mixture may be emulsified this way. PFCE generates more stable and easy to handle nanoemulsions than PFP; in addition, it offers a possibility of monitoring *in-vivo* nanodroplet biodistribution using ^{19}F-MRI since twenty equivalent fluorine nuclei in a PFCE molecule generate a sharp peak in MR spectra. A phase state of perfluorocarbon/copolymer formulations depends on the PFC/copolymer concentration ratio as shown schematically in (Fig. 13.2) (Gao et al. 2008). At low concentration, PFC is dissolved in micelle cores (zone 1, Fig. 13.2). When the PFC concentration exceeds a limit of solubility in micelle cores, nanodroplets evolve into a separate phase. In this process, former micelle cores turn into droplet shells.

A nanodroplet shell contains two layers: the inner layer, formed by a hydrophobic block of a block copolymer (*e.g.* polylactide or polycaprolactone), and the outer layer, formed by a hydrophilic block, usually PEG, as shown schematically in Fig. 13.3a. A lipophilic drug initially encapsulated in micelle cores moves with the hydrophobic block into the inner layer of a droplet shell, as exemplified by the laser confocal imaging of DOX encapsulating droplets (Fig. 13.3b).

In some ranges of PFC/copolymer concentration ratios, micelles coexist with nanodroplets (zone 2, Fig. 13.2). As PFC concentration increases, all block copolymer is used for droplet stabilization and micelles disappear; only droplets are observed in zone 3. The droplet size in PFC nanoemulsions ranges from 200 to 750 nm depending on the type of the stabilizing copolymer, perfluorocarbon-to-copolymer concentration ratio and emulsification conditions (Gao et al. 2008). An example of a size distribution diagram for a 1 %PFCE/5 %PEG-PDLA formulation is presented in Fig. 13.4, revealing coexisting micelles and nanodroplets (corresponding to zone 2 of the phase diagram).

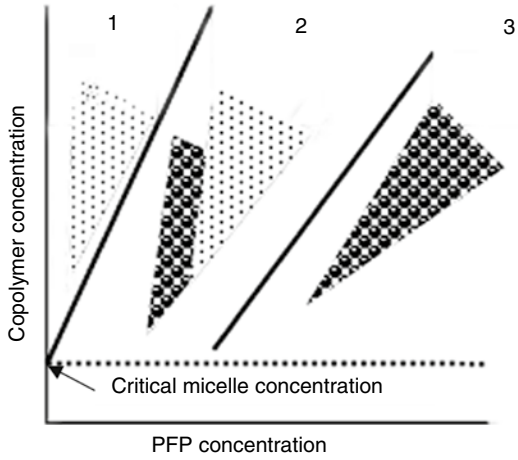

Fig. 13.2 Schematic representation of the phase diagram of a perfluorocarbon/block copolymer formulation in aqueous solution (Reprinted with permission from (Gao et al. 2008))

13.3.2 Droplet-to-bubble Phase Transition in PFP Nanoemulsions

Starting with a pioneering work by Apfel, it was shown that perfluorocarbon droplets can convert into microbubbles under ultrasound irradiation

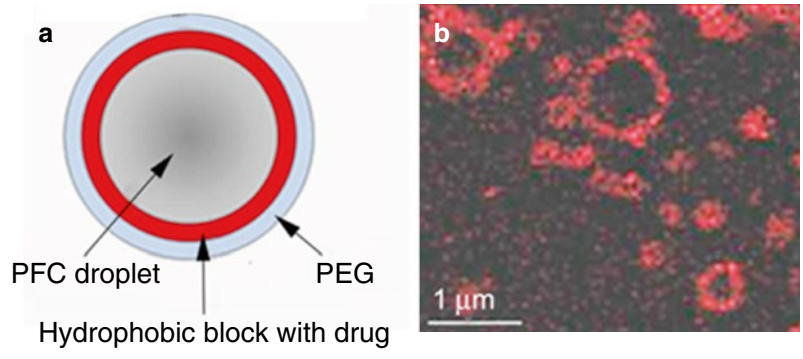

Fig. 13.3 Schematic representation of a drug-loaded nanodroplet (**a**) and laser confocal image of DOX-loaded PFP/PEG-PLLA droplets; scale bar 1 µm (**b**); micron-sized droplets were produced to better visualize drug location on the droplet surface

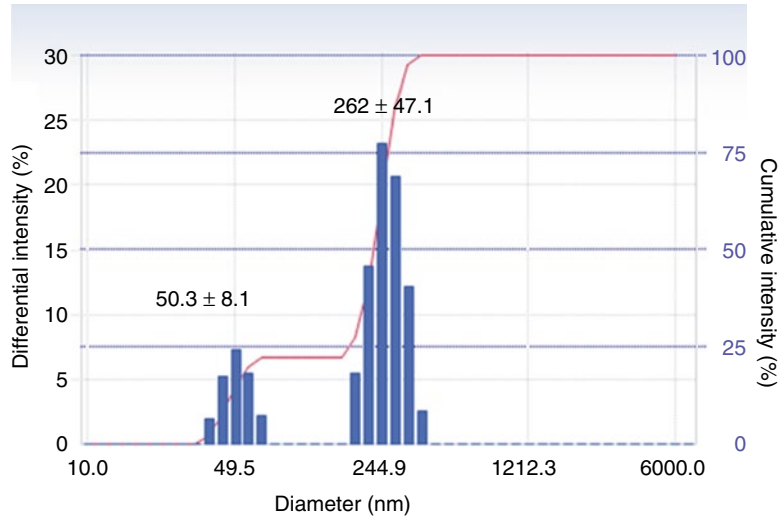

Fig. 13.4 Particle size distribution in a 1 % PECE/5 % PEG-PDLA formulation (zone 2 of the phase diagram, see Fig. 14.2); left peak – PEG-PDLA micelles with dissolved PFP; right peak – PFCE nanodroplets. Only one (nanodroplets) peak would be observed in zone 3 (*i.e.* at higher PFP concentrations). Particle sizes in all zones depend on PFCE and PEG-PDLA concentrations and concentration ratios (Reprinted with permission from (Rapoport et al. 2013))

(Apfel 1998). This effect, called acoustic droplet vaporization (ADV), has been thoroughly investigated by the Fowlkes group (Fabiilli et al. 2009, 2010a, b; Kripfgans et al. 2000, 2002, 2004, 2005; Lo et al. 2006, 2007; Miller et al. 2000; Wong et al. 2011; Zhang et al. 2010), the De Jong and Versluis groups (Chen et al. 2013; Faez et al. 2013; Kokhuis et al. 2013; Kooiman et al. 2014; Maresca et al. 2013; Reznik et al. 2013, 2014; Segers and Versluis 2014; Shpak et al. 2013, 2014; Ten Kate et al. 2013; Thomas et al. 2013) and Rapoport group (Gao et al. 2008; Nam et al. 2009; O'Neill and Rapoport 2011; Rapoport et al. 2009a, b, 2010a, 2012a). In medical applications, acoustic droplet vaporization was tested for temporal and spatial control of tissue occlusion (Kripfgans et al. 2002; Kripfgans et al. 2005; Zhang et al. 2010), as well as for cavitation nucleation agents for non-thermal ultrasound therapy (Miller et al. 2000; Miller and Song 2002), for enhancing gene transfer, for phase aberration correction (Kripfgans et al. 2002) and for the ultrasound-enhanced drug delivery; for reviews on the latter application, see (Rapoport 2012a, b).

13.3.2.1 Vaporization of the PFP Droplets: Mechanism and Therapeutic Applications

It was found that micrometer-sized albumin-coated PFP droplets vaporized into gas bubbles with the application of short tone bursts in the diagnostic frequency range of 1.5–8 MHz (Kripfgans et al. 2000). The resulting bubbles were 20–80 μm in diameter. The threshold for vaporization decreased with increasing ultrasound frequency and sonication time, and in the presence of microbubbles as nucleation agents (Kripfgans et al. 2000; Lo et al. 2007). The vaporization threshold was higher for smaller droplets (Kripfgans et al. 2004). These experiments were complemented with the optical imaging of the droplet-to-bubble transition using the ultra-high speed imaging camera (Wong et al. 2011).

Physico-chemical aspects of the PFP droplet vaporization were discussed by Rapoport et al. (2009a, b, 2010a). PFP has a boiling temperature of 29 °C at atmospheric pressure and therefore manifests high propensity for vaporization under heating. However, for small droplets stabilized by elastic copolymer shells, the Laplace pressure (*i.e.* the pressure difference between the inside and outside of a droplet) may substantially increase boiling temperature. This effect is caused by the surface tension at the interface between a droplet and a bulk liquid. The Laplace pressure is given by

$$\Delta P = P_{inside} - P_{outside} = \frac{2\sigma}{r} \qquad (13.1)$$

where P_{inside} is the pressure inside a droplet, P_{outside} is the pressure outside a droplet, σ is the surface tension and r is a droplet radius.

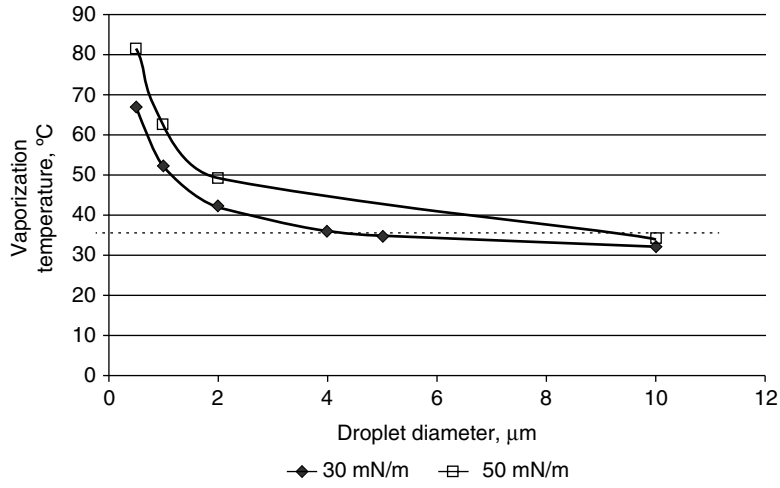

Fig. 13.5 Dependence of the PFP boiling temperature in nanodroplets on droplet size calculated for two characteristic values of interfacial energy, 30 and 50 mN/m (Reprinted with permission from (Rapoport et al. 2013))

Excessive pressure inside a droplet results in an increase in PFP boiling temperature. This phenomenon has important consequences for drug delivery. Laplace pressure is inversely proportional to droplet size according to Eq. 13.1, meaning smaller droplets have higher boiling temperatures than larger droplets. The surface tension at the PFP/water interface for "naked" (*i.e.* not surfactant-coated) PFP droplets is 56 ± 1 mN/m. Using the known parameters of the Antoine equation for the pressure dependence of PFP vaporization temperature (Barber and Cady 1956), the dependence of the PFP droplet vaporization temperature on droplet size was calculated for two values of the interfacial tension 30 and 50 mN/m, typical values for PEG-coated colloid particles (Alexandridis et al. 1994) (Fig. 13.5) (Rapoport et al. 2009a). As indicated by Fig. 13.5, PFP boiling temperature in droplets smaller than 4 µm is higher than physiological temperature. These droplets remain in the liquid state at physiological temperatures, while droplets larger than 4 µm vaporize. Therefore, droplets larger than 4 µm should be excluded from pharmaceutical PFP emulsion formulations as they would prematurely vaporize upon systemic injection. The fact that micron-sized droplets would not extravasate is equally important. Hence, in Rapoport's works, paclitaxel (PTX)-loaded PFP nanodroplets were prepared with the average size of 250–300 nm and relatively low polydispersity (see Fig. 13.4). These nanodroplets circulated as liquid nanodroplets and gradually extravasated into tumor tissue, upon which their conversion into microbubbles, which led to a localized drug release, was triggered by tumor-directed ultrasound.

Note of warning: Droplet-to-bubble transition upon injection of PFP nanoemulsion may be induced by shear stresses generated during injection through a small diameter (high-gauge) needle (Rapoport et al. 2009a, b). This phenomenon was first observed in Echogen microemulsions; its clinical implications have been discussed in ref. (Becher and Burns 2000). Though some generation of microbubbles in the vascular bed may be beneficial for increasing ultrasound-induced vascular permeability (Caskey et al. 2007, 2009a, b; Chen et al. 2010; Chen et al. 2011; Kinoshita et al. 2006; Matula and Guan 2011; Stieger et al. 2007), substantial transition of nanodroplets into microbubbles inside blood vessels should be avoided unless occlusion therapies have been considered. For safety reasons, PFP nanoemulsions should be injected either by infusion or through low-gauge needles.

Upon complete PFP droplet vaporization inside a copolymer wall, particle diameter increases fivefold due to a 125-fold density difference between liquid and gaseous PFP phases (Gao et al. 2008; Kripfgans et al. 2000; Rapoport et al. 2007). Therefore, a 500-nm diameter droplet would generate a 2.5-µm bubble upon complete vaporization. However, bubbles of much larger sizes were observed upon ultrasound-induced

PFP droplet vaporization (Kripfgans et al. 2000; Lo et al. 2007; Rapoport et al. 2009a, b). These were secondary bubbles formed from primary 2.5-μm bubbles. At least two different mechanisms of bubble growth beyond the size of primary bubbles may be considered: bubble coalescence with droplets or between themselves; diffusion of dissolved air and/or PFP from small bubbles into larger bubbles (*i.e.* Oswald ripening). Oswald ripening may also play a predominant role in gel or solid matrices, where droplet and bubble diffusion and collisions are restricted or stalled.

The increase of bubble size upon ultrasound-induced vaporization was tested in embolotherapy. Experiments performed on the externalized rabbit kidney using albumin-coated PFP microdroplets with an initial diameter less than 6 μm showed more than a 70 % perfusion reduction following ADV (Kripfgans et al. 2005). The authors hypothesized that this effect may be sufficient for cell death and tumor treatment via ischemic necrosis. It was also suggested that radiofrequency ablation of tumors might also benefit from ADV due to reduced perfusion and heat loss. These experiments were later extended to externalized canine kidneys (Zhang et al. 2010). Substantial reduction of cortex perfusion was achieved in some cases.

To elucidate physical mechanisms behind acoustic vaporization of PFP droplets, the relationship between ADV and inertial cavitation (IC) thresholds was studied (Fabiilli et al. 2009; Giesecke and Hynynen 2003; Kawabata et al. 2006; Lo et al. 2007; Schad and Hynynen 2010). Most of these experiments were performed with albumin- or lipid-coated microbubbles and showed that the ADV threshold was lower than the inertial cavitation threshold, indicating that the droplet-to-bubble transition preceded inertial cavitation. Measurements of the inertial cavitation threshold were performed for micrometer-sized albumin-shelled droplets containing various PFC cores, including those with higher boiling temperatures than that of PFP (*i.e.* perfluorohexane and perfluoromethylcyclohexane) (Giesecke and Hynynen 2003). The authors found that inertial cavitation thresholds did not noticeably depend on perfluorocarbon molecular weights and boiling temperatures, and thus, the droplets did not need to be in a superheated state to be cavitated by ultrasound bursts. This was later confirmed in experiments with nanosized perfluoro-15-crown-5-ether (PFCE) droplets that effectively converted into bubbles at ultrasound pressures that were only slightly higher than those for PFP nanodroplets (Rapoport et al. 2011). The mechanism of a droplet-to-bubble conversion with high boiling temperature perfluorocarbon compounds is most probably fundamentally different from true vaporization (see below). It was also found that nanometer-sized droplets containing a mixture of perfluoropentane (DDFP) and 2H,3H-perfluoropentane could be vaporized at diagnostic ultrasound frequencies (4–7.8 MHz) and that the vaporization threshold could be changed by altering relative concentrations of the two PFCs in the droplet (Kawabata et al. 2005). The authors hypothesized that the vaporization of a higher boiling temperature 2H,3H-perfluoropentane may have been caused not only by a directly delivered ultrasound energy, but also by the energy deposited by ultrasonically induced PFP bubbles. Droplet-to-bubble transition in PFP nanodroplets was shown to be catalyzed by pre-existing larger droplets or microbubbles. The catalytic effect was stronger at lower ultrasound frequencies (Rapoport et al. 2009a, b). This suggested that the droplet-to-bubble transition in nanoscaled droplets can be effectively catalyzed not only by mixing PFCs of various boiling temperatures, but also by using a bimodal or broad droplet size distribution in initial formulations. This is given that the conversion of larger droplets at lower power levels would catalyze droplet-to-bubble transition of smaller droplets.

Given that there is a large mismatch between the ultrasound wavelength and the droplet size, detailed physical mechanisms of droplet vaporization today remain elusive. Nevertheless, a new mechanism was recently proposed (Kooiman et al. 2014; Reznik et al. 2014; Shpak et al. 2014). The authors concluded that droplet vaporization is initiated by a combination of two phenomena:

highly nonlinear distortion of the acoustic wave before it hits the droplet, and focusing of the distorted wave by the droplet itself. At high excitation pressures, nonlinear distortion causes significant superharmonics with wavelengths of the order of the droplet size. These superharmonics strongly contribute to the focusing effect; therefore, this proposed mechanism also explains the observed pressure thresholding effect. This interpretation is validated with experimental data on the positions of the nucleation spots captured with an ultrahigh-speed camera; excellent agreement with the theoretical predictions was observed. The authors suggested a number of ways to decrease ultrasound pressure required for droplet vaporization: mixing different liquids to vary the acoustic impedance; to use dual or multiple frequency transducers to optimize the amplitudes and phases of the transmitted waves for maximal constructive interference, thus maximizing the focusing on the droplet. Still, the conclusions of the paper were not promising for delivering nanodroplet-loaded drugs into tumor interstitium using the ADV effect because nucleation of vaporization strongly depended on droplet sizes and manifested low probability for nanosized droplets. Small droplets would require higher ultrasound frequencies for vaporization; the latter don't penetrate deep into the interior of the body due to enhanced attenuation. On the other hand, micron-sized droplets that require lower ultrasound frequencies for nucleation and manifest higher probability of vaporization would not extravasate. Despite these apparent issues, excellent therapeutic results were obtained with drug-loaded nanosized droplets and ultrasound (see Sect. 13.4). Note that droplet-to-bubble transition is not necessarily associated with true perfluorocarbon vaporization as discussed in the next section.

13.3.2.2 Droplet-to-bubble Phase Transitions in Perfluoro-15-crown-5-ether Nanoemulsions

PFCE has a much higher boiling temperature than PFP (146 °C at atmospheric pressure). However, initiating droplet-to-bubble transition in PFCE nanodroplets required only slightly higher ultrasound energies than those for PFP (Rapoport et al. 2011), confirming the previously reported data (Giesecke and Hynynen 2003). The droplet-to-bubble transition in PFCE nanodroplets was induced by both continuous wave or pulsed ultrasound; the latter caused insignificant heating (Rapoport et al. 2011), confirming that the mechanism of droplet-to-bubble transition in a PFCE nanoemulsion was non-thermal. A possible mechanism of ultrasound-induced droplet-to-bubble transition in PFCE has been suggested (Rapoport et al. 2011). Perfluorocarbon emulsions differ from other emulsions by very high gas solubility, particularly for oxygen. This feature has allowed the use of perfluorocarbon emulsions as blood substitutes (Cohn and Cushing 2009). According to Henry's law, the solubility of gases increases with pressure. It has been hypothesized that a pressure drop during a rarefactional phase of ultrasound led to the evolution of PFC-dissolved oxygen in a gas phase inside the nanodroplet shell, followed by a rectified diffusion of dissolved gases from the surrounding liquid into the resulting nanobubble. According to this hypothesis, PFCE bubbles should predominantly contain a mixture of oxygen and other ambient gases, rather than PFCE vapor (though a bubble will also contain a low fraction of PFCE vapor in equilibrium with PFCE liquid phase). The bubbles formed this way are transient in nature; when the ultrasound is turned off, the equilibrium between nanodroplets and surrounding medium is restored; gases with super-equilibrium concentrations diffuse out of bubbles, thus restoring PFCE nanodroplets. This was confirmed experimentally. A PFCE nanoemulsion was placed in a long test tube; only the lower part of a test tube was sonicated. Bubbles that formed in the ultrasound field moved up due to buoyancy, but converted back to heavy droplets upon leaving the ultrasound field. On the way down towards the bottom of the test tube, droplets entered the ultrasound field and converted back to bubbles. Ultimately, nanoparticles "danced" at the border of the ultrasound field.

This proposed mechanism has been corroborated by the fact that degassing PFCE nanoemulsions inhibited the droplet-to-bubble transition

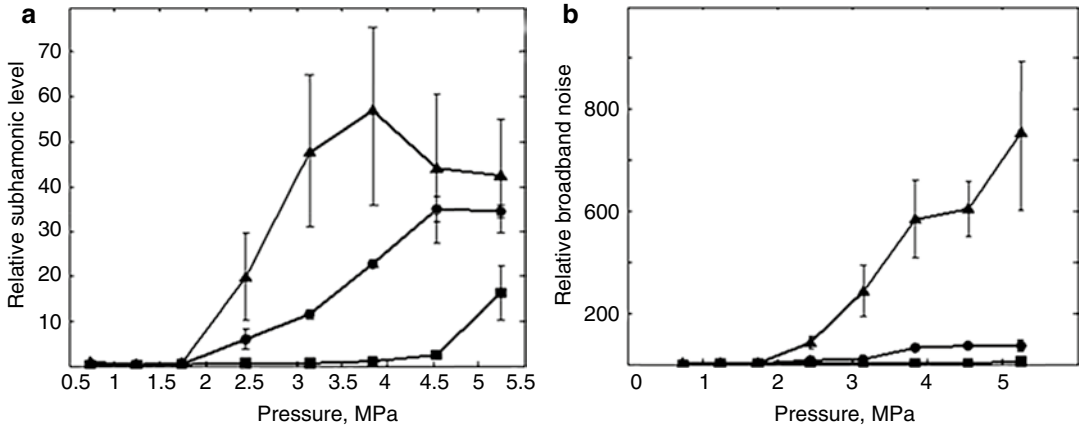

Fig. 13.6 Relative subharmonic (**a**) and broadband noise (**b**) levels generated under the action of 1-MHz focused ultrasound (HIFU) at room temperature by PFP and PFCE nanodroplets inserted into 0.6 % agarose gel. Nanodroplets were stabilized by a mixture of 0.25 % PEG-PLAA/0.25 % PEG-PCL copolymer. Triangles – PFP droplets; circles – PFCE droplets; squares – pure agarose gel (Reprinted with permission from (Rapoport et al. 2010a))

that was restored after contact with air was re-established. The bubble formation mechanism suggested above is different from true vaporization of nanodroplets, which is involved in the formation of PFP bubbles. Bubbles formed from either PFP or PFCE nanodroplets were shown to cavitate in the ultrasound field, as manifested by the generation of harmonic frequencies in the fast Fourier transform (FFT) spectra of the scattered ultrasound beam (Rapoport et al. 2009a, 2010a, 2011). Stable cavitation was observed in both an aqueous environment and agarose gel used as a tissue phantom (Fig. 13.6a). However, a broadband noise (characteristic of inertial cavitation) was not generated by PFCE droplets (Fig. 13.6b). Droplet-to-bubble conversion *in-vivo* was recently confirmed by ultrasound imaging (Matsunaga et al. 2012; Wilson et al. 2012). The material presented above implies that drug-loaded nanodroplets may serve as nano-scaled microbubble precursors that have a prospect of accumulating in tumors due to their nanoscaled sizes, and then convert into microbubbles *in-situ* under the action of tumor-directed ultrasound. Using this approach, successful therapy for breast, ovarian, and pancreatic cancer was achieved in animal model preclinical studies as described below.

13.4 Therapeutic Outcomes and Anticipated Mechanisms of Ultrasound-Mediated Drug Delivery using Phase-shift Perfluorocarbon Nanoemulsions as Drug Carriers

Successful *in-vitro* ultrasound-triggered delivery of paclitaxel (PTX) to monolayers of prostate cancer cells was reported for a phospholipid-coated perfluorohexane nanoemulsion developed by ImaRx (Dayton et al. 2006). Promising *in-vitro* results were also obtained for delivery of a chemotherapeutic drug camptothecin to melanoma and ovarian cancer cells. Ultrasound-activated perfluorocarbon nanodroplets of diameters 220–420 nm were stabilized by phospholipids and/or Pluronic F68. Confocal laser scanning microscopy confirmed nanoemulsion uptake by the cells (Zhou et al. 2009). Albumin/soybean oil-coated PFP microdroplets were tested *in-vitro* for the delivery of a lipophilic drug chlorambucil (Fabiilli et al. 2010a). Application of ultrasound almost doubled cell killing by the drug.

Tumor therapy with drug-loaded perfluorocarbon nanoemulsions combined with ultrasound

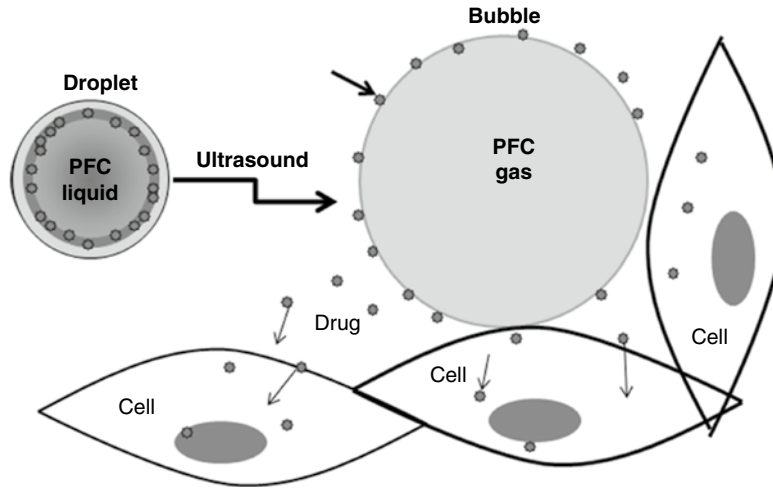

Fig. 13.7 Schematic representation of the mechanism of a drug release from a perfluorocarbon nanodroplet triggered by ultrasound-induced phase shift (Reprinted with permission from (Rapoport et al. 2009b))

was also studied *in-vivo*. Strong therapeutic effects were achieved with drug-loaded lipid-stabilized perfluorooctylbromide (PFOB) or PFCE nanoemulsions (Kaneda et al. 2009; Soman et al. 2009; Tran et al. 2007; Winter et al. 2007). In the experiments by the Lanza and Wickline group, a technology was developed to impart active targeting properties to lipid-coated nanodroplets. Integrin-targeted perfluorocarbon-based nanoparticles (250 nm diameter) were used for imaging $\alpha_v\beta(3)$-integrin receptor expression in tumors. The tumor-to-muscle droplet accumulation ratio was found to be 7 for targeted nanodroplets, and only 3 for non-targeted nanodroplets. This group also used molecularly targeted lipid-coated perfluorocarbon-based nanoparticles for *in-vivo* delivery of a highly toxic amphipathic cytolytic peptide, melittin, to tumor bearing mice. Melittin was incorporated into the outer lipid monolayer of a perfluorocarbon nanoparticle. The authors observed a dramatic reduction in tumor growth, without any apparent signs of toxicity. Furthermore, it was demonstrated that molecularly targeted nanocarriers selectively delivered melittin to multiple tumor targets, including endothelial and cancer cells, supposedly through a hemifusion mechanism. For review on lipid-coated perfluorocarbon nanoparticles for ^{19}F molecular imaging and targeted drug delivery agents in cancer and cardiovascular diseases see Kaneda et al. 2009. Targeted nanodroplets were also used for diagnosis and therapy of atherosclerosis (Caruthers et al. 2009; Wickline et al. 2007; Winter et al. 2008).

The mechanism of ultrasound-mediated drug delivery proposed in these publications is based on the enhancing effect of the ultrasound radiation force on the droplet/cell contacts. This facilitates fusion between cell membranes and phospholipid-coated nanodroplets, which results in drug transfer from nanodroplets into the interior of the cell. The mechanism suggested above is presumably operative for lipid-coated particles; however it would hardly function for block copolymer-stabilized nanodroplets that expose PEG chains on the surfaces. An alternative mechanism was proposed for these nanodroplets. The mechanism is based on the ultrasound-induced droplet-to-bubble transition as presented schematically in Fig. 13.7 (Rapoport et al. 2009b). Upon the droplet-to-bubble transition, the nanoparticle volume increases dramatically, while the thickness of the droplet shell, as well as block copolymer concentration on the particle surface, decreases correspondingly. This allows the drug to be "ripped off" the droplet surface. Drug transition from bubbles to cells under the action of ultrasound was observed in model experiments (Rapoport et al. 2007).

In-vivo, PTX was shown to be tightly retained in PFP/PEG-PLLA nanodroplets, as manifested by the experiments with bi-lateral ovarian carcinoma tumors (Fig. 13.8).

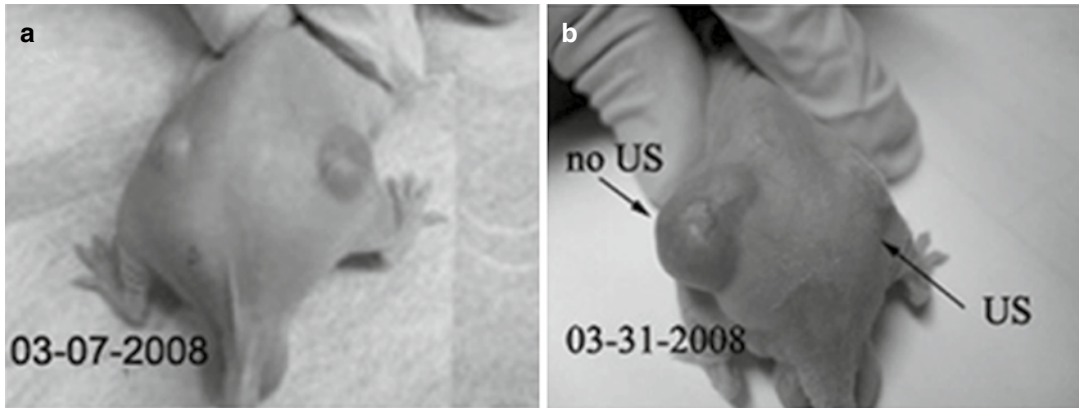

Fig. 13.8 Photographs of a mouse bearing two ovarian carcinoma tumors (**a**) – immediately before and (**b**) – 3 weeks after the treatment; mouse treated by four systemic injections of nanodroplets-encapsulated PTX (20 mg/kg as PTX) given twice weekly; the right tumor was sonicated by 1-MHz CW ultrasound (nominal output power density 3.4 W/cm^2, exposure duration 1 min) delivered 4 h after the injection of the drug formulation. Ultrasound was delivered through a water bag coupled to a transducer and mouse skin by Aquasonic coupling gel. Reprinted with permission from (Rapoport et al. 2009b)

A mouse was treated with four systemic injections of PTX-loaded nanodroplets (20 mg/kg PTX) twice weekly for 2 weeks; only one tumor (right side) was sonicated by unfocused 1-MHz continuous wave (CW) ultrasound at a nominal output power density 3.4 W/cm^2 with exposure duration of 1 min. The non-sonicated tumor (left side) grew with the same rate as control tumors, indicating that the drug did not reach this tumor in therapeutic concentrations. In contrast, the size of the sonicated tumor decreased dramatically, and the tumor appeared completely resolved after the treatment. This data suggests that without ultrasound, PTX was tightly retained by the PFP droplets, but was effectively released under the action of tumor-directed therapeutic ultrasound. Tight drug retention by the nanodroplet carrier *in-vivo* provides protection for healthy tissues; on the other hand, effective ultrasound-induced localized drug release into the tumor results in efficient tumor regression.

Very promising results on the therapeutic action of drug-loaded PFP or PFCE nanoemulsions combined with 1- or 3-MHz ultrasound were confirmed in experiments with breast and pancreatic tumors (Rapoport et al. 2009b, 2011). Effective therapy of pancreatic ductal adenocarcinoma is especially important because other treatment modalities tested for this devastating disease have so far proved ineffective. In our experiments, pancreatic tumor cells were transfected with red fluorescent protein to allow monitoring of tumor size and cell survival in orthotopically inoculated PDA tumors using intravital fluorescence imaging. In initial experiments tumors were treated with unfocused 1-MHz ultrasound and PTX was encapsulated in PFP/PEG-PLLA nanodroplets (Rapoport et al. 2010b, 2011). Though development of drug resistance was observed in the course of treatment, the results (extended life span, decreased metastasizing and ascites) (Rapoport et al. 2010b; Shea et al. 2011) were considered encouraging and stimulated transition to experiments with focused ultrasound delivered under the MRI control designated as MRgFUS. Temperature rise during treatment was monitored using MRI thermometry (Rapoport et al. 2013) as shown schematically in Fig. 13.9.

The ultrasound beam was steered in a single plane within the tumor; hence the treated volume was much smaller than the whole tumor volume. In these experiments, PTX was encapsulated in a second generation of block copolymer coated perfluorocarbon nanodroplets, PFCE/PEG-PDLA nanodroplets that manifested a number of important improvements over the PFP/PEG-PLLA formulation used earlier. The improvements were

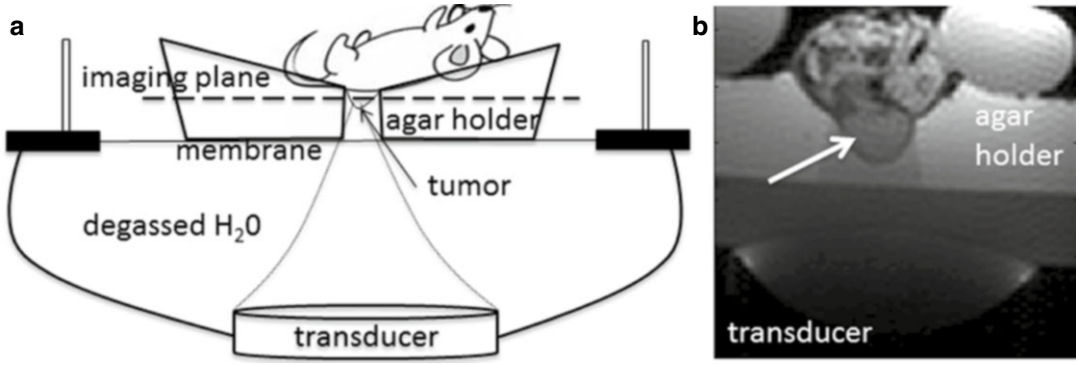

Fig. 13.9 Schematic representation of a mouse positioning on the small animal MRgFUS device. (**a**) An axial image of a mouse on the small animal MRgFUS device. (**b**) The white arrow indicates the tumor (initial size 455 mm^3) (Reprinted with permission from (Rapoport et al. 2013))

provided by both a different compound of the droplet core, and a different structure of the block copolymer that forms an elastic rather than solid shell. Importantly, the development of the drug resistance was prevented, presumably due to the action of the PEG-PDLA unimers that were in equilibrium with PEG-PDLA micelles (Alakhova et al. 2010; Batrakova et al. 1998, 2001).

A PFCE core allows the use of ^{19}F MR imaging for monitoring nanodroplet biodistribution since PFCE contains 20 equivalent fluorine nuclei that generate a sharp single resonance peak in ^{19}F magnetic resonance spectra (Ahrens et al. 2005; Noth et al. 1997; Yu et al. 2005). The results obtained shed light on some important aspects of the mechanisms involved in the combined therapy with drug-loaded perfluorocarbon nanodroplets and ultrasound. It is important to underline that ultrasound power levels used in this study were always subablative. After a single treatment with PTX-loaded nanodroplets and MRgFUS applied 6–8 h after the injection, PDA tumors in four of twenty-eight mice were completely resolved and never recurred. Additionally, the life span of other mice was very significantly extended over the treatment with the same formulation without ultrasound (Table 13.1).

No effect of MRgFUS was observed when ultrasound was applied either before or 2 h after the nanodroplet injection. The average life span of mice treated with pulsed ultrasound was significantly lower than that of mice treated with CW ultrasound. The treatment with empty droplets with or without ultrasound did not produce any therapeutic effect; moreover, treatment with empty droplets combined with MRgFUS was either inefficient or detrimental. Also, increasing ultrasound power above 4.6 acoustic watts (but remaining in the subablative power levels) exerted a detrimental effect on the tumor growth and animal survival. These data indicate that the main therapeutic effect was caused by the drug, and not by ultrasound. Even without ultrasound, treatment with PTX-loaded PFCE/PEG-PDLA nanodroplets considerably extended mouse life span (Table 13.1). Still, for the optimal combinations of ultrasound parameters, MRgFUS significantly enhanced the action of the drug. It is noteworthy that despite only a small fraction of

Table 13.1 Average mouse life span for various treatment parameters. MRgFUS was applied 8 h after the drug injection

Treatment group	Average life span, weeks
Control	3.5 ± 0.5
No injection, MRgFUS (N = 6)	4.8 ± 2.3
Empty droplets, MRgFUS (N = 6)	3.5 ± 2.1
PTX droplets, no MRgFUS (N = 7)	7 ± 0.8
PTX droplets, MRgFUS CW (N = 8)	10.3 ± 1.6
PTX droplets, MRgFUS (N = 4)	6 ± 1.4

the total tumor being treated by ultrasound, a substantial delay of the tumor growth was observed, which suggests that drug was effectively disseminated from the sonicated areas by enhanced convection or diffusion. The data of this study implied that ultrasound may exert both positive and negative effects on biological tissue. Positive effects may be related to ultrasound-increased drug carrier and drug extravasation, drug release from carrier, and drug internalization by tumor cells. On the other hand, vasodilation or vasoconstriction in response to ultrasound and cavitating microbubbles may result in negative effects such as inflammation, edema, hemorrhaging effects *etc*.

Tissue response to ultrasound-induced heating is multifaceted. In the absence of drug, the response to sub-ablative heating may be negative due to enhanced perfusion that promotes tumor growth. In contrast, in the presence of drug, enhanced perfusion is a positive factor that promotes drug delivery to tumor tissue. In addition, hyperthermia increases vascular wall and plasma membrane permeability, thus increasing drug internalization by tumor cells. The ultimate biological response to ultrasound presumably depends on the prevalence of positive or negative factors, which is expected to depend on the treatment protocol.

Taken together, these results suggest that drug-loaded perfluorocarbon nanoemulsion in combination with ultrasound treatment can provide efficient therapy for a broad spectrum of diseases.

13.5 Conclusions and Future Prospects

Targeted drug delivery has been a goal of the bioengineering community ever since the 'magic bullet' concept was introduced by Paul Ehrlich over a century ago. By combining tissue targeting of drug-loaded nanodroplets with active release mechanisms, this formerly elusive goal is turning into medical reality. The unprecedented opportunity to localize drug delivery is associated with developing stimuli responsive drug carriers, particularly ultrasound-responsive phase-shift perfluorocarbon nanoemulsions. Their important properties combine drug carrying, tumor-targeting, enhancing intracellular drug delivery and enhancing the ultrasound contrast of tumors. This novel technology has demonstrated excellent therapeutic potential in murine cancer models.

Much preclinical work remains to be done for introducing phase-shift nanoparticles into clinical practice. Transition to experiments on larger animal models is a critical task. Passive targeting of nanoparticles may prove more challenging in larger animals (and humans) than in small animal models due to much smaller tumor-to-body volume ratio in larger animals. Actively targeted phase-shift nanoemulsions may be required for effective tumor accumulation. For this, identifying more selective surface receptors on tumor cells is a crucial task.

Design of optimal clinical drug delivery systems involves the identification of targets, tracking delivery systems in the body, guidance of therapy and monitoring of immediate and delayed therapeutic responses. More research needs to be carried out on biodistribution and pharmacokinetics of the components of nanoemulsion formulations, as well as optimization of ultrasound parameters and time of ultrasound application. These problems remain to be addressed in future translational studies.

References

Ahrens ET, Flores R, Xu H, Morel PA (2005) In vivo imaging platform for tracking immunotherapeutic cells. Nat Biotechnol 23:983–987

Alakhov V, Moskaleva E, Batrakova EV, Kabanov AV (1996) Hypersensitization of multidrug resistant human ovarian carcinoma cells by pluronic P85 block copolymer. Bioconjug Chem 7:209–216

Alakhova DY, Rapoport NY, Batrakova EV, Timoshin AA, Li S, Nicholls D, Alakhov VY, Kabanov AV (2010) Differential metabolic responses to pluronic in MDR and non-MDR cells: a novel pathway for chemosensitization of drug resistant cancers. J Control Release 142:89–100

Alexandridis P, Holzwarth JF, Hatton TA (1994) Micellization of poly(ethylene oxide)-poly(propylene oxide)-poly(ethylene oxide) triblock copolymers in

aqueous solutions: thermodynamics of copolymer association. Macromolecules 27:2414–2425
Apfel RE (1998) Activatable infusable dispersions containing drops of a superheated liquid for methods of therapy and diagnosis, US Patent 5840276, 1998
Barber EJ, Cady GH (1956) Vapor pressures of perfluoropentanes. J Phys Chem 60:504–505
Batrakova EV, Han HY, Miller DW, Kabanov AV (1998) Effects of pluronic P85 unimers and micelles on drug permeability in polarized BBMEC and Caco-2 cells. Pharm Res 15:1525–1532
Batrakova E, Lee S, Li S, Venne A, Alakhov V, Kabanov A (1999) Fundamental relationships between the composition of pluronic block copolymers and their hypersensitization effect in MDR cancer cells. Pharm Res 16:1373–1379
Batrakova EV, Li S, Elmquist WF, Miller DW, Alakhov VY, Kabanov AV (2001) Mechanism of sensitization of MDR cancer cells by pluronic block copolymers: selective energy depletion. Br J Cancer 85:1987–1997
Batrakova EV, Li S, Alakhov VY, Elmquist WF, Miller DW, Kabanov AV (2003) Sensitization of cells overexpressing multidrug-resistant proteins by pluronic P85. Pharm Res 20:1581–1590
Becher H, Burns PN (2000) Handbook for contrast echocardiography. Springer, Frankfurt/New York
Becher H, Lofiego C, Mitchell A, Timperley J (2005) Current indications for contrast echocardiography imaging. Eur J Echocardiogr 6(Suppl 2):S1–S5
Borden MA, Kruse DE, Caskey CF, Zhao S, Dayton PA, Ferrara KW (2005) Influence of lipid shell physicochemical properties on ultrasound-induced microbubble destruction. IEEE Trans Ultrason Ferroelectr Freq Control 52:1992–2002
Borden MA, Zhang H, Gillies RJ, Dayton PA, Ferrara KW (2008) A stimulus-responsive contrast agent for ultrasound molecular imaging. Biomaterials 29:597–606
Burke CW, Klibanov AL, Sheehan JP, Price RJ (2011) Inhibition of glioma growth by microbubble activation in a subcutaneous model using low duty cycle ultrasound without significant heating. J Neurosurg 114(6): 1654–1661
Campbell RB (2006) Tumor physiology and delivery of nanopharmaceuticals. Anticancer Agents Med Chem 6:503–512
Caruthers SD, Cyrus T, Winter PM, Wickline SA, Lanza GM (2009) Anti-angiogenic perfluorocarbon nanoparticles for diagnosis and treatment of atherosclerosis. Wiley Interdiscip Rev Nanomed Nanobiotechnol 1:311–323
Caskey CF, Stieger SM, Qin S, Dayton PA, Ferrara KW (2007) Direct observations of ultrasound microbubble contrast agent interaction with the microvessel wall. J Acoust Soc Am 122:1191–1200
Caskey CF, Qin S, Dayton PA, Ferrara KW (2009a) Microbubble tunneling in gel phantoms. J Acoust Soc Am 125:EL183–EL189
Caskey CF, Qin S, Ferrara KW (2009b) Ultrasound mediated drug delivery: the effect of microbubbles on a gel boundary. Conf Proc IEEE Eng Med Biol Soc 2009:134–136
Chen H, Brayman AA, Bailey MR, Matula TJ (2010) Blood vessel rupture by cavitation. Urol Res 38: 321–326
Chen H, Kreider W, Brayman AA, Bailey MR, Matula TJ (2011) Blood vessel deformations on microsecond time scales by ultrasonic cavitation. Phys Rev Lett 106:034301
Chen X, Wang J, Versluis M, de Jong N, Villanueva FS (2013) Ultra-fast bright field and fluorescence imaging of the dynamics of micrometer-sized objects. Rev Sci Instrum 84:063701
Cohn CS, Cushing MM (2009) Oxygen therapeutics: perfluorocarbons and blood substitute safety. Crit Care Clin 25:399–414, Table of Contents
Dalecki D (2004) Mechanical bioeffects of ultrasound. Annu Rev Biomed Eng 6:229–248
Dayton P, Klibanov A, Brandenburger G, Ferrara K (1999) Acoustic radiation force in vivo: a mechanism to assist targeting of microbubbles. Ultrasound Med Biol 25:1195–1201
Dayton PA, Zhao S, Bloch SH, Schumann P, Penrose K, Matsunaga TO, Zutshi R, Doinikov A, Ferrara KW (2006) Application of ultrasound to selectively localize nanodroplets for targeted imaging and therapy. Mol Imaging 5:160–174
Deckers R, Moonen CT (2010) Ultrasound triggered, image guided, local drug delivery. J Control Release 148(1):25–33
Dewhirst MW, Vujaskovic Z, Jones E, Thrall D (2005) Re-setting the biologic rationale for thermal therapy. Int J Hyperthermia 21:779–790
Dreher MR, Liu W, Michelich CR, Dewhirst MW, Yuan F, Chilkoti A (2006) Tumor vascular permeability, accumulation, and penetration of macromolecular drug carriers. J Natl Cancer Inst 98:335–344
Dromi S, Frenkel V, Luk A, Traughber B, Angstadt M, Bur M, Poff J, Xie J, Libutti SK, Li KC, Wood BJ (2007) Pulsed-high intensity focused ultrasound and low temperature-sensitive liposomes for enhanced targeted drug delivery and antitumor effect. Clin Cancer Res 13:2722–2727
Fabiilli ML, Haworth KJ, Fakhri NH, Kripfgans OD, Carson PL, Fowlkes JB (2009) The role of inertial cavitation in acoustic droplet vaporization. IEEE Trans Ultrason Ferroelectr Freq Control 56:1006–1017
Fabiilli ML, Haworth KJ, Sebastian IE, Kripfgans OD, Carson PL, Fowlkes JB (2010a) Delivery of chlorambucil using an acoustically-triggered perfluoropentane emulsion. Ultrasound Med Biol 36:1364–1375
Fabiilli ML, Lee JA, Kripfgans OD, Carson PL, Fowlkes JB (2010b) Delivery of water-soluble drugs using acoustically triggered perfluorocarbon double emulsions. Pharm Res 27:2753–2765
Faez T, Emmer M, Kooiman K, Versluis M, van der Steen A, de Jong N (2013) 20 years of ultrasound contrast agent modeling. IEEE Trans Ultrason Ferroelectr Freq Control 60:7–20
Ferrara KW (2008) Driving delivery vehicles with ultrasound. Adv Drug Deliv Rev 60:1097–1102
Ferrara K, Pollard R, Borden M (2007) Ultrasound microbubble contrast agents: fundamentals and application

to gene and drug delivery. Annu Rev Biomed Eng 9:415–447
Frenkel V, Kimmel E, Iger Y (2000a) Ultrasound-facilitated transport of silver chloride (AgCl) particles in fish skin. J Control Release 68:251–261
Frenkel V, Kimmel E, Iger Y (2000b) Ultrasound-induced intercellular space widening in fish epidermis. Ultrasound Med Biol 26:473–480
Frenkel V, Etherington A, Greene M, Quijano J, Xie J, Hunter F, Dromi S, Li KC (2006) Delivery of liposomal doxorubicin (Doxil) in a breast cancer tumor model: investigation of potential enhancement by pulsed-high intensity focused ultrasound exposure. Acad Radiol 13:469–479
Frulio N, Trillaud H, Deckers R, Lepreux S, Moonen C, Quesson B (2010) Influence of ultrasound induced cavitation on magnetic resonance imaging contrast in the rat liver in the presence of macromolecular contrast agent. Invest Radiol 45:282–287
Gaber MH, Wu NZ, Hong K, Huang SK, Dewhirst MW, Papahadjopoulos D (1996) Thermosensitive liposomes: extravasation and release of contents in tumor microvascular networks. Int J Radiat Oncol Biol Phys 36:1177–1187
Gaitan DF, Tessien RA, Hiller RA, Gutierrez J, Scott C, Tardif H, Callahan B, Matula TJ, Crum LA, Holt RG, Church CC, Raymond JL (2010) Transient cavitation in high-quality-factor resonators at high static pressures. J Acoust Soc Am 127:3456–3465
Gao Z, Fain HD, Rapoport N (2004) Ultrasound-enhanced tumor targeting of polymeric micellar drug carriers. Mol Pharm 1:317–330
Gao Z, Kennedy AM, Christensen DA, Rapoport NY (2008) Drug-loaded nano/microbubbles for combining ultrasonography and targeted chemotherapy. Ultrasonics 48:260–270
Giesecke T, Hynynen K (2003) Ultrasound-mediated cavitation thresholds of liquid perfluorocarbon droplets in vitro. Ultrasound Med Biol 29:1359–1365
Hancock H, Dreher MR, Crawford N, Pollock CB, Shih J, Wood BJ, Hunter K, Frenkel V (2009a) Evaluation of pulsed high intensity focused ultrasound exposures on metastasis in a murine model. Clin Exp Metastasis 26:729–738
Hancock HA, Smith LH, Cuesta J, Durrani AK, Angstadt M, Palmeri ML, Kimmel E, Frenkel V (2009b) Investigations into pulsed high-intensity focused ultrasound-enhanced delivery: preliminary evidence for a novel mechanism. Ultrasound Med Biol 35: 1722–1736
Hauck ML, LaRue SM, Petros WP, Poulson JM, Yu D, Spasojevic I, Pruitt AF, Klein A, Case B, Thrall DE, Needham D, Dewhirst MW (2006) Phase I trial of doxorubicin-containing low temperature sensitive liposomes in spontaneous canine tumors. Clin Cancer Res 12:4004–4010
Hayat H, Friedberg I (1986) Heat-induced alterations in cell membrane permeability and cell inactivation of transformed mouse fibroblasts. Int J Hyperthermia 2:369–378
Hernot S, Klibanov AL (2008) Microbubbles in ultrasound-triggered drug and gene delivery. Adv Drug Deliv Rev 60:1153–1166
Hitchcock KE, Holland CK (2010) Ultrasound-assisted thrombolysis for stroke therapy: better thrombus break-up with bubbles. Stroke 41:S50–S53, a journal of cerebral circulation
Hitchcock KE, Ivancevich NM, Haworth KJ, Caudell Stamper DN, Vela DC, Sutton JT, Pyne-Geithman GJ, Holland CK (2011) Ultrasound-enhanced rt-PA thrombolysis in an ex vivo porcine carotid artery model. Ultrasound Med Biol 37:1240–1251
Hobbs SK, Monsky WL, Yuan F, Roberts WG, Griffith L, Torchilin VP, Jain RK (1998) Regulation of transport pathways in tumor vessels: role of tumor type and microenvironment. Proc Natl Acad Sci U S A 95:4607–4612
Holland CK, McPherson DD (2009) Echogenic lipsomes for targeted drug delivery. Proc IEEE Int Symp Biomed Imaging 2009:755–758
Iyer AK, Khaled G, Fang J, Maeda H (2006) Exploiting the enhanced permeability and retention effect for tumor targeting. Drug Discov Today 11:812–818
Kaneda MM, Caruthers S, Lanza GM, Wickline SA (2009) Perfluorocarbon nanoemulsions for quantitative molecular imaging and targeted therapeutics. Ann Biomed Eng 37:1922–1933
Kawabata K, Sugita N, Yoshikawa H, Azama T, Umemura S (2005) Nanoparticles with multiple perfluorocarbons for controllable ultrasound-induced phase shift. Jpn J Appl Phys 44:4548–4552
Kawabata K, Yoshizawa A, Asami R (2006) Site-specific contrast imaging with locally induced microbubble from liquid precursors. Proc IEEE Int Ultrasonic Symp 517–520
Kheirolomoom A, Dayton PA, Lum AF, Little E, Paoli EE, Zheng H, Ferrara KW (2007) Acoustically-active microbubbles conjugated to liposomes: characterization of a proposed drug delivery vehicle. J Control Release 118:275–284
Kheirolomoom A, Mahakian LM, Lai CY, Lindfors HA, Seo JW, Paoli EE, Watson KD, Haynam EM, Ingham ES, Xing L, Cheng RH, Borowsky AD, Cardiff RD, Ferrara KW (2010) Copper-doxorubicin as a nanoparticle cargo retains efficacy with minimal toxicity. Mol Pharm 7:1948–1958
Kinoshita M, McDannold N, Jolesz FA, Hynynen K (2006) Noninvasive localized delivery of Herceptin to the mouse brain by MRI-guided focused ultrasound-induced blood–brain barrier disruption. Proc Natl Acad Sci U S A 103:11719–11723
Klibanov AL (2007) Ultrasound molecular imaging with targeted microbubble contrast agents. J Nucl Cardiol 14:876–884
Klibanov AL, Shevchenko TI, Raju BI, Seip R, Chin CT (2010) Ultrasound-triggered release of materials entrapped in microbubble-liposome constructs: A tool for targeted drug delivery. J Control Release 148(1):13
Kokhuis TJ, Garbin V, Kooiman K, Naaijkens BA, Juffermans LJ, Kamp O, van der Steen AF, Versluis M, de Jong N (2013) Secondary bjerknes forces deform

targeted microbubbles. Ultrasound Med Biol 39: 490–506

Kong G, Dewhirst MW (1999) Hyperthermia and liposomes. Int J Hyperthermia 15:345–370

Kong G, Anyarambhatla G, Petros WP, Braun RD, Colvin OM, Needham D, Dewhirst MW (2000a) Efficacy of liposomes and hyperthermia in a human tumor xenograft model: importance of triggered drug release. Cancer Res 60:6950–6957

Kong G, Braun RD, Dewhirst MW (2000b) Hyperthermia enables tumor-specific nanoparticle delivery: effect of particle size. Cancer Res 60:4440–4445

Kong G, Braun RD, Dewhirst MW (2001) Characterization of the effect of hyperthermia on nanoparticle extravasation from tumor vasculature. Cancer Res 61:3027–3032

Kooiman K, Vos HJ, Versluis M, de Jong N (2014) Acoustic behavior of microbubbles and implications for drug delivery. Adv Drug Deliv Rev 72C:28–48

Kripfgans OD, Fowlkes JB, Miller DL, Eldevik OP, Carson PL (2000) Acoustic droplet vaporization for therapeutic and diagnostic applications. Ultrasound Med Biol 26:1177–1189

Kripfgans OD, Fowlkes JB, Woydt M, Eldevik OP, Carson PL (2002) In vivo droplet vaporization for occlusion therapy and phase aberration correction. IEEE Trans Ultrason Ferroelectr Freq Control 49:726–738

Kripfgans OD, Fabiilli ML, Carson PL, Fowlkes JB (2004) On the acoustic vaporization of micrometer-sized droplets. J Acoust Soc Am 116:272–281

Kripfgans OD, Orifici CM, Carson PL, Ives KA, Eldevik OP, Fowlkes JB (2005) Acoustic droplet vaporization for temporal and spatial control of tissue occlusion: a kidney study. IEEE Trans Ultrason Ferroelectr Freq Control 52:1101–1110

Krupka T, Dremann D, Exner A (2009) Time and dose dependence of pluronic bioactivity in hyperthermia-induced tumor cell death. Exp Biol Med (Maywood) 234:95–104

Laing ST, Moody M, Smulevitz B, Kim H, Kee P, Huang S, Holland CK, McPherson DD (2011) Ultrasound-enhanced thrombolytic effect of tissue plasminogen activator-loaded echogenic liposomes in an in vivo rabbit aorta thrombus model–brief report. Arterioscler Thromb Vasc Biol 31:1357–1359

Lo AH, Kripfgans OD, Carson PL, Fowlkes JB (2006) Spatial control of gas bubbles and their effects on acoustic fields. Ultrasound Med Biol 32:95–106

Lo AH, Kripfgans OD, Carson PL, Rothman ED, Fowlkes JB (2007) Acoustic droplet vaporization threshold: effects of pulse duration and contrast agent. IEEE Trans Ultrason Ferroelectr Freq Control 54:933–946

Lubner MG, Brace CL, Hinshaw JL, Lee FT Jr (2010) Microwave tumor ablation: mechanism of action, clinical results, and devices. J Vasc Interv Radiol 21: S192–S203

Lum AF, Borden MA, Dayton PA, Kruse DE, Simon SI, Ferrara KW (2006) Ultrasound radiation force enables targeted deposition of model drug carriers loaded on microbubbles. J Control Release 111:128–134, Epub 2005 Dec 2027

Manthe RL, Foy SP, Krishnamurthy N, Sharma B, Labhasetwar V (2010) Tumor ablation and nanotechnology. Mol Pharm 7:1880–1898

Maresca D, Renaud G, van Soest G, Li X, Zhou Q, Shung KK, de Jong N, van der Steen AF (2013) Contrast-enhanced intravascular ultrasound pulse sequences for bandwidth-limited transducers. Ultrasound Med Biol 39:706–713

Matsunaga TO, Sheeran PS, Luois S, Streeter JE, Mullin LB, Banerjee B, Dayton PA (2012) Phase-change nanoparticles using highly volatile perfluorocarbons: toward a platform for extravascular ultrasound imaging. Theranostics 2:1185–1198

Matula T, Guan J (2011) Using optical scattering to measure properties of ultrasound contrast agent shells. J Acoust Soc Am 129:1675

McDannold NJ, Vykhodtseva NI, Hynynen K (2006) Microbubble contrast agent with focused ultrasound to create brain lesions at low power levels: MR imaging and histologic study in rabbits. Radiology 241:95–106

McDannold N, Vykhodtseva N, Hynynen K (2008) Effects of acoustic parameters and ultrasound contrast agent dose on focused-ultrasound induced blood–brain barrier disruption. Ultrasound Med Biol 34:930–937, Epub 2008 Feb 2021

McWilliams JP, Lee EW, Yamamoto S, Loh CT, Kee ST (2010) Image-guided tumor ablation: emerging technologies and future directions. Semin Intervent Radiol 27:302–313

Miller DL, Song J (2002) Lithotripter shock waves with cavitation nucleation agents produce tumor growth reduction and gene transfer in vivo. Ultrasound Med Biol 28:1343–1348

Miller MW, Miller DL, Brayman AA (1996) A review of in vitro bioeffects of inertial ultrasonic cavitation from a mechanistic perspective. Ultrasound Med Biol 22: 1131–1154

Miller DL, Kripfgans OD, Fowlkes JB, Carson PL (2000) Cavitation nucleation agents for nonthermal ultrasound therapy. J Acoust Soc Am 107:3480–3486

Mohan P, Rapoport N (2010) Doxorubicin as a molecular nanotheranostic agent: effect of doxorubicin encapsulation in micelles or nanoemulsions on the ultrasound-mediated intracellular delivery and nuclear trafficking. Mol Pharm 7:1959–1973

Nam KH, Christensen DA, Kennedy AM and Rapoport N (2009) Acoustic droplet vaporization, cavitation, and therapeutic properties of copolymer-stabilized perfluorocarbon nanoemulsions. Am Inst Phys Conf Proc 1113:124–128

Needham D, Anyarambhatla G, Kong G, Dewhirst MW (2000) A new temperature-sensitive liposome for use with mild hyperthermia: characterization and testing in a human tumor xenograft model. Cancer Res 60: 1197–1201

Negussie AH, Yarmolenko PS, Partanen A, Ranjan A, Jacobs G, Woods D, Bryant H, Thomasson D, Dewhirst MW, Wood BJ, Dreher MR (2011) Formulation and characterisation of magnetic resonance imageable thermally sensitive liposomes for use

with magnetic resonance-guided high intensity focused ultrasound. Int J Hyperthermia 27:140–155
Noth U, Morrissey SP, Deichmann R, Jung S, Adolf H, Haase A, Lutz J (1997) Perfluoro-15-crown-5-ether labelled macrophages in adoptive transfer experimental allergic encephalomyelitis. Artif Cells Blood Substit Immobil Biotechnol 25:243–254
O'Neill BE, Rapoport N (2011) Phase-shift, stimuli-responsive drug carriers for targeted delivery. Ther Deliv 2:1165–1187
O'Neill BE, Vo H, Angstadt M, Li KP, Quinn T, Frenkel V (2009) Pulsed high intensity focused ultrasound mediated nanoparticle delivery: mechanisms and efficacy in murine muscle. Ultrasound Med Biol 35:416–424
Poon RTP, Borys N (2009) Lyso-thermosensitive liposomal doxorubicin: a novel approach to enhance efficacy of thermal ablation of liver cancer. Expert Opin Pharmacother 10:333–343
Qin S, Caskey CF, Ferrara KW (2009) Ultrasound contrast microbubbles in imaging and therapy: physical principles and engineering. Phys Med Biol 54:R27–R57
Rapoport N (2007) Physical stimuli-responsive polymeric micelles for anti-cancer drug delivery. Prog Polym Sci 32:962–990
Rapoport N (2012a) Phase-shift, stimuli-responsive perfluorocarbon nanodroplets for drug delivery to cancer. Wiley Interdiscip Rev Nanomed Nanobiotechnol 4(5):492–510
Rapoport N (2012b) Ultrasound-mediated micellar drug delivery. Int J Hyperthermia 28:374–385
Rapoport N, Gao Z, Kennedy A (2007) Multifunctional nanoparticles for combining ultrasonic tumor imaging and targeted chemotherapy. J Natl Cancer Inst 99: 1095–1106
Rapoport NY, Efros AL, Christensen DA, Kennedy AM, Nam KH (2009a) Microbubble generation in phase-shift nanoemulsions used as anticancer drug carriers. Bubble Sci Eng Technol 1:31–39
Rapoport NY, Kennedy AM, Shea JE, Scaife CL, Nam K-H (2009b) Controlled and targeted tumor chemotherapy by ultrasound-activated nanoemulsions/microbubbles. J Control Release 138:268–276
Rapoport N, Christensen DA, Kennedy AM, Nam KH (2010a) Cavitation properties of block copolymer stabilized phase-shift nanoemulsions used as drug carriers. Ultrasound Med Biol 36:419–429
Rapoport N, Kennedy AM, Shea JE, Scaife CL, Nam KH (2010b) Ultrasonic nanotherapy of pancreatic cancer: lessons from ultrasound imaging. Mol Pharm 7:22–31
Rapoport N, Nam K-H, Gupta R, Gao Z, Mohan P, Payne A, Todd N, Liu X, Kim T, Shea J, Scaife C, Kennedy AM, Parker DL, Jeong E-K (2011) Ultrasound-mediated tumor imaging and nanotherapy using drug loaded, block copolymer stabilized perfluorocarbon nanoemulsions. J Control Release 153:4–15
Rapoport N, Payne A, Dillon C, Shea J, Scaife C, Gupta R (2013) Focused ultrasound-mediated drug delivery to pancreatic cancer in a mouse model. J Ther Ultrasound 1
Reznik N, Williams R, Burns PN (2011) Investigation of vaporized submicron perfluorocarbon droplets as an ultrasound contrast agent. Ultrasound Med Biol 37: 1271–1279
Reznik N, Shpak O, Gelderblom EC, Williams R, de Jong N, Versluis M, Burns PN (2013) The efficiency and stability of bubble formation by acoustic vaporization of submicron perfluorocarbon droplets. Ultrasonics 53:1368–1376
Reznik N, Lajoinie G, Shpak O, Gelderblom EC, Williams R, de Jong N, Versluis M, Burns PN (2014) On the acoustic properties of vaporized submicron perfluorocarbon droplets. Ultrasound Med Biol 40:1379–1384
Schad KC, Hynynen K (2010) In vitro characterization of perfluorocarbon droplets for focused ultrasound therapy. Phys Med Biol 55:4933–4947
Schroeder A, Avnir Y, Weisman S, Najajreh Y, Gabizon A, Talmon Y, Kost J, Barenholz Y (2007) Controlling liposomal drug release with low frequency ultrasound: mechanism and feasibility. Langmuir 23:4019–4025
Schroeder A, Honen R, Turjeman K, Gabizon A, Kost J, Barenholz Y (2009) Ultrasound triggered release of cisplatin from liposomes in murine tumors. J Control Release 137(1):63–68
Segers T, Versluis M (2014) Acoustic bubble sorting for ultrasound contrast agent enrichment. Lab Chip 14: 1705–1714
Shaw GJ, Meunier JM, Huang SL, Lindsell CJ, McPherson DD, Holland CK (2009) Ultrasound-enhanced thrombolysis with tPA-loaded echogenic liposomes. Thromb Res 124:306–310
Shea JE, Nam KH, Rapoport N, Scaife CL (2011) Genexol inhibits primary tumour growth and metastases in gemcitabine-resistant pancreatic ductal adenocarcinoma. HPB (Oxford) 13:153–157
Sheeran PS, Luois S, Dayton PA, Matsunaga TO (2011) Formulation and acoustic studies of a new phase-shift agent for diagnostic and therapeutic ultrasound. Langmuir 27:10412–10420
Shortencarier MJ, Dayton PA, Bloch SH, Schumann PA, Matsunaga TO, Ferrara KW (2004) A method for radiation-force localized drug delivery using gas-filled lipospheres. IEEE Trans Ultrason Ferroelectr Freq Control 51:822–831
Shpak O, Kokhuis TJ, Luan Y, Lohse D, de Jong N, Fowlkes B, Fabiilli M, Versluis M (2013) Ultrafast dynamics of the acoustic vaporization of phase-change microdroplets. J Acoust Soc Am 134:1610–1621
Shpak O, Verweij M, Vos HJ, de Jong N, Lohse D, Versluis M (2014) Acoustic droplet vaporization is initiated by superharmonic focusing. Proc Natl Acad Sci U S A 111:1697–1702
Smith DA, Vaidya SS, Kopechek JA, Huang SL, Klegerman ME, McPherson DD, Holland CK (2010) Ultrasound-triggered release of recombinant tissue-type plasminogen activator from echogenic liposomes. Ultrasound Med Biol 36:145–157
Soman NR, Marsh JN, Hughes MS, Lanza GM, Wickline SA (2006) Acoustic activation of targeted liquid perfluorocarbon nanoparticles does not compromise endothelial integrity. IEEE Trans Nanobioscience 5: 69–75

Soman NR, Baldwin SL, Hu G, Marsh JN, Lanza GM, Heuser JE, Arbeit JM, Wickline SA, Schlesinger PH (2009) Molecularly targeted nanocarriers deliver the cytolytic peptide melittin specifically to tumor cells in mice, reducing tumor growth. J Clin Invest 119: 2830–2842

Staruch R, Chopra R, Hynynen K (2011) Localised drug release using MRI-controlled focused ultrasound hyperthermia. Int J Hyperthermia 27:156–171

Stieger SM, Caskey CF, Adamson RH, Qin S, Curry FR, Wisner ER, Ferrara KW (2007) Enhancement of vascular permeability with low-frequency contrast-enhanced ultrasound in the chorioallantoic membrane model. Radiology 243:112–121

Stone MJ, Frenkel V, Dromi S, Thomas P, Lewis RP, Li KC, Horne M 3rd, Wood BJ (2007) Pulsed-high intensity focused ultrasound enhanced tPA mediated thrombolysis in a novel in vivo clot model, a pilot study. Thromb Res 121:193–202

Sutton JT, Haworth KJ, Pyne-Geithman G, Holland CK (2013a) Ultrasound-mediated drug delivery for cardiovascular disease. Expert Opin Drug Deliv 10:573–592

Sutton JT, Ivancevich NM, Perrin SR Jr, Vela DC, Holland CK (2013b) Clot retraction affects the extent of ultrasound-enhanced thrombolysis in an ex vivo porcine thrombosis model. Ultrasound Med Biol 39: 813–824

Tartis MS, McCallan J, Lum AF, LaBell R, Stieger SM, Matsunaga TO, Ferrara KW (2006) Therapeutic effects of paclitaxel-containing ultrasound contrast agents. Ultrasound Med Biol 32:1771–1780

Ten Kate GL, van den Oord SC, Sijbrands EJ, van der Lugt A, de Jong N, Bosch JG, van der Steen AF, Schinkel AF (2013) Current status and future developments of contrast-enhanced ultrasound of carotid atherosclerosis. J Vasc Surg 57:539–546

Thakkar D, Gupta R, Monson K, Rapoport N (2013) Effect of ultrasound on the permeability of vascular wall to nano-emulsion droplets. Ultrasound Med Biol 39:1804–1811

Thomas DH, Sboros V, Emmer M, Vos H, de Jong N (2013) Microbubble oscillations in capillary tubes. IEEE Trans Ultrason Ferroelectr Freq Control 60: 105–114

Tran TD, Caruthers SD, Hughes M, Marsh JN, Cyrus T, Winter PM, Neubauer AM, Wickline SA, Lanza GM (2007) Clinical applications of perfluorocarbon nanoparticles for molecular imaging and targeted therapeutics. Int J Nanomedicine 2:515–526

Treat LH, McDannold N, Vykhodtseva N, Zhang Y, Tam K, Hynynen K (2007) Targeted delivery of doxorubicin to the rat brain at therapeutic levels using MRI-guided focused ultrasound. Int J Cancer 121:901–907

Unger EC, Porter T, Culp W, Labell R, Matsunaga T, Zutshi R (2004) Therapeutic applications of lipid-coated microbubbles. Adv Drug Deliv Rev 56:1291–1314

Vujaskovic Z, Kim DW, Jones E, Lan L, McCall L, Dewhirst MW, Craciunescu O, Stauffer P, Liotcheva V, Betof A, Blackwell K (2010) A phase I/II study of neoadjuvant liposomal doxorubicin, paclitaxel, and hyperthermia in locally advanced breast cancer. Int J Hyperthermia 26:514–521

Vykhodtseva N, McDannold N, Hynynen K (2006) Induction of apoptosis in vivo in the rabbit brain with focused ultrasound and optison. Ultrasound Med Biol 32:1923–1929

Vykhodtseva N, McDannold N, Hynynen K (2008) Progress and problems in the application of focused ultrasound for blood–brain barrier disruption. Ultrasonics 48:279–296, Epub 2008 Apr 2014

Wheatley MA, Forsberg F, Oum K, Ro R, El-Sherif D (2006) Comparison of in vitro and in vivo acoustic response of a novel 50:50 PLGA contrast agent. Ultrasonics 44:360–367

Wickline SA, Neubauer AM, Winter PM, Caruthers SD, Lanza GM (2007) Molecular imaging and therapy of atherosclerosis with targeted nanoparticles. J Magn Reson Imaging 25:667–680

Wilson K, Homan K, Emelianov S (2012) Biomedical photoacoustics beyond thermal expansion using triggered nanodroplet vaporization for contrast-enhanced imaging. Nat Commun 3:618

Winter PM, Cai K, Caruthers SD, Wickline SA, Lanza GM (2007) Emerging nanomedicine opportunities with perfluorocarbon nanoparticles. Expert Rev Med Devices 4:137–145

Winter PM, Caruthers SD, Zhang H, Williams TA, Wickline SA, Lanza GM (2008) Antiangiogenic synergism of integrin-targeted fumagillin nanoparticles and atorvastatin in atherosclerosis. JACC Cardiovasc Imaging 1:624–634

Wong Z, Krifgans O, Qamar A, Fowlkes J, Bull J (2011) Bubble evolution in acoustic droplet vaporization at physiological temperature via ultra-high speed imaging. Soft Matter 7:4009–4016

Yarmolenko PS, Zhao Y, Landon C, Spasojevic I, Yuan F, Needham D, Viglianti BL, Dewhirst MW (2010) Comparative effects of thermosensitive doxorubicin-containing liposomes and hyperthermia in human and murine tumours. Int J Hyperthermia 26:485–498

Yu JX, Kodibagkar VD, Cui W, Mason RP (2005) 19 F: a versatile reporter for non-invasive physiology and pharmacology using magnetic resonance. Curr Med Chem 12:819–848

Yuh EL, Shulman SG, Mehta SA, Xie J, Chen L, Frenkel V, Bednarski MD, Li KC (2005) Delivery of systemic chemotherapeutic agent to tumors by using focused ultrasound: study in a murine model. Radiology 234:431–437

Zhang M, Fabiilli ML, Haworth KJ, Fowlkes JB, Kripfgans OD, Roberts WW, Ives KA, Carson PL (2010) Initial investigation of acoustic droplet vaporization for occlusion in canine kidney. Ultrasound Med Biol 36:1691–1703

Zheng H, Kruse DE, Stephens DN, Ferrara KW, Sutcliffe P, Gardner E (2008) A sensitive ultrasonic imaging method for targeted contrast microbubble detection. Conf Proc IEEE Eng Med Biol Soc 2008:5290–5293

Zhou HF, Chan HW, Wickline SA, Lanza GM, Pham CT (2009) Alphavbeta3-targeted nanotherapy suppresses inflammatory arthritis in mice. FASEB J 23:2978–2985

Bubble-Assisted Ultrasound: Application in Immunotherapy and Vaccination

14

Jean-Michel Escoffre, Roel Deckers, Clemens Bos, and Chrit Moonen

Abstract

Bubble-assisted ultrasound is a versatile technology with great potential in immunotherapy and vaccination. This technology involves the exposure of immune cells (i.e., dendritic cells, lymphocytes) *in-vitro* or diseased tissues (i.e., brain, tumor) *in-vivo* to ultrasound treatment with gas bubbles. Bubble destruction leads to physical forces that induce the direct delivery of weakly permeant immuno-stimulatory molecules either into the cytoplasm of immune cells, or through the endothelial barrier of diseased tissues. Hence, therapeutic antibodies (i.e., antibody-based immunotherapy) and cytokine-encoding nucleic acids (i.e., cytokine gene therapy) can be successfully delivered into diseased tissues, thus improving immune responses. In addition, protein antigens, as well as antigen-encoding nucleic acids (pDNA, mRNA), can be delivered into dendritic cells (i.e., dendritic cell-based vaccines), thus leading to a long-lasting prophylactic or therapeutic immunization. This chapter focuses on the state-of-the-art of bubble-assisted ultrasound in the field of immunotherapy and vaccination.

Keywords

Ultrasound • Bubble • Immunotherapy • Vaccination

14.1 Introduction

Immunotherapy and vaccination are promising strategies for inducing long-lasting therapeutic or prophylactic immunization against bacterial and viral infections, as well as brain diseases and cancer (Fig. 14.1). Immunotherapy aims to stimulate immune response in diseased patients by delivering immuno-stimulating molecules (i.e., antibodies,

J.-M. Escoffre (✉) • R. Deckers • C. Bos (✉)
C. Moonen
Imaging Division, University Medical Center Utrecht, Utrecht, The Netherlands
e-mail: j.r.escoffre@umcutrecht.nl; c.bos@umcutrecht.nl

© Springer International Publishing Switzerland 2016

J.-M. Escoffre, A. Bouakaz (eds.), *Therapeutic Ultrasound*, Advances in Experimental Medicine and Biology, Vol. 880, DOI 10.1007/978-3-319-22536-4_14

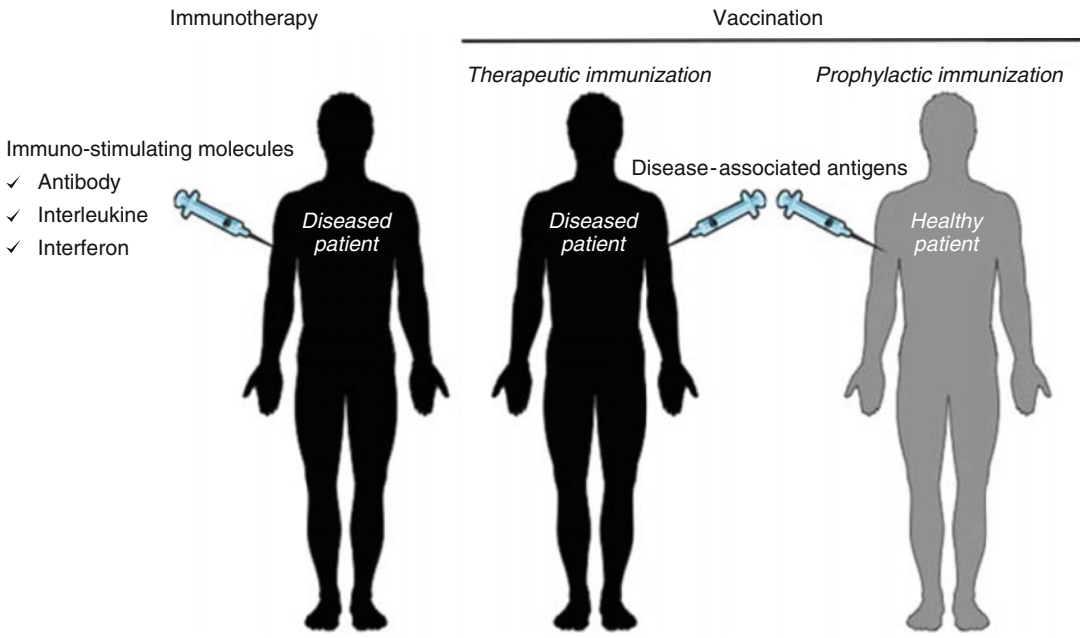

Fig. 14.1 Immunotherapy and vaccination

interferons, interleukines) natively produced by the immune cells. In the vaccination field, prophylactic and therapeutic immunizations are reported. The prophylactic vaccination aims to induce immune response against disease by administrating disease-associated antigens (Ags) in healthy patients while the therapeutic vaccination, also defined as an immunotherapy, intends to stimulate the immune response in diseased patients. Prophylactic immunization will lead to rapid and efficient immune response during the disease occurrence. The immuno-stimulating molecules and Ags can be delivered either in the form of recombinant protein or encoded by nucleic acids (i.e., pDNA, mRNA). However, the physico-chemical properties including charge, hydrophilicity, size, and molecular weight reduce their access to the biological targets (i.e., immune cells, skin, skeletal muscle) thus limiting the therapeutic effectiveness. Consequently, the clinical development of these therapies requires the use of safe and efficient methods that deliver the immuno-stimulating molecules and Ags. A suitable delivery method has to overcome several biological obstacles: (i) it should protect the recombinant protein and nucleic acids against degradation by enzymes present in the blood or in the target tissues; (ii) it ought to increase their passage through biological barriers (i.e., vascular endothelium, plasma membrane) and (iii) it should improve their diffusion in interstitial tissue. Strategies for the delivery of nucleic acids as well as recombinant proteins including the use of viral, physical and chemical methods have been proposed.

Among the delivery methods tested, the combination of high frequency ultrasound (1–10 MHz) and gas bubbles (e.g., microbubble, nanobubble, liposomal bubble) was introduced as a physical, non-viral method that is currently under evaluation for gene and drug delivery (See Chaps. 12, 13, 14, 15, 16, 17, 18, and 19). Bubble-assisted ultrasound involves the treatment of a desired volume of cells *in-vitro* or tissue *in-vivo* with ultrasound in the presence of bubbles. These bubbles are formulated as lipid, albumin or polymer shelled micrometer (e.g., microbubbles) or nanometer (i.e., nanobubbles, liposomal bubbles) sized gas bodies in aqueous suspension (See Chap. 11). They are then mixed with cells *in-vitro* or administered by intravascular/intratissue injection *in-vivo*. The exposure of bubbles to ultrasound causes their periodic oscillations (also referred to as stable cavitation) and/or their

collapse (inertial cavitation) under suitable acoustic conditions (See Chap. 9). It is now known that bubble oscillations can induce physical phenomena (e.g., shock waves, micro-streamings, micro-jets) that can disturb the integrity of biological barriers (Doinikov and Bouakaz 2010; Ohl et al. 2006; Ohl and Wolfrum 2003). The use of bubble-assisted ultrasound to deliver therapeutic molecules to diseased tissues has been extensively explored over the past decade. Indeed, this technology has been successfully used to transfer nucleic acids into the heart, vessels, liver, skeletal muscle and tumors (Escoffre et al. 2013b). In addition, *in-vivo* local delivery of low molecular weight chemotherapeutics has been reported (Escoffre et al. 2013a; Iwanaga et al. 2007) and is now under clinical investigation (Kotopoulis et al. 2013). For both *in-vitro* and *in-vivo* applications, this technology enables delivery of exogenous molecules with minimal cell or tissue damage, inflammation and/or immunological response (Hauff et al. 2005; Taylor et al. 2007; Escoffre et al. 2010a). In addition, ultrasound can be non-invasively targeted to a specific volume of superficial tissue (e.g., skin), as well as deeply embedded organs (e.g., liver). Together, these properties make bubble-assisted ultrasound an innovative and compelling method for the delivery of nucleic acids, antibodies (Abs), cytokines and Ags.

Recently, the applications of bubble-assisted ultrasound have been extended to immunotherapy and vaccination, especially for the treatment of brain diseases and cancer. The focus of this chapter is to review the current applications of bubble-assisted ultrasound in these fields. The limitations and the future developments of bubble-assisted ultrasound will be further discussed.

14.2 Ab-Based Immunotherapy

14.2.1 Applications in Neurology

The increasing knowledge of molecular mechanisms of brain diseases and the absence of successful therapies allowed the advent of Ab-based immunotherapies for the treatment of neurodegenerative diseases. Nevertheless, this attractive therapeutic option is restricted by a physiological barrier, the blood-brain barrier (BBB) (Wong et al. 2013). This barrier plays a major role in the brain homeostasis. The BBB consists of pericytes, astrocytes, neurons and microglia and endothelial cells in close contact. The endothelial cells of the central nervous system (CNS) are unique cells that are tightly fused to each other by intercellular attachments known as tight junctions. The BBB limits the passage of most molecules (e.g., nucleic acids or antibodies) from the circulation into the brain parenchyma, thus precluding their use in the treatment of neurodegenerative diseases and brain tumors. The factors that determine molecular extravasation are their molecular charge and size (e.g., 150 kDa for Abs), their lipid solubility (e.g., Abs are hydrophilic) and whether or not these molecules use any transport processes across the BBB (e.g., transcytosis).

To overcome these limitations, different strategies of antibody delivery across the intact BBB have been evaluated. These include chemical or genetic modification of the antibodies with cationic compounds (i.e., absorptive-mediated transcytosis) or with endogenous molecules necessary for normal brain function (i.e., receptor-mediated transcytosis) (Chacko et al. 2013). However, the main limitation of these approaches is the putative loss of Ab function. Transient BBB disruption (BBBD) is another strategy that improves intracerebral delivery of antibodies. Indeed, intra-arterial (i.a.) injection of hyperosmotic solutions (e.g., 1.6 M mannitol) or pharmacological agents (e.g., bradykinin) has been used to induce a transient BBBD, which was, however, non-focal and involved the entire brain tissue supplied by the injected artery branch. Local BBBD can be clinically performed by direct stereotaxis-guided injection of molecules into the targeted brain site, however this method remains invasive.

Nowadays, many efforts are being made to increase the BBB permeability to facilitate local delivery of therapeutics into the brain. Since the 1990s, local BBBD using microbubble-assisted ultrasound under magnetic resonance imaging

(MRI) guidance is under investigation (Aryal et al. 2014; Burgess and Hynynen 2014). Thus, ultrasound-driven microbubble oscillations near the BBB may promote the extravasation and the uptake of antibodies into the desired brain region. MRI provides the identification of the target location, and allows the assessment of the efficacy of the BBBD on the basis of the extravasation of MRI contrast agents. Owing to this method, several groups around the world have successfully reported the targeted delivery of chemotherapeutics, genes, therapeutic Abs and the extravasation of immune or stem cells into the CNS (See Chap. 16).

Example – Alzheimer's disease

Alzheimer's disease (AD) is a progressive and incurable neurodegenerative disorder that affects several tens of millions of people worldwide. AD pathogenesis is thought to be correlated to the accumulation of beta-amyloid (Aβ) plaques and hyperphosphorylated tau tangles (Ittner and Gotz 2011). New knowledge of the pathogenesis of AD has allowed emerging diagnostic and therapeutic strategies that aim at detecting and reducing Aβ plaques. Ab-based immunotherapy is a promising therapeutic option for Aβ plaque clearance, either by active immunization with Aβ peptides or genes, or by passive immunization after administration of anti-Aβ Abs (Liu et al. 2012). Current treatment of AD patients requires long-term intravenous (i.v.) perfusion of high doses of anti-Aβ Abs in order to remove Aβ plaques from the brain (Opar 2008; Wilcock and Colton 2008). In AD mouse models, i.v. and i.a. injection of a high dose of 500 μg anti-Aβ Abs resulted in clearance of Aβ plaques and cognitive progress, while pharmacokinetic analyses revealed that less than 1 % of Abs actually reached the brain (Bard et al. 2000; DeMattos et al. 2001; Banks et al. 2002). However, Thakker et al.., reported that the intracerebral injection of 40 μg anti-Aβ Abs was more efficient at clearing Aβ plaques than intra-peritoneal (i.p.) administration of 200 μg Abs (Thakker et al. 2009). Hence, targeted intracerebral delivery of anti-Aβ Abs allows an effective amount of Ab access to the Aβ plaque-heavy anatomical regions, thus leading to an improved treatment in AD mice models. However, most technical procedures required to achieve this are invasive. In this context, Raymond et al. investigated anti-Aβ Ab delivery into the brain of AD mouse models using MRI-guided and microbubble-assisted focused ultrasound (MRIgFUS) (Raymond et al. 2008). MRI guidance allowed selective treatment and monitoring of affected brain regions (Fig. 14.2a, b).

After i.v. injection of anti-Aβ Abs (0.1 mL of 53 mg/mL whole serum), mice were sonicated (0.69 MHz, PRF[1] of 1 Hz, DC[2] of 1 %, PNP[3] of 0.67–0.8 MPa, duration of 40–45 s) with concomitant i.v. administration of Definity® microbubbles (0.01 mL 1:10 diluted contrast agent). Subsequently, BBB disruption was monitored with T1-weighted fast spin echo MRI following i.v. injection of Magnevist® (MR contrast agent; 62.5 μL/kg). The results revealed that sonicated brain regions displayed a 2.7 ± 1.2-fold increase in anti-Aβ Abs binding to Aβ plaques. No Ab extravasation was detected in the unsonicated regions. In addition, T1-weighted fast-spin echo MRI and anti-Aβ Abs detection in sonicated regions showed a positive correlation between the MRI intensity change and Ab concentration, thus indicating that the BBBD was responsible for the intracerebral delivery of anti-Aβ Abs. Afterwards, this procedure was successfully reproduced in two different transgenic strains (i.e., APPswe:PSEN1dE9, PDAPP) across a large age range (i.e., 9–26 months). Little or no tissue damage (i.e., scattered petechia) was detected in sonicated brain tissues, thus revealing the safety of this approach.

This same group then continued to investigate the therapeutic benefit of anti-Aβ Abs with FUS-mediated BBBD in a transgenic AD mouse model (i.e., TgCRND8) (Jordao et al. 2010). Following a similar procedure, the mice brains were targeted with ultrasound (0.558 MHz, 10 ms burst/Hz, PNP of 0.3 MPa, duration of 120 s) after i.v. co-administration of Definity® (160 μL/kg), Gadovist® (MR contrast agents; 0.1 mL/kg) and 40 μg of anti-Aβ Abs (BAM-10) (Fig. 14.2a).

[1] *PRF* pulse repetition frequency.

[2] *DC* duty cycle.

[3] *PNP* peak negative pressure.

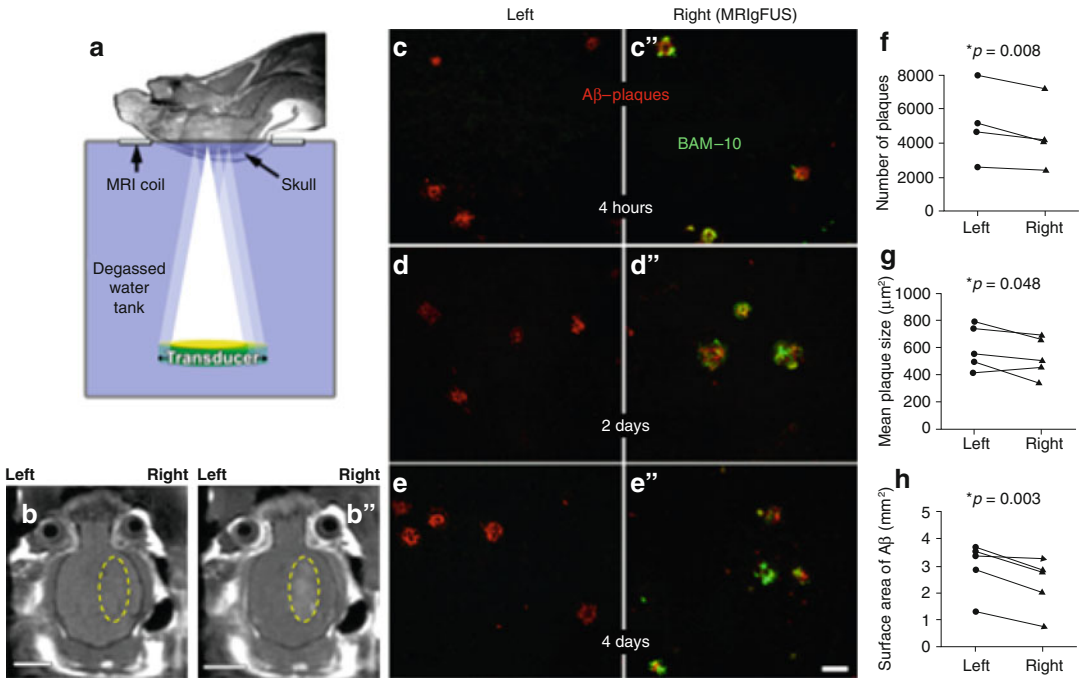

Fig. 14.2 Anti-Aβ Abs (BAM-10) delivery using microbubble-assisted FUS under MRI guidance (MRIgFUS). Mice were positioned in a supine position (**a**). The right sides of mice brains were targeted with FUS after i.v. co-injection of Definity®, Gadovist® and anti-Aβ Abs (BAM-10). T1-weighted contrast-enhanced MRI scans were used to position ultrasound foci prior to (**b**) and following (**b′**) transcranial FUS treatment. BAM-10 antibodies (*green stain*) and Aβ plaques (*red stain*) were detected using immunofluorescence assays at 4 h (**c**, **c′**), 2 days (**d**, **d′**) and 4 days (**e**, **e′**) post-treatment (scale bar 50 μm). In 4 days, the mean count (**f**), size (**g**) and surface area (**h**) of Aβ plaques of right sonicated and left unsonicated sides of mice brains were determined (Reprinted with permission from Jordao et al. (2010))

Within minutes following the sonication, Gadovist® was taken up in the targeted brain tissues (Fig. 14.2b) and anti-Aβ Abs were later detected bound to Aβ plaques (Fig. 14.2c–e). Four days post-treatment, the number and mean size of Aβ plaques as well as surface area of Aβ were significantly decreased in right sonicated side of mice brain compared to left unsonicated side of brain (Fig. 14.2f–h). In conclusion, microbubble-assisted FUS under MRI guidance is a promising non-invasive technology for the local delivery of low but therapeutic doses of anti-Aβ Abs.

14.2.2 Applications in Oncology

Cancer therapy has considerably developed over the past decade, especially in the area of therapeutic Abs (Scott et al. 2012). Unlike chemotherapy, Abs are able to distinguish between healthy and tumor tissues, thus potentially providing efficient therapy, while minimizing adverse side effects to healthy tissues. Abs potentially provide effective therapy by targeting specific molecular targets involved in biological pathways of tumor growth and dissemination, thus leading to tumor cell growth inhibition. In *in-vivo* experiments, Abs activity is found to depend on natural killer cell action, identifying antibody-dependent cellular cytotoxicity (ADCC) as the main mechanism of Abs action. Recently, the FDA and EMA have approved several Ab-based immunotherapies for the clinical treatment of hematological malignancies (e.g., Zevalin®, Rituxan®) and solid tumors (e.g., Erbitux®, Herceptin®). In clinical trials, these Abs decreased mortality in patients with metastatic or early cancer, either as a monotherapy or combined with chemotherapy.

However, Ab-based immunotherapy is rarely curative in solid tumor. Owing to their poor intratumoral (i.t.) bioavailability, systemic injection of high or frequent Ab doses is necessary to reach therapeutic efficacy. Consequently, these Ab doses are associated with severe side effects and this immunotherapy becomes an expensive option. Indeed, the limited success of this approach for solid tumors is due to a number of factors, including Ab physicochemical properties, and the biological characteristics of the tumor microenvironment (Frenkel 2008). The large size of antibodies (150 kDa) may provide a long circulatory half-life ($t_{1/2}$>21 days in humans), but on the other hand decreases its extravasation and penetration into tumor tissues. Contrary to healthy tissues, tumor tissues have a high interstitial fluid pressure due to their leaky vasculature and lack of functional lymphatics (Boucher et al. 1990). These high pressures establish an outward fluid motion from the periphery of the solid tumor and reduce fluid infiltration across the vascular wall. As a result, the extravasation and tumor accumulation of convection-dependent macromolecules, such as Abs, are severely limited. The increase in mean distance between tumor cells and vessels is another limitation for insufficient delivery of Abs. Indeed, high cell proliferation levels lead to tumor cells forcing vessels apart, thus resulting in a decrease in vascular density and a limitation in the access of Abs to distant tumor cells (Minchinton and Tannock 2006). Once in the tumor interstitium, extracellular matrix and binding-site barriers limit the interstitial transport of Abs through non-specific and specific interactions, respectively. Altogether these limitations prevent sufficient and uniform distribution of Abs in solid tumors. Recently, microbubble-assisted ultrasound has been investigated to improve Ab delivery in oncology.

Example 1: Cetuximab and Head and Neck Squamous Cell Carcinoma

Head and neck squamous cell carcinoma (HNSCC) is the sixth most common cancer worldwide with an estimated global incidence of 500,000 new cases and is known for its rapid clinical progression. During the past 25 years, treatments combining surgery, radiotherapy and chemotherapy have improved disease outcome, but this is linked to significant patient morbidity and an increase in treatment-related deaths (Price and Cohen 2012). The increasing knowledge on HNSCC pathogenesis allowed the identification of a new molecular target, the epidermal growth factor receptor (EGFR) (Bose et al. 2013). EGFR was found to be overexpressed in HNSCC and has been associated with more advanced disease and unfavorable outcomes. These investigations led to the development of a novel targeted therapeutic, cetuximab (Erbitux®), a chimeric human:murine IgG1 monoclonal antibody that targets EGFR. Clinical trials have revealed modest outcome improvements in HNSCC treated with this Ab, especially when combined with radiotherapy (Bonner et al. 2006). In addition, adverse side effects of cetuximab treatment alone or combined with other therapies still significantly contribute to patient morbidity (Logan 2009). In this context, any method increasing in intra-tumor cetuximab bioavailability, while simultaneously minimizing side effects to healthy tissues, would be an attractive method for HNSCC therapy.

Recently, Heath et al. examined the therapeutic benefit of cetuximab delivery by microbubble-assisted ultrasound for the treatment of HNSCC (Heath et al. 2012). *In-vitro* results showed that this method (Definity® microbubbles; 1 MHz, MI[4] of 0.5, PRP[5] of 0.01 s, DC of 20 %, duration of 5 min) resulted in a 30 % increase in intracellular uptake of cetuximab in HNSCC cells compared to cetuximab treatment alone. In agreement with previous data, this enhanced Ab incorporation was positively correlated to a significant increase in cell apoptosis. *In-vivo* cetuximab delivery using microbubble-assisted ultrasound (Definity® microbubbles; 1 MHz, MI of 0.5, PRP of 5 s, DC of 20 %, duration of 5 min) in subcutaneous HNSCC tumor xenografts led to a 30 % decrease in tumor size compared to cetuximab treatment alone. Histopathological analyses of

[4] *MI* mechanical index.

[5] *PRP* pulse repetition period.

tumors revealed that the reduction in tumor size was positively correlated to a decrease in microvessel density and to an increase in apoptosis. In addition, no tissue damage was reported in the tumor surrounding tissues after treatment. In conclusion, cetuximab delivery using microbubble-assisted ultrasound showed a therapeutic benefit.

Example 2 – Trastuzumab and Brain Metastatic Breast Cancer

Breast cancer is the most common cancer in women worldwide and the principle cause of death from cancer among women. Moreover, 25–30 % of human breast cancers overexpress the human epidermal growth factor receptor (HER-2), which is predictive of poor clinical outcome (Arteaga et al. 2012). HER-2 positive breast cancer has been found to metastasize to the CNS more frequently than all other breast cancer types (Leyland-Jones 2009). The prognosis for patients with CNS metastases is in majority very poor. The standard treatments are steroids combined with radiotherapy, surgery or stereotaxic radiosurgery (Chang and Lo 2003). As previously described, chemotherapy is generally excluded as an effective therapeutic option due to the BBB. However, in most primary brain tumors and metastases, the permeability of the tumor vasculature is heterogeneous, thus facilitating free access of toxic concentrations of chemotherapeutics to a small subset of highly perfused metastases (Eichler et al. 2011). Nevertheless, metastatic seeds could be protected by the BBB of the surrounding healthy tissues. Thus, the BBB remains one of the main hindrances to patient cure. Unfortunately today, facing the lack of efficient therapeutic alternatives, the number of women with CNS metastases and recurrence after radiotherapy is still increasing.

Trastuzumab (Herceptin®) is a humanized monoclonal Ab that targets HER-2 overexpressed in breast tumors (Hudis 2007). This immunotherapy decreases mortality in patients with early and metastatic breast cancer, either as a monotherapy or combined with chemotherapy and/or radiotherapy (Joensuu et al. 2006; Horton et al. 2010). This survival benefit is mostly due to control of systemic disease, with the CNS remaining a sanctuary site. Nevertheless, clinical investigations have reported that the increasing use of trastuzumab has resulted in a higher incidence of brain metastases from primary tumors (Bendell et al. 2003).

In order to effectively treat CNS metastases, trastuzumab will need to overcome the limitations imposed by the BBB and the tumor microenvironment. Recently, Kinoshita et al. investigated the use of microbubble-assisted ultrasound to deliver trastuzumab into the brain of healthy mice (Kinoshita et al. 2006). Using a 0.69 MHz focused ultrasound transducer and the i.v. co-injection of trastuzumab (20 mg/kg) and Optison® microbubbles (1.6 mL/kg) with Magnevist® (1.6 mL/kg), the BBB was non-invasively opened under MRI guidance. After 0.6 MPa or 0.8 MPa sonication (PRF of 1 Hz, DC of 1 %, duration of 40s), the amount of trastuzumab in the targeted brain tissue increased to 1.50 and 3.25 ng/g of tissue, respectively. No trastuzumab was detected in unsonicated brain tissues. This intracerebral delivery was positively correlated to BBBD monitored by T1-weighted fast-spin echo MRI. In addition, histopathological analyses revealed that the sonication resulted in few scattered, extravasated red blood cells and apoptotic cells, whose the numbers increased with increasing acoustic pressure. However, no ischemic neurons were detected in the sonicated brain tissue. In conclusion, this technology is a promising method to increase the intracerebral bioavailability of trastuzumab.

Six years later, Park et al. assessed the therapeutic benefit of this method in a rat model of breast cancer metastases in the brain (Park et al. 2012). To this end, HER-2 positive human breast cancer cells (i.e., BT-474) were intracranially implanted into nude rats. Animals received 6 weekly sonication treatments (0.69 MHz, PRF of 1 Hz, DC of 1 %, PNP of 0.69 MPa, duration of 60s) under MRI guidance, combined with i.v. injection of trastuzumab (2 mg/kg), Magnevist® (0.2 mL/kg) and Definity® microbubbles (10 µL/kg) (Fig. 14.3). Tumor growth and survival rates were monitored using MRI for 7 weeks after treat-

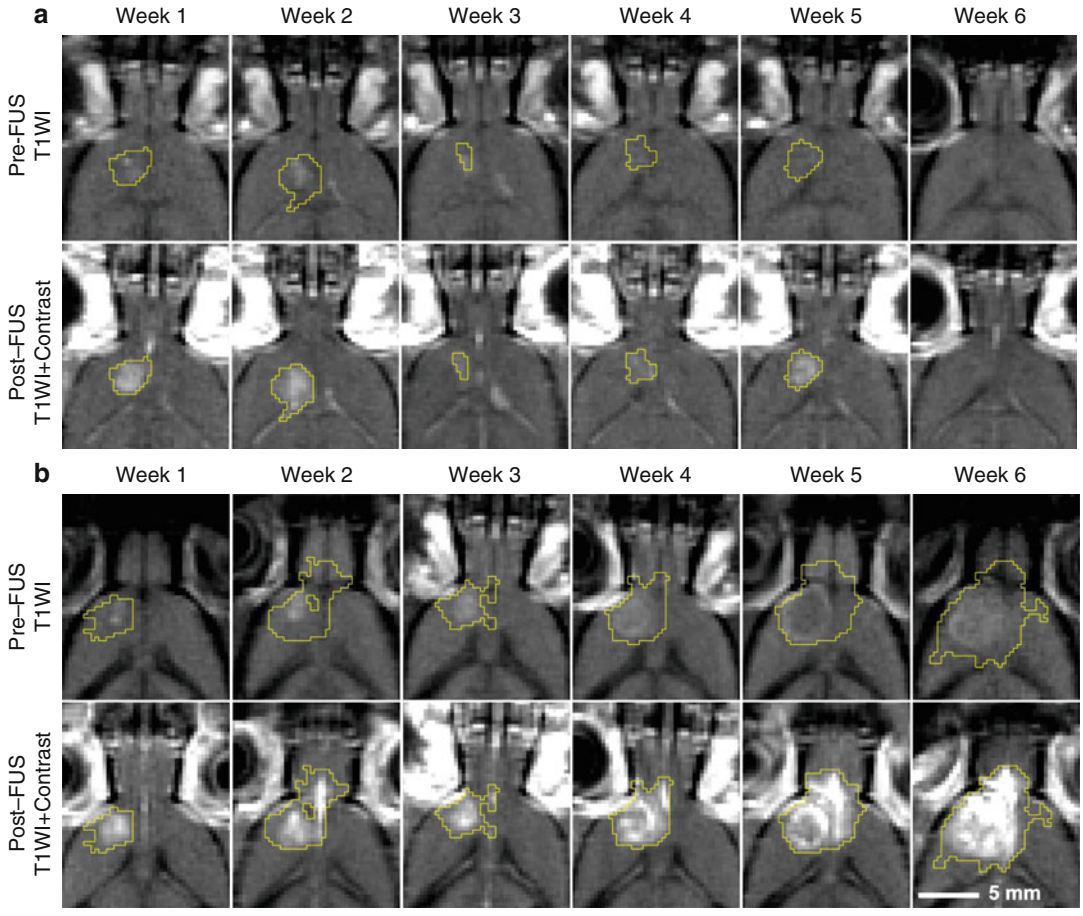

Fig. 14.3 Trastuzumab delivery using microbubble-assisted FUS under MRI guidance (MRgFUS). Serial T1-weighted images (T1WI) were acquired before (Pre-FUS) and after (Post-FUS) six treatments with trastuzumab delivered by microbubble-assisted FUS. Human HER-2 positive breast tumor disappeared after 6 weeks (**a**) and another one did not exhibit a strong response (**b**). Post-treatment images were acquired after Magnevist® injection. *Yellow contours* show the brain regions where the signal intensity was at least 5 % above that in non-sonicated brain regions (Reprinted with permission from Park et al. (2012))

ment. Trastuzumab delivery using microbubble-assisted ultrasound resulted in a significant decrease in tumor volume compared to Ab treatment alone (Fig. 14.3a, b). At the study endpoint, tumor eradication was only observed in rats treated by microbubble-assisted ultrasound combined with trastuzumab administration. More than half treated rats survived, resulting in a median survival time of more than 83 days (i.e., at least 17 % longer than trastuzumab treatment alone). To conclude, trastuzumab delivery using microbubble-assisted ultrasound showed a significant therapeutic benefit compared to trastuzumab treatment alone.

14.3 Dendritic Cell-Based Vaccination

Dendritic cells (DCs) are the most potent antigen presenting cells (APCs), and they are able to prime and activate cytotoxic T-lymphocytes (CTL or $CD8^+$ T cells) and T helper lymphocytes (Th or $CD4^+$ T cells) responses (Abbas and Lichtman

2006). $CD8^+$ T cells are involved in the elimination of infected or transformed cells, whereas $CD4^+$ T cells essentially support efficient and long-lasting T and B lymphocyte responses through cytokine production and intercellular interactions. Free Ags induce a potent $CD4^+$ T cell response, while the induction of $CD8^+$ T cell responses is efficiently achieved as a result of the cross-presentation of particle-coupled Ags. In addition, DCs are also involved in the generation of Ab responses through their interactions with B lymphocytes. Immature DCs function as sentinel cells throughout the organism periphery where they recognize and engulf Ags. These Ags are subsequently processed, and DCs migrate to afferent/draining lymph nodes (i.e., secondary lymphoid organs) where the local initiation of immune responses occurs. DCs mature into APCs during their migration, and these mature DCs present epitope peptides derived from Ags via major histocompatibility complex (MHC) class I molecules and MHC class II molecules. At the same time, exogenous Ags may have direct access to the draining lymph node where they are recognized by resident DCs, and a suitable profile of adaptive immune responses is generated under the control of environment-mediated signals. While innocuous Ags usually activate tolerogenic cells, Ags associated with danger signals, such as harmful pathogens, ultimately trigger effector immune cells.

Currently, immunization techniques using live attenuated and killed pathogen-based vaccines have proven efficient immune response induction, thus controlling various infections (Andre 2003). However, such vaccines are not useful for the prevention or the treatment of cancer, autoimmune and allergic disorders. Besides, the use of live attenuated pathogens for vaccination raises extensive safety issues. To overcome these limitations, subunit vaccines based on recombinant or purified Ags have emerged as an alternative option (Foged 2011). Nevertheless, these Ags are poorly immunogenic. Addition of immune-modulating molecules/adjuvants has successfully been described to increase the immunogenicity of recombinant Ag-based vaccines. For decades, research has focused on the development of efficient and safe methods to deliver Ags, peptides, mRNA and pDNA into DCs (Cintolo et al. 2012). These methods include the absorption or covalent linkage of Ags to particles (e.g., lipid or polymer-based nano- or micro-particles), mineral salts (e.g., alum) and antibodies, as well as their encapsulation inside particles. The efficiency of these methods relies on their ability to prevent Ag degradation, thus delivering effective concentrations of Ags into DCs to activate them. The combination of efficient Ag delivery methods with immuno-stimulating molecules could be crucial for the induction of efficient and long-lasting effector and memory immunities. Recently, several studies reported bubble-assisted ultrasound as a promising and efficient method to deliver Ags into DCs (Lemmon et al. 2011; Un et al. 2010, 2011; Oda et al. 2012; De Temmerman et al. 2011). Indeed, recombinant Ags, peptides or nucleic acids can be loaded on gas bubbles during their assembly. Besides, bubbles provide additional protection against Ag degradation. In the following examples, the combination of these intelligent carriers with ultrasound has been successfully reported for the delivery of Ags into DCs for the treatment of melanoma lung metastasis.

Example 1: Delivery of Melanoma-derived Ag Proteins

Melanoma is the leading cause of skin cancer death worldwide and has early tendency to metastasize (Black and Brockway-Lunardi 2013; Ferlay et al. 2013). The 5-year survival of patients with localized melanoma (i.e., confined to the primary site) is between 80 and 90 %, while patients with metastasized melanoma have a 5-year survival below 20 %. The chemoresistance of melanoma, along with the highly tumor heterogeneous response rate for any single or combination of chemotherapeutics, explains that metastatic melanoma leads to the majority of melanoma deaths. As a result, the development of effective therapeutic options, including DC-based immunotherapy, is becoming a challenge for the treatment of metastasized melanoma (Sanlorenzo et al. 2014).

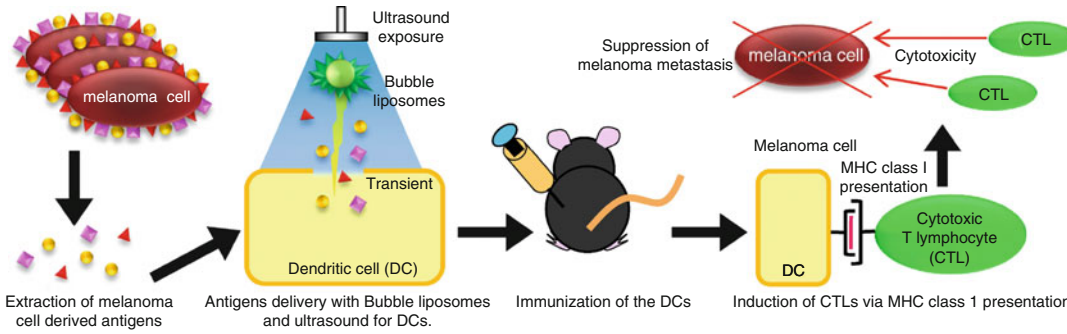

Fig. 14.4 Prophylactic immunization with BLs and ultrasound-treated dendritic cells (Reprinted with permission from Oda et al. (2012))

Recently, prophylactic immunization with DCs, exposed to Ags during bubble liposome (BL)-assisted ultrasound, was investigated for preventing melanoma lung metastasis (Oda et al. 2012). In this approach, the Ags were extracted from melanoma cells and were delivered (50 μg) into DCs using BL-assisted ultrasound (2 MHz, DC of 10 %, burst rate 2 Hz, 2 W/cm^2, 3 × 10s with time interval of 10 s; 120 μg of BLs) (Fig. 14.4).

The delivery efficiency was approximately 74 %. Unlike Ag delivery methods previously described, relying on endocytotic pathways; BL-assisted ultrasound directly delivers the melanoma-associated Ags (MAA) into the cytosol. Accordingly, this approach induces MHC class I-restricted MAA presentation on DCs. To assess the *in-vivo* prophylactic immunization, C57BL/6 mice were immunized twice with DCs before i.v. injection of B16/BL6 melanoma cells. Histopathological analyses revealed that DC-based immunotherapy provided a fourfold decrease in the frequency of melanoma lung metastasis. This investigation demonstrated that BL-assisted ultrasound is an encouraging method for Ag protein delivery into DCs (Fig. 14.5).

Example 2: Delivery of Ag-encoding pDNA

To obtain high therapeutic efficiency from DNA vaccination (also known as genetic vaccination) using tumor-specific Ag-encoding pDNA, it is crucial to deliver pDNA selectively and efficiently into APCs; including DCs (splenic CD11$^+$ cells) and macrophages (non-parenchymal liver cells) (Aurisicchio and Ciliberto 2012). Nevertheless, the two main limitations of this strategy are: (i) the low *in-vitro* and *in-vivo* transfer efficiency of pDNA into APCs using current delivery methods; (ii) the low number of organ APCs, thus limiting the selective delivery of pDNA. Since APCs express a large number of mannose receptors, many research groups have designed mannose-modified non-viral carriers for pDNA delivery into APCs.

Un et al. developed mannose receptor-targeted bubble lipoplexes (BL), which were shown selectivity with regard to APCs and respond to ultrasound (Un et al. 2010). Using a luciferase reporter gene, they demonstrated that the *in-vivo* i.v. injection of targeted BL (400 μL BL incorporating 50 μg pDNA), followed by a transdermal ultrasound exposure (1 MHz, DC of 50 %, burst rate of 10 Hz, intensity of 1 W/cm^2, insonation time 2 min) to the abdominal area, induced a selective 500–800-fold higher luciferase expression in APCs (i.e., splenic CD11$^+$ cells and non-parenchymal liver cells). This enhanced gene expression was positively correlated to the improvement of pDNA delivery efficiency to targeted organs (i.e., spleen and liver). The authors did not observe any severe side effects, such as liver toxicity, with this procedure. Using pDNA-encoding ovalbumin as a model antigen, the authors showed that thrice immunization induced high production of interferon-γ (IFN-γ) by splenic CD11$^+$ cells, thus leading to significant enhancement in the differentiation of helper T cells into Th1 cells. This led to CTL activation with high specific anti-tumor activity against ovalbumin-expressing cells. To investigate the prophylactic effects, ovalbumin-expressing

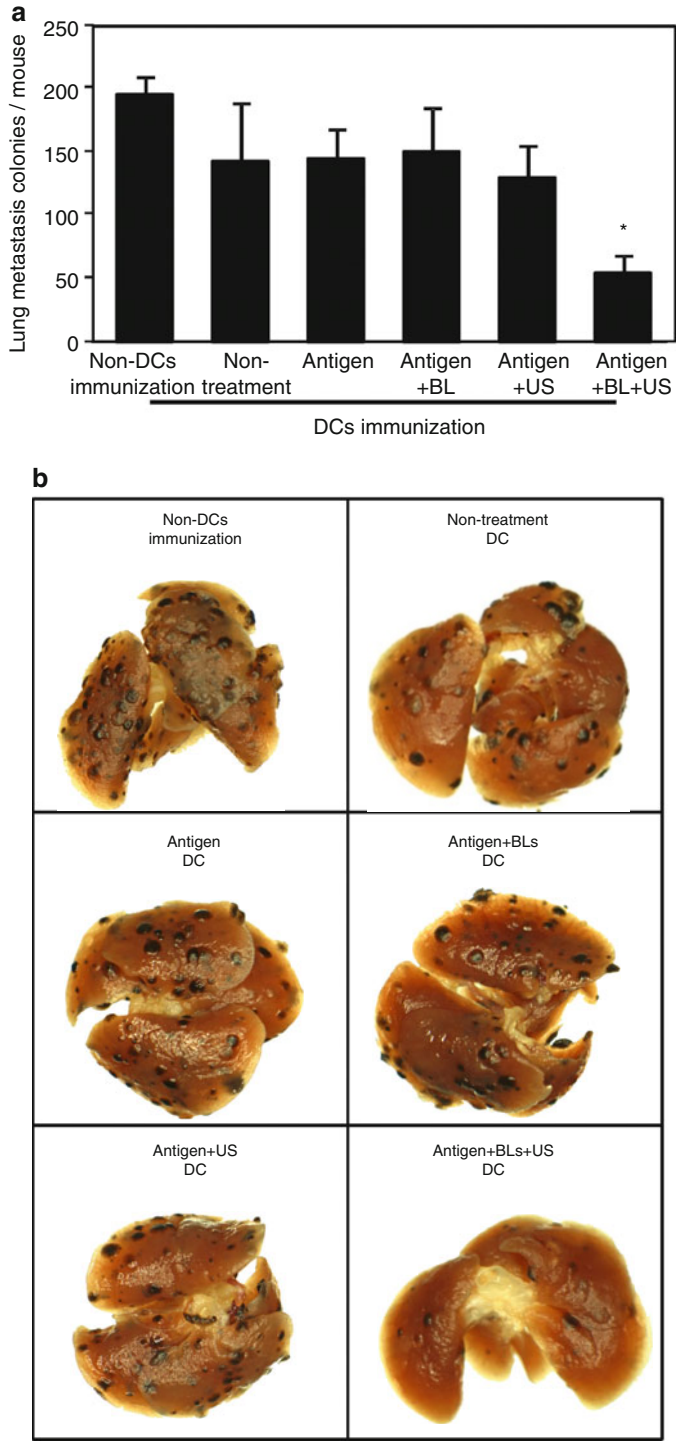

Fig. 14.5 Reduction of melanoma lung metastasis following prophylactic immunization. MAA were delivered in DCs by BL-assisted ultrasound. Mice were immunized with the DCs twice with 1-week interval. One week later, melanoma cells were inoculated through the tail vein. Two weeks after the injection of tumor cells, mice were euthanized. The lungs were visualized by stereomicroscopy (**a**) and the number of lung metastatic colonies was determined (**b**) (Reprinted with permission from Oda et al. (2012))

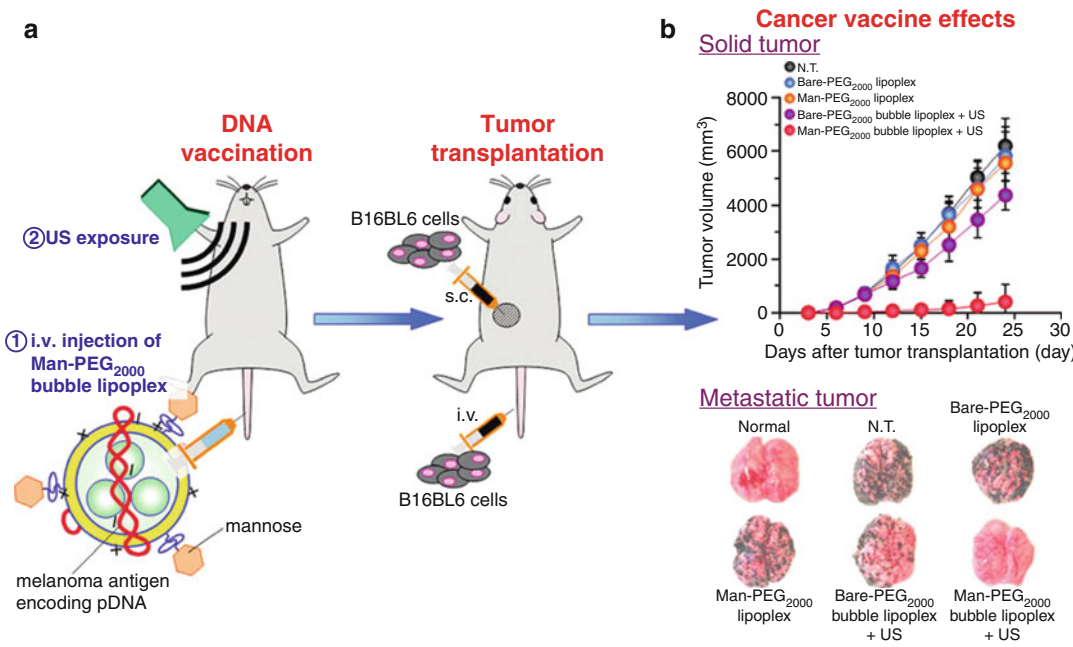

Fig. 14.6 Suppression of melanoma primary tumor and lung metastasis following Ag-encoding pDNA using Man-PEG_{2000} bubble lipoplex-assisted ultrasound. Prophylactic immunization (**a**) induces the inhibition of solid tumor growth (**b**) and lung metastasis (**c**) (Reprinted with permission from Un et al. (2011). Copyright © 2011 American Chemical Society)

tumor cells were subcutaneously transplanted after thrice immunization. Results revealed that DNA vaccination using targeted BL and ultrasound led to a 4.5–5-fold decrease in tumor volume, compared to an immunization with either untargeted BL-assisted ultrasound or with i.v. injection of targeted or bare lipoplexes alone. The survival, as well, of vaccinated mice was significantly prolonged by this DNA immunization procedure. In addition, tumor re-transplantation to completely tumor-rejected mice revealed that anti-tumor effects obtained from this delivery method were maintained for at least 80 days.

A year later, the same authors investigated this DNA vaccination method for metastatic and relapsed murine melanoma (i.e., B16BL6) (Un et al. 2011) (Fig. 14.6a).

Following DNA immunization using targeted BL carrying pDNA, which expressed ubiquitylated melanoma-specific Ags (i.e., gp 100, tyrosinase-related protein 2), the secretion of Th1 cytokines (i.e., IFN-γ, tumor necrosis factor-α) and CTL activities were specifically enhanced in the presence of B16BL6 melanoma Ags. In addition, the authors succeeded in obtaining potent and long-lasting DNA immunization against primary and solid melanoma tumors, as well as melanoma lung metastasis (Fig. 14.6b, c). A complete tumor rejection was reported in 70 % of immunized mice. In addition, these mice showed significantly prolonged survival (80 % at 100 days after tumor transplantation) compared to control groups, where no mouse survived longer than 60 days post-tumor inoculation.

As compared to DNA vaccination, mRNA-based immunization presents several advantages including (i) no integration into the host genome, rendering its method much safer; (ii) the nuclear envelope is a cell barrier for pDNA transfer into the nucleus, especially in non-dividing cells (iii) mRNA generates only transient gene expression which is necessary and sufficient for Ag processing and presentation by DCs. Bubble-assisted ultrasound is currently under investigation for mRNA-based (De Temmerman et al. 2011).

14.4 Cytokine Gene Therapy

The increase of host anti-tumor immunity by the local or systemic expression of cytokines seems to be the favorable therapeutic strategy for affecting growth of all types of tumors. Several Th-1 cytokines, including interleukin-2 (IL-2) (Chi et al. 2003), IL-12 (Suzuki et al. 2010), IL-27 (Zolochevska et al. 2011), INF-γ (Sakakima et al. 2005) and granulocyte macrophage colony stimulating factor (GM-CSF) (Chi et al. 2003) induce significant inhibitions in tumor growth and metastases, as well as significantly increasing survival. In general, the intra-tumor delivery and expression of cytokine pDNA are very well tolerated, and the severe systemic side effects reported with the use of recombinant cytokines are not observed. Complete tumor regression, followed by long-lasting anti-tumor immunity, has been reported in response to pDNA encoding Th-1 cytokines (Suzuki et al. 2010; Zolochevska et al. 2011). These promising results indicate that host immunity against primary and metastatic cancer diseases can be stimulated after local cytokine pDNA based immunotherapy, provided that an efficient, safe and targeted delivery of pDNA can be achieved.

Naked pDNA is covalently closed-circular double-stranded DNA, which is unable to freely cross through biological barriers, such as the cell plasma membrane or vascular endothelium (Escoffre et al. 2010b). pDNA can carry larger coding sequences and is easier and inexpensive to mass-produce compared to viral vectors. Low immunogenicity and lack of integration of pDNA make it a greatly attractive molecule for gene therapy, especially for immunotherapy. Previously, the direct injection of pDNA into target tissue was a simple and safe technique available to achieve pDNA delivery and expression. However, the main limitations of this method are low levels of gene expression, limited intratissue distribution and inter-individual heterogeneity. In order to improve the efficiency of pDNA delivery, physical methods, including bubble-assisted ultrasound have been investigated (Escoffre et al. 2013b). These methods have received special interest since they can bypass many undesired effects associated with direct delivery methods and they allow repeated pDNA delivery to achieve the therapeutic effectiveness.

Using bubble-assisted ultrasound for pDNA delivery, the simplest approach is the co-administration of bubbles with pDNA. Both components are mixed *in-vitro* before their intra-vascular or intratissue injection. The target tissue is then exposed to ultrasound. Using this approach, bubbles and pDNA can be independently handled before their administration, allowing thus the adjustment of the treatment through change in the relative ratio of components, as well as adding or substituting one component. Nevertheless, this approach has two potential limitations: (i) Naked pDNA is sensitive to serum and tissue DNAses, causing it to be rapidly cleared; (ii) Bubbles and pDNA may not distribute identically in the target tissue. To overcome these effects, cationic lipids or polymers are used to condense and protect pDNA from DNAses. Lipoplexes and polyplexes are formed and co-administered with bubbles. pDNA can also be loaded on bubbles during their assembly, or by incubation of pDNA with cationic bubbles. In addition, lipoplexes and polyplexes can be loaded on bubbles through electrostatic interactions or covalent linkages. Thus, bubbles provide an additional protection of pDNA from DNAses and both components are consequently distributed identically. To our knowledge, no study supports the use of pDNA-loaded bubbles for cytokine-based immunotherapy. Currently, the intra-tumor delivery of a mixture of bubbles and cytokine pDNA is the most current strategy used in cytokine-based immunotherapy. Several reports have demonstrated the feasibility and the therapeutic benefit of this approach for the delivery of cytokine pDNA, including INF-γ and IL-27 (Sakakima et al. 2005; Zolochevska et al. 2011). The example of IL-12 based immunotherapy using bubble-assisted ultrasound is described in the next paragraph.

Example: IL-12 based immunotherapy

IL-12 is a heterodimeric protein composed of p35 and p40 subunits produced by DCs and macrophages (Abbas and Lichtman 2006). This cytokine has a variety of immunomodulatory and anti-tumor effects, including the induction of IFN-γ secretion

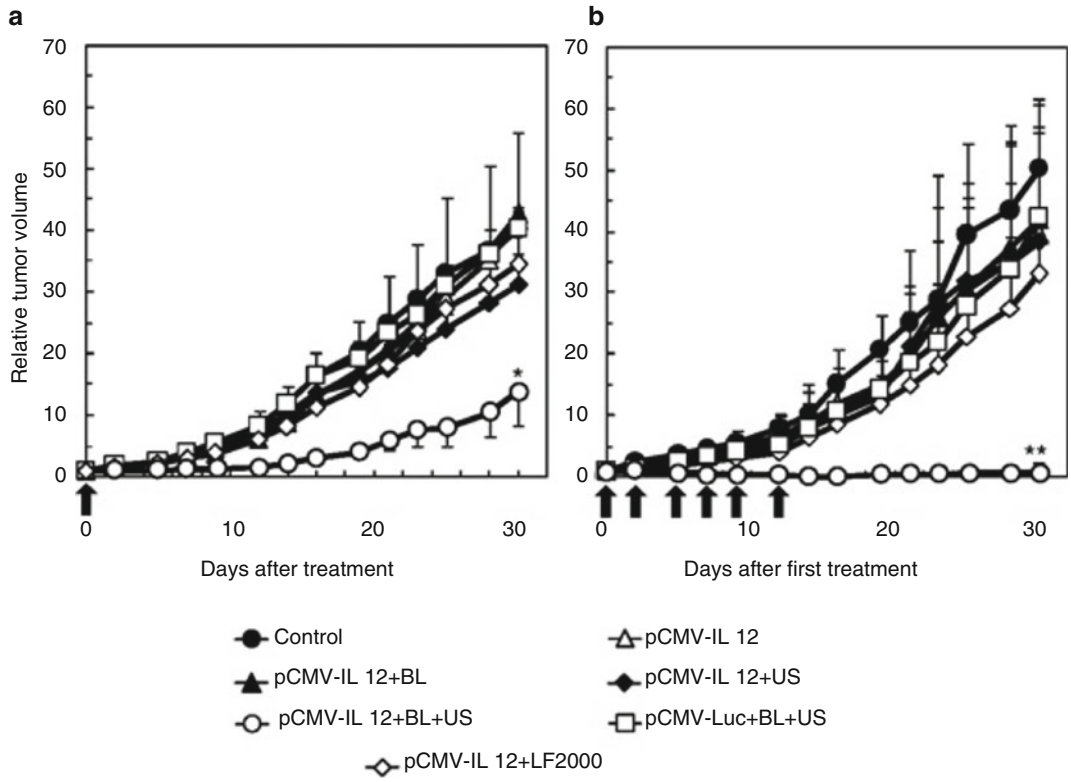

Fig. 14.7 IL-12 based immunotherapy. Mice were intradermally inoculated with murine ovarian carcinoma cells. (**a**) Single gene therapy. (**b**) Repetitive gene therapy. Each treatment (*arrow*) consists of an i.t. delivery of IL-12 encoding pDNA using BL-assisted ultrasound or Lipofectamine-2000 (LF2000). The volume of the growing tumors was measured (Reprinted with permission from Suzuki et al. (2010))

by stimulation of T lymphocytes and natural killer (NK) cells, and the increase in $CD8^+$ T and NK cell proliferation and cytotoxicity (i.e., promotion and the development of T-helper 1 (Th-1) responses). Moreover, this cytokine induces anti-angiogenic effects, mainly through IFN-γ-dependent production of interferon-inducible protein-10. IL-12 could be a versatile cytokine with great potential as an immunotherapeutic agent for the treatment of cancer. Recombinant protein rhIL-12 therapy has had some success, but has unfortunately been associated with toxicity. Indeed, clinical phase I and II trials reported that the systemic administration of rhIL-12 induced multiple serious adverse effects, including renal and systemic toxicity (Gollob et al. 2000; Alatrash et al. 2004). High-dose levels were linked to transient immune suppression, which would be unfavorable for effective immunotherapy. Nevertheless, preclinical studies support that the local delivery of IL-12 into tumors seems to be less toxic, while retaining an effective immunotherapeutic effect (Heller and Heller 2010; Lucas et al. 2002). More recently, new preclinical and phase I trials have been reported with intra-tumoral (i.t.) delivery of IL-12 gene using non-viral and viral vectors (Daud et al. 2008; Mahvi et al. 2007; Ren et al. 2003). All of these IL-12 based immunotherapies were well tolerated.

Among these vectors, Suzuki et al. have evaluated the delivery of IL-12 pDNA using bubble liposome-assisted ultrasound in an ovarian carcinoma mouse model (Suzuki et al. 2010). Seven days after intradermally inoculation of murine ovarian carcinoma OV-HM cells, a mixture of experimental bubbles (2.5 μg) and IL-12 pDNA (10 μg) was inter-tumorally (i.t) injected and ultrasound (1 MHz, 0.7 W/cm^2, 60 s) was transder-

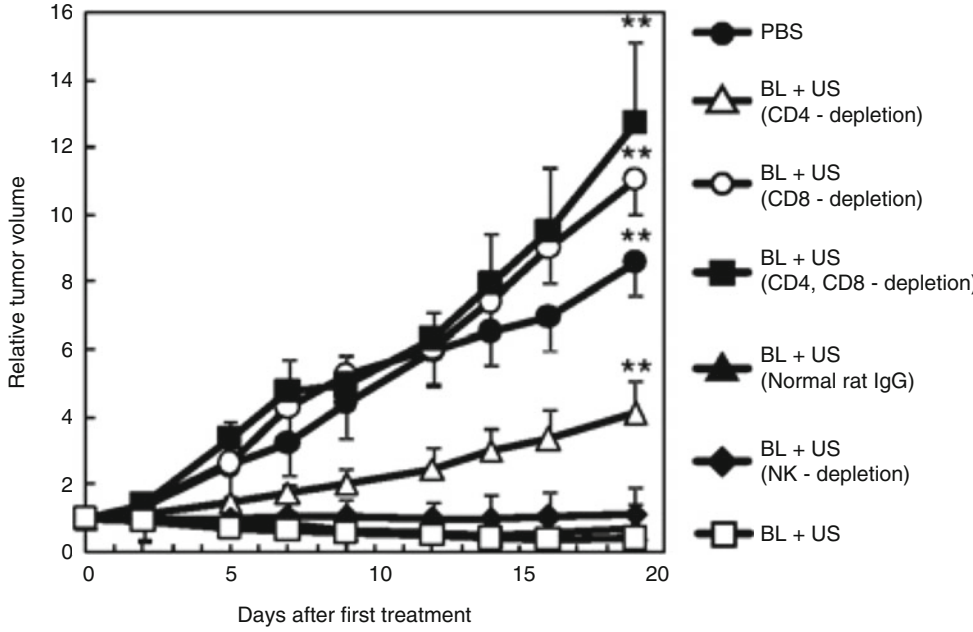

Fig. 14.8 Determination of immune cells responsible for the anti-tumor effect induced by IL-12 based immunotherapy. Mice were intradermally inoculated with murine ovarian carcinoma cells. $CD8^+$, $CD4^+$ and NK cells were depleted by the i.p. injection of specific antisera. Repetitive gene therapy was performed using BL-assisted ultrasound. The volume of the growing tumors was measured (Reprinted with permission from (Suzuki et al. 2010))

mally applied to the tumor tissue. A conventional lipofection method using lipofectamine was also investigated and compared to bubble-assisted ultrasound. Lipofectamine-2000 (20 μg) was mixed with IL-12 pDNA (10 μg) for 20 min to form polyplexes. Subsequently, these polyplexes were injected into the tumor. The authors showed that IL-12 was more effectively expressed in solid tumors using bubble-assisted ultrasound than using lipofection. The therapeutic effect of a single delivery of IL-12 pDNA was also examined. While pDNA delivery using bubbles, ultrasound or lipofection only showed no significant anti-tumor effect, tumor growth was significantly suppressed in mice treated with i.t. delivery of IL-12 pDNA using bubble-assisted ultrasound (Fig. 14.7a).

However, complete tumor regression was not observed. Consequently, the authors examined the therapeutic benefit of repeated IL-12 based immunotherapy. Six treatments using bubble-assisted ultrasound led to tumor suppression and complete regression in 80 % of the tumor-bearing mice (Fig. 14.7b). In addition, these mice showed prolonged survival. No adverse side effects related to IL-12 based immunotherapy were observed.

To investigate the anti-tumor mechanism of this immunotherapy, the authors examined the individual contributions of $CD8^+$, $CD4^+$ T and NK cells. Through *in-vivo* analysis of $CD8^+$, $CD4^+$ and NK cell depletions, they demonstrated that $CD8^+$ CTLs, activated by $CD4^+$ Th cells, were the predominant effector cells in this immunotherapy (Fig. 14.8). This conclusion was supported by immunohistochemical analyses. Indeed, tumors treated with IL-12 pDNA using bubble-assisted ultrasound showed increased infiltration of $CD8^+$ CTLs compared to control groups. In addition, the presence of high levels of perforin (i.e., the major cytotoxic molecule in activated $CD8^+$ cells) in the treated tumors supported the infiltration of activated $CD8^+$ CTLs into these tumors. In summary, the authors demonstrated that bubble-assisted ultrasound effectively delivers IL-12 pDNA into tumor tissue. The local IL-12 production induces immune responses resulting in tumor eradication.

14.5 Conclusions and Future Prospects

Bubble-assisted ultrasound is under investigation as a promising non-viral delivery method. This technology combines the use of gas bubbles and the application of ultrasound in such a way that the ultrasound-mediated destruction of bubbles induces physical phenomena, which transiently increase the permeability of biological barriers (i.e., plasma membrane, vascular endothelium) to poorly permeant molecules. Although the precise molecular and cellular mechanisms involved in bubble-assisted ultrasound are still unclear, this method has received special interest in the fields of anticancer chemotherapy, gene therapy, regenerative medicine, and very recently in the areas of immunotherapy and vaccination. Indeed, bubble-assisted ultrasound successfully delivers immuno-stimulatory components, such as therapeutic Abs (i.e., Ab-based immunotherapy) or cytokine-encoding nucleic acids (i.e., cytokine gene therapy) *in-vivo*, thus stimulating and improving immune responses against brain diseases and cancer. Moreover, protein Ags or Ag-encoding nucleic acids, can be efficiently delivered into dendritic cells (i.e., dendritic cell-based vaccines), thus resulting in a long-lasting immunization against cancer.

Most recent data available on bubble-assisted ultrasound in the fields of immunotherapy and vaccination show that proofs of principle have been mainly achieved for oncological applications in accessible tumors, such as melanoma or subcutaneous xenograft tumor models. However, ultrasound is also a promising technology for non-invasive and targeted treatment of deep-seated tumor tissues by focusing the ultrasound. Where the i.t. injection of bubbles and immuno-stimulating molecules and Ags seems to be the best administration route for cutaneous and subcutaneous tumors, i.v. injection should be favored for deep-seated tumors. Indeed, even though i.t. ultrasound-guided needle delivery can be performed, the i.v. route is the cheap and safe way used for the administration of therapeutics in the human clinic. The i.v. delivery of therapeutic Abs using bubble-assisted ultrasound is only reported in brain tissue. Consequently, further investigations are still required to demonstrate that the improvement of immune responses and long-lasting immunization can be achieved by bubble-assisted ultrasound through i.v. delivery of immuno-stimulating molecules and Ags.

Moreover, most proofs of principle have been essentially attained using small animals, thus demonstrating the therapeutic benefit of this technology as a site-specific and non-invasive therapeutic method. As previously described for gene therapy or chemotherapy using bubble-assisted ultrasound, large animal studies, as well as human proof-of-concepts, are still lacking and might face challenging and unexpected limitations. Efficacy trials, especially in large animals, require a very efficient delivery of therapeutic molecules. The improvement of this method relies on two main strategies:

(i) *Design of bubbles dedicated for therapeutic purposes*: In current studies, commercial UCAs (i.e., SonoVue®, Definity®) are employed for the delivery of immune-stimulating molecules and Ags. The use of these clinically approved microbubbles may facilitate the clinical translation of microbubble-assisted ultrasound, but any undesired side effect might have a negative impact on these UCAs in ultrasound-based diagnostics. In addition, the use of commercial UCAs restricts the delivery of immuno-stimulating compounds and Ags using the co-administration approach. Indeed, the modification of these UCAs for therapeutic applications would prevent their clinical translation, thus requiring new validation from the regulatory and healthy authorities. The coadministration approach seems to be especially interesting for Ab-based immunotherapy, where antibodies have a long circulation lifetime. However, the development of loaded bubbles should allow to carry optimal amounts of immuno-stimulating molecules and Ags and to protect them from degradation for therapeutic application including DC-based vaccination and cytokine gene therapy.

(ii) *Development of therapeutic ultrasound protocols*: Although the influence of acoustic parameters on the effectiveness of therapeutic molecule delivery has been described for gene therapy and chemotherapy, no exhaustive optimization of these parameters for the delivery of immuno-stimulating molecules and Ags has been reported. Note that, it is not straightforward to compare the results of these studies directly, due to the absence of common units concerning the applied US parameters and the large parameter space (US frequency, pressure, pulse duration, pulse repetition rate, total duration, spatial coverage). Consequently, further investigations are still required to show the influence of these parameters in the activation/stimulation, and the duration of immune responses. In addition, homemade US devices and probes are mainly used in these studies, while it seems obvious nowadays that the use of diagnostic US imaging systems (linear array) could facilitate the clinical translation of this technology. On the other hand, dedicated ultrasound probes, such as two-dimensional arrays, should be designed specifically for therapeutic applications. The two-dimensional ultrasound arrays are composed of thousands of small transducers with the ability to steer in three dimensions, thus allowing high and homogeneous delivery of therapeutic molecules. Future preclinical studies should evaluate the effectiveness of diagnostic US imaging systems and two-dimensional ultrasound arrays to deliver immuno-stimulating molecules and Ags.

References

Abbas AK, Lichtman AH (2006) Basic immunology: functions and disorders of the immune system. Saunders Edition, Philadelphia

Alatrash G, Hutson TE, Molto L, Richmond A, Nemec C, Mekhail T, Elson P, Tannenbaum C, Olencki T, Finke J, Bukowski RM (2004) Clinical and immunologic effects of subcutaneously administered interleukin-12 and interferon alfa-2b: phase I trial of patients with metastatic renal cell carcinoma or malignant melanoma. J Clin Oncol 22:2891–2900

Andre FE (2003) Vaccinology: past achievements, present roadblocks and future promises. Vaccine 21:593–595

Arteaga CL, Sliwkowski MX, Osborne CK, Perez EA, Puglisi F, Gianni L (2012) Treatment of HER2-positive breast cancer: current status and future perspectives. Nat Rev Clin Oncol 9:16–32

Aryal M, Arvanitis CD, Alexander PM, Mcdannold N (2014) Ultrasound-mediated blood-brain barrier disruption for targeted drug delivery in the central nervous system. Adv Drug Deliv Rev 72C:94–109

Aurisicchio L, Ciliberto G (2012) Genetic cancer vaccines: current status and perspectives. Expert Opin Biol Ther 12:1043–1058

Banks WA, Terrell B, Farr SA, Robinson SM, Nonaka N, Morley JE (2002) Passage of amyloid beta protein antibody across the blood-brain barrier in a mouse model of Alzheimer's disease. Peptides 23:2223–2226

Bard F, Cannon C, Barbour R, Burke RL, Games D, Grajeda H, Guido T, Hu K, Huang J, Johnson-Wood K, Khan K, Kholodenko D, Lee M, Lieberburg I, Motter R, Nguyen M, Soriano F, Vasquez N, Weiss K, Welch B, Seubert P, Schenk D, Yednock T (2000) Peripherally administered antibodies against amyloid beta-peptide enter the central nervous system and reduce pathology in a mouse model of Alzheimer disease. Nat Med 6:916–919

Bendell JC, Domchek SM, Burstein HJ, Harris L, Younger J, Kuter I, Bunnell C, Rue M, Gelman R, Winer E (2003) Central nervous system metastases in women who receive trastuzumab-based therapy for metastatic breast carcinoma. Cancer 97:2972–2977

Black D, Brockway-Lunardi L (2013) The melanoma research alliance: the power of patient advocacy to accelerate research and novel therapies. Cancer Immunol Res 1:357–361

Bonner JA, Harari PM, Giralt J, Azarnia N, Shin DM, Cohen RB, Jones CU, Sur R, Raben D, Jassem J, Ove R, Kies MS, Baselga J, Youssoufian H, Amellal N, Rowinsky EK, Ang KK (2006) Radiotherapy plus cetuximab for squamous-cell carcinoma of the head and neck. N Engl J Med 354:567–578

Bose P, Brockton NT, Dort JC (2013) Head and neck cancer: from anatomy to biology. Int J Cancer 133:2013–2023

Boucher Y, Baxter LT, Jain RK (1990) Interstitial pressure gradients in tissue-isolated and subcutaneous tumors: implications for therapy. Cancer Res 50:4478–4484

Burgess A, Hynynen K (2014) Drug delivery across the blood-brain barrier using focused ultrasound. Expert Opin Drug Deliv 11:711–721

Chacko AM, Li C, Pryma DA, Brem S, Coukos G, Muzykantov V (2013) Targeted delivery of antibody-based therapeutic and imaging agents to CNS tumors: crossing the blood-brain barrier divide. Expert Opin Drug Deliv 10:907–926

Chang EL, Lo S (2003) Diagnosis and management of central nervous system metastases from breast cancer. Oncologist 8:398–410

Chi CH, Wang YS, Lai YS, Chi KH (2003) Anti-tumor effect of in vivo IL-2 and GM-CSF electrogene therapy in murine hepatoma model. Anticancer Res 23:315–321

Cintolo JA, Datta J, Mathew SJ, Czerniecki BJ (2012) Dendritic cell-based vaccines: barriers and opportunities. Future Oncol 8:1273–1299

Daud AI, Deconti RC, Andrews S, Urbas P, Riker AI, Sondak VK, Munster PN, Sullivan DM, Ugen KE, Messina JL, Heller R (2008) Phase I trial of interleukin-12 plasmid electroporation in patients with metastatic melanoma. J Clin Oncol 26:5896–5903

De Temmerman ML, Dewitte H, Vandenbroucke RE, Lucas B, Libert C, Demeester J, De Smedt SC, Lentacker I, Rejman J (2011) mRNA-Lipoplex loaded microbubble contrast agents for ultrasound-assisted transfection of dendritic cells. Biomaterials 32:9128–9135

Demattos RB, Bales KR, Cummins DJ, Dodart JC, Paul SM, Holtzman DM (2001) Peripheral anti-A beta antibody alters CNS and plasma A beta clearance and decreases brain A beta burden in a mouse model of Alzheimer's disease. Proc Natl Acad Sci U S A 98:8850–8855

Doinikov AA, Bouakaz A (2010) Acoustic microstreaming around a gas bubble. J Acoust Soc Am 127: 703–709

Eichler AF, Chung E, Kodack DP, Loeffler JS, Fukumura D, Jain RK (2011) The biology of brain metastases-translation to new therapies. Nat Rev Clin Oncol 8:344–356

Escoffre JM, Kaddur K, Rols MP, Bouakaz A (2010a) In vitro gene transfer by electrosonoporation. Ultrasound Med Biol 36:1746–1755

Escoffre JM, Teissie J, Rols MP (2010b) Gene transfer: how can the biological barriers be overcome? J Membr Biol 236:61–74

Escoffre JM, Novell A, Serriere S, Lecomte T, Bouakaz A (2013a) Irinotecan delivery by microbubble-assisted ultrasound: in vitro validation and a pilot preclinical study. Mol Pharm 10:2667–2675

Escoffre JM, Zeghimi A, Novell A, Bouakaz A (2013b) In-vivo gene delivery by sonoporation: recent progress and prospects. Curr Gene Ther 13:2–14

Ferlay J, Steliarova-Foucher E, Lortet-Tieulent J, Rosso S, Coebergh JW, Comber H, Forman D, Bray F (2013) Cancer incidence and mortality patterns in Europe: estimates for 40 countries in 2012. Eur J Cancer 49:1374–1403

Foged C (2011) Subunit vaccines of the future: the need for safe, customized and optimized particulate delivery systems. Ther Deliv 2:1057–1077

Frenkel V (2008) Ultrasound mediated delivery of drugs and genes to solid tumors. Adv Drug Deliv Rev 60:1193–1208

Gollob JA, Mier JW, Veenstra K, Mcdermott DF, Clancy D, Clancy M, Atkins MB (2000) Phase I trial of twice-weekly intravenous interleukin 12 in patients with metastatic renal cell cancer or malignant melanoma: ability to maintain IFN-gamma induction is associated with clinical response. Clin Cancer Res 6:1678–1692

Hauff P, Seemann S, Reszka R, Schultze-Mosgau M, Reinhardt M, Buzasi T, Plath T, Rosewicz S, Schirner M (2005) Evaluation of gas-filled microparticles and sonoporation as gene delivery system: feasibility study in rodent tumor models. Radiology 236:572–578

Heath CH, Sorace A, Knowles J, Rosenthal E, Hoyt K (2012) Microbubble therapy enhances anti-tumor properties of cisplatin and cetuximab in vitro and in vivo. Otolaryngol Head Neck Surg 146:938–945

Heller LC, Heller R (2010) Electroporation gene therapy preclinical and clinical trials for melanoma. Curr Gene Ther 10:312–317

Horton JK, Halle J, Ferraro M, Carey L, Moore DT, Ollila D, Sartor CI (2010) Radiosensitization of chemotherapy-refractory, locally advanced or locally recurrent breast cancer with trastuzumab: a phase II trial. Int J Radiat Oncol Biol Phys 76:998–1004

Hudis CA (2007) Trastuzumab–mechanism of action and use in clinical practice. N Engl J Med 357:39–51

Ittner LM, Gotz J (2011) Amyloid-beta and tau–a toxic pas de deux in Alzheimer's disease. Nat Rev Neurosci 12:65–72

Iwanaga K, Tominaga K, Yamamoto K, Habu M, Maeda H, Akifusa S, Tsujisawa T, Okinaga T, Fukuda J, Nishihara T (2007) Local delivery system of cytotoxic agents to tumors by focused sonoporation. Cancer Gene Ther 14:354–363

Joensuu H, Kellokumpu-Lehtinen PL, Bono P, Alanko T, Kataja V, Asola R, Utriainen T, Kokko R, Hemminki A, Tarkkanen M, Turpeenniemi-Hujanen T, Jyrkkio S, Flander M, Helle L, Ingalsuo S, Johansson K, Jaaskelainen AS, Pajunen M, Rauhala M, Kaleva-Kerola J, Salminen T, Leinonen M, Elomaa I, Isola J, Finher Study I (2006) Adjuvant docetaxel or vinorelbine with or without trastuzumab for breast cancer. N Engl J Med 354:809–820

Jordao JF, Ayala-Grosso CA, Markham K, Huang Y, Chopra R, Mclaurin J, Hynynen K, Aubert I (2010) Antibodies targeted to the brain with image-guided focused ultrasound reduces amyloid-beta plaque load in the TgCRND8 mouse model of Alzheimer's disease. PLoS One 5:e10549

Kinoshita M, Mcdannold N, Jolesz FA, Hynynen K (2006) Noninvasive localized delivery of Herceptin to the mouse brain by MRI-guided focused ultrasound-induced blood-brain barrier disruption. Proc Natl Acad Sci U S A 103:11719–11723

Kotopoulis S, Dimcevski G, Gilja OH, Hoem D, Postema M (2013) Treatment of human pancreatic cancer using combined ultrasound, microbubbles, and gemcitabine: a clinical case study. Med Phys 40:072902

Lemmon JC, Mcfarland RJ, Rybicka JM, Balce DR, Mckeown KR, Krohn RM, Matsunaga TO, Yates RM (2011) In vitro and in vivo transfection of primary phagocytes via microbubble-mediated intraphagosomal sonoporation. J Immunol Methods 371:152–158

Leyland-Jones B (2009) Human epidermal growth factor receptor 2-positive breast cancer and central nervous system metastases. J Clin Oncol 27:5278–5286

Liu YH, Giunta B, Zhou HD, Tan J, Wang YJ (2012) Immunotherapy for Alzheimer disease: the challenge of adverse effects. Nat Rev Neurol 8:465–469

Logan RM (2009) Advances in understanding of toxicities of treatment for head and neck cancer. Oral Oncol 45:844–848

Lucas ML, Heller L, Coppola D, Heller R (2002) IL-12 plasmid delivery by in vivo electroporation for the successful treatment of established subcutaneous B16. F10 melanoma. Mol Ther 5:668–675

Mahvi DM, Henry MB, Albertini MR, Weber S, Meredith K, Schalch H, Rakhmilevich A, Hank J, Sondel P (2007) Intratumoral injection of IL-12 plasmid DNA–results of a phase I/IB clinical trial. Cancer Gene Ther 14:717–723

Minchinton AI, Tannock IF (2006) Drug penetration in solid tumours. Nat Rev Cancer 6:583–592

Oda Y, Suzuki R, Otake S, Nishiie N, Hirata K, Koshima R, Nomura T, Utoguchi N, Kudo N, Tachibana K, Maruyama K (2012) Prophylactic immunization with Bubble liposomes and ultrasound-treated dendritic cells provided a four-fold decrease in the frequency of melanoma lung metastasis. J Control Release 160:362–366

Ohl CD, Wolfrum B (2003) Detachment and sonoporation of adherent HeLa-cells by shock wave-induced cavitation. Biochim Biophys Acta 1624:131–138

Ohl CD, Arora M, Ikink R, De Jong N, Versluis M, Delius M, Lohse D (2006) Sonoporation from jetting cavitation bubbles. Biophys J 91:4285–4295

Opar A (2008) Mixed results for disease-modification strategies for Alzheimer's disease. Nat Rev Drug Discov 7:717–718

Park EJ, Zhang YZ, Vykhodtseva N, Mcdannold N (2012) Ultrasound-mediated blood-brain/blood-tumor barrier disruption improves outcomes with trastuzumab in a breast cancer brain metastasis model. J Control Release 163:277–284

Price KA, Cohen EE (2012) Current treatment options for metastatic head and neck cancer. Curr Treat Options Oncol 13:35–46

Raymond SB, Treat LH, Dewey JD, Mcdannold NJ, Hynynen K, Bacskai BJ (2008) Ultrasound enhanced delivery of molecular imaging and therapeutic agents in Alzheimer's disease mouse models. PLoS One 3:e2175

Ren H, Boulikas T, Lundstrom K, Soling A, Warnke PC, Rainov NG (2003) Immunogene therapy of recurrent glioblastoma multiforme with a liposomally encapsulated replication-incompetent Semliki forest virus vector carrying the human interleukin-12 gene–a phase I/II clinical protocol. J Neurooncol 64:147–154

Sakakima Y, Hayashi S, Yagi Y, Hayakawa A, Tachibana K, Nakao A (2005) Gene therapy for hepatocellular carcinoma using sonoporation enhanced by contrast agents. Cancer Gene Ther 12:884–889

Sanlorenzo M, Vujic I, Posch C, Dajee A, Yen A, Kim S, Ashworth M, Rosenblum MD, Algazi A, Osella-Abate S, Quaglino P, Daud A, Ortiz-Urda S (2014) Melanoma immunotherapy. Cancer Biol Ther 15:665–674

Scott AM, Wolchok JD, Old LJ (2012) Antibody therapy of cancer. Nat Rev Cancer 12:278–287

Suzuki R, Namai E, Oda Y, Nishiie N, Otake S, Koshima R, Hirata K, Taira Y, Utoguchi N, Negishi Y, Nakagawa S, Maruyama K (2010) Cancer gene therapy by IL-12 gene delivery using liposomal bubbles and tumoral ultrasound exposure. J Control Release 142:245–250

Taylor SL, Rahim AA, Bush NL, Bamber JC, Porter CD (2007) Targeted retroviral gene delivery using ultrasound. J Gene Med 9:77–87

Thakker DR, Weatherspoon MR, Harrison J, Keene TE, Lane DS, Kaemmerer WF, Stewart GR, Shafer LL (2009) Intracerebroventricular amyloid-beta antibodies reduce cerebral amyloid angiopathy and associated micro-hemorrhages in aged Tg2576 mice. Proc Natl Acad Sci U S A 106:4501–4506

Un K, Kawakami S, Suzuki R, Maruyama K, Yamashita F, Hashida M (2010) Development of an ultrasound-responsive and mannose-modified gene carrier for DNA vaccine therapy. Biomaterials 31:7813–7826

Un K, Kawakami S, Suzuki R, Maruyama K, Yamashita F, Hashida M (2011) Suppression of melanoma growth and metastasis by DNA vaccination using an ultrasound-responsive and mannose-modified gene carrier. Mol Pharm 8:543–554

Wilcock DM, Colton CA (2008) Anti-amyloid-beta immunotherapy in Alzheimer's disease: relevance of transgenic mouse studies to clinical trials. J Alzheimers Dis 15:555–569

Wong AD, Ye M, Levy AF, Rothstein JD, Bergles DE, Searson PC (2013) The blood-brain barrier: an engineering perspective. Front Neuroeng 6:7

Zolochevska O, Xia X, Williams BJ, Ramsay A, Li S, Figueiredo ML (2011) Sonoporation delivery of interleukin-27 gene therapy efficiently reduces prostate tumor cell growth in vivo. Hum Gene Ther 22: 1537–1550

Sonoporation: Applications for Cancer Therapy

15

Jiale Qin, Tzu-Yin Wang, and Jürgen K. Willmann

Abstract

Therapeutic efficacy of both traditional chemotherapy and gene therapy in cancer is highly dependent on the ability to deliver drugs across natural barriers, such as the vessel wall or tumor cell membranes. In this regard, sonoporation induced by ultrasound-guided microbubble (USMB) destruction has been widely investigated in the enhancement of therapeutic drug delivery given it can help overcome these natural barriers, thereby increasing drug delivery into cancer. In this chapter we discuss challenges in current cancer therapy and how some of these challenges could be overcome using USMB-mediated drug delivery. We particularly focus on recent advances in delivery approaches that have been developed to further improve therapeutic efficiency and specificity of various cancer treatments. An example of clinical translation of USMB-mediated drug delivery is also shown.

Keywords

Sonoporation • Drug delivery • Cancer

15.1 Introduction

Cancer has emerged as the leading cause of human death worldwide (Jemal et al. 2011). In 2012, approximately 14.1 million patients were diagnosed and about 8.2 million patients died from cancer (Ferlay et al. 2014). This high mortality primarily results from a lack of effective therapy in many cancer types. Current treatment approaches include either surgical removal with and without adjuvant radiation and/or systemic chemotherapy, primary radiation or chemotherapy (Minchinton and Tannock 2006; Jain 1998). However, most chemotherapeutics lack tumor specificity, leading to high systemic toxicity. In addition to chemotherapy, gene therapy has been investigated as an alternative treatment approach

J. Qin • T.-Y. Wang • J.K. Willmann (✉)
Department of Radiology,
Molecular Imaging Program at Stanford,
Stanford University, School of Medicine,
Stanford, CA, USA
e-mail: willmann@stanford.edu

© Springer International Publishing Switzerland 2016

J.-M. Escoffre, A. Bouakaz (eds.), *Therapeutic Ultrasound*, Advances in Experimental Medicine and Biology, Vol. 880, DOI 10.1007/978-3-319-22536-4_15

as it has demonstrated promising antitumor effects in preclinical studies. However, major hurdles still exist for this treatment approach in terms of safe methods to selectively deliver therapeutic genes into tumor cells and high enough gene expression levels to efficiently eradicate tumors *in-vivo* (Shillitoe 2009; Tong et al. 2009).

Over the last two decades, several methods have been developed to deliver drugs, including genes, to the tumor target location using an externally applied "trigger" (Waite and Roth 2012; Guarneri et al. 2012). Among these methods, ultrasound-guided microbubble (USMB) destruction has great potential for clinical translation in oncology because it is a safe, non-invasive, cost-effective and non-ionizing modality (Edelstein et al. 2007). Importantly, this approach can create temporary and reversible openings in vessel walls and cellular membranes through a process called "sonoporation", allowing enhanced transport of therapeutic agents across these biological barriers in the insonated region (Tzu-Yin et al. 2014; Kaneko and Willmann 2012).

An in-depth description of the mechanisms of sonoporation can be found in previous chapters of this book. Here, we focus on the *in-vitro* and *in-vivo* investigations on USMB-mediated drug delivery in various tumor models for improved cancer therapy. Specifically, we discuss how USMB assists in overcoming the challenges of drug delivery into tumors, general treatment protocols, current status in preclinical and clinical applications, as well as future directions for clinical translation of this technique.

15.2 Tumor Microenvironment and Pathways of Sonoporation-Mediated Drug Delivery

Although many anticancer agents are effective in killing monolayer tumor cells grown in culture, their treatment effects are significantly reduced *in-vivo* because the *in-vivo* tumor microenvironment creates several barriers for drug delivery into tumor cells (Lozano et al. 2012). Most solid tumors are composed of proliferating tumor cells, tumor stroma (including the extracellular matrix of tumors) and angiogenic vessels, which are different from normal tissues. The tumor vasculature is chaotic in terms of spatial distribution, microvessel length and diameter. Vessels are also tortuous and saccular, possessing haphazard interconnections (Wang and Yuan 2006) and they show leaky pores, allowing for larger particles up to a few hundred nanometers to pass through (Hobbs et al. 1998). Also, the tumor architecture generally lacks adequate lymphatic drainage. The combination of high vascular permeability and inadequate lymphatic drainage results in an increased interstitial fluid pressure, which severely limits convection-dependent transport of agents in the interstitium (Boucher et al. 1990). Furthermore, the extracellular matrix of tumors, a combination of proteoglycans, collagens and additional molecules (Mow et al. 1984), can limit interstitial transport and prevent sufficient and uniform distribution of anti-cancer agents (Wang and Yuan 2006). Finally, actively proliferating tumor cells can force the vessels apart, leading to an increased distance between the tumor cells and the blood vessels. The tumor cells can be separated from the blood vessels by more than 100 μm (Minchinton and Tannock 2006). Due to high interstitial fluid pressures, transport barriers in the extracellular matrix, and an increased distance from the vessels to the cells, usually only limited quantities of therapeutic agents reach tumor cells by diffusion only.

USMB-mediated drug delivery has been reported to result in a 20–80 % improvement in tumor response to drug treatment compared with administration of drugs alone in preclinical murine models (Yu et al. 2013; Sorace et al. 2012; Pu et al. 2014; Duvshani-Eshet et al. 2007; Carson et al. 2012). In an USMB delivery system, hydrophobic gas-filled microbubbles, stabilized by a lipid, protein or polymer shell, are exposed to ultrasound (Sirsi and Borden 2014). During exposure, the microbubbles can undergo volumetric change and/or violent collapse, a process called cavitation (Tzu-Yin et al. 2014). Cavitation can occur in two forms: stable and inertial. Stable cavitation occurs when the microbubbles oscillate stably around a resonant

diameter at low acoustic intensities. At higher intensities, the microbubbles undergo much more violent expansion, contraction and forcible collapse, generating shock waves in the vicinity of the microbubbles, a process called inertial cavitation (Newman and Bettinger 2007). Both forms of cavitation can create pores on the nearby cellular membranes (Matsuo et al. 2011; Zhang et al. 2012) and vessel walls (Bekeredjian et al. 2007; Bohmer et al. 2010), allowing for transport of particles. In addition, the fluid motion induced during the cavitation process may enhance the transportation of drugs into the interstitium, increasing the quantities of agents that can reach more distant tumor cells (Eggen et al. 2013).

While multiple novel treatment approaches are being explored, in this chapter we focus on two USMB-mediated drug delivery approaches currently being investigated for cancer therapy. The first approach aims to kill tumor parenchymal cells by delivering cytotoxic or cytostatic antitumor therapeutics across the vessel, through the interstitium, and into tumor cells, *i.e.*, a transvascular-interstitial-transmembrane pathway. The second approach aims to destroy tumor vasculature by either killing the vascular endothelial cells or mechanically destructing the tumor vasculature in order to compromise tumor blood supply. Both approaches are discussed in the following sections.

15.2.1 Tumor Treatment Through a Transvascular-Interstitial-Intracellular Pathway

The major challenge of drug delivery into tumor cells through this pathway is the need to push therapeutic agents across several barriers: (1) across vessels, (2) interstitial transport, and (3) passage into tumor cell.

15.2.1.1 Transvascular Transport by Modulating Vascular Integrity

Inertial cavitation of microbubbles in the lumen of tumor vessels may disrupt vascular endothelial integrity due to shock waves and jetting during collapse of microbubbles (Qin et al. 2009). On the other hand, stable cavitation is thought to temporarily increase the gap-junction distance between vascular endothelial cells by a volumetric change of the oscillating microbubbles. In the expansion phase, the large microbubbles may cause a circumferential displacement of the vessel, and the contraction phase may cause invagination of the interacted vessel (Chen et al. 2011; Caskey et al. 2007). Both forms of cavitation can lead to pores on the vessel wall, allowing for circulating therapeutic agents to extravasate across the vessels wall into the tumor interstitium (Fig. 15.1a).

Bekeredjian et al. (2007)) injected Evans blue dye (a highly charged low molecular weight marker that binds to serum albumin (about 69 kDa) to become a high molecular weight intravascular tracer protein) (Hoffmann et al. 2011; Elodie Debefve et al. 2013) and lipid microbubbles into hepatoma-bearing rats and insonated the tumors with ultrasound (1.3 MHz, mechanical index 1.6, bursting pulses every 4 cardiac cycles for 15 min). They showed an approximate five-fold higher Evans blue dye accumulation in insonated compared to non-insonated tumors. The amount of Evans blue extravasation has also been shown to be affected by both the microbubble type and the acoustic conditions. Bohmer et al. (2010)) showed that ultrasound (10,000 cycles of 1.2 MHz ultrasound pulsed at 2 MPa pressure and a pulsing rate of 0.25 Hz for 5 min) increased Evans blue extravasation by a factor of 2.3 in the presence of lipid-shelled mircobubbles, compared to a factor of 1.6 in the presence of polymer-shelled microbubbles in murine colon cancers subcutaneously established in mice. This difference likely occurred because the cavitation threshold is lower for lipid-shelled microbubbles. In the same study, two acoustic conditions were compared: Pulse lengths of 100 and 10,000 cycles. The results showed that the spatial extent of extravasation was significantly smaller for 100 cycles per pulse than for 10,000 cycles (6 ~ 9 mm vs. 18 ~ 20 mm), while other ultrasound parameters (1.2 MHz, 2 MPa pressure and pulsing rate of 0.25 Hz for 5 min) and the microbubble type (polymer-shelled microbubbles) were kept the same.

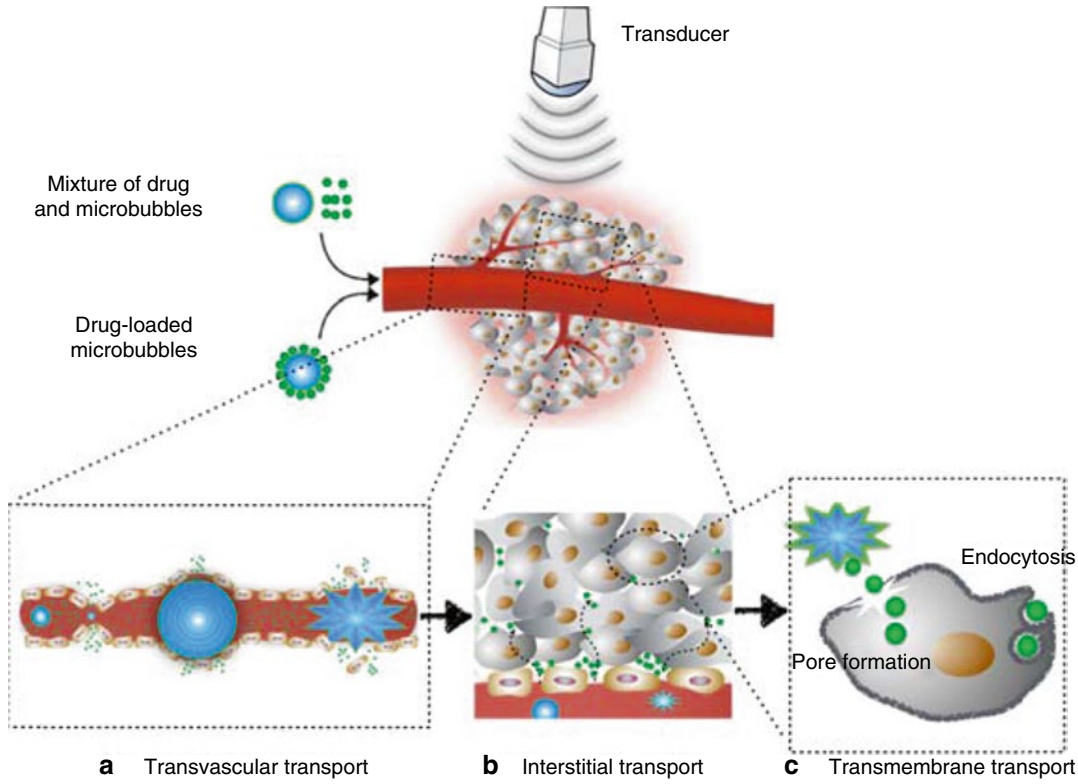

Fig. 15.1 Schematic summary of the transvascular-interstitial-transmembrane pathway in USMB-mediated drug delivery. (**a**) Potential mechanisms responsible for the passage across the vessels include creation of temporary gaps between vascular endothelial cells by volumetric expansion and contraction of the oscillating microbubbles. Also, cavitation of microbubbles may disrupt vascular endothelial cell integrity during violent collapse of microbubbles, creating ruptures in the vascular endothelial layer. (**b**) Interstitial transport of drugs/genes within the extracellular matrix may be enhanced by ultrasound radiation force. (**c**) USMB may induce membrane disruption and/or enhance active transport, such as endocytosis, thereby enhancing cellular permeability

Since Evans blue dye bound to serum albumin is relatively small (7 nm) (Elodie Debefve et al. 2013) compared to many therapeutic agents, another study assessed whether USMB can also increase tumor delivery of other model drugs that are larger in size. Carlisle et al. (2013)) demonstrated that USMB (ultrasound: 0.5 MHz, 50,000 cycles pulse length, 0.5 Hz pulse repetition frequency, 1.2 MPa peak rarefactional pressure for 4 min; SonoVue® microbubbles) increased extravasation and intratumoral (i.t.) distribution of a 130-nm luciferase labeled polymer-coated adenovirus in a breast cancer mouse model. Compared with non-insonated tumor, USMB resulted in a 5-fold increase in the amount of delivered adenovirus within 100 μm of blood vessels, and an increase of 40 fold beyond 100 μm. This suggests that USMB may not only increase the amount of drug extravasation, but also enhance drug penetration in the tumor interstitium, as shown in the following section.

15.2.1.2 Interstitial Transport

The high interstitial fluid pressure in tumors can reduce the convectional transport of drugs and particles throughout the extracellular matrix and, hence, only a small population of neoplastic cells located close to blood vessels is exposed to therapeutic agents by diffusion (Bae 2009; Davies Cde et al. 2004). Application of ultrasound has been shown to facilitate drug penetration beyond the close proximity of tumor vessels, potentially through radiation force caused by ultrasound (Fig. 15.1b). Radiation force is produced by the pressure gradient caused by a momentum transfer from the wave to the attenuating media, arising

either from absorption or reflection of the wave. This momentum transfer from ultrasound beam to a particle causes the transport of the particle in the direction of wave propagation. Due to higher tissue absorption at higher frequencies, the radiation force increases with increasing frequencies.

In a study performed by Eggen et al. (2013), prostate tumors established in mice were exposed to ultrasound (1 or 0.3 MHz, 13.35 W/cm^2, mechanical index 2.2, 5 % duty cycle, total exposure 10 min) 24 h after the administration of liposomes. At this time point, liposomes had passively extravasated into the tumor via the enhanced permeability and retention (EPR) effect, with a very low remaining concentration in the circulation (only approximately 10 % of liposomes in the circulation 24 h after injection). Since the blood liposome concentrations at 24 h was so low, changes of liposomal tumor distribution following ultrasound application was considered to be caused by its effect on already extravasated liposomes, rather than liposomes still in circulation. The study showed that liposomes in tumors insonated with ultrasound were more scattered throughout the tumor volume and penetrated two-fold more from blood vessels compared to those in non-insonated tumors. Moreover, the penetration distance was larger when the higher frequency (1 MHz) was applied. One potential explanation for this phenomenon is that the acoustic radiation force enhances drug transport. As the ultrasound frequency increased from 0.3 to 1 MHz, the radiation force could be increased, thus facilitating the transport of particles in the interstitium. This study demonstrated that radiation force from ultrasound may propel interstitial transport of extravasated therapeutic agents within the interstitial space. The increased penetration depth may allow the therapeutic agents to act on deeper lying tumor cells, eventually improving the outcome of tumor drug therapy.

However, the penetration depth of therapeutic agents varies at different spatial locations within tumors. Eggen et al. (2014) showed that USMB had a different impact on drug delivery in the periphery versus the core of tumors. In a prostatic cancer mouse model, USMB resulted in an increased nanoparticle penetration distance of 0.5–1 nm in the tumor periphery compared to the tumor core. This phenomenon was potentially caused by the heterogeneous distribution of interstitial fluid pressure across tumors. Indeed, in other studies using subcutaneous rat breast cancer models (Boucher et al. 1990) and a subcutaneous human osteosarcoma xenograft model (Eikenes et al. 2004), the interstitial fluid pressure rose with increased distance from the tumor periphery to the core within the first 400 μm, and then plateaued afterwards. The elevated interstitial fluid pressure may hinder transport of the extravasated particles in the interstitial space, resulting in shorter penetration in the tumor core.

15.2.1.3 Transmembrane Transport of Tumor Parenchymal Cells

The process of USMB-mediated permeability enhancement of tumor cells can be induced by pore formation and/or active transport across the membrane (Fig. 15.1c).

Pore formation in tumor cells has been visualized in many *in-vitro* studies, such as melanoma C32 cells (Matsuo et al. 2011) and prostate cancer DU145 cells (Zhang et al. 2012) by electron microscopy. Stable and inertial cavitations have been shown to cause cell membrane displacement and disruption for improved drug delivery across cellular membranes (Taniyama et al. 2002; van Wamel et al. 2004). Pore sizes between 100 nm and a few micrometers have been reported (Schlicher et al. 2006). This implies that exogenous antitumor agents with sizes smaller than the pore size could passively diffuse into the cytoplasm *in-vitro* via pores created by USMB. However, these observations were made in a simple *in-vitro* setting with monolayers of cells cultured in a fluid environment. It is not clear whether USMB also causes pore formation *in-vivo*, where tumor parenchymal cells are located in a densely packed solid tissue environment.

In addition to passive diffusion through nonspecific pores on tumor cell membranes, USMB has also been shown to assist in active drug transport mechanisms into the cytoplasm, such as endocytosis, especially for larger molecules (>500 kDa). Meijering et al. (2009) and Juffermans et al. (2014) demonstrated that cellular uptake of larger molecules relied on endocytosis alone; whereas cellular uptake of smaller

molecules involved both pore formation and endocytosis. Chuang et al. (2014) used microscopy to show the endocytotic process (24 h) by which albumin-shelled microbubbles loaded with paclitaxel (1.91 μm) enter breast cancer cells in presence of acoustic exposure, resulting in increased transport of albumin microbubbles into tumor cells. The exact mechanism behind USMB-induced endocytosis has not been completely elucidated. It has been speculated that ultrasound exposure and microbubble cavitation trigger changes in the membrane ion channels and the cytoskeletal arrangement, leading to an increase in intracellular Ca^{2+} (Parvizi et al. 2002) and polymerization of microtubules (Hauser et al. 2009). The changes may lead to enhanced endocytotic activity, thereby causing an increase in extracellular drug uptake in insonated cells. A detailed description on the microbubble-membrane interaction can be found in previous chapters of this book.

Indeed, the interaction between microbubbles and cells occurs within close proximity to the cells (Tzu-Yin et al. 2014). *In-vivo*, since microbubbles are spatially limited within the vessels, USMB induced in the vessel may only affect very few parenchymal cells near the vasculature (Ward et al. 2000). Therefore, successful drug delivery into distant parenchymal cells may require combination of USMB and other slow release therapeutic carrier systems. While USMB allows for passage of the therapeutic carriers across the vessels, the extravasated therapeutic carriers diffuse into the tumor parenchyma and slowly release the drug payload into tumor cells (Cochran et al. 2011a).

15.2.2 Destruction of Tumor Vascular

An alternative approach to cancer therapy is to destroy tumor vasculature by USMB. Exposure of tumor vessels to oscillating and imploding microbubbles can not only increase vascular endothelial cell membrane permeability, thereby enhancing uptake of anti-tumoral or anti-angiogenic in the vessels, but can also directly and mechanically destroy tumor vasculature. Both phenomena can cause blood vessel shut down with decreased supply of nutrients to tumor tissue (Molema et al. 1998).

15.2.2.1 Enhanced Cellular Uptake of Drugs in Vascular Endothelial Cells

The ultrasound-microbubble-cell interaction in the lumen of tumor vessels can selectively stimulate uptake of cytotoxic or anti-angiogenic drugs in vascular endothelial cells, leading to cellular apoptosis and subsequent disruption of the tumor vasculature (Fig. 15.2a).

In-vitro, this enhanced endothelial cellular uptake has been demonstrated using a dye, as well as fluorescently labeled molecules with difference sizes, such as propidium iodide (0.8 nm) (van Wamel et al. 2006), DiI (1 nm) (Patil et al. 2011), dextran (4.4 kDa) (Meijering et al. 2009), 5-carboxytetramethylrhodamine labeled small interfering RNA (siRNA about 15 kDa) (Juffermans et al. 2014), fluorescein isothiocyanate (FITC)-labeled dextran (500 kDa) (Taniyama et al. 2002) and Cy3-labeled plasmid DNA (about 3,500 kDa) (van Wamel et al. 2004). *In-vivo*, Fujii et al. (2013) demonstrated enhanced uptake of plasmid in endothelial cells in a heterotopic mammary adenocarcinoma model. In this study, vascular endothelial growth factor receptor-2 (VEGFR2) short hairpin (sh)RNA plasmid delivered by USMB (1.3 MHz, 0.9 W power, 10 s pulsing intervals for 20 min; cationic lipid-shelled microbubbles) resulted in increased knockdown of VEGFR2, as examined by PCR, immunostaining and western blotting. *In-vivo* contrast-enhanced ultrasound imaging further confirmed decreased tumor microvascular blood volume and blood flow in tumors treated with plasmid and USMB compared to tumors treated with plasmid alone.

15.2.2.2 Mechanical Destruction of the Tumor Vasculature

In addition to delivering anti-angiogenic therapeutics, USMB alone without adding therapeutic agents has been shown to have a direct anti-angiogenic effect in tumors (Fig. 15.2b). Wood et al. (2008) observed an acute shutdown of blood flow (as measured by Power Doppler) along with increased necrosis and apoptosis by histology following the administration of Definity® microbubbles and low intensity ultrasound (1 MHz at 2.2 $W.cm^{-2}$ or 3 MHz at 2.4 $W.cm^{-2}$; treatment for 3 min) in a murine melanoma model. Similarly, an acute

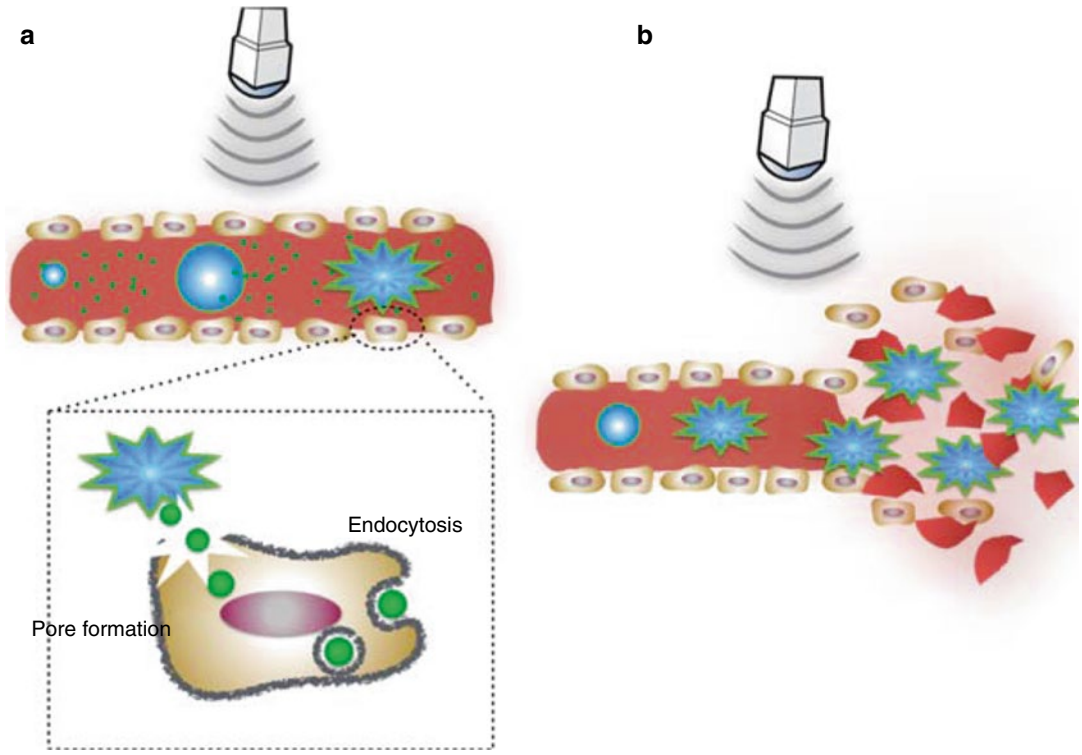

Fig. 15.2 Schematic drawing of destruction of tumor vasculature in USMB treatment. (**a**) Ultrasound-microbubble-cell interaction in the lumen of tumor vessels can stimulate uptake of cytotoxic or anti-angiogenic drugs in vascular endothelial cells by either creating pores on the cellular membrane and/or stimulating active transport, such as endocytosis. (**b**) USMB alone can directly produce an anti-angiogenic effect by mechanically disrupting tumor vasculature

decrease of blood flow by USMB alone (1 MHz, 0.1 ms pulse length, 1.6 MPa, Definity® microbubbles) was demonstrated in an *in-vivo* breast cancer model by Todorova et al. (2013). In this study, vessels in the tumor center were more preferentially disrupted versus those in the tumor periphery.

15.3 Treatment Protocols in Preclinical Experiments

USMB treatments require sufficient accumulation of microbubbles and drugs and appropriate ultrasound waves at the target tissues (Panje et al. 2012). The microbubbles and drugs can be delivered through different routes (intravenous (i.v.), intratumoral (i.t.) or intraperitoneal (i.p.)). The drugs can be mixed in the microbubble solution prior to administration or loaded on the microbubbles. Once the microbubbles and drugs reach the target tissues, appropriate ultrasound waves need to be delivered in a timely manner to produce optimal release of drugs (Willmann et al. 2008, Fig. 15.3).

In general, USMB treatment protocols involve systemic or local administration of microbubbles, along with a combination of therapeutic agents, followed by imaging-guided application of extracorporeal acoustic energy to actuate sonoporation at the desired delivery site. Delivery outcomes can be influenced by several factors, including but not limited to (1) whether drugs are mixed with or loaded on microbubbles, (2) routes of microbubble and drug administration, (3) ultrasound parameters, and (4) the temporal sequence of treatment. Several studies have investigated the influence of these factors on drug delivery efficiency in order to optimize treatment outcomes in cancer and to ultimately prepare this technique for clinical translation.

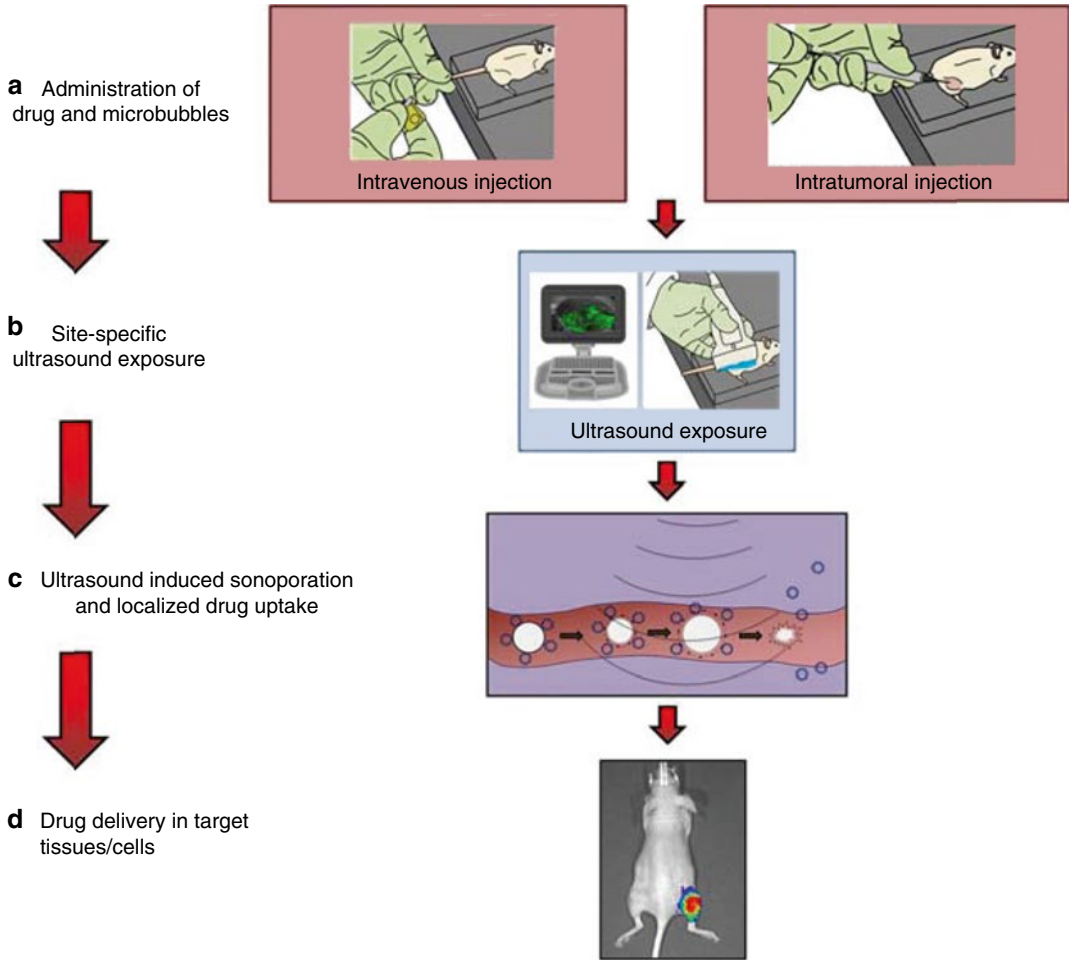

Fig. 15.3 Typical treatment protocol of USMB-mediated drug delivery in preclinical *in-vivo* experiments. (**a**) Microbubbles and therapeutic agents are administered either systemically via intravenous injection or locally through, for example, intratumoral injection. (**b**, **c**) Site-specific ultrasound exposure with the presence of microbubbles triggers sonoporation, facilitating the uptake of therapeutic agents. (**d**) Drug delivery outcomes could be quantified and monitored noninvasively using, for example, bioluminescence imaging shown here or other imaging modalities. Here, focal bioluminescent signal on the right hind limb of a mouse shows successful delivery of a reporter gene to the right hind limb tumor, while no imaging signal is observed elsewhere, demonstrating site-specific delivery limited to the region of insonation (This figure is adapted with permission from Panje et al. (2013))

15.3.1 Mixing Drugs with Microbubbles Versus Loading a Drug onto Microbubbles

15.3.1.1 Mixture of Drug and Microbubbles

One approach to USMB-mediated drug delivery is co-injecting a mixture of microbubbles and therapeutic agents. The advantage of this approach is the accessibility of already commercially available clinical grade microbubbles, such as Optison®, Definity® and Lumason®, all of which are FDA-approved for clinical contrast-enhanced ultrasound imaging. Sorace et al. (2012) intravenously injected Taxol, a chemotherapeutic for breast cancer, along with Definity® in breast cancer bearing xenografts in

mice followed by ultrasound insonation (1.0 MHz, 5 s pulse repetition period, mechanical index 0.5, 20 % duty cycle for 5 min). Over a 3-week treatment period, these tumors showed almost a 40 % increased inhibition and a higher degree of necrosis compared to the tumors treated with drugs alone. Wang et al. 2013a intravenously injected SonoVue® along with a suicide gene, herpes simplex virus-thymidine kinase gene (HSV-TK), for USMB treatment (mechanical index 1.2 for 10 min). They observed that USMB resulted in a 47-fold enhanced TK mRNA expression and a more than 2-fold apoptosis rate in an ovarian cancer model in mice. More examples (Sorace et al. 2012; Duvshani-Eshet et al. 2007; Matsuo et al. 2011; Carlisle et al. 2013; Wang et al. 2013a, b; Nie et al. 2008; Liao et al. 2012; Kotopoulis et al. 2014; Zhao et al. 2012; Suzuki et al. 2010; Yamaguchi et al. 2011; Heath et al. 2012; Iwanaga et al. 2007) are summarized in Table 15.1.

15.3.1.2 Drug-Loaded Microbubbles

The drawbacks of co-injecting drugs freely along with microbubbles are (1) faster degradation of certain drugs (nucleic acid (Zhou et al. 2010; Greco et al. 2010; Haag et al. 2006) and RNA (Carson et al. 2012)), and (2) potentially increased toxicity to other organs (other than liver and spleen in which microbubbles are usually cleared). To address these issues, microbubbles have been exploited as drug delivery vehicles as they are amenable for surface modification. Several strategies have been proposed for conjugating therapeutic agents onto or into microbubble carriers, which are further detailed in Chap. 11. For example, drugs can be embedded within the microbubble shell, dissolved in an oily layer between the gas core and the shell, or linked to the surface of the microbubbles. However, the drug loading capacity using these approaches is generally low. To improve this, alternative techniques coupling drug loaded liposomes or nanoparticles onto the microbubble shell have been reported (Wang et al. 2012; Sirsi SR and Borden MA (2014) State-of-the-art materials for ultrasound-triggered drug delivery. Advanced drug delivery reviews.

15.3.2 Routes of Microbubbles and Antitumor Agent Administration

Several drug administration routes have been explored including i.v., i.t., and i.p. injections. Direct i.t. and i.p. injection allow delivery of high local concentrations but are invasive.

15.3.2.1 Intravenous Injection

In most studies on USMB-mediated drug delivery for cancer therapy in preclinical animal models, microbubbles and drugs are administered intravenously. The potential drawbacks of this approach are the potential systemic toxicity and, in the case of gene delivery, the rapid degradation of the agent in the circulation. Both disadvantages can be overcome by either attaching drugs directly onto microbubbles or by loading them into nanoparticles.

Another potential drawback of systemic administration is that the delivery efficiency may be limited in hypovascularized tumors, such as pancreatic cancer (Fukumura and Jain 2007), because this route relies on sufficient tumoral vascularity for circulating microbubbles and drugs to float into target lesions.

15.3.2.2 Intratumoral Injection

Several early proof-of-concept animal studies have used this approach and demonstrated improved drug delivery after ultrasound exposure (Duvshani-Eshet et al. 2007; Iwanaga et al. 2007; Haag et al. 2006). The main advantage of i.t. injection is the ability to deliver high concentrations of drugs directly to the site of desired treatment while minimizing systemic toxicity (Duvshani-Eshet et al. 2007). However, this method of administration is invasive and can be challenging if the target lesion is located in an area that is difficult to access.

15.3.2.3 Intraperitoneal Injection

This approach may be useful for primary peritoneal cancers or cancers with i.p. spread as local drug concentration can be increased at the tumor sites (Pu et al. 2014; Kotopoulis et al. 2014). It has been shown that i.p. injection of drugs can

Table 15.1 Examples of animals studies using ultrasound and microbubbles to deliver drugs/genes for cancer therapy

Cancer types	References	Animal models	Drugs	MBs	Techniques	Routes	Treatment outcomes
HCC	Cochran et al. (2011b)	sc 3924a rats	DOX	Drug-loaded polymer MBs	1 MHz, MI 0.4–0.45, 20 min	i.v., MBs, single	Drug concentration in liver tumors was increased by 7-fold compared to administration of free DOX, while drug concentrations in plasma and myocardium were reduced to 1/5 and 1/2, respectively.
	Nie et al. (2008)	sc Hepa1-6 mice	HSV-TK pDNA GCV	SonoVue®	1 MHz, 50 % DC, 2 W/cm^2, 5 min	i.v., MBs, pDNA i.p. GCV daily for 10 days	Tumor volume was approximately 1/2 of control group treated with TK and MBs at day 28. MST was significantly longer than control (survival ratio at day 100 was 50 % vs. 0 %)
	Zhou et al. (2010)	sc H22 mice	HSV-TK pDNA GCV	pDNA-loaded lipids MBs	1 MHz, 2 W/cm^2, 5 min	i.v., MBs, pDNA i.p. GCV daily for 14 days	Tumor growth was further inhibited by 37 % compared to HSV-TK pDNA alone. Longer MST and better life quality in an 80-day continuous observation period.
	Yu et al. (2013)	sc HepG2 mice	HSV-TK pDNA Timp3 pDNA	Liposomes MBs	1.3 MHz, MI 1.3, 1 s interval time for 5 min	i.v., MBs, pDNA i.p. GCV daily for 4 days	Tumor growth was further inhibited by 30 % in treatment with both pDNA and USMB compared to treatments with single gene under the same USMB settings.
PC	Kotopoulis et al. (2014)	Orthotopic MIA PaCa-2 mice	Gemcitabine	SonoVue®	1 MHz, MI 0.2, 40 % DC, 10 min	i.v., MBs i.p. Gemcitabine weekly for 8 wks	The primacy tumor presented only 1/3 size of those treated with drug alone. A slower onset of metastatic development was observed.

HCC LC Glioma	Liao et al. (2012)	sc/orthotopic BNL mice Orthotopic LL/2 mice Orthotopic RT-2 mice	Endostatin Calreticulin pDNA polytreated with DOX, GM-CSF or IL-12	SonoVue®	1 MHz, 0.4 W/cm^2, 20 % DC, 200 Hz PRF	i.m., MBs, pDNA, intermittent (weekly for 4 wks) or consecutive (daily for the initial 4 days) i.p. DOX twice i.t. GM-CSF & IL-12 single	Tumors significantly regressed in all groups. Intermittent regimen was much more effective than consecutive regimen. Administration of multiple therapeutic agents resulted in better treatment outcome than administration of single agent.
BC	Sorace et al. (2012)	sc 2LMP mice	PTX	Definity®	1 MHz, 5 s PRP, 20 % DC, 5 min, MI 0.1, 0.5, 1 or 2	i.v., MBs, PTX twice a wk for 3 wks	All 4 pressure levels resulted in decreased tumor growth. Among them, MI of 0.5 resulted in the highest percentage of necrosis.
	Yan et al. (2013)	sc 4 T1 mice	PTX	Drug-loaded liposomes MBs	2.25 MHz, 1 % DC 1 Hz PRF, 10 ms BL, 1.9 MPa, 10 min	i.v., MBs, 3 more times at 3-day intervals	Drug accumulation was 3.54- or 4.31- fold higher in tumors compared to the groups without MBs or ultrasound, while the accumulation was lower in liver & kidney.
	Zhao et al. (2012)	sc MDA-MB-435 mice	Liposomal-DOX	Lipids MBs	1 MHz, 0.3 W/cm^2 50 % DC, 10 s	i.v., MBs, drug every 2 days	Tumor growth was inhibited using either of the three treatment schedules (USMB applied 2 h before, 2 h after, or simultaneously with drug administration), although the effect in the group treated with USMB applied 2 h after drug administration was inferior to the others.

(continued)

Table 15.1 (continued)

Cancer types	References	Animal models	Drugs	MBs	Techniques	Routes	Treatment outcomes
BC	Carlisle et al. (2013)	sc ZR75-1 mice	Oncolytic adenovirus (polymer)	SonoVue®	0.5 MHz, 50,000 cycles/pulse length, 0.5 Hz PRF, 1.2 MPa, 4 min	i.v., MBs & polymer, single	Circulation half-life of oncolytic adenovirus was improved by more than 50-fold. Tumor infection was enhanced by more than 30-fold, resulting in improved tumor growth retardation and prolonged MST.
OC	Suzuki et al. (2010)	sc OV-HM mice	IL-12 pDNA	Liposome MBs	1 MHz, 0.7 W/cm^2, 1 min	i.t., MBs, pDNA single & 12-day repetitive treatments	Tumor growth was suppressed in both treatments. Complete tumor regression in 80 % of mice receiving repetitive treatments.
	Pu et al. (2014)	Orthotopic A2780/DDP mice	PTX	LHRHa-targeted drug-loaded MBs	0.3 MHz, 1 W/cm^2 50 % DC, 3 min	i.p., MBs every 3 days for 15 days	Tumor cell apoptosis increased by 38 %, angiogenesis reduced by 39 % in comparison to the non-targeted PTX-loaded MBs + US group.

Prostatic Cancer	Goertz et al. (2012)	sc PC3 mice	Docetaxel	Polymer MBs	1 MHz, 50 ms burst, 1.65 MPa, 3 min	i.v., MBs & drug, single & 4-week repetitive treatment	Compared to drug alone, single treatment of USMB and drug induced a four-fold increase in necrosis, and repetitive treatment delayed tumor growth with prolonged doubling time from 0.1 to 6.9 weeks.
	Duvshani-Eshet et al. (2007)	sc PC2 mice	Hemopexin-like domain fragment pDNA	Optison®	1 MHz, 2 W/cm^2, 30 % DC 20 min	i.t., MBs, pDNA single & 4-wk repetitive treatments	Tumor growth was inhibited by 50 % after single treatment and by 80 % after repetitive treatments.
	Greco et al. (2010)	sc DU-145 DU-Bcl-xL mice	Cancer terminator virus	Virus-loaded targeson	MI 0.7 m 1.8 MPa, 10 min	i.v., MBs weekly for 4 weeks	Primary and metastatic tumors and therapy-resistant tumors were completely eradicated. No tumor regrowth occurred 3 months after cessation of the therapy.
	Haag et al. (2006)	sc LNCaPbl mice	Androgen receptor AO	AO-loaded lipid MBs	1.5, 2.5 or 7 MHz, MI 1.9, 9 min	i.t., & i.v., MBs single	Stronger gene uptake in tumor tissue was detected after gene-loaded MB injection and ultrasound compared to MB complex alone (16~49 % vs. 2~18 %).

(continued)

Table 15.1 (continued)

Cancer types	References	Animal models	Drugs	MBs	Techniques	Routes	Treatment outcomes
Melanoma	Matsuo et al. (2011)	sc C32 mice	Melphalan	Sonazoid®	1.011 MHz, 0.064 W/cm^2, 0.5 Hz burst rate, 50 % DC, 2 min	i.t., MBs, drug. Every 2 days for 2 weeks	Tumor growth ratio was significantly reduced by nearly 2.5 fold compared to drug alone.
	Yamaguchi et al. (2011)	sc C32 mice	IFN-β pDNA	Sonazoid®	1.011 MHz, 0.22 W/cm^2, 50 % DC, 3 min	i.t., MBs, pDNA, weekly for 4 weeks	Tumor growth ratio was significantly reduced by 2-fold and nearly 1.5-fold compared to blank control and gene alone, respectively.
SCC	Heath et al. (2012)	sc SCC-5 mice	Cisplatin Cetuximab	Definity®	1 MHz, MI 0.5, 5 s PRP, 20 % DC, 5 min	i.v., MBs & drugs, twice weekly for 4 weeks	Tumors treated with USMB and drug exhibited a 21 ~ 26 % decrease in tumor size compared with drug alone.
	Iwanaga et al. (2007)	sc Ca9-22 mice	Bleomycin Cdt-B pDNA	Optison®	1 MHz, 2 W/cm^2, 50 % DC	i.t., MBs, pDNA. Every 2 days in the first and third wks	Tumor was completely suppressed at the end of experimental period (56 days) in the group of cdtB pDNA and USMB, and nearly disappeared in bleomycin and USMB.
	Carson et al. (2012)	sc SCC-VII mice	EGFR-siRNA	Gene-loaded lipids MBs	1.3 MHz, MI 1.6, 30 min	i.v., MBs, 3 times	EGFR knockdown was distributed widely (80 %) throughout treated tumors. Tumor doubling time was prolonged from 2.7 to 8.5 days compared to gene alone.

Glioma	Liu et al. (2010)	Orthotopic C6 rats	Carmustine	SonoVue®	0.4 MHz, 0.62 MPa, 10 ms burst length, 1 Hz PRF, 30 s	i.v., MBs & drug, single	Drug delivery was enhanced by two-fold. Tumor growth was inhibited. MST was prolonged from 33 to 53 days compared to drug alone.
	Treat et al. (2012)	Orthotopic 9 L rats	Liposomal-DOX	Definity®	1.7 MHz, 1.2 MPa, 10 ms burst length, 1 Hz PRF for 1–2 min repeated every 5 min	i.t., MBs, drug, single	Tumor doubling time was prolonged from 2.7 days to 3.7 days compared to drug alone. MST was improved.
	Ting et al. (2012)	Orthotopic C6 rats	Carmustine	Drug-loaded MBs	0.7 MPa, 10 ms burst length, 5 % DC, 5 Hz PRF, 1 min	i.v., MBs, twice	Circulation drug half-life was prolonged by four-fold. Drug accumulation in the liver was reduced fivefold compared to drug alone. Tumor growth ratio was significantly reduced from 117.4 to 39.6 % and MST was improved from 29.5 to 32.5 days compared to drug alone.

PC pancreatic cancer, *Wks* weeks, *LC* lung cancer, *BC* breast cancer, *PTX* paclitaxel, *BL* burst length, *LNCaPbl* androgen hypersensitive LNCaP subline, *AO* antisense oligonucleotide, *IFN*-β interferon-β, *SCC* squamous cell carcinoma, *Cdt-B* Cytolethal distending toxin B, *HCC* hepatocellular cancer, *MBs* microbubbles, *DOX* doxorubicin, *DC* duty cycle, *MI* mechanical index, *PRF* pulse repetition frequency, *PRP* pulse repetition period, *i.v.* intravenous, *i.t.* intratumoral, *i.p.* intreperitoneal, *i.m.* intramuscular, *HSV-TK/GCV* herpes simplex thymidine kinase gene/ganciclovir, *LHRH-R* luteinizing hormone-resealing hormone receptor, *TIMP3* tissue inhibitor of metalloproteinase 3, *GM-CSF* granulocyte-macrophage colony-stimulating factor, *IL-12* interleukin-12, *pDNA* plasmid DNA, *MST* mean survival time

result in 20- to 1,000-fold higher peritoneal drug concentrations compared to plasma concentrations (Zimm et al. 1987; Markman et al. 1992). Micron-sized microbubbles, injected intraperitoneally, can stably persist in the peritoneal cavity without rapid clearance through the lymphatic drainage (Pu et al. 2014; Kohane et al. 2006; Tsai et al. 2007). Recently, in a mouse model of metastatic peritoneal lesions of ovarian cancer, Pu et al. (2014) injected luteinizing hormone-releasing hormone (LHRH) receptor-targeted paclitaxel-loaded microbubbles into the mouse peritoneal cavity and exposed the abdomen to ultrasound for sonporation. These microbubbles specifically bind to tumor cells expressing LHRH, and upon exposure to ultrasound, encapsulated drugs can be locally released at the tumor sites. Compared to treatment with paclitaxel alone, this approach resulted in an approximately two-fold higher apoptosis rate, an extended median survival time of treated mice from 37 to 47 days, and an approximately 55 % reduced tumor angiogenesis. In patients, however, peritoneal spread of cancer is usually diffuse and further studies are needed to assess clinical practicability of this approach to efficiently treat a diffuse disease process, such as peritoneal carcinomatosis using USMB.

15.3.3 Ultrasound Parameters

Most studies have shown successful USMB-guided drug delivery using already available clinical ultrasound imaging systems; however, the reported delivery efficiency is inconsistent (Newman and Bettinger 2007), likely due to there being so far no standardization of the acoustic parameters. To date, standardized ultrasound parameters for drug delivery have not been determined on any of the current clinical ultrasound systems, possibly because the systems have limited tunable acoustic parameters. This makes it difficult to perform a systematic and parametric study for optimal drug delivery on these systems. Optimizing ultrasound parameters tailored for the purpose of drug delivery has the potential to improve treatment outcomes (Yu et al. 2013). To determine an optimal setting for effective delivery, some studies compared drug delivery outcomes using custom-built ultrasound systems with more flexibility in the acoustic parameters. A wider range of ultrasound parameters was tested in drug delivery into cells *in-vitro* (Sonoda et al. 2007; Ghoshal et al. 2012) and *in-vivo* (Sorace et al. 2012; Wang et al. 2013a, Haag et al. 2006). So far, standard ultrasound parameters for USMB drug delivery have not been established. *In-vivo* ultrasound settings suggested by current literature are as follows:

Ultrasound frequency: 0.4 ~ 3 MHz. Lower frequencies are more preferable in general because the pressure threshold to initiate cavitation is reduced in the low frequency range (Apfel and Holland 1991).

Ultrasound intensities: 0.3 ~ 3 W/cm^2. This range lies close to or above the level used in diagnostic ultrasound (0.1–100 mW/cm^2), but below that of high-intensity focused ultrasound (Dubinsky et al. 2008; Leslie and Kennedy 2006). This allows for drug delivery into tumors while minimizing damage to normal tissues.

Mechanical index: 0.2 ~ 1.9. Mechanical index is defined as the ratio of peak negative pressure in MPa and the square root of center frequency in MHz. This index indicates the likelihood of cavitation generation. The likelihood of cavitation increases with increasing ultrasound intensity and decreasing frequency, and the mechanical index of an acoustic field is used as a safety gauge on clinical ultrasound imaging systems. The FDA stipulated limitation of mechanical index for clinical diagnosis is 1.9. It is thought that cavitation is unlikely to occur at a mechanical index of less than 0.7 (Newman and Bettinger 2007). However, the presence of microbubbles in the acoustic field significantly reduces this threshold by a rather unpredictable degree. This allows for USMB-enhanced drug delivery under a mechanical index lower than 1.9 (Newman and Bettinger 2007).

Duty cycles: <1–90 %. Duty cycle specifies the percentage of time pulsed ultrasound transmission occurs (O'Brien 2007). Applied duty

cycles vary substantially among various publications and usually depend on the ultrasound intensity used. In general, long duty cycles combined with high intensities can cause thermal damage to tissues. To avoid unnecessary thermal effects, duty cycles are kept low when high intensities are used and vice versa.

Duration of ultrasound exposure: 10 s ~ 30 min. The exposure duration needs to be sufficiently long for complete destruction of the administered microbubbles. However, for safety reasons, the exposure duration should be shortened to the minimally required time to avoid excess tissue damage. Most investigators apply ultrasound for a period of 1–5 min.

15.3.4 Treatment Schedule

The treatment schedule, including the temporal sequence of drug administration, USMB treatment, and the length and interval durations of repeated treatment cycles can have substantial effects on treatment efficiency.

Given that USMB only increases the permeability for a few seconds to a few hours (Tzu-Yin et al. 2014; Fan et al. 2012; Sheikov et al. 2008; Park et al. 2012a), administration of therapeutic agents at different time points following USMB treatment could result in substantially different treatment outcomes, as recently demonstrated in an *in-vivo* model by Zhao et al. (2012). In their experiment, three different treatment schedules (USMB applied 2 h before, 2 h after, or simultaneously with the injection of doxorubicin-loaded liposomes) were tested in a human breast cancer model in mice. Tumor suppression was smallest in mice treated with USMB applied 2 h after drug administration, and comparable in the other two treatment groups. This indicates a lingering therapeutic window for drug delivery of at least 2 h after USMB. Knowing the therapeutic window after a certain USMB treatment is critical to maximize therapeutics in cancer.

The influence of treatment interval length on USMB therapeutic outcomes was further assessed by Liao et al. (2012). Two different USMB treatment schedules, combined with the administration of anti-angiogenic gene therapy using endostatin and calreticulin, were evaluated in a subcutaneous hepatocellular cancer model in mice. In the first group of animals, USMB was applied once a week over 4 weeks. In the second group, USMB was applied daily over the first 4 days and all tumors were observed over a 4-week period. Therapeutic effects were more pronounced in the first group compared to the second one, suggesting that a continuous systemic concentration of angiogenesis inhibitors administrated weekly may be more effective in tumor growth inhibition than the administration of a high dose during a short time period (Grossman et al. 2011; Kisker et al. 2001).

It is expected that in the future optimized treatment schedules may need to be assessed for different tumor types and different therapeutic agents to enable maximum treatment effects.

15.4 Application in Cancer Therapies

Numerous studies have shown successful USMB-mediated drug delivery to a number of different cancer types (Table 15.1). This technique has shown enhanced systemic chemotherapy tumoricidal effects, improved biodistribution with preferential local accumulation in tumor tissue, and reversal of drug resistance of certain cancer types. It has also been proposed as an adjuvant treatment to other cancer therapies, as well as a potential approach to cancer vaccination. In the following section, the current status of USMB-mediated drug delivery in different types of cancer therapies *in-vitro* and in preclinical animal models is reviewed.

15.4.1 Cancer Therapy

15.4.1.1 Enhanced Tumoricidal Effects

Multiple *in-vitro* and *in-vivo* studies have demonstrated that USMB improves tumoricidal effects, as evidenced by a reduction of tumor growth, increase in tumor apoptosis and necrosis,

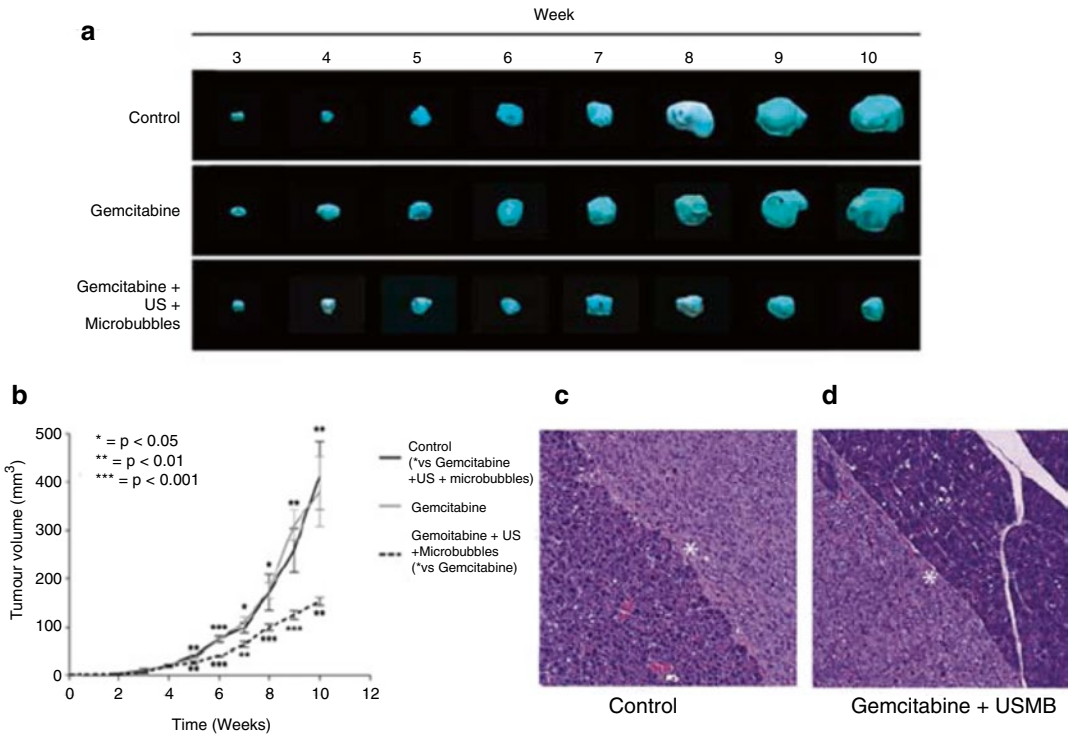

Fig. 15.4 Enhanced tumoricidal effect of USMB-mediated gemcitabine delivery in orthotopic pancreatic tumors in mice. (**a**) Compared to mice receiving weekly treatment of gemcitabine alone or no treatment (control), mice treated with USMB and gemcitabine presented a significantly suppressed tumor growth, as visualized in 3D tumor volumetric ultrasound images over time. (**b**) A statistically significant difference can be seen between the combined treatment group and the gemcitabine alone and/or control group after two treatment cycles. Histology images show a more invasive border between normal and tumor tissue in the control group (**c**), and a less invasive border in the gemcitabine and USMB group (**d**) (as indicated by the *asterisks*) (This figure is adapted with permission from Kotopoulis et al. (2014))

decrease in angiogenesis and regulation of relative protein expressions (Fig. 15.4).

For example, in a prostate tumor bearing mouse model (Goertz et al. 2012), intravenous injection of the chemotherapeutic docetaxel, along with microbubbles and ultrasound treatment, resulted in four-fold increase in necrosis compared to treatment with docetaxel alone at 24 h. In a mouse ovarian cancer model, Xing et al. (2008) investigated the level of tumor suppressor p53 after treatment with paclitaxel-loaded microbubbles and ultrasound. They showed that p53 expression was down-regulated 33 % more than in the paclitaxel alone group. Greco et al. (2010) treated mice with prostate cancer xenografts using USMB-assisted delivery of cancer terminator virus (CTV) with CTV-loaded microbubbles. They showed complete tumor response with complete tumor eradication following several weeks of weekly treatment. Even when animals were followed up to 3 months after the treatment, there was no tumor recurrence or metastatic spread in any of the mice. Similar complete response results were also reported in other murine cancer models, including head and neck squamous cell carcinoma (2007) and ovarian cancer (Greco et al. 2010).

Delivery of multiple medications, or polytherapy, using USMB can further enhance tumoricidal effects. Yu et al. (2013) administered a mixture of two therapeutic plasmids, HSV-TK/GCV and the tissue inhibitor of metalloproteinase 3 (Timp3), along with cationic microbubbles into mice bearing subcutaneous hepatocellular carcinomas and insonated the tumors with ultrasound. An additional 30 % improvement of tumor suppression was

observed compared with USMB-mediated delivery of either gene alone. Liao et al. (2012) treated orthotropic liver tumors in mice using USMB-assisted delivery of a combination of endostation (an anti-angiogenic gene) and interleukin-12 (an immunotherapeutic drug that prompts the immune system to fight cancer). The treatment resulted in an average tumor volume reduction to 7 % of the original size, while USMB-assisted delivery of either endostation or interleukin-12 alone resulted in a tumor volume reduction to only 52 % and 56 %, respectively.

Tumoricidal effects were observed not only in primary tumors but also in their metastases. Park et al. (2012b) studied treatment of breast cancer brain metastasis using USMB. A chemotherapeutic, trastuzumab, was co-injected along with Definity® microbubbles, and brain metastatic lesions were insonated by transcranial ultrasound. In animals treated with USMB and trastuzumab, an overall longer survival time, significant tumor suppression and even complete remission in some cases were observed compared to animals treated with intravenously injected trastuzumab alone. Pu et al. (2014) developed a method for treating metastatic ovarian cancer peritoneal lesions using the complex of LHRHa-targeted paclitaxel-loaded microbubbles. Five consecutive treatments with i.p. injection of this complex, followed by ultrasound exposure to the abdomen, resulted in approximately two-fold more cell apoptosis and 50 % lower microvessel density in peritoneal implants compared to the treatment with i.p. injection of paclitaxel alone.

In summary, USMB has demonstrated benefits in improving outcomes of many anti-cancer therapeutics in various preclinical tumor models, resulting in significantly increased tumoricidal effects, even complete remission in some cases.

15.4.1.2 Reduction of Toxicity of Chemotherapeutics

One of the most notorious problems of chemotherapy is its significant systemic toxicity, including cardiotoxicity and myelosuppression (Rahman et al. 2007). This issue could be addressed by the aforementioned technique of drug-loaded microbubbles with a spatially confined release of the encapsulated drug in the region exposed to ultrasound, while the drug remains on the microbubbles or nanoparticles, and rapidly clears before free drug exposes healthy tissues. For example, Cochran et al. (2011b) demonstrated preferential drug accumulation in the tumor, and smaller levels in normal organs, using doxorubicin-loaded microbubbles and ultrasound in a subcutaneous hepatoma mouse model. Specifically, the drug concentration was eight-fold higher in hepatoma (2.491 vs. 0.373 %/g tissue) and 50 % lower in the myocardium (0.168 vs. 0.320 %/g tissue) in mice treated with doxorubicin-loaded microbubbles, with ultrasound relative to the mice treated with the same dose of free drug (Fig. 15.5). Similar results were reported by Yan et al. (2013) in mice bearing breast cancer xenografts treated with paclitaxel liposome-loaded microbubbles and ultrasound. In tumors, a 3.5-fold higher paclitaxel tumor concentration could be obtained, along with significantly reduced levels of paclitaxel in normal liver and kidney tissues, compared to mice treated by free paclitaxel liposomes and ultrasound without microbubbles.

The lower drug concentration in the non-insonated healthy organ might reduce the toxicity of chemotherapeutics. Additionally, the preferential accumulation in insonated tumors suggests that the systemically administered dose may be reduced and yet still produce a comparable treatment effect in the diseased tissues. This may reduce the drug deposition in healthy organs, thus reducing the systemic toxicity. This feature has significant clinical implications in that it may reduce the systemic side effects in patients, as well as the financial burden of the cost of expensive chemotherapy drugs.

15.4.1.3 Reversal of Drug Resistance

Drug resistance is a common chemotherapy challenge resulting in failure of successful therapy in many cancers. For example, 75 % of pancreatic cancer patients are resistant to gemcitabine, even though it is the first-line chemotherapeutic agent for pancreatic adenocarcinoma (Ducreux et al. 1998). In breast cancer, only 60–70 % patients respond to anthracycline-based chemotherapy,

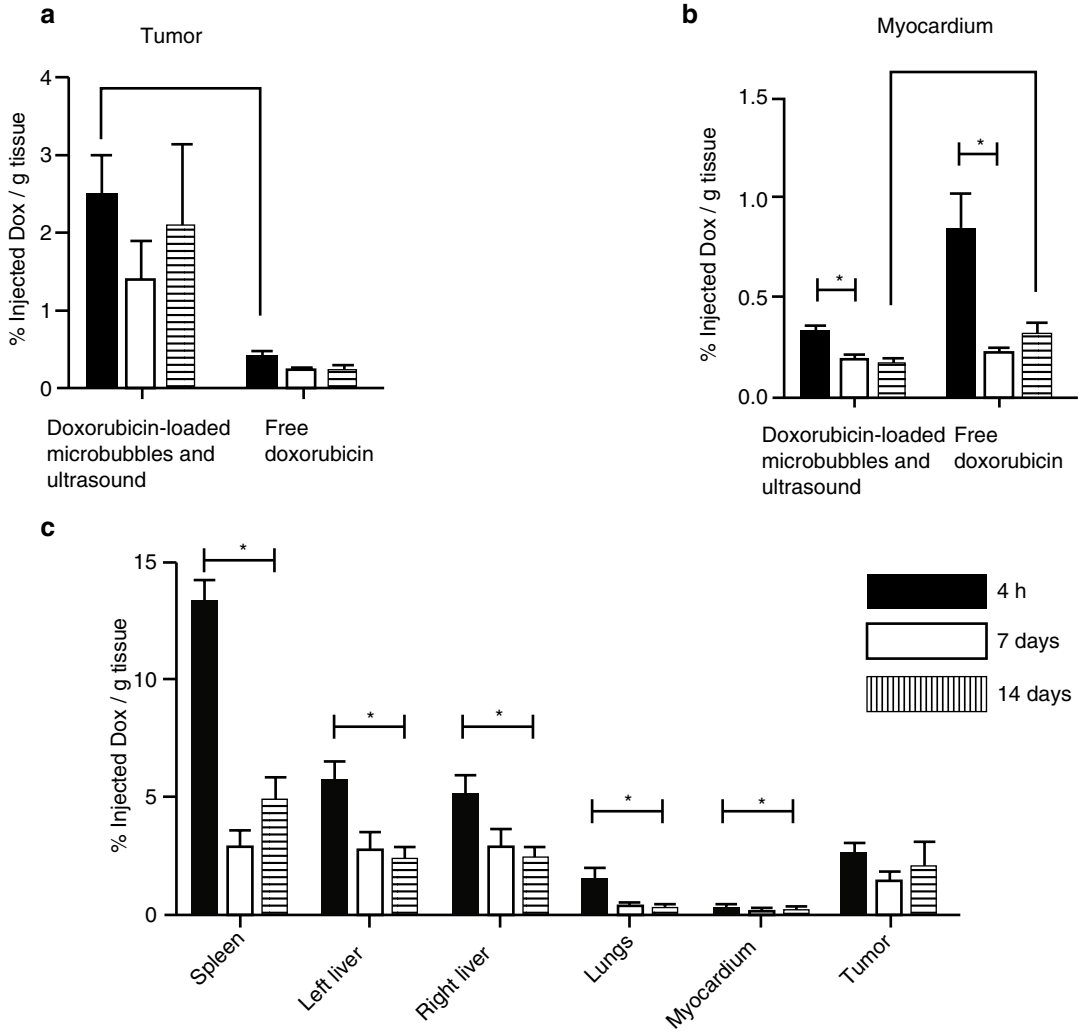

Fig. 15.5 Temporal and spatial distribution of doxorubicin in subcutaneous hepatoma-bearing mice treated with doxorubicin-loaded microbubbles and ultrasound or free doxorubicin alone. Compared to tumors treated with free doxorubicin, the treatment of doxorubicin-loaded microbubbles and ultrasound resulted in a higher doxorubicin concentration in the tumors (**a**) and lower concentrations in the myocardium (**b**). Doxorubicin levels in the spleen, liver, lungs, and myocardium all peaked at 4 h and dropped significantly after 14 days, whereas those in the tumor showed no significant drop from day 0 to day 14 (**c**). *$p<0.05$ (This figure is adapted with permission from Cochran et al. (2011b)

with only 14 % of them being completely responsive (Carey et al. 2006).

Drug resistance is often caused by the up-regulation of special transporters across the cancer cell membranes, preventing cellular uptake of drugs and/or ejecting drugs from the cytoplasm. An example is the multidrug resistance associated protein pumps, also known as P-glycoproteins, which are exporters of ATP-binding cassette transporters (Gottesman 2002; Szakacs et al. 2006).

Deng et al. (2013) observed that the use of USMB could help reduce drug resistance by down-regulating the level of P-glycoprotein in breast cancer cells *in-vitro*. Doxorubicin-resistant MCF-7 breast cancer cells were exposed to doxorubicin-liposome-microbubble complexes and insonated by ultrasound. Cells treated with doxorubicin-liposome-microbubble complex and ultrasound showed a more rapid cellular uptake, enhanced nuclear accumulation of drugs, and less

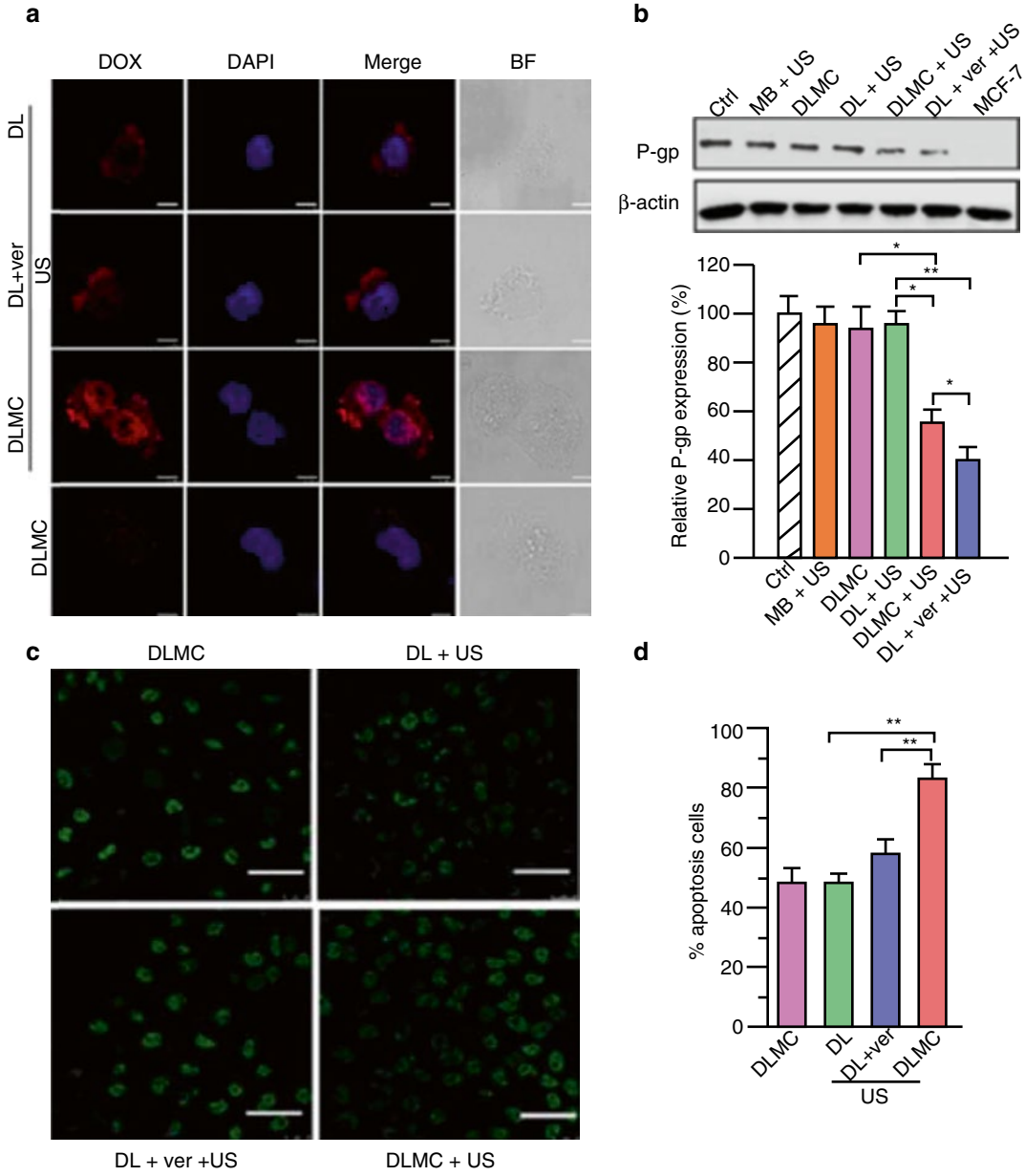

Fig. 15.6 Doxorubicin-resistant MCF-7 breast cancer cells were exposed to doxorubicin-liposome (DL)+ultrasound (US), DL+verapamil (ver) (a compound which reverses multidrug resistance by inhibiting drug efflux)+US, doxorubicin-liposome-microbubble complexes (DLMC)+US, and DLMC only. (a) Confocal microscopic images of intracellular doxorubicin distribution showed a more rapid cellular uptake and enhanced nuclear accumulation of doxorubicin using DLMC+US compared to other treatments. (b) Western-blotting showed down-regulated expression of P-glycoprotein using DLMC+US. (c) Apoptosis was detected by terminal deoxynucleotidyl transferase dUTP nick end labeling. (d) Quantitative analysis of apoptosis staining indicated significantly enhanced apoptosis using DLMC+US. *$p < 0.05$, **$p<0.01$ (This figure is adapted with permission from Deng et al. (2014))

drug efflux. Importantly, P-glycoprotein levels were substantially reduced in treated cells compared to non-treated cells (Fig. 15.6). Although the exact mechanism of reduced P-glycoprotein expression levels by USMB treatment remains unclear, it has been speculated that the

P-glycoprotein could have been mechanically removed from the cell membranes due to shear force induced by ultrasound-triggered microbubble cavitation (Brayman et al. 1999).

Alternatively, drug resistant tumors can be transfected with therapeutic genes to increase membrane transporters that shuffle drugs into tumor cells. This concept has been shown *in-vitro* in gemcitabine-resistant cells (dilazep-treated HEK293) transfected with human concentrative nucleoside transporter 3 (hCNT3) gene using USMB (Paproski et al. 2013). This resulted in a more than 2,000-fold increase of hCNT3 mRNA expression, and a subsequent more than 3,400-fold increased cellular uptake of gemcitabine relative to that in non-transfected cancer cells.

These two examples demonstrate that both physical impact of USMB on tumor cells and USMB-assisted transfection of transporter genes could potentially help overcome tumor cell drug resistance. However, so far experiments on this topic have only been performed under *in-vitro* conditions and further studies in animal models are warranted.

15.4.2 Adjuvant Treatment to Other Cancer Therapies

Adjuvant chemotherapy or radiotherapy is often applied following surgical resection in order to minimize local tumor recurrence and reduce tumor metastases. USMB-mediated drug delivery into a resection bed could become a part of a multimodality treatment approach of certain cancer types to reduce local recurrence rates. Sorace et al. (2014) proposed the use USMB-mediated delivery of cetuximab as adjuvant therapy following surgical resection of head and neck cancer in mice (1 MHz, 0.9 MPa peak negative pressure, 15 s pulse repetition period, 5 % duty cycle for 5 min). Tumors were resected at various degrees (0, 50, or 100 %), followed by adjuvant therapy with USMB-assisted delivery of cetuximab. During a 60-day post surgery observation period, there was no tumor recurrence in mice treated with complete tumor resection and USMB-aided drug treatment, while the recurrence rate was 66 % in animals receiving complete resection but no adjuvant USMB-guided therapy.

15.4.3 Cancer Vaccination

Cancer vaccination refers to the mediation that stimulates or restores the immune system's capability to treat existing cancer or prevent cancer development in certain high-risk individuals. The "classic" vaccine is currently achieved using tumor antigens isolated from surgical specimens or cancer cell lines, and made non-viable in *ex-vivo* conditions (Chiang et al. 2010). The non-viable antigens are then injected into the patient. The antigens can be taken up by the dendritic cells, processed intracellularly and subsequently expressed on the cell surface (Timmerman and Levy 1999). In the presence of antigen-presenting cells, the naïve T-cells are activated and play a central role in cell-mediated immunity to eliminate cancerous cells before they can do any harm. However, most clinical trials investigating cancer vaccination have failed or had very modest responses. A possible explanation is that the immune system of cancer patients is suppressed, with dendritic cells not recognizing the antigens to trigger an appropriate immune response in order to kill cancer cells.

USMB is currently being explored as a tool for *in-vivo* transfection of dendritic cells for cancer vaccination with improved transfection efficiency. It was found that antigen-encoding RNA intranodally injected into lymph nodes can be taken up by resident lymph node dendritic cells. Transfection of the dendritic cells propagated a T-cell attracting and stimulatory intralymphatic milieu, leading to efficient expansion of antigen-specific T cells, eliciting a protective and therapeutic anti-tumoral immune response (De Temmerman et al. 2011). The uptake of antigen-encoding RNA by dendritic cells could be further enhanced by the assistance of USMB. On the other hand, intradermally injected microbubbles can migrate to and successfully accumulate in lymph nodes (Sever et al. 2009). The accumulation of microbubbles can enhance

image contrast and facilitate *in-vivo* transfection of dendritic cells in the lymph nodes.

Oda et al. (2012) performed a first *in-vitro* proof-of-principle experiment and extracted tumor-specific antigens from melanoma cells. These were then delivered into dendritic cells with the assistance of USMB. This treatment induced 74.1 % of dendritic cells to present melanoma-derived antigens on their cell surface, relative to only 5.7 % in the group without USMB. These antigen-presenting dendritic cells were then intradermally injected twice into the backs of mice to assess effects in preventing melanoma lung metastases *in-vivo*. The results demonstrated a four-fold decrease in lung metastasis frequency after USMB-assisted prophylactic vaccination.

15.5 First Clinical Case Study

Recently, USMB was explored in a first clinical case study conducted by Kotopoulis et al. (Kotopoulis et al. 2013) in five patients with locally advanced pancreatic cancer. In this study, the patients were administered standardized gemcitabine treatment followed by sequential treatment with SonoVue® microbubbles and customized commercial ultrasound scanning over a period of 31.5 min (1.9 MHz, mechanical index 0.49, 1 % duty cycle, 5 kHz repetition rate, and 0.27 MPa peak negative pressure). The results showed that compared with a historical control group of 80 patients treated with gemcitabine alone, the 5 patients were able to tolerate a greater number of chemotherapy cycles (16 ± 7 *vs.* 9 ± 6 cycles). The tumor size was temporally or permanently reduced in 2 out of 5 patients, and the other 3 patients showed reduced tumor growth. No adverse effects related to this procedure were reported in this study.

This is the first report on sonoporation performed in a clinical setting, representing an important first step toward clinical development and hopefully also supporting subsequent clinical trials to be performed in additional institutions. However, this study has several limitations. Firstly, the treatment protocol has not been optimized, including ultrasound parameters and doses of drug and microbubbles. Future studies are warranted to explore this in the clinical setting. Secondly, only five patients were included for this pilot study and it remains unclear whether there was a true clinical benefit for the treated patients since there was no report on standard oncological outcomes, such as time to progression and overall survival time. Finally, long-term safety needs to be assessed for this treatment protocol.

An ongoing clinical trial conducted by the same research team including more patients with pancreatic cancer is expected to confirm this promising outcome (Helse Bergen and Georg 2010). Additionally, a clinical trial about the safety of USMB-assisted chemotherapy for the treatment of malignant neoplasms of the digestive system is currently being performed in China (Kun and Lin 2014). In this study, pancreatic cancer patients with liver metastases in whom routine chemotherapy has failed will be recruited. These patients will undergo treatment with USMB (SonoVue® microbubbles) and chemotherapy (platinum or gemcitabine). The tumor response rate and the safety limits on the mechanical index and ultrasound treatment time will be explored.

15.6 Prospects and Conclusions

Exciting results in preclinical studies and promising results in a first clinical case study show great potential for USMB-mediated drug delivery in cancer therapy. To further improve this technique and to develop it as a safe and efficient therapeutic approach, several issues need to be addressed.

15.6.1 Mechanisms of Microbubble-Tissue Interaction In-vivo

While multiple studies have provided some insight into the dynamic interaction between cavitating microbubbles and tumor cells for successful cellular drug delivery in a well-controlled *in-vitro* setup, successful drug delivery in an *in-vivo* environment is more complex and challenging. For a

drug to reach the target tumor cells *in-vivo*, several biological barriers have to be overcome. New insights into the mechanisms of sonoporation in *in-vivo* tumor tissue need to be further explored to allow optimal use of the biological implications of USMB-mediated drug delivery. The cavitation dynamics of microbubbles may be altered *in-vivo* compared to *in-vitro* settings due to the confinement from the surrounding tissues.

15.6.2 Advance in Multifunctional Microbubbles

Microbubbles play a key role in USMB-mediated drug delivery systems. Improved clinical outcomes may be achieved by the development of new microbubble formulations, with increased drug loading capacity and improved site-specific targeting. Several studies have been initiated towards these aims. For example, Borden et al. (2007) designed a multilayer construction using cationic polymers on the surface of positively charged microbubbles. These increased loading capacity of microbubbles for DNA by ten-fold. Covalently binding nanocarriers to microbubbles is an alternative approach, increasing loading capacity 34-fold without significantly increasing the diameter of the microbubble drug carrier (Sirsi and Borden 2014). In terms of further improvement of the targeting specificity, molecularly targeted microbubbles could be used that bind to markers differentially overexpressed on the tumor vasculature, such as VEGFR2, $\alpha_v\beta_3$ integrins or thymocyte differentiation antigen 1 (Lutz et al. 2014; Foygel et al. 2013; Bachawal et al. 2013; Wilson et al. 2013; Kircher and Willmann 2012a, b; Kiessling et al. 2012; Pysz and Willmann 2011; Deshpande et al. 2010; Schneider 2008).

15.6.3 Optimization of Drug Delivery Protocol

One of the main aims of USMB-mediated drug delivery research is to develop an optimal treatment protocol for improved drug delivery into tumor tissues. As mentioned above, several studies have investigated the influence of various ultrasound parameters, microbubble types and drug dosages, as well as routes of microbubble and drug administration, in order to identify more optimized settings for an USMB-assisted drug delivery approach. Unfortunately, so far, most optimization studies have been performed in cell culture experiments (Sonoda et al. 2007; Ghoshal et al. 2012), with only a few studies performed *in-vivo* (Sorace et al. 2012; Panje et al. 2012), these being limited to mouse tumor models. It is unclear whether these results obtained in mice are applicable in larger animals and even patients, where concerns of limited acoustic window and higher attenuation may arise for deeply seated tissues. Future research, systematically assessing the influences of various delivery parameters on the efficiency and safety of USMB-mediated drug delivery in larger animals is needed.

15.6.4 Development of a Dedicated Ultrasound System for Drug Delivery

USMB-mediated drug delivery can be achieved using clinical ultrasound imaging systems or custom-built ultrasound systems; however, limitations exist in both types of systems. The clinical imaging systems have very limited range of tunable pulse parameters and temporal pulsing sequences, which may result in less effective drug delivery outcomes. The custom-built ultrasound systems have more flexibility in pulse parameter and sequence design; however, these systems are usually assembled with a single element transducer. Mechanical motion of the transducer is often needed for a 3-dimensional raster scan over the entire tumor volume, which can be a time-consuming procedure. To address these issues, a more flexible system capable of generating a wide range of tunable pulse parameters and equipped with an array transducer capable of 3D electronic beam steering is essential. Development of a new system dedicated for drug delivery may substantially improve the therapeutic outcomes with minimally required treatment time.

15.6.5 Safety Studies

Although diagnostic ultrasound and contrast agents are considered safe and have been approved for use in clinical diagnostic imaging, safety of using ultrasound and microbubbles for therapeutic purposes needs to be systematically studied. A few preclinical studies in small animals so far have evaluated the safety of USMB using simple parameters, such as weight, eating habits and mobility (Pu et al. 2014; Kotopoulis et al. 2014; Zhou et al. 2010). However, more formal toxicity studies are likely required for various treatment protocols before clinical development.

Conclusions

The future success of cancer therapy is dependent on the development of noninvasive delivery methods that can efficiently and selectively deliver therapeutic agents to target cells with minimal systemic toxicity. Sonoporation, triggered by USMB, is a promising technique to fulfill this need. It is likely that drug delivery with USMB will benefit greatly from future improvements in molecular targeting strategies, engineering of new microbubble, and the development of precisely focusable ultrasound probes with optimized technical parameters of the ultrasound beam and optimized therapeutic temporal delivery sequences. This approach may provide much-needed therapeutic breakthroughs in cancer therapy, especially in cases where only palliative treatment is available.

References

Apfel RE, Holland CK (1991) Gauging the likelihood of cavitation from short-pulse, low-duty cycle diagnostic ultrasound. Ultrasound Med Biol 17:179–185

Bachawal SV, Jensen KC, Lutz AM, Gambhir SS, Tranquart F, Tian L, Willmann JK (2013) Earlier detection of breast cancer with ultrasound molecular imaging in a transgenic mouse model. Cancer Res 73:1689–1698

Bae YH (2009) Drug targeting and tumor heterogeneity. J Control Release 133:2–3

Bekeredjian R, Kroll RD, Fein E, Tinkov S, Coester C, Winter G, Katus HA, Kulaksiz H (2007) Ultrasound targeted microbubble destruction increases capillary permeability in hepatomas. Ultrasound Med Biol 33:1592–1598

Bohmer MR, Chlon CH, Raju BI, Chin CT, Shevchenko T, Klibanov AL (2010) Focused ultrasound and microbubbles for enhanced extravasation. J Control Release 148:18–24

Borden MA, Caskey CF, Little E, Gillies RJ, Ferrara KW (2007) DNA and polylysine adsorption and multilayer construction onto cationic lipid-coated microbubbles. Langmuir 23:9401–9408

Boucher Y, Baxter LT, Jain RK (1990) Interstitial pressure gradients in tissue-isolated and subcutaneous tumors: implications for therapy. Cancer Res 50:4478–4484

Brayman AA, Coppage ML, Vaidya S, Miller MW (1999) Transient poration and cell surface receptor removal from human lymphocytes in-vitro by 1 MHz ultrasound. Ultrasound Med Biol 25:999–1008

Carey LA, Perou CM, Livasy CA, Dressler LG, Cowan D, Conway K, Karaca G, Troester MA, Tse CK, Edmiston S, Deming SL, Geradts J, Cheang MC, Nielsen TO, Moorman PG, Earp HS, Millikan RC (2006) Race, breast cancer subtypes, and survival in the Carolina Breast Cancer Study. JAMA 295:2492–2502

Carlisle R, Choi J, Bazan-Peregrino M, Laga R, Subr V, Kostka L, Ulbrich K, Coussios CC, Seymour LW (2013) Enhanced tumor uptake and penetration of virotherapy using polymer stealthing and focused ultrasound. J Natl Cancer Inst 105:1701–1710

Carson AR, McTiernan CF, Lavery L, Grata M, Leng X, Wang J, Chen X, Villanueva FS (2012) Ultrasound-targeted microbubble destruction to deliver siRNA cancer therapy. Cancer Res 72:6191–6199

Caskey CF, Stieger SM, Qin S, Dayton PA, Ferrara KW (2007) Direct observations of ultrasound microbubble contrast agent interaction with the microvessel wall. J Acoust Soc Am 122:1191–1200

Chen H, Kreider W, Brayman AA, Bailey MR, Matula TJ (2011) Blood vessel deformations on microsecond time scales by ultrasonic cavitation. Phys Rev Lett 106:034301

Chiang CL, Benencia F, Coukos G (2010) Whole tumor antigen vaccines. Semin Immunol 22:132–143

Chuang YH, Wang YH, Chang TK, Lin CJ, Li PC (2014) Albumin acts like transforming growth factor beta1 in microbubble-based drug delivery. Ultrasound Med Biol 40:765–774

Cochran MC, Eisenbrey J, Ouma RO, Soulen M, Wheatley MA (2011a) Doxorubicin and paclitaxel loaded microbubbles for ultrasound triggered drug delivery. Int J Pharm 414:161–170

Cochran MC, Eisenbrey JR, Soulen MC, Schultz SM, Ouma RO, White SB, Furth EE, Wheatley MA (2011b) Disposition of ultrasound sensitive polymeric drug carrier in a rat hepatocellular carcinoma model. Acad Radiol 18:1341–1348

Davies Cde L, Lundstrom LM, Frengen J, Eikenes L, Bruland SO, Kaalhus O, Hjelstuen MH, Brekken C (2004) Radiation improves the distribution and uptake of liposomal doxorubicin (caelyx) in human osteosarcoma xenografts. Cancer Res 64:547–553

De Temmerman ML, Dewitte H, Vandenbroucke RE, Lucas B, Libert C, Demeester J, De Smedt SC, Lentacker I, Rejman J (2011) mRNA-Lipoplex loaded microbubble contrast agents for ultrasound-assisted transfection of dendritic cells. Biomaterials 32: 9128–9135

Deng Z, Yan F, Jin Q, Li F, Wu J, Liu X, Zheng H (2014) Reversal of multidrug resistance phenotype in human breast cancer cells using doxorubicin-liposome-microbubble complexes assisted by ultrasound. J Control Release 174:109–116

Deshpande N, Needles A, Willmann JK (2010) Molecular ultrasound imaging: current status and future directions. Clin Radiol 65:567–581

Dubinsky TJ, Cuevas C, Dighe MK, Kolokythas O, Hwang JH (2008) High-intensity focused ultrasound: current potential and oncologic applications. Am J Roentgenol 190:191–199

Ducreux M, Rougier P, Fandi A, Clavero-Fabri MC, Villing AL, Fassone F, Fandi L, Zarba J, Armand JP (1998) Effective treatment of advanced biliary tract carcinoma using 5-fluorouracil continuous infusion with cisplatin. Ann Oncol 9:653–656

Duvshani-Eshet M, Benny O, Morgenstern A, Machluf M (2007) Therapeutic ultrasound facilitates antiangiogenic gene delivery and inhibits prostate tumor growth. Mol Cancer Ther 6:2371–2382

Edelstein ML, Abedi MR, Wixon J (2007) Gene therapy clinical trials worldwide to 2007--an update. J Gene Med 9:833–842

Eggen S, Afadzi M, Nilssen EA, Haugstad SB, Angelsen B, Davies Cde L (2013) Ultrasound improves the uptake and distribution of liposomal Doxorubicin in prostate cancer xenografts. Ultrasound Med Biol 39:1255–1266

Eggen S, Fagerland SM, Morch Y, Hansen R, Sovik K, Berg S, Furu H, Bohn AD, Lilledahl MB, Angelsen A, Angelsen B, de Lange DC (2014) Ultrasound-enhanced drug delivery in prostate cancer xenografts by nanoparticles stabilizing microbubbles. J Control Release 187:39–49

Eikenes L, Bruland OS, Brekken C, Davies Cde L (2004) Collagenase increases the transcapillary pressure gradient and improves the uptake and distribution of monoclonal antibodies in human osteosarcoma xenografts. Cancer Res 64:4768–4773

Elodie Debefve YW, Krueger T, van den Bergh H (2013) Photodynamic therapy for increased delivery of anticancer drugs. In: Handbook of photomedicine. CRC Press, Florida

Fan Z, Liu H, Mayer M, Deng CX (2012) Spatiotemporally controlled single cell sonoporation. Proc Natl Acad Sci U S A 109:16486–16491

Ferlay J, Soerjomataram I, Ervik M, Dikshit R, Eser S, Mathers C, Rebelo M, Parkin DM, Forman D, Bray F (2014) Cancer worldwide. In: Stewart BW, Wild CP (eds) World cancer report 2014, vol 3. International Agency for Research on Cancer (IARC), Lyon, pp 16–80

Foygel K, Wang H, Machtaler S, Lutz AM, Chen R, Pysz M, Lowe AW, Tian L, Carrigan T, Brentnall TA, Willmann JK (2013) Detection of pancreatic ductal adenocarcinoma in mice by ultrasound imaging of thymocyte differentiation antigen 1. Gastroenterology 4:885–894

Fujii H, Matkar P, Liao C, Rudenko D, Lee PJ, Kuliszewski MA, Prud'homme GJ, Leong-Poi H (2013) Optimization of ultrasound-mediated anti-angiogenic cancer gene therapy. Mol Ther Nucleic Acids 2, e94

Fukumura D, Jain RK (2007) Tumor microenvironment abnormalities: causes, consequences, and strategies to normalize. J Cell Biochem 101:937–949

Ghoshal G, Swat S, Oelze ML (2012) Synergistic effects of ultrasound-activated microbubbles and doxorubicin on short-term survival of mouse mammary tumor cells. Ultrason Imaging 34:15–22

Goertz DE, Todorova M, Mortazavi O, Agache V, Chen B, Karshafian R, Hynynen K (2012) Antitumor effects of combining docetaxel (taxotere) with the antivascular action of ultrasound stimulated microbubbles. PLoS One 7, e52307

Gottesman MM (2002) Mechanisms of cancer drug resistance. Annu Rev Med 53:615–627

Greco A, Di Benedetto A, Howard CM, Kelly S, Nande R, Dementieva Y, Miranda M, Brunetti A, Salvatore M, Claudio L, Sarkar D, Dent P, Curiel DT, Fisher PB, Claudio PP (2010) Eradication of therapy-resistant human prostate tumors using an ultrasound-guided site-specific cancer terminator virus delivery approach. Mol Ther 18:295–306

Grossman R, Tyler B, Hwang L, Zadnik P, Lal B, Javaherian K, Brem H (2011) Improvement in the standard treatment for experimental glioma by fusing antibody Fc domain to endostatin. J Neurosurg 115: 1139–1146

Guarneri V, Dieci MV, Conte P (2012) Enhancing intracellular taxane delivery: current role and perspectives of nanoparticle albumin-bound paclitaxel in the treatment of advanced breast cancer. Expert Opin Pharmacother 13:395–406

Haag P, Frauscher F, Gradl J, Seitz A, Schafer G, Lindner JR, Klibanov AL, Bartsch G, Klocker H, Eder IE (2006) Microbubble-enhanced ultrasound to deliver an antisense oligodeoxynucleotide targeting the human androgen receptor into prostate tumours. J Steroid Biochem Mol Biol 102:103–113

Hauser J, Hauser M, Muhr G, Esenwein S (2009) Ultrasound-induced modifications of cytoskeletal components in osteoblast-like SAOS-2 cells. J Orthop Res 27:286–294

Heath CH, Sorace A, Knowles J, Rosenthal E, Hoyt K (2012) Microbubble therapy enhances anti-tumor properties of cisplatin and cetuximab in-vitro and in-vivo. Otolaryngol Head Neck Surg 146:938–945

Helse Bergen H, Georg D (2010) Treatment of pancreatic adenocarcinoma by combining contrast agent and gemcitabine under sonication. Helse Bergen HF, Haukeland Unversity Hospital, Bergen

Hobbs SK, Monsky WL, Yuan F, Roberts WG, Griffith L, Torchilin VP, Jain RK (1998) Regulation of transport pathways in tumor vessels: role of tumor type and

microenvironment. Proc Natl Acad Sci U S A 95: 4607–4612

Hoffmann A, Bredno J, Wendland M, Derugin N, Ohara P, Wintermark M (2011) High and low molecular weight fluorescein isothiocyanate (FITC)-dextrans to assess blood-brain barrier disruption: technical considerations. Transl Stroke Res 2:106–111

Iwanaga K, Tominaga K, Yamamoto K, Habu M, Maeda H, Akifusa S, Tsujisawa T, Okinaga T, Fukuda J, Nishihara T (2007) Local delivery system of cytotoxic agents to tumors by focused sonoporation. Cancer Gene Ther 14:354–363

Jain RK (1998) Delivery of molecular and cellular medicine to solid tumors. J Control Release 53:49–67

Jemal A, Bray F, Center MM, Ferlay J, Ward E, Forman D (2011) Global cancer statistics. CA Cancer J Clin 6:69–90

Juffermans LJ, Meijering BD, Henning RH, Deelman LE (2014) Ultrasound and microbubble-targeted delivery of small interfering RNA into primary endothelial cells is more effective than delivery of plasmid DNA. Ultrasound Med Biol 40:532–540

Kaneko OF, Willmann JK (2012) Ultrasound for molecular imaging and therapy in cancer. Quant Imaging Med Surg 2:87–97

Kiessling F, Fokong S, Koczera P, Lederle W, Lammers T (2012) Ultrasound microbubbles for molecular diagnosis, therapy, and theranostics. J Nucl Med 53:345–348

Kircher MF, Willmann JK (2012a) Molecular body imaging: MR imaging, CT, and US. Part I. Principles. Radiology 263:633–643

Kircher MF, Willmann JK (2012b) Molecular body imaging: MR imaging, CT, and US. Part II. Applications. Radiology 264:349–368

Kisker O, Becker CM, Prox D, Fannon M, D'Amato R, Flynn E, Fogler WE, Sim BK, Allred EN, Pirie-Shepherd SR, Folkman J (2001) Continuous administration of endostatin by intraperitoneally implanted osmotic pump improves the efficacy and potency of therapy in a mouse xenograft tumor model. Cancer Res 61:7669–7674

Kohane DS, Tse JY, Yeo Y, Padera R, Shubina M, Langer R (2006) Biodegradable polymeric microspheres and nanospheres for drug delivery in the peritoneum. J Biomed Mater Res A 77:351–361

Kotopoulis S, Dimcevski G, Gilja OH, Hoem D, Postema M (2013) Treatment of human pancreatic cancer using combined ultrasound, microbubbles, and gemcitabine: a clinical case study. Med Phys 40:072902

Kotopoulis S, Delalande A, Popa M, Mamaeva V, Dimcevski G, Gilja OH, Postema M, Gjertsen BT, McCormack E (2014) Sonoporation-enhanced chemotherapy significantly reduces primary tumour burden in an orthotopic pancreatic cancer xenograft. Mol Imaging Biol 16:53–62

Kun Y, Lin S (2014) Safety study of combining ultrasound microbubbles and chemotherapy to treat malignant neoplasms of liver metastases from gastrointestinal tumors and pancreatic carcinoma. Beijing Cancer Hospital, Beijing

Leslie TA, Kennedy JE (2006) High-intensity focused ultrasound principles, current uses, and potential for the future. Ultrasound Q 22:263–272

Liao ZK, Tsai KC, Wang HT, Tseng SH, Deng WP, Chen WS, Hwang LH (2012) Sonoporation-mediated anti-angiogenic gene transfer into muscle effectively regresses distant orthotopic tumors. Cancer Gene Ther 19:171–180

Liu HL, Hua MY, Chen PY, Chu PC, Pan CH, Yang HW, Huang CY, Wang JJ, Yen TC, Wei KC (2010) Blood-brain barrier disruption with focused ultrasound enhances delivery of chemotherapeutic drugs for glioblastoma treatment. Radiology 255:415–425

Lozano R, Naghavi M, Foreman K, Lim S, Shibuya K, Aboyans V, Abraham J, Adair T, Aggarwal R, Ahn SY, Alvarado M, Anderson HR, Anderson LM, Andrews KG, Atkinson C, Baddour LM, Barker-Collo S, Bartels DH, Bell ML, Benjamin EJ, Bennett D, Bhalla K, Bikbov B, Bin Abdulhak A, Birbeck G, Blyth F, Bolliger I, Boufous S, Bucello C, Burch M, Burney P, Carapetis J, Chen H, Chou D, Chugh SS, Coffeng LE, Colan SD, Colquhoun S, Colson KE, Condon J, Connor MD, Cooper LT, Corriere M, Cortinovis M, de Vaccaro KC, Couser W, Cowie BC, Criqui MH, Cross M, Dabhadkar KC, Dahodwala N, De Leo D, Degenhardt L, Delossantos A, Denenberg J, Des Jarlais DC, Dharmaratne SD, Dorsey ER, Driscoll T, Duber H, Ebel B, Erwin PJ, Espindola P, Ezzati M, Feigin V, Flaxman AD, Forouzanfar MH, Fowkes FG, Franklin R, Fransen M, Freeman MK, Gabriel SE, Gakidou E, Gaspari F, Gillum RF, Gonzalez-Medina D, Halasa YA, Haring D, Harrison JE, Havmoeller R, Hay RJ, Hoen B, Hotez PJ, Hoy D, Jacobsen KH, James SL, Jasrasaria R, Jayaraman S, Johns N, Karthikeyan G, Kassebaum N, Keren A, Khoo JP, Knowlton LM, Kobusingye O, Koranteng A, Krishnamurthi R, Lipnick M, Lipshultz SE, Ohno SL, Mabweijano J, MacIntyre MF, Mallinger L, March L, Marks GB, Marks R, Matsumori A, Matzopoulos R, Mayosi BM, McAnulty JH, McDermott MM, McGrath J, Mensah GA, Merriman TR, Michaud C, Miller M, Miller TR, Mock C, Mocumbi AO, Mokdad AA, Moran A, Mulholland K, Nair MN, Naldi L, Narayan KM, Nasseri K, Norman P, O'Donnell M, Omer SB, Ortblad K, Osborne R, Ozgediz D, Pahari B, Pandian JD, Rivero AP, Padilla RP, Perez-Ruiz F, Perico N, Phillips D, Pierce K, Pope CA 3rd, Porrini E, Pourmalek F, Raju M, Ranganathan D, Rehm JT, Rein DB, Remuzzi G, Rivara FP, Roberts T, De Leon FR, Rosenfeld LC, Rushton L, Sacco RL, Salomon JA, Sampson U, Sanman E, Schwebel DC, Segui-Gomez M, Shepard DS, Singh D, Singleton J, Sliwa K, Smith E, Steer A, Taylor JA, Thomas B, Tleyjeh IM, Towbin JA, Truelsen T, Undurraga EA, Venketasubramanian N, Vijayakumar L, Vos T, Wagner GR, Wang M, Wang W, Watt K, Weinstock MA, Weintraub R, Wilkinson JD, Woolf AD, Wulf S, Yeh PH, Yip P, Zabetian A, Zheng ZJ, Lopez AD, Murray CJ, AlMazroa MA, Memish ZA (2012) Global and regional mortality from 235 causes of death for 20 age groups in 1990

and 2010: a systematic analysis for the Global Burden of Disease Study 2010. Lancet 380:2095–2128

Lutz AM, Bachawal SV, Drescher CW, Pysz MA, Willmann JK, Gambhir SS (2014) Ultrasound molecular imaging in a human CD276 expression-modulated murine ovarian cancer model. Clin Cancer Res 5: 1313–1322

Markman M, Rowinsky E, Hakes T, Reichman B, Jones W, Lewis JL Jr, Rubin S, Curtin J, Barakat R, Phillips M et al (1992) Phase I trial of intraperitoneal taxol: a Gynecoloic Oncology Group study. J Clin Oncol 10: 1485–1491

Matsuo M, Yamaguchi K, Feril LB Jr, Endo H, Ogawa K, Tachibana K, Nakayama J (2011) Synergistic inhibition of malignant melanoma proliferation by melphalan combined with ultrasound and microbubbles. Ultrason Sonochem 18:1218–1224

Meijering BD, Juffermans LJ, van Wamel A, Henning RH, Zuhorn IS, Emmer M, Versteilen AM, Paulus WJ, van Gilst WH, Kooiman K, de Jong N, Musters RJ, Deelman LE, Kamp O (2009) Ultrasound and microbubble-targeted delivery of macromolecules is regulated by induction of endocytosis and pore formation. Circ Res 104:679–687

Minchinton AI, Tannock IF (2006) Drug penetration in solid tumours. Nat Rev Cancer 6:583–592

Molema G, Meijer DK, de Leij LF (1998) Tumor vasculature targeted therapies: getting the players organized. Biochem Pharmacol 55:1939–1945

Mow VC, Mak AF, Lai WM, Rosenberg LC, Tang LH (1984) Viscoelastic properties of proteoglycan subunits and aggregates in varying solution concentrations. J Biomech 17:325–338

Newman CM, Bettinger T (2007) Gene therapy progress and prospects: ultrasound for gene transfer. Gene Ther 14:465–475

Nie F, Xu HX, Lu MD, Wang Y, Tang Q (2008) Anti-angiogenic gene therapy for hepatocellular carcinoma mediated by microbubble-enhanced ultrasound exposure: an in-vivo experimental study. J Drug Target 16:389–395

O'Brien WD Jr (2007) Ultrasound-biophysics mechanisms. Prog Biophys Mol Biol 93:212–255

Oda Y, Suzuki R, Otake S, Nishiie N, Hirata K, Koshima R, Nomura T, Utoguchi N, Kudo N, Tachibana K, Maruyama K (2012) Prophylactic immunization with Bubble liposomes and ultrasound-treated dendritic cells provided a four-fold decrease in the frequency of melanoma lung metastasis. J Control Release 160:362–366

Panje CM, Wang DS, Pysz MA, Paulmurugan R, Ren Y, Tranquart F, Tian L, Willmann JK (2012) Ultrasound-mediated gene delivery with cationic versus neutral microbubbles: effect of DNA and microbubble dose on in-vivo transfection efficiency. Theranostics 2: 1078–1091

Panje CM, Wang DS, Willmann JK (2013) Ultrasound and microbubble-mediated gene delivery in cancer: progress and perspectives. Invest Radiol 48:755–769

Paproski RJ, Yao SY, Favis N, Evans D, Young JD, Cass CE, Zemp RJ (2013) Human concentrative nucleoside transporter 3 transfection with ultrasound and microbubbles in nucleoside transport deficient HEK293 cells greatly increases gemcitabine uptake. PLoS One 8, e56423

Park J, Zhang Y, Vykhodtseva N, Akula JD, McDannold NJ (2012a) Targeted and reversible blood-retinal barrier disruption via focused ultrasound and microbubbles. PLoS One 7, e42754

Park EJ, Zhang YZ, Vykhodtseva N, McDannold N (2012b) Ultrasound-mediated blood-brain/blood-tumor barrier disruption improves outcomes with trastuzumab in a breast cancer brain metastasis model. J Control Release 163:277–284

Parvizi J, Parpura V, Greenleaf JF, Bolander ME (2002) Calcium signaling is required for ultrasound-stimulated aggrecan synthesis by rat chondrocytes. J Orthop Res 20:51–57

Patil AV, Rychak JJ, Klibanov AL, Hossack JA (2011) Real-time technique for improving molecular imaging and guiding drug delivery in large blood vessels: in-vitro and ex vivo results. Mol Imaging 10:238–247

Pu C, Chang S, Sun J, Zhu S, Liu H, Zhu Y, Wang Z, Xu RX (2014) Ultrasound-mediated destruction of LHRHa-targeted and paclitaxel-loaded lipid microbubbles for the treatment of intraperitoneal ovarian cancer xenografts. Mol Pharm 11:49–58

Pysz MA, Willmann JK (2011) Targeted contrast-enhanced ultrasound: an emerging technology in abdominal and pelvic imaging. Gastroenterology 140:785–790

Qin S, Caskey CF, Ferrara KW (2009) Ultrasound contrast microbubbles in imaging and therapy: physical principles and engineering. Phys Med Biol 54:R27–R57

Rahman AM, Yusuf SW, Ewer MS (2007) Anthracycline-induced cardiotoxicity and the cardiac-sparing effect of liposomal formulation. Int J Nanomed 2:567–583

Schlicher RK, Radhakrishna H, Tolentino TP, Apkarian RP, Zarnitsyn V, Prausnitz MR (2006) Mechanism of intracellular delivery by acoustic cavitation. Ultrasound Med Biol 32:915–924

Schneider M (2008) Molecular imaging and ultrasound-assisted drug delivery. J Endourol 22:795–802

Sever A, Jones S, Cox K, Weeks J, Mills P, Jones P (2009) Preoperative localization of sentinel lymph nodes using intradermal microbubbles and contrast-enhanced ultrasonography in patients with breast cancer. Br J Surg 96:1295–1299

Sheikov N, McDannold N, Sharma S, Hynynen K (2008) Effect of focused ultrasound applied with an ultrasound contrast agent on the tight junctional integrity of the brain microvascular endothelium. Ultrasound Med Biol 34:1093–1104

Shillitoe EJ (2009) Gene therapy: the end of the rainbow? Head Neck Oncol 1:7

Sirsi SR, Borden MA (2014) State-of-the-art materials for ultrasound-triggered drug delivery. Adv Drug Deliv Rev 72:3–14

Sonoda S, Tachibana K, Uchino E, Yamashita T, Sakoda K, Sonoda KH, Hisatomi T, Izumi Y, Sakamoto T (2007) Inhibition of melanoma by ultrasound-microbubble-aided drug delivery suggests membrane permeabilization. Cancer Biol Ther 6:1276–1283

Sorace AG, Warram JM, Umphrey H, Hoyt K (2012) Microbubble-mediated ultrasonic techniques for

improved chemotherapeutic delivery in cancer. J Drug Target 20:43–54
Sorace AG, Korb M, Warram JM, Umphrey H, Zinn KR, Rosenthal E, Hoyt K (2014) Ultrasound-stimulated drug delivery for treatment of residual disease after incomplete resection of head and neck cancer. Ultrasound Med Biol 40:755–764
Suzuki R, Namai E, Oda Y, Nishiie N, Otake S, Koshima R, Hirata K, Taira Y, Utoguchi N, Negishi Y, Nakagawa S, Maruyama K (2010) Cancer gene therapy by IL-12 gene delivery using liposomal bubbles and tumoral ultrasound exposure. J Control Release 142:245–250
Szakacs G, Paterson JK, Ludwig JA, Booth-Genthe C, Gottesman MM (2006) Targeting multidrug resistance in cancer. Nat Rev Drug Discov 5:219–234
Taniyama Y, Tachibana K, Hiraoka K, Namba T, Yamasaki K, Hashiya N, Aoki M, Ogihara T, Yasufumi K, Morishita R (2002) Local delivery of plasmid DNA into rat carotid artery using ultrasound. Circulation 105:1233–1239
Timmerman JM, Levy R (1999) Dendritic cell vaccines for cancer immunotherapy. Annu Rev Med 50:507–529
Ting CY, Fan CH, Liu HL, Huang CY, Hsieh HY, Yen TC, Wei KC, Yeh CK (2012) Concurrent blood-brain barrier opening and local drug delivery using drug-carrying microbubbles and focused ultrasound for brain glioma treatment. Biomaterials 33:704–712
Todorova M, Agache V, Mortazavi O, Chen B, Karshafian R, Hynynen K, Man S, Kerbel RS, Goertz DE (2013) Antitumor effects of combining metronomic chemotherapy with the antivascular action of ultrasound stimulated microbubbles. Int J Cancer 132:2956–2966
Tong AW, Jay CM, Senzer N, Maples PB, Nemunaitis J (2009) Systemic therapeutic gene delivery for cancer: crafting Paris' arrow. Curr Gene Ther 9:45–60
Treat LH, McDannold N, Zhang Y, Vykhodtseva N, Hynynen K (2012) Improved anti-tumor effect of liposomal doxorubicin after targeted blood-brain barrier disruption by MRI-guided focused ultrasound in rat glioma. Ultrasound Med Biol 38:1716–1725
Tsai M, Lu Z, Wang J, Yeh TK, Wientjes MG, Au JL (2007) Effects of carrier on disposition and antitumor activity of intraperitoneal Paclitaxel. Pharm Res 24:1691–1701
Tzu-Yin W, Wilson KE, Machtaler S, Willmann JK (2014) Ultrasound and microbubble guided drug delivery: mechanistic understanding and clinical implications. Curr Pharm Biotechnol 14:743–752
van Wamel A, Bouakaz A, Versluis M, de Jong N (2004) Micromanipulation of endothelial cells: ultrasound-microbubble-cell interaction. Ultrasound Med Biol 30:1255–1258
van Wamel A, Kooiman K, Emmer M, ten Cate FJ, Versluis M, de Jong N (2006) Ultrasound microbubble induced endothelial cell permeability. J Control Release 116:e100–e102
Waite CL, Roth CM (2012) Nanoscale drug delivery systems for enhanced drug penetration into solid tumors: current progress and opportunities. Crit Rev Biomed Eng 40:21–41
Wang Y, Yuan F (2006) Delivery of viral vectors to tumor cells: extracellular transport, systemic distribution, and strategies for improvement. Ann Biomed Eng 34:114–127
Wang DS, Panje C, Pysz MA, Paulmurugan R, Rosenberg J, Gambhir SS, Schneider M, Willmann JK (2012) Cationic versus neutral microbubbles for ultrasound-mediated gene delivery in cancer. Radiology 264:721–732
Wang XL, Zhao XY, Li S, Jia CJ, Jiang L, Shi TM, Ren WD (2013a) A novel plasmid and SonoVue formulation plus ultrasound sonication for effective gene delivery in nude mice. Life Sci 93:536–542
Wang Y, Bai WK, Shen E, Hu B (2013b) Sonoporation by low-frequency and low-power ultrasound enhances chemotherapeutic efficacy in prostate cancer cells. Oncol Lett 6:495–498
Ward M, Wu J, Chiu JF (2000) Experimental study of the effects of optison concentration on sonoporation in-vitro. Ultrasound Med Biol 26:1169–1175
Willmann JK, van Bruggen N, Dinkelborg LM, Gambhir SS (2008) Molecular imaging in drug development. Nat Rev Drug Discov 7:591–607
Wilson KE, Wang TY, Willmann JK (2013) Acoustic and photoacoustic molecular imaging of cancer. J Nucl Med 54:1851–1854
Wood AK, Bunte RM, Price HE, Deitz MS, Tsai JH, Lee WM, Sehgal CM (2008) The disruption of murine tumor neovasculature by low-intensity ultrasound-comparison between 1- and 3-MHz sonication frequencies. Acad Radiol 15:1133–1141
Xing W, Gang WZ, Yong Z, Yi ZY, Shan XC, Tao RH (2008) Treatment of xenografted ovarian carcinoma using paclitaxel-loaded ultrasound microbubbles. Acad Radiol 15:1574–1579
Yamaguchi K, Feril LB Jr, Tachibana K, Takahashi A, Matsuo M, Endo H, Harada Y, Nakayama J (2011) Ultrasound-mediated interferon beta gene transfection inhibits growth of malignant melanoma. Biochem Biophys Res Commun 411:137–142
Yan F, Li L, Deng Z, Jin Q, Chen J, Yang W, Yeh CK, Wu J, Shandas R, Liu X, Zheng H (2013) Paclitaxel-liposome-microbubble complexes as ultrasound-triggered therapeutic drug delivery carriers. J Control Release 166(3):246–255
Yu BF, Wu J, Zhang Y, Sung HW, Xie J, Li RK (2013) Ultrasound-targeted HSVtk and Timp3 gene delivery for synergistically enhanced antitumor effects in hepatoma. Cancer Gene Ther 20:290–297
Zhang JZ, Saggar JK, Zhou ZL, Hu B (2012) Different effects of sonoporation on cell morphology and viability. Bosn J Basic Med Sci 12:64–68
Zhao YZ, Dai DD, Lu CT, Lv HF, Zhang Y, Li X, Li WF, Wu Y, Jiang L, Li XK, Huang PT, Chen LJ, Lin M (2012) Using acoustic cavitation to enhance chemotherapy of DOX liposomes: experiment in-vitro and in-vivo. Drug Dev Ind Pharm 38:1090–1098
Zhou S, Li S, Liu Z, Tang Y, Wang Z, Gong J, Liu C (2010) Ultrasound-targeted microbubble destruction mediated herpes simplex virus-thymidine kinase gene treats hepatoma in mice. J Exp Clin Cancer Res 29:170
Zimm S, Cleary SM, Lucas WE, Weiss RJ, Markman M, Andrews PA, Schiefer MA, Kim S, Horton C, Howell SB (1987) Phase I/pharmacokinetic study of intraperitoneal cisplatin and etoposide. Cancer Res 47:1712–1716

Microbubble-Assisted Ultrasound for Drug Delivery in the Brain and Central Nervous System

16

Alison Burgess and Kullervo Hynynen

Abstract

The blood-brain barrier is a serious impediment to the delivery of pharmaceutical treatments for brain diseases, including cancer, neurodegenerative and neuropsychatric diseases. Focused ultrasound, when combined with microbubbles, has emerged as an effective method to transiently and locally open the blood-brain barrier to promote drug delivery to the brain. Focused ultrasound has been used to successfully deliver a wide variety of therapeutic agents to pre-clinical disease models. The requirement for clinical translation of focused ultrasound technology is considered.

Keywords

Focused ultrasound • Blood-brain barrier • Drug delivery • Alzheimer's disease • Glioblastoma

16.1 Barriers Protecting the Central Nervous System (CNS)

The brain and spinal cord are separated from the rest of the body by permeability barriers. The concept behind the blood-brain barrier (BBB) and blood-spinal cord barrier (BSCB) emerged in the late 1800s when Paul Ehrlich discovered that injection of intravenous dyes stained all organs except for the brain. Follow-up studies in the 1900s injected the same dyes into the spinal cord and found that only the brain and spinal cord were stained (Goldmann 1909). These studies led to the conceptualization that a blood-CNS barrier might exist (Hawkins and Davis 2005).

A. Burgess
Physical Sciences, Sunnybrook Research Institute, Toronto, ON, Canada

K. Hynynen (✉)
Physical Sciences, Sunnybrook Research Institute, Toronto, ON, Canada

Medical Biophysics, University of Toronto, Toronto, ON, Canada
e-mail: khynynen@sri.utoronto.ca

© Springer International Publishing Switzerland 2016
J.-M. Escoffre, A. Bouakaz (eds.), *Therapeutic Ultrasound*, Advances in Experimental Medicine and Biology, Vol. 880, DOI 10.1007/978-3-319-22536-4_16

Although the barriers were first thought to represent a physical barrier to block the entry of molecules into the CNS, further studies demonstrated that molecular entry into the CNS depends on molecular weight, size, binding affinities, electric charge and lipid solubility. These findings indicated that the barriers represent dynamic, complicated structures, functioning to selectively limit the entry and exit of molecules into the CNS.

The blood-CNS barriers are formed by specialized endothelial cells and are supported by the neurovascular unit to restrict molecular passage into or out of the CNS. The presence of these barriers is vital for maintaining a microenvironment that supports neuronal function. However, the barriers are also an obstruction to the delivery of therapeutics to treat CNS disorders.

Note that this chapter will focus on the BBB since the brain represents the majority of the current scientific literature. However, the same principles apply to the BSCB and its limitation for drug delivery to treat spinal cord disorders.

16.2 Formation of the BBB

The BBB is formed by the monolayer of endothelial cells that line the blood vessels in the brain. However, the endothelial cells in the brain and spinal cord are connected by tight junctions, which reduce the intercellular space between the endothelial cells. The tight junctions have abundant transmembrane proteins, including claudin, occludin and junctional adhesion molecules (JAM's). These are all anchored in the cell by the zonula occludens family of cytoskeletal proteins (Kniesel and Wolburg 2000). The tight junction proteins bind to their identical counterparts on adjacent endothelial cells, forming a continuous cellular layer that significantly restricts the passage of molecules between endothelial cells and into the brain parenchyma (Abbott et al. 2010). In addition to the upregulation of tight junction proteins, the endothelial cells in the brain also have reduced fenestrations and pinocytotic vesicles; further reducing the transport of molecules that transcytose through the endothelial cells into the brain (Fenstermacher et al. 1988; Sedlakova et al. 1999)

The endothelial cells are central to BBB functions, but their actions are regulated by adjacent astrocytes, pericytes, neurons, microglia and extracellular matrix molecules (Fig. 16.1). Together, these components function as the neurovascular unit. Astrocyte projections form endfeet that wrap around the microvessels. In addition to the physical support they provide, the endfeet also provide growth factors and other types of neurochemical support to induce and maintain the barrier-like properties of the brain endothelial cells (Janzer and Raff 1987). The necessity of pericytes and the extracellular matrix in formation of the BBB and its normal function has been demonstrated, but the exact role of these two substructures is yet to be determined (Armulik et al. 2010; Daneman et al. 2010; Tilling et al. 2002).

In combination, these neurovascular unit components work to form a functional BBB that can maintain the delicate microenvironment required for the neuronal population. The BBB regulates ion and neurotransmitter ranges within a very narrow range, and also prevents the entry of pathogens from the peripheral system. The barrier is essential for preventing damage to the brain since the brain itself has very limited ability to repair after injury.

While the BBB is crucial for maintaining health, it is also a serious obstruction to pharmacological agents that could repair the brain after injury or disease. Lipid-soluble drugs smaller than 400 Da are able to cross the barrier; however, this means that over 98 % of potential small-molecule and 100 % of large molecule therapeutics potentially effective for treating brain disorders, are unable to pass the BBB in appreciable quantities (Pardridge 2005). The BBB is also equipped with ATP-binding cassette (ABC) efflux transporters, such as p-glycoprotein and multidrug resistance protein. These active transporters ensure that any toxic or foreign molecules, including therapeutic agents, are shuttled back across the BBB. The prevalence of brain diseases, including neurodegenerative diseases, brain tumors and psychiatric illnesses, is increasing at alarming rates, and currently there

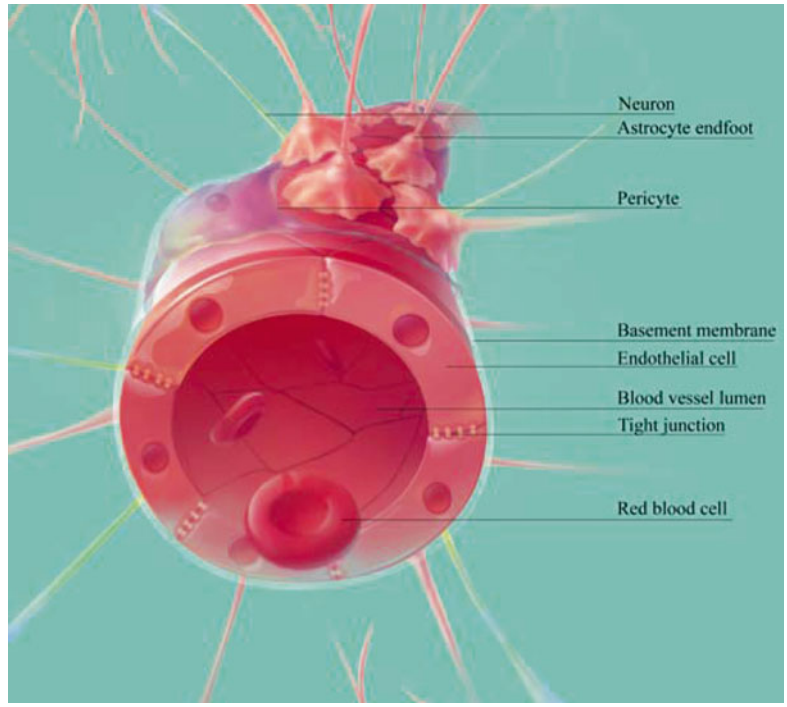

Fig. 16.1 The Blood-Brain Barrier (BBB) is composed of endothelial cells that are connected to each other via tight junctions. The endothelial cells are supported by the cells of the neurovascular unit, including pericytes, astrocytes, neurons and the basement membrane

are very few effective treatments. This is primarily due to the presence of the BBB.

16.3 Bypassing the BBB for Effective Drug Delivery

There are limitations to the methods used to overcome the BBB for drug delivery. In some clinical trials, investigators have attempted to directly inject the drug into the targeted brain region using MRI and neuronavigation systems to position needles and pumps (Gross et al. 2011; White et al. 2010). Although this method of drug delivery is effective, the potential risks and undesirable surgical procedures prevent patients from receiving these treatments. Other methods to bypass the BBB include pharmacological modification of the drug targets in order to increase uptake through the barrier. One successful example of this technique is the addition of cysteine, a small neutral amino acid, to a non-transportable drug. This makes the drug appear to be a large amino acid, thereby allowing it to be taken up into the BBB (Killian et al. 2007). Although drug modification can be effective for bypassing the BBB, there are challenges in achieving therapeutic concentrations in the target region.

As an effort to address the limitations regarding drug delivery methods, researchers have attempted to find new 'non-invasive' methods to circumvent the BBB. Recent successes with intranasal delivery of therapeutic agents have gained attention. The highly vascularized nasal mucosa is adjacent to the cerebrospinal fluid (CSF), thus rapid blood concentrations can lead to therapeutic CSF drug concentrations. It has been suggested that drugs travel to the CSF via the olfactory neuroepithelium or via neuronal transport (Pires et al. 2009). Recent studies have shown that fluorescent tracers delivered intranasally may move through the perivascular spaces to reach the brain (Lochhead and Thorne 2012). These experiments have been promising in rodent models, but may be difficult to validate in humans where drug penetration throughout large brain regions is limited (Pardridge 2012).

Focused ultrasound (FUS) has been used to non-invasively and transiently open the BBB to allow drugs to pass from the blood stream into

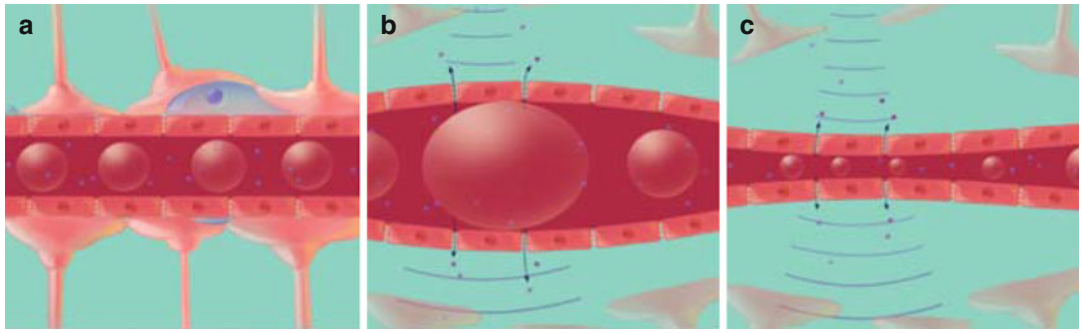

Fig. 16.2 (**a**) Microbubbles flow through the vasculature. (**b**) When ultrasound is applied, the microbubbles expand and (**c**) contract at the frequency of the ultrasound. The expansion and contraction of microbubbles leads to BBB opening

the brain (Hynynen et al. 2001). FUS has been effective as a method for delivering small and large therapeutic agents in preclinical disease models. The first clinical trials are rapidly approaching, and FUS has the potential to revolutionize drug delivery methods and be the first step to effective treatment of brain disorders.

16.4 Focused Ultrasound (FUS)-Mediated Barrier Opening

The use of focused ultrasound in the brain has been investigated since the 1950s (Fry and Fry 1960). It was first observed that heating of brain tissue through application of continuous ultrasound could result in BBB opening, but this was often accompanied by hemorrhage (Bakay et al. 1956; Shealy and Crafts 1965) or tissue coagulation (Patrick et al. 1990). At the time, both thermal- and cavitation-related mechanisms were thought to contribute to BBB opening. Further studies have confirmed that thermal mechanisms can lead to increased drug uptake by endothelial cells (Cho et al. 2002), but that thermally-induced BBB opening has so far been accompanied by tissue damage (McDannold et al. 2004). As an alternative, cavitation-related BBB opening has been explored using pulsed ultrasound application. Cavitation refers to ultrasound-induced generation, oscillation, and in its extreme form, subsequent collapse of bubbles within a tissue. Similar to thermal mechanisms, in the 1980s and 1990s, cavitation-mediated ultrasound-induced BBB opening was unpredictable and often related to damage of the surrounding blood vessels and brain tissues (Vykhodtseva et al. 1995). Several parameters were investigated, and in general it was observed that tissue damage occurred more often as pulse duration, number of pulses and repetition frequency increased (Vykhodtseva et al. 1995; Mesiwala et al. 2002).

In 2001 it was demonstrated for the first time that preformed microbubbles, delivered intravenously, could be used as cavitation nuclei, thereby reducing the ultrasound energy required to induce BBB opening, producing much more consistent results (Hynynen et al. 2001). When the circulating microbubbles pass through the focal area of the ultrasound, they concentrate the acoustic energy inside the blood vessel. The ultrasound energy causes the microbubbles to expand and contract at the frequency of the ultrasound, a process known as stable cavitation (Fig. 16.2).

It is important to note the considerable differences between the high pressure generation and collapse of bubbles observed during the initial attempts at ultrasound-mediated BBB opening (Vykhodtseva et al. 1995), and then the stable oscillation of preformed bubbles that was introduced in 2001 (Hynynen et al. 2001). The addition of microbubbles has reduced the amount of ultrasound energy required to open the BBB by 100-fold. Since less energy is required, the risk of skull heating by the ultrasound is reduced, thereby making clinical treatments feasible. Also, at lower ultrasound pressures, the risk of brain tissue hemorrhage and damage is significantly

reduced. Instead, the gently oscillating microbubbles interact with the endothelial cells and stimulate the opening of the tight junctions and increase transcellular molecular transport, leading to safe and effective drug delivery to the brain (Hynynen et al. 2001, 2006).

Following this first study, several groups have reported effective drug delivery using different ultrasound parameters in the presence of microbubbles. The factor that most significantly affects the amount of BBB opening is the ultrasound pressure. There is a delicate balance between applying enough ultrasound pressure to induce BBB opening for drug delivery, but limiting the ultrasound to avoid damage to the vessels and surrounding brain tissue. As pressure increases, the amount of microbubble expansion and contraction also increases, but too much pressure can lead to microbubble collapse and ensuing tissue damage. The relative amount of BBB opening required is based on the relative size of the therapeutic agent that needs to cross the BBB. Recent studies have demonstrated that greater ultrasound pressure is required to allow a 2000 kDa drug to cross the BBB, compared to the ultrasound pressure required for a 70 kDa drug (Chen and Konofagou 2014). The threshold of ultrasound pressure required for BBB opening is related to the mechanical index, defined as the peak negative pressure *in-vivo* by the square root of the frequency (McDannold et al. 2008a, b).

In rodents, ultrasound frequencies ranging from 28 kHz (Liu et al. 2010a, b) to 8 MHz (Bing et al. 2009) have been used to open the BBB. The size of the focal spot (or the treatment area) decreases with higher frequency, so conceptually, a higher frequency transducer would be better suited for targeting small brain nuclei. However, higher ultrasound pressures are required to induce opening when higher frequencies are used (McDannold et al. 2008a, b), therefore, the clinically relevant frequency range for therapeutic ultrasound is likely between 0.2 and 1.5 MHz. In addition to frequency, the duration of the ultrasound burst and the frequency of the burst repetitions have both been investigated to better understand their effects on BBB opening. Ultrasound burst length ranging from a few microseconds to a 100 ms have been reported, and in general BBB opening is greater as the burst length is increased, with no real benefit observed after 10 ms (McDannold et al. 2008a, b; Choi et al. 2011, O'Reilly et al. 2010). The repetition frequency of the bursts has not significantly impacted the amount of BBB opening (McDannold et al. 2008b), however it is understood that if the burst repetition frequency is too high, the microbubbles cannot reperfuse the area, thereby limiting the effectiveness of the low ultrasound energy (McDannold et al. 2007; Yang et al. 2008; Goertz et al. 2010; Weng et al. 2010; Choi et al. 2010; Vlachos et al. 2011). The microbubbles themselves can impact BBB opening. As microbubble size and dose are increased, there is greater BBB opening and potential for damage (Samiotaki et al. 2012; Wang et al. 2014).

Until recently, FUS-mediated BBB opening was monitored by post-treatment magnetic resonance imaging (MRI) and histological methods; however these methods were limited in their ability to provide feedback during FUS treatments. Over the past few years, several different groups have developed methods to detect and evaluate microbubble activity *in-vivo* (McDannold et al. 2006; Tung et al. 2011; O'Reilly and Hynynen 2012, 2013; Arvanitis et al. 2012). It was demonstrated that the frequency content emitted from the microbubbles during the ultrasound treatment can be used for online control of the exposures (O'Reilly and Hynynen 2012).

16.5 Advantages of FUS for Drug Delivery Through the BBB

There are several advantages to FUS-induced BBB opening with microbubbles over other methods used.

Targeted The ultrasound is focused so that the BBB is only opened in the targeted region of interest. The ultrasound is focused using one of two methods. Firstly, if using a single element transducer, as is common in preclinical studies, the surface of the transducer is curved so that the natural geometric focus comes to a point at a set

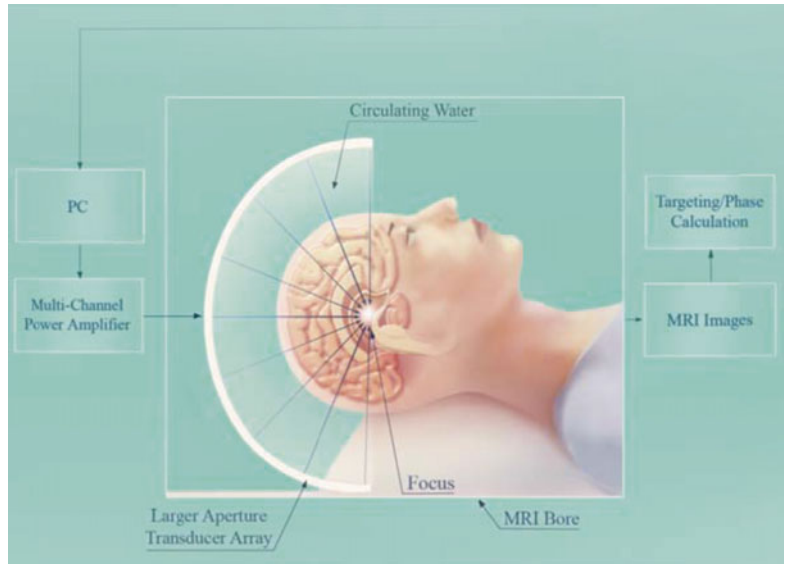

Fig. 16.3 For clinical application of FUS to open the BBB, a multi-element hemispherical ultrasound array is used. The elements can be steered electronically to target regions away from the midline. The ultrasound is combined with MR imaging to improve targeting accuracy to ~1 mm. These systems have been used to coagulate deep brain tissue in human patients

distance from the transducer. Secondly, for a multi-element hemispherical transducer, which is commonly used for clinical applications, the elements have a geometric focus at the center of the sphere. To target areas away from the midline of the brain, the elements can be electronically steered to produce off-center focal points. These phased arrays are also needed for trans-skull focusing in humans since the variable thickness of the human skull distorts the propagating ultrasound wave, such that sharp focus is not achieved from a single element focused transducer (Hynynen and Jolesz 1998). The phased array allows precise control of the phase and the amplitude of the ultrasound wave emitted by each array element, thus providing a method for distortion correction and sharp, through skull focusing (Clement et al. 2001). By combining the phased array with MR imaging (Hynynen et al. 2004), targeting accuracy in order of 1 mm has been achieved when these focused beams have been used to coagulate deep human patient brain tissue (McDannold et al. 2010; Lipsman et al. 2013; Fig. 16.3).

Some of the original methods used to open the BBB, including osmotic and chemical opening, produced widespread permeabilization of the brain and allowed potentially toxic components of the blood to access the entire nervous system (Rapoport 2001). Current and developing methods to overcome the BBB include modifying drugs so that they mimic antigens of endogenous brain endothelial receptors (Pardridge and Boado 2012). Although this method can be successful, drug delivery can be diffuse and it can be difficult to achieve therapeutic concentrations in the target region.

Transient Following BBB opening with FUS, the BBB has been found to be closed when evaluated with a clinical MRI contrast agent dose approximately 6 h after opening. The BBB remained impenetrable for up to 4 weeks, the longest time point tested (Hynynen et al. 2001, 2006). The reversibility of BBB permeability is related to the extent of BBB opening. Therefore, the period of time before the BBB closes may be related to the pressure and pulse length of the ultrasound used to open the BBB (Samiotaki et al. 2012; Samiotaki and Konofagou 2013). There have been other reports that suggest that the BBB can remain open up to 24 h using similar pressure levels (Choi et al. 2007). Further research is required to fully understand the impact frequency, pulse length, acoustic pressure and the method used in determining the closure

has on the reversibility of BBB permeability. However, it is not clear yet if the long term openings are also associated with some degree of tissue damage. This is given that detailed histological studies investigating ischemia, apoptosis and surviving neuron numbers have only been conducted at exposures that result in BBB closure approximately 6 h after opening, as determined by clinically applicable MRI methods (Hynynen et al. 2005, 2006).

Non-invasive Ultrasound energy is capable of transmitting through the skull and brain tissue when appropriate frequencies and parameters are used. The non-invasive nature of this treatment eliminates the need for surgical procedures (Hynynen et al. 2001). In addition, the microbubbles that are required to create reproducible and safe BBB opening can be delivered intravenously.

Safe When FUS is applied within an appropriate range of parameters and in conjunction with microbubbles, BBB opening can be achieved with no histological evidence of ischemia or apoptosis (Hynynen et al. 2005, 2006; McDannold et al. 2005). It has been suggested that BBB opening allows the entry of toxic blood components, including red blood cells and albumin. However, studies have shown that minor extravasations following transient, targeted BBB opening are cleared by glial cells, and have no effect on the neuronal populations (Alonso et al. 2011). Furthermore, cognitive and motor tests following repeated BBB opening with ultrasound have shown no adverse effects on behavior (McDannold et al. 2012). In a mouse model of Alzheimer's disease, repeated application of FUS led to improved cognitive function and increased neurogenesis in the targeted brain areas (Burgess et al. 2014). Applying too much acoustic pressure may result in tissue damage (Hynynen et al. 2005), therefore the development of acoustic monitoring techniques to monitor and control the applied pressure will ensure a consistent and safe level of BBB opening (McDannold et al. 2006).

16.6 Mechanisms of FUS

FUS has proven to be an effective method for transiently opening the BBB and allowing therapeutic agents to cross into the brain parenchyma. Yet, the physical and cellular mechanisms by which the barrier is opened are still unknown. It has been shown that at low ultrasound pressures, microbubble oscillations put stress on the vascular endothelium (Hosseinkhah and Hynynen 2012), which responds to dynamic shear stress (Krizanac-Bengez et al. 2004). Although both the expansion and the contraction phases of the bubble under ultrasound can impact the blood vessel wall, recent evidence has indicated that the majority of changes occur during the contraction phase (Chen et al. 2011). Bubble contraction exerts forces that pull the vessel wall towards the interior of the lumen. There are also circumferential stresses and radiation forces that are generated by an oscillating microbubble that may activate the mechanosensitive ion channels in the vascular endothelium (Traub et al. 1999).

At higher pressure, microbubble oscillation can turn into violent collapse, a process known as inertial cavitation. It has been suggested that inertial cavitation could be a potential mechanism for BBB opening, but due to the extreme local temperature rise and microjetting, it is suspected that inertial cavitation is linked to red blood cell extravasation and more serious vessel damage (Nyborg 2001; Deng et al. 2004; Vykhodtseva et al. 2008). Recently developed methods, which monitor microbubble acoustic emissions during ultrasound exposure, have determined that BBB opening can occur in the absence of inertial cavitation. Analysis of the acoustic emissions demonstrated rises in subharmonics, harmonics and ultra harmonics due to bubble oscillation. These harmonic changes are correlated to BBB opening (McDannold et al. 2008b; O'Reilly and Hynynen 2012). The acoustic emissions observed during inertial cavitation show increased broadband emission, and these signals are correlated experimentally with red blood cell extravasation and damage, thus confirming that BBB opening is not due to inertial cavitation.

Less is known about the cellular mechanisms of FUS. Initial studies delivered labeled endogenous IgG and tracked its entry through the BBB following FUS in the presence of microbubbles (Sheikov et al. 2004, 2008). The studies suggested that antibodies passed through the BBB using both the paracellular and transcellular delivery routes.

Firstly, the paracellular space was increased in the FUS application region. This widening of the tight junctions was accompanied by a reduction in the quantity of tight junction proteins (Sheikov et al. 2004, 2008), suggesting increased paracellular transport following FUS application. Specifically, there was a reduction in key tight junction proteins (occludin, claudin-5 and zonula occludens) between 1 and 2 h after FUS application, but these levels were returned to normal within 4 h (Sheikov et al. 2004). These studies have been supported by research using oxidants to open the BBB, in which there was a consistent and similar reduction in occludin and zonula occludens (Musch et al. 2006). With respect to FUS, it has been hypothesized that FUS induces either protein reorganization in the tight junction which masks the antigens, or that the proteins are downregulated (Sheikov et al. 2008). It is known that FUS can downregulate other proteins, such as the gap junction protein Connexin 43 (Alonso et al. 2011). The change in gap junction proteins was suggested to buffer the hyperexcitability of the brain, which may occur after BBB opening (Alonso et al. 2011).

Secondly, there was labeled antibody present inside vesicles within the endothelial cells. Along with an increase in the number of cytoplasmic channels and vesicles in FUS-treated regions, it was evident that antibody was being taken up by the endothelial cells and passed through the BBB transcellularly (Sheikov et al. 2004, 2008). Related studies have demonstrated both *in-vitro* and *in-vivo* that caveolin, a membrane protein involved in receptor independent endocytosis, is upregulated after FUS (Lionetti et al. 2009; Deng et al. 2012). Uptake of the drug into the cells may occur during the deformation of the endothelial cells due to the shear stress generation by the microbubble in the ultrasound field (van Wamel et al. 2006; Meijering et al. 2009).

In-vivo, two-photon microscopy has been used to visualize FUS-mediated BBB opening. Two studies have attempted to fit the leakage observed during imaging sessions to the cellular mechanisms of FUS (Raymond et al. 2008; Cho et al. 2011). In these studies, fluorescent dye (10–70 kDa) was injected intravenously to visualize the vasculature and to observe the leakage kinetics as the dye passed through the BBB. Two different patterns of dye leakage from a single vessel were observed. Fast leakage was characterized by the dye rapidly crossing across the BBB within the first 5 min after FUS application, as well as appearing to arise from a point source along the vessel wall (Cho et al. 2011). Conversely, slow leakage began 5–15 min after the onset of FUS and occurred along the length of the vessel (Cho et al. 2011). The authors speculated that these leakage types corresponded to the different cellular mechanisms of FUS. Fast leakage was hypothesized to occur when tight junction proteins were downregulated, leading to tight junction widening and 'fast' leakage of dye through the BBB. Slow leakage was hypothesized to occur when the endothelial cells were stimulated to uptake dye and transfer it through the BBB. A next step will be to correlate two-photon microscopy with acoustic emission analysis to understand the relationship between the dye leakage type and the microbubble emissions.

16.7 FUS and Microbubbles for Drug Delivery

Over 100 primary research studies have used FUS to deliver tracers or therapeutic agents through the BBB and into the brain. Evaluation of BBB opening and quantification of drug delivery is done by delivery of a contrast agent or tracer molecule. Most commonly, gadolinium-based MRI contrast agents (500–900 Da) are delivered during FUS treatment, and the extravasation of these agents into the brain is used to confirm and evaluate BBB opening using MRI (Hynynen et al. 2001). MRI images are analyzed and the hyperintense regions, indicative of

contrast agent delivery, are measured and used as an indicator of the 'amount' of BBB opening (Treat et al. 2007). It has been demonstrated that the relative enhancement of the hyperintense regions is correlated to the amount of vessel damage that occurs in the brain (Hynynen et al. 2001; McDannold et al. 2008a, b; O'Reilly and Hynynen 2012). Within the safe range of BBB opening (enhancement <30 %), there is the clear advantage of more drug delivery when the BBB is opened to a greater extent. This is particularly true when delivering large molecules. As an example, Jordao et al. measured the amount of endogenous IgM, an antibody that weighs 6 times more than the more abundant IgG. They demonstrated that the percentage increase in IgM in the brain after FUS-mediated BBB opening is positively correlated to relative amount of BBB opening, quantified by increased enhancement on MR images (Jordão et al. 2013). There is room for further experimentation in this area to precisely optimize the amount of BBB opening during each treatment with respect to the drug that is being delivered. It is understood that larger drugs require more BBB opening to reach therapeutic concentrations in the brain, and balancing optimal drug delivery with the risk of vessel damage will be important (Yang et al. 2011; Nhan et al. 2013; Chen and Konofagou 2014). Many other studies have supported these findings and have validated the use of MRI, not only as a method to choose the target location, but also as a method to evaluate drug delivery and success of the treatment (Kinoshita et al. 2006; Treat et al. 2007; Liu et al. 2010b; Aryal et al. 2013; Fan et al. 2013a). It is also possible to combine the therapeutic agents with MRI contrast agent molecules, and thus directly quantify the amount of drug delivered (Ting et al. 2012; Fan et al. 2013a, b).

16.7.1 Drug Delivery to the Brain in Rodent Models

Delivery of fluorescent and colorimetric dyes has provided knowledge on the localization of the BBB opening to the region of interest and relative quantity of potential drug delivery. Trypan blue and Evan's blue (~70 kDa when bound to albumin *in-vivo*), horseradish peroxidase (40 kDa) and fluorescently tagged dextrans (3–2000 kDa) have all served as models of drug delivery (Sheikov et al. 2004; Raymond et al. 2007; Cho et al 2011; Choi et al 2010).

A major focus of FUS-mediated drug delivery has been on its application for brain tumors. Several types of chemotherapeutic agents have been delivered effectively to the brain in rodent models. Doxorubicin, a chemotherapeutic compound with widespread use, has limited success in the brain because of the BBB. In rat brain tumor models, FUS-mediated BBB opening has delivered therapeutic concentrations of doxorubicin to the tumor (Treat et al. 2007; Fan et al. 2013a, b). Repeated delivery of doxorubicin using FUS leads to significant increases in median survival times over animals treated with doxorubicin alone (Treat et al. 2012; Aryal et al. 2013). In addition to doxorubicin, methotrexate (Mei et al. 2009), 1,3-bis(2-chloroethyl)-1-nitrosourea (BCNU; Chen et al. 2010) and epirubicin (Liu et al. 2010a, b) have also been effectively delivered with FUS and show tumor-suppressing effects in the brain.

Antibodies represent another class of drugs effective for cancer treatment. Herceptin, a monoclonal antibody that targets the HER2/neu receptor found in 30 % of breast cancers, is effective against breast tumors. On the other hand, it is unable to treat brain metastases. It was first demonstrated by Kinoshita and colleagues that antibodies are able to be delivered through the BBB using FUS (Kinoshita et al. 2006), and ongoing treatment results in significant improvements in tumor reduction and survival time (Park et al. 2012). As a novel method to treat brain tumors expressing HER2/neu receptors, natural killer cells expressing a Her2 antigen were delivered to the brain using FUS (Alkins et al. 2013). The immune cells entered the brain in the brain tumor region in quantities that were sufficient for tumor reduction.

Although tumors have been a focus for drug delivery to the brain, FUS-mediated BBB opening has other additional applications. Several

studies have suggested that FUS-mediated BBB opening may be an integral part of the treatment strategy for neurodegenerative disease. FUS and microbubbles were used to open the BBB in a transgenic mouse model of Alzheimer's disease and their non-transgenic littermates. No quantifiable differences in the opening or closing behaviors were detected (Choi et al. 2008). With the knowledge that antibodies could be delivered through the BBB from the Herceptin study, two research groups used FUS to deliver amyloid antibodies into mouse models of Alzheimer's disease (Raymond et al. 2008; Jordão et al. 2010). Amyloid antibodies were found bound to plaques in the regions treated with FUS and microbubbles (Raymond et al. 2008; Jordão et al. 2010). Furthermore, the antibodies delivered by FUS were found to significantly reduce mean plaque size and number after 4 days compared to control treated animals (Jordão et al. 2010).

Other therapeutics, such as neurotrophic factors, have been investigated for applications in Alzheimer's and Parkinson's disease where growth factor levels are reduced. Despite their short half-life *in-vivo*, brain-derived neurotrophic factor (BDNF; Baseri et al. 2012), neurturin (Baseri et al. 2012) and glial-derived neurotrophic factor (GDNF; Wang et al. 2012) have been delivered to the brain in significant amounts using FUS and microbubbles. *In-vivo,* BDNF levels were high enough to stimulate pro-survival signaling pathways, indicating that the compounds are still effective after delivery through the BBB (Baseri et al. 2012). Large biological therapeutics, including stem cells and gene therapy agents, have also been delivered through the BBB despite their size (Fig. 16.4). Neural stem cells were delivered to the striatum and the hippocampus of the rat brain and were shown to have begun differentiating into neurons after delivery through the BBB (Burgess et al. 2011). Nanoparticles (Etame et al. 2012; Diaz et al. 2014), adeno-associated viruses (Thévenot et al. 2012; Alonso et al. 2013; Hsu et al. 2013) and siRNA (Burgess et al. 2012) have also been delivered to various regions of the brain and have the potential to be effective drug carriers for treatment of neurodegenerative diseases.

16.7.2 Drug Delivery to the Primate Brain

The translation of studies on BBB opening and drug delivery to clinical applications requires treatment and analysis of non-human primates. Ultrasound transmission is more problematic in non-human primates and humans who have skulls with varying thicknesses and densities. Clinical, hemispherical transducer arrays reduce the aberrations in ultrasound propagation caused by varying skull thickness and spread heat over the entire surface of the skull (Hynynen et al. 2004). FUS-mediated BBB opening has been performed in non-human primates, using both a single element transducer (Marquet et al. 2011; Tung et al. 2011) and the commercially available, clinical ultrasound transducer array (McDannold et al. 2012). In one key study, non-human primates were treated multiple times in multiple locations within the brain. Prior to and following the FUS-mediated BBB opening treatments, the non-human primates were tested in a series of visual and learning tests. It was found that the non-human primates performed as well on the tests following treatment as they did prior to treatment (McDannold et al. 2012).

16.7.3 Effects of FUS Alone on the Brain

In recent studies, it has been shown that FUS is more than just a method for drug delivery. A novel role for FUS-mediated BBB opening in neurogenesis has been discovered. In one study, healthy mice were injected with a thymidine analog, bromodeoxyuridine (BrdU), immediately following BBB opening in one hemisphere (Scarcelli et al. 2014). BrdU incorporates into the DNA of dividing cells and is used to identify newly born cells in the neurogenic regions of the hippocampus. Post-mortem analysis of the hippocampus showed an increase in the number of new neurons in the FUS-treated hemisphere compared to the contralateral hemisphere, suggesting that FUS can stimulate new neuron growth (Scarcelli et al. 2014). These data were

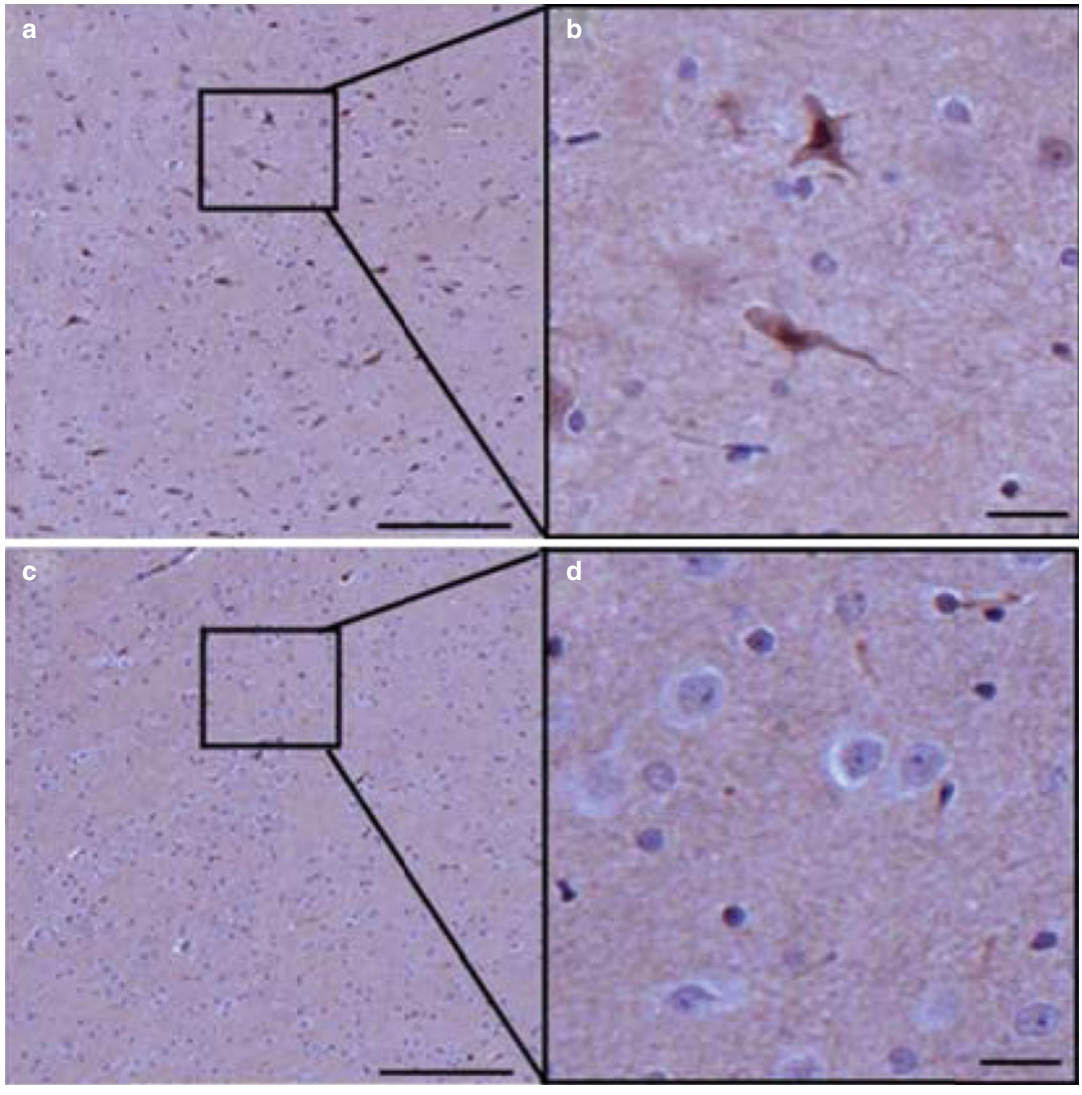

Fig. 16.4 FUS and microbubbles have been used to effectively deliver large biological agents, including stem cells. GFP immunohistochemistry was performed on brain sections following FUS-mediated delivery of GFP-expressing stem cells to the brain. FUS was applied to the left hemisphere. GFP-expressing cells are only observed in the left hemisphere (**a**, **b**), but not in the right, untreated hemisphere (**c**, **d**) (Figure adapted from Burgess et al. 2011)

supported in another study using a mouse model of Alzheimer's disease. Burgess and colleagues showed that FUS significantly increased the number of immature neurons in the hippocampus of transgenic mice treated with FUS (Burgess et al. 2014). The increase in new neurons in the hippocampus was correlated to improved performance in the Y maze, suggesting that the new neurons improved cognition (Burgess et al. 2014). The mechanisms behind FUS-induced neurogenesis in the hippocampus are unknown, but the data is consistent with previous studies. Firstly, it was demonstrated that ultrasound exposure to the brain, using different exposure parameters and without microbubles, leads to increased production of brain-derived neurotrophic factor (BDNF), which is a modulator of neurogenesis in the hippocampus (Tufail et al. 2010). Secondly, BDNF protein levels can be increased by upregulation of the pro-survival Akt

signaling pathway. Akt activation was detected following FUS-mediated BBB opening with microbubbles, consequently providing a potential mechanism by which FUS stimulates neurogenesis (Jalali et al. 2010).

In other studies looking at FUS in Alzheimer's disease, FUS-mediated BBB opening has been shown to reduce plaque pathology, even in the absence of drug delivery (Jordão et al. 2013; Burgess et al. 2014). Jordao and colleagues presented two possible mechanisms. Initially, they indicated that the plaque was reduced by endogenous immunoglobulins, which passed through the BBB from the peripheral circulation. Then, BBB opening led to activation of microglia and astrocytes, which then internalize the amyloid. Regardless of the precise mechanisms, these data present new evidence that FUS-mediated BBB opening, even in the absence of any exogenous drug delivery, could lead to significant improvements in pathology and behavior in animal disease models.

16.8 Future Considerations

The BBB has been identified as the single most important factor limiting pharmaceutical treatment of brain disorders. There are many research streams aimed at circumventing the BBB to improve drug accumulation in the brain, but only FUS is non-invasive, targeted, transient, safe and effective.

Despite the significant advances in FUS since the introduction of microbubbles in 2001, there are still significant hurdles to overcome before FUS is adopted into widespread clinical use. Further research is necessary to better understand specific drug concentrations, so that therapeutic concentrations can be achieved while simultaneously limiting the potential for toxicity in the periphery. Although research using tracer molecules has begun to address some of these questions (Nhan et al. 2013), future studies using clinically appropriate drugs in relevant animal models need to be established. Since drug dosages currently used for treatment may need to be adjusted in order to achieve therapeutic doses in the brain, close monitoring of the kinetics of these agents will be important.

Furthermore, most of the studies completed to date have been performed in healthy animals with a strong BBB. The BBB is a target in many diseases, and in fact some research indicates that breakdown of the BBB may be the precipitating factor compromised in many diseases.

References

Abbott NK, Patabendige AA, Doman DE, Yusof SR, Begley DG (2010) Structure and function of the blood-brain barrier. Neurobiol Dis 37:13–25

Alkins R, Burgess A, Ganguly M, Francia G, Kerbel R, Wels WS, Hynynen K (2013) Focused ultrasound delivers targeted immune cells to metastatic brain tumors. Cancer Res 73:1892–1899

Alonso A, Reinz E, Fatar M, Hennerici MG, Meairs S (2011) Clearance of albumin following ultrasound-induced blood-brain barrier opening is mediated by glial but not neuronal cells. Brain Res 1411:9–16

Alonso A, Reinz E, Leuchs B, Kleinschmidt J, Fatar M, Geers B, Lentacker I, Hennerici MG, de Smedt SC, Meairs S (2013) Focal delivery of AAV2/1-transgene into the rat brain by localized ultrasound induced BBB opening. Mol Ther Nucleic Acids 2:e73

Armulik A, Genové G, Mäe M, Nisancioglu MH, Wallgard E, Niaudet C, He L, Norlin J, Lindblom P, Strittmatter K, Johansson BR, Betsholtz C (2010) Pericytes regulate the blood-brain barrier. Nature 468:557–561

Arvanitis CD, Livingstone MS, Vykhodtseva N, McDannold N (2012) Controlled ultrasound-induced blood-brain barrier disruption using passive acoustic emissions monitoring. PLoS One 7:e45783

Aryal M, Vykhodtseva N, Zhang YZ, Park J, McDannold N (2013) Multiple treatments with liposomal doxorubicin and ultrasound-induced disruption of blood-tumor and blood-brain barriers improve outcomes in a rat glioma model. J Control Release 169:103–111

Bakay L, Ballantine HT Jr, Hueter TF, Sosa D (1956) Ultrasonically produced changes in the blood-brain barrier. AMA Arch Neurol Psychiatry 76:457

Baseri B, Choi JJ, Deffieux T, Samiotaki G, Tung YS, Olumolade O, Small SA, Morrison B III, Konofagou EE (2012) Activation of signaling pathways following localized delivery of systemically administered neurotrophic factors across the blood-brain barrier using focused ultrasound and microbubbles. Phys Med Biol 57:65–81

Bing KF, Howles GP, Qi Y, Palmeri ML, Nightingale KR (2009) Blood-brain barrier (BBB) disruption using a diagnostic ultrasound scanner and definity in mice. Ultrasound Med Biol 35:1298–1308

Burgess A, Ayala-Grosso CA, Ganguly M, Jordão JF, Aubert I, Hynynen K (2011) Targeted delivery of

neural stem cells to the brain using MRI-guided focused ultrasound to disrupt the blood-brain barrier. PLoS One 6:e27877

Burgess A, Huang Y, Querbes W, Sah DW, Hynynen K (2012) Focused ultrasound for targeted delivery of siRNA and efficient knockdown of Htt expression. J Control Release 163:125–129

Burgess A, Dubey S, Yeung S, Hough O, Eterman N, Aubert I, Hynynen K (2014) Alzheimer disease in a mouse model: MR imaging-guided focused ultrasound targeted to the hippocampus opens the blood-brain barrier and improves pathologic abnormalities and behavior. Radiology 273:736–745

Chen H, Konofagou EE (2014) The size of blood-brain barrier opening induced by focused ultrasound is dictated by acoustic pressure. J Cereb Blood Flow Metab 34:1197–1204

Chen PY, Liu HL, Hua MY, Yang HW, Huang CY, Chu PC, Lyu LA, Tseng IC, Feng LY, Tsai HC, Chen SM, Lu YJ, Wang JJ, Yen TC, Ma YH, Wu T, Chen JP, Chuang JI, Shin JW, Hseuh C, Wei KC (2010) Novel magnetic/ultrasound focusing system enhances nanoparticle drug delivery for glioma treatment. Neuro Oncol 12:1050–1060

Chen H, Kreider W, Brayman AA, Bailey MR, Matula TJ (2011) Blood vessel deformations on microsecond time scales by ultrasonic cavitation. Phys Rev Lett 106:034301

Cho CW, Liu W, Cobb N, Henthorn TK, Lillehei K, Christians U (2002) Ultrasound induced mild hyperthermia as a novel approach to increase drug uptake in brain microvessel endothelial cells. Pharm Res 19:1123–1129

Cho EE, Drazic J, Ganguly M, Stefanovic B, Hynynen K (2011) Two-photon fluorescence microscopy study of cerebrovascular dynamics in ultrasound-induced blood–brain barrier opening. J Cereb Blood Flow Metab 31:1852–1862

Choi JJ, Pernot M, Small SA, Konofagou EE (2007) Noninvasive transcranial and localized opening of the blood-brain barrier using focused ultrasound in mice. Ultrasound Med Biol 33:95–104

Choi JJ, Wang S, Brown TR, Small SA, Duff KE, Konofagou EE (2008) Noninvasive and transient blood-brain barrier opening in the hippocampus of Alzheimer's double transgenic mice using focused ultrasound. Ultrason Imaging 30:189–200

Choi JJ, Feshitan JA, Baseri B, Wang S, Tung YS, Borden MA, Konofagou EE (2010) Microbubble-size dependence of focused ultrasound-induced blood-brain barrier opening in mice in vivo. IEEE Trans Biomed Eng 57:145–154

Choi JJ, Selert K, Gao Z, Baseri B, Konofagou EE (2011) Noninvasive and localized blood-brain barrier disruption using focused ultrasound can be achieved at short pulses lengths and low repetition frequencies. J Cereb Blood Flow Metab 31:725–737

Clement GT, Sun J, Hynynen K (2001) The role of internal reflection in transskull phase distortion. Ultrasonics 39:109–113

Daneman R, Zhou L, Kebede AA, Barres BA (2010) Pericytes are required for blood-brain barrier integrity during embryogenesis. Nature 468:562–566

Deng CX, Sieling F, Pan H, Cui J (2004) Ultrasound-induced cell membrane porosity. Ultrasound Med Biol 30:519–526

Deng J, Huang Q, Wang F, Liu Y, Wang Z, Wang Z, Zhang Q, Lei B, Cheng Y (2012) The role of caveolin-1 in blood-brain barrier disruption induced by focused ultrasound combined with microbubbles. J Mol Neurosci 46:677–687

Diaz RJ, McVeigh PZ, O'Reilly MA, Burrell K, Bebenek M, Smith C, Etame AB, Zadeh G, Hynynen K, Wilson BC, Rutka JT (2014) Focused ultrasound delivery of Raman nanoparticles across the blood-brain barrier potential for targeting experimental brain tumours. Nanomedicine 10:1075–1087

Etame AB, Diaz RJ, O'Reilly MA, Smith CA, Mainprize TG, Hynynen K, Rutka JT (2012) Enhanced delivery of gold nanoparticles with therapeutic potential into the brain using MRI-guided focused ultrasound. Nanomedicine 8:1133–1142

Fan CH, Ting CY, Lin HJ, Wang CH, Liu HL, Yen TC, Yeh CK (2013a) SPIO-conjugated, doxorubicin-loaded microbubbles for concurrent MRI and focused-ultrasound enhanced brain-tumor drug delivery. Biomaterials 34:3706–3715

Fan CH, Ting CY, Liu HL, Huang CY, Hsieh HY, Yen TC, Wei KC, Yeh CK (2013b) Antiangiogenic-targeting drug-loaded microbubbles combined with focused ultrasound for glioma treatment. Biomaterials 34:2142–2155

Fenstermacher J, Gross P, Sposito N, Acuff V, Pettersen S, Gruber K (1988) Structural and functional variations in capillary systems within the brain. Ann N Y Acad Sci 529:21–30

Fry WJ, Fry FJ (1960) Fundamental neurological research and human neurosurgery using intense ultrasound. IRE Trans Med Electron 7:166–181

Goertz DE, Wright C, Hynynen K (2010) Contrast agent kinetics in the rabbit brain during exposure to therapeutic ultrasound. Ultrasound Med Biol 36:916–924

Goldmann EE (1909) Die aussere und innere Sekretion des gesunden und kranken Organismus im Lichte det 'vitalenFarbung'. Beitraege Klinischen Chirurgie 64:192–265

Gross ME, Nelson ET, Mone MC, Hansen HJ, Sklow B, Glasgow RE, Scaife CL (2011) A comparison of post-operative outcomes utilizing a continuous preperitoneal infusion versus epidural for midline laparotomy. Am J Surg 202:765–770

Hawkins BT, Davis TP (2005) The blood-brain barrier/neurovascular unit in health and disease. Pharmacol Rev 57:173–185

Hosseinkhah N, Hynynen K (2012) A three-dimensional model of an ultrasound contrast agent gas bubble and its mechanical effects on microvessels. Phys Med Biol 57:785–808

Hsu PH, Wei KC, Huang CY, Wen CJ, Yen TC, Liu CL, Lin YT, Chen JC, Shen CR, Liu HL (2013) Noninvasive and targeted gene delivery into the brain using microbubble-facilitated focused ultrasound. PLoS One 8:e57682

Hynynen K, Jolesz FA (1998) Demonstration of potential noninvasive ultrasound brain therapy through an intact skull. Ultrasound Med Biol 24:275–283

Hynynen K, McDannold N, Vykhodtseva N, Jolesz FA (2001) Noninvasive MR imaging-guided focal opening of the blood-brain barrier in rabbits. Radiology 220:640–646

Hynynen K, Clement GT, McDannold N, Vykhodtseva N, King R, White PJ, Vitek S, Jolesz FA (2004) 500-element ultrasound phased array system for noninvasive focal surgery of the brain: a preliminary rabbit study with ex vivo human skulls. Magn Reson Med 52:100–107

Hynynen K, McDannold N, Sheikov NA, Jolesz FA, Vyhodtseva N (2005) Local and reversible blood-brain barrier disruption by noninvasive focused ultrasound at frequencies suitable for trans-skull sonications. Neuroimage 24:12–20

Hynynen K, McDannold N, Vykhodtseva N, Raymond S, Weissleder R, Jolesz FA, Sheikov N (2006) Focal disruption of the blood-brain barrier due to 260 kHz ultrasound bursts: a method for molecular imaging and targeted drug delivery. J Neurosurg 105: 445–454

Jalali S, Huang Y, Dumont DJ, Hynynen K (2010) Focused ultrasound-mediated bbb disruption is associated with an increase in activation of AKT: experimental study in rats. BMC Neurol 10:114

Janzer RC, Raff MC (1987) Astrocytes induce blood-brain barrier properties in endothelial cells. Nature 325:253–257

Jordão JF, Ayala-Grosso CA, Markham K, Huang Y, Chopra R, McLaurin J, Hynynen K, Aubert I (2010) Antibodies targeted to the brain with image-guided focused ultrasound reduces amyloid-beta plaque load in the TgCRND8 mouse model of Alzheimer's disease. PLoS One 5:e10549

Jordão JF, Thévenot E, Markham-Coultes K, Scarcelli T, Weng YQ, Xhima K, O'Reilly M, Huang Y, McLaurin J, Hynynen K, Aubert I (2013) Amyloid-ß plaque reduction, endogenous antibody delivery and glial activation by brain-targeted, transcranial focused ultrasound. Exp Neurol 248:16–29

Killian DM, Hermeling S, Chikhale PJ (2007) Targeting the cerebrovascular large neutral amino acid transporter (LAT1) isoform using a novel disulfide-based brain drug delivery system. Drug Deliv 14:25–31

Kinoshita M, McDannold N, Jolesz FA, Hynynen K (2006) Noninvasive localized delivery of Herceptin to the mouse brain by MRI-guided focused ultrasound-induced blood-brain barrier disruption. Proc Natl Acad Sci U S A 103:11719–11723

Kniesel U, Wolburg H (2000) Tight junctions of the blood-brain barrier. Cell Mol Neurobiol 20:1347–1357

Krizanac-Bengez L, Mayberg MR, Janigro D (2004) The cerebral vasculature as a therapeutic target for neurological disorders and the role of shear stress in vascular homeostatis and pathophysiology. Neurol Res 26: 846–853

Lionetti V, Fittipaldi A, Agostini S, Giacca M, Recchia FA, Picano E (2009) Enhanced caveolae-mediated endocytosis by diagnostic ultrasound in vitro. Ultrasound Med Biol 35:136–143

Lipsman N, Schwartz ML, Huang Y, Lee L, Sankar T, Chapman M, Hynynen K, Lozano AM (2013) MR-guided focused ultrasound thalamotomy for essential tremor: a proof-of-concept study. Lancet Neurol 12:462–468

Liu HL, Pan CH, Ting CY, Hsiao MJ (2010a) Opening of the blood-brain barrier by low-frequency (28 kHz) ultrasound: a novel pinhole assisted mechanical scanning device. Ultrasound Med Biol 36:325–335

Liu HL, Hua MY, Chen PY, Chu PC, Pan CH, Yang HW, Huang CY, Wang JJ, Yen TC, Wei KC (2010b) Blood-brain barrier disruption with focused ultrasound enhances delivery of chemotherapeutic drugs for glioblastoma treatment. Radiology 255:415–425

Lochhead JJ, Thorne RG (2012) Intranasal delivery of biologics to the central nervous system. Adv Drug Deliv Rev 64:614–628

Marquet F, Tung YS, Teichert T, Ferrera VP, Konofagou EE (2011) Noninvasive, transient and selective blood-brain barrier opening in non-human primates in vivo. PLoS One 6:e22598

McDannold N, Vykhodsteva N, Jolesz FA, Hynynen K (2004) MRI investigation of the threshold for thermally induced blood-brain barrier disruption and brain tissue damage in the rabbit. Magn Reson Med 51: 913–923

McDannold N, Vykhodtseva N, Raymond S, Jolesz F, Hynynen K (2005) MRI-guided targeted blood-brain barrier disruption with focused ultrasound: histological findings in rabbits. Ultrasound Med Biol 31:1527–1537

McDannold N, Vykhodtseva N, Hynynen K (2006) Targeted disruption of the blood-brain barrier with focused ultrasound: association with cavitation activity. Phys Med Biol 51:793–807

McDannold N, Vykhodtseva N, Hynynen K (2007) Use of ultrasound pulses combined with definity for targeted blood-brain barrier disruption; a feasibility study. Ultrasound Med Biol 33:584–590

McDannold N, Vykhodtseva N, Hynynen K (2008a) Blood-brain barrier disruption by focused ultrasound and circulating preformed microbubbles appears to be characterized by the mechanical index. Ultrasound Med Biol 34:834–840

McDannold N, Vykhodtseva N, Hynynen K (2008b) Effects of acoustic parameters and ultrasound. Ultrasound Med Biol 34:930–937

McDannold N, Clement GT, Black P, Jolesz F, Hynynen K (2010) Transcranial magnetic resonance imaging – guided focused ultrasound surgery of brain tumors: initial findings in 3 patients. J Neurosurg 66:323–332

McDannold N, Arvanitis CD, Vykhodtseva N, Livingstone MS (2012) Temporary disruption of the blood-brain barrier by use of ultrasound and microbubbles: safety and efficacy evaluation in rhesus macaques. Cancer Res 72:3652–3663

Mei J, Cheng Y, Song Y, Yang Y, Wang F, Liu Y, Wang Z (2009) Experimental study on targeted methotrexate delivery to the rabbit brain via magnetic resonance imaging-guided focused ultrasound. J Ultrasound Med 28:871–880

Meijering BD, Juffermans LJ, van Wamel A, Henning RH, Zuhorn IS, Emmer M, Versteilen AM, Paulus WJ, van Gilst WH, Kooiman K, de Jong N, Musters RJ, Deelman LE, Kamp O (2009) Ultrasound and microbubble-targeted delivery of macromolecules is regulated by induction of endocytosis and pore formation. Circ Res 104:679–687

Mesiwala AH, Farrell L, Wenzel HJ, Silbergeld DL, Crum LA, Winn HR, Mourad PD (2002) High-intensity focused ultrasound selectively disrupts the blood-brain barrier in vivo. Ultrasound Med Biol 28:389–400

Musch MW, Walsh-Reitz MM, Chang EB (2006) Roles of ZO-1, occludin, and actin in oxidant-induced barrier disruption. Am J Physiol Gastrointest Liver Physiol 290:222–231

Nhan T, Burgess A, Cho EE, Stefanovic B, Lilge L, Hynynen K (2013) Drug delivery to the brain by focused ultrasound induced blood-brain barrier disruption: quantitative evaluation of enhanced permeability of cerebral vasculature using two-photon microscopy. J Control Release 172:274–280

Nyborg WL (2001) Biological effects of ultrasound: development of safety guidelines. Part II: general review. Ultrasound Med Biol 27:301–333

O'Reilly MA, Hynynen K (2012) Blood-brain barrier: real-time feedback-controlled focused ultrasound disruption by using an acoustic emissions-based controller. Radiology 263:96–106

O'Reilly MA, Hynynen K (2013) A super-resolution ultrasound method for brain vascular mapping. Med Phys 40:100701

O'Reilly MA, Waspe AC, Ganguly M, Hynynen K (2010) Focused ultrasound disruption of the blood-brain barrier using closely-timed short pulses: influence of sonication parameters and injection rate. Ultrasound Med Biol 37:587–594

Pardridge WM (2005) The blood-brain barrier: bottleneck in brain drug development. NeuroRx 2:3–14

Pardridge WM (2012) Drug transport across the blood-brain barrier. J Cereb Blood Flow Metab 32:1959–1972

Pardridge WM, Boado RJ (2012) Reengineering biopharmaceuticals for targeted delivery across the blood-brain barrier. Methods Enzymol 503:269–292

Park EJ, Zhang YZ, Vykhodtseva N, McDannold N (2012) Ultrasound-mediated blood-brain/blood-tumor barrier disruption improves outcomes with trastuzumab in a breast cancer brain metastasis model. J Control Release 163:277–284

Patrick JT, Nolting MN, Goss SA, Dines KA, Clendenon JL, Rea MA, Heimburger RF (1990) Ultrasound and the blood-brain barrier. Adv Exp Med Biol 267:369–381

Pires A, Fortuna A, Alves G, Falcao A (2009) Intranasal drug delivery: how, why and what for? J Pharm Pharm Sci 12:288–311

Rapoport SI (2001) Advances in osmotic opening of the blood-brain barrier to enhance CNS chemotherapy. Expert Opin Investig Drugs 10:1809–1818

Raymond SB, Skoch J, Hynynen K, Bacskai BJ (2007) Multiphoton imaging of ultrasound/optison mediated cerebrovascular effects in vivo. J Cereb Blood Flow Metab 27:393–403.

Raymond SB, Treat LH, Dewey JD, McDannold NJ, Hynynen K, Bacskai BJ (2008) Ultrasound enhanced delivery of molecular imaging and therapeutic agents in Alzheimer's disease mouse models. PLoS One 3:e2175

Samiotaki G, Konofagou EE (2013) Dependence of the reversibility of focused- ultrasound-induced blood-brain barrier opening on pressure and pulse length in vivo. IEEE Trans Ultrason Ferr 60:2257–2265

Samiotaki G, Vlachos F, Tung YS, Konofagou EE (2012) A quantitative pressure and microbubble-size dependence study of focused ultrasound induced blood-brain barrier opening reversibility in vivo using MRI. Magn Reson Med 67:769–777

Scarcelli T, Jordao JF, O'Reilly MA, Ellens N, Hynynen K, Aubert I (2014) Stimulation of hippocampal neurogenesis by transcranial focused ultrasound and microbubbles in adult mice. Brain Stimul 7:304–307

Sedlakova R, Shivers RR, Del Maestro RF (1999) Ultrastructure of the blood-brain barrier in the rabbit. J Submicrosc Cytol Pathol 31:149–161

Shealy CN, Crafts D (1965) Selective alteration of the blood-brain barrier. J Neurosurg 23:484–487

Sheikov N, McDannold N, Vykhodtseva N, Jolesz F, Hynynen K (2004) Cellular mechanisms of the blood-brain barrier opening induced by ultrasound in presence of microbubbles. Ultrasound Med Biol 30: 979–989

Sheikov N, Mcdannold NJ, Sharma S, Hynynen K (2008) Effect of focused ultrasound applied with an ultrasound contrast agent on the tight junctional integrity of the brain microvascular endothelium. Ultrasound Med Biol 34:1093–1104

Thévenot E, Jordão JF, O'Reilly MA, Markham K, Weng YQ, Foust KD, Kaspar BK, Hynynen K, Aubert I (2012) Targeted delivery of scAAV9 to the brain using MRI-guided focused ultrasound. Human Gene Ther 23:1144–1155

Tilling T, Engelbertz C, Decker S, Korte D, Hüwel S, Galla HJ (2002) Expression and adhesive properties of basement membrane proteins in cerebral capillary endothelial cells cultures. Cell Tissue Res 310:19–29

Ting CY, Fan CH, Liu HL, Huang CY, Hsieh HY, Yen TC, Wei KC, Yeh CK (2012) Concurrent blood-brain barrier opening and local drug delivery using drug carrying microbubbles and focused ultrasound for brain glioma treatment. Biomaterials 33:704–712

Traub O, Ishida T, Ishida M, Tupper JC, Berk BC (1999) Shear-stress-mediated extracellular signal-related kinase activation is regulated by sodium in endothelial cells. Potential role for a voltage-dependent sodium channel. J Biol Chem 274:20144–20150

Treat LH, McDannold N, Vykhodtseva N, Zhang Y, Tam K, Hynynen K (2007) Targeted delivery of doxorubicin to the rat brain at therapeutic levels using MRI-guided focused ultrasound. Int J Cancer 121:901–907

Treat LH, McDannold N, Zhang Y, Vykhodtseva N, Hynynen K (2012) Improved anti-tumor effect of

liposomal doxorubicin after targeted blood-brain barrier disruption by mri-guided focused ultrasound in rat glioma. Ultrasound Med Biol 38:1716–1725

Tufail Y, Matyushov A, Baldwin N, Tauchmann ML, Georges J, Yoshihiro A, Tillery SIH, Tyler WJ (2010) Transcranial pulsed ultrasound stimulates intact brain circuits. Neuron 66:681–694

Tung YS, Marquet F, Teichert T, Ferrera V, Konofagou EE (2011) Feasibility of noninvasive cavitation-guided blood-brain barrier opening using focused ultrasound and microbubbles in nonhuman primates. Appl Phys Lett 98:163704

van Wamel A, Kooiman K, Harteveld M, Emmer M, ten Cate FJ, Versluis M, de Jong N (2006) Vibrating microbubbles poking individual cells: drug transfer into cells via sonoporation. J Control Release 112:149–155

Vlachos F, Tung YS, Konofagou EE (2011) Permeability dependence study of the focused ultrasound-induced blood-brain barrier opening at distinct pressures and microbubble diameters using DCE-MRI. Magn Reson Med 66:821–830

Vykhodtseva N, Hynynen K, Damianou C (1995) Histologic effects of high intensity pulsed ultrasound exposure with subharmonic emission in rabbit brain in vivo. Ultrasound Med Biol 21:969–979

Vykhodtseva N, McDannold N, Hynynen K (2008) Progress and problems in the application of focused ultrasound for blood–brain barrier disruption. Ultrasonics 48:279–296

Wang F, Shi Y, Lu L, Liu L, Cai Y, Zheng H, Liu X, Yan F, Zou C, Sun C, Shi J, Lu S, Chen Y (2012) Targeted delivery of GDNF through the blood–brain barrier by MRI-guided focused ultrasound. PLoS One 7:e52925

Wang S, Samiotaki G, Olumolade O, Feshitan JA, Konofagou EE (2014) Microbubble type and distribution dependence of focused ultrasound-induced blood-brain barrier opening. Ultrasound Med Biol 40:130–137

Weng JC, Wu SK, Yang FY, Tseng WY (2010) Pulse sequence and timing of contrast-enhanced MRI for assessing blood-brain barrier disruption after transcranial focused ultrasound in the presence of haemorrhage. J Magn Reson Imaging 31:1323–1330

White E, Woolley M, Bienemann A, Johnson DE, Wyatt M, Murray G, Taylor H, Gill SS (2010) A robust MRI-compatible system to facilitate highly accurate stereotactic administration of therapeutic agents to targets within the brain of a large animal model. J Neurosci Methods 195:78–87

Yang FY, Fu WM, Chen WS, Yeh WL, Lin WL (2008) Quantitative evaluation of the use of microbubbles with transcranial focused ultrasound on blood-brain barrier disruption. Ultrason Sonochem 15:636–643

Yang FY, Lin YS, Kang KH, Chao TK (2011) Reversible blood-brain barrier disruption by repeated transcranial focused ultrasound allows enhanced extravasation. J Control Release 150:111–116

Microbubbles and Ultrasound: Therapeutic Applications in Diabetic Nephropathy

17

Wei J. Cao, Pratiek N. Matkar, Hao H. Chen, Azadeh Mofid, and Howard Leong-Poi

Abstract

Diabetic nephropathy (DN) remains one of the most common causes of end-stage renal disease. Current therapeutic strategies aiming at optimization of serum glucose and blood pressure are beneficial in early stage DN, but are unable to fully prevent disease progression. With the limitations of current medical therapies and the shortage of available donor organs for kidney transplantation, the need for novel therapies to address DN complications and prevent progression towards end-stage renal failure is crucial. The development of ultrasound technology for non-invasive and targeted *in-vivo* gene delivery using high power ultrasound and carrier microbubbles offers great therapeutic potential for the prevention and treatment of DN. The promising results from preclinical studies of ultrasound-mediated gene delivery (UMGD) in several DN animal models suggest that UMGD offers a unique, non-invasive platform for gene- and cell-based therapies targeted against DN with strong clinical translation potential.

Keyword

Diabetic nephropathy • Ultrasound • Gene delivery • Microbubble

17.1 Introduction

Despite the widespread adoption of renoprotective strategies, diabetic nephropathy (DN) remains the leading cause of end-stage renal disease (Rosolowsky et al. 2011); with rising prevalence in the United States that parallels the increasing prevalence of diabetes (de Boer et al. 2011; Selvin et al. 2012). Among diabetics, prevalence of DN is unaffected by the increased use of glucose-lowering medications and

W.J. Cao • P.N. Matkar • H.H. Chen • A. Mofid
H. Leong-Poi (✉)
Division of Cardiology, Department of Medicine, Keenan Research Centre for Biomedical Science, Li Ka Shing Knowledge Institute, St. Michael's Hospital, University of Toronto, Toronto, ON, Canada
e-mail: leong-poih@smh.ca

© Springer International Publishing Switzerland 2016

J.-M. Escoffre, A. Bouakaz (eds.), *Therapeutic Ultrasound*, Advances in Experimental Medicine and Biology, Vol. 880, DOI 10.1007/978-3-319-22536-4_17

renin-angiotensin-aldosterone antagonists, suggesting the necessity for newer, more effective therapies (Rosolowsky et al. 2011). Current interventions for the prevention and treatment of DN include optimal blood glucose control, management of hypertension and the use of renin-angiotensin system (RAS) blockers. While important for the management of DN, these approaches have only modest utility and are ineffective at preventing progression of the disease. Renal replacement therapies through pancreatic islet and kidney transplantation are most beneficial for patients with end-stage renal disease (ESRD) (Abecassis et al. 2008). However, the scarcity of available donor organs for transplantation and life-long intake of immunosuppressive agents are major limitations for its widespread utility.

Alternatively, gene therapy is emerging as a promising therapeutic strategy for treatment of various genetic and acquired diseases, including DN. Unlike the short-lived effects of pharmacological therapies, gene therapy offers a more sustained therapeutic effect, with prolonged transgene expression at the cellular level depending on the vector utilized. However, to date, there are no human studies on gene therapy approaches for the treatment of chronic kidney disease. A major roadblock to gene therapy applications in clinical trials is the lack of a safe and efficient route of gene delivery. Although gene transfection using viral vectors is highly efficient, the potential systemic side effects of cytotoxicity and high immunogenicity remain a concern for human use (Raper et al. 2003).

Several attempts have been made to overcome the limitations of viral vectors, aiming for a more targeted gene therapy strategy. *Ultrasound-mediated gene delivery (UMGD)* offers an alternative therapeutic strategy with minimum invasiveness. This technique makes use of carrier microbubble agents to facilitate delivery of genes to a targeted area. The DNA vectors (most commonly plasmid DNA) are loaded onto cationic carrier microbubbles to form a microbubble-DNA complex that can be administered intravenously. Targeted transfection is achieved in the tissue of interest through external application of high-power triggered ultrasound (Leong-Poi 2012; Smith et al. 2011). The noninvasive nature of UMGD allows repeated gene delivery for prolonged therapeutic effects (Fujii et al. 2011; Smith et al. 2012). Also, the use of targeted high-power ultrasound results in organ specific transfection with minimum off-target effects (Chen et al. 2003; Bekeredjian et al. 2003; Leong-Poi et al. 2007). UMGD has great therapeutic potential for targeted gene therapy against various diseases, including DN.

17.2 Diabetic Nephropathy

Diabetic nephropathy (DN) is the leading cause of end-stage renal failure in most countries around the world (Lewis and Maxwell 2014; Collins et al. 2013). The presence of DN is associated with substantially higher cardiovascular risk factors (Groop et al. 2009) and is prevalent in both type 1 and type 2 diabetes mellitus (DM). Approximately 20–30 % of patients with type 1 or type 2 DM develop overt DN, and while a smaller percentage of type 2 DM patients will progress to ESRD, given the greater prevalence, type 2 DM patients make up the majority of ESRD patients on chronic dialysis (Sanchez and Sharma 2009; Molitch et al. 2004). DN increases morbidity and premature mortality in diabetic patients due to its associated complications (Rosolowsky et al. 2011; Molitch et al. 2004).

17.2.1 Pathophysiology of Diabetic Nephropathy

DN is primarily caused by angiopathy of capillaries in the kidney glomeruli and can be characterized by structural abnormalities, including glomerular hypertrophy, thickening of tubular and glomerular basement membranes, and accumulation of extracellular matrix in these membranes. This is referred to as Kimmelstiel-Wilson lesions and is the classic underlying pathology. These structural changes ultimately lead to tubulointerstitial and glomerular fibrosis and sclerosis (Najafian et al. 2011; Tang and Lai

2012; Kolset et al. 2012; Reidy et al. 2014; Ponchiardi et al. 2013). The earliest clinical sign of DN is the presence of albumin in urine, known as microalbuminuria. Based on the amount of urinary albumin excretion per day, DN is classified into overt DN, referring macroalbuminuria (>300 mg per day) (Zelmanovitz et al. 1998), and incipient DN, referring microalbuminuria (3–300 mg per day) (Bangstad et al. 1991). The amount of albuminuria is correlated with a decline in glomerular filtration rate, progression of chronic kidney disease (Adler et al. 2003) and increased risk of adverse cardiovascular events (MacLeod et al. 1995; KDOQI 2007).

17.2.2 Causes of DN

There are various factors that contribute to the development of DN; genetic factors, familial disease predisposition, race and other environmental factors have combined effects towards DN development. Several studies have suggested that age, gender, smoking and hypertension also contribute to the pathogenesis and progression of DN (Ponchiardi et al. 2013; Gross et al. 2005; Marcantoni et al. 1998). It is known that hyperglycemia alone is not enough to cause the complications of DN. However, prolonged exposure to diabetes, poor glycemic control and hypertension are still recognized as the major risk factors for both DN and associated cardiovascular complications (Gaede et al. 2008; Holman et al. 2008).

17.2.3 Endothelial Dysfunction

The endothelium is defined as the inner lining of blood and lymphatic vessels. Endothelial dysfunction can be broadly defined as an imbalance between vasodilating and vasoconstricting molecules that are either produced by or act on the endothelium. DN-associated endothelial dysfunction is generally caused by two major factors: Insulin resistance and hyperglycemia. Insulin resistance promotes release of free fatty acids from adipose tissue, which in turn produces protein kinase C (PKC) (Griffin et al. 1999). Activation of PKC following hyperglycemia in endothelial cells stimulates overproduction of free radicals. Both insulin resistance and hyperglycemia inhibit production of nitric oxide (NO) in endothelial and vascular smooth muscle cells by blocking endothelial nitric oxide synthase (eNOS), thus increasing oxidative stress and generation of reactive oxygen species (ROS). The result of reduced bioavailability of NO for various pathways leads to smooth muscle cell migration, monocyte activation, adhesion, migration and expression of soluble adhesion molecules, which all contribute to DN associated microvasculature permeability. The permeability of the microvasculature is a result of increased expression of vascular endothelial growth factors (VEGF), a key angiogenic cytokine associated with diabetic retinopathy and atherosclerotic macrovascular disease (Costa and Soares 2013).

17.3 Animal Models of Diabetic Nephropathy

The progression towards end-stage kidney disease in the majority of patients with DN has propelled vigorous research towards development of novel therapies. The availability of animal models to mimic the human phenotypic pathology is essential for the development and pre-clinical testing of novel therapies. There are several rodent animal models currently available which closely recapitulate the features of DN in humans. However, due to the nephropathy resistant nature of most rodents, a model that truly mimics the progression to ESRD, as seen in human patients, is currently not available.

The Animal Models of Diabetic Complications Consortium (AMDCC) has defined criteria for the validation of murine models of nephropathy. These include: A greater than 50 % decrease in glomerular filtration rate (GFR), a greater than tenfold increase in albuminuria, a greater than 50 % thickening of the glomerular basement membrane and the presence of advanced

Table 17.1 Animal models of diabetic nephropathy

Model	Model establishment	Advantages	Disadvantages
STZ Wei et al. (2003)	Type 1: chemical toxicity of STZ to target insulin-producing β cells	Inexpensive; can be established in different strains; easy to breed	Toxicity & off-target effects of STZ; degree of renal injury is strain dependent
Akita Yoshioka et al. (1997)	Type 1: mutation in Ins2 gene resulting in pancreatic β cell failure	Autosomal dominant trait; stable insulin resistant diabetes phenotype; diabetes onset is not through systemic immunogenic alteration	Modest renal injury only available in C57BL/6 strain
NOD Anderson and Bluestone (2005)	Type 1: autoimmune destruction of pancreatic islets	Commercially available; spontaneous defective β cells	Ketoacidocis is mild; females are more susceptible to the diabetic phenotype
db/db Chen et al. (1996)	Type II: mutation in *leptin receptor* gene	Widely used Predictable elevation in albuminuria and mesangial expansion	Autosomal recessive trait; homozygotes are infertile; albuminuria may not be progressive
OVE26 Zheng et al. (2004)	Type I: overexpression of *calmodulin* gene leading to β cell toxicity	Hyperalbuminuria; High blood pressure & GFR decrease; Enlarged glomeruli & tubulointerstitial fibrosis. Available on the more sensitive FVB background	Difficult to maintain & high mortality rate; Requirement for FVB background limits breeding of OVE26 mice with KO mice on other backgrounds
Agouti yellow obese (A^y/a) Yen et al. (1994)	Type II: mutation of the *agouti* gene resulting in insulin resistance	Available in KK & C57BL/6 strain; Phenotype in KK background is more pronounced (renal injury with high albuminuria); Intact Leptin signaling pathway	Only males develop overt hyperglycemia; Nephropathy phenotype is less robust in strains other than KK; Susceptible to tumor development
Goto-Kakizaki Goto et al. (1976)	Type II: decreased pancreatic β cell mass & impaired insulin sensitivity	Insulin deficient & resistant. Thickening of glomerular & tubular basement membranes; Renal lesions, peripheral nerve changes, retinal abnormalities	Moderate hyperglycemia; No progressive proteinuria & glomerulosclerosis; Expensive
Zucker Diabetic Fatty Finegood et al. (2001)	Type II: mutation in the Leptin receptor resulting in high circulating Leptin levels	Insulin resistant at young age with progressive hyperglycemia, Defective β cells; Widely studied	Males are more susceptible to developing diabetic phenotype

mesangial matrix expansion, arteriolar hyalinosis and tubulointerstitial fibrosis (Brosius et al. 2009). Although the ideal animal model should comprise all these phenotypes, no current animal model has them all. These criteria are not strict requirements, but are guidelines for future development of DN animal models.

The background strain from which the rodent model was initially derived is critical in determining the susceptibility to renal injury and diabetes (Breyer et al. 2005). From studies comparing the effect of background strain on the susceptibility to nephropathy, it was noted that the rodent models from the C57BL/6 mouse strain are highly nephropathy resistant, while the DBA/2 strain has high susceptibility to nephropathy (Qi et al. 2005). FVB mice have a predisposition of developing renal fibrosis as a result of diabetes. OVE26 mice, which were derived from the FVB strain, show advanced renal injury compared to other rodent models of DN (Brosius et al. 2009). Table 17.1 details the characteristics of various available rodent models of DN.

17.4 Current Therapeutic Strategies and Challenges

Current therapeutic strategies for management of DN are centered on treatment of the known predisposing risk factors: Hypertension, hyperglycemia, dyslipidemia and occurrence of cardiovascular events. Glycemic control, bodyweight reduction through bariatric surgery, lipid management etc. have been some of the standard approaches for metabolic control (Fernandez-Fernandez et al. 2014). Although these therapeutic strategies offer renoprotective benefits to slow down the progression of DN, they fail to fully protect against progression to ESRD. We will be addressing some of the primary therapeutic strategies against DN and their associated challenges in the next section.

17.4.1 Glycemic Control

Intensive blood glucose control can decelerate the development of microvascular complications in patients with DN (Gross et al. 2005). In the Kumamoto Study, type 2 diabetic patients receiving multiple insulin therapies for strict glycemic control had slower progression of nephropathy and microvascular complications, including retinopathy (Shichiri et al. 2000). However, the beneficial effects of strict glycemic control are restricted to early-stage DN, prior to the development of albuminuria. Even with strict glycemic control, diabetic patients with developed microalbuminuria do not benefit from a decreased rate of progression to macroabuminuria. (DCCT 1995 and Microalbuminuria Collaborative Study Group 1995).

17.4.2 Renin Angiotensin System (RAS) Blockade

Renin-angiotensin system (RAS) blockade, with angiotensin-converting enzyme (ACE) inhibitors or angiotensin receptor blockers (ARBs), produce positive effects on DN-related albuminuria. Both ACE inhibitors and ARBs are not only effective treatment options for hypertension, but also have an additional renoprotective effect independent of blood pressure reduction. This renoprotective effect is associated with diminished intraglomerular pressure and flow of proteins into the proximal tubule (Thurman and Schrier 2003). This renoprotective effect decreases urine albumin excretion (UAE) and progression to more advanced stages of DN. Various clinical studies have shown that ACE inhibitor and ARB therapies can decrease the rate of progression towards overt DN (Parving et al. 2001) and reduce UAE (Viberti and Wheeldon 2002; Andersen et al. 2003). However, in a recent large-scale clinical study involving 1448 type II diabetic patients, increased adverse effects of combined RAS blockade (ACE inhibitors in combination with ARBs) for treatment of DN have been reported (Fried et al. 2013). The study was terminated early due to safety concerns. Similarly, several other clinical trials with PKC inhibitors, ACE, advanced glycation end products (AGEs), aldose reductase *etc.* have failed to generate positive effects against DN.

17.4.3 Kidney Transplantation

DN is the leading cause of ESRD in the western world (2). For patients with ESRD, the only treatment options available are either dialysis or kidney transplantation (Go et al. 2004). Although dialysis is a lifesaving alternative that can clear out waste and toxins from the blood similar to the kidneys, it is only equivalent to 10 % of healthy kidney function. Besides, long-term dialysis is associated with various complications, such as cardiovascular disease, hernia, peritonitis, *etc.* (Collins et al. 2009; Diaz-Buxo et al. 2013; Lok and Foley 2013; Stuart et al. 2009). The average life expectancy of a patient starting on dialysis is generally 3–5 years (Stokes 2011 and USRDS 2009). The best therapeutic strategy for ESRD patients is kidney transplantation. Kidney transplantation can extend the life expectancy of patients compared to those who stay on dialysis. On average, transplant of a living donor kidney

can function for 12–20 years, and a deceased donor kidney from 8 to 12 years (Traynor et al. 2012). Studies have shown that kidney transplantation is especially beneficial for younger patients, but even older adults can favor from an average of 4 or more years of life span compared to patients on dialysis (Briggs 2001; Knoll 2013). However, kidney transplantation is a major surgery with phased recovery. The long-term success of the transplant is limited by the host's immune response to the foreign kidney graft. Clinical studies have shown that transplants from human leukocyte antigen (HLA)-identical siblings result in highest graft survival (99.17 %, 91.84 %, and 88.96 % at 1, 3, and 5 years, respectively) (Kessaris et al. 2008). To prevent immune rejection, transplanted patients will be required to routinely take immunosuppressant drugs for the rest of their lives. The prolonged immunosuppressant therapies have various adverse effects, including bone disease, hyperglycemia, and most importantly increased susceptibility to opportunistic infections (Alangaden et al. 2006; Marcen 2009). Another major drawback of kidney transplantation, like in any other form of transplantation, is the lack of organ donors. Due to the existing imbalance between demand for kidney transplantation and the number of donor organs, many patients suffering from kidney disease have no option but to remain on dialysis.

17.5 Gene Therapy: Techniques and Vectors – Applications in Diabetic Nephropathy

Many diseases, including DN, result from dysregulation of endogenous genes. Gene therapy aims to overcome deficiencies in endogenous gene expression and regulation, with the goal of restoring normal structure and function. Unlike the short-lived effect of pharmaceutical drug treatments, gene therapy offers a more prolonged cellular protein expression for a sustained therapeutic effect. The success of gene therapy largely depends on the development of vectors or vehicles that can selectively and efficiently deliver genes to targeted cells with minimal toxicity. Broadly, the gene delivery systems can be divided into two categories: Viral and non-viral based.

17.5.1 Viral Gene Delivery

The viral vector delivery system is a popular method of transfection due to its ease of production, having a high functional titer and its ability to infect various cell types (Loiler et al. 2003; Work et al. 2009). A gene of interest can be integrated into a viral vector, and exposure of the virus to the targeted cells can lead to transfection. This leads to expression of the transgene in the host cell, resulting in a desired therapeutic effect. There are several pre-clinical studies using viral vectors for targeting DN (Table 17.2). Although this method has been used for clinical studies of cardiovascular disease (Jessup et al. 2011; Grines et al. 2003), there are as yet no clinical studies of viral gene transfection against DN. Despite being approved for clinical trials, the use of viral vectors has several potential drawbacks, including cytotoxicity, expensive production, high immunogenicity and the risk of mutagenesis in the host genome (Thomas et al. 2003).

Fatal accidental deaths have been reported form studies after systemic administration of adenoviral vectors due to over activation of the innate immune response (Marshall 1999). Adeno-associated virus (AAV) has moved to the forefront as the most attractive viral vector. The recombinant form remains almost completely episomal, with only minimal genomic integration in mice (Inagaki et al. 2008) and humans (Kaeppel et al. 2013). While clinical trial experience is growing rapidly with recombinant AAV vectors, immune responses to the capsid and toxicity remain potential concerns. As a result, research into the development of non-viral vectors continues to evolve.

17.5.2 Non-viral Gene Delivery

The strong inflammatory response elicited by viral vectors during *in-vivo* gene delivery has boosted research into developing non-viral gene

Table 17.2 Preclinical studies of gene therapy (non-UMGD) in diabetic nephropathy

Study	Gene	Animal model	Delivery method	Major findings
Dobrzynski et al. (2002)	Human adrenomedullin (AM)	STZ-induced diabetic rats	iv injection of adenovirus vector	Reduced renal hyperglycemia-induced glycogen accumulation and tubular damage; Increased cAMP & cGMP levels in urine, pAkt & membrane-bound GLUT4 levels in skeletal muscle; Increased body weight & prevented renal dysfunction via Akt signaling pathways
Dai et al. (2004)	Human hepatocyte growth factor (HGF)	Male STZ-induced diabetic mice	iv injection of naked pDNA	Decreased albuminuria & proteinuria; Improved development of DN by reducing fibronectin & collagen deposition; Prevented glomerular mesangial growth; Inhibited myofibroblast activation & kidney cell apoptosis; Attenuated urinary TGF-β1 protein level
Kagawa et al. (2006)	Human HGF	C57BL/KsJ-db/db mice	im injection of adenovirus vector	Ameliorated creatinine clearance, renal tubule fibrosis & glomerular sclerosis; Decreased TGF-β1 expression; Reduced glomerular endothelial cell & tubular epithelial cell apoptosis; Improved renal function along with long-term survival
Zhang et al. (2006)	Translocase of inner mitochondrial membrane 44 (TIM44)	STZ-induced diabetic CD-1 mice	iv injection of hemagglutination virus of Japan-envelope vector	Increased import of antioxidative enzymes into mitochondria; Suppressed cell proliferation & apoptosis; Reduced proteinuria & renal cell hypertrophy
Yuan et al. (2007)	Human tissue kallikrein (HK)	STZ-induced diabetic rats	iv injection of recombinant adeno-associated virus	Ameliorated clearance of creatinine; Increased urinary osmolarity; Reduced urinary micro-albuminuria; Reduced diabetic renal damage
Kondo et al. (2008)	Soluble TGF-β2 receptor	STZ-induced diabetic mice	im injection of adenovirus vector	Reduced fibrosis in glomeruli & renal tubules; No effect on glucose metabolism, albumin excretion in urine & renal function
Ortiz-Munoz et al. (2010)	SOCS-1 & SOCS-3	STZ-induced diabetic mice	iv (renal vein) injection of adenovirus vector	Improved renal function; Reduced renal lesions; Decreased action of STAT-1 & -3, expression of pro-inflammatory & fibrotic proteins; Inhibited mesangial expansion, fibrosis & influx of macrophages
Shi et al. (2010)	SOCS-1	STZ-induced diabetic mice	iv (tail vein) injection of naked pDNA	Reduced renal hypertrophy & albuminuria; Inhibited expression of TGF-β1 and MCP-1; Activation of STAT-1 & -3

(continued)

Table 17.2 (continued)

Study	Gene	Animal model	Delivery method	Major findings
Liu et al. (2012)	Megsin	STZ-induced diabetic CD-1 mice	iv (tail vein) injection of naked pDNA encoding anti-Megsin siRNA	Decreased proteinuria & collagen IV buildup in glomeruli; Reduced renal cell proliferation by regulating MMP-2 and tissue inhibitor of MMP-2
Tang et al. (2012)	Mitofusin-2 (Mfn-2)	STZ-induced diabetic rats	Intra-arterial (renal artery) injection of adenovirus vector	Reduced proteinuria; Improved enlargement of glomeruli & accumulation of ECM; Reduced synthesis of collagen IV & thickening of the basement membrane; No prevention of apoptosis; activation of p38 & ROS buildup were decreased
Flaquer et al. (2012)	HGF	Female C57BLKS mice (db/db)	im injection of naked pDNA	Improved expression of SDF-1; Increased number of monocyte-derived macrophages contributing to renal tissue repair & regeneration
Wang et al. (2014)	Histone deacetylase-4 (HDAC-4)	STZ-induced diabetic rats & db/db mice	Intraparenchymal injection of naked pDNA encoding anti-HDAC-4 siRNA	Prevented podocyte injury; Reduced renal dysfunction in diabetic rats through regulation of HDAC-1/STAT-1 signaling
Yuan et al. (2014)	Globular adiponectin (ADPN)	STZ-induced diabetic rats	ip injection of naked pDNA	Decreased urine albumin excretion; Increased glomerular mesangial expansion; Decreased production of ROS; Prevented interstitial fibrosis; Promoted renal expression of eNOS & inhibited TGF-β1 expression
Zhou et al. (2014)	Suppressor of cytokine signaling −2 (SOCS-2)	STZ-induced diabetic rats	iv (renal vein) injection of adenovirus vector	Reduced glomerular hypertrophy, hyper-filtration, inflammation, fibrosis & renal lesions; Decreased level of pro-inflammatory proteins such as TNF-α, IL-6 and MCP-1, and profibrotic proteins such as TGF-β, collagen IV & fibronectin
Yang et al. (2014)	Thrombomodulin domain-1 (THBDD-1)	Male C57BLKs/J db/db mice	iv injection of adeno-associated virus vector	Improved albuminuria & renal function as well as renal interstitial inflammation & glomerular sclerosis by inhibition of mitochondria-derived apoptosis; Prevented activation of NF-κB pathway & NLRP-3 inflammasome & facilitated nuclear translocation of NRF-2

vectors that may be safer for clinical applications. New classes of chemical vectors and physical delivery systems have been developed which are economical; provide stable transfection with minimum immunogenicity. Although the transfection efficiency of non-viral vectors is lower compared to the viral vectors, they are believed to be attractive alternatives for their lack of specific immune response, versatility, ease of large-scale production and simplicity of usage. Non-viral based gene therapy can be broadly classified into chemical and physical methods.

17.5.2.1 Chemical Methods

Chemical methods utilize cationic lipids, cationic polymers and cell-penetrating peptides that can be synthesized to target specific cells locally or systemically. Chemical vectors overcome the safety concerns associated with disease-causing viral vectors and can also be custom engineered according to the purpose. The primary mechanism for non-viral transfection using chemical vectors is through endocytosis by the target cell (Hoekstra et al. 2007). Cationic lipids/liposomes have been designed to facilitate efficient binding of nucleic acid vectors to their surface. The efficiency of *in-vivo* transfection with cationic lipids/liposomes is highly dependent on the lipid structure, DNA properties and size (Alatorre-Meda et al. 2010; Liang et al. 2013). Although the association of nucleic acids to the cationic lipid is through electrostatic interaction, due to the lack of mechanisms for recognition of cell surface markers, *in-vivo* transfection with cationic lipids/liposomes is non-specific with remote off-target effects. Studies have implemented antibody-conjugated liposomes to improve cell specificity (Asgeirsdottir et al. 2008), but these are still unable to achieve organ specificity. Additionally, primary cells, progenitor cells and stem cells have proven more difficult to transfect using chemical vectors. Many viral and chemical vectors have limited efficiency in transfecting non-dividing cells. Thus, the limitations of non-viral cationic lipid vectors for *in-vivo* and *in-vitro* studies have encouraged development of newer physical method-based delivery techniques for increasing target specific transfection.

17.5.2.2 Physical Methods

The most common methods of physical gene transfer include electroporation and sonoporation. Electroporation can be defined as the application of an external electrical field to a cell population or a tissue for a fixed duration to increase cell permeability to nucleic acids and small proteins by forming localized transient pores in the cell membrane (Andre and Mir 2010). Electroporation has successfully transfected both dividing and non-dividing cells, which has been a major limitation of viral and chemical-based methods. Although electroporation may be able to efficiently transport nucleic acids into cells, this advantage usually comes at a cost of low cell viability. Low cell viability has been associated with irreversible damage to the cell membrane and increased cytotoxicity occurring due to changes in pH. Thus, an ideal gene delivery technique would require provision of: (1) Maximized transfection efficiency of the therapeutic gene, (2) good safety profile, (3) minimal invasion during gene delivery, (4) enhanced target specificity for improved localization of exogenous genes without off-target effects, (5) high cell viability, and (6) repeatability as required. Table 17.2 lists pre-clinical studies using non-viral vectors to combat DN.

Comparable to electroporation, high-power ultrasound has exhibited the ability to induce pore formation in cell membranes through cavitation mechanisms. This phenomenon has been termed sonoporation, and allows for transport of nucleic acids/proteins/drugs into the cell cytosol. Cavitation and subsequent tissue transfection has been shown to be enhanced with the use of ultrasound contrast agents, known as microbubbles. This combined delivery of therapeutic ultrasound and microbubbles, conjugated with gene vectors/antibodies/drugs, comes under several headings, including ultrasound-mediated gene delivery (UMGD, or ultrasound-targeted microbubble destruction (UTMD). As discussed earlier, this is

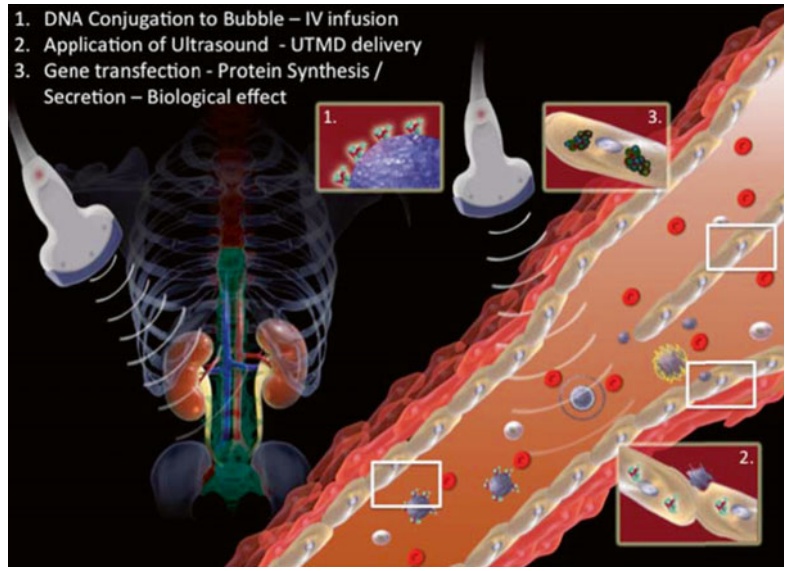

Fig. 17.1 Schematic diagram of ultrasound-mediated gene delivery (UMGD) to the kidney. Firstly, co-injection (intra-venous or intra-arterial) of nucleic acids (DNA) and microbubbles; Next, application of external high power ultrasound over the kidney(s); Bioeffects of ultrasound destruction within target tissue/organ leading to vascular and extravascular transfection, protein synthesis/secretion or knockdown, and resultant biological effect on diabetic nephropathy

a non-invasive and target-specific method of gene transfer that fulfills most of the requirements of an ideal gene therapy platform.

17.6 Ultrasound-Mediated Gene Delivery

UMGD is a unique gene delivery platform that results in targeted transfection with increased *in-vivo* transfection efficiency of non-viral gene vectors. This technique can achieve high organ-specific transfection, with minimum invasiveness and immunogenicity. Also referred to as ultrasound-targeted microbubble destruction, UMGD employs high power ultrasound and gene-bearing carrier microbubbles for achieving targeted gene delivery.

17.6.1 Microbubbles

The carrier agents for UMGD are microbubbles; very small, gas-filled bubbles. The gas-filled core is usually made up of a high molecular weight gas, such as decafluorobutane, perfluoropropane or sulfur hexafluoride, while the outer shell is composed of biocompatible lipids or proteins (Klibanov 2006). The low diffusivity and solubility properties of the heavy gas core allows for prolonged stability in circulation. The rheology of microbubbles is comparable to that of red blood cells, with a mean diameter of approximately 2–4 μm; giving them the ability to freely traverse through the microvasculature without being impeded (Lindner et al. 2002). Microbubble contrast agents have been conventionally used as a diagnostic contrast agent for clinical use with ultrasound (Mulvagh et al. 2008; Honos et al. 2007). The ability to modify microbubbles to become a carrier vessel for nucleic acid vectors, such as plasmid DNA, microRNA (miRNA) and silencing-RNA (siRNA) allows them to be used for UMGD.

17.6.2 UMGD: Methodology and Mechanisms

A schematic diagram of UMGD is depicted in Fig. 17.1. Firstly, microbubble-nucleic acid complexes are generated. This is either by direct incorporation of nucleic acids during microbubble sonication, by conjugation of nucleic acids (plasmid DNA, siRNAs, miRNAs or viral DNA) to the outer surface of microbubbles via electrostatic interactions (charge-coupling), or by simple mixing/co-administration. Secondly, the microbubble-nucleic acid complexes are administered intravenously. Thirdly, the complex circu-

lates through the systemic vascular system during transmission of high power triggered ultrasound over the target tissue/organ. The destructive power of ultrasound causes acoustic disruption of the gas-filled microbubbles and facilitates the nucleic acid uptake by the endothelium and surrounding cells/interstitium. This uptake is via several mechanisms, including formation of microjets, induction of transient pores at the cellular membrane and endocytosis (Christiansen et al. 2003; Kodama et al. 2006; Meijering et al. 2009).

While transfection efficiency of UMGD is relatively modest compared to viral vectors, studies using marker genes, such as luciferase, have demonstrated that transfection can be optimized by (1) using longer pulsing intervals for triggered delivery. This allows replenishment of the microvasculature by microbubble-DNA complexes within the target tissue/organ between destructive delivery pulses of ultrasound (Chen et al. 2003; Song et al. 2002). Conversely, continuous ultrasound transmission results in minimal transfection due to continual destruction of microbubble-DNA complexes as soon as they enter the ultrasound beam, (2) using higher acoustic powers for ultrasound application, with low transmission frequency and a greater mechanical index (Chen et al. 2003). This method must however be balanced against higher adverse bioeffects, especially when applied to the kidney (Williams et al. 2007), (3) the use of intra-arterial injections of carrier microbubbles versus intravenous delivery (Song et al. 2002; Christiansen et al. 2003) also results in greater tissue damage and vessel hemorrhage, and (4) use of repeated deliveries resulting in a more sustained duration of transgene expression (Bekeredjian et al. 2003).

17.6.3 UMGD: In-Vivo Applications

There have been numerous studies of UMGD in multiple organs, delivering gene therapy in many pre-clinical models of human disease. Studies have demonstrated the efficacy of UMGD for therapeutic angiogenesis in a rat model of peripheral arterial disease (PAD). UMGD of a plasmid DNA encoding VEGF and green fluorescent protein (GFP) in a bicistronic vector resulted in increased microvascular perfusion and vessel density (Leong-Poi et al. 2007). Using the same vector and PAD model, UMGD was more effective for therapeutic angiogenesis compared to direct intramuscular (im) injection of the VEGF/GFP plasmid, despite lower transgene expression. The higher efficiency of pro-angiogenic gene therapy by UMGD was likely due to its targeted vascular transfection, as compared to IM injections. While IM injections resulted in local transfection of myocytes and perivascular regions, UMGD resulted in more diffuse transfection of arteriole and capillary endothelium and surrounding myocytes (Kobulnik et al. 2009). UMGD can be effective for targeted cardiac transfection, including delivery of pro-angiogenic genes in pre-clinical models of myocardial infarction (Fujii et al. 2009, 2011) and heart failure (Lee et al. 2013). A major advantage of UMGD is its noninvasive nature, which allows for delivery of multiple genes through repeated gene therapy (Fujii et al. 2011; Smith et al. 2012). Using multiple UMGD deliveries of plasmid DNA encoding for stem cell factor and stromal cell derived factor-1 (SDF-1) in a rat model of myocardial infarction, Fujii et al. showed increased vascular density in the peri-infarct region and greater myocardial perfusion and ventricular function compared with untreated animals (Fujii et al. 2011). The use of UMGD for *in-vivo* gene transfer has been applied for targeted gene transfection in other organs and tissues that can be imaged by diagnostic ultrasound, including kidney, pancreas (Chen et al. 2006, 2007, 2010) and tumors (Fujii et al. 2013; Carson et al. 2011, 2012).

17.7 Ultrasound-Mediated Gene Delivery: Applications in Diabetic Nephropathy

Gene therapy offers a promising approach for the treatment of chronic kidney diseases; both inherited genetic disorders, like hereditary nephritis

(Alport syndrome), and acquired diseases, including nephropathy. Despite promising results of numerous pre-clinical studies of gene therapy in animal models of kidney diseases, translation to the clinic has been remarkably slow. Major questions that limit clinical translation include choice of target gene, which vector, optimal route of delivery, what dose, how many doses and at what intervals between doses. A comprehensive discussion of the different routes, vehicles and delivery techniques for gene therapy has been carried out in Sect. 17.5.

Studies have demonstrated transfection of the kidney using UMGD. Azuma and colleagues published the very first report of UMGD to the kidney in 2003 (Azuma et al. 2003). They used UMGD with Optison™ (a commercially available microbubble contrast agent, GE) to transfect fluorescein isothiocyanate (FITC) labeled NFκB-decoy into donor kidneys to prevent acute kidney rejection and prolong survival in a rat renal allograft model. They also used UMGD to transfect luciferase reporter gene to the kidney, showing that transfection occurred in 70–80 % of glomeruli and most tubular cells (Azuma et al. 2003). From a mechanistic standpoint, Zhang et al. (2014) demonstrated that the interactions of ultrasound (frequency 7 MHz, mechanical index = 0.9, peak negative acoustic pressure = 2.38 MPa) and microbubbles used for UMGD increases renal interstitial capillary permeability, as measured by Evan's blue extravasation in rats with early DN induced with streptozotocin (STZ). Importantly, hemorrhage or necrosis was not observed. Figure 17.2 shows fluorescent confocal microscopic images of a control non-transfected kidney and a kidney where UMGD was performed. Initially, 2.5 μg of red fluorescent (Alexa Fluor BlockIT Red, Invitrogen) control microRNA was charge-coupled onto 1×10^9 cationic lipid microbubbles. Then this solution was intravenously administered during external application of intermittent high-powered ultrasound (frequency 5 MHz, 2 cm depth, power 120 V) at a pulsing interval of 10s (internal timer). UMGD resulted in fairly diffuse transfection throughout the kidney parenchyma, including glomeruli and tubules.

Preclinical studies using UMGD have shown benefits in various models of kidney disease, including DN, using multiple different gene targets. Table 17.3 provides important details on all studies to date of UMGD in a variety of preclinical models of kidney disease, many of which targeted DN. Lan et al. (2003) investigated UMGD to specifically target the transforming growth factor (TGF)-β/Smad pathway, and subsequently renal fibrosis in a rat unilateral ureteral obstruction model. Ultrasound-mediated doxycycline-regulated Smad7 gene transfer resulted in increased Smad7 expression and inhibited tubulointerstitial fibrosis, thus providing a novel therapeutic strategy against renal fibrosis. For UMGD, Optison™ microbubbles in saline were mixed with 25 μg of chosen plasmid, and then 0.5 mL of the mixture was injected into the left renal artery. The ultrasound transducer (Ultax UX-301; Celcom Medico Inc., Japan) was placed directly onto one side of the left kidney, with a continuous-wave output of 1-MHz ultrasound at 5 % power output, for a total of 60 s with 30 s intervals.

With the role of TGF-β1 being established as critical in nephropathy, Chen and colleagues were the first to test UMGD in DN. They investigated the protective role of Smad7 in diabetic kidney disease in streptozotocin-induced diabetic mice and rats (Chen et al. 2011). Overexpression of Smad7 by UMGD was associated with reduction in the development of microalbuminuria, TGF-β/Smad3-mediated renal fibrosis and NFκB/p65-mediated renal inflammation and macrophage infiltration. The type of microbubbles and ultrasound parameters used during UMGD were similar to this group's prior studies – Optison™ mixed with 25 μg of the designated plasmids in 0.5 mL saline. This was injected via the left renal artery with temporary cutting off of the renal blood supply for 5 min. Subsequently, the same group of researchers showed that overexpression of Smad7 by UMGD significantly repressed activation of TGF-β/Smad and NFκB signaling in renal tissue, improving type 2 diabetic kidney injuries in a db/db mouse model of type 2 diabetes (Ka et al. 2012). In this study, Optison™ was mixed with 15 μg of

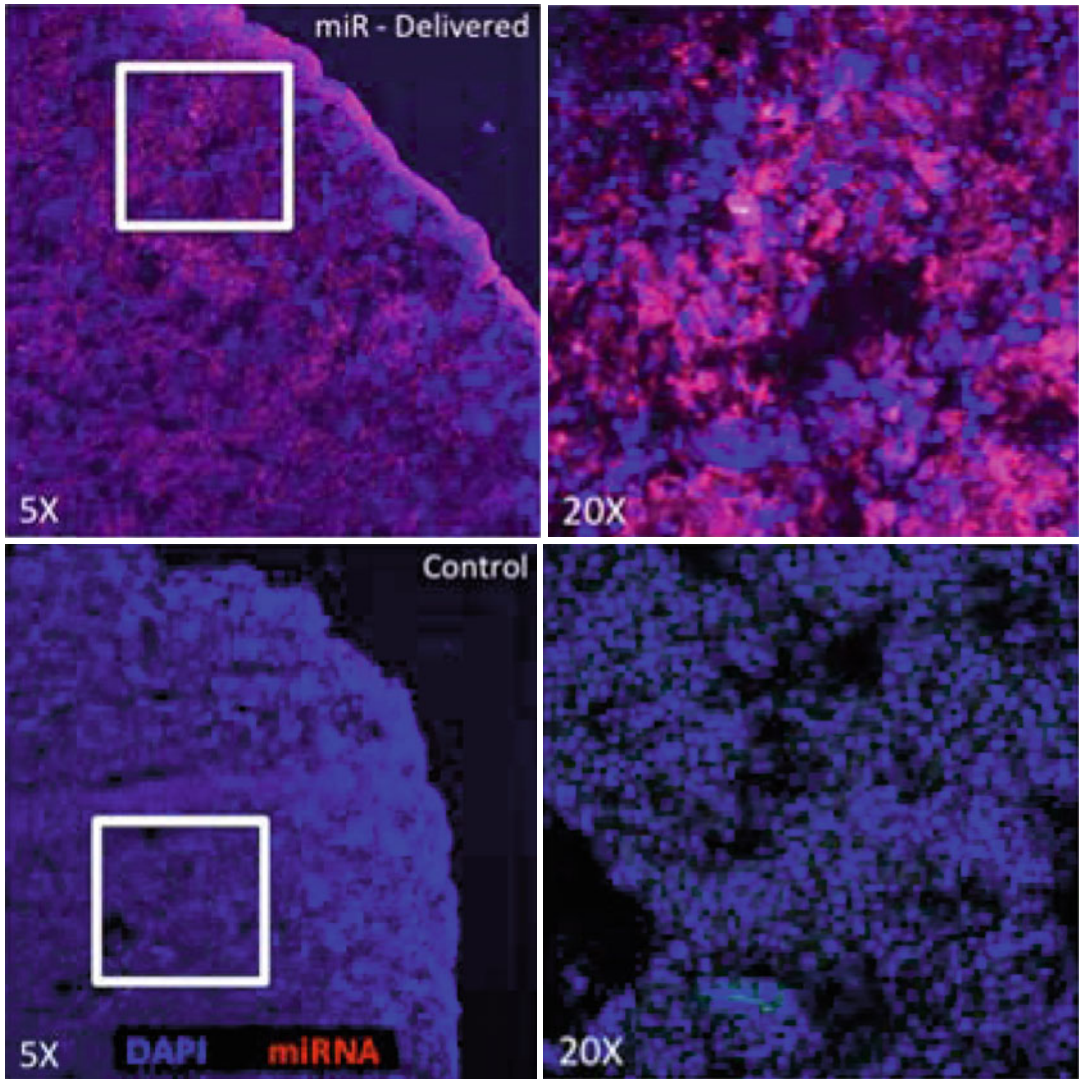

Fig. 17.2 *In-vivo* transfection by UMGD to the kidney. UMGD of fluorescent-labeled control miRNA (*red*) to the kidney via a phased array transducer. A transmission frequency of 5 MHz at 120 V and pulsing interval of 5 s were used. *In-vivo* UMGD delivery of fluorescent-labeled oligonucleotides to the kidney resulted in high and diffuse *in-vivo* transfection (*Top panels*), as compared to control non-delivered kidneys (*Bottom panels*)

designated Smad7 plasmids and delivered intravenously via the tail vein. The animals received ultrasound to their backs on both sides, thus targeting both kidneys (Sonoplus 590, 1 MHz; Ernaf-Nonius, Delft, Netherlands), at a frequency of 1 MHz for 30 s on one side, and then 30 s on the other side, for approximately 10 min.

More recently, nucleic acid therapeutics has begun focusing on miRNAs. These are a class of evolutionarily conserved and small (~22 nucleotides) regulatory non-coding RNAs that regulate the expression of a large number of genes. They do this by post-transcriptionally repressing gene expression by targeting 3-untranslated regions of messenger RNAs (mRNAs). miRNAs have been found to be functionally important in the regulation of many pathological states, including DN (Kato and Natarajan 2014; Figueira et al. 2014; Hagiwara et al. 2013), and are being exploited to develop new therapeutic

Table 17.3 Preclinical UMGD studies in kidney disease

Reference	Gene/target	Animal model	Ultrasound settings	Microbubble	Major findings
Azuma et al. (2003)	NF-κB	Wistar-Lewis rat renal allograft model	2 MHz 2.5 W/cm^2 30 s – 8 min	Optison	Inhibited action of inflammatory molecules associated with graft rejection; preserved histological structure; indication of prolonged graft survival & prolonged animal survival compared to controls
Lan et al. (2003)	Smad-7	Rat unilateral ureteral obstruction model	1 MHz 5 % power out 60 s with 30 s intervals	Optison	Inhibited tubulointerstitial fibrosis; Resulted in complete inhibition of Smad-2 & -3 action, thus provided a novel therapeutic strategy against renal fibrosis
Hou et al. (2005)	Smad-7	Rat remnant kidney model	1 MHz 5 % power output 60 s with 30 s intervals	Albumin perflutren-filled microbubbles	Reduced renal & vascular sclerosis; Inhibited Smad-2 & -3 activation; Prevented progressive renal injury by inhibiting the rise of proteinuria & serum creatinine
Ng et al. (2005)	Smad-7	Rat remnant kidney model	1 MHz 2 min	Optison	Inhibited IL-1β & TNF-α expressions; Blocked NF-κB activation; Attenuated proteinuria & high serum creatinine; Increased creatinine clearance; Inhibited renal inflammatory pathways, like ICAM-1 & iNOS; Glomerular & tubule interstitial accumulation of macrophages & T cells
Ka et al. (2007)	Smad-7	Mouse model of autoimmune crescentic glomerulonephritis in C57BL/6×DBA/2 J F1 hydrid mice receiving DBA/2 J donor lymphocytes	1 MHz Continuous wave 30 s on one side, then 30 s on the other side. Total time 10 min	Optison	Inhibited accumulation of α-smooth muscle actin, collagen I, III & IV; Inhibited expression of inflammatory cytokines such as IL-1β & IL-6; Inhibitied expression of ICAM-1, MCP-1 & iNOS; Prevented leukocyte infiltration, severe histologic damage, like glomerular crescent formation & tubule-interstitial injury; Inhibited functional injury, *i.e.,* proteinuria
Chen et al. (2011)	Smad-7	SZT-induced diabetic mice & rats	1 MHz 5 % power output for 60 s with 30 s interval	Albumin perflutren-filled microbubbles	Reduced development of microalbuminuria. TGF-β/Smad-3 mediated renal fibrosis & NF-κB/p65 mediated renal inflammation & macrophage infiltration
Ka et al. (2012)	Smad-7	db/db mice	1 MHz Continuous wave For 30 s one side then 30 s on the other side, for a total of 10 min	Optison	Inhibited local activation of TGF-β/SMAD and NF-κB signaling pathways; Inhibited renal function impairment, such as proteinuria, renal fibrosis, such as glomerular sclerosis & tubule-interstitial collagen matrix abundance, & renal inflammatory responses, such as INOS-Il 1b & MCP-1 upregulation, macrophage infiltration, podocyte & endothelial cell injury

Zhang et al. (2013)	BM-MSCs	SZT-induced diabetic rats	7 MHz MI 0.9 5 min	Perfluoropropane gas-filled lipid-shelled microbubbles	Increased permeability of interstitial renal capillaries, thereby enhancing the homing & retention of MSCs in the kidney
Qiao et al. (2013)	Intermedin	Rat model of renal ischemia-reperfusion injury	0.95 MHz Continuous wave 5 % power output For a total of 60 s with 30 s interval	SonoVue	Inhibited myeloperoxidase activity, apoptosis & the expression of ICAM-1, P-Selectin & ET-1 following ischemia/reperfusion injury of kidney; Improved renal function by prevention of ROS production & oxidative stress
Zhong et al. (2013)	miR-21	db/db mice	1 MHz Continuous wave 1 W power output 5 min/side	SonoVue	Decreased micro-albuminuria, renal fibrosis & inflammation in diabetic kidneys
Li et al. (2013)	miR-433	Rat unilateral ureteral obstruction model	1 MHz Continuous wave For 30 s one side then 30 s on the other side, for a total of 10 min	SonoVue	Prevented fibrosis in the obstructive kidney model by regulating TGF-β/Smad-3 induced renal fibrosis pathways
Xiao et al. (2014)	Rap-1b	SZT-induced diabetic rats	1 MHz 5 % power output For a total of 60 s with 30 s intervals	SonoVue	Ameliorated renal tubular mitochondrial dysfunction, oxidative stress & apoptosis; Increased C/EBP-β and PGC-1α
Liu et al. (2014)	Smad-7	Mouse model of Ang-II induced hypertensive kidney disease	1 MHz 5 % power output For a total of 60 s with 30 s intervals	Optison	Inhibited Ang-II induced up-regulation of SMURF-2 & Sp1; Blocked TGF-β/Smad-3 mediated renal fibrosis; Suppressed NF-κB mediated renal inflammation; Prevented Ang-II induced loss of renal miR-29b, an inhibitor in both TGF-β/Smad-3 & NF-κB pathways; Prevented Ang-II induced hypertensive nephropathy by inhibiting proteinuria & improving the glomerular filtration rate
Chen et al. (2014)	miR-29b	Male db/db mice	1 MHz 2 W/cm^2 5 min	SonoVue	Loss of renal miR-29b was associated with progressive diabetic kidney injury, including microalbuminuria, renal fibrosis & inflammation; Restored miR-29b by UTMD induced attenuation of diabetic kidney complications by inhibiting NF-κB mediated inflammation & TGF-β driven fibrosis

strategies. In this regard, Chen et al. (2014) reported that microRNA (miR)-29b was largely down-regulated under diabetic conditions, and loss of renal miR-29b was linked to progressive diabetic kidney disease, including renal fibrosis and inflammation. Targeted transfection of miR-29b via UMGD to the kidneys was capable of attenuating diabetic kidney complications in db/db mice by inhibiting NFκB-mediated inflammation and TGF-β driven fibrosis. Plasmids encoding miR-29b, along with SonoVue™ microbubbles, (Bracco) were delivered intravenously via tail vein injections. This was followed immediately by ultrasound application (2 W/cm^2) using an ultrasound transducer (Sonoplus 590, 1 MHz; Ernaf-Nonius, Delft, Netherlands) placed directly on the skin over the kidneys for 5 min.

Similarly, Zhong et al. (2013) knocked down miR-21 in the kidneys of diabetic db/db mice using UMGD of miR-21 short-hairpin plasmids (doxycycline-inducible). SonoVue™ microbubbles (Bracco SA, Switzerland) were administered intravenously via the tail vein, with continuous wave ultrasound at an output of 1 MHz at 1 W power for 5 min per kidney. In this model, miR-21 knockdown restored Smad7 levels, leading to amelioration of DN, with less microalbuminuria, fibrosis and renal inflammation (Zhong et al. 2013). These studies on Smad7 gene therapy and associated miRNAs collectively indicate that the TGF-β/Smad pathway may be a prime therapeutic target for the treatment of diabetes-associated nephropathy.

The TGF-β/Smad pathway is not the only gene target for UMGD to the kidney in DN. Xiao et al. (2014) used UMGD to deliver doxycycline-induced plasmids encoding Rap1, a small GTPase that regulates cell adhesion, proliferation and cell survival. This was delivered to the kidneys in a streptozotocin-induced diabetic model in Sprague–Dawley rats. This strategy resulted in attenuation of tubular injury and reduced progression of DN by modulation of renal mitochondrial dysfunction.

Recently, multipotent and self-renewing bone-marrow-derived mesenchymal stem cells (BM-MSCs) have been widely considered for the treatment of DN owing to their pivotal characteristics. Several preclinical studies have been published using cell delivery in combination with ultrasound and microbubbles in various disease settings (Kuliszewski et al. 2011), including kidney diseases. In 2013, Zhang et al. used UTMD for renal-targeted delivery of BM-MSCs in streptozotocin-induced diabetic rats. They showed that UTMD had the ability to increase permeability of interstitial renal capillaries, thereby enhancing the homing and retention of MSCs in the kidney. Self-made perfluoropropane-filled microbubbles with lipid shells were used for this study. A diagnostic ultrasound system (S2000, Siemens, Germany) was used with a high-frequency probe of 9 L4 placed over the right kidney. The parameters were fixed at 7 MHz frequency; mechanical index of 0.9; depth of 3 cm; duration of 5 min. This cell delivery method in combination with therapeutic UTMD, if successful in clinical studies, could act as a personal stem cell therapy for treating DN.

Finally, several studies have shown the use of UMGD directed to the pancreas. Here, UMGD is used to regenerate islet cells for improving glycemic control (Chen et al. 2010), deliver genes involved in islet cell development (Chen et al. 2007) and deliver insulin-associated genes (Chen et al. 2006). These in turn may attenuate the progression of DN. In summary, many studies have provided a line of evidence and demonstrated the potential of UMGD as a novel strategy for targeted gene therapy against DN.

17.8 Future Perspectives on UMGD for Diabetic Nephropathy

The utility of microbubbles in diagnostic contrast enhanced ultrasound has extended its usage into therapeutics in the past decade and the prospect of this technology is promising. UMGD has proven to be an effective modality for targeted gene therapy in several disease conditions, including kidney diseases. While high power ultrasound in combination with intravenous microbubbles has been demonstrated to be clinically successful and safe for enhanced thrombolysis in stroke (Molina et al. 2006), to date UMGD has not been investigated in human subjects. Although this strategy is minimally invasive and offers targeted transfec-

tion, there are several challenges and limitations of this technique in terms of transfection efficiency and safety profiles that need to be addressed before proceeding to human clinical trials.

Several studies have reported adverse bioeffects of ultrasound-microbubble interactions, such as localized hemorrhage or petechiae, microvascular leakage, apoptotic cell death and inflammation, at least in preclinical models including the kidney (Miller et al. 2008, 2009, 2012, 2014). Safety profiles need to be improved by optimization of ultrasound parameters/dosimetry and proper designing of microbubbles. In turn, this will minimize bioeffects mediated by UMGD, ensuring an optimal benefit to risk ratio for patients. Many types of microbubbles have been used for pre-clinical studies of UMGD, including commercially available microbubble contrast agents (Optison™, SonoVue™) and custom-designed microbubbles, both neutral and cationic microbubbles. While the majority of UMGD studies for DN were performed with commercial microbubbles, studies have shown that cationic microbubbles are more effective than neutral microbubbles, with greater transgene expression, including commercially available agents (Sun et al. 2013; Nomikou et al. 2012; Sun et al. 2014). Future pre-clinical studies of UMGD for DN should include testing of cationic microbubbles. Targeted microbubbles using conjugated microbubbles with antibodies or microbubbles conjugated with DNA vectors containing tissue-specific promoters open the door for enhanced targeted therapy (Xie et al. 2012). While several UMGD studies in DN used intra-renal artery injections, intravenous delivery will increase the likelihood of clinical translation by facilitating a non-invasive platform for gene delivery. Ultrasound deliveries in UMGD kidney studies have used a variety of transmission probes at various frequencies and durations (Table 17.3). Settings for human studies will have to be tested, and ideally ultrasound transmission via an imaging probe would help facilitate targeted delivery to each kidney, using a more posterior approach via the flanks to avoid gene delivery to other adjacent tissues.

The TGF-β/Smad pathway has been the predominant target for UMGD studies in DN, and given the wealth of pre-clinical data, it is likely the best initial target for human translational studies. More preclinical work needs to be undertaken to identify other potential therapeutic targets and transfection sites in the kidney for the treatment of DN. Low transfection efficiency of exogenous genes has been considered to be a significant limitation of this technique. Rapid progress has been made in this avenue with the development of newer, more potent plasmids/non-viral vectors, such as mini-intronic plasmids and minicircles that have enhanced transfection efficiency owing to their small size and lack of bacterial elements (Gill et al. 2009; Lu et al. 2013). The ability of microbubbles to penetrate into tissues with severely compromised vasculature (ischemia, necrotic tissue and infarction) is hampered, however, for initial therapy of DN in which perfusion or blood flow is augmented, this would not prove to be a major drawback. With these critical facets in mind, UMGD certainly exhibits the potential to offer innovative-targeted therapy to prevent and treat DN.

References

Abecassis M, Bartlett ST, Collins AJ, Davis CL, Delmonico FL, Friedewald JJ, Hays R, Howard A, Jones E, Leichtman AB, Merion RM, Metzger RA, Pradel F, Schweitzer EJ, Velez RL, Gaston RS (2008) Kidney transplantation as primary therapy for end-stage renal disease: a National Kidney Foundation/Kidney Disease Outcomes Quality Initiative (NKF/KDOQITM) conference. Clin J Am Soc Nephrol 3:471–480

Adler AI, Stevens RJ, Manley SE, Bilous RW, Cull CA, Holman RR (2003) Development and progression of nephropathy in type 2 diabetes: the United Kingdom Prospective Diabetes Study (UKPDS 64). Kidney Int 63:225–232

Alangaden GJ, Thyagarajan R, Gruber SA, Morawski K, Garnick J, El-Amm JM, West MS, Sillix DH, Chandrasekar PH, Haririan A (2006) Infectious complications after kidney transplantation: current epidemiology and associated risk factors. Clin Transplant 20:401–409

Alatorre-Meda M, Taboada P, Krajewska B, Willemeit M, Deml A, Klosel R, Rodriguez JR (2010) DNA-poly(diallyldimethylammonium chloride) complexation and transfection efficiency. J Phys Chem B 114:9356–9366

Andersen S, Brochner-Mortensen J, Parving HH (2003) Kidney function during and after withdrawal of long-term irbesartan treatment in patients with type 2 diabetes and microalbuminuria. Diabetes Care 26:3296–3302

Anderson MS, Bluestone JA (2005) The NOD mouse: a model of immune dysregulation. Annu Rev Immunol 23:447–485

Andre FM, Mir LM (2010) Nucleic acids electrotransfer in vivo: mechanisms and practical aspects. Curr Gene Ther 10:267–280

Asgeirsdottir SA, Zwiers PJ, Morselt HW, Moorlag HE, Bakker HI, Heeringa P, Kok JW, Kallenberg CG, Molema G, Kamps JA (2008) Inhibition of proinflammatory genes in anti-GBM glomerulonephritis by targeted dexamethasone-loaded AbEsel liposomes. Am J Physiol Renal Physiol 294:F554–F561

Azuma H, Tomita N, Kaneda Y, Koike H, Ogihara T, Katsuoka Y, Morishita R (2003) Transfection of NFkappaB-decoy oligodeoxynucleotides using efficient ultrasound-mediated gene transfer into donor kidneys prolonged survival of rat renal allografts. Gene Ther 10:415–425

Bangstad HJ, Try K, Dahl-Jorgensen K, Hanssen KF (1991) New semiquantitative dipstick test for microalbuminuria. Diabetes Care 14:1094–1097

Bekeredjian R, Chen S, Frenkel PA, Grayburn PA, Shohet RV (2003) Ultrasound-targeted microbubble destruction can repeatedly direct highly specific plasmid expression to the heart. Circulation 108:1022–1026

Breyer MD, Bottinger E, Brosius FC 3rd, Coffman TM, Harrris RC, Heilig CW, Sharma K, AMDCC (2005) Mouse models of diabetic nephropathy. J Am Soc Nephrol 16:27–45

Briggs JD (2001) Causes of death after renal transplantation. Nephrol Dial Transplant 16:1545–1549

Brosius FC 3rd, Alpers CE, Bottinger EP, Breyer MD, Coffman TM, Gurley SB, Harris RC, Kakoki M, Kretzler M, Leiter EH, Levi M, McIndoe RA, Sharma L, Smithies O, Susztak K, Takahashi N, Takahashi T, Animal Models of Diabetic Complications Consortium (2009) Mouse models of diabetic nephropathy. J Am Soc Nephrol 20:2503–2512

Carson AR, McTiernan CF, Lavery L, Hodnick A, Grata M, Leng X, Wang J, Chen X, Modzekewski RA, Villanueva FS (2011) Gene therapy of carcinoma using ultrasound-targeted microbubble destruction. Ultrasound Med Biol 37:393–402

Carson AR, McTiernan CF, Lavery L, Grata M, Leng X, Wang J, Chen X, Villanueva FS (2012) Ultrasound-targeted microbubble destruction to deliver siRNA cancer therapy. Cancer Res 72:6191–6199

Chen H, Charlat O, Tartaglia LA, Woolf EA, Weng X, Ellis SJ, Lakey ND, Culpepper J, Moore KJ, Breitbart RE, Duyk GM, Tepper RI, Morgenstern JP (1996) Evidence that the diabetes gene encodes the leptin receptor: identification of a mutation in the leptin receptor gene in db/db mice. Cell 84:491–495

Chen S, Shohet RV, Bekeredjian R, Frenkel P, Grayburn PA (2003) Optimization of ultrasound parameters for cardiac gene delivery of adenoviral or plasmid deoxyribonucleic acid by ultrasound-targeted microbubble destruction. J Am Coll Cardiol 42:301–308

Chen S, Ding JH, Bekeredjian R, Yang BZ, Shohet RV, Johnston SA, Hohmeier HE, Newgard CB, Grayburn PA (2006) Efficient gene delivery to pancreatic islets with ultrasonic microbubble destruction technology. Proc Natl Acad Sci U S A 103:8469–8474

Chen S, Ding J, Yu C, Yang B, Wood DR, Grayburn PA (2007) Reversal of streptozotocin-induced diabetes in rats by gene therapy with betacellulin and pancreatic duodenal homeobox-1. Gene Ther 14:1102–1110

Chen S, Shimoda M, Wang MY, Ding J, Noguchi H, Matsumoto S, Grayburn PA (2010) Regeneration of pancreatic islets in vivo by ultrasound-targeted gene therapy. Gene Ther 17:1411–1420

Chen HY, Huang XR, Wang W, Li JH, Heuchel RL, Chung A, Lan HY (2011) The protective role of Smad7 in diabetic kidney disease: mechanism and therapeutic potential. Diabetes 60:590–601

Chen HY, Zhong X, Huang XR, Meng XM, You Y, Chung AC, Lan HY (2014) MicroRNA-29b inhibits diabetic nephropathy in db/db mice. Mol Ther 22:842–853

Christiansen JP, French BA, Klibanov AL, Kaul S, Lindner JR (2003) Targeted tissue transfection with ultrasound destruction of plasmid-bearing cationic microbubbles. Ultrasound Med Biol 29:1759–1767

Collins AJ, Foley RN, Gilbertson DT, Chen SC (2009) The state of chronic kidney disease, ESRD, and morbidity and mortality in the first year of dialysis. Clin J Am Soc Nephrol 4(Suppl 1):S5–S11

Collins AJ, Foley RN, Herzog C et al (2013) US renal data system 2012 annual data report. Am J Kidney Dis 61(A7):e1–e476

Costa PZ, Soares R (2013) Neovascularization in diabetes and its complications. Unraveling the angiogenic paradox. Life Sci 92:1037–1045

Dai C, Yang J, Bastacky S, Xia J, Li Y, Liu Y (2004) Intravenous administration of hepatocyte growth factor gene ameliorates diabetic nephropathy in mice. J Am Soc Nephrol 15:2637–2647

DCCT (1995) Effect of intensive therapy on the development and progression of diabetic nephropathy in the Diabetes Control and Complications Trial. The Diabetes Control and Complications Research Group. *Kidney international* 47:1703–1720

de Boer IH, Rue TC, Hall YN, Heagerty PJ, Weiss NS, Himmelfarb J (2011) Temporal trends in the prevalence of diabetic kidney disease in the United States. JAMA 305:2532–2539

Diaz-Buxo JA, White SA, Himmele R (2013) Frequent hemodialysis: a critical review. Semin Dial 26:578–589

Dobrzynski E, Montanari D, Agata J, Zhu J, Chao J, Chao L (2002) Adrenomedullin improves cardiac function and prevents renal damage in streptozotocin-induced diabetic rats. Am J Physiol Endocrinol Metab 283:E1291–E1298

Fernandez-Fernandez B, Ortiz A, Gomez-Guerrero C, Egido J (2014) Therapeutic approaches to diabetic nephropathy-beyond the RAS. Nat Rev Nephrol 10:325–346

Figueira MF, Monnerat-Cahli G, Medei E, Carvalho AB, Morales MM, Lamas ME, da Fonseca RN, Souza-Menezes J (2014) MicroRNAs: potential therapeutic targets in diabetic complications of the cardio-

vascular and renal systems. Acta Physiol (Oxf) 211: 491–500

Finegood DT, McArthur MD, Kojwang D, Thomas MJ, Topp BG, Leonard T, Buckingham RE (2001) Beta-cell mass dynamics in Zucker diabetic fatty rats. Rosiglitazone prevents the rise in net cell death. Diabetes 50:1021–1029

Flaquer M, Franquesa M, Vidal A, Bolaños N, Torras J, Lloberas N, Herrero-Fresneda I, Grinyó JM, Cruzado JM (2012) Hepatocyte growth factor gene therapy enhances infiltration of macrophages and may induce kidney repair in db/db mice as a model of diabetes. Diabetologia 55:2059–2068.

Fried LF, Emanuele N, Zhang JH, Brophy M, Conner TA, Duckworth W, Leehey DJ, McCullough PA, O'Connor T, Palevsky PM, Reilly RF, Seliger SL, Warren SR, Watnick S, Peduzzi P, Guarino P, VA NEPHRON-D Investigators (2013) Combined angiotensin inhibition for the treatment of diabetic nephropathy. N Engl J Med 369:1892–1903

Fujii H, Sun Z, Li SH, Wu J, Fazel S, Weisel RD, Rakowski H, Lindner J, Li RK (2009) Ultrasound-targeted gene delivery induces angiogenesis after a myocardial infarction in mice. JACC Cardiovasc Imaging 2:869–879

Fujii H, Li SH, Wu J, Miyagi Y, Yau TM, Rakowski H, Egashira K, Guo J, Weisel RD, Li RK (2011) Repeated and targeted transfer of angiogenic plasmids into the infarcted rat heart via ultrasound targeted microbubble destruction enhances cardiac repair. Eur Heart J 32: 2075–2084

Fujii H, Matkar P, Liao C, Rudenko D, Lee PJ, Kuliszewski MA, Prud'homme GJ, Leong-Poi H (2013) Optimization of ultrasound-mediated anti-angiogenic cancer gene therapy. Mol Ther Nucleic Acids 2:e94

Gaede P, Lund-Andersen H, Parving HH, Pedersen O (2008) Effect of a multifactorial intervention on mortality in type 2 diabetes. N Engl J Med 358:580–591

Gill DR, Pringle IA, Hyde SC (2009) Progress and prospects: the design and production of plasmid vectors. Gene Ther 16:165–171

Go AS, Chertow GM, Fan D, McCulloch CE, Hsu CY (2004) Chronic kidney disease and the risks of death, cardiovascular events, and hospitalization. N Engl J Med 351:1296–1305

Goto Y, Kakizaki M, Masaki N (1976) Production of spontaneous diabetic rats by repetition of selective breeding. Tohoku J Exp Med 119:85–90

Griffin ME, Marcucci MJ, Cline GW, Bell K, Barucci N, Lee D, Goodyear LJ, Kraegen EW, White MF, Shulman GI (1999) Free fatty acid-induced insulin resistance is associated with activation of protein kinase C theta and alterations in the insulin signaling cascade. Diabetes 48:1270–1274

Grines C, Rubanyi GM, Kleiman NS, Marrott P, Watkins MW (2003) Angiogenic gene therapy with adenovirus 5 fibroblast growth factor-4 (Ad5FGF-4): a new option for the treatment of coronary artery disease. Am J Cardiol 92:24n–31n

Groop PH, Thomas MC, Moran JL, Waden J, Thorn LM, Makinene VP, Rosengard-Barlund M, Saraheimo M, Hietala K, Heikkila O, Forsblom C, FinnDiane Study Group (2009) The presence and severity of chronic kidney disease predicts all-cause mortality in type 1 diabetes. Diabetes 58:1651–1658

Gross JL, de Azevedo MJ, Silveiro SP, Canani LH, Caramori ML, Zelmanovitz T (2005) Diabetic nephropathy: diagnosis, prevention, and treatment. Diabetes Care 28:164–176

Hagiwara S, McClelland A, Kantharidis P (2013) MicroRNA in diabetic nephropathy: renin angiotensin, aGE/RAGE, and oxidative stress pathway. J Diab Res 2013:173783

Hoekstra D, Rejman J, Wasungu L, Shi F, Zuhorn I (2007) Gene delivery by cationic lipids: in and out of an endosome. Biochem Soc Trans 35:68–71

Holman RR, Paul SK, Bethel MA, Matthews DR, Neil HA (2008) 10-year follow-up of intensive glucose control in type 2 diabetes. N Engl J Med 359:1577–1589

Honos G, Amyot R, Choy J, Leong-Poi H, Schnell G, Yu E (2007) Contrast echocardiography in Canada: Canadian Cardiovascular Society/Canadian Society of Echocardiography position paper. Can J Cardiol 23: 351–356

Hou CC, Wang W, Huang XR, Fu P, Chem TH, Sheikh-Hamad D, Lan HY (2005) Ultrasound-microbubble-mediated gene transfer of inducible Smad7 blocks transforming growth factor-beta signaling and fibrosis in rat remnant kidney. Am J Pathol 166:761–771

Inagaki K, Piao C, Kotchey NM, Wu X, Nakai H (2008) Frequency and spectrum of genomic integration of recombinant adeno-associated virus serotype 8 vector in neonatal mouse liver. J Virol 82:9513–9524

Jessup M, Greenberg B, Mancini D, Cappola T, Pauly DF, Jaski B, Yaroshinsky A, Zsebo KM, Dittrich H, Hajjar RJ, Investigators CUPID (2011) Calcium Upregulation by Percutaneous Administration of Gene Therapy in Cardiac Disease (CUPID): a phase 2 trial of intracoronary gene therapy of sarcoplasmic reticulum Ca2+-ATPase in patients with advanced heart failure. Circulation 124:304–313

Ka SM, Huang XR, Lan HY, Tsai PY, Yang SM, Shui HA, Chen A (2007) Smad7 gene therapy ameliorates an autoimmune crescentic glomerulonephritis in mice. J Am Soc Nephrol 18:1777–1788

Ka SM, Yeh YC, Huang XR, Chao TK, Hung YJ, Yu CP, Lin TJ, Wu CC, Lan HY, Chen A (2012) Kidney-targeting Smad7 gene transfer inhibits renal TGF-beta/MAD homologue (SMAD) and nuclear factor kappaB (NF-kappaB) signalling pathways, and improves diabetic nephropathy in mice. Diabetologia 55:509–519

Kaeppel C, Beattie SG, Fronza R, van Logtenstein R, Salmon F, Schmidt S, Wolf S, Nowrouzi A, Glimm H, von Kalle C, Petry H, Gaudet D, Schmidt M (2013) A largely random AAV integration profile after LPLD gene therapy. Nat Med 19:889–891

Kagawa T, Takemura G, Kosai K, Murata I, Ohno T, Takahashi Esaki M, Maruyama R, Fujiwara T, Ohashi H, Fujiwara H (2006) Hepatocyte growth factor gene therapy slows down the progression of diabetic nephropathy in db/db mice. Nephron Physiol 102:92–102

Kato M, Natarajan R (2014) Diabetic nephropathy-emerging epigenetic mechanisms. Nat Rev Nephrol 10:517–530

KDOQI (2007) Clinical Practice Guidelines and Clinical Practice Recommendations for Diabetes and Chronic Kidney Disease. *American Journal of Kidney Diseases: the official journal of the National Kidney Foundation* 49:S12–154

Kessaris N, Mukherjee D, Chandak P, Mamode N (2008) Renal transplantation in identical twins in United States and United Kingdom. Transplantation 86: 1572–1577

Klibanov AL (2006) Microbubble contrast agents: targeted ultrasound imaging and ultrasound-assisted drug-delivery applications. Invest Radiol 41:354–362

Knoll GA (2013) Kidney transplantation in the older adult. Am J Kidney Dis 61:790–797

Kobulnik J, Kuliszewski MA, Stewart DJ, Lindner JR, Leong-Poi H (2009) Comparison of gene delivery techniques for therapeutic angiogenesis ultrasound-mediated destruction of carrier microbubbles versus direct intramuscular injection. J Am Coll Cardiol 54:1735–1742

Kodama T, Tomita Y, Koshiyama K, Blomley MJ (2006) Transfection effect of microbubbles on cells in superposed ultrasound waves and behavior of cavitation bubble. Ultrasound Med Biol 32:905–914

Kolset SO, Reinholt FP, Jenssen T (2012) Diabetic nephropathy and extracellular matrix. J Histochem Cytochem 60:976–986

Kondo T, Takemura G, Kosai K, Ohno T, Takahashi T, Esaki M, Goto K, Maruyama R, Murata I, Minatoguchi S, Fujiwara T, Fujiwara H (2008) Application of an adenoviral vector encoding soluble transforming growth factor-beta type II receptor to the treatment of diabetic nephropathy in mice. Clin Exp Pharmacol Physiol 35:1288–1293

Kuliszewski MA, Kobulnik J, Lindner JR, Stewart D, Leong-Poi H (2011) Vascular gene transfer of SDF-1 promotes endothelial progenitor cell engraftment and enhances angiogenesis in ischemic muscle. Mol Ther 19:895–902

Lan HY, Mu W, Tomita N, Huang XR, Li JH, Zhu HJ, Morishita R, Johnson RJ (2003) Inhibition of renal fibrosis by gene transfer of inducible Smad7 using ultrasound-microbubble system in rat UUO model. J Am Soc Nephrol 14:1535–1548

Lee PJ, Rudenko D, Kuliszewski MA, Liao C, Kabor MG, Connelly KA, Leong-Poi H (2013) Survivin gene therapy attenuates left ventricular systolic dysfunction in doxorubicin cardiomyopathy by reducing apoptosis and fibrosis. Cardiovasc Res 101:423–433

Leong-Poi H (2012) Contrast ultrasound and targeted microbubbles: diagnostic and therapeutic applications in progressive diabetic nephropathy. Semin Nephrol 32:494–504

Leong-Poi H, Kuliszewski MA, Lekas M, Sibbald M, Teichert-Kuliszewska K, Klibanov AL, Stewart DJ, Lindner JR (2007) Therapeutic arteriogenesis by ultrasound-mediated VEGF165 plasmid gene delivery to chronically ischemic skeletal muscle. Circ Res 101:295–303

Lewis G, Maxwell AP (2014) Risk factor control is key in diabetic nephropathy. Practitioner 258:13–17

Li R, Chung AC, Dong Y, Yang W, Zhong X, Lan HY (2013) The microRNA miR-433 promotes renal fibrosis by amplifying the TGF-beta/Smad3-Azin1 pathway. Kidney Int 84:1129–1144

Liang X, Li X, Chang J, Duan Y, Li Z (2013) Properties and evaluation of quaternized chitosan/lipid cation polymeric liposomes for cancer-targeted gene delivery. Langmuir 29:8683–8693

Lindner JR, Song J, Jayaweera AR, Sklenar J, Kaul S (2002) Microvascular rheology of Definity microbubbles after intra-arterial and intravenous administration. J Am Soc Echocardiogr 15:396–403

Liu M, Zhang Y, Chi Y, Zhai S, Wang B, Shi Y, Li Y (2012) Delivery of megsin siRNA plasmid reveals therapeutic potential against diabetic nephropathy by down-regulating p27(kip1) level. J Nephrol 25:418–425

Liu GX, Li YQ, Huang XR, Wei LH, Zhang Y, Feng M, Meng XM, Chen HY, Shi YJ, Lan HY (2014) Smad7 inhibits AngII-mediated hypertensive nephropathy in a mouse model of hypertension. Clin Sci (Lond) 127:195–208

Loiler SA, Conlon TJ, Song S, Tang Q, Warrington KH, Agarwal A, Kapturczak M, Li C, Ricordi C, Atkinson MA, Muzyczka N, Flotte TR (2003) Targeting recombinant adeno-associated virus vectors to enhance gene transfer to pancreatic islets and liver. Gene Ther 10:1551–1558

Lok CE, Foley R (2013) Vascular access morbidity and mortality: trends of the last decade. Clin J Am Soc Nephrol 8:1213–1219

Lu J, Zhang F, Kay MA (2013) A mini-intronic plasmid (MIP): a novel robust transgene expression vector in vivo and in vitro. Mol Ther 21:954–963

MacLeod JM, Lutale J, Marshall SM (1995) Albumin excretion and vascular deaths in NIDDM. Diabetologia 38:610–616

Marcantoni C, Ortalda V, Lupo A, Maschio G (1998) Progression of renal failure in diabetic nephropathy. Nephrol Dial Transplant 13(Suppl 8):16–19

Marcen R (2009) Immunosuppressive drugs in kidney transplantation: impact on patient survival, and incidence of cardiovascular disease, malignancy and infection. Drugs 69:2227–2243

Marshall E (1999) Gene therapy death prompts review of adenovirus vector. Science 286:2244–2245

Meijering BD, Juffermans LJ, van Wamel A, Henning RH, Zuhorn IS, Emmer M, Versteilen AM, Paulus WJ, van Gilst WH, Kooiman K, de Jong N, Musters RJ, Deelman LE, Kamp O (2009) Ultrasound and microbubble-targeted delivery of macromolecules is regulated by induction of endocytosis and pore formation. Circ Res 104:679–687

Microalbuminuria Collaborative Study Group (1995) Intensive therapy and progression to clinical albuminuria in patients with insulin dependent diabetes melli-

tus and microalbuminuria. United Kingdom. *BMJ (Clinical research ed)* 311:973–977

Miller DL, Averkiou MA, Brayman AA, Everbach EC, Holland CK, Wible JH Jr, Wu J (2008) Bioeffects considerations for diagnostic ultrasound contrast agents. J Ultrasound Med 27:611–632

Miller DL, Dou C, Wiggins RC (2009) Glomerular capillary hemorrhage induced in rats by diagnostic ultrasound with gas-body contrast agent produces intratubular obstruction. Ultrasound Med Biol 35:869–877

Miller DL, Smith NB, Bailey MR, Czarnota GJ, Hynynen K, Makin IR (2012) Overview of therapeutic ultrasound applications and safety considerations. J Ultrasound Med 31:623–634

Miller DL, Suresh MV, Dou C, Yu B, Raghavendran K (2014) Characterization of ultrasound-induced pulmonary capillary hemorrhage in rats. Microvasc Res 93:42–45

Molina CA, Ribo M, Rubiera M, Montaner J, Santamarina E, Delgado-Mederos R, Arenillas JF, Huertas R, Purroy F, Delgado P, Alvarez-Sabin J (2006) Microbubble administration accelerates clot lysis during continuous 2-MHz ultrasound monitoring in stroke patients treated with intravenous tissue plasminogen activator. Stroke 37:425–429

Molitch ME, DeFronzo RA, Franz MJ, Keane WF, Mogensen CE, Parving HH, Steffes MW, American Diabetes Association (2004) Nephropathy in diabetes. Diabetes Care 27(Suppl 1):S79–S83

Mulvagh SL, Rakowski H, Vannan MA et al (2008) American Society of Echocardiography consensus statement on the clinical applications of ultrasonic contrast agents in echocardiography. J Am Soc Echocardiogr 21:1179–1201

Najafian B, Alpers CE, Fogo AB (2011) Pathology of human diabetic nephropathy. Contrib Nephrol 170:36–47

Ng YY, Hou CC, Wang W, Huang XR, Lan HY (2005) Blockade of NFkappaB activation and renal inflammation by ultrasound-mediated gene transfer of Smad7 in rat remnant kidney. Kidney Int Suppl(94):S83–91

Nomikou N, Tiwari P, Trehan T, Gulati K, McHale AP (2012) Studies on neutral, cationic and biotinylated cationic microbubbles in enhancing ultrasound-mediated gene delivery in vitro and in vivo. Acta Biomater 8:1273–1280

Ortiz-Munoz G, Lopez-Parra V, Lopez-Franco O, Fernandez-Vizarra P, Mallavia B, Flores C, Sanz A, Blanco J, Mezzano S, Ortiz A, Egido J, Gomez-Guerrero C (2010) Suppressors of cytokine signaling abrogate diabetic nephropathy. J Am Soc Nephrol 21:763–772

Parving HH, Lehnert H, Brochner-Mortensen J, Gomis R, Andersen S, Arner P (2001) The effect of irbesartan on the development of diabetic nephropathy in patients with type 2 diabetes. N Engl J Med 345:870–878

Ponchiardi C, Mauer M, Najafian B (2013) Temporal profile of diabetic nephropathy pathologic changes. Cur Diab Rep 13:592–599

Qi Z, Fujita H, Jin J, Davis LS, Wang Y, Fogo AB, Breyer MD (2005) Characterization of susceptibility of inbred mouse strains to diabetic nephropathy. Diabetes 54:2628–2637

Qiao X, Li RS, Li H, Zhu GZ, Huang XG, Shao S, Bai B (2013) Intermedin protects against renal ischemia-reperfusion injury by inhibition of oxidative stress. Am J Physiol Renal Physiol 304:F112–F119

Raper SE, Chirmule N, Lee FS, Wivel NA, Bagg A, Gao GP, Wilson JM, Batshaw ML (2003) Fatal systemic inflammatory response syndrome in a ornithine transcarbamylase deficient patient following adenoviral gene transfer. Mol Genet Metab 80:148–158

Reidy K, Kang HM, Hostetter T, Susztak K (2014) Molecular mechanisms of diabetic kidney disease. J Clin Invest 124:2333–2340

Rosolowsky ET, Skupien J, Smiles AM, Niewczas M, Roshan B, Stanton R, Eckfeldt JH, Warram JH, Krolewski AS (2011) Risk for ESRD in type 1 diabetes remains high despite renoprotection. J Am Soc Nephrol 22:545–553

Sanchez AP, Sharma K (2009) Transcription factors in the pathogenesis of diabetic nephropathy. Expert Rev Mol Med 11:e13

Selvin E, Juraschek SP, Coresh J (2012) Kidney disease in people with diabetes: the expanding epidemic. Am J Kidney Dis 59:340–342

Shi Y, Du C, Zhang Y, Ren Y, Hao J, Zhao S, Yao F, Duan H (2010) Suppressor of cytokine signaling-1 ameliorates expression of MCP-1 in diabetic nephropathy. Am J Nephrol 31:380–388

Shichiri M, Kishikawa H, Ohkubo Y, Wake N (2000) Long-term results of the Kumamoto Study on optimal diabetes control in type 2 diabetic patients. Diabetes Care 23(Suppl 2):B21–B29

Smith AH, Fujii H, Kuliszewski MA, Leong-Poi H (2011) Contrast ultrasound and targeted microbubbles: diagnostic and therapeutic applications for angiogenesis. J Cardiovasc Trans Res 4:404–415

Smith AH, Kuliszewski MA, Liao C, Rudenko D, Stewart DJ, Leong-Poi H (2012) Sustained improvement in perfusion and flow reserve after temporally separated delivery of vascular endothelial growth factor and angiopoietin-1 plasmid deoxyribonucleic acid. J Am Coll Cardiol 59:1320–1328

Song J, Chappell JC, Qi M, VanGieson EJ, Kaul S, Price RJ (2002) Influence of injection site, microvascular pressure and ultrasound variables on microbubble-mediated delivery of microspheres to muscle. J Am Coll Cardiol 39:726–731

Stokes JB (2011) Consequences of frequent hemodialysis: comparison to conventional hemodialysis and transplantation. Trans Am Clin Climatol Assoc 122:124–136

Stuart S, Booth TC, Cash CJ, Hameeduddin A, Googde JA, Harvey C, Malhotra A (2009) Complications of continuous ambulatory peritoneal dialysis. Radiographics 29:441–460

Sun L, Huang CW, Wu J, Chen KJ, Li SH, Weisel RD, Rakowski H, Sung HW, Rk L (2013) The use of cationic microbubbles to improve ultrasound-targeted gene delivery to the ischemic myocardium. Biomaterials 34:2107–2116

Sun RR, Noble ML, Sun SS, Song S, Miao CH (2014) Development of therapeutic microbubbles for enhancing ultrasound-mediated gene delivery. J Control Release 182:111–120

Tang SC, Lai KN (2012) The pathogenic role of the renal proximal tubular cell in diabetic nephropathy. Nephrol Dial Transplant 27:3049–3056

Tang WX, Wu WH, Zeng XX, Bo H, Huang SM (2012) Early protective effect of mitofusion 2 overexpression in STZ-induced diabetic rat kidney. Endocrine 41:236–247

Thomas CE, Ehrhardt A, Kay MA (2003) Progress and problems with the use of viral vectors for gene therapy. Nat Rev Genet 4:346–358

Thurman JM, Schrier RW (2003) Comparative effects of angiotensin-converting enzyme inhibitors and angiotensin receptor blockers on blood pressure and the kidney. Am J Med 114:588–598

Traynor C, Jenkinson A, Williams Y et al (2012) Twenty-year survivors of kidney transplantation. Am J Transplant 12:3289–3295

USRDS (2009) Annual Data Report. US Renal Data Systems. National Institutes of Health, National Institute of Diabetes and Digestive and Kidney Diseases. Bethesda MD.

Viberti G, Wheeldon NM (2002) Microalbuminuria reduction with valsartan in patients with type 2 diabetes mellitus: a blood pressure-independent effect. Circulation 106:672–678

Wang X, Liu J, Zhen J, Zhang C, Wan Q, Liu G, Wei X, Zhang Y, Wang Z, Han H, Xu H, Bao C, Song Z, Zhang X, Li N, Yi F (2014) Histone deacetylase 4 selectively contributes to podocyte injury in diabetic nephropathy. Kidney Int 86:712–725

Wei M, Ong L, Smith MT, Ross FB, Schmid K, Hoey AJ, Burstow D, Brown L (2003) The streptozotocin-diabetic rat as a model of the chronic complications of human diabetes. Heart Lung Circ 12:44–50

Williams AR, Wiggins RC, Wharram BL, Goyal M, Dou C, Johnson KJ, Miller DL (2007) Nephron injury induced by diagnostic ultrasound imaging at high mechanical index with gas body contrast agent. Ultrasound Med Biol 33:1336–1344

Work LM, Nicklin SA, Brain NJ, Dishart KL, Von Seggern DJ, Hallek M, Buning H, Baker AH (2009) Development of efficient viral vectors selective for vascular smooth muscle cells. Mol Ther 9:198–208

Xiao L, Zhu X, Yang S, Liu F, Zhou Z, Zhan M, Xie P, Zhang D, Li J, Song P, Kanwar YS, Sun L (2014) Rap1 ameliorates renal tubular injury in diabetic nephropathy. Diabetes 63:1366–1380

Xie A, Belcik T, Qi Y, Morgan TK, Champaneri SA, Taylor S, Davidson BP, Zhao Y, Klibanov AL, Kuliszewsli MA, Leong-Poi H, Ammi A, Lindner JR (2012) Ultrasound-mediated vascular gene transfection by cavitation of endothelial-targeted cationic microbubbles. JACC Cardiovasc Imaging 5:1253–1262

Yang SM, Ka SM, Wu HL, Yeh YC, Kuo CH, Hua KF, Shi GY, Hung YJ, Hsiao FC, Yang SS, Shieh YS, Lin SH, Wi CW, Lee JS, Yang CY, Chen A (2014) Thrombomodulin domain 1 ameliorates diabetic nephropathy in mice via anti-NF-kappaB/NLRP3 inflammasome-mediated inflammation, enhancement of NRF2 antioxidant activity and inhibition of apoptosis. Diabetologia 57:424–434

Yen TT, Gill AM, Frigeri LG, Barsh GS, Wolff GL (1994) Obesity, diabetes, and neoplasia in yellow A(vy)/- mice: ectopic expression of the agouti gene. FASEB J 8:479–488

Yoshioka M, Kayo T, Ikeda T, Koizumi A (1997) A novel locus, Mody4, distal to D7Mit189 on chromosome 7 determines early-onset NIDDM in nonobese C57BL/6 (Akita) mutant mice. Diabetes 46:887–894

Yuan G, Deng J, Wang T, Zhao C, Xu X, Wang P, Voltz JW, Edin ML, Xiao X, Chao L, Chao J, Zhang XA, Zedlin DC, Wang DW (2007) Tissue kallikrein reverses insulin resistance and attenuates nephropathy in diabetic rats by activation of phosphatidylinositol 3-kinase/protein kinase B and adenosine 5′-monophosphate-activated protein kinase signaling pathways. Endocrinology 148:2016–2026

Yuan F, Liu YH, Liu FY, Peng YM, Tian JW (2014) Intraperitoneal administration of the globular adiponectin gene ameliorates diabetic nephropathy in Wistar rats. Mol Med Rep 9:2293–2300

Zelmanovitz T, Gross JL, Oliveira J, de Azevedo MJ (1998) Proteinuria is still useful for the screening and diagnosis of overt diabetic nephropathy. Diabetes Care 21:1076–1079

Zhang Y, Wada J, Hashimoto I, Eguchi J, Yasuhara A, Kanwar YS, Shikata K, Makino H (2006) Therapeutic approach for diabetic nephropathy using gene delivery of translocase of inner mitochondrial membrane 44 by reducing mitochondrial superoxide production. J Am Soc Nephrol 17:1090–1101

Zhang Y, Ye C, Wang G, Gao Y, Tan K, Zhuo Z, Liu Z, Xia H, Yang D, Li P (2013) Kidney-targeted transplantation of mesenchymal stem cells by ultrasound-targeted microbubble destruction promotes kidney repair in diabetic nephropathy rats. BioMed Res Int 2013:526367

Zhang Y, Ye C, Xu Y, Dong X, Li J, Liu R, Gao Y (2014) Ultrasound-mediated microbubble destruction increases renal interstitial capillary permeability in early diabetic nephropathy rats. Ultrasound Med Biol 40:1273–1281

Zheng S, Noonan WT, Metreveli NS, Coventry S, Kralik PM, Carlson EC, Epstein PN (2004) Development of late-stage diabetic nephropathy in OVE26 diabetic mice. Diabetes 53:3248–3257

Zhong X, Chung AC, Chen HY, Dong Y, Meng XM, Li R, Yang W, Hou FF, Lan HY (2013) miR-21 is a key therapeutic target for renal injury in a mouse model of type 2 diabetes. Diabetologia 56:663–674

Zhou Y, Lv C, Wu C, Chen F, Shao Y, Wang Q (2014) Suppressor of cytokine signaling (SOCS) 2 attenuates renal lesions in rats with diabetic nephropathy. Acta Histochem 116:981–988

Drug and Gene Delivery using Sonoporation for Cardiovascular Disease

18

Jason Castle and Steven B. Feinstein

Abstract

Using the improvements made in diagnostic contrast enhanced ultrasound, researchers have made significant progress in the field of ultrasound-mediated sonoporation for drug delivery. Many programs take advantage of commercial products; both ultrasound imaging systems and contrast agents to better enable translation from preclinical to first-in-man studies (Kotopoulis et al., Med Phys 40:072902, 2013). Particularly well-suited targets for this novel therapy are diseases of the cardiovascular system. This chapter will highlight several recent studies addressing treatment of both acute and chronic conditions.

Keywords

Cardiovascular • Microbubble • Targeted drug delivery • Contrast enhanced ultrasound (CEUS)

18.1 Treatment Paradigms: Times Are Changing

Today's treatment designs are evolving to emphasize personalized medicine and include advances in therapeutic approaches for the treatment of rare and neglected diseases. These interests have spawned development of novel approaches for both acute and chronic therapies, including revisiting gene therapy.

The revitalized interest in gene therapy has been approached with caution and scrutiny due to the unproven safety record of traditional gene delivery techniques associated with viral vectors. Previous efforts resulted in tragic deaths from unforeseen mutagenesis and toxicities (Hacein-Bey-Abina et al. 2003a, b). Concerns remain over the potential for chromosomal insertion leading to the development of cancer. Several recent reviews of alternative vehicle delivery systems have outlined the similarities

J. Castle
Translational Sciences Lab, GE Global Research, Niskayuna, NY, USA
e-mail: Castle@ge.com

S.B. Feinstein (✉)
SonoGene LLC, Glen Ellyn, IL, USA

Section of Cardiology, Rush University Medical Center, Chicago, IL, USA
e-mail: Steven_Feinstein@rush.edu

© Springer International Publishing Switzerland 2016

J.-M. Escoffre, A. Bouakaz (eds.), *Therapeutic Ultrasound*, Advances in Experimental Medicine and Biology, Vol. 880, DOI 10.1007/978-3-319-22536-4_18

and differences inherent in the respective methods (Wang et al. 2013).

The focus of this chapter will be the use of biologics and non-viral mediated gene therapy, specifically sonoporation techniques that use commercial, acoustic microspheres as drug vehicles. This will provide a limited review of more recent therapeutic approaches, with a particular focus on clinical and preclinical studies for the treatment of cardiovascular (CV) diseases. For a more detailed review of gene- and ultrasound-mediated therapies, see the following excellent references. (Fishbein et al. 2010; Sirsi and Borden 2012; Chen et al. 2013; Wang et al. 2013)

18.2 Mode of Delivery: Enteral *vs* Parenteral

Traditionally, most acute therapy utilizes parenteral delivery, and often requires serial or periodic infusions for sustained, systemic effects for maintenance of a chronic condition (*e.g.*, oncology). This standard of therapy presents a reasonable requirement for acute therapeutic interventions that necessitate rapid and timely applications to alter the course of an imminent deleterious consequence. Such examples include the use of thrombolytics for acute coronary occlusions, anti-arrhythmics for treatment of lethal arrhythmias, and vasopressors, inotropic or chronotopic agents for immediate control of blood pressure or heart rates.

Generally, enteric therapies have been reserved for maintenance of chronic, non-acute diseases and atherosclerosis, anticoagulation or osteoporosis. However, this dichotomous paradigm is shifting due to the innovation of effective therapeutic agents and corresponding innovative delivery systems. As an example, newer agents for the treatment of osteoporosis and osteopenia are designed for annual parenteral infusions, thus avoiding weekly or monthly enteric preparations (Lambrinoudaki et al. 2008; Black et al. 2007).

An example of the effectiveness of an annual intravenous therapy for osteoporosis includes the medication Zoledronic acid (Reclast) (Deeks and Perry 2008). A 15 min treatment infusion is required in an outpatient setting. This annual infusion therapy is in stark contrast to the prior use of similarly effective medications that were prescribed on a daily, weekly or monthly basis. It is anticipated that there will be continued emphasis on non-enteral therapies for both acute and chronic disease states, and as the delivery vehicles improve, additional site-specific long-acting medications will be developed. This approach provides patients and third party providers the benefits of improved: (a) Compliance, (b) convenience and (c) cost.

To further illustrate the growing trend towards parental therapies, Walgreens Pharmacy in 2008 purchased the rights to use an infusion center for oncologic therapy applications. This acquisition of OptionCare for $850 M represented the largest purchase in Walgreens' 110-year history, and made Walgreens the nation's largest independent specialty-pharmacy company (Merrick 2008).

18.3 Parenteral Therapy and Clinical Applications: Lipid Therapy (mAb, Proteins, Gene Therapy)

Specifically with regard to parenteral and subcutaneous therapies for the treatment of dyslipidemia, a number of pharmaceutical companies have embarked on the treatment of elevated low-density lipoprotein cholesterol (LDL-C) using antibodies to increase liver LDL receptors, and thereby lower serum LDL by almost 50 % (referred to as PCSK9 therapy). These novel therapies use monoclonal antibodies (mAb) to effectively block the PCSK9 protein, permitting prolongation of an active LDL receptor site, thus lowering circulating serum LDL (Pollack 2012). As a result, rare autosomal dominant familial hypercholesterolemia becomes a new target for personalized therapies. Similarly, a number of pharmaceutical companies have initiated trials using siRNA (antisense oligonucleotides) gene silencing technology, resulting in increased LDL receptors and decreased circulating LDL in mice (Ason et al. 2011; Tadin-Strapps et al. 2011; Suzuki et al. 2010).

Despite the newly developed models for LDL cholesterol treatment, the ability to increase de novo (functional) high-density lipoprotein (HDL) remains a dilemma, and at the present time there is no effective therapy for HDL insufficiency. Historically, reduced or absent serum HDL is a well-established CV risk factor, yet all efforts to increase effective serum HDL, and reduce CV mortality and morbidity, have been largely unsuccessful. In fact, the failure of recent clinical trials has called into question the HDL hypothesis. The two major cholesteryl ester transfer protein (CETP) inhibitor clinical trials (Torcetrapib and Dalcetrapib) failed to reduce atherosclerotic events, and did not reveal beneficial therapeutic effects on biomarkers when evaluated in randomized clinical trials (Nissen et al. 2007; Rader and deGoma 2014). In addition, although nicotinic acid preparations are known to elevate HDL serum levels, recent clinical trials were unsuccessful in demonstrating CV benefits (Boden et al. 2011; Landray et al. 2014). The presumed etiology of HDL therapy failure is likely to be based on the underlying complex nature of HDL; its functional state and the related sub-fractions that appear to confer both functional and dysfunctional metabolic activities (Fisher et al. 2012; Zheng and Aikawa 2013; Yamamoto et al. 2012; Gomaraschi et al. 2013). Several of the HDL subfractions exhibit beneficial anti-atherosclerotic, anti-inflammatory, anti-oxidant and anti-apoptotic properties, while other HDL particles appear to be ineffective and "dysfunctional", and may actually be pro-inflammatory.

However, as observed with LDL therapy, newer therapies and delivery systems provide an optimistic view for future HDL therapy. Esperion, a start-up biotechnology company, conducted preclinical and clinical trials that resulted in significant intra-plaque lipid reduction and plaque regression in both rabbit and human trials using intravenous infusions of recombinant Milano ApoA-I proteins (Chiesa et al. 2002; Nicholls et al. 2006). In addition, r-ApoA-I infusions were found to reduce atheroma volume in clinical trials (Shaw et al. 2008). Esperion investigators established proof-of-concept by showing that *de novo* ApoA-I is an effective therapy for the treatment of systemic atherosclerosis. This enthusiasm was however dampened due to the subsequent limitations associated with r-ApoA-I, including hepatic immunotoxicity (protein loads), production costs and product standardization. Based on these, and other recent studies, lipid experts have developed a consensus that enhanced ApoA-I production may be the preferred method of choice for increasing circulating and functional HDL.

18.4 Newer Therapeutic Delivery Systems: Acoustic Microspheres

Contrast Enhanced Ultrasound (CEUS) was developed to provide improved ultrasound imaging for diagnostic applications. Indeed, today CEUS is being used to monitor diseases, providing an unsurpassed degree of spatial and temporal resolution without invoking ionizing radiation (Darge et al. 2013). CEUS has established itself as a diagnostic modality, providing intimate resolution of microvascular tissue/organ blood flow and volume. New ultrasound technology (3D/4D) will permit a true volumetric analysis of the intraplaque microvessel density (vasa vasorum) within tumors, and specifically within carotid artery plaques (Staub et al. 2010). These ultrasound-based systems will have distinct advantages for diagnostic imaging over traditional imaging modalities, including: (1) Utilization of non-ionizing, acoustic energy, (2) high spatial and temporal resolution, (3) real-time processing and interpretation, (4) large established user base, (5) ease of operation, (6) portability and (7) favorable economics.

To effectively compete with CT, nuclear and PET imaging in clinical practice, ultrasound systems are evolving to provide 3D/4D acquisition, thus reducing operator variability and dependency. Additionally, due in part to heightened public awareness of excessive or unnecessary ionizing radiation exposure derived from medical imaging; there is a trend toward reducing excessive radiation exposure to the population. Ultrasound

imaging provides a welcome portal for both patients and clinicians, forecasting a prominent role in diagnostic imaging in the near future.

Over the last several decades, the value of diagnostic CEUS has undergone a transformation into a powerful therapeutic platform for site-specific, agent delivery systems. Briefly, when activated by external ultrasound energy, the acoustic microspheres serve as catalysts for and vehicles of drug/gene intravascular packages, providing a direct, transient and non-destructive access to whole tissues and organs. This access is the result of the creation of transient "pores" within endothelial cells, permitting transmission of "products" into the cytoplasm (Juffermans et al. 2009). Thus, CEUS now includes a novel therapeutic application built upon the traditional diagnostic use. In the future, optimization studies will be required to provide "recipes" for a complex set of parameters that include (a) specific acoustically active microspheres, (b) acoustic parameters, (c) specific targets (organ/tissue) and of course (d) the therapeutic agent (gene/drug). These ongoing efforts require a more complete understanding of the interactions between the desired target organ, the acoustic microsphere shell properties and drug or gene physicochemical characteristics. Investigators are now attempting to elucidate the multiple inter-related mechanisms of sonoporation to achieve the highest therapeutic yields (Deng et al. 2004; Juffermans et al. 2009; Pan et al. 2004).

As an historical note, the earliest efforts to use CEUS as a therapeutic technology may be attributed to Ken Ishihara. In his US patent, Ishihara described the preferred usage of Albunex combined with 5Flurouracil (5FU) for oncology therapy (Ishihara 1993). Over the last two decades, the therapeutic CEUS field has dramatically expanded and has been the subject of several excellent reviews (Fishbein et al. 2010; Sirsi and Borden 2012; Chen et al. 2013).

In addition to the multiple inter-related aspects of sonoporation, analytic data will be required to ascertain the local delivery yields, nucleic acid biodistribution, mutagenicity and related host tissue effects, including off-target effects. Accordingly, newer ultrasound hardware and software will be required to provide dual functions for disease monitoring, progression *vs* regression, and treatment.

18.5 Therapeutic Cardiovascular Applications of Sonoporation

We will present a selected application that highlights the exciting and near-term promises of CEUS therapy applications.

18.5.1 Sonothrombolysis

Several years ago, researchers at VU University Medical Center in Amsterdam, The Netherlands, began what is progressing to be a worldwide clinical trial utilizing sonothrombolysis for the treatment of patients with acute ST elevation myocardial infarctions (STEMI) (Slikkerveer et al. 2012). In the Sonolysis trial, this group of leading scientists and clinicians conducted a pilot study of ten patients presenting a first acute STEMI. They assessed the safety and feasibility of the combined use of acoustic microspheres and external ultrasound with tPA (tissue Plasminogen Activator). Success was demonstrated in that there was no difference in adverse events and clinical outcome was statistically the same for both the treated and control (placebo, no U/S) groups.

A similar application of sonothrombolysis has been published for the early treatment of cerebral vascular accidents. Other investigators, similar to the work of Slikkerveer, have shown that the combined effects of external ultrasound and acoustic microspheres result in a disruption of the culprit thrombosis within the respective coronary and cerebral vasculature (Rubiera et al. 2008). The clinical trials at VU University were based on the earlier data using ultrasound and microbubbles to dissolve thrombi (Culp et al. 2001; Tsutsui et al. 2006).

Following the Sonolysis study, further refinements have been made to the acoustic parameters required for optimal thrombus dissolution in the preclinical setting. New trials are now underway in Brazil, utilizing improved techniques and early results appear promising (Mathias et al. 2014).

18.5.2 Suppression of Arterial Neointimal Formation

In the days and weeks following percutaneous intervention, a major concern for the patient is the development of neointimal formation and inflammation at the site of the arterial injury. In these cases, restenosis rates can be quite high, ranging from 25 to 50 % (Reis et al. 2000). As a potential therapy to inhibit the contributing factors, researchers in Japan have begun examining the delivery of Intercellular Adhesion Molecule-1 (ICAM-1) siRNA. ICAM-1 is a protein-coding gene expressed on endothelial cells and cells of the immune system. As such, it plays an integral role in proinflammatory responses and leukocyte binding to endothelial cells. In excess, these functions contribute to the restenosis process following vascular insult. By suppressing ICAM-1, mice that had undergone vascular injury showed a limited inflammatory response and thereby reduced development of neointimal formation. In using ultrasound-meditated microbubble delivery, the authors were able to overcome two of the largest hurdles facing RNAi intervention; rapid degradation of circulating siRNA and sufficient concentration at the target organ to elicit a response. Further, this method eliminates the need for viral vectors, while effectively diminishing T cell and adhesion molecule positive cell accumulation to suppress arterial neointimal formation. This represents a potentially safe and efficacious treatment of a common CV disease using siRNA delivered via microbubble-induced sonoporation.

18.5.3 Generation of *de novo* HDL Cholesterol

In an effort to address an unmet clinical need, investigators at SonoGene LLC have combined three commercial components to deliver an effective HDL therapeutic product, including: (1) Human ApoA-I plasmids, (2) acoustic microspheres (Optison™ microspheres, GE Healthcare), and (3) commercial ultrasound imaging systems (GE VIVID *i* system) (Castle et al. 2014). All prescribed doses of ultrasound energy used remained within recommended guidelines for diagnostic applications. The standard infusion process is as follows: 1 mL of microspheres mixed with 1 mL of human ApoA-I plasmids (8 mg/mL) are co-administered and injected intravenously (2.0 mL over 90 s). Simultaneous with the infusion, an external ultrasound probe is placed on the abdomen and is used for both liver imaging and therapy (pulsed acoustic energy). This process induces microsphere disruption, resulting in transient, localized endothelial cell porosity, thus facilitating plasmid entry into the cells (Juffermans et al. 2009; Deng et al. 2004; Pan et al. 2004). Within hours of treatment, human mRNA can be identified in the liver cells of rats, with subsequent production of serum human ApoA-I protein.

This rapidly formed ApoA-I protein facilitates a significant increase in HDL circulating in treated rats (Fig. 18.1). With additional testing and process refinement, this minimally invasive technique could hold promise for both acute coronary syndrome and chronic HDL disorders.

Similarly, confirmatory data was reported from China in which investigators produced a therapeutic effect of the scavenger receptor B type I (SRBI) gene. This serves as a receptor for HDL when delivered by combining cationic liposomal microbubbles (CLMs) and ultrasound in hypercholesterolemic rats (Liu et al. 2013). Researchers found delivery of the SRBI gene resulted in a significant decrease in circulating lipid levels. Much like the direct increase in HDL generation, as demonstrated by ApoA-I gene therapy, the upregulation of HDL receptors in this study may exert a protective role in hypercholesterolemia.

18.6 Summary of CEUS for Cardiovascular Diagnostic and Therapeutic Applications

As an alternative to viral-mediated therapies, non-viral-mediated gene therapies provide a unique opportunity to advance the field through the use of acoustic microspheres. These serve as a non-invasive, monitoring systems coupled with the opportunity to provide a localized delivery

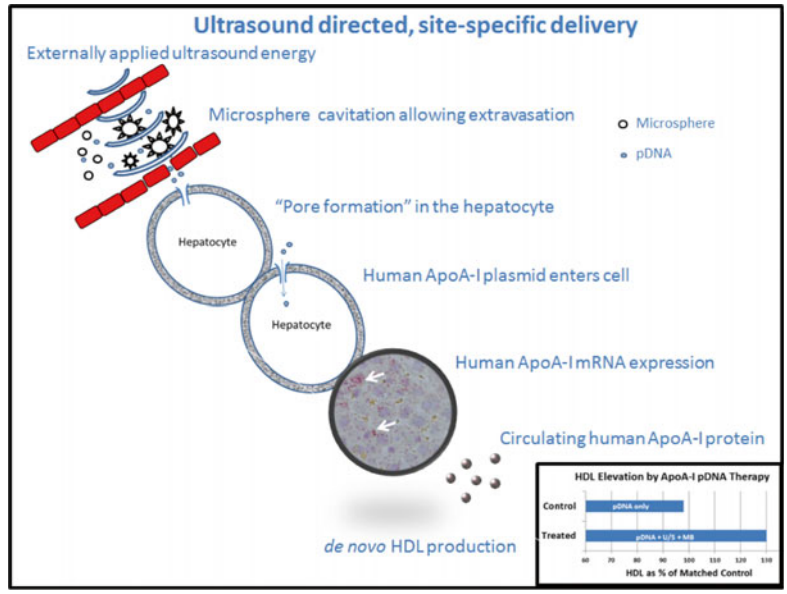

Fig. 18.1 The representative cascade of events involved in sonoporation for gene therapy is as follows. Externally applied acoustic energy disrupts the intravascular acoustic microspheres, generating transient porosity within the endothelial cell borders. ApoA-I plasmids enter the cells, resulting in expression of human ApoA-I messenger RNA with resultant generation of circulating human ApoA-I protein, and finally production of *de novo* serum HDL, *White arrows* indicate presence of human ApoA-I messenger RNA in treated rat liver

method, without the associated risks of ionizing radiation or potential chromosomal insertion (mutagenesis). The ongoing work of the investigators from the University of Bergen have broken new ground with their report of the use of acoustic microspheres to both monitor and better deliver chemotherapy to patients suffering from pancreatic cancer (Kotopoulis et al. 2013). The dual approach to therapy has been realized and presents a propitious beginning. Due to the advent and improvement of this technology, the list of potential applications of drug UTMD (ultrasound-targeted microbubble destruction) – from small molecules to plasmid DNA – is seemingly limitless. To this end, CV microbubble drug delivery may encompass the three forms of intervention, including pre-event management; HDL regulation via gene therapy, and intra-event relief; vascular reperfusion by sonothrombolyis, and post-event maintenance; prevention of restenosis through siRNA silencing.

The CEUS migration from diagnostic to therapeutic applications has opened new horizons for the volumetric analyses of microvascular perfusion monitoring and therapeutic delivery of localized agents. The ongoing developments in this technology provide a platform for designer therapies useful in complex diseases. In addition, the concurrent advancement of acoustic hardware, software and "wetware" will accelerate this progress. Collaborations between academia, industry and pharma should begin to focus their efforts to further define the underlying mechanisms, as well as determine the most relevant technology applications. This coupling of investigations and optimization for acoustic sonoporation will provide an opportunity to advance the field of medicine (Castle et al. 2013). This will require forward–looking study design, which has the highest potential for translational success, as research advances from discovery through to early clinical trials. In doing so, the concept of using microspheres to safely and effectively administer therapy is rapidly becoming a reality.

References

AIM-HIGH Investigators; Boden WE, Probstfield JL, Anderson T, Chaitman BR, Desvignes-Nickens P, Koprowicz K, McBride R, Teo K, Weintraub W (2011) Niacin in patients with low HDL cholesterol levels receiving intensive statin therapy. N Engl J Med 365:2255–2267

Ason B, Castro-Perez J, Tep S, Stefanni A, Tadin-Strapps M, Roddy T, Hankemeier T, Hubbard B, Sachs AB, Michael Flanagan W, Kublin NA, Mitnaul LJ (2011) ApoB siRNA-induced liver steatosis is resistant to clearance by the loss of fatty acid transport protein 5 (Fatp5). Lipids 46:991–1003

Black DM, Delmas PD, Eastell R, Reid R, Boonen S, Cauley JA, Cosman F, Lakatos P, Leung PC, Man Z, Mautalen C, Mesenbrink P, Hu H, Caminis J, Tong K, Rosario-Jansen T, Krasnow J, Hue TF, Sellmeyer D, Eriken EF, Cummings SR, HORIZON Pivotal Fracture Trial (2007) Once-yearly zoledronic acid for treatment of postmenopausal osteoporosis. N Engl J Med 356:1809–1822

Castle J, Butts M, Healey A, Kent K, Marino M, Feinstein SB (2013) Ultrasound-mediated targeted drug delivery: recent success and remaining challenges. Am J Physiol Heart Circ Physiol 304:H350–H357

Castle J, Roberts J, Feinstein SB (2014) Localized gene delivery for the elevation of HDL. Paper presented at the 29th annual advances in contrast ultrasound – ICUS Bubble conference, Chicago, 17–19 Sept 2014

Chen ZY, Lin Y, Yang F, Jiang L, Ge SP (2013) Gene therapy for cardiovascular disease mediated by ultrasound and microbubbles. Cardiovasc Ultrasound 11:11

Chiesa G, Monteggia E, Marchesi M, Lorenzon P, Laucello M, Lorusso V, Di Mario C, Karvouni E, Newton RS, Bisgaier CL, Franceschini G, Sirtori CR (2002) Recombinant apolipoprotein A-I(Milano) infusion into rabbit carotid artery rapidly removes lipid from fatty streaks. Circ Res 90:974–980

Culp WC, Porter TR, Xie F, Goertzen TC, McCowan TC, Vonk BN, Baxter BT (2001) Microbubble potentiated ultrasound as a method of declotting thrombosed dialysis grafts: experimental study in dogs. Cardiovasc Intervent Radiol 24:407–412

Darge K, Papadopoulou F, Ntoulia A, Bulas DI, Coley BD, Fordham LA, Paltiel HJ, McCarville B, Volberg FM, Cosgrove DO, Goldberg BB, Wilson SR, Feinstein SB (2013) Safety of contrast-enhanced ultrasound in children for non-cardiac applications: a review by the Society for Pediatric Radiology (SPR) and the International Contrast Ultrasound Society (ICUS). Pediatr Radiol 43:1063–1073

Deeks ED, Perry CM (2008) Zoledronic acid: a review of its use in the treatment of osteoporosis. Drugs Aging 25:963–986

Deng CX, Sieling E, Pan H, Cui J (2004) Ultrasound-induced cell membrane porosity. Ultrasound Med Biol 30:519–526

Fishbein I, Chorny M, Levy RJ (2010) Site-specific gene therapy for cardiovascular disease. Curr Opin Drug Discov Devel 13:203–213

Fisher EA, Feig JE, Hewing B, Hazen SL, Smith JD (2012) High-density lipoprotein function, dysfunction, and reverse cholesterol transport. Arterioscler Thromb Vasc Biol 32:2813–2820

Gomaraschi M, Ossoli A, Favari E, Adorni MP, Sinagra G, Cattin L, Veglia F, Bernini F, Franceschini G, Calabresi L (2013) Inflammation impairs eNOS activation by HDL in patients with acute coronary syndrome. Cardiovasc Res 100:36–43

Hacein-Bey-Abina S, von Kalle C, Schmidt M, Le Deist F, Wulffraat N, McIntyre E, Radford I, Villeval JL, Fraser CC, Cavazzana-Calvo M, Fischer A (2003a) A serious adverse event after successful gene therapy for X-linked severe combined immunodeficiency. N Engl J Med 348:255–256

Hacein-Bey-Abina S, von Kalle C, Schmidt M, McCormack MP, Wulffraat N, Leboulch P, Lim A, Osborne CS, Pawliuk R, Morillon E, Sorensen R, Forster A, Fraser P, Cohen JI, de Saint Basile G, Alexander I, Wintergerst U, Frebourg T, Aurias A, Stoppa-Lyonnet D, Romana S, Radford-Weiss I, Gross F, Valensi F, Delabesse E, McIntytre E, Sigaux F, Soulier J, Leiva LE, Wissler M, Prinz C, Rabbitts TH, Le Deist F, Fischer A, Cavazzana-Calvo M (2003b) LMO2-associated clonal T cell proliferation in two patients after gene therapy for SCID-X1. Science 302:415–419

HPS2-THRIVE Collaborative Group; Landray MJ, Haynes R, Hopewell JC Parish S, Aung T, Tomson J, Wallendszus K, Craig M Jiang L, Collins R, Armitage J (2014) Effects of extended-release niacin with laropiprant in high-risk patients. N Engl J Med 371:203–212

Ishihara K (1993) Administering anticancer drugs to specific locations in human bodies. USA Patent US 5190766 A

Juffermans LJ, van Dijk A, Jongenelen CA, Drukarch B, Reijerkerk A, de Vries HE, Kamp O, Musters RJ (2009) Ultrasound and microbubble-induced intra- and intercellular bioeffects in primary endothelial cells. Ultrasound Med Biol 35:1917–1927

Kotopoulis S, Dimcevski G, Gilja OH, Hoem D, Postema M (2013) Treatment of human pancreatic cancer using combined ultrasound, microbubbles, and gemcitabine: a clinical case study. Med Phys 40:072902

Lambrinoudaki I, Vlachou S, Galapi F, Papadimitriou D, Papadias K (2008) Once-yearly zoledronic acid in the prevention of osteoporotic bone fractures in post-menopausal women. Clin Interv Aging 3:445–451

Liu F, Zhu J, Huang Y, Guo W, Rui M, Xu Y, Hu B (2013) Hypolipidemic effect of SR-BI gene delivery by combining cationic liposomal microbubbles and ultrasound in hypercholesterolemic rats. Mol Med Rep 7:1965–1969

Mathias W, Kamp O and Porter T (2014) Sonothrombolysis the SAMI study. Paper presented at the 29th annual advances in contrast ultrasound – ICUS Bubble conference. Chicago, 1719 Sept 2014

Merrick A (2008) How Walgreen changed its prescription for growth. Wall Street J, p. B1

Nicholls SJ, Tuzcu EM, Sipahi I, Schoenhagen P, Crowe T, Kapadia S, Nissen SE (2006) Relationship between atheroma regression and change in lumen size after infusion of apolipoprotein A-I Milano. J Am Coll Cardiol 47:992–997

Nissen SE, Tardif JC, Nicholls SJ, Revkin JH, Shear CL, Duggan WT, Ruzyllo W, Bachinsky WB, Lasala GP, Tuzcu E, ILLUSTRATE Investigators (2007) Effect of torcetrapib on the progression of coronary atherosclerosis. N Engl J Med 356:1304–1316

Pan H, Zhou Y, Sieling F, Shi J, Cui J, Deng C (2004) Sonoporation of cells for drug and gene delivery. Conf Proc IEEE Eng Med Biol Soc 5:3531–3534

Pollack A (2012) New drugs for lipids set off race. New York Times. November 5, 2012 page B1

Rader DJ, deGoma EM (2014) Future of cholesteryl ester transfer protein inhibitors. Annu Rev Med 65:385–403

Reis ED, Roque M, Dansky H, Fallon JT, Badimon JJ, Cordon-Cardo C, Shiff SJ, Fisher EA (2000) Sulindac inhibits neointimal formation after arterial injury in wild-type and apolipoprotein E-deficient mice. Proc Natl Acad Sci U S A 97:12764–12769

Rubiera M, Ribo M, Delgado-Mederos R, Santamarina E, Maisterra O, Delgado P, Montaner J, Alvarez-Sabin J, Molina CA (2008) Do bubble characteristics affect recanalization in stroke patients treated with microbubble-enhanced sonothrombolysis? Ultrasound Med Biol 34:1573–1577

Shaw JA, Bobik A, Murphy A, Kanellakis P, Blombery P, Mukhamedova N, Woollard K, Lyon S, Sviridov D, Dart AM (2008) Infusion of reconstituted high-density lipoprotein leads to acute changes in human atherosclerotic plaque. Circ Res 103:1084–1091

Sirsi SR, Borden MA (2012) Advances in ultrasound mediated gene therapy using microbubble contrast agents. Theranostics 2:1208–1222

Slikkerveer J, Kleijn SA, Appelman Y, Porter TR, Veen G, van Rossum AC, Kamp O (2012) Ultrasound enhanced prehospital thrombolysis using microbubbles infusion in patients with acute ST elevation myocardial infarction: pilot of the Sonolysis study. Ultrasound Med Biol 38:247–252

Staub D, Schinkel AFL, Coll B, Coli S, van der Steen AF, Reed JD, Krueger C, Thomenius KE, Adam D, Sijbrands EJ, ten Cate FJ, Feinstein SB (2010) Contrast-enhanced ultrasound imaging of the vasa vasorum from early atherosclerosis to the identification of unstable plaques. JACC Cardiovasc Imaging 3:761–771

Suzuki J, Ogawa M, Takayama K, Taniyama Y, Morishita R, Hirata Y, Nagai R, Isobe M (2010) Ultrasound-microbubble–mediated intercellular adhesion molecule-1 small interfering ribonucleic acid transfection attenuates neointimal formation after arterial injury in mice. J Am Coll Cardiol 55:904–913

Tadin-Strapps M, Peterson LB, Cumiskey AM, Rosa RL, Mendoza VH, Castro-Perez J, Puig O, Zhang L, Strapps WR, Yendluri S, Andrews L, Pickering V, Rice J, Luo L, Chen Z, Tep S, Ason B, Somers EP, Sachs AB, Bartz SR, Tian J, Chin J, Hubbard BK, Wong KK, Mitnaul LJ (2011) SiRNA-induced liver ApoB knockdown lowers serum LDL-cholesterol in a mouse model with human-like serum lipids. J Lipid Res 52:1084–1097

Tsutsui JM, Feng X, Johanning J, Lof J, Cory B, He A, Thomas L, Matsunaga T, Unger E, Porter TR (2006) Treatment of deeply located acute intravascular thrombi with therapeutic ultrasound guided by diagnostic ultrasound and intravenous microbubbles. J Ultrasound Med 25:1161–1168

Wang W, Li W, Ma N, Steinhoff G (2013) Non-viral gene delivery methods. Curr Pharm Biotechnol 14:46–60

Yamamoto S, Yancey PG, Ikizler TA, Jerome WG, Kaseda R, Cox B, Bian A, Shintani A, Fogo AB, Linton MF, Fazio S, Kon V (2012) Dysfunctional high-density lipoprotein in patients on chronic hemodialysis. J Am Coll Cardiol 60:2372–2379

Zheng C, Aikawa M (2013) High-density lipoproteins: from function to therapy. J Am Coll Cardiol 60: 2380–2383

Sonothrombolysis

19

Kenneth B. Bader, Guillaume Bouchoux, and Christy K. Holland

Abstract

Thrombo-occlusive disease is a leading cause of morbidity and mortality. In this chapter, the use of ultrasound to accelerate clot breakdown alone or in combination with thrombolytic drugs will be reported. Primary thrombus formation during cardiovascular disease and standard treatment methods will be discussed. Mechanisms for ultrasound enhancement of thrombolysis, including thermal heating, radiation force, and cavitation, will be reviewed. Finally, *in-vitro*, *in-vivo* and clinical evidence of enhanced thrombolytic efficacy with ultrasound will be presented and discussed.

Keywords

Ultrasound • Thrombus • Cardiovascular disease

19.1 Clinical Challenges of Thrombo-Occlusive Disease

Cardiovascular disease is the number one cause of death worldwide (17.3 million deaths in 2008) (World Health Organization 2013), with a 15% projected mortality rate increase between 2010 and 2020 (Mathers and Loncar 2006). In the United States of America, more than one third of adults (~83.6 million) have one or more forms of cardiovascular disease (Go et al. 2013). Cardiovascular disease is characterized by occlusion of blood flow through the vasculature, in part due to the presence of blood clots, or thrombi.

19.1.1 Thrombus Formation During Cardiovascular Disease

The primary function of thrombus formation is to prevent bleeding from injured blood vessels (Gregg 2003). Platelets adhere to the injury site to initiate the formation of a fibrin mesh (Furie and Furie 2008), a protein network that stabilizes

K.B. Bader • G. Bouchoux • C.K. Holland (✉)
Division of Cardiovascular Health and Disease, Department of Internal Medicine, College of Medicine, University of Cincinnati, Cincinnati, OH, USA
e-mail: Christy.Holland@uc.edu

© Springer International Publishing Switzerland 2016

J.-M. Escoffre, A. Bouakaz (eds.), *Therapeutic Ultrasound*, Advances in Experimental Medicine and Biology, Vol. 880, DOI 10.1007/978-3-319-22536-4_19

the clot architecture. Under normal circumstances, fibrin strands are cleaved by plasmin as the injured vessel is repaired. In pathologic cases, however, excessive blood clotting occurs in response to Virchow's triad: hypercoagulability, hemodynamic changes (stasis or turbulence) or endothelial injury (Watson et al. 2009). Atherosclerosis, a disease known to induce Virchow's triad, is the build-up of lipids, cholesterol, and other substances in arterial tissue (Saric and Kronzon 2012). Lipid-rich plaques are vulnerable and their rupture can cause the formation of platelet- and fibrin-rich thrombi. Thrombi may also form in stagnated blood, such as in the heart during atrial fibrillation (Watson et al. 2009).

Thrombus composition varies based on conditions during formation (Liebeskind et al. 2011). "White" thrombi are formed due to platelet activity in the arterial system, whereas "red" thrombi originate from trapped erythrocytes within a fibrin mesh in the low-pressure venous system (Tan and Lip 2003). Thrombi retrieved from patients exhibit an underlying commonality of histological components and morphology, regardless of origin (Marder et al. 2006). Thromboembolism occurs when a thrombus breaks free and blocks blood flow in the distal vasculature. Hypoxic conditions in tissues distal to the occlusive thrombus cause infarction and tissue death. Depending on the anatomical location of the obstruction, tissue death can occur in the brain (ischemic stroke), extremities and lungs (deep vein thrombosis and pulmonary thromboembolism, respectively), or heart (myocardial infarction).

19.1.1.1 Stroke

Stroke, or brain impairment due to loss of oxygen, is the fourth leading cause of death in the United States (Go et al. 2013), and a leading cause of death worldwide (Mathers et al. 2008). Stroke is classified as either hemorrhagic (13% of cases) or ischemic (87% of cases) (Go et al. 2013). Hemorrhagic stroke has a 40–50% 30-day mortality rate and a 6-month functional independence rate of only 20% (Adeoye et al. 2010). Hemorrhagic stroke results from a weakened vessel that ruptures and bleeds, compressing the surrounding brain tissue. Bleeding can occur in different brain compartments: intracerebral (10% of all stroke cases) or subarachnoid (3% of all stroke cases) (Go et al. 2013). Bleeding extends into the ventricles for 45% of intracerebral cases and 25% of subarachnoid cases (Mohr et al. 1983; Brott et al. 1986). In contrast, ischemic stroke is the result of a thrombus obstructing blood flow to the brain, with a 30-day mortality rate of 8–13% (Rosamond et al. 2007). Thrombi responsible for ischemic stroke are primarily cardioembolic in origin, but can also be atherothromboembolic (Marder et al. 2006). Clinical outcomes are best in patients with distal middle cerebral artery (MCA) occlusions and worst in internal carotid artery occlusions, potentially due to larger thrombus burden and impaired collateral blood flow in the latter (Puetz et al. 2008).

19.1.1.2 Deep Vein Thrombosis and Pulmonary Embolism

Deep vein thrombosis (DVT) is the formation of thrombi in a deep vein, primarily in the calf of the leg (Kearon 2003). Thrombi form due to stagnation of blood in the deep veins (Markel 2005), resulting in "red" thrombi (Hirsh and Hoak 1996). If left untreated, post-thrombotic syndrome, a cause of increased morbidity and disability, can progress due to incompetent valves in deep and superficial veins (Markel 2005). Approximately 20% of venous thrombi occur in the tibial and popliteal veins (Kakkar et al. 1969). Dislodged thrombi, or emboli, travel to the lung in 26–67% of DVT cases (Markel 2005), a condition called pulmonary embolism (PE). The increased workload by the blockage enlarges the heart, potentially resulting in right ventricular dysfunction (Kearon 2003). PE has a 25% morality rate, with a 30-day survival rate of 59.1% (Go et al. 2013). Approximately 10% of PE cases cause death within 1 h of onset (Bell and Simon 1982).

19.1.1.3 Myocardial Infarction

One cause of myocardial infarction (MI), more commonly known as a "heart attack," is embolic atherosclerotic debris (White and Chew 2008) within the coronary arteries (Saric and Kronzon

2012). There are 600,000 annual incidents of MI, with a mortality rate of 15% (Go et al. 2013). Thrombus formation in the atherosclerotic build-up is composed of a platelet-rich core surrounded by an erythrocyte-rich fibrin mesh. Early platelet thrombus is unstable and fragile (Falk 1991), and may embolize unless stabilized by fibrin (Silvain et al. 2011). Transmural MI results in necrosis in all three muscle layers of the heart (endocardium, myocardium, and epicardium), and is associated with total occlusion of the coronary artery (Turgut and Bates 2000). Non-transmural MI is characterized by ischemic necrosis that does not extend across the full thickness of the myocardial wall, and is limited to the myocardium and the endocardium or the endocardium (Fardanesh and Kian 2014). Vasospasm from endothelial dysfunction, concurrent with chronic atherosclerosis, can also reduce flow and increase ischemia (Fuster 1994). Dissection of the coronary artery is an additional cause of infarction in the absence of occlusive atherosclerosis or vasospasm (Casscells 2003).

19.1.2 Frontline Therapy: Thrombolytic Drugs

Recanalization of the occluded vessels is correlated with functional clinical outcome for DVT (Hirsh and Hoak 1996), MI (Pasceri et al. 1996) and ischemic stroke (Rha and Saver 2007). Regardless of the vascular origin of the thrombus, recanalization can be accelerated with thrombolytic drugs or mechanical intervention. An excellent review of current thrombolytics is provided by Weisel and Litvinov (2008). Most thrombolytic drugs cleave plasminogen bonds to create plasmin. Plasmin, which can also be used as a direct thrombolytic agent (Novokhatny et al. 2004), lyses fibrin to initiate thrombolysis. Early thrombolytic drugs, such as streptokinase (SK) (Baruah et al. 2006) and recombinant urokinase (UK) (Reuning et al. 2003) are administered for treatment of PE and MI. However, both UK and SK lack specificity to fibrin, and their bacterial origin contributes to adverse effects (Perler 2005). These limitations prompted the advent of the fibrin-specific thrombolytic recombinant tissue type plasminogen activator (rt-PA) (Higgins and Bennett 1990; Baruah et al. 2006; Watson et al. 2009), and its derivatives (Baruah et al. 2006; Labreuche et al. 2010; Saric and Kronzon 2012; Jauch et al. 2013). The rt-PA drug is currently the primary thrombolytic in use (Turi et al. 1993; Watson et al. 2009; Jauch et al. 2013).

Strict exclusion criteria (Turi et al. 1993) limit the administration of rt-PA to only 1.5% of total stroke cases (Go et al. 2013). Mechanical thrombolysis with catheter-based intervention has gained some clinical traction in removing or disrupting thrombi (Gralla et al. 2011), either as a stand-alone or adjuvant therapy for ischemic stroke (Jauch et al. 2013) and PE (Jaff et al. 2011). These mechanical devices employ aspiration (The Penumbra Pivotal Stroke Trial Investigators 2009), microcatheters (Smith et al. 2008) or stents (Castano et al. 2010) to remove thrombi. However, endovascular recanalization techniques are reserved for dedicated stroke centers, limiting their widespread use (Gralla et al. 2011). Furthermore, recent studies indicate mechanical intervention has limited clinical improvement compared to rt-PA alone (Ciccone et al. 2013), questioning the value of such an invasive procedure. To improve therapeutic outcome, there is an unmet need for techniques that would either locally increase the efficacy of thrombolytic drugs, or allow a safe and minimally invasive mechanical disruption of the thrombus without drugs. Sonothrombolysis has the potential for both.

19.2 Mechanisms of Thrombolytic Enhancement

The interaction of acoustic waves with tissue is well documented (Nyborg and Miller 1982) and can generally be categorized as thermal, primary mechanical effects (e.g., radiation force), or secondary mechanical effects (acoustic cavitation). The contributions of each of these interactions to thrombolytic enhancement are reviewed in the following sections.

19.2.1 Thermal Effects of Ultrasound

Heating of biological tissues exposed to ultrasound is generated by absorption of the incident wave. *In-vitro* studies have shown rt-PA clot lysis to be well described by a Arrhenius temperature dependence (Shaw et al. 2007). Increasing the ambient temperature increases enzymatic activity and expedites thrombolysis. However, several studies have shown negligible thermal effects in bench-top (Francis et al. 1992; Shaw et al. 2006; Damianou et al. 2014) or clinical studies (Barlinn and Alexandrov 2013). Numerical computations confirm a negligible temperature rise in clots due to 0.12–3.5 MHz insonations during thrombolysis (Nahirnyak et al. 2007; Bouchoux et al. 2014). In contrast, Sakharov et al. (2000) attributed increased thrombolytic efficacy from 1-MHz insonation *in-vitro* due to the combined effect of heating and acoustic streaming. However, the *in-vitro* model employed by Sakharov et al. lacked flow to accelerate the diffusion of heat around the clot.

19.2.2 Primary Mechanical Effects

Ultrasound energy imparts momentum to tissue through absorption and scattering mechanisms. The resultant force, known as the acoustic radiation force, is well described by Nyborg (1953). Radiation force can initiate fluid motion, or acoustic streaming (Lighthill 1978). Fluid mixing may help a thrombolytic drug penetrate a clot (Francis et al. 1995). Traveling wave insonation generates greater acoustic streaming than standing wave insonation (Devcic-Kuhar et al. 2002). Pfaffenberger et al. (2003) found increased thrombolytic efficacy employing 2-MHz traveling waves instead of standing waves in an *in-vitro* clot model. Furthermore, the thrombolytic efficacy was optimized at a 1-Hz pulse repetition frequency of the traveling wave. These acoustic streaming effects are similar to mild stirring of the medium surrounding the clot (Sakharov et al. 2000).

Displacement of clot surfaces has also been observed due to acoustic radiation force (Wright et al. 2012b). Frenkel et al. (2006), using both an *in-vitro* clot model and a numerical model to calculate clot displacement, found a correlation between thrombolytic efficacy and acoustic radiation force at 1 MHz. Bader et al. (2015) found a correlation between the root-mean-square velocity of displaced *in-vitro* human whole blood clots and the lytic rate with sub-megahertz insonation. Radiation force is known to act on bubbles (Leighton 1994), and several groups have shown microbubbles forced into clots *in-vitro* (Caskey et al. 2009; Acconcia et al. 2013; Everbach and Guarini 2013) (Fig. 19.1). The presence of microbubbles could modify both the attenuation and sound speed of the thrombus (Commander and Prosperetti 1989), thereby increasing the acoustic radiation force on the clot (Nyborg 1965).

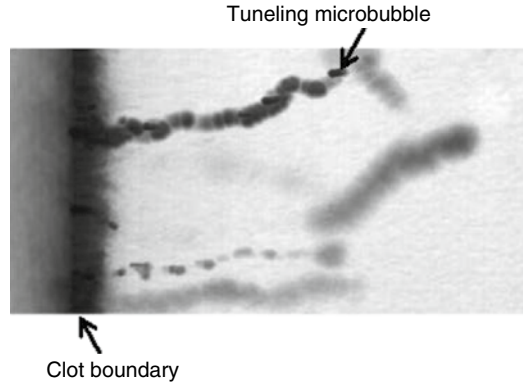

Fig. 19.1 Microbubble tunneling though a fibrin clot (fluid-clot boundary at left) caused by acoustic radiation force (1 MHz, 0.4 MPa). The blurred, dark line is a motion artifact from deflection of the clot boundary due to radiation force (Acconcia et al. 2013)

19.2.3 Secondary Mechanical Effects (Acoustic Cavitation)

19.2.3.1 Classification of Cavitation

Acoustic cavitation has been a topic of study since the early twentieth century (Rayleigh 1917) and has been extensively reviewed elsewhere (Flynn 1964; Apfel 1981; Leighton 1994; Lauterborn and Kurz 2010). Acoustic cavitation refers to both the formation and oscillation of bubbles due to an acoustic pressure. Cavitation activity can generally be categorized as inertial or stable.

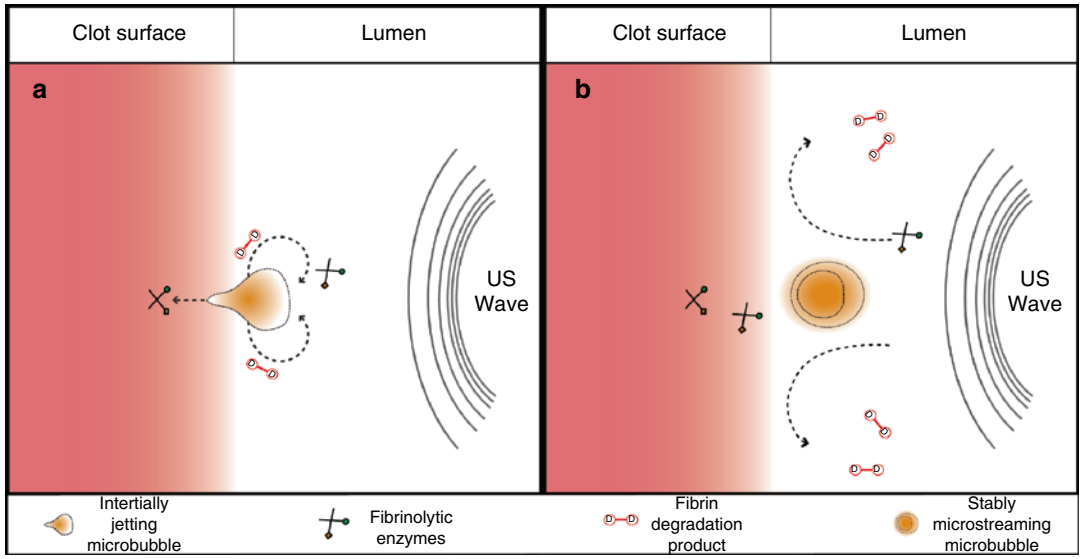

Fig. 19.2 Interaction of cavitating microbubbles with thrombi. (**a**) Illustration of inertial cavitation. The asymmetric boundary condition causes a liquid jet to form during the final stages of collapse during inertial cavitation (Brujan et al. 2001). The jet will impinge on the thrombus, resulting in direct mechanical damage and erosion of clot surface. (**b**) Illustration of stable cavitation. Sustained bubble motion promotes strong fluid mixing through microstreaming (Elder 1959). Local pressure gradients around the microbubble cause enhanced mixing of the fibrinolytic enzymes, and removal of fibrin degradation products from the clot (Datta et al. 2008) (Figure Adapted from Sutton et al. (2013a))

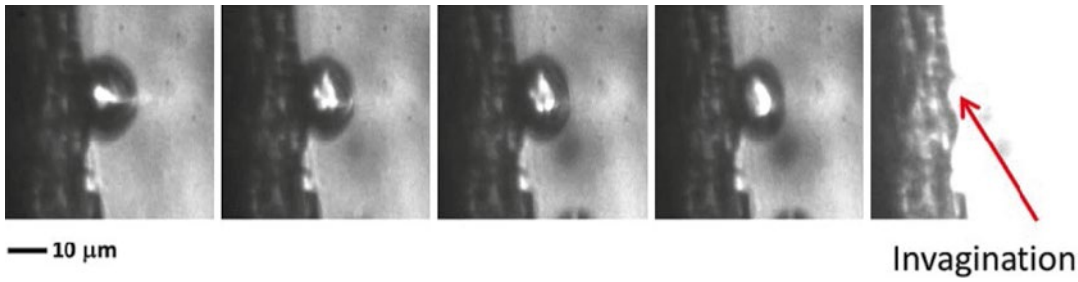

Fig. 19.3 Interaction of inertially cavitating microbubble with thrombus (1 MHz, 1.5 MPa) recorded at 5 Mfps (200 ns interframe time). As the microbubble disappears at the completion of the inertial collapse, there is a residual "pit" at the thrombus site (Chen et al. 2014)

Inertial cavitation encompasses bubble motion dominated by the inertia of the surrounding fluid. Large expansions of the bubbles occur due to relatively large tension generated in the liquid by the acoustic excitation (Holland and Apfel 1989). During the final stages of bubble collapse, the converging liquid compresses and heats the contents of the bubble, creating a high energy density (Young 2005). The sudden halt of the converging liquid generates shock waves (Holzfuss et al. 1998), light emissions (Gaitan et al. 1992), and free radicals (Riesz and Kondo 1992). If the collapse occurs along a surface, a liquid jet with speeds in excess of 1 km/s may form (Brujan et al. 2001). These jets are associated with mechanical damage or deformation of clots (Weiss et al. 2013) (Fig. 19.2a).

Chen et al. (2014) used high-speed imaging to observe the formation of a defect in a thrombus surface at the location of a microbubble jet after

ultrasound exposure (Fig. 19.3). Inertial cavitation can be detected acoustically as broadband emissions (Everbach and Francis 2000; Datta et al. 2008). Chuang et al. (2010) found a positive correlation between the dose of broadband acoustic emissions and the thrombolytic efficacy *in-vitro*. Similarly, Leeman et al. (2012) observed significant fibrinolysis *in-vitro* only when insonation of microbubbles produced broadband acoustic emissions. Broadband acoustic emissions have also been detected *in-vivo* during thrombolysis in porcine (Shi et al. 2011; Maxwell et al. 2011) and rabbit (Wright et al. 2012a) models. Xie et al. (2009) found significant thrombolytic enhancement in a canine model only when microbubbles nucleated inertial cavitation. However, Wu et al. (2014) found that thrombolytic efficacy did not correlate with the amplitude of *in-vitro* broadband acoustic emissions. They concluded instead that strong inertial cavitation shielded the acoustic energy from the thrombus. Although strong inertial activity appears to enhance thrombolysis in some cases (Chen et al. 2009; Maxwell et al. 2009), sustained bubble activity is difficult (Prokop et al. 2007), potentially due to the destruction of cavitation nuclei (Datta et al. 2006).

Stable cavitation is a sustained bubble motion (Datta et al. 2006) where the converging liquid inertia is offset by the restoring force of the gaseous contents of the bubble (Flynn 1964). The acoustic pressure amplitude required to initiate stable oscillations is generally lower than that required for inertial cavitation (Bader and Holland 2012). The highly nonlinear nature of these oscillations generates microstreaming of the surrounding fluid (Elder 1959), promotes strong fluid mixing (Collis et al. 2010) and attracts particulates via secondary radiation force (Nyborg and Miller 1982). Such strong fluid mixing hastens enzymatic fibrinolysis, enhancing the penetration of both rt-PA and plasminogen into clots (Datta et al. 2008; Sutton et al. 2013a) (Fig. 19.2b).

In contrast to the broadband emissions from inertial cavitation, stable cavitation generates harmonic, ultraharmonic, and subharmonic emission lines in the acoustic spectra. Depending on the relative size of the bubble compared to the resonant size (Bader and Holland 2012), harmonic (integer multiples of the fundamental) (Choi and Coussios 2012), subharmonic (rational fractions of the fundamental less than one) (Prokop et al. 2007), or ultraharmonic (rational fractions of the fundamental greater than one) (Datta et al. 2006) emissions can be used to detect stable cavitation acoustically. Datta et al. (2008) found a correlation between thrombolytic enhancement and ultraharmonic emissions *in-vitro*. Subsequent studies from the same group (Hitchcock et al. 2011) found increased thrombolytic efficacy using an intermittent insonation scheme that optimized ultraharmonic emissions from stable cavitation.

Bader et al. (2015)) used an *in-vitro* model to monitor the instantaneous reduction in clot width and ultraharmonic emissions from stable cavitation nucleated from Definity® microbubbles. The energy of ultraharmonic emissions was found to correlate significantly with the instantaneous reduction in clot width (i.e., thrombolytic efficacy). Prokop et al. (2007) suggested a correlation between increased thrombolytic efficacy *in-vitro* and the presence of subharmonic emissions from stable cavitation. The correlation between subharmonic or ultraharmonic emissions established by Prokop et al. (2007), Datta et al. (2008), and Bader et al. (2015)) illustrate the importance of stable cavitation in assisting enzymatic fibrinolysis.

To gauge both types of cavitation activity incited, Apfel (1981) recommends the use of three golden rules: Know thy sound field, Know thy liquid, and Know when something happens. These rules can help optimize sonothrombolysis treatments employing acoustic cavitation.

19.2.3.2 Know Thy Sound Field

Consistent insonification is necessary for safe and efficient sonothrombolysis. Several ultrasound exposure approaches have been proposed, as summarized in Fig. 19.4.

Ultrasound Catheter

Ultrasound-emitting catheters have been applied to a wide variety of pathologies (Doomernik et al. 2011). The catheter is inserted into the thrombus allowing combined exposure to ultrasound and local drug infusion. A relatively

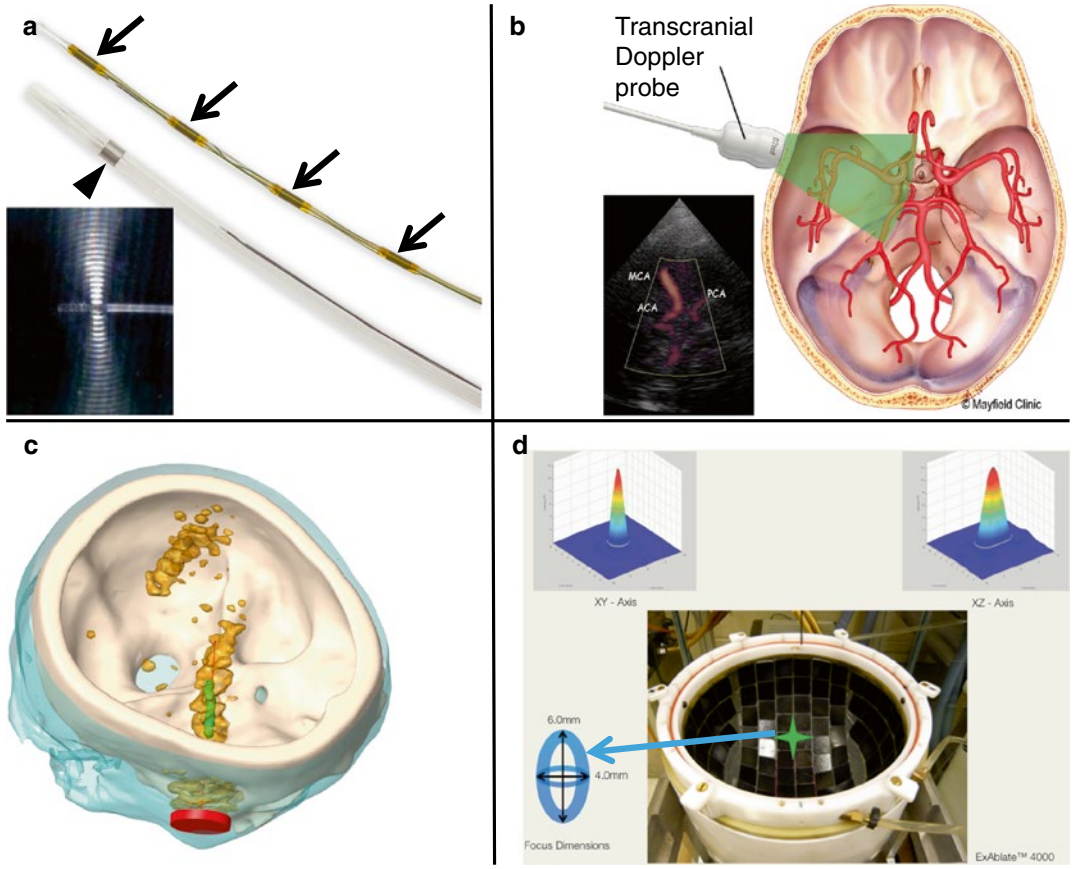

Fig. 19.4 Ultrasound insonation schemes for sonothrombolysis. (**a**) *Ultrasound-assisted thrombolysis catheter* composed of a 5.2-Fr multi-sidehole drug infuser (*arrowhead*). Ultrasound elements along central core (*small arrows*) shown separately. During treatment, the central core is placed inside the infusion catheter (Engelberger and Kucher 2014). The omnidirectional ultrasound field promotes cavitation and acoustic streaming, driving thrombolytics into the clot. Images provided by EKOS Corporation (Bothell, WA, USA). (**b**) *Transcranial Doppler*. Schematic representation of the penetration of 2-MHz TCCS through the skull. Images reprinted with permission from Mayfield Clinic (Cincinnati, OH, USA). (**c**) *Unfocused, Sub-megahertz Ultrasound.* Simulated acoustic fields generated by an unfocused, transcranial sub-megahertz (120 kHz) ultrasound system in a human skull (*white*). The M1 segment of the MCA is shown in green and the transducer in red. The orange contour indicates the regions where the acoustic pressure is larger than half the maximum pressure in the M1 region of interest (Bouchoux et al. 2014). (**d**) *MR-Guided Focused Ultrasound.* Top view of ExAblate™ 4000 HIFU hemispherical 1000-element system for MR-guided transcranial focused ultrasound exposure. A sharp 4 mm × 6 mm focus is created along the lateral and elevational orientations, respectively (Hölscher et al. 2013)

uniform ultrasound field covering large clots can be obtained using a series of miniaturized unfocused transducers aligned in the lumen of the catheter (Soltani et al. 2007). The acoustic pressure decreases rapidly with distance from the catheter because the transducers are small and unfocused. Nevertheless, effective ultrasound-catheter sonothrombolysis was achieved in large thrombi caused by intracerebral hemorrhage (Newell et al. 2011).

Transcranial Doppler

Extracorporeal insonation of the thrombus, combined with an intravenous injection of a thrombolytic drug and/or microbubbles, is an appealing minimally invasive approach for the treatment of ischemic stroke. The cranial bone attenuates, reflects and distorts the ultrasound waves (Fry et al. 1970). Hence, bone constitutes a major obstacle for transcranial sonothrombolysis. The temporal bone acoustic window is routinely

used for transcranial Doppler (TCD) examination of cerebral blood flow (Aaslid et al. 1982). TCD, or transcranial color-coded sonography (TCCS), exposure through the temporal bone accelerates rt-PA thrombolysis (Cintas et al. 2002; Alexandrov et al. 2004; Eggers et al. 2008). TCD and TCCS sonothrombolysis use similar frequencies (around 2 MHz) and similar pulsed-ultrasound waveforms, and comparable results were obtained in clinical trials (Saqqur et al. 2013).

TCD is operator dependent, and the lack of trained operators is an obstacle for widespread adoption (Barlinn et al. 2012). To overcome this limitation, a sonothrombolysis device has been designed in order to be simpler to put into place and is less operator-dependent than TCD (Barlinn et al. 2013). A frame is fixed to the patient's head using simple landmarks. Eighteen transducers are mounted on the head frame in order to insonify the most frequent locations of thrombi during ischemic stroke through the temporal and suboccipital acoustic windows. The acoustic parameters used by this device are based on those used in FDA-approved TCD devices (2 MHz, 100 kPa derated peak rarefactional pressure). The safety and relevance of this device has been demonstrated in phase I and II clinical trials (Barreto et al. 2013).

Ultrasound waves at 2 MHz are transmitted poorly through the bone (Ammi et al. 2008), which prevents TCD examination in 18% of patients (Wijnhoud et al. 2008). Barlinn et al. (2012) estimated the *in-situ* acoustic pressure for 20 subjects treated with TCD in the TUCSON trial using a simple attenuation model based on CT data. The calculated *in-situ* acoustic pressures were higher for patients functionally independent at 3 months. Hence, some patients may receive an insufficient acoustic pressure for thrombolysis enhancement with TCD insonification.

Sub-megahertz Ultrasound

Efficient acoustic transmission through the skull can be achieved in the sub-megahertz frequency range. Ammi et al. (2008) measured a pressure reduction resulting from bone between 77.1 and 96.6% at 2 MHz in 5 human skull specimens. A pressure reduction between 22.5 and 45.5% was observed at 120 kHz. Therefore, sub-megahertz sonothrombolysis may allow a more consistent insonation than 2-MHz TCD. Sub-megahertz (300 kHz) insonation was used in the TRUMBI clinical trial (Daffertshofer et al. 2005). However, a significantly higher rate of symptomatic hemorrhage occurred in the ultrasound group. Baron et al. (2009) numerically simulated TRUMBI trial insonation parameters and concluded that standing waves, due to acoustic reflections in the cranial cavity, could have caused unexpected local pressure maxima. Reflection from contralateral bone and associated constructive interference are less likely for 2-MHz TCD because the wave is significantly attenuated while propagating in the brain tissue. The TRUMBI trial and subsequent studies revealed the necessity of producing a well-controlled transcranial ultrasound field for safe and efficient sonothrombolysis.

Taking into account these findings, revised sub-megahertz transcranial sonothrombolysis devices were designed. A dual-frequency array capable of performing 2.5-MHz TCCS and emitting a 500-kHz sonothrombolysis beam was developed for transcranial insonation (Azuma et al. 2010). The transcranial ultrasound field produced by this device was evaluated *in-vitro* and the safety of this approach was demonstrated in a healthy primate model (Shimizu et al. 2012). Bouchoux et al. (2014) simulated 120 and 500-kHz transcranial ultrasound fields from the head CT scans of 20 ischemic stroke patients using a validated acoustic propagation numerical model (Bouchoux et al. 2012). Consistent and homogeneous insonation of the M1 segment of the MCA was achieved at both 120 and 500 kHz. A positioning strategy based on external head landmarks, which did not require the knowledge of the position of the thrombus, was proposed by Bouchoux et al. and was found to perform similarly to an optimized transducer positioning technique based on CT data analysis. Local acoustic pressure maxima, due to reflection from the contralateral bone, were well controlled and similar to the amplitude in the targeted M1 segment of the MCA.

Transcranial exposure with sub-megahertz ultrasound may allow simple and consistent

insonation of the thrombus in ischemic patients, without excluding subjects with an insufficient temporal bone window for TCD or TCCS. Sub-megahertz sonothrombolysis devices should be developed and evaluated carefully. The transcranial ultrasound field can be evaluated by simulation or *in-vitro* measurements in several skulls. Moreover, sub-megahertz sonothrombolysis devices should be evaluated in a large animal model accounting for constructive interference due to standing waves. Random frequency modulation of the wave can also be employed to suppress standing waves (Tang and Clement 2010; Furuhata and Saito 2013).

Focused Ultrasound

Thrombolysis with focused ultrasound is also a promising approach. A highly focused ultrasound beam allows accurate spatial targeting of the clot. High-pressure amplitudes can be applied locally with a low risk of side effects outside the focal zone. Therefore, thrombolysis based on erosion of the clot by inertial cavitation may be possible with focused ultrasound without a thrombolytic drug. Maxwell et al. (2011) treated acute thrombi in juvenile pig femoral arteries using a 1-MHz transducer with a 1.9×13.5 mm focus (−6 dB). Similarly, a 1.5-MHz transducer (0.9×7.1 mm focal zone) was used to lyse clots in rabbit femoral arteries (Wright et al. 2012a). These studies demonstrated the feasibility of high intensity focused sonothrombolysis using accurate clot targeting. However, the focal zone is usually larger than the targeted vessels. Therefore careful studies on the side effects on tissue surrounding the clot are needed. The treatment of ischemic stroke with a MR-guided transcranial focused ultrasound device (ExAblate™ 4000, InSightec Inc., Tirat Carmel, Israel) was also proposed (Hölscher et al. 2013). This device is a hemispheric 1000-element 220-kHz phased array that can produce an electronically-steered 4×6 mm transcranial focal spot. Nevertheless, the work reported by Hölscher et al. (2013) is in a very early stage and more studies are needed to assess the efficacy and safety of this approach. Safe and efficient intracerebral hemorrhage (ICH) clot liquefaction with a similar MR-guided transcranial ultrasound device was demonstrated in an *in-vivo* porcine model and in a human cadaver model (Monteith et al. 2013). Though large aperture, focused ultrasound for transcranial insonation appears promising, numerical studies by Pajek and Hynynen (2012) indicate that these devices currently appear to be limited to treatment near the center of the brain (basilar artery and the proximal end of the M1 segment of the middle cerebral artery).

19.2.3.3 Know Thy Liquid (i.e., Know Thy Cavitation Nuclei)

The type and threshold for cavitation activity incited depends highly on the nuclei that are present.

Endogenous Nuclei

Thresholds for cavitation activity depend on the purity of the medium (Roy et al. 1985). However, cavitation thresholds in even the purest sources of water (Herbert et al. 2006; Bader et al. 2012; Maxwell et al. 2013) are much less than theoretically predicted (Church 2002). This discrepancy is generally attributed to nanometer-sized nuclei (Bader et al. 2012; Maxwell et al. 2013) that are difficult to extract from the medium (Flynn 1964). Such nuclei are however not likely to be found *in-vivo* due to the body's natural filtration system. Instead, Yount (1979) proposed nuclei composed of an elastic organic skin of amphiphilic molecules which would stabilize bubbles against dissolution. The cavitation thresholds of endogenous nuclei in tissue are summarized by Church (2015). Maxwell et al. (2013) measured the thresholds for a wide range of *ex-vivo* tissues with short 1-MHz pulses, including clots, using a regime of therapeutic ultrasound termed histotripsy (Xu et al. 2004). The cavitation threshold of clots was similar to that of pure water, suggesting similar nanometer-sized nuclei to that observed in water.

Cavitation from endogenous nuclei has been observed during sonothrombolysis. Maxwell et al. (2011) observed microbubble clouds as regions of hyperechogenicity using 10-MHz diagnostic ultrasound imaging while insonating thrombi in a porcine femoral vein artery at

1 MHz. Additional studies have observed acoustic emissions from inertial (Everbach and Francis 2000; Wright et al. 2012a) or stable cavitation (Datta et al. 2006) during ultrasound-enhanced thrombolysis.

Exogenous Nuclei

Introducing exogenous nuclei allows control of the type and location of cavitation activity. Hydrophobic particulates (Soltani 2013), perfluorocarbon droplets (Pajek et al. 2014) and focused laser pulses (Cui et al. 2013) have been used to nucleate cavitation effectively during sonothrombolysis. However, ultrasound contrast agents (UCAs), or stabilized microbubbles, are also used to nucleate cavitation. Excellent reviews of the principles of UCAs are provided by Stride and Saffari (2003) and Cosgrove (2006). The specific use of UCAs for sonothrombolysis is reviewed by de Saint et al. (2014). Briefly, most commercially available UCAs are composed of a high-molecular-weight inert gas core surrounded by a lipid shell (Faez et al. 2013). The use of a gas with low solubility in the blood stream and pegylation of the lipid shell increases the circulation lifetime (Sarkar et al. 2009). The large compressibility of the gas compared to the surrounding tissue results in a high backscatter of incident acoustic pulse. UCAs are excellent blood pooling agents for left ventricular opacification (Radhakrishnan et al. 2013), detection of focal lesions in the liver (Claudon et al. 2013) and evaluation of brain perfusion (Claudon et al. 2008). UCAs range in size from 1 to 10 μm in diameter (Bouakaz and de Jong 2007), which prevents filtration of UCAs by the lungs (Hogg 1987). In addition, UCAs of this size are resonant at diagnostic imaging frequencies (1–10 MHz). Current FDA-approved use of UCAs is restricted to left ventricular opacification, although there is a growing interest in using UCAs for therapeutic applications as well (Cosgrove and Harvey 2009; Stride et al. 2009).

To gauge the potential for generating therapeutic cavitation activity from UCAs, Bader and Holland (2012) investigated the nucleation and detection of stable cavitation numerically. The cavitation index (I_{CAV}) was devised to gauge the likelihood of stable cavitation activity from UCAs in terms of the peak rarefactional pressure in MPa (P_r) and center frequency in MHz (f):

$$I_{CAV} = P_r / f.$$

Bader and Holland found there was an increased likelihood of nucleating cavitation activity by rupturing the UCA shell when $I_{CAV} > 0.02$, and an increased likelihood of detecting subharmonic emissions from stable cavitation when $I_{CAV} > 0.09$. Subharmonic emissions are more likely from inertial cavitation when $I_{CAV} > 0.45$. The parameter space predicted by the cavitation index necessary to promote beneficial bioeffects from stable cavitation is in agreement with reported literature values, including sonothrombolysis studies (Fig. 19.5).

19.2.3.4 Know When Something Happens

Apfel's final golden rule refers to the detection of cavitation activity. While some *in-vitro* studies used high-speed imaging to monitor cavitation activity during sonothrombolysis (Caskey et al. 2009; Acconcia et al. 2013; Chen et al. 2014), such observations are not possible *in-vivo*. Devising methods to monitor cavitation is important to translate these treatments through the regulatory process and into the clinic (Harris 2009). The most common method of monitoring cavitation activity in sonothrombolysis studies is passive cavitation detection (Everbach and Francis 2000; Datta et al. 2006; Prokop et al. 2007), whereby cavitation acoustic emissions are passively received by a transducer. The frequency spectrum of the signal is inspected for the presence of either broadband emissions to indicate the presence of inertial cavitation, harmonic, subharmonic, or ultraharmonic emissions to indicate the presence of stable cavitation. The strength of these characteristic cavitation emissions can be correlated with thrombolytic efficacy in order to gain insight into the type of cavitation activity required to promote maximal thrombolytic efficacy. Chuang et al. (2010) found a positive correlation between the thrombolytic efficacy and the strength of broadband acoustic emissions in an *in-vitro* human clot model. In contrast, Datta

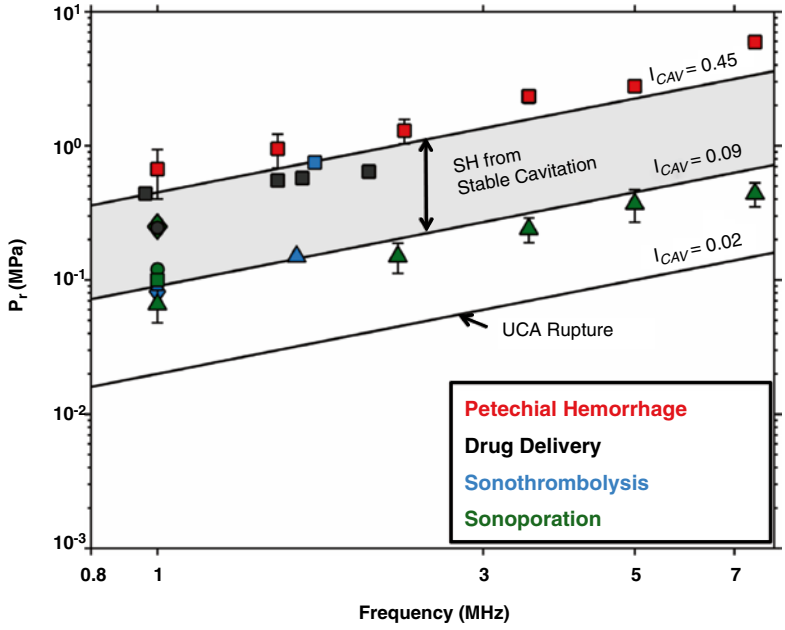

Fig. 19.5 Comparison of cavitation index to selected bioeffects (Bader and Holland 2012). The line labeled $I_{CAV}=0.45$ indicates the peak rarefractional pressure (P_r) required to initiate shell rupture of ultrasound contrast agents. The lines labeled $I_{CAV}=0.09$ and $I_{CAV}=0.45$ bordering the shaded region demarcate the parameter space over which subharmonic (SH) emissions from stable cavitation are likely. The cavitation index is well suited for predicting beneficial bioeffects associated with stable cavitation, such as drug delivery (Hitchcock et al. 2010; McDannold et al. 2008), sonoporation (Greenleaf et al. 1998; Miller and Dou 2004; Rahim et al. 2006; Juffermans et al. 2009) and sonothrombolysis (Porter et al. 2001; Prokop et al. 2007; Petit et al. 2012a). Beyond $I_{CAV}=0.45$, subharmonic emissions originate from inertial cavitation. Bioeffects associated with inertial cavitation, such as petechial hemorrhage (Miller et al. 2008), occur at a cavitation index above 0.45

et al. (2008) and Bader et al. (2015) found a positive correlation between thrombolytic efficacy and the strength of ultraharmonic emissions in *in-vitro* models.

Passive cavitation detection with single-element transducers provides limited information on the spatial distribution of cavitation activity. A new method of cavitation detection, passive cavitation imaging (PCI) (Salgaonkar et al. 2009; Haworth et al. 2012; Jensen et al. 2012), beamforms received cavitation signals from multiple-element arrays. The resulting passive cavitation images resolve the location and type of cavitation activity. Vignon et al. (2013) demonstrated the feasibility of PCI to detect and map cavitation activity *in-vivo* for thrombolysis studies. Shi et al. (2011) implemented the technique to monitor cavitation nucleated from Doppler exposure of Definity® in an *in-vivo* porcine model. Cavitation emissions mapped within the porcine skull were a mixture of both stable and inertial cavitation at the lower Doppler amplitudes (0.46 mechanical index). Only inertial cavitation was observed at the higher Doppler amplitudes (1.7 mechanical index).

19.3 Experimental Evidence for Ultrasound-Enhanced Efficacy

19.3.1 Assessment of Sonothrombolysis in the Laboratory

Since the first demonstration of ultrasound-enhanced thrombolysis by Sobbe et al. in 1974, nearly 500 studies have been published on sonothrombolysis (Scopus search engine,

Accessed 9 July 2014). These studies have included "bench top" experiments, designed to elucidate and maximize the mechanisms of ultrasound that enhance thrombolysis. The conclusions of these studies depend on the type of study (i.e., *in-vitro, ex-vivo,* or *in-vivo*), modeling of biological parameters (i.e., clot manufacturing process, thrombolytic metric, etc.), and the ultrasound exposure conditions.

19.3.1.1 *In-Vitro*, *Ex-Vivo*, and *In-Vivo* Studies

In-vitro studies minimize the complexity associated with biological systems to assess the interaction of ultrasound with clots in a controlled setting. Clot models have been developed through strict protocols in order to produce consistent, clinically-relevant clots (Holland et al. 2008). Coagulation is initiated by incubating fresh or recalcified blood at physiologic temperature (37 °C) (Roessler et al. 2011). Coagulation can also be initiated by the addition of thrombin to plasma (Lauer et al. 1992; Suchkova et al. 1998). Fibrin clots, which are optically translucent, are also used for optical studies (Acconcia et al. 2013). The degree of clot retraction can be modified by altering the properties of the surface in contact with incubated blood (Sutton et al. 2013b), or by storing the clot at low temperatures (<4 °C) for several days post-incubation (Shaw et al. 2006). Thrombolytic metrics have included mass loss (Datta et al. 2006), dimensional reduction on an image (Cheng et al. 2005; Kim et al. 2012; Petit et al. 2012a), or the presence of fibrin degradation products (Francis et al. 1992; Kimura et al. 1994; Pfaffenberger et al. 2003; Alonso et al. 2009). Interested readers are invited to review an exhaustive list of recent *in-vitro* studies compiled by Petit et al. (2012b).

Ex-vivo studies incorporate excised living tissue as a first step towards understanding the interaction of vascular tissue exposed to thrombolytics and ultrasound. Excised arteries have been employed to determine the effect on the endothelium during sonothrombolysis (Rosenschein et al. 2000; Hitchcock et al. 2011). Clot models are similar to those used *in-vitro*, and mass loss is used as the thrombolytic metric.

In-vivo animal models allow the full biological response of a living organism to ultrasound and thrombolytics to be assessed, including the efficacy of the treatment, the ability to track and monitor treatment progress, physiologic alterations, and the potential for collateral damage. These studies are required prior to U.S. Food and Drug Administration approval for new clinical devices (Harris 2009). A variety of *in-vivo* thrombosis models have been developed and are summarized by Hossmann (1998), Verbeuren (2006), and Mousa (2010). Small animal models, such as rodent (Daffertshofer et al. 2004) and rabbit (Hölscher et al. 2012), are used in sonothrombolysis due to their low cost, ease of handling, and accumulation of data from previous studies. Large animal models, such as swine (Culp 2004) and primates (Shimizu et al. 2012), are needed to model the propagation of ultrasound through the skull and brain architecture. Thrombus formation can be initiated by incubation of autologous blood within a stenotic artery (Culp 2004; Damianou et al. 2014). High-intensity laser pulses can also be used to induce clot formation (Yamashita et al. 2009; Chen et al. 2013). Flow velocity (Maxwell et al. 2011), degree of thrombus size burden (Stone et al. 2007), or the presence of fibrin degradation products (Xie et al. 2005; Yamashita et al. 2009) can be used to assess thrombolytic efficacy. Potential side effects are evaluated using imaging techniques, post-mortem histology and immunohistochemistry techniques.

19.3.1.2 Ultrasound Exposure Conditions

Insonation of thrombi to initiate lysis have been employed with and without thrombolytic drugs. UCAs have also been used to nucleate cavitation activity in both cases. The degree of thrombolysis is dependent on the ultrasound exposure conditions (Holland et al. 2008; Petit et al. 2012a).

Ultrasound Therapy Without a Thrombolytic

In the absence of a thrombolytic drug, lysis is initiated by the mechanical interaction of ultrasound energy with the thrombus. Maxwell et al. employed 1-MHz histotripsy pulses (Xu et al.

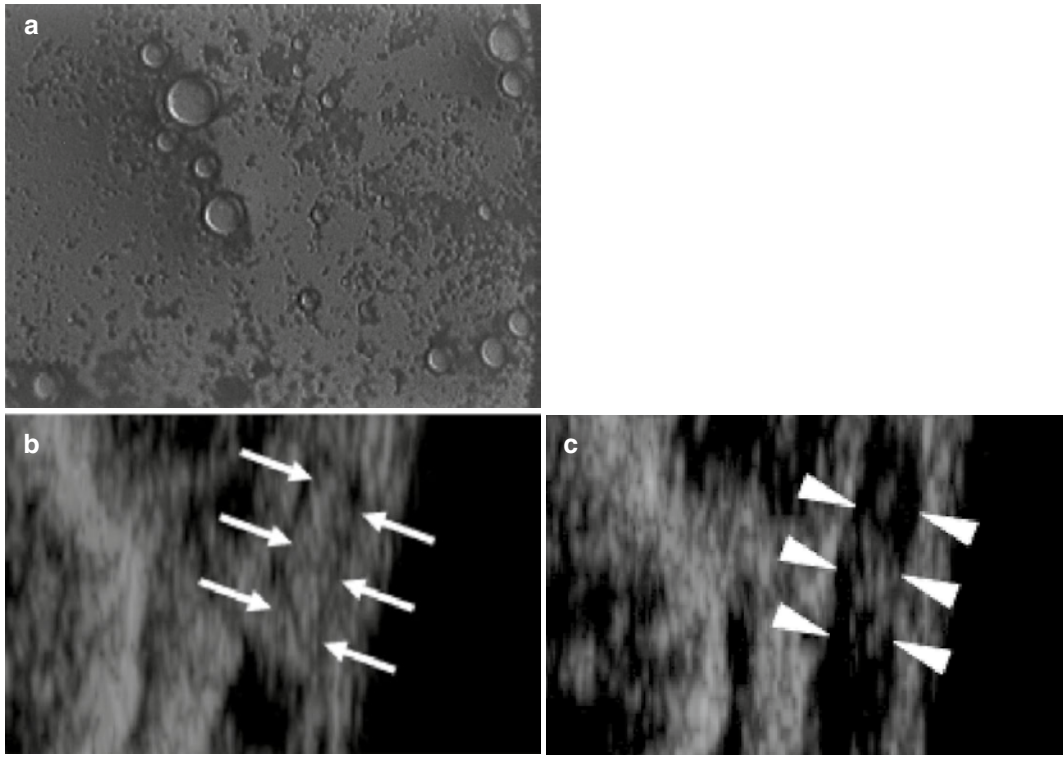

Fig. 19.6 (**a**) Photograph of thrombus-targeted microbubble bound to human whole blood clot *in-vitro*. Non-targeted microbubbles did not bind to the clot (Unger et al. 1998). (**b**) Thrombus-targeted bubble liposomes (*white arrows*) accumulate on thrombus within an occluded iliac artery in a rabbit model of thromboembolism. (**c**) After insonation of the thrombus-targeted bubble liposomes, flow was restored and the hyperechogenic area within the iliac artery was reduced (*white arrowheads*) (Hagisawa et al. 2013)

2004) to lyse clots *in-vitro* completely within 5 min (Maxwell et al. 2009). This technique reduced the thrombus size in 10 of 12 cases in an *in-vivo* swine model (Maxwell et al. 2011). Westermark et al. (1999) determined pulsed ultrasound increased the thrombolytic efficacy compared to continuous wave ultrasound *in-vitro*. Similarly, Rosenschein et al. (2000) and Wright et al. (2012a) found efficient thrombolysis with pulsed ultrasound both *in-vitro* and *in-vivo*. Moderate collateral damage was observed *in-vivo* in the form of coagulative necrosis (Rosenschein et al. 2000), hemorrhage (Wright et al. 2012a; Burgess et al. 2012), or denudation of the endothelium (Maxwell et al. 2011). These deleterious effects could be explained by the relatively small size of the vessel relative to the focal zone of the transducer (Maxwell et al. 2011), or by standing waves (Burgess et al. 2012).

Ultrasound Therapy with Microbubbles, but Without a Thrombolytic

Sonothrombolysis was investigated in several *in-vitro* (Borrelli et al. 2012) and *in-vivo* (Birnbaum et al. 1998; Culp et al. 2003; Xie et al. 2005) studies by insonation of microbubbles alone to initiate thrombolysis. These studies confirm thrombolytic efficacy using ultrasound and microbubbles alone, emphasizing the importance of cavitation activity. Several groups have developed thrombus-specific microbubbles with the ability to target clots for both imaging (Unger et al. 1998; Chen et al. 2009) and therapy (Alonso et al. 2009; Hagisawa et al. 2013) (Fig. 19.6).

Culp (2004) investigated thrombolytic efficacy of a clot-targeted microbubble formulation in a porcine model. In a follow-up study (Culp et al. 2011), a rabbit carotid stroke model insonated with pulsed, 1-MHz ultrasound and

microbubbles alone had a significantly smaller infarct volume than with rt-PA alone, or rt-PA with ultrasound exposure. However, there was no significant difference in the infarct volume if targeted or non-targeted microbubbles were used. Several additional studies demonstrated enhanced thrombolytic efficacy *in-vitro* (Unger et al. 1998; Chen et al. 2009) and *in-vivo* (Alonso et al. 2009; Hagisawa et al. 2013) using targeted microbubbles. It should be noted that the treatment parameters employed in several other studies did not produce appreciable thrombolytic efficacy with ultrasound alone (Frenkel et al. 2006; Datta et al. 2006; Prokop et al. 2007; Shaw et al. 2008; Petit et al. 2012a) or with microbubbles (Datta et al. 2008; Petit et al. 2012a; Bader et al. 2015).

Ultrasound Therapy with a Thrombolytic

Although lysis with ultrasound alone is a promising means to overcome strict contraindication criteria of thrombolytic drugs (Turi et al. 1993), drug-mediated thrombolysis remains the gold-standard in clinical practice. In this treatment regime, ultrasound is considered an adjuvant therapy, without the intent of completely replacing thrombolytic drugs. Early *in-vitro* studies by Lauer et al. (1992), and later by Francis and his colleagues (Francis et al. 1992; Blinc et al. 1993; Francis et al. 1995), found enhancement of rt-PA with ultrasound exposure. Meunier et al. (2007) found an increasing thrombolytic efficacy over rt-PA alone as a function of duty cycle over the range 10–80% at 120 kHz. However, subsequent studies by the same group found no distinct trend with duty cycle (Holland et al. 2008). Datta et al. (2006) demonstrated thrombolytic enhancement only when cavitation emissions were detected.

Ultrasound Therapy with Microbubbles and a Thrombolytic

Introducing ultrasound contrast agents, or stabilized microbubbles, can reduce the threshold for cavitation activity. De Saint et al. (2014) provides an extensive review of the use of microbubbles in sonothrombolysis. Tachibana and Tachibana (1995) pioneered the use of microbubbles in sonothrombolysis, insonating Albunex® with urokinase at 170 kHz to increase thrombolytic efficacy over urokinase alone, or urokinase with ultrasound exposure. Subsequent studies confirmed the thrombolytic enhancement *in-vitro,* with sub-megahertz ultrasound exposure (Datta et al. 2008; Hitchcock et al. 2011; Bader et al. 2015) as well as with diagnostic imaging frequencies (Kondo et al. 1999; Cintas et al. 2004; Xie et al. 2011). Nedelmann et al. (2010) found an increase in thrombolytic efficacy *in-vivo* with transcranial color-coded duplex Doppler, SonoVue®, and rt-PA when compared with rt-PA alone. Edema and lesion volumes were significantly smaller when microbubbles and rt-PA were exposed to ultrasound than exposed to rt-PA alone. However, Brown et al. (2011) found the infarct volume in a rabbit carotid artery model was not significantly smaller when Definity® and rt-PA were insonified compared to rt-PA alone. Hitchcock et al. (2011) developed a novel *ex-vivo* porcine carotid model and measured significant thrombolytic efficacy when Definity® and rt-PA were exposed to sub-megahertz ultrasound over rt-PA alone. Sutton et al. (2013b) extended this model, and showed that increased thrombolysis occurred only in unretracted clots. Xie et al. (2013) noted that epicardial recanalization was greatest in a porcine atherosclerotic model when Doppler pulses induced cavitation activity from Definity® in the presence of rt-PA.

Drug-loaded microbubbles also show potential as a "theragnostic" approach for enhancing thrombolytic efficacy. Echogenic liposomes (ELIP), liposomes containing air-filled microbubbles, can be used as a vector for therapeutic drugs. Incorporation of rt-PA into ELIP, or t-ELIP, allows acoustic activation (Smith et al. 2010) for localized drug delivery. *In-vitro* studies have demonstrated enhanced thrombolytic efficacy of t-ELIP and ultrasound over rt-PA alone (Shaw et al. 2009), or over rt-PA, ultrasound and Optison™ combined (Tiukinhoy-Laing et al. 2007). Hua et al. (2014) treated thrombi in a rabbit femoral artery using targeted microbubbles loaded with rt-PA and 2-MHz ultrasound. The recanalization rates obtained with rt-PA targeted microbubbles were similar to those with a combination of untargeted microbubbles and free rt-PA.

19.3.1.3 Conclusions of Bench Top Studies

Ultrasound is well established to enhance thrombolysis *in-vitro* (Datta et al. 2006; Prokop et al. 2007), *ex-vivo* (Hitchcock et al. 2011), and *in-vivo* (Culp 2004; Xie et al. 2013). Mechanical effects, particularly acoustic cavitation (Petit et al. 2012a; Wu et al. 2014; Bader et al. 2015), are clearly responsible for enhanced thrombolysis. These bench top experiments provide proof of concept for a particular insonation scheme, but the results are restricted to the particular clot model employed (Xie et al. 2011). Given the variability in thrombi composition *in-vivo* (Liebeskind et al. 2011), future studies should focus on both the insonation regime and subtype of clot in order to employ the optimal treatment regime. For example, thrombolytic enhancement was not possible for low-amplitude (<0.25 MPa peak negative pressure), sub-megahertz insonation of retracted clots treated with Definity® and rt-PA (Sutton et al. 2013b). Other insonation schemes need to be developed for these stiff, retracted thrombi. Studies are also needed to determine the thrombus type, for example using elastography techniques (Viola et al. 2004) to determine the optimal ultrasound approach. Finally, methods to monitor and quantify the dose of cavitation energy, possibly employing PCI (Haworth et al. 2012), need to be further developed in order to monitor treatment progress.

19.3.2 Clinical Trials

19.3.2.1 Catheter-Directed Thrombolysis

Significant progress has been made over the past decade to translate ultrasound from the bench to the bedside. Catheter-directed ultrasound-accelerated thrombolysis has been successfully employed to treat peripheral arterial occlusions (Greenberg et al. 1999), stroke (The IMS II Trial Investigators 2007), deep venous thrombosis (Raabe 2006), and pulmonary embolism (PE) (Engelberger and Kucher 2014). Catheter-based ultrasound initiated complete or partial recanalization in 87.9% of cases in a review of 340 clinical cases (Doomernik et al. 2011). Overall rates of non-response (8.2%), complications (7.1%), bleeding (4.1%) and re-occlusion (2.1%) were low compared to conventional thrombolytic treatment. No distal embolization was reported during treatment. Engelberger and Kucher (2014) compiled the results from clinical studies of PE treatment with ultrasound catheter-directed thrombolysis and found similar clinical outcomes compared to administration of the thrombolytic tenecteplase, a genetically modified version of rt-PA (Baruah et al. 2006). In the first randomized trial employing an ultrasound catheter device, 59 patients with acute PE were treated with either the EKOS Endovascular System and rt-PA, or anticoagulation therapy alone (Kucher et al. 2013). The authors concluded ultrasound-assisted thrombolysis was the superior treatment versus anticoagulation at 24 h, without an increased bleeding risk.

19.3.2.2 Transcranial Insonation

The therapeutic effect of transcranial insonation during intravenous rt-PA treatment for acute stroke has been investigated independently by three stroke therapy centers: University of Texas-Houston Medical School (Alexandrov et al. 2000), University of Lübeck, Germany (Eggers et al. 2003), and University Hospital Ostrava, Czech Republic (Skoloudik et al. 2008). Based on these findings, randomized studies employing either TCD in the CLOTBUST trial (Alexandrov et al. 2004), or TCCS in the Eggers study (Eggers et al. 2008) were conducted (Fig. 19.7). Both studies found significant improved recanalization for the sonothrombolysis groups, with an improvement in neurological deficits after 4 days and functional independence after 3 months. The CLOTBUST trial however found no difference in the rate of symptomatic intracranial hemorrhage between the control and sonothrombolysis groups. The Eggers study found no significant correlation between exposure to TCCS and symptomatic cerebral bleeding. Preliminary studies found further thrombolytic enhancement when employing TCD in combination with Levovist® (Molina et al. 2006) or TCCS with SonoVue® (Perren et al. 2007), and there was

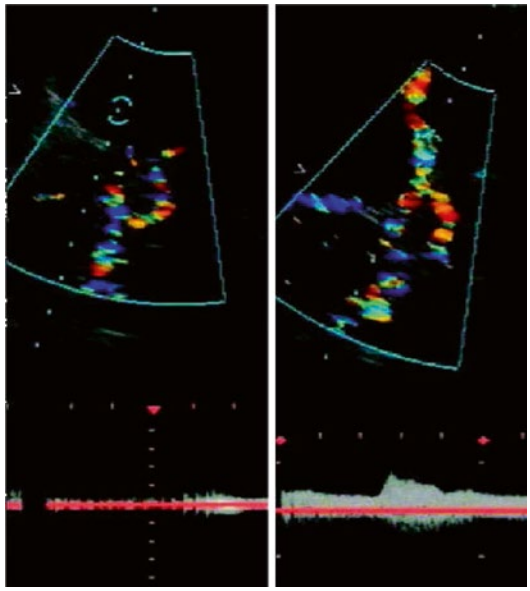

Fig. 19.7 Transcranial color-coded sonography in an ischemic stroke patient with an MCA occlusion. Proximal middle cerebral artery stem occlusion (*left*) with complete recanalization 1 h after intravenous rt-PA plus TCCS exposure (*right*) (Eggers et al. 2003)

no report of an increase in intracranial bleeding. A randomized trial employing MRX-801 (ImaRx Therapeutics, Inc., Redmond, WA, USA), a microbubble developed purposely for enhancing sonothrombolysis, exposed to TCD was discontinued by the sponsor after microbubble dose-escalation resulted in increased bleeding (Molina et al. 2009). The combination of TCD, MRX-801, and rt-PA demonstrated increased early recanalization and clinical recovery rates compared to rt-PA alone.

Performing meta-analysis of the results from ten clinical studies of both randomized control trials and case control studies, Saqqur et al. (2013) found TCD and TCCS sonothrombolysis was safe, effective and had more than a twofold likelihood of favorable long-term outcome. Furthermore, subgroup analysis of the use of ultrasound and microbubbles was both safe and more effective than thrombolytic therapy alone, when symptomatic intracranial hemorrhage was considered as the primary safety outcome. In contrast, a meta-analysis by Ricci et al. (2012) of seven randomized control trials found an increased risk of hemorrhage in connection with microbubbles and ultrasound, when both symptomatic and asymptomatic cerebral bleeding were considered. The success of using TCD and TSSC during treatment of ischemic stroke has prompted a host of ongoing trials (Dwedar et al. 2014; Haukeland University Hospital 2014; la Santa Creu i Sant Pau 2014), including successful completion of phase II trials employing a hands-free therapeutic device (Barreto et al. 2013).

19.3.2.3 Conclusions of Clinical Studies

The success of these clinical trials motivates the viability of ultrasound as a therapy for thrombo-occlusive disease. The prospect of co-administration of thrombolytic drugs with microbubbles is especially encouraging. Cavitation detection schemes should be implemented in future studies to inform what specific type of bubble activity promotes thrombolysis. Future TCD studies employing user-free devices may help decrease the patient-to-patient variability (Barlinn et al. 2013). The means to obtain reproducible and predictable transcranial sub-megahertz ultrasound fields have been devised (Bouchoux et al. 2014), and the approach appears safe in large primate models (Shimizu et al. 2012).

19.4 Conclusions and Future Directions

Thrombosis is a major contributor to mortality and morbidity in cardiovascular disease. Although administration of thrombolytic drugs is the current standard clinical treatment, adjuvant therapies are under development. Ultrasound has been demonstrated as an effective adjuvant for thrombolytic drugs *in-vitro*, *in-vivo*, and in clinical trials. Of particular interest are insonation schemes that obviate the need for thrombolytic drugs. A considerable degree of variability in clot models exists amongst bench top experiments (Petit et al. 2012b). Thrombus architecture and lytic susceptibility varies depending on the origin of the thrombus (Silvain et al. 2011). Ultrasound-

enhanced thrombolysis studies at present have only rarely considered the effect of thrombus composition (Sutton et al. 2013b). Thus a single insonation parameter set may not be effective for all thrombus subtypes. Future studies should focus on the effect of ultrasound on a particular subtype of thrombus to determine what treatment type is optimal for each thrombus type.

Radiation force and acoustic streaming are proposed mechanisms for ultrasound enhancement. In addition, mechanisms related to cavitation are strongly correlated with the enhancement of thrombolytic efficacy. Therefore, potent sonothrombolysis may be achieved by promoting cavitation. In particular, the use of microbubbles to nucleate cavitation both expedites the lytic rate and improves the functional outcome, both *in-vivo* and in clinical studies. Although these findings are most promising, UCAs are currently only FDA-approved for diagnostic purposes. Furthermore, specific devices designed to produce and monitor safe and efficient cavitation activity are needed. Thus, substantial work is still underway to identify standards to monitor and control therapies employing both spontaneous and UCA nucleated microbubble activity.

In summary, ultrasound shows great promise in the treatment of acute and chronic thrombotic disease. While further bench top measurements are needed to elucidate the mechanisms and assess potential risks, clinical trials are also required for optimal and safe clinical implementation.

References

Aaslid R, Markwalder TM, Nornes H (1982) Noninvasive transcranial Doppler ultrasound recording of flow velocity in basal cerebral arteries. J Neurosurg 57: 769–774

Acconcia C, Leung BYC, Hynynen K, Goertz DE (2013) Interactions between ultrasound stimulated microbubbles and fibrin clots. Appl Phys Lett 103:053701

Adeoye O, Clark JF, Khatri P, Wagner KR, Zuccarello M, Pyne-Geithman GJ (2010) Do current animal models of intracerebral hemorrhage mirror the human pathology? Transl Stroke Res 2:17–25

Alexandrov AV, Demchuk AM, Felberg RA, Christou I, Barber PA, Burgin WS, Malkoff M, Wojner AW, Grotta JC (2000) High rate of complete recanalization and dramatic clinical recovery during tPA infusion when continuously monitored with 2-MHz transcranial Doppler monitoring. Stroke 31:610–614

Alexandrov AV, Molina CA, Grotta JC, Garami Z, Ford SR, Alvarez-Sabin J, Montaner J, Saqqur M, Demchuk AM, Moyé LA, Hill MD, Wojner AW, Clotbust Investigators (2004) Ultrasound-enhanced systemic thrombolysis for acute ischemic stroke. N Engl J Med 351:2170–2178

Alonso A, Dempfle C-E, Martina Della A, Stroick M, Fatar M, Zohsel K, Allémann E, Hennerici MG, Meairs S (2009) In vivo lysis of human thrombus with intravenous abciximab immunobubbles and ultrasound. Thromb Res 124:70–74

Ammi AY, Mast TD, Huang IH, Abruzzo TA, Coussios CC, Shaw GJ, Holland CK (2008) Characterization of ultrasound propagation through ex-vivo human temporal bone. Ultrasound Med Biol 34:1578–1589

Apfel RE (1981) Acoustic cavitation. In: Edmonds PD (ed) Methods in experimental physics. Academic, New York, pp 355–411

Azuma T, Ogihara M, Kubota J, Sasaki A, Umemura S, Furuhata H (2010) Dual-frequency ultrasound imaging and therapeutic bilaminar array using frequency selective isolation layer. IEEE Trans Ultrason Ferrelectr Freq Control 57:1211–1224

Bader KB, Holland CK (2012) Gauging the likelihood of stable cavitation from ultrasound contrast agents. Phys Med Biol 58:127–144

Bader KB, Raymond JL, Mobley J, Church CC, Felipe Gaitan D (2012) The effect of static pressure on the inertial cavitation threshold. J Acoust Soc Am 132:728

Bader KB, Gruber MJ, Holland CK (2015) Shaken and stirred: mechanisms enhancing thrombolysis with submegahertz ultrasound. Ultrasound Med Biol 41: 187–196

Barlinn K, Alexandrov AV (2013) Sonothrombolysis in ischemic stroke. Curr Treat Options Neurol 15:91–103

Barlinn K, Tsivgoulis G, Molina CA, Alexandrov DA, Schafer ME, Alleman J, Alexandrov AV, TUCSON Investigators (2012) Exploratory analysis of estimated acoustic peak rarefaction pressure, recanalization, and outcome in the transcranial ultrasound in clinical sonothrombolysis trial. J Clin Ultrasound 41:354–360

Barlinn K, Barreto AD, Sisson A, Liebeskind DS, Schafer ME, Alleman J, Zhao L, Shen L, Cava LF, Rahbar MH, Grotta JC, Alexandrov AV (2013) CLOTBUST-hands free: initial safety testing of a novel operator-independent ultrasound device in stroke-free volunteers. Stroke 44:1641–1646

Baron C, Aubry J-F, Tanter M, Meairs S, Fink M (2009) Simulation of intracranial acoustic fields in clincial trials of sonothrombolysis. Ultrasound Med Biol 35:1148–1158

Barreto AD, Alexandrov AV, Shen L, Sisson A, Bursaw AW, Sahota P, Peng H, Ardjomand-Hessabi M, Pandurengan R, Rahbar MH, Barlinn K, Indupuru H, Gonzales NR, Savitz SI, Grotta JC (2013) CLOTBUST-Hands Free: pilot safety study of a novel

operator-independent ultrasound device in patients with acute ischemic stroke. Stroke 44:3376–3381
Baruah DB, Dash RN, Chaudhari MR, Kadam SS (2006) Plasminogen activators: a comparison. Vasc Pharmacol 44:1–9
Bell WR, Simon TL (1982) Current status of pulmonary thromboembolic disease: pathophysiology, diagnosis, prevention, and treatment. Am Heart J 103:239–262
Birnbaum Y, Luo H, Nagai T, Fishbein MC, Peterson TM, Li S, Kricsfeld D, Porter TR, Siegel RJ (1998) Noninvasive in vivo clot dissolution without a thrombolytic drug: recanalization of thrombosed iliofemoral arteries by transcutaneous ultrasound combined with intravenous infusion of microbubbles. Circulation 97:130–134
Blinc A, Francis CW, Trudnowski JL, Carstensen EL (1993) Characterization of ultrasound-potentiated fibrinolysis in vitro. Blood 81:2636–2643
Borrelli MJ, O'Brien WD, Hamilton E, Oelze ML, Wu J, Bernock LJ, Tung S, Rokadia H, Culp WC (2012) Influences of microbubble diameter and ultrasonic parameters on in vitro sonothrombolysis efficacy. J Vasc Interv Radiol 23:1677–1684
Bouakaz A, de Jong N (2007) WFUMB safety symposium on echo-contrast agents: nature and types of ultrasound contrast agents. Ultrasound Med Biol 33:187–196
Bouchoux G, Bader KB, Korfhagen JJ, Raymond JL, Shivashankar R, Abruzzo TA, Holland CK (2012) Experimental validation of a finite-difference model for the prediction of transcranial ultrasound fields based on CT images. Phys Med Biol 57: 8005–8022
Bouchoux G, Shivashankar R, Abruzzo TA, Holland CK (2014) In silico study of low-frequency transcranial ultrasound fields in acute ischemic stroke patients. Ultrasound Med Biol 40:1154–1166
Brott T, Thalinger K, Hertzberg V (1986) Hypertension as a risk factor for spontaneous intracerebral hemorrhage. Stroke 17:1078–1083
Brown AT, Flores R, Hamilton E, Roberson PK, Borrelli MJ, Culp WC (2011) Microbubbles improve sonothrombolysis in vitro and decrease hemorrhage in vivo in a rabbit stroke model. Invest Radiol 46:202–207
Brujan E, Nahen K, Schmidt P, Vogel A (2001) Dynamics of laser-induced cavitation bubbles near an elastic boundary. J Fluid Mech 433:251–281
Burgess A, Huang Y, Waspe AC, Ganguly M, Goertz DE, Hynynen K (2012) High-Intensity Focused Ultrasound (HIFU) for dissolution of clots in a rabbit model of embolic stroke. PLoS One 7:e42311
Caskey CF, Qin S, Dayton PA, Ferrara KW (2009) Microbubble tunneling in gel phantoms. J Acoust Soc Am 125:EL183
Casscells W (2003) Vulnerable atherosclerotic plaque: a multifocal disease. Circulation 107:2072–2075
Castano C, Dorado L, Guerrero C, Millan M, Gomis M, Perez de la Ossa N, Castellanos M, Garcia MR, Domenech S, Davalos A (2010) Mechanical thrombectomy with the solitaire AB device in large artery occlusions of the anterior circulation: a pilot study. Stroke 41:1836–1840
Chen SC, Ruan JL, Cheng PW, Chuang YH, Li PC (2009) In vitro evaluation of ultrasound-assisted thrombolysis using a targeted ultrasound contrast agent. Ultrason Imaging 31:235–246
Chen R, Paeng D-G, Lam KH, Zhou Q, Shung KK, Matsuoka N, Humayun MS (2013) In vivo sonothrombolysis of ear marginal vein of rabbits monitored with high-frequency ultrasound needle transducer. J Med Biol Eng 33:103–110
Chen X, Leeman JE, Wang J, Pacella JJ, Villanueva FS (2014) New insights into mechanisms of sonothrombolysis using ultra-high-speed imaging. Ultrasound Med Biol 40:258–262
Cheng JY, Shaw GJ, Holland CK (2005) In vitro microscopic imaging of enhanced thrombolysis with 120-kHz ultrasound in a human clot model. Acoust Res Lett Online 6:25–29
Choi JJ, Coussios CC (2012) Spatiotemporal evolution of cavitation dynamics exhibited by flowing microbubbles during ultrasound exposure. J Acoust Soc Am 132:3538
Chuang YH, Cheng PW, Chen SC, Ruan JL, Li PC (2010) Effects of ultrasound-induced inertial cavitation on enzymatic thrombolysis. Ultrason Imaging 32:81–90
Church CC (2002) Spontaneous homogeneous nucleation, inertial cavitation and the safety of diagnostic ultrasound. Ultrasound Med Biol 28:1349–1364
Church CC, Labuda C, Nightingale K (2015) A theoretical study of inertial cavitation from acoustic radiation force impulse (ARFI) imaging and implications for the mechanical index. Ultrasound Med Biol 41:472–485
Ciccone A, Valvassori L, Nichelatti M, Sgoifo A, Ponzio M, Sterzi R, Boccardi and SYNTHESIS Expansion Investigators (2013) Endovascular treatment for acute ischemic stroke. N Engl J Med 368:904–913
Cintas P, Le Traon AP, Larrue V (2002) High rate of recanalization of middle cerebral artery occlusion during 2-MHz transcranial color-coded doppler continuous monitoring without thrombolytic drug. Stroke 33:626–628
Cintas P, Nguyen F, Boneu B, Larrue V (2004) Enhancement of enzymatic fibrinolysis with 2-MHz ultrasound and microbubbles. J Thromb Haemost 2:1163–1166
Claudon M, Cosgrove D, Albrecht T, Bolondi L, Bosio M, Calliada F, Correas JM, Darge K, Dietrich C, D'Onofrio M, Evans DH, Filice C, Greiner L, Jager K, Nd J, Leen E, Lencioni R, Lindsell D, Martegani A, Meairs S, Nolsoe C, Piscaglia F, Ricci P, Seidel G, Skjoldbye B, Solbiati L, Thorelius L, Tranquart F, Weskott HP, Whittingham T (2008) Guidelines and good clinical practice recommendations for Contrast Enhanced Ultrasound (CEUS) – update 2008. Ultraschall Med 29:28–44
Claudon M, Dietrich CF, Choi BI, Cosgrove D, Kudo M, Nolsoe C, Piscaglia F, Wilson SR, Barr RG, Chammas MC, Chaubal NG, Chen MH, Clevert DA, Correas JM, Ding H, Forsberg F, Fowlkes JB, Gibson RN, Goldberg BB, Lassau N, Leen EL, Mattrey RF, Moriyasu F, Solbiati L, Weskott HP, Xu HX, World Federation for Ultrasound in Medicine, European

Federation of Societies for Ultrasound (2013) Guidelines and good clinical practice recommendations for Contrast Enhanced Ultrasound (CEUS) in the liver-update 2012. Ultrasound Med Biol 39:187–210
Collis J, Manasseh R, Liovic P, Tho P, Ooi A, Petkovic-Duran K, Zhu Y (2010) Cavitation microstreaming and stress fields created by microbubbles. Ultrasonics 50:273–279
Commander KW, Prosperetti A (1989) Linear pressure waves in bubbly liquids: comparison between theory and experiments. J Acoust Soc Am 85:1–15
Cosgrove D (2006) Ultrasound contrast agents: an overview. Eur J Radiol 60:324–330
Cosgrove D, Harvey C (2009) Clinical uses of microbubbles in diagnosis and treatment. Med Biol Eng Comput 47:813–826
Cui H, Zhang T, Yang X (2013) Laser-enhanced cavitation during high intensity focused ultrasound 102: 133702
Culp WC (2004) Intracranial clot lysis with intravenous microbubbles and transcranial ultrasound in swine. Stroke 35:2407–2411
Culp WC, Porter TR, McCowan TC, Roberson PK, James CA, Matchett WJ, Moursi M (2003) Microbubble-augmented ultrasound declotting of thrombosed arteriovenous dialysis grafts in dogs. J Vasc Interv Radiol 14:343–347
Culp WC, Flores R, Brown AT, Lowery JD, Roberson PK, Hennings LJ, Woods SD, Hatton JH, Culp BC, Skinner RD, Borrelli MJ (2011) Successful microbubble sonothrombolysis without tissue-type plasminogen activator in a rabbit model of acute ischemic stroke. Stroke 42:2280–2285
Daffertshofer M, Huang Z, Fatar M, Popolo M, Schroeck H, Kuschinsky W, Moskowitz MA, Hennerici MG (2004) Efficacy of sonothrombolysis in a rat model of embolic ischemic stroke. Neurosurgery 361:115–119
Daffertshofer M, Gass A, Ringleb P, Sitzer M, Sliwka U, Els T, Sedlaczek O, Koroshetz WJ, Hennerici MG (2005) Transcranial low-frequency ultrasound-mediated thrombolysis in brain ischemia: increased risk of hemorrhage with combined ultrasound and tissue plasminogen activator: results of a phase II clinical trial. Stroke 36:1441–1446
Damianou C, Hadjisavvas V, Mylonas N, Couppis A, Ioannides K (2014) MRI-guided sonothrombolysis of rabbit carotid artery. J Stroke Cerebrovasc 23:e113–e121
Datta S, Coussios C-C, McAdory LE, Tan J, Porter T, De Courten-Myers G, Holland CK (2006) Correlation of cavitation with ultrasound enhancement of thrombolysis. Ultrasound Med Biol 32:1257–1267
Datta S, Coussios C-C, Ammi AY, Mast TD, de Courten-Myers GM, Holland CK (2008) Ultrasound-enhanced thrombolysis using Definity® as a cavitation nucleation agent. Ultrasound Med Biol 34:1421–1433
de Saint VM, Crake C, Coussios CC, Stride E (2014) Properties, characteristics and applications of microbubbles for sonothrombolysis. Expert Opin Drug Deliv 11:187–209
Devcic-Kuhar B, Pfaffenberger S, Grschl M, Kollmann C, Benes E, Gottsauner-Wolf M (2002) In vitro thrombolysis enhanced by standing and travelling ultrasound wave fields. Ultrasound Med Biol 28: 1181–1187
Doomernik DE, Schrijver AM, Zeebregts CJ, de Vries JP, Reijnen MM (2011) Advancements in catheter-directed ultrasound-accelerated thrombolysis. J Endovasc Ther 18:418–434
Dwedar AZ, Ashour S, Haroun M, El Nasser AA, Moustafa RR, Ibrahim MH, Elsadek A (2014) Sonothrombolysis in acute middle cerebral artery stroke. Neurol India 62:62–65
Eggers J, Koch B, Meyer K, Konig I, Seidel G (2003) Effect of ultrasound on thrombolysis of middle cerebral artery occlusion. Ann Neurol 53:797–800
Eggers J, Konig IR, Koch B, Handler G, Seidel G (2008) Sonothrombolysis with transcranial color-coded sonography and recombinant tissue-type plasminogen activator in acute middle cerebral artery main stem occlusion: results from a randomized study. Stroke 39:1470–1475
Elder SA (1959) Cavitation microstreaming. J Acoust Soc Am 31:54–64
Engelberger RP, Kucher N (2014) Ultrasound-assisted thrombolysis for acute pulmonary embolism: a systematic review. Eur Heart J 35:758–764
Everbach EC, Francis CW (2000) Cavitational mechanisms in ultrasound-accelerated thrombolysis at 1 MHz. Ultrasound Med Biol 26:1153–1160
Everbach EC, Guarini A (2013) Modeling of microbubbles pushed through clots via acoustic radiation force. In: International congress on acoustics montreal, New York, NY 2–7 June 2013
Faez T, Emmer M, Kooiman K, Versluis M, van der Steen A, de Jong N (2013) 20 years of ultrasound contrast agent modeling. IEEE Trans Ultrason Ferroelectr Freq Control 60:7–20
Falk E (1991) Coronary thrombosis: pathogenesis and clinical manifestations. Am J Cardiol 68:B28–B35
Fardanesh R, Kian L (2014) Nontransmural myocardial infarcion. In: White CS, Haramati LB, Chen JJ-S, Levsky JM (eds) Cardiac imaging, 1st edn. Oxford University Press, Oxford, pp 269–272
Flynn HG (1964) Physics of acoustic cavitation in liquids. In: Mason WP (ed) Physical acoustics. Academic, New York, pp 58–172
Francis CW, Onundarson PT, Carstensen EL, Blinc A, Meltzer RS, Schwarz K, Marder VJ (1992) Enhancement of fibrinolysis in vitro by ultrasound. J Clin Invest 90:2063–2068
Francis CW, Blinc A, Lee S, Cox C (1995) Ultrasound accelerates transport of recombinant tissue plasminogen activator into clots. Ultrasound Med Biol 21:419–424
Frenkel V, Oberoi J, Stone MJ, Park M, Deng C, Wood BJ, Neeman Z, Home M 3rd, Li KC (2006) Pulsed high-intensity focused ultrasound enhances thrombolysis in an in vitro model 1. Radiology 239:86–93
Fry FJ, Heimburger RF, Gibbons LV, Eggleton RC (1970) Ultrasound for visualization and modification of brain tissue. IEEE Trans Ultrason Ferroelectr Freq Control 17:165–169
Furie B, Furie BC (2008) Mechanisms of thrombus formation. N Engl J Med 359:938–949

Furuhata H, Saito O (2013) Comparative study of standing wave reduction methods using random modulation for transcranial ultrasonication. Ultrasound Med Biol 39:1440–1450

Fuster V (1994) Lewis A. Conner Memorial Lecture. Mechanisms leading to myocardial infarction: insights from studies of vascular biology. Circulation 90:2126–2146

Gaitan DF, Crum LA, Church CC, Roy RA (1992) Sonoluminescence and bubble dynamics for a single, stable, cavitation bubble. J Acoust Soc Am 91:3166

Go AS, Mozaffarian D, Roger VL, Benjamin EJ, Berry JD, Blaha MJ, Dai S, Ford ES, Fox CS, Franco S, Fullerton HJ, Gillespie C, Hailpern SM, Heit JA, Howard VJ, Huffman MD, Judd SE, Kissela BM, Kittner SJ, Lackland DT, Lichtman JH, Lisabeth LD, Mackey RH, Magid DJ, Marcus GM, Marelli A, Matcher DB, McGuire DK, Mohler ER 3rd, Moy CS, Mussolino ME, Neumar RW, Nichol G, Pandey DK, Paynter NP, Reeves MJ, Sorlie PD, Stein J, Towfighi TA, Turan TN, Virani SS, Wing ND, Woo D, Turner MB, American Heart Association Statistics Committee and Stroke Statistics Subcommittee (2013) Heart disease and stroke statistics–2013 update: a report from the American Heart Association. Circulation 127:e6–e245

Gralla J, Brekenfeld C, Mordasini P, Schroth G (2011) Mechanical thrombolysis and stenting in acute ischemic stroke. Stroke 43:280–285

Greenberg R, Ivancev K, Ouriel K (1999) High frequency ultrasound thrombolysis: phase I results. Am J Cardiol 84:42

Greenleaf WJ, Bolander ME, Sarkar G, Goldring MB, Greenleaf JF (1998) Artifical cavitation nuclei significantly enhance acoustically induced cell transfection. Ultrasound Med Biol 24:587–595

Gregg D (2003) Platelets and cardiovascular disease. Circulation 108:88e–90e

Hagisawa K, Nishioka T, Suzuki R, Maruyama K, Takase B, Ishihara M, Kurita A, Yoshimoto N, Nishida Y, Iida K, Luo H, Siegel RJ (2013) Thrombus-targeted perfluorocarbon-containing liposomal bubbles for enhancement of ultrasonic thrombolysis: in vitro and in vivo study. J Thromb Haemost 11:1565–1573

Harris GR (2009) FDA regulation of clinical high intensity focused ultrasound (HIFU) devices. In: 31st annual international conference of the IEEE EMBS. IEEE, Minneapolis, pp 145–148

Haukeland University Hospital The Norwegian Sonothrombolysis in Acute Stroke Study. In: clinicaltrials.gov. http://clinicaltrials.gov/show/NCT01949961. Accessed 19 May 2014

Haworth KJ, Mast TD, Radhakrishnan K, Burgess MT, Kopecheck JA, Huang SL, McPherson DD, Holland CK (2012) Passive imaging with pulsed ultrasound insonations. J Acoust Soc Am 132:544

Herbert E, Balibar S, Caupin F (2006) Cavitation pressure in water. Phys Rev E 74:041603

Higgins DL, Bennett RM (1990) Tissue plasminogen-activator – the biochemistry and pharmacology of variants produced by mutagenesis. Ann Rev Pharmacol 30:91–121

Hirsh J, Hoak J (1996) Management of deep vein thrombosis and pulmonary embolism. Circulation 93: 2212–2245

Hitchcock KE, Caudell DN, Sutton JT, Klegerman ME, Vela D, Pyne-Geithman GJ, Abruzzo T, Cyr PE, Geng YJ, McPherson DD, Holland CK (2010) Ultrasound-enhanced delivery of targeted echogenic liposomes in a novel ex vivo mouse aorta model. J Control Release 144:288–295

Hitchcock KE, Ivancevich NM, Haworth KJ, Caudell Stamper DN, Vela DC, Sutton JT, Pyne-Geithmann GJ, Holland CK (2011) Ultrasound-enhanced rt-PA thrombolysis in an ex vivo porcine carotid artery model. Ultrasound Med Biol 37:1240–1251

Hogg JC (1987) Neutrophil kinetics and lung injury. Physiol Rev 67:1249–1295

Holland CK, Apfel RE (1989) Improved theory for the prediction of microcavitation thresholds. IEEE Trans Ultras Ferroelectr Freq Control 36:204–208

Holland CK, Vaidya SS, Datta S, Coussios CC, Shaw GJ (2008) Ultrasound-enhanced tissue plasminogen activator thrombolysis in an in vitro porcine clot model. Thromb Res 121:663–673

Hölscher T, Fisher DJ, Ahadi G, Voie A (2012) Introduction of a rabbit carotid artery model for sonothrombolysis research. Transl Stroke Res 3: 397–407

Hölscher T, Ahadi G, Fisher D, Zadicario E, Voie A (2013) MR-guided focused ultrasound for acute stroke: a rabbit model. Stroke 44:S58–S60

Hölscher T, Raman R, Fisher DJ, Ahadi G, Zadicario E, Voie A (2013) Effects of varying duty cycle and pulse width on high-intensity focused ultrasound (HIFU)-induced transcranial thrombolysis. J Therap Ultrasound 1:18–22

Holzfuss J, Rüggeberg M, Billo A (1998) Shock wave emissions of a sonoluminescing bubble. Phys Rev Lett 81:5434–5437

Hossmann KA (1998) Experimental models for the investigation of brain ischemia. Cardiovasc Res 39: 106–120

Hua X, Zhou L, Liu P, He Y, Tan K, Chen Q, Gao Y, Gao Y (2014) In vivo thrombolysis with targeted microbubbles loading tissue plasminogen activator in a rabbit femoral artery thrombus model. J Thromb Thrombolysis 38:57–64

Jaff MR, McMurtry MS, Archer SL, Cushman M, Goldenberg N, Goldhaber SZ, Jenkins JS, Kline JA, Michaels AD, Thistlethwaite P, Vedantham S, White RJ, Zierler BK, American Heart Association Council on Cardiopulmonary, Critical Care, Perioperative and Resuscitation, American Heart Association Council on Peripheral Vascular Disease, American Hear Association Council on Arteriosclerosis, Thrombosis and Vascular Biology (2011) Management of massive and submassive pulmonary embolism, iliofemoral deep vein thrombosis, and chronic thromboembolic pulmonary hypertension: a scientific statement from the American Heart Association. Circulation 123:1788–1830

Jauch EC, Saver JL, Adams HP, Brino A, Connors JJ, Demaerschalk BM, Khatri P, McMullan PW Jr, Qureshi A, Rosenfield K, Scott PA, Summers DR, Wang DZ, Wintermark M, Yonas H, American Heart Association Stroke Council, Council on Cardiovascular Nursing, Council on Peripheral Vascular Disease, Council on Clinical Cardiology (2013) Guidelines for the early management of patients with acute ischemic stroke: a guideline for healthcare professionals from the American Heart Association/American Stroke Association. Stroke 44:870–947

Jensen CR, Ritchie RW, Gyöngy M, Collin JR, Leslie T, Coussios CC (2012) Spatiotemporal monitoring of high-intensity focused ultrasound therapy with passive acoustic mapping. Radiology 262:252–261

Juffermans LJM, van Dijk A, Jongenelen CAM, Drukarch B, Reijerkerk A, de Vries HE, Kamp O, Musters RJ (2009) Ultrasound and microbubble-induced intra- and intercellular bioeffects in primary endothelial cells. Ultrasound Med Biol 35:1917–1927

Kakkar VV, Flanc C, Howe CT, Clarke MB (1969) Natural history of postoperative deep-vein thrombosis. Lancet 2:230–232

Kearon C (2003) Natural history of venous thromboembolism. Circulation 107:I22–I30

Kim JS, Leeman JE, Kagemann L, Yu FT, Chen X, Pacella JJ, Schuman JS, Villanueva FS, Kim K (2012) Volumetric quantification of in vitrosonothrombolysis with microbubbles using high-resolution optical coherence tomography. J Biomed Opt 17:0705021

Kimura M, Iijima S, Kobayashi K, Furuhata H (1994) Evaluation of the thrombolytic effect of tissue-type plasminogen activator with ultrasonic irradiation: in vitro experiment involving assay of the fibrin degradation products from the clot. Biol Pharm Bull 17:126–130

Kondo I, Mizushige K, Ueda T, Masugata H, Ohmori K, Matsuo H (1999) Histological observations and the process of ultrasound contrast agent enhancement of tissue plasminogen activator thrombolysis with ultrasound exposure. Jap Circ J (English Edition) 63:478–484

Kucher N, Boekstegers P, Müller OJ, Kupatt C, Beyer-Westendorf J, Heitzer T, Tebbe U, Horstkotte J, Muller R, Blessing E, Greid M, Lange P, Hoffmann RT, Werth S, Barmeyer A, Hartel D, Greunwald H, Empen K, Baumgartner I (2013) Randomized, controlled trial of ultrasound-assisted catheter-directed thrombolysis for acute intermediate-risk pulmonary embolism. Circulation 129:479–486

la Santa Creu i Sant Pau de FI de R de L Sonothrombolysis Potentiated by Microbubbles for Acute Ischemic Stroke. In: clinicaltrials.gov. http://clinicaltrials.gov/ct2/show/NCT01678495?term=sonothrombolysis&rank=2. Accessed 19 May 2014

Labreuche J, Deplanque D, Touboul PJ, Bruckert E, Amarenco P (2010) Association between change in plasma triglyceride levels and risk of stroke and carotid atherosclerosis: systematic review and meta-regression analysis. Atherosclerosis 212:9–15

Lauer CG, Burge R, Tang DB, Bass BG, Gomez ER, Alving BM (1992) Effect of ultrasound on tissue-type plasminogen activator-induced thrombolysis. Circulation 86:1257–1264

Lauterborn W, Kurz T (2010) Physics of bubble oscillations. Rep Prog Phys 73:106501

Leeman JE, Kim JS, Yu FTH, Chen X, Kim K, Wang J, Chen X, Villanueva FS, Pacella JJ (2012) Effect of acoustic conditions on microbubble-mediate microvascular sonothrombolysis. Ultrasound Med Biol 38:1589–1598

Leighton TG (1994) The acoustic bubble. Academic, London

Liebeskind DS, Sanossian N, Yong WH, Starkman S, Tsang MP, Moya AL, Zheng DD, Abolian AM, Kim D, Ali LK, Shah SH, Towfighi A, Ovbiagele B, Kidwell CS, Tateshima S, Jahan R, Duckwiler GR, Vinuela F, Salamon N, Villablanca JP, Vinters HV, Marder VJ, Saver JL (2011) CT and MRI early vessel signs reflect clot composition in acute stroke. Stroke 42:1237–1243

Lighthill SJ (1978) Acoustic streaming. J Sound Vib 61: 391–418

Marder VJ, Chute DJ, Starkman S, Abolian AM, Kidwell C, Liebeskind D, Ovbiagele B, Vinuela F, Duckwiler G, Jahan R, Vespa PM, Selco S, Rajajee V, Kim D, Sanossian N, Saver JL (2006) Analysis of thrombi retrieved from cerebral arteries of patients with acute ischemic stroke. Stroke 37:2086–2093

Markel A (2005) Origin and natural history of deep vein thrombosis of the legs. Sem Vasc Med 5:65–74

Mathers CD, Loncar D (2006) Projections of global mortality and burden of disease from 2002 to 2030. PLoS Med 3:e442

Mathers C, Fat DM, Boerma JT (2008) The global burden of disease: 2004 update. World Health Organization, Geneva, Switzerland

Maxwell AD, Cain CA, Duryea AP, Yuan L, Gurm HS, Xu Z (2009) Noninvasive thrombolysis using pulsed ultrasound cavitation therapy – histotripsy. Ultrasound Med Biol 35:1982–1994

Maxwell AD, Owens G, Gurm HS, Ives K, Myers DD Jr, Xu Z (2011) Noninvasive treatment of deep venous thrombosis using pulsed ultrasound cavitation therapy (histotripsy) in a porcine model. J Vasc Interv Radiol 22:369–377

Maxwell AD, Cain CA, Hall TL, Fowlkes JB, Xu Z (2013) Probability of cavitation for single ultrasound pulses applied to tissues and tissue-mimicking materials. Ultrasound Med Biol 39:449–465

McDannold N, Vykhodtseva N, Hynynen K (2008) Blood-brain barrier disruption induced by focused ultrasound and circulating preformed microbubbles appears to be characterized by the mechanical index. Ultrasound Med Biol 34:834–840

Meunier JM, Holland CK, Lindsell CJ, Shaw GJ (2007) Duty cycle dependence of ultrasound enhanced thrombolysis in a human clot model. Ultrasound Med Biol 33:576–583

Miller DL, Dou C (2004) Membrane damage thresholds for 1- to 10-MHz pulsed ultrasound exposure of phagocytic cells loaded with contrast agent gas bodies in vitro. Ultrasound Med Biol 30:973–977

Miller DL, Dou C, Wiggins RC (2008) Frequency dependence of kidney injury induced by contrast-aided

diagnostic ultrasound in rats. Ultrasound Med Biol 34:1678–1687

Mohr G, Ferguson G, Khan M, Malloy D, Watts R, Benoit R, Weir B (1983) Intraventricular hemorrhage from ruptured aneurysm: retrospective analysis of 91 cases. J Neurosurg 58:482–487

Molina CA, Ribo M, Rubiera M, Montaner J, Santamarina E, Delgado-Mederos R, Arenillas JF, Huertas R, Purroy F, Delgado P, Alvarez-Sabin J (2006) Microbubble administration accelerates clot lysis during continuous 2-MHz ultrasound monitoring in stroke patients treated with intravenous tissue plasminogen activator. Stroke 37:425–429

Molina CA, Barreto AD, Tsivgoulis G, Sierzenski P, Malkoff MD, Rubiera M, Gonzales N, Mikulik R, Pate G, Ostrem J, Singleton W, Manvelian G, Unger EC, Grotta JC, Schellinger PD, Alexandrov AV (2009) Transcranial ultrasound in clinical sonothrombolysis (TUCSON) trial. Ann Neurol 66:28–38

Monteith SJ, Harnof S, Medel R, Popp B, Wintermark M, Lopes MB, Kassell NF, Elias WJ, Snell J, Eames M, Zadicario E, Moldovan K, Sheehan J (2013) Minimally invasive treatment of intracerebral hemorrhage with magnetic resonance–guided focused ultrasound. J Neurosurg 118:1035–1045

Mousa SA (2010) In vivo models for the evaluation of antithrombotics and thrombolytics. In: Methods in molecular biology. Humana Press, Totowa, pp 29–107

Nahirnyak V, Mast TD, Holland CK (2007) Ultrasound-induced thermal elevation in clotted blood and cranial bone. Ultrasound Med Biol 33:1285–1295

Nedelmann M, Ritschel N, Doenges S, Langheirich AC, Acker T, Reuter P, Yeniguen M, Pukropski J, Kaps M, Mueller C, Bachmann G, Gerriets T (2010) Combined contrast-enhanced ultrasound and rt-PA treatment is safe and improves impaired microcirculation after reperfusion of middle cerebral artery occlusion. J Cereb Blood Flow Metab 30:1712–1720

Newell DW, Shah MM, Wilcox R, Hansmann DR, Melnychuk E, Muschelli J, Hanley DF (2011) Minimally invasive evacuation of spontaneous intracerebral hemorrhage using sonothrombolysis. J Neurosurg 115:592–601

Novokhatny VV, Jesmok GJ, Landskroner KA, Vander VJ, Zimmerman TP (2004) Locally delivered plasmin: why should it be superior to plasminogen activators for direct thrombolysis? Trends Pharmacol Sci 25: 72–75

Nyborg WL (1953) Acoustic streaming due to attenuated plane waves. J Acoust Soc Am 25:68

Nyborg WL (1965) Acoustic streaming. In: Mason WP (ed) Physical acoustics. Academic, Waltham, pp 265–331

Nyborg WL, Miller DL (1982) Biophysical implications of bubble dynamics. Appl Sci Res 38:17–24

Pajek D, Hynynen K (2012) The design of a focused ultrasound transducer array for the treatment of stroke: a simulation study. Phys Med Biol 57:4951–4968

Pajek D, Burgess A, Huang Y, Hynynen K (2014) High-intensity focused ultrasound sonothrombolysis: The use of perfluorocarbon droplets to achieve clot lysis at reduced acoustic power. Ultrasound Med Biol 40:2131–2161

Pasceri V, Andreotti F, Maseri A (1996) Clinical markers of thrombolytic success. Eur Heart J 17(Suppl E): 35–41

Perler B (2005) Thrombolytic therapies: the current state of affairs. J Endovasc Ther 12:224–232

Perren F, Loulidi J, Poglia D, Landis T, Sztajzel R (2007) Microbubble potentiated transcranial duplex ultrasound enhances IV thrombolysis in acute stroke. J Thromb Thrombolysis 25:219–223

Petit B, Gaud E, Colevret D, Arditi M, Yan F, Tranquart F, Allemann E (2012a) In vitro sonothrombolysis of human blood clots with BR38 microbubbles. Ultrasound Med Biol 38:1222–1233

Petit B, Yan F, Tranquart F, Allemann E (2012b) Microbubbles and ultrasound-mediated thrombolysis: a review of recent in vitro studies. J Drug Deliv Sci Tec 22:381–392

Pfaffenberger S, Devcic-Kuhar B, El-Rabadi K, Groschl M, Speidl WS, Weiss TW, Huber K, Benes E, Maurer G, Wojta J, Gottsauner-Wolf M (2003) 2MHz ultrasound enhances t-PA-mediated thrombolysis: comparison of continuous versus pulsed ultrasound and standing versus travelling acoustic waves. Thromb Haemost 89:583–589

Porter TR, Kricsfeld D, Lof J, Everbach EC, Xie F (2001) Effectiveness of transcranial and transthoracic ultrasound and microbubbles in dissolving intravascular thrombi. J Ultrasound Med 20:1313–1325

Prokop AF, Soltani A, Roy RA (2007) Cavitational mechanisms in ultrasound-accelerated fibrinolysis. Ultrasound Med Biol 33:924–933

Puetz V, Dzialowski I, Hill MD, Subramaniam S, Sylaja PN, Krol A, O'Reilly C, Hudon ME, Hu WY, Coutts SB, Barber PA, Watson T, Roy J, Demchuk AM, Calgary CTA Study Group (2008) Intracranial thrombus extent predicts clinical outcome, final infarct size and hemorrhagic transformation in ischemic stroke: the clot burden score. Int J Stroke 3:230–236

Raabe RA (2006) Ultrasound facilitated thrombolysis in treating DVT. Endovascular Today 4:1–14

Radhakrishnan K, Bader KB, Haworth KJ, Kopechek JA, Raymond JL, Huang SL, McPherson DD, Holland CK (2013) Relationship between cavitation and loss of echogenicity from ultrasound contrast agents. Phys Med Biol 58:6541–6563

Rahim A, Taylor SL, Bush NL, ter Haar GR, Bamber JC, Porter CD (2006) Physical parameters affecting ultrasound/microbubble-mediated gene delivery efficiency in vitro. Ultrasound Med Biol 32:1269–1279

Rayleigh L (1917) On the pressure developed in a liquid during the collapse of a spherical cavity. Philos Mag 34:94–98

Reuning U, Magdolen V, Hapke S, Schmitt M (2003) Molecular and functional interdependence of the urokinase-type plasminogen activator system with integrins. Biol Chem 384:1119–1131

Rha JH, Saver JL (2007) The impact of recanalization on ischemic stroke outcome: a meta-analysis. Stroke 38:967–973

Ricci S, Dinia L, Del Sette M, Anzola P, Mazzoli T, Cenciarelli S, Gandolfo C (2012) Sonothrombolysis for acute ischaemic stroke. Cochrane Database Syst Rev 10:CD008348

Riesz P, Kondo I (1992) Free-radical formation induced by ultrasound and its biological implications. Free Radical Bio Med 13:247–270

Roessler FC, Ohlrich M, Marxsen JH, Stellmacher F, Sprenger A, Dempfle CE, Seidel G (2011) The platelet-rich plasma clot: a standardized in-vitro clot formation protocol for investigations of sonothrombolysis under physiological flows. Blood Coagul Fibrin 22:407–415

Rosamond W, Flegal K, Friday G, Furie K, Go A, Greenlund K, Haase N, Ho M, Howard V, Kissela B, Kittner S, Lloyd-Jones D, McDermott M, Meigs J, Moy C, Nichol G, O'Donnell CJ, Roger V, Rumsfeld J, Sorlie P, Steinberger J, Thom T, Wasserthiel-Smoller S, Hong Y, American Heart Association Statistics Committee and Stroke Statistics Subcommitee (2007) Heart disease and stroke statistics–2007 update: a report from the American Heart Association Statistics Committee and Stroke Statistics Subcommittee. Circulation 115:e69–e171

Rosenschein U, Furman V, Kerner E, Fabian I, Bernheim J, Eshel Y (2000) Ultrasound imaging-guided noninvasive ultrasound thrombolysis: preclinical results. Circulation 102:238–245

Roy RA, Atchley AA, Crum LA, Fowlkes JB, Reidy JJ (1985) A precise technique for the measurement of acoustic cavitation thresholds and some preliminary results. J Acoust Soc Am 78:1799–1805

Sakharov DV, Hekkenberg RT, Rijken DC (2000) Acceleration of fibrinolysis by high-frequency ultrasound: the contribution of acoustic streaming and temperature rise. Thromb Res 100:333–340

Salgaonkar VA, Datta S, Holland CK, Mast TD (2009) Passive cavitation imaging with ultrasound arrays. J Acoust Soc Am 126:3071

Saqqur M, Tsivgoulis G, Nicoli F, Skoloudik D, Vk S, Larrue V, Eggers J, Perren F, Charalampidis P, Stories D, Shuaib A, Alexandrov AV (2013) The role of sonolysis and sonothrombolysis in acute ischemic stroke: a systematic review and meta-analysis of randomized controlled trials and case-control studies. J Neuroimaging 24:209–220

Saric M, Kronzon I (2012) Aortic atherosclerosis and embolic events. Curr Cardiol Rep 14:342–349

Sarkar K, Katiyar A, Jain P (2009) Growth and dissolution of an encapsulated contrast microbubble: effects of encapsulation permeability. Ultrasound Med Biol 35:1385–1396

Shaw GJ, Bavani N, Dhamija A, Lindsell CJ (2006) Effect of mild hypothermia on the thrombolytic efficacy of 120 kHz ultrasound enhanced thrombolysis in an in-vitro human clot model. Thromb Res 117:603–608

Shaw GJ, Dhamija A, Bavani N, Wagner KR, Holland CK (2007) Arrhenius temperature dependence of in vitro tissue plasminogen activator thrombolysis. Phys Med Biol 52:2953–2967

Shaw GJ, Meunier JM, Lindsell CJ, Holland CK (2008) Tissue plasminogen activator concentration dependence of 120 kHz ultrasound-enhanced thrombolysis. Ultrasound Med Biol 34:1783–1792

Shaw GJ, Meunier JM, Huang SL, Lindsell CJ, McPherson DD, Holland CK (2009) Ultrasound-enhanced thrombolysis with tPA-loaded echogenic liposomes. Thromb Res 124:306–310

Shi WT, Porter TR, Vignon F, Powers JE, Shunji G, Jinjin L, Feng X, Drvol L, Lof J, Everbach EC (2011) Investigation of image-guided sonothrombolysis in a porcine acute ischemic stroke model. In: 2011 IEEE International Ultrasonics Symposium (IUS), Orlando, FL. pp 5–8

Shimizu J, Fukuda T, Abe T, Ogihara M, Kubota J, Sasaki A, Azuma T, Sasaki K, Shimizu K, Oishi T, Umemura S, Furuhata H (2012) Ultrasound safety with midfrequency transcranial sonothrombolysis: preliminary study on normal macca monkey brain. Ultrasound Med Biol 38:1040–1050

Silvain J, Collet JP, Nagaswami C, Beygui F, Edmondson KE, Bellemain-Appaix A, Cayla G, Pena A, Brugier D, Barthelemy O, Montalescot G, Wisel JW (2011) Composition of coronary thrombus in acute myocardial infarction. J Am Coll Cardiol 57:1359–1367

Skoloudik D, Bar M, Skoda O, Vaclavik D, Hradilek P, Allendoerfer J, Sanak D, Hlustik P, Langova K, Herzig R, Kanovsky P (2008) Safety and efficacy of the sonographic acceleration of the middle cerebral artery recanalization: results of the pilot thrombotripsy study. Ultrasound Med Biol 34:1775–1782

Smith WS, Sung G, Saver J, Budzik R, Duckwiler G, Liebeskind DS, Lutsep HL, Rymer MM, Higashida RT, Starkman S, Gobin YP, MERCI Multi Investigators, Frei D, Grobelny T, Hellinger F, Huddle D, Kidwell C, Koroshetz W, Marks M, Nesbit G, Silverman IE (2008) Mechanical thrombectomy for acute ischemic stroke: final results of the multi MERCI trial. Stroke 39:1205–1212

Smith DAB, Vaidya SS, Kopechek JA, Huang SL, Klegerman ME, McPherson DD, Holland CK (2010) Ultrasound-triggered release of recombinant tissue-type plasminogen activator from echogenic liposomes. Ultrasound Med Biol 36:145–157

Soltani A (2013) Application of cavitation promoting surfaces in management of acute ischemic stroke. Ultrasonics 53:580–587

Soltani A, Singhal R, Garcia JL, Raju NR (2007) Absence of biological damage from prolonged exposure to intravascular ultrasound: a swine model. Ultrasonics 46:60–67

Stone MJ, Frenkel V, Dromi S, Thomas P, Lewis RP, Li KC, Horne M 3rd, Wood BJ (2007) Pulsed-high intensity focused ultrasound enhanced tPA mediated thrombolysis in a novel in vivo clot model, a pilot study. Thromb Res 121:193–202

Stride E, Saffari N (2003) Microbubble ultrasound contrast agents: a review. Proc Inst Mech Eng H 217:429–447

Stride EP, Coussios CC, Wells PNT (2009) Cavitation and contrast: the use of bubbles in ultrasound imaging and therapy. Proc Inst Mech Eng H 224:171–191

Suchkova V, Siddiqi FN, Carstensen EL, Dalecki D, Child S, Francis CW (1998) Enhancement of fibrinolysis with 40-kHz ultrasound. Circulation 98:1030–1035

Sutton JT, Haworth KJ, Pyne-Geithman G, Holland CK (2013a) Ultrasound-mediated drug delivery for cardiovascular disease. Expert Opin Drug Deliv 10:573–592

Sutton JT, Ivancevich NM, Perrin SR Jr, Vela DC, Holland DC (2013b) Clot retraction affects the extent of ultrasound-enhanced thrombolysis in an ex vivo porcine thrombosis model. Ultrasound Med Biol 39:813–824

Tachibana K, Tachibana S (1995) Albumin microbubble echo-contrast material as an enhancer for ultrasound accelerated thrombolysis. Circulation 92:1148–1150

Tan KT, Lip GYH (2003) Red vs white thrombi: treating the right clot is crucial. Arch Intern Med 163:2534–2535– author reply 2535

Tang SC, Clement GT (2010) Standing-wave suppression for transcranial ultrasound by random modulation. IEEE Trans Biomed Eng 57:203–205

The IMS II Trial Investigators (2007) The Interventional Management of Stroke (IMS) II study. Stroke 38:2127–2135

The Penumbra Pivotal Stroke Trial Investigators (2009) The penumbra pivotal stroke trial: safety and effectiveness of a new generation of mechanical devices for clot removal in intracranial large vessel occlusive disease. Stroke 40:2761–2768

Tiukinhoy-Laing SD, Huang S, Klegerman M, Holland DC, McPherson DD (2007) Ultrasound-facilitated thrombolysis using tissue-plasminogen activator-loaded echogenic liposomes. Thromb Res 119:777–784

Turgut T, Bates ER (2000) Acute transmural myocardial infarction. Curr Treat Options Cardiovasc Med 2:13–18

Turi ZG, Goldberg S, LittleJohn JK, Vander Ark C, Shadoff N, Karlsberg R, Williams J, Butman S, Stadius ML, Wise K (1993) Dose-related efficacy and bleeding complications of double-chain tissue plasminogen activator in acute myocardial infarction. Am J Cardiol 71:1009–1014

Unger EC, McCreery TP, Sweitzer RH et al (1998) In vitro studies of a new thrombus-specific ultrasound contrast agent. Am J Cardiol 81:58G–61G

Verbeuren TJ (2006) Experimental models of thrombosis and atherosclerosis. Therapie 61:379–387

Vignon F, Shi WT, Powers JE, Everbach EC, Liu J, Gao S, Xie F, Porter TR (2013) Microbubble cavitation imaging. IEEE Trans Ultrason Ferroelectr Freq Control 60:661–670

Viola F, Kramer MD, Lawrence MB, Oberhauser JP, Walker WF (2004) Sonorheometry: a noncontact method for the dynamic assessment of thrombosis. Ann Biomed Eng 32:696–705

Watson T, Shantsila E, Lip GY (2009) Mechanisms of thrombogenesis in atrial fibrillation: Virchow's triad revisited. Lancet 373:155–166

Weisel JW, Litvinov RI (2008) The biochemical and physical process of fibrinolysis and effects of clot structure and stability on the lysis rate. Cardiovasc Hematol Agents Med Chem 6:161–180

Weiss HL, Selvaraj P, Okita K, Matsumoto Y, Voie A, Hoelscher T, Szeri AJ (2013) Mechanical clot damage from cavitation during sonothrombolysis. J Acoust Soc Am 133:3159

Westermark S, Wiksell H, Elmqvist H, Hultenby K, Berglund H (1999) Effect of externally applied focused acoustic energy on clot disruption in vitro. Clin Sci 97:67–71

White HD, Chew DP (2008) Acute myocardial infarction. Lancet 372:570–584

Wijnhoud AD, Franckena M, van der Lugt A, Koudstaal PJ, Dippel ED (2008) Inadequate acoustical temporal bone window in patients with a transient ischemic attack or minor stroke: role of skull thickness and bone density. Ultrasound Med Biol 34:923–929

World Health Organization (2011) Global status report on noncommunicable diseases 2010. Geneva, Switzerland

Wright C, Hynynen K, Goertz D (2012a) In vitro and in vivo high-intensity focused ultrasound thrombolysis. Invest Radiol 47:217–225

Wright CC, Hynynen K, Goertz DE (2012b) Pulsed focused ultrasound-induced displacements in confined in vitro blood clots. IEEE Trans Biomed Eng 59:842–851

Wu J, Xie F, Kumar T, Liu J, Lof J, Shi W, Everbach EC, Porter ER (2014) Improved sonothrombolysis from a modified diagnostic transducer delivering impulses containing a longer pulse duration. Ultrasound Med Biol 40:1545–1553

Xie F, Tsutsui JM, Lof J, Unger EC, Johanning J, Culp WC, Matsunaga T, Porter TR (2005) Effectiveness of lipid microbubbles and ultrasound in declotting thrombosis. Ultrasound Med Biol 31:979–985

Xie F, Lof J, Everbach C, He A, Bennet RM, Matsunaga T, Johanning J, Porter TR (2009) Treatment of acute intravascular thrombi with diagnostic ultrasound and intravenous microbubbles. J Am Coll Cardiol 2:511–518

Xie F, Everbach EC, Gao S, Drvol LK, Shi WT, Vignon F, Powers JE, Lof J, Porter TR (2011) Effects of attenuation and thrombus age on the success of ultrasound and microbubble-mediated thrombus dissolution. Ultrasound Med Biol 37:280–288

Xie F, Gao S, Wu J, Lof J, Radio S, Vignon F, Shi W, Powers J, Unger E, Everbach EC, Liu J, Porter TR (2013) Diagnostic ultrasound induced inertial cavitation to non-invasively restore coronary and microvascular flow in acute myocardial infarction. PLoS One 8:e69780

Xu Z, Ludomirsky A, Eun LY, Hall TL, Tran BC, Fowlkes JB, Cain CA (2004) Controlled ultrasound tissue erosion. IEEE Trans Ultrason Ferroelectr Freq Control 51:726–736

Yamashita T, Ohtsuka H, Arimura N, Sonoda S, Kato C, Ushimaru K, Hara N, Tachibana K, Sakamoto T (2009) Sonothrombolysis for intraocular fibrin formation in an animal model. Ultrasound Med Biol 35:1845–1853

Young FR (2005) Sonoluminescence. CRC Press, Boca Raton

Yount DE (1979) Skins of varying permeability: a stabilization mechanism for gas cavitation nuclei. J Acoust Soc Am 65:1429

Part III

Other Ultrasound Therapy

Ultrasound-Mediated Polymeric Micelle Drug Delivery

20

Hesheng Xia, Yue Zhao, and Rui Tong

Abstract

The synthesis of multi-functional nanocarriers and the design of new stimuli-responsive means are equally important for drug delivery. Ultrasound can be used as a remote, non-invasive and controllable trigger for the stimuli-responsive release of nanocarriers. Polymeric micelles are one kind of potential drug nanocarrier. By combining ultrasound and polymeric micelles, a new modality (*i.e.,* ultrasound-mediated polymeric micelle drug delivery) has been developed and has recently received increasing attention. A major challenge remaining in developing ultrasound-responsive polymeric micelles is the improvement of the sensitivity or responsiveness of polymeric micelles to ultrasound. This chapter reviews the recent advance in this field. In order to understand the interaction mechanism between ultrasound stimulus and polymeric micelles, ultrasound effects, such as thermal effect, cavitation effect, ultrasound sonochemistry (including ultrasonic degradation, ultrasound-initiated polymerization, ultrasonic in-situ polymerization and ultrasound site-specific degradation), as well as basic micellar knowledge are introduced. Ultrasound-mediated polymeric micelle drug delivery has been classified into two main streams based on the different interaction mechanism between ultrasound and polymeric micelles; one is based on the ultrasound-induced physical disruption of the micelle and reversible release of payload. The other is based on micellar ultrasound mechanochemical disruption and irreversible release of payload.

Keywords

Ultrasound • HIFU • Polymer micelle • Stimuli-responsive • Drug release

H. Xia (✉) • R. Tong
State Key Laboratory of Polymer Materials Engineering, Polymer Research Institute, Sichuan University, Chengdu 610065, China
e-mail: xiahs@scu.edu.cn

Y. Zhao (✉)
Département de Chimie, Université de Sherbrooke, Sherbrooke, Québec J1K 2R1, Canada
e-mail: yue.zhao@usherbrooke.ca

© Springer International Publishing Switzerland 2016

J.-M. Escoffre, A. Bouakaz (eds.), *Therapeutic Ultrasound*, Advances in Experimental Medicine and Biology, Vol. 880, DOI 10.1007/978-3-319-22536-4_20

20.1 Introduction

For many years, most scientific research worldwide has been focused on cancer therapeutics, including more effective drug treatments and advanced diagnostic devices. Novel multi-functional drug nanocarriers and controlled drug release are under development in order to improve therapeutic drug efficiency and alleviate patient suffering.

Drug nanocarriers generally include polymeric micelles, liposomes, polymer-drug conjugates, polymer dendrimers and metal or inorganic nanoparticles. A nanocarrier with a size of several tens to hundreds of nanometers can diffuse or extravasate into tumor tissues by the enhanced permeability and retention (EPR) effect. Experiments suggest that the threshold particle size for extravasation into tumors is ~400 nm (Peer et al. 2007; Yuan et al. 1995). Surface functionalization for the drug nanocarrier, such as PEGylation and ligand grafting, improves the longevity, stability and safety of drugs within the circulatory system, and also the targeting of specific cells. Passively targeting nanocarriers, based on liposomes and polymer–protein conjugates, went into clinical trials in the 1980s, and were commercialized in the 1990s (Peer et al. 2007). However, the translation of the enhanced permeability, retention effect and ligand recognition into the clinic still needs to be improved (Mura et al. 2013; Fleige et al. 2012; Musyanovych and Landfester 2014).

Stimuli-responsive nanocarriers are nanosized active delivery vehicles with a special structure that can respond to an external signal and can control drug release. The concept of stimuli-responsive drug delivery was first suggested in the late 1970s with the use of thermosensitive liposomes for the local release of drugs through hyperthermia (Mura et al. 2013). Generally, the responsive mechanism includes stimuli-induced oxidation/reduction, protonation, hydrolysis, enzymolysis, bond cleavage or molecular conformational change. The non-invasive and remote on/off stimulus, with spatial-, temporal- and dosage-controlled modes, are expected since some particular drugs are often restricted to a narrow dosing range, and may also be restricted to a particular target tissue (Kost and Langer 2001; Timko et al. 2010; Nakayama et al. 2014; Kost et al. 1989). The stimuli that trigger drug release from nanocarriers can be broadly classified into internal (pH, glutathione, enzymes) and external (physical stimuli, *i.e.,* heat, light, magnetic, electrical field and ultrasound). Two mechanisms according to the nature of the interaction between the drug and nanocarriers exist: For drug physically entrapped within the nanocarrier, the release can be triggered by structural nanocarrier change, while for drug chemically linked to the nanocarrier, such as drug-polymer conjugates, the triggered release involves the breaking of chemical bonds between the drug and carrier. The synthesis of multi-functional nanocarriers for drug delivery and the design of new stimuli-responsive means are equally important and still need to be developed. The major challenge lies in the creation and understanding of the optimized molecular coupling interactions between the external stimuli and the microscopic nanocarrier, and its amplifying effect.

Ultrasound is a powerful physical modality for spatial and temporal control of on-demand drug delivery (Lin and Thomas 2003; Mitragotri 2005; Kim et al. 2006, Geest et al. 2007, Park 2010; Oerlemans et al. 2010). Amphiphilic copolymer micelles that consist of a hydrophobic inner core and a hydrophilic corona in aqueous solution are one kind of potential nanocarrier for hydrophobic drugs. Ultrasound-mediated polymeric micelle drug delivery is now attracting more and more interest. This chapter will focus on this topic.

20.2 Ultrasound

Ultrasound is high frequency sound above 20 kHz that is inaudible to the human ear (Ashihara et al. 2006). In medicine, ultrasound has been widely used, for example in tissue ablation, stone crushing, ultrasound contrast and transdermal drug delivery (Schroeder et al. 2009). As one kind of trigger, ultrasound may have some unique advantages over other types of stimuli, in particular with focused, high-frequency diagnos-

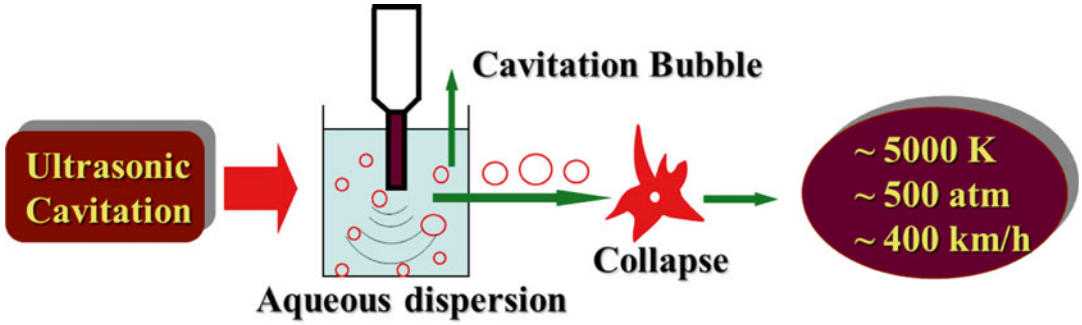

Fig. 20.1 Ultrasound cavitation

tic ultrasound. In addition to the possibility of temporal and spatial control, ultrasound can easily penetrate deep into the body in a noninvasive and remote way by selecting the time of ultrasound application and the targeted action area (around the focal region of the sound beams). In contrast to this, light does have selective times and locations, and a limited penetration depth, particularly when concerning ultraviolet light.

In general, according to the frequency of ultrasound, ultrasound can be divided into low frequency ultrasound (20–200 kHz) and high frequency ultrasound (>200 KHz). Similar to light waves, ultrasonic waves can also be focused on a volume of which the dimensions are as small as about half the wavelength. Low frequency ultrasound has some advantages, such as deeper penetration and lower attenuation. However, low frequency ultrasound can produce a strong cavitation effect, and long wavelength ultrasound is difficult to focus. Therefore, when low frequency ultrasound passes through the human body, ultrasonic cavitation may destroy healthy and vital tissues. In the case of high frequency ultrasound, the ultrasonic wave can be focused in a small area. This means that the intensity is quite high only in the focal spot, while in other areas the intensity can be sufficiently low and accepted by the human body. So for drug delivery applications, high frequency ultrasound is a promising trigger. However, with high frequency ultrasound the cavitation becomes weak. This makes high frequency ultrasound less effective in disrupting polymeric micelles. This problem can be resolved by designing more ultrasound-sensitive copolymers. When a medium or tissue is exposed to ultrasound, ultrasound can induce two different effects: Thermal or cavitation effects.

20.2.1 The Thermal Effect of Ultrasound

When ultrasonic waves pass through a tissue, ultrasound attenuation will occur by both scattering and absorption. The attenuation of high frequency ultrasound is much stronger than low frequency ultrasound. The strong attenuation of high frequency ultrasound prevents its deep penetration into the body. This is a drawback for the use of high frequency ultrasound as the trigger for drug delivery. The ultrasound attenuation energy will convert into heat. Thus, the thermal effect of high frequency ultrasound is much stronger than low frequency ultrasound (Phenix et al. 2014). The thermal effect may not be the main activating effect for ultrasound-triggered drug release from micelles, but it must be considered.

20.2.2 The Cavitation Effect of Ultrasound

The most significant effect of ultrasound is the cavitation effect. When an ultrasonic wave transmits through a liquid medium, a large number of microbubbles form, grow and collapse during very short periods of time (a few microseconds). This is a process called ultrasonic cavitation and is illustrated in Fig. 20.1. Cavitation is the

formation, rapid growth and collapse of bubbles (inertial cavitation), or sustained oscillatory motion of bubbles (stable cavitation). The cavitation effect is very common when ultrasound is applied in any aqueous environment. There is a distinction between the two types of cavitation. In inertial cavitation, bubbles oscillate in an unstable manner around their equilibrium, expanding to 2 or 3 times their resonant size, before violently collapsing during a single compression half-cycle. By contrast, in stable cavitation bubbles exist for a considerable number of acoustic cycles, while the radius of each bubble varies around an equilibrium value. Sonochemical theoretical calculations, and corresponding experiments, suggested that ultrasonic cavitation can generate a local temperature as high as 5000 K, a local pressure as high as 500 atm, heating and cooling rates greater than 109 K/s, a very strong shock wave and microstreaming (Luche 1998; Cravotto et al. 2013; Suslick 1990). Inertial cavitation is considered a major mechanism for causing alterations to medium.

20.2.3 Ultrasound Sonochemistry

Ultrasound has been used to invent novel chemical reactions and to enhance the reaction rate. This is called sonochemistry. Ultrasonic cavitation converts acoustics into extreme physics, creating a vigorous environment. Such special physical and chemical effects provide a new route for chemical reactions that are difficult or impossible to achieve under conventional conditions. During bubble collapse, radicals can be generated due to decomposition of solvents and monomers, or rupture of polymer chains. This initiates further chemical reaction, *e.g.,* monomer polymerization (Mason and Lorimer 1988; Kruus 1983; Price et al. 1992). Since the first report about sonochemistry by Richards and Loomis (1927), sonochemistry has initiated growing interest in many areas of synthetic chemistry, especially in polymer science.

20.2.3.1 Ultrasound Degradation

A well-known use of ultrasound is the degradation of polymers to lower molecular weights and their distribution control. Previous research suggests that ultrasonic depolymerization is a non-random process, with the chain scission occurring preferentially at the polymer chain midpoints, and with larger molecules degrading the fastest (Mason and Lorimer 1988). Another unique feature is that ultrasonic degradation reduces the molecular weight simply by splitting the most susceptible chemical bond in the chain (Gronroos et al. 2001). The factors affecting ultrasonic polymer degradation and its mechanisms have been investigated in detail, typically for polymers in solution (Price and Smith 1991; Tabata and Sohma 1980; Malhotra 1982). Moreover, by the performance of degradation in the presence of the radical scavenger, it has been proven that ultrasound can degrade polymer chains to macroradicals (Chen et al. 1985). Reich reported that at an ultrasound intensity of 40 W and above, a significant reduction in the molecular weight of poly (lactic acid) (PLA) and poly(lactic-co-glycolic acid) (PLGA) could be observed, even after short exposure times of 30 or 20 s, respectively (Reich 1988). EI-sherif et al. (2004) also observed the degradation of PLGA under a high frequency ultrasound of 5–10 MHz. By controlling the reaction parameters influencing the degradation of polymer chains and the copolymerization of added monomers, one can produce various grafts or block copolymers with tailored structures in systems containing either a mixture of homopolymers or a mixture of polymers and monomers (Zhang et al. 1990; Fujiwara et al. 1992, 1994). Therefore, ultrasonic irradiation can provide an effective method for polymer design.

The exact mechanism of ultrasonic degradation still remains obscure, but it is well accepted that the large shear fields and instantaneous hot spots produced by ultrasonic cavitation are primarily responsible for polymer degradation (Kawasaki et al. 2007; Liu et al. 1992). It is believed that at the stage of cavity collapse induced by ultrasound waves, radiated friction forces and shock waves generate the stresses on the surface of a polymer chain, and/or more possibly within the polymer coil, resulting in macromolecular chain bond breaking in the liquid. This is similar to hydrodynamic shear degradation

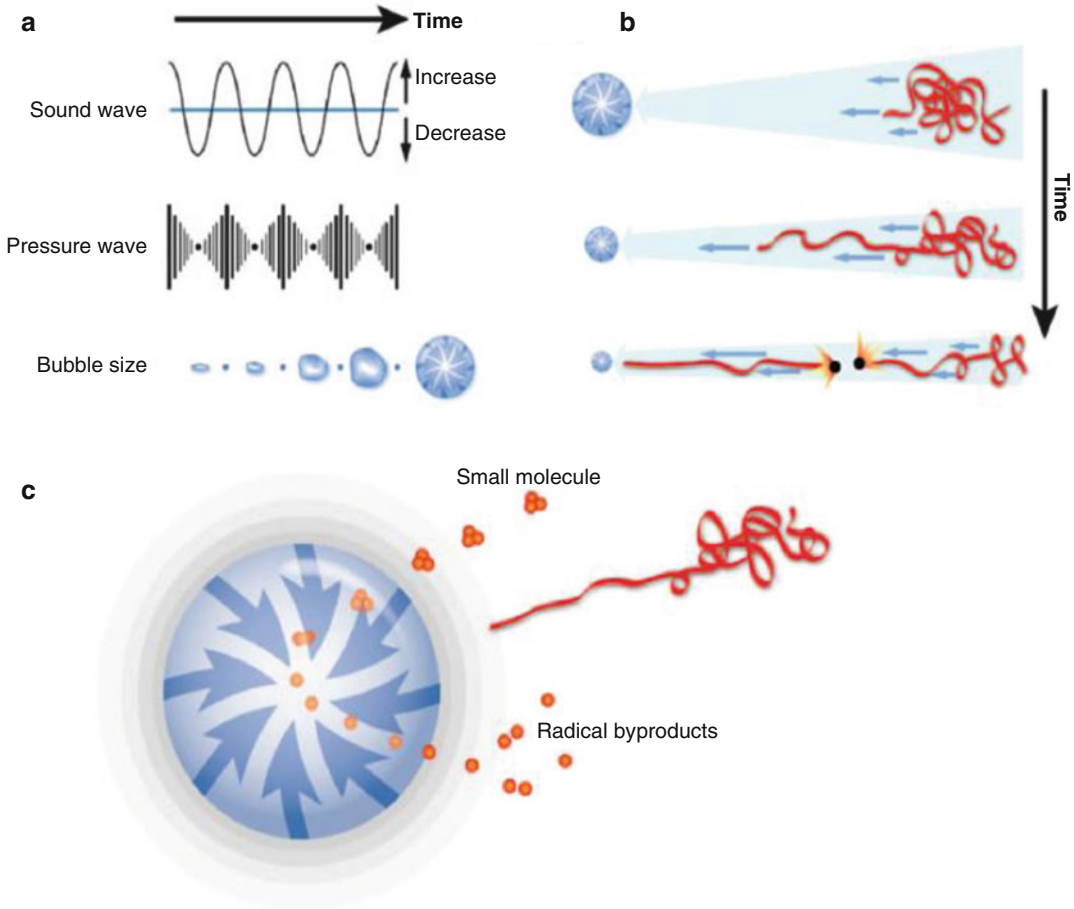

Fig. 20.2 Mechanism of ultrasound-induced polymer chain scission. (**a**) Gradual bubble formation; (**b**) Rapid bubble collapse generates solvodynamic shear to make polymer chain breaks; (**c**) Small molecules undergo pyrolytic cleavage to form radical byproducts (Cravotto and Angew 2007)

(Mason and Lorimer 1988). When the microbubbles collapse, polymer segments in the high-gradient shear field, near the collapsing bubbles, move at a higher velocity than those segments far away from the collapsing bubbles (Fig. 20.2). Thus, the polymer chain becomes elongated and this finally leads to chain scission (Cravotto and Angew 2007; Caruso et al. 2009).

20.2.3.2 Ultrasound-Initiated Polymerization

The use of ultrasound to initiate the bulk or solution polymerization of monomers has been reported. Kruus and Price et al. successfully produced poly(methyl methacrylate) (PMMA) and proved that monomers could decompose to free radicals to initiate polymerization (Kruus and Patraboy 1985; Price et al. 1992). In addition, Makino et al. (1983) reported that water molecules were dissociated to high concentrations of OH · and H · radicals under ultrasonic irradiation. Henglein (1954) produced poly(acrylonitrile) in an aqueous solution in this way. By combining the advantages of sonochemistry and emulsion polymerization together, ultrasonically-initiated emulsion polymerization of methyl methacrylate, styrene and butyl acrylate/vinyl acetate has been reported (Liu et al. 1994; Chou and Stoffer 1999; Biggs and Grieser 1995; Xia et al. 2002). Compared with ultrasonically-initiated bulk or solution polymerization, ultrasonically-initiated emulsion polymerization can produce faster

polymerization, higher monomer conversion and higher molecular weight polymers. Moreover, due to the intense dispersion, emulsifying and disrupting effects of ultrasound waves, nanoscale latex particles can be produced. This technique provides an alternative route to undergo mini- and micro-emulsion polymerization to produce polymeric nanoparticles (Zhang et al. 2002; Xia et al. 2001).

20.2.3.3 Ultrasonic In-situ Polymerization

Ultrasonic in-situ polymerization technology is a new technology to prepare polymer nanocomposites containing inorganic nanocomposites. By taking advantage of the multiple effects of ultrasound, *i.e.,* dispersion, pulverizing, activation and initiation, the aggregation and entanglement of inorganic nanoparticles in aqueous solution can be broken down. At the same time, in-situ monomer polymerization of inorganic nanoparticles occurs on the surface. Consequently, the inorganic nanoparticles are coated by the formed polymer. Using ultrasonic in-situ polymerization, polymer-SiO_2, polymer-Al_2O_3, polymer/carbon nanotubes, polymer-TiO_2, polymer-Fe_3O_4 and polymer-montmorillonite nanocomposites were prepared (Xia and Wang 2002, Xia and Wang 2003, Xia et al. 2001, 2003; Wang et al. 2001, 2005; Qiu et al. 2007). This method has the following advantages: (i) Use of aqueous media, (ii) ease of operation and (iii) ability to design the encapsulated polymer layer to meet different requirements.

20.2.3.4 Site-Specific Ultrasound Degradation

Site-specific ultrasound degradation is a process in which degradation occurs at well-designed sites among polymer chains. The polymer normally contains a labile group, which can be broken under ultrasonic irradiation, initiating structural and property changes. This is also defined as mechanochemistry, and the reactions are much dependent on the molecular weight of the polymer, *i.e.,* there exists a minimum molecular weight for the chain scission. In 2007 and 2009, Moore and colleagues proposed the

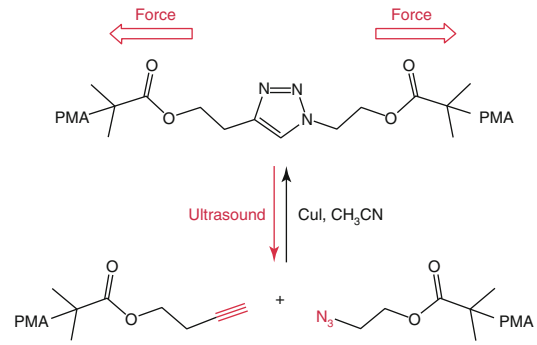

Fig. 20.3 Ultrasound-induced site-specific cleavage of 1,2,3-triazole mechanophore-containing polymers (Brantley et al. 2011)

mechanophore concept (Hickenboth et al. 2007, David et al. 2009). They introduced the mechanophore, such as benzocyclobutene, spiropyrans (SP) or dicyanocyclobutane, into PEG and poly (methyl acrylate) PMA chains. They found that ultrasound irradiation can induce structural conformation change, or site-specific degradation, by exerting the mechanical force on these mechanophore groups (Brantley et al. 2013; May and Moore 2013; Wiggins et al. 2013; Brantley et al. 2012; Ariga et al. 2012; Kryger et al. 2010). Such ultrasound-sensitive polymers are expected to have many potential applications, such as self-healable materials. Several distinguished research groups, including Moore, Craig, Bielawski and Sijbesma, are very active in this research field. The ultrasound mechanoresponsive materials can basically be divided into four kinds according to the research group: (1) Moore et al.: Benzocyclobutene (BCB) based PEG-BCB-PEG, spiropyran (SP)-based PMA-SP-PMA, dicyanocyclobutane(DCCB)-based PMA-DCCB-PAM; (2) Craig et al.: Gem-dichlorocyclopropane (gDCCs)-based poly(1,4-butadiene) PBD-DCC, (3) Bielawski et al.: Oxanorbornene Diels-Alder bond-based PMA-DA-PMA; 1,2,3-triazole-based PMA-triazole-PMA (Fig. 20.3); and (4) Sijbesma et al.: Bis(N-heterocyclic carbene) metal ligand poly(tetrahydrofuran). These researches are highly innovative and the molecular designs are elegant. However, some challenges remain: (1) The ultrasound power was too high: ~100 W, intensity ~10 $W.cm^{-2}$, frequency 20 kHz; (2) The

sonication time was too long, ~2 h; (3) The used organic solvent, like acetonitrile, is not environment-friendly, limiting the application to some degree. More rapid responsive mechanophores are still needed to be developed. On the other hand, Xia and Zhao focused their efforts trying to develop sensitive mechanophores in aqueous solution. They introduced the block copolymer with its micelle mechanophore concept, and established a new mechanochemical way to break the copolymer micelle. This has potential applications for controlled drug release (Wang et al. 2009; Zhang et al. 2009; Li et al. 2010).

20.2.4 High Intensity Focused Ultrasound (HIFU)

HIFU refers to the high frequency focused ultrasound of ultrasound beams that are emitted from a specially designed and curved transducer or phased arrays. The HIFU ultrasound beams are focused to a very small volume of several millimeters, which makes HIFU a more promising trigger for polymeric micelle drug delivery systems. At the focused spot, the ultrasonic intensity is very strong, while the intensity is very weak at other areas. A typical HIFU system consists of a signal generator, a power amplifier and an acoustic lens transducer. The signal generator controls the frequency and initial amplitude of the input signal, which is amplified using the power amplifier. The amplified signals are transmitted to the HIFU transducer to generate the desired ultrasound beam. They are constructed to make ultrasound beams converge and deposit maximum acoustic energy into the focal millimeter-sized volume. The acoustic lens transducer can determine the focal dimensions by the geometry of the transducer (aperture and focal length) and its operating frequency. The first report of HIFU application in humans was in 1960 (Fry and Fry 1960). However, this technique did not gain significant clinical acceptance until the 1990s, despite successful ophthalmological treatments before that date. In recent years, HIFU treatment has been increasingly used as a non-contact and remote control approach in medical treatment.

Compared with other techniques, such as cryotherapy, laser, microwave and radiofrequency, HIFU has some distinct advantages (Dogra et al. 2009). It is noninvasive and nonionizing, which means it can be repeated many times because it has no long-term cumulative effects. Due to the viscoelastic characteristics of human tissues, acoustic energy is lost and converted to heat; HIFU treatment can raise the focal area tissue temperature in seconds, and can maintain this temperature for 1 s or longer (Haar and Coussios 2007). Ultrasonic energy absorption within the focal volume induces high temperatures that can also be focused precisely on tissue volumes as small as several cubic millimeters, with temperatures outside this region being kept at noncytotoxic levels. This important HIFU lesion features makes the damage spatially confined, without damaging the intervening or surrounding tissue. Since the focal dimensions can be determined by the acoustic lens transducer, the desired size and shape of a larger HIFU target can be achieved by multiple sonications, combining individual lesions in a matrix format. Nowadays, a challenge in designing an optimal drug delivery system is the targeted, controlled and enhanced drug release in targeted areas. Compared to other stimuli, HIFU could be an ideal trigger to solve this issue because it can be focused and its parameters can be tuned in a remote way.

20.3 Micelles

Traditional surfactants include a hydrophilic head group and a hydrophobic long chain alkane. It can self-assemble into micelles in aqueous solution when the concentration is above critical micelle concentration (CMC). Similar to traditional surfactants, the polymer micelle is formed by self-assembly of amphiphilic copolymers, which include at least one hydrophilic block forming the shell, and at least one hydrophobic block forming the core. The polymer micelle diameter is about 10–100 nm. As a kind of smart material, stimuli-responsive amphiphilic copolymer micelles are of great interest, and have been extensively investigated as a delivery system for

biomedical applications. This type of nanocontainer can encapsulate various poorly water-soluble pharmaceuticals in the hydrophobic core, and can be soluble or dispersible due to the hydrophilic corona. When polymeric micelles get into the human circulatory system, drug-containing micelles will accumulate at tumor cells by the enhanced permeability and retention effect.

For normal polymeric micelles without stimuli-responsiveness, drugs can only be released by diffusion and/or slow degradation of polymer materials; the responsive and release behavior of these micelles are usually uncontrollable. The stimuli-responsive polymeric micelles are of particular interest as they may have the following three advantages: (a) Better solubilization of hydrophobic drugs; (b) prolongation of the drug circulation time; (c) the release of guest molecules in a controlled way by external stimuli. Generally, hydrophobic drugs in the micelle can be released in response to a variety of stimuli, such as pH change,(Su et al. 2011; Zhou et al. 2011), temperature change (Eissa and Khosravi 2011, Liu et al. 2011), exposure to light (Knezevic et al. 2011; Yan et al. 2011) or enzymes (Coll et al. 2011; Pritchard et al. 2011). Ultrasound, which possesses the strong penetration effect and remote controllability, is a promising tool and attracts lots of interest as one kind of stimulus for polymeric micelle drug delivery systems. In recent years, there has been growing interest in using ultrasound as a stimulus to induce the disruption of copolymeric micelles and trigger the release of payloads (Geest et al. 2007; Geers et al. 2011; Pitt et al. 2004; Lensen et al. 2011).

20.4 Ultrasound-Mediated Polymeric Micelle Drug Delivery

Ultrasound is known as a powerful physical modality for spatial and temporal control of drug delivery. Ultrasound can effectively penetrate deep into the interior of the body in a noninvasive way. Fellinger and Schmid (1954) reported that ultrasound could enhance the percutaneous absorption of drugs, *i.e.,* phonophoresis or sonophoresis. Skauen and Zentner (1984) proposed the concept of phonophoresis. Kost et al. (1989) firstly proposed the concept of releasing drugs entrapped in a solid polymer matrix through ultrasonic polymer degradation and erosion. Recently, ultrasound-triggered release from liposomes (Lin and Thomas 2003), polyelectrolyte microcontainers (Shchukin et al. 2006), multilayered capsules (Skirtach et al. 2007), microemulsions (Lee et al. 2008) and micelles (Rapoport et al. 1999; Husseini et al. 2000, 2002a, b, c; Husseini and Pitt 2008; Marin et al. 2002; Smith et al. 2008; Zhang and Pitt 2006) have been widely investigated. For ultrasound-mediated micellar drug delivery, the pioneer work was done by Pitt, Rapoport, Husseini et al. They first introduced ultrasound to control the drug release from polymeric micelles mainly by using low frequency ultrasound. The release mechanism is based on the physical disruption of the micelle and reversible release of payload. Xia and Zhao proposed the concept of ultrasound mechanochemically responsive polymeric micelles for drug delivery, mainly using high intensity focused ultrasound (HIFU). The release mechanism is based on chain scission, chemical disruption of the micelle and irreversible release of payload. Other groups include Deckers et al. (2013), Ugarenko et al. (2009), Myhr and Moan (2006) and Hasanzadeh et al. (2011).

20.4.1 Ultrasound-Triggered Physical Breakdown of Micelle and Reversible Release of Payload

In 1997, Rapoport and Pitt investigated ultrasonic-activated drug delivery from Pluronic P-105 polymeric micelles. They found the combination of ultrasound and micellar drug carriers can lower the effective dosage of an anti-cancer drug and reduce the toxic side effects associated with high doses of chemotherapeutic drugs (Munshi et al. 1997). Therefore, they established a novel modality for drug delivery and targeting, *i.e.,*

encapsulating the anti-cancer drug in micellar carriers, and then focusing ultrasound on the tumor site for controlled drug release. Since 1997, Rapoport, Pitt and Husseini et al. have carried out many investigations on ultrasound-mediated micellar drug delivery, which are summarized in some comprehensive reviews (Pitt and Husseini and Kherbeck 2013; Husseini and Pitt 2008, Sirsi and Borden 2014, Kiessling et al. 2014). In their research, the ultrasound-triggered release mechanism is "physical", and can be described as follows: The micelle is disrupted or disassembled under ultrasound perturbation resulting from ultrasonic cavitation or mechanical effect, and the payload is released from the micelle. Once the ultrasound ceases, the micelle can be reassembled again, and the payload can be re-encapsulated. For this mechanism, the micelle disruption is temporary and the drug release is reversible.

The work of Rapoport, Pitt and Husseini et al. is not only pioneered, but also comprehensive. The effect of ultrasound factors, including ultrasound intensity, low or high frequency, pulsed or continuous wave, were examined, and also the ultrasound triggered release kinetics and mechanism were investigated in-depth. For the micelle carrier, they mainly used the FDA-approved Pluronic micelle, composed of triblock copolymer poly(ethylene oxide)-poly(propylene oxide)-poly(ethylene oxide) (PEO-PPO-PEO), or stabilized Pluronic micelle by crosslink or interpenetrating network. Most importantly, they did a lot of excellent work on ultrasound-triggered *in-vitro* drug (mainly doxorubicin) release to different cancer cells, such as promyelocytic leukemia HL-60, MDR ovarian carcinoma and breast cancer cells MCF-7, A2780, MDA-MB-231. Additionally, they studied *in-vivo* drug release in animal models, such as rat hind leg with a colon carcinogen DHD/K12/TRb tumor cell, and mouse with colon or breast cancer. All *in-vitro* and *in-vivo* experimental results were positive. Under action of the new modality, *i.e.,* ultrasound-mediated micellar drug delivery, the cellular drug uptake was improved, and consequently cancer cells were destroyed and tumor reduction was significant.

Husseini et al. investigated the factors affecting acoustically-triggered drug release from polymeric micelles (Husseini et al. 2000). Real-time fluorescence detection was used to measure the drug release from Pluronic P-105 micelles under continuous wave or pulsed ultrasound in the frequency range of 20–90 kHz. Two fluorescent drugs (Doxorubicin and Ruboxyl) were used. The drug release was found to decrease at higher frequencies, indicating an important role for transient cavitation in drug release. The release of doxorubicin (DOX) was higher than that of Ruboxyl due to stronger interaction and deeper insertion of Ruboxyl into the core of the micelles. Drug release was higher at lower Pluronic concentrations, and increased with increasing power density. At constant power density, peak release under pulsed ultrasound, with duration longer than 0.1 s, was the same as that under continuous ultrasound. Released drug was quickly re-encapsulated between the ultrasound pulses, suggesting the non-extravasated and non-internalized drug would circulate in the encapsulated form upon ultrasound halts, thus preventing unwanted drug interactions with normal tissues. Marin et al. also studied the effect of a continuous wave and pulsed 20-kHz ultrasound on DOX uptake by HL-60 cells from phosphate buffered saline solution (PBS) and Pluronic micellar solutions (Marin et al. 2001a, b). Under both the continuous wave and pulsed wave ultrasound, DOX uptake from PBS and Pluronic micelle solutions can be enhanced. Drug uptake can be further enhanced under higher ultrasound power, accompanied by extensive cell sonolysis. The drug uptake also increased with increasing pulse duration in the range 0.1–2 s. Over 2 s pulses, the uptake was similar to that under continuous-wave (CW) ultrasound. At an ultrasound frequency of 20 kHz and power density of 58 mW/cm^2, no significant drug release was observed when exposed to ultrasound for less than 0.1 s. This shows a threshold time value. Above this threshold, the amount of release was shown to increase as the pulse length increased up to 0.6 s. Under ultrasound treatment, micelles were destructed because of the shock waves produced by collapsing bubbles, inducing the release of hydrophobic

drugs. After the ultrasound treatment halted, micelles could be reassembled and drugs could be re-encapsulated.

Regarding the effect of ultrasound frequency on polymeric micelle drug release, there is no doubt that low frequency is more effective than high frequency. However, there are some inconsistent results. In 2002, *Marin* et al. observed a DOX release of ~8.5 % at a power density of ~7 W/cm^2 under high frequency 1 MHz ultrasound (Marin et al. 2002). On the other hand, Diaz de la Rosa (2007) found no DOX release occurs at 500 kHz high frequency ultrasound, even at an ultrasound intensity of 20 W/cm^2. It should be mentioned that they didn't investigate the effect of HIFU on drug release. Kobayashi et al. (2012) investigated the release of hydrophobic dye from Pluronic micelles under low frequency ultrasound. They also found the hydrophobic dye is more easily released under lower frequency ultrasound. Compared with the thermal effect, mechanical cavitation is more significant.

Husseini et al. (2002a, b, c) measured the kinetics of acoustic release of DOX from and subsequent re-encapsulation of DOX in Pluronic P105 micelles. Several physical models and their corresponding mathematical solutions were analyzed to see which model most closely fitted the data. The model of zero-order release with first-order re-encapsulation appears to represent data from this polymeric system better than other models.

Stevenson-Abouelnasr et al. (2007) investigated the release mechanism and release kinetics of DOX from Pluronic P105 micelles during ultrasonication and its subsequent re-encapsulation upon cessation of insonation. The mechanisms included micelle destruction, destruction of cavitating nuclei, reassembly of micelles and the re-encapsulation of Dox. The micelles are destroyed because of cavitation events produced by collapsing nuclei. The slow destruction of cavitating nuclei results in a slow partial recovery phase when a small amount of Dox is re-encapsulated. The reassembly of micelles and the re-encapsulation of Dox are independent of ultrasound. Parameters for the model were determined based upon the best-observed fit to experimental data.

Concerning the drug release mechanism from Pluronic micelles, there is no doubt that ultrasound indeed physically breaks the polymer micelle. However, it is not so clear how the ultrasound breaks the micelle. In other words, what is the interaction mechanism between the micelle and the ultrasound wave? Cavitation or mechanical vibration? Marin et al. (2002) studied the relationship between ultrasound intensities and DOX release, as well as the relationship between the radical concentration and ultrasound intensity. They found that for 10 % DOX drug release from Pluronic micelles, the required ultrasound intensities are: 20 kHz: 0.058 W/cm^2; 67 kHz: 2.8 W/cm^2; 1.0 MHz: 7.2 W/cm^2. However, the radical trapping experiments showed that the radial formation thresholds under ultrasound were: 20 kHz: 0.08 W/cm^2; 67 kHz: 1.0 W/cm^2; 1.0 MHz: 3.6 W/cm^2. This result implies that the DOX release was not directly related to the ultrasonic cavitation, which can be characterized by radical formation. Husseini et al. (2005) re-investigated the role of cavitation in acoustically-activated drug delivery. The acoustic spectra were collected and analyzed at the same spatial position as fluorescence data to explore the role of cavitation in drug release. The results showed a strong correlation between percentage drug release and subharmonic acoustic emissions, and the drug release was attributed to the collapse cavitation that perturbs the structure of the micelle and releases drug. Since then, the mechanism of cavitation for micelle disruption was widely accepted.

Regarding the carrier design, Pitt, Rapoport and Husseini mainly focused on Pluronic micelles. However, they also made some valuable modifications on the carrier system. One disadvantage for P-105 micelles is that they are not very stable under dilution. Rapoport et al. (1999) designed three routes to overcome this problem: (1) Radical crosslinking of micelle cores; (2) introducing vegetable oil into the Pluronic solutions, and (3) polymerization of the temperature-responsive LCST hydrogel in the core of Pluronic micelles, called Plurogel. They confirmed the

third route is the best one, and found that the ultrasonication actually enhanced intracellular drug uptake from dense plurogel micelles.

Husseini et al. (2002a, b, c) prepared P-105 micelles stabilized with an interpenetrating network of N,N-diehtylacrylamide NanoDeliv (TM). The results showed that 2 % DOX can be released within 2 s from the stabilized micelles under ultrasound at 70 kHz, which was not significantly different from unstabilized P-105 micelles. The drug re-encapsulation upon insonation cessation was also complete. In 2007, they measured the release of DOX from unstabilized Pluronic 105 micelles, Pluronic P105 micelles stabilized with an interpenetrating network of N,N-diethylacrylamide and poly(ethylene oxide)-b-poly (N-isopropylacrylamide)-b-poly(oligolactylmethacrylate) micelles with stabilized cores. It seemed that they obtained the opposite conclusion to the previous experiment, *i.e.,* the DOX release from unstabilized Pluronic micelles is much greater than that from the stabilized and crosslinked micelles, however the onset of release occurs at the same ultrasonic power density for the three kinds of carriers investigated (Husseini et al. 2007). In 2009, they found that ultrasound at frequencies 70 and 476 kHz, with a mechanical index of 0.9, can disrupt stabilized micellar covalent networks (NanoDeliv^{TM}), but the network degradation time constant is very long compared to the time constant pertaining for drug release from micelles. After exposure to 70 kHz and 476 kHz ultrasound for 1 h, no significant difference between the network degradation was observed (Husseini et al. 2009).

Zeng and Pitt (2006) prepared a polymeric micelle system with a hydrolysable segment for drug delivery. This micelle is composed of an amphiphilic copolymer, poly(ethylene oxide)-b-poly(N-isopropylacrylamide-co-2-hydroxyethyl methacrylate-lactate$_n$), and has a half-life of about 48 h at 40 °C. The DOX release was ~ 4 % at body temperature under ultrasound, and the drug was returned to the polymeric micelles when insonation ceased. Smith et al. (2008) confirmed that high intensity focused ultrasound can trigger drug release from the pH responsive PEGylated micelles and can improve drug uptake by H69 human carcinoma cells *in-vitro*. Husseini et al. (2013) reported the use of the Pluronic P105 micelles with a folate-targeting moiety containing DOX, and investigated the acoustic release of the drug. The maximum amount of release reached ~ 14 % at an ultrasound power density of 5.4 W/cm^2. The novel, well-designed folated Pluronic micelle, combined with external ultrasound stimulus, can reduce the adverse side effects of chemotherapy by preferentially and actively targeting tumor cells.

Deckers et al. (2013) investigated the CW, low frequency, high intensity focused ultrasound (HIFU)-triggered payload release from non-cross-linked (NCL) and core cross-linked (CCL) poly(ethylene glycol)-b-poly[N-(2-hydroxypropyl) methacrylamide-lactate] (mPEG-b-p(HPMAm-Lacn)) micelles. Under ultrasound action, up to 85 % Nile Red was released from NCL and CCL micelles. No change in micelle size distribution after CW and pulsed-wave (PW) HIFU exposure was observed, and no polymer chain degradation occurred. They hypothesized that the polymeric micelles are temporally destabilized upon HIFU exposure due to radiation induced shear forces, not due to the cavitation, leading to NR release on demand.

Rapoport et al. (1999) investigated the effect of Pluronic P-105 micelle structure and ultrasound on the uptake by HL-60 cells of two anthracycline drugs, doxorubicin and ruboxyl. The results showed that insonation with 70 kHz ultrasound enhanced intracellular HL-60 cell uptake of drugs encapsulated in dense Pluronic micelles. The drug uptake mechanism was investigated by using two fluorescent probes, Lysosensor Green and Cell Tracker Orange CMTMR. It was confirmed that the increase in drug accumulation in the cells was not due to an increase in endocytosis, but due to ultrasonication. They hypothesized that sonoporation played an important role in the acoustically activated drug delivery of chemotherapy drugs delivered by Pluronic micelles (Husseini et al. 2002a, b, c).

Nelson et al. (2002) reported ultrasonically activated chemotherapeutic drug delivery in a rat model using a novel stabilized micellar drug delivery system. Forty-two BDIX rats were

inoculated in each hind leg with a DHD/K12/TRb tumor cell line. The results showed significant tumor reduction for rats receiving ultrasound at 20 and 70 kHz, along with encapsulated DOX at 2.67 mg/kg. It is suggested that ultrasound released the DOX from the micelles, and also assisted the drug and/or carriers to extravasate and enter the tumor cells.

In 2006, a novel on-demand delivery system based on paclitaxel encapsulated in polymeric micelles, in conjunction with triggered release of the drug by local ultrasonic irradiation of the tumor, was evaluated by Howard et al. (2006) *in-vitro* and *in-vivo* using a drug-resistant human MCF-7/ADM breast cancer cell line. Using this new modality, the drug uptake from micellar paclitaxel increased more than 20-fold, and cellular proliferation was inhibited by nearly 90 %. Ultrasound causes local perturbation of polymeric micelles and cell membranes, thereby enhancing micellar drug release and boosting local intracellular uptake. This treatment modality could be successfully used for the therapy of both drug-sensitive and drug-resistant tumors Howard et al. (2006).

Studies on the mechanism underlying ultrasonic enhancement of cytotoxic drug uptake show that ultrasound enhanced both the intracellular uptake of Pluronic micelles and Pluronic trafficking into cell nuclei. Under ultrasound treatment, the equilibrium between encapsulated drug and free drug is shifted in the direction of free drug due to micelle perturbation. The equilibrium between extracellular and internalized drug is shifted to the intracellular drug due to the ultrasound-induced cellular changes that enhance the accessibility of drugs to various cellular structures (Marin et al. 2001a, b).

Looking into the future with regards to ultrasound-triggered drug release from polymer micelles, Pitt et al. pointed out that the next question to be answered is whether these micelles are efficient at higher frequencies that are easy to focus. Also, they emphasized the needs to develop not only more effective sequestration in combination with higher sensitivity to shear-stress induced drug release, but also more creative molecular designs (Pitt and Husseini and Kherbeck 2013).

20.4.2 Ultrasound-Triggered Chemical Disruption of Polymeric Micelles and Irreversible Payload Release

Inspired by the concept of light-breakable micelles, Xia and Zhao proposed a new ultrasound-triggered release mechanism, *i.e.,* ultrasound-triggered chemical micelle disruption and irreversible release of payload (Zhang et al. 2009; Wang et al. 2009). This mechanism is based on the use of amphiphilic block copolymers of designed molecular structures susceptible to respond to ultrasound. When the micelle solution was subjected to ultrasonic irradiation, the ultrasound-responsive copolymer was specifically degraded and the amphiphilic copolymer structure was broken. Likewise, the hydrophobic/hydrophilic balance was shifted, and consequently the micelle was disrupted and the encapsulated payload was irreversibly released. Figure 20.4 illustrates this new mechanism in terms of ultrasound-responsive PEG-COO-S-S-PPG micelles. Three kinds of copolymers were designed and synthesized. One is copolymer with labile or ultrasound sensitive links in the junction point between hydrophobic and hydrophilic segments. The second is copolymer with a cleavable side group in the hydrophobic segment. The third is copolymer with multi-labile bonds in the hydrophobic segment.

HIFU equipment used in their experiments comprises three main components: Arbitrary waveform generator, RF power amplifier and acoustic lens transducer. The acoustic lens transducer, with a high acoustic focal pressure within a long focal volume and a geometric focal length, was mounted at the bottom of a tank filled with water, and the beams of ultrasound were pointed upwards and focused on a specific spot.

Zhang et al. (2009) prepared diblock copolymer, poly(ethylene glycol)-block- poly(lactic acid) (PEG-b-PLA) and it's micelles. The payload Nile Red (NR) was used to examine the HIFU-induced release behavior by fluorescence emission spectra. At a HIFU power output of 200 W, the percentage of released NR for 60 min reached ~ 65 %. By adjusting the HIFU time,

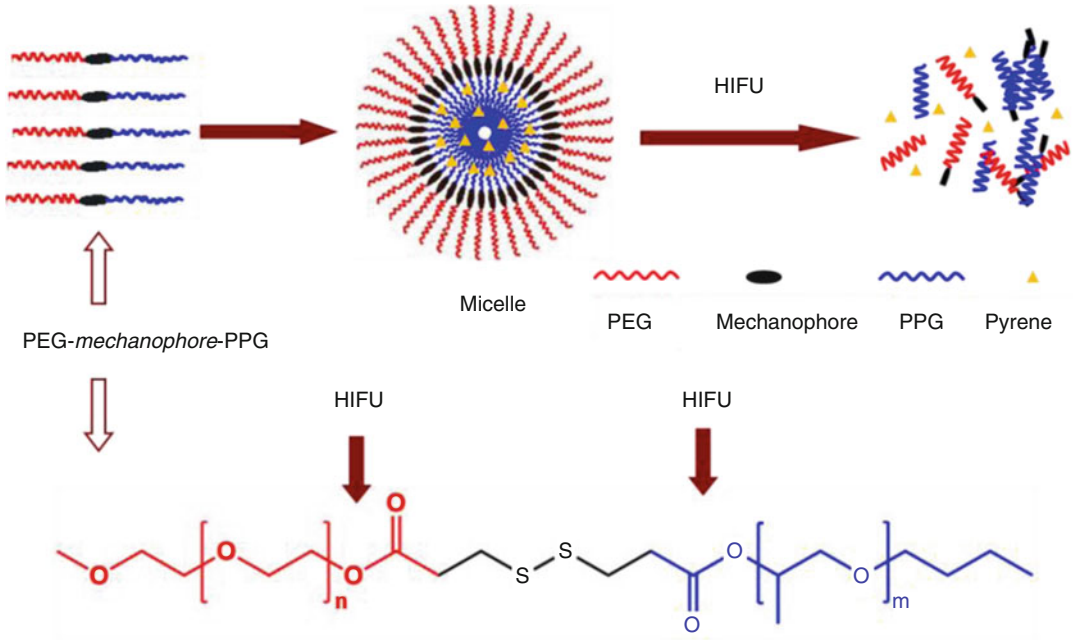

Fig. 20.4 HIFU-responsive behavior of the PEG-COO-S-S-PPG micelle

intensity and location of reactor, the NR release behavior can be tuned. For the controlled block copolymer PEO-PPO-PEO micelle, nearly no NR release was observed after 120 min HIFU treatment, instead a better NR solubilization effect was observed under HIFU treatment. It was found that no reversible encapsulation of the dye occurred after the HIFU was turned off. The irreversible release of NR from PLA-b-PEG micelle was attributed to a chemical breaking of the micelle structure due to the degradation of PLA-b-PEG chain, resulting from transient cavitation in the HIFU focal spot. It was assumed that ultrasonic degradation of PLA-b-PEG block copolymer is due to the scission of the ester bond connecting PEG and PLA block. This study opened up a new way for HIFU-copolymer micelle drug delivery.

However, the HIFU-responsive rate for PLA-b-PEG is not ideal, especially at a lower HIFU power owing to the relatively weak cavitation effect of HIFU. In order to improve the ultrasound response rate and lower ultrasound power, it is of fundamental interest to develop block copolymer micelles that can be rapidly and efficiently disrupted by HIFU. For such a purpose, the copolymer should contain weak bonds, ideally mechano-labile ones that are sensitive to the mechanical effects associated with the ultrasonic cavitation. The labile and redox sensitive disulfide bond was introduced into the central linkage site of PEG-b-PLA, and dual responsive diblock copolymer PEG-S-S-PLA micelles were prepared (Li et al. 2010). The hydrophobic pyrene payload was used to examine HIFU-induced release behavior by fluorescence emission spectra. Like the redox responsive behavior of other copolymer micelles with disulfide bonds, PEG-S-S-PLA micelles could be disrupted slowly under GSH reducing agent due to disulfide bond cleavage. Consequently, hydrophobic payloads in the micellar core were slowly released. Under HIFU treatment, PEG-S-S-PLA micelles were disrupted quickly due to the HIFU-induced decomposition of the block copolymer. Key evidence for this mechanism is that the average molecular weight number of PEG-S-S-PLA copolymer decreases rapidly with HIFU time. The released pyrene reached ~ 90 % in 10 min at a power of 80 W, while there is almost no release in such a short time under GSH treatment. Moreover, the release rate and release percentage

could be easily tuned by adjusting the HIFU time, power output, etc. Combining the two stimuli, GSH and HIFU, the encapsulated cargos could be released in a remote and controllable way. Compared with the control sample, PEG-PLA and PEG-S-PLA with monosulfide bonds, PEG-S-S-PLA with disulfide bonds has a quick response to HIFU, owing to this labile disulfide bond.

In order to confirm the mechanism of HIFU-micelle behavior, a Pluronic copolymer micelle type (PEG-COO-SS-PPG) was prepared with ester and disulfide bonds in the central linkage site between hydrophilic PEG block and hydrophobic PPG block (Tong et al. 2014). It was found that in this copolymer, the central ester bond is more easily broken than the central disulfide bond with weak bond energy in aqueous solution. This result suggests that the mechanophore sensitivity to ultrasound is dependent upon the environmental media. In protic solvents, heterolytic bond cleavage possibly occurs more easily. Under HIFU treatment at 70 W, the hydrophobic pyrene dye can be released up to ~80 % in 10 min, much faster than under DTT treatment. Under the combined treatment of HIFU and DTT, the release rate can be further enhanced. The finding that mechanochemical cleavage occurs preferentially at the central ester bond rather than at the disulfide bond in the micelle aqueous solution may open up a new approach in the design of novel HIFU-responsive micelles for drug release.

The metallo-supramolecular copolymer micelle could also be used for advanced encapsulation and release of both hydrophilic and hydrophobic molecules in the field of nanoreactors, nanocatalysis and drug/gene delivery (Whittell et al. 2011; Gohy et al. 2002). This kind of novel micelle containing a metal-ligand bond located at the junction between two blocks offers the possibility of constructing HIFU-responsive micelles. The metal-ligand coordination bond is highly directional and can be easily broken by ultrasonic cavitation (Karthikeyan et al. 2008; Paulusse and Sijbesma 2008). The metal-ligand bond interaction strength can be tuned by changing the types of metal ion and ligand, which is helpful for the selection of ultrasound intensity. Liang et al. (2014) developed novel ultrasound-responsive metallo-supramolecular block copolymer micelles by coupling metal-ligand bonds with the remote HIFU stimulus, and carried out HIFU-controlled release of the encapsulants from micelles. The diblock polypropylene glycol (PPG) and polyethylene glycol (PEG) copolymers, containing a HIFU-responsive mechanolabile Cu(II)-terpyridine (Tpy) bond in the junction point (PPG-[Cu]-PEG), were synthesized and the micellar HIFU-responsive behavior was investigated. The estimated pyrene payload release percentage reaches ~ 75 % in 30 min at a low HIFU power output of 2 W, while for the control samples PPG-[Ru]-PEG and PEO – PPO – PEO micelles, no release was observed at HIFU power outputs of 2 and 7 W. The release behavior was attributed to a dynamic micelle disruption process resulting from the breakage of the weak Cu(II) – Tpy bonds in the PPG-[Cu]-PEG chain due to the cavitation in the HIFU focal spot. The incorporation of labile metal – ligand bonds into the copolymer micelle system would provide a unique opportunity for HIFU-triggered drug release from the polymer micelles due to the adjustability of the metal – ligand bond strength.

Block copolymers with ultrasound cleavable side groups in the hydrophobic segment were also investigated. Wang et al. (2009) prepared micelles of diblock copolymers composed of poly(ethylene oxide) and poly(2-tetrahydropyranyl methacrylate), and found they were sensitive to high frequency ultrasound (1.1 MHz). More interestingly, the spectroscopic characterization results suggest the occurrence of hydrolysis of the THPMA side groups induced upon exposure to HIFU beams. Thus, hydrophobic THPMA groups convert to hydrophilic MAA groups, creating a shift in the hydrophilic-hydrophobic balance, inducing the disruption of micelles and release of hydrophobic dyes. The micelle disruption process could be changed by adjusting the HIFU time, intensity and location. This study shows the possibility of rationally designing ultrasound sensitive block copolymer micelles with labile chemical linkages in the side group.

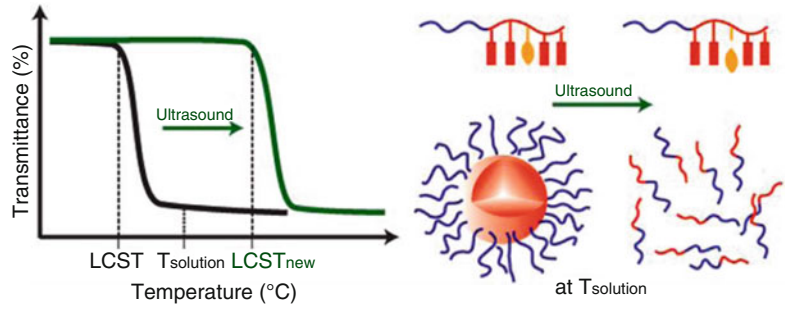

Fig. 20.5 Amplification mechanism for ultrasound-disrupted block copolymeric micelles based on an ultrasound-induced increase in the lower critical solution temperature (LCST) of the hydrophobic block (Xuan et al. 2012)

In order to find possible polymer structures that are susceptible to be affected by ultrasound, a comparative study on the disruption of the micelles formed by various block copolymers, and the concomitant release of encapsulated NR by HIFU, was conducted by Xuan et al. (2011). Four different block copolymer (BCP) micelles, PEG-b-PTHPMA, poly(ethylene oxide)-block-poly[1-(isobutoxy)ethylmethacrylate] (PEO-b-PIBMA), poly(ethylene oxide)-block-poly[(2-tetrahydrofuranyloxy)ethyl methacrylate] (PEO-b-PTHFEMA) and poly(ethylene oxide-block-poly(methyl methacrylate) (PEO-b-PMMA) were examined. Combining the characterization results, they found that all the four micelles formed from the four block copolymers could be disrupted by ultrasound, resulting in the release of hydrophobic NR payload, but the extent of micellar disruption and the release of NR were significantly different due to the different chemical structures of the micelle-core-forming hydrophobic polymethacrylates. For the PEO-b-PIBMA and PEO-b-PTHPMA micelles, whose hydrophobic blocks have a labile acetal unit in the side group, they are more likely to undergo ester hydrolysis and could be disrupted more severely by ultrasound, giving rise to a faster NR release. By contrast, for PEO-b-PMMA micelles, whose polymethacrylate block is more stable, they appear to be more resistant to ultrasound and exhibit a slower rate of NR release than other micelles.

Based on the finding that the PEO-b-PTHPMA micelle is more sensitive to ultrasound irradiation, a new approach for amplifying the effect of HIFU in disassembling amphiphilic block copolymer micelles in aqueous solution was developed (Xuan et al. 2012). The diblock copolymer PEO-b-P(MEO_2MA-co-THPMA) is comprised of a water-soluble poly(ethylene oxide) (PEO) block, and a block of poly(2-(2-methoxyethoxy) ethyl methacrylate ($PMEO_2MA$), that is hydrophobic at temperatures above its lower critical solution temperature (LCST). By introducing a small amount of HIFU-labile 2-tetrahydropyranyl methacrylate (THPMA) comonomer units into the $PMEO_2MA$ that forms the micelle core at T > LCST, ultrasound irradiation of a micellar solution could induce the hydrolysis of THPMA groups. Then, the LCST of the polymer increases due to the conversion of the hydrophobic THPMA group into a hydrophilic MAA group. Consequently, the micelles can be disrupted without changing the solution temperature because the new LCST is above the solution temperature (Fig. 20.5). This approach of changing LCST by HIFU is general and could be applied by further exploring other ultrasound-labile moieties in polymer micelle design.

To further improve ultrasound responsibility, copolymers with multiple labile bonds in the hydrophobic segment were designed. Based on the finding of Wiita et al. (2006) that the exchange reaction between disulfide bonds and thiol groups can be accelerated due to the stretch of disulfide bonds under external mechanical stress, Tong et al. (2013) designed a novel polyurethane (PU)-based tri-block copolymer PEG-PU(SS)-PEG. This contained lots of disulfide bonds incorporated in the hydrophobic block. Pyrene was used as the payload for the PEG-PU(SS)-PEG copolymer micelle. It was found that the redox responsive behavior of the micelle and the pyrene release rate were dependent on the amount of disulfide bonds within the copolymer. Interestingly, under the HIFU treatment in the

presence of reducing agent DTT, the release rate of the copolymer micelle could be significantly enhanced due to the HIFU-induced acceleration of the reaction between disulfide bond and thiol groups. For the copolymer micelles of which each of the repeat units in hydrophobic blocks contains a disulfide bond, ~90 % of the payloads could be released in 12 min with 10 mM DTT at 37 °C. Additionally, it takes only 2 min to release 90 % of the payloads for the same micelles under the combined HIFU (80 W) and DTT treatment.

20.5 Perspectives

Ultrasound is a remote, non-invasive and controllable trigger for the stimuli-responsive release of polymer micelles. Ultrasound-mediated polymeric micelle drug delivery has been successfully used for *in-vitro* cell and *in-vivo* animal experiments and should have a promising future. However, the use of ultrasound as a means to control polymeric micelle disruption remains largely unexplored. A major challenge remains in developing ultrasound-responsive polymeric micelles is to improve the sensitivity or responsiveness of polymer micelles to ultrasound. It is expected to reduce the ultrasound intensity required for effective activation. To achieve this goal, more exploration is required into the use of ultrasound-responsive chemical bonds, which are more susceptible to breaking by ultrasound, and can be used in polymeric micelle drug delivery systems. Also, more useful strategies on introducing weak chemical bonds into polymer structures need to be developed.

Another practical challenge remaining in polymer micelles is their low *in-vivo* stability, which possibly leads to premature payload release once introduced into the body, and thus reduced ability to release the payload on the target. In order to overcome this obstacle, crosslinking of the polymer chains constituting the micelles has been proved to be effective. However, the chain crosslinking may slow down the ultrasound response rate or reduce the efficiency of drug release. Therefore, in order to minimize this conflicting effect, it is important to develop polymer micelles with dynamic crosslinked chemical bonds that can be rapidly disintegrated or opened upon exposure to ultrasound after arrival on the target site.

References

Ariga K, Mori T, Hill JP (2012) Mechanical control of nanomaterials and nanosystems. Adv Mater 24: 158–176

Ashihara K, Kurakata K, Mizunami T, Matsushita K (2006) Hearing threshold for pure tones above 20 kHz. Acoust Sci Tech 2006(27):12–19

Biggs S, Grieser F (1995) Preparation of polystyrene latex with ultrasonic irradiation. Macromolecules 28: 4877–4882

Brantley JN, Wiggins KM, Bielawski CW (2011) Unclicking the click: mechanically facilitated 1,3-dipolar cycloreversions. Science 333:1606–1609

Brantley JN, Wiggins KM, Bielawski CW (2012) Polymer mechanochemistry: the design and study of mechanophores. Polym Int 62:2–12

Brantley JN, Bailey CB, Wiggins KM, Ketinge-Clay AT, Bielawski CW (2013) Mechanobiochemistry: harnessing biomacromolecules for force-responsive materials. Polym Chem 4:3916–3928

Caruso MM, Davis DA, Shen QS, Odom SA, Sottos NR, White SR, Moore JS (2009) Mechanically-induced chemical changes in polymeric materials. Chem Rev 109:5755–5798

Chen KQ, Ye S, Li HL, Xu XJ (1985) Studies on ultrasonic degradation and block/graft copolymerization of hydroxyethyl cellulose and poly(ethylene oxide). J Macromol Sci Chem 22:455–469

Chou H, Stoffer JO (1999) Ultrasonically initiated free radical-catalyzed emulsion polymerization of methyl methacrylate. J Appl Polym Sci 72:797–825

Coll C, Mondragón L, Martínez-Máñez R, Sancenón F, Marcos MD, Soto J, Amorós P, Pérez-Payá E (2011) Enzyme-mediated controlled release systems by anchoring peptide sequences on mesoporous silica supports. Angew Chem Int Ed Engl 50:2138–2140

Cravotto G, Angew CP (2007) Forcing and controlling chemical reactions with ultrasound. Angew Chem Int Ed Engl 46:5476–5478

Cravotto G, Gaudino EC, Cintas P (2013) On the mechanochemical activation by ultrasound. Chem Soc Rev 42:7521–7534

David DA, Hamilton A, Yang J, Cremar LD, Van Goug D, Potisek SL, Ong MT, Braun PV, Matinez TJ, White SR, Moore JS, Sottos NR (2009) Force-induced activation of covalent bonds in mechanoresponsive polymeric materials. Nature 459:68–72

de Geest BG, Skirtach AG, Mamedov AA, Antipov AA, Kotov NA, de Smedt AC, Sukhorukov B (2007) Ultrasound-triggered release from multilayered capsules. Small 3:804–808

Diaz de la Rosa MA (2007) High-Frequency Ultrasound Drug Delivery And Cavitation. MSc thesis, Brigham Young University, USA

Deckers R, Paradissis A, Oerlemans C, Talelli M, Storm G, Hennink WE, Nijsen JFW (2013) New insights into the HIFU-triggered release from polymer micelles. Langmuir 29:9483–9490

Dogra VS, Zhang M, Bhatt S (2009) High-intensity focused ultrasound (HIFU) therapy applications. Ultrasound Clin 4:307–327

EI-sherif DM, Lathia JD, Le NT, Wheatley MA (2004) Ultrasound degradation of novel polymer contrast agents. J Biomed Mater Res A 68A:71–78

Eissa AM, Khosravi E (2011) Synthesis of a new smart temperature responsive glycopolymerisation. Eur Polym J 47:61–69

Fellinger K, Schmid J (1954) Klinik and therapies des chromischen gelenkreumatismus. Maudrich Vienna, Austria, pp 549–555

Fleige E, Quadir MA, Haag R (2012) Stimuli-responsive polymeric nanocarriers for the controlled transport of active compounds: concepts and applications. Adv Drug Deliv Rev 64:866–884

Fry WJ, Fry FJ (1960) Fundamental neurological research and human neurosurgery using intense ultrasound. IRE Trans Med Electron 7:166–181

Fujiwara H, Kimura T, Segi M, Nakataka T, Nakamura H (1992) Mechanochemical block copolymerization in heterogeneous systems of the solid poly(vinyl chloride) with styrene by ultrasonic irradiation. Polym Bull 28:189–196

Fujiwara H, Kikyu T, Nanbu H, Honda T (1994) Mechanochemical block copolymerization in heterogeneous systems of the solid poly(vinyl chloride) with styrene by ultrasonic irradiation. Polym Bull 33:317–323

Geers B, Lentacker I, Sanders NN, Demeester J, Meairs S, De Smedt SC (2011) Self-assembled liposome-laoded microbubbles: the missing link for safe and efficient ultrasound triggered drug delivery. J Control Release 152:249–256

Gohy JF, Lohmeijer BGG, Schubert US (2002) Metallosupramolecular block copolymer micelles. Macromolecules 35:4560–4563

Gronroos A, Pirkonen P, Heikkinen J, Ihalainen J, Mursunen H, Sekki H (2001) Ultrasonic depolymerization of aqueous polyvinyl alcohol. Ultrason Sonochem 8:259–264

Haar GT, Coussios C (2007) High intensity focused ultrasound: physical principles and devices. Int J Hyperthermia 23:89–104

Hasanzadeh H, Mokhtari-Dizaji M, Bathaie SZ, Hassan ZM (2011) Effect of local dual frequency sonication on drug distribution from polymeric nanomicelles. Ultrason Sonochem 18:1165–1171

Henglein VA (1954) Die Auslösung und der Verlauf der Polymerisation des Acrylamids unter dem Einfluß von Ultraschallwellen. Makromol Chem 14:15–39

Hickenboth CR, Moore JS, White SR, Sottos NR, Baudry J, Wilson SR (2007) Biasing reaction pathways with mechanical force. Nature 446:423–427

Howard B, Gao Z, Lee SW, Seo MH, Rapoport N (2006) Ultrasound-enhanced chemotherapy of drug-resistant breast cancer tumors by micellar-encapsulated paclitaxel. Am J Drug Deliv 4:97–104

Husseini GA, Pitt WG (2008) Micelles and nanoparticles for ultrasonic drug and gene delivery. Adv Drug Deliv Rev 60:1137–1152

Husseini GA, Myrup G, Pitt WG, Christensen DA, Rapoport NY (2000) Factors affecting acoustically triggered release of drugs from polymeric micelles. J Control Release 69:43–52

Husseini GA, Christensen DA, Rapoport NY, Pitt WG (2002a) Ultrasonic release of doxorubicin from Pluronic P105 micelles stabilized with an interpenetrating network of N, N-diethylacrylamide. J Control Release 83:303–305

Husseini GA, Rapoport NY, Christensen DA, Pruitt J, Pitt WG (2002b) Kinetics of ultrasonic release of doxorubicin from pluronic P105 micelles. Colloids Surf B 24:253–264

Husseini GA, Runyan CM, Pitt WG (2002c) Investigating the mechanism of acoustically activated uptake of drugs from Pluronic cells. BMC Cancer 2:20

Husseini GA, Diaz de la Rosa MA, Richardson ES, Christensen DA, Pitt WG (2005) The role of cavitation in acoustically activated drug delivery. J Control Release 107:253–261

Husseini GA, Diaz de la Rosa MA, Gabuji T, Zeng Y, Christensen DA, Pitt WG (2007) Release of doxorubicin from unstabilized and stabilized micelles under the action of ultrasound. J Nanosci Nanotechnol 7: 1028–1033

Husseini GA, Pitt WG, Christensen DA, Dicknson DJ (2009) Degradation kinetics of stabilized Pluronic micelles under the action of ultrasound. J Control Release 138:45

Husseini GA, Velluto D, Kherbeck L, Pitt WG, Hubbell JA, Christensen DA (2013) Investigating the acoustic release of doxorubicin from targeted micelles. Colloids Surf B Biointerfaces 101:153–155

Karthikeyan S, Potisek SL, Piermattei A, Sijbesma RP (2008) Highly efficient mechanochemical scission of silver-carbene coordination polymers. J Am Chem Soc 130:14968–14969

Kawasaki H, Takeda Y, Arakawa R (2007) Mass spectrometric analysis for high molecular weight synthetic polymers using ultrasonic degradation and the mechanism of degradation. Anal Chem 79:4182–4187

Kiessling F, Fokong S, Bzyl J, Lederle W, Palmowski M, Lammer T (2014) Recent advances in molecular, multimodal and theranostic ultrasound imaging. Adv Drug Deliv Rev 72:15–27

Kim HJ, Matsuda H, Zhou HS, Honma I (2006) Ultrasound-triggered smart drug release from a poly(dimethylsiloxane)- mesoporous silica composite. Adv Mater 18:3083–3088

Knezevic NZ, Trewyn BG, Lin VSY (2011) Functionalized mesoporous silica nanoparticle-based visible light responsive controlled release delivery system. Chem Commun (camb) 47:2817–2819

Kobayashi D, Karasawa M, Takahashi T, Otake K and Shono A (2012) Effluence of internal substances from pluronic micelle using ultrasound. Jpn J Appl Phys 51:07GD10

Kost J, Langer R (2001) Responsive polymeric delivery systems. Adv Drug Deliv Rev 46:125–148

Kost J, Leong K, Langer R (1989) Ultrasound-enhanced polymer degradation and release of incorporated substances. Proc Natl Acad Sci U S A 86:7663–7666

Kruus P (1983) Polymerization resulting from ultrasonic cavitation. Ultrasonics 21:201–204

Kruus P, Patraboy TJ (1985) Initiation of polymerization with ultrasound in methyl methacrylate. J Phys Chem 89:3379–3384

Kryger MJ, Ong MT, Odom SA, Sottos NR, White SR, Martinez TJ, Moore JS (2010) Masked cyanoacrylates unveiled by mechanical force. J Am Chem Soc 132: 4558–4559

Lee MH, Lin HY, Chen HC, Thomas JL (2008) Ultrasound mediated the release of curcumin from microemulsions. Langmuir 24:1707–1713

Lensen D, Gelderblom EC, Vriezema DM, Marmottant P, Verdonschot N, Versluis M, de Jong N, van Hest JCM (2011) Biodegradable polymeric microscapsules for sequential ultrasound-triggered drug delivery. Soft Matter 7:5417–5422

Li Y, Tong R, Xia H, Zhang H, Xuan J (2010) High intensity focused ultrasound and redox dual responsive polymer micelles. Chem Commun 46:7739–7741

Liang B, Tong R, Wang Z, Guo S, Xia H (2014) High intensity focused ultrasound responsive metallosupramolecular block copolymer micelles. Langmuir 30:9524–9532

Lin HY, Thomas JL (2003) PEG-lipids and oligo(ethylene glycol) surfactants enhance the ultrasonic permeabilizability of liposomes. Langmuir 19:1098–1105

Liu LS, Kost J, D'Emanuele A, Langer R (1992) Experimental approach to elucidate the mechanism of ultrasound-enhanced polymer erosion and release of incorporated substances. Macromolecules 25:123–128

Liu Y, Chou H, Stoffer JO (1994) Analysis of ultrasonically induced free radicals in the emulsion polymerization system by GC-MS. J Appl Polym Sci 53:247–254

Liu X, Zhou T, Du Z, Wei Z, Zhang J (2011) Recognition ability of temperature responsive molecularly imprinted polymer hydrogels. Soft Matter 7:1986–1993

Luche JL (1998) Synthetic Organic Sonochemistry, Springer Science+Business Media, LLC

Makino K, Mossoba M, Reisz P (1983) Chemical effects of ultrasound on aqueous solutions. Formation of hydroxyl radicals and hydrogens atoms. J Phys Chem 87:1369–1377

Malhotra SL (1982) Ultrasonic modification of polymers. II. Degradation of polystyrene, substituted polystyrene, and poly(n-vinyl carbazole) in the presence of flexible chain polymers. J Macromol Sci Chem 18:1055–1085

Marin A, Muniruzzaman M, Rapoport N (2001a) Acoustic activation of drug delivery from polymeric micelles: effect of pulsed ultrasound. J Control Release 71:239–249

Marin A, Muniruzzaman M, Rapoport N (2001b) Mechanism of the ultrasonic activation of micellar drug delivery. J Control Release 75:69–81

Marin A, Sun H, Husseini GA, Pitt WG, Christensen DA, Rapoport NY (2002) Drug delivery in pluronic micelles: effect of high-frequency ultrasound on drug release from micelles and intracellular uptake. J Control Release 84:39–47

Mason TJ, Lorimer JP (1988) Sonochemistry: theory, application and uses of ultrasound in chemistry. Ellis Norwood, Chichester

May PA, Moore JS (2013) Polymer mechanochemistry: techniques to generate molecular force via elongational flows. Chem Soc Rev 42:7497–7506

Mitragotri S (2005) Healing sound: the use of ultrasound in drug delivery and other therapeutic appilications. Nature Rev. Nat Rev Drug Discov 4:255–260

Munshi N, Rapoport N, Pitt WG (1997) Ultrasonic activated drug delivery from Pluronic P-105 micelles. Cancer Lett 118:13–19

Mura S, Nicolas J, Couvreur P (2013) Stimuli-responsive nanocarriers for drug delivery. Nat Mater 12:991–1003

Musyanovych A, Landfester K (2014) Polymer microand nanocapsules as biological carriers with multifunctional properties. Macromol Biosci 14:458–477

Myhr G, Moan J (2006) Synergistic and tumour selective effects of chemotherapy and ultrasound treatment. Cancer Lett 232:206–213

Nakayama M, Akimoto J, Okano T (2014) Polymeric micelles with stimuli-triggering systems for advanced cancer drug targeting. J Drug Target 22:584–599

Nelson JL, Roeder BL, Carmen JC, Roloff F, Pitt WG (2002) Ultrasonically activated chemotherapeutic drug delivery in a rat model. Cancer Res 62:7280–7283

Oerlemans C, Bult W, Bos M, Storm G, Nijsen JFW, Hennink WE (2010) Polymeric micelles in anticancer therapy: targeting, imaging and triggered release. Pharm Res 27:2569–2589

Park K (2010) Focused ultrasound for targeted nanoparticle delivery to tumors. J Control Release 146:263

Paulusse JMJ, Sijbesma RP (2008) Selectivity of mechanochemical chain scission in mixed palladium(II) and platinum(II) coordination polymers. Chem Commun 37:4416–4418

Peer D, Karp JM, Hong S, Farokhzad OC, Margalit R, Langer R (2007) Nanocarriers as an emerging platform for cancer therapy. Nature Nanotechnol 2:751–760

Phenix CP, Togtema M, Pichardo S, Zehbe I, Curiel L (2014) High intensity focused ultrasound technology, its scope and applications in therapy and drug delivery. J Pharm Pharm Sci 17:136–153

Pitt WG, Husseini GA, Staples BJ (2004) Ultrasonic drug delivery – a general review. Expert Opin Drug Deliv 1:37–56

Pitt WG, Husseini GA, Kherbeck LN (2013) Smart Materials for Drug Delivery. RSC Publishing 6(1):169–171

Price GJ, Smith PF (1991) The use of ultrasound for the controlled degradation of polymer solutions. Polym Int 3:159–164

Price GJ, Norris DJ, West PJ (1992) Polymerization of methyl methacrylate initiated by ultrasound. Macromolecules 25:6447–6454

Pritchard EM, Valentin T, Boison D, Kaplan DL (2011) Incorporation of proteinase into silk-based delivery devices for enhanced control of degradation and drug release. Biomaterials 32:909–918

Qiu G, Wang Q, Wang C, Lau W, Guo Y (2007) Polystyrene/Fe3O4 magnetic emulsion and nanocomposite prepared by ultrasonically initiated miniemulsion polymerization. Ultrasonic Sonochem 14:55–61

Rapoport NY (1999) Stabilization and activation of pluronic micelles for the tumor-targeted drug delivery. Colloids Surf B Biointerfaces 16:93–111

Rapoport NY, Herron JN, Pitt WG (1999) Micellar delivery of doxorubicin and its paramagnetic analog, ruboxyl, to HL-60 cells: effect of micelle structure and ultrasound on the intracellular drug uptake. J Control Release 58:153–162

Reich G (1988) Ultrasound-induced degradation of PLA and PLGA during microsphere processing: influence of formulation variables. Eur J Pharm Biopharm 45:165–171

Richards WT, Loomis AL (1927) The chemical effects of high frequency sound waves I. A preliminary survey. J Am Chem Soc 49:3086–3100

Schroeder A, Kost J, Barenholz Y (2009) Ultrasound, liposomes, and drug delivery: principles for using ultrasound to control the release of drugs from liposomes. Chem Phys Lipids 162:1–16

Shchukin DG, Gorin DA, Moehwald H (2006) Ultrasonically induced opening of polyelectrolyte microcontainers. Langmuir 22:7400–7404

Sirsi SR, Borden MA (2014) State-of-the-art materials for ultrasound-triggered drug delivery. Adv Drug Deliv Rev 72:3–14

Skauen D, Zentner G (1984) Phonophoresis. Int J Pharm 20:235–245

Skirtach AG, De Geest BG, Mamedov A, Antipov AA, Kotov NA, Sukhorukov GBJ (2007) Ultrasound stimulated release and catalysis using polyelectrolyte multilayer capsules. J Mater Chem 17:1050–2054

Smith MJ, Eccleston ME, Slater NK (2008) The effect of high intensity focussed ultrasound (HIFU) on pH responsive PEGylated micelles. J Acoust Soc Am 123:3223

Stevenson-Abouelnasr D, Husseini GA, Pitt WG (2007) Further investigations of the mechanism of Doxorubicin release from P105 micelles using kinetic models. Colloids Surf B Biointerfaces 55:59–66

Su J, Chen F, Cryns VL, Messersmith PB (2011) Catechol polymers for pH-responsive, targeted drug delivery to cancer cells. J Am Chem Soc 133:11850–11853

Suslick KS (1990) Sonochemistry. Science 247:1439–1445

Tabata M, Sohma J (1980) Direct evidence of main-chain scissions induced by ultrasonic irradiation of benzene solutions of polymers. Chem Phys Lett 73:178–180

Timko BP, Dvir T, Kohane DS (2010) Remotely triggerable drug delivery systems. Adv Mater 22:4925–4943

Tong R, Xia H, Lu X (2013) Fast release behavior of block copolymer micelles under high intensity focused ultrasound/redox combined stimulis. J Mater Chem B 1:886–894

Tong R, Lu X, Xia H (2014) A facile mechanophore functionalization of an amphiphilic block copolymer towards remote ultrasound and redox dual stimulus responsiveness. Chem Commun 50:3575–3578

Ugarenko M, Chan CK, Nudelman A, Rephaeli A, Cutts SM, Phillips DR (2009) Development of pluronic micelle-encapsulated doxorubicin and formaldehyde-releasing prodrugs for localized anticancer chemotherapy. Oncol Res 17:283–299

Wang Q, Xia H, Zhang C (2001) Preparation of polymer/inorganic nanoparticles composites through ultrasonic irradiation. J Appl Polymer Sci 80:1478–1488

Wang C, Wang Q, Chen X (2005) Intercalated PS/Na^+-MMT nanocomposites prepared by ultrasonically initiated in situ emulsion polymerization. Macromol Mater Eng 290:920–926

Wang J, Pelletier M, Zhang H, Xia H, Zhao Y (2009) High-frequency ultrasound-responsive block copolymer micelle. Langmuir 25:13201–13205

Whittell GR, Hager MD, Schubert US, Manners I (2011) Functional soft materials from metallopolymers and metallosupramolecular polymers. Nat Mater 10: 176–188

Wiggins KM, Brantley JN, Bielawski CW (2013) Methods for activating and characterizing mechanically responsive polymers. Chem Soc Rev 42:7130–7147

Wiita AP, Ainavarapu SRK, Huang HH, Fernandez JM (2006) Force-dependent chemical kinetics of disulfide bond reduction observed with single-molecule techniques. Proc Natl Acad Sci U S A 103:7222–7227

Xia H, Wang Q (2001) Synthesis and characterization of conductive polyaniline nanoparticle through ultrasonic assisted inverse microemulsion polymerization. J Nanopart Res 3:401–411

Xia H, Wang Q (2002) Ultrasonic irradiation: a novel way to prepare conductive polyaniline/nanocrystalline TiO_2 particles composites. Chem Mater 14:2158–2165

Xia H, Wang Q (2003) Preparation of conductive polyaniline/nanosilica particle composites through ultrasonic irradiation. J Appl Polymer Sci 87:1811–1817

Xia H, Zhang C, Wang Q (2001) Study on ultrasonic induced encapsulating emulsion polymerization in presence of nanoparticles. J Appl Polymer Sci 80:1130–1139

Xia H, Wang Q, Liao Y, Xu X (2002) Polymerization rate and mechanism of ultrasonically initiated emulsion polymerization of n-butyl acrylate. Ultrasonics Sonochem 9:151–158

Xia H, Wang Q, Qiu G (2003) Polymer-encapsulated carbon nanotubes prepared through ultrasonically initiated in-situ emulsion polymerization. Chem Mater 15:3879–3886

Xuan J, Pelletier M, Xia H, Zhao Y (2011) Ultrasound-induced disruption of amphiphilic block copolymer micelles. Macromol Chem Phys 212:498–506

Xuan J, Boissière O, Zhao Y, Yan B, Tremblay L, Lacelle S, Xia H, Zhao Y (2012) Ultrasound-responsive block copolymer micelles based on a new amplification mechanism. Langmuir 28:16463–16468

Yan B, Boyer JC, Branda NR, Zhao Y (2011) Near-infrared light-triggered dissociated of block copolymer micelles using upconverting nanoparticles. J Am Chem Soc 133:19714–19717

Yuan F, Dellian M, Fukumura D, Leunig M, Berk DA, Torchilin VP, Jain RK (1995) Vascular-permeability in a human tumor xenograft – Molecular-size dependence and cutoff size. Cancer Res 55:3752–3756

Zeng Y, Pitt WG (2006) A polymeric micelle system with a hydrolysable segment for drug delivery. J Biomater Sci Polym Ed 17:591–604

Zhang Y, Pitt WGJ (2006) A polymeric micelle system with a hydrolysable segment for drug delivery. J Biomater Sci Polym Ed 17:591–604

Zhang J, Chen KQ, Liu QR, Xu X (1990) Ultrasonic heterogeneous copolymerization of poly (ethylene oxide) with hexyl methacrylate. Acta Polym Sin 3:271–276

Zhang C, Wang Q, Xia H, Qiu G (2002) Ultrasonic-induced microemulsion polymerization of styrene. Eur Polymer J 38:1769–1776

Zhang H, Xia H, Wang J, Li Y (2009) High intensity focused ultrasound-responsive release behavior of PLA-b-PEG copolymer micells. J Control Release 139:31–39

Zhou K, Wang Y, Huang X, Luby-Phelps K, Sumer BD, Gao J (2011) Tunable, ultrasensitive pH-responsive nanoparticles targeting specific endocytic organelles in living cells. Angew Chem Int Ed Engl 50:6109–6114

Stimulation of Bone Repair with Ultrasound

21

Frédéric Padilla, Regina Puts, Laurence Vico, Alain Guignandon, and Kay Raum

Abstract

This chapter reviews the different options available for the use of ultrasound in the enhancement of fracture healing or in the reactivation of a failed healing process: LIPUS, shock waves and ultrasound-mediated delivery of bioactive molecules, such as growth factors or plasmids. The main emphasis is on LIPUS, or Low Intensity Pulsed Ultrasound, the most widespread and studied technique. LIPUS has pronounced bioeffects on tissue regeneration, while employing intensities within a diagnostic range. The biological response to LIPUS is complex as the response of numerous cell types to this stimulus involves several pathways. Known to-date mechanotransduction pathways involved in cell responses include MAPK and other kinases signaling pathways, gap-junctional intercellular communication, up-regulation and clustering of integrins, involvement of the COX-2/PGE2 and iNOS/NO pathways, and activation of the ATI mechanoreceptor. Mechanisms at the origin of LIPUS biological effects remain intriguing, and analysis is hampered by the diversity of experimental systems used *in-vitro*. Data point to clear evidence that bioeffects can be modulated by direct and indirect mechanical effects, like acoustic radiation force, acoustic streaming, propagation of surface waves, heat, fluid-flow induced circulation and redistribution of nutrients, oxygen and signaling molecules. One of the future engineering challenge is therefore the design of dedicated experimental set-ups allowing control of these

F. Padilla (✉)
Inserm U1032, LabTau, Université de Lyon, Lyon 69003, France
e-mail: frederic.padilla@inserm.fr

R. Puts • K. Raum
Berlin-Brandenburg School for Regenerative Therapies, Charité – Universitätsmedizin Berlin, Föhrerstr. 15, 13353 Berlin, Germany

L. Vico • A. Guignandon
Inserm U1059 Lab Biologie intégrée du Tissu Osseux, Université de Saint-Etienne, St-Etienne 42023, France

© Springer International Publishing Switzerland 2016

J.-M. Escoffre, A. Bouakaz (eds.), *Therapeutic Ultrasound*, Advances in Experimental Medicine and Biology, Vol. 880, DOI 10.1007/978-3-319-22536-4_21

different mechanical phenomena, and to relate them to biological responses. Then, the derivation of an 'acoustic dose' and the cross-calibration of the different experimental systems will be possible. Despite this imperfect knowledge of LIPUS biophysics, the clinical evidence, although most often of low quality, speaks in favor of the clinical use of LIPUS, when the economics of nonunion and the absence of toxicity of this ultrasound technology are taken into account.

Keywords
Bone repair • Low intensity pulsed ultrasound

21.1 Introduction

There are several ways by which ultrasound can influence bone fracture healing. Ultrasound has played, or has the potential to play, a role in different aspects of the process of bone regeneration. It can act on the biological components of the regeneration process via promotion of cell proliferation, cell pre-conditioning to orient their differentiation during culture (Claes and Willie 2007; Cui et al. 2007) or cell transfection (Sheyn et al. 2008). Ultrasound can modulate the micro-environment by triggering delivery of growth factors or gene expression in engineered cells (Chappell et al. 2008; Fabiilli et al. 2013), or by modulating the physical environment by heat deposition or mechanical stimulation (Kruse et al. 2008). Ultrasound can also be useful in tissue engineering approaches by acting on the scaffolds for improvements of scaffold integration, characterization and control of the rate of scaffold degradation (Mather et al. 2008; Parker et al. 2011; Winterroth et al. 2011; Kim et al. 2008). Within this arsenal, LIPUS (or Low Intensity Pulsed Ultrasound) techniques aim at modulating the physical environment of the cells, in particular by mechanical stimulation.

Different forms of ultrasound treatment (LIPUS, Shock Waves) have been proposed to stimulate or induce bone repair. Biophysical effects of ultrasound, and in particular of therapeutic ultrasound used for thermal ablation or drug delivery, have been documented (O'Brien 2007). However, the mechanisms by which ultrasound can interact with cells and/or their microenvironments during fracture healing are still open to debate.

Clinical results obtained with ultrasound stimulation of bone healing are still controversial, suggesting a potential effective role, but depending on the medical history of previous treatments, site and type of fracture or bone loss (like bone lengthening), pathology (fresh fracture *vs* delayed unions) and treatment modality (daily treatment duration, intensity, frequency…). Thus suggesting the need for standardization of treatment dose and for further randomized controlled trials (Martinez de Albornoz et al. 2011; Romano et al. 2009; Claes and Willie 2007; Busse et al. 2009). Moreover, the lack of understanding of the relevant mechanisms that trigger a positive biological response suggests that optimization of technology devices and treatment regimens remains to be fulfilled.

The main purpose of this chapter is to give the reader a general idea on existing ultrasound applications for the stimulation of bone healing and treatment of nonunions. The main focus is placed on the LIPUS technique, which has pronounced bioeffects on tissues regeneration, while employing intensities within a diagnostic range (Romano et al. 2009; Claes and Willie 2007; Pounder and Harrison 2008). The updated state of LIPUS biological and clinical knowledge is summarized and discussed through the prism of plausible physical effects implicated with observed biological phenomena. The core of the chapter is based on a previously published review (Padilla et al. 2014), which has been revised and updated, and upgraded with a Sect. 21.7.

21.2 LIPUS Physics

21.2.1 LIPUS Exposure Conditions

Heating, cavitation and acoustic streaming have been proposed to be the main physical mechanisms to stimulate cells *in-vitro*. LIPUS stimulation studies have been conducted with frequencies between 45 kHz and 3 MHz, intensity levels between 5 and 1000 mW/cm^2 (SATA: spatial average, time average), in continuous or burst mode, and with daily exposure times between 1 and 20 min.

The vast majority of the published studies were performed with devices similar to the commercial system Exogen (SAFHS, Exogen, NJ). This system uses unfocused circular transducers with effective surface areas of 3.88 cm^2, and the following typical stimulation conditions: Frequency 1.5 MHz, intensity 30 mW/cm^2 (SATA), burst mode 200 µs ON/800 µs OFF (*i.e.,* pulse repetition rate 1 kHz) and daily exposure 20 min (Lu et al. 2009). Other studies report the use of unfocused transducers with different surface areas, ultrasound frequencies between 45 kHz (Reher et al. 2002) and 3 MHz (Nakamura et al. 2011), intensity levels between 5 and 2400 mW/cm^2 (Reher et al. 2002; Li et al. 2002), and duty cycles (*e.g.,* 2 ms ON at 100 Hz pulse repetition rate, or continuous wave mode) (Nakamura et al. 2011).

For lossless linear plane wave propagation, the relation between acoustic impedance $Z = \rho c$, particle velocity v and acoustic pressure P is:

$$P = Zv \tag{21.1}$$

The intensity is proportional to the square of the acoustic pressure:

$$I = \frac{|p_r|^2}{2Z} \tag{21.2}$$

where $|p_r|^2$ is the absolute acoustic peak rarefractional pressure of the wave. The mechanical index MI is defined as:

$$MI = \frac{p_r}{\sqrt{f_0}} \tag{21.3}$$

where f_0 is the frequency of the acoustic wave. The spatial intensity distribution of a plane circular transducer is shown in Fig. 21.1. For LIPUS studies, the spatially and temporally averaged intensity (I_{SATA}) is commonly reported. The latter is determined by means of the acoustic radiation force F_{rad} acting on a large absorber that is placed perpendicular to the beam axis in the sound field (*i.e.,* a radiation force balance):

$$F_{rad} = \frac{W}{c_0} \tag{21.4}$$

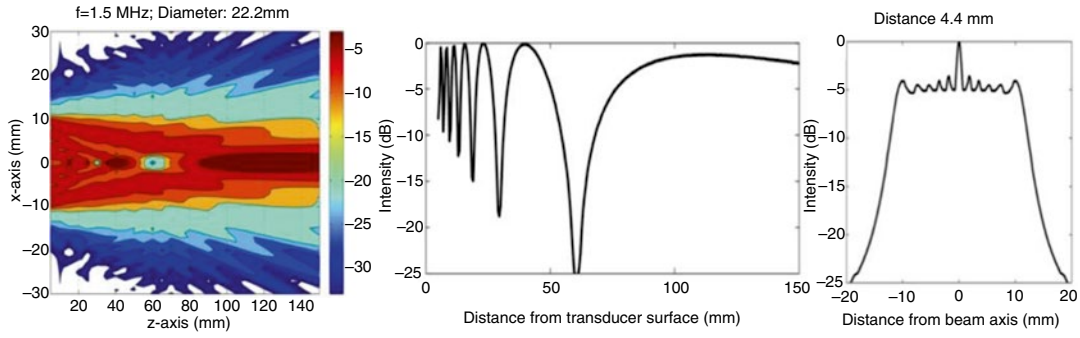

Fig. 21.1 *Left*: Temporal peak intensity (I_{TP}) distribution of a plane circular transducer of 22 mm in diameter. The transducer is centered at the origin of the coordinate system in the x, y plane. *Middle*: Axial intensity (I_{TP}) distribution along the beam axis (x, y = 0). *Right*: Lateral intensity (I_{TP}) distribution at a distance of 4.4 mm from the transducer surface

where W and c_0 are the total acoustic output power and the sound velocity in the medium, respectively. The force can be measured with an ultrasonic power balance. For example, the acoustic output power of 1 mW produces a force of 0.69 μN in water (Humphrey 2007). Total acoustic output power is related to the transducer surface area a, I_{SATA} by:

$$I_{SATA} = \frac{W}{a} \tag{21.5}$$

21.2.2 Rationale for LIPUS

It is important to consider the spatial and temporal characteristics of the acoustic waveform used in LIPUS studies. For a continuous wave, the radiation force is time invariant. However, for pulsed excitation, the force varies periodically at the pulse repetition frequency (*i.e.,* the inverse of the period between the emissions of two consecutive pulses). For the commonly used burst excitation at 1 kHz pulse repetition frequency ($\tau_{on} = 200$ μs), the relation between temporal peak (I_{TP}) and temporal averaged (I_{TA}) intensity is:

$$I_{TA} = \tau_{on} \cdot PRF \cdot I_{TP} = 0.2 \cdot I_{TP} \tag{21.6}$$

The spatial and temporal variations of I_{TA} within the acoustic beam give rise to local radiation pressure variations, and resulting strain and motion at frequencies independent of the emission acoustic frequency, but related to the *PRF*. The local radiation pressure averaged over the pulse duration τ_{on} is:

$$P_{rad} = \frac{1}{2}\frac{|p_r|^2}{\rho_0 c_0^2} = \frac{I_{PA}}{c_0} \tag{21.7}$$

I_{PA} denotes intensity averaged over the pulse duration τ_{on}. Amplitude and direction of the radiation force depend on the properties of the interrogated material. For small-unbound particles, local radiation pressure gradients can result in particle movement. In the special case of standing waves, this can in turn lead to a separation of particles or cells at nodes/antinodes depending on the properties of the particles and fluid. This effect is utilized for example in acoustic tweezers (Ding et al. 2012). The assumption that the low frequency of the radiation force, but not the pressure alteration at the ultrasound excitation frequency, is responsible for the biological effect observed in LIPUS led to studies investigating direct stimulation at the modulating frequency of 1 kHz. This suggested that the radiation force is indeed an important component of the stimulation (Argadine et al. 2005, 2006). This may also imply that the *PRF*, *i.e.,* the frequency of the resulting radiation pressure, could have an impact on the biological outcome if cells are sensitive in this range of cyclic loading, an assumption that is supported by recent experimental evidence obtained with varying *PRF* (Marvel et al. 2010).

Attenuation, nonlinear sound propagation (*i.e.,* the conversion of acoustic energy from fundamental to harmonic frequencies) and divergence of the acoustic waves in the far-field of the transducer lead to a gradual decrease of the radiation pressure with increasing distance from the acoustic source. The attenuation in pure water is (Pinkerton 1949): $\alpha = 2.17 \cdot 10^{-15} \cdot f^2 \left(dB/cm\right)$, whereas in soft tissues it is typically assumed that attenuation is linear with frequency and varies as $\propto = 0.3$ dB/cm/MHz.

This radiation pressure gradient gives rise to a net force directed away from the transducer and a resulting fluid flow in liquids (Fig. 21.2). Solid interfaces hinder this fluid flow induced mass transport. However, it has been shown that fluid streaming can build up again in the acoustic beam behind a membrane (Humphrey 2007).

Experimentally, it was observed that acoustic streaming (i) increases with increasing proportion of nonlinear acoustic propagation, *i.e.,* with the generation of harmonics at higher intensities, (ii) gradually increases with increasing distance from the transducer, and (iii) builds up 60 % of the free streaming velocity within 1 mm after solid interfaces (Humphrey 2007). The streaming velocity in water and amniotic fluid was measured at 3.5 MHz (a = 2.82 cm^2, focus distance: 95 mm,

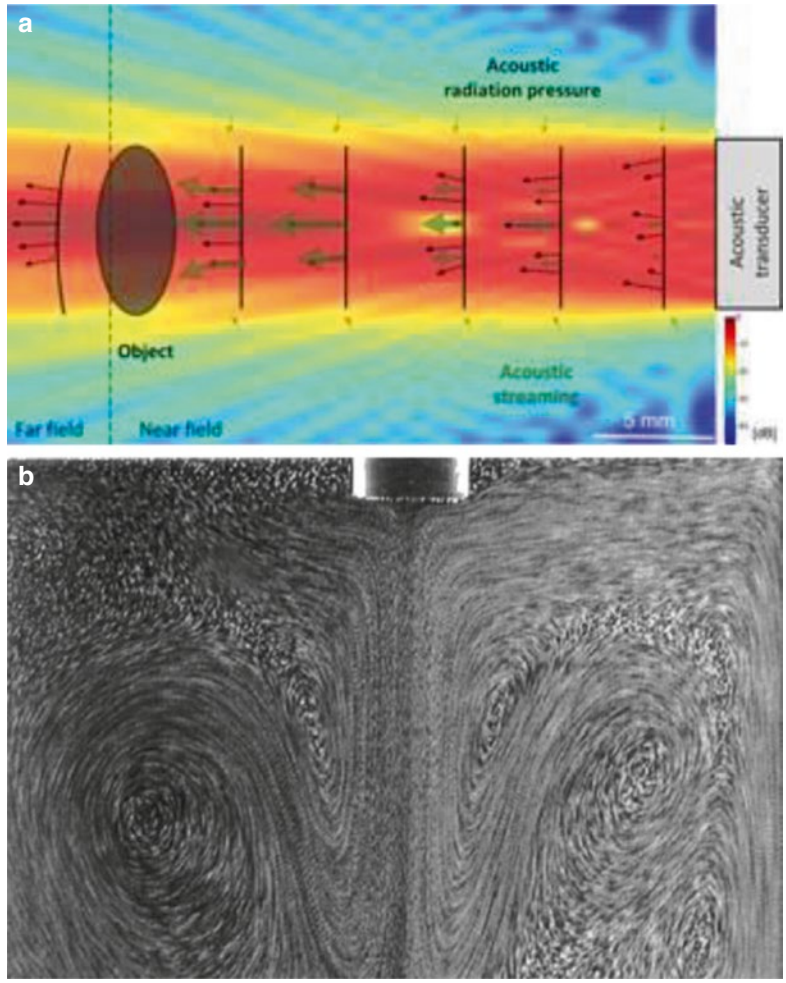

Fig. 21.2 Acoustic radiation force and streaming action on objects in the sound field generated by an acoustic source. *Top*: In liquids, the radiation force (*black arrows*) gives rise to acoustic streaming (*green arrows*). The inhomogeneous intensity distribution in the near field results in a regional dependence of the direction and the amplitude of the radiation force. Acoustic streaming velocity is gradually increasing from the transducer surface to the focus region. Solid interfaces interrupt the flow, but not the radiation pressure. *Bottom*: Acoustic streaming, visualized by ten superimposed images taken at 200 ms intervals of corn starch particles in the field of a 32-MHz plane transducer (Nowicki et al. 1998)

CW, W = 140 mW, P_A = 0.23 MPa, I_{SATA} ~ 50 mW/cm^2) to be in the order of 3 cm·s^{-1} (Zauhar et al. 2006). Much higher velocities (up to 9 cm·s^{-1}) were observed for high-amplitude short pulse excitation (W = 140 mW, P_A = 4 MPa, I_{SATA} ~ 50 mW/cm^2). In cell culture flasks, values of 0.4, 6.0 and 19.4 cm/s at 130, 480 and 1770 mW/cm^2, respectively, were measured at 3 MHz and continuous wave excitation (Harle et al. 2005). In this later study, no cavitation events could be recorded for intensities below 500 mW/cm^2.

Several groups investigated the temperature rise possibly induced by LIPUS. They generally ruled out temperature effects as the measured temperature increase was typically below 0.2 °C for intensities (SATP: spatial average, temporal peak) below 500 mW/cm^2 (Harle et al. 2005) or

even 2400 mW/cm^2 (Li et al. 2002). This was for experimental setups where the cell dish was positioned in the focal plane with a special absorbing chamber, preventing multiple reflections within the dish (see next section). The issue of temperature rise is however highly dependent on the experimental set-up. These effects have been studied in detail by Leskinen and Hynynen (2012), reporting maximum temperature rises of 3 °C at 30 mW/cm^2 (I_{SATA}) in experimental set-ups in which the transducer was coupled to the bottom of culture plates with coupling gel. In contrast, a maximum elevation of 0.2 °C was observed if the transducer was immersed in water. This effect is related to the heating of the ultrasound transducer. The poor heat transfer properties of surrounding air leads to a heat transfer through the coupling gel into the well plate. Therefore, temperature-related biological effects may be induced in cell culture systems in which the transducer is not properly cooled, but not in systems in which the transducer is immersed in a temperature controlled water tank.

Besides temperature elevation, radiation pressures, streaming and standing waves effects, propagation of surface shear waves and Lamb waves have been reported to take place *in-vitro* due to mode conversions at the bottom of plastic wells (Leskinen and Hynynen 2012). These waves can in turn be responsible for bioeffects and can propagate to neighboring wells, jeopardizing the attempt to precisely control the stimulus delivered to a given cell monolayer.

It appears therefore that only cavitation can be ruled out for stimulation intensities below 500 mW/cm^2. Mechanical forces resulting from spatial and temporal gradients of radiation pressure and acoustic streaming, propagation of surface and guided waves are likely sources for biological effects observed in LIPUS stimulation studies. Temperature effects can be ruled out in experimental set-ups with water coupling, but its potential role in setups using gel coupling cannot be ignored.

21.2.3 The Influence of Geometrical Configurations on In-vitro Stimulation

For the exposure the ultrasound transducer has to be coupled to the cell culture dish. Different set-ups have been used, *i.e.,* (i) immersion of the sterilized transducer from the top directly into the culture medium in close distance (3–5 mm) to the cell layer (Fig. 21.3a), (ii) direct coupling to the bottom of the culture dish via coupling gel (Fig. 21.3b), (iii) exposure from the bottom of the culture dish with the cell layer place in the focal plane and immersion of a special sound absorption chamber (Fig. 21.3c), and (iv) the propagation of the sound through a culture flask (Fig. 21.3d).

Considering the spatial and temporal sound field dimensions, as illustrated by Fig. 21.1, and the limited dimension of the culture dishes, several sound propagation phenomena, *e.g.,* inhomogeneous pressure distribution in the near field, multiple reflections at interfaces, standing waves and acoustic streaming have to be considered.

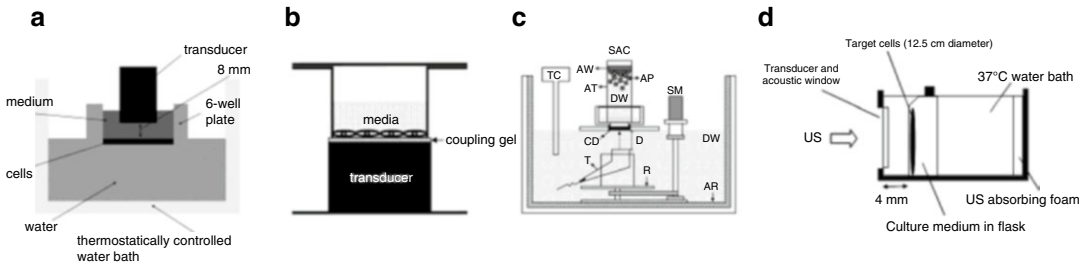

Fig. 21.3 Different sound exposure set-ups used for *in-vitro* LIPUS stimulation. (**a**) (Gleizal et al. 2006) (**b**) (Sena et al. 2005), (**c**) (Lai et al. 2010) and (**d**) (Dalla-Bona et al. 2006)

The sound propagation distance in the cell culture dish or flask (a few mm) is generally much smaller compared to the total propagation distance a wave can travel before it is attenuated. The attenuation in water at 1 MHz and 37 °C is very low (0.0014 dB/cm (Hensel et al. 2011)). If the incoming waves are not properly absorbed or directed away from the culture dish, they will be reflected several times at internal interfaces. Due to the long pulse duration of at least 200 µs (which is equal to 300 cycles, or in terms of wavelength: 300 × 1 mm = 0.3 m at 1.5 MHz), any interface perpendicular to the sound propagation direction, *e.g.,* liquid/plastic, liquid/air, or liquid/transducer, will result in the development of standing waves, ring interferences and a remarkable prolongation of the duty cycle (Fig. 21.4). As a consequence, the effective peak and time average intensity levels, and the resulting modulation of the radiation force between ON and OFF phases, is considerably different from that measured in an interface-free medium. The estimation of the effects of standing waves is not straightforward as the development of nodes depends on multiple factors (Hensel et al. 2011).

Another important factor is the transmission and reflection of the sound waves through the well plate walls. Multiple reflections inside the plastic result in pronounced oscillations of the transmitted and reflected amplitudes. The resonance frequencies for maximum transmission (f_{Tn}) and reflection (f_{Rn}) are:

$$f_{Tn} = \frac{nc}{d}, \quad n = 1,2,3,\ldots \tag{21.8}$$

$$f_{Rn} = \frac{nc}{2d}, \quad n = 1,2,3,\ldots \tag{21.9}$$

where c and d are sound velocity and thickness of the plate, respectively.

If the ultrasound frequency is set to the anti-resonance value, the transmitted or reflected wave amplitudes can be completely diminished (Leskinen and Hynynen 2012). For a typical polystyrene well-chamber with a longitudinal sound velocity of 2305 m/s at 37 °C and a well bottom thickness of 1.22 mm, the transmission and reflection resonance frequencies are at intervals of 1916 and 958 kHz, respectively. Therefore, stimulations conducted with the same set-up, but different frequencies, may result in different exposure levels in the well, if the sound has to be propagated through the well plate bottom.

21.2.4 The LIPUS 'Dose' and the Need for Standardization

Standardization of experimental settings, both *in-vitro* and *in-vivo*, is a crucial factor in order to not only compare studies, but also to be able to iden-

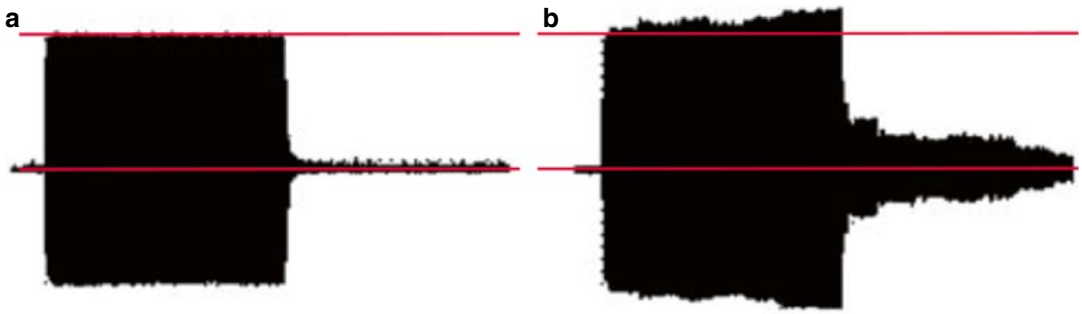

Fig. 21.4 LIPUS temporal wave pattern in a culture dish with the transducer placed on the bottom of the dish and (**a**) in presence or (**b**) absence of a silicon absorbing chamber on the top of the dish (Reproduced from Fig. 1 of Iwabuchi et al. (2005)). Without an absorbing chamber, a gradual increase of intensity during the ON cycle and a gradual decay during the OFF cycle can be seen, leading to effective slight and remarkable increases of the applied temporal peak (I_{TP}) and temporal average (I_{TA}) intensities, respectively

tify relevant parameters and subsequent physical and biological effects. This is particularly important *in-vitro* because both the positioning of the culture plates/wells with respect to the ultrasound source and the output of the source can be regarded as responsible for a lack of reproducibility of LIPUS treatments of cells. In particular, the formation of standing wave patterns have been reported to be very sensitive to the height of the fluid in the wells, and to be responsible for very large spatial variations of the peak pressure applied on the cells (Williams et al. 2013; Hensel et al. 2011). The effects of intensities have indeed been reported to influence the outcome of *in-vitro* experiments.

The concept of an acoustic 'dose' for LIPUS that could be standardized is difficult to derive. Similarly to therapeutic thermal ultrasound (Duck 2011), the dose should be related to the amount of bioeffect induced. However, given the lack of understanding of which parameters of the stimulation are responsible for any given bioeffects, the dose is so far a lacking concept in the field of LIPUS. We therefore suggest that precise data on transducer geometry, intensity, peak pressure, duty cycle, pulse duration, center frequency are reported. Concerning the *in-vitro* cases, great care should be given to the geometry of the experimental set-up to evaluate the aforementioned parameters in the well and in particular to avoid the formation of standing wave patterns and heating by the transducer. For historical reasons, most of the studies have been performed using parameters similar to the Exogen commercial system, *i.e.,*: plane transducer, $I_{SATA} = 30$ m W/cm^2, 200 µs pulses, 1 kHz *PRF*, treatment time 20 min daily. Unless otherwise mentioned, our discussion is focused on data obtained using these settings.

21.3 Potential Bio-effects of LIPUS

The difficulty in interpreting LIPUS experiments lies in the complexity of the triggered physical phenomena that can in turn potentially induce bio-effects. Compared to experimental designs implying laser traps, controlled fluid shear stress or magnetic bead twisting, it is difficult to isolate a single pattern of mechanical stimulation by a propagating ultrasound wave. This problem is even more severe as several of these potential acoustical phenomena can be activated with similar acoustic output parameters to a variable extent, depending on the particular geometry of the stimulation system, (Hensel et al. 2011) and that the biological response to the treatment may depend on cell and tissue types (Claes and Willie 2007).

Potential LIPUS physical effects that may induce a biological response can be divided into thermal and non-thermal effects.

21.3.1 Thermal Effects

Temperature rises associated with LIPUS can range from a few tenths of a degree, to a few degrees at the bottom of the culture well when coupling gel is used (Leskinen and Hynynen 2012). These changes can be significant enough to regulate thermo-sensitive enzymes, such as metalloproteinase, which support threefold reaction rate increases per 2 °C temperature rise and are important enzymes for bone matrix remodeling (Kusano et al. 1998; Welgus et al. 1981). These associated effects should be further investigated. For water-coupling experimental setups, it is a fair assumption to consider that thermal effects are not determining, but rather additive to the non-thermal effects.

21.3.2 Non-thermal effects

Non-thermal effects imply dynamic mechanical forces at various frequencies (from quasi-stationary up to the acoustic excitation frequency) (Sarvazyan et al. 2010; Argadine et al. 2005, 2006). A bulk ultrasonic wave is a propagating mechanical perturbation of the medium, and for a frequency of 1 MHz (typical center frequency for LIPUS devices) the correspond-

ing wavelength is about 1.5 mm in soft tissues or in culture medium. This wave can directly affect the mechanosensitive elements (see next section) by inducing oscillatory strains at very high frequency (typically thousands to a few million oscillations per second) compared to physiological strains. The strain amplitudes will be a function of the applied intensity, and are typically of the order of 10^{-5} for low intensity ultrasound. Secondary mechanisms at lower frequencies can also be triggered by the acoustic radiation force (Sarvazyan et al. 2010) – an oscillatory strain acting at the frequency corresponding to the pulse repetition frequency for pulsed ultrasound (typically 1 kHz for LIPUS-type stimulation), resulting in a low frequency cyclic mechanical stimulus (Argadine et al. 2005, 2006). Inhomogeneities in the acoustic near field, or caused standing waves and ring interferences, can also generate local strain gradients. Finally, fluid-flow related phenomena can also be induced, such as acoustic streaming, resulting in a quasi-stationary fluid flow (Zauhar et al. 2006) and microstreaming, *i.e.,* fluid streaming around oscillating particles.

The relevant scale at which these effects will influence the cellular and tissue biological responses in the context of bone healing remains an open question.

21.3.3 Effects at the Tissue and Cellular Scales

Radiation force, fluid flow and strain gradients can create shear stresses on cell membranes. Acoustic streaming and microstreaming, often used in the literature interchangeably but consequences of two separate physical phenomena, are thought to play important roles in LIPUS action, especially *in-vitro*. Acoustic streaming. The former is associated with a transfer of momentum to the fluid that will result in nutrient redistribution in the culture medium *in-vitro* and perturbation of local homeostasis, thus triggering biological responses. Microstreaming The latter is generated in response to oscillating gas bubbles, or other small acoustic inhomogeneities, causing circulatory fluid movement. Microstreaming around gas bubbles in response to LIPUS is not likely to occur in bone tissue or in the fracture callus *in-vivo* because the pressure levels applied by LIPUS systems are well below cavitation thresholds. However, it can be hypothesized that the wave propagation through the highly porous network of soft and mineralized tissues in the fracture callus may induce fluid micromovement in the pores. Fluid flow, created by either acoustic streaming or microstreaming, can modulate the extracellular matrix and can apply shear stress, in turn activating mechanoreceptors on the cell membranes.

21.3.4 Intracellular Effects

Direct mechanical action of the ultrasound wave on cell membranes or proteins may trigger a biological response. At intensities between 1 and 2 W/cm^2 (*i.e.,* much higher than applied by typical LIPUS), the very low strains induced by ultrasound on cells *in-vitro* have been reported to induce a prompt fluidization of the cytoskeleton, resulting in accelerated cytoskeletal remodeling events (Mizrahi et al. 2012). These mechanisms, similar to those caused by physiological strains of higher amplitude and much lower frequency, could contribute to LIPUS bioeffects.

Other proposed mechanisms of pulsed ultrasound action at the intracellular scale include the hypothesis of relative oscillatory displacements between intracellular elements of different densities (Or and Kimmel 2009), such as cell nuclei and the structures in which they are embedded. By modeling the linear oscillations of such structures with different rheological models, Or and Kimmel (2009) suggested that LIPUS can trigger cyclic intracellular displacements. These are comparable with, and even larger than, the mean thermal fluctuations, with resonance frequencies in the range of tens to hundreds of kHz, so within the range of direct oscillatory movement caused by the ultrasound wave or by the acoustic radia-

tion pressure. Additionally, the 'bilayer sonophore' model (Krasovitski et al. 2011) they proposed describes a mechanism where the intramembranous hydrophobic space between the two lipid monolayer leaflets inflates and deflates periodically when exposed to ultrasound. Accordingly, being pulled apart during the depression phase (negative pressure) of an ultrasound cycle, and pushed back together by the positive pressure. Here, the main assumption being that negative acoustic pressures are large enough to overcome the molecular attractive forces of the two cell membrane leaflets. Published data showed that this effect can occur at levels below cavitation thresholds, but were obtained with intensity levels higher than typically used in LIPUS treatment (1 W/cm^2 at 1 MHz). Nevertheless, this is an interesting model that would merit further investigation with LIPUS-type ultrasound fields.

Another mathematical model was proposed to predict ultrasound-induced intra-cellular stresses and strain using a biphasic (solid elastic structures and macromolecules on one side, fluid cytosol on the other side) description of the cells in a harmonic standing wave field (Louw et al. 2013). Modeling results predict that stresses and strain are maximized within the cell at two distinct resonant frequencies, which are cell-type dependent through the geometric and mechanical characteristics of its different components. Stress gradients are induced through dilatational deformation, resulting in net forces acting on the nucleus, possibly triggering transduction by the nucleus and leading to load-inducible gene expression. Stimulated load-inducible gene expression should therefore be maximized when excitation frequency matches the cell resonant frequency, a prediction that was confirmed by experimental data (Louw et al. 2013).

21.3.5 Molecular Effects

At the molecular scale, it is well known that ultrasound can interact with molecules. This interaction is used in the field of "molecular acoustics" to probe molecular properties, based on the measurement of variations in ultrasound velocity (Sarvazyan 1991) or absorption (Morse et al. 1999). These measurements utilize the changes in molecular compressibility (and in ultrasound velocity) or in ultrasound absorption following changes in conformation, in solvent-molecule interactions or in hydration. All these effects are the results of intra and intermolecular forces, interaction potentials, electrostatic interactions, rigidities of interatomic bonds and relaxation phenomena. For example, lipids, constituting the second most prevalent component of dry weight of many tissues after proteins, interact with ultrasound. Lipids and structures associated with the cell membrane exhibit an absorption behavior for ultrasound, probably linked to relaxation phenomena with relaxation frequencies in the range 1–16 MHz. In large unilamellar vehicles, these relaxation phenomena are linked to the interaction of ultrasound with the hydrophobic side chains, leading to a structural reorganization of small molecular domains (Morse et al. 1999). These interactions can affect the function of biological molecules. At very high intensities, ultrasound can damage biological molecules, *e.g.,* DNA degradation in the presence (Elsner and Lindblad 1989) or in the absence of cavitation (Hawley et al. 1963). Nonetheless, these intensities are much higher than those typically used in low intensity pulsed ultrasound stimulation or other techniques mentioned in this review (for an *in-vivo* use of ultrasound, safety guidelines are provided by scientific societies or regulatory agencies in order to avoid such effects). At lower intensities however, where absorption is a result of ultrasound interaction with molecules, can the deposited ultrasound energy induce transient conformational changes, or changes in molecule-molecule or molecule-solvent interactions, which in turn could modify the biological functions of these proteins? It has been suggested that ultrasound could disrupt multimolecular complexes (Johns 2002), although intensities and mechanisms (cavitation or not) at which these phenomena could occur were not specified. A change of protein conformation is believed to be responsible for cytoskeleton fluidization observed after low intensity

therapeutic ultrasound treatment at 1 MHz center frequency, with 20 % duty cycle and pressures in the order of 200 kPa (Mizrahi et al. 2012). The origin of these phenomena is thought to be due to the local strains applied by ultrasound that could be large enough to disrupt weak nonspecific bonds, altering protein conformation and triggering structural remodeling of the cytoskeleton.

21.3.6 Other Effects

Finally, some reported that ultrasound bioeffects are difficult to categorize due to the lack of knowledge of the physics underlying them. In particular, ultrasound can affect intracellular trafficking, and this would be relevant in the stimulation of bone healing processes. It has been recently reported that after a few minutes of exposure to 1 MHz ultrasound (at I_{SATA} of 0.3 W/cm^2, 50 % duty cycle and 5 Hz PRF), cells that had already internalized plasmids (delivered using calcium phosphate co-precipitates) expressed higher transfection rates than the non-ultrasound treated cells (Hassan et al. 2012). The mechanisms of these effects are not clearly understood. Plausible explanations are either a destabilization of the endosomal vesicles or an increase in the net diffusivity of the pDNA through the cytoplasm, an inhibitory action on enzymatic levels or assistance in the permeabilization of the nuclear envelope. Whatever the exact mechanism, this study clearly demonstrated that ultrasound levels below cavitation thresholds can modulate intracellular trafficking of pDNA, and by extension could more generally modulate intracellular trafficking of other molecules, thereby eventually triggering or enhancing a possible mechanoresponse.

21.4 LIPUS and Mechanotransduction

Conventionally, 'mechanotransduction' is the process in which specific cellular machineries switch a physical stimulus into chemical activities to trigger downstream signaling. Conformational changes in proteins, such as stretch-activated ion channels or mechanosensitive adhesion structures, often mediate conversion of force into chemical signaling. Given the modalities of mechanical stimulation of LIPUS shown in Sect. 21.4, it is difficult at this stage to specify a biological response to a particular strain range. Nevertheless, the magnitude of interfragmentary movement, the rate and timing of micromotion application and the number of loading cycles are mechanical boundaries susceptible to impact signal transduction pathways, and subsequently gene up- or down-regulation, thereby influencing cell phenotype and function.

A variety of mechanosensitive membrane molecules and microdomains have been identified, including ion channels, receptors, G-proteins, adhesion molecules, caveolae, the glycocalyx and primary cilia. As the intracellular cytoskeleton ultimately bears the impact of force applied on cells, it also represents a major class of mechanosensitive structures. The activation, reinforcement and/or redistribution of membrane-bound complexes, and the reorganization of the cytoskeleton and extracellular matrix, are all immediate responses to forces. These events critically influence cell metabolism, protein synthesis, cell survival and stem cell commitment, in addition to migration, spreading and contraction. Compared to other types of mechanical stimuli (such as shear stress or extracellular deformation), ultrasound-induced mechanotransduction pathways are less well defined. We will present mechanosensitive structures that should potentially come into play knowing that the sensor molecules that initially sense the different varieties and orders of magnitude of mechanical stimuli are not fully defined.

Changes in free intracellular calcium concentration are one of the first responses against environmental stress and are important biological signals in mechanotransduction: Upon ion channel activation, calcium is mobilized into the cytoplasm from outside the cell membrane or from intracellular reservoirs, including endoplasmic reticulum, sarcoplasmic reticulum and mitochondria. There is experimental evidence suggesting that ultrasound, even at low intensity, increases

intracellular calcium concentration (Parvizi et al. 2002), and that blocking this rise with intracellular calcium chelating agents or inhibiting Ca^{2+}/ATP-ase, abolishes the stimulatory effect of ultrasound on proteoglycan synthesis by chondrocytes. Proliferative LIPUS effects were also shown to depend on the release of ATP/purines through Ca^{2+} and P2Y receptors (Alvarenga et al. 2010). Calcium is a product generated indirectly from enzymatic activities, such as phospholipase C. In consequence of the intracellular calcium increase, calcium acts as a secondary messenger by allosterically binding to proteins including calmodulin, troponin-C and annexin, as well as calpain, and then the complex triggers downstream cellular processes. Recently, it has been shown that Ca^{2+} signals are oscillatory (Kim et al. 2009), and that these oscillatory Ca^{2+} signals are crucial for a variety of cellular functions, such as bone marrow-derived mesenchymal stem cell (HMSCs) differentiation (D'Souza et al. 2001; den Dekker et al. 2001). In HMSCs, calcium oscillation can be regulated by electrical stimulation (Sun et al. 2007) or substrate rigidity (Kim et al. 2009). In this later study, Ca^{2+} oscillation occurred via the RhoA GTPase pathways. These are major cytoskeleton regulators, although sometimes not correlated with cytoskeleton activities (Kobayashi and Sokabe 2010). However, at this stage we do not have evidence that oscillatory Ca^{2+} signals are a target for LIPUS stimulation, and further studies should address whether intracellular calcium rise is a primary target or a downstream event.

Another major factor in mechanotransduction of adherent cells, being at the center of cell integration of internal and external signals, is the "cytoskeleton-focal adhesion-extracellular matrix (ECM) connection". Integrin-mediated focal adhesions (FAs) are large, multi-protein complexes that link the actin cytoskeleton to the ECM and take part in adhesion-mediated signaling. FAs insure cell adhesion to ECM via integrin-regulated organization. They undergo maturation wherein they grow and differentially change composition to provide traction and to transduce the signals that drive cell migration. This is crucial to various biological processes, including wound healing. FAs are related to signaling networks and dynamically modulate the strength of the linkage between integrin and actin, and control the organization of the actin cytoskeleton (Kuo et al. 2011; Schiller et al. 2011). In response to mechanical force, these force-sensitive focal adhesion proteins may undergo structural rearrangement or enzymatic modifications that change their binding preferences with respect to other associated proteins. This then further modulates the protein association with focal complexes (del Rio et al. 2009). It has been shown that forces in the physiological range (2–20 pN) are sufficient to stretch FA molecules (such as talin), exposing cryptic binding sites for others molecules (such as vinculin), suggesting a role for protein binding in the talin-vinculin system in the mechanotransduction process. LIPUS-type mechanical stimulation has been shown to alter the role of integrins (Whitney et al. 2012). It was shown to activate the integrin/phosphatidylinositol 3-OH kinase/Akt pathway which is associated with cell proliferation (Takeuchi et al. 2008). It was also shown to trigger phosphorylation of FA signaling molecules, such as FAK, Src and p130Cas, which in turn phosphorylate and activate Erk and MAP Kinases. LIPUS signal transduction to the nucleus via the integrin/MAPK pathway influences numerous cellular processes, including migration and a wide range of gene regulations (Whitney et al. 2012; Sato et al. 2014).

Integrin-mediated signals can be modulated by changes in ECM characteristics (composition/mechanical properties). ECM compounds were also stimulated by LIPUS exposure: Type IX-collagen in chondrocytes in 3D matrices (Takeuchi et al. 2008), proteoglycans and growth factors with their receptors (BMP2, FGF7, TGF-β R, EGFR, VEGF) in nucleus pulposus cell line (Kobayashi et al. 2009). However, other potential candidates should be investigated, including (i) stretch-activated ion channels or G-protein coupled receptors (Liedert et al. 2006), (ii) the glycocalyx, a pericellular GAG-proteoglycan rich layer surrounding the cell membrane that creates a drag force when fluid flow passes over causing plasma membrane deformation (Morris et al. 2010), and (iii) the primary cilium, an immotile

microtubule-based organelle that protrudes like an antenna from the apical cell surface. This already has implications as a mechanosensor in a variety of cell types, including mesenchymal stem cells MSCs (Malone et al. 2007).

Along with transmembrane integrins, direct cell-to-cell communication is important for mechanotransduction. The connexins not only experience the different biomechanical forces within the system, but also act as effector proteins in coordinating responses within groups of cells against these forces. Improved cell-to-cell communication via gap junctions assessed by dye transfer assay was reported after LIPUS exposure in rat MSCs. Inhibition of gap junctions led to decreased activation of Erk1/2 and p38 MAPK kinases, and attenuated alkaline phosphatase (ALP) activity in response to LIPUS, implying that gap junctions are essential for LIPUS effects on osteogenic differentiation of MSCs (Sena et al. 2011). Activation of p38 and Erk1/2 MAPK kinases in rat MSCs, and Erk1/2 MAPK kinase in murine pre-osteoblastic MC3T3-E1 cells, has been confirmed by other investigators (Angle et al. 2011; Bandow et al. 2007).

Activation of another mechanoreceptor on the surface of osteoblasts, angiotensin II type I receptor (ATI), has been suggested by Bandow et al. (2007). ATI receptor expression increased with osteoblast maturation, and inhibition of the receptor resulted in ablation of LIPUS-induced cytokine expression and Erk1/2 phosphorylation. To date, integrins remain the most studied receptors known to transmit ultrasound-induced signals into cells. Further investigation is required into other mechanoreceptors of which their mechanofunction is not well understood, like ATI, as well as more detailed function elucidation of signaling pathways transmitting the converted intracellular mechanical stimuli.

Among genes whose expression is promoted by LIPUS are chemokines such as monocyte chemoattractant protein (MCP)-1, macrophage-inflammatory protein (MIP)-1 and RANKL in osteoblastic cells (Bandow et al. 2007), and TNF-α in macrophagic cells (Iwabuchi et al. 2008). In line with these results, LIPUS inhibits osteoblast lipopolysaccharide-induced inflammatory responses through TLR4-MyD88 dissociation (Nakao et al. 2014).

Mechanical loading plays a key role in bone formation and maintenance. While unloading induces osteocyte apoptosis and bone loss *in-vivo*, mechanical stimuli prevent osteocyte death through a mechanism involving beta-catenin accumulation and ERK nuclear translocation, establishing osteocytes as primary mechanosensors (Temiyasathit and Jacobs 2010). To understand the cellular mechanisms underlying LIPUS on enhanced fracture healing in a rat model, Fung et al. (2014) investigated the effect of ultrasound axial distances on osteocytes and mechanotransduction between osteocytes and pre-osteoblasts (bone-forming cells) through paracrine signaling. They demonstrated the positive effects of far field LIPUS on stimulating osteocyte nitric oxide production and promoting mechanotransduction between osteocytes and osteoblasts.

Although much work has focused on dissecting the adhesive and structural components of the cell responsible for transducing external mechanical forces into biochemical signaling cascades, how mechanical signals are transmitted to the nucleus and activate specific gene expression programs have only been recently suggested. One necessary step in these processes is the transport of signaling molecules from the cytoplasm to the nucleus; a common theme in mechanotransduction (Sharili and Connelly 2014). The SRF (serum-response factor) and YAP (Yes-associated protein)/TAZ (transcriptional co-activator with PDZ-binding motif) pathways are known mediators of this process in multiple cell types, including mesenchymal stem cells (Costa et al. 2012). In addition, recent evidence suggests a potential role of YAP/TAZ for β-catenin and Smad signaling in mechanotransduction, both critical for osteogenic differentiation (Halder et al. 2012). YAP/TAZ accumulates in the nucleus of cells cultured on stiff gels or large ECM micropatterns, and promotes osteogenic MSC differentiation (Dupont et al. 2011). This response requires RhoA and cytoskeletal contractility, preventing YAP/TAZ from being targeted for degradation by phosphorylation. It has been established

that LIPUS influences the multilineage differentiation of mesenchymal stem and progenitor cell lines through a ROCK dependent pathway (Kusuyama et al. 2014). YAP/TAZ nuclear translocation under mechanical stimulation therefore provides another mechanism for linking biophysical cues to transcriptional responses and cell differentiation. To our knowledge, there is no evidence that LIPUS could activate YAP/TAZ in exposed cells, but it could represent a clear demonstration of mechanosensory pathway activation by LIPUS.

It is also important to consider that continuous mechanical stimulation received by cells can be deleterious for integrity of large structures, such as microfilaments or microtubules, but also for individual proteins. In muscle cells, contractile apparatus is subject to intense mechanical stress, leading to irreversible protein 3D structure modification, such as the actin-crosslinking protein filamin. A chaperone dependent process facilitates the degradation of damaged filamin through selective autophagy. Recent seminal work in Jorg Hohfeld's lab identified a chaperone-assisted selective autophagy (Klionsky et al. 2012) as a tension-induced autophagy pathway (Arndt et al. 2010; Ulbricht et al. 2013). A mechanosensitive chaperone (BAG3) utilizes its WW domain to engage in YAP/TAZ signaling in order to stimulate filamin transcription to maintain actin anchoring and crosslinking under mechanical tension (Ulbricht and Höhfeld 2013). By integrating tension sensing, via autophagosome formation and transcription regulation during mechanotransduction, the chaperone-assisted selective autophagy (CASA) machinery ensures tissue homeostasis and regulates fundamental cellular processes, such as adhesion, migration and proliferation. In this context, it is conceivable that LIPUS exposure could alter many mechanosensitive proteins, leading to their recycling and renewal using a CASA mechanism. Activation of autophagy by LIPUS may explain many, if not all, of the above-described mechano-mimetic effects, especially on stem cell differentiation.

Furthermore, how LIPUS-induced cues from the nanoscale- to the tissue-level compromise tensional homeostasis still need to be investigated to provide a comprehensive understanding of coordinated mechanoresponsiveness.

21.5 LIPUS-Induced Bone Healing: Biological Evidence

Bone healing is a complex biological phenomenon composed of a temporally and spatially overlapping sequence of four basic stages: Inflammation, soft callus formation, bone formation and bone remodeling. To some extent these stages recapitulate the development of bone formation processes (Gerstenfeld et al. 2003, 2006). LIPUS has been reported to actively influence all these stages, *i.e.,* (1) mitigation of the soft tissue phases (inflammation and soft callus formation), (2) potential acceleration of the onset of bone formation and (3) influence of the biomechanical properties of remodeled bone (Azuma et al. 2001). There are various ways by which LIPUS might play a role in this orchestrated sequence of events, affecting migration, proliferation, differentiation of several cell types (*e.g.,* MSCs, osteoblasts, chondrocytes, osteoclasts, fibroblasts, endothelial cells and inflammatory cells), and ECM production and remodeling. In particular, MSCs possess multiple lineage differentiating potentials, and can form cells from bone, cartilage, fat, muscle, tendon etc. They are therefore receiving more and more attention in the field of regeneration therapies (Pittenger et al. 1999).

Numerous phenomenological studies have investigated cellular events in response to LIPUS exposure. Figure 21.5 illustrates possible ultrasound effects on the sequence of events in a healing bone fracture, summarizing gene expression and release of chemical messengers in response to ultrasound as determined by *in-vitro* studies. This is described in more detail in Sect. 21.5.1. Furthermore, signaling pathways generated by LIPUS important for transduction of mechanostimuli are discussed in Sect. 21.5.3 and summarized in Table 21.1. Lastly, the possible role of ultrasound in maintenance of extracellular fluid homeostasis is discussed in the Sect. 21.5.4.

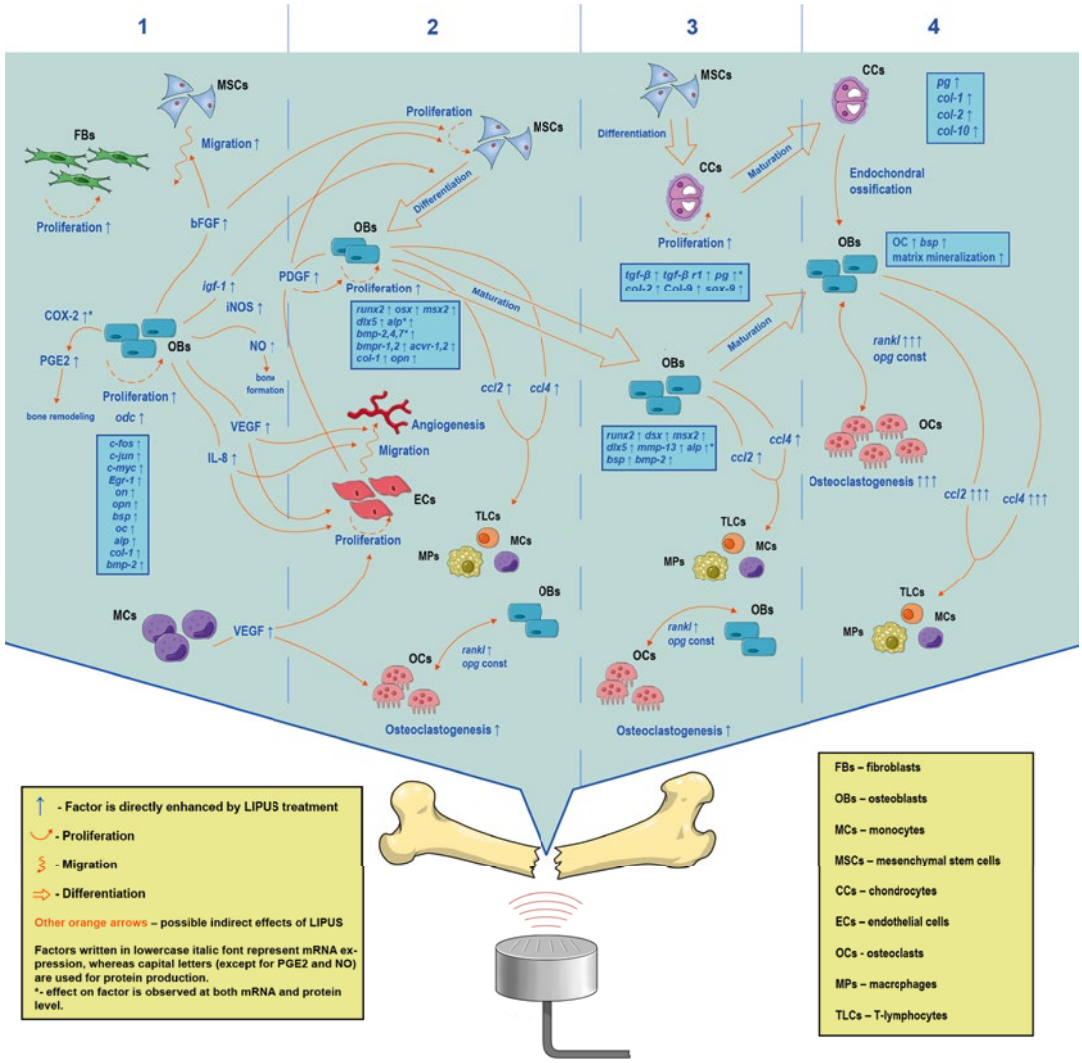

Fig. 21.5 Summary of hypothetical LIPUS effects on cellular events from published *in-vitro* data. The columns represent the four phases during *in-vivo* endochondral bone fracture healing: *Phase 1* – early events soon after the bone injury, *i.e.,* hematoma formation, inflammation and migration of osteogenic precursors; *phase 2* – angiogenesis, proliferation of MSCs and osteoblasts, and osteogenic differentiation; *phase 3* – chondrogenesis and maturation of osteoblasts; *phase 4* – maturation of chondrocytes, woven bone formation and remodeling

21.5.1 LIPUS-Stimulated Gene Expression and Signaling Molecule Release

Figure 21.5 depicts the effect of ultrasound on each stage of fracture healing. The data have been gathered from *in-vitro* reports and are presented in the figure within four distinct phases corresponding to the four basic stages of the bone healing process. Phase 1 illustrates the possible early effects of LIPUS observed soon after the bone injury, including hematoma formation, inflammation and migration of precursor cells. Phase 2 shows LIPUS-effect on angiogenesis, MSC proliferation, osteoblast proliferation and differentiation. Phase 3 depicts LIPUS-enhanced chondrogenesis and osteoblast maturation. Phase 4 represents further differentiation of

Table 21.1 Ultrasound-induced intracellular signaling pathways

Reference	Signaling molecule	US signal/conditions	Cells	Exposure time	Time of the effect	Additional information
Zhou et al. (2004)	RhoA-GTP ↑ p-Erk1/2 ↑	1.5 MHz, 30 mW/cm^2 200 μs burst, 1 kHz PRF Transducer is from the bottom via coupling gel	Human primary skin fibroblasts	11 min	Peak after 10–20 min	These signaling molecules are suggested to be involved in US-induced DNA synthesis
Mahoney et al. (2009)	Rac ↑	1.5 MHz, 30 mW/cm^2 1 kHz PRF Transducer is from the bottom via coupling gel	Mouse embryonic fibroblasts (WT & syndecan-4 –/– mutant)	30 min	30 min post-US	PKCα, mediating Rac activity in the presence of syndecan-4, was not involved in US-induced activity of the protein
Tang et al. (2006)	p-FAF ↑ p-85 of PI3K ↑ p-Akt ↑ Activation of canonical NF-κB pathway PGE2 ↑	1.5 MHz, 30 mW/cm^2 200 μs burst, 1 kHz PRF Transducer is from the top, 5–6 mm away from the cells	MC3T3-E1 mouse preosteoblasts, primary osteoblasts	20 min	Peak after 10–30 min 6 h post-US Peaking at 24 h	The activation of the listed pathways is implicated with enhanced COX-2 expression, which is supported by higher secretion of PGE2 in the medium
Ren et al. (2013)	p-p38 ↑	1 MHz, 90 mW/cm^2 (not clear how it is pulsed)	Human periodontal ligament cells	20 min	Peak after 30 min and sustained for 6 h	Inhibition of p-38 reduces US-increased ALP activity, OC secretion and matrix mineralization
Hou et al. (2009)	Ras ↑ p-Raf-1 ↑ p-MEK1/2 ↑ p-Erk1/2 ↑ p-IKKα/β ↑ p-IκBα ↑ p-p65 ↑	1.5 MHz, I_{SATA} = 30 mW/cm^2, 200 μs burst at 1 kHz PRF, transducer is from the top, 5 mm away from the cells	MC3T3-E1 mouse pre-osteoblasts	20 min	15 min post-US 30 min post-US	US increased activation of the listed signaling molecules, resulting in up-regulated iNOS production
Ikeda et al. (2006)	p-ERK 1/2 ↑ p-p38 ↑ p-p38 ↑	1.5 MHz, 70 mW/cm^2, 2 ms burst 100 Hz PRF Transducer is from the top, 3–4 mm away from the cells	C2C12 mouse myoblasts	20 min	60 min post-US Starting at 10 min Peaking at 30 min 10 min post-US	The pathways drive cell differentiation into chondroblastic/osteoblastic lineages

Reference	Signaling molecule	US signal/conditions	Cells	Exposure time	Time of the effect	Additional information
Takeuchi et al. (2008)	p-Akt ↑ p-ERK 1/2 ↑	1.5 MHz, 30 mW/cm^2, 200 μs burst, 1 kHz PRF Transducer is from the bottom via coupling gel	Primary pig chondrocytes in 3D collagen matrix	20 min/day for 7 days	2 h post-US on day 7	Akt pathway is involved in US-increased chondrocyte proliferation, which is confirmed by Cyclins D1 & B1 up-regulation
Whitney et al. (2012)	p-FAK (Y397) ↑ p-Src (Y416) ↑ p-p130Cas (Y249) ↑ p-CrkII (Y221) ↑ p-Erk1/2 ↑	5 MHz in continuous mode, Spatial averaged pressure 14 kPa, Transducer immersed in the media 6 mm away from the bottom	Human primary chondrocytes	3 min	60 min post-US 5 min post-US Decrease by 60 min	Integrins and Src inhibitors lowered US-induced Erk1/2 phosphorylation, implying that they function upstream from the protein.
Parvizi et al. (2002)	Intracellular [Ca^{2+}] ↑	1 MHz, 111–450 kPa, 200 μs burst, 1 kHz PRF	Neonatal rat primary chondrocytes	2 s-10 min	Right after US	Transient increase at 111 kPa and sustained rise at 450 kPa. Increased [Ca^{2+}] was established to be implicated in US-induced proteoglycan synthesis
Sena et al. (2011)	p-Erk1/2 ↑ p-p38 ↑	1.5 MHz, 30 mW/cm^2, 200 μs burst, 1 kHz PRF Transducer is from the bottom via coupling gel	Rat bone marrow stromal cells	20 min	30 min post-US	The inhibition of gap-junctions abolishes US-enhanced p-Erk1/2 and p38 phosphorylation
Angle et al. (2011)	p-Erk1/2 ↑ p-p38 ↑	1.5 MHz, 2, 15 or 30 mW/cm^2, 200 μs burst, 1 kHz PRF	Rat bone marrow stromal cells (in osteogenic media)	20 min	30 min post-US	More intense p-p38 phosphorylation is seen at 15 mW/cm^2, whereas p-Erk1/2 phosphorylation is only more pronounced at 30 mW/cm^2
Bandow et al. (2007)	p-Erk1/2 ↑	1.5 MHz, 30 mW/cm^2, 200 μs burst, 1 kHz PRF Transducer is 13 cm away from the bottom in the water tank	Mouse MC3T3-E1 cells (3 weeks differentiated)	20 min	5 min post-US	AT1 receptor inhibitor down-regulates LIPUS-induced enhanced Erk1/2 activation

DC duty cycle, *PRF* pulse repetition frequency, *US* ultrasound, *WT* wild type

chondrocytes, LIPUS-accelerated woven bone formation and remodeling. The information gathered in Fig. 21.5 and in Table 21.1 does not recapitulate the entire complexity of the biological mechanisms underlying the response to ultrasound treatment, but rather represents an attempt to reconstitute a hypothetical consequence of cellular events which were observed during *in-vitro* studies performed in various cell types and species. We will now review this data in more detail.

21.5.1.1 Inflammation

Soon after the bone fracture, fibroblasts form a granulation tissue to support the damaged site and a hematoma is formed. The influence of ultrasound stimulation on proliferation of fibroblasts within 24 h post-exposure has been reported in several studies (Zhou et al. 2004; Doan et al. 1999; Reher et al. 1998). Hematoma formation is accompanied by the release of chemotactic factors, recruiting inflammatory cells, MSCs and other progenitors to the fracture site. Kumagai et al. (2012) reported recruitment of local osteoprogenitors and osteogneic precurors from systemic circulation to the fracture site in an *in-vivo* mouse model after LIPUS treatment (Fig. 21.5, ph. 1).

21.5.1.2 Angiogenesis

It has been shown that LIPUS up-regulates interleukin-8 (IL-8) secretion in human mandibular osteoblasts (Doan et al. 1999) and IL-8 gene expression in murine pre-osteoblasts (Bandow et al. 2007) (Fig. 21.5, ph. 1). IL-8 is a cytokine known to induce endothelial cells proliferation and migration, which, in turn, are crucial for new blood vessel formation (angiogenesis) in fracture healing (Li et al. 2003a; Koch et al. 1992) (Fig. 21.5, ph. 2).

Enhanced production of vascular endothelial growth factor (VEGF) by human mandibular osteoblasts, human peripheral blood monocytes (Doan et al. 1999) and human osteoblasts (hFOB1.19, MG-63 and SaOS-2) (Wang et al. 2004) has also been reported in response to LIPUS (Fig. 21.5, ph. 1). VEGF is a critical player in angiogenesis. It regulates mitogenesis and the recruitment of endothelial cells (Ferrara et al. 2003), and is also involved in osteoblast differentiation and osteoclast activation (Street et al. 2002; Ishiduka et al. 1999) (Fig. 21.5, ph. 2). Basic fibroblast growth factor (bFGF), another cytokine regulating angiogenesis in the healing fracture (Montesano et al. 1986; Hayek et al. 1987), has been found to be up-regulated by LIPUS treatment in human mandibular osteoblasts (Doan et al. 1999). bFGF enhances fracture healing through an unknown mechanism by promoting migration (Fig. 21.5, ph. 1) and mitogenesis of MSCs and osteoblasts (Radomsky et al. 1998; Kim et al. 2007; Globus et al. 1988) (Fig. 21.5, ph. 2).

Co-cultures of human osteoblast SaOS-2 and human umbilical vein endothelial cells exhibited higher levels of platelet-derived growth factor (PDGF) secretion upon LIPUS exposure (Ito et al. 2000; Kilian et al. 2004; Canalis et al. 1989). PDGF is a mitogenic factor for MSCs and osteoblasts (Ito et al. 2000; Kilian et al. 2004; Canalis et al. 1989) (Fig. 21.5, ph. 2).

21.5.1.3 NO and PGE2

Nitric oxide (NO), a free radical gas, was found to be an important contributor to bone formation in response to mechanical loading (Fox et al. 1996). The up-regulation of NO production in response to LIPUS was demonstrated to be involved in the regulation of VEGF expression in human osteoblasts (hFOB1.19) (Wang et al. 2004) (Fig. 21.5, ph. 1). The increase of NO production is in agreement with findings from Reher et al. (2002), also showing that NO concentration in human primary mandibular osteoblasts increases using both continuous and pulsed ultrasound systems. Moreover, they established that this increase was regulated by inducible NO synthase (iNOS) (Fig. 21.5, ph. 1).

Secretion of prostaglandin E2 (PGE2) has been shown to be up-regulated in response to ultrasound exposure in osteoblasts from various species (Tang et al. 2006; Reher et al. 2002; Sun et al. 2001; Naruse et al. 2003). PGE2 is an arachidonic acid-derived metabolite associated with bone formation and resorption (Nefussi and Baron 1985). Cyclooxygenase-2 (COX-2) is a rate-limiting enzyme in the PGE2 production reaction. It has been reported that LIPUS

increases COX-2 gene expression in mouse pre-osteoblasts (Kokubu et al. 1999) (Fig. 21.5, ph. 1). In cells pretreated with a COX-2 specific inhibitor, PGE2 production in response to ultrasound was significantly decreased.

21.5.1.4 Early Osteogenesis

Insulin-like growth factor-1 (IGF-1) mRNA has been reported to be up-regulated by LIPUS in both the murine ST2 bone marrow derived cell line and rat osteoblasts within the first day of stimulation (Naruse et al. 2000, 2003) (Fig. 21.5, ph. 1). IGF-1 mediates expression of osterix (Osx), a transcription factor involved in differentiation of pre-osteoblasts into mature osteoblasts (Fig. 21.5, ph. 2) (Celil and Campbell 2005; Nakashima et al. 2002). The up-regulated expression of Osx has also been shown by Suzuki et al. (2009b) in a rat osteosarcoma-derived cell line expressing an osteoblastic phenotype, starting on day 7 of LIPUS exposure and persisting until the end of week 2 (Fig. 21.5, ph. 2, 3).

The up-regulation of early response gene c-fos following ultrasound treatment has been reported in rat MSCs, rat UMR-106 osteoblast-like cells, primary rat osteoblasts and murine ST2 cells (Naruse et al. 2000, 2003; Stein et al. 1996; Sena et al. 2005; Warden et al. 2001) (Fig. 21.5, ph. 1). Enhanced expression of c-jun, c-myc and Egr-1 genes in rat MSCs 3 h after 20 min LIPUS-stimulation has been demonstrated by Sena et al. (2005) (Fig. 21.5, ph. 1). The genes c-myc and Egr-1 encode for transcriptional factors involved in osteoblast proliferation and differentiation (Suva et al. 2013; Siggelkow et al. 1998; Kirstein and Baglioni 1988). The combination of c-jun and c-fos proteins forms an activator protein-1 (AP-1) transcriptional factor complex. AP-1 binding sites are encountered in several promoters that are important for the expression of osteogenic markers, *i.e.,* collagen type 1 (Col-1) and osteocalcin (OC) (Bozec et al. 2010). The early up-regulation of these proteins, as well as other important osteogenic markers (*e.g.,* osteonectin (ON), osteopontin (OPN), bone sialoprotein (BSP), alkaline phosphatase (ALP), bone morphogenetic protein 2 (BMP-2)), has been demonstrated in cells with an osteoblastic phenotype within 1 day following ultrasound exposure (Naruse et al. 2000, 2003; Gleizal et al. 2006; Yang et al. 2005; Maddi et al. 2006) (Fig. 21.5, ph. 1)

21.5.1.5 Proliferation of Osteoprogenitors and Osteoblasts

Proliferation of osteogenic progenitors is not directly affected by LIPUS exposure *in-vitro* as reported by Hasegawa et al. (2009). This group found that the number of human hematoma-derived progenitor cells remained the same within 7 days of stimulation, whereas differentiation of the cells was significantly enhanced within 28 days of LIPUS-exposure. LIPUS effects on osteoblast proliferation appear to be controversial. Doan et al. (1999) and Reher et al. (1998) demonstrated that DNA synthesis in human mandibular osteoblasts was increased 24 h post-exposure (Fig. 21.5, ph. 1). Hayton et al. (2005) showed an increase in gene expression of ornithine decarboxylase (ODC), a cell growth marker, 8 h following LIPUS-treatment in the human SaOS-2 osteosarcoma cell line (Fig. 21.5, ph. 2). These results are in agreement with a study by Wang et al. (2004) showing increased DNA synthesis 24-h post-ultrasound exposure in cultures of human osteoblasts hFOB1.19, MG-63 and SaOS-2. Several more studies reported an elevated proliferation rate in cells with osteoblastic phenotype within 4 days of LIPUS stimulation (Sant'Anna et al. 2005; Suzuki et al. 2009b; Gleizal et al. 2006; Li et al. 2003b; Hayton et al. 2005). In contrast to these findings, upon ultrasound-stimulation Suzuki et al. and Dalla-Bona et al. did not see any change in proliferation of rat ROS 17/2.8 osteosarcoma cells and the mouse OCCM-30 cementoblast cell line, respectively. Sawai et al. looked at proliferation of mouse MC3T3-E1 osteoblasts and osteosarcoma (mouse LM8 and human SaOS-2), renal cancer, prostate cancer and lung cancer cell lines. They found that it was not affected by 3 days of LIPUS stimulation, arguing for beneficial effects of ultrasound usage in patients with bone cancers and bone metastases. Increased proliferation of murine primary calvarial osteoblasts reported in

Gleizal et al. (2006) study was accompanied by enhanced expression of osteogenic markers, *i.e.,* ALP, BMP-2, BMP-7, OPN, Col-1 etc. Expression of these markers was normalized to expression of a housekeeping gene, compensating for a potential increased cell number. Therefore, it is not yet completely clear whether the beneficial effects of LIPUS concerning the fast and favorable healing of the *in-vivo* fracture are due to enhanced differentiation of osteoblasts, or to a more complex combination of accelerated proliferation, differentiation and maturation, finally leading to an increased tissue size.

21.5.1.6 Ossification

Another transcriptional factor with an essential role in the development of an osteogenic phenotype is Runx2. It has been reported that Runx2 can be up-regulated following ultrasound stimulation. Up-regulation can start from day 2 following ultrasound in the osteoblastic cell line ROS 17/2.8 and in rat MSCs (Suzuki et al. 2009b; Sant'Anna et al. 2005). Up-regulation can last up to 2 weeks following ultrasound in mouse calvarial primary osteoblasts (Sant'Anna et al. 2005; Suzuki et al. 2009b; Gleizal et al. 2006). Runx2 is encoded by the Cbfa1 gene (core-binding factor-1) and is only found in cells of osteoblast lineage (Ducy et al. 1999). Mice with Cbfa1$^{-/-}$ homozygous mutation are not capable of either intramembranous or endochondral ossification (Komori et al. 1997; Otto et al. 1997). Runx2 is a transcription factor regulating differentiation of MSCs into osteogenic lineage by directing expression of ALP, Col-1, matrix metalloproteinase-13 (MMP-13), BSP, OPN and OC genes (Ducy et al. 1999). Enhanced expressions of ALP and MMP13 have been observed on day 10, and elevated ALP activity was detected on day 6 in LIPUS-treated murine MC3T3-E1 cells (Unsworth et al. 2007) (Fig. 21.5, ph. 3). Up-regulated OPN and ALP expressions by ultrasound-exposure were also shown in osteoprogenitors and osteoblast-like cells (Sant'Anna et al. 2005; Naruse et al. 2000; Suzuki et al. 2009b; Gleizal et al. 2006; Unsworth et al. 2007; Maddi et al. 2006) (Imai et al. 2014). MSCs derived from adipose tissue also possess osteogenic potential, which can be enhanced by LIPUS stimulation in osteoinductive media (Yue et al. 2013). However, when the same cells were cultured in the media with adipogenic reagents, LIPUS supported adipogenic differentiation of the cells (Fu et al. 2013). In contrast to these results, it was shown that LIPUS could suppress the expression of phenotypic features of 3 T3-L1 adipocytes, down-regulate the expression of adipogenesis-related markers and up-regulate expression of osteogenesis-related markers in murine ST2 MSCs and MC3T3-E1 pre-osteoblasts (Kusuyama et al. 2014). These later results suggest that LIPUS stimulation suppresses adipogenesis and promotes osteogenesis of MSCs.

An effect of ultrasound on Dlx5 and Msx2 gene expression has been reported by Suzuki et al. (2009b). Increased gene expression of both Dlx5 and Msx2 was observed within the first 2 weeks of LIPUS treatment in rat osteoblast-like cells. The functional mechanisms of these proteins are not entirely understood. However, it is known that the Dlx5 gene is important for osteoblast differentiation and maturation, whereas Msx2 is in majority expressed during osteoblast proliferation and it antagonizes Runx2 (Ryoo et al. 1997). Dlx5 in turn binds to Msx2, therefore rescuing a prominent Runx2 transcriptional activity (Ryoo et al. 1997).

Physical immobility accompanying some bone fractures or other injuries can result in reduced rate of osteogenesis and induce adipogenesis of MSCs. However, when adipose tissue-derived hMSCs were placed in microgravity conditions, mimicking the lack of physical movement in humans, they experienced higher expression of Runx2, Osx, ALP and RANKL when treated with LIPUS. Conversely, they showed reduced expression of OPG, indicating a potential for LIPUS to restore normal osteogenic differentiation of MSCs from disuse by daily short duration stimulation (Uddin and Qin 2013).

21.5.1.7 BMPs

Bone morphogenetic proteins (BMPs), cytokines of the transforming growth factor-β (TGF- β) superfamily, perform a plethora of functions throughout diverse tissues, regulating cellular events based on the context (Ruschke et al. 2012).

BMP-2, 4 and 7 are important players in bone healing and regulate the differentiation of MSCs to the osteoblastic and chondroblastic lineages (Ahrens et al. 1993; Shen et al. 2010). BMPs signal through Smad, a family of transcription factors, and other cascades including mitogen-activated protein kinase (MAPK) pathways, like p38 and Erk1/2 (Heldin et al. 1997; Moustakas and Heldin 2005).

These proteins, as well as BMP receptors (BMPR-I, II) and activin receptors (ACVR- I, II), were found to be up-regulated after 7 days of LIPUS treatment in the rat osteosarcoma ROS 17/2.8 cell line (Suzuki et al. 2009a). Enhanced expression of BMP-2 from day 5 until day 14 has also been shown in these cells (Suzuki et al. 2009b). Smad1 activation, a signaling molecule downstream from BMPR receptors, was observed 5 min after LIPUS exposure.

21.5.1.8 Chondrogenesis

During the third stage of bone repair, proliferating MSCs start differentiating into chondrocytes and endochondral ossification begins (Fig. 21.5, ph. 3). Lee et al. (2006) reported that low intensity ultrasound delivered in a continuous wave mode promoted enhanced expression of chondrogenic markers Col-2, aggrecan (proteoglycan (PG)) and Sox-9 (a gene encoding for a transcriptional factor prominent for chondrocyte differentiation) at week 1 and 2 in rabbit MSCs (Fig. 21.5, ph. 3). Schumann et al. (2006) demonstrated that hMSCs seeded in 3D scaffold and stimulated with 40 min a day LIPUS for 1 week, and then left in the incubator for another 2 weeks, have a more pronounced chondrogenic phenotype on day 21, expressing higher aggrecan, Col-1, Col-2 and Col-10 (Fig. 21.5, ph. 4). Other studies showed that LIPUS supported differentiation of rat and pig primary chondrocytes within the first 2 weeks of the treatment and up–regulated expressions of TGF-β, TGF-β R1, PG, Col-2 and Col-9 (Mukai et al. 2005; Takeuchi et al. 2008; Kobayashi et al. 2009) (Fig. 21.5, ph. 3). Parvizi et al. (2002) reported that proteoglycan increase in rat chondrocytes treated by ultrasound was governed by increase of intracellular Ca^{2+} concentration.

Besides their differentiation state, viability of chondrocytes was also affected by LIPUS. Several studies have shown that proliferation of chondrocytes from rat, pig and the human nucleus pulposus cell line (HNPSV-1) was accelerated within 2 weeks of LIPUS treatment (Mukai et al. 2005; Takeuchi et al. 2008; Kobayashi et al. 2009) (Fig. 21.5, ph. 3).

LIPUS is a potential candidate for cartilage repair in patients suffering from osteoarthritis (OA). It has been shown that LIPUS has a beneficial effect on the migratory ability of bovine chondrogenic progenitor cells, which were recruited by ultrasound to the mechanically damaged cartilage through focal adhesion kinase (FAK) activation (Jang et al. 2014). Rabbits with anterior cruciate ligament transection have been used as a model for OA. It was found that chondrocytes from this model produced higher amounts of Col-2 and aggrecan at both the mRNA and protein level when stimulated with LIPUS, whereas MMP-1 and MMP-13 levels were reduced after the ultrasound application (Cheng et al. 2014).

21.5.1.9 Bone Remodeling

At the primary spongiosa level, chondrocytes become hypertrophic and begin to secrete ALP, which initiates matrix mineralization. The mineralized cartilage matrix provides a scaffold for migration of osteoprogenitor cells, which then differentiate and produce osteoid, the organic matrix of mineralized bone tissue (Fig. 21.5, ph. 4). Enhanced expression of maturating osteoblast markers, like OC and BSP, and calcium deposition in response to ultrasound has been confirmed throughout several studies (Yang et al. 2005; Suzuki et al. 2009b; Unsworth et al. 2007; Angle et al. 2011; Dalla-Bona et al. 2006; Ren et al. 2013). Osteoblast receptor activator of NF-κB ligand (RANKL) and osteoprotegerin (OPG) protein expression is responsible for regulation of osteoclast function. While RANKL activates osteoclasts (Lacey et al. 1998), OPG antagonizes their action by binding to the receptor activator of NF-κB (RANK) (Hsu et al. 1999). The most pronounced peak (about tenfold compared to unstimulated controls) of RANKL gene expression was found during the third week of LIPUS-treatment

in differentiating murine osteoblasts, while it was only slightly up-regulated during 1st, 2nd and 4th week of stimulation. Conversely, OPG expression levels remained constant throughout 3 weeks of LIPUS-stimulation (Bandow et al. 2007). These results imply that LIPUS enhances osteoclastogenesis throughout the entire time-course of bone regeneration (Fig. 21.5, ph. 2, 3, 4), peaking at week 3, which corresponds to woven bone resorption and lamellar bone formation in mice.

21.5.1.10 Immune Response

Immune cells assure inaccessibility of any foreign particles into the vulnerable cellular environment of the fracture, and thus, perform a prominent function in bone healing. The enhanced production of monocyte chemoattractant protein-1 MCP-1 (CCL2) and macrophage-inflammatory protein-1 MIP-1β (CCL4) mRNAs were observed during LIPUS treatment of differentiating murine pre-osteoblasts (Bandow et al. 2007). The increase persisted from week 1 until week 4, peaking on week 3. CCL2 and CCL4 are inflammatory cytokines that recruit monocytes, T-lymphocytes, macrophages and other immune cells that can potentially maintain proper fracture healing (Yoshie 2000) (Fig. 21.5, ph. 2, 3, 4). Interestingly, osteoblasts previously exposed to lipopolysaccharides and eliciting strong immune responses were found to express less inflammatory cytokines, *i.e.,* CXCL1, CXCL10 and RANKL, when treated with LIPUS (Nakao et al. 2014). Similar results were obtained with porcine mandibular condylar chondrocytes exposed to the inflammatory cytokine IL-1β: A concomitant treatment of the cells with LIPUS significantly reduced COX-2 mRNA expression levels compared to the cells treated with cytokine alone (Iwabuchi et al. 2014). The results of these studies suggest an anti-inflammatory effect of LIPUS.

21.5.2 Regeneration of Tissues Other than Bone in Response to LIPUS

There is growing evidence of LIPUS effectiveness in situations other than bone healing. The non-invasive character of LIPUS has a great potential to be used for regeneration of dental and periodontal tissues. Application of LIPUS led to enhanced expression of Col-1 and dentin matrix protein-1 (DMP-1) in human *ex-vivo* 3-D tooth culture. There was no effect on odontoblast viability and predentin layer thickness (Al-Daghreer et al. 2013). LIPUS also had beneficial effects on orthodontically induced inflammatory root resorption in beagle dogs, where LIPUS treatment reduced the size of the resorption lacunae, and resulted in higher cell counts in the periodontal ligament (Al-Daghreer et al. 2014). During the 2-week long treatment, LIPUS exposure increased the differentiation of human periodontal ligament cells (hPDLCs) as quantified by increased ALP activity, OC secretion and both mRNA and protein expression of Runx2. This promotion of osteogenic differentiation was found to be mediated in human periodontal ligament cells by integrin β1, relaying the LIPUS-induced mechanical stimuli intracellulary (Hu et al. 2014).

A higher proliferation rate of primary rat tenocytes was observed 24 h after LIPUS stimulation. The cells also secreted higher levels of TGF-β1 and MMP-13, and expressed more MMP-13, c-fos and c-jun (Chao et al. 2011). These results suggest LIPUS effectiveness in regeneration of tendon tissue.

LIPUS has been used to treat chronic venous wound healing caused by venous ulcer (VU). Treatment of human VU with LIPUS resulted in a decrease in the ulcer area, compared to no change in the group treated with topical antiseptic (de Ávila Santana et al. 2013), showing promising application of LIPUS for epithelial tissue regeneration.

Some promising results in regeneration of peripheral nerve tissue by LIPUS have been reported. Induced pluripotent stem cells-derived neural crest stem cells had higher viability when treated with LIPUS, as well as up-regulated expression of neural differentiation markers, *i.e.,* NF-M, Tuj1, S100β and GFAP 2 days after exposure (Lv et al. 2013). The LIPUS-supported neural differentiation was also reported in human gingival progenitor cells, where co-application of neuroinductive medium and ultrasound enhanced

expression of neurofilament and vimentin, two neurodifferentiation markers (El-Bialy et al. 2014).

21.5.3 Mechanotransduction Signaling Pathways Associated with LIPUS

Integrins, evolutionary conserved mechanoreceptors, are expressed by various cell types and convert mechanical signals into biochemical responses (Ingber 1991). Integrins have been proposed to be key players in the transduction of the ultrasound signal (Pounder and Harrison 2008). However, the type of activated integrins and their roles in the response to ultrasound stimulation vary with cell types and origin, as described below.

21.5.3.1 Transmembrane Mechanoreceptors

Increased surface expression of α2, α5, β1 and β3 integrins, and clustering of β1 and β3 integrins, have been shown to be upregulated in rat primary osteoblasts within 24 h after 20-min LIPUS treatment (Tang et al. 2006). In the same cell type but using continuous ultrasound exposure, enhanced expression of α2, α5 and β1 integrins has also been reported (Yang et al. 2005). After ultrasound exposure, gene expression of α2, α5 and β1 integrins was also significantly up-regulated in mouse osteoblasts isolated from long bones, whereas only expression of α5 was enhanced in mouse mandibular and calvaria-derived osteoblasts stimulated with LIPUS (Watabe et al. 2011).

Inhibiting β1 integrin in human primary skin fibroblasts, by blocking antibody or RGD-peptide, led to restoration of basal DNA synthesis levels that had been previously up-regulated in response to ultrasound (Zhou et al. 2004).

Cooperative functioning of integrin α2β1 with syndecan-4 receptors defines a successful outcome in wound healing (Echtermeyer et al. 2001). In mouse embryonic fibroblasts (MEF) ablation of the syndecan-4 receptor (syndecan-$4^{-/-}$) led to disruption of focal adhesion formation when stimulated with the soluble syndecan-4 ligand (Mahoney et al. 2009).

However, when the mutant cells were treated with LIPUS, cells formed focal adhesions and activation of intracellular signaling pathways occurred. LIPUS elevated transient expression of GTP-Rac1 protein, signaling downstream from syndecan-4 receptor, and enhanced formation of focal adhesions in syndecan-$4^{-/-}$ mouse embryonic fibroblasts. Interestingly, PKCα protein kinase, mediating Rac1 activity in the presence of syndecan-4, is not involved in ultrasound-induced signaling events. Instead, Mahoney et al. (2009) suggested that LIPUS acts downstream from these proteins or transmits its signal through an unknown signaling pathway. The ability of LIPUS to substitute for syndecan-4 receptor and to induce focal adhesion formation through Rac1 activation has been confirmed in another study (Roper et al. 2012).

21.5.3.2 Pathways Associated with PGE2 and NO Signaling Messengers

COX-2 expression, important for PGE2 production, was found to be regulated by signaling of focal adhesion kinase (FAK), and MAPK, Erk1/2, PI3K and Akt kinases in response to ultrasound treatment in murine MC3T3-E1 pre-osteoblasts (Tang et al. 2006). These signaling pathways were antagonized when the cells were treated with integrin inhibitors, and no enhanced phosphorylation of the proteins was observed after the ultrasound exposure, showing that integrins serve as an important link for converting mechanical signal into intracellular signaling.

Signaling pathways involved in regulation of iNOS expression in murine MC3T3-E1 pre-osteoblasts were also investigated. iNOS is another important enzyme in bone metabolism. It was found that ultrasound induces iNOS expression via the canonical NF-kB pathway in these cells, which is preceded by activation of Ras, Raf -1, MEK, Erk and IKKα/β kinases (Hou et al. 2009).

21.5.3.3 Osteogenesis-Associated Pathways

Human periodontal ligament cells (HPDLC), which are similar to MSCs, can undergo osteogenic differentiation (Choi et al. 2011). Ren et al.

(2013) have reported that p38 MAPK kinase is crucial for LIPUS-induced enhanced-differentiation of HPDLC cells. Treatment of cells with p38 inhibitor significantly reduced ALP activity, OC concentration and matrix mineralization in response to LIPUS, compared to the control group involving no inhibitor addition.

Naruse et al. (2003), using a set of inhibitors have demonstrated that enhanced differentiation of ST2 murine bone marrow-derived cells treated with LIPUS could be linked to the PI3K and p38 kinases pathways, but not Erk1/2 MAPK kinase signaling. Ikeda et al. (2006) has shown that the murine pluripotent mesenchymal cell line C2C12 can be committed to the osteoblastic or chondroblastic lineage when they are treated by LIPUS, and this is through activation of p38 and Erk1/2 MAPK kinase pathways. The discrepancy between these two studies concerning the activation of Erk1/2 signaling in response to LIPUS could be due to the different cell types, or to the inhibitors used that could have abrogated osteogenic marker expression in the study by Naruse et al. (2003). In the study by Ikeda et al. (2006), direct effects on protein phosphorylation were examined. The differences could also be attributed to the differences in the US set-up parameters, which are discussed in more detail in Chap. 8.

21.5.3.4 Chondrogenesis-Associated Pathways

The MAPK/ERK pathway has also been implicated in a very recent study (Louw et al. 2013) showing that blocking ERK phosphorylation abrogates the low-intensity ultrasound-induced expression of early response genes c-Fos, c-Jun and c-Myc in bovine chondrocytes. Further transcriptional induction of these genes is frequency-dependent, with highest c-series gene expression obtained at 5 MHz when compared to 2 and 8 MHz.

Low intensity ultrasound in continuous mode caused more intense phosphorylation of FAK, Src, p130Cas, CrkII and Erk1/2 in primary human chondrocyte cultures, suggesting that this pathway is involved in the US-induced mechanotransduction mechanism (Whitney et al. 2012). Increased proliferation rate of primary pig articular chondrocytes in response to LIPUS has been linked to the integrin/PI3K/Akt pathway (Takeuchi et al. 2008).

21.5.4 Ultrasound-Mediated Modulation of the Extra-Cellular Environment

Along with the direct effect of ultrasound on cellular mechanosensitive receptors/channels of the cell, and the indirect effect of acoustic streaming-governed shear stress on the cell surface, there is in fact another significant, yet often underappreciated effect: the acoustic streaming. Acoustic streaming, giving rise to a unidirectional bulk fluid movement, can improve molecular circulation within the extracellular matrix in the culture well, or trigger fluid flow *in-vivo*. This thereby increases the delivery of cytokines secreted by other cell participants or other essential nutrients, and removes cellular waste products (Argintar et al. 2011). The accessibility of the crucial factors to the compromised cells supports their viability and maintains the indispensable microenvironment in the healing fracture through the regulation of pH, oxygenation etc. which may be enhanced by the ultrasound treatment.

A mechanism of improved oxygen and nutrient transport in response to ultrasound has been suggested by Pitt and Ross (2003), who observed the effect of acoustic streaming on different strains of bacteria. Thicker biofilms were formed in response to low intensity, low frequency ultrasound exposure (100-ms bursts at 2 Hz PRF, 70 kHz ultrasound frequency, $I = 2\ W/cm^2$, type of intensity was not reported). The same group had previously shown that combining 2 h of continuous ultrasound with antibiotic Gentamicin could eliminate up to 99 % of bacteria, whereas treatment with the antibiotic alone achieved only 82 % (Peterson and Pitt 2000). Biofilms, formed during bacteria population, represent a strong barrier against penetration by oxygen, nutrients and more importantly, against penetration by antibiotics (Walters et al. 2003; Borriello et al. 2004). Lack of oxygen and nutrients slows down bacterial metabolism in the biofilm, decreasing

their susceptibility to antibiotics (Brown and Williams 1985). It is believed that improved transport of molecules due to acoustic streaming, not only delivers antibiotics to the bacteria, but also paves their way through the film by "reactivating" the bacteria and increasing the effectiveness of the drug (Peterson and Pitt 2000). This finding is critical for patients with open fractures and/or patients receiving bone transplants or replacements that could be at risk of bacterial infections and biofilm formation. Therefore, complementary treatment of ultrasound with antibiotic therapy appears to be a potential way of improving clinical outcomes for these patients.

Radial diffusion of Trypan blue dye was shown by Park et al. (2010) using 22 kHz frequency, 30 mW/cm^2 intensity and up to 10 min indirect low intensity ultrasound stimulation. This group reported that proliferation and uptake of glucose by adipose organoids was significantly increased, while TNF-α expression was markedly decreased in response to ultrasound, indicating increased metabolic activity. These effects could be explained by an improved supply of oxygen and transfer of nutrients to organoids occurring when cells can have limited access to the diffusing molecules.

The assumption that acoustic streaming could be responsible for an increase mass transport and could trigger the aforementioned effects is supported by other experimental evidence. Similarly to the ultrasound-induced acoustic streaming effect, bulk fluid flow can also be achieved by using perfusion bioreactors. Static 3D cultures usually fail to reproduce the tissue-like morphology and function because of the poor mass transfer to the cells in the center of the scaffolds. Dynamic culture serves as a good alternative to that (Potier et al. 2007; Li et al. 2009; Pisanti et al. 2012). Oxygen concentration can directly affect cell viability. Moreover, it has been shown that oxygen level can influence osteogenic differentiation. Volkmer et al. (2008) showed that MC3T3-E1 cells grown for 5 days in 3D static culture died in the center of the scaffold, where oxygen level was about 0 %, while the cells survived on the periphery. When the same cells were grown under the dynamic conditions, the cell death in the center was prevented and the oxygen gradient was lowered. Furthermore, hMSCs grown in hypoxic conditions experience downregulated expression of osteogenic phenotype genes, like Runx2, OC and Col-1 (Potier et al. 2007). Improved mass transfer was also confirmed by Pisanti et al. (2012) who showed that mesenchymal cells grown in dynamic 3D culture exhibited a higher proliferation rate, and this seemed to depend on pore size, with bigger pore size promoting higher rates. The authors hypothesized that larger pores improved the transport of nutrients, increasing therefore the proliferation rate. The same authors found improved osteogenic differentiation of cells under the dynamic conditions, which was evaluated by BMP-2 and ALP expression.

It should be noted that it is not always obvious to attribute the improved differentiation of the cells to the increased mass transport or to the shear stress agitation of the cellular membrane. To differentiate these two contributors, Li et al. (2009) manipulated the generated shear stress in a 3D-perfused hMSC culture by changing either the fluid viscosity at a fixed flow rate, or by changing the flow rate at a constant fluid shear stress. The study showed that by increasing shear stress, ALP activity was significantly increased on culture day 28 at 3 ml/min flow rate. Increasing flow rate from 3 to 6 ml/min at the same shear stress also significantly increased ALP activity. Osteopontin secretion was enhanced in response to each of the two parameters, implying that both mechanisms regulate osteogenic differentiation of hMSCs.

Since the principle behind acoustic streaming is movement of fluid, it is most likely that its effect is most pronounced during the earlier *in-vivo* healing stage, *i.e.,* during hematoma and soft callus formation. The impaired vascularization at the fracture site can no longer fulfill the needs of the compromised cells. Similarly to a perfusion system, the ultrasound-generated acoustic fluid flow is hypothesized to provide the cells with oxygen and nutrients, rescuing the viability and supporting the phenotype of the cells. Therefore, acoustic streaming may be an indirect, yet prominent effector of enhanced bone fracture healing.

The development of acoustic streaming is facilitated when the ultrasound propagates in one direction. While this condition may usually be fulfilled for *in-vivo* applications, *in-vitro* systems for which the sound is reflected several times between the interfaces (Fig. 21.3a, b), may prevent the development of an unidirectional fluid flow. Therefore, the aforementioned effects induced by acoustic streaming may not occur in some *in-vitro* cell culture stimulation systems.

21.6 Other Forms of Ultrasound Treatments Improving Bone Regeneration

LIPUS relies on a direct stimulation of the cells implicated in the bone healing processes. In this section we will review other LIPUS uses, including their synergistic combination with hormones or growth factors, but also other forms of ultrasound that have been carried out for the purpose of stimulating bone repair.

21.6.1 Synergistic Effect of LIPUS Combined with Essential Participants in Bone and Cartilage Regeneration

Due to the accelerated bone healing ability of LIPUS, there has been increased interest in combining the treatment with application of other essential participants already known to have bone-healing efficacy.

Combined treatment of LIPUS and a calcium-regulating hormone implicated in improved fracture healing, 1,25-dihydroxyvitamin D3 ($1,25\text{-}(OH)_2D_3$), has shown a synergistic effect on the expression of PDGF on day 5 in co-culture of human umbilical vein endothelial cells (HUVEC) and human osteoblasts SaOS-2 (Ito et al. 2000). In the presence of either LIPUS or $1,25\text{-}(OH)_2D_3$, the production of PDGF has been demonstrated. PDGF is an important factor for the regulation of MSCs and osteoblasts in the bone fracture. However, the highest effect was achieved when the two treatments were combined.

A significant improvement in chondrogenic differentiation has been reported in response to treatment of LIPUS with TGF-β_3 in a pellet culture of hMSCs (Ebisawa et al. 2004). The hMSCs treated with both LIPUS and TGF-β_3 exhibited more intense Alcian blue staining and an approximate threefold increase in aggrecan production, compared to the pellets treated solely with TGF-β3. Similar results were reported in another study where cells were grown in monolayers and TGF-β_1 was used instead of TGF-β_3 (Lai et al. 2010). Moreover, elevated Sox9 (a gene encoding a transcriptional factor prominent for chondrocyte differentiation), aggrecan and Col-2 expression were observed in response to the combined treatment. Intriguingly, in the first weeks of LIPUS-type stimulation of MSCs embedded in polyglycolic acid PGA scaffolds implanted in the back of nude mice, it was observed that LIPUS up-regulated chondrogenic differentiation of rabbit MSCs, even in the absence of TGF-β. Afterwards, a dominant osteogenic area could be observed in the later phase of the study (6 weeks post-implantation) (Cui et al. 2006, 2007). These data suggest that *in-vitro* LIPUS preconditioning could be effective in up-regulating chondrogenic differentiation of MSCs implanted in scaffolds *in-vivo* for cartilage tissue engineering applications.

BMP-2 and BMP-7 are the morphogenes approved by the FDA (Food and Drug Administration) for the treatment of bone fractures. Despite their promising bone healing ability, numerous side effects are associated with these cytokines (Argintar et al. 2011). Given the fact that BMPs are multifunctional players found in various tissues, the dose administration for a fractured bone should be stringently controlled. Due to growing knowledge of the synergistic effects of LIPUS combined with various macromolecule treatments, simultaneous application of LIPUS and BMPs appears to be an appealing tool in dose-controlled mediation of fracture healing.

In an *in-vivo* rat ectopic implant model, BMP-2 loaded on bovine Col-1 scaffolds with simultaneous LIPUS application induced more intensive bone formation after 4 weeks of stimu-

lation, compared to rats treated with BMP-2 alone (Lee et al. 2013). Interestingly, so far the synergistic combined effect of LIPUS and BMP-2 has not been confirmed *in-vitro*. Stimulation of hMSCs with combined LIPUS and BMP-2 treatment did not affect gene expression of Runx2, Col-1, Col-2 and ALP expression on day 3 (Lai et al. 2010). Similarly, there was no pronounced influence of the treatments on Runx2 and ALP gene expression, but a moderate up-regulation of Col-1 and osteopontin on day 3 and 5 in rat MSCs (Sant'Anna et al. 2005). Thus, the mechanism of the synergistic action of BMP-2 and LIPUS observed *in-vivo* requires further *in-vitro* investigation. One of the possible signaling mechanisms may be explained by a study of the mechanical cyclic loading of human fetal osteoblasts (hFOB). This reported a synergistic effect with treatment of BMP-2 through phosphorylation of Smad1, 5 and 8, followed by nuclear translocation of the proteins and regulation of genes involved in bone morphogenesis (Kopf et al. 2012).

In contrast to the aforementioned *in-vitro* experiments, combined exposure to LIPUS and BMP-7 has been shown to influence the osteogenic differentiation of human hematoma-derived progenitor cells (Lee et al. 2013). Compared to cultures treated exclusively with BMP-7, the combined treatment LIPUS + BMP-7 resulted in an increased expression of ALP, Runx2 and OPN on day 21, OC on day 14 and 21, as well as elevated ALP activity on day 14.

Not only vitamins and growth factors have been investigated for a potential effect on accelerated fracture healing with simultaneous LIPUS exposure, but also MSCs, inevitable cells in bone regeneration. These have shown an improved healing effect when combined with US in a rat model (Cheung et al. 2013). Rat GFP-labeled MSCs were exogenously injected and migrated to the fracture site, independent of the LIPUS treatment. However, in the group where MSCs were combined with ultrasound, the fracture healed faster, which was assessed by quantification of callus width and area, as well as bone volume to tissue ratio. Treatment with MSCs, regardless of LIPUS presence, resulted in faster bone remodeling.

LIPUS has also been combined with gene therapy. In a mouse model of ectopic bone formation in the muscle, gene transfer of BMP-4 by electroporation and subsequent application of LIPUS resulted in an accelerated maturation of ectopic bone formation (Watanuki et al. 2009).

21.6.2 Acoustic Shock Waves

Acoustic shock waves have been studied for their potential to promote beneficial therapeutic effects on different bone–related clinical complications. Acoustic shock wave treatments are very different to LIPUS-type treatments due to the very different nature of the stimulation applied in tissues (Rassweiler et al. 2011). A shock wave is a short-duration (<10 μs) acoustic pressure wave consisting of a compressive phase (peak pressure: 30–100 MPa) followed by a tensile phase (negative pressure). When propagating into tissues, it will be associated with the generation of very high compressive, tensile and shear stresses, as well as generation and collapse of bubbles (inertial cavitation). Shock waves can be generated by different types of sources: Electrohydraulic, *i.e.,* a spark source which generates a shock wave that is focused by an ellipsoidal reflector, electromagnetic, *i.e.,* using an electrical coil in close proximity to a metal plate as an acoustic source, or piezoelectric, *i.e.,* using a large focused transducer. In shock wave lithotripsy, acoustic energy is focused to a relatively small zone surrounding the focal point of the lithotripter. This is an elongated, elliptical "cigar-shaped" volume of typically a few tenths of a single mm in length, versus a few mm in width. Lithotripsy treatment to induce kidney stonecomminution, and in application of shock waves to bones, will consist of the application of 500–2000 consecutive shock waves, at repetition frequencies of typically 1 Hz. Historically, the application of shock waves in medicine by lithotripsy was in situations where stones that form in the kidney, bladder, ureter or gallbladder were fragmented into passable size. Shock wave lithotripsy has become a standard procedure in urology. Applications in the bone context are more recent. So far, shock waves have

been used for the treatment of nonunions, pseudarthrosis (Birnbaum et al. 2002), loosening of bone cement during revision arthroplasty (Weinstein et al. 1988), bone regeneration in hip necrosis (Mont et al. 2007), healing at the bone-tendon junction (Wang et al. 2008b) and enhancement of bone callus formation during bone lengthening (Narasaki et al. 2003). To date, they are currently two FDA-approved indications for the use of shock waves in orthopedics; treatment of plantar fasciitis and lateral epicondylitis (Foldager et al. 2012). In the treatment of bone fractures and femoral head osteonecrosis, shock waves have been reported to promote bone remodeling, but also angiogenesis (Wang et al. 2008a; Ma et al. 2007) and the ability to restore the healing process in the case of nonunion (Padilla and Cleveland 2009). Mechanisms of action are possibly related to the induction of micro-fractures in bony tissues due to the very high stresses induced by the propagation of shock waves (Da Costa Gómez et al. 2004; Padilla and Cleveland 2009). These in turn could trigger the initiation of remodeling cycles; the stimulation of neovascularization (Wang et al. 2003a; Ma et al. 2007). This is possibly associated with an inflammatory response following induced trauma in soft tissues due to shock-wave induced inertial cavitation phenomena (Delius et al. 1990); together with direct effects on cell proliferation, membrane polarization, expression of bone morphogenic proteins and activation of mechanotransduction pathway cascades (Wang et al. 2001, 2003b, 2008a; Chen et al. 2004; Yip et al. 2008).

21.6.3 Ultrasound and Tissue Engineering

Ultrasound has also shown potential in bone tissue engineering strategies. Engineering tissue regeneration relies on the delivery of biologics, *i.e.,* cells, signaling molecules and genetic materials via degradable and non-degradable scaffolds (Hollister 2009). The process of tissue engineering is therefore often described as a "triad", including scaffolds, cells and microenvironments (signaling molecules and the physical environment). Ultrasound has played, or has a potential to play, a role in all these aspects of tissues engineering processes.

For the biologics: Ultrasound can be used to promote cell proliferation, or to pre-condition cells to orient their differentiation during culture, as reviewed earlier with LIPUS. Additionally, ultrasound can be used to transfect cells. Ultrasound associated with microbubbles, such as acoustic contrast agents, is a technique aimed at transiently altering the permeability of cell membranes– so called sonoporation. This is a powerful way to induce internalization of genetic materials (Mehier-Humbert et al. 2007). This method has been applied to induce ectopic bone formation by sonoporation of naked DNA encoding for an osteogenic gene (rhBMP-9) into mice thigh muscles (Sheyn et al. 2008). *In-vitro* transfection with ultrasound and microbubbles has also been used to genetically modify MSCs before their implantation with siRNA to knock down PTEN mRNA expression and activation of Akt, a mediator of a survival signaling pathway (Otani et al. 2009).

Furthermore, ultrasound can be used for the monitoring and the control of scaffold degradation rate, for the manufacturing of scaffolds, for the characterization of scaffold properties and their quality control, and for improving scaffold integration (Mather et al. 2008; Parker et al. 2011; Winterroth et al. 2011; Kim et al. 2008).

21.6.4 Ultrasound-Triggered Delivery of Growth Factors

Ultrasound can be used to control delivery of growth factors or gene expression of engineered cells, but it can also modulate the physical environment by heat deposition or mechanical stimulation in order to promote regeneration. Delivery of bioactive molecules as instructive cues to engineered tissues can also benefit from the specificity of ultrasound-mediated delivery techniques. Microbubbles have been combined with growths factors for a spatio-temporal control of their release (Chappell et al. 2008). We recently developed a delivery system composed of fibrin

hydrogels doped with growth factor-loaded double emulsion for applications in tissue regeneration and on-demand release of growths factors (Fabiilli et al. 2013). We also demonstrated that growth factor production could be remotely controlled both temporally and spatially with ultrasound by using engineered cells transfected with a heat-shock-activated, rapamycin-dependent gene switch (Wilson et al. 2014).

21.7 Clinical Data

21.7.1 Regulatory Agreement

In the USA, the first FDA premarket approval (PMA) for a LIPUS device was granted in 1994 to Exogen, a Smith & Nephew company, for the generation of the first Exogen device. The approved indications included acceleration of the time for fracture healing of, (1) fresh, closed, posteriorly displaced distal radius fractures, and (2) fresh, closed or grade I open tibial diaphyseal fractures in skeletally mature individuals. This is when fractures are orthopaedically managed by closed reduction and cast immobilization. This approval was based on data submitted from two randomized, double-blind, placebo-controlled trials (Heckman et al. 1994; Kristiansen et al. 1997).

This approval was then extended in 2000 for the non-invasive treatment of established nonunions, excluding skull and vertebra. The approval was based on prospective studies where individuals served as their own control (case series n = 74) and on a case series of 41 nonunions (Nolte et al. 2001).

The Exogen system is currently distributed by Bioventus, a joint venture between Smith & Nephew and Essex Woodlands, a private equity firm.

The ultrasound signal approved for clinical use by the American FDA consists of a 1.5 MHz ultrasound wave pulsed at 1 kHz, with a 20 % duty cycle at an intensity of 30 mW/cm^2 I_{SATA} (spatial average temporal average intensity) applied for 20 min per day. The device is composed of a main operating unit, with an external power supply, that is connected to a treatment head module (transducer) that is affixed to a mounting fixture centered over the fracture site. The device is intended for individual use in the home setting in one daily 20-min treatment until healing is confirmed.

21.7.2 Clinical Evidence

In 1994 and 2000, PMA were granted on the basis of three clinical studies (Heckman et al. 1994; Kristiansen et al. 1997; Nolte et al. 2001) that reported stimulation of the acceleration of the normal fracture-repair process of, (1) grade I open tibia fractures (67 patients, 33 treated, 34 placebo), and (2) distal radial fractures (60 patients, 30 treated, 30 placebo), when both types of fractures were treated with a cast. These two studies demonstrated the usefulness of LIPUS for the treatment of challenging, established nonunions (29 patients including tibia, femur, radius/ulna, scaphoid, humerus, metatarsal and clavicle fractures).

Several retrospective reports (case series, case reports, data from a registry of users, and randomized, double-blind, placebo-controlled trials) have since indicated the beneficial effects of LIPUS: Promotion of healing of fresh distal radius and tibial diaphyseal fractures, acceleration of healing for nonunion of other fracture sites (including the clavicle, humerus, femur, tibia, and the metatarsals and metacarpals). However, the quality of the methodology of some of these studies, the lack of large-scale clinical studies and the heterogeneity in outcomes has rendered it difficult to make a definitive conclusion about the effectiveness of LIPUS. Various outcomes have been used to assess effectiveness of the treatment: Directly assessed functional end points (time to return to active duty, Olerud-Molander score, time to full weight bearing, time to patient reported fracture healing and resumption of household activities, work or sports), or surrogate outcomes, such as radiographical healing; the most commonly reported end point.

A number of systematic reviews and meta-analyses have examined the available clinical data (Malizos et al. 2006; Romano et al. 2009; Claes and Willie 2007; Pounder and Harrison

2008; Busse et al. 2009; Martinez de Albornoz et al. 2011; Hannemann et al. 2014; Griffin et al. 2014). These conclude that the quality of the evidence is low to moderate, and at times appears conflicting.

Two of these reviews and meta-analysis have conducted a selection of eligible randomized controlled trials. These were based on a GRADE system of rating quality of evidence for each outcome (Busse et al. 2009), or by assessing the risk of bias according to the criteria in the Cochrane Handbook for Systematic Reviews of Interventions (Hannemann et al. 2014). Some other publications applied less stringent filters, like inclusion of prospective clinical studies, randomized controlled trials or quasi-randomized trials (Martinez de Albornoz et al. 2011; Griffin et al. 2014), whereas others did not report applying quality-based selections of the studies discussed (Romano et al. 2009; Malizos et al. 2006).

In a meta-analysis published in 2009, Busse et al. (2009) concluded that the evidence to support the use of low-intensity pulsed ultrasonography for fracture healing was limited and inconsistent; with most trials reporting surrogate outcomes. Their meta-analysis of eligible randomized controlled trials found 13 eligible trials, with only five directly assessing functional end points, among them only one was positive.

A consensus is however reached that numerous factors will influence the outcome of the treatment: Types of injuries (fresh, malunion or nonunion), types of fractures (metaphyseal or diaphyseal), fracture site (upper or lower limb), type of bone, management (non-operative or operative) and for nonunion, the stability at the site of fracture. Effectiveness of LIPUS must therefore be analyzed on a case-by-case basis.

For operatively managed fresh fractures, the evidence to support the use of low intensity pulsed ultrasonography suggested low quality evidence of the benefit of LIPUS (Busse et al. 2009), with inconsistencies between trials which may (or may not) be explained by differences in the patient populations or by duration of low intensity pulsed ultrasonography use. A more recent meta-analysis also concluded that current evidence did not support the assumption that LIPUS could reduce time to heal surgically managed fresh fractures (Hannemann et al. 2014).

On the contrary, although supported by low quality evidence, it was shown that the effect of LIPUS on fresh fractures, not undergoing operative treatment, resulted in a mean acceleration of the time to radiological union of approximately 27 days, and 20 days for upper limb fractures (Hannemann et al. 2014; Busse et al. 2009). LIPUS may also accelerate the time to clinical union for acute diaphyseal fractures (Hannemann et al. 2014), with an average reduction of time to clinical union by 18 days.

Studies concerning nonunions are more difficult to analyze due to the large variation in fracture site, initial fracture severity, initial fracture treatment (LIPUS not been used as a first line treatment) and the number of subsequent surgical interventions. Moreover, these studies are not blinded, and thus harbor potential bias. Patients are usually their own controls and treatment's success is assessed based on radiological or clinical healing, which usually prevents distinguishing pure effects of LIPUS from potential effects of previous treatments. With all these considerations in mind, the results of these level IV clinical studies appear to suggest that LIPUS promotes healing in established nonunions, with reported union rate ranging from 70 to 93 % (Malizos et al. 2006) (Romano et al. 2009).

The clinical evidence is therefore positive, but generally weak. A large registry study (Mayr 2000) has provided quite robust estimates of absolute healing rates, with LIPUS for delayed union and nonunion fractures of different long bones. One randomized controlled trial, that compared LIPUS with placebo in a mixed population of patients with delayed and nonunion fractures of the tibia (Schofer et al. 2010), failed to detect significant improvements in the rate of healing with LIPUS. On the other hand, they detected significant improvements in indicators of progression towards healing (bone mineral density and bone gap area).

The effect of LIPUS on patients with established scaphoid nonunion, and treated with vascularized pedicle bone graft, versus those exposed to a sham device was studied with a placebo-controlled design

(Ricardo 2006). It was found that LIPUS accelerated healing by a mean difference of 38 days, but the small sample size (21 patients) provides only low quality evidence for a benefit of LIPUS in accelerating healing of established nonunions managed with bone graft (Busse et al. 2009).

Current evidence from randomized trials is also insufficient to conclude a benefit of LIPUS on reducing the incidence of nonunion when used for treatment in acute fractures (Hannemann et al. 2014).

Other available evidence comes from case series, which are difficult to summarize due to differences in the reported outcomes.

21.7.3 Health Economics of LIPUS

The analysis of the cost-effectiveness of ultrasound treatment of bone fractures is complex, given that analyses have compared treated to non-treated patients, and also ultrasound to other treatment strategies. The actual economic burden of a treatment method is a complex entity that should not be judged from surgery or implant costs alone, but requires analysis of direct and indirect costs, as well as the impact on quality of life. The potential cost-saving of ultrasound stimulation has therefore to be evaluated from a global and social perspective, both for health care system costs (direct health care costs, including governmental, insurer and patient costs) and costs of productivity losses (indirect health care costs).

It is recognized from a health economics view, that the longer the delay to union, the greater the total cost for the treatment of the fracture. Cost increase is due to productivity losses and to secondary procedures costs, such as intramedullary nailing, bone grafting, external fixation or BMP-7 grafting. This is particularly relevant for nonunions, for which an econometrics study conducted in England in 2007 had estimated associated costs of around £16 k in a best case scenario, highlighting the economic burden of these types of fractures.

The costs of tibial shaft fractures, treated with either casting or intramedullary nailing, was modeled by Heckman and Sarasohn-Kahn (1997). They incorporated direct healthcare costs, outpatient costs and workers' compensation costs. The use of LIPUS as an adjunct to casting resulted in cost savings of approximately 15,000$ US per case, with savings attributed to a reduction in secondary procedures and a shortened healing time, reducing the amount of Workers' Compensation payments.

This trend was confirmed by Busse et al. (2005), who also conducted an economic analysis for four competing treatment strategies of closed or grade I open tibial fractures: (1) Casting alone, (2) casting with therapeutic ultrasound, (3) operative treatment with non-reamed intramedullary nailing, and (4) operative treatment with reamed intramedullary nailing. Their results suggested that casting with therapeutic ultrasound may hold promise in terms of cost-saving over operative management by non-reamed intramedullary nailing and casting alone. This was with time lost at work included in the analysis.

The most recent cost-analysis study was conducted in 2013 (available online: http://www.nice.org.uk/guidance/mtg12/resources/exogen-ultrasound-bone-healing-system-for-long-bone-fractures-with-nonunion-or-delayed-healing-assessment-report2) as part of a review process for the English National Institute of Health. It was based on a model including patients with fractures of the tibia initially treated by surgical insertion of an intramedullary nail. It concluded that the use of LIPUS, followed by surgery only if needed after a further 6 months, was estimated to save about £1200 per patient, compared with immediate surgery in patients with nonunion fractures of the tibia. They also deduced that early use of LIPUS for delayed union was around £500 more expensive than waiting for surgery at nonunion. These data partly motivated the UK National Institute for Health and Care Excellence (NICE) to issue a positive recommendation in their provisional guidance for the use of LIPUS in the management of nonunion.

Large, prospective, randomized controlled trials that include cost-effectiveness analyses would be needed to further define the financial burden associated with LIPUS. However, evidence of acceleration of healing rates, although of low

level, and of decreased secondary procedures, tend to favor LIPUS as a cost-saving modality.

A 2008 review in the Journal of Bone and Joint Surgery (American edition), although failing to include negative trials, reported that there was "overwhelmingly positive clinical data supporting low intensity pulsed ultrasound as a treatment for fracture repair" (Khan and Laurencin 2008). This over-optimistic assessment is unfortunately not yet supported by the available clinical data. The encouraging case series and small size randomized studies suggest that LIPUS may accelerate the time of heal of non-surgically managed fresh fractures, and that it may promote healing in established nonunions. Although of low quality, this evidence, together with the economics of nonunion and the absence of toxicity, speak in favor of the clinical use of LIPUS.

It should also be kept in mind that even if a consensus seems to have been reached that LIPUS may prove beneficial for patients via an accelerated improvement in function, the evidence of acceleration of fracture repair, as observed by radiographic assessment, may not directly translate into important patient benefits. Therefore, large, methodologically sound trials on the effect of LIPUS on fracture, particularly operatively-managed fresh fractures and nonunion, that assess important outcomes, such as quality of life and return to function, are still needed to fully establish the potential role of LIPUS in clinical practice.

21.8 Discussion

The biological response to LIPUS is complex, as different bio-effects can be induced either directly or indirectly by the acoustic waves, and various cell types respond to these stimuli in a concerted manner involving several pathways. Among the difficulties understanding the mechanistic basis of the observed stimulatory effects, are the technical limitations by which ultrasound has commonly been used *in-vivo* and in cell culture stimulation systems. LIPUS has been introduced as a simple and wearable *in-vivo* device that supports and accelerates the healing of human bone fractures (Heckman et al. 1994). The dimension of the sound field produced by the flat circular transducer ensures easy handling and deposition of the majority of the acoustic energy in the fracture repair region. Driven by the encouraging clinical outcomes, the same or similar systems have been used to investigate the mechanistic effects of LIPUS stimulation *in-vivo* in small animal models and *in-vitro* cell cultures. The translation of the clinical stimulation system to a small animal model or a cell culture system appears to be challenging due to the physical dimensions of the acoustic sound field and the various physical effects induced by the propagating waves. For typical application in human fractures, the ultrasound waves are predominantly emitted in the fracture repair region and the same device irradiates the entire bone, including surrounding soft tissues in small animals. *In-vivo* applications may prevent the development of standing waves due to irregular organ and tissue morphology, resulting in divergence, scattering and attenuation of the emitted waves, the regular dimensions and interfaces perpendicular to the sound propagation direction. Additionally, the low attenuation in the culture medium and culture dish materials lead to multiple reflections, standing waves and potential heating artifacts. Therefore, for a particular ultrasound transducer that emits a well-defined acoustic intensity pattern in an interface-free fluid, not only the acoustic intensity, but also the induced physical mechanisms, may be remarkably different between *in-vivo* and *in-vitro* conditions, even between *in-vitro* experiments with different exposure geometries. In consequence, care must be taken when comparing the findings of different LIPUS studies.

Several set-up parameters have to be taken into account in order to achieve agreeable data in response to ultrasound treatment. The geometry, affecting transmission, reflection, as well as spatial and temporal distributions of pressures and intensities exerted on the cells during *in-vitro* experiments, are factors that can jeopardize experimental results. The physical characteristics, *e.g.,* ultrasound frequency, intensity, duty cycle and duration of application of the applied ultrasound beam have indeed been reported to

potentially affect the outcome of the stimulation, both *in-vitro* and *in-vivo*.

Using similar frequency and temporal settings (1.5 MHz center frequency, 200 μs pulses, for 5–20 min daily), Tsai et al. (1992) found that while 0.5 W/cm^2 (I_{SATA}) significantly accelerated bone repair, 1.0 W/cm^2 suppressed it. Similarly, Reher et al. (1997) reported that while 0.1 W/cm^2 stimulated collagen and non-collagenous protein synthesis, 0.5–2 W/cm^2 inhibited it (at 3 MHz center frequency, 2 ms pulses for 5 min). Similar data showed that increasing I_{SATA} from 30 to 150 mW/cm^2 did not improve bone volume fraction or failure torque in a model of closed femoral fractures in rats (Fung et al. 2012). Likewise, Wang et al. (1994) reported that 1.5 MHz center frequency could accelerate fracture repair with greater stiffness in a rat model of closed femoral shaft fractures. However, 0.5 MHz frequency did not accelerate repair, all other parameters being constant (30 mW/cm^2, 200 μs pulses, 1 kHz PRF). Changing the PRF from 1 Hz to 1 kHz has also been shown to affect the biological response to LIPUS (Marvel et al. 2010). Several studies suggested that continuous mode or bursts with long duty cycles might inhibit osteoclastogenesis (Maddi et al. 2006; Yang et al. 2005; Sun et al. 2001), illustrated by the absence of changes in RANKL expression or even the decrease in number of osteoclast or tartrate-resistant acid phosphatase (TRAP) positive osteoclasts. Positioning of the cells within the acoustic field might also be a factor influencing the biological outcome: A positive effect on differentiation of pre-osteoblastic mouse MC3T3-E1 cells was observed when the culture plate was directly coupled to the transducer as illustrated in (Fig. 21.3b) (Unsworth et al. 2007), whereas no effect was observed when the plate was placed in the far field, as illustrated in (Fig. 21.3b) (Bandow et al. 2007). All other parameters were similar (1.5 MHz ultrasound burst of 200 μs at 1 kHz and $I_{SATA} = 30$ mW/cm^2). In the same way, osteocyte positioned in the far field of the transducer released the most NO after only 5 min of stimulation, while the peak of NO release was observed after 20 min when the cells were placed in the near field of the transducer (Ryoo et al. 1997).

Cell site-specificity can also alter the outcomes of LIPUS stimulation. Using rat UMR-106 bone-forming cells with osteoblast-like features (Warden et al. 2001), or mouse ST2 bone-marrow-derived stromal cells that can differentiate into osteoblasts (Naruse et al. 2000), different expression levels and time courses were observed for IGF-1, BSP and OC. Similarly, osteoblasts from calvaria and long bones differently expressed osteogenic resorption and survival markers after LIPUS stimulation when compared to mandible-derived primary mouse osteoblasts (Watabe et al. 2011).

These examples demonstrate the necessity to design experimental setups in which acoustic peak pressure levels, temporal variation of intensity, resulting radiation pressure and acoustic streaming can be well controlled. More important than the documentation of the acoustic output levels are type, amplitude and duration of the 'dose' experienced by the cells. Furthermore, it is crucial to develop studies, which can differentiate contribution of each of the previously described US bioeffects. These approaches should help in achieving more reproducible outcomes of cell stimulation studies and contribute to the understanding of the biophysical mechanisms of LIPUS action.

Conclusion

There are different directions that can now be addressed to improve ultrasound stimulation of bone formation.

The first ones are technological. The previous sections illustrated the necessity of carefully designing experimental setups and documenting the acoustic output levels, and more importantly the type, amplitude and duration of the stimulation 'dose' experienced by the cells. These issues can be addressed *in-vitro*, where acoustic fields can be well controlled and where side effects that can potentially influence the response, like standing waves or heating by the transducer, can be avoided. Systems operating in the far field of unfocused transducers, with an absorbing chamber behind the stimulated cell layer, seem to be the most predictable designs so

far. Controlling the sound propagation path length in the culture medium could allow precise control of the acoustic streaming in the stimulated well, and will allow experimental designs that can differentiate the contributions of each of the previously described ultrasound bioeffects. Alternatively to the use of plane wave transducers, focusing the ultrasound wave *in-vivo* to areas similar in size to the dimensions of a fracture, or osteotomy in small animal models, can also be used. Then, the entire acoustic energy can be deposited in the repair region, which we believe should allow a better control of the deposited dose. We anticipate that such systems will provide a better convergence of *in-vitro* and *in-vivo* results.

A second direction of research is the combination of ultrasound imaging and therapy for both stimulation and response monitoring. Different approaches, such as focused through-transmission (Rohrbach et al. 2013) or axial transmission (Machado et al. 2010, 2011; Protopappas et al. 2008; Potsika et al. 2013) can distinguish fibrous or cartilaginous tissues from mineralized ones, and could be useful for real-time monitoring of bone healing *in-vivo*.

A third direction that merits attention is the passage from *in-vitro* experiments to clinical use. The passage from *in-vitro* to small animal models and then to large, weight-bearing and functional models is not trivial. Among the most challenging issues for the comparability of *in-vitro* and *in-vivo* studies are the different boundary conditions. *In-vivo* bone regeneration involves a plethora of cells of different origin (residing osteocytes, stem cells, immune cells, macrophages) which have to orchestrate the synthesis of tissue under highly compromised conditions, *i.e.,* diminished nutrition and waste transport, inflammatory tissue response, disrupted tissue architecture. On the other hand, *in-vitro* conditions are usually optimized to obtain a maximum cell response with respect to proliferation, differentiation and matrix production. Under such conditions, stimulatory effects may be much less pronounced or the response may be different compared to the *in-vivo* situation. One of the advantages of ultrasound technology, at least LIPUS, is the absence of reported side effects. We can therefore expect that obtaining reproducible *in-vitro* results in more complex biological systems could pave the way for new clinical trials. To mimic relevant *in-vitro* conditions, future studies should aim at working with more complex biological systems and at compromising the supplies of nutrients and growth factors, as well as investigating the synergistic effects of cell-cell interactions. This can be achieved using co-cultures, organoids or 3D tissue engineering that seeds several cell types in scaffolds. These types of culture will also allow exploration of the effects of ultrasound on increased mass transport, which could benefit tissue grafts during the immediate post-implant period, when blood supply to the implanted tissue is suboptimal, as reported recently (Park et al. 2010).

A recent editorial in the *J Orthop Trauma* (Bhandari and Schemitsch 2010) argued that innovation in the management of bone fractures was likely to come from a 'biologic; a drug or device that further enhances the healing potential of fractures treated with modern day implant fixation' that could come at a reasonable cost. In this context, ultrasound technologies have a role to play due to their therapeutic potential, possibly combined with monitoring, that comes at low costs compared to other non-healing fracture management strategies. Improvements will probably come from a combination of ultrasound with 'biologic' components, *e.g.,* growth factors, scaffolds, gene therapies or drug delivery vehicles, the effects of which could be potentiated by ultrasound. Ultrasound-based drug delivery approaches are currently intensively investigated and it is likely that combination of this approach with the intrinsic stimulatory potential of ultrasound will open way for new applications in the orthopedic field.

In summary, ultrasound can enhance fracture healing or reactivate a failed healing process. There are several options available for

the use of ultrasound in this context, either to induce a direct physical effect (LIPUS, shock waves) to deliver bioactive molecules, such as growth factors, or to transfect cells with osteogenic plasmids. The clinical evidence, although often of low quality, speaks nevertheless in favor of a clinical use of LIPUS when analyzed in combination with the economics of nonunion and the absence of toxicity of this ultrasound technology.

We have focused in this chapter mainly on LIPUS-type stimulation of fracture healing as it is the most widespread and studied. The biological response to LIPUS is complex, as numerous cell types respond to this stimulus involving several pathways. Mechanotransduction pathways seem to be involved in cell responses, as demonstrated by the role of MAPK and other kinase pathways, the role of gap-junctional cell-to-cell intercellular communication, up-regulation and clustering of integrins, involvement of the COX-2/PEG2 pathway and activation of the ATI receptor. The mechanisms by which ultrasound can trigger these effects remain intriguing. To some extent, these responses can be compared to the responses to well-controlled mechanical stimuli, such as shear stresses. Possible mechanisms include direct mechanical effects, like acoustic radiation force, acoustic streaming, propagation of surface waves and indirect effects, such as fluid-flow induced mixing and redistribution of nutrients, oxygen and signaling molecules. Temperature is usually ruled out, but it's possible influence cannot be neglected for some *in-vitro* set-ups. Although *in-vitro* studies are not appropriate to identify the full complexity of biological effects, they are of interest to study specific mechanisms of action. However, great care has to be given to the design of dedicated experimental set-ups in which the different ultrasound contributions can be controlled. This will enable the study of the various influencing parameters and to relate the variations of these parameters to the induced biological responses. Then, it should become possible to derive an 'acoustic dose' required for particular responses and to transfer such *in-vitro* findings to *in-vivo* applications.

Acknowledgments The authors thank Ruslan PUTS for his help in the design and drawing of Fig. 21.5.

References

Ahrens M, Ankenbauer T, Schröder D, Hollnagel A, Mayer H, Gross G (1993) Expression of human bone morphogenetic proteins-2 or -4 in murine mesenchymal progenitor C3H10T1/2 cells induces differentiation into distinct mesenchymal cell lineages. DNA Cell Biol 12:871–880

Al-Daghreer S, Doschak M, Sloan AJ, Major PW, Heo G, Scurtescu C, Tsui YY, El-Bialy T (2013) Short-term effect of low-intensity pulsed ultrasound on an ex-vivo 3-D tooth culture. Ultrasound Med Biol 39: 1066–1074

Al-Daghreer S, Doschak M, Sloan AJ, Major PW, Heo G, Scurtescu C, Tsui YY, El-Bialy T (2014) Effect of low-intensity pulsed ultrasound on orthodontically induced root resorption in beagle dogs. Ultrasound Med Biol 40:1187–1196

Alvarenga EC, Rodrigues R, Caricati-Neto A, Silva-Filho FC, Paredes-Gamero EJ, Ferreira AT (2010) Low-intensity pulsed ultrasound-dependent osteoblast proliferation occurs by via activation of the P2Y receptor: role of the P2Y1 receptor. Bone 46:355–362

Angle SR, Sena K, Sumner DR, Virdi AS (2011) Osteogenic differentiation of rat bone marrow stromal cells by various intensities of low-intensity pulsed ultrasound. Ultrasonics 51:281–288

Argadine HM, Kinnick RR, Bolander ME, Greenleaf J (2005) 1 kHz low power sound stimulates ATDC5 chondrocytes. Proc IEEE Ultrason Symp 996–998

Argadine H, Bolander ME, Greenleaf J (2006) Stimulation of proteglycan synthesis with low-intensity 1 kHz vibration IEEE. Proc IEEE Ultrason Symp 849–851

Argintar E, Edwards S, Delahay J (2011) Bone morphogenetic proteins in orthopaedic trauma surgery. Injury 42:730–734

Arndt V, Dick N, Tawo R, Dreiseidler M, Wenzel D, Hesse M, Fürst DO, Saftig P, Saint R, Fleischmann BK, Hoch M, Höhfeld J (2010) Chaperone-assisted selective autophagy is essential for muscle maintenance. Curr Biol 20:143–148

Azuma Y, Ito M, Harada Y, Takagi H, Ohta T, Jingushi S (2001) Low-intensity pulsed ultrasound accelerates rat femoral fracture healing by acting on the various cellular reactions in the fracture callus. J Bone Miner Res 16:671–680

Bandow K, Nishikawa Y, Ohnishi T, Kakimoto K, Soejima K, Iwabuchi S, Kuroe K, Matsuguchi T (2007) Low-intensity pulsed ultrasound (LIPUS) induces RANKL, MCP-1, and MIP-1beta expression in osteoblasts through the angiotensin II type 1 receptor. J Cell Physiol 211:392–398

Bhandari M, Schemitsch EH (2010) Stimulation of fracture healing: osteobiologics, bone stimulators, and beyond. J Orthop Trauma 24 Suppl 1:S1

Birnbaum K, Wirtz DC, Siebert CH, Heller KD (2002) Use of extracorporeal shock-wave therapy (ESWT) in the treatment of non-unions. A review of the literature. Arch Orthop Trauma Surg 122:324–330

Borriello G, Wermer E, Roe F, Kim AM, Ehrlich GD, Stewart PS (2004) Oxygen limitation contributes to antibiotic tolerance of Pseudomonas aeruginosa in biofilms. Antimicrob Agents Chemother 48:2659–2664

Bozec A, Wermer E, Roe F, Kim AM, Ehrlich GD, Stewart PS (2010) Fra-2/AP-1 controls bone formation by regulating osteoblast differentiation and collagen production. J Cell Biol 190:1093–1106

Brown MR, Williams P (1985) Influence of substrate limitation and growth phase on sensitivity to antimicrobial agents. J Antimicrob Chemother 15 Suppl A:7–14

Busse JW, Bhandari M, Sprague S, Johnson-Masotti AP, Gafni A (2005) An economic analysis of management strategies for closed and open grade I tibial shaft fractures. Acta Orthop 76:705–712

Busse JW, Kaur J, Mollon B, Bhandari M, Tornetta P 3rd, Schünemann HJ, Guyatt GH (2009) Low intensity pulsed ultrasonography for fractures: systematic review of randomised controlled trials. BMJ 338:b351

Canalis E, McCarthy TL, Centrella M (1989) Effects of platelet-derived growth factor on bone formation in vitro. J Cell Physiol 140:530–537

Celil AB, Campbell PG (2005) BMP-2 and insulin-like growth factor-I mediate Osterix (Osx) expression in human mesenchymal stem cells via the MAPK and protein kinase D signaling pathways. J Biol Chem 280:31353–31359

Chao YH, Tsuang YH, Sun JS, Cheng CK, Chen MH (2011) The cross-talk between transforming growth factor-beta1 and ultrasound stimulation during mechanotransduction of rat tenocytes. Connect Tissue Res 52:313–321

Chappell JC, Song J, Burke CW, Klibanov AL, Price RJ (2008) Targeted delivery of nanoparticles bearing fibroblast growth factor-2 by ultrasonic microbubble destruction for therapeutic arteriogenesis. Small 4:1769–1777

Chen YJ, Kuo YR, Yang KD, Wang CJ, Sheen Chen SM, Huang HC, Yang YJ, Yi-Chih S, Wang FS (2004) Activation of extracellular signal-regulated kinase (ERK) and p38 kinase in shock wave-promoted bone formation of segmental defect in rats. Bone 34:466–477

Cheng K, Xia P, Lin Q, Shen S, Gao M, Ren S, Li X (2014) Effects of low-intensity pulsed ultrasound on integrin-FAK-PI3K/Akt mechanochemical transduction in rabbit osteoarthritis chondrocytes. Ultrasound Med Biol 40:1609–1618

Cheung WH, Chin WC, Wei FY, Li G, Leung KS (2013) Applications of exogenous mesenchymal stem cells and low intensity pulsed ultrasound enhance fracture healing in rat model. Ultrasound Med Biol 39:117–125

Choi HD, Noh WC, Park JW, Lee JM, Suh JY (2011) Analysis of gene expression during mineralization of cultured human periodontal ligament cells. J Periodontal Implant Sci 41:30–43

Claes L, Willie B (2007) The enhancement of bone regeneration by ultrasound. Prog Biophys Mol Biol 93: 384–398

Costa P, Almeida FVM, Connelly JT (2012) Biophysical signals controlling cell fate decisions: how do stem cells really feel? Int J Biochem Cell Biol 44: 2233–2237

Cui JH, Park K, Park SR, Min BH (2006) Effects of low-intensity ultrasound on chondrogenic differentiation of mesenchymal stem cells embedded in polyglycolic acid: an in vivo study. Tissue Eng 12:75–82

Cui JH, Park SR, Park S, Choi BH, Min BH (2007) Preconditioning of mesenchymal stem cells with low-intensity ultrasound for cartilage formation in vivo. Tissue Eng 1:351–360

Da Costa Gómez TM, Radtke CL, Kalscheur VL, Swain CA, Scollay MC, Edwards RB, Santschi EM, Markel MD, Muir P (2004) Effect of focused and radial extracorporeal shock wave therapy on equine bone microdamage. Vet Surg 33:49–55

Dalla-Bona DA, Tanaka E, Oka H, Yamano E, Kawai N, Miyauchi M, Takata T, Tanne K (2006) Effects of ultrasound on cementoblast metabolism in vitro. Ultrasound Med Biol 32:943–948

de Ávila Santana L, Alves JM, Andrade TA, Kajiwara JK, Garcia SB, Gomes FG, Frade MA (2013) Clinical and immunohistopathological aspects of venous ulcers treatment by Low-Intensity Pulsed Ultrasound (LIPUS). Ultrasonics 53:870–879

del Rio A, Perez-Jimenez R, Liu R, Roca-Cusachs P, Fernandez JM, Sheetz MP (2009) Stretching single talin rod molecules activates vinculin binding. Science 323:638–641

Delius M, Jordan M, Liebich HG, Brendel W (1990) Biological effects of shock waves: effect of shock waves on the liver and gallbladder wall of dogs--administration rate dependence. Ultrasound Med Biol 16:459–466

den Dekker E, Molin DG, Breikers G, van Oerle R, Akkerman JW, van Eys GJ, Heemskerk JW (2001) Expression of transient receptor potential mRNA isoforms and Ca(2+) influx in differentiating human stem cells and platelets. Biochim Biophys Acta 1539:243–255

Ding X, Lin SC, Kiraly B, Yue H, Li S, Chiang IK, Benkovic SJ, Huang TJ (2012) On-chip manipulation of single microparticles, cells, and organisms using surface acoustic waves. Proc Natl Acad Sci USA 109:11105–11109

Doan N, Reher P, Meghji S, Harris M (1999) In vitro effects of therapeutic ultrasound on cell proliferation, protein synthesis, and cytokine production by human fibroblasts, osteoblasts, and monocytes. J Oral Maxillofac Surg 57:409–419

D'Souza SJ, Pajak A, Balazso K, Dagnino L (2001) Ca2+ and BMP-6 signaling regulate E2F during epidermal keratinocyte differentiation. J Biol Chem 276: 23531–23538

Duck FA (2011) A new definition for acoustic dose. J Phys Conf Ser 279:012006

Ducy P, Starbuck M, Priemel M, Shen J, Pinero G, Geoffroy V, Amling M, Karsenty G (1999) A Cbfa1-dependent genetic pathway controls bone formation beyond embryonic development. Genes Dev 13: 1025–1036

Dupont S, Morsut L, Aragona M, Enzo E, Giulitti S, Cordenonsi M, Zanonato F, Le Digabel J, Forcato M, Bicciato S, Elvassore N, Piccolo S (2011) Role of YAP/TAZ in mechanotransduction. Nature 474:179–183

Ebisawa K, Hata K, Okada K, Kimata K, Ueda M, Torii S, Watanabe H (2004) Ultrasound enhances transforming growth factor beta-mediated chondrocyte differentiation of human mesenchymal stem cells. Tissue Eng 10:921–929

Echtermeyer F, Streit M, Wilcox-Adelman S, Saoncella S, Denhez F, Detmar M, Goetinck P (2001) Delayed wound repair and impaired angiogenesis in mice lacking syndecan-4. J Clin Invest 107:R9–R14

El-Bialy T, Alhadlaq A, Wong B, Kucharski C (2014) Ultrasound effect on neural differentiation of gingival stem/progenitor cells. Ann Biomed Eng 42:1406–1412

Elsner HI, Lindblad EB (1989) Ultrasonic degradation of DNA. DNA 8:697–701

Fabiilli ML, Wilson CG, Padilla F, Martin-Saavedra FM, Fowlkes JB, Franceschi RT (2013) Acoustic droplet-hydrogel composites for spatial and temporal control of growth factor delivery and scaffold stiffness. Acta Biomater 9:7399–7409

Ferrara N, Gerber HP, LeCouter J (2003) The biology of VEGF and its receptors. Nat Med 9:669–676

Foldager CB, Kearney C, Spector M (2012) Clinical application of extracorporeal shock wave therapy in orthopedics: focused versus unfocused shock waves. Ultrasound Med Biol 38:1673–1680

Fox SW, Chambers TJ, Chow JW (1996) Nitric oxide is an early mediator of the increase in bone formation by mechanical stimulation. Am J Physiol 270: E955–E960

Fu N, Yang X, Ba K, Fu Y, Wei X, Yue Y, Li G, Yao Y, Chen J, Liang C, Ge Y, Lin Y (2013) Low-intensity pulsed ultrasound induced enhanced adipogenesis of adipose-derived stem cells. Cell Prolif 46:312–319

Fung CH, Cheung WH, Pounder NM, de Ana FJ, Harrison A, Leung KS (2012) Effects of different therapeutic ultrasound intensities on fracture healing in rats. Ultrasound Med Biol 38:745–752

Fung CH, Cheung WH, Pounder NM, Harrison A, Leung KS (2014) Osteocytes exposed to far field of therapeutic ultrasound promotes osteogenic cellular activities in pre-osteoblasts through soluble factors. Ultrasonics 54(5):1358–1365.

Gerstenfeld LC, Cullinane DM, Barnes GL, Graves DT, Einhorn TA (2003) Fracture healing as a post-natal developmental process: molecular, spatial, and temporal aspects of its regulation. J Cell Biochem 88:873–884

Gerstenfeld LC, Alkhiary YM, Krall EA, Nicholls FH, Stapleton SN, Fitch JL, Bauer M, Kayal R, Graves DT, Jepsen KJ, Einhorn TA (2006) Three-dimensional reconstruction of fracture callus morphogenesis. J Histochem Cytochem 54:1215–1228

Gleizal A, Li S, Pialat JB, Beziat JL (2006) Transcriptional expression of calvarial bone after treatment with low-intensity ultrasound: an in vitro study. Ultrasound Med Biol 32:1569–1574

Globus RK, Patterson-Buckendahl P, Gospodarowicz D (1988) Regulation of bovine bone cell proliferation by fibroblast growth factor and transforming growth factor beta. Endocrinology 123:98–105

Griffin XL, Parsons N, Costa ML, Metcalfe D (2014) Ultrasound and shockwave therapy for acute fractures in adults. Cochrane Database Syst Rev 6: CD008579

Halder G, Dupont S, Piccolo S (2012) Transduction of mechanical and cytoskeletal cues by YAP and TAZ. Nat Rev Mol Cell Biol 13:591–600

Hannemann PF, Mommers EH, Schots JP, Brink PR, Poeze M (2014) The effects of low-intensity pulsed ultrasound and pulsed electromagnetic fields bone growth stimulation in acute fractures: a systematic review and meta-analysis of randomized controlled trials. Arch Orthop Trauma Surg 134:1093–1106

Harle J, Mayia F, Olsen I, Salih V (2005) Effects of ultrasound on transforming growth factor-beta genes in bone cells. Eur Cell Mater 10:70–76

Hasegawa T, Miwa M, Sakai Y, Niikura T, Kurosaka M, Komori T (2009) Osteogenic activity of human fracture haematoma-derived progenitor cells is stimulated by low-intensity pulsed ultrasound in vitro. The Journal of bone and joint surgery. British volume 91(2):264–270.

Hassan MA, Ahmed IS, Campbell P, Kondo T (2012) Enhanced gene transfection using calcium phosphate co-precipitates and low-intensity pulsed ultrasound. Eur J Pharm Sci 47:768–773

Hawley SA, Macleod RM, Dunn F (1963) Degradation of DNA by intense, noncavitating ultrasound. J Acoust Soc Am 35:1285

Hayek A, Culler FL, Beattie GM, Lopez AD, Cuevas P, Baird A (1987) An in vivo model for study of the angiogenic effects of basic fibroblast growth factor. Biochem Biophys Res Commun 147:876–880

Hayton MJ, Dillon JP, Glynn D, Curran JM, Gallagher JA, Buckley KA (2005) Involvement of adenosine 5'-triphosphate in ultrasound-induced fracture repair. Ultrasound Med Biol 31:1131–1138

Heckman JD, Sarasohn-Kahn J (1997) The economics of treating tibia fractures. The cost of delayed unions. Bull Hosp Jt Dis 56:63–72

Heckman JD, Ryaby JP, McCabe J, Frey JJ, Kilcoyne RF (1994) Acceleration of tibial fracture-healing by non-invasive, low-intensity pulsed ultrasound. J Bone Joint Surg 76:26–34

Heldin CH, Miyazono K, Ten Dijke P (1997) TGF-beta signalling from cell membrane to nucleus through SMAD proteins. Nature 390:465–471

Hensel K, Mienkina MP, Schmitz G (2011) Analysis of ultrasound fields in cell culture wells for in vitro ultrasound therapy experiments. Ultrasound Med Biol 37:2105–2115

Hollister SJ (2009) Scaffold design and manufacturing: from concept to clinic. Adv Mater 21:3330–3342

Hou CH, Lin J, Huang SC, Hou SM, Tang CH (2009) Ultrasound stimulates NF-kappaB activation and iNOS expression via the Ras/Raf/MEK/ERK signaling pathway in cultured preosteoblasts. J Cell Physiol 220:196–203

Hsu H, Lacey DL, Dunstan CR, Solovyev I, Colombero A, Timms E, Tan HL, Elliott G, Kelley MJ, Wang L, Xia XZ, Elliott R, Chiu L, Black T, Scully S, Capparelli C, Morony S, Shimamoto G, Bass MB, Boyle WJ (1999) Tumor necrosis factor receptor family member RANK mediates osteoclast differentiation and activation induced by osteoprotegerin ligand. Proc Natl Acad Sci USA 96:3540–3545

Hu B, Zhang Y, Zhou J, Li J, Deng F, Wang Z, Song J (2014) Low-intensity pulsed ultrasound stimulation facilitates osteogenic differentiation of human periodontal ligament cells. PLoS One 9:e95168

Humphrey VF (2007) Ultrasound and matter--physical interactions. Prog Biophys Mol Biol 93:195–211

Ikeda K, Takayama T, Suzuki N, Shimada K, Otsuka K, Ito K (2006) Effects of low-intensity pulsed ultrasound on the differentiation of C2C12 cells. Life Sci 79:1936–1943

Imai Y, Hasegawa T, Takeda D, Akashi M, Lee SY, Niikura T, Shibuya Y, Kurosaka M, Komori T (2014) The osteogenic activity of human mandibular fracture haematoma-derived cells is stimulated by low-intensity pulsed ultrasound in vitro. Int J Oral Maxillofac Surg 43:367–372

Ingber D (1991) Integrins as mechanochemical transducers. Curr Opin Cell Biol 3:841–848

Ishiduka Y, Mochizuki R, Yanai K, Takatsuka M, Nonomura T, Niida S, Horiguchi H, Maeda N, Fukamizu A (1999) Induction of hydroxyapatite resorptive activity in bone marrow cell populations resistant to bafilomycin A1 by a factor with restricted expression to bone and brain, neurochondrin. Biochim Biophys Acta 1450:92–98

Ito M, Azuma Y, Ohta T, Komoriya K (2000) Effects of ultrasound and 1,25-dihydroxyvitamin D3 on growth factor secretion in co-cultures of osteoblasts and endothelial cells. Ultrasound Med Biol 26:161–166

Iwabuchi S, Ito M, Hata J, Chikanishi T, Azuma Y, Haro H (2005) In vitro evaluation of low-intensity pulsed ultrasound in herniated disc resorption. Biomaterials 26:7104–7114

Iwabuchi S, Ito M, Chikanishi T, Azuma Y, Haro H (2008) Role of the tumor necrosis factor-alpha, cyclooxygenase-2, prostaglandin E2, and effect of low-intensity pulsed ultrasound in an in vitro herniated disc resorption model. J Orthop Res 26:1274–1278

Iwabuchi Y, Tanimoto K, Tanne Y, Inubushi T, Kamiya T, Kunimatsu R, Hirose N, Mitsuyoshi T, Su S, Tanake E, Tanne K (2014) Effects of low-intensity pulsed ultrasound on the expression of cyclooxygenase-2 in mandibular condylar chondrocytes. J Oral Facial Pain Headache 28:261–268

Jang KW, Ding L, Seol D, Lim T, Buckwalter JA, Martin JA (2014) Low-intensity pulsed ultrasound promotes chondrogenic progenitor cell migration via focal adhesion kinase pathway. Ultrasound Med Biol 40:1177–1186

Johns LD (2002) Nonthermal effects of therapeutic ultrasound: the frequency resonance hypothesis. J Athl Train 37:293–299

Khan Y, Laurencin CT (2008) Fracture repair with ultrasound: clinical and cell-based evaluation. J Bone Joint Surg 90:138–144

Kilian O, Flesch I, Wenisch S, Taborski B, Jork A, Schnettler R, Jonuleit T (2004) Effects of platelet growth factors on human mesenchymal stem cells and human endothelial cells in vitro. Eur J Med Res 9:337–344

Kim SJ, Kim SY, Kwon CH, Kim YK (2007) Differential effect of FGF and PDGF on cell proliferation and migration in osteoblastic cells. Growth Factors 25:77–86

Kim K, Jeong CG, Hollister SJ (2008) Non-invasive monitoring of tissue scaffold degradation using ultrasound elasticity imaging. Acta Biomater 4:783–790

Kim TJ, Seong J, Ouyang M, Sun J, Lu S, Hong JP, Wang N, Wang Y (2009) Substrate rigidity regulates Ca2+ oscillation via RhoA pathway in stem cells. J Cell Physiol 218:285–293

Kirstein M, Baglioni C (1988) Tumor necrosis factor stimulates proliferation of human osteosarcoma cells and accumulation of c-myc messenger RNA. J Cell Physiol 134:479–484

Klionsky DJ, Abdalla FC, Abeliovich H et al (2012) Guidelines for the use and interpretation of assays for monitoring autophagy. Autophagy 8:445–544

Kobayashi T, Sokabe M (2010) Sensing substrate rigidity by mechanosensitive ion channels with stress fibers and focal adhesions. Curr Opin Cell Biol 22:669–676

Kobayashi Y, Sakai D, Iwashina S, Iwabuchi S, Mochida J (2009) Low-intensity pulsed ultrasound stimulates cell proliferation, proteoglycan synthesis and expression of growth factor-related genes in human nucleus pulposus cell line. Eur Cell Mater 17:15–22

Koch AE, Polverini PJ, Kunkel SL, Harlow LA, DiPietro LA, Elner VM, Elner SG, Strieter RM (1992) Interleukin-8 as a macrophage-derived mediator of angiogenesis. Science 258:1798–1801

Kokubu T, Matsui N, Fujioka H, Tsunoda M, Mizuno K (1999) Low intensity pulsed ultrasound exposure increases prostaglandin E2 production via the induction of cyclooxygenase-2 mRNA in mouse osteoblasts. Biochem Biophys Res Commun 256:284–287

Komori T, Yagi H, Nomura S, Yamaguchi A, Sasaki K, Deguchi K, Shimizu Y, Bronson RT, Gao YH, Inada M, Sato M, Okamoto R, Kitamura Y, Yoshiki S, Kishimoto T (1997) Targeted disruption of Cbfa1 results in a complete lack of bone formation owing to maturational arrest of osteoblasts. Cell 89:755–764

Kopf J, Petersen A, Duda GN, Knaus P (2012) BMP2 and mechanical loading cooperatively regulate immediate

early signalling events in the BMP pathway. BMC Biol 10:37

Krasovitski B, Frenkel V, Shoham S, Kimmel E (2011) Intramembrane cavitation as a unifying mechanism for ultrasound-induced bioeffects. Proc Natl Acad Sci USA 108:3258–3263

Kristiansen TK, Ryaby JP, McCabe J, Frey JJ, Roe LR (1997) Accelerated healing of distal radial fractures with the use of specific, low-intensity ultrasound. A multicenter, prospective, randomized, double-blind, placebo-controlled study. J Bone Joint Surg 79:961–973

Kruse DE, Mackanos MA, O'Connell-Rodwell CE, Contag CH, Ferrara KW (2008) Short-duration-focused ultrasound stimulation of Hsp70 expression in vivo. Phys Med Biol 53:3641–3660

Kumagai K, Takeuchi R, Ishikawa H, Yamaguchi Y, Fujisawa T, Kuniya T, Takagawa S, Muschler GF, Saito T (2012) Low-intensity pulsed ultrasound accelerates fracture healing by stimulation of recruitment of both local and circulating osteogenic progenitors. J Orthop Res 30:1516–1521

Kuo JC, Han X, Hsiao CT, Yates JR 3rd, Waterman CM (2011) Analysis of the myosin-II-responsive focal adhesion proteome reveals a role for β-Pix in negative regulation of focal adhesion maturation. Nat Cell Biol 13:383–393

Kusano K, Miyaura C, Inada M, Tamura T, Ito A, Nagase H, Kamoi K, Suda T (1998) Regulation of matrix metalloproteinases (MMP-2, -3, -9, and -13) by interleukin-1 and interleukin-6 in mouse calvaria: association of MMP induction with bone resorption. Endocrinology 139:1338–1345

Kusuyama J, Bandow K, Shamoto M, Kakimoto K, Ohnishi T, Matsuguchi T (2014) Low Intensity Pulsed Ultrasound (LIPUS) influences the multilineage differentiation of mesenchymal stem and progenitor cell lines through ROCK-Cot/Tpl2-MEK- signaling pathway. J Biol Chem 289:10330–10344

Lacey DL, Timms E, Tan HL et al (1998) Osteoprotegerin ligand is a cytokine that regulates osteoclast differentiation and activation. Cell 93:165–176

Lai CH, Chen SC, Chiu LH, Yang CB, Tsai YH, Zuo CS, Chang WH, Lai WF (2010) Effects of low-intensity pulsed ultrasound, dexamethasone/TGF-beta1 and/or BMP-2 on the transcriptional expression of genes in human mesenchymal stem cells: chondrogenic vs. osteogenic differentiation. Ultrasound Med Biol 36:1022–1033

Lee HJ, Choi BH, Min BH, Son YS, Park SR (2006) Low-intensity ultrasound stimulation enhances chondrogenic differentiation in alginate culture of mesenchymal stem cells. Artificial organs 30(9):707–715.

Lee SY, Koh A, Niikura T, Oe K, Koga T (2013) Low-intensity pulsed ultrasound enhances BMP-7-induced osteogenic differentiation of human fracture hematoma-derived progenitor cells in vitro. J Orthop Trauma 27:29–33

Leskinen JJ, Hynynen K (2012) Study of factors affecting the magnitude and nature of ultrasound exposure with in vitro set-ups. Ultrasound Med Biol 38:777–794

Li JG, Chang WH, Lin JC, Sun JS (2002) Optimum intensities of ultrasound for PGE(2) secretion and growth of osteoblasts. Ultrasound Med Biol 28:683–690

Li A, Dubey S, Varney ML, Dave BJ, Singh RK (2003a) IL-8 directly enhanced endothelial cell survival, proliferation, and matrix metalloproteinases production and regulated angiogenesis. J Immunol 170:3369–3376

Li JK, Chang WH, Lin JC, Ruaan RC, Liu HC, Sun JS (2003b) Cytokine release from osteoblasts in response to ultrasound stimulation. Biomaterials 24:2379–2385

Li D, Tang T, Lu J, Dai K (2009) Effects of flow shear stress and mass transport on the construction of a large-scale tissue-engineered bone in a perfusion bioreactor. Tissue Eng 15:2773–2783

Liedert A, Kaspar D, Blakytny R, Claes L, Ignatius A (2006) Signal transduction pathways involved in mechanotransduction in bone cells. Biochem Biophys Res Commun 349:1–5

Louw TM, Budhiraja G, Viljoen HJ, Subramanian A (2013) Mechanotransduction of ultrasound is frequency dependent below the cavitation threshold. Ultrasound Med Biol 39:1303–1319

Lu H, Qin L, Lee K, Cheung W, Chan K, Leung K (2009) Identification of genes responsive to low-intensity pulsed ultrasound stimulations. Biochem Biophys Res Commun 378:569–573

Lv Y, Zhao P, Chen G, Sha Y, Yang L (2013) Effects of low-intensity pulsed ultrasound on cell viability, proliferation and neural differentiation of induced pluripotent stem cells-derived neural crest stem cells. Biotechnol Lett 35:2201–2212

Ma HZ, Zeng BF, Li XL (2007) Upregulation of VEGF in subchondral bone of necrotic femoral heads in rabbits with use of extracorporeal shock waves. Calcif Tissue Int 81:124–131

Machado CB, de Albuquerque Pereira WC, Talmant M, Padilla F, Laugier P (2010) Computational evaluation of the compositional factors in fracture healing affecting ultrasound axial transmission measurements. Ultrasound Med Biol 36:1314–1326

Machado CB, Pereira WC, Granke M, Talmant M, Padilla F, Laugier P (2011) Experimental and simulation results on the effect of cortical bone mineralization in ultrasound axial transmission measurements: a model for fracture healing ultrasound monitoring. Bone 48:1202–1209

Maddi A, Hai H, Ong ST, Sharp L, Harris M, Meghji S (2006) Long wave ultrasound may enhance bone regeneration by altering OPG/RANKL ratio in human osteoblast-like cells. Bone 39:283–288

Mahoney CM, Morgan MR, Harrison A, Humphries MJ, Bass MD (2009) Therapeutic ultrasound bypasses canonical syndecan-4 signaling to activate rac1. J Biol Chem 284:8898–8909

Malizos KN, Hantes ME, Protopappas V, Papachristos A (2006) Low-intensity pulsed ultrasound for bone healing: an overview. Injury 37:S56–S62

Malone AM, Anderson CT, Tummala P, Kwon RY, Johnston TR, Stearns T, Jacobs CR (2007) Primary cilia mediate mechanosensing in bone cells by a calcium-independent mechanism. Proc Natl Acad Sci USA 104:13325–13330

Martinez de Albornoz P, Khanna A, Longo UG, Forriol F, Maffulli N (2011) The evidence of low-intensity pulsed ultrasound for in vitro, animal and human fracture healing. Br Med Bull 100:39–57

Marvel S, Okrasinski S, Bernacki SH, Loboa E, Dayton PA (2010) The development and validation of a LIPUS system with preliminary observations of ultrasonic effects on human adult stem cells. IEEE Trans Ultrason Ferroelectr Freq Control 57:1977–1984

Mather ML, Crowe JA, Morgan SP, White LJ, Kalashikov AN, Ivchenko VG, Howdle SM, Shakesheff KM (2008) Ultrasonic monitoring of foamed polymeric tissue scaffold fabrication. J Mater Sci 19: 3071–3080

Mayr E, Frankel V, Rüter A (2000) Ultrasound – an alternative healing method for nonunions? Arch Orthop Trauma Surg 120(1-2):1-8.

Mehier-Humbert S, Yan F, Frinking P, Scheinder M, Ruy RH, Bettinger T (2007) Ultrasound-mediated gene delivery: influence of contrast agent on transfection. Bioconjug Chem 18:652–662

Mizrahi N, Zhou EH, Lenormand G, Krishnan R, Weihs D, Butler JP, Weitz DA, Fredberg JJ, Kimmel E (2012) Low intensity ultrasound perturbs cytoskeleton dynamics. Soft Matter 8:2438–2443

Mont MA, Jones LC, Seyler TM, Marulanda GA, Saleh KJ, Delanois RE (2007) New treatment approaches for osteonecrosis of the femoral head: an overview. Instr Course Lect 56:197–212

Montesano R, Vassalli JD, Baird A, Guillemin R, Orci L (1986) Basic fibroblast growth factor induces angiogenesis in vitro. Proc Natl Acad Sci USA 83:7297–7301

Morris HL, Reed CI, Haycock JW, Reilly GC (2010) Mechanisms of fluid-flow-induced matrix production in bone tissue engineering. Proc Inst Mech Eng H 224:1509–1521

Morse R, La LD, Magin RL, Dunn F (1999) Ultrasound interaction with large unilamellar vesicles at the phospholipid phase transition: perturbation by phospholipid side chain substitution with deuterium. Chem Phys Lipids 103:1–10

Moustakas A, Heldin CH (2005) Non-Smad TGF-beta signals. J Cell Sci 118:3573–3584

Mukai S, Ito H, Nakagawa Y, Akiyama H, Miyamoto M, Nakamura T (2005) Transforming growth factor-beta1 mediates the effects of low-intensity pulsed ultrasound in chondrocytes. Ultrasound Med Biol 31: 1713–1721

Nakamura T, Fujihara S, Yamamoto-Nagata K, Katsura T, Inubushi T, Tanaka E (2011) Low-intensity pulsed ultrasound reduces the inflammatory activity of synovitis. Ann Biomed Eng 39:2964–2971

Nakao J, Fujii Y, Kusuyama J, Bandow K, Kakimoto K, Ohnishi T, Matsuguchi T (2014) Low-intensity pulsed ultrasound (LIPUS) inhibits LPS-induced inflammatory responses of osteoblasts through TLR4-MyD88 dissociation. Bone 58:17–25

Nakashima K, Zhou X, Kunkel G, Zhang Z, Deng JM, Behringer RR, de Crombrugghe B (2002) The novel zinc finger-containing transcription factor osterix is required for osteoblast differentiation and bone formation. Cell 108:17–29

Narasaki K, Shimizu H, Beppu M, Aoki H, Takagi M, Takashi M (2003) Effect of extracorporeal shock waves on callus formation during bone lengthening. J Orthop Sci 8:474–481

Naruse K, Mikuni-Takagaki Y, Azuma Y, Ito M, Oota T, Kameyama K, Itoman M (2000) Anabolic response of mouse bone-marrow-derived stromal cell clone ST2 cells to low-intensity pulsed ultrasound. Biochem Biophys Res Commun 268:216–220

Naruse K, Miyauchi A, Itoman M, Mikuni-Takagaki Y (2003) Distinct anabolic response of osteoblast to low-intensity pulsed ultrasound. J Bone Miner Res 18:360–369

Nefussi JR, Baron R (1985) PGE2 stimulates both resorption and formation of bone in vitro: differential responses of the periosteum and the endosteum in fetal rat long bone cultures. Anat Rec 211:9–16

Nolte PA, van der Krans A, Patka P, Janssen M, Ryaby JP, Albers GH (2001) Low-intensity pulsed ultrasound in the treatment of nonunions. J Trauma 51:693–702; discussion 702–703

Nowicki A, Kowalewski T, Secomski W, Wojcik J (1998) Estimation of acoustical streaming: theoretical model, Doppler measurements and optical visualisation. Eur J Ultrasound 7:73–81

O'Brien WD (2007) Ultrasound-biophysics mechanisms. Prog Biophys Mol Biol 93:212–255

Or M, Kimmel E (2009) Modeling linear vibration of cell nucleus in low intensity ultrasound field. Ultrasound Med Biol 35:1015–1025

Otani K, Yamahara K, Ohnishi S, Obata H, Kitamura S, Nagaya N (2009) Nonviral delivery of siRNA into mesenchymal stem cells by a combination of ultrasound and microbubbles. J Control Release 133:146–153

Otto F, Thornell AP, Crompton T, Denzel A, Gilmour KC, Rosewell IR, Stamp GW, Beddington RS, Mundlos S, Olsen BR, Selby PB, Owen MJ (1997) Cbfa1, a candidate gene for cleidocranial dysplasia syndrome, is essential for osteoblast differentiation and bone development. Cell 89:765–771

Padilla F, Cleveland R (2009) Numerical simulation of shock wave propagation in fractured cortical bone. AIP Conf Proc 1113:185–189

Padilla F, Puts R, Vico L, Raum K (2014) Stimulation of bone repair with ultrasound: a review of the possible mechanic effects. Ultrasonics 54(5):1125-45. doi: 10.1016/j.ultras.2014.01.004.

Park H, Yip MC, Chertok B, Kost J, Kobler JB, Langer R, Zeitels SM (2010) Indirect low-intensity ultrasonic stimulation for tissue engineering. J Tissue Eng 2010:973530

Parker NG, Mather ML, Morgan SP, Povey MJ (2011) Longitudinal acoustic properties of poly(lactic acid) and poly(lactic-co-glycolic acid). Biomed Mater 5:055004

Parvizi J, Parpura V, Greenleaf JF, Bolander ME (2002) Calcium signaling is required for ultrasound-

stimulated aggrecan synthesis by rat chondrocytes. J Orthop Res 20:51–57
Peterson RV, Pitt WG (2000) The effect of frequency and power density on the ultrasonically-enhanced killing of biofilm-sequestered Escherichia coli. Colloids Surf B Biointerfaces 17:219–227
Pinkerton J (1949) The absorption of ultrasonic waves in liquids and its relation to molecular constitution. Proc Phys Soc B 62:129
Pisanti P, Yeatts AB, Cardea S, Fisher JP, Reverchon E (2012) Tubular perfusion system culture of human mesenchymal stem cells on poly-L-lactic acid scaffolds produced using a supercritical carbon dioxide-assisted process. J Biomed Mater Res A 100:2563–2572
Pitt WG, Ross SA (2003) Ultrasound increases the rate of bacterial cell growth. Biotechnol Prog 19: 1038–1044
Pittenger MF, Mackay AM, Beck SC, Jaiswal RK, Douglas R, Mosca JD, Moorman MA, Simonetti DW, Craig S, Marshak DR (1999) Multilineage potential of adult human mesenchymal stem cells. Science 284: 143–147
Potier E, Ferreira E, Andriamanalijaona R, Pujol JP, Oudina K, Logeart-Avramoglou D, Petite H (2007) Hypoxia affects mesenchymal stromal cell osteogenic differentiation and angiogenic factor expression. Bone 40:1078–1087
Potsika VT, Grivas KN, Protopappas VC, Vavva MG, Raum K, Rohrbach D, Polyzos D, Fotiadis DJ (2013) Application of an effective medium theory for modeling ultrasound wave propagation in healing long bones. Ultrasonics 54:1219–1230
Pounder NM, Harrison AJ (2008) Low intensity pulsed ultrasound for fracture healing: a review of the clinical evidence and the associated biological mechanism of action. Ultrasonics 48:330–338
Protopappas VC, Vavva MG, Fotiadis DI, Malizos KN (2008) Ultrasonic monitoring of bone fracture healing. IEEE Trans Ultrason Ferroelectr Freq Control 55:1243–1255
Radomsky ML, Thompson AY, Spiro RC, Poser JW (1998) Potential role of fibroblast growth factor in enhancement of fracture healing. Clin Orthop Relat Res 355(Suppl):S283–S293
Rassweiler JJ, Knoll T, Köhrmann KU, McAteer JA, Lingeman JE, Cleveland RO, Bailey MR, Chaussy C (2011) Shock wave technology and application: an update. Eur Urol 59:784–796
Reher P, Elbeshir el-NI, Harvey W, Meghji S, Harris M (1997) The stimulation of bone formation in vitro by therapeutic ultrasound. Ultrasound Med Biol 23:1251–1258
Reher P, Doan N, Bradnock B, Meghji S, Harris M (1998) Therapeutic ultrasound for osteoradionecrosis: an in vitro comparison between 1 MHz and 45 kHz machines. Eur J Cancer 34:1962–1968
Reher P, Harris M, Whiteman M, Hai HK, Meghji S (2002) Ultrasound stimulates nitric oxide and prostaglandin E2 production by human osteoblasts. Bone 31:236–241
Ren L, Yang Z, Song J, Wang Z, Deng F, Li W (2013) Involvement of p38 MAPK pathway in low intensity pulsed ultrasound induced osteogenic differentiation of human periodontal ligament cells. Ultrasonics 53:686–690
Ricardo M (2006) The effect of ultrasound on the healing of muscle-pediculated bone graft in scaphoid non-union. Int Orthop 30:123–127
Rohrbach D, Preininger B, Hesse B, Gerigk H, Perka C, Raum K (2013) The early phases of bone healing can be differentiated in a rat osteotomy model by focused transverse-transmission ultrasound. Ultrasound Med Biol 39:1642–1653
Romano CL, Romano D, Logoluso N (2009) Low-intensity pulsed ultrasound for the treatment of bone delayed union or nonunion: a review. Ultrasound Med Biol 35:529–536
Roper J, Harrison A, Bass MD (2012) Induction of adhesion-dependent signals using low-intensity ultrasound. J Vis Exp 63:e4024
Ruschke K, Hiepen C, Becker J, Knaus P (2012) BMPs are mediators in tissue crosstalk of the regenerating musculoskeletal system. Cell Tissue Res 347: 521–544
Ryoo HM, Hoffmann HM, Beumer T, Frenkel B, Towler DA, Stein GS, Stein JL, van Wijnen AJ, Lian JB (1997) Stage-specific expression of Dlx-5 during osteoblast differentiation: involvement in regulation of osteocalcin gene expression. Mol Endocrinol 11:1681–1694
Sant'Anna EF, Leven RM, Virdi AS, Sumner DR (2005) Effect of low intensity pulsed ultrasound and BMP-2 on rat bone marrow stromal cell gene expression. J Orthop Res 23:646–652
Sarvazyan AP (1991) Ultrasonic velocimetry of biological compounds. Ann Rev Biophys Biophys Chem 20: 321–342
Sarvazyan AP, Rudenko OV, Nyborg WL (2010) Biomedical applications of radiation force of ultrasound: historical roots and physical basis. Ultrasound Med Biol 36:1379–1394
Sato M, Nagata K, Kuroda S, Horiuchi S, Nakamura T, Karima M, Inubushi T, Tanaka E (2014) Low-intensity pulsed ultrasound activates integrin-mediated mechanotransduction pathway in synovial cells. Ann Biomed Eng 42:2156–2163
Schiller HB, Friedel CC, Boulegue C, Fässler R (2011) Quantitative proteomics of the integrin adhesome show a myosin II-dependent recruitment of LIM domain proteins. EMBO Rep 12:259–266
Schofer MD, Block JE, Aigner J, Schmelz A (2010) Improved healing response in delayed unions of the tibia with low-intensity pulsed ultrasound: results of a randomized sham-controlled trial. BMC Musculoskelet Disord 11:229
Schumann D, Kujat R, Zellner J, Angele MK, Nerlich M, Mayr E, Angele P (2006) Treatment of human mesenchymal stem cells with pulsed low intensity ultrasound enhances the chondrogenic phenotype in vitro. Biorheology 43:431–443

Sena K, Leven RM, Mazhar K, Sumner DR, Virdi AS (2005) Early gene response to low-intensity pulsed ultrasound in rat osteoblastic cells. Ultrasound Med Biol 31:703–708

Sena K, Angle SR, Kanaji A, Aher C, Karwo DG, Sumner DR, Virdi AS (2011) Low-intensity pulsed ultrasound (LIPUS) and cell-to-cell communication in bone marrow stromal cells. Ultrasonics 51:639–644

Sharili AS, Connelly JT (2014) Nucleocytoplasmic shuttling: a common theme in mechanotransduction. Biochem Soc Trans 42:645–649

Shen B, Wei A, Whittaker S, Williams LA, Tao H, Ma DD, Diwan AD (2010) The role of BMP-7 in chondrogenic and osteogenic differentiation of human bone marrow multipotent mesenchymal stromal cells in vitro. J Cell Biochem 109:406–416

Sheyn D, Kimelman-Bleich N, Pelled G, Zilberman Y, Gazit D, Gazit Z (2008) Ultrasound-based nonviral gene delivery induces bone formation in vivo. Gene Ther 15:257–266

Siggelkow H, Niedhart C, Kurre W, Ihbe A, Schulz A, Atkinson MJ, Hüfner M (1998) In vitro differentiation potential of a new human osteosarcoma cell line (HOS 58). Differentiation 63:81–91

Stein GS, Lian JB, Stein JL, Van Wijnen AJ, Montecino M (1996) Transcriptional control of osteoblast growth and differentiation. Physiol Rev 76:593–629

Street J, Bao M, deGuzman L, Bunting S, Peale FV Jr, Ferrara N, Steinmetz H, Hoeffel J, Cleland JL, Daugherty A, van Bruggen N, Redmond HP, Carano RA, Filvaroff EH (2002) Vascular endothelial growth factor stimulates bone repair by promoting angiogenesis and bone turnover. Proc Natl Acad Sci USA 99:9656–9661

Sun JS, Hong RC, Chang WH, Chen LT, Lin FH, Liu HC (2001) In vitro effects of low-intensity ultrasound stimulation on the bone cells. J Biomed Mater Res 57:449–456

Sun S, Liu Y, Lipsky S, Cho M (2007) Physical manipulation of calcium oscillations facilitates osteodifferentiation of human mesenchymal stem cells. FASEB J 21: 1472–1480

Suva LJ, Towler DA, Harada S, Gaub MP, Rodan GA (2013) Characterization of retinoic acid- and cell-dependent sequences which regulate zif268 gene expression in osteoblastic cells. Mol Endocrinol 8:1507–1520

Suzuki A, Takayama T, Suzuki N, Kojima T, Ota N, Asano S, Ito K (2009a) Daily low-intensity pulsed ultrasound stimulates production of bone morphogenetic protein in ROS 17/2.8 cells. J Oral Sci 51:29–36

Suzuki A, Takayama T, Suzuki N, Sato M, Fukuda T, Ito K (2009b) Daily low-intensity pulsed ultrasound-mediated osteogenic differentiation in rat osteoblasts. Acta Biochim Biophys Sin 41:108–115

Takeuchi R, Ryo A, Komitsu N, Mikuni-Takagaki Y, Fukui A, Shiraishi T, Morishita S, Yamazaki Y, Kumagai K, Aoki I, Saito T (2008) Low-intensity pulsed ultrasound activates the phosphatidylinositol 3 kinase/Akt pathway and stimulates the growth of chondrocytes in three-dimensional cultures: a basic science study. Arthritis Res Ther 10:R77

Tang CH, Yang RS, Huang TH, Lu DY, Chuang WJ, Huang TF, Fu WM (2006) Ultrasound stimulates cyclooxygenase-2 expression and increases bone formation through integrin, focal adhesion kinase, phosphatidylinositol 3-kinase, and Akt pathway in osteoblasts. Mol Pharmacol 69:2047–2057

Temiyasathit S, Jacobs CR (2010) Osteocyte primary cilium and its role in bone mechanotransduction. Ann N Y Acad Sci 1192:422–428

Tsai CL, Chang WH, Liu TK (1992) Preliminary studies of duration and intensity of ultrasonic treatments on fracture repair. Chin J Physiol 35:21–26

Uddin SMZ, Qin YX (2013) Enhancement of osteogenic differentiation and proliferation in human mesenchymal stem cells by a modified low intensity ultrasound stimulation under simulated microgravity. PLoS One 8:e73914

Ulbricht A, Höhfeld J (2013) Tension-induced autophagy: may the chaperone be with you. Autophagy 9:920–922

Ulbricht A, Eppler FJ, Tapia VE et al (2013) Cellular mechanotransduction relies on tension-induced and chaperone-assisted autophagy. Curr Biol 23:430–435

Unsworth J, Kaneez S, Harris S, Ridgway J, Fenwick S, Chenery D, Harrison A (2007) Pulsed low intensity ultrasound enhances mineralisation in preosteoblast cells. Ultrasound Med Biol 33:1468–1474

Volkmer E, Drosse I, Otto S, Stangelmayer A, Stengele M, Kallukalam BC, Mutscher W, Schieker M (2008) Hypoxia in static and dynamic 3D culture systems for tissue engineering of bone. Tissue Eng 14:1331–1340

Walters MC 3rd, Roe F, Bugnicourt A, Franklin MJ, Stewart PS (2003) Contributions of antibiotic penetration, oxygen limitation, and low metabolic activity to tolerance of Pseudomonas aeruginosa biofilms to ciprofloxacin and tobramycin. Antimicrob Agents Chemother 47:317–323

Wang SJ, Lewallen DG, Bolander ME, Chao EY, Ilstrup DM, Greenleaf JF (1994) Low intensity ultrasound treatment increases strength in a rat femoral fracture model. J Orthop Res 12:40–47

Wang FS, Wang CJ, Huang HJ, Chung H, Chen RF, Yang KD (2001) Physical shock wave mediates membrane hyperpolarization and Ras activation for osteogenesis in human bone marrow stromal cells. Biochem Biophys Res Commun 287:648–655

Wang CJ, Wang FS, Yang KD, Weng LH, Hsu CC, Huang CS, Yang LC (2003a) Shock wave therapy induces neovascularization at the tendon-bone junction. A study in rabbits. J Orthop Res 21:984–989

Wang FS, Yan KD, Kuo YR, Wang CJ, Sheen-Chen SM, Huang HC, Chen YJ (2003b) Temporal and spatial expression of bone morphogenetic proteins in extracorporeal shock wave-promoted healing of segmental defect. Bone 32:387–396

Wang FS, Kuo YR, Wang CJ, Yang KD, Chang PR, Huang YT, Huang HC, Syn YC, Yang YJ, Chen YJ

(2004) Nitric oxide mediates ultrasound-induced hypoxia-inducible factor-1alpha activation and vascular endothelial growth factor-A expression in human osteoblasts. Bone 35:114–123

Wang CJ, Wang FS, Ko JY, Huang HY, Chen CJ, Sun YC, Yang YJ (2008a) Extracorporeal shockwave therapy shows regeneration in hip necrosis. Rheumatology (Oxford) 47:542–546

Wang L, Qin L, Lu HB, Cheung WH, Yang H, Wong WN, Chan KM, Leung KS (2008b) Extracorporeal shock wave therapy in treatment of delayed bone-tendon healing. Am J Sports Med 36:340–347

Warden SJ, Favaloro JM, Bennell KL, McMeeken JM, Ng KW, Zajac JD, Wark JD (2001) Low-intensity pulsed ultrasound stimulates a bone-forming response in UMR-106 cells. Biochem Biophys Res Commun 286: 443–450

Watabe H, Furuhama T, Tani-Ishii N, Mikuni-Takagaki Y (2011) Mechanotransduction activates $\alpha_5\beta_1$ integrin and PI3K/Akt signaling pathways in mandibular osteoblasts. Exp Cell Res 317:2642–2649

Watanuki M, Kishimoto KN, Kotajima S, Iwabuchi S, Kokubun S (2009) Effect of low-intensity pulsed ultrasound on scaffold-free ectopic bone formation in skeletal muscle. Ups J Med Sci 114:242–248

Weinstein JN, Oster DM, Park JB, Park SH, Leoning S (1988) The effect of the extracorporeal shock wave lithotriptor on the bone-cement interface in dogs. Clin Orthop Relat Res 235:261–267

Welgus HG, Jeffrey JJ, Eisen AZ (1981) Human skin fibroblast collagenase. Assessment of activation energy and deuterium isotope effect with collagenous substrates. J Biol Chem 256:9516–9521

Whitney NP, Lamb AC, Louw TM, Subramanian A (2012) Integrin-mediated mechanotransduction pathway of low-intensity continuous ultrasound in human chondrocytes. Ultrasound Med Biol 38:1734–1743

Williams R, Wright C, Cherin E, Reznik N, Lee M, Gorelikov I, Foster FS, Matsuura N, Burns PN (2013) Characterization of submicron phase-change perfluorocarbon droplets for extravascular ultrasound imaging of cancer. Ultrasound Med Biol 39: 475–489

Wilson CG, Martin-Saavedra FM, Padilla F, Fabiilli ML, Zhang M, Baez AM, Bonkowski CJ, Kripfgans OD, Voellmy R, Vilaboa N, Fowlkes JB, Franceschi RT (2014) Patterning expression of regenerative growth factors using high intensity focused ultrasound. Tissue Eng Part C Methods 20:769–779

Winterroth F, Lee J, Kuo S, Fowlkes JB, Feinberg SE, Hollister SJ, Hollman KW (2011) Acoustic microscopy analyses to determine good vs. failed tissue engineered oral mucosa under normal or thermally stressed culture conditions. Ann Biomed Eng 39:44–52

Yang RS, Lin WL, Chen YZ, Tang CH, Huang TH, Lu BY, Fu WM (2005) Regulation by ultrasound treatment on the integrin expression and differentiation of osteoblasts. Bone 36:276–283

Yip HK, Chang LT, Sun CK, Youssef AA, Sheu JJ, Wang CJ (2008) Shock wave therapy applied to rat bone marrow-derived mononuclear cells enhances formation of cells stained positive for CD31 and vascular endothelial growth factor. Circ J 72:150–156

Yoshie O (2000) Immune chemokines and their receptors: the key elements in the genesis, homeostasis and function of the immune system. Springer Semin Immunopathol 22:371–391

Yue Y, Yang X, Wei X, Chen J, Fu N, Fu Y, Ba K, Li G, Yao Y, Liang C, Zhang J, Cai X, Wang M (2013) Osteogenic differentiation of adipose-derived stem cells prompted by low-intensity pulsed ultrasound. Cell Prolif 46:320–327

Zauhar G, Duck FA, Starritt HC (2006) Comparison of the acoustic streaming in amniotic fluid and water in medical ultrasonic beams. Ultraschall Med 27: 152–158

Zhou S, Schmelz A, Seufferlein T, Li Y, Zhao J, Bachem MG (2004) Molecular mechanisms of low intensity pulsed ultrasound in human skin fibroblasts. J Biol Chem 279:54463–54469

Sonodynamic Therapy: Concept, Mechanism and Application to Cancer Treatment

22

Anthony P. McHale, John F. Callan, Nikolitsa Nomikou, Colin Fowley, and Bridgeen Callan

Abstract

Sonodynamic therapy (SDT) represents an emerging approach that offers the possibility of non-invasively eradicating solid tumors in a site-directed manner. It involves the sensitization of target tissues with a non-toxic sensitizing chemical agent and subsequent exposure of the sensitized tissues to relatively low-intensity ultrasound. Essentially, both aspects (the sensitization and ultrasound exposure) are harmless, and cytotoxic events occur when both are combined. Due to the significant depth that ultrasound penetrates tissue, the approach provides an advantage over similar alternative approaches, such as photodynamic therapy (PDT), in which less penetrating light is employed to provide the cytotoxic effect in sensitized tissues. This suggests that sonodynamic therapy may find wider clinical application, particularly for the non-invasive treatment of less accessible lesions. Early SDT-based approaches employed many of the sensitizers used in PDT, although the manner in which ultrasound activates the sensitizer differs from activation events in PDT. Here we will review the currently accepted mechanisms by which ultrasound activates sensitizers to elicit cytotoxic effects. In addition, we will explore the breath of evidence from *in-vitro* and *in-vivo* SDT-based studies, providing the reader with an insight into the therapeutic potential offered by SDT in the treatment of cancer.

Keywords

Sonodynamic therapy • Ultrasound • Sonosensitizer • Reactive oxygen species • Cancer

A.P. McHale • J.F. Callan (✉) • C. Fowley
B. Callan
School of Pharmacy and Pharmaceutical Sciences,
University of Ulster, Coleraine, Co. Derry
BT2 1SA, UK
e-mail: j.callan@ulster.ac.uk

N. Nomikou
Division of Surgery and Interventional Science,
University College London,
4th Floor, 67-73 Riding House St,
London W1W 7EJ, England, UK

© Springer International Publishing Switzerland 2016

J.-M. Escoffre, A. Bouakaz (eds.), *Therapeutic Ultrasound*, Advances in Experimental Medicine and Biology, Vol. 880, DOI 10.1007/978-3-319-22536-4_22

22.1 Background

22.1.1 Conventional Approaches to Cancer Treatment

Owing to the focal nature of many cancers, the search for therapeutic approaches over the past 100 years has yielded a number of major clinical options. These include direct surgical intervention to remove the lesion(s), an extensive battery of chemotherapeutic regimes, approaches involving the use of radiation to essentially ablate the lesion(s) and combinations thereof. Essentially, those approaches were originally based on the premise that cancer was a relatively homogenous disease, but we now know that this is, unfortunately, far from the truth. Indeed, modern approaches to studying the character of the disease at the molecular genetics and epigenetic levels have demonstrated that, even in a single tumor in an individual, uncontrolled evolution continues, even over extremely short time frames. Additionally, in many cases these changes evolve as a result of selective pressure placed upon target cell populations by the therapeutic options described above (Sciacovelli et al. 2014; Holohan 2014). Although each of the conventional options above have provided very significant benefits to patients over the years, continuing recognition of the limitations pertaining to the existing clinical mainstays of cancer treatment has driven the search for more effective treatment options that offer patients enhanced survival and quality of life. Based on our knowledge of the molecular events that control the various stages of cancer and its progression, efforts have sought to fine-tune chemotherapy-based approaches by identifying more specific and distinguishing features of tumors, and then designing drugs to specifically target them. In doing so, it was suggested that adverse effects associated with the off-target actions of conventional cancer chemotherapy would be ameliorated. This approach has led to the release of well-known biopharmaceuticals, such as bevacizumab (Avastin®) and trastuzumab (Herceptin®) onto the market, and these are currently being exploited together with conventional chemotherapeutics in the treatment of a variety of cancers (Tonder 2014; Fabi 2014). This described approach offers a very brief and limited example of how recognition of the limitations of existing chemotherapy-based approaches could, potentially, be enhanced by the application of modern molecular strategies. Nevertheless, even these highly targeted molecular therapies exhibit off-target effects and can lead to the development of resistance (Mokuyasu 2014; Liu and Kurzrock 2014; Tonder et al. 2014; Fabi et al. 2014). Regarding many of these approaches, it remains clear that the short-term evolutionary adaptive survival capabilities of cancer cells, even within a single lesion, can lead to a failure to completely eradicate the disease. Treatment with chemotherapy or targeted chemotherapy drugs is further complicated by the unique environment presented by solid tumors. In many cases, delivery of chemotherapeutic drugs, or specific targeted agents, to a tumor exploits the vascular system, and yet we know the tumor microvasculature and lymphatics in many solid tumors are atypical. Capillaries are mal-formed with aberrant features such as blind ends or closed loops, and vessels are also extremely leaky (Siemann 2011). These features, together with atypical and dysfunctional lymphatics for efficient tissue drainage, lead to high interstitial fluid pressure within the tumor tissues. This has long been recognized as a significant obstacle for delivery of chemotherapy drugs (Heldin et al. 2004). It would appear therefore that delivery of chemotherapeutic agents via the vasculature to tumors is confounded by attributes uniquely associated with the microarchitecture presented by tumors. Paradoxically, it is one of these very features that is being exploited in the development of alternative targeting strategies for drugs, and this will be addressed further below.

As previously mentioned, cancer is in many cases a focal disease, and direct surgical intervention to remove any identified lesions would seem an obvious therapeutic option. Although surgical intervention will, for the foreseeable future, remain an essential component of cancer treatment when possible, reducing the degree of intervention has always been recognized as beneficial to patients in terms of outcome and quality of life. Indeed, many advances in surgical oncology have basically sought to reduce the invasive

nature of surgical procedures (Bianchi et al. 2014; Tran Cao et al. 2014). Obviously when a lesion is anatomically positioned to preclude surgery, then the major therapeutic options include chemotherapy and/or radiotherapy. From a totally non-invasive perspective, external beam and stereotactic radiotherapy provide the mainstay of current clinical practice in terms of achieving stimulus-responsive, site-specific tumor ablation, and certainly provide major patient benefit. External beam or stereotactic radiotherapy are of course not without risk and adverse effects associated with their use are well documented (Rodriguez et al. 2013; Herrera et al. 2014). Despite continuous development of more precise delivery approaches, such as CyberKnife®, awareness of the potential adverse effects associated with radiotherapy as a non-invasive stimulus has also supplied impetus to the search for alternative approaches that do not carry the inherent negative attributes or perceptions associated with radiation.

22.1.2 Alternatives to Convention: Stimulus-responsive Therapeutic Approaches

At least partially in response to the negative perceptions associated with the use of radiation, the search for alternative stimuli has led to the development of minimally-invasive ablative procedures, including radiofrequency (RFA) and microwave ablation (MWA) (Chu and Dupuy 2014). RFA involves the placement of an electrode into the lesion to enable delivery of an alternating electric current that oscillates in the radiofrequency range, and preferably at approximately 500 kHz. Hyperthermia around the inserted probe results from friction caused by ions attempting to follow the rapidly alternating current (Ni et al. 2005). Microwave ablation again involves the insertion of a probe directly into the lesion that serves as an antenna for the delivery of electromagnetic waves at frequencies in the microwave range, typically ranging from 900 to 2500 MHz. The oscillating electromagnetic field induces hyperthermia by forcing molecules, such as water, that have intrinsic dipoles to continuously align with the oscillating field (Chu and Dupuy 2014). It has been suggested that the latter provides advantage over RFA induction of hyperthermia since it does not depend on the passage of an electric current through tissues and therefore is not subject to variations in tissue conductivity. Accordingly, it enables the treatment of larger tumor volumes. These approaches rapidly progressed through the 1990s with the emergence of image guidance technologies such as ultrasound, CT and MRI. Offering a more precise alternative to surgery, and without the negative aspects associated with external beam radiation, these approaches offered a viable alternative to conventional therapies. With both of these approaches, energy deposition is such that a number of zones occur around the tip of the inserted probe. These include a central mass that is closest to the tip of the probe and undergoes coagulation necrosis, in which catastrophic effects such as collapse of membranes, protein denaturation and mitochondrial dysfunction occur. Further out from the probe tip a transitional zone exists where the cells are exposed to sub lethal doses of thermal energy, resulting in some degree of injury occurring. Injury in this zone can result in the production of pro-inflammatory factors that recruit immune cells to the area and it has been suggested that this can result in conditioning of dendritic cells/native T cells, potentially enhancing tumor-free survival in certain patients (Chu and Dupuy 2014; Hiroishi et al. 2010). Whilst both of these approaches, together with similar therapies such as cryotherapy and percutaneous irreversible electroporation (IRE), are clearly site-specific stimulus-responsive therapies, and provide alternative clinical options in the treatment of cancer, they are minimally invasive. Essentially, they have however sacrificed one of the most valuable aspects associated with external beam radiotherapy, *i.e.* it's completely non-invasive nature.

Due to its tissue penetrating capabilities and concurrent with the development of the above approaches, ultrasound has emerged as a truly non-invasive stimulus for the induction of localized hyperthermia. Developments in this area since the early 1940s have resulted in the development of HIFU and its association with

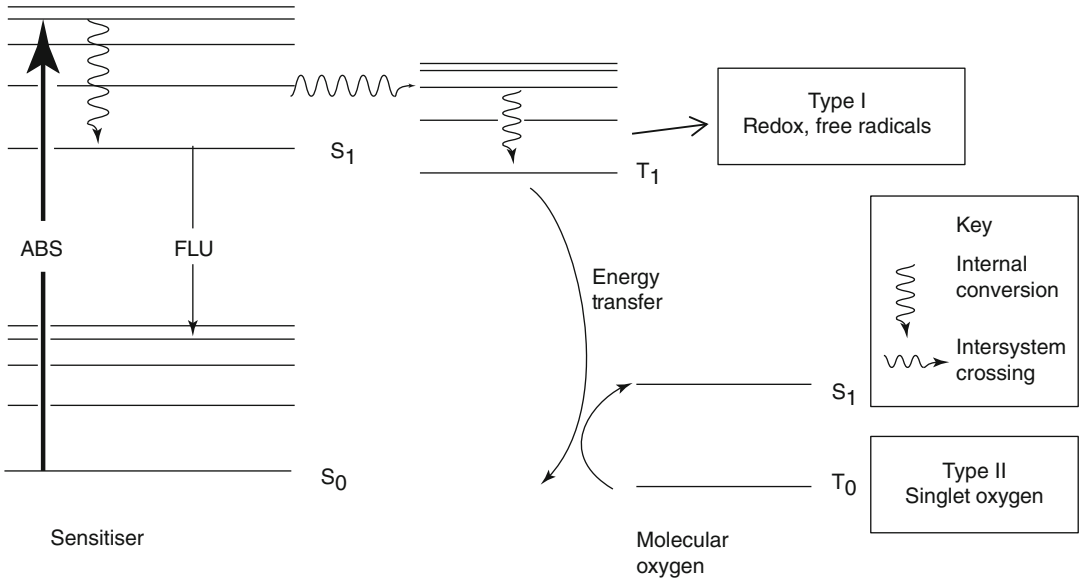

Fig. 22.1 Jablonski diagram outlining the photochemical processes involved in PDT

MRI guidance systems. Briefly, as this is the subject of Part I of this volume, HIFU has been employed in the clinic to enable non-invasive thermal ablation for the treatment of a variety of cancers (Li et al. 2014a, b, c; Nishikawa and Osaki 2013). Clinical data also appear to suggest that HIFU is comparable with RFA for the treatment of hepatocellular carcinoma, with the exception that HIFU is truly non-invasive (Nishikawa and Osaki 2013). It is also worth noting that reports are emerging which suggest that, in addition to providing a tumor ablative function, HIFU also offers the potential to provide tumor specific immunity (Huang et al. 2012). Although the above-mentioned approaches facilitate minimally or completely non-invasive approaches to the treatment of focal disease, they all employ stimuli that are destructive.

22.1.3 Photodynamic Therapy

In an ideal scenario, it would be very valuable if an approach could be devised to exploit a harmless stimulus that could trigger a cytotoxic event specifically at the target site. In the early 1970s an approach known as photodynamic therapy emerged which was based on the use of a harmless photosensitizer to sensitize tumor tissues and relatively low intensity light to activate the photosensitizer (Dougherty et al. 1975). Irradiation of the sensitizer with light of an appropriate wavelength in the presence of molecular oxygen generates singlet oxygen and/or other reactive oxygen species (ROS) that are potent intracellular cytotoxins. The photochemical processes involved in the generation of ROS are illustrated in the Jablonski diagram shown in Fig. 22.1.

Upon absorption (ABS) of light energy by the sensitizer, an electron is promoted from the singlet ground state (S_0) to a higher energy singlet excited state (S_1, S_2…). Any electrons that occupy orbitals higher than S_1 return to S_1 via a non-radiative process known as internal conversion. From S_1 the electron has two options; (i) it can return to S_0 emitting its excited energy as fluorescence (FLU), or (ii) undergo a process known as intersystem crossing (ISC), where the spin state of the excited electron is changed, forming a triplet excited state (T_1). Triplet excited states have significantly longer lifetimes than singlet excited states, enabling T_1 to partake in non-radiative processes kinetically unavailable to singlet excited states. In PDT, such processes are usually classified as Type I or Type II reactions. In Type I photoreactions, certain molecular substrates can be

directly oxidized by the excited sensitizer, resulting in a reduced sensitizer that can further interact with molecular oxygen to generate superoxide ion (O_2^-) and its derivative series of ROS (Macdonald and Dougherty 2001). In Type II photoreactions, the T_1 state interacts directly with molecular oxygen, which itself has an uncharacteristic triplet ground state (T_0), via an energy transfer process to produce singlet oxygen ($^1O_2$). While both Type I and Type II reactions can occur simultaneously, Type II reactions typically dominate in aerobic media. Due to the high reactivity and short half-life (0.04 μs) of singlet oxygen, its diffusion radius is less than 20 nm. This implies that only cells close to the site of its generation are affected (Moan and Berg 1991). Several factors influence the efficiency of ROS generation in PDT, such as the type of sensitizer used, its concentration, the light dose (both wavelength and fluence) and the amount of available oxygen. While PDT is extremely effective at treating superficial lesions and is a recognized first line treatment for non-melanoma skin cancer, its use for the treatment of deeper-seated solid tumors has been restricted by the inability of light to penetrate to depth through human tissue. The penetration of light through human tissue depends on its wavelength, with longer wavelength light penetrating deeper than shorter wavelength light. Indeed, the phototherapeutic window, where tissue has maximum transparency to light, is in the 750–900 nm range (Starkey et al. 2008). Unfortunately, the absorption maximum of currently approved sensitizers is in the 400–600 nm range, limiting penetration depth to millimeters. While significant progress has been made with the development of so-called third generation sensitizers, in particular the bacteriochlorins with strong absorption bands in the 720–740 nm region (Fukuzumi et al. 2008), the difficulty remains in delivering light to sites that are deep within the body.

22.2 Sonodynamic Therapy (SDT)

22.2.1 The Concept

The observation that relatively low intensity ultrasound can enhance chemotherapeutic drug action has been well documented by our own group and many others (Rosenthal et al. 2004; Tachibana et al. 2008; Li et al. 2008a, b; Nomikou et al. 2010). The mechanisms by which ultrasound enhances the action of chemotherapeutic drugs are varied and range from; (a) the ability of ultrasound to 'porate' cell membranes (a phenomenon known as sonoporation) to enhance entry of the chemotherapeutic drug into target cells to (b) the ability of ultrasound to promote dispersion of chemotherapeutic drugs through poorly vascularized tissues in solid tumors (Li et al. 2008a; Nomikou et al. 2010). Some have interpreted this as the drug sensitizing the tumor tissues since the approach reduces the effective dose of the chemotherapeutic drug that needs to be used to obtain a cytotoxic effect (Rosenthal et al. 2004). Thus in the field, some refer to this extremely broad interpretation as sonodynamic therapy. However, in 1989 it was recognized by Yumita and Umemura that hematoporphyrin, a well-known photosensitizer, could be used to elicit cytotoxic effects in acoustic fields. They then went on to coin the phrase 'sonodynamic approach' in 1992 to describe the activation of the porphyrin by ultrasound (Yumita et al. 1989; Umemura et al. 1992). It is now generally recognized that the term sonodynamic therapy refers more specifically to sensitizer-dependent sonochemical or sonophotochemical events in an acoustic field that lead to cytotoxicity. For the purposes of this review we will deal with this more narrow definition of SDT. Although we will review SDT in more detail below, the concept offers very significant advantage over alternative approaches involving the use of external stimuli, primarily because it exploits ultrasound at relatively low intensities. Essentially, the stimulus is non-thermal and as such is recognized as being non-toxic. In addition, with few exceptions, the approach exploits sensitizers that are commonly employed as photosensitizers in PDT, and these are also regarded as relatively non-toxic entities. Therefore, in comparison with the stimulus-dependent approaches described above, SDT offers the advantage of minimizing adverse effects and maximizing on-target responses. The approach also provides a very significant benefit over PDT because unlike light,

ultrasound may be focused deeply within tissues to a single discrete point in three dimensions, whereas light diffuses very significantly as it passes through tissues and the depth to which it penetrates is extremely limited. Indeed, the latter is one of the major reasons why the use of PDT has been restricted to treatment of less accessible lesions. In addition, the use of a chemical agent that is non-toxic in the absence of the stimulus also adds another level of control and distinguishes the more narrow definition of SDT from the broader definition where ultrasound is employed to enhance the action of an already toxic chemical. In SDT, off-target effects associated with virtually all cancer chemotherapeutic drugs, even at lower doses, are circumvented.

22.2.2 Sonosensitizers

As mentioned above, many of the sensitizers originally used in SDT-based studies were porphyrin-based molecules that had been used as photosensitizers and these included hematoporphyrin and Photofrin®, a commercially available hematoporphyrin derivative that is employed in clinical PDT. Table 22.1 lists a selected group of sensitizers that have been studied extensively in the context of SDT. Even in the very early studies reporting sonodynamic effects, it was very clearly demonstrated that the porphryin-based sensitizers produced ROS when exposed to ultrasound and it was suggested that these ROS mediated ultrasound-responsive cytotoxicity in much the same way as in PDT. Indeed, it was demonstrated in a single study, using the same acoustic field properties, that protoporphryin IX appeared to be more active as a sonosensitizing agent than hematoporphyrin, although subsequent studies suggested that this was due to the observation that cells had simply taken up more protoporphryin IX (Liu et al. 2007; Zhu et al. 2010). Although porphyrins had been demonstrated to be capable of sonodynamic effects, it was recognized that these are relatively hydrophobic and although taken up preferentially by tumors to some degree, their distribution in other tissues is ubiquitous and clearance from those tissues is prolonged (Liu et al. 2007). If one wished to realize the major potential benefit offered by SDT, *i.e*. non-invasive access to deeper lesions, then it would be of benefit if the sensitizer did not exist in tissues anatomically positioned between the ultrasound source and the target.

On the other hand, others have reported the use of xanthene dyes, such as rose bengal, as sensitizers and demonstrated ultrasound-stimulated ROS generation in cell free systems and cytotoxic effects *in-vitro* (Kawabata and Umemura 1997; Umemura et al. 1999; McCaughan et al. 2011). Although extremely effective as a sonosensitizer *in-vitro*, its use is contraindicated *in-vivo* because of its extremely rapid sequestration in the liver and subsequent clearance (Sugita et al. 2007). Prompted by the latter and suggestions that for selective uptake of porphyrins by tumors, amphilicity was key, Sugita et al. (2007, 2010) sought to develop amphiphilic preparations of rose bengal using a combination of alkylation and carboxylation. The resulting drug, known as rose bengal derivative, was shown to be more effective as a sonosensitizing drug because it exhibited enhanced uptake by murine tumors (Sugita et al. 2007, 2010).

In addition to serving as sonosensitizers, the agents selected for Table 22.1 all exhibit the ability to serve as photosensitizers, with the exception of DCPH-P-Na (I) (13,17-bis(1-carboxyethyl)-8-[2,4 dichlorophenyl-hydrazonoethylidene]-e-ethenyl-7-hydroxy2,7,12,18-tetramethylchlorin, disodium salt). Synthesized from protoporphyrin IX dimethyl ester, this sensitizer has been compared with ATX-70, a commonly used Ga-porphyrin-based sonosensitizer (Hachimine et al. 2007). In examining the ability of both sensitizers to provide cytotoxic effects following exposure to light, it was found that whilst ATX-70 exhibited very significant phototoxicity, DCPH-P-Na (I) exhibited low phototoxicity. In this study it was shown that both agents exhibited similar absorption profiles, although DCPH-P-Na (I) also exhibited an absorption band at about 720 nm. Since a halogen lamp was employed for irradiation in these studies, it would be interesting to determine whether or not DCPH-P-Na (I) could serve as a photosensitizer at longer wavelengths of light. In any case, it was

Table 22.1 A selection of sensitizers used in SDT

Sensitizer	ROS	Ultrasound frequency	Reference
5-Aminolevulinic acid	N/A	1.04 MHz	Ohmura et al. (2011)
Acridine orange	$^1O_2$ + ·OH	2 MHz	Suzuki et al. (2007)
ATX-70	$^1O_2$ + ·OH	500 KHz	Ding et al. (2006)
Chlorin-e6	$^1O_2$ + ROO	1.56 MHz	Yumita et al. (2008)
ClAl-phthalocyanine	N/A	3 MHz	Yumita and Umemura (2004b)
DCPH-P-Na(I)	$^1O_2$	1 MHz	Hachimine et al. (2007)
Hematoporphyrin	$^1O_2$	1.92 MHz	Yumita et al. (1990)
Hypocrellin SL052	N/A	1 MHz	Meng et al. (2010)
Indocyanine green	N/A	1 MHz	Nomikou et al. (Nomikou et al. 2012a, b)
Methylene blue	·OH	2 MHz	Komori et al. (2009)
Photofrin	$^1O_2$	1 MHz	Xu et al. (2013)
Phthalocyanine	N/A	1 MHz	Kolarova et al. (2009)
Protoporphyrin IX	$^1O_2$	1 MHz	Guo et al. (2013)
Rose Bengal	$^1O_2$	0.8–5.9 MHz	Umemura et al. (1999)
Rose Bengal derivative	$^1O_2$	1.92 MHz	Sugita et al. (2010)

N/A information not available in the cited report

interesting that DCPH-P-Na (I) was able to serve as an efficient sonosensitizer whilst only exhibiting a low degree of photosensitivity. We will discuss this observation later. In addition to the porphryins and the xanthenes, it is perhaps not so surprising that the chlorins can also serve as sonosensitizers, and reports are emerging chlorin E6 may be employed in combined approaches involving the use of light and ultrasound (Li et al. 2014a, b). The approach, known as sonodynamic photodynamic therapy, or SPDT, is sometimes confused with SDT, and we will discuss this further below.

From Table 22.1 it can be seen that many of the sonosensitizers listed give rise to the generation of either singlet oxygen ($^1O_2$) or hydroxyl radicals (·OH) in the presence of an acoustic field and as mentioned above it has been suggested that these mediate the cytotoxic effects observed in SDT. The drug, 5-aminolevulinic acid (5-ALA), is a protoporphyrin IX precursor and even though it does not have an associated ROS listed in Table 22.1, many studies have demonstrated the generation of ROS by its anabolic product, protoporphyrin IX, when exposed to ultrasound. Precisely how ultrasound and the sensitizer generate these radicals is discussed in the next section. It should also be noted from Table 22.1 that all of these sonosensitizers respond to ultrasound at relatively low frequencies ranging from 0.4 to 3 MHz and this further supports the suggestion that an SDT approach for the treatment of less accessible lesions is feasible since there is an inverse relationship between ultrasound attenuation or penetration through tissues, and frequency. Whilst not shown in Table 22.1, it is interesting to note that many of the cited reports with these sensitizers provide an ultrasound intensity/power density and this ranged from 0.5 to 4 W/cm^2, with the exception of both the Ohmura et al. (2011) and the Sugita et al. (2010) citations. Ohmura et al. (2011) report the use of focused ultrasound at 10 W/cm^2, but acoustic pressure was not reported. Similarly, Sugita et al. (2010) employed ultrasound at an intensity of 8.3 W/cm^2, but again the acoustic pressure was not cited. From our own studies with indocyanine green, we employed a planar transducer emitting ultrasound at a frequency of 1 MHz (Nomikou et al. 2012a, b). Significant effects on cell viability in the presence of indocyanine green were observed following exposure to ultrasound at power densities of 0.5 to 2 W/cm^2. With this transducer the acoustic pressures delivered at these ultrasound intensities were calculated to range from 0.086 to 0.172 MPa. In addition, Hachimine et al. (2007), using a

similarly designed transducer, employed ultrasound power densities of 0.5–2 W/cm^2, at a frequency of 1 MHz, when studying the effects of DCPH-P-Na (I) in acoustic fields. The transducer employed in these studies delivered acoustic pressures ranging from 0.108 – 0.217 MPa. The key issue here is that sonodynamic effects are observed in the above two examples using ultrasound that delivers mechanical indices (MI) ranging between 0.08 and 0.217; which are well below the recommended MI limit of 1.9 for diagnostic ultrasound devices.

Despite many of the sonosensitizers listed in Table 22.1 being preferentially sequestered by solid tumors, it should also be noted that residual quantities of these sensitizers are taken up by other tissues and indeed this has been identified as a challenge in PDT as patients exhibit hypersensitivity to light for relatively prolonged periods of time. If similar sensitizers were employed for SDT, then the same effect would occur in patients. As previously mentioned, one of the major perceived benefits of SDT is that it could provide a non-invasive means of targeting lesions deep within the body. In order for this approach to be fully realized it would be necessary for the sensitizer to be absent from tissues that lie between the ultrasound source and the target deep within the body. In PDT the first clinically approved form of hematoporphyrin was chemically modified in order to circumvent issues relating to its low solubility. We have already described how rose bengal could be chemically modified in order to enhance tumor retention. Recent reports suggest that exploiting emerging drug delivery platforms could provide an alternative means of facilitating tumor-specific delivery of sonosensitizers. Such approaches could enhance the tumor specificity of existing sensitizers, as well as providing a means of exploiting sensitizers that have, in the past, been identified as excellent sonosensitizers but ignored because of either a lack of adequate tumor retention or premature clearance. In attempts to address the latter we decided to examine the possibility of using an ultrasound-responsive, microbubble-based delivery system in order to circumvent the issues relating to rose bengal (Nomikou et al. 2012a, b). As described in Part II of this volume, microbubbles are conventionally employed to provide enhanced contrast in ultrasonography, although more recently, they are being examined as mediators of drug and gene delivery. In our studies we covalently attached this efficient sonosensitizer to a lipid-shelled microbubble and were able to demonstrate that ROS production was enhanced in the presence of an acoustic field. This, in turn, led to enhanced ultrasound-mediated cytotoxic effects on target cells. Preliminary data, obtained using human xenograft tumor models, further supported these results and suggest that this approach could provide enhanced therapeutic effects. In addition to using ultrasound to activate a sonosensitizer payload at a chosen target site, drug delivery platforms based on the use of microbubbles could provide a means of targeting sensitizer to tumors. If a conventional photosensitizer was employed in such a delivery system for an SDT-based approach, then issues associated with whole patient sensitization to light would be precluded.

Other innovations in the delivery of sensitizers to tumors have exploited nanotechnology-based approaches. As mentioned above it is well known that solid tumors present a unique microarchitecture that is characterized by deficiencies in vascularization (Narang and Varia 2011). As a result of this atypical vasculature, gas and mass transfer are compromised. Since the integrity of tumor capillaries is compromised, they tend to be leaky and this, in combination with atypical lymphatics and inefficient drainage, results in a high interstitial fluid pressure. From a drug delivery perspective, non-vascularized regions of the tumor combined with a high interstitial fluid pressure within the tumor, present very significant challenges. Paradoxically, it has been shown that nanoparticles, ranging in size from 20 to 200 nm in diameter, can escape from the leaky tumor vasculature and become trapped within the extracellular tumor matrix as a result of inefficient tumor drainage. Known as the tumor enhanced permeation and retention effect (EPR), it has been suggested that this phenomenon could be exploited in order to enhance delivery of active agents to tumors (Torchilin 2001).

It has been further suggested that this approach could benefit PDT-based approaches and this has been reviewed recently by Master et al. (2013). In further developments Ren et al. (2014)) demonstrated the potential of this approach by co-incorporating the conventional photosensitizer hematoporphyrin together with the chemotherapeutic drug doxorubicin and using the formulation to enable drug resistance reversal and tumor ablation. Based on the demonstrated advantages attributed to nanotechnology-based platforms for use in PDT it seems logical to assume that such approaches would also benefit SDT-based regimes. Indeed it could be suggested that the delivery capabilities of these treatments could be further enhanced using ultrasound. This would be particularly useful for penetration of payloads into the impermeable regions of tumors, as it has previously been demonstrated that ultrasound can enhance dispersion of agents through impermeable tissues (Nomikou et al. 2012a, b; Bhatnagar et al. 2014). Indeed, reports are beginning to emerge that describe the use of nanoparticle-based sonosensitizers in SDT. Sazgarnia et al. (2011) have reported the use of protoporphyrin IX conjugated to gold nanoparticles for use in SDT-based treatment using an animal model for colon cancer. Due to their tumor-specific nature it seems clear that nanotechnology-based approaches will play a very significant role in the emergence of SDT as a means of enabling the treatment of more deeply seated lesions.

22.2.3 Mechanism(s) of Activation

As shown in Table 22.1, there appears to be a clear link between ultrasound exposure, presence of the sonosensitizer and the generation of ROS, and most agree that it is the generation of ROS that elicits cytotoxic effects. Whilst the generation of cytotoxic effects resulting from photodynamic activation has been explained at the molecular level, it is less clear how ultrasound interacts with the sensitizer to produce ROS. Here we will explore how ultrasound interacts with the sensitizer to elicit cytotoxic effects.

22.2.3.1 Direct Ultrasound-Mediated Generation of ROS

As mentioned stated, the recognition that exposure of porphyrins to ultrasonic fields could result in cytotoxic effects gave rise to the more accepted definition of sonodynamic therapy. In further characterizing this effect it was demonstrated that exposure of porphyrins, and subsequently many other agents, to ultrasound resulted in the generation of ROS, and it was suggested that these brought about cytotoxicity. So how are these ROS produced in an ultrasonic field, and why does the presence of a sonosensitizer enhance this effect? To address this issue one needs to examine the effects of ultrasound on liquids/tissues. As ultrasound travels through a liquid/tissue, any microbubbles in the liquid are forced to oscillate in the applied acoustic field. At increasing acoustic pressure, this oscillation becomes unstable and eventually the bubble will catastrophically implode. At the time of implosion extreme temperatures and pressures exist and energy is released as heat and in some cases as light. It has been suggested that as a result of these extremes in pressure and temperature the collapsing bubble may be viewed as a sonochemical reactor (Misik and Riesz 2000). Although this is a relatively naïve and perhaps oversimplified view, essentially the bubble serves as a means of concentrating the ultrasonic energy applied to a sample.

Many of the earlier studies relating to identification of cytotoxic ROS species produced during sonodynamic activation of porphyrins were performed with free radical scavengers such as histidine (to detect singlet oxygen and hydroxyl radicals), mannitol (to detect hydroxyl radicals but not singlet oxygen) and superoxide dismutase (SOD) (to explore the involvement of superoxide radicals) (Umemura et al. 1990). In this study, because it was performed in D_2O, and singlet oxygen has an extended half-life in that medium, it was suggested that the singlet oxygen played a significant role in cytotoxicity elicited by SDT. The authors used hematoporphyrin as the sensitizer with ultrasound at a frequency of 1.9 MHz and a power density of 1.8 W/cm^2. In addition, SOD provided a degree of protection

and so it was presumed that superoxide played some role in eliciting cytotoxicity. In the absence of hematoporphyrin, but using D_2O in combination with the above list of scavangers, it was found that singlet oxygen did not play a big role in ultrasound-mediated cytotoxicity. Conversely, using prolonged exposure to ultrasound at a frequency of 48 kHz and an electron paramagnetic resonance spectroscopy (EPR)-based method for the detection of singlet oxygen, Miyoshi et al. (2000) suggested that sonodynamic activation of hematoporphyrin did not result in the generation of singlet oxygen. Instead it was suggested that cytotoxic effects resulted from sonochemical activation of the sonosensitizer that is proximal to a collapsing cavitation bubble, forming sensitizer-derived free radicals either by direct cavitation-induced pyrolysis or by reaction with hydroxyl radicals and H atoms resulting from cavitation-induced pyrolysis of water (Miyoshi et al. 2000; Misik and Riesz 2000). These studies ruled out the role of singlet oxygen as a mediator of ultrasound-induced cytotoxicity, at least under their own chosen ultrasound parameters. In a subsequent report, Hiraoka et al. (2006) compared the separate sonodynamic and photodynamic effects with commonly used photosensitizers on free radical formation and cell killing. In those studies ultrasound was used at a frequency of 1.2 MHz and intensities ranging from 0.5 to 3.1 W/cm^2 (spatial average-temporal average; I_{SATA}). An EPR-based approach using 2,2,6,6-tetramethyl-4-piperidone (TMPD) was employed to detect singlet oxygen by measuring the production of 2,2,6,6-tetramethyl-4-piperidione-N-oxyl (TAN). Sensitizers examined in this study included hematoporphyrin and rose bengal. The authors also measured hydroxyl radical formation in their cell free systems as a means of identifying ultrasound conditions that induced inertial cavitation. In this study, when hematoporphyrin was exposed to light, TAN was observed, suggesting that singlet oxygen was produced during stimulation. When ultrasound was used however, TAN was produced in the absence of hematoporphyrin, and in its presence TAN production was enhanced. It was interesting to note that with ultrasound treatment, TAN did not increase in a time dependent manner as it did during photoactivation. It should be emphasized that in the ultrasound studies, intensities above the inertial cavitation threshold were employed. It would have been very interesting to determine what would have happened at intensities lower than the threshold. In addition, it was found that hematoporphyrin served to suppress hydroxyl radical formation during ultrasound exposure by scavenging, although no carbon-centered radicals were detected using EPR in combination with 3,5-dibromo-nitrosobenzene sulfonic acid (DBNBS) as a spin trap. It was also noted that under the ultrasound exposure conditions employed, ultrasound itself had a significant effect on cell viability whilst no immediate effects were observed on sensitizer-dependent cell viability. The effects of exposure to ultrasound and hematoporphyrin on cell viability 24 or 48 h after ultrasound treatment were not described in this report. Based on these data, the authors concluded that neither singlet oxygen, nor hydroxyl radicals or carbon-centered sensitizer radicals played a role in mediating sonodynamic cytotoxicity. Perhaps if the study had included an examination of the effects of lower intensity ultrasound on singlet oxygen production, a different conclusion may have been made, particularly in the context of generating stable cavitation that would result in sonoluminescence. This is discussed further below.

Whilst contradictory literature reports exist relating to the identity of ROS mediating cytotoxic effects in SDT, the balance of evidence to date does suggest some role in SDT. This is further supported by more recent reports describing cell membrane lipid peroxidation induced by ROS generated upon exposure of DCPH-P-Na(I) treated cells to ultrasound. These effects were inhibited by histidine, but unaffected by mannitol, suggesting a role for singlet oxygen (Yumita et al. 2010). Using an alternative approach to the detection of ROS generation in the presence of ultrasound, the use of a ROS trap (1,3 diphenylisobenzofuran; DPBF) by our own group in a cell free system demonstrated that rose bengal conjugated to lipid-based microbubbles results in the enhanced production of ROS (Nomikou et al.

2012a, b). We have further confirmed this using singlet oxygen sensor green (SOSG), a commercially available diagnostic for the presence of singlet oxygen (McEwan et al. (2015)). Essentially there seems to be little doubt that ROS are involved in SDT-based mechanisms, and the only degree of uncertainty relates to how those are generated. It is also clear from the literature that the nature of ROS generated as a result of exposure to ultrasound varies with the nature of the sensitizer (Table 22.1).

22.2.3.2 The Role of Sonoluminescence

In earlier reports on SDT by Umemura et al. (1990), the authors suggested a role for sonoluminescence (SL). SL is the emission of light from cavitating bubbles, and although the precise mechanism by which light is produced is still uncertain, it has been suggested that it may result from blackbody radiation, bremsstrahlung radiation, recombination radiation or combinations of these (Byun et al. 2005). It has been suggested that it results from inertial cavitation events when bubbles implode, however SL from systems generating stable cavitation have been reported (Saksena and Nyborg 1970; Gaitan et al. 1992). In their studies on SDT, Umemura et al. (1990) were able to demonstrate emission of light from saline solutions using ultrasound conditions that were employed to elicit sonodynamic effects. The spectrum of emitted SL light indicated a peak at 400–450 nm and they were also able to demonstrate that hematoporphyrin absorbed the SL emissions in this region. The authors suggested that SL light could serve to activate hematoporphyrin since it is a photosensitizer. In effect, this would explain the generation of singlet oxygen during sonodynamic activation. The possibility that SL may play a role in sonodynamic activation was reinforced by the demonstration by He et al. (2002) that SL could be detected *in-vivo*, although this study employed ultrasound at a lower frequency (40 kHz) and an acoustic pressure of 0.2 MPa. Nevertheless, this was a key study in that it suggested that SL could occur *in-vivo*. Using water as the medium and a therapeutic ultrasound device, Pickworth et al. (1988) already demonstrated that SL could be observed at a driving frequency of 1 MHz and at ultrasound power densities of as low as 0.25 W/cm^2. The acoustic pressure at this lower limit was determined to be 0.14 MPa. This study was also interesting because it demonstrated that SL in aqueous solutions at this frequency increased with increasing temperature between 22 and 44 °C. In the latter context, it is worth noting that Misik and Riesz (2000) precluded involvement of SL in the sonodynamic activation of the porphyrin-based sonosensitizer, ATX-70, because it had been suggested that SL decreased with increasing temperature. Effectively, this has been reproduced, but is most apparent at lower frequencies, and one should note that Misik and Riesz (2000) employed ultrasound at a frequency of 47 kHz in their study. Although the above reports suggest a possible role for SL in SDT, one report using DPCH-P-Na(I) suggested that SL did not play a significant role as this sensitizer was shown to exhibit sonosensitizing capabilities, but was 'devoid' of photosensitizing capabilities (Hachimine et al. 2007). Although the authors claimed that this sensitizer was devoid of photosensitizing capabilities, the data did however indicate a statistically relevant slightly negative impact on cell viability following exposure to light. They also performed ROS scavenging experiments with histidine and mannitol and were able to demonstrate that singlet oxygen played some role in the cytotoxic effect observed with ultrasound. From a clinical perspective, this sensitizer would provide considerable benefit because it would preclude one of the major side effects of currently used sensitizers, *i.e.* prolonged sensitivity to light. However, from a mechanistic perspective, one wonders if the limited effects of light exposure that were observed can be completely ignored, and if not, could SL still be playing some role in the mechanism of action of this sensitizer? In a more recent study, Sazgarnia et al. (2013) succeeded in demonstrating SL in gel-based phantoms using protoporphyrin IX coupled to gold nanoparticles. Ultrasound at a frequency of 1.1 MHz and acoustic intensities of 1 and 2 W/cm^2 were used. The authors suggested that the gold nanoparticles served as nucleation centers for cavitation. Integrated SL signals at 350–450, 450–550 and 550–650 nm were detected, and it was suggested that the longer

wavelength emissions resulted from sensitizer fluorescence. This study is also interesting in that SL was observed in agar gels and the enhanced bulk medium afforded by the gel could result in SL as a consequence of stable cavitation. From the data available, particularly with respect to SL derived from stable cavitating bubbles, reports of SL in gel-based systems and detection of SL *in-vivo*, SL cannot be ruled out as a potential mediator of ultrasound-induced activation of sensitizers. The concept of SL derived from stable cavitating bubbles is an attractive one because it could potentially facilitate a degree of amplification that has not been previously envisaged.

22.2.3.3 Sensitizer-Dependent Destabilization of Cell Membranes

Although most agree that there is some involvement of ROS in SDT, it has been suggested that SDT may be based on sonomechanical mechanisms (Hiraoka et al. 2006). This conclusion was based on observations that hematoporphyrin-sensitized cells were sensitive to ultrasound at intensities that were shown not to induce inertial cavitation. It is interesting to note however, that the ultrasound intensities employed in this study that did not give rise to inertial cavitation, could, quite possibly have given rise to sonoluminescence via stable cavitation. It would have been interesting if the authors had determined whether or not singlet oxygen was produced in the presence of hematoporphyrin using those lower ultrasound intensities. Using a range of sensitizers in their study, including rhodamine derivatives such as rose bengal, they suggested that sensitivity to ultrasound seemed to be associated with sensitizer hydrophobicity. In this context, and on the basis of their previously reported results, they suggest that mechanical disruption of membranes by ultrasound is augmented by the rhodamine derivatives (Hiraoka et al. 2006; Feril et al. 2005). Indeed, it is well known that porphyrins interact with cell membranes and the manner of this interaction has been modeled (Stepniewski et al. 2012). Although there may be some truth in the suggestion that interaction of a hydrophobic entity with a cell membrane may result in that membrane exhibiting hypersensitivity to ultrasound, other evidence suggests that chemical modification of the membrane lipids results from ultrasound exposure in the presence of a sensitizer (Tang et al. 2008). In this study the authors demonstrated that treatment of cells with hematoporphyrin and ultrasound resulted in reduced membrane fluidity as a result of lipid peroxidation. This reduced membrane fluidity resulted in an observed decrease in adenylate and guanylate cyclase activities. Cell membrane lipid peroxidation was also reported by Yumita and Umemura (2004a) during SDT with Photofrin®. More recently, Yumita et al. (2010) further demonstrated membrane lipid peroxidation using DCPH-P-Na (I)-mediated SDT. One can only conclude that sensitization is not solely due to a physical destabilization of the cell membrane by interaction with the sensitizer, particularly in the case of porphyrins. It is interesting to note that in PDT-based studies with Photofrin®, interaction of the sensitizer solely with the cell membrane and subsequent to light exposure, resulted in membrane damage that led to a necrotic phenotype (Hsieh et al. 2003). The implication of this finding from a PDT perspective was that controlling the form of cell death could have an impact on the development of tumor immunity. Promotion of an inflammatory response via necrosis could provide a means of addressing metastatic disease. One wonders if the same might apply to SDT-based therapies. In a relatively recent report it was suggested that gas molecules partitioning into lipid bilayers can serve as nucleation centers for the formation of gas bubbles between the layers of the bilayer (Wrenn et al. 2013). Although this report related to the study of artificial bilayers and the use of low frequency ultrasound to facilitate payload release from membrane-enclosed vesicles, they do raise the possibility of such a phenomenon existing in natural cell membrane bilayers. If this was so, then membrane-associated sensitizers would be in very close proximity to an acoustically sensitive entity (*i.e.* a nucleated bubble) within the membrane. If this nucleated bubble was subject to cavitation within the membrane layers at lower ultrasound intensities, the membrane-stabilized

bubble could result in sonoluminescence, and this may provide one explanation for SDT-based membrane lipoperoxidation.

All of the above suggested mechanisms for SDT must of course be taken in context and it is important to consider that many of the above studies are performed in highly defined environments. To identify what might be happening at atomic and molecular levels in systems containing target cells and media is somewhat more challenging. Mechanisms have been explored, as mentioned above, using specific ROS scavengers, such as histidine, mannitol and SOD. It does appear from the literature that different sensitizers appear to behave differently in ultrasonic fields. It also appears that a given sensitizer may result in differential effects that depend upon the frequency and intensity of the ultrasound. It is generally accepted that it is very difficult to distinguish between sonochemical and sonomechanical effects using ultrasound at relatively low intensities. In exploring the exciting aspects of these mechanisms it can sometimes be extremely easy to lose sight of the basic observation in the above cited literature; that in SDT, as with PDT, neither the stimulus nor the sensitizer are toxic, but when both are combined, regardless of the precise mechanism, a cytotoxic event occurs at a single point in space and depth in tissue.

22.3 Application of SDT in the Treatment of Cancer

In the following sections we will explore the evidence suggesting that SDT could provide us with a means to exploit a harmless stimulus and drug, to non-invasively target less accessible solid tumors.

22.3.1 In-Vitro Studies Examining SDT Efficacy

The term 'sonodynamic' was first employed by Yumita and Umemura in their studies reporting the effects of combining a sensitiser with ultrasound to elicit a cytotoxic effect (Yumita et al. 1989; Umemura et al. 1992). This differed from existing alternative approaches using ultrasound to enhance cancer chemotherapeutic action in that the chemical entity exhibited no toxicity in the absence of the stimulus. In these original studies, the authors used two cell lines, a rat hepatoma cell line (AH-130) and a mouse sarcoma from a metastatic site (sarcoma 180). These were both harvested from ascites fluid in the relevant host animal and cell suspensions were treated with hematoporphryin as the sonosensitizer. Cells were treated with ultrasound at a frequency of 1.92 MHz with varying intensities. Using a dye exclusion assay to determine cell viability, the authors noted that AH-130 cells treated with sensitizer and ultrasound were completely lysed, whereas treatment of the sarcoma 180 cells resulted in cell permeability to the dye but lysis was less severe (Yumita et al. 1989). The authors suggested that the differential response may have been due to AH-130 cell membrane hypersensitization. Since these studies were published, many cell lines representing an extremely wide range of cancers have been tested for their susceptibility to SDT and a list of chosen examples is shown in Table 22.2. One particular study using DCPH-P-Na (I) as the sensitizer by Hachimine et al. (2007) examined a wide range of cancer cell lines in addition to those listed, including breast, lung, liver and prostate lines. Although the studies shown in Table 22.2 employ ultrasound at frequencies ranging from 0.4 to 2 MHz, it is important to note that a significant number of studies have also been performed at ultrasound frequencies that are much lower (Miyoshi et al. 2000; Misik and Riesz 2000). As mentioned above from a mechanistic perspective, data support the observation that differential frequency-dependent effects occur during SDT. The data also support the fact that SDT could provide very significant benefits in the treatment of a wide range of cancers.

In addition to demonstrating efficacy in a wide range of cell lines, *in-vitro* studies have also demonstrated that SDT, like PDT, can induce apoptosis or programmed cell death, although the extent to which this occurs depends on the sonosensitizer used, the characteristics of the ultrasound

Table 22.2 *In-vitro* cytotoxic studies using SDT

Target	Ultrasound frequency (MHz)	Maximum intensity ($W/cm^{2)}$	Reference
S 180 (sarcoma/mouse)	2	2	Suzuki et al. (2007)
KLN205 (lung/mouse)	1 and 3	1–3	Osaki et al. (2011)
MKN-1 (gastric/human)	1	2	Hachimine et al. (2007)
QGP-1 (pancreatic/human)	1	2	Hachimine et al. (2007)
THP-1 (leukemia/human)	1	0.5	Zheng et al. (2014)
HO-8910 (ovarian/human)	1.7	0.46	Xiang et al. (2011)
AH-130 (hepatoma/rat)	1.92	3.18	Yumita et al. (1989)
GSC (glioblastoma/human)	1	0.5	Xu et al. (2013)
G361 (melanoma/human)	1	2	Kolarova et al. (2009)
MDA-MB-231 (breast/human)	1.1	1	Li et al. (2012)
RIF-1 (sarcoma/mouse)	1	1.5	Nomikou et al. (2012a, b)

and the nature of the target (Kuroki et al. 2007). It had previously been felt that apoptosis was desirable because it minimized immune activation and inflammation. However, it is becoming increasingly recognized that necrotic mechanisms of cell death (such as more catastrophic effects, including cell lysis or fragmentation following traumatic insult), may induce immunological responses that yield therapeutic benefit. Cell fragments serve as antigens in the generation of tumor immunity that may in turn, preclude tumor reoccurrence and/or serve to minimize or eradicate metastatic disease. In PDT-based studies a non-apoptotic form of cell death known as autophagy has been described and it has been suggested that autophagy may underpin the reports that low dose PDT could potentially yield anti-tumor vaccines (Kessel et al. 2006). Autophagy is a process whereby cytosol or organelles are encapsulated in autophagosomes. These subsequently fuse with lysosomes in order to recycle damaged cellular components. It the past autophagy had been viewed as a survival response to stress, although it has subsequently been recognized as a form of programmed cell death that plays a significant role in development and has been suggested to play a role in mediating the effects of some chemotherapeutic drugs (Kondo et al. 2005). Using mouse sarcoma 180 cells, Wang et al. (2010) demonstrated that autophagy played some role in cell death using SDT. Paradoxically, their data suggested that autophagy was providing a means of rescuing cells that had been treated. They demonstrated this using autophagy inhibitors and were able to show enhanced SDT-mediated death in the presence of inhibitors. Although these observations appear contradictory, it is likely that signaling pathways controlling autophagy have a degree of discriminatory control that provides a trigger for rescue or termination. Regardless of the mechanism by which cells die following treatment with SDT, there is now a very significant body of evidence from *in-vitro* studies on a wide range of cancer cell lines indicating efficacy of the approach. Again we emphasize that in SDT the agent employed to facilitate sonosensitization and the ultrasound employed to deliver the sonodynamic effect are, in their own right, non-toxic.

22.3.2 In-Vivo Studies Examining SDT Efficacy

As already discussed, ultrasound can be employed to facilitate therapeutic effects and the major clinical approach, HIFU, is the subject of Part I of this volume. With HIFU, the ultrasound itself is cytotoxic and one of the major challenges in this area is delivering the energy to the required target region whilst ensuring adequate dose delivery to facilitate complete ablation of the lesion. In SDT, the site-directed specificity of the approach is delivered by uptake of a relatively harmless agent by the tumor tissues and subsequent delivery of relatively harmless low intensity ultrasound to

Table 22.3 Therapeutic efficacy of SDT for the treatment of selected *in-vivo* tumor models

Tumor/Source	Host	Ultrasound frequency (MHz)	Ultrasound intensity ($W/cm^{2)}$	Reference
Glioma/Rat	Rat	1.04	10	Ohmura et al. (2011)
Colon/Mouse	Mouse	2	3	Yumita et al. (1996)
Breast/Rat	Rat	1.92	3	Yumita et al. (2007)
Liver/Mouse	Mouse	1.56	4	Shi (2011)
Colon/Human	Mouse	3	1.92	Yumita and Umemura (2004b)
Gastric/Human	Mouse	1	0.5–2	Hachimine et al. (2007)
Myeloma/Mouse	Mouse	1	0.8	Meng et al. (2010)
Sarcoma/Mouse	Mouse	1	3.5	Nomikou et al. (2012a, b)
Glioma/Rat	Rat	1	1	Tserkovsky et al. (2012)
Colon/Mouse	Mouse	1.1	2	Shanei et al. (2012)
Prostate/Human	Mouse	1	1.5	Nomikou et al. (2012a, b)
Tongue/Human	Mouse	1.1	2.0	Guo et al. (2013)

that site. Essentially, the spatial specificity is afforded by the necessity to have both the sensitizer and stimulus present at the same point in space and time. Of course one needs to ensure that the sensitizer is not present in high concentrations in the tissues that lie between the ultrasound-emitting surface and the target tissues. We have already discussed how enhanced tumor specificity with respect to sensitizer uptake can be accomplished in Sect. 22.2.2. Here we will explore the evidence that SDT can provide a therapeutic effect in the whole organism.

In one of the earliest reports describing *in-vivo* sonodynamic effects, Yumita et al. (1996) described the use of ATX-70 (a gallium porphyrin complex) to treat an ectopic mouse model of colon adenocarcinoma (colon 26 in CDF_1 mice). Following intravenous administration of ATX-70 (dose of 2.5 mg/kg), the authors demonstrated that ATX-70 reached a maximum concentration in the tumor at 6 h after administration and was cleared from the plasma faster than from the tumor. It was also found that when the skin ATX-70 concentration was examined, the tumor to skin ratio increased up to 24 h and as a consequence, ultrasound treatment was performed 24 h after drug administration. Using ultrasound at 2 MHz and at an intensity of 3 W/cm^2 to treat tumors with an average diameter of almost 1 cm, tumors reduced to less than half their original size 3 days after treatment. Although the tumors did appear to increase in size after days 5–7, the authors suggested that SDT was compatible with multiple treatments and suggested this as an option. In a later report these authors also described the use of SDT to treat 7,12 dimethylanthracene (DMBA)-induced rat mammary tumors (Yumita et al. 2007). Using ATX-70 and an ultrasound intensity of 3 W/cm^2, tumor volumes decreased and no re-growth was observed. Table 22.3 illustrates a selection of reports describing SDT to treat a variety of tumor targets derived from mouse, rat and human sources, and tested in hosts such as mouse and rat. The ultrasound frequency in all of those studies ranges from 0.8 to 3 MHz, with most employing frequencies around 1 MHz. In many cases, the intensity of ultrasound used ranged from 0.8 to 3.5 W/cm^2, with the exception of that reported by Ohmura et al. (2011), where an intensity of 10 W/cm^2 was employed. In this study the authors used an orthotopic rat glioma model. In a series of studies with their transducer and using normal brain as a target, they were able to show that this ultrasound intensity had no effect on the histological integrity of normal brain. Although the ultrasound intensity seems high, it should be noted that a focused transducer was employed, but acoustic pressure was not reported. The authors also demonstrated a significant reduction in tumor size following sensitization with 5-aminolevulinic acid (5-ALA) and reported no damage to tissues that were anatomically positioned between the target and the emitting surface

of the transducer. In a similar study using a rat glioma model, albeit an ectopic model, Tserkovsky et al. (2012) demonstrated significant tissue damage following treatment with a modified chlorin e6 sensitizer. Ultrasound at a frequency of 1 MHz and a power density of 0.7 W/cm^2 was used. They did however observe necrosis following treatment with ultrasound in the absence of sensitizer and this appeared to be dose dependent with respect to the ultrasound intensity. It was interesting to note that Yoshino et al. (2009) demonstrated ultrasound-mediated localized disruption of the blood brain barrier in the presence of a sensitizer using focused ultrasound, although in this case the ultrasound intensity reported was much higher than that used in the study by Ohmura et al. (2011). Nevertheless, these reports do suggest that SDT may provide potential benefits in the treatment of less accessible lesions, particularly in the brain.

It has been suggested for PDT that, in addition to direct cytotoxic effects on tumor cells, the tumor vascular endothelium also serves as a major target, resulting in vascular shut down and consequential starvation of the tumor (Roberts et al. 1994). Using 5-ALA as a precursor for intratumoral generation of protoporphyrin IX, Guo et al. (2013) demonstrated that exposure of a human tongue squamous cell carcinoma xenograft model in mice to ultrasound, at a frequency of 1.1 MHz and an intensity of 2 W/cm^2, reduced tumor growth and had a profound effect on the tumor vasculature. This treatment also inhibited expression of vascular endothelial growth factor (VEGF). In the same study it was found that exposure of 5-ALA treated primary human umbilical vein endothelial cells (HUVECs) to ultrasound at the same frequency, using an intensity of 1 W/cm^2, inhibited cell proliferation, migration, invasion and tube formation. On this basis the authors concluded that SDT exhibited an anti-angiogenic effect in their system. In conventional PDT, the sensitizer is administered and a time delay prior to exposure to light is necessary in order to enhance clearance of systemic sensitizer. When porphyrins are used, this time delay can be 24–48 h post administration of the sensitizer. For PDT it had been suggested that if the conventional therapy sensitizer dose was divided into two, administered at 4 h and 15 min prior to delivery of light, then both the vasculature and the perivascular space would be exposed to circulating levels of sensitizer as it would not be completely cleared. Therefore endothelial cells in the tumor microvasculature would be exposed to this uncleared sensitizer fraction. This approach was found to have a superior therapeutic impact on PDT-mediated therapy of an orthotopic breast tumor model in mice, even though the same overall dose of the sensitizer had been administered (Dolmans et al. 2002). Based on these observations and their own findings, Guo et al. (2013) suggested that a similar approach may benefit SDT.

It has been known for some time that PDT-based protocols can lead to apoptosis and necrosis that stimulate the host immune system. This is in contrast to conventional cancer treatments, such as radiotherapy and chemotherapy, which tend to be immunosuppressive. It has been suggested that the acute inflammation induced by PDT could result in the presentation of tumor-derived antigens to T cells, thereby providing an immune response that would inhibit tumor re-occurrence and suppress metastatic disease (Castano et al. 2006). Using a porphyrin-based sensitizer named SF1 to treat S-180 tumors in mice, together with ultrasound at a frequency of 1 MHz and a maximum intensity of 1.1 W/cm^2, Wang et al. (2008), in addition to demonstrating dramatic SDT-mediated inhibitory effects on tumor growth, also noted inflammation around the target site shortly after treatment. In some of our own studies we have also noted this phenomenon; however, whether or not this could yield an anti-tumor immunological effect that may provide benefit in limiting tumor re-occurrence or controlling metastatic disease remains to be seen.

In discussing sensitizers that are employed in SDT, we mentioned a number of preparations that are provided in a nano-particulate form. Based on exploiting the tumor EPR, such preparations could lead to a reduction of uptake by normal tissues and this would be of particular benefit in targeting less accessible lesions. Using a gold nanoparticle-protoporphyrin IX conjugate

as a sensitizer to treat an ectopic mouse colon carcinoma tumor model (CT26), together with ultrasound at a frequency of 1.1 MHz and an intensity of 2 W/cm^2, Sazgarnia et al. (2011) demonstrated that this preparation was an effective sensitizer that led to reduced tumor volumes with enhanced host survival. The authors suggested that the enhanced activity of the novel nanoparticle-based preparation over free protoporphyrin IX in SDT resulted from a variety of factors, including enhanced cellular uptake of the nanoparticles and enhanced cavitation promoted by the presence of the nanoparticles. As mentioned above in a different context, we have used a microbubble-sensitizer conjugate to treat a human prostate xenograft cancer model (LNCaP-Luc) in mice, together with ultrasound at a frequency of 1 MHz and an intensity of 3.5 W/cm^2 (Nomikou et al. 2012a, b). Treatment with ultrasound resulted in a rapid and very significant reduction in tumor size. The microbubble was lipid-based, and the sensitizer (rose bengal) was covalently coated on the exterior of the microbubble. It was interesting to note that when ROS production by both the free and microbubble-conjugated sensitizer was compared in cell free systems during exposure to ultrasound, ROS generation was far superior in the latter preparation. On the basis of these studies, we suggested that ultrasound-responsive microbubbles could provide a convenient means of both targeting and activating sensitizers at a specific site.

22.3.3 Towards Clinical Trials with SDT

Despite the accumulation of an ever-increasing body of work demonstrating the potential benefits of SDT, we are unaware of any clinical trials that have been embarked upon to date. A number of studies have been performed in patients; however, these have been reported to exploit a combination of light and ultrasound to stimulate a sensitizer (Wang et al. 2009; Kenyon et al. 2009). The approach has become known as sonodynamic photodynamic therapy (SPDT), or next generation PDT (NGPDT), and has attracted considerable negative press for a variety of reasons. Unfortunately, because of the use of the word 'sonodynamic' in the title of the former publication, SDT has incorrectly become associated with SPDT and NGPDT. From a purely scientific perspective, the rationale for using ultrasound together with PDT in the former study was based on the success reported in a preclinical mouse model using SDT with a chlorin-based sensitizer known as SF-1 (Wang et al. 2009). The SPDT study involved the treatment of three patients with advanced breast cancer that had exhausted all conventional therapeutic approaches. The study employed debulking strategies, administration of the sensitizer (SF-1) and subsequent exposure to light and ultrasound treatment. Although the authors reported reductions in tumor sizes in all three patients, from a scientific perspective, it was difficult to identify the precise nature of the treatments (dose per tumor), or indeed to deduce whether or not these results were obtained as a result of enhancing chemotherapeutic/radiotherapeutic effects that had been applied for debulking, enhancing PDT or indeed combinations of these possibilities. In the absence of any data describing drug pharmacokinetic behavior and tissue distribution, it was difficult to determine the logic associated with whole body exposure to light. Indeed, with the light and ultrasound-emitting devices employed it was also difficult to envisage how deeply the stimuli had penetrated into tissues. It will be interesting to monitor further work emerging from this group in the future. It is perhaps noteworthy that this study prompted a relatively negative response from a number of investigators that have been active in the PDT field (Huang et al. 2010). Although much of the commentary relates to the SPDT approach actually used by Wang et al. (2009), the authors do offer their opinion in relation to SDT and state that '*There is no convincing data that shows that ultrasound used in this way is effective in the treatment of primary tumor and multiple metastases*'. They cite two reviews published in 2004 and one research paper published in 2008. Indeed in the research paper cited, the conclusion is that '*SDT could kill C6 glioma cells in-vitro and possibility through*

induction of apoptosis and necrosis' (Li et al. 2008a, b). In the second study using NGPDT in patients cited above (Kenyon et al. 2009), although therapeutic benefit was reported using the combination of light and ultrasound after sensitization, rigorous diagnostic data before and after treatment were somewhat lacking and again, the basis for whole body exposure to light and stimulus penetration to depth was difficult to appreciate from this report (Kenyon et al. 2009). Since both of the above-listed studies involving the use of patients describe the use of ultrasound to enhance PDT, they really cannot be interpreted as a test of the therapeutic efficacy of SDT.

Essentially the major question here is whether or not these two studies, taken together with the very considerable and ever-increasing body of preclinical data accumulating from *in-vitro* and *in-vivo* experimentation, warrants embarking on clinical trials to assess SDT in its own right. It is clear from *in-vitro* and *in-vivo* studies on SDT that; (i) the effects obtained are dose dependent with respect to the sensitizer and ultrasound; (ii) neither the drug nor the stimulus (ultrasound) result in toxicity, and cytotoxic events require the presence of both drug and ultrasound which delivers a degree of spatial control at depth with minimal risk that is unprecedented in targeted cancer therapy; (iii) many of the drugs employed for SDT have a clinical history as a result of their use in PDT. Indeed it could be argued that the wealth of accumulated data on the use of these drugs for SDT at concentrations similar to those employed for PDT would provide a very supportive platform upon which to design SDT-based clinical trials; (iv) cytotoxic effects are mediated by ROS and this is similar to mediators of cytotoxicity in PDT; (v) therapeutic efficacy of SDT has been demonstrated in recognized pre-clinical animal models and finally (vi) focused ultrasound is currently employed in the clinic, albeit at much higher intensities that would be required for clinical SDT. Indeed studies exploiting focused ultrasound, but using lower ultrasound intensities than those used in HIFU-based applications, can be employed to elicit SDT-based effects (Tang et al. 2009; Nonaka et al. 2009; Jeong et al. 2012). It should be noted that in the latter example a focused transducer was not used and focusing was achieved using a conical tissue contact configuration (Jeong et al. 2012). On the basis of the above it is surprising that clinical trials have not yet been embarked upon. From a safety perspective, it could be argued that there is much more pre-clinical evidence out there relating to the use of SDT than there was prior to clinical testing of PDT or some the more recent chemotherapeutic agents currently undergoing clinical trials or emerging into the clinic (*e.g.* some of the tyrosine kinase inhibitors). From a conceptual perspective, and given the similarities between SDT and PDT, it is perhaps not surprising that SDT would be perceived as an approach that would compete very effectively with PDT. From a PDT perspective, many developments in the area have been based on approaches that can facilitate delivery of light to less accessible lesions and this has presented a variety of device opportunities in the field, including the development of lasers, high intensity semiconductor-based light sources and endoscopic light-delivery devices. Emergence of SDT into the clinic could preclude the necessity for such devices. The authors noted a recent web-based description of SDT from a reputable institution (Moseley et al. 2014) with considerable experience in the PDT field. In the context of SDT they state 'Often the light is delivered externally' which indicates a complete misunderstanding of SDT, its scientific origins, developments and potential. They also cite Huang et al. (2010) as being a critical appraisal of a clinical application of SDT. As mentioned above, Huang et al. (2010) is actually a critical appraisal of NGPDT in three patients. Whilst we do appreciate that these authors were criticizing the NGPDT-based work referred to above, we would have expected these authors to have been able to differentiate between SDT and NGPDT, particularly since SDT presents a very realistic alternative to PDT. Ultimately the people that are disadvantaged as a result of ill-informed interpretations such as these are patients that could benefit from SDT in the future. Nevertheless, despite the negative impact relating to NGPDT and the incorrect association with SDT, we feel confident that the wealth of data that has emerged since the word 'sonodynamic' was

coined in 1992 should provide the basis for clinical trials in the very near future with a view towards offering this approach to patients.

References

Bhatnagar S, Schiffter H, Coussios CC (2014) Exploitation of acoustic cavitation-induced microstreaming to enhance molecular transport. J Pharm Sci 103:1903–1912

Bianchi PP, Petz W, Luca F, Biffi R, Spinoglio G, Montorsi M (2014) Laparoscopic and robotic total mesorectal excision in the treatment of rectal cancer. Brief review and personal remarks. Front Oncol 4:98

Byun KT, Kim KY, Kwak HY (2005) Sonoluminescence characteristics from micron and submicron bubbles. J Korean Phys Soc 47:1010–1022

Castano AP, Mroz P, Hamblin MR (2006) Photodynamic therapy and anti-tumour immunity. Nat Rev Cancer 6:35–545

Chu KF, Dupuy DE (2014) Thermal ablation of tumours: biological mechanisms and advances in therapy. Nat Rev Cancer 14:199–208

Ding C, Da Xing D (2006) Studies on the sonosensitization mechanism of ultrasound with ATX-70 in sonodynamic therapy. Life Sci J 3:85–89

Dolmans DEJGJ, Kadambi A, Hill JS, Flores KR, Gerber JN, Walker JP, Borel Rinkes IH, Jain RK, Fukumura D (2002) Targeting tumor vasculature and cancer cells in orthotopic breast tumor by fractionated dosing photodynamic therapy. Cancer Res 2:4289–4294

Dougherty TJ, Grindley GB, Fiel R, Weishaupt KR, Boyle DG (1975) Photoradiation therapy. II. Cure of animal tumors with hematoporphyrin and light. J Natl Cancer Inst 55:115–121

Fabi A, Mottolese M, Segatto O (2014) Therapeutic targeting of ERBB2 in breast cancer: understanding resistance in the laboratory and combating it in the clinic. J Mol Med 92:681–695

Feril LB, Kondo T, Cui ZG, Tabuchi Y, Zhao QL, Ando H, Misaki T, Yoshikawa H, Umemura S (2005) Apoptosis induced by the sonomechanical effects of low intensity pulsed ultrasound in a human leukemia cell line. Cancer Lett 221:145–152

Fukuzumi S, Ohkubo K, Zheng X, Chen Y, Pandley RK, Zhan R, Kadish KM (2008) Metal bacteriochlorins which act as dual singlet oxygen and superoxide generators. J Phys Chem B 6:2733–2746

Gaitan DF, Crum LA, Church CC, Roy RA (1992) Sonoluminescence and bubble dynamics for a single, stable, cavitation bubble. J Acoust Soc Am 91:3166–3183

Guo S, Sun X, Cheng J, Xu H, Dan J, Shen J, Zhou Q, Zhang Y, Meng L, Cao W, Tian Y (2013) Apoptosis of THP-1 macrophages induced by protoporphyrin IX-mediated sonodynamic therapy. Int J Nanomedicine 8:2239–2246

Hachimine K, Shibaguchi H, Kuroki M, Yamada H, Kinugasa T, Nakae Y, Asano R, Sakata I, Yamashita Y, Shirakusa T, Kuroki M (2007) Sonodynamic therapy of cancer using a novel porphyrin derivative, DCPH-P-Na(I), which is devoid of photosensitivity. Cancer Sci 98:916–920

He Y, Xing D, Tan S, Tang Y, Ueda K (2002) In vivo sonoluminescence imaging with the assistance of FCLA. Phys Med Biol 47:1535–1541

Heldin CH, Rubin K, Pietras K, Ostman A (2004) High interstitial fluid pressure – an obstacle in cancer therapy. Nat Rev Cancer 4:806–813

Herrera FG, Santa Cruz O, Achtari C, Bourhis J, Ozsahin M (2014) Long-term outcome and late side effects in endometrial cancer patients treated with surgery and postoperative radiation therapy. Ann Surg Oncol 21:2390–2397

Hiraoka W, Honda H, Feril LB Jr, Kudo N, Kondo T (2006) Comparison between sonodynamic effect and photodynamic effect with photosensitizers on free radical formation and cell killing. Ultrason Sonochem 13:535–542

Hiroishi K, Eguchi J, Toshiyuki B, Shimazaki T, Ishii S, Hiraide A, Sakaki M, Doi H, Uozomi S, Omori R, Matsumura T, Yanagawa T, Ito T, Imawari M (2010) Strong $CD8^+$ T-cell responses against tumor-associated antigens prolong the recurrence-free interval after tumor treatment in patients with hepatocellular carcinoma. J Gastroenterol 45:451–458

Holohan C, Van Schaeybroeck S, Longley DB, Johnston PG (2014) Cancer drug resistance: an evolving paradigm. Nat Rev Cancer 13:714–726

Hsieh YJ, Wu CC, Chang CJ, Yu JS (2003) Subcellular localization of Photofrin® determines the death phenotype of human epidermoid carcinoma A431 cells triggered by photodynamic therapy: when plasma membranes are the main targets. J Cell Physiol 194: 363–375

Huang Z, Moseley H, Bown S (2010) Rationale of combined PDT and SDT modalities for treating cancer patients in terminal stage: the proper use of photosensitizer. Integr Cancer Ther 9:317–319

Huang X, Yuan F, Liang M, Lo HW, Shinohara ML, Robertson C, Zhong P (2012) M-HIFU inhibits tumor growth, suppresses STAT3 activity and enhances tumor specific immunity in a transplant tumor model of prostate cancer. PLoS One 7, e41632

Jeong EJ, Seo SJ, Ahn YJ, Choi KH, Kim KH, Kim JK (2012) Sonodynamically induced antitumour effects of 5-aminolevulinic acid and fractionated ultrasound irradiation in an orthotopic rat glioma model. Ultrasound Med Biol 38:2143–2150

Kawabata K, Umemura S (1997) Xanthene dyes for reducing acoustic cavitation threshold in aqueous solution. Ultrasonics 35:469–474

Kenyon JN, Fulle RJ, Lewis TJ (2009) Activated cancer therapy using light and ultrasound – a case series of sonodynamic photodynamic therapy in 115 patients over a 4 year period. Curr Drug Ther 4:179–193

Kessel D, Vicente MG, Reiners JJ (2006) Initiation of apoptosis and autophagy by photodynamic therapy. Lasers Surg Med 38:482–488

Kolarova H, Tomankova K, Bajgar R, Kolar P, Kubinek R (2009) Photodynamic and sonodynamic treatment by phthalocyanine on cancer cell lines. Ultrasound Med Biol 35:1397–1404

Komori C, Okada K, Kawamura K, Chida S, Suzuki T (2009) The sonodynamic antitumor effect of methylene blue on sarcoma180 cells in vitro. Anticancer Res 29:2411–2416

Kondo Y, Kanzawa T, Sawaya T, Kondo S (2005) The role of autophagy in cancer development and response to therapy. Nat Rev Cancer 5:726–734

Kuroki M, Hachimine K, Abe H, Shibaguchi H, Kuroki M, Maekawa S, Yanagisawa J, Kinugasa T, Tanaka T, Yamashita Y (2007) Sonodynamic therapy of cancer using novel sonosensitisers. Anticancer Res 27:3673–3678

Li JH, Song DY, Xu YG, Huang Z, Yue W (2008a) In vitro study of hematoporphyrin monomethyl ether-mediated sonodynamic effects on C6 glioma cells. Neurol Sci 29:229–235

Li YS, Reid CN, McHale AP (2008b) Enhancing ultrasound-mediated cell membrane permeabilisation (sonoporation) using a high frequency pulse regime and implications for ultrasound-aided cancer chemotherapy. Cancer Lett 266:156–162

Li Y, Wang P, Zhao P, Zhu S, Wang X, Liu Q (2012) Apoptosis induced sonodynamic treatment by protoporphyrin IX MDA-MB-231 cells. Ultrasonics 52: 490–496

Li D, Kang J, Madoff DC (2014a) Locally ablative therapies for primary and metastatic liver cancer. Expert Rev Anticancer Ther 14:931–945

Li Q, Liu Q, Wang P, Feng X, Wang H, Wang X (2014b) The effects of Ce6-mediated sono-photodynamic therapy on cell migration, apoptosis and autophagy in mouse mammary 4T1 cell line. Ultrasonics 54:981–989

Li Y, Wang P, Wang X, Su X, Liu Q (2014c) Involvement of mitochondrial and reactive oxygen species in the sonodynamic toxicity of chlorin e6 in human leukemia K562 cells. Ultrasound Med Biol 40:990–1000

Liu S, Kurzrock R (2014) Toxicity of targeted therapy: implications for response and impact of genetic polymorphisms. Cancer Treat Rev 40:883–891

Liu QH, Wang XB, Wang P, Xiao L, Hao Q (2007) Comparison between sonodynamic effect with protoporphyrin IX and hematoporphyrin on sarcoma 180. Cancer Chemother Pharmacol 60:671–680

Macdonald IJ, Dougherty TJ (2001) Basic principles of photodynamic therapy. J Porphyrins Phthalocyanines 5:105–129

Master A, Livingston M, Sen Gupta A (2013) Potodynamic nanomedicine in the treatment of solid tumors: perspectives and challenges. J Control Release 168:88–102

McCaughan B, Rouanet C, Fowley C, Nomikou N, McHale AP, McCarron PA, Callan JF (2011) Enhanced ROS production and cell death through combined photo- and sono-activation of conventional photosensitising drugs. Bioorg Med Chem Lett 21:5750–5752

McEwan C, Owen J, Stride E, Fowley C, Nesbitt H, Cochrane D, Coussios Constantin. C, Borden M, McHale AP, Callan JF (2015) Oxygen carrying microbubbles for enhanced sonodynamic therapy of hypoxic tumours. J Controlled Release 203:51–56

Meng Y, Zou C, Madiyalakan R, Woo T, Huang M, Yang X, Swanson E, Chen J, Xing JZ (2010) Water-soluble and biocompatible sono/photosensitizer nanoparticles for enhanced cancer therapy. Nanomedicine 5: 1559–1569

Misik V, Riesz P (2000) Free radical intermediates in sonodynamic therapy. Ann N Y Acad Sci 899: 335–348

Miyoshi N, Igarashi T, Riesz P (2000) Evidence against singlet oxygen formation by sonolysis of aqueous oxygen-saturated solutions of hematoporphyrin and rose bengal. The mechanism of sonodynamic therapy. Ultrason Sonochem 7:121–124

Moan J, Berg K (1991) The photodegradation of porphyrins in cells can be used to estimate the lifetime of singlet oxygen. Photochem Photobiol 53:549–553

Mokuyasu S, Suzuki Y, Kawahara E, Seto T, Tokuda Y (2014) High-sensitivity cardiac troponin I detection for 2 types of drug-induced cadiotoxicity in patients with breast cancer. Breast Cancer (in press) DOI: 10.1007/s12282-014-0520-8

Moseley H, Eljamel S Moghissi K (2014) Sonodynamic therapy. http://www.yorkshirelasercentre.org/index.php/sonodynamic-therapy. Accessed 26 June 2014

Narang AS, Varia S (2011) Role of tumor vascular architecture in drug delivery. Adv Drug Deliv Rev 63: 640–658

Ni Y, Mulier S, Miao Y, Michel L, Marchal G (2005) A review of the general aspects of radiofrequency ablation. Abdom Imaging 30:381–400

Nishikawa H, Osaki Y (2013) Comparison of high-intensity focused ultrasound therapy and radiofrequency ablation for recurrent hepatocellular carcinoma. Hepatobiliary Surg Nutr 2:168–170

Nomikou N, Li YS, McHale AP (2010) Ultrasound-enhanced drug dispersion through solid tumours and its possible role in aiding ultrasound-targeted cancer chemotherapy. Cancer Lett 288:94–98

Nomikou N, Fowley C, Byrne NM, McCaughan B, McHale AP, Callan JF (2012a) Microbubble-sonosensitiser conjugates as therapeutics in sonodynamic therapy. Chem Commun 48:8332–8334

Nomikou N, Sterrett C, Arthur C, McCaughan B, Callan JF, McHale AP (2012b) The effects of ultrasound and light on indocyanine-green-treated tumour cells and tissues. ChemMedChem 7:1465–1471

Nonaka M, Yamamoto M, Yoshino S, Umemura S, Sasaki K, Fukushima T (2009) Sonodynamic therapy consisting of focused ultrasound and a photosensitiser causes a selective antitumor effect in a rat intracranial glioma model. Anticancer Res 29:943–950

Ohmura T, Fukushima T, Shibaguchi H, Yoshizawa S, Inoue T, Kuroki M, Sasaki K, Umemura S (2011) Sonodynamic therapy with 5-aminolevulinic acid and focused ultrasound for deep-seated intracranial glioma in rat. Anticancer Res 31:2527–2534

Osaki T, Tajima M, Okamoto Y, Takagi S, Tsuka T, Imagawa T, Minami S (2011) Sonodynamic antitumor

effect of benzoporphyrin derivative monoacid ring a on KLN205 cells. J Cancer Ther 2:99–104

Pickworth MJW, Dendy PP, Leighton TG, Twentyman PR (1988) Studies of the cavitational effects of clinical ultrasound by sonolumenescence: 2. Thresholds for sonoluminescence from a therapeutic ultrasound beam and the effect of temperature and duty cycle. Phys Med Biol 33:1249–1260

Ren Y, Wang R, Liu Y, Guo H, Zhou X, Yuan X, Liu C, Tian J, Yin H, Wang Y, Zhang N (2014) A hematoporphyrin-based drug delivery system for drug resistance reversal and tumor ablation. Biomaterials 35:2462–2470

Roberts D, Cairnduff F, Driver I, Dixon B, Brown S (1994) Tumor vascular shutdown following photodynamic therapy based on polyhematoporphyrin or 5-aminolevulinic acid. Int J Oncol 5:763–768

Rodriguez N, Sanz X, Dengra J, Foro P, Membrive I, Reig A, Quera J, Fernandez-Velilla E, Pera O, Lio J, Lozano J, Algara M (2013) Five-year outcomes, cosmesis and toxicity with 3-dimensional conformal external beam radiation therapy to deliver accelerated partial breast irradiation. Int J Radiat Oncol Biol Phys 87:1051–1057

Rosenthal I, Sostaric JZ, Riesz P (2004) Sonodynamic therapy – a review of the synergistic effects of drugs and ultrasound. Ultrason Sonochem 11:349–363

Saksena TK, Nyborg WL (1970) Sonoluminescence from stable cavitation. J Chem Phys 53:1722–1733

Sazgarnia A, Shanei A, Meibodi NT, Eshghi H, Nassirli H (2011) A novel sonosensitizer for sonodynamic therapy: in vivo study on a colon tumor model. J Ultrasound Med 30:1321–1329

Sazgarnia A, Shanei A, Eshghi H, Hassanzadeh-Khayyat M, Esmaily H, Shanei MM (2013) Detection of sonoluminescence signals in a gel phantom in the presence of protoporphyrin IX conjugated to gold nanoparticles. Ultrasonics 53:29–35

Sciacovelli M, Gaude E, Hilvo M, Frezza C (2014) The metabolic alterations of cancer cells. Methods Enzymol 542:1–23

Shanei A, Sazgarnia A, Meibodi N, Hassanzadeh-Khayyat M, Esmaily H, Attaran Kakhki N (2012) Sonodynamic therapy using protoporphyrin IX conjugated to gold nanoparticles: an in vivo study on a colon tumor model. Iran J Basic Med Sci 15:759–767

Shi H, Liu Q, Qin X, Wang P, Wang X (2011) Pharmacokinetic study of a novel sonosensitizer chlorin-e6 and its sonodynamic anti-cancer activity in hepatoma-22 tumor-bearing mice. Biopharm Drug Dispos 32:319–332

Siemann DW (2011) The unique characteristics of tumour vasculature and preclinical evidence for its selective disruption of tumour-vascular disrupting agents. Cancer Treat Rev 37:63–74

Starkey JR, Rebane AK, Drobizhev MA, Meng F, Gong A, Elliot A, McInnerney K, Splangler CW (2008) New two-photon activated photodynamic therapy sensitizers induce xenograft tumor regressions after near-IR laser treatment though the body of the host mouse. Clin Cancer Res 14:6564–6573

Stepniewski M, Kepczynski M, Jamroz D, Nowakowska M, Rissanen S, Vattulainen I, Rog T (2012) Interaction of hematoporphyrin with lipid membranes. J Phys Chem B 116:4889–4897

Sugita N, Kawabata K, Sasaki K, Sakata I, Umemura S (2007) Synthesis of amphiphilic derivatives of rose bengal and their tumor accumulation. Bioconjug Chem 18:866–873

Sugita N, Iwase Y, Yumita N, Ikeda T, Umemura S (2010) Sonodynamically induced cell damage using rose bengal derivative. Anticancer Res 30:3361–3366

Suzuki N, Okada K, Chida S, Komori C, Shimada Y, Suzuki T (2007) Antitumor effect of acridine orange under ultrasonic irradiation in vitro. Anticancer Res 27:4179–4184

Tachibana K, Feril LB, Ikeda-Dantsuji Y (2008) Sonodynamic therapy. Ultrasonics 24:253–259

Tang W, Liu Q, Wang X, Mi N, Wang P, Zhang J (2008) Membrane fluidity altering and enzyme inactivating in sarcoma 180 cells post the exposure to sonoactivated hematoporphyrin in vitro. Ultrasonics 48:66–73

Tang W, Liu Q, Wang X, Wang P, Zhang J, Cao B (2009) Potential mechanism in sonodynamic therapy and focused ultrasound induced apoptosis in sarcoma 180 cells in vitro. Ultrasonics 49:86–793

Tonder M, Eisele G, Weiss T, Hofer Sm Seystahl K, Valavanis A, Stupp R, Weller M, Roth P (2014) Addition of lomustine for bevacizumab-refractory recurrent glioblastoma. Acta Oncol 26:1–4

Torchilin V (2001) Tumor delivery of macromolecular drugs based on the EPR effect. Adv Drug Deliv Rev 63:131–135

Tran Cao HS, Lopez N, Chang DC, Lowy A, Bouvet M, Baumgartner JM, Talamini MA, Sicklick JK (2014) Improved perioperative outcomes with minimally invasive distal pancreatectomy: results from a population-based study. JAMA Surg 149:237–243

Tserkovsky DA, Alexandrova EN, Chalau VN, Istomin YP (2012) Effects of combined sonodynamic and photodynamic therapies with photolon on a glioma C6 tumor model. Exp Oncol 34:332–335

Umemura S, Yumita N, Nishigaka R, Umemura K (1990) Mechanism of cell damage by ultrasound in combination with hematoporphyrin. Jpn J Cancer Res 81:962–966

Umemura S, Kawabata K, Nishigaki R, Umemura K (1992) Sonodynamic approach to tumor treatment. Proc IEEE Ultrason Symp 9:1231–1240

Umemura S, Yumita N, Umemura K, Nishigaki R (1999) Sonodynamically induced effect of rose bengal on isolated sarcoma 180 cells. Cancer Chemother Pharmacol 43:389–393

Wang X, Lewis TJ, Mitchell D (2008) The tumoricidal effect of sonodynamic therapy (SDT) on S-180 sarcoma in mice. Integr Cancer Ther 7:96–102

Wang X, Zhang W, Xu Z, Luo Y, Mitchell D, Moss RW (2009) Sonodynamic and photodynamic therapy in advanced breast carcinoma: a report of 3 cases. Integr Cancer Ther 8:283–287

Wang X, Liu Q, Wang Z, Wang P, Zhao P, Zhao X, Yang L, Li Y (2010) Role of autophagy in sonodynamic

therapy-induced cytotoxicity in S180 cells. Ultrasound Med Biol 36:1933–1946

Wrenn SP, Small E, Dan N (2013) Bubble nucleation in lipid bilayers: a mechanism for low frequency ultrasound disruption. Biochim Biophys Acta 1828:1192–1197

Xiang J, Xia X, Leung AW, Wang X, Xu J, Wang P, Yu H, Bai D, Xu C (2011) Apoptosis of ovarian cancer cells induced by methylene blue-mediated sonodynamic action. Ultrasonics 1:390–395

Xu ZY, Wang K, Li XQ, Chen S, Deng JM, Cheng Y, Wang ZG (2013) The ABCG2 transporter is a key molecular determinant of the efficacy of sonodynamic therapy with Photofrin in glioma stem-like cells. Ultrasonics 53:232–238

Yoshino SI, Fukushima T, Hayashi S, Nanola M, Ogawa K, Sasaki K, Umemura S (2009) Effects of focused ultrasound sonodynamic treatment on the rat blood-brain barrier. Anticancer Res 29:889–896

Yumita N, Umemura S (2004a) Sonodynamic antitumour effect of chloroaluminum phthalocyanine tetrasulfonate on murine solid tumor. J Pharm Pharmacol 56: 85–90

Yumita N, Umemura S (2004b) Ultrasonically induced cell damage and membrane lipid peroxidation by photofrin II: mechanism of sonodynamic activation. J Med Ultrason 31:35–40

Yumita N, Nishigaki R, Umemura K, Umemura S (1989) Hematoporphyrin as a sensitizer of cell-damaging effect of ultrasound. Jpn J Cancer Res 80:219–222

Yumita N, Nishigaki R, Umemura K, Umemura S (1990) Synergistic effect of ultrasound and hematoporphyrin on sarcoma 180. Jpn J Cancer Res 81: 304–308

Yumita N, Sasaki K, Umemura S, Nishigaki R (1996) Sonodynamically induced antitumor effect of a gallium-porphyrin complex, ATX-70. Jpn J Cancer Res 87:310–316

Yumita N, Okuyama N, Sasaki K, Umemura S (2007) Sonodynamic therapy on chemically induced mammary tumor: pharmacokinetics, tissue distribution and sonodynamically induced antitumor effect of gallium-porphyrin complex ATX-70. Cancer Chemother Pharmacol 60:891–897

Yumita N, Han QS, Kitazumi I, Umemura S (2008) Sonodynamically-induced apoptosis, necrosis, and active oxygen generation by mono-l-aspartyl chlorin e6. Cancer Sci 99:166–172

Yumita N, Iwase Y, Nishi K, Ikeda T, Umemura S, Sakata I, Momose Y (2010) Sonodynamically induced cell damage and membrane lipid peroxidation by novel porphyrin derivative, DCPH-P-Na (I). Anticancer Res 30:2241–2246

Zheng L, Sun X, Zhu X, Lv F, Zhong Z, Zhang F, Guo W, Cao W, Yang L, Tian Y (2014) Apoptosis of THP-1 derived macrophages induced by sonodynamic therapy using a new sonosensitizer hydroxyl acetylated curcumin. PLoS One 9, e93133

Zhu B, Liu Q, Want Y, Wang X, Wang P, Zhang L, Su S (2010) Comparison of accumulation, subcellular location and sonodynamic cytotoxicity between hematoporphyrin and protoporphyrin IX in L1210 cells. Chemotherapy 56:403–410

Index

© Springer International Publishing Switzerland 2016

J.-M. Escoffre, A. Bouakaz (eds.), *Therapeutic Ultrasound*, Advances in Experimental Medicine and Biology Vol. 880, DOI 10.1007/978-3-319-22536-4

T